frontiers | Research Topics

Potential biomarkers in neurovascular disorders

Edited by
Yuzhen Xu, Jinming Han, Wen-Jun Tu and John Zhang

Published in
Frontiers in Neurology

FRONTIERS EBOOK COPYRIGHT STATEMENT

The copyright in the text of individual articles in this ebook is the property of their respective authors or their respective institutions or funders. The copyright in graphics and images within each article may be subject to copyright of other parties. In both cases this is subject to a license granted to Frontiers.

The compilation of articles constituting this ebook is the property of Frontiers.

Each article within this ebook, and the ebook itself, are published under the most recent version of the Creative Commons CC-BY licence. The version current at the date of publication of this ebook is CC-BY 4.0. If the CC-BY licence is updated, the licence granted by Frontiers is automatically updated to the new version.

When exercising any right under the CC-BY licence, Frontiers must be attributed as the original publisher of the article or ebook, as applicable.

Authors have the responsibility of ensuring that any graphics or other materials which are the property of others may be included in the CC-BY licence, but this should be checked before relying on the CC-BY licence to reproduce those materials. Any copyright notices relating to those materials must be complied with.

Copyright and source acknowledgement notices may not be removed and must be displayed in any copy, derivative work or partial copy which includes the elements in question.

All copyright, and all rights therein, are protected by national and international copyright laws. The above represents a summary only. For further information please read Frontiers' Conditions for Website Use and Copyright Statement, and the applicable CC-BY licence.

ISSN 1664-8714
ISBN 978-2-8325-2240-0
DOI 10.3389/978-2-8325-2240-0

About Frontiers

Frontiers is more than just an open access publisher of scholarly articles: it is a pioneering approach to the world of academia, radically improving the way scholarly research is managed. The grand vision of Frontiers is a world where all people have an equal opportunity to seek, share and generate knowledge. Frontiers provides immediate and permanent online open access to all its publications, but this alone is not enough to realize our grand goals.

Frontiers journal series

The Frontiers journal series is a multi-tier and interdisciplinary set of open-access, online journals, promising a paradigm shift from the current review, selection and dissemination processes in academic publishing. All Frontiers journals are driven by researchers for researchers; therefore, they constitute a service to the scholarly community. At the same time, the *Frontiers journal series* operates on a revolutionary invention, the tiered publishing system, initially addressing specific communities of scholars, and gradually climbing up to broader public understanding, thus serving the interests of the lay society, too.

Dedication to quality

Each Frontiers article is a landmark of the highest quality, thanks to genuinely collaborative interactions between authors and review editors, who include some of the world's best academicians. Research must be certified by peers before entering a stream of knowledge that may eventually reach the public - and shape society; therefore, Frontiers only applies the most rigorous and unbiased reviews. Frontiers revolutionizes research publishing by freely delivering the most outstanding research, evaluated with no bias from both the academic and social point of view. By applying the most advanced information technologies, Frontiers is catapulting scholarly publishing into a new generation.

What are Frontiers Research Topics?

Frontiers Research Topics are very popular trademarks of the *Frontiers journals series*: they are collections of at least ten articles, all centered on a particular subject. With their unique mix of varied contributions from Original Research to Review Articles, Frontiers Research Topics unify the most influential researchers, the latest key findings and historical advances in a hot research area.

Find out more on how to host your own Frontiers Research Topic or contribute to one as an author by contacting the Frontiers editorial office: frontiersin.org/about/contact

Potential biomarkers in neurovascular disorders

Topic editors

Yuzhen Xu — Tongji University, China

Jinming Han — Capital Medical University, China

Wen-Jun Tu — Chinese Academy of Medical Sciences and Peking Union Medical College, China

John Zhang — Loma Linda University, United States

Citation

Xu, Y., Han, J., Tu, W.–J., Zhang, J., eds. (2023). *Potential biomarkers in neurovascular disorders*. Lausanne: Frontiers Media SA.

doi: 10.3389/978-2-8325-2240-0

Table of contents

08 Editorial: Potential biomarkers in neurovascular disorders
Yuzhen Xu, Jinming Han, Wen-Jun Tu and John Zhang

10 Serum Irisin as a Potential Biomarker for Cognitive Decline in Vascular Dementia
Feng Zhang, Guangshun Hou, Guangjian Hou, Congan Wang, Bin Shi and Yuekun Zheng

17 Hypertension With High Homocysteine Is Associated With Default Network Gray Matter Loss
Yanliang Kong, Xin Li, Lina Chang, Yuwei Liu, Lin Jia, Lei Gao and Lijuan Ren

25 Increased Systemic Immune-Inflammation Index Is Associated With Delayed Cerebral Ischemia in Aneurysmal Subarachnoid Hemorrhage Patients
Liuwei Chen, Sajan Pandey, Rui Shen, Yi Xu and Quanbin Zhang

33 Association Between *CST3* Gene Polymorphisms and Large-Artery Atherosclerotic Stroke
Yarong Ding, Zhe Xu, Yuesong Pan, Xia Meng, Xianglong Xiang, Hao Li, Liping Liu and Yongjun Wang on behalf of the CNSR-III Study Group

42 Clinical Features and Prognostic Factors of Acute Ischemic Stroke Related to Malignant Gastrointestinal Tumor
Yating Liu, Xin Li, Feixue Song, Xin Yan, Zhijian Han, Futian Tang and Yumin Li

50 Association Between Types of Posterior Staphyloma and Refractive Error After Cataract Surgery for High Myopia
Jing Wu, Ruochen Wang, Can Liu, Yu Zhou, Ziyuan Jiang and Fang Liu

58 Investigation of Altered Spontaneous Brain Activities in Patients With Moyamoya Disease Using Percent Amplitude of Fluctuation Method: A Resting-State Functional MRI Study
Chu-Qi Li, Qian-Min Ge, Hui-Ye Shu, Xu-Lin Liao, Yi-Cong Pan, Jie-Li Wu, Ting Su, Li-Juan Zhang, Rong-Bin Liang, Yi Shao and Er-Ming Zeng

70 Altered Expression of Specific MicroRNAs in Plasma of Aneurysmal Subarachnoid Hemorrhage Patients
Lina Zheng, Xin Zhang, Liping Liu and Yuehua Pu

79 Lipidomics Profiles Revealed Alterations in Patients With Meibomian Gland Dysfunction After Exposure to Intense Pulsed Light
Hui Zhao, Shi-Nan Wu, Yi Shao, Dong Xiao, Li-Ying Tang, Zhe Cheng and Jie Peng

92 Characterization of a Novel Monoclonal Antibody for Serine-129 Phosphorylated α-Synuclein: A Potential Application for Clinical and Basic Research
Weijin Liu, Qidi Zhang, Hao Xing, Ge Gao, Jia Liu, Yue Huang and Hui Yang

108 Gut Microbiota and Targeted Biomarkers Analysis in Patients With Cognitive Impairment
Shourong Lu, Ying Yang, Qiao Xu, Shuqiang Wang, Jie Yu, Bingshan Zhang, Zhuo Wang, Yunyun Zhang, Wenwei Lu and Kan Hong

117 Brain Activity Changes in Slow 5 and Slow 4 Frequencies in Patients With Optic Neuritis: A Resting State Functional MRI Study
Kai Yan, Wen-Qing Shi, Ting Su, Xu-Lin Liao, Shi-Nan Wu, Qiu-Yu Li, Jing Yu, Hui-Ye Shu, Li-Juan Zhang, Yi-Cong Pan and Yi Shao

126 Correlation Between Blood Glucose Variability and Early Therapeutic Effects After Intravenous Thrombolysis With Alteplase and Levels of Serum Inflammatory Factors in Patients With Acute Ischemic Stroke
Yun Cai, Hongtao Zhang, Qiang Li and Peilan Zhang

133 Optical Coherence Tomography Angiography Biomarkers of Retinal Thickness and Microvascular Alterations in Sjogren's Syndrome
Ren Liu, Yan Wang, Qiuyu Li, Qiang Xia, Tian Xu, Ting Han, Shuang Cai, Shuilin Luo, Rui Wu and Yi Shao

145 *Eucommia ulmoides Oliver-Tribulus terrestris* L. Drug Pair Regulates Ferroptosis by Mediating the Neurovascular-Related Ligand-Receptor Interaction Pathway- A Potential Drug Pair for Treatment Hypertension and Prevention Ischemic Stroke
Qian Zhang, Jie Yang, Chuanhua Yang, Xuesong Yang and Yongzhi Chen

162 Serum Neuroglobin as a Potential Prognostic Biomarker for Cognitive Impairment After Intracerebral Hemorrhage
Yu Gao, Bo Wang, Ye Miao and Yu Han

168 Advances in the Role of Endothelial Cells in Cerebral Small Vessel Disease
Tao Bai, Shijia Yu and Juan Feng

181 hsa-miR-518-5p/hsa-miR-3135b Regulates the REL/SOD2 Pathway in Ischemic Cerebral Infarction
Boyan Zhao and Xiaofan Jiang

194 Association of Blood Pressure Within 6 h After Endovascular Thrombectomy and Functional Outcomes in Ischemic Stroke Patients With Successful Recanalization
Xuening Zhang, Ting Cui, Qiange Zhu, Changyi Wang, Anmo Wang, Yuan Yang, Shucheng Li, Fayun Hu and Bo Wu

203 Caveolin-1 Promoted Collateral Vessel Formation in Patients With Moyamoya Disease
Jinbing Zhao, Zhiqiang Yu, Yanping Zhang, Cheng Qiu, Guangxu Zhang, Lijiu Chen, Shengxue He and Jun Ma

214 MicroRNA-Based Diagnosis and Therapeutics for Vascular Cognitive Impairment and Dementia
Weijie Zhai, Meng Zhao, Guimei Zhang, Zicheng Wang, Chunxiao Wei and Li Sun

225 Expression and Potential Biomarkers of Regulators for M7G RNA Modification in Gliomas
Zhen Chen, Zhe Zhang, Wei Ding, Jie-hui Zhang, Zi-long Tan, Yu-ran Mei, Wei He and Xiao-jing Wang

239 Intracranial Aneurysms Induced by *RUNX1* Through Regulation of *NFKB1* in Patients With Hypertension-An Integrated Analysis Based on Multiple Datasets and Algorithms
Yang Li, Zhen Zhang and Donghua Liu

252 Brain Activity in Different Brain Areas of Patients With Dry Eye During the Female Climacteric Period According to Voxel-Based Morphometry
Meng-Yan Hu, Li-Juan Zhang, Min Kang, Yi-Cong Pan, Qian-min Ge, Qiu-yu Li, Lin Yang, Chong-Gang Pei and Yi Shao

260 miR-17-5p/*HOXA7* Is a Potential Driver for Brain Metastasis of Lung Adenocarcinoma Related to Ferroptosis Revealed by Bioinformatic Analysis
Quanfang Chen, Qingyun Pan, Han Gao, Yingju Wang and Xiaoning Zhong

273 15-Hydroxyprostaglandin Dehydrogenase Is a Predictor of Stroke-Associated Pneumonia
Yunfei Xu, Haoduo Qiao, Shun Yang, Lin Zhou, Yao Zhao, Qing Xu, Shuying Miao, Dun Yuan, Jie Zhao and Ying Liu

280 Decreased Macular Retinal Thickness in Patients With Pterygium
Feng Wang, Li Qi Liu, Rong Bin Liang, Li Juan Zhang, Hui Ye Shu, Xu Lin Liao, Yi Cong Pan, Jie Li Wu, Ting Su and Yi Shao

289 Clinical Features and Influencing Factors for the Prognosis of Patients With Sudden Deafness
Wei Lin, Gaoyun Xiong, Kailei Yan, Wumin Yu, Xiaoxing Xie, Ze Xiang, Jian Wu, Yanping Ge and Ying Wang

295 Hypoxia- and Inflammation-Related Transcription Factor SP3 May Be Involved in Platelet Activation and Inflammation in Intracranial Hemorrhage
Ding Wan, Jin Feng, Peng Wang, Zhenxing Yang and Tao Sun

308 MicroRNAs Promote the Progression of Sepsis-Induced Cardiomyopathy and Neurovascular Dysfunction Through Upregulation of NF-kappaB Signaling Pathway-Associated HDAC7/ACTN4
Qiancheng Luo, Hanning Ma, Enwei Guo, Lin Yu, Ling Jia, Bingyu Zhang, Gang Feng and Rui Liu

322 Detection of Vascular Notch3 Deposits in Unfixed Frozen Skin Biopsy Sample in CADASIL
Akihiko Ueda, Makoto Nakajima, Yohei Misumi, Keiichi Nakahara, Satoru Shinriki, Masayoshi Tasaki, Hirotaka Matsui and Mitsuharu Ueda

331 Neuroimaging Markers of Chronic Eye Diseases and Their Application Values
Chen-Yu Yu, Rong Huang, Shi-Qi Li and Yi Shao

337 Admission Serum Calcium Level and Short-Term Mortality After Acute Ischemic Stroke: A Secondary Analysis Based on a Norwegian Retrospective Cohort
Yuzhao Lu, Xin Ma, Kiarash Tazmini, Ming Yang, Xiaobing Zhou and Yang Wang

348 Role of Ultrasound Imaging in the Prediction of *TRIM67* in Brain Metastases From Breast Cancer
Zhidong Xuan, Ting Ma, Yue Qin and Yajie Guo

362 Associations of Abdominal Visceral Fat Content and Plasma Adiponectin Level With Intracranial Atherosclerotic Stenosis: A Cross-Sectional Study
Fei-Hong Wang, Long-Yan Meng, Tong-Ya Yu, Yan Tan, Hui Quan, Jia-Yu Hu, Qing-Ke Bai, Jun-Chao Xie and Yan-Xin Zhao

371 Altered Intrinsic Brain Activity in Patients With Toothache Using the Percent Amplitude of a Fluctuation Method: A Resting-State fMRI Study
Jun Yang, Yi Shao, Yan-Kun Shen, Hong-Shui Zhu, Bin Li, Qiu-Yue Yu, Min Kang, San-Hua Xu, Ping Ying, Qian Ling, Jie Zou, Hong Wei and Yu-Lin He

383 Application and Research Progress of High Frequency Ultrasound in the Diagnosis of Chronic Inflammatory Neuropathies
Xishun Ma, Lizhen Du, Wenqing Yuan and Tongliang Han

390 Early Changes in the White Matter Microstructure and Connectome Underlie Cognitive Deficit and Depression Symptoms After Mild Traumatic Brain Injury
Wenjing Huang, Wanjun Hu, Pengfei Zhang, Jun Wang, Yanli Jiang, Laiyang Ma, Yu Zheng and Jing Zhang

401 TGFβ1 as a Predictive Biomarker for Collateral Formation Within Ischemic Moyamoya Disease
Yuanbing Chen, Miao Tang, Hui Li, Hongwei Liu, Junyu Wang and Jun Huang

411 Association of Serum Interleukin-8 and Serum Amyloid A With Anxiety Symptoms in Patients With Cerebral Small Vessel Disease
Li-Li Shan, Yi-Lin Wang, Tian-Ci Qiao, Yue-Feng Bian, Ya-Jing Huo, Cen Guo, Qian-Yun Liu, Zi-Dong Yang, Ze-Zhi Li, Ming-Yuan Liu and Yan Han

419 Cervical Cancer Imaging Features Associated With *ADRB1* as a Risk Factor for Cerebral Neurovascular Metastases
Xingju Zheng, Shilin Xu and JiaYing Wu

433 Detection of Abnormal Spontaneous Brain Activity Patterns in Patients With Orbital Fractures Using Fractional Amplitude of Low Frequency Fluctuation
Min Kang, YuXuan Gao, LiJuan Zhang, RongBin Liang, QiuYu Li, HuiYe Shu, YiCong Pan, Ping Ying, SanHua Xu and Shao Yi

442 Absence of Susceptibility Vessel Sign in Patients With Malignancy-Related Acute Ischemic Stroke Treated With Mechanical Thrombectomy
Morin Beyeler, Nebiyat F. Belachew, Moritz Kielkopf, Enrique B. Aleman, Alejandro Xavier León Betancourt, Kotryna Genceviciute, Christoph Kurmann, Lorenz Grunder, Barbara Birner, Thomas R. Meinel, Adrian Scutelnic, Philipp Bücke, David J. Seiffge, Tomas Dobrocky, Eike I. Piechowiak, Sara Pilgram-Pastor, Heinrich P. Mattle, Pasquale Mordasini, Marcel Arnold, Urs Fischer, Thomas Pabst, Jan Gralla, Martin D. Berger, Simon Jung and Johannes Kaesmacher

450 The endogenous neuropeptide calcitonin gene-related peptide after spontaneous subarachnoid hemorrhage–A potential psychoactive prognostic serum biomarker of pain-associated neuropsychological symptoms
Elisabeth Bründl, Martin Proescholdt, Eva-Maria Störr, Petra Schödel, Sylvia Bele, Florian Zeman, Christoph Hohenberger, Martin Kieninger, Nils Ole Schmidt and Karl-Michael Schebesch

465 Machine learning for infection risk prediction in postoperative patients with non-mechanical ventilation and intravenous neurotargeted drugs
Yi Du, Haipeng Shi, Xiaojing Yang and Weidong Wu

477 Consensus clustering of gene expression profiles in peripheral blood of acute ischemic stroke patients
Zhiyong Yang, Guanghui Wang, Nan Luo, Chi Kwan Tsang and Li'an Huang

496 Non-HDL-C/HDL-C ratio is associated with carotid plaque stability in general population: A cross-sectional study
Anran Wang, Yapeng Li, Lue Zhou, Kai Liu, Shaohua Li, Ce Zong, Bo Song, Yuan Gao, Yusheng Li, Chuansheng Tian, Yurong Xing, Yuming Xu and Longde Wang

505 Association between serum transthyretin and intracranial atherosclerosis in patients with acute ischemic stroke
Jinfeng He, Jiamin Zhu, Wenyuan Zhang, Zhenxiang Zhan, Fangwang Fu and Qiongqiong Bao

514 Clinical study on the feasibility of new thrombus markers in predicting massive cerebral infarction
Xiaoxia Zhao, Siyu Yang, Ruining Lei, Qiaoyan Duan, Jundong Li, Jiangtao Meng and Lei Sun

frontiers | Frontiers in Neurology

TYPE Editorial
PUBLISHED 11 April 2023
DOI 10.3389/fneur.2023.1186852

Check for updates

OPEN ACCESS

EDITED AND REVIEWED BY
Anastasia Bougea,
National and Kapodistrian University of Athens, Greece

*CORRESPONDENCE
Yuzhen Xu
✉ tianyayizhe@126.com

SPECIALTY SECTION
This article was submitted to Neurological Biomarkers, a section of the journal Frontiers in Neurology

RECEIVED 15 March 2023
ACCEPTED 21 March 2023
PUBLISHED 11 April 2023

CITATION
Xu Y, Han J, Tu W-J and Zhang J (2023) Editorial: Potential biomarkers in neurovascular disorders. *Front. Neurol.* 14:1186852. doi: 10.3389/fneur.2023.1186852

COPYRIGHT
© 2023 Xu, Han, Tu and Zhang. This is an open-access article distributed under the terms of the Creative Commons Attribution License (CC BY). The use, distribution or reproduction in other forums is permitted, provided the original author(s) and the copyright owner(s) are credited and that the original publication in this journal is cited, in accordance with accepted academic practice. No use, distribution or reproduction is permitted which does not comply with these terms.

Editorial: Potential biomarkers in neurovascular disorders

Yuzhen Xu[1]*, Jinming Han[2], Wen-Jun Tu[3] and John Zhang[4]

[1]The Second Affiliated Hospital of Shandong First Medical University, Taian, Shandong, China, [2]Department of Neurology, Xuanwu Hospital, Capital Medical University, Beijing, China, [3]Peking Union Medical College, Chinese Academy of Medical Sciences, Beijing, China, [4]Department of Physiology and Pharmacology, Loma Linda University, Loma Linda, CA, United States

KEYWORDS

neurovascular, biomarkers, peripheral blood, cerebrospinal fluid, mechanisms

Editorial on the Research Topic
Potential biomarkers in neurovascular disorders

Neurovascular disorders are a leading cause of disability and death in adults by affecting the arteriovenous system and blood supply. Neurological disorders accounted for 92 million disability-adjusted life-years (DALYs) in 2005 and are projected to reach 103 million worldwide by 2030 (1), serving as the leading cause of DALYs and the second leading cause of death. The annual economic burden due to neurovascular disorders is USD 765 billion in the United States and EUR 788 billion in Europe (2, 3). In view of the huge economic burden and high morbidity of neurovascular disorders, the identification of potential early biomarkers is crucial.

Ischemic stroke is the most common neurovascular disorder. He et al. found that the decreased serum transthyretin level in patients with acute ischemic stroke may serve as one major cause of intracranial atherosclerosis. Wang F.-H. et al. indicated that the decreased plasma adiponectin levels and increased visceral adipose tissue (VAT) to subcutaneous adipose tissue (SAT) ratio may be involved in intracranial atherosclerotic stenosis. Based on the report from Ding et al., Cystatin C, encoded by CST3, is a potential biomarker of atherosclerosis, with its rs13038305 and rs911119 polymorphisms independently affecting large artery atherosclerotic stroke. Furthermore, Wang A. et al. showed that the stability of atherosclerotic plaque can be affected by the non-high-density lipoprotein cholesterol (non-HDL-C)/high-density of lipoprotein cholesterol (HDL-C) ratio. The higher the ratio, the less stable the atherosclerotic plaque appears to be. The understanding of blood glucose management with intravenous thrombolysis and blood pressure management after endovascular thrombectomy (EVT) in patients with acute cerebral infarction has also been expanded by new research. Cai et al. found that patients with stroke who treated with intravenous thrombolysis can aggravate the prognosis through inflammatory response and increased blood glucose fluctuation. Zhang Q. et al. found that early blood pressure management after EVT may be important for the functional outcome of acute cerebral infarction patients with a successful recanalization.

Subarachnoid hemorrhage (SAH) is a type of hemorrhagic stroke with a high mortality and disability, accounting for 5–10% of stroke. High levels of systemic immune-inflammation index (SII) predict delayed cerebral ischemia (DCI) after SAH (Chen et al.). In addition, significantly downregulated specific plasma miRNAs, including miR-23b-3p, miR-590-5p, miR-20b-5p, miR-142-3p and miR-29b-3p, may play a role in the regulation of SAH progression (Zheng et al.).

It is estimated that there are ∼50 million people living with dementia today, and this number will grow to 152 million by 2050 (4). Vascular dementia (VD) is the second largest type of dementia after Alzheimer's disease. Specifically, the new myosin hormone irisin is considered to be associated with VD and reduced serum irisin levels can predict cognitive impairment in VD patients (Zhang F. et al.). The prevalence of post-stroke cognitive impairment (PSCI) ranges from 20 to 80% (5). Gao et al. found that neuroglobin is associated with cognitive impairment after intracranial hemorrhage and low levels of neuroglobin may be used as a biomarker of cognitive impairment after intracranial hemorrhage. Recent studies regarding the involvement of gut microbiota and cognitive function have gradually emerged. Lu et al. analyzed the differences in intestinal flora between cognitive impairment group and control group, providing novel insights for subsequent research.

Moyamoya disease is a disorder characterized by narrowing and blockage of arteries in the brain, which eventually leads to ischemic stroke, hemorrhagic stroke or/and seizures. The percent amplitude of fluctuation (PerAF) can be used as an effective indicator of ocular complications and emotional complications in patients with Moyamoya disease (Li et al.). Angiogenesis and reconstruction are widely used treatments for Moyamoya disease. Caveolin-1 (Cav-1) may serve as a biomarker driving angiogenesis and collateral formation in patients with Moyamoya disease after the bypass surgery (Zhao et al.). In addition, Chen et al. showed that the TGFβ1/VEGF pathway may be a key mechanism involved in vascular remodeling in patients with Moyamoya disease.

Optic nerve and vascular lesions are important parts of neurovascular disorders in the central nervous system. Using fMRI to scan patients with optic neuritis and orbital fractures in the resting state, it was found that the amplitude of low-frequency fluctuations (ALFF) can predict abnormal functional activities at different frequencies and brain regions (Yan et al.; Kang et al.). Hu et al. used voxel-based morphometry (VBM) to analyze imaging data to investigate potential morphological changes in the brains of female patients with menopausal dry eye (DE), and analyzed the relationship between VBM and behavioral performance, suggesting that DE patients have brain changes during menopause. Abnormal spontaneous activity of the region may be the underlying pathological mechanism causing the disease. Interestingly, retinal thickness is considered as a potential biomarker for both Sjogren's syndrome (Liu et al.) and Pterygium (Wang F. et al.).

Author contributions

YX and JH drafted the manuscript. All authors contributed to the article and approved the submitted version.

Funding

The present study was funded by the Shandong Medical and Health Technology Development Fund (202103070325), the Shandong Province Traditional Chinese Medicine Science and Technology Project (M-2022216), the Natural Science Foundation of Shandong Province (ZR2022MH124), and the Nursery Project of the Shandong First Medical University Youth Science Fund Cultivation Funding Program (202201-105).

Acknowledgments

We would like to thank all the authors who participated in the subject collection and all the reviewers who were involved in the review process, and we are very grateful to all the editors who assisted us in processing the manuscripts.

Conflict of interest

The authors declare that the research was conducted in the absence of any commercial or financial relationships that could be construed as a potential conflict of interest.

Publisher's note

All claims expressed in this article are solely those of the authors and do not necessarily represent those of their affiliated organizations, or those of the publisher, the editors and the reviewers. Any product that may be evaluated in this article, or claim that may be made by its manufacturer, is not guaranteed or endorsed by the publisher.

References

1. Kaddumukasa M, Mugenyi L, Kaddumukasa MN, Ddumba E, Devereaux M, Furlan A, et al. Prevalence and incidence of neurological disorders among adult Ugandans in rural and urban Mukono district, a cross-sectional study. *BMC Neurol.* (2016) 16:227. doi: 10.1186/s12883-016-0732-y

2. Feigin VL, Vos T, Alahdab F, Amit AML, Bärnighausen TW, Beghi E, et al. Burden of Neurological Disorders Across the US From 1990-2017: A Global Burden of Disease Study. *JAMA Neurol.* (2021) 78:165–76. doi: 10.1001/jamaneurol.2020.4152

3. Deuschl G, Beghi E, Fazekas F, Varga T, Christoforidi KA, Sipido E, et al. The burden of neurological diseases in Europe: an analysis for the Global Burden of Disease Study 2017. *Lancet Public Health.* (2020) 5:e551–67. doi: 10.1016/S2468-2667(20)30190-0

4. Wang Q, Xu Y, Qi C, Liu A, Zhao Y. Association study of serum soluble TREM2 with vascular dementia in Chinese Han population. *Int J Neurosci.* (2020) 130:708–12. doi: 10.1080/00207454.2019.1702548

5. Wang Q, Wang K, Ma Y, Li S, Xu Y. Serum galectin-3 as a potential predictive biomarker is associated with poststroke cognitive impairment. *Oxid Med Cell Longev.* (2021) 2021:5827812. doi: 10.1155/2021/5827812

frontiers in Neurology

ORIGINAL RESEARCH
published: 13 September 2021
doi: 10.3389/fneur.2021.755046

Serum Irisin as a Potential Biomarker for Cognitive Decline in Vascular Dementia

Feng Zhang[1], *Guangshun Hou*[2], *Guangjian Hou*[1], *Congan Wang*[1], *Bin Shi*[1] *and Yuekun Zheng*[1]*

[1] Neck-Shoulder and Lumbocrural Pain Hospital of Shandong First Medical University, Shandong First Medical University and Shandong Academy of Medical Sciences, Jinan, China, [2] Qilu Children's Hospital of Shandong University, Shandong University, Jinan, China

Background: Irisin, a new exercise-related myokine, has been shown to be associated with a variety of diseases including serious neurological disorders. However, whether irisin is involved in the pathogenesis of vascular dementia (VD) has not yet been reported. Our aim is to determine the serum irisin level in patients with VD and investigate its relationship with cognitive function.

Methods: The subjects of the study were VD patients and controls with normal cognitive function who were hospitalized in the Neck-Shoulder and Lumbocrural Pain Hospital of Shandong First Medical University from July 2018 to June 2020. Upon admission, a cognitive function assessment was performed. Enzyme-linked immunosorbent assay (ELISA) was used to determine the concentration of irisin in serum.

Results: During the study period, 187 subjects (82 controls and 105 VD patients) were included in the analysis. The serum irisin level of VD patients was significantly lower than that of the control group ($p < 0.001$). Spearman analysis showed that irisin was positively correlated with HLD-C and MoCA, and negatively correlated with all clinical characteristics except for HCY. Logistic regression analysis showed that after adjusting for all clinical characteristics, the serum irisin of VD patients still had a significant correlation with MoCA ($\beta = 0.304$, $p = 0.029$). According to receiver operating characteristic (ROC) curve analysis, the diagnostic accuracy for serum irisin levels on VD was 76% with the sensitivity and 71% with specificity respectively.

Conclusions: These data indicate that a decrease in serum irisin levels is a powerful biological marker for cognitive decline in patients with VD, even after adjustment for risk factors. Further multi-center studies need to confirm this connection, which may pave the way for new treatment options.

Keywords: irisin, biomarker, vascular dementia, cognitive, ELISA

OPEN ACCESS

Edited by:
Yuzhen Xu,
Tongji University, China

Reviewed by:
Yihong Ma,
Kumamoto University, Japan
Zhenpeng Song,
University of Calgary, Canada

***Correspondence:**
Yuekun Zheng
zhengyuekun888@163.com

Specialty section:
This article was submitted to Neurological Biomarkers, a section of the journal Frontiers in Neurology

Received: *07 August 2021*
Accepted: *23 August 2021*
Published: *13 September 2021*

Citation:
Zhang F, Hou G, Hou G, Wang C, Shi B and Zheng Y (2021) Serum Irisin as a Potential Biomarker for Cognitive Decline in Vascular Dementia. Front. Neurol. 12:755046. doi: 10.3389/fneur.2021.755046

INTRODUCTION

Vascular dementia (VD) is generally considered to be the second largest subtype of dementia (1, 2). It accounts for about 15–20% of dementia cases in Europe and America, and it is even higher in developing countries, especially in Asia, at about 30% (3). The incidence of VD increases sharply with age, and its prevalence in countries around the world is increasing with the advent of an aging society (4). According to reports, there are currently ∼35.6 million people suffering from dementia in the world, and the number of patients will increase by two times and three times by 2030 and 2050, respectively (5, 6). Unfortunately, similar to Alzheimer's disease (AD), the pathogenic mechanism of VD has not yet been fully identified and understood (7). Therefore, identifying the potential pathogenic biomarkers of VD and adopting targeted interventions are public health problems to be solved urgently.

Irisin, first described by Böstrom et al. in 2012, is a small polypeptide with 123 amino acids released into the blood from the membrane protein fibronectin type III domain-containing protein 5 (FNDC5), which is cleaved at the carboxy terminus by protease in skeletal muscle (8). FNDC5 is a well-defined myokine, which is also considered to be an adipokine. FNDC5/irisin axis was activated by exercise and is relatively conserved in evolution across a number of species (9). Although the research on irisin has received extensive attention in the past few years, the cleavage mechanisms of FNDC5 protein and the regulation pathways of irisin are still unclear (10).

Initial studies have shown that the expression of irisin is related to obesity, type 2 diabetes, and metabolic syndrome (11). More studies have shown that irisin is closely related to the prognosis of stroke and affective disorder after stroke (12, 13). However, whether irisin plays a role in the pathogenesis of VD is unclear. Therefore, in this study, we studied the correlation between irisin concentration and cognitive function in VD.

METHODS

Study Population

The study population were VD patients and controls with normal cognitive function who were hospitalized in the Neck-Shoulder and Lumbocrural Pain Hospital of Shandong First Medical University from July 2018 to June 2020 (**Figure 1**). VD was defined according to the International Statistical Classification of Diseases and Related Health Problems 11 (ICD-11) (14) and the Diagnostic and Statistical Manual of Mental Disorders 5th edition (DSM-5) (15). The exclusion criteria are as follows: (1) previous diagnosis of other types of dementia; (2) various malignant tumors; (3) metabolic syndrome other than diabetes; (4) mental dysfunction or taking antipsychotic drugs; (5) severe heart, liver and kidney dysfunction; (6) recent history of trauma, stroke, or surgery. All research subjects signed an informed consent form. The age, gender, Body Mass Index (BMI) and blood pressure information of all subjects were collected at the time of enrollment. This study complies with the principles of the Declaration of Helsinki and was approved by the Ethics Committee of Neck-Shoulder and Lumbocrural Pain Hospital of Shandong First Medical University.

Cognitive Scale Assessment

The Montreal Cognitive Assessment (MoCA) is a simple cognitive screening tool, which is widely used in many countries around the world with good psychometric characteristics and excellent sensitivity. MoCA is a 30-point screening tool that takes about 10 min to evaluate attention, orientation, language, memory, visual space, and executive function. The recommended normal range of MoCA is 26–30 points (16, 17). The MoCA scale is evaluated by experienced neurologists, who are blind to the grouping of study subjects and serum biomarkers.

Blood Collection and Laboratory Test

All blood samples were collected within 24 h of admission in a fasting state and rested for at least 10 min. The blood sample was centrifuged at 1,200 g for 20 min, and the separated serum was aliquoted and stored at −80°C for later use (18, 19). Standard laboratory methods are used for biochemical determination including total cholesterol, triglycerides, high density lipoprotein cholesterol, low density lipoprotein cholesterol, fasting plasma glucose and homocysteine. A commercial enzyme stained immunosorbent assay (ELISA) kit (Aviscera Bioscience, Santa Clara, CA, USA) was used to determine the concentration of irisin in the serum of VD patients. The specific operation was carried out in accordance with the instructions.

Statistical Analysis

The results of categorical variables are represented by n or percentages, and the results of continuous variables are represented by mean ± standard deviation (SD). Categorical variables are compared by chi-square test, while continuous variables are analyzed by student's *t*-test. Spearman rank correlation was used for bivariate correlation. The relationship between serum irisin concentration and clinical characteristics was evaluated by logistic stepwise regression analysis. Sensitivity and specificity of measured variable for VD diagnosis were determined by receiver operating characteristic (ROC). All statistical analyses were performed using SPSS for Windows, version 23.0 (SPSS Inc., Chicago, IL, USA). Statistical significance is defined as two-tailed $P < 0.05$.

RESULTS

Baseline Clinical Characteristics of Subjects

A total of 82 normal cognitive function controls and 105 VD patients were enrolled in this study. The baseline clinical characteristics of all subjects are shown in **Table 1**. There was no significant difference in baseline data such as age, gender, BMI, SBP, DBP, TC, TG, LDL-C, HDL-C, FBG and HCY between the two groups ($p > 0.05$). The serum irisin concentrations of the control group and the VD group were (127.80 ± 11.15) and (79.37 ± 8.74) ng/ml, respectively, and there are significant differences between the two groups ($p < 0.001$).

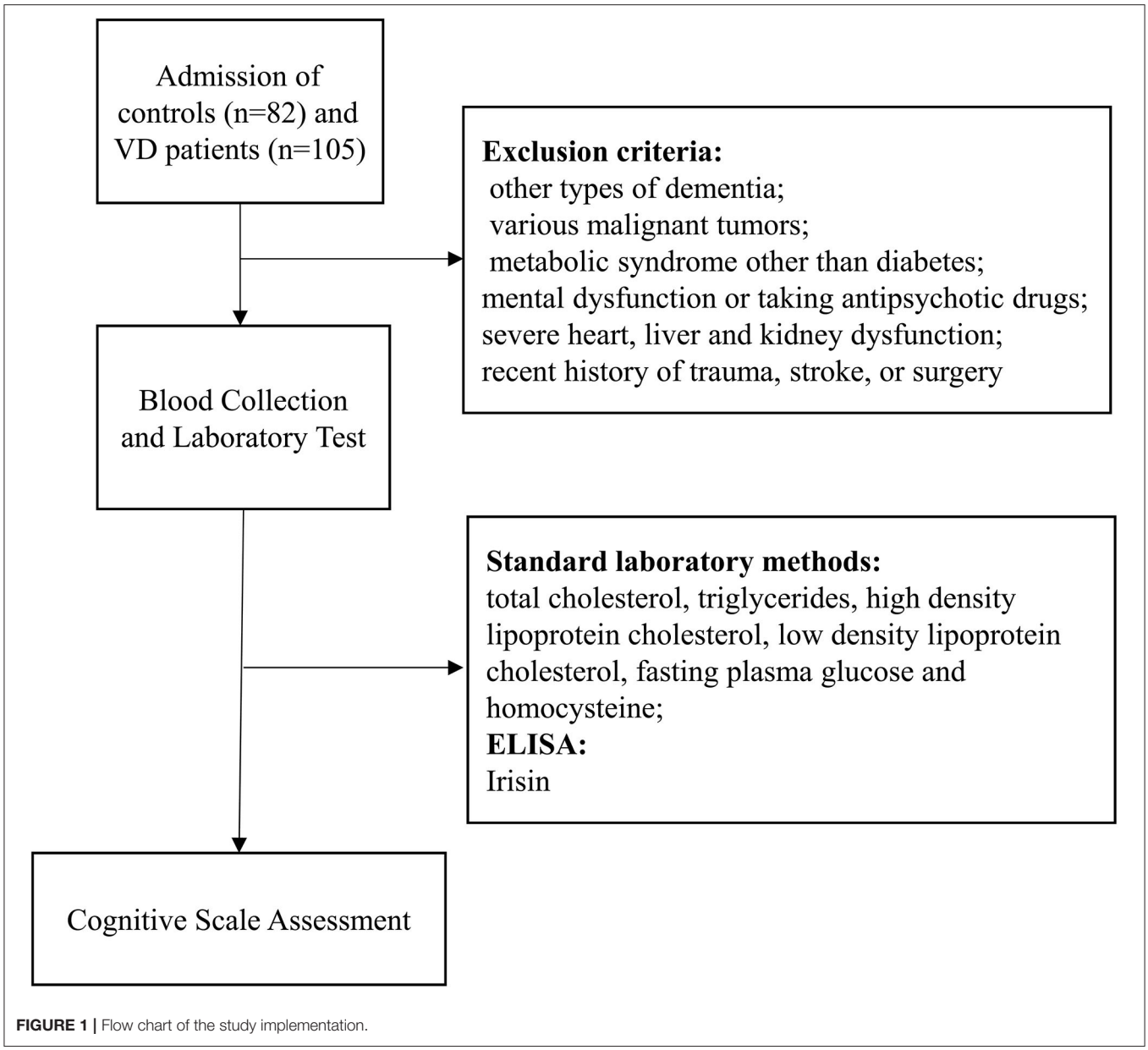

FIGURE 1 | Flow chart of the study implementation.

Spearman's Correlation Test

In the Spearman rank correlation test, the serum irisin of VD patients was significantly negatively correlated with age ($r = -0.231$, $p < 0.001$), gender ($r = -0.174$, $p = 0.005$), BMI ($r = -0.159$, $p < 0.001$), SBP ($r = -0.254$, $p < 0.001$), DBP ($r = -0.217$, $p < 0.001$), TC ($r = -0.322$, $p = 0.013$), TG ($r = -0.283$, $p < 0.001$), LDL-C ($r = -0.195$, $p < 0.001$) and FBG ($r = -0.170$. $p < 0.001$), and positively correlated with HDL-C ($r = 0.272$, $p < 0.001$) and MoCA scores ($r = 0.316$, $p < 0.001$). There was no significant correlation between serum irisin and HCY in patients with VD ($r = -0.308$, $p = 0.094$). The results of the Spearman rank correlation test are shown in **Table 2**.

Logistic Regression Analysis

The logistic regression analysis results are shown in **Table 3**. After controlling for age, gender and BMI in Model 1, there is a significant correlation between the serum irisin concentration of VD patients and the MoCA score ($\beta = 0.385$, $p < 0.001$). After further controlling of SBP, DBP, TC, TG, LDL-C, HDL-C and FBG in Model 2, the serum irisin concentration of VD patients still has a significant correlation with the MoCA score ($\beta = 0.336$, $p = 0.008$). HCY is considered to be an important factor affecting cognitive function, we pulled it into Model 3. Finally, after controlling of all baseline clinical characteristics in Model 3, the correlation between serum irisin concentration and MoCA score in VD patients is still significant ($\beta = 0.304$, $p = 0.029$).

TABLE 1 | Baseline clinical characteristics of all subjects.

	Controls ($n = 82$)	VD ($n = 105$)	*P*-values
Age (years)	61.6 ± 6.2	62.0 ± 7.4	0.695
Male (*n*)	43	60	0.524
BMI (Kg/m^2)	24.2 ± 1.7	24.1 ± 1.9	0.709
SBP (mmHg)	136.3 ± 8.0	136.9 ± 7.8	0.606
DBP (mmHg)	80.5 ± 4.6	81.4 ± 5.1	0.213
TC (mmol/L)	4.71 ± 0.73	4.73 ± 0.67	0.846
TG (mmol/L)	1.57 ± 0.26	1.59 ± 0.30	0.632
LDL-C (mmol/L)	2.45 ± 0.34	2.51 ± 0.35	0.240
HLD-C (mmol/L)	1.17 ± 0.21	1.14 ± 0.22	0.346
HCY (mmol/L)	12.3 ± 1.2	12.6 ± 1.6	0.159
FBG (mmol/L)	6.27 ± 0.79	6.19 ± 0.83	0.505
Irisin (ng/ml)	127.80 ± 11.15	79.37 ± 8.74	<0.001
MoCA scores (points)	27.9 ± 1.1	22.3 ± 1.6	<0.001

VD, vascular dementia; BMI, Body Mass Index; SBP, systolic blood pressure; DBP, diastolic blood pressure; TC, total cholesterol; TG, triglycerides; HDL-C, high density lipoprotein cholesterol; LDL-C, low density lipoprotein cholesterol; FBG, fasting plasma glucose; HCY, homocysteine; homocysteine.

TABLE 2 | Clinical correlations between irisin and various characteristics in VD.

	Spearman's correlation coefficient	*P*
Age (years)	−0.231	<0.001
Gender	−0.174	0.005
BMI (Kg/m^2)	−0.159	<0.001
SBP (mmHg)	−0.254	<0.001
DBP (mmHg)	−0.217	<0.001
TC (mmol/L)	−0.322	0.013
TG (mmol/L)	−0.283	<0.001
LDL-C (mmol/L)	−0.195	<0.001
HLD-C (mmol/L)	0.272	<0.001
HCY (mmol/L)	−0.308	0.094
FBG (mmol/L)	−0.170	<0.001
MoCA scores (points)	0.316	<0.001

VD, vascular dementia; BMI, Body Mass Index; SBP, systolic blood pressure; DBP, diastolic blood pressure; TC, total cholesterol; TG, triglycerides; HDL-C, high density lipoprotein cholesterol; LDL-C, low density lipoprotein cholesterol; FBG, fasting plasma glucose; HCY, homocysteine; homocysteine.

TABLE 3 | Association between irisin and MoCA scores in VD.

	Regression coefficient	*P*
Model 1	0.385	<0.001
Model 2	0.336	0.008
Model 3	0.304	0.029

Model 1: adjusted for age, gender and BMI; Model 2: further adjusted for SBP, DBP, TC, TG, LDL-C, HDL-C and FBG; Model 3: further adjusted for HCY. VD, vascular dementia; BMI, Body Mass Index; SBP, systolic blood pressure; DBP, diastolic blood pressure; TC, total cholesterol; TG, triglycerides; HDL-C, high density lipoprotein cholesterol; LDL-C, low density lipoprotein cholesterol; FBG, fasting plasma glucose; HCY, homocysteine; homocysteine.

ROC Curve Analysis

To evaluate the diagnostic value of serum irisin levels as a potential marker for VD, ROC curve analysis was performed (**Figure 2**). The area under the curve (AUC) was 0.846. The diagnostic accuracy for serum irisin levels on VD was 76% with the sensitivity and 71% with specificity, respectively.

DISCUSSION

This is the first time to study the relationship between cognitive decline and serum irisin concentration in VD patients. Our results show that the serum irisin concentration of VD patients is significantly lower than that of controls with normal cognitive function, and there is a significant positive correlation with the MoCA score. This relationship still exists after adjusting the clinical baseline data, suggesting that serum irisin may be used as a biomarker of cognitive function for VD.

In recent years, irisin has been confirmed to be related to the onset of many diseases. Yeon-Kyung Choi et al. found that serum irisin concentration was lower in newly-onset type 2 diabetes patients and is affected by blood sugar levels, suggesting that irisin played an important role in the pathogenesis of type 2 diabetes (20). The study of Graziana Colaianni et al. showed that irisin could enhance bone mass and improve the strength of skeletal cortex, suggesting that irisin may not only be responsible for the skeletal connection of muscles and bones, but may also become an important means for the treatment of osteoporosis (21). Another study pointed out that serum irisin was a biomarker of metabolic syndrome and cardiovascular disease (22). A study from Taiwan found that the serum irisin level of patients with chronic kidney disease was reduced, and it couldalso affect the cholesterol level and energy metabolism of patients with chronic kidney disease (23).

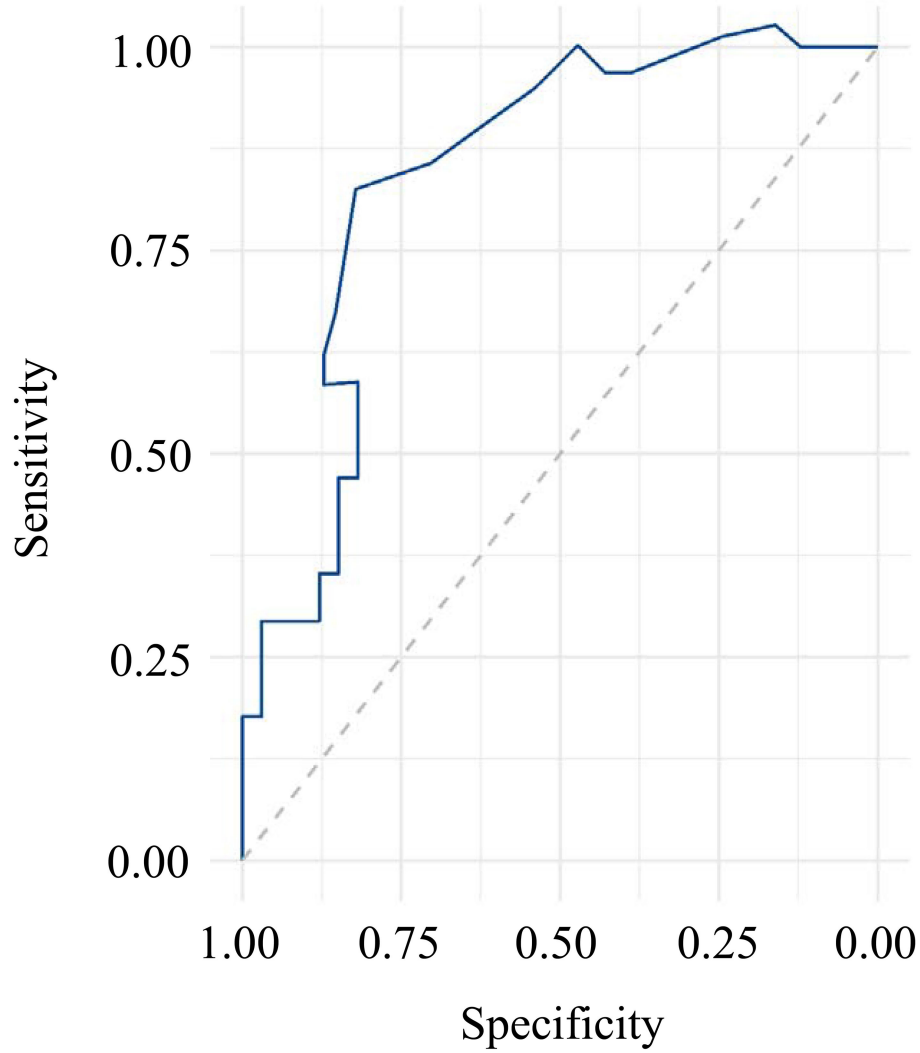

FIGURE 2 | ROC curve analysis for serum irisin levels in all subjects.

More and more evidences showed that irisin could also participate in the pathogenesis of a series of neurological diseases. Wen-Jun Tu's team found that serum irisin level was a powerful biological marker for the risk of post-stroke depression (12). The team also found that the decreased serum irisin concentration was a risk factor for the prognosis of acute stroke patients (13). The above two studies have shown that serum irisin is involved in the pathogenesis of acute stroke, but the specific mechanism is still unclear. Irisin is released by the cleavage of the membrane-bound precursor protein FNDC5, which is highly expressed in the hippocampus, while the level of FNDC5/irisin in the AD hippocampus and cerebrospinal fluid is reduced. Therefore, knocking out FNDC5/irisin may impair the cognitive function of mice. On the contrary, overexpression of FNDC5/irisin has neuroprotective effects on synaptic plasticity and memory in mice (24). The protective effect of irisin on AD is also believed to be related to the regulation of inflammation (25). Studies have confirmed that irisin can regulate the release of inflammatory factors in astrocytes and promote the survival of neurons (26). Studies from animal experiments showed that intraperitoneal injection of irisin could increase the expression of neurotrophic genes in the brain of mice and had a certain neuroprotective effect (27). Although irisin is associated with a variety of neurological diseases, there are relatively few reports on its protective effect on cognitive function. The mechanism of irisin involved in cognitive protection deserves further study.

Our research has some limitations. First of all, our research subjects come from a single region and the sample size is relatively small. Secondly, exercise can affect the level of irisin (28). We did not collect information on the subjects' exercise habits in the clinical baseline data. Thirdly, some drugs have potential effects on the level of serum irisin, but we have not

collected the patient's medication status. Finally, we did not analyze the relationship between serum irisin and different cognitive domains. Nevertheless, our research is the first study to report the role of irisin in the pathogenesis of VD, which still has great clinical significance.

CONCLUSIONS

This study shows that a decrease in serum irisin level is a potential biological marker of cognitive impairment in VD patients, even after adjustment for confounding factors. Future studies *in vivo* and *in vitro* are needed to further confirm this connection, which may provide a novel treatment for VD.

DATA AVAILABILITY STATEMENT

The raw data supporting the conclusions of this article will be made available by the authors, without undue reservation.

ETHICS STATEMENT

The studies involving human participants were reviewed and approved by the Ethics Committee of the Neck-Shoulder and Lumbocrural Pain Hospital of Shandong First Medical University. The patients/participants provided written informed consent to participate in this study.

AUTHOR CONTRIBUTIONS

YZ designed this research and wrote the manuscript. BS, CW, FZ, GuangjH, and GuangsH participated in data collection, experimental process, and data analysis. All authors contributed to the article and approved the submitted version.

ACKNOWLEDGMENTS

All authors are grateful to the Neck-Shoulder and Lumbocrural Pain Hospital of Shandong First Medical University.

REFERENCES

1. Wang Q, Yang W, Zhang J, Zhao Y, Xu Y. TREM2 overexpression attenuates cognitive deficits in experimental models of vascular dementia. *Neural Plast.* (2020) 2020:8834275. doi: 10.1155/2020/8834275
2. Xu Y, Wang Q, Qu Z, Yang J, Zhang X, Zhao Y. Protective effect of hyperbaric oxygen therapy on cognitive function in patients with vascular dementia. *Cell Transplant.* (2019) 28:1071–5. doi: 10.1177/0963689719853540
3. Wolters FJ, Ikram M A. Epidemiology of vascular dementia: nosology in a time of epiomics. *Arterioscler Thromb Vasc Biol.* (2019) 39:1542–9. doi: 10.1161/ATVBAHA.119.311908
4. Li J, Li S, Song Y, Zhou W, Zhu X, Xu S, et al. Association of serum FAM19A5 with cognitive impairment in vascular dementia. *Dis Markers.* (2020) 2020:8895900. doi: 10.1155/2020/8895900
5. Xu Y, Wang Q, Cui R, Lu K, Liu Y, Zhao Y. Uric acid is associated with vascular dementia in Chinese population. *Brain Behav.* (2017) 7:e00617. doi: 10.1002/brb3.617
6. Wang Q, Xu Y, Qi C, Liu A, Zhao Y. Association study of serum soluble TREM2 with vascular dementia in Chinese Han population. *Int J Neurosci.* (2020) 130:708–12. doi: 10.1080/00207454.2019.1702548
7. Romay MC, Toro C, Iruela-Arispe ML. Emerging molecular mechanisms of vascular dementia. *Curr Opin Hematol.* (2019) 26:199–206. doi: 10.1097/MOH.0000000000000502
8. Byun K, Lee S. The potential role of irisin in vascular function and atherosclerosis: a review. *Int J Mol Sci.* (2020) 21:184. doi: 10.3390/ijms21197184
9. Kelly DP. Irisin, light my fire. *Science.* (2012) 336:42–3. doi: 10.1126/science.1221688
10. Albrecht E, Schering L, Buck F, Vlach K, Schober H-C, Drevon CA, et al. Irisin: still chasing shadows. *Mol Metab.* (2020) 34:124–35. doi: 10.1016/j.molmet.2020.01.016
11. Yan B, Shi X, Zhang H, Pan L, Ma Z, Liu S, et al. Association of serum irisin with metabolic syndrome in obese Chinese adults. *PLoS ONE.* (2014) 9:e94235. doi: 10.1371/journal.pone.0094235
12. Tu WJ, Qiu HC, Cao JL, Liu Q, Zeng XW, Zhao JZ. Decreased concentration of irisin is associated with poor functional outcome in ischemic stroke. *Neurotherapeutics.* (2018) 15:1158–67. doi: 10.1007/s13311-018-0651-2
13. Tu WJ, Qiu HC, Liu Q, Li X, Zhao JZ, Zeng X. Decreased level of irisin, a skeletal muscle cell-derived myokine, is associated with post-stroke depression in the ischemic stroke population. *J Neuroinflammation.* (2018) 15:133. doi: 10.1186/s12974-018-1177-6
14. First MB, Reed GM, Hyman SE, Saxena S. The development of the ICD-11 clinical descriptions and diagnostic guidelines for mental and behavioural disorders. *World Psychiatry.* (2015) 14:82–90. doi: 10.1002/wps.20189
15. Reisberg B. Diagnostic criteria in dementia: a comparison of current criteria, research challenges, and implications for DSM-V. *J Geriatr Psychiatry Neurol.* (2006) 19:137–46. doi: 10.1177/0891988706291083
16. Xu Y, Wang Q, Liu Y, Cui R, Zhao Y. Is *Helicobacter pylori* infection a critical risk factor for vascular dementia? *Int J Neurosci.* (2016) 126:899–903. doi: 10.3109/00207454.2015.1081387
17. Wu PH, Lin YT, Wu PY, Huang JC, Chen SC, Chang JM, et al. Low ankle-brachial index and high brachial-ankle pulse wave velocity are associated with poor cognitive function in patients undergoing hemodialysis. *Dis Markers.* (2019) 2019:9421352. doi: 10.1155/2019/9421352
18. Zhang J, Tang L, Hu J, Wang Y, Xu Y. Uric acid is associated with cognitive impairment in the elderly patients receiving maintenance hemodialysis-A two-center study. *Brain Behav.* (2020) 10:e01542. doi: 10.1002/brb3.1542
19. Xu Y, Wang Q, Liu Y, Cui R, Lu K, Zhao Y. Association between *Helicobacter pylori* infection and carotid atherosclerosis in patients with vascular dementia. *J Neurol Sci.* (2016) 362:73–7. doi: 10.1016/j.jns.2016.01.025
20. Choi YK, Kim MK, Bae KH, Seo HA, Jeong JY, Lee WK, et al. Serum irisin levels in new-onset type 2 diabetes. *Diabetes Res Clin Pract.* (2013) 100:96–101. doi: 10.1016/j.diabres.2013.01.007
21. Colaianni G, Cuscito C, Mongelli T, Pignataro P, Buccoliero C, Liu P, et al. The myokine irisin increases cortical bone mass. *Proc Natl Acad Sci USA.* (2015) 112:12157–62. doi: 10.1073/pnas.1516622112
22. Park KH, Zaichenko L, Brinkoetter M, Thakkar B, Sahin-Efe A, Joung KE, et al. Circulating irisin in relation to insulin resistance and the metabolic syndrome. *J Clin Endocrinol Metab.* (2013) 98:4899–907. doi: 10.1210/jc.2013-2373
23. Wen MS, Wang CY, Lin SL, Hung KC. Decrease in irisin in patients with chronic kidney disease. *PLoS ONE.* (2013) 8:e64025. doi: 10.1371/journal.pone.0064025
24. Lourenco MV, Frozza RL, de Freitas GB, Zhang H, Kincheski GC, Ribeiro FC, et al. Exercise-linked FNDC5/irisin rescues synaptic plasticity and memory defects in Alzheimer's models. *Nat Med.* (2019) 25:165–75. doi: 10.1038/s41591-018-0275-4
25. Kim OY, Song J. The role of irisin in Alzheimer's disease. *J Clin Med.* (2018) 7:407. doi: 10.3390/jcm7110407
26. Wang K, Li H, Wang H. Wang J-h, Song F, Sun Y. Irisin exerts neuroprotective effects on cultured neurons by regulating

astrocytes. *Mediat Inflamm.* (2018) 2018:9070341. doi: 10.1155/2018/9070341
27. Natalicchio A, Marrano N, Biondi G, Dipaola L, Spagnuolo R, Cignarelli A, et al. Irisin increases the expression of anorexigenic and neurotrophic genes in mouse brain. *Diabetes Metab Res Rev.* (2020) 36:e3238. doi: 10.1002/dmrr.3238
28. de Freitas GB, Lourenco MV, De Felice FG. Protective actions of exercise-related FNDC5/Irisin in memory and Alzheimer's disease. *J Neurochem.* (2020) 155:602–11. doi: 10.1111/jnc.15039

Conflict of Interest: The authors declare that the research was conducted in the absence of any commercial or financial relationships that could be construed as a potential conflict of interest.

Publisher's Note: All claims expressed in this article are solely those of the authors and do not necessarily represent those of their affiliated organizations, or those of the publisher, the editors and the reviewers. Any product that may be evaluated in this article, or claim that may be made by its manufacturer, is not guaranteed or endorsed by the publisher.

Copyright © 2021 Zhang, Hou, Hou, Wang, Shi and Zheng. This is an open-access article distributed under the terms of the Creative Commons Attribution License (CC BY). The use, distribution or reproduction in other forums is permitted, provided the original author(s) and the copyright owner(s) are credited and that the original publication in this journal is cited, in accordance with accepted academic practice. No use, distribution or reproduction is permitted which does not comply with these terms.

frontiers in Neurology

ORIGINAL RESEARCH
published: 28 September 2021
doi: 10.3389/fneur.2021.740819

Hypertension With High Homocysteine Is Associated With Default Network Gray Matter Loss

*Yanliang Kong[1], Xin Li[2], Lina Chang[1], Yuwei Liu[1], Lin Jia[1], Lei Gao[3] and Lijuan Ren[1,2]**

[1] Department of Radiology, People's Hospital of Tongchuan City, Tongchuan, China, [2] Department of Ultrasound, People's Hospital of Tongchuan City, Tongchuan, China, [3] Department of Radiology, Zhongnan Hospital of Wuhan University, Wuhan, China

Hypertension with high homocysteine (Hcy, ≥10 μmol/L) is also known as H-type hypertension (HHT) and proposed as an independent risk factor for stroke and cognitive impairment. Although previous studies have established the relationships among hypertension, Hcy levels, and cognitive impairment, how they affect brain neuroanatomy remains unclear. Thus, we aimed to investigate whether and to what extent hypertension and high Hcy may affect gray matter volume in 52 middle-aged HHT patients and 51 demographically matched normotensive subjects. Voxel-based morphological analysis suggested that HHT patients experienced significant gray matter loss in the default network. The default network atrophy was significantly correlated with Hcy level and global cognitive function. These findings provide, to our knowledge, novel insights into how HHT affects brain gray matter morphology through blood pressure and Hcy.

Keywords: hypertension, homocysteine, VBM, default mode network, cognitive impairment

OPEN ACCESS

Edited by:
Yuzhen Xu,
Tongji University, China

Reviewed by:
Anastasia Bougea,
National and Kapodistrian University of Athens, Greece
Nafisa M. Jadavji,
Midwestern University, United States

***Correspondence:**
Lijuan Ren
1027452890@qq.com

Specialty section:
This article was submitted to Neurological Biomarkers, a section of the journal Frontiers in Neurology

Received: *13 July 2021*
Accepted: *24 August 2021*
Published: *28 September 2021*

Citation:
Kong Y, Li X, Chang L, Liu Y, Jia L, Gao L and Ren L (2021) Hypertension With High Homocysteine Is Associated With Default Network Gray Matter Loss. Front. Neurol. 12:740819. doi: 10.3389/fneur.2021.740819

INTRODUCTION

Hypertension is a well-known risk factor for stroke and cognitive impairment. In China, about 75% of primary hypertension is accompanied by high homocysteine (plasma Hcy ≥ 10 μmol/L) and is defined as H-type hypertension (HHT) (1). High Hcy is an independent risk factor for cerebrovascular events (2, 3) and cognitive impairment (4–7). Despite these prominent dual toxic effects, little is known about the neuroanatomical basis for cognitive impairment in HHT. Investigation upon the neuroanatomical basis may help to understand how dual cerebrovascular risk factors exacerbate the impact of brain morphological integrity, promoting a targeted prevention of risk factors and progression monitoring.

One potential neuroimaging biomarker that encodes cognitive impairment is integrity of the default mode network (DMN). The DMN was first proposed by Raichle et al. (8) and anatomically comprises the posterior cingulate/precuneus, bilateral inferior parietal lobule, lateral temporal, and hippocampus (9, 10). The DMN regions show less activity during goal-directed tasks and greater activity during resting state or several particular social cognitive tasks (9, 10). The DMN is considered to be a critical basis for advanced cognition of humans during development and evolution. Moreover, the DMN has been proposed as a neural biomarker for cognitive impairment in neuroimaging community. For example, DMN connectivity differentiates Alzheimer disease (11), mild cognitive impairment (12), mild traumatic injury (13, 14), and chemotherapy-related (15) cognitive impairment.

Previous studies on primary hypertension have shown evidence on the DMN. For example, primary hypertension is associated with increased coupling between the core and the dorsal medial subpart of the DMN during resting state (16) and abnormal spontaneous activity in DMN in a rodent model (17).

Etiologically, hypertension is a group of syndromes with high heterogeneity; each subgroup classification may represent different outcomes. Among the various types of hypertensions, HHT is the most common in China and has been suggested to predict more adverse consequences and outcomes (1). Essentially, HHT is a, at least, silent, cerebrovascular disease, often associated with higher silent infarcts, white matter hyperintensity (WMH), and gray matter loss (1, 18–24). These silent lesions represent physical dysconnectivity, compromised coordination between interconnected gray matter regions, and progressive atrophy itself. We know that cortical gray matter integrity is the neuroanatomical basis of large-scale brain networks that support human behaviors and cognition, and mounting evidence links gray matter atrophy to cognitive impairment (25–30). However, it is unclear that whether and to what extent HHT may affect the DMN gray matter morphometry.

Voxel-based morphometry (VBM) serves as a non-invasive, automatic framework for predicting brain disease and aging related model (31–34). Previously, it has been reported that hypertensive individuals experienced shrinkage of gray matter (35). Moreover, in dementia and mild cognitive impairment, the DMN appears to be the most impacted and has the ability to be a potential imaging biomarker (16, 36, 37). In both human and rodent studies, higher serum Hcy is associated with significant brain atrophy (38, 39); for more details, please see de Jager (40). Together, these evidences suggest that HHT is an adverse factor in the atrophy of DMN and cognitive performance and may interact with particular ways.

Here, we aimed to investigate whether HHT is associated with significant gray matter loss in the DMN and the relationships among the DMN atrophy, Hcy level, and global cognition. We hypothesized that HHT was associated with significant gray matter loss in the DMN, and Hcy level significantly mediated the relationship between DMN atrophy and global cognitive behavioral variables in patients with HHT.

MATERIALS AND METHODS

Subjects

Fifty-two H-type hypertensive subjects (26 females and 26 males, mean age 53.20 ± 10.98 years) and 51 normotensive healthy adults (33 females and 18 males, mean age 50.84 ± 9.92 years) were enrolled in this study. Informed consent was obtained from all the participants, and the Ethical Committee for Human Research at the People's Hospital of Tongchuan City approved all the procedures in accordance with the *Declaration of Helsinki*.

All of subjects were screened and diagnosed by a physician. All the subjects received comprehensive neurological examination and blood and neurocognitive tests. The inclusion criteria for the HHT subjects were as follows: (a) 18–65 years; (b) right-handed; (c) conforming to diagnostic criteria for HHT, i.e., serum Hcy ≥ 10 μmol/L and clinical systolic pressure >140 mmHg and/or diastolic pressure >90 mmHg; (d) currently not receiving systemically antihypertensive treatment; and (e) no contraindications for magnetic resonance imaging (MRI) examination.

Exclusion criteria were as follows: (a) any previous cardiovascular or cerebrovascular event; (b) large-scale old cerebral infarction and cerebral hemorrhage; (c) major diseases, including psychiatric diseases, renal failure (serum creatinine level >176 mmol/L), liver damage (aspartate aminotransferase or alanine aminotransferase >40 IU/L), coronary heart disease, congestive heart failure, or history of malignant tumors; (d) structural abnormalities that could impair cognitive function; and (e) low education years (<6 years).

Data Collection

We used a standardized questionnaire to record demographic information, life style, and medical history for each participant. Medical history including cardiovascular factors (hypertension, hyperlipidemia, stroke, coronary artery disease), diabetes complications, medication use, and age of diabetes onset were recorded using a standardized questionnaire. Body mass index (BMI) was calculated as weight/height (kg/m^2). Neurocognitive tests were administered to examine global cognition function with the Mini-Mental State Examination (MMSE) (41, 42). Neurocognitive tests and questionnaire were administered by a trained neuropsychologist and nurse staff. The diastolic and systolic blood pressures were measured by a trained staff after resting for at least 5 min in a seated position.

MRI Acquisition and Data Processing

Structural brain images, including 3D T1-weighted fast field echo (3D T1-FFE, repetition time = 8.29 ms, echo time = 3.81 ms, flip angle = 8°, slice thickness = 1 mm, 160 axial slices covering whole brain) high-resolution anatomical and T2-fluid-attenuated inversion recovery (FLAIR, repetition time = 8,000 ms, echo time = 140 ms, inversion time = 2,200 ms, flip angle = 90°, slice thickness = 1 mm, 160 axial slices covering whole brain) images, were acquired on a 1.5T MRI (Phillips, Achieva, Andover, MA, USA) scanner equipped with an eight-channel head coil.

T1 structural images were processed using the computational anatomy toolbox (CAT, version 12.6; http://www.neuro.uni-jena.de/cat/) implanted in SPM12 (www.fil.ion.ucl.ac.uk/spm). Briefly, T1 images were first visually inspected and manually reoriented to ensure image quality and whole brain covering and further segmented into gray matter, white matter, and cerebral spinal fluid, with the diffeomorphic anatomical registration through an exponentiated lie algebra (DARTEL) algorithm (31). The individual gray matter images were then spatially normalized into the Montreal Neurological Institute (MNI) standard space and modulated. The modulated and spatial normalized gray matter images were then smoothed with an isotropic Gaussian kernel of 8 mm full-width at half-maximum. The FLAIR images were used for manually calculating white matter hyperintensity (WMH) volume for each participant.

Two HHT subjects and one control were excluded from the analysis due to poor image quality or segment failure.

TABLE 1 | Clinical and demographic information.

Variable	HHT	Controls	Statistic, *t* (*p*)
Demographic data			
Age, mean (SD), years	53.20 (10.98)	50.84 (9.92)	1.128, 0.26
Sex/gender: males/females	26M/24F	18M/32F	2.60, 0.11
Education, mean (SD), years	11.68 (2.35)	11.46 (2.84)	0.338, 0.51
History of smoking: yes, *n* (%)	24 (48%)	16 (32%)	2.67, 0.10
Obesity: obese, *n* (%)	11 (22%)	5 (10%)	2.68, 0.10
Alcohol	28 (56%)	21 (42)	1.96, 0.16
MMSE	27.22 (0.89)	27.74 (0.96)	-2.805, $p = 0.006$
BP Systolic	159.86 (17.33)	117.92 (7.50)	15.593, $p < 0.001$***
BP Diastolic	98.86 (14.83)	77.71 (5.85)	9.312, $p < 0.001$***
Hcy (μmol/L)	21.79 (10.97)	11.47 (7.65)	5.462, $p < 0.001$***
BMI	24.42 (3.05)	23.48 (2.60)	1.658, 0.102

****$p < 0.001$; SD, standard deviation; MMSE, Mini Mental State Examination; BP, blood pressure; Hcy, homocysteine; BMI, body mass index; HHT, hypertension with high homocysteine.*

TABLE 2 | Gray matter VBM results.

Brain regions	Cluster size	*t*-value	MNI coordinates		
			x	*y*	*z*
Parietal_Inf_L	1,334	4.157	−33	−69	41
Rectus_R	1,685	4.068	13	32	−22
OFCmed_L	2,201	4.065	−16	30	−19
Ventral medial prefrontal	2,423	3.994	2	62	−19
Cerebellum_Crus1_L	1,515	3.941	−19	−87	−21
Precuneus_R	4,548	3.913	6	−46	16
Precuneus_R	2,601	3.810	12	−49	56
OFCant_R	676	3.556	31	54	−14
Occipital_Sup_R	478	3.527	26	−90	13
Temporal_Mid_L	1,418	3.463	−45	−67	14
Parietal_Sup_R	343	3.449	28	−60	64
Frontal_Sup_2_L	392	3.367	−20	−13	55
Frontal_Mid_2_L	363	3.260	−41	53	20
Precentral_L	417	3.160	−49	−3	23
Temporal_Mid_L	1,132	3.138	−52	−34	−4
Temporal_Mid_R	405	2.983	55	−64	3

Regions were automatically labeled using the AAL3 atlas. These results were reported with voxel-wise $p < 0.001$ and family-wise error (FWE) cluster corrected at cluster-level $p < 0.05$. Regions were automatically reported and labeled using BSPMVIEW (http://www.bobspunt.com/software/bspmview) and automated anatomical labeling atlas 3 (https://www.gin.cnrs.fr/en/tools/aal/).
MNI, Montreal Neurological Institute; x, y, and z, MNI coordinates in the left–right, anterior–posterior, and inferior–superior dimensions, respectively.

Statistical Analysis

Demographic and clinical variables, Hcy, and cognitive tests were analyzed using SPSS 16 (SPSS Inc., USA). Categorical variables (including gender, diabetes, obesity, smoking, drinking, etc.) were tested using the chi-square test, while the remaining variables were tested using independent two-sample *t*-tests. The significance was set at $p < 0.05$. Differences/associations with a $p < 0.05$ were considered to be statistically significant.

Mediation Analysis

Since prior research has suggested that Hcy level (X, independent variable) can predict cognitive functions (Y, dependent variable) (43), we considered to take the DMN gray matter volume as a mediator (M) and build a mediation model. The mediation analysis was conducted by using the Hayes Process macro (44) (http://www.afhayes.com/), which is an observed least-squares regressions path analysis modeling tool. We used a model 4, with the independent factor as Hcy level and dependent variable as the cognitive measures (i.e., the MMSE scores), and the proposed mediator was DMN gray matter size. Age, gender, and education were controlled as nuisance of no interest. Statistical significance was set at $p < 0.05$.

RESULTS

Demographic and Clinical Data

Demographic and clinical data of all the participants are presented in **Table 1**. We excluded two HHT subjects and one control subject from data analysis due to poor image quality or segment failure; thus, a total of 100 subjects were finally included. The HHT subjects demonstrated an average Hcy of 21.79 ± 10.97 μmol/L compared with the normotensive controls (11.47 ± 7.65 μmol/L, $p < 0.05$). In addition, the HHT subjects demonstrated lower MMSE scores ($p = 0.006$) and higher but non-significant frequency of vascular risks, including diabetes mellitus, hyperlipidemia, and obesity ($p > 0.05$). However, the hypertensive subjects were generally comparable with normotensive controls on age, gender, and education ($p > 0.05$).

Voxel-Wise Gray Matter Volume

To investigate gray matter volume differences, we performed voxel-based morphological analysis. Our findings showed that HHT subjects exhibited smaller gray matter volume in several clusters in the DMN, including the left inferior parietal, right medial prefrontal, precuneus, and bilateral middle temporal gyri and additionally in the left lateral frontal, left precentral, and right superior occipital and left cerebellum crus regions [**Table 2**, **Figure 1**; voxel-wise $p < 0.001$ and family-wise error (FWE) cluster corrected at cluster-level $p < 0.05$].

Brain Size and White Matter Lesion Burden

The HHT subjects showed larger intracranial volume ($p = 0.042$) and cerebrospinal fluid volumes ($p = 0.049$), and higher WMH burden ($p = 0.015$), but comparable gray matter and white matter sizes (**Table 3**).

Association Analyses

To determine the relationships between brain (WMH and gray matter volume) and behavioral and physiological parameters, we conducted linear correlation analyses. Results showed that gray matter in the DMN and thalamus was negatively correlated with WMH but positively correlated with MMSE scores. In other words, the DMN gray matter size predicted white matter lesion

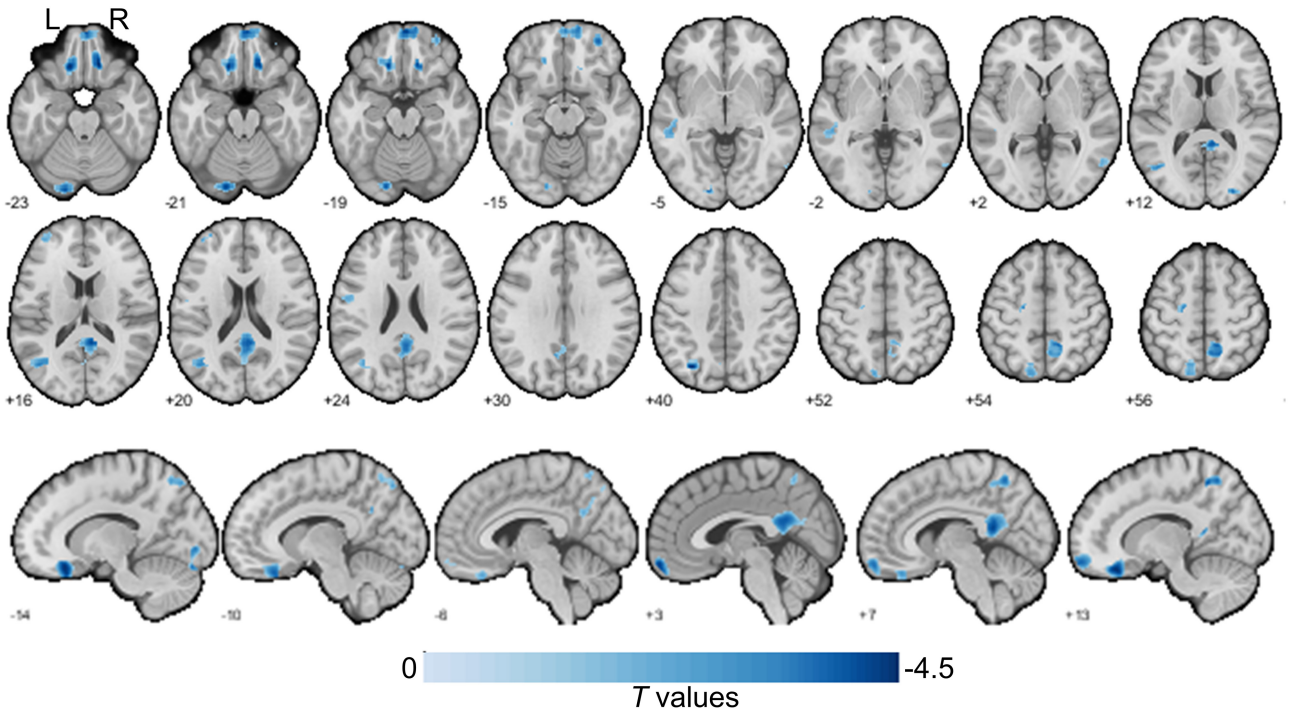

FIGURE 1 | Gray matter size difference between the H-type hypertensive and normotensive subjects. The axial slices are labeled with Z coordinates and sagittal slices with Y coordinates. The results were reported with voxel-wise $p < 0.001$ and family-wise error (FWE) cluster corrected at cluster-level $p < 0.05$. A negative colorbar indicates gray matter losses in the H-type hypertensive subjects. Regions were automatically reported and labeled using BSPMVIEW (http://www.bobspunt.com/software/bspmview) and automated anatomical labeling atlas 3 (https://www.gin.cnrs.fr/en/tools/aal/). L, left; R, right.

TABLE 3 | Gross segment volumes and white matter hyperintensity burden in the two groups included in this study.

Variable	HHT	Controls	Statistic, *t* (*p*)
TIV (ml)	1,379.93 (129.08)	1,325.52 (134.79)	2.061, 0.042*
GM (ml)	582.94 (57.34)	573.30 (55.58)	−0.854, 0.40
WM (ml)	508.59 (61.56)	487.42 (60.91)	1.728, 0.087
CSF (ml)	286.62 (61.19)	263.61 (53.80)	1.996, 0.049*
WMH (ml)	1.78 (1.45)	1.19 (0.87)	−2.484, 0.015*

**p < 0.05; HHT, hypertension with high homocysteine; TIV, total intracranial volume; GM, gray matter; WM, white matter; CSF, cerebrospinal fluid; WMH, white matter hyperintensity.*

load and general cognition, although there was no significant relationship between WMH and MMSE.

We also found that increased systolic blood pressure was associated with decreased gray matter size within the thalamus and DMN (**Figures 2**, **3**). We also determined correlations between the whole brain (excluding the significant clusters) voxel-wise gray matter volume and blood pressure (BP), MMSE, Hcy, and WMH loads (**Figure 3**).

Mediation Analyses

To investigate whether the gray matter loss significantly affected the association between Hcy and cognitive performance, we used a mediation model to answer this issue. Unfortunately, we did not find any mediation effect of gray matter volume on the reported significant clusters.

DISCUSSION

In this study, we investigated gray matter atrophy underlying HHT and the associations with cognitive performance and plasma Hcy, while considering multiple vascular variables. We found that HHT patients showed significant DMN atrophy, which can reflect Hcy level, global cognitive function (MMSE), and WMH load. HHT patients demonstrated parallelized gray matter atrophy and global cognitive decline, suggesting that both hypertension and high Hcy aggravate the neuroanatomical and cognitive toxic effects.

Consistent with our hypothesis and previous published reports (16, 35), we found significant gray matter loss in the DMN and sensorimotor regions in the HHT subjects. The DMN has been well-characterized in advanced cognitive functions, including autobiographical memory, social cognition, memory consolidation, and reasoning; for more details, please see Buckner and DiNicola (9) and Raichle (10). Brain regions that constitute the DMN include the inferior parietal lobule that is associated with spatial orientation, the medial prefrontal cortex that is linked to reasoning, precuneus that is linked to social cognition, and middle temporal region that is involved

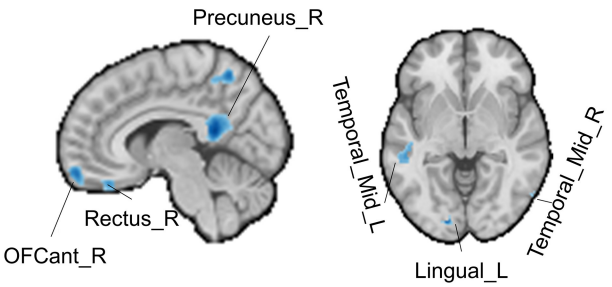

B

Brain regions	BP	HCY	MMSE
Rectus_R	-0.06	-0.02	0.309
Precuneus_R	-0.34	-0.02	0.372
Lingual_L	-0.22	-0.31	0.472
OFCant_R	-0.15	0.045	0.398
Temporal_Mid_L	-0.39	-0.02	0.064
Temporal_Mid_R	-0.08	0.166	0.353

FIGURE 2 | Associations between gray matter size within the significant clusters and clinical (blood pressure), physiological (Hcy level), and behavioral (MMSE scores) parameters in H-type hypertensive subjects. **(A)** Among the significant clusters, brain regions showing at least one significant correlation **(B)** are marked out. **(B)** Heatmap showing Pearson's correlation coefficients between gray matter size within the significant clusters and clinical (blood pressure), physiological (Hcy level), and behavioral (MMSE scores) parameters in H-type hypertensive subjects. Significant correlations are marked with warm (positive) or cold (negative) colors, and non-significant correlations are marked with white color. BP, blood pressure based measure, here hypertension grades 1–3; HCY, homocysteine; MMSE, Mini-Mental State Examination.

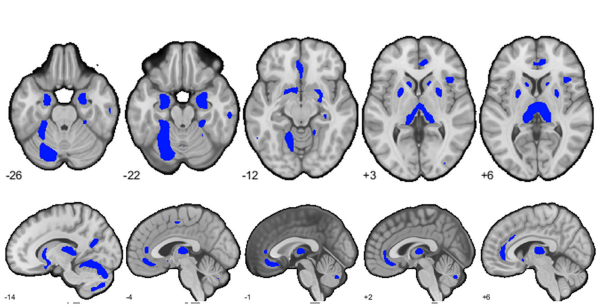

B

Brain regions	BP	HCY	MMSE	WMH
Cerebelum_8_L	-0.443	0	0	-0.524
Fusiform_L	-0.508	0	0	-0.469
Amygdala_R	-0.439	0	0	-0.728
Hippocampus_R	-0.432	-0.426	0.4487	-0.66
Thalamus_L	-0.459	0	0	-0.678
Thalamus_R	-0.426	0	0	-0.552
Cingulum_Ant_R	-0.46	0	0	-0.652
Angular_R	-0.503	0	0	0
Hippocampus_L	0	0	0.3957	-0.728

FIGURE 3 | Associations between whole brain gray matter size (excluding the significant clusters) and clinical (blood pressure), physiological (Hcy level), and behavioral (MMSE scores) parameters, and lesion (WMH load) in H-type hypertensive subjects. **(A)** Excluding the significant clusters, brain regions showing at least one significant correlation **(B)** are marked out. **(B)** Heatmap showing Pearson's correlation coefficients between gray matter size within the significant clusters and clinical (blood pressure), physiological (Hcy level), and behavioral (MMSE scores) parameters, and lesion (WMH load) in H-type hypertensive subjects. Significant correlations are marked with warm (positive) or cold (negative) colors, and non-significant correlations are marked with white color. BP, blood pressure based measure, here hypertension grades 1–3; Hcy, homocysteine; MMSE, Mini-Mental State Examination; WMH, white matter hyperintensity.

in multimodal sensory processing and social cognition. These components are crucial to advanced cognitive functions (43), have been linked to cognitive impairment in Alzheimer's disease (37, 45), and also generally align to the findings from rodents and other animals (39, 46) in HHT. Anatomically, lateral temporal regions receive anterior circulation whose arteries emerge from the Sylvian fissure, thus a potential focus that is targeted by the hypertension-induced hypoperfusion. Also, these key DMN regions are a marker for cognitive impairment and heavily hit regions of altered hemodynamics. Thus, the DMN atrophy reported here is consistent but beyond the previous published reports on sole or mixed primary hypertension.

Apart from the DMN, we also identified gray matter loss in the left lateral prefrontal, left precentral, right occipital, and cerebellum regions. These regions are mainly involved in sensory and motor processing. For example, the left inferior frontal region is a classical Broca's area, responsible for speech and other higher motor functions, and is also a vulnerable foci for stroke and other cerebrovascular events (47). The precentral region is involved in the somatomotor system and associated with physical fitness and well-being (48, 49). The occipital is also largely a primary sensory cortex and involved in visuospatial processing. Visuospatial deficit is also supposed as a biomarker of Alzheimer's disease (50).

Beyond the gray matter atrophy, we also found significant associations. We first report the associations between significant atrophic clusters with blood pressure, Hcy, and MMSE scores. Gray matter volume in the precuneus and left middle temporal gyrus was negatively correlated with blood pressure; gray matter volume in the left lingual cortex was negatively correlated with plasma Hcy. Nevertheless, we found that the MMSE scores were correlated with almost all the significant clusters, thereby suggesting the role of these regions in global cognition. This finding is in line with many studies investigating the brain anatomical correlates with global cognition (25–30). The precuneus is a core of the DMN, and this result is also in line with other published reports on vascular cognitive impairment (51–53). The middle temporal gyrus is a vulnerable

locus attacked by the vascular pathologies. For example, in patients with carotid stenosis, the same region is the most impacted (51–53).

The finding that HHT showed higher WMH load and correlated with lower gray matter is generally consistent with previous reports. For example, previous cohort studies have reported positive associations between elevated Hcy and WMH and silent infarction (54–56) but inconsistent findings on whether these factors act as mediators (54). However, in healthy aging and some major brain diseases, WMH load tends to associate with regional gray matter atrophy (57, 58).

Hcy and cognitive impairment together promote brain atrophy, especially when they cross a threshold level (40). Therefore, we were also interested in investigating whether there is a relationship between high Hcy and cognitive decline mediated by gray matter atrophy in HHT subjects. Unfortunately, due to the lack of a significant correlation between Hcy and global cognition, our mediation model could not confirm this hypothesis. One possibility is that Hcy is a non-specific measure, especially when it is associated with non-specific global cognitive measures such as MMSE. Another possibility, as mentioned at the beginning of this paragraph, is that Hcy needs to reach a certain threshold level to establish a parallel relationship with cognitive impairment, which makes this problem more complicated. In addition, HHT, as a kind of vascular cognitive impairment, may need more sensitive tests focused on specific cognitive domains (59–63). We also found slightly elevated Hcy in the controls, suggesting independent risk factor in this population. Although this does not necessarily provide any indications, it suggests a possibility that there may be regional and dietary predisposition in this population, which may also be the reason for the high incidence of HHT (64). Nevertheless, investigations on this topic are still lacking. However, HHT subjects demonstrated far higher Hcy; this may become highly unfavorable.

We found that the HHT group had larger intracranial and cerebrospinal fluid volumes. One reason is that the HHT group had a higher proportion of males, although there was no statistical difference in the gender ratio; thus, we included gender as a nuisance covariate in all the analyses. At the same time, patients with hypertension have more WMHs, which is consistent with clinical observation and previous published report (24), thereby suggesting that HHT is accompanied by more white matter damage burden than the normotensive controls.

Although we have reported some novel findings, several limitations of our study cannot be neglected. First, we could not build the casual relationship between Hcy and hypertension, which might affect the statistical model; nonetheless the current findings suggest dual adverse effects from HHT. Further study may validate the casual relationship by considering more variables, including WMH load, blood pressure classification, vitamins, and other risk factors. Second, factors affecting gray matter atrophy also include hemodynamic changes (65) and lacunar infarction (66–68). Although these two aspects are still poorly characterized, they may contribute to brain atrophy to varying degrees. Future research should include these factors as explanatory variables and promote a more comprehensive model. Third, we only measured global cognition for each subject; this could hamper the ability to classify between-group differences. Increasing evidence suggests that vascular cognitive impairment is more likely to affect processing speed and semantic/recall memory, which is different from the pattern of global cognitive impairment caused by Alzheimer's disease (60, 69–71). Therefore, we need to further include domain-specific tests, such as the Digit Symbol (72) and the Rey Auditory Verbal Learning Tests (73), to accurately characterize the affected cognitive domains that are most sensitive to HHT and its underlying neuroanatomical and physiological basis.

CONCLUSION

In conclusion, this study reports that HHT is associated with default network atrophy and correlated with WMH, Hcy level, and MMSE score. These results provide, to our knowledge, the first insights into how HHT affects brain gray matter morphology and how these three risk factors interact with one another.

DATA AVAILABILITY STATEMENT

The original contributions presented in the study are included in the article/supplementary material, further inquiries can be directed to the corresponding author.

ETHICS STATEMENT

The studies involving human participants were reviewed and approved by the Ethical Committee for Human Research at the People's Hospital of Tongchuan City. The patients/participants provided their written informed consent to participate in this study.

AUTHOR CONTRIBUTIONS

YK collected data and wrote the draft. XL wrote the draft. LC, YL, and LJ collected data and analyzed data. LG analyzed data and proofread the manuscript. LR conceived and revised the manuscript. All authors contributed to the article and approved the submitted version.

FUNDING

This work was supported by the Natural Science Foundation of China (Grant No. 82001799).

ACKNOWLEDGMENTS

We thank all the subjects for their active participation and cooperation. We also thank Dr. Yawen Ren (Clinical Laboratory Director), Xiaoyan Yan (Division of Chronic Disease), Baiqiang Yang (Medical Department), Xiaoping He (General Medicine Section), and Liping Cheng (Branch Training Section) of People's Hospital of Tongchuan City for their kind help in subject recruitment and data collection.

REFERENCES

1. Lu Z, Li J, Li X, Ding M, Mao C, Zhu X, et al. Hypertension with hyperhomocysteinemia increases the risk of early cognitive impairment after first-ever ischemic stroke. *Eur Neurol.* (2019) 82:75–85. doi: 10.1159/000504704
2. Hassan A, Hunt BJ, O'Ullivan M, Bell R, D'Ouza R, Jeffery S, et al. Homocysteine is a risk factor for cerebral small vessel disease, acting via endothelial dysfunction. *Brain.* (2004) 127:212–9. doi: 10.1093/brain/awh023
3. Ostrakhovitch EA, Tabibzadeh S. Homocysteine and age-associated disorders. *Ageing Res Rev.* (2019) 49:144–64. doi: 10.1016/j.arr.2018.10.010
4. Garcia A, Zanibbi K. Homocysteine and cognitive function in elderly people. *CMAJ.* (2004) 171:897–904. doi: 10.1503/cmaj.1031586
5. Price BR, Wilcock DM, Weekman EM. Hyperhomocysteinemia as a risk factor for vascular contributions to cognitive impairment and dementia. *Front Aging Neurosci.* (2018) 10:350. doi: 10.3389/fnagi.2018.00350
6. Sala I, Sánchez-Saudinós MB, Molina-Porcel L, Lázaro E, Gich I, Clarimón J, et al. Homocysteine and cognitive impairment. *Dement Geriatr Cogn Disord.* (2008) 26:506–12. doi: 10.1159/000173710
7. Zhou S, Chen J, Cheng L, Fan K, Xu M, Ren W, et al. Age-dependent association between elevated homocysteine and cognitive impairment in a post-stroke population: a prospective study. *Front Nutr.* (2021) 8:691837. doi: 10.3389/fnut.2021.691837
8. Raichle ME, MacLeod AM, Snyder AZ, Powers WJ, Gusnard DA, Shulman GL. A default mode of brain function. *Proc Nat Acad Sci USA.* (2001) 98:676–82. doi: 10.1073/pnas.98.2.676
9. Buckner RL, DiNicola LM. The brain's default network: updated anatomy, physiology and evolving insights. *Nat Rev Neurosci.* (2019) 20:593–608. doi: 10.1038/s41583-019-0212-7
10. Raichle ME. The brain's default mode network. *Annu Rev Neurosci.* (2015) 38:433–47. doi: 10.1146/annurev-neuro-071013-014030
11. Greicius MD, Srivastava G, Reiss AL, Menon V. Default-mode network activity distinguishes Alzheimer's disease from healthy aging: evidence from functional MRI. *Proc Nat Acad Sci USA.* (2004) 101:4637–42. doi: 10.1073/pnas.0308627101
12. Bai F, Zhang Z, Yu H, Shi Y, Yuan Y, Zhu W, et al. Default-mode network activity distinguishes amnestic type mild cognitive impairment from healthy aging: a combined structural and resting-state functional MRI study. *Neurosci Lett.* (2008) 438:111–5. doi: 10.1016/j.neulet.2008.04.021
13. Sharp DJ, Beckmann CF, Greenwood R, Kinnunen KM, Bonnelle V, De Boissezon X, et al. Default mode network functional and structural connectivity after traumatic brain injury. *Brain.* (2011) 134:2233–47. doi: 10.1093/brain/awr175
14. Zhou Y, Milham MP, Lui YW, Miles L, Reaume J, Sodickson DK, et al. Default-mode network disruption in mild traumatic brain injury. *Radiology.* (2012) 265:882–92. doi: 10.1148/radiol.12120748
15. Kesler SR, Wefel JS, Hosseini SH, Cheung M, Watson CL, Hoeft F. Default mode network connectivity distinguishes chemotherapy-treated breast cancer survivors from controls. *Proc Nat Acad Sci USA.* (2013) 110:11600–5. doi: 10.1073/pnas.1214551110
16. Gu Y, Liu R, Qin R, Chen X, Zou J, Jiang Y, et al. Characteristic changes in the default mode network in hypertensive patients with cognitive impairment. *Hypertension Res.* (2019) 42:530–40. doi: 10.1038/s41440-018-0176-4
17. Huang S, Wu Y, Peng S, Peng H, Huang T, Ho K, et al. Inter-strain differences in default mode network: a resting state fmri study on spontaneously hypertensive rat and Wistar Kyoto rat. *Sci Rep.* (2016) 6:21697. doi: 10.1038/srep21697
18. Ji Y, Li X, Teng Z, Li X, Jin W, Lv PY. Homocysteine is associated with the development of cerebral small vessel disease: retrospective analyses from neuroimaging and cognitive outcomes. *J Stroke Cerebrovasc Dis.* (2020) 29:105393. doi: 10.1016/j.jstrokecerebrovasdis.2020.105393
19. Dufouil C, Alpérovitch A, Ducros V, Tzourio C. Homocysteine, white matter hyperintensities, and cognition in healthy elderly people. *Ann Neurol.* (2003) 53:214–21. doi: 10.1002/ana.10440
20. Feng L, Isaac V, Sim S, Ng T, Krishnan KRR, Chee MW. Associations between elevated homocysteine, cognitive impairment, and reduced white matter volume in healthy old adults. *Am J Geriatric Psychiatry.* (2013) 21:164–72. doi: 10.1016/j.jagp.2012.10.017
21. Glodzik L, Rusinek H, Tsui W, Pirraglia E, Kim H, Deshpande A, et al. Different relationship between systolic blood pressure and cerebral perfusion in subjects with and without hypertension. *Hypertension.* (2019) 73:197–205. doi: 10.1161/HYPERTENSIONAHA.118.11233
22. Lee KO, Woo M, Chung D, Choi J, Kim N, Kim O, et al. Differential impact of plasma homocysteine levels on the periventricular and subcortical white matter hyperintensities on the brain. *Front Neurol.* (2019) 10:1174. doi: 10.3389/fneur.2019.01174
23. Li T, Liu X, Diao S, Kong Y, Duan X, Yang S, et al. H-type hypertension is a risk factor for cerebral small-vessel disease. *BioMed Res Int.* (2020) 2020:6498903. doi: 10.1155/2020/6498903
24. Li X, Liang Y, Chen Y, Zhang J, Wei D, Chen K, et al. Disrupted frontoparietal network mediates white matter structure dysfunction associated with cognitive decline in hypertension patients. *J Neurosci.* (2015) 35:10015–24. doi: 10.1523/JNEUROSCI.5113-14.2015
25. Fein G, Di Sclafani V, Tanabe J, Cardenas V, Weiner MW, Jagust WJ, et al. Hippocampal and cortical atrophy predict dementia in subcortical ischemic vascular disease. *Neurology.* (2000) 55:1626–35. doi: 10.1212/WNL.55.11.1626
26. Han Y, Lui S, Kuang W, Lang Q, Zou L, Jia J. Anatomical and functional deficits in patients with amnestic mild cognitive impairment. *PLoS ONE.* (2012) 7:e28664. doi: 10.1371/journal.pone.0028664
27. Jack CR, Shiung MM, Weigand SDO, Brien PC, Gunter JL, Boeve BF, et al. Brain atrophy rates predict subsequent clinical conversion in normal elderly and amnestic MCI. *Neurology.* (2005) 65:1227–31. doi: 10.1212/01.wnl.0000180958.22678.91
28. Li J, Gao L, Wen Z, Zhang J, Wang P, Tu N, et al. Structural covariance of gray matter volume in HIV vertically infected adolescents. *Sci Rep.* (2018) 8:1182. doi: 10.1038/s41598-018-19290-5
29. Mok V, Wong KK, Xiong Y, Wong A, Schmidt R, Chu W, et al. Cortical and frontal atrophy are associated with cognitive impairment in age-related confluent white-matter lesion. *J Neurol Neurosurg Psychiatry.* (2011) 82:52–7. doi: 10.1136/jnnp.2009.201665
30. van de Mortel LA, Thomas RM, van Wingen GA, Alzheimer's Disease Neuroimaging Initiative. Grey matter loss at different stages of cognitive decline: a role for the thalamus in developing Alzheimer's disease. *J Alzheimer's Dis.* (2021) 83:705–20. doi: 10.3233/JAD-210173
31. Ashburner J. A fast diffeomorphic image registration algorithm. *Neuroimage.* (2007) 38:95–113. doi: 10.1016/j.neuroimage.2007.07.007
32. Ashburner J, Friston KJ. Why voxel-based morphometry should be used. *Neuroimage.* (2001) 14:1238–43. doi: 10.1006/nimg.2001.0961
33. Jónsson BA, Bjornsdottir G, Thorgeirsson TE, Ellingsen LM, Walters GB, Gudbjartsson DF, et al. Brain age prediction using deep learning uncovers associated sequence variants. *Nat Commun.* (2019) 10:5409. doi: 10.1038/s41467-019-13163-9
34. Mechelli A, Price CJ, Friston KJ, Ashburner J. Voxel-based morphometry of the human brain: methods and applications. *Curr Med Imaging.* (2005) 1:105–13. doi: 10.2174/1573405054038726
35. Schaare HL, Mueller K, Babayan A, Erbey M, Gaebler M, Kumral D, et al. Higher blood pressure is associated with lower regional grey matter density in healthy, young adults. *Autonomic Neurosci.* (2015) 192:97. doi: 10.1016/j.autneu.2015.07.138
36. Kesler SR. Default mode network as a potential biomarker of chemotherapy-related brain injury. *Neurobiol Aging.* (2014) 35:S11–9. doi: 10.1016/j.neurobiolaging.2014.03.036
37. Lee E, Yoo K, Lee Y, Chung J, Lim J, Yoon B, et al. Default mode network functional connectivity in early and late mild cognitive impairment. *Alzheimer Dis Assoc Disord.* (2016) 30:289–96. doi: 10.1097/WAD.0000000000000143
38. Madsen SK, Rajagopalan P, Joshi SH, Toga AW, Thompson PM, Alzheimer's Disease Neuroimaging Initiative (ADNI). Higher homocysteine associated with thinner cortical gray matter in 803 participants from the Alzheimer's Disease Neuroimaging Initiative. *Neurobiol Aging.* (2015) 36:S203–10. doi: 10.1016/j.neurobiolaging.2014.01.154
39. Matt,é C., Mussulini BHM, Dos Santos TM, Soares FM, Simão F, Matt,é A., et al. Hyperhomocysteinemia reduces glutamate uptake in parietal cortex of rats. *Int J Dev Neurosci.* (2010) 28:183–7. doi: 10.1016/j.ijdevneu.2009.11.004

40. de Jager CA. Critical levels of brain atrophy associated with homocysteine and cognitive decline. *Neurobiol Aging.* (2014) 35:S35–S9. doi: 10.1016/j.neurobiolaging.2014.03.040
41. Cockrell JR, Folstein MF. Mini-mental state examination. In: Abou-Saleh MT, Katona CLE, Anand KA, editors. *Principles and Practice of Geriatric Psychiatry*. Chichester; West Sussex: John Wiley & Sons, Ltd. (2002). p. 140-1. doi: 10.1002/0470846410.ch27(ii)
42. Tombaugh TN, McIntyre NJ. The mini-mental state examination: a comprehensive review. *J Am Geriatr Soc.* (1992) 40:922–35. doi: 10.1111/j.1532-5415.1992.tb01992.x
43. Nelson ME, Andel R, Nedelska Z, Martinkova J, Cechova K, Markova H, et al. The association between homocysteine and memory in older adults. *J Alzheimer's Dis*. (2021) 81:413–26. doi: 10.3233/JAD-201558
44. Hayes AF. *Introduction to Mediation, Moderation, and Conditional Process Analysis: A Regression-Based Approach (2nd ed.).* New York, NY: Guilford Press (2018).
45. Glodzik L, Mosconi L, Tsui W, de Santi S, Zinkowski R, Pirraglia E, et al. Alzheimer's disease markers, hypertension, and gray matter damage in normal elderly. *Neurobiol Aging.* (2012) 33:1215–27. doi: 10.1016/j.neurobiolaging.2011.02.012
46. Willette AA, Gallagher C, Bendlin BB, McLaren DG, Kastman EK, Canu E, et al. Homocysteine, neural atrophy, and the effect of caloric restriction in rhesus monkeys. *Neurobiol Aging.* (2012) 33:670–80. doi: 10.1016/j.neurobiolaging.2010.06.003
47. Nishitani N, Schurmann M, Amunts K, Hari R. Broca's region: from action to language. *Physiology.* (2005) 20:60–9. doi: 10.1152/physiol.00043.2004
48. Belcher BR, Zink J, Azad A, Campbell CE, Chakravartti SP, Herting MM. The roles of physical activity, exercise, and fitness in promoting resilience during adolescence: effects on mental well-being and brain development. *Biol Psychiatry.* (2020) 6:225–37. doi: 10.1016/j.bpsc.2020.08.005
49. Wei G, Xu T, Fan F, Dong H, Jiang L, Li H, et al. Can Taichi reshape the brain? A brain morphometry study. *PLoS ONE.* (2013) 8:e61038. doi: 10.1371/journal.pone.0061038
50. Mandal PK, Joshi J, Saharan S. Visuospatial perception: an emerging biomarker for Alzheimer's disease. *J Alzheimer's Dis.* (2012) 31:S117–35. doi: 10.3233/JAD-2012-120901
51. Chen L, Song J, Cheng R, Wang K, Liu X, He M, et al. Cortical thinning in the medial temporal lobe and precuneus is related to cognitive deficits in patients with subcortical ischemic vascular disease. *Front Aging Neurosci.* (2020) 12:536. doi: 10.3389/fnagi.2020.614833
52. Wang R, Liu N, Tao Y, Gong X, Zheng J, Yang C, et al. The application of rs-fMRI in vascular cognitive impairment. *Front Neurol.* (2020) 11:951. doi: 10.3389/fneur.2020.00951
53. Yi L, Wang J, Jia L, Zhao Z, Lu J, Li K, et al. Structural and functional changes in subcortical vascular mild cognitive impairment: a combined voxel-based morphometry and resting-state fMRI study. *PLoS One*. (2012) 7:e44758. doi: 10.1371/journal.pone.0044758
54. Censori B, Partziguian T, Manara O, Poloni M. Plasma homocysteine and severe white matter disease. *Neurol Sci.* (2007) 28:259–63. doi: 10.1007/s10072-007-0832-y
55. Vermeer SE, Van Dijk EJ, Koudstaal PJ, Oudkerk M, Hofman A, Clarke R, et al. Homocysteine, silent brain infarcts, and white matter lesions: The Rotterdam Scan Study. *Ann Neurol.* (2002) 51:285–9. doi: 10.1002/ana.10111
56. Wright CB, Paik MC, Brown TR, Stabler SP, Allen RH, Sacco RL, et al. Total homocysteine is associated with white matter hyperintensity volume: the Northern Manhattan Study. *Stroke.* (2005) 36:1207–11. doi: 10.1161/01.STR.0000165923.02318.22
57. Arvanitakis Z, Fleischman DA, Arfanakis K, Leurgans SE, Barnes LL, Bennett DA. Association of white matter hyperintensities and gray matter volume with cognition in older individuals without cognitive impairment. *Brain Struct Funct.* (2016) 221:2135–46. doi: 10.1007/s00429-015-1034-7
58. Wen W, Sachdev PS, Chen X, Anstey K. Gray matter reduction is correlated with white matter hyperintensity volume: a voxel-based morphometric study in a large epidemiological sample. *Neuroimage.* (2006) 29:1031–9. doi: 10.1016/j.neuroimage.2005.08.057
59. de Jager CA, Hogervorst E, Combrinck M, Budge MM. Sensitivity and specificity of neuropsychological tests for mild cognitive impairment, vascular cognitive impairment and Alzheimer's disease. *Psychol Med.* (2003) 33:1039–50. doi: 10.1017/S0033291703008031
60. Dichgans M, Leys D. Vascular cognitive impairment. *Circ Res.* (2017) 120:573–91. doi: 10.1161/CIRCRESAHA.116.308426
61. Ghafar MZAA, Miptah HN, O'Caoimh R. Cognitive screening instruments to identify vascular cognitive impairment: a systematic review. *Int J Geriatr Psychiatry.* (2019) 34:1114–27. doi: 10.1002/gps.5136
62. Nyenhuis DL, Gorelick PB, Geenen EJ, Smith CA, Gencheva E, Freels S, et al. The pattern of neuropsychological deficits in vascular cognitive impairment-no dementia (vascular CIND). *Clin Neuropsychol.* (2004) 18:41–9. doi: 10.1080/13854040490507145
63. Van Der Flier WM, Skoog I, Schneider JA, Pantoni L, Mok V, Chen CL, et al. Vascular cognitive impairment. *Nat Rev Disease Primers.* (2018) 4:1–16. doi: 10.1038/nrdp.2018.3
64. Huo Y, Li J, Qin X, Huang Y, Wang X, Gottesman RF, et al. Efficacy of folic acid therapy in primary prevention of stroke among adults with hypertension in China: the CSPPT randomized clinical trial. *JAMA.* (2015) 313:1325–35. doi: 10.1001/jama.2015.2274
65. Lattanzi S, Carbonari L, Pagliariccio G, Bartolini M, Cagnetti C, Viticchi G, et al. Neurocognitive functioning and cerebrovascular reactivity after carotid endarterectomy. *Neurology.* (2018) 90:e307–15. doi: 10.1212/WNL.0000000000004862
66. Blanco-Rojas L, Arboix A, Canovas D, Grau-Olivares M, Morera JCO, Parra O. Cognitive profile in patients with a first-ever lacunar infarct with and without silent lacunes: a comparative study. *BMC Neurol.* (2013) 13:1–7. doi: 10.1186/1471-2377-13-203
67. Grau-Olivares M, Arboix A, Junqué C., Arenaza-Urquijo EM, Rovira M, Bartrés-Faz D. Progressive gray matter atrophy in lacunar patients with vascular mild cognitive impairment. *Cerebrovasc Dis.* (2010) 30:157–66. doi: 10.1159/000316059
68. Nam K, Kwon H, Jeong H, Park J, Kwon H, Jeong S. Serum homocysteine level is related to cerebral small vessel disease in a healthy population. *Neurology.* (2019) 92:e317–25. doi: 10.1212/WNL.0000000000006816
69. Gao L, Ruan Z, Xiao Y, Xu H. Surface-based cortical morphometry, white matter hyperintensity, and multidomain cognitive performance in asymptomatic carotid stenosis. *Neuroscience.* (2021) 467:16–27. doi: 10.1016/j.neuroscience.2021.05.013
70. Gao L, Wang T, Qian T, Xiao F, Bai L, Zhang J, et al. Severe asymptomatic carotid stenosis is associated with robust reductions in homotopic functional connectivity. *Neuroimage Clin.* (2019) 24:102101. doi: 10.1016/j.nicl.2019.102101
71. Gao L, Xiao Y, Xu H. Gray matter asymmetry in asymptomatic carotid stenosis. *Hum Brain Mapp.* (2021) 1–12. doi: 10.1002/hbm.25645
72. Strauss E, Sherman EMS, Spreen O. *A Compendium of Neuropsychological Tests: Administration, Norms and Commentary*. New York, NY: Oxford University Press (2006).
73. Schmidt M. *Rey Auditory Verbal Learning Test: A Handbook*. Los Angeles, CA: Western Psychological Services (1996).

Conflict of Interest: The authors declare that the research was conducted in the absence of any commercial or financial relationships that could be construed as a potential conflict of interest.

Publisher's Note: All claims expressed in this article are solely those of the authors and do not necessarily represent those of their affiliated organizations, or those of the publisher, the editors and the reviewers. Any product that may be evaluated in this article, or claim that may be made by its manufacturer, is not guaranteed or endorsed by the publisher.

Copyright © 2021 Kong, Li, Chang, Liu, Jia, Gao and Ren. This is an open-access article distributed under the terms of the Creative Commons Attribution License (CC BY). The use, distribution or reproduction in other forums is permitted, provided the original author(s) and the copyright owner(s) are credited and that the original publication in this journal is cited, in accordance with accepted academic practice. No use, distribution or reproduction is permitted which does not comply with these terms.

frontiers in Neurology

ORIGINAL RESEARCH
published: 11 October 2021
doi: 10.3389/fneur.2021.745175

Increased Systemic Immune-Inflammation Index Is Associated With Delayed Cerebral Ischemia in Aneurysmal Subarachnoid Hemorrhage Patients

*Liuwei Chen†, Sajan Pandey†, Rui Shen, Yi Xu and Quanbin Zhang**

Department of Neurosurgery, Shanghai Tenth People's Hospital, Tongji University School of Medicine, Shanghai, China

OPEN ACCESS

Edited by:
Yuzhen Xu,
Tongji University, China

Reviewed by:
Damien Bouvier,
Centre Hospitalier Universitaire de Clermont-Ferrand, France
Verena Rass,
Medizinische Universität Innsbruck, Austria

***Correspondence:**
Quanbin Zhang
quanbinzhang@aliyun.com

†These authors have contributed equally to this work and share first authorship

Specialty section:
This article was submitted to Neurological Biomarkers, a section of the journal Frontiers in Neurology

Received: *21 July 2021*
Accepted: *06 September 2021*
Published: *11 October 2021*

Citation:
Chen L, Pandey S, Shen R, Xu Y and Zhang Q (2021) Increased Systemic Immune-Inflammation Index Is Associated With Delayed Cerebral Ischemia in Aneurysmal Subarachnoid Hemorrhage Patients. Front. Neurol. 12:745175. doi: 10.3389/fneur.2021.745175

Background: Systemic immune-inflammation index (SII) is a novel biomarker that reflects the state of a patient's inflammatory and immune status. This study aimed to determine the clinical significance of SII as a predictor of delayed cerebral ischemia (DCI) in patients with aneurysmal subarachnoid hemorrhage (SAH).

Methods: Retrospective data were collected from aneurysmal SAH patients who had been admitted to our hospital between January 2015 and October 2019. Both univariate and multivariate analyses were performed to investigate whether SII was an independent predictor of DCI. In addition, the receiver operating characteristic (ROC) curve and area under the curve (AUC) were also evaluated.

Results: There were 333 patients with aneurysmal SAH included in this study. Multivariate logistic analysis revealed that a modified Fisher grade 3 and 4 score [odds ratio (OR) = 7.851, 95% confidence interval (CI): 2.312–26.661, $P = 0.001$] and elevated SII (OR = 1.001, 95% CI: 1.001–1.002, $P < 0.001$) were independent risk factors for DCI. ROC curves showed that SII could predict DCI with an AUC of 0.860 (95% CI: 0.818–0.896, $P < 0.001$). The optimal cut-off value for SII to predict DCI was 1,424, and an SII $\geq$ 1,424 could predict DCI with a sensitivity of 93.1% and a specificity of 68.1%. Patients with higher SII value on admission tended to have higher incidence of acute hydrocephalus and DCI, greater modified Fisher and Hunt-Hess scales, and poorer outcomes.

Conclusions: SII is an independent predictor of DCI in patients with aneurysmal SAH. The SII system can be implemented in a routine clinical setting to help clinicians diagnose patients with high risk of DCI.

Keywords: systemic immune-inflammation index, delayed cerebral ischemia, inflammation, aneurysmal subarachnoid hemorrhage, hemorrhagic stroke

INTRODUCTION

Aneurysmal subarachnoid hemorrhage (SAH) is a critical cerebrovascular accident with high financial and disease (mortality and morbidity) burdens (1, 2). The mechanisms of cerebral injury following aneurysmal SAH remain largely unclear. However, it is believed that the risks of inflammation and thrombosis may be increased after aneurysmal SAH (3, 4).

Delayed cerebral ischemia (DCI) is often associated with poor functional outcomes in patients who survived the first-time SAH (5, 6). DCI can lead to poorer prognostic outcomes, greater disease severity, and higher mortality rates in patients with aneurysmal SAH (7). The pathophysiological characteristics of DCI include cerebral inflammation, microthrombosis, perfusion mismatch, spreading depolarization, and neurovascular uncoupling, all of which culminate in an infarction event (8). Therefore, identifying aneurysmal SAH patients who are at high risk of DCI can improve the survival outcomes of these patients.

Leukocytosis and platelet activation occur after aneurysmal SAH due to the stimulation of systemic immune reaction (9). Elevated inflammatory biomarkers, such as neutrophil-lymphocyte ratio (NLR) and platelet-lymphocyte ratio (PLR), have been employed to predict DCI development and functional outcome following aneurysmal SAH (10). Systemic immune-inflammation index (SII) is a novel biomarker reflecting the balance of inflammatory and immune status, which can be calculated as platelet count × neutrophil count/lymphocyte count. SII has recently been shown to exhibit a good prognostic value in predicting different malignant conditions (11–13). However, the ability of SII to predict DCI remains unclear. Therefore, this study aimed to evaluate the potential of SII as a predictive biomarker of DCI and to compare its effectiveness with other inflammatory biomarkers.

METHODS

Patients

We retrospectively collected and analyzed data from aneurysmal SAH patients who received treatment in our hospital between January 2015 to October 2019. The patients were included if they met the following criteria: (i) aneurysmal SAH confirmed by CT angiography and/or digital subtraction angiography, (ii) endovascular coiling or surgical clipping within 48 h following admission, and (iii) <24 h between symptom onset and hospital admission. The patients were excluded if they had (i) additional cerebral vascular disease (e.g., arteriovenous malformation or moyamoya disease), (ii) prior severe systemic disease (e.g., renal, hepatic, immune, hematologic, and/or infectious diseases) or history of malignancy, (iii) death within 3 days of admission, and (iv) missing data. Ethical approval for this study was obtained from the institutional ethics review board.

Demographical, Clinical, and Laboratory Parameters

The collected data included age, gender, medical history, radiological characteristics (modified Fisher grade, acute hydrocephalus), clinical status at admission (Hunt-Hess grade), aneurysm location and size, treatment approach (coiling or clipping), and DCI occurrence. Acute hydrocephalus was characterized as the presence of hydrocephalus symptoms and ventricle enlargement (bicaudate index $\geq$ 0.20 on CT scan) within 72 h following aneurysmal SAH. According to the AHA/ASA (14), DCI was defined as new focal neurological impairment or a decrease of two points on the Glasgow Coma Scale, which did not appear immediately following aneurysm occlusion. The management of SAH patients and DCI was carried out according to the SAH management guideline (15, 16). In sedated or poor-grade SAH patients, transcranial doppler ultrasonography is routinely used to detect vasospasm and DCI (16). Functional outcomes were evaluated using the modified Rankin Scale (mRS) score at 3 months. Data were obtained by telephone or outpatient interview. For analysis purposes, the data were dichotomized as follows: modified Fisher scale ("1–2" and "3–4"), Hunt-Hess scale ("1–3" and "4–5"), aneurysm location ("anterior cerebral artery," "internal cerebral artery," "middle cerebral artery," and "vertebrobasilar artery"), aneurysm size (">10 mm," "5–10 mm," and "<5 mm"), treatment approach ("clipping" and "coiling"), and functional outcome (">2" and "≤2"). Blood specimens were collected before treatment at admission and analyzed by an autoanalyzer (XE-2100, Sysmex Company, Japan) within 1 h after venipuncture. SII was calculated as platelet count × neutrophil count/lymphocyte count; NLR was calculated as neutrophil count/lymphocyte count, and PLR was calculated as platelet count/lymphocyte count.

Statistical Analysis

All statistical tests were conducted with SPSS v21.0 and Medcalc v19.1. Continuous variables were expressed as median (interquartile range, IQR), while categorical variables were presented as numbers (percentages). Mann-Whitney U test was used to analyze the continuous univariate variables, whereas χ^2-test or Fisher exact-test was employed to assess the categorical univariate variables. Potential predictors of DCI were examined through analysis of multicollinearity by stepwise regression. Significant univariate variables in univariate logistic analysis ($P < 0.10$) were inputted into a multivariate regression model. Receiver operating characteristic (ROC) curves were constructed to determine the discriminative abilities of SII, NLR, and PLR for predicting DCI. Area under the curve (AUC) was subsequently evaluated. The ROC curves were also employed to establish the optimal cut-off point at which the sum of the sensitivity and specificity values was the highest. The discriminative performances of the NLR, PLR, and SII were compared using the DeLong test. A two-sided P-value of <0.05 was deemed statistically significant.

RESULTS

Three hundred thirty-three aneurysmal SAH patients, including 205 (61.6%) female and 128 (38.4%) male, were enrolled into this study (**Figure 1**). The median age at the time of admission was 59 years (range, 51–66). In addition, 81 (24.3%) and 252

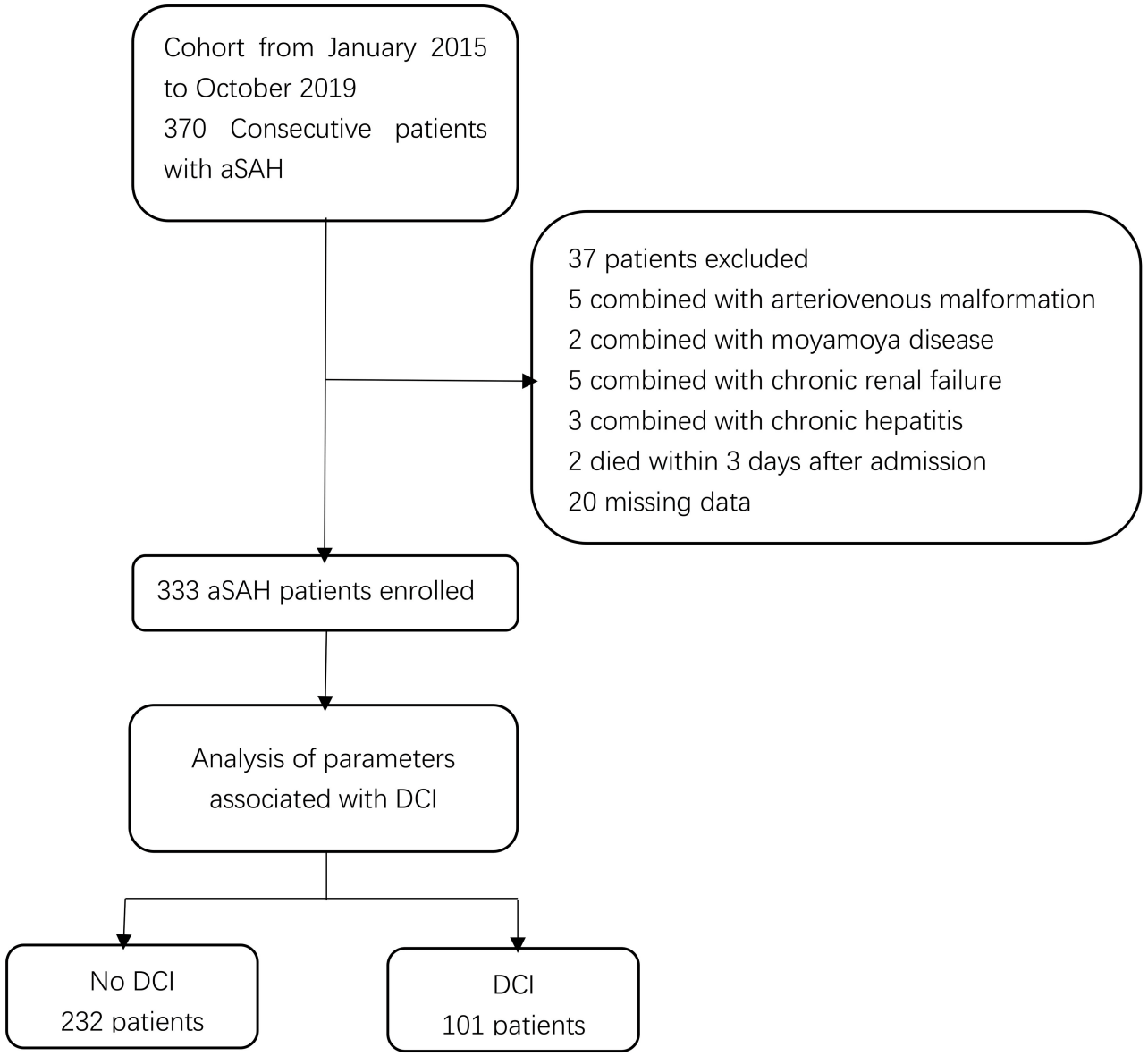

FIGURE 1 | Flow chart of study patients. aSAH, aneurysmal subarachnoid hemorrhage; DCI, delayed cerebral ischemia.

(75.7%) patients received surgical clipping and endovascular coiling, respectively. Furthermore, DCI occurred in 101 (30.3%) patients.

All patients were assigned to two groups based on the occurrence of DCI. Univariate analysis revealed that aneurysmal SAH patients with DCI tended to have higher incidence of acute hydrocephalus, to have greater modified Fisher and Hunt-Hess scores, and to be treated by surgical clipping (**Table 1**). Moreover, the red blood cell count, hemoglobin, and lymphocyte percentage were remarkably lower in patients with DCI than those without DCI (**Table 1**). Meanwhile, the white blood cell count, c-reactive protein (CRP), and SII value were markedly higher (**Table 1**). Multivariate logistic regression analysis demonstrated that modified Fisher grade 3 and 4 score [odds ratio (OR) = 7.851, 95% confidence interval (CI): 2.312–26.661, $P = 0.001$] and SII (OR = 1.001, 95% CI: 1.001–1.002, $P < 0.001$) were independent risk factors for DCI development (**Table 2**). ROC curves showed that SII could predict DCI with an AUC of 0.860 (95% CI: 0.818–0.896, $P < 0.001$; **Figure 2**). The AUC for SII was obviously greater compared to PLR, but the difference was not significant between NLR and SII (**Table 3**). The optimal cut-off value for SII to predict DCI was 1,424, and an SII $\geq$ 1,424 could predict DCI with a sensitivity of 93.1% (95% CI: 86.2–97.2%), a specificity of 68.1% (95% CI: 61.7–74.1%), a positive predictive value of 56.0% (95% CI: 51.1–60.7%), and a negative predictive value of 95.8% (95% CI: 91.7–97.9%).

TABLE 1 | Comparison of demographic, clinical, and laboratory data in patients with aneurysmal SAH according to the development of delayed cerebral ischemia.

Variable	Total ($n = 333$)	DCI		*P*-value
		Yes ($n = 101$)	No ($n = 232$)	
Age (years)	59 (51–66)	60 (53–67)	59 (50–66)	0.288
Sex (female)	205 (61.6%)	56 (55.4%)	149 (64.2%)	0.130
Hypertension	189 (56.8%)	55 (54.5%)	134 (57.8%)	0.576
Diabetes	45 (13.5%)	13 (12.9%)	32 (13.8%)	0.821
Hunt-Hess grade				<0.001
Grade 1,2,3	235 (70.6%)	37 (36.6%)	198 (85.3%)	
Grade 4,5	98 (29.4%)	64 (63.4%)	34 (14.7%)	
Modified Fisher grade				<0.001
Grade 1,2	101 (30.3%)	4 (4.0%)	97 (41.8%)	
Grade 3,4	232 (69.7%)	97 (96.0%)	135 (58.2%)	
Location				0.118
ACA	115 (34.5%)	35 (34.7%)	80 (34.5%)	
ICA	123 (36.9%)	33 (32.7%)	90 (38.8%)	
MCA	50 (15.0%)	22 (21.8%)	28 (12.1%)	
VBA	45 (13.5%)	11 (10.9%)	34 (14.7%)	
Size (mm)				0.272
<5	193 (58.0%)	53 (52.5%)	140 (60.3%)	
5–10	114 (34.2%)	41 (40.6%)	73 (31.5%)	
>10	26 (7.8%)	7 (6.9%)	19 (8.2%)	
Treatment				0.001
Coiling	252 (75.7%)	64 (63.4%)	188 (81.0%)	
Clipping	81 (24.3%)	37 (36.6%)	44 (19.0%)	
Acute hydrocephalus	48 (14.4%)	31 (30.7%)	17 (7.3)	<0.001
RBC, $\times 10^9$	4.1 (3.6–4.4)	3.9 (3.2–4.4)	4.1 (3.7–4.4)	0.023
Hemoglobin	122 (110–135)	118 (100–134)	124 (114–135)	0.007
WBC, $\times 10^9$	9.7 (7.7–12.2)	11.9 (10.3–15.1)	8.6 (7.4–11.3)	<0.001
Neutrophil %	83.6 (78.0–87.8)	84.4 (78.4–89.3)	83.0 (77.5–87.5)	0.115
Lymphocyte %	10.7 (8.0–15.7)	9.8 (6.5–15.7)	11.6 (8.0–15.7)	0.073
Platelet, $\times 10^9$	183 (150–227)	187 (157–232)	181 (146–224)	0.129
CRP	7.1 (2.6–17.3)	17.0 (5.8–30.0)	5.6 (2.1–11.1)	<0.001
SII	1,445 (821–2,187)	2,260 (1,747–3,218)	1,061 (737–1,671)	<0.001

Data are n (%), or median (interquartile).
DCI, delayed cerebral ischemia; ACA, anterior cerebral artery; ICA, internal carotid artery; MCA, middle cerebral artery; VBA, vertebrobasilar artery; RBC, red blood cell; WBC, white blood cell; CRP, c-reactive protein; SII, systemic immune-inflammation index.

TABLE 2 | The univariate and multivariate logistic analysis of predictors for delayed cerebral ischemia.

Predictors	Univariate analysis		Multivariate analysis	
	OR (95% CI)	*P*-value	OR (95% CI)	*P*-value
Age	1.008 (0.989–1.028)	0.401		
Sex	1.443 (0.897–2.321)	0.131		
Hypertension	0.874 (0.546–1.400)	0.576		
Diabetes	0.923 (0.462–1.844)	0.821		
Hunt-Hess grade	10.073 (5.845–17.360)	<0.001	1.635 (0.678–3.946)	0.274
Modified Fisher grade	17.424 (6.199–48.975)	<0.001	7.851 (2.312–26.661)	**0.001**
Location	1.020 (0.810–1.283)	0.868		
Size	1.174 (0.818–1.684)	0.385		
Clipping	2.470 (1.467–4.160)	0.001	1.685 (0.780–3.639)	0.184
Acute hydrocephalus	5.601 (2.924–10.730)	<0.001	1.689 (0.656–4.346)	0.277
RBC, $\times 10^9$	0.558 (0.376–0.829)	0.004	0.665 (0.205–2.153)	0.496
Hemoglobin	0.981 (0.969–0.995)	0.006	0.997 (0.961–1.035)	0.886
WBC, $\times 10^9$	1.286 (1.192–1.387)	<0.001	1.099 (0.979–1.234)	0.109
Neutrophil %	1.018 (0.989–1.049)	0.225		
Lymphocyte %	0.996 (0.992–1.001)	0.076	1.034 (0.984–1.086)	0.189
Platelet, $\times 10^9$	1.021 (0.986–1.054)	0.236		
CRP	1.025 (1.015–1.036)	<0.001	1.011 (0.998–1.025)	0.109
SII	1.001 (1.001–1.002)	<0.001	1.001 (1.001–1.002)	**<0.001**

OR, odds ratio; CI, confidence interval.
P < 0.05, significant P values are bold.

Patients were further assigned to two groups based on the SII threshold (**Table 4**). Patients with an SII level of ≥1,424 had greater modified Fisher and Hunt-Hess scores as well as higher incidence of acute hydrocephalus and DCI. The functional outcome at 3 months was comparatively poorer in patients with SII ≥ 1,424 than those with SII < 1,424 [mRS score 3–6: SII ≥ 1,424 = 77/168 (45.8%) vs. SII < 1,424 = 15/165 (9.1%); $P < 0.001$]. Furthermore, the risk of DCI was also associated with SII value (SII ≥ 1,424 vs. SII < 1,424, OR: 17.793; 95% CI: 6.948–45.564; $P < 0.001$) as a dichotomous variable in the logistic regression model (**Table 5**).

DISCUSSION

DCI is the leading determinant of poor functional outcomes in patients who have survived after an aneurysmal SAH. We evaluated the SII value for its potential as a novel biomarker for DCI prediction in aneurysmal SAH patients. Our findings indicated that aneurysmal SAH patients with an SII value of ≥1,424 on admission tended to have a worse neurological status and more severe clinical course (e.g., acute hydrocephalus), DCI, and poorer functional outcomes. The SII value on admission was independently associated with the occurrence of DCI. ROC curve analysis demonstrated that SII could predict the occurrence of DCI (AUC = 0.860), suggesting that the SII value on admission may be a promising predictive biomarker for DCI in aneurysmal SAH patients (17).

Aneurysmal SAH is associated with systemic inflammatory response syndrome. Bleeding in the subarachnoid space triggers a rapid activation of the inflammatory cascades, leading to leukocytosis and platelet aggregation (9, 18, 19). Patients with a higher Hunt-Hess grade tended to have obvious alterations in these parameters, indicating that the degree of platelet aggregation and inflammation is positively correlated with early brain injury. Inflammation and thrombotic formation

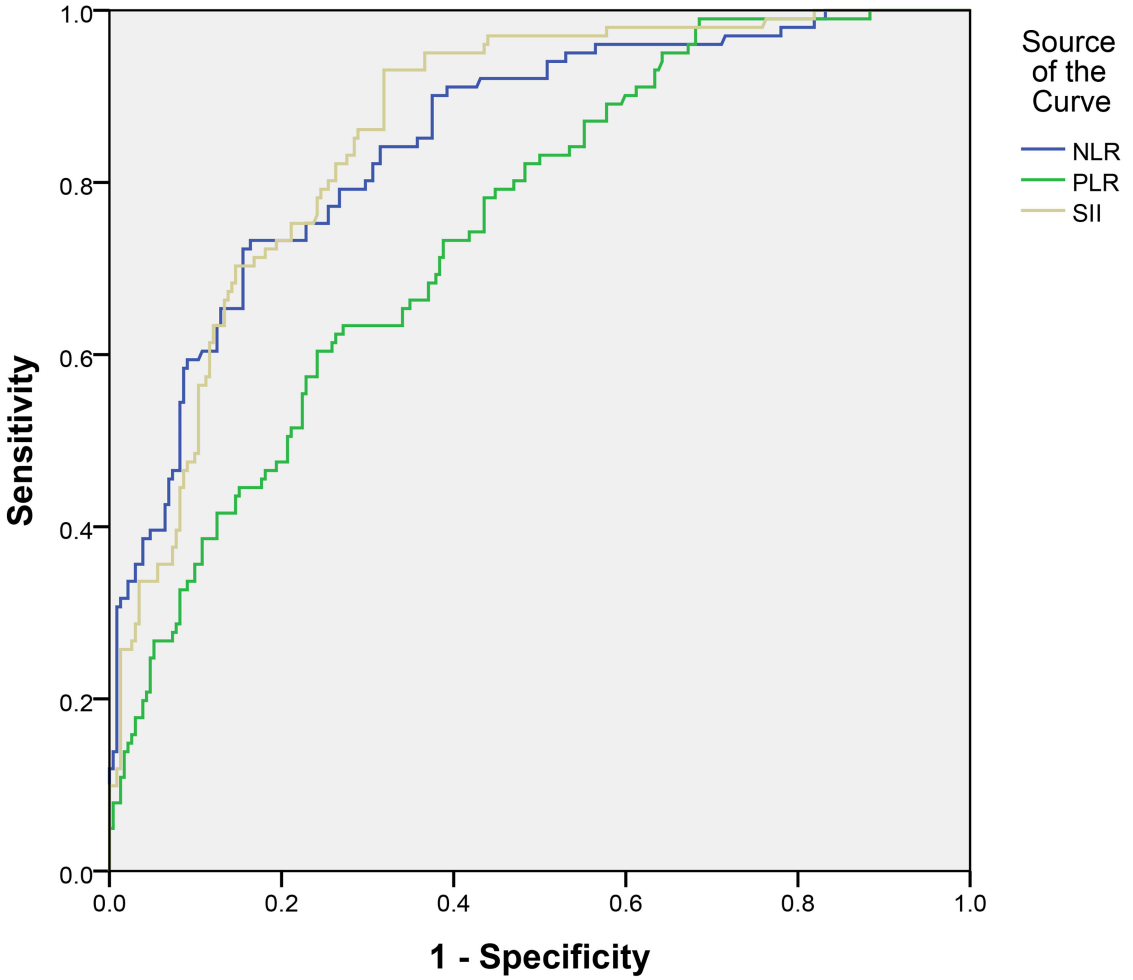

FIGURE 2 | Discriminative ability of the SII, NLR, and PLR for DCI. SII, systemic immune-inflammation index; NLR, neutrophil-lymphocyte ratio; PLR, platelet-lymphocyte ratio.

TABLE 3 | Diagnostic values of SII, NLR, and PLR for delayed cerebral ischemia.

Variable	AUC (95% CI)	*P*-value[a]
SII	0.860 (0.818–0.896)	Reference
NLR	0.848 (0.805–0.885)	0.3230
PLR	0.745 (0.695–0.791)	<0.001

NLR, neutrophil to lymphocyte ratio; PLR, platelet to lymphocyte ratio; AUC, area under the curve.

[a]*The discriminative performances of SII vs. NLR and SII vs. PLR were compared using the DeLong test.*

also participate in the pathophysiological process following aneurysmal SAH (18, 20) and can increase the susceptibility to DCI (21). SII is calculated as platelet count × neutrophil count/lymphocyte count, which reflects the balance of a person's inflammatory and immune status. An elevated SII value represents both pro-thrombotic (higher platelet counts) and immune dysregulation (higher neutrophil counts and lower lymphocyte counts) states. Collectively, our study reveals that SII is an independent risk factor for DCI development, which adds to the growing evidence that inflammation and thrombotic formation participate in the pathogenesis of DCI.

Previous studies have shown the clinical significance of SII in hemorrhagic stroke. An increased SII obtained at admission or obtained at 1 day after initial hemorrhage is associated with poor functional outcomes in patients with spontaneous intracerebral hemorrhage (22, 23). However, secondary intracerebral hemorrhage, including SAH, was ruled out in these studies. Yun et al. have performed an analysis for SII in patients with SAH. They found that an elevated SII at admission was an independent risk factor of poor functional outcomes in SAH patients (24). However, it is still unknown whether SII could predict the occurrence of DCI in SAH patients. This study is the first to establish an association between SII and DCI.

TABLE 4 | Baseline characteristics of included SAH patients dichotomized to the identified SII threshold (1,424).

Variable	SII ≥ 1424 $n = 168$	SII < 1,424 $n = 165$	*P*-value
Age (years)	59 (50–66)	59 (53–67)	0.654
Sex (women)	106 (63.1%)	99 (60.0%)	0.562
Hypertension	95 (56.5%)	94 (57.0%)	0.938
Diabetes	23 (13.7%)	22 (13.3%)	0.924
Hunt-Hess grade			<0.001
Grade 1,2,3	92 (54.8%)	143 (86.7%)	
Grade 4,5	76 (45.2%)	22 (13.3%)	
Modified Fisher grade			<0.001
Grade 1,2	31 (18.5%)	70 (42.4%)	
Grade 3,4	137 (81.5%)	95 (57.6%)	
Location			0.504
ACA	60 (35.7%)	55 (33.3%)	
ICA	56 (33.3%)	67 (40.6%)	
MCA	26 (15.5%)	24 (14.5%)	
VBA	26 (15.5%)	19 (11.5%)	
Size (mm)			0.101
<5	91 (54.2%)	102 (61.8%)	
5–10	59 (35.1%)	55 (33.3%)	
>10	18 (10.7%)	8 (4.8%)	
Acute hydrocephalus	40 (23.8%)	8 (4.8%)	<0.001
DCI	94 (56.0%)	7 (4.2%)	<0.001
mRS			<0.001
0–2	91 (54.2%)	150 (90.9%)	
3–6	77 (45.8%)	15 (9.1%)	

Data are n (%), or median (interquartile).
mRS, modified Rankin scale.

TABLE 5 | Associations of the SII with delayed cerebral ischemia.

	Univariate analysis		Multivariate analysis	
	OR (95% CI)	*P*-value	OR (95% CI)	*P*-value
SII[a]	1.001 (1.001–1.002)	<0.001	1.001 (1.001–1.002)	<0.001
SII[b]	28.672 (12.678–68.840)	<0.001	17.793 (6.948–45.564)	<0.001

Multivariate logistic regression analysis with adjustment for Hunt-Hess grade, modified Fisher grade, treatment methods, acute hydrocephalus, RBC, hemoglobin, WBC, lymphocyte %, and CRP.
[a]*SII as a continuous variable.*
[b]*SII as a dichotomous variable.*

Previous research has shown that other inflammatory markers, such as CRP, total leukocyte count, PLR, and NLR, are associated with the development of DCI (10, 25). However, in our study, CRP and total leukocyte count were not independent risk factors for DCI. In the ROC analysis, the AUC for SII was larger than those for NLR and PLR, though the difference was not significant between NLR and SII. SII may be considered as a combination of NLR and PLR because the components of each parameter are encompassed within the SII. When SII was set as a dichotomous variable, we found that the SII value of ≥1,424 was associated with a 17.79-fold increased risk toward DCI, which implied its strong predictive impact. SII is a novel prognostic biomarker in the area of cancer research (11–13). It has several advantages over other inflammation biomarkers. The measurement of SII is affordable, rapid, and widely available in routine laboratory testing. It reflects both the inflammatory and thrombotic status of patients. Additionally, due to the fact that this index is derived from a ratio of two fitted parameters, SII is likely more reliable than other parameters (26).

We postulate here a few reasons why the SII value is elevated in aneurysmal SAH patients with DCI. Firstly, a high SII value can reflect a severe inflammatory response following aneurysmal SAH. Neuro-inflammation may cause disruption in the blood-brain barrier, synaptic injury, neuronal death, white matter injury, and loss of long-term potentiation, all of which ultimately lead to brain injury (27). Several inflammatory molecules and signaling pathways have been found to participate in the development of vasospasm (28). Secondly, an elevated SII value reflects a prothrombotic state and stronger aggregation ability of platelet. Platelet aggregation may induce micro-thrombosis, ischemia, and cerebral tissue death after aneurysmal SAH (29). Thirdly, an elevated SII value also reflects an immune dysregulation state (27, 30). Activation of an innate immune response, which is characterized by increased neutrophil counts, may lead to secondary brain injury after SAH. Microglia cells are part of the brain's innate immune system. Inflammatory reaction following an aneurysmal SAH can trigger microglia cells in the microvasculature, thereby leading to neuronal cell death (31). This evidence suggests that an elevated SII represents a severe inflammation response, a pro-thrombotic state, and an immune dysregulation state, making it easier to understand why an elevated SII value may be associated with the development of DCI. However, more studies are warranted to validate this hypothesis.

The use of transcranial doppler ultrasonography, CT perfusion imaging, and electroencephalography is recommended for monitoring DCI (16). However, compared with these monitoring methods, SII measurement is more convenient and widely available. We postulate that an elevated SII represents a severe inflammation response, a pro-thrombotic state, and an immune dysregulation state. The SII can be used in clinical settings to estimate a patient's susceptibility to DCI and help clinicians recognize patients who are at high risk. It can also guide decisions about which patients should receive prophylaxis against DCI. For example, several studies have shown the safety and efficacy of antiplatelet therapy in SAH (32–34). Antiplatelet drugs with both an anti-platelet and an anti-inflammatory action can reduce their risk of DCI. It may be appropriate to start antiplatelet therapy for patients with higher SII, as these patients are likely to be in a severe inflammation response and a pro-thrombotic state.

Nevertheless, there are some limitations that need to be addressed. Firstly, this was a single-center retrospective observational study. Therefore, it may prone to bias and limit the

generalizability of the findings. Secondly, we did not assess the changes in SII values over time after hospital admission. Thirdly, the definition of DCI, especially as applied to patients who are sedated or comatose, may exclude patients who have actually developed DCI. Fourthly, we did not explore the relationship between SII and functional outcomes in patients with aneurysmal SAH. Clinical observational studies may overestimate the causality between the SII and DCI, and a prospective, multi-center study is needed to verify our findings in the near future.

CONCLUSION

SII is an independent predictor of DCI in patients with aneurysmal SAH. The SII value of ≥1,424 on admission may guide clinicians to screen for patients who are at high risk for DCI.

DATA AVAILABILITY STATEMENT

The raw data supporting the conclusions of this article will be made available by the authors, without undue reservation.

ETHICS STATEMENT

The studies involving human participants were reviewed and approved by The Ethics Committee of the Shanghai Tenth People's Hospital. The patients/participants provided their written informed consent to participate in this study.

AUTHOR CONTRIBUTIONS

QZ: conception, design, and administrative support. LC and SP: provision of study materials or patients. SP: collection and assembly of data. RS and YX: data analysis and interpretation. All authors manuscript writing and final approval of manuscript.

REFERENCES

1. Galea J, Ogungbenro K, Hulme S, Patel H, Scarth S, Hoadley M, et al. Reduction of inflammation after administration of interleukin-1 receptor antagonist following aneurysmal subarachnoid hemorrhage: results of the Subcutaneous Interleukin-1Ra in SAH (SCIL-SAH) study. *J Neurosurg.* (2018) 128:515–23. doi: 10.3171/2016.9.JNS16615
2. Ridwan S, Urbach H, Greschus S, von Hagen J, Esche J, Boström A. Health care costs of spontaneous aneurysmal subarachnoid hemorrhage for rehabilitation, home care, and in-hospital treatment for the first year. *World Neurosurg.* (2017) 97:495–500. doi: 10.1016/j.wneu.2016.09.123
3. Sabri M, Ai J, Lakovic K, D'Abbondanza J, Ilodigwe D, Macdonald RL. Mechanisms of microthrombi formation after experimental subarachnoid hemorrhage. *Neuroscience.* (2012) 224:26–37. doi: 10.1016/j.neuroscience.2012.08.002
4. Zheng VZ, Wong GKC. Neuroinflammation responses after subarachnoid hemorrhage: a review. *J Clin Neurosci.* (2017) 42:7–11. doi: 10.1016/j.jocn.2017.02.001
5. Haegens NM, Gathier CS, Horn J, Coert BA, Verbaan D, van den Bergh WM. Induced hypertension in preventing cerebral infarction in delayed cerebral ischemia after subarachnoid hemorrhage. *Stroke.* (2018) 49:2630–6. doi: 10.1161/STROKEAHA.118.022310
6. Platz J, Güresir E, Wagner M, Seifert V, Konczalla J. Increased risk of delayed cerebral ischemia in subarachnoid hemorrhage patients with additional intracerebral hematoma. *J Neurosurg.* (2017) 126:504–10. doi: 10.3171/2015.12.JNS151563
7. Duan W, Pan Y, Wang C, Wang Y, Zhao X, Wang Y, et al. Risk factors and clinical impact of delayed cerebral ischemia after aneurysmal subarachnoid hemorrhage: analysis from the China National Stroke Registry. *Neuroepidemiology.* (2018) 50:128–36. doi: 10.1159/000487325
8. Foreman B. The pathophysiology of delayed cerebral ischemia. *J Clin Neurophysiol.* (2016) 33:174–82. doi: 10.1097/WNP.0000000000000273
9. Kasius KM, Frijns CJ, Algra A, Rinkel GJ. Association of platelet and leukocyte counts with delayed cerebral ischemia in aneurysmal subarachnoid hemorrhage. *Cerebrovasc Dis.* (2010) 29:576–83. doi: 10.1159/000306645
10. Tao C, Wang J, Hu X, Ma J, Li H, You C. Clinical value of neutrophil to lymphocyte and platelet to lymphocyte ratio after aneurysmal subarachnoid hemorrhage. *Neurocrit Care.* (2017) 26:393–401. doi: 10.1007/s12028-016-0332-0
11. Shi H, Jiang Y, Cao H, Zhu H, Chen B, Ji W. Nomogram based on systemic immune-inflammation index to predict overall survival in gastric cancer patients. *Dis Markers.* (2018) 2018:1787424. doi: 10.1155/2018/1787424
12. Xie QK, Chen P, Hu WM, Sun P, He WZ, Jiang C, et al. The systemic immune-inflammation index is an independent predictor of survival for metastatic colorectal cancer and its association with the lymphocytic response to the tumor. *J Transl Med.* (2018) 16:273. doi: 10.1186/s12967-018-1638-9
13. Zhang W, Wang R, Ma W, Wu Y, Maskey N, Guo Y, et al. Systemic immune-inflammation index predicts prognosis of bladder cancer patients after radical cystectomy. *Ann Transl Med.* (2019) 7:431. doi: 10.21037/atm.2019.09.02
14. Vergouwen MD, Vermeulen M, van Gijn J, Rinkel GJ, Wijdicks EF, Muizelaar JP, et al. Definition of delayed cerebral ischemia after aneurysmal subarachnoid hemorrhage as an outcome event in clinical trials and observational studies: proposal of a multidisciplinary research group. *Stroke.* (2010) 41:2391–5. doi: 10.1161/STROKEAHA.110.589275
15. Connolly ES, Rabinstein AA, Carhuapoma JR, Derdeyn CP, Dion J, Higashida RT, et al. Guidelines for the management of aneurysmal subarachnoid hemorrhage: a guideline for healthcare professionals from the American Heart Association/american Stroke Association. *Stroke.* (2012) 43:1711–37. doi: 10.1161/STR.0b013e3182587839
16. Diringer MN, Bleck TP, Claude Hemphill J, Menon D, Shutter L, Vespa P, et al. Critical care management of patients following aneurysmal subarachnoid hemorrhage: recommendations from the Neurocritical Care Society's Multidisciplinary Consensus Conference. *Neurocrit Care.* (2011) 15:211–40. doi: 10.1007/s12028-011-9605-9
17. Ray P, Le Manach Y, Riou B, Houle TT. Statistical evaluation of a biomarker. *Anesthesiology.* (2010) 112:1023–40. doi: 10.1097/ALN.0b013e3181d47604
18. Frontera JA, Provencio JJ, Sehba FA, McIntyre TM, Nowacki AS, Gordon E, et al. The role of platelet activation and inflammation in early brain injury following subarachnoid hemorrhage. *Neurocrit Care.* (2017) 26:48–57. doi: 10.1007/s12028-016-0292-4
19. Sehba FA, Mostafa G, Friedrich V, Bederson JB. Acute microvascular platelet aggregation after subarachnoid hemorrhage. *J Neurosurg.* (2005) 102:1094–100. doi: 10.3171/jns.2005.102.6.1094
20. Romano JG, Rabinstein AA, Arheart KL, Nathan S, Campo-Bustillo I, Koch S, et al. Microemboli in aneurysmal subarachnoid hemorrhage. *J Neuroimaging.* (2008) 18:396–401. doi: 10.1111/j.1552-6569.2007.00215.x
21. McMahon CJ, Hopkins S, Vail A, King AT, Smith D, Illingworth KJ, et al. Inflammation as a predictor for delayed cerebral ischemia after aneurysmal subarachnoid haemorrhage. *J Neurointerv Surg.* (2013) 5:512–7. doi: 10.1136/neurintsurg-2012-010386
22. Li Y, Wen D, Cui W, Chen Y, Zhang F, Yuan M, et al. The prognostic value of the acute phase systemic immune-inflammation index in patients with intracerebral hemorrhage. *Front Neurol.* (2021) 12:628557. doi: 10.3389/fneur.2021.628557

23. Trifan G, Testai FD. Systemic Immune-Inflammation (SII) index predicts poor outcome after spontaneous supratentorial intracerebral hemorrhage. *J Stroke Cerebrovasc Dis.* (2020) 29:105057. doi: 10.1016/j.jstrokecerebrovasdis.2020.105057
24. Yun S, Yi HJ, Lee DH, Sung JH. Systemic inflammation response index and systemic immune-inflammation index for predicting the prognosis of patients with aneurysmal subarachnoid hemorrhage. *J Stroke Cerebrovasc Dis.* (2021) 30:105861. doi: 10.1016/j.jstrokecerebrovasdis.2021.105861
25. Srinivasan A, Aggarwal A, Gaudihalli S, Mohanty M, Dhandapani M, Singh H, et al. Impact of early leukocytosis and elevated high-sensitivity C-reactive protein on delayed cerebral ischemia and neurologic outcome after subarachnoid hemorrhage. *World Neurosurg.* (2016) 90:91–5. doi: 10.1016/j.wneu.2016.02.049
26. Balta S, Ozturk C. The platelet-lymphocyte ratio: a simple, inexpensive and rapid prognostic marker for cardiovascular events. *Platelets.* (2015) 26:680–1. doi: 10.3109/09537104.2014.979340
27. Provencio JJ. Inflammation in subarachnoid hemorrhage and delayed deterioration associated with vasospasm: a review. *Acta Neurochir Suppl.* (2013) 115:233–8. doi: 10.1007/978-3-7091-1192-5_42
28. Miller BA, Turan N, Chau M, Pradilla G. Inflammation, vasospasm, and brain injury after subarachnoid hemorrhage. *Biomed Res Int.* (2014) 2014:384342. doi: 10.1155/2014/384342
29. Friedrich V, Flores R, Sehba FA. Cell death starts early after subarachnoid hemorrhage. *Neurosci Lett.* (2012) 512:6–11. doi: 10.1016/j.neulet.2012.01.036
30. el-Hag A, Clark RA. Immunosuppression by activated human neutrophils. Dependence on the myeloperoxidase system. *J Immunol (Baltimore, Md: 1950).* (1987) 139:2406–13.
31. Atangana E, Schneider UC, Blecharz K, Magrini S, Wagner J, Nieminen-Kelhä M, et al. Intravascular inflammation triggers intracerebral activated microglia and contributes to secondary brain injury after experimental subarachnoid hemorrhage (eSAH). *Transl Stroke Res.* (2017) 8:144–56. doi: 10.1007/s12975-016-0485-3
32. Nagahama Y, Allan L, Nakagawa D, Zanaty M, Starke RM, Chalouhi N, et al. Dual antiplatelet therapy in aneurysmal subarachnoid hemorrhage: association with reduced risk of clinical vasospasm and delayed cerebral ischemia. *J Neurosurg.* (2018) 129:702–10. doi: 10.3171/2017.5.JNS17831
33. Darkwah Oppong M, Gembruch O, Pierscianek D, Köhrmann M, Kleinschnitz C, Deuschl C, et al. Post-treatment antiplatelet therapy reduces risk for delayed cerebral ischemia due to aneurysmal subarachnoid hemorrhage. *Neurosurgery.* (2019) 85:827–33. doi: 10.1093/neuros/nyy550
34. Shimamura N, Naraoka M, Matsuda N, Ohkuma H. Safety of preprocedural antiplatelet medication in coil embolization of ruptured cerebral aneurysms at the acute stage. *Interv Neuroradiol.* (2014) 20:413–7. doi: 10.15274/INR-2014-10035

Conflict of Interest: The authors declare that the research was conducted in the absence of any commercial or financial relationships that could be construed as a potential conflict of interest.

Publisher's Note: All claims expressed in this article are solely those of the authors and do not necessarily represent those of their affiliated organizations, or those of the publisher, the editors and the reviewers. Any product that may be evaluated in this article, or claim that may be made by its manufacturer, is not guaranteed or endorsed by the publisher.

Copyright © 2021 Chen, Pandey, Shen, Xu and Zhang. This is an open-access article distributed under the terms of the Creative Commons Attribution License (CC BY). The use, distribution or reproduction in other forums is permitted, provided the original author(s) and the copyright owner(s) are credited and that the original publication in this journal is cited, in accordance with accepted academic practice. No use, distribution or reproduction is permitted which does not comply with these terms.

frontiers in Neurology

ORIGINAL RESEARCH
published: 13 October 2021
doi: 10.3389/fneur.2021.738148

Association Between *CST3* Gene Polymorphisms and Large-Artery Atherosclerotic Stroke

Yarong Ding[1,2,3,4], *Zhe Xu*[1,2,3,4], *Yuesong Pan*[1,2,3,4], *Xia Meng*[1,2,3,4], *Xianglong Xiang*[1,2,3,4], *Hao Li*[1,2,3,4], *Liping Liu*[1,2,3,4] *and Yongjun Wang*[1,2,3,4*] *on behalf of the CNSR-III Study Group*

[1] Department of Neurology, Beijing Tiantan Hospital, Capital Medical University, Beijing, China, [2] China National Clinical Research Center for Neurological Diseases, Beijing, China, [3] Center of Stroke, Beijing Institute for Brain Disorders, Beijing, China, [4] Beijing Key Laboratory of Translational Medicine for Cerebrovascular Disease, Beijing, China

Objective: Cystatin C, a marker of atherosclerosis, is encoded by *CST3*. We aimed to evaluate whether two single-nucleotide polymorphisms (SNPs) of *CST3* are correlated with large-artery atherosclerotic stroke (LAAS) and prognosis.

Methods: This subgroup analysis of the Third China National Stroke Registry (CNSR-III) enrolled acute ischemic stroke (AIS) patients within 7 days from August 2015 to March 2018 in China. rs13038305 and rs911119 of *CST3* were selected based on the strong association with cystatin C concentration.

Results: Two loci of *CST3* (rs13038305 and rs911119) were analyzed in 3,833 ischemic stroke patients. Carriers of T allele in rs13038305 and C allele in rs911119 tend to have lower serum cystatin C levels ($p < 0.05$). Compared with C/C as a reference in rs13038305, odds ratio (OR) of T/T was 0.486, 95% CI 0.237–0.994, $p = 0.048$. Per C allele of rs13038305 also showed an increased level of low-density lipoprotein cholesterol (LDL-C), β (95% CI) was 1.335 (1.008–1.250), $p = 0.044$. No correlation was found between the selected SNPs and stroke prognosis (functional outcome, recurrence, and mortality).

Conclusions: Carriers of the T allele in rs13038305 tend to have a lower proportion of LAAS. rs13038305 and rs911119 polymorphisms were likely to affect cystatin C concentration independently of kidney function.

Keywords: cystatin C, polymorphism, biomarker, ischemic stroke, prognosis

OPEN ACCESS

Edited by:
Wen-Jun Tu,
Chinese Academy of Medical Sciences and Peking Union Medical College, China

Reviewed by:
Huihui Liu,
Second Affiliated Hospital of Soochow University, China
Chenghe Fan,
Peking University First Hospital, China

***Correspondence:**
Yongjun Wang
yongjunwang@ncrcnd.org.cn

Specialty section:
This article was submitted to Neurological Biomarkers, a section of the journal Frontiers in Neurology

Received: *08 July 2021*
Accepted: *07 September 2021*
Published: *13 October 2021*

Citation:
Ding Y, Xu Z, Pan Y, Meng X, Xiang X, Li H, Liu L and Wang Y (2021) Association Between CST3 Gene Polymorphisms and Large-Artery Atherosclerotic Stroke. Front. Neurol. 12:738148. doi: 10.3389/fneur.2021.738148

INTRODUCTION

Cystatin C (CysC, encoded by *CST3* on 20p11.21) is a candidate marker of glomerular filtration rate (1, 2). As a competitive inhibitor of cysteine proteases, CysC is also involved in the process of atherosclerotic plaque remodeling (3) and independently associated with cerebral artery stenosis and prognosis in stroke patients (4). The imbalance expression between CysC and cysteine proteases is a key factor of atherosclerosis. Although the effects of CysC on metabolic syndrome and atherosclerosis-related factors have been confirmed in observational studies (5), the underlying mechanism is still unclear (2, 6). The causal involvement or directionality of any causal effect on artery stenosis and ischemic stroke is yet to be proven (7).

Cerebrovascular disease is one of the leading causes of death in China, especially for ischemic stroke (IS) (8, 9). Intracranial and extracranial large-artery stenotic disease is one of the most common causes of ischemic stroke worldwide (10, 11). Large-artery atherosclerotic stroke (LAAS) was the most frequent subtype based on the Trial of Org 10 172 in Acute Stroke Treatment (TOAST) system (12), which was typically caused by intracranial artery stenosis (ICAS) and extracranial artery stenosis (ECAS). The stenosis of intracranial or extracranial arteries is also an important indicator of atherosclerosis. CysC has been proposed to participate in the process of atherosclerosis, thereby influencing the risk of cardiovascular disease (13). However, its role as a marker of atherosclerosis is still controversial. In this study, we aimed to assess whether two selected single-nucleotide polymorphisms (SNPs) of the *CST3* gene are correlated with LAAS and large-vessel stenosis as well as stroke prognosis.

METHODS

Study Design and Subjects

This study was conducted based on the Third China National Stroke Registry (CNSR-III), a nationwide, multicenter, prospective registry study launched in China between August 2015 and March 2018, aiming to evaluate etiology, imaging, and biological markers of acute ischemic stroke (AIS). Detailed descriptions of the CNSR-III study have been reported previously (14). Blood samples were collected from 171 study sites for this prespecified biomarker subgroup analysis. We selected two SNPs of the *CST3* gene (rs13038305 and rs911119) as the robust association with the circulating concentration of CysC based on the previous study. Of note, these two SNPs were reported not associated with creatinine-based measures of renal function (15, 16). Finally, 3,833 subjects were included in our analysis. The protocol of the CNSR-III study was approved by the ethics committee of Beijing Tiantan Hospital.

Data Collection and Blood Sample Test

Blood samples were collected on the first day of enrollment and transported through the cold chain to the central laboratory in Beijing Tiantan Hospital, where all serum specimens were stored at −80°C until testing was performed. Blood samples were sent to the laboratory to extract serum, plasma, and white blood cells and tested uniformly in the central laboratory of Beijing Tiantan Hospital according to the standardized methods.

The value of CysC was measured by the immunoturbidimetric method (Roche Cobas c501 analyzer with CysC assay); coefficient of variation (CV) of CysC was 2%. SNP analysis was accomplished by Kompetitive allele-specific polymerase chain reaction (KASP) method, which is also called allele-specific quantitative polymerase chain reaction (AQP)-based genotyping assay. To verify the accuracy of the KASP method and sample numbers, the quality controls required that the consistency between KASP and first-generation sequencing results in verified loci was >99%. The laboratory indices [including high-sensitivity C-reactive protein (hs-CRP), creatinine, high-density lipoprotein (HDL), low-density lipoprotein (LDL), triglyceride (TG), total cholesterol(TC), and creatinine] were tested by the central laboratory of Beijing Tiantan Hospital after admission. All measurements were performed by laboratory personnel blinded to the study status. Stroke subtypes are classified according to the TOAST system. The degree of stenosis was assessed according to

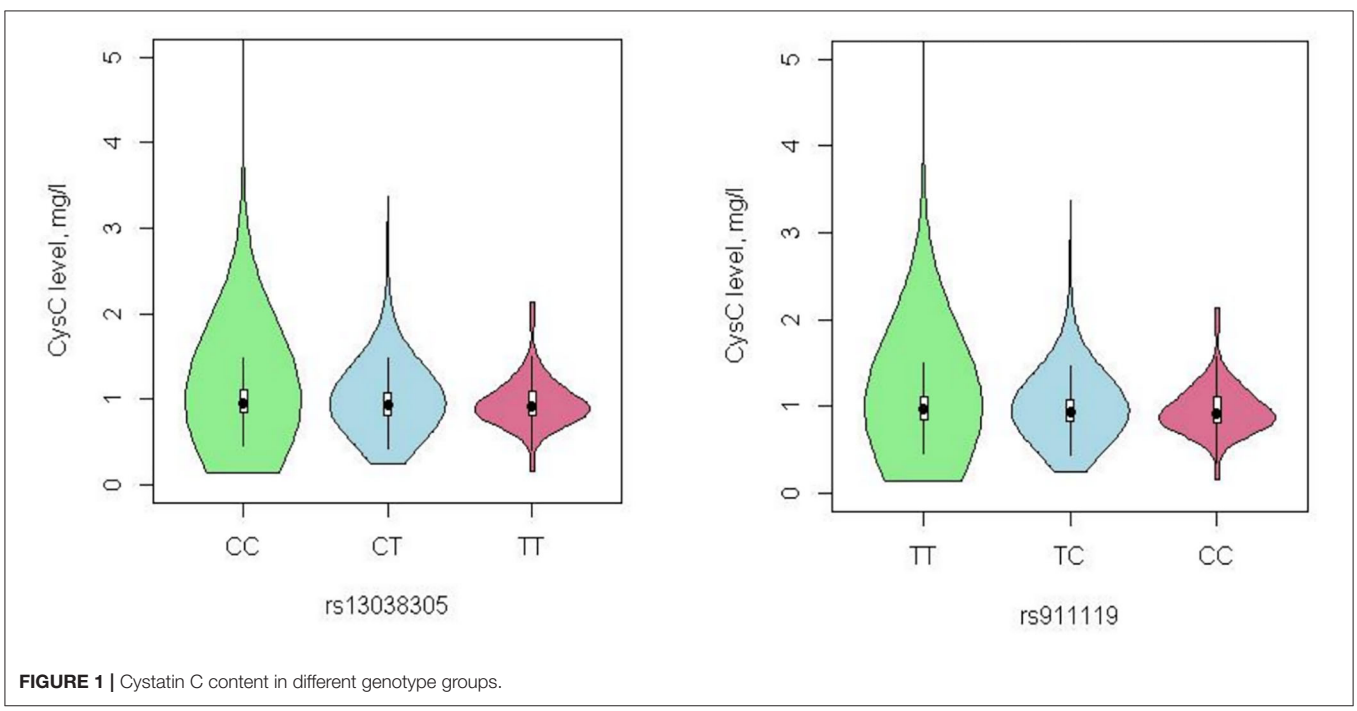

FIGURE 1 | Cystatin C content in different genotype groups.

computed tomographic angiography (CTA), magnetic resonance angiography (MRA) imaging, or conventional ultrasonography. More than 50% caliber reduction of the intracranial and extracranial artery was defined as ICAS and ECAS, respectively. To ensure the diagnosis standard was consistent, all images were independently evaluated by two trained neuroradiologists blinded to clinical information. A third neuroradiologist was involved for additional assessment if there was disagreement in certain cases.

Outcome Assessment

The primary objective was to explore the impact of SNPs on LAAS and large-vessel stenosis. Additionally, we evaluated the association between individual SNPs and the poor functional outcome of modified Rankin scale (mRS 3–6) score, stroke recurrence, all-cause mortality, and the combined vascular events during 1 year of follow-up. The outcomes were obtained through clinic or telephone in 1-year follow-up. Assessment of endpoints was completed by trained research coordinators who were blinded to patients' baseline clinical information.

Statistical Analysis

Haploview analysis software (http://www.broadinstitute.org/haploview) was used to perform Hardy–Weinberg equilibrium analysis. Pearson's χ^2-test or Fisher's exact test was used for comparisons of LAAS and control group (indicating an etiological diagnosis of non-LAAS based on the TOAST system). Logistic regression and Cox regression analyses were performed to compute odds ratios (ORs) and hazard ratio (HR) with 95% confidence intervals (CIs) after adjusting the covariates to assess the correlation between *CST3* gene polymorphisms and outcomes in an addictive and dominant model. We also performed the ordinal logistic regression analysis between per major allele of the selected SNPs and atherosclerosis risk factors including CysC. Effect sizes (β) are presented as standard deviations of each trait per major allele to facilitate comparison between traits. Statistical analyses were performed using SAS software (version 9.4; SAS Institute, Cary, NC, USA). The level of significance was defined as $p < 0.05$ (two-sided).

RESULTS

Baseline Characteristics

As a subgroup analysis of CNSR-III, two loci of the *CST3* gene (rs13038305 and rs911119) were analyzed in 3,833 ischemic stroke patients. Characteristics of enrolled patients compared with the entire CNSR-III cohort are shown in

TABLE 1 | Characteristics of enrolled patients.

Characteristics*	Total (*N* = 3,833)	LAAS group (*N* = 1,005)	Control group† (*N* = 2,828)	*p*-value
Age, years, mean ± SD	62.8 ± 11.3	63.3 ± 11.2	62.6 ± 11.3	0.068
Male sex	2,602 (67.9)	697 (69.4)	1,905 (67.4)	0.246
NIHSS score at admission				<0.001
0–3	2,024 (52.8)	449 (44.7)	1,575 (55.7)	
≥4	1,809 (47.2)	556 (55.3)	1,253 (44.3)	
BMI	24.6 (22.7–26.7)	24.3 (22.5–26.7)	24.7 (22.8–26.7)	0.553
Medical history				
Ischemic stroke	904 (23.6)	267 (26.6)	637 (22.5)	0.010
Coronary artery disease	456 (11.9)	137 (13.6)	319 (11.3)	0.048
Hyperlipidemia	326 (8.5)	86 (8.6)	240 (8.5)	0.945
Diabetes mellitus	933 (24.3)	282 (28.1)	651 (23.0)	0.001
Hypertension	2,405 (62.7)	662 (65.9)	1,743 (61.6)	0.017
Smoking	1,193 (31.1)	323 (32.1)	870 (30.8)	0.419
Alcohol drinking	543 (14.2)	140 (13.9)	403 (14.3)	0.803
Laboratory data				
hs-CRP, mg/l	1.510 (0.700–4.420)	1.975 (0.805–5.410)	1.390 (0.670–4.040)	<0.001
CysC, mg/l	0.960 (0.850–1.100)	0.960 (0.848–1.100)	0.960 (0.850–1.100)	<0.001
TG, mmol/l	1.400 (1.060–1.900)	1.360 (1.070–1.800)	1.410 (1.060–1.920)	0.005
TC, mmol/l	3.980 (3.330–4.740)	3.940 (3.280–4.720)	3.990 (3.350–4.750)	<0.001
LDL-C, mmol/l	2.420 (1.830–3.130)	2.430 (1.840–3.110)	2.420 (1.830–3.130)	0.004
HDL-C, mmol/l	0.940 (0.760–1.130)	0.930 (0.770–1.111)	0.950 (0.760–1.140)	<0.001
eGFRcr, ml/min/1.73 m^2	91.914 (79.770–100.972)	91.908 (80.546–100.591)	91.914 (79.622–101.00)	0.331
Concomitant medication				
Antiplatelets	3,733 (97.4)	982 (97.7)	2,751 (97.3)	0.458
Anticoagulants	399 (10.4)	101 (10.1)	298 (10.5)	0.664

SD, standard deviation; LAAS, large-artery atherosclerosis stroke; CysC, cystatin C; NIHSS, National Institutes of Health Stroke Scale; BMI, body mass index; hs-CRP, high sensitivity C-reactive protein; TG, triglyceride; TC, total cholesterol; HDL, high-density lipoprotein; LDL, low-density lipoprotein; eGFRcr, creatinine-calculated estimated glomerular filtration rate.

**Variables were presented as median (interquartile range) or counts (percentages) unless otherwise indicated.*

†Control group indicating etiological diagnosis of non-LAAS based on The Trial of Org 10 172 in Acute Stroke Treatment (TOAST) system.

Supplementary Table 1. Patients enrolled in our analysis have more proportion of ischemic stroke, coronary artery disease, and higher National Institutes of Health Stroke Scale (NIHSS).

The distribution of alleles and genotypes of the two groups follows the Hardy–Weinberg equilibrium (rs13038305, $p = 0.853$; rs911119, $p = 0.331$). **Figure 1** shows the organ diagram of CysC content in different genotype groups. Median CysC concentrations per genotype for rs13038305 were as follows: 1.012 mg/l (C/C), 0.990 mg/l (C/T), and 0.969 mg/l (T/T); for rs911119 were as follows: 1.014 mg/l (T/T), 0.988 mg/l (T/C), and 0.971 mg/l (C/C). **Table 1** summarizes the clinical characteristics of enrolled LAAS patients and control subjects. There were no differences between the two groups in the clinical characteristic aspects of age, sex, body mass index (BMI), medical history of hyperlipidemia, smoking, alcohol drinking, creatinine-calculated estimated glomerular filtration rate (eGFRcr), and concomitant medication of antiplatelets and anticoagulants. NIHSS scores at admission are higher in the LAAS group ($p < 0.001$). Besides, the LAAS group showed more proportion of ischemic stroke, coronary artery disease, diabetes mellitus, and hypertension ($p < 0.05$).

TABLE 2 | Genotype and allelic frequencies of *CST3* SNPs in LAAS and control subjects.

SNPs sites		LAAS group, *n* (%)	Control group*, *n* (%)	Univariate analysis		Multivariate analysis†	
				OR (95%CI)	*p*-value	Adjusted OR (95% CI)	*p*-value
rs 13038305	C/C	778 (71.4)	2,135 (75.5)	Reference		Reference	
Genotypes	C/T	218 (21.7)	643 (22.7)	0.930 (0.782–1.107)	0.417	0.922 (0.774–1.099)	0.365
	T/T	9 (0.9)	50 (1.8)	0.494 (0.242–1.009)	0.053	0.486 (0.237–0.994)	0.048
	C/T+T/T	227 (22.6)	693 (24.5)	0.899 (0.758–1.066)	0.222	0.891 (0.750–1.057)	0.186
Allele	C	1,774 (88.3)	4,913 (86.9)	Reference			
	T	236 (11.7)	743 (13.1)	0.880 (0.752–1.028)	0.108	0.872 (0.746–1.020)	0.088
rs 911119	T/T	751 (74.7)	2,080 (73.6)	Reference		Reference	
Genotypes	C/T	244 (24.3)	695 (24.6)	0.972 (0.822–1.150)	0.744	0.961 (0.812–1.138)	0.648
	C/C	10 (1.0)	53 (1.9)	0.523 (0.265–1.032)	0.062	0.517 (0.261–1.023)	0.058
	C/T+C/C	254 (25.3)	748 (26.5)	0.940 (0.797–1.109)	0.4661	0.930 (0.788–1.098)	0.391
Allele	T	1,746 (86.9)	4,855 (85.8)	Reference		Reference	
	C	264 (13.1)	801 (14.2)	0.916 (0.789–1.064)	0.253	0.908 (0.781–1.055)	0.206

SNPs, single-nucleotide polymorphisms; LAAS, large-artery atherosclerosis stroke; CI, confidence interval; OR, odds ratio.

**Control group indicating etiological diagnosis of non-LAAS based on The Trial of Org 10 172 in Acute Stroke Treatment (TOAST) system.*

†Adjusted covariates including sex, age, smoking and drinking, hyperlipidemia, diabetes mellitus, hypertension, ischemic stroke, and coronary artery disease history.

TABLE 3 | Genotype and allelic frequencies of *CST3* SNPs in ICAS or ECAS group.

SNP sites		ICAS or ECAS group, *n* (%)	Control group*, *n* (%)	Univariate analysis		Multivariate analysis†	
				OR (95% CI)	*p*-value	Adjusted OR (95% CI)	*p*-value
rs 13038305	C/C	1,273 (76.2)	1,374 (76.1)	Reference		Reference	
Genotypes	C/T	366 (21.9)	406 (22.5)	1.028 (0.875–1.207)	0.738	1.012 (0.860–1.192)	0.882
	T/T	31 (1.9)	26 (1.4)	0.777 (0.459–1.316)	0.348	0.755 (0.443–1.286)	0.301
	C/T+T/T	1,273 (76.2)	1,374 (76.1)	1.008 (0.862–1.179)	0.919	0.992 (0.847–1.163)	0.921
Allele	C	2,912 (87.2)	3,154 (87.3)	Reference		Reference	
	T	428 (12.8)	458 (12.7)	0.988 (0.858–1.138)	0.867	0.973 (0.843–1.123)	0.709
rs 911119	T/T	1,237 (74.1)	1,338 (74.1)	Reference		Reference	
Genotypes	C/T	400 (24.0)	440 (24.4)	1.017 (0.870–1.189)	0.833	1.001 (0.855–1.173)	0.986
	C/C	33 (2.0)	28 (1.6)	0.784 (0.471–1.306)	0.350	0.768 (0.459–1.286)	0.316
	C/T+C/C	433 (25.9)	468 (25.9)	0.999 (0.858–1.163)	0.992	0.984 (0.843–1.147)	0.833
Allele	T	2,874 (86.1)	3,116 (86.3)	Reference		Reference	
	C	466 (14.0)	496 (13.7)	0.982 (0.857–1.125)	0.791	0.968 (0.843–1.111)	0.644

SNPs, single-nucleotide polymorphisms; ICAS, intracranial artery stenosis; ECAS extracranial artery stenosis; CI, confidence interval; OR, odds ratio.

**Control group indicating patients without intracranial and extracranial artery stenoses.*

†Adjusted covariates including sex, age, smoking and drinking, hyperlipidemia, diabetes mellitus, hypertension, ischemic stroke, and coronary artery disease history.

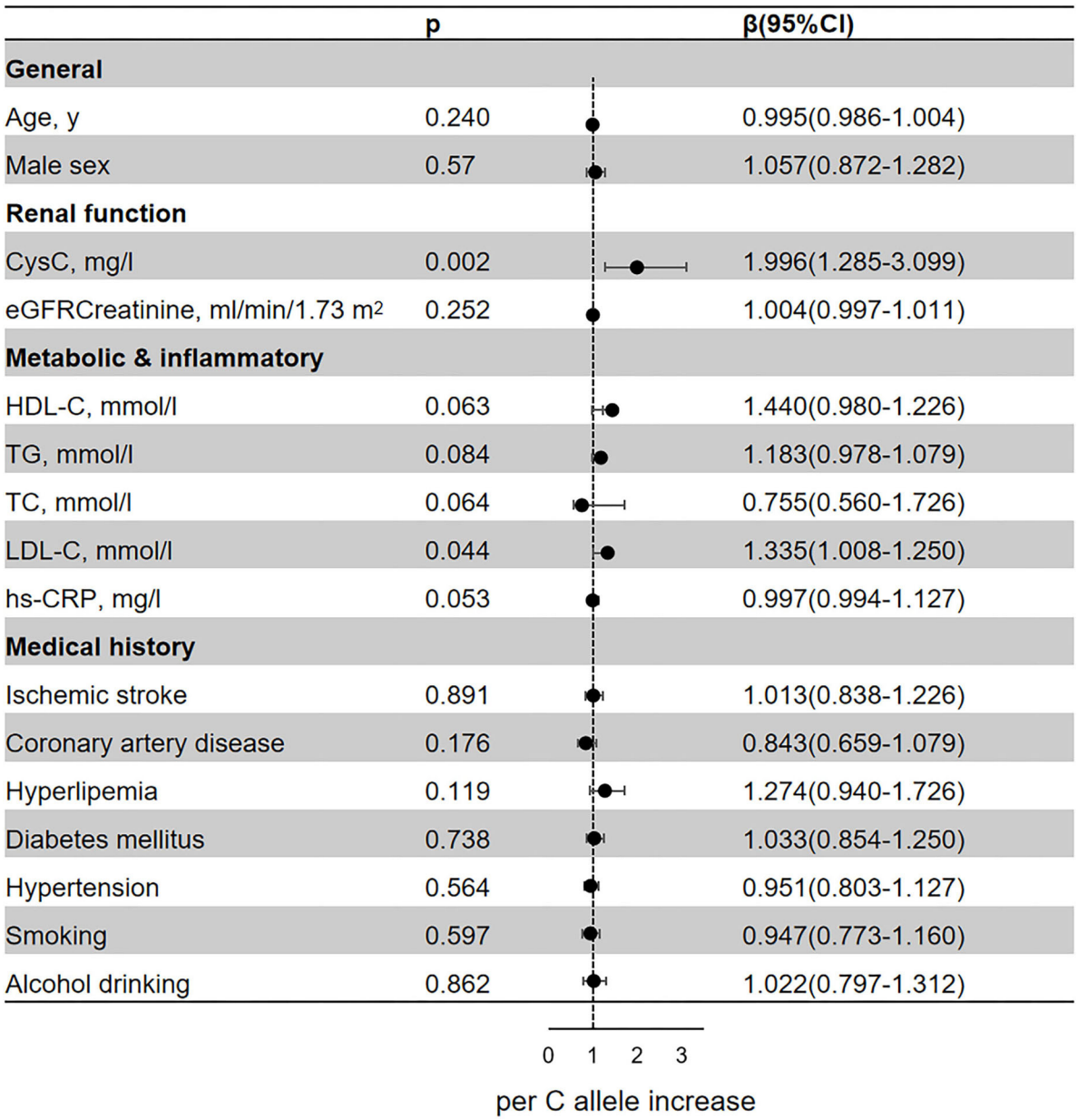

FIGURE 2 | Association of the genetic variant (rs13038305 polymorphisms) with cardiovascular risk factors and traits. Effect sizes (β) are presented as standard deviations of each trait per major allele to facilitate comparison between traits. Adjusted for age, sex, CysC, eGFRcr, HDL-C, TG, TC, LDL-C, hs-CRP, smoking, alcohol drinking, ischemic stroke, coronary artery disease, hyperlipidemia, diabetes mellitus, and hypertension. BMI, body mass index; CysC, cystatin C; eGFRcr, creatinine-calculated estimated glomerular filtration rate; LDL, low-density lipoprotein; HDL, high-density lipoprotein; TG, triglyceride; TC, total cholesterol; hs-CRP, high-sensitivity C-reactive protein; CI, confidence interval.

Association Between Two Single-Nucleotide Polymorphisms of the *CST3* Gene and Large-Artery Atherosclerotic Stroke

The distributions of the alleles and genotypes were following Hardy–Weinberg equilibrium in both groups (rs13038305, $\chi^2 = 0.317$, $p = 0.853$; rs911119, $\chi^2 = 2.206$, $p = 0.331$). **Table 1** shows that carriers of the T allele of the SNP rs13038305 tend to have a lower rate of LAAS. Compared with C/C as a reference, the *CST3* allelic frequency OR of T/T in the univariate analysis is 0.494, 95% CI 0.242–1.009, $p = 0.053$. After adjusting for covariate in multivariate analysis, adjusted OR was 0.486, 95% CI 0.237–0.994, $p = 0.048$. Carriers of the C allele of the SNP rs911119 tend to have a lower rate of LAAS. However, no statistically significant differences between genotypes and allele frequencies were found for SNP rs911119 between LAAS and control group (**Table 2**).

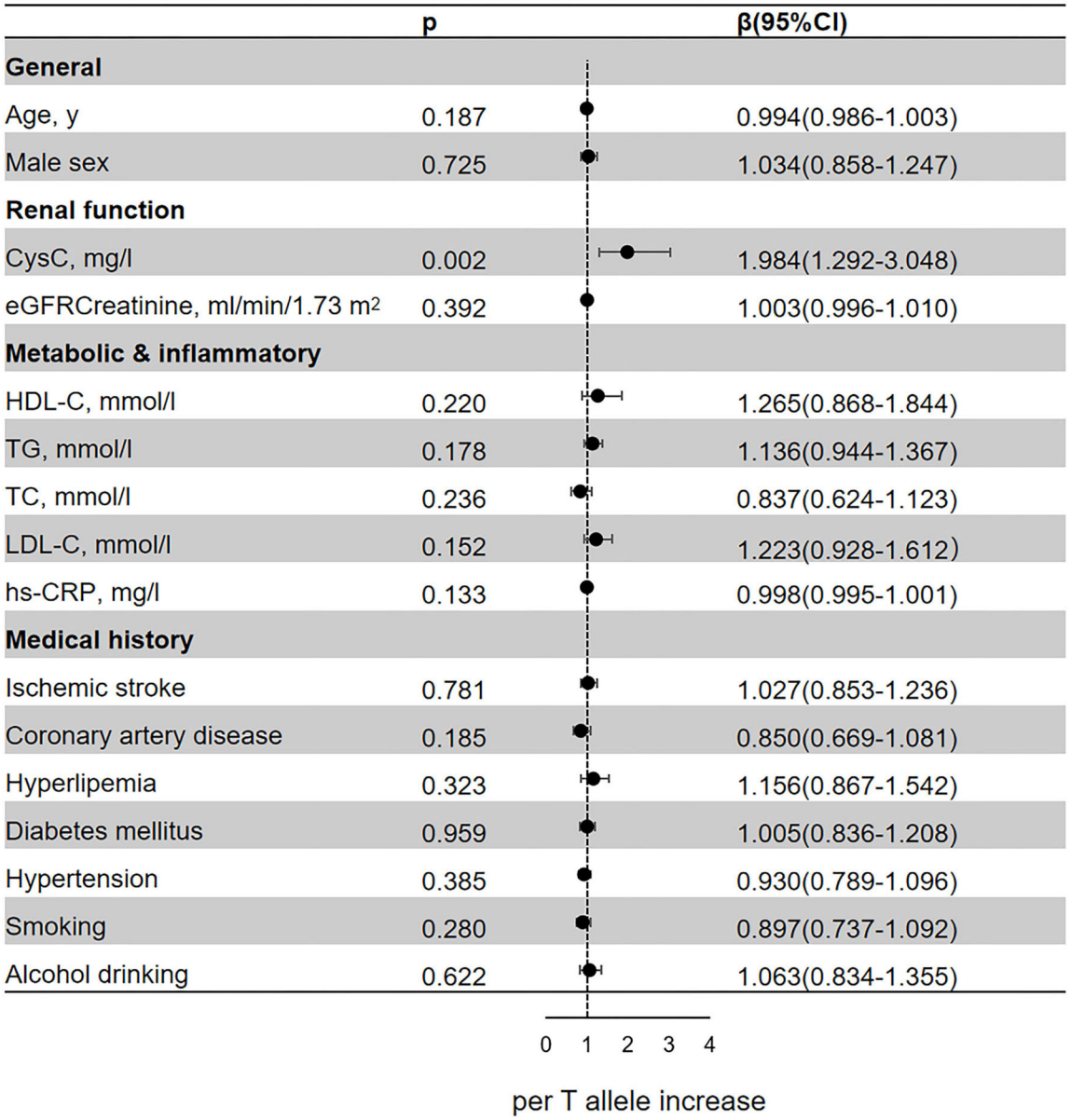

FIGURE 3 | Association of the genetic variant (rs911119 polymorphisms) with cardiovascular risk factors and traits. Effect sizes (β) are presented as standard deviations of each trait per major allele to facilitate comparison between traits. Adjusted for age, sex, CysC, eGFRcr, HDL-C, TG, TC, LDL-C, hs-CRP, smoking, alcohol drinking, ischemic stroke, coronary artery disease, hyperlipidemia, diabetes mellitus, and hypertension. BMI, body mass index; CysC, cystatin C; eGFRcr, creatinine-based estimated glomerular filtration rate; LDL, low-density lipoprotein; HDL, high-density lipoprotein; TG triglyceride; TC, total cholesterol; hs-CRP, high-sensitivity C-reactive protein; CI, confidence interval.

Association Between Two Single-Nucleotide Polymorphisms of the *CST3* Gene and Intracranial Artery Stenosis or Extracranial Artery Stenosis

Table 3 shows the correlation between the two selected SNPs and large-artery stenosis. There was no association between the two SNPs and either ICAS or ECAS.

Genetic Variant and Cardiovascular Risk Factors

In the regression analyses, rs13038305 and rs911119 were all related to the content of serum CysC ($p < 0.05$; **Figures 2**, **3**). Of note, per C allele of rs13038305 also showed an increased level of LDL cholesterol (LDL-C), β was 1.335, and 95% CI 1.008–1.250 after adjustment [adjusted for age, sex, CysC, eGFRcr,

TABLE 4 | Clinical outcomes in different *CST3* polymorphisms.

SNP sites	Outcomes	Genotypes	No. of events/total no. (%)	Model 0*		Model 1†	
				HR (95% CI)	*p*-value	Adjusted HR (95% CI)	*p*-value
rs13038305	Poor functional outcome (mRS score 3–6)	C/C	362 (12.6)	–		–	
		T/C	118 (13.9)	1.118 (0.894–1.398)	0.327	1.104 (0.877–1.389)	0.399
		T/T	7 (11.9)	0.933 (0.420–2.069)	0.864	0.890 (0.395–2.005)	0.779
		C/T+T/T	125 (13.8)	1.106 (0.889–1.376)	0.817	1.089 (0.870–1.363)	0.456
	Stroke recurrence	C/C	279 (9.6)	(Reference)		(Reference)	
		T/C	84 (9.8)	1.018 (0.798–1.299)	0.887	1.016 (0.796–1.296)	0.901
		T/T	6 (10.2)	1.051 (0.468–2.359)	0.904	1.036 (0.461–2.325)	0.932
		C/T+T/T	90 (9.8)	1.020 (0.804–1.293)	0.871	1.017 (0.802–1.290)	0.890
	All-cause mortality	C/C	81 (2.8)	(Reference)		(Reference)	
		T/C	33 (3.8)	1.386 (0.925–2.078)	0.114	1.356 (0.905–2.033)	0.140
		T/T	2 (3.4)	1.212 (0.298–4.929)	0.788	1.178 (0.290–4.793)	0.819
		C/T+T/T	35 (3.8)	1.375 (0.925–2.044)	0.116	1.345 (0.904–1.999)	0.143
	Combined vascular events	C/C	292 (10.0)	–		–	
		T/C	87 (10.1)	1.008 (0.793–1.280)	0.951	1.005 (0.791–1.277)	0.967
		T/T	7 (11.9)	1.170 (0.553–2.476)	0.681	1.151 (0.544–2.436)	0.713
		C/T+T/T	94 (10.2)	1.018 (0.807–1.285)	0.879	1.015 (0.804–1.280)	0.902
rs911119	Poor functional outcome (mRS score 3–6)	T/T	351 (12.6)	–		–	
		T/C	128 (13.8)	1.112 (0.895–1.383)	0.338	1.102 (0.881–1.377)	0.396
		C/C	8 (12.7)	1.010 (0.477–2.138)	0.980	0.967 (0.450–2.081)	0.933
		C/T+C/C	136 (13.7)	1.106 (0.894–1.368)	0.355	1.093 (0.878–1.359)	0.426
	Stroke recurrence	T/T	270 (9.5)	–		–	
		T/C	93 (9.9)	1.036 (0.818–1.311)	0.771	1.033 (0.816–1.308)	0.786
		C/C	6 (9.5)	0.984 (0.438–2.209)	0.969	0.971 (0.432–2.180)	0.943
		C/T+C/C	99 (9.9)	1.032 (0.820–1.300)	0.787	1.029 (0.818–1.296)	0.806
	All-cause mortality	T/T	80 (2.8)	–		–	
		T/C	34 (3.6)	1.286 (0.861–1.921)	0.219	1.266 (0.848–1.892)	0.249
		C/C	2 (3.2)	1.115 (0.274–4.535)	0.879	1.081 (0.266–4.396)	0.914
		C/T+C/C	36 (3.6)	1.275 (0.861–1.890)	0.226	1.254 (0.846–1.859)	0.259
	Combined vascular events	T/T	283 (10.0)	–		–	
		T/C	96 (10.2)	1.020 (0.809–1.285)	0.868	1.017 (0.807–1.283)	0.883
		C/C	7 (11.1)	1.094 (0.517–2.316)	0.814	1.077 (0.509–2.281)	0.845
		C/T+C/C	103 (10.3)	1.025 (0.818–1.284)	0.832	1.021 (0.815–1.280)	0.855

SNPs, single-nucleotide polymorphisms; CI, confidence interval; HR, hazard ratio; mRS, modified Rankin Scale.

**Model 0 was unadjusted.*

†*Model 1 was adjusted for age (in year, continuous) and sex (male or female).*

HDL cholesterol (HDL-C), TG, TC, LDL-C, hs-CRP, smoking, alcohol drinking, ischemic stroke, coronary artery disease, hyperlipidemia, diabetes mellitus, and hypertension]. However, rs13038305 and rs911119 showed no significant association with other cardiovascular risk factors and traits in the increase of per major allele in the adjusted model. Besides, there is no correlation between these two SNPs and creatinine, but they are strongly correlated with the content of CysC.

Clinical Outcomes in Different *CST3* Polymorphisms

We evaluated the risk prediction of genotype (rs13038305 and rs911119) for stroke prognosis during 1 year of follow-up (**Table 4**). No statistically significant association between the polymorphism rs13038305 or rs911119 and any outcome was observed.

DISCUSSION

Previous observational studies on CysC have confirmed that it was not simply a marker of renal function to affect cardiovascular and stroke outcomes (17–19). CysC might change metabolic status and promote the progress of metabolic disorders (20). Besides, since CysC is a potent competitive inhibitor of cysteine proteases (3) and involved in the progression of atherosclerosis, the balance cysteine protease and protease inhibitor (CysC) plays an important role in the pathogenesis of cerebral injury and functional rehabilitation (21). However, underlying mechanisms remain to be fully elucidated.

Our previous study has proven the relationship between CysC levels and poor functional outcome independent of renal function in 1 year after ischemic stroke (22). In this study, we selected two SNPs that have been reported to be strongly related to serum CysC level and tried to investigate the impact of SNPs

on LAAS and large-vessel stenosis. We found that carriers of the T allele of SNP rs13038305 tend to have a lower proportion of LAAS. However, no correlation was found between the two SNPs and either ICAS or ECAS. The possible reason is that large-artery stenosis is not the only factor leading to LAAS, and our classification method to assess intracranial and extracranial large-vessel stenosis may miss some detailed information about the degree of vascular stenosis and the state of atherosclerotic plaque. T allele of the SNP rs13038305 tends to have a lower CysC level and higher CysC-based eGFR (eGFRcys) (6, 23). The minor allele of rs911119 was also associated with decreased serum CysC (2, 24). Consistent with previous research, we reported a strong association between the CysC concentration and the two SNPs. A lower CysC level may also indicate a lower risk of atherosclerosis and therefore a lower LAAS proportion. Besides, per major allele (C) of rs13038305 seems related to higher LDL-C concentration, which may cause changes in metabolic status. The observational study also found that the effect of CysC on prognosis might be modified by LDL-C level because of a potential interaction between lipids and CysC (25, 26). Our research indicated that CysC might be an important marker in determining subclinical atherosclerosis.

Although elevated CysC concentration was associated with cardiovascular risk factors and prognosis (17, 27, 28), Mendelian randomization studies based on the two selected SNPs revealed that genetic *CST3* seems not to be a causal risk factor of cardiovascular disease in the population-based prospective cohort study (2, 6, 29). In our study, we failed to find any association between these two SNPs and stroke outcome at 1 year. Previous studies have also confirmed that although the epidemiological relationship between plasma CysC level and coronary heart disease exists and is statistically independent of other risk factors such as atherosclerosis and renal function, there is insufficient genetic evidence. Even if the two selected SNPs were associated with increased CysC level, our study did not find that the genetic polymorphisms of these two loci resulted in impaired renal function, nor did it affect other risk factors that may cause impaired renal function. However, the specific functions of these two SNPs and the causal relationship between CysC concentration remain to be elucidated.

Although this subgroup analysis was based on the data from a large, multicenter, progressive cohort study, there were still several limitations. First, MRA, CTA, and ultrasonography are not the gold standards for assessing intracranial and extracranial stenosis; hierarchical evaluation of 50% instead of the detailed value of stenotic severity might be less accurate to some extent. Second, since there is a fluctuant level of inflammatory and metabolic markers, a one-time examination of plasma level might confound the mediator concentration. The concentration peak of biomarkers might be missed, and the variation could not be observed as well. However, even if we conducted plasma level examination for one time, the SNP frequency was consistent under normal circumstances. The variation of CysC levels might have less impact on the primary outcome. Third, the investigated cohort of ischemic stroke patients only enrolled a proportion of patients in China; thereby, the results are not necessarily applicable to a general population. The correlation between *CST3* and ischemic stroke needs further exploration.

CONCLUSIONS

In conclusion, our study indicated that carriers of the T allele of the SNP rs13038305 tend to have a lower proportion of LAAS. rs13038308 and rs911119 polymorphisms were likely to affect CysC concentration independently of kidney function. Per major allele (C) of rs13038305 related to higher LDL-C concentration. However, no correlation was found between stroke prognosis and the polymorphisms at rs13038305 or rs911119.

DATA AVAILABILITY STATEMENT

The original contributions presented in the study are included in the article/**Supplementary Material**, further inquiries can be directed to the corresponding author/s.

ETHICS STATEMENT

The studies involving human participants were reviewed and approved by the Ethics Committee of Beijing Tiantan Hospital. The patients/participants provided their written informed consent to participate in this study.

AUTHOR CONTRIBUTIONS

YW had full access to all the data in the study, takes responsibility for the integrity of the data and the accuracy of the data analysis, and designed and conceptualized this study. YD performed the experiments and drafted the manuscript. ZX interpreted the data. XM revised the article for intellectual content. HL interpreted the data and revised the manuscript. YP conducted the statistical analysis and interpreted the data. LL revised the article for intellectual content. XX conducted the statistical analysis. All authors contributed to the article and approved the submitted version.

FUNDING

This work was supported by grants from the National Key R&D Program of China (2016YFC0901002 and 2018YFC1312903), National Science and Technology Major Project (2017ZX09304018), and Beijing Municipal Science & Technology Commission (D171100003017002 and Z181100001818001).

ACKNOWLEDGMENTS

We gratefully acknowledge all of the participating hospitals in the study and all research patients for their dedication to this study.

SUPPLEMENTARY MATERIAL

The Supplementary Material for this article can be found online at: https://www.frontiersin.org/articles/10.3389/fneur.2021.738148/full#supplementary-material

REFERENCES

1. Goddard KAB, Olson JM, Payami H, Voet MVD, Tromp G. Evidence of linkage and association on chromosome 20 for late-onset Alzheimer disease. *Neurogenetics.* (2004) 5:121–8. doi: 10.1007/s10048-004-0174-3
2. van der Laan SW, Fall T, Soumaré A, Teumer A, Sedaghat S, Baumert J, et al. Cystatin C and cardiovascular disease. *J Am Coll Cardiol.* (2016) 68:934–45. doi: 10.1016/j.jacc.2016.05.092
3. Sukhova GK, Wang B, Libby P, Pan JH, Zhang Y, Grubb A, et al. Cystatin C deficiency increases elastic lamina degradation and aortic dilatation in apolipoprotein E–null mice. *Circ Res.* (2005) 96:368–75. doi: 10.1161/01.RES.0000155964.34150.F7
4. Xu Z, Leng C, Yang B, Wang H, Zhu J. Serum cystatin C is associated with large cerebral artery stenosis in acute ischemic stroke. *Oncotarget*. (2017) 8:67181–8. doi: 10.18632/oncotarget.18061
5. Maahs DM, Prentice N, McFann K, Snell-Bergeon JK, Jalal D, Bishop FK, et al. Age and sex influence cystatin C in adolescents with and without type 1 diabetes. *Diabetes Care.* (2011) 34:2360–2. doi: 10.2337/dc11-0829
6. Svensson-Färbom P, Almgren P, Hedblad B, Engström G, Persson M, Christensson A, et al. Cystatin C is not causally related to coronary artery disease. *PLoS ONE.* (2015) 10:e129269. doi: 10.1371/journal.pone.0129269
7. Chen HH. Is cystatin C an important prognostic marker independent of renal function? *J Am Coll Cardiol.* (2010) 56:1937–8. doi: 10.1016/j.jacc.2010.06.049
8. Wang Y, Li Z, Gu H, Zhai Y, Jiang Y, Zhao X, et al. China stroke statistics 2019: a report from the national center for healthcare quality management in neurological diseases, china national clinical research center for neurological diseases, the Chinese stroke association, national center for chronic and non-communicable disease control and prevention, Chinese center for disease control and prevention and institute for global neuroscience and stroke collaborations. *Stroke Vasc Neurol.* (2020) 5:211–39. doi: 10.1136/svn-2020-000457
9. Chao B, Yan F, Hua Y, Liu J, Yang Y, Ji X, et al. Stroke prevention and control system in China: CSPPC-Stroke Program. *Int J Stroke.* (2021) 16:265–72. doi: 10.1177/1747493020913557
10. Holmstedt CA, Turan TN, Chimowitz MI. Atherosclerotic intracranial arterial stenosis: risk factors, diagnosis, and treatment. *Lancet Neurol.* (2013) 12:1106–14. doi: 10.1016/S1474-4422(13)70195-9
11. Gorelick PB, Wong KS, Bae HJ, Pandey DK. Large artery intracranial occlusive disease: a large worldwide burden but a relatively neglected frontier. *Stroke.* (2008) 39:2396–9. doi: 10.1161/STROKEAHA.107.505776
12. Adams HP, Bendixen BH, Kappelle LJ, Biller J, Love BB, Gordon DL, et al. Classification of subtype of acute ischemic stroke. Definitions for use in a multicenter clinical trial. TOAST. Trial of ORG 10172 in acute stroke treatment. *Stroke.* (1993) 24:35–41. doi: 10.1161/01.str.24.1.35
13. Eriksson P, Deguchi H, Samnegard A, Lundman P, Boquist S, Tornvall P, et al. Human evidence that cystatin c gene is implicated in focal progression of coronary artery disease. *Arterioscler Thromb Vasc Biol.* (2004) 24:551–7. doi: 10.1161/01.ATV.0000117180.57731.36
14. Wang Y, Jing J, Meng X, Pan Y, Wang Y, Zhao X, et al. The third China national stroke registry (CNSR-III) for patients with acute ischaemic stroke or transient ischaemic attack: design, rationale and baseline patient characteristics. *Stroke Vasc Neurol.* (2019) 4:158–64. doi: 10.1136/svn-2019-000242
15. Köttgen A, Pattaro C, Böger CA, Fuchsberger C, Fox CS. New loci associated with kidney function and chronic kidney disease. *Nat Genet.* (2010) 42:376–84. doi: 10.1055/s-0030-1266452
16. Köttgen A, Glazer NL, Dehghan A, Hwang SJ, Katz R, Li M, et al. Multiple loci associated with indices of renal function and chronic kidney disease. *Nat Genet.* (2009) 41:712–7. doi: 10.1038/ng.377
17. Keller T, Messow CM, Lubos E, Nicaud V, Wild PS, Rupprecht HJ, et al. Cystatin C and cardiovascular mortality in patients with coronary artery disease and normal or mildly reduced kidney function: results from the AtheroGene study. *Eur Heart J.* (2009) 30:314–20. doi: 10.1093/eurheartj/ehn598
18. Mussap M, Plebani M. Biochemistry and clinical role of human cystatin C. *Crit Rev Clin Lab Sci.* (2004) 41:467–550. doi: 10.1080/10408360490504934
19. Kaeser SA, Herzig MC, Coomaraswamy J, Kilger E, Selenica ML, Winkler DT, et al. Cystatin C modulates cerebral β-amyloidosis. *Nat Genet.* (2007) 39:1437–9. doi: 10.1038/ng.2007.23
20. Kang YH, Jeong DW, Son SM. Prevalence of reduced kidney function by estimated glomerular filtration rate using an equation based on creatinine and cystatin C in metabolic syndrome and its components in Korean adults. *Endocrinol Metab.* (2016) 31:446–53. doi: 10.3803/EnM.2016.31.3.446
21. Song H, Zhou H, Qu Z, Hou J, Chen W, Cai W, et al. From analysis of ischemic mouse brain proteome to identification of human serum clusterin as a potential biomarker for severity of acute ischemic stroke. *Transl Stroke Res.* (2019) 10:546–56. doi: 10.1007/s12975-018-0675-2
22. Ding Y, Liu L, Chen Z, Li H, Pan Y, Wang J, et al. Serum cystatin C predicts stroke clinical outcomes at 1-year independent of renal function. *Front Neurol.* (2021) 12:676872. doi: 10.3389/fneur.2021.676872
23. Maniwa K, Yano S, Sheikh AM, Onoda K, Mitaki S, Isomura M, et al. Association between cystatin C gene polymorphism and the prevalence of white matter lesion in elderly healthy subjects. *Sci Rep.* (2020) 10:4688. doi: 10.1038/s41598-020-61383-7
24. Jiang G, Luk AOY, Tam CHT, Xie F, Carstensen B, Lau ESH, et al. Progression of diabetic kidney disease and trajectory of kidney function decline in Chinese patients with type 2 diabetes. *Kidney Int.* (2019) 95:178–87. doi: 10.1016/j.kint.2018.08.026
25. Zhu Z, Zhong C, Xu T, Wang A, Peng Y, Xu T, et al. Prognostic significance of serum cystatin C in acute ischemic stroke patients according to lipid component levels. *Atherosclerosis.* (2018) 274:146–51. doi: 10.1016/j.atherosclerosis.2018.05.015
26. Weng R, Wei X, Yu B, Zhu S, Yang X, Xie F, et al. Combined measurement of plasma cystatin C and low-density lipoprotein cholesterol: a valuable tool for evaluating progressive supranuclear palsy. *Parkinsonism Relat Disord.* (2018) 52:37–42. doi: 10.1016/j.parkreldis.2018.03.014
27. Magnusson M, Molvin J, Engström G, Svensson-Färbom P, Persson M, Christensson A, et al. Cystatin C and risk of diabetes and the metabolic syndrome-biomarker and genotype association analyses. *PLoS ONE.* (2016) 11:e155735. doi: 10.1371/journal.pone.0155735
28. Shlipak MG, Matsushita K, Ärnlöv J, Inker LA, Katz R, Polkinghorne KR, et al. Cystatin C versus creatinine in determining risk based on kidney function. *New Engl J Med.* (2013) 369:932–43. doi: 10.1056/NEJMoa1214234
29. O'Seaghdha CM, Tin A, Yang Q, Katz R, Liu Y, Harris T, et al. Association of a cystatin C gene variant with cystatin C levels, CKD, and risk of incident cardiovascular disease and mortality. *Am J Kidney Dis.* (2014) 63:16–22. doi: 10.1053/j.ajkd.2013.06.015

Conflict of Interest: The authors declare that the research was conducted in the absence of any commercial or financial relationships that could be construed as a potential conflict of interest.

Publisher's Note: All claims expressed in this article are solely those of the authors and do not necessarily represent those of their affiliated organizations, or those of the publisher, the editors and the reviewers. Any product that may be evaluated in this article, or claim that may be made by its manufacturer, is not guaranteed or endorsed by the publisher.

Copyright © 2021 Ding, Xu, Pan, Meng, Xiang, Li, Liu and Wang. This is an open-access article distributed under the terms of the Creative Commons Attribution License (CC BY). The use, distribution or reproduction in other forums is permitted, provided the original author(s) and the copyright owner(s) are credited and that the original publication in this journal is cited, in accordance with accepted academic practice. No use, distribution or reproduction is permitted which does not comply with these terms.

frontiers in Neurology

ORIGINAL RESEARCH
published: 25 November 2021
doi: 10.3389/fneur.2021.777483

Clinical Features and Prognostic Factors of Acute Ischemic Stroke Related to Malignant Gastrointestinal Tumor

Yating Liu[1,2†], *Xin Li*[3†], *Feixue Song*[1], *Xin Yan*[2], *Zhijian Han*[2], *Futian Tang*[2] *and Yumin Li*[2*]

[1] Department of Oncology, Lanzhou University Second Hospital, Lanzhou, China, [2] Key Laboratory of the Digestive System Tumors of Gansu Province, Lanzhou University Second Hospital, Lanzhou, China, [3] Department of Neurology, Lanzhou University Second Hospital, Lanzhou, China

Objectives: To analyze the clinical and imaging features of acute ischemic stroke (AIS) related to gastrointestinal malignant tumor, and to explore the prognostic factors.

Methods: Clinical data of consecutive patients with gastrointestinal malignant tumor complicated with AIS admitted to the Department of Neurology and Oncology in Lanzhou University Second Hospital from April 2015 to April 2019 were retrospectively analyzed. Patients were divided into good prognosis (mRS 0–2) and poor prognosis (mRS > 2) based on a 90-day mRS score after discharge. The multivariate logistic regression model was used to analyze the prognostic factors.

Results: A total of 68 patients were enrolled with an average age of 61.78 ± 6.65 years, including 49 men (72.06%). There were 18 patients in the good prognosis group and 50 patients in the poor prognosis group. The univariate analysis showed that Hcy, D-dimer, thrombin–antithrombin complex (TAT), and three territory sign in magnetic resonance imaging (MRI) were the risk factors for poor prognosis. Multivariate analysis showed that increased D-dimer (OR 4.497, 95% CI 1.014–19.938) and TAT levels (OR 4.294, 95% CI 1.654–11.149) were independent risk factors for the prognosis in such patients.

Conclusion: Image of patients with gastrointestinal malignant tumor-related AIS is characterized by three territory sign (multiple lesions in different vascular supply areas). Increased TAT and D-dimer levels are independent prognostic risk factors. TAT is more sensitive to predict prognosis than D-dimer.

Keywords: gastrointestinal malignant tumor, acute ischemic stroke, D-dimer (DD), TAT, prognosis

OPEN ACCESS

Edited by:
Yuzhen Xu,
Tongji University, China

Reviewed by:
Yongjun Cao,
The Second Affiliated Hospital of Soochow University, China
Taizen Nakase,
Tohoku University, Japan

***Correspondence:**
Yumin Li
liym@lzu.edu.cn

†These authors have contributed equally to this work and share first authorship

Specialty section:
This article was submitted to Neurological Biomarkers, a section of the journal Frontiers in Neurology

Received: *15 September 2021*
Accepted: *07 October 2021*
Published: *25 November 2021*

Citation:
Liu Y, Li X, Song F, Yan X, Han Z, Tang F and Li Y (2021) Clinical Features and Prognostic Factors of Acute Ischemic Stroke Related to Malignant Gastrointestinal Tumor. Front. Neurol. 12:777483. doi: 10.3389/fneur.2021.777483

INTRODUCTION

Armand Trousseau first reported the relation between thrombosis and malignant tumors in 1865 (1). Subsequent studies have confirmed that thrombosis is a common complication of malignant tumors, which is the second leading cause of death in patients with cancer (2). Thrombotic complications of cancer include arterial or venous thromboembolism and disseminated intravascular coagulation (DIC) (3, 4). Up to 15% of patients with malignant tumors have a history of acute ischemic stroke (AIS) (5), and about 20% of patients with AIS

due to an unknown cause (cryptogenic stroke) may have latent malignant tumors (6). Previous studies on gastrointestinal malignant tumor-related thromboembolism mainly focused on venous thromboembolism (7), and clinical studies on the associated AIS focused on a single type of gastrointestinal tumor (8), leading to a paucity of systematic analysis of different gastrointestinal tumor types. The present work retrospectively analyzes the 5-year clinical data of consecutive patients with gastrointestinal malignant tumor-related AIS in a single center. Prognostic factors are analyzed to improve clinical understanding of the gastrointestinal malignant tumor-related AIS.

THE MECHANISMS OF MALIGNANT TUMOR-RELATED AIS

Abnormal coagulation function is the main cause of AIS in patients with malignant tumor. Abnormal cerebrovascular coagulation is seen in patients with malignant tumors including breast cancer, leukemia, and lymphoma, after performing autopsy, which indicated the association between malignant tumors and coagulation and thrombosis (9). Kim et al. (10) conducted a prospective study and found that D-dimer levels in tumor-related cerebral infarction patients were significantly higher with increased incidence of multifocal cerebral infarction compared with conventional stroke risk factors. Tumor onset and progression are often accompanied by hypercoagulability, resulting in systemic and cerebral–arterial or venous thrombosis (11).

Adenocarcinomas, especially those of the pancreas, colon, breast, lung, prostate, and ovary induce thrombosis by producing and releasing mucin (a high-molecular weight molecule that is glycosylated and secreted by the endothelial cells) directly into the blood, which promotes a hypercoagulation state. Mucin can also interact with certain cellular adhesion molecules on endothelial cells, platelets, and lymphocytes, triggering the formation of microthrombi, which is rich in platelets (12). Meanwhile, tumor cells can produce cancer coagulants (cysteine protease that can independently activate coagulation X factor), tissue factors (binding with coagulation factor VII), and release inflammatory and vascular endothelial growth factors that can mediate coagulation and thrombosis (13–15). For example, tumor necrosis factor-α (TNF-α) affects the anticoagulant properties of the vascular endothelial cells through tissue factors, which promotes thrombin production, fibrin clot formation, and fibrin deposition in blood vessels, and can reduce fibrinolysis by inhibiting tPA activity (16). Tumors may also be associated with acute or chronic DIC. Due to excessive activation of the coagulation process, the imbalance between coagulation and fibrinolysis will eventually lead to thrombosis and arterial occlusion, resulting in AIS (17). The binding of malignant tumor cells with certain nonspecific immune signaling molecules, such as selectin, chemokines, and the corresponding receptors, is conducive to tumor invasion, migration, and adhesion. This will damage cellular connection and cause endothelial injury (18). The activation of the host immune system and the release of inflammatory factors will damage vascular endothelium and thus promote thrombosis (19). **Figure 1** shows the formation mechanism of hypercoagulable state in malignant tumors.

Nonbacterial thrombotic endocarditis (NBTE) caused by platelet thrombotic inflammatory complex is another important cause of malignant tumor-related AIS. In a work which consisted of 2,627 cases of postmortem examination, found that in 16 patients with malignant tumor complicated with NBTE, seven were complicated with cerebral infarction (20). This indicated that detaching of cardiac embolus in patients with malignant tumor complicated with NBTE can directly lead to AIS. In addition, infection (21, 22), tumor-related chemotherapy (23), endocrine therapy (24, 25) and, radiotherapy (26) can also lead to AIS in patients with a malignant tumor.

MATERIALS AND METHODS

Study Population

The clinical baseline data of patients with gastrointestinal malignant tumor complicated with AIS admitted to the Department of Neurology and Oncology in Lanzhou University Second Hospital from April 2015 to April 2019, were retrospectively analyzed. Eligible patients were required to meet the following criteria: (1) patients aged $\geq$18 years; (2) diagnosed with acute cerebral infarction conforming to Chinese Guidelines for the Diagnosis and Treatment of Acute Ischemic Stroke (2014) (5); (3) having clear imaging evidence in magnetic resonance imaging (MRI); (4) within 7 days of onset; (5) with a history of active malignant gastrointestinal tumor in the past or during follow-up. Patients were excluded if they had the following characteristics: (1) a history of TIA or cerebral hemorrhage; (2) primary tumors of the central nervous system, hematological, and other systems; (3) incomplete medical records; (4) poor prognosis due to tumor progression or chemotherapy.

Study Measures

Baseline and MRI Data

General information of the patients was retrieved, including gender, age, medical history and complications, laboratory tests on the second day of admission, tumor related data, and the results of echocardiography. The MRI data of the patients were collected. The location and the number of lesions on DWI were recorded. Lesions in both hemispheres were defined as bilateral infarction, and multiple infarctions referred to more than two lesions. Distribution patterns of the lesions were categorized into the following: (1) one territory sign: single or multiple lesions in unilateral anterior or posterior circulation; (2) two territory sign: single or multiple lesions in unilateral anterior and posterior circulations, or in bilateral anterior circulations; (3) three territory sign: bilateral single or multiple lesions in bilateral anterior and posterior circulations. Prognosis of the patients was evaluated by mRS, 90 days after discharge. An mRS score of 0–2 was defined as good prognosis, and score >2 was regarded as poor prognosis.

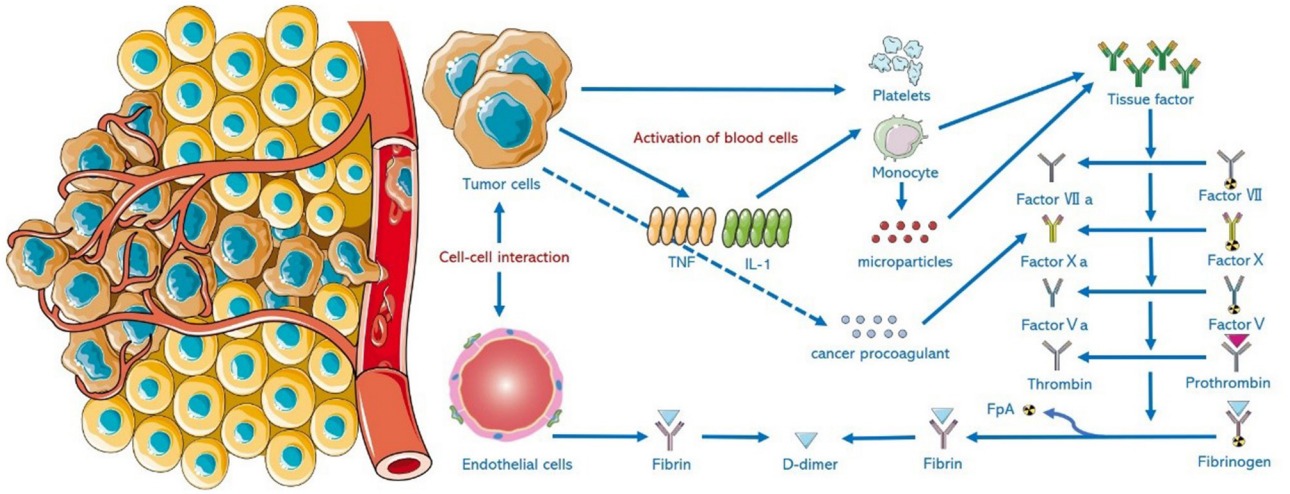

FIGURE 1 | Mechanism of hypercoagulable state in malignant tumors. Tumor cells activate cellular systems *in vivo* through intercellular interactions and injured endothelial cells. Tumor cells can directly release tissue factor (TF) and cancer procoaparticles (CP). Tumor cells produce cytokines including interleukin-1 (IL-1) and tumor necrosis factor (TNF). Activated blood cells (such as monocytes and platelets) and the microparticles (MP) produced by these cells work synergistically to increase TF expression and activate the coagulation system *in vivo*.

Statistical Analysis

Statistical analysis was performed by the SPSS 25.0. Enumeration data were recorded in ratio or proportion using $\chi 2$ or Fisher tests for comparisons among groups. Normally distributed measurement data was expressed as X ± S, using *t*-test for comparisons among groups. Median and range (M, P25–P75) were used if the measurement data were not normally distributed, and the Mann–Whitney U test was used for comparisons among groups. Variables with $P < 0.05$ in univariate analysis were taken as independent variables with a 90-day prognosis as dependent variable. Multivariate logistic regression analysis was used to screen out independent risk factors for prognosis. $P < 0.05$ was considered statistically significant.

RESULTS

A total of 68 patients with gastrointestinal cancer complicated with AIS were enrolled in this study, including 49 (72.09%) men and 19 (27.91%) women, with a mean age of 61.78 ± 6.65 years. Cases of complications included hypertension, diabetes, hyperlipidemia, and coronary heart disease, and were 45 (66.18%), 38 (55.88%), 43 (63.24%), and 45 (66.18%), respectively. Patients with a history of drinking and smoking accounted for 50.00 and 35.29%, respectively. Fifteen (22.06%) cases and 14 (20.59%) cases had a history of atrial fibrillation and stroke, respectively. The types of gastrointestinal malignant tumors included gastric cancer (42/68, 61.76%), colorectal cancer (17/68, 25.00%), gallbladder cancer (4/68, 5.88%), pancreatic cancer (2.68, 2.94%), liver cancer (2/68, 2.94%), and esophageal cancer (1/68, 1.47%). Adenocarcinoma was the main pathological tumor type, accounting for 63/68 cases (92.65%). Fifty-two (76.47%) cases had a history of malignant tumor, 16 (23.53%) cases without a previous history of tumor. Malignant tumors were diagnosed during hospitalization or follow-up due to AIS. MRI showed multiple scattered lesions. Patients with two and three territory signs accounted for 25 (36.76%) and 30 (44.12%) cases, respectively; one territory sign was only observed in seven (10.29%) cases. **Figure 2** shows the characteristics of gastrointestinal malignant tumor-related AIS in MRI.

The baseline characteristics of all study population and univariate regression analysis of prognosis are summarized in **Table 1**, with 18 patients in the good prognosis group and 50 patients in the poor prognosis group. Compared with the good prognosis group, patients in the poor prognosis group of three territory sign in MRI (52.00 vs. 22.22%, $P = 0.029$) showed higher levels of Hcy (8.84 ± 3.03 vs. 17.00 ± 3.40 μmol/L, $P = 0.047$) and D-dimer (2.12 ± 0.78 vs. 1.24 ± 0.70 mg/L, $P < 0.001$), and also higher levels of TAT (8.07 ± 3.99 vs. 3.75 ± 1.40 ng/ml, $P < 0.001$), all with significant differences ($P < 0.05$).

Table 2 shows the multivariate analysis of prognosis. The results showed higher levels of D-dimer (OR 4.497, 95% CI 1.014–19.938) and TAT (OR 4.294, 95% CI 1.654–11.149) which are independent risk factors for the prognosis in patients with gastrointestinal malignant tumor-related AIS ($P < 0.05$).

The baseline levels of D-dimer and thrombin–antithrombin (TAT) were 1.89 ± 0.85 and 6.93 ± 3.98 ng/ml, respectively. The levels of D-dimer at 3, 6, and 9-month follow-up were 1.65 ± 0.80, 1.52 ± 0.97, and 1.39 ± 1.02 mg/L, respectively; the levels of TAT were 8.46 ± 6.17, 9.88 ± 8.61, and 9.33 ± 8.82 ng/ml, respectively. An ROC curve analysis showed that when the AUC of D-dimer was 0.894 with a cutoff value of 1.60 mg/L FEU, the diagnostic sensitivity and specificity were 78.0 and 94.4%, respectively; when the AUC of TAT was 0.926 with a cutoff value of 5.05 ng/mL, the diagnostic sensitivity and specificity

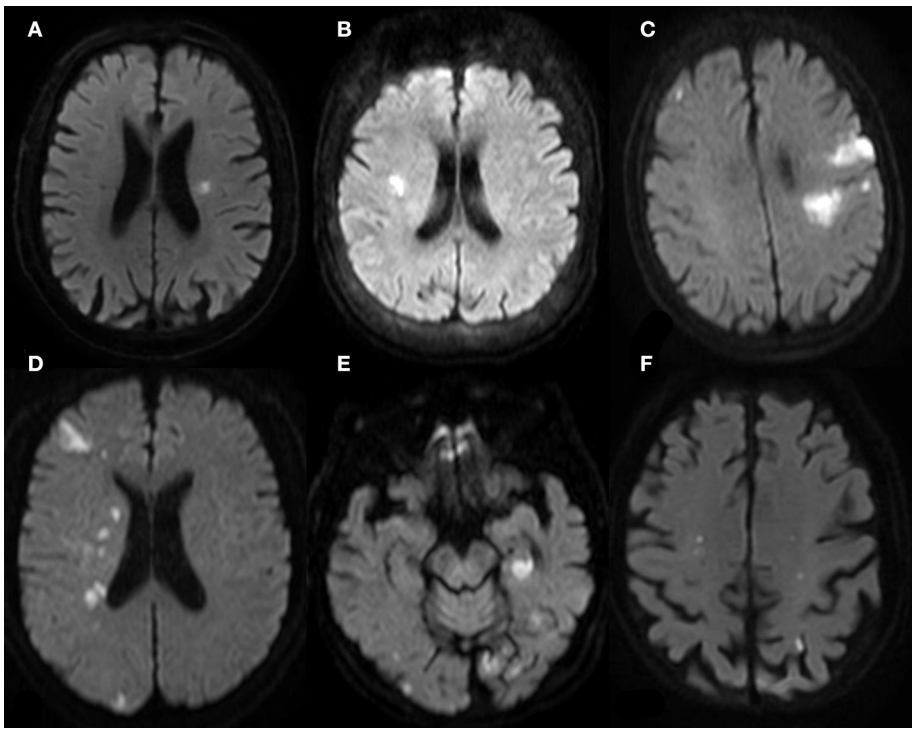

FIGURE 2 | MR (DWI) of patients with gastrointestinal malignant tumor-related AIS. **(A,B)** One Territory Sign (different patients): lesions with hyperintense signal in the supply area of LMCA in **(A)**; lesions with hyperintense signal in the supply area of RMCA. **(C,D)** Two Territory Sign (different patients): multiple lesions in the supply area of LMCA and RACA in **(C)**, involving cortex and deep white matter region; multiple lesions in the supply area of RMCA and RPCA in **(D)**. **(E,F)** Three Territory Sign (the same patient): massive lesions in the left posterior hippocampus region supplied by the posterior choroid artery of LPCA; scattered lesions in bilateral occipital cortex and subcortex, more prominent on the left side. **(E)** shows two dotted lesions in the supply area of bilateral internal carotid arteries.

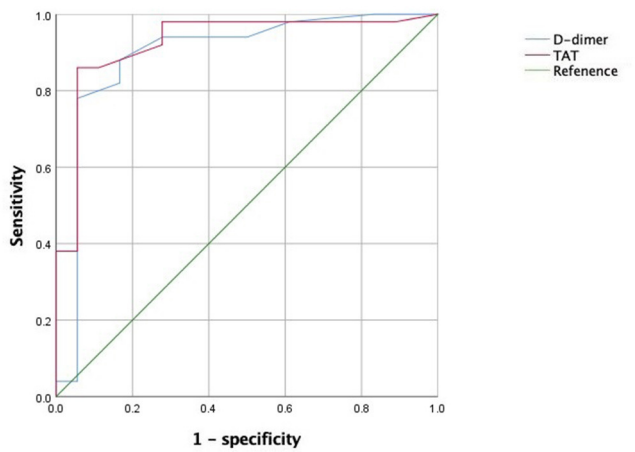

FIGURE 3 | ROC curve of TAT and D-dimer levels for prognosis in patients with gastrointestinal malignant tumor-related AIS.

of TAT were 86.0 and 94.4%, respectively. **Figure 3** show ROC curve of TAT and D-dimer levels for prognosis in patients with gastrointestinal malignant tumor-related AIS.

DISCUSSION

Acute ischemic stroke may be identified prior to malignant tumor, which may be an early evidence of potential malignant tumor. Previous studies have found that patients with malignant tumor and with AIS as an initial symptom accounted for 0.4–3.0% of hospitalized stroke patients, and about 5.3–20% of latent stroke patients were diagnosed with malignant tumor during hospitalization, commonly including lung, breast, liver, stomach, and prostate cancers (27, 28). Malignant tumor-related AIS is prone to early neurological deterioration, with high recurrence and poor prognosis, and the prognosis varies in patients with different types of such cerebral infarctions (29). Based on the 2020 data from the International Agency for Research on Cancer (IARC), colorectal, liver, and gastric cancers were the third to fifth common malignant tumors in men, and colorectal cancer is the second common cancer in women (30). Analyzing the characteristics of gastrointestinal malignant tumor-related AIS is the basis for the treatment of such kinds of disease.

Prognostic Factors in Patients With Gastrointestinal Malignant Tumor-Related AIS

The results showed no significant difference between good and poor prognosis groups in common risk factors of AIS

TABLE 1 | Univariate regression analysis of poor prognosis in patients with gastrointestinal malignant tumor-related AIS.

Item	Total (68)	Good prognosis (18)	Poor prognosis (50)	*P*-value
Male, *n* (%)	49 (72.06)	14 (77.78)	35 (70.00)	0.528
Age, years	61.78 ± 6.65	61.78 ± 6.11	61.78 ± 6.90	0.741
Hypertension, *n* (%)	45 (66.18)	9 (50.00)	36 (72.00)	0.091
Diabetes, *n* (%)	38 (55.88)	7 (38.89)	31 (62.00)	0.090
Hyperlipidemia, *n* (%)	43 (63.24)	9 (50.00)	34 (68.00)	0.174
AF, *n* (%)	15 (22.06)	2 (11.11)	13 (26.00)	0.330
CHD, *n* (%)	37 (54.41)	8 (44.44)	29 (58.00)	0.322
Stroke, *n* (%)	14 (20.59)	4 (22.22)	10 (20.00)	1.000
Smoking, *n* (%)	24 (35.29)	6 (33.33)	18 (36.00)	0.839
Drinking, *n* (%)	34 (50.00)	10 (55.56)	24 (48.00)	0.582
Previous tumor history, *n* (%)	52 (76.47)	11 (61.11)	41 (82.00)	0.574
MT to stroke after tumor, month	6.15 ± 3.21	6.86 ± 2.26	5.64 ± 3.02	0.812
Diagnosis after stroke, *n* (%)	16 (23.53)	7 (38.89)	9 (18.00)	0.871
MT to tumor after stroke, month	12.39 ± 4.12	13.21 ± 3.22	10.18 ± 2.41	0.072
RBC (×1012/L)	4.51 ± 0.75	4.62 ± 0.90	4.47 ± 0.69	0.833
WBC (×109/L)	7.01 ± 2.10	7.76 ± 2.02	6.74 ± 2.08	0.810
PLT (×109/L)	314.22 ± 20.85	306.33 ± 29.53	317.06 ± 16.14	0.326
Hb, g/L	119.09 ± 10.34	122.56 ± 15.30	117.84 ± 7.69	0.231
LDL-C, mmol/L	4.11 ± 0.72	3.89 ± 0.70	4.19 ± 0.72	0.130
Hcy, μmol/L	18.35 ± 3.21	17.00 ± 3.40	18.84 ± 3.03[a]	0.047
Fib, g/L	4.30 ± 0.60	4.18 ± 0.57	4.34 ± 0.61	0.981
D-dimer, mg/L	1.89 ± 0.85	1.24 ± 0.70	2.12 ± 0.78[a]	<0.001
TAT, ng/ml	6.93 ± 3.98	3.75 ± 1.40	8.07 ± 3.99[a]	<0.001
One territory sign	7 (10.29)	4 (22.22)	3 (6.00)	0.136
Two territory sign	25 (36.76)	4 (22.22)	21 (42.00)	0.136
Three territory sign	30 (44.12)	4 (22.22)	26 (52.00)[a]	0.029
Cardiac valvular vegetations	13 (19.12)	2 (11.11)	11 (22.00)	0.511

CHD, coronary heart disease; AF, atrial fibrillation; MT, mean time; RBC, Red blood cell; WBC, White blood cell; PLT, Platelet; Hb, Hemoglobin; LDL-C, low-density lipoprotein cholesterol; Hcy, homocysteine; Fib, fibrinogen; TAT, thrombin-antithrombin complex. [a]*P < 0.05, as compared to poor prognosis.*

TABLE 2 | Multivariate analysis of poor prognosis in patients with gastrointestinal malignant tumor-related AIS.

Variables	β	SE	Wals	Df	*P*-value	OR	95% CI
Hcy	0.259	0.164	2.493	1	0.114	1.296	0.939–1.788
D-dimer	1.503	0.76	3.914	1	0.048	4.497	1.014–19.938
TAT	1.457	0.487	8.957	1	0.003	4.294	1.654–11.149
Three territory sign	2.2	1.216	3.271	1	0.071	9.021	0.832–97.827

including hypertension, coronary heart disease, diabetes, and hyperlipidemia. Higher levels of fibrinogen, TAT, and D-dimer, and greater proportion of patients with multiple scattered infarctions were observed in the poor prognosis group, which indicated a different mechanism of tumor-related AIS from the common atherosclerotic infarction. It has been proposed that tumor necrosis factors or cytokines produced by tumor cells can promote coagulation through DIC and form microthrombi (31). The mechanisms of malignant tumor-related AIS include hypercoagulability, NBTE, infection, tumor-related chemotherapy, endocrine therapy, and radiotherapy, among which, hypercoagulability plays the most important role. This study found that increased levels of D-dimer and TAT are independent prognostic factors of such patients, which is consistent with the results of previous studies (32). Results of this study also confirmed that hypercoagulation may be the major mechanism of cerebral infarction in patients with a malignant tumor.

TAT as a Better Prognostic Factor Than D-Dimer in Tumor-Related AIS

D-dimer has been proposed as a predictor of AIS in patients with a malignant tumor (33, 34). However, the limitations of the testing methods, interference by rheumatoid factor, immune complex, and intake of antitumor drugs or immunoenhancing drugs may lead to false positive results (35). With the updated testing methods, TAT and other indicators become more suitable for clinical application. These indicators are molecular markers of thrombosis and fibrinolysis that can reflect the state of coagulation and fibrinolysis in patients with a malignant tumor

(36, 37). TAT is a complex formed by thrombin and antithrombin III. As a molecular marker of thrombin formation, TAT directly reflects the activation of the coagulation system. Increased TAT is a hint of procoagulant activation and inhibitor depletion and is one of the earliest indicators of coagulation dysfunction (38). Fidan et al. found that the level of TAT in gastric cancer patients was significantly higher than that in the control group, with stable expression at different tumor stages, which was a reliable marker for the hypercoagulation state of malignant tumors (39). The present study also confirmed that TAT expression was significantly correlated with the clinical prognosis in patients with gastrointestinal malignancy, and was more sensitive and specific than D-dimer. Therefore, we believe that TAT is better than D-dimer in predicting the prognosis of patients with malignant tumor-related thrombotic events, which is consistent with the results of Cui et al. (40).

MRI Features of Gastrointestinal Malignant Tumor-Related AIS

Previous research found that in AIS patients complicated with malignant tumor the incidence of infarction simultaneously involving three main intracranial arterial supply areas was six times that of patients with atrial fibrillation (41). A significant increase of D-dimer is a characteristic of malignant tumor-related AIS (42–44). In this study, most patients showed infarction in three territories on DWI (44.12%), which was an independent risk factor for prognosis.

Echocardiogram was performed in all the patients to identify potential cardiogenic embolism, and 19.12% (13/68) of the patients were found to have NBTE which is basically consistent with the proportion of NBTE in about 19% of patients with malignant tumors found by Edoute et al. (45). NBTE is most common in lung or gastrointestinal adenocarcinoma-related AIS associated with lung cancer or gastrointestinal adenocarcinoma, which is also reported in pancreatic and biliary cancer (46). However, NBTE was not found in patients with pancreatic and biliary cancer in this study.

Prognosis, the Temporal Relation Between Gastrointestinal Malignant Tumor, and AIS

It has been reported that the mortality of AIS was higher in patients complicated with malignant tumor than those without the tumor (47). The former research showed that a 3-month mortality rate of 46.9% in patients with malignant tumor complicated with AIS after receiving relevant treatment and 50% of the survivors had neurological sequela (48). Another study showed that an average follow-up of 29 months for 24 patients with cerebral infarction complicated with latent tumor, with mortality reaching 79%. At a 1-year follow-up, 73.53% (50/68) of the patients showed poor outcomes (mRS $>$ 2) including deaths (27). The poor therapeutic effects may be attributed to the complex mechanisms of cancer, or the onset of AIS leading to aggravation of the general condition of the patients, even affecting, or interrupting antitumor therapy.

Selvik et al. (49) found an average interval of 14 months from the onset of AIS, to the diagnosis of the tumor. In the present study, 16 patients (23.53%) were diagnosed with malignant gastrointestinal tumor 12.39 $\pm$ 4.12 months after AIS; 52 patients (76.47%) developed AIS after the diagnosis of tumor, with an average interval of 6.15 $\pm$ 3.21 months, which is basically consistent with previous results showing an interval of 1.5–9 months (50).

CONCLUSIONS

Patients with AIS related to gastrointestinal malignant tumor have a relatively poor prognosis. Increased levels of TAT and D-dimer are independent risk factors for poor prognosis. TAT has a better performance than D-dimer in predicting prognosis in patients with gastrointestinal malignant tumor-related AIS.

LIMITATIONS

Some limitations have to be admitted for we report a retrospective study with a relatively small number of patients. Due to the limited number of the included cases, tumor stage and treatment were not analyzed, which could limit the statistical significance of the results. Multicenter studies and larger sample are required for analysis to better summarize the clinical characteristics of malignant tumor patients complicated with AIS in future.

DATA AVAILABILITY STATEMENT

The raw data supporting the conclusions of this article will be made available by the authors, without undue reservation.

ETHICS STATEMENT

The studies involving human participants were reviewed and approved by Lanzhou University Second Hospital Ethics Committee. The patients/participants provided their written informed consent to participate in this study. Written informed consent was obtained from the individual(s) for the publication of any potentially identifiable images or data included in this article.

AUTHOR CONTRIBUTIONS

YLiu and XL contributed to the study design and drafted the manuscript. FS and XY analyzed the data in the literature and edited the manuscript. YLi contributed to the study design, supervised writing of the manuscript, critically reviewed the paper, and supervised the research project. All authors contributed to the article and approved the submitted version.

FUNDING

This work was supported by grants from the Science and Technology Foundation for Young Scientist of Gansu Province, China (Grant no. 21JR1RA163), The Natural Science Foundation of Gansu Province, China (Grant no. 21JR1RA136), The Science and Technology Project of CuiYing, Lanzhou University Second Hospital, China (Grant no. CY2018-MS06), and Major Science and Technology Projects of Gansu Province, China (20ZD7FA003).

SUPPLEMENTARY MATERIAL

The Supplementary Material for this article can be found online at: https://www.frontiersin.org/articles/10.3389/fneur.2021.777483/full#supplementary-material

REFERENCES

1. Prandoni P, Falanga A, Piccioli A. Cancer and venous thromboembolism. *Lancet Oncol.* (2005) 6:401–10. doi: 10.1016/S1470-2045(05)70207-2
2. Noble S, Pasi J. Epidemiology and pathophysiology of cancer-associated thrombosis.*Br J Cancer.* (2010) 102 Suppl 1:S2–9. doi: 10.1038/sj.bjc.6605599
3. Levi M. Cancer-related coagulopathies. *Thromb Res.* (2014) 133 Suppl 2:S70–5. doi: 10.1016/S0049-3848(14)50012-6
4. Eichinger S. Cancer associated thrombosis: risk factors and outcomes. *Thromb Res*. (2016) 140 Suppl 1:S12–S17. doi: 10.1016/S0049-3848(16)30092-5
5. Grisold W, Oberndorfer S, Struhal W. Stroke and cancer: a review. *Acta Neurol Scand.* (2009) 119:1–16. doi: 10.1111/j.1600-0404.2008.01059.x
6. Kim SJ, Park JH, Lee MJ, Park YG, Ahn MJ, Bang OY. Clues to occult cancer in patients with ischemic stroke. *PLoS ONE.* (2012) 7:e44959. doi: 10.1371/journal.pone.0044959
7. Larsen AC, Dabrowski T, Frøkjær JB, Fisker RV, Iyer VV, Møller BK, et al. Prevalence of venous thromboembolism at diagnosis of upper gastrointestinal cancer. *Br J Surg.* (2014) 101:246–53. doi: 10.1002/bjs.9353
8. Kuan AS, Chen SC, Yeh CM, Hung MH, Hung YP, Chen TJ, et al. Risk of ischemic stroke in patients with gastric cancer: a nationwide population-based cohort study. *Medicine.* (2015) 94:e1336. doi: 10.1097/MD.0000000000001336
9. Collins RC, Al-Mondhiry H, Chernik NL, Posner JB. Neurologic manifestations of intravascular coagulation in patients with cancer. A clinicopathologic analysis of 12 cases. *Neurology.* (1975) 25:795–806. doi: 10.1212/WNL.25.9.795
10. Kim SG, Hong JM, Kim HY, Lee J, Chung PW, Park KY, et al. Ischemic stroke in cancer patients with and without conventional mechanisms: a multicenter study in Korea. *Stroke.* (2010) 41:798–801. doi: 10.1161/STROKEAHA.109.571356
11. Schwarzbach CJ, Schaefer A, Ebert A, Held V, Bolognese M, Kablau M, et al. Stroke and cancer: the importance of cancer-associated hypercoagulation as a possible stroke etiology. *Stroke.* (2012) 43:3029–34. doi: 10.1161/STROKEAHA.112.658625
12. Dearborn JL, Urrutia VC, Zeiler SR. Stroke and Cancer-A Complicated Relationship. *J Neurol Transl Neurosci.* (2014) 2:1039.
13. Selvik HA, Thomassen L, Logallo N, Næss H. Prior cancer in patients with ischemic stroke: the Bergen NORSTROKE study. *J Stroke Cerebrovasc Dis.* (2014) 23:919–25. doi: 10.1016/j.jstrokecerebrovasdis.2013.07.041
14. Lee AY. Cancer and thromboembolic disease: pathogenic mechanisms. *Cancer Treat Rev*. (2002) 28:137–40. doi: 10.1016/S0305-7372(02)00044-0
15. Franco AT, Corken A, Ware J. Platelets at the interface of thrombosis, inflammation, and cancer. *Blood.* (2015) 126:582–8. doi: 10.1182/blood-2014-08-531582
16. Peng Z, Shu B, Zhang Y, Wang M. Endothelial response to pathophysiological stress. *Arterioscler Thromb Vasc Biol.* (2019) 39:e233–43. doi: 10.1161/ATVBAHA.119.312580
17. Lefkovitz NW, Roessmann U, Kori SH. Major cerebral infarction from tumor embolus. *Stroke.* (1986) 17:555–7. doi: 10.1161/01.STR.17.3.555
18. Friedl P, Alexander S. Cancer invasion and the microenvironment: plasticity and reciprocity. *Cell.* (2011) 147:992–1009. doi: 10.1016/j.cell.2011.11.016
19. Elkind MS. Inflammatory mechanisms of stroke. *Stroke.* (2010) 41(10 Suppl):S3–S8. doi: 10.1161/STROKEAHA.110.594945
20. Ojeda VJ, Frost F, Mastaglia FL. Non-bacterial thrombotic endocarditis associated with malignant disease: a clinicopathological study of 16 cases. *Med J Aust.* (1985) 142:629–31. doi: 10.5694/j.1326-5377.1985.tb113555.x
21. Zembower TR. Epidemiology of infections in cancer patients. *Cancer Treat Res.* (2014) 161:43–89. doi: 10.1007/978-3-319-04220-6_2
22. Bos MM, Smeets LS, Dumay I, de Jonge E. Bloodstream infections in patients with or without cancer in a large community hospital. *Infection.* (2013) 41:949–58. doi: 10.1007/s15010-013-0468-1
23. Saynak M, Cosar-Alas R, Yurut-Caloglu V, Caloglu M, Kocak Z, Uzal C. Chemotherapy and cerebrovascular disease. *J BUON.* (2008) 13:31–6.
24. Robinson D, Garmo H, Lindahl B, Van Hemelrijck M, Adolfsson J, Bratt O. et al. Ischemic heart disease and stroke before and during endocrine treatment for prostate cancer in PCBaSe Sweden. *Int J Cancer.* (2012) 130:478–87. doi: 10.1002/ijc.26022
25. Mosca L, Grady D, Barrett-Connor E, Collins P, Wenger N, Abramson BL, et al. Effect of raloxifene on stroke and venous thromboembolism according to subgroups in postmenopausal women at increased risk of coronary heart disease. *Stroke.* (2009) 40:147–55. doi: 10.1161/STROKEAHA.108.518621
26. Scott AS, Parr LA, Johnstone PA. Risk of cerebrovascular events after neck and supraclavicular radiotherapy: a systematic review. *Radiother Oncol.* (2009) 90:163–5. doi: 10.1016/j.radonc.2008.12.019
27. Taccone FS, Jeangette SM, Blecic SA. First-ever stroke as initial presentation of systemic cancer. *J Stroke Cerebrovasc Dis.* (2008) 17:169–74. doi: 10.1016/j.jstrokecerebrovasdis.2008.01.007
28. Ikushima S, Ono R, Fukuda K, Sakayori M, Awano N, Kondo K. Trousseau's syndrome: cancer-associated thrombosis. *Jpn J Clin Oncol.* (2016) 46:204–8. doi: 10.1093/jjco/hyv165
29. Kneihsl M, Enzinger C, Wünsch G, Khalil M, Culea V, Urbanic-Purkart T, et al. Poor short-term outcome in patients with ischaemic stroke and active cancer. *J Neurol.* (2016) 263:150–6. doi: 10.1007/s00415-015-7954-6
30. Sung H, Ferlay J, Siegel RL, Laversanne M, Soerjomataram I, Jemal A, et al. Global Cancer Statistics 2020: GLOBOCAN Estimates of Incidence and Mortality Worldwide for 36 Cancers in 185 Countries. *CA Cancer J Clin*. (2021) 71:209–49. doi: 10.3322/caac.21660
31. Yigit M, Sogut O, Yigit E, Turkdogan KA, Kaplan O, Dur A, et al. The relationship between anemia and recurrence of ischemic stroke in patients with Trousseau's syndrome: a retrospective cross-sectional study. *Turk J Emerg Med*. (2016) 16:65–8. doi: 10.1016/j.tjem.2015.11.013
32. Tsushima M, Metoki N, Hagii J, Saito S, Shiroto H, Yasujima M, et al. D-dimer and C-reactive Protein as Potential Biomarkers for Diagnosis of Trousseau's Syndrome in Patients with Cerebral Embolism. *J Stroke Cerebrovasc Dis.* (2020) 29:104534. doi: 10.1016/j.jstrokecerebrovasdis.2019.104534
33. Chen W, He Y, Su Y. Multifocal cerebral infarction as the first manifestation of occult malignancy: case series of trousseau's syndrome and literature review. *Brain Circ.* (2018) 4:65–72. doi: 10.4103/bc.bc_1_18
34. Sorgun MH, Kuzu M, Ozer IS, Yilmaz V, Ulukan C, Cotur Levent H, et al. Risk Factors, Biomarkers, Etiology, Outcome and Prognosis of Ischemic Stroke in Cancer Patients. *Asian Pac J Cancer Prev*. (2018) 19:649–53. doi: 10.22034/APJCP.2018.19.3.649
35. Reitter EM, Kaider A, Ay C, Quehenberger P, Marosi C, Zielinski C, et al. Longitudinal analysis of hemostasis biomarkers in cancer patients during antitumor treatment. *J Thromb Haemost.* (2016) 14:294–305. doi: 10.1111/jth.13218

36. Nakano K, Sugiyama K, Satoh H, Arifuku H, Fujimatsu T, Yoshida N, et al. Effect of Thrombomodulin Alfa on Disseminated Intravascular Coagulation in Patients with Lung Cancer. *Intern Med.* (2017) 56:1799–806. doi: 10.2169/internalmedicine.56.7143
37. Lee SY, Niikura T, Iwakura T, Sakai Y, Kuroda R. Kurosaka M. Thrombin-antithrombin III complex tests. *J Orthop Surg.* (2017) 25:170840616684501. doi: 10.1177/0170840616684501
38. Kvolik S, Jukic M, Matijevic M, Marjanovic K, Glavas-Obrovac L. An overview of coagulation disorders in cancer patients. *Surg Oncol.* (2010) 19:e33–46. doi: 10.1016/j.suronc.2009.03.008
39. Fidan E, Kavgaci H, Orem A, Yilmaz M, Yildiz B, Fidan S, et al. Thrombin activatable fibrinolysis inhibitor and thrombin-antithrombin-III-complex levels in patients with gastric cancer. *Tumour Biol.* (2012) 33:1519–25. doi: 10.1007/s13277-012-0403-6
40. Cui CJ, Cui W, Gao J, Li J, Yan CE, Yu MY. TAT and PIC better than Ddimer in monitoring hypercoagulability of cancer patients. *Chin J Lab Med.* (2019) 42:853–7. doi: 10.3760/cma.j.issn.1009-8158.2019.10.008
41. Nouh AM, Staff I, Finelli PF. Three territory sign: an MRI marker of malignancy-related ischemic stroke (Trousseau syndrome). *Neurol Clin Pract.* (2019) 9:124–8. doi: 10.1212/CPJ.0000000000000603
42. Chi X, Zhao R, Pei H, Xing A, Hu S, Chen J, et al. Diffusion-weighted imaging-documented bilateral small embolic stroke involving multiple vascular territories may indicate occult cancer: a retrospective case series and a brief review of the literature. *Aging Med.* (2020) 3:53–9. doi: 10.1002/agm2.12105
43. Selvik HA, Bjerkreim AT, Thomassen L, Waje-Andreassen U, Naess H, Kvistad CE. When to Screen Ischaemic Stroke Patients for Cancer. *Cerebrovasc Dis.* (2018) 45:42–7. doi: 10.1159/000484668
44. Prugger C, Luc G, Haas B, Morange PE, Ferrieres J, Amouyel P, et al. Multiple biomarkers for the prediction of ischemic stroke: the PRIME study. *Arterioscler Thromb Vasc Biol.* (2013) 33:659–66. doi: 10.1161/ATVBAHA.112.300109
45. Edoute Y, Haim N, Rinkevich D, Brenner B, Reisner SA. Cardiac valvular vegetations in cancer patients: a prospective echocardiographic study of 200 patients. *Am J Med.* (1997) 102:252–8. doi: 10.1016/S0002-9343(96)00457-3
46. Liu J, Frishman WH. Nonbacterial thrombotic endocarditis: pathogenesis, diagnosis, and management. *Cardiol Rev.* (2016) 24:244–7. doi: 10.1097/CRD.0000000000000106
47. Zhang YY, Cordato D, Shen Q, Sheng AZ, Hung WT, Chan DK. Risk factor, pattern, etiology and outcome in ischemic stroke patients with cancer: a nested case-control study. *Cerebrovasc Dis.* (2007) 23:181–7. doi: 10.1159/000097639
48. Cutting S, Wettengel M, Conners JJ, Ouyang B, Busl K. Three-Month Outcomes Are Poor in Stroke Patients with Cancer Despite Acute Stroke Treatment. *J Stroke Cerebrovasc Dis.* (2017) 26:809–15. doi: 10.1016/j.jstrokecerebrovasdis.2016.10.021
49. Selvik HA, Thomassen L, Bjerkreim AT, Næss H. Cancer-associated stroke: the Bergen NORSTROKE study. *Cerebrovasc Dis Extra.* (2015) 5:107–13. doi: 10.1159/000440730
50. Sørensen HT, Mellemkjaer L, Olsen JH, Baron JA. Prognosis of cancers associated with venous thromboembolism. *N Engl J Med.* (2000) 343:1846–50. doi: 10.1056/NEJM200012213432504

Conflict of Interest: The authors declare that the research was conducted in the absence of any commercial or financial relationships that could be construed as a potential conflict of interest.

Publisher's Note: All claims expressed in this article are solely those of the authors and do not necessarily represent those of their affiliated organizations, or those of the publisher, the editors and the reviewers. Any product that may be evaluated in this article, or claim that may be made by its manufacturer, is not guaranteed or endorsed by the publisher.

Copyright © 2021 Liu, Li, Song, Yan, Han, Tang and Li. This is an open-access article distributed under the terms of the Creative Commons Attribution License (CC BY). The use, distribution or reproduction in other forums is permitted, provided the original author(s) and the copyright owner(s) are credited and that the original publication in this journal is cited, in accordance with accepted academic practice. No use, distribution or reproduction is permitted which does not comply with these terms.

frontiers in Neurology

ORIGINAL RESEARCH
published: 30 November 2021
doi: 10.3389/fneur.2021.736404

Association Between Types of Posterior Staphyloma and Refractive Error After Cataract Surgery for High Myopia

Jing Wu[1,2†], *Ruochen Wang*[3†], *Can Liu*[1], *Yu Zhou*[1], *Ziyuan Jiang*[1] *and Fang Liu*[1,2*]

[1] *Department of Ophthalmology, Tenth People's Hospital Affiliated of Tongji University, Shanghai, China,* [2] *Department of Ophthalmology, Tenth People's Hospital Chongmin Branch, Shanghai, China,* [3] *Department of Epidemiology, University of Michigan School of Public Health, Ann Arbor, MI, United States*

OPEN ACCESS

Edited by:
Jinming Han,
Capital Medical University, China

Reviewed by:
Yunpeng Zhang,
Brandeis University, United States
Tao Li,
Fudan University, China
Yan Yan,
Shanghai JiaoTong University, China
Ashish Markan,
Post Graduate Institute of Medical Education and Research (PGIMER), India
Enrique García Gen,
Universidad CEU Cardenal Herrera, Spain

***Correspondence:**
Fang Liu
fangliu_2004@yahoo.com

†These authors have contributed equally to this work

Specialty section:
This article was submitted to Neurological Biomarkers, a section of the journal Frontiers in Neurology

Received: *05 July 2021*
Accepted: *29 October 2021*
Published: *30 November 2021*

Citation:
Wu J, Wang R, Liu C, Zhou Y, Jiang Z and Liu F (2021) Association Between Types of Posterior Staphyloma and Refractive Error After Cataract Surgery for High Myopia. Front. Neurol. 12:736404. doi: 10.3389/fneur.2021.736404

Purpose: To investigate the association between different types of posterior staphyloma (PS) and refractive error (RE) after cataract surgery in patients with high myopia.

Methods: This retrospective study included 113 eyes of 113 highly myopic patients with PS. PS was detected using a wide-field fundus imaging system. PS was classified into wide macular, narrow macular, and other types. RE equaled the actual spherical equivalent (SE) minus the targeted SE values 3 months after cataract surgery.

Results: The rates of wide macular, narrow macular, and other types of PS were 46.02, 39.82, and 14.16%, respectively. There were no significant differences in best corrected distance visual acuity (BCDVA) or SE among the three classifications of PS before cataract surgery ($P > 0.05$). However, postoperative BCDVA and SE were significantly different among the three types of PS patients ($P < 0.05$). The average RE values were 0.98 ± 1.00 D, 0.19 ± 0.87 D, 0.13 ± 0.59 D, respectively; the statistical differences of RE were <0.01, <0.01, and 0.81 (wide macular vs. narrow macular, wide macular vs. other types, narrow macular vs. other types), respectively. Multivariate linear regression analysis revealed that higher hyperopia RE after surgery was associated with wide macular staphyloma ($P < 0.001$), more myopic SE ($P = 0.003$), and increased BCDVA ($P = 0.002$) before surgery.

Conclusions: Wide macular PS may be associated with more hyperopic RE; it may serve as a critical biomarker of hyperopic RE after cataract surgery in highly myopic patients.

Keywords: high myopia, refractive error, posterior staphyloma, cataract surgery, biomarker

INTRODUCTION

High myopia is considered a neurovascular disease and may affect both the retinal microvascular network and optic nerve, causing visual impairment (1–4). The prevalence of high myopia is increasing worldwide, and remains the leading cause of irreversible vision loss in adults due to associated complications (5, 6). Posterior staphyloma (PS) is a hallmark of myopic retinopathy (7, 8), which was defined by Spaide in 2013 as "an outpouching of the wall of the eye that has a

radius of curvature that is less than the surrounding curvature of the wall of the eye" (9). PS is present in about one in three to one in two of highly myopic eyes in adults, and the prevalence of PS is associated with increasing age and longer axial length (10–12).

In 1977, Curtin first classified PS into 10 types according to its morphological characteristics on fundoscopic examination (13); this classification is still used in clinical practice. Recently, PS has become more easily detected using new instruments such as optical coherence tomography and high-resolution, three-dimensional magnetic resonance imaging (3D-MRI) (14, 15). However, traditional fundus images often cannot include the entire border of the PS, in particular, in wide macular staphyloma; in addition, screening with 3D-MRI may not be feasible in the clinic. In 2014, Ohno-Matsui analyzed the morphological characteristics of the whole eye by applying wide-field fundus imaging, so that even a large field of PS could be imaged directly and comprehensively. More importantly, this method simplified the classification of PS according to its location and distribution, in contrast to traditional classification (10, 16).

Complicated cataract is a common complication in patients with high myopia (17); however, precise measurement of intraocular lens (IOL) power in highly myopic eyes with cataract remains a challenge. It is known that greater axial length ($>$ 26 mm) affects the precision of the IOL power estimates in highly myopic eyes (18). As PS is accompanied by axial length elongation and morphological changes to the eyeball of highly myopic eyes, PS is classified into different types based on location and distribution. However, few previous studies have focused on whether different types of PS may affect postoperative refractive errors (RE) in highly myopic eyes. Thus, the purpose of this study was to examine the associations between different types of PS and RE after cataract surgery in patients with high myopia, using wide-field fundus imaging technology.

MATERIALS AND METHODS

This study retrospectively reviewed preoperative medical records of 113 eyes of 113 highly myopic patients with PS (spherical equivalent values of more than −6.00 D or axial length of $>$26 mm). For patients with both eyes involved, only data from the right eye were used for statistical analyses. All patients underwent cataract surgery between January 1, 2018, and July 31, 2020, at the cataract clinic of the Shanghai Tenth People's Hospital affiliated with Tongji University. Cataract was graded at the slit lamp according to the Lens Opacification Classification System (LOCS) lll classification (1) as follows: nuclear opalescence (NO); nuclear color (NC); cortical cataract (C) and posterior subcapsular cataract (P). This study was approved by the Clinical Research Ethical Committee of the Shanghai Tenth People's Hospital affiliated with Tongji University and adhered to the principles of the Declaration of Helsinki (clinical study registered at www.chictr.org.cn, accession number ChiCTR2000036875). Written informed consent was provided for the use of the participants' medical data for clinical research purposes. The ocular exclusion criteria were as follows: (a) irregular corneal astigmatism, glaucoma, uveitis, retinal detachment, and the presence of a full-thickness macular hole; (b) history of eye trauma or previous ocular surgery that may affect ocular morphology; (c) serious myopic retinopathy such as choroidal neovascularization (CNV), macular epiretinal membranes, macular retinoschisis and so on; (d) cataract which exceeded N5, C4, and P4.

All participants underwent a complete preoperative examination. Baseline characteristics of patients with highly myopic eyes with PS were recorded, including age, sex, best corrected distance visual acuity (BCDVA), and spherical equivalent (SE). Keratometry (K) measurements were performed using an anterior segment swept-source optical coherence tomography SS-1000 (Tomey Corporation, Nagoya, Japan). Preoperative IOL calculations and axial lengths were measured using an IOLMaster 700 (Carl Zeiss, Meditec AG, Germany). The actual refractive outcomes of the participants were recorded 3 months after the surgery. RE was calculated based on the achieved postoperative SE minus the targeted SE.

Surgical Technique for IOL Implantation

All cataract surgeries were performed by a single experienced surgeon. In highly myopic patients with complicated cataracts, lens aspiration followed by implantation of a foldable posterior chamber IOL (ZCB00, Abbott Medical Optics, Santa Ana, CA, USA) into the capsular bag was performed. The IOL power was calculated based on the Barrett Universal II formulas. The predicted refractive outcomes targeted approaching −3 (D) under correction.

Classification of Posterior Staphyloma

PS was determined and classified using wide-field fundus imaging of 200° of the retina, based on Ohno-Matsui K's definition (10). After dilution, fundus imaging was performed using an Optos 200Tx scanning laser ophthalmoscope (Optos PLC, Dunfermline, UK). Two experienced doctors determined the types of PS, which included wide macular staphyloma, narrow macular staphyloma, and other types of staphylomas, based on location and distribution. Wide macular staphylomas were defined as the nasal edge of the macular staphyloma placed more nasally beyond the nasal edge of the optic disc. While the nasal edge of the macular staphyloma was along the nasal edge of the optic disc, the eyes were considered to be narrow macular staphyloma.

The study slightly modified the classification of PS described by Ohno-Matsui because wide macular staphyloma and narrow macular staphyloma are the most common types of PS, according to our clinical observation and previous studies (12); the remaining PS types (including inferior staphyloma, peripapillary staphyloma, nasal staphyloma, and types not otherwise specified by the Ohno-Matsui classification) were grouped as the "other" type of PS in this study. **Figure 1** shows representative wide-field fundus images of the different types of PS. We repeated three times of the measurements by the experienced physicians to make sure the reliability of our results.

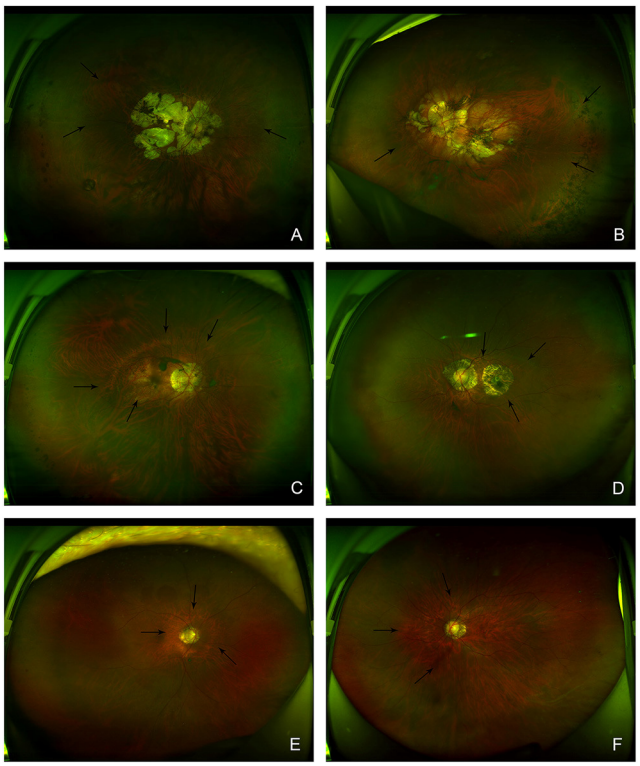

FIGURE 1 | Representative wide-field fundus images of posterior staphyloma. **(A,B)** Eyes with a wide macular staphyloma. Posterior fundus shows fibrovascular tissue and focal chorioretinal atrophy. Focal chorioretinal atrophy has spread widely and the posterior fundus shows a bare sclera appearance. **(C,D)** Eyes with a narrow macular staphyloma. Posterior fundus shows a relatively narrower focal chorioretinal atrophy. **(E,F)** Eyes with other types of staphylomas. In a typical peripapillary staphyloma, focal chorioretinal atrophy is closer-set and tends to be restricted to the optic disc. Arrows shows the edge of posterior staphyloma.

Statistical Analyses

SPSS version 22.0 software (Chicago, IL, USA) was used for statistical analyses. Data were presented as the mean ± standard deviation. BCDVA was presented as the logarithm of the minimum angle of resolution. One-way analysis of variance (ANOVA) followed by a *post-hoc* test was used to compare the results of different types of PS. Univariate and multivariate analyses using linear regression models were performed to analyze the impact of various variables on RE. Statistical significance was set at $P < 0.05$.

RESULTS

Among 113 patients, 64 (56.64%) patients were female. A total of 52 (46.02%), 45 (39.82%), and 16 (14.16%) eyes had wide macular, narrow macular and other types of staphylomas respectively. And other types of staphylomas included 10 (8.85%), 4 (3.54%), and 2 (1.77%) eyes with the peripapillary, inferior, and other staphyloma types, respectively. There was no significant difference in age, axial length, Km, BCDVA, or SE among the groups before cataract surgery (all $P > 0.05$). The patients' preoperative baseline characteristics are presented in **Table 1**.

Postoperative Refractive Outcomes of Highly Myopic Eyes With PS

Three months after cataract surgery in 113 highly myopic eyes with PS, postoperative refractive outcomes including BCDVA, actual SE, targeted SE, and RE were compared among the three subclassifications (**Table 2**). Postoperative BCDVA was better in eyes with narrow macula and other types of PS than in eyes with wide macular staphyloma ($P = 0.01$, 0.02, respectively). Among the three categories, the actual SE values were -2.00 ± 1.17 D, -2.92 ± 0.61 D, -2.90 ± 0.61 D in wide macular, narrow macular, and other types of PS groups, respectively. RE presented a hyperopic trend after IOL implantation, with a much greater deviation from the targeted refractive outcome in the macular wide staphyloma group than in the other two groups ($P < 0.01$, $P = 0.01$, respectively).

Refractive Error in Different Types of Posterior Staphyloma

The distributions of RE in different types of PS after cataract surgery are shown in **Figure 2**. There was a hyperopic trend in highly myopic patients after IOL implantation. The RE (mean ± SD) values of the wide macular, narrow macular, and other types of PS groups were 0.98 ± 1.00 D, 0.19 ± 0.87 D, 0.13 ± 0.59 D, respectively, indicating statistically significant differences between wide macular vs. narrow macular ($P < 0.01$) and wide macular vs. other types of PS ($P < 0.01$). However, there was no difference between the narrow macula and other types of PS in this parameter ($P = 0.81$).

Risk Factors Associated With Refractive Error in Highly Myopic Eyes With PS

Univariate and multivariate linear regression analyses were used to examine preoperative risk factors associated with RE after cataract surgery, including the types of PS, age, anterior chamber depth, Km, axial length, preoperative SE, and BCDVA (**Table 3**). The presence of wide macular staphyloma ($P < 0.001$), higher preoperative myopic SE ($P = 0.003$), and worse preoperative BCDVA ($P = 0.002$) were positively associated with higher hyperopic RE in the multivariate analyses.

Factors Associated With Refractive Error in Different PS Types

In the univariate and multivariate analysis (**Table 4**), in eyes with wide macular staphyloma worse preoperative BCDVA was significantly associated with higher postoperative refractive errors ($P < 0.05$); however, there was no significant association between axial length ($P < 0.05$) and postoperative refractive errors. In eyes with narrow macular staphyloma, a longer axial length ($P < 0.05$) was significantly associated with higher postoperative refractive errors. In eyes with other types of posterior staphyloma, none of the examined risk factors was

TABLE 1 | Preoperative baseline characteristics of patients with highly myopic cataract eyes and posterior staphyloma.

	All	Wide, macular	Narrow, macular	Other types	*P*-value
No. of eyes (%)	113	52 (46.02%)	45 (39.82%)	16 (14.16%)	–
Age, year	64.73 ± 7.47	65.92 ± 7.14	64.00 ± 7.56	62.94 ± 8.14	0.27
Gender (male/female)	49/64	22/30	20/25	7/9	0.77
ACD, mm	3.47 ± 0.46	3.50 ± 0.41	3.47 ± 0.55	3.35 ± 0.34	0.52
AL, mm	28.78 ± 1.69	29.04 ± 2.03	28.60 ± 1.41	28.44 ± 1.03	0.32
Km, D	44.00 ± 1.28	43.94 ± 1.20	44.12 ± 1.39	43.85 ± 1.26	0.69
BCDVA, logMAR	0.52 ± 0.32	0.59 ± 0.27	0.46 ± 0.37	0.44 ± 0.27	0.06
SE, D	−11.49 ± 3.35	−11.52 ± 3.76	−11.49 ± 2.99	−11.42 ± 3.08	0.99

*Data are shown as mean ± standard deviation. *Statistically significant at $p < 0.05$. ACD, anterior chamber depth; AL, axial length; BCDVA, best corrected distance visual acuity; D, diopter; Km, mean keratometry; Log MAR, logarithm of the minimum angle of resolution; SE, spherical equivalent.*

TABLE 2 | Postoperative refractive characteristics of patients with highly myopic eyes and posterior staphyloma.

	Posterior staphyloma			*P*-value		
	Wide, macular	Narrow, macular	Other types	Wide, macular vs. Narrow, macular	Wide, macular vs. Other types	Narrow, macular vs. Other types
BCDVA, logMAR	0.29 ± 0.39	0.14 ± 0.14	0.11 ± 0.10	0.01*	0.02*	0.66
Targeted SE, D	−2.97 ± 0.46	−3.11 ± 0.53	−3.02 ± 0.47	0.16	0.70	0.55
Actual SE, D	−2.00 ± 1.17	−2.92 ± 1.19	−2.90 ± 0.61	<0.01*	0.01*	0.63
RE, D	0.98 ± 1.00	0.19 ± 0.87	0.13 ± 0.59	<0.01*	<0.01*	0.81

*Data are shown as mean ± standard deviation. *Significant at $p < 0.05$. BCDVA, best corrected distance visual acuity; D, diopter; Log MAR, logarithm of the minimum angle of resolution; SE, spherical equivalent; RE, refractive error. RE equals the measured postoperative actual SE minus the targeted SE.*

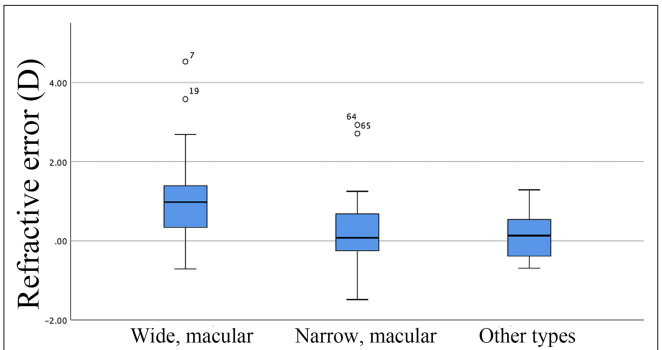

FIGURE 2 | Distribution of postoperative refractive errors in different posterior staphyloma groups.

significantly correlated with postoperative refractive errors (all $P > 0.05$).

DISCUSSION

High myopia has a complex and variable course, and the associated mechanisms remain unclear (3, 19). PS is a common complication and one among other major causes of developing myopic maculopathy, which is identified as an outpouching of a circumscribed region of the posterior fundus prudent (16). Precise estimates of IOL power are critical to cataract surgery outcomes in patients with PS in highly myopic eyes. Axial length is the main risk factor affecting postoperative RE, in particular, in patients with high myopia (20). Using more advanced optical coherence interferometry instruments to measure axial length and revise the IOL power calculation formulas may help improve outcomes (21–23). Presently, IOL power prediction is more accurate than before; however, an unexpected significant RE (usually hyperopic) is not uncommon after cataract surgery for eyes with PS.

Except for axial length elongation in PS, a wide variation was observed in the morphological characteristics of eyeballs with PS (3). However, to our knowledge, there have been no studies on the association between different types of PS and RE after cataract surgery.

Advances in wide-field imaging have enabled the visualization of 200° of the retinal area, providing more detailed and accurate assessments of PS than those available previously (10, 12). Compared with conventional 50° fundus photography, wide-field imaging may detect the entire extent of PS, which is especially important for identifying the border of wide macular staphyloma. In our study, we used wide-field fundus imaging to detect different types of PS. In 113 highly myopic eyes with PS, the rates of wide, narrow, and other types of PS were 46.02, 39.82, and 14.16%, respectively. Shinohara et al. compared the rates of PS types in 117 eyes with retinoschisis and staphyloma, reporting 47.86, 48.72, and 3.42% of wide macular staphyloma, narrow macular staphyloma, and other types of PS, respectively (19). The reason for this discrepancy in findings may be the differences

TABLE 3 | Univariate and multivariate analyses of risk factors for postoperative refractive errors.

Variables	Univariate			Multivariate		
	β	95%CI	*P*	β	95%CI	*P*
PS						
Others	Reference	Reference	–	Reference	Reference	-
Wide, macular	0.792	0.428, 1.157	<0.001*	0.726	0.330, 1.041	<0.001*
Narrow, macular	−0.065	−0.586, 0.456	0.805	−0.010	−0.551, 0.443	0.969
Age, year	0.004	−0.021, 0.029	0.745	−0.015	−0.035, 0.009	0.202
ACD, mm	0.175	−0.226, 0.575	0.390	−0.048	−0.415, 0.322	0.797
Km, D	−0.019	−0.163, 0.125	0.794	0.048	−0.092, 0.179	0.486
AL, mm	0.082	−0.025, 0.188	0.132	0.073	−0.063, 0.153	0.161
SE, D	0.075	0.020, 0.129	0.057	0.077	0.021, 0.124	0.003*
BCDVA, logMAR	1.056	0.514, 1.597	<0.001*	0.886	0.353, 1.462	0.002*

**Significant at $p < 0.05$. β =coefficient value. ACD, anterior chamber depth; AL, axial length; BCDVA, best corrected distance visual acuity; PS, posterior staphyloma; SE, spherical equivalent. Other type of staphyloma as the reference when comparing the different groups of PS associated with refractive error.*

TABLE 4 | Impact of risk factors on postoperative refractive errors in wide macular, narrow macular, and other types of posterior staphyloma.

Variables	Univariate			Multivariate		
	β	95%CI	*P*	β	95%CI	*P*
Wide, macular (*n* = 52)						
Age, year	0.012	−0.028, 0.052	0.552	−0.012	−0.053, 0.029	0.573
ACD, mm	0.129	−0.561, 0.818	0.709	−0.022	−0.690, 0.646	0.948
Km, D	0.028	−0.210, 0.266	0.814	−0.024	−0.259, 0.211	0.838
AL, mm	−0.022	−0.162, 0.118	0.752	−0.011	−0.181, 0.160	0.901
SE, D	0.056	−0.018, 0.130	0.133	0.072	−0.016, 0.160	0.104
BCDVA, logMAR	1.331	0.353, 2.309	0.009*	1.635	0.504, 2.766	0.006*
Narrow, macular (*n* = 45)						
Age, year	−0.023	−0.058, 0.011	0.180	−0.033	−0.067, 0.000	0.051
ACD, mm	0.140	−0.349, 0.629	0.568	−0.121	−0.612, 0.369	0.619
Km, D	0.001	−0.193, 0.191	0.990	0.117	−0.083, 0.318	0.243
AL, mm	0.202	0.040, 0.363	0.016*	0.197	0.020, 0.375	0.030*
SE, D	0.070	−0.017, 0.156	0.113	0.072	−0.014, 0.158	0.099
BCDVA, logMAR	0.573	−0.126, 1.271	0.105	0.447	−0.301, 1.195	0.234
Others (*n* = 16)						
Age, year	0.003	−0.039, 0.045	0.890	0.029	−0.050, 0.108	0.424
ACD, mm	−0.112	−1.117, 0.893	0.814	−0.602	−2.777, 1.574	0.547
Km, D	−0.129	−0.388, 0.129	0.301	−0.230	−0.645, 0.186	0.243
AL, mm	0.095	−0.229, 0.419	0.538	0.172	−0.251, 0.594	0.382
SE, D	−0.004	−0.114, 0.106	0.942	0.037	−0.162, 0.235	0.679
BCDVA, logMAR	0.401	−0.824, 1.625	0.494	0.060	−1.753, 1.873	0.942

**Significant at $P < 0.05$. β = coefficient value. ACD, anterior chamber depth; AL, axial length; BCDVA, best corrected distance visual acuity; PS, posterior staphyloma; SE, spherical equivalent.*

in study populations; the present participants were high myopia patients with PS who had undergone cataract surgery.

In our study, different types of PS were associated with RE. The development of staphyloma is usually accompanied various kinds of myopic lesions, such as CNV, macular epiretinal membranes and macular retinoschisis, which may influence the RE, therefore our research excluded these serious myopic retinopathies. There were significant differences in postoperative RE among wide macular staphyloma with narrow macular staphyloma and other types of PS in highly myopic eyes. Eyes with wide macular staphyloma have a higher risk of hyperopic RE after cataract surgery in highly myopic patients. In fact, the proposed subclassification of PS emerged as a functional factor that may play an essential role in predicting postoperative RE.

Our results have shown that highly myopic patients with wide macular staphyloma had lower corrected visual acuity than those with narrow macula and other types of staphylomas after cataract surgery (**Table 1**). Although there was no significant difference in BCDVA among patients with different PS before cataract surgery, we inferred that it may be partly affected by the clouded lens. The loss of BCDVA is closely related to the degree of myopic retinopathy. With the enlargement of myopic retinopathy, wide macular staphyloma may lead to a higher incidence of myopia-associated complications, such as diffuse chorioretinal atrophy, myopic choroidal neovascularization, and patchy chorioretinal pathological changes (24). The present findings were consistent with those of Ohno-Matsui, showing that the progression of visual impairment was significantly different among different types of PS in high myopia (10).

In highly myopic patients, there is a significant association between axial length elongation and increased RE after cataract surgery. In the present study, there was no significant difference in axial length among different types of PS (**Table 1**); however, the RE varied significantly among the different subclassifications after cataract surgery (**Figure 2**), which indicated that axial length may not be an accurate predictor of RE in highly myopic patients in clinical practice. This finding suggests that wide macular staphyloma may lead to a more hyperopic RE shift after cataract surgery (**Table 2**, **Figure 2**), which means that the type of PS might be a more effective predictor of postoperative RE in eyes with high myopia and PS.

Univariate and multivariate linear regression analyses further demonstrated that the presence of wide macular staphyloma was a significant predictor of postoperative RE (**Table 3**). The causal relationship between PS classification and postoperative RE warrants further study. Classifications of PS may interfere with accurate calculation of the RE in eyes with high myopia. First, axial length measurements are not accurate in myopic eyes with different types of PS, as the eye shapes are non-spherical and deformed due to PS (25). Axial length is the distance from the pre-surface of the central cornea to the fovea. When the eye is spherical, the diameter of the spherical globe is the same, and the axial length measurement is accurate. However, if the eye is irregularly deformed, the axial length is not a diameter, and the measured axial length is usually shorter than the actual axial length. Second, poor central fixation stability of the fovea caused by PS may affect refractive outcomes. In physical conditions, the magnitudes of central fixation movements of healthy eyes are small, while in eyes with myopic retinopathy, central fixation stability of the fovea is impaired and fluctuates greatly (26). Zhu et al. reported that poor fixation stability might have a positive relationship with RE after cataract surgery in eyes with high myopia (27). Wide macular staphyloma tends to be associated with more serious myopic retinopathy than is narrow macular staphyloma or other types of PS (12, 28, 29), which may account for the impairment of central fixation stability of the fovea. Third, a more advanced fundus status with wide macular staphyloma may affect the accuracy of axial length measurement, which would increase the refractive power of the eye. In our study, among eyes with wide macular staphyloma, there was no statistically significant association between axial length and postoperative refractive error; however, in eyes with narrow macular staphyloma, a statistically significant association between axial length and postoperative RE was detected (**Table 4**). Overall, these findings suggest that patients with wide macular staphyloma have larger RE than do other patients after cataract surgery; meanwhile, axial length is not the main factor affecting postoperative RE. However, as we just did the primary research on the relationship between wide macular staphyloma and RE after cataract surgery, the inner causal relationship between PS classification and postoperative RE warrants further study.

Our findings highlight that wide macular staphyloma may serve as an important source of postoperative RE in highly myopic cases. The present findings suggest that even highly myopic cases seem to present no significant difference in axial length, depending on the subclassification of PS evaluated by wide-field fundus imaging. The present findings are consistent with those of previous studies on eyes with high myopia and PS (30), showing that refractive outcomes vary significantly among different types of PS after cataract surgery. In addition, a significant correlation between posterior staphyloma classification and postoperative RE was observed. Wide macular staphyloma type was more strongly associated with postoperative RE than was narrow macular and other types staphyloma types; this finding suggests that, to a certain extent, it may serve as a biomarker for predicting higher RE after cataract surgery.

There are some limitations to the present study. First, the number of PS types was relatively small, which partly limited the statistical power of the analysis. Second, Ohno-Matsui's classification of PS involves six types (wide macular staphyloma, narrow macular staphyloma, inferior staphyloma, peripapillary staphyloma, and nasal staphyloma, and types not otherwise specified). We combined the latter four types into the "other" types of PS (14.16% of PS in our study); however, it remains difficult to differentiate refractive outcomes of these four types. Lastly, except posterior staphyloma, dome shaped macula, myopic choroidal neovascularization, and macular atrophy are the very common complications of high myopia, which might be potential predictive biomarkers for visual acuity after cataract surgery in highly myopic eyes. In our future study, we aim to include larger samples of PS and compare the rates of myopic retinal complications among the different types, such as dome-shaped macula, myopic choroidal neovascularization, or macular atrophy, to examine factors associated with RE after cataract surgery and we will research and comment on the types of myopic retinopathy among different kinds of staphyloma in this context. Besides, the depth of PS detected by wide-field OCT may have an impact on postoperative RE, which deserves further study.

In conclusion, this study classified the PS of highly myopic patients with cataract surgery according to their morphologic characteristics, identified using wide-field fundus imaging, and examined refractive outcomes among the three types of PS. The subclassification of staphyloma may be a useful biomarker for future prediction of postoperative RE in highly myopic eyes; wide macular staphyloma might have a detrimental effect on

the accuracy of postoperative refractive outcome prediction. Therefore, PS classification should be considered in clinical practice, specifically, for highly myopic patients due to undergo cataract surgery with wide macular staphyloma.

DATA AVAILABILITY STATEMENT

The original contributions presented in the study are included in the article/supplementary material, further inquiries can be directed to the corresponding author.

ETHICS STATEMENT

The studies involving human participants were reviewed and approved by the Clinical Research Ethical Committee of Shanghai Tenth People's Hospital affiliated with Tongji University. The patients/participants provided their written informed consent to participate in this study.

AUTHOR CONTRIBUTIONS

JW: writing the original draft and data analysis. RW: data analysis and editing. CL, YZ, and ZJ: data collection. FL: supervision and editing. All authors contributed to the article and approved the submitted version.

FUNDING

This study was supported by the Clinical Research and Cultivation Project of Shanghai Municipal Hospital (SHDC12019X30) and Science and Technology Commission of Shanghai Municipality (20142203200).

ACKNOWLEDGMENTS

We would like to thank Editage (www.editage.com) for English language editing.

REFERENCES

1. Li M, Yang Y, Jiang H, Gregori G, Roisman L, Zheng F, et al. Retinal microvascular network and microcirculation assessments in high myopia. *Am J Ophthalmol.* (2017) 174:56–67. doi: 10.1016/j.ajo.2016.10.018
2. Ruiz-Medrano J, Montero JA, Flores-Moreno I, Arias L, García-Layana A, Ruiz-Moreno JM. Myopic maculopathy: current status and proposal for a new classification and grading system (ATN). *Prog Retin Eye Res.* (2019) 69:80–115. doi: 10.1016/j.preteyeres.2018.10.005
3. Ohno-Matsui K, Lai TY, Lai CC, Cheung CM. Updates of pathologic myopia. *Prog Retin Eye Res.* (2016) 52:156–87. doi: 10.1016/j.preteyeres.2015.12.001
4. Bedggood P, Mukherjee S, Nguyen BN, Turpin A, McKendrick AM. Geometry of the retinal nerve fibers from emmetropia through to high myopia at both the temporal raphe and optic nerve. *Invest Ophthalmol Vis Sci.* (2019) 60:4896–903. doi: 10.1167/iovs.19-27539
5. Wong YL, Saw SM. Epidemiology of pathologic myopia in asia and worldwide. *Asia Pac J Ophthalmol.* (2016) 5:394–402. doi: 10.1097/APO.0000000000000234
6. Ikuno Y. Overview of the complications of high myopia. *Retina.* (2017) 37:2347–51. doi: 10.1097/IAE.0000000000001489
7. Ohno-Matsui K, Kawasaki R, Jonas JB, Cheung CM, Saw SM, Verhoeven VJ, et al. International photographic classification and grading system for myopic maculopathy. *Am J Ophthalmol.* (2015) 159:877–83.e7. doi: 10.1016/j.ajo.2015.01.022
8. Hsia Y, Ho TC. Posterior staphyloma of extreme pathologic myopia. *JAMA Ophthalmol.* (2020) 138:e191663. doi: 10.1001/jamaophthalmol.2019.1663
9. Spaide RF. Staphyloma: part 1. In: Spaide RF, Ohno- Matsui K, Yannuzzi LA, editors. *Pathologic Myopia*. New York, NY: Springer (2013). p. 167–76. doi: 10.1007/978-1-4614-8338-0_12
10. Ohno-Matsui K. Proposed classification of posterior staphylomas based on analyses of eye shape by three-dimensional magnetic resonance imaging and wide-field fundus imaging. *Ophthalmology.* (2014) 121:1798–809. doi: 10.1016/j.ophtha.2014.03.035
11. Zheng F, Wong CW, Sabanayagam C, Cheung YB, Matsumura S, Chua J, et al. Prevalence, risk factors and impact of posterior staphyloma diagnosed from wide-field optical coherence tomography in Singapore adults with high myopia. *Acta Ophthalmol.* (2020) 99:e144–53. doi: 10.1111/aos.14527
12. Mimura R, Mori K, Torii H, Nagai N, Suzuki M, Minami S, et al. Ultra-widefield retinal imaging for analyzing the association between types of pathological myopia and posterior staphyloma. *J Clin Med.* (2019) 8:1505. doi: 10.3390/jcm8101505
13. Curtin BJ. The posterior staphyloma of pathologic myopia. *Trans Am Ophthalmol Soc.* (1977) 75:67–86.
14. Ikuno Y, Tano Y. Retinal and choroidal biometry in highly myopic eyes with spectral-domain optical coherence tomography. *Invest Ophthalmol Vis Sci.* (2009) 50:3876–80. doi: 10.1167/iovs.08-3325
15. Guo X, Xiao O, Chen Y, Wu H, Chen L, Morgan IG, et al. Three-dimensional eye shape, myopic maculopathy, and visual acuity: the zhongshan ophthalmic center-brien holden vision institute high myopia cohort study. *Ophthalmology.* (2017) 124:679–87. doi: 10.1016/j.ophtha.2017.01.009
16. Ohno-Matsui K, Jonas JB. Posterior staphyloma in pathologic myopia. *Prog Retin Eye Res.* (2019) 70:99–109. doi: 10.1016/j.preteyeres.2018.12.001
17. Li T, Guadie A, Feng L, Fan J, Jiang Z, Liu F. Influence of cataract surgery on macular vascular density in patients with myopia using optical coherence tomography angiography. *Exp Ther Med.* (2020) 20:258. doi: 10.3892/etm.2020.9388
18. Chong EW, Mehta JS. High myopia and cataract surgery. *Curr Opin Ophthalmol.* (2016) 27:45–50. doi: 10.1097/ICU.0000000000000217
19. Shinohara K, Tanaka N, Jonas JB, Shimada N, Moriyama M, Yoshida T, et al. Ultrawide-field OCT to investigate relationships between myopic macular retinoschisis and posterior staphyloma. *Ophthalmology.* (2018) 125:1575–86. doi: 10.1016/j.ophtha.2018.03.053
20. Kora Y, Koike M, Suzuki Y, Inatomi M, Fukado Y, Ozawa T. Errors in IOL power calculations for axial high myopia. *Ophthalmic Surg.* (1991) 22:78–81. doi: 10.3928/1542-8877-19910201-06
21. Wan KH, Lam TCH, Yu MCY, Chan TCY. Accuracy and precision of intraocular lens calculations using the new hill-RBF version 2.0 in eyes with high axial myopia. *Am J Ophthalmol.* (2019) 205:66–73. doi: 10.1016/j.ajo.2019.04.019
22. Melles RB, Holladay JT, Chang WJ. Accuracy of intraocular lens calculation formulas. *Ophthalmology.* (2018) 125:169–78. doi: 10.1016/j.ophtha.2017.08.027
23. Yang CM, Lim DH, Kim HJ, Chung TY. Comparison of two swept-source optical coherence tomography biometers and a partial coherence interferometer. *PLoS One.* (2019) 14:e0223114. doi: 10.1371/journal.pone.0223114
24. Fang Y, Yokoi T, Nagaoka N, Shinohara K, Onishi Y, Ishida T, et al. Progression of myopic maculopathy during 18-year follow-up. *Ophthalmology.* (2018) 125:863–877. doi: 10.1016/j.ophtha.2017.12.005
25. Wakazono T, Yamashiro K, Miyake M, Nakanishi H, Oishi A, Ooto S, et al. Association between eye shape and myopic traction maculopathy in high myopia. *Ophthalmology.* (2016) 123:919–21. doi: 10.1016/j.ophtha.2015.10.031

26. Molina-Martín A, Pérez-Cambrodí RJ, Piñero DP. Current clinical application of microperimetry: a review. *Semin Ophthalmol.* (2018) 33:620–8. doi: 10.1080/08820538.2017.1375125
27. Zhu X, He W, Sun X, Dai J, Lu Y. Fixation stability and refractive error after cataract surgery in highly myopic eyes. *Am J Ophthalmol.* (2016) 169:89–94. doi: 10.1016/j.ajo.2016.06.022
28. Ohno-Matsui K, Akiba M, Modegi T, Tomita M, Ishibashi T, Tokoro T, et al. Association between shape of sclera and myopic retinochoroidal lesions in patients with pathologic myopia. *Invest Ophthalmol Vis Sci.* (2012) 53:6046–61. doi: 10.1167/iovs.12-10161
29. Frisina R, Baldi A, Cesana BM, Semeraro F, Parolini B. Morphological and clinical characteristics of myopic posterior staphyloma in Caucasians. *Graefes Arch Clin Exp Ophthalmol.* (2016) 254:2119–2129. doi: 10.1007/s00417-016-3359-1
30. Alfonso-Bartolozzi B, Villota E, Fernandez-Vega-Gonzalez A, Fernandez-Vega-Cueto L, Fernandez-Vega A, Alfonso JF. Implantation of a trifocal intraocular lens in high myopic eyes with nasal-inferior staphyloma. *Clin Ophthalmol.* (2020) 14:721–7. doi: 10.2147/OPTH.S227670

Conflict of Interest: The authors declare that the research was conducted in the absence of any commercial or financial relationships that could be construed as a potential conflict of interest.

Publisher's Note: All claims expressed in this article are solely those of the authors and do not necessarily represent those of their affiliated organizations, or those of the publisher, the editors and the reviewers. Any product that may be evaluated in this article, or claim that may be made by its manufacturer, is not guaranteed or endorsed by the publisher.

Copyright © 2021 Wu, Wang, Liu, Zhou, Jiang and Liu. This is an open-access article distributed under the terms of the Creative Commons Attribution License (CC BY). The use, distribution or reproduction in other forums is permitted, provided the original author(s) and the copyright owner(s) are credited and that the original publication in this journal is cited, in accordance with accepted academic practice. No use, distribution or reproduction is permitted which does not comply with these terms.

frontiers in Neurology

ORIGINAL RESEARCH
published: 24 December 2021
doi: 10.3389/fneur.2021.801029

Investigation of Altered Spontaneous Brain Activities in Patients With Moyamoya Disease Using Percent Amplitude of Fluctuation Method: A Resting-State Functional MRI Study

Chu-Qi Li[1,2†], Qian-Min Ge[1†], Hui-Ye Shu[1], Xu-Lin Liao[3], Yi-Cong Pan[1], Jie-Li Wu[4], Ting Su[4,5], Li-Juan Zhang[1], Rong-Bin Liang[1], Yi Shao[1] and Er-Ming Zeng[1*]*

[1] Department of Neurosurgery and Ophthalmology, The First Affiliated Hospital of Nanchang University, Nanchang, China, [2] The First Clinical Medical College, Nanchang University, Nanchang, China, [3] Department of Ophthalmology and Visual Sciences, The Chinese University of Hong Kong, Shatin, Hong Kong SAR, China, [4] Fujian Provincial Key Laboratory of Ophthalmology and Visual Science, Department of Ophthalmology, Eye Institute of Xiamen University, Xiang'an Hospital of Xiamen University, Xiamen University School of Medicine, Xiamen, China, [5] Department of Ophthalmology, Massachusetts Eye and Ear, Harvard Medical School, Boston, MA, United States

OPEN ACCESS

Edited by:
Yuzhen Xu,
Tongji University, China

Reviewed by:
Wensi Tao,
University of Miami Health System, United States
Fei Dong,
University of Cincinnati, United States
Junyi Li,
Medical School of Nanjing University, China

***Correspondence:**
Yi Shao
freebee99@163.com
Er-Ming Zeng
ermingzeng@aliyun.com

[†]These authors have contributed equally to this work and share first authorship

Specialty section:
This article was submitted to Neurological Biomarkers, a section of the journal Frontiers in Neurology

Received: 24 October 2021
Accepted: 24 November 2021
Published: 24 December 2021

Citation:
Li C-Q, Ge Q-M, Shu H-Y, Liao X-L, Pan Y-C, Wu J-L, Su T, Zhang L-J, Liang R-B, Shao Y and Zeng E-M (2021) Investigation of Altered Spontaneous Brain Activities in Patients With Moyamoya Disease Using Percent Amplitude of Fluctuation Method: A Resting-State Functional MRI Study. Front. Neurol. 12:801029. doi: 10.3389/fneur.2021.801029

Background: Moyamoya disease (MMD) is a chronic progressive cerebrovascular abnormality characterized by chronic occlusion of large intracranial vessels with smoky vascular development at the base of the skull. In patients with MMD, abnormal spontaneous brain activity would be expected.

Purpose: To assess the brain activity changes in patients with MMD by resting-state functional MRI (rs-fMRI), using the percent amplitude of fluctuation (PerAF) analysis method.

Materials and Methods: A total of 17 patients with MMD (3 males and 14 females) and 17 healthy control (HC) subjects with matched gender and age were recruited for this study. We used rs-fMRI to scan all the patients with MMD. Spontaneous neural activity was evaluated using the PerAF approach. The receiver operating characteristic (ROC) curve analysis was used to assess the ability of the PerAF to distinguish patients with MMD from HCs. The Hospital Anxiety and Depression Scale (HADS) tests were performed to assess the emotional status of patients with MMD and retinal nerve fiber layer thickness (RNFLT) was measured using high-resolution optical coherence tomography (hr-OCT). The relationship between the HADS scores, RNFLT values, and the PerAF signals was assessed using the Pearson's correlation analysis.

Results: Compared with HCs, the PerAF signals in patients with MMD were decreased in the Frontal_Sup_Medial_R and Precentral_L, whereas those in the Caudate_L were increased. The areas under the ROC curves indicated that signals in these brain regions could distinguish between patients with MMD and HCs. The PerAF value of Frontal_Sup_Medial_R was positively correlated with the left and right eye RNFLT values and negatively correlated with the HADS scores.

Conclusion: In patients with MMD, reduced PerAF signals in the Frontal_Sup_Medial_R, Precentral_L, and Caudate_L may be associated with psychiatric diseases including anxiety and depression and decreased RNFLT may be associated with ophthalmic complications due to the compression of terminal branches of the internal carotid artery in the retinal fiber layer. The PerAF can be used as an effective indicator of ocular complications of MMD and to study the neural mechanism underpinning emotional complications in patients with MMD.

Keywords: percent amplitude of fluctuation (PerAF), resting-state functional magnetic resonance imaging (rs-fMRI), retinal nerve fiber layer thickness (RNFLT), anxiety, depression, moyamoya disease (MMD)

INTRODUCTION

Moyamoya disease (MMD) is a non-atherosclerotic cerebrovascular structural abnormality, which results from progressive stenosis of the intracranial internal carotid arteries and their proximal branches, with insufficient blood supply to the supraclinoid anterior circulation. Due to compensation for cerebral ischemia (1), patients with MMD will have abundant growth of collateral vessels, which contribute to most of the clinical symptoms of MMD. The main complications of MMD include transient ischemic attack (TIA), hemiparesis, hemorrhagic stroke, seizure, epilepsy, and other symptoms caused by repeated cerebral ischemia and stroke such as memory loss, headache, and progressive loss of cognitive ability (2). According to studies conducted between 1997 and 2011, MMD has a 10-fold higher prevalence in Asian populations than in other ethnic groups. For example, prevalence rates of 1/280,000 have been reported in China and 1/89,000 in Japan, but 1/1,100,000 in the US and 1/2,130,000 in Denmark and prevalence is increasing in both the East Asia and the US (2–5). As the most common pediatric cerebrovascular disease in East Asian regions, MMD is mostly diagnosed in children between 10 and 14 years old or in adults after 40 years old, with females at higher risk (6) (**Figure 1**).

Digital subtraction angiography (DSA) is widely used in clinical practice and allows blood vessels to be visualized through bone and soft tissues. Doctors can obtain the image as the difference between images before and after administration of the contrast medium. Since its first use in the 1970's, DSA has been widely used in the diagnosis of MMD and is considered to be the gold standard. Some studies indicate that the nephrotoxic contrast agent may cause kidney damage, but X-ray is also harmful for patients, so DSA cannot provide dynamic information and references to clinicians in the diagnosis and treatment of MMD. Functional MRI (fMRI) is a widely used imaging technique, which can detect structural changes in brain regions of interest (ROI) at rest. It is non-invasive and can produce three-dimensional (3D) images without harmful X-rays or nephrotoxic contrast agents (7) and there are no reports of ionizing radiation injury in patients with MMD who have undergone MRI scanning. MRI scanning can also provide images with high tissue structure resolution and its multiple sequencing can provide information to help localize the disease lesion and determine its size (8). The diagnostic signs of MMD in an MRI scan include disappearance of the occlusive vascularity effect and increased vascularity in collateral circulation (9, 10) fMRI has been applied in investigation of the neural mechanisms of neurological diseases. The percent amplitude of fluctuation (PerAF) is a new method of fMRI analysis. Instead of measuring the blood oxygenation level-dependent (BOLD) signal at voxel level, the PerAF reflects the percent signal change by measuring the percentage of BOLD fluctuations relative to the mean BOLD signal intensity for each time point and averaging across the whole time series that directly reflects the resting-state BOLD signal fluctuations (11). It is not influenced by the raw signals due to it do not contain arbitrary units, so the PerAF values are less affected by signal strength errors, more accurate and more suitable for ensuing statistical analysis than other MRI analysis methods such as amplitude of low frequency fluctuation, regional homogeneity, and degree centrality (12–14). In addition, the PerAF can be used for group-level statistical analysis and is unaffected by the confounding mixture of voxel-specific fluctuation amplitude in the amplitude of low-frequency fluctuation method (11). For these reasons, the PerAF can measure voxel-level brain activity changes with higher accuracy and efficiency and is a promising analysis method of voxel-level spontaneous BOLD activity. So far, the PerAF has not been used to explore the pathogenesis and clinical complications of cerebrovascular diseases.

Currently, DSA is the main diagnostic method of MMD and study on brain anomalies in MMD is lacking. We speculate that using the PerAF method to study changes of brain activity in MMD will provide information for diagnosis and the underlying neurological basis including biological indicators. In this study, we used the PerAF analysis to assess spontaneous brain activity and mean retinal nerve fiber layer thickness (RNFLT) in sufferers with MMD. We examined the association between the PerAF signals and clinical characteristics, which may help to reveal the underlying neural mechanisms of MMD and help clinicians to predict the disease and protect their patients from potential complications.

MATERIALS AND METHODS

Subjects

A total of 17 sufferers with MMD (3 males and 14 females) were enrolled in this study. The inclusion criteria were: (1) Patients with typical bilateral MMD diagnosed using DSA; (2) No contraindications to head scan of MRI such as implanted metal devices; and (3) Age between 18 and 60 years. The exclusion

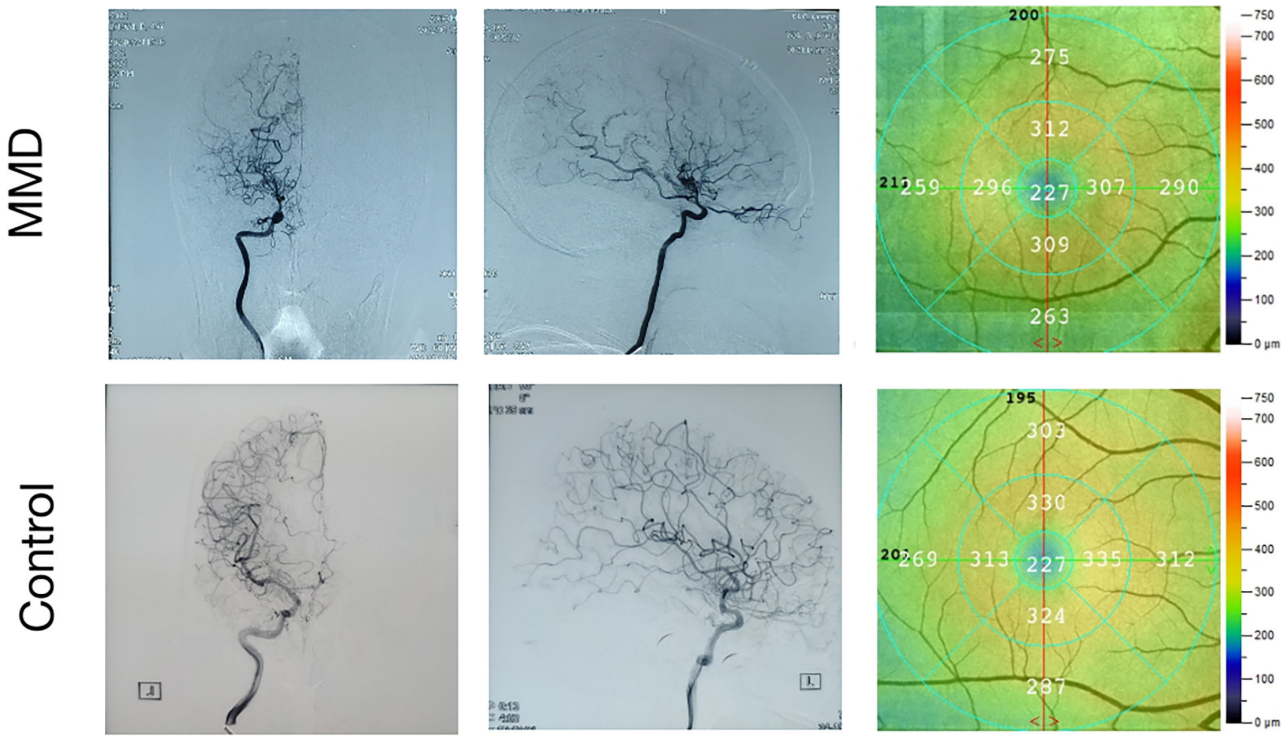

FIGURE 1 | A moyamoya disease (MMD) angiography illustration and a fundus camera illustration. Internal carotid in the digital subtraction angiography (DSA). Undeveloped anterior and middle cerebral arteries and multiple anomalous vascular networks at the base of the skull.

criteria were: (1) Patients with atypical MMD or moyamoya syndrome; (2) History of craniocerebral surgery; (3) Severe medical disease and visual and hearing impairment; (4) History of stroke; (5) Addiction (for example, to drugs or alcohol); and (6) Contraindications to MRI examination.

This study also enrolled 17 healthy control (HC) subjects (4 males and 13 females) matched for age, gender, and education level. The inclusion criteria were: (1) No MMD diagnosis; (2) No other defects in brain function (such as cerebrovascular diseases and tumors); (3) No serious organic diseases such as heart disease or hypertension; (4) No history of neurologic or psychiatric disorders (anxiety disorders or delusions); and (5) No contraindication to MRI examination. The RNFLT values were measured at baseline, using high-resolution optical coherence tomography (hs-OCT), following a previously described protocol (15).

The Ethics Committee of the First Affiliated Hospital of Nanchang University approved this study. In this study, all the procedures followed the principles of the Declaration of Helsinki and Medical Ethics guidelines. Every subject voluntarily underwent the study procedures and was informed about the aim of this study as well as the potential risks. Each subject signed an informed consent form before recruitment.

Digital Subtraction Angiography

Digital subtraction angiography of the brain was performed. A digital subtraction vascular machine was used. The patient was instructed to adopt the supine position, the towel was disinfected, femoral artery puncture was performed, and a 5F sheath was inserted 2 cm below the inguinal ligament of the lower extremity of patient. A Pigtail catheter was inserted into the aortic arch and 30 ml contrast agent was injected into the aortic arch at a constant rate. The Pigtail catheter was replaced and a 5F vertebral artery angiography tube was inserted into the common carotid artery, internal carotid artery, subclavian artery, and vertebral artery along with the arterial sheath and DSA was performed in the anteroposterior, lateral, oblique, and Torontonian positions.

Resting-State FMRI (Rs-FMRI) Protocol

Magnetic resonance imaging scans in this study were implemented on a Trio 3-Tesla MRI scanner using the total imaging matrix method (Siemens, Berlin, UK). All the subjects were instructed to breathe steadily without moving their heads during the scan. To obtain T1-weighted images, all the subjects were scanned using parameters reported in previous studies (16).

Resting-State FMRI Data Analysis

The functional data were prefiltered to remove incomplete data with MRIcro program (https://crnl.readthedocs.io/). We deleted the first 10 volumes from each data of subject to balance the signal. Then, we use Data Processing Assistant for rs-fMRI version 4.0 (http://rfmri.org/DPARSF) and Statistical Parametric Mapping version 8 (http://www.fil.ion.ucl.ac.uk/spm) for head movement correction and spatial normalization; then, we exported the data to a Digital Imaging Communication System. The images were smoothened with $6 \times 6 \times 6$ mm^3 voxel size and full width of 6 mm. The scan data of the participants with head movement over 3 mm were deleted and head movement correction was applied to other valid data (17). The automated anatomical labeling (AAL) was used as a template in the study. Linear regression would filtered out the false variable values (18) and we use echo plane image template to standardize the fMRI scans, with the guidance of the Montreal Neurological Institute standards.

The PerAF method used in this study differs from that of previous study. The average BOLD signal values were calculated on the basis of measurements and the percentage of BOLD fluctuation was measured at different time points in relation to the average BOLD value, which was then averaged over the whole time series to acquire the PerAF. The PerAF value for each voxel was calculated using the equations below.

$$PerAF = \frac{1}{n}\sum_{n=1}^{n}\left|\frac{x_i - \mu}{\mu}\right| \times 100\% \quad (1)$$

$$\mu = \frac{1}{n}\sum_{i=1}^{n} x_i \quad (2)$$

In these equations, x_i is the signal strength at the i_{th} time point, n is the number of all the time points, and μ is the average value across the time series.

Brain–Behavior Correlation Analysis

Brain regions were classified into ROIs based on the PerAF findings, with the resting state fMRI data analysis toolkit (REST) program (https://sourceforge.net/projects/resting-fmri/). The average PerAF value of each ROI was extracted by averaging the PerAF values on all the voxels. Lastly, the relationship between the average PerAF signal of each brain region of MMDs and corresponding functional abnormalities was discussed through correlation analysis.

All the participants completed the Hospital Anxiety and Depression Scale (HADS) questionnaire and the result was evaluated by the Pearson's correlation analysis ($p < 0.05$). The SPSS software version 20.0 (IBM Corporation, Armonk, New York, USA) were used to perform linear correlation.

Statistical Analysis

After controlling for age and sex, the SPSS software (IBM Corporation, Armonk, New York, USA) was used to perform independent samples *t*-tests comparing the demographic data, RNFLT, and visual acuity (VA) between patients with MMD and HCs. $p < 0.05$ was considered as statistically significant. The 2-sample *t*-test was used to evaluate the differences in the PerAF values between the two groups using the REST program. The Gaussian random field theory was applied to determine the voxel-wide threshold in multiple comparisons as $p < 0.005$. The AlphaSim correction was also applied to clusters over 103 voxels. The receiver operating characteristic (ROC) curve analysis was performed to compare the average PerAF between the two groups using the area under the ROC curve (AUC). The Pearson's correlation analysis was utilized to evaluate the associations between the PerAF values in clusters and the HADS scores as well as RNFLT.

RESULTS

Demographics and Clinical Indicators

No significant differences in age (unpaired *t*-test, $p = 0.90$), sex (chi-squared test, $p > 0.99$), or body weight (unpaired *t*-test, $p = 0.917$) were found between the MMD and HC groups. VA-left

TABLE 1 | Basic information of participants in the study.

Condition	MMD	HCs	t	P-value*
Male/female	3/14	3/14	N/A	>0.99
Age (years)	50.11 ± 5.58	49.88 ± 5.29	0.126	0.90
Weight (kg)	61.22 ± 5.12	60.12 ± 9.15	0.196	0.917
Handedness	17R	17R	N/A	>0.99
Duration of MMD (Mons)	3.12 ± 0.24	N/A	N/A	N/A
Best-corrected VA-left eye	0.029 ± 0.014	0.023 ± 0.013	0.298	0.768
Best-corrected VA-right eye	0.064 ± 0.019	0.064 ± 0.019	<0.001	>0.99
IOP-Left	15.05 ± 0.40	14.86 ± 0.34	0.363	0.719
IOP-Right	15.94 ± 0.39	15.26 ± 0.42	1.165	0.253
RNFLT-right (μm)	117.06 ± 17.35	138.76 ± 12.07	4.235	<0.001
RNFLT-left (μm)	115.76 ± 19.22	136.41 ± 11.63	3.789	<0.001#
Higher education/HSEB	8/9	8/9	N/A	N/A

MM, independent t-tests comparing two groups ($p < 0.05$); HCs, healthy controls; N/A, not applicable.
*Significant at *$P < 0.05$; #$P < 0.001$.*

($p = 0.768$) and VA-right ($p > 0.99$) also showed no significant differences between the groups. However, significant between-group differences were found in RNFL thickness of the right ($p < 0.001$) and left eye ($p < 0.001$) (**Table 1**).

Percent Amplitude of Fluctuation in MMD

The PerAF values in Frontal_Sup_Medial_R and Precentral_L regions were significantly lower in MMD than in HC, while values in the Caudate_L

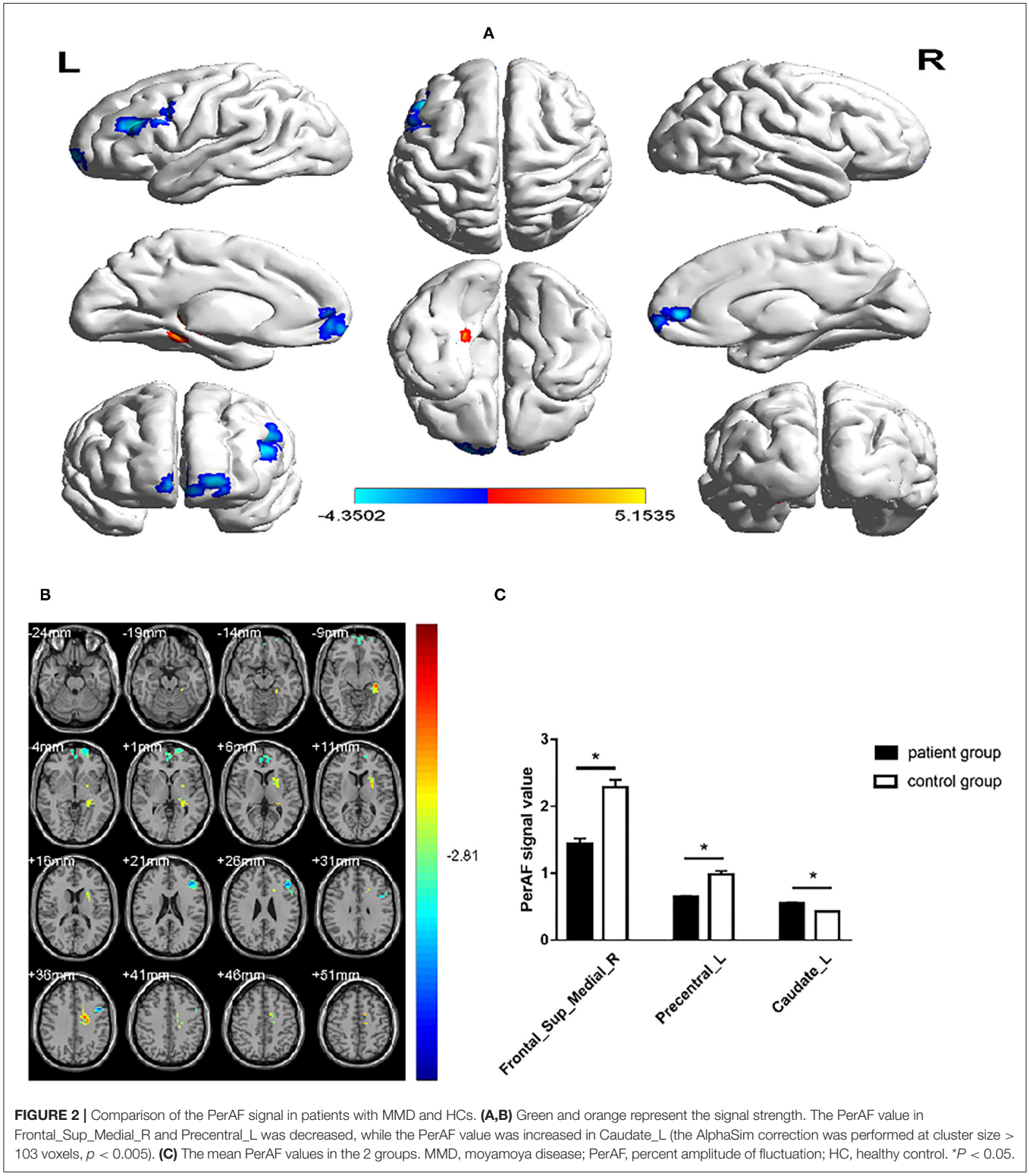

FIGURE 2 | Comparison of the PerAF signal in patients with MMD and HCs. **(A,B)** Green and orange represent the signal strength. The PerAF value in Frontal_Sup_Medial_R and Precentral_L was decreased, while the PerAF value was increased in Caudate_L (the AlphaSim correction was performed at cluster size > 103 voxels, $p < 0.005$). **(C)** The mean PerAF values in the 2 groups. MMD, moyamoya disease; PerAF, percent amplitude of fluctuation; HC, healthy control. *$P < 0.05$.

TABLE 2 | Brain areas with significantly different AF values between patients with MMD and HCs.

Brain areas	MNI coordinates			BA	Number of voxels	T value
	X	Y	Z			
Patient < HC						
Frontal_Sup_Medial_R	6	51	3	24	159	−3.8795
Precentral_L	−48	9	36	1	135	−4.3502
Patient > HC						
Caudate_L	−18	15	9	0	104	3.8544

The statistical threshold was set at a voxel level with $p < 0.005$ for multiple comparisons using Gaussian random field theory (the AlphaSim corrected at cluster > 103 voxels, $p < 0.05$). PerAF, percent amplitude of fluctuation; HC, healthy control; MNI, Montreal Neurological Institute; MMD, moyamoya disease.

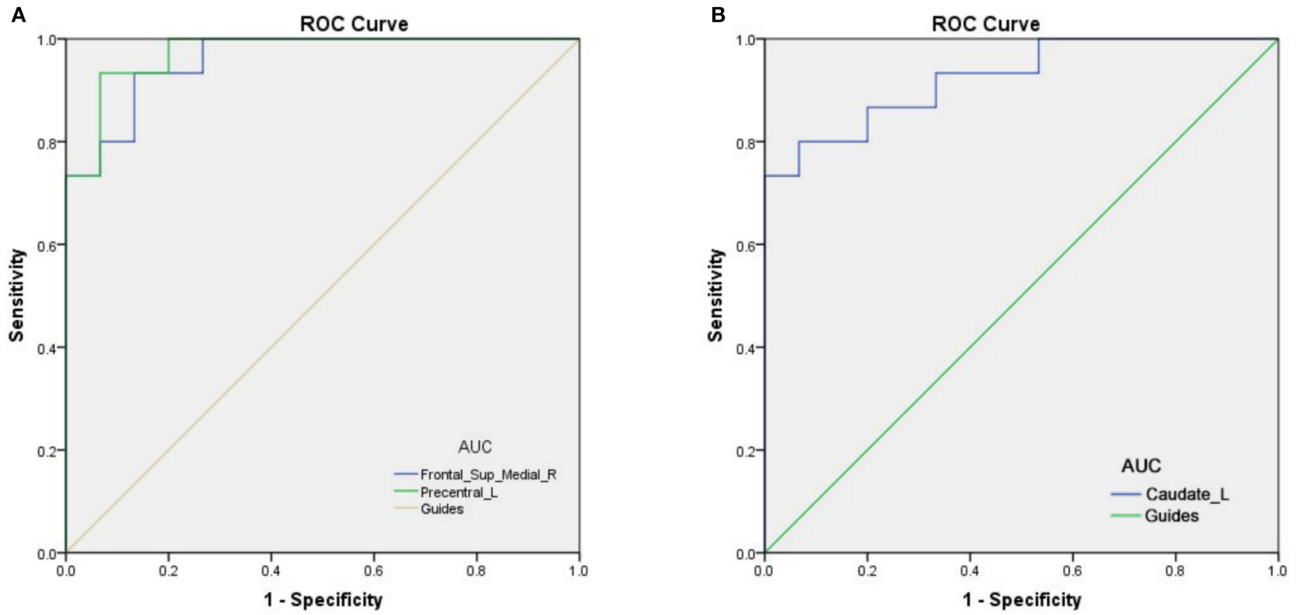

FIGURE 3 | The ROC curve analysis of the mean PerAF values of different brain regions. **(A)** The AUCs for Frontal_Sup_Medial_R and Precentral_L were 0.960 ($p <$ 0.0001; 95% CI: 0.900–1.000) and 0.973 ($p < 0.0001$; 95% CI: 0.926–1.000), respectively **(B)** The AUC was 0.924 ($p < 0.0001$; 95% CI: 0.831–1.000) for Caudate_L. ROC, receiver operating characteristic; AUC, area under the ROC curve; MMD, moyamoya disease; PerAF, percent amplitude of fluctuation.

were higher in MMD than in HC (**Figure 2**, **Table 2**).

Receiver Operating Characteristic Curve

The AUCs for Frontal_Sup_Medial_R and Precentral_L were 0.960 ($p < 0.0001$; 95% CI: 0.900–1.000) and 0.973 ($p < 0.0001$; 95% CI: 0.926–1.000), respectively, and the AUCs for Caudate_L was 0.924 ($p < 0.0001$; 95% CI: 0.831–1.000) (**Figure 3**).

Correlation Analysis

In patients with MMD, the RNFLT-left and RNFLT-right were positively associated with the PerAF value of the Frontal_Sup_Medial_R ($r = 0.727$, $p < 0.01$ and $r = 0.748$, $p <$ 0.01, respectively) (**Figure 4A**, **Table 3**). In patients with MMD, the anxiety score (AS) and depression score (DS) were negatively associated with the PerAF value of the Frontal_Sup_Medial_R ($r = -0.772$, $p < 0.01$ and $r = 0.806$, $p < 0.01$, respectively) (**Figure 4B**).

DISCUSSION

The PerAF reflects the resting-state BOLD signal fluctuations directly, it does not use arbitrary units, and is not influenced by raw signals, so the PerAF values are less affected by signal strength errors, more accurate, and more suitable for ensuing statistical analysis than other MRI analysis methods. The PerAF has been used in some studies of neurological disorders (**Table 4**) (14, 19–21), but this study is the first to use the PerAF to study changes in brain activity in a cerebrovascular disorder. The results showed that the PerAF values in MMD were decreased in Frontal_Sup_Medial_R and Precentral_L, but increased in Caudate_L compared with HCs (**Figure 5**).

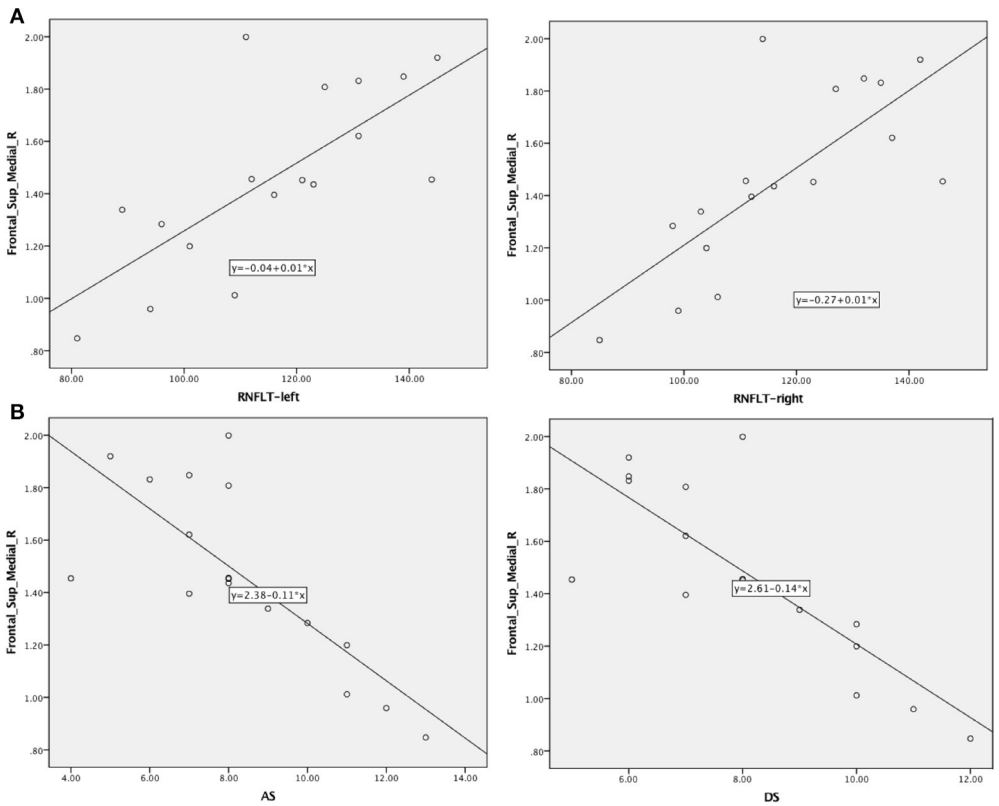

FIGURE 4 | Correlations between AS/DS and RNFLT and the PerAF signal intensity in patients with MMD. **(A)** Negative associations were found between the AS/DS and the PerAF value in the Frontal_Sup_Medial_R. **(B)** Positive associations were found between left-RNFLT, right-RNFLT, and the PerAF value in Frontal_Sup_Medial_R. AS, anxiety score; DS, depression score; RNFLT, retinal nerve fiber layer thickness; PerAF, percent amplitude of fluctuation.

TABLE 3 | The results of the HADS test in patients with MMD and HCs.

Patients	AS	DS	HCs	AS	DS
Patient 1	7	7	HC 1	3	2
Patient 2	4	5	HC 2	3	2
Patient 3	6	6	HC 3	3	2
Patient 4	9	9	HC 4	3	1
Patient 5	8	8	HC 5	4	3
Patient 6	11	10	HC 6	4	2
Patient 7	10	10	HC 7	3	2
Patient 8	7	7	HC 8	1	2
Patient 9	12	11	HC 9	1	1
Patient 10	8	8	HC 10	1	2
Patient 11	8	8	HC 11	3	3
Patient 12	11	10	HC 12	3	2
Patient 13	7	6	HC 13	2	2
Patient 14	8	7	HC 14	3	2
Patient 15	13	12	HC 15	5	3
Patient 16	5	6	HC 16	3	1
Patient 17	8	9	HC 17	4	3

MMD, moyamoya disease; HC, healthy control; HADS, Hospital Anxiety and Depression Scale.

The AS and DS from the HADS questionnaire were negatively associated with the PerAF in the Frontal_Sup_Medial_R in sufferers with MMD, indicating an association between MMD and psychiatric disorders. RNFLT value can be measured by OCT *in vivo* accurately and reproducibly, which provides high diagnostic ability in discriminating between healthy and glaucomatous eyes (22). RNFLT is now more and more commonly used in the staging system of glaucoma in the clinical practice. Previous studies demonstrated that the measurement of RNFLT provides important information for discriminating patients with ocular hypertension without any type of damage from those patients that do not show any functional damage, but have early structural glaucomatous signs (23, 24). The RNFLT-left and RNFLT-right were positively correlated with the PerAF value of the Frontal_Sup_Medial_R. Since we did not study the relationship between the PerAF and the course and progression of MMD, we are unable to determine whether RNFLT is related to the course of MMD. However, because changes in RNFLT are associated with various ocular diseases such as glaucoma, retinitis pigmentosa, ischemic optic neuropathy, optic neuritis, and cranial lesions that destroy or damage the optic nerve (25), the PerAF values as measured in this study can be used as an effective indicator of ocular complications associated with MMD.

TABLE 4 | The PerAF methods applied in neurogenic diseases.

PerAF method applied in neurogenic diseases				
	References	**Disease**	**Brain areas**	
			PerAF increased	**PerAF decreased**
Neurogenic diseases	Wang et al. (20)	ET-1	B1-4: vermis VIII, B1-3: LCL VIII, B1-4: LPG	B5: vermis VIII, B4-5: LCL VIII, B5: LPG
	Zeng et al. (21)	Sleep Deprivation	BVC, BSC	BDPC, BCPL
	Yu et al. (19)	MCID	ILPHGs, TG	N/A

ET-1, Type I epilepsy; B1-4, frequency band B1, B2, B3, B4; B1-3, frequency band B1, B2, B3; B5, frequency band 5; B4-5, frequency band B4, B5; LCL VIII, left cerebellar lobule VIII; LPG, left precentral gyrus; BVC, bilateral vision cortex; BSC, bilateral sensorimotor cortex; LPG, left para-hippocampus gyrus; MCID, mild cognitive impairment with depression symptom; TG, temporal gyrus; BDPC, bilateral dorsolateral prefrontal cortex; BCPL, bilateral cerebellum posterior lobe. PerAF, percent amplitude of fluctuation.

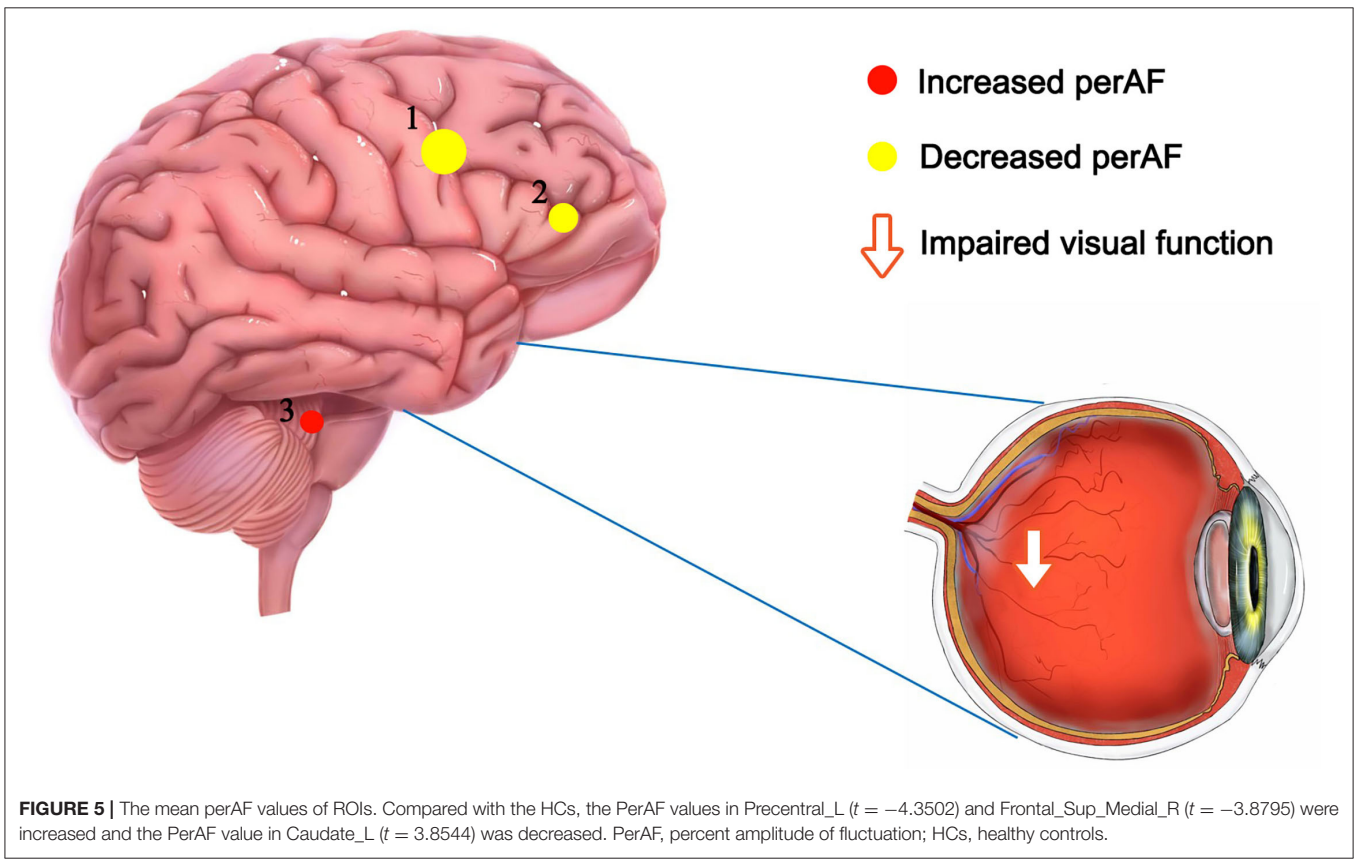

FIGURE 5 | The mean perAF values of ROIs. Compared with the HCs, the PerAF values in Precentral_L ($t = -4.3502$) and Frontal_Sup_Medial_R ($t = -3.8795$) were increased and the PerAF value in Caudate_L ($t = 3.8544$) was decreased. PerAF, percent amplitude of fluctuation; HCs, healthy controls.

On the other hand, patients with MMD may have higher risk of developing eye diseases that are associated with abnormal RNFLT such as glaucoma, optic neuritis, and retinitis pigmentosa.

The superior frontal gyrus (SFG) is an important component of the third frontal lobe of the human brain and plays a crucial role in the regulation of movement, working memory, cognitive ability, self-awareness, and emotional regulation, in coordination with sensory systems (26). Fried et al. (27) found that electrical stimulation of the SFG triggered laughter in an epileptic patient. A higher level of electrical current increased the duration and intensity of laughter, from a smile at low currents to robust laughter with head waving at high current. The patient said her laughter was caused by the sensation of merriment and explained the laughter differently each time, attributing it to several external factors such as decor of the room or the content of the paragraph she was asked to read (27). The SFG is also involved in the perception and regulation of stress including acute psychosocial stress (28) and chronic life

stress (29). Altered SFG gray matter volume was found in stress-related diseases such as major depression (30) and social anxiety disorder (31).

In this study, the PerAF was lower in the SFG of patients with MMD compared to controls. Combined with the above evidence, we deduce from our findings that sensory system impairment is likely in MMD, with reduced brain activity in the SFG. Therefore, patients with MMD may suffer from emotional disorders (depression and anxiety) resulting from decreased neural activity in the SFG. The risk of suffering from other disorders related to dysfunctions in the SFG such as cognitive disability and dyskinesia would also increase. The treatment of sufferers with MMD should include strategies for mood adjustment to avoid the development of depression and anxiety symptoms.

Furthermore, the mean PerAF value of the Frontal_Sup_Medial_R was negatively associated with the thickness of the left and right RNFL. Reduction in RNFLT is associated with various ocular diseases such as glaucoma, retinitis pigmentosa, ischemic optic neuropathy, optic neuritis, and cranial lesions that destroy or damage the optic nerve (25) (**Figure 6**). This may suggest that the PerAF analysis can be used as an early biomarker for ocular complications associated with MMD.

The precentral gyrus (PG) contains the primary motor cortex, which controls the regulation of voluntary movement of the

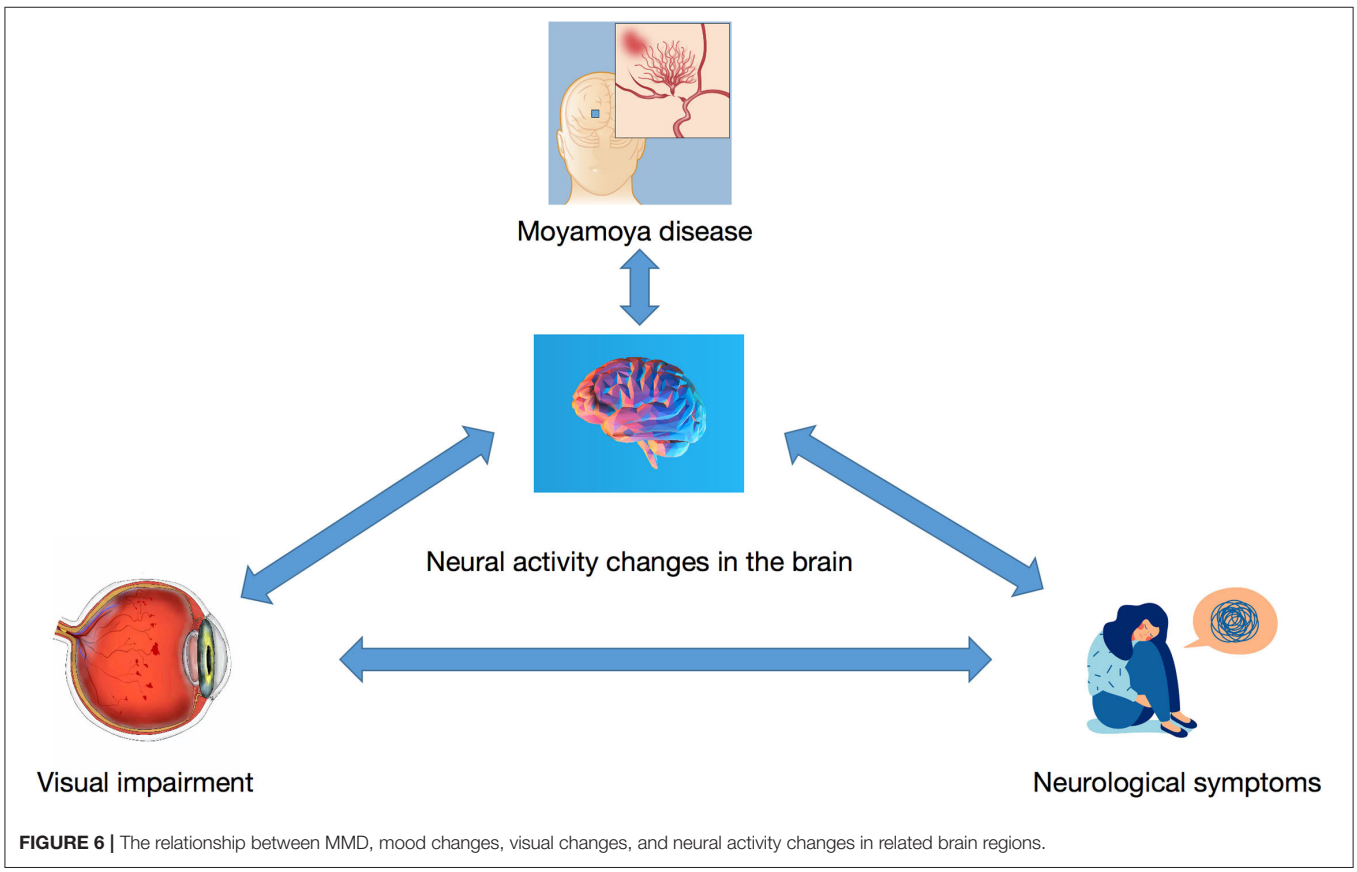

FIGURE 6 | The relationship between MMD, mood changes, visual changes, and neural activity changes in related brain regions.

TABLE 5 | Brain regions alternation and its potential impact.

Brain regions	Experimental result	Brain function	Anticipated results
Frontal_Sup_Medial_R	MMD < HCs	Motor movement, working memory, cognitive ability, emotional regulation	Social and emotional problems, motor function defects, stress disorders and depression, cognitive disorders.
Precentral_L	MMD < HCs	Speech articulation, motor movement, planning of movement	Aphasia, muscle weakness, paralysis
Caudate_L	MMD > HCs	Motor processing, spatial mnemonic processing, procedural learning, associative learning, inhibitory control of action	Parkinson's disease, Alzheimer's disease, spatial movement disorder, defects in working memory, aesthetic obstacles, linguistic barrier

MMD, moyamoya disease; HC, healthy control.

contralateral side of the body (32). PG also comprises part of the supplementary motor cortex, which is responsible for the control of voluntary muscle contraction of the upper and lower limbs (33). When PG lesions occur, patients show dysfunction of the upper motor neurons with associated muscle weakness, abnormal muscle tone, contralateral paralysis (facial, leg, and arm paralysis), and pathological muscle stretch reflexes (such as Babinski sign) (34). Combining the above evidence with the decreased PG PerAF in this study, we can speculate that the extending terminal branches of the carotid artery may, to some extent, be compressed and cause PG dysfunction. The risks of contracting diseases related to PG, such as ataxia, contralateral paralysis, and dysmetria, would be increased in this situation.

The caudate nucleus is an important component of the corpus striatum, which controls spatial movement (35), spatial mnemonic processing, procedural learning (36), and associative learning (37). As part of the cortico-basal ganglia-thalamic loop, it also functions as a component of the reward system (38). The caudate nucleus receives input from the dopaminergic neurons projecting from the substantia nigra and from other associated brain regions. Previous studies indicate that the caudate nucleus is associated with the dysfunction of spatial working memory in patients with Alzheimer's disease as well as its abnormal dopamine supply to the striatum. Compared with non-spatial tasks, increased neural activity in the caudate nucleus is observed when undertaking tasks requiring spatial and motor memories (39). The caudate nucleus also takes part in regulating the speed and accuracy of directed body movements. Arushanian and Tolpyshev (40) removed the caudate nucleus in felines and observed defects in regulation of movement distance and accuracy. In another group in which the caudate nucleus was partially removed in felines, upper limb movement was delayed after stimulation, with constant adjustment of body posture and apparent failure to localize stimulation. A similar animal experiment conducted on monkeys involved the use of cocaine to damage the caudate nucleus. Uncontrolled forward movement and forward leaping were observed in the caudate-damaged monkeys, indicating that the caudate nucleus inhibits spontaneous forward movement when there is no resistance in the forward direction (41). The dorsal-prefrontal subcortical loop in the caudate nucleus is also associated with working memory. Hannan et al. (42) found in normal human subjects that the caudate nucleus is highly activated during working memory tasks, while in patients with schizophrenia, defects in working memory are linked to reduced innervation of the caudate nucleus. The amygdala sends projections to the caudate nucleus and they both have projections into the hippocampus. It is well established that the amygdala is important in memory processing. Lesions of connections between these structures obstruct the infusion of oxotremorine into the caudate nucleus, preventing its memory-enhancing effect and demonstrating the caudate nucleus function in memory processing in cooperation with amygdala. Combining the above evidence with the result of this study that higher PerAF signal was found in the caudate nucleus in sufferers with MMD, we may speculate that dysfunction in the MMD motor control system may cause compensatory overactivation of the caudate nucleus. Therefore, we hypothesize that increased neural activity in the caudate nucleus would cause disorders in motor control and memory learning, which is related to the function of this brain region. In clinical practice, interventions can be made to avoid these potential risks. Based on the above evidence, **Table 5** illustrates the changed activation of brain regions in MMD, functions of those regions, and anticipated clinical outcomes.

In conclusion, changes of the PerAF signals are found in specific brain regions in sufferers with MMD, with decreases in the Frontal_Sup_Medial_R and Precentral_L and an increase in the Caudate_L. Patients with MMD may be at higher risk of diseases that are related to the dysfunction of these brain regions. This study had some limitations. For example, all the subjects were recruited from one province. As MMD is a relatively rare disease, the number of subjects that can be recruited is very limited and a relatively large and equal number of male and female subjects could not be included in this study. But since MMD is a rare disease, the incidence ranges from 1/280,000 to 1/89,000 in Japan and China to 1/1,100,000 in the US. The incidence of the disease in our country is much lower than that in the west. Thus, we have merely collected 46 cases with definite diagnosis and only 17 out of the 46 patients are willing to participate in this study. Therefore, the recruitment of experimental subjects has a certain degree of difficulty. Since our hospital is a well-known hospital in our country for treatment of MMD, patients come not only from the local, but from all over the country. Although it is a single-centered study, the subjects in this study are still representative. Therefore, the sample included large differences in the numbers of male and female participants. However, this study is the first study to use the PerAF to study neural activity changes in MMD. This study found altered brain activity in certain brain regions in sufferers with MMD and disclosed the neural mechanisms underlying clinical features such as anxiety and depression in patients with MMD. This study will also help to advance understanding of the pathogenesis of MMD and its complications, which will, in turn, lead to improvements in the diagnosis and treatment of MMD.

DATA AVAILABILITY STATEMENT

The raw data supporting the conclusions of this article will be made available by the authors, without undue reservation.

ETHICS STATEMENT

The studies involving human participants were reviewed and approved by the Ethics Committee of The First Affiliated Hospital of Nanchang University. The patients/participants provided their written informed consent to participate in this study.

AUTHOR CONTRIBUTIONS

YS and E-MZ contributed to the guarantor of integrity of the entire study. H-YS and Y-CP contributed to the study concepts and design. Q-MG contributed to the literature search. TS

and J-LW contributed to the clinical studies. L-JZ and C-QL contributed to the experimental studies/data analysis. R-BL and X-LL contributed to the statistical analysis. C-QL contributed to the editing and preparation of manuscript. All authors contributed to the article and approved the submitted version.

FUNDING

This study was supported by the National Natural Science Foundation (No: 82160195), the Central Government Guides Local Science and Technology Development Foundation (No: 20211ZDG02003), the Key Research Foundation of Jiangxi Province (Nos: 20181BBG70004 and 20203BBG73059), the Excellent Talents Development Project of Jiangxi Province (No: 20192BCBL23020), the Natural Science Foundation of Jiangxi Province (No: 20181BAB205034), the Grassroots Health Appropriate Technology Spark Promotion Plan Project of Jiangxi Province (No: 20188003), the Health Development Planning Commission Science Foundation of Jiangxi Province (Nos: 20201032 and 202130210), and the Health Development Planning Commission Science TCM Foundation of Jiangxi Province (Nos: 2018A060 and 2020A0087).

ACKNOWLEDGMENTS

The authors would like to express their gratitude to Charlesworth Author Services (www.cwauthors.com) for the expert linguistic services provided.

REFERENCES

1. Suzuki J, Takaku A. Cerebrovascular "moyamoya" disease. disease showing abnormal net-like vessels in base of brain. *Arch Neurol.* (1969) 20:288–99. doi: 10.1001/archneur.1969.00480090076012
2. Shang S, Zhou D, Ya J, Li S, Yang Q, Ding Y, et al. Progress in moyamoya disease. *Neurosurg Rev.* (2020) 43:371–82. doi: 10.1007/s10143-018-0994-5
3. Goto Y, Yonekawa Y. Worldwide distribution of moyamoya disease. *Neurol Med Chir.* (1992) 32:883–6. doi: 10.2176/nmc.32.883
4. Kuroda S, Houkin K. Moyamoya disease: current concepts and future perspectives. *Lancet Neurol.* (2008) 7:1056–66. doi: 10.1016/S1474-4422(08)70240-0
5. Hishikawa T, Sugiu K, Date I. Moyamoya disease: a review of clinical research. *Acta Med Okayama.* (2016) 70:229–36. doi: 10.18926/AMO/54497
6. Scott RM, Smith ER. Moyamoya disease and moyamoya syndrome. *N Engl J Med.* (2009) 360:1226–37. doi: 10.1056/NEJMra0804622
7. Biswal BB. Resting state fMRI: a personal history. *Neuroimage.* (2012) 62:938–44. doi: 10.1016/j.neuroimage.2012.01.090
8. Wang X, Cui D, Zheng L, Yang X, Yang H, Zeng J. Combination of blood oxygen level-dependent functional magnetic resonance imaging and visual evoked potential recordings for abnormal visual cortex in two types of amblyopia. *Mol Vis.* (2012) 18:909–19. doi: 10.7150/ijms.9.115
9. Conner IP, Odom JV, Schwartz TL, Mendola JD. Monocular activation of V1 and V2 in amblyopic adults measured with functional magnetic resonance imaging. *J aapos.* (2007) 11:341–50. doi: 10.1016/j.jaapos.2007.01.119
10. Liang M, Xie B, Yang H, Yin X, Wang H, Yu L, et al. Altered interhemispheric functional connectivity in patients with anisometropic and strabismic amblyopia: a resting-state fMRI study. *Neuroradiology.* (2017) 59:517–24. doi: 10.1007/s00234-017-1824-0
11. Jia XZ, Sun JW, Ji GJ, Liao W, Lv YT, Wang J, et al. Percent amplitude of fluctuation: A simple measure for resting-state fMRI signal at single voxel level. *PLoS ONE.* (2020) 15:e0227021. doi: 10.1371/journal.pone.0227021
12. Smitha KA, Akhil Raja K, Arun KM, Rajesh PG, Thomas B, Kapilamoorthy TR, et al. Resting state fMRI: a review on methods in resting state connectivity analysis and resting state networks. *Neuroradiol J.* (2017) 30:305–17. doi: 10.1177/1971400917697342
13. Zhao N, Yuan LX, Jia XZ, Zhou XF, Deng XP, He HJ, et al. Intra- and inter-scanner reliability of voxel-wise whole-brain analytic metrics for resting state fMRI. *Front Neuroinform.* (2018) 12:54. doi: 10.3389/fninf.2018.00054
14. Yang YC, Li QY, Chen MJ, Zhang LJ, Zhang MY, Pan YC, et al. Investigation of changes in retinal detachment-related brain region activities and functions using the percent amplitude of fluctuation method: a resting-state functional magnetic resonance imaging study. *Neuropsychiatr Dis Treat.* (2021) 17:251–60. doi: 10.2147/NDT.S292132
15. Serbecic N, Beutelspacher SC, Kircher K, Reitner A, Schmidt-Erfurth U. Interpretation of RNFLT values in multiple sclerosis-associated acute optic neuritis using high-resolution SD-OCT device. *Acta Ophthalmol.* (2012) 90:540–5. doi: 10.1111/j.1755-3768.2010.02013.x
16. Li CQ, Yao F, Yu CY, Shu HY, Zhang LJ, Pan YC, et al. Investigation of changes in activity and function in acute unilateral open globe injury-associated brain regions based on percent amplitude of fluctuation method: a resting-state functional MRI study. *Acta Radiol.* (2021) 2841851211034035. doi: 10.1177/02841851211034035
17. Liu X, Yan Z, Wang T, Yang X, Feng F, Fan L, et al. Connectivity pattern differences bilaterally in the cerebellum posterior lobe in healthy subjects after normal sleep and sleep deprivation: a resting-state functional MRI study. *Neuropsychiatr Dis Treat.* (2015) 11:1279–89. doi: 10.2147/NDT.S84204
18. Fox MD, Snyder AZ, Vincent JL, Corbetta M, Van Essen DC, Raichle ME. The human brain is intrinsically organized into dynamic, anticorrelated functional networks. *Proc Natl Acad Sci U S A.* (2005) 102:9673–8. doi: 10.1073/pnas.0504136102
19. Yu Y, Li Z, Lin Y, Yu J, Peng G, Zhang K, et al. Depression affects intrinsic brain activity in patients with mild cognitive impairment. *Front Neurosci.* (2019) 13:1333. doi: 10.3389/fnins.2019.01333
20. Wang B, Wang J, Cen Z, Wei W, Xie F, Chen Y, et al. Altered cerebello-motor network in familial cortical myoclonic tremor with epilepsy type 1. *Mov Disord.* (2020) 35:1012–20. doi: 10.1002/mds.28014
21. Zeng B, Zhou J, Li Z, Zhang H, Li Z, Yu P. Altered percent amplitude of fluctuation in healthy subjects after 36 h sleep deprivation. *Front Neurol.* (2020) 11:565025. doi: 10.3389/fneur.2020.565025
22. Brusini P. OCT glaucoma staging system: a new method for retinal nerve fiber layer damage classification using spectral-domain OCT. *Eye.* (2018) 32:113–9. doi: 10.1038/eye.2017.159
23. Lisboa R, Leite MT, Zangwill LM, Tafreshi A, Weinreb RN, Medeiros FA. Diagnosing preperimetric glaucoma with spectral domain optical coherence tomography. *Ophthalmology.* (2012) 119:2261–9. doi: 10.1016/j.ophtha.2012.06.009
24. Jeoung JW, Kim TW, Weinreb RN, Kim SH, Park KH, Kim DM. Diagnostic ability of spectral-domain versus time-domain optical coherence tomography in preperimetric glaucoma. *J Glaucoma.* (2014) 23:299–306. doi: 10.1097/IJG.0b013e318274 1cc4
25. Cui D, Hou X, Li J, Qu X, Yu T, Song A. Relationship between peripapillary choroidal thickness and retinal nerve fiber layer in young people with myopia. *J Int Med Res.* (2021) 49:3000605211032780. doi: 10.1177/0300060521103 2780
26. Goldberg II, Harel M, Malach R. When the brain loses its self: prefrontal inactivation during sensorimotor processing. *Neuron.* (2006) 50:329–39. doi: 10.1016/j.neuron.2006.03.015
27. Fried I, Wilson CL, MacDonald KA, Behnke EJ. Electric current stimulates laughter. *Nature.* (1998) 391:650. doi: 10.1038/35536
28. Pruessner JC, Dedovic K, Khalili-Mahani N, Engert V, Pruessner M, Buss C, et al. Deactivation of the limbic system during acute psychosocial stress: evidence from positron emission tomography and functional magnetic resonance imaging studies. *Biol Psychiatry.* (2008) 63:234–40. doi: 10.1016/j.biopsych.2007.04.041

29. Li G, Ma X, Bian H, Sun X, Zhai N, Yao M, et al. A pilot fMRI study of the effect of stressful factors on the onset of depression in female patients. *Brain Imaging Behav.* (2016) 10:195–202. doi: 10.1007/s11682-015-9382-8
30. Liu J, Ren L, Womer FY, Wang J, Fan G, Jiang W, et al. Alterations in amplitude of low frequency fluctuation in treatment-naïve major depressive disorder measured with resting-state fMRI. *Hum Brain Mapp.* (2014) 35:4979–88. doi: 10.1002/hbm.22526
31. Qiu C, Feng Y, Meng Y, Liao W, Huang X, Lui S, et al. Analysis of altered baseline brain activity in drug-naive adult patients with social anxiety disorder using resting-state functional MRI. *Psychiatry Investig.* (2015) 12:372–80. doi: 10.4306/pi.2015.12.3.372
32. Ribas GC. The cerebral sulci and gyri. *Neurosurg Focus.* (2010) 28:E2. doi: 10.3171/2009.11.FOCUS09245
33. Lemon RN. Descending pathways in motor control. *Annu Rev Neurosci.* (2008) 31:195–218. doi: 10.1146/annurev.neuro.31.060407.125547
34. Ostergard TA, Miller JP. Surgery for epilepsy in the primary motor cortex: a critical review. *Epilepsy Behav.* (2019) 91:13–9. doi: 10.1016/j.yebeh.2018.06.036
35. Çirak M, Yagmurlu K, Kearns KN, Ribas EC, Urgun K, Shaffrey ME, et al. The caudate nucleus: its connections, surgical implications, and related complications. *World Neurosurg.* (2020) 139:e428–38. doi: 10.1016/j.wneu.2020.04.027
36. Bick SK, Patel SR, Katnani HA, Peled N, Widge A, Cash SS, et al. Caudate stimulation enhances learning. *Brain.* (2019) 142:2930–7. doi: 10.1093/brain/awz254
37. Anderson BA, Kuwabara H, Wong DF, Roberts J, Rahmim A, Brašić JR, et al. Linking dopaminergic reward signals to the development of attentional bias: a positron emission tomographic study. *Neuroimage.* (2017) 157:27–33. doi: 10.1016/j.neuroimage.2017.05.062
38. Yager LM, Garcia AF, Wunsch AM, Ferguson SM. The ins and outs of the striatum: role in drug addiction. *Neuroscience.* (2015) 301:529–41. doi: 10.1016/j.neuroscience.2015.06.033
39. Postle BR, D'Esposito M. Dissociation of human caudate nucleus activity in spatial and nonspatial working memory: an event-related fMRI study. *Brain Res Cogn Brain Res.* (1999) 8:107–15. doi: 10.1016/S0926-6410(99)00010-5
40. Arushanian EB, Tolpyshev BA. [The effect of caudate nucleus stimulation on phenamine stereotypy in cats]. *Zh Vyssh Nerv Deiat Im I P Pavlova.* (1975) 25:171–8.
41. White NM. Some highlights of research on the effects of caudate nucleus lesions over the past 200 years. *Behav Brain Res.* (2009) 199:3–23. doi: 10.1016/j.bbr.2008.12.003
42. Hannan KL, Wood SJ, Yung AR, Velakoulis D, Phillips LJ, Soulsby B, et al. Caudate nucleus volume in individuals at ultra-high risk of psychosis: a cross-sectional magnetic resonance imaging study. *Psychiatry Res.* (2010) 182:223–30. doi: 10.1016/j.pscychresns.2010.02.006

Conflict of Interest: The authors declare that the research was conducted in the absence of any commercial or financial relationships that could be construed as a potential conflict of interest.

Publisher's Note: All claims expressed in this article are solely those of the authors and do not necessarily represent those of their affiliated organizations, or those of the publisher, the editors and the reviewers. Any product that may be evaluated in this article, or claim that may be made by its manufacturer, is not guaranteed or endorsed by the publisher.

Copyright © 2021 Li, Ge, Shu, Liao, Pan, Wu, Su, Zhang, Liang, Shao and Zeng. This is an open-access article distributed under the terms of the Creative Commons Attribution License (CC BY). The use, distribution or reproduction in other forums is permitted, provided the original author(s) and the copyright owner(s) are credited and that the original publication in this journal is cited, in accordance with accepted academic practice. No use, distribution or reproduction is permitted which does not comply with these terms.

frontiers in Neurology

ORIGINAL RESEARCH
published: 15 February 2022
doi: 10.3389/fneur.2022.842888

Altered Expression of Specific MicroRNAs in Plasma of Aneurysmal Subarachnoid Hemorrhage Patients

*Lina Zheng, Xin Zhang, Liping Liu and Yuehua Pu**

Department of Neurology, Beijing Tiantan Hospital, Capital Medical University, Beijing, China

Background: Aneurysmal subarachnoid hemorrhage (aSAH) is a life-threatening condition with high disability and mortality. MicroRNAs (miRNAs) are reported to play a modulating role in aSAH. We investigated specific plasma microRNAs (miRNAs) associated with aSAH and gained comprehensive insight into its pathological mechanisms.

Methods: This is a prospective case–control study. We used a two-stage approach, with primary screening and ensuing two-step validation stages. Significantly differentially expressed plasma miRNAs between aSAH patients and neurologically healthy controls were initially screened by microarray analysis. These miRNAs were then validated in two groups of independent cohorts using reverse transcription quantitative real-time polymerase chain reaction assays. Functional annotation of these miRNA targets was performed by Gene Ontology and Kyoto Encyclopedia of Genes and Genomes pathway enrichment analyses.

Results: In the primary screening stage, 14 miRNAs were identified as differentially expressed at a significance level of $P < 0.05$ and fold change >2 between 5 aSAH patients and 5 neurologically healthy controls. In the two validation steps (20 patients vs. 20 control; 40 patients vs. 30 controls), miR-23b-3p, miR-590-5p, miR-20b-5p, miR-142-3p, and miR-29b-3p were found to be significantly down-regulated in patients with aSAH compared with controls. Through these 5 miRNAs, we obtained 32 overlapping target genes, including TGM2, EREG, EDN1, and COL4A1, in three databases that may affect the progression of aSAH. The results of functional annotation revealed mechanisms mainly related to inflammation, smooth muscle cell proliferation and cell adhesion, potentially contributing to the occurrence of aSAH.

Conclusion: We demonstrate that specific miRNAs in plasma, including miR-23b-3p, miR-590-5p, miR-20b-5p, miR-142-3p, and miR-29b-3p, are significantly down-regulated in aSAH patients and may play a modulating role in its progression.

Keywords: subarachnoid hemorrhage, microRNAs, intracranial aneurysm, microarray, genes

OPEN ACCESS

Edited by:
Wen-Jun Tu,
Chinese Academy of Medical Sciences and Peking Union Medical College, China

Reviewed by:
Jun Zhang,
Texas Tech University Health Sciences Center, United States
Yujie Chen,
Army Medical University, China

****Correspondence:***
Yuehua Pu
sophiepu@me.com

Specialty section:
This article was submitted to Neurological Biomarkers, a section of the journal Frontiers in Neurology

Received: *24 December 2021*
Accepted: *24 January 2022*
Published: *15 February 2022*

Citation:
Zheng L, Zhang X, Liu L and Pu Y (2022) Altered Expression of Specific MicroRNAs in Plasma of Aneurysmal Subarachnoid Hemorrhage Patients. Front. Neurol. 13:842888. doi: 10.3389/fneur.2022.842888

INTRODUCTION

Aneurysmal subarachnoid hemorrhage (aSAH) is a life-threatening condition with high disability and mortality worldwide, accounting for 5–10% of stroke (1). Early identification of aSAH is particularly important. Current diagnostic methods mainly depend on digital subtraction angiography (DSA). However, false negative results

may occur in the presence of vasospasm or thrombosis in ruptured aneurysms. In addition, DSA is an invasive operation with underlying risks. Therefore, biomarkers based on the pathophysiology of ruptured aneurysms that distinguish patients with aSAH from a healthy population are urgently needed.

MicroRNAs (miRNAs), molecules 19–25 nucleotides in length, comprise a class of endogenous, non-coding, single-stranded sequences that play critical roles in post-transcriptional regulation by pairing with the 3′ or 5′ -untranslated region (UTR) of target mRNAs and repressing their translation (2). It has been previously demonstrated that miRNAs are stably expressed in the circulating blood at sufficient levels and have great potential for serving as novel, non-invasive biomarkers (3). Recent studies have investigated circulating miRNA profiling as an indicator for cardiovascular diseases (4). Other studies report significant differences in levels of circulating miRNAs at different pathological processes and physiological aneurysm formation stages, including the inflammatory response, endothelial dysfunction and vascular smooth muscle cell phenotypic modulation (5). In this study, we aimed to investigate specific plasma microRNAs (miRNAs) associated with aSAH and to gain comprehensive insight into the pathological mechanisms of this condition.

MATERIALS AND METHODS

Study Design and Subjects

This was a case-control study using a two-stage approach to analyse differential expression of plasma miRNAs between patients with aSAH and age- and sex-matched neurologically healthy controls, including primary screening and ensuing validation stages. We performed microarray analysis in the primary screening stage to identify differentially expressed plasma miRNA profiles. Then, we carried out validation via reverse transcription quantitative real-time polymerase chain reaction (RT-qPCR) assays twice by recruiting two groups of independent cohorts. Based on the two sets of validated significantly expressed miRNAs between patients with aSAH and neurologically healthy controls, we obtained targeted genes and related biological processes through databases.

Patients meeting the following criteria were enrolled prospectively in the current study: 1) age between 20 and 60 years old; 2) aSAH with at least one intracranial aneurysm confirmed by digital subtraction angiography (DSA) in Beijing Tiantan Hospital; and 3) within 10 days after the onset of symptoms. Those with previous cardiovascular diseases, neurological diseases such as dementia and encephalitis, or prior systemic disorders such as severe renal, liver or heart failure and malignancy were excluded. We enrolled neurologically healthy controls from the health physical examination center in Beijing Tiantan Hospital whose age and sex matched the included aSAH patients. First-degree relatives of the controls had no history of intracranial aneurysm or subarachnoid hemorrhage (SAH). Baseline demographic data, including characteristics regarding vascular risk factors such as hypertension, diabetes, smoking, and alcohol consumption, were collected. We collected the time from blood sampling to the aSAH onset in the patients. We also evaluated the imaging features of intracranial aneurysms including aneurysmal number, location, type and size and assessed the Hunt Hess scale (6), modified Fisher scale (7) in the aSAH patients. Moreover, we dichotomized the neurological functional outcomes at discharge of the aSAH patients as good and poor outcomes, which were defined by modified Rankin Scale 0–2 and 3–6, respectively. This study was evaluated and approved by the medical ethics committee of Beijing Tiantan Hospital, Capital Medical University (KY2012-002-01). All participants or their legal representatives provided written informed consent to participate in the study.

Sample Processing and RNA Isolation

Peripheral venous blood samples were collected into EDTA-containing tubes on the day after admission, processed within 30 min to prevent blood clotting and cell lysis and promptly centrifuged at 2,200 × g for 10 min at room temperature. The plasma was aliquoted into 1.5-mL nuclease-free tubes and stored at −80°C until RNA isolation.

Total RNA, including miRNA, was extracted from venous blood samples using mirVana RNA Isolation Kit (Ambion) according to the manufacturer's standard protocols. The concentration of isolated RNA was measured using a NanoDrop 2000 spectrophotometer (Thermo Scientific, USA), and the RNA integrity was assessed using an Agilent Bioanalyzer 2100 (Agilent Technologies).

miRNA Microarray Experiment

Qualified total RNA was dephosphorylated, denatured and labeled with Cyanine-3-CTP. The purified labeled RNAs were hybridized onto an Agilent Human miRNA microarray (8∗60K, Design ID: 046064) containing 2006 miRNA probes at 55°C for 20 h. After washing, the miRNA microarrays were scanned with an Agilent Scanner G2505C (Agilent Technologies).

Reverse Transcription Quantitative Real-Time Polymerase Chain Reaction

To validate the microarray-generated plasma miRNAs, we conducted two independent validation stages. In the first stage, we measured levels of miRNAs obtained in the screening stage. In the second stage, we validated the miRNAs identified in the first stage and added miRNA-29b-3p, which was closely related to aneurysm formation (8).

miRNA levels were measured using RT-qPCR, with two reaction processes: reverse transcription (RT) and real-time polymerase chain reaction (qPCR). The RT reaction was performed with GeneAmp® PCR System 9700 (Applied Biosystems, USA); qPCR was performed using a LightCycler® 480 II Real-time PCR Instrument (Roche, Switzerland). Exogenous cel-miR-39 was added as an external control, and expression levels of miRNAs were normalized (9). The reactions were run in triplicate, and we used average values of miRNA levels. The ΔCt (threshold cycle) value was calculated by subtracting the Ct value of the exogenous miRNA (cel-miR-39) from that of the target miRNA. The ΔΔCt value was calculated by subtracting the ΔCt value of the miRNA of the control group from that of the target miRNA. Ultimately, the relative

expression levels of miRNAs were calculated via the $2^{-\Delta\Delta Ct}$ method (10). miRNAs were verified in the validation stages when the level differed significantly ($P < 0.05$) and fold change was >2 between the two groups. Investigators performing the whole screening and validation processes above were blinded to the group of samples.

Functional Annotation

We employed a total of three databases, TargetScan, PITA and microRNAorg, separately to obtain a gene list predicted to be targeted by the differentially expressed miRNAs using GeneSpring13.1 software. Functional annotation of miRNA target genes was performed by Gene Ontology (GO) analysis (11) and Kyoto Encyclopedia of Genes and Genomes (KEGG) pathway enrichment analysis (12). GO was used to uncover the biological functions of the miRNA target genes, including biological process, cellular component and molecular function, and KEGG pathway enrichment analysis was performed to detect potential pathways of the miRNA target genes based on the KEGG pathway database, which is a recognized and comprehensive database including various types of biochemistry pathways. We counted the number of target genes and calculated the statistical significance for each GO and pathway entry. The calculation resulted in a *P*-value, with a smaller value indicating that the target gene was more enriched.

Statistical Analysis

Baseline characteristics are presented as percentages for categorical variables and means and standard deviations for continuous variables. Chi-square tests and *t*-tests were used to compare categorical and continuous variables between the patients and controls. miRNA levels were compared using the *t*-test. A two-sided *P*-value of <0.05 was considered statistically significant. All statistical analyses were performed using SPSS 24.0 (IBM Corp, Armonk, NY).

RESULTS

Clinical Characteristics

A total of 65 aSAH patients and 55 healthy controls were included in the study (**Figure 1**). The baseline characteristics of the 120 participants in each case–control cohort are shown in **Table 1**. Among the 65 aSAH patients, 36 (55.4%) were male, and the mean age was 47.28 years. The mean age of the controls was 47.70 years, and 26 (47.3%) of them were male. There were no significant differences between the risk factors between aSAH patients and controls in each case–control cohort. The median time of blood sampling after the aSAH onset was 2 days (interquartile range 2–3). None of the subjects had a history of anticoagulation or antiplatelet drug use.

There were 74 aneurysms in the 65 aSAH patients. Seven patients had multiple aneurysms: five patients had two aneurysms, and two had three aneurysms. The percentage of anterior communicating arteries was highest, and most aneurysms were saccular and had a size less than 5 mm. Most patients were with grade 2 of the initial Hunt Hess scale (58.5%) and grade 3 of modified Fisher scale (30.8%, **Table 2**).

Differently Expressed miRNAs Screened by Microarray Analysis

The microarray study screened expression levels of approximately 2006 miRNAs isolated from the plasma of 10 participants (5 aSAH patients and 5 controls), who were the first 5 aSAH patients admitted to the hospital and 5 age- and sex- matched neurologically healthy controls. Among 113 miRNAs detected on chips, 14 were differentially expressed between 5 aSAH patients and 5 controls at an adjusted significance level of $P < 0.05$ and fold change >2. Among those, 6 miRNAs were up-regulated and 8 down-regulated in aSAH patients compared to the controls (**Table 3**). The results of two-way hierarchical clustering of the 14 important miRNAs are presented in a heatmap (**Figure 2**).

Validation of Candidate miRNAs With RT-qPCR

We enrolled 40 independent samples (20 aSAH patients vs. 20 controls) in the first small-scale preliminary experiment and validated the 14 initial candidate miRNAs that were significantly expressed in the screening stage by RT-qPCR, and only four miRNAs, hsa-miR-23b-3p, miR-590-5p, miR-20b-5p, and miR-142-3p, were still significantly expressed. According to the results

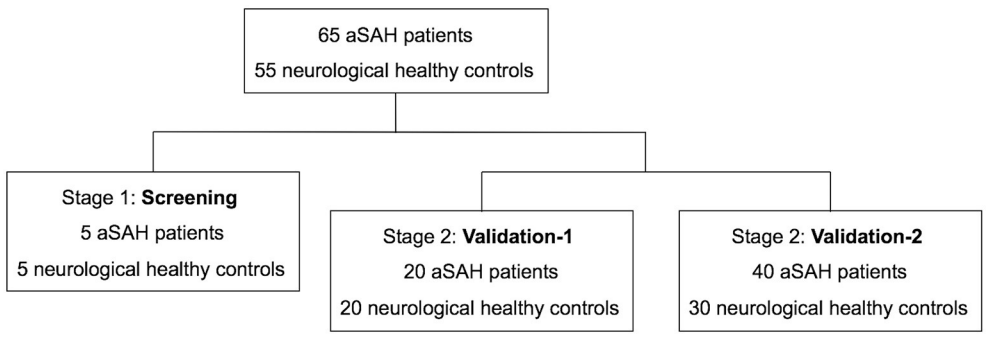

FIGURE 1 | Study flow diagram. aSAH indicates aneurysmal subarachnoid hemorrhage.

TABLE 1 | General characteristics of patients with aneurysmal subarachnoid hemorrhage and controls*.

	Screening			Validation-1			Validation-2		
	Patients ($n = 5$)	**Controls ($n = 5$)**	***P*-value**	**Patients ($n = 20$)**	**Controls ($n = 20$)**	***P*-value**	**Patients ($n = 40$)**	**Controls ($n = 30$)**	***P*-value**
Age, years	46.80 ± 6.14	46.34 ± 7.13	-	48.50 ± 9.08	47.89 ± 8.83	0.653	46.18 ± 7.64	47.60 ± 7.53	0.637
Sex, male	2 (40.0)	2 (40.0)	-	8 (40.0)	6 (30.0)	0.507	26 (65.0)	18 (60.0)	0.668
Risk factor									
Hypertension	2 (40.0)	1 (20.0)	-	10 (50.0)	8 (40.0)	0.525	13 (32.5)	6 (20.0)	0.244
Diabetes mellitus	0 (0.0)	0 (0.0)	-	2 (10.0)	1 (5.0)	1.000	0 (0.0)	0 (0.0)	-
Hyperlipidemia	0 (0.0)	1 (20.0)	-	1 (5.0)	1 (5.0)	1.000	2 (5.0)	2 (6.7)	1.000
Smoking	1 (20.0)	2 (40.0)	-	7 (35.0)	5 (25.0)	0.490	16 (40.0)	11 (36.7)	0.777
Alcoholism	1 (20.0)	1 (20.0)	-	4 (20.0)	3 (15.0)	1.000	13 (32.5)	8 (26.7)	0.598
Time of blood sampling (days after onset)	3 (2–4)	-	-	2 (1-3)	-	-	2 (2-3.5)	-	-

*Values are mean ± standard deviation or number (%); Student's *t*-tests were used for comparison of continuous variables and χ^2-tests for categorical variables.

TABLE 2 | Radiologic and clinical features of patients with aneurysmal subarachnoid hemorrhage*.

Variable	**aSAH patients ($n = 65$)**
Aneurysm	
Number	
1	58 (89.2)
2	5 (7.7)
3	2 (3.1)
Location	
ACom	29 (39.2)
PCom	16 (21.6)
ACA	4 (5.4)
ICA	7 (9.5)
MCA	15 (20.3)
PCA	0 (0.0)
VA	1 (1.4)
BA	2 (2.7)
Type	
Saccular	54 (73.0)
Irregular	19 (25.7)
Dissecting	1 (1.4)
Size, diameter (mm)	
<5	42 (56.8)
5–10	26 (35.1)
11–25	6 (8.1)
>25	0 (0.0)
Initial Hunt Hess scale	
Grade 1 (Minimal symptoms)	21 (32.3)
Grade 2 (Severe headache)	38 (58.5)
Grade 3 (Lethargy)	5 (7.7)
Grade 4 (Hemiparesis or stupor)	1 (1.5)
Grade 5 (Coma, posturing)	0 (0.0)
Modified Fisher scale	
Grade 0 (No blood)	0 (0.0)
Grade 1 (Thin SAH)	30 (4.6)
Grade 2 (Thin SAH and bilateral IVH)	15 (23.1)
Grade 3 (Thick SAH)	20 (30.8)
Grade 4 (Thick SAH and bilateral IVH)	0 (0.0)
Outcome, mRS at discharge	
Good (0-2)	62 (95.4)
Poor (3-6)	3 (4.6)

*Values are number (%) and median (interquartile range).
aSAH indicates aneurysmal subarachnoid hemorrhage; ACom, anterior communicating artery; PCom, posterior communicating artery; ACA, anterior cerebral artery; ICA, internal carotid artery; MCA, middle cerebral artery; PCA, posterior cerebral artery; VA, vertebral artery; BA, basilar artery and mRS, the modified Rankin Scale.

of the experiment, we chose to validate these four miRNAs and added miR-29b-3p, which is reported to be closely related to intracranial aneurysm formation, in another independent cohort of 70 individuals (40 aSAH patients vs. 30 controls) (8). Among the miRNAs identified, all 5 miRNAs were significantly down-regulated in the aSAH patients compared with the controls (all

$P < 0.05$; **Figure 3**), consistent with the preliminary validation experiment results.

Target Gene Prediction and Functional Annotation

We identified 32 common target genes based on the intersection of results from three databases, TargetScan, PITA and microRNAorg (**Figure 4A**), and displayed these 32 genes which were shared by all these three databases in **Table 4**. Several of these target genes have been reported to be closely related to the formation, growth and rupture of intracranial aneurysms, including transglutaminase 2 (TGM2), epiregulin (EREG), endothelin-1 (EDN1) and alpha 1 type IV collagen (COL4A1).

We performed GO enrichment analysis to systematically understand the pathological roles of the target genes. The results revealed a broad range of enriched biological processes or molecular function categories (**Figure 4B**), such as connective tissue development, angiogenesis, signaling pathways, cell proliferation, collagen catabolic process, extracellular matrix organization, and smooth muscle tissue development.

In addition, we carried out pathway analysis using the KEGG database, which indicated the transforming growth factor (TGF)-β signaling pathway (ID: hsa04350) as the most significantly enriched (P = 1.11E-08). Several related pathways involved in sSAH disease were also enriched, including the Hippo signaling pathway (hsa04390), p53 signaling pathway (hsa04115), cellular senescence (hsa04218), AMP-activated protein kinase (AMPK) signaling pathway (hsa04152), focal adhesion (hsa04510), osteoclast differentiation (hsa04380) and cell cycle (hsa04110) (**Figure 4C**).

DISCUSSION

The major discovery in our study is that, compared with neurologically healthy individuals, 14 plasma miRNAs were significantly altered in aSAH patients, regardless of the characteristics of the aneurysms, such as location, type and size. In the verification study, 4 miRNAs, hsa-miR-23b-3p, miR-590-5p, miR-20b-5p, and miR-142-3p, expression profiling and supplement one miR-29b-3p, were significantly altered, and we identified 32 putative target genes involved in the progression of aSAH, including TGM2, EREG, EDN1, and COL4A1. Connective tissue development and the TGF-β signaling pathway were the most significantly enriched biological processes and pathways.

Studies on miRNAs associated with intracranial aneurysms are ongoing. Among the five miRNAs screened and validated in our study, it had been previously reported that miRNA-29b and miRNA-23b-3p are differentially expressed in intracranial aneurysm tissues compared with normal tissues (5); in addition, miR-20b-5p might affect the occurrence and development of intracranial aneurysms by regulating actin cytoskeleton biogenesis (13). miR-23b was also found to result in an impaired inhibitory effect on inflammatory cytokine expression and to be closely related to the inflammatory response. It has been demonstrated that downregulation of miR-590-5p promotes angiotensin II-induced endothelial cell apoptosis in aSAH (14). To date, however, there is no report that miR-142-3p is associated with aSAH or intracranial aneurysms, though a mouse study demonstrated that down-regulation of miR-142-3p affects macrophages involved in age-related inflammatory diseases (15). Moreover, some studies have demonstrated that miR-142-3p is a key regulator of the TGF-β-mediated contractile phenotype of vascular smooth muscle cells that acts by inhibiting cell migration (16). Notably, the TGF-β signaling pathway was found to be involved in the progression of aSAH in our study, and we hypothesize that miR-142-3p is involved in the formation of intracranial aneurysms.

We obtained 32 common target genes in total based on intersection of the results from three databases, demonstrating that each miRNA can participate in regulating expression of multiple target genes and that the same gene may also be regulated by several miRNAs. TGM2 is reported to play a key role in positive regulation of the inflammatory response, smooth muscle cell proliferation and cell adhesion and to participate in blood vessel remodeling (17). In addition to TGM2, EREG, coregulated by miR-142-3p, miR-150-5p, miR-20b-5p, and miR-4793-3p, is closely related to the regulation of smooth muscle cell differentiation and proliferation, epidermal growth factor receptor activity and signaling pathways, epithelial cell proliferation and angiogenesis (18, 19). By targeting EDN1, a potent vasoconstrictor produced by endothelial cells, miR-4443 positively regulates smooth muscle cell proliferation and blood vessel morphogenesis (20). Furthermore, COL4A1 appears to be involved in the maintenance of the integrity of the extracellular matrix of the arterial wall, as genetic variation in COL4A1 leads to disruption of collagen type 4 in the basement membrane (21).

By analyzing the results of GO enrichment, we found that a large part of the cause of intracranial aneurysms is related to the structure of the blood vessel wall, including connective tissue development, smooth muscle cell proliferation and endothelial cell inflammation. Endothelial cells are present in the innermost wall of arteries, which are in direct contact with blood. Endothelial cell differentiation and proliferation or inflammation can increase the formation of aneurysms by generating reactive oxygen species (22). Extracellular connective components and vascular smooth muscle cells together form the medial membrane of the vascular wall, which is the main load-bearing structure. Changes in the collagen catabolic process, extracellular matrix tissue and vascular smooth muscle will inevitably lead to a significant decrease in wall tensile strength (23, 24). Although intracranial aneurysms appear to be focal lesions, there is sufficient evidence to suggest that the entire vascular system is altered in patients with intracranial aneurysms. Our study also found that systemic mechanisms such as stem cell differentiation, positive regulation of angiogenesis and venous blood vessel development are involved in the formation of aneurysms.

With regard to target gene-associated pathways, TGF-β signaling was the most significant pathway revealed in KEGG analysis. This finding is consistent with a previous study, which indicated that the TGF-β pathway plays a pivotal role

TABLE 3 | Plasma miRNAs with significant differences between aSAH patients and controls, as determined by microarray.

miRNAs	Regulation	Fold change	Sequence	Chromosome locus
miR-4793-3p	Up	14.09	AGCCAGCCAACTCAC	chr3
miR-4436-3p	Up	4.03	TTGTCCACTTCTTCCTG	chr2
miR-5010-5p	Up	3.46	AATTTTGCTCTGCCATCC	chr17
miR-30c-2-3p	Up	3.35	AGAGTAAACAGCCTTCTC	chr6
miR-3190-3p	Up	3.26	TCTCTGGCCGTCTACC	chr19
miR-4443	Up	2.03	AAAACCCACGCCTCC	chr3
miR-4449	Down	−12.36	TGCCTCGCGCAGC	chr4
miR-31-5p	Down	−8.20	AGCTATGCCAGCATCTT	chr9
miR-6130	Down	−4.81	CATACAATCCACTCCCT	chr21
miR-150-5p	Down	−4.72	CACTGGTACAAGGGTTGG	chr19
miR-142-3p	Down	−2.55	TCCATAAAGTAGGAAACACTAC	chr17
miR-20b-5p	Down	−2.44	CTACCTGCACTATGAGCAC	chrX
miR-590-5p	Down	−2.22	CTGCACTTTTATGAATAAGCTC	chr7
miR-23b-3p	Down	−2.08	GGTAATCCCTGGCAATG	chr9

aSAH indicates aneurysmal subarachnoid hemorrhage.

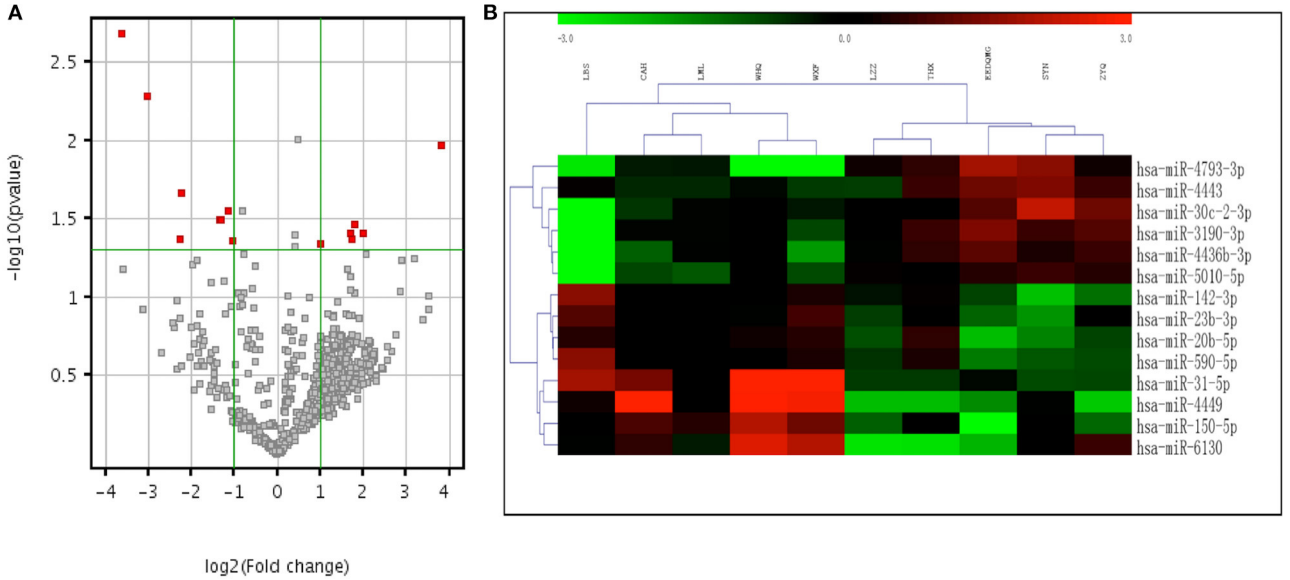

FIGURE 2 | Volcano plot and heatmap expression profiles of differentially expressed miRNAs between aSAH patients and controls in the screening stage. **(A)** Volcano plot of all miRNAs. The –log (P) of each miRNA is plotted against the log2 ratio of aSAH intensity to normal intensity. The green horizontal line indicates the significance level at $P = 0.05$. The green vertical line indicates a fold change level >2. miRNAs that were significantly up-regulated or down-regulated in aSAH patients are indicated by red dots. **(B)** Two-way hierarchical clustering of 14 significant miRNAs. Relatively higher expression levels are represented by red, and relatively lower expression levels are represented by green. miRNAs indicate microRNAs and aSAH, aneurysmal subarachnoid hemorrhage.

in Loeys-Dietz syndrome by affecting smooth muscle cells, with characteristic arterial tortuosity and aneurysms (25). Another study found that TGF-β signal transduction participates in intracranial aneurysm pathogenesis through endothelial cells, corresponding well with enriched GO categories (26). Furthermore, the Hippo signaling pathway is reported to be essential for angiogenesis and vascular barrier formation and maturation, and cellular senescence is associated with the formation of micro-aneurysm in old-age human retinas (27).

There are some limitations to our study. First, we only enrolled patients with aSAH but none with unruptured intracranial aneurysms. So far, there are relatively few literatures on the effect of aneurysm rupture process on the change of plasma miRNAs. Despite previous studies have shown that the change in miRNA expression levels is consistent in patients with intracranial aneurysms, regardless of their status (either ruptured or unruptured), compared to healthy controls (28), whether the aneurysm rupture process has effect on the expression of

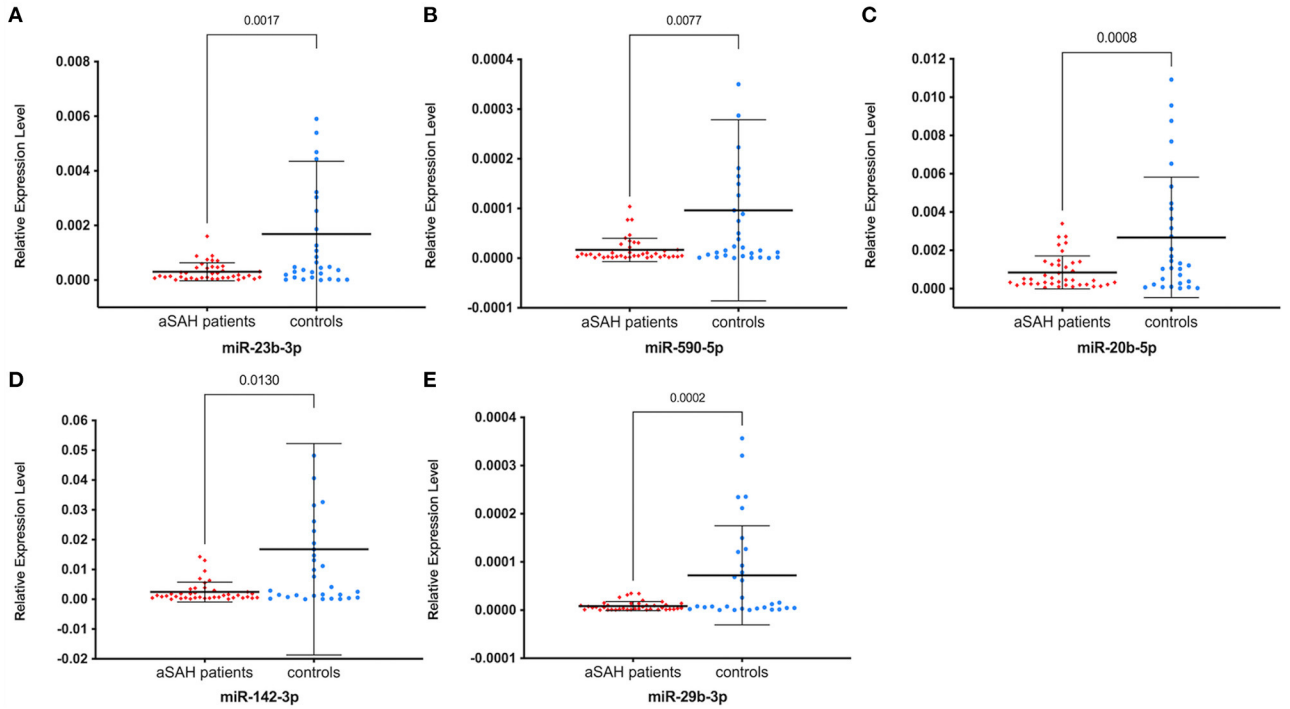

FIGURE 3 | Relative expression levels of five miRNAs between aSAH patients and controls in the validation stage. **(A)** miR-23b-3p; **(B)** miR-590b-5p; **(C)** miR-20b-5p; **(D)** miR-142b-3p; **(E)** miR-29b-3p. Relative expression levels were all significantly lower in aSAH patients than in controls (all $P < 0.05$). miRNAs indicate microRNAs and aSAH, aneurysmal subarachnoid hemorrhage.

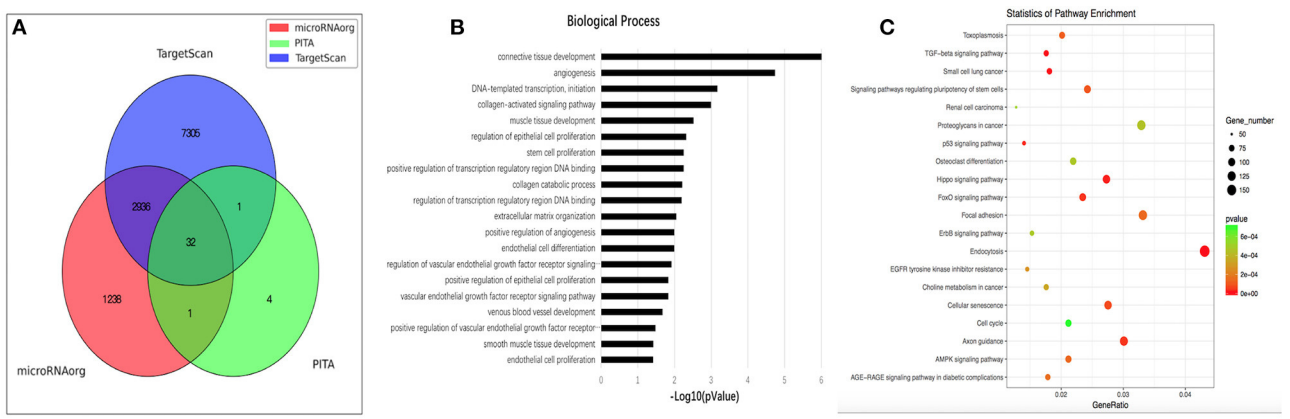

FIGURE 4 | Target genes and results of GO and KEGG analyses. **(A)** 3 targetsbase_venn. Venn diagram of target genes from three databases, TargetScan, PITA, and microRNAorg. **(B)** GO_barplot. Enrichment *P*-value histograms for each GO branch (sorted by *P*-value). **(C)** KEGG_dotplot. A bubble map for the result of KEGG branch enrichment (each KEGG branch is sorted by the *P*-value, taking the first 20 KEGG results). The abscissa is the ratio of the number of genes associated with the KEGG term in the target gene to the number of genes enriched in the KEGG database. The ordinate is the KEGG term. The color scale represents the *P*-value; when the color tends toward red, the *P*-value is smaller. The size of the circle indicates the number of differentially expressed genes in the pathway: the larger the point, the more significant in the gene. GO indicates gene ontology; KEGG, Kyoto Encyclopedia of Genes and Genomes; TGF, transforming growth factor and AMPK, AMP-activated protein kinase.

plasma miRNAs warrants further prospective and large scale studies to investigate. Second, the sample size of this study was relatively small, especially after splitting into 3 cohorts, which might have led to some bias in the results. In addition, we only analyzed the miRNAs in plasma, which might be influenced by the conditions of peripheral organs after aSAH. Therefore, further studies are needed to explore miRNAs in aSAH.

TABLE 4 | Target gene list obtained from three databases.

TGM2	EREG	EDN1	COL4A1	CTNND1	VIM	PDE4B	ME1
KRT10	FNTB	VAMP3	CPEB3	CCNT2	CUL5	ZNF217	LZTFL1
PLEKHA1	GAB1	TMEM59	GTF2A1	CHIC1	PDE8A	EHF	SYPL1
NCK2	MARCKS	LRRC32	C9orf72	CLTA	SKI	MMD	NAV3

In conclusion, we demonstrate that miR-23b-3p, miR-590-5p, miR-20b-5p, miR-142-3p, and miR-29b-3p are significantly down-regulated in aSAH patients, which suggests that these 5 miRNAs are associated with aSAH disease. In addition, mechanisms mainly involving inflammation, smooth muscle cell proliferation and cell adhesion potentially contribute to the occurrence of disease. These results provide a foundation for future research to identify genetic differences between the aSAH population and controls, which may lead to a better understanding of the underlying molecular and pathological mechanisms of aSAH and novel therapeutic targets.

DATA AVAILABILITY STATEMENT

The data cannot be shared as participants were assured that their data would be kept private and confidential to the extent permitted by law, and that only the research team would have access to the data. However, summarized and de-identified data can be available at reasonable request to the corresponding author.

ETHICS STATEMENT

The studies involving human participants were reviewed and approved by the Medical Ethics Committee of Beijing Tiantan Hospital, Capital Medical University. The patients/participants provided their written informed consent to participate in this study.

AUTHOR CONTRIBUTIONS

LZ designed the study, analyzed the data, interpreted the findings, and wrote the manuscript. XZ contributed to data collection and analyses. LL provided critical comments and revisions of the manuscript. YP is responsible for the overall content. All authors have read and approved the manuscript.

FUNDING

This study was supported by National Natural Science Foundation of China (31271192). The funders of the study had no role in study design, data collection, data analysis, data interpretation, or writing of the report.

REFERENCES

1. Feigin VL, Lawes CMM, Bennett DA, Barker-Collo SL, Parag V. Worldwide stroke incidence and early case fatality reported in 56 population-based studies: a systematic review. *Lancet Neurol.* (2009) 8:355–69. doi: 10.1016/S1474-4422(09)70025-0
2. Luo D, Fu J. Identifying characteristic mirnas-genes and risk pathways of multiple sclerosis based on bioinformatics analysis. *Oncotarget.* (2018) 9:5287–300. doi: 10.18632/oncotarget.23866
3. Chen X, Ba Y, Ma L, Cai X, Yin Y, Wang K, et al. Characterization of micrornas in serum: a novel class of biomarkers for diagnosis of cancer and other diseases. *Cell Res.* (2008) 18:997–1006. doi: 10.1038/cr.2008.282
4. Bayoumi AS, Aonuma T, Teoh J-p, Tang Y-l, Kim I-m. Circular noncoding rnas as potential therapies and circulating biomarkers for cardiovascular diseases. *Acta Pharmacol Sin*. (2018) 39:1100–9. doi: 10.1038/aps.2017.196
5. Jiang YG, Zheng MM, He H, Chen J, Zeng H, Li J, et al. Microrna/mrna profiling and regulatory network of intracranial aneurysm. *BMC Med Genomics.* (2013) 6:36. doi: 10.1186/1755-8794-6-36
6. Willianme H, Robert MH. Surgical risk as related to time of intervention in the repair of intracranial aneurysms. *J Neurosurg.* (1967) 28:14–20. doi: 10.3171/jns.1968.28.1.0014
7. Frontera JA, Claassen J, Schmidt JM, Wartenberg KE, Temes R, Connolly ES, et al. Prediction of symptomatic vasospasmafter subarachnoid hemorrhage: the modified fisher scale. *Neurosurgery.* (2006) 59:21–7. doi: 10.1227/01.NEU.0000218821.34014.1B
8. Maegdefessel L, Azuma J, Tsao PS. Microrna-29b regulation of abdominal aortic aneurysm development. *Trends Cardiovasc Med.* (2014) 24:1–6. doi: 10.1016/j.tcm.2013.05.002
9. Sanders I, Holdenrieder S, Walgenbach-Brünagel G, von Ruecker A, Kristiansen G, Müller SC, et al. Evaluation of reference genes for the analysis of serum mirna in patients with prostate cancer, bladder cancer and renal cell carcinoma. *Int J Urol.* (2012) 19:1017–25. doi: 10.1111/j.1442-2042.2012.03082.x
10. Livak KJ, Schmittgen TD. Analysis of relative gene expression data using real-time quantitative PCR and the $2^{-\Delta\Delta CT}$ method. *Methods.* (2001) 25:402–8. doi: 10.1006/meth.2001.1262
11. Ashburner M, Ball CA, Blake JA, Botstein D, Butler H, Cherry JM, et al. Gene ontology: tool for the unification of biology. The Gene Ontology Consortium. *Nat Genet.* (2000) 25:25–9. doi: 10.1038/75556
12. Kanehisa M, Goto S. Kegg: kyoto encyclopedia of genes and genomes. *Nucleic Acids Res.* (2000) 28:27–30. doi: 10.1093/nar/28.1.27
13. Tromp G, Weinsheimer S, Ronkainen A, Kuivaniemi H. Molecular basis and genetic predisposition to intracranial aneurysm. *Ann Med.* (2014) 46:597–606. doi: 10.3109/07853890.2014.949299
14. Luo P, Zhang WF, Qian ZX, Xiao LF, Wang H, Zhu TT, et al. Mir-590-5p-meidated lox-1 upregulation promotes angiotensin ii-induced endothelial cell apoptosis. *Biochem Biophys Res Commun.* (2016) 471:402–8. doi: 10.1016/j.bbrc.2016.02.074
15. Leng X, Fang H, Leung TWH, Mao C, Miao Z, Liu L, et al. Impact of collaterals on the efficacy and safety of endovascular treatment in acute ischaemic stroke: a systematic review and meta-analysis. *J Neurol Neurosurg Psychiatry.* (2016) 87:537–44. doi: 10.1136/jnnp-2015-310965
16. Kim K, Yang DK, Kim S, Kang H. Mir-142-3p is a regulator of the tgfbeta-mediated vascular smooth muscle cell phenotype. *J Cell Biochem.* (2015) 116:2325–33. doi: 10.1002/jcb.25183

17. Eligini S, Fiorelli S, Tremoli E, Colli S. Inhibition of transglutaminase 2 reduces efferocytosis in human macrophages: role of cd14 and sr-ai receptors. *Nutr Metab Cardiovasc Dis.* (2016) 26:922–30. doi: 10.1016/j.numecd.2016.05.011
18. Radom-Aizik S, Zaldivar FP, Jr., Haddad F, Cooper DM. Impact of brief exercise on circulating monocyte gene and microrna expression: implications for atherosclerotic vascular disease. *Brain Behav Immun.* (2014) 39:121–9. doi: 10.1016/j.bbi.2014.01.003
19. Takahashi M, Hayashi Ki, Yoshida K, Ohkawa Y, Komurasaki T, Kitabatake A, et al. Epiregulin as a major autocrine/paracrine factor released from erk- and p38mapk-activated vascular smooth muscle cells. *Circulation.* (2003) 108:2524–9. doi: 10.1161/01.CIR.0000096482.02567.8C
20. Jacobs ME, Wingo CS, Cain BD. An emerging role for microrna in the regulation of endothelin-1. *Front Physiol.* (2013) 4:22. doi: 10.3389/fphys.2013.00022
21. Plaisier E, Gribouval O, Alamowitch S, Mougenot B, Prost C, Verpont MC, et al. Col4a1 mutations and hereditary angiopathy, nephropathy, aneurysms, and muscle cramps. *N Engl J Med.* (2007) 357:2687–95. doi: 10.1056/NEJMoa071906
22. Tulamo R, Frösen J, Hernesniemi J, Niemelä M. Inflammatory changes in the aneurysm wall: a review. *J Neurointerv Surg.* (2018) 10:i58–i67. doi: 10.1136/jnis.2009.002055.rep
23. Chalouhi N, Ali MS, Jabbour PM, Tjoumakaris SI, Gonzalez LF, Rosenwasser RH, et al. Biology of intracranial aneurysms: role of inflammation. *J Cereb Blood Flow Metab.* (2012) 32:1659–76. doi: 10.1038/jcbfm.2012.84
24. Frösen J. Smooth muscle cells and the formation, degeneration, and rupture of saccular intracranial aneurysm wall—a review of current pathophysiological knowledge. *Transl Stroke Res.* (2014) 5:347–56. doi: 10.1007/s12975-014-0340-3
25. Loeys BL, Schwarze U, Holm T, Callewaert BL, Thomas GH, Pannu H, et al. Aneurysm syndromes caused by mutations in the tgf-beta receptor. *N Engl J Med.* (2006) 355:788–98. doi: 10.1056/NEJMoa055695
26. Xu Z, Rui YN, Hagan JP, Kim DH. Intracranial aneurysms: pathology, genetics, and molecular mechanisms. *Neuromolecular Med.* (2019) 21:325–43. doi: 10.1007/s12017-019-08537-7
27. Lo pez-Luppo M CJ, Ramos D, et al. Cellular senescence is associated with human retinal microaneurysm formation during aging. *Invest Ophthalmol Vis Sci.* (2017) 58:7. doi: 10.1167/iovs.16-20312
28. Li P, Zhang Q, Wu X, Yang X, Zhang Y, Li Y, et al. Circulating micrornas serve as novel biological markers for intracranial aneurysms. *J Am Heart Assoc.* (2014) 3:e000972. doi: 10.1161/JAHA.114.000972

Conflict of Interest: The authors declare that the research was conducted in the absence of any commercial or financial relationships that could be construed as a potential conflict of interest.

Publisher's Note: All claims expressed in this article are solely those of the authors and do not necessarily represent those of their affiliated organizations, or those of the publisher, the editors and the reviewers. Any product that may be evaluated in this article, or claim that may be made by its manufacturer, is not guaranteed or endorsed by the publisher.

Copyright © 2022 Zheng, Zhang, Liu and Pu. This is an open-access article distributed under the terms of the Creative Commons Attribution License (CC BY). The use, distribution or reproduction in other forums is permitted, provided the original author(s) and the copyright owner(s) are credited and that the original publication in this journal is cited, in accordance with accepted academic practice. No use, distribution or reproduction is permitted which does not comply with these terms.

frontiers in Neurology

ORIGINAL RESEARCH
published: 15 February 2022
doi: 10.3389/fneur.2022.827544

Lipidomics Profiles Revealed Alterations in Patients With Meibomian Gland Dysfunction After Exposure to Intense Pulsed Light

Hui Zhao[1*†], *Shi-Nan Wu*[2†], *Yi Shao*[2], *Dong Xiao*[1], *Li-Ying Tang*[3], *Zhe Cheng*[3] and *Jie Peng*[1]

[1] Department of Ophthalmology, Xinhua Hospital Affiliated to Shanghai Jiao Tong University School of Medicine, Shanghai, China, [2] Department of Ophthalmology, Jiangxi Province Ocular Disease Clinical Research Center, The First Affiliated Hospital of Nanchang University, Nanchang, China, [3] Department of Ophthalmology, Fujian Provincial Key Laboratory of Ophthalmology and Visual Science, School of Medicine, Xiamen University, Eye Institute of Xiamen University, Xiamen, China

OPEN ACCESS

Edited by:
Yuzhen Xu,
Tongji University, China

Reviewed by:
Yi Zhou,
Amgen, United States
Lan Gong,
Eye, Ear, Nose, and Throat Hospital of Fudan University, China

***Correspondence:**
Hui Zhao
20887787@qq.com

[†]These authors have contributed equally to this work and share first authorship

Specialty section:
This article was submitted to Neurological Biomarkers, a section of the journal Frontiers in Neurology

Received: 02 December 2021
Accepted: 04 January 2022
Published: 15 February 2022

Citation:
Zhao H, Wu S-N, Shao Y, Xiao D, Tang L-Y, Cheng Z and Peng J (2022) Lipidomics Profiles Revealed Alterations in Patients With Meibomian Gland Dysfunction After Exposure to Intense Pulsed Light. Front. Neurol. 13:827544. doi: 10.3389/fneur.2022.827544

So far, intense pulsed light (IPL) has been widely used in the treatment of meibomian gland dysfunction (MGD), but there was still a lack of research on its specific mechanism. Determining whether there was a correlation between liposome changes and remission of clinical signs in patients with MGD treated with IPL was of great significance in the clinical evaluation of efficacy in patients with MGD. Our study enrolled the 10 healthy subjects and 26 adult patients, who were diagnosed with MGD and had not received any alternative treatments for at least 3 months. Each patient received a series of three treatments at 3-week intervals. The meibum was collected before the first treatment (T0) and the third treatment (T2). The significant changes in ocular surface parameters before and after IPL treatment were analyzed. The results showed that IPL significantly improved the symptoms of MGD, including ocular surface disease index (OSDI), tear breakup time (TBUT), redness of conjunctival (CR), corneal fluorescein staining (CF), the meibomian gland expressibility (MGE), and meibum quality (all $p < 0.05$). Lipidomics analysis of the meibum characterized the changes in lipid profiles induced by IPL. A total of 323 lipid species compounds were identified in the spectrum. A total of 41 lipid species were significantly different in patients with MGD (T0) vs. healthy controls. Following IPL treatment (T2), 24 lipid species were significantly different compared with T0: TG (10 lipid species), LPC (6 lipid species), OAHFA (4 lipid species), Cer (2 lipid species), SM (1 lipid species), and PE (1 lipid specie). Among these lipids, 4 of the lipids was a high correlation with TBUT, 5 was TH, 6 was CR, and 11 was meibum quality. In a ward, IPL treatment can achieve the therapeutic effect by changing the alternations of tear film lipids in patients with MGD. The changes in lipid expression profiles are potential indexes to evaluate the therapeutic effectiveness of IPL treatment or other treatments on MGD.

Keywords: intense pulsed light, dry eye, disease markers, lipidomics, meibomian gland dysfunction

INTRODUCTION

The meibomian gland (MG) is a lipid-rich tissue that is the main source of lipids for the tear film. Meibomian gland dysfunction (MGD) is a chronic, diffuse abnormality of the MGs, commonly characterized by terminal duct obstruction and/or qualitative or quantitative changes in glandular secretion. It may result in alteration of the tear film, symptoms of eye irritation, clinically apparent inflammation, and ocular surface disease (1). An epidemiological meta-analysis of MGD showed that the overall clinical prevalence rate was 35.8%. The prevalence rate of men was significantly higher than that of women (odds ratio = 1.24) (2). The MG is one of the components of the ocular surface microenvironment and its secretion plays an important role in tear film homeostasis (3). MGD was regarded as the leading cause of evaporative dry eye (DE) worldwide (4), especially related to the evaporative DE which is the most common ocular surface disease worldwide. Long-term MG lesions can cause inflammatory reactions in the ocular surface, which in turn lead to corresponding changes in the cornea and conjunctiva (5). In severe cases, visual acuity declines, resulting in a poor prognosis. At present, there is no uniform diagnostic standard for MGD (6). The widely accepted definition of "MGD" is a chronic diffuse abnormality of the MG, usually characterized by terminal duct obstruction and/or qualitative or quantitative changes in glandular secretions. This can lead to tear film changes, eye irritation, clinical inflammation, and ocular surface diseases. The commonly used diagnostic method is the generic diagnosis and systematic assessments, and its main inclusion indicators include the patient's symptoms, altered gland secretions, and changes in tear film (6, 7). Any of the above signs in combination with ocular symptoms are indicative of MGD. Due to the lack of symptomatic specificity assigned to MGD, it is often misdiagnosed and mistreated. These limitations in arriving at accurate diagnosis are prompting increasing attention by researchers in gaining insight into the pathophysiology underlying MGD.

The meibum, secretions of the MG, spreads onto the tear film to reduce the evaporation of the tear component and protects the eye from dust and microbial agents. The lipids secreted by MGs played a critical role in the homeostasis of the tear film. According to the related studies, the contents of triglycerides, cholesterol, and monounsaturated fatty acids in lipids in patients with MGD changed significantly (8). The meibum consists of an extremely complex mixture of lipids that is mainly composed of wax lipids, cholesterol lipids, free fatty acids, phospholipids, and a small amount of protein. More than 100 components of meibum lipids have been found, and hundreds of subtypes have not been identified thus far (9–11). Accurate evaluation of the changes in lipid expression profile is conducive to the treatment effect or disease progression of patients with MGD.

Numbers of therapeutics have been applied to treat MGD, such as antiinflammatory agents, immunosuppressors, tetracycline, lubricant ointments, artificial lubricants, eyelid hygiene, eyelid warming, massage (12), IPL (13), etc. However, there was not a standardized treatment for MGD. IPL is a noncoherent polychromatic light source with a broad wavelength spectrum of 500–1,200 nm (14, 15). As an established commercial technology, IPL treatment is broadly used in diseases involving facial rosacea. It has been shown that IPL is effective for the treatment of the eyelid sebaceous gland, also termed MG (16–18). Thus, IPL is a promising new therapy for MGD. Currently, IPL treatment is regarded as a more time-efficient and effective method to ameliorate the symptoms of DE (13). Although the efficacy and safety of IPL have been confirmed by ocular surface symptoms (18), the exact therapeutic effect of IPL on the MG remains unclear, especially the lipid metabolism. In this study, a comprehensive evaluation of clinical signs and changes in the lipid composition of meibum were conducted in patients with MGD after at least three exposures to IPL. A comparison of clinical assessment and alteration of the meibum were also conducted in patients treated with IPL and those without MGD. The results of this study would be helpful to understand the mechanisms of IPL in MGD treatment by providing insightful data.

PATIENTS AND METHODS

Patients

Adult patients, who were diagnosed with MGD and had not received any alternative treatments for at least 3 months, were enrolled in the study. The inclusion criteria were as follows: diagnosis of MGD according to the Japanese MGD diagnostic criteria (9), including ocular symptoms, plugged gland orifices, vascularity of lid margins, irregularity of lid margins, and decreased meibum quality and quantity. The exclusion criteria were as follows: previous ocular surgery or trauma, blepharal dysraphism, history of blepharal and periorbital skin disease within 1 month prior to enrollment, acute inflammation, rheumatic immune systemic diseases, excessive sun exposure within 1 month prior to enrollment, history of herpes zoster infection, pregnancy, and use of photosensitive drugs or foods.

Informed consent was provided by all patients following an explanation of the nature and possible consequences of the study. This study was approved by the Institutional Review Board of the Xin Hua Hospital of Shanghai Jiao Tong University School of Medicine (Shanghai, China) and was registered with the Chinese Clinical Trial Registry prior to enrollment of the first patient. This study adhered to the tenets of the Declaration of Helsinki. All examiners were blinded to the treatment group. The

Abbreviations: IPL, intense pulsed light; MGD, meibomian gland dysfunction; T0, before treatment; T2, after treatment; TBUT, tear breakup time; MGE, meibomian gland expressibility; DE, dry eye; UHPLC-MS/MS, ultrahigh pressure liquid chromatography liquid chromatography-tandem mass spectrometry; CR, redness of conjunctival; CF, fluorescein staining; TG, triglyceride; Cer, ceramide; PC, phosphatidylcholine; SM, sphingomyelin; CerG1, simple Glc series G1; SO, sphingosine; LPC, lysophosphatidylcholine; LPE, lysophosphatidylethanolamine; MGDG, monogalactosyldiacylglycerol; PS, phosphatidylserine; DGDG, digalactosyldiacylglycerol; OAHFA, (O-acyl)-1-hydroxy fatty acid; PE, phosphatidylethanolamine; DGMG, digalactosylmonoacylglycerol; WE, wax ester; CerG2, simple Glc series G2; CO, coenzyme; LPG, lysophosphatidylglycerol; PG, phosphatidylglycerol; DG, diglyceride; LPI, lysophosphatidylinositol; LPS, lysophosphatidylserine; LSM, lysosphingomyelin; MGMG, monogalactosylmonoacylglycerol; PI, phosphatidylinositol; StE, stigmasterol ester; PCA, principal component analysis.

study was enlisted in the clinical trial registry (trial registration no.: ChiCTR2000033454).

IPL Treatment

Each patient received a series of three treatments at 3-week intervals. The patients had to use proparacaine hydrochloride eye drops (Benoxil, Santen Pharmaceutical Co., Ltd. Japan) at least 2 days prior to each treatment (19). A modular laser multiapplication platform (Quantum^{TM}, Lumenis, USA) was used to administer treatment to the periorbital area. During the IPL procedure, patients were required to wear opaque goggles, and the coolant was applied around the eyelids under both eyes. Makeup and contact lenses were removed before treatment. Depending on the patient tolerance, each subject in the patient group received 2–3 light pulses. The intensity of IPL treatment (14–16 J/cm^2) depends on the Fitzpatrick skin with a 590-nm filter (19).

Clinical Assessment

Visual acuity and intraocular pressure were recorded in the case-report form. The standard patient evaluation of eye dryness questionnaire was completed by each patient. Schirmer I test, corneal staining, meibum quality, and meibomian gland expressibility (MGE), lid margin abnormality, redness of conjunctival (CR), MG opening position, and corneal fluorescein staining (CF) were measured through slit-lamp microscopy. A noncontact infrared meibography system was used to assess tear breakup time (TBUT), MG dropout, and tear meniscus height (TH).

Meibum Acquisition

The use of makeup, artificial tears, and cleaning the rim more than 3 h prior to the collection of the material was prohibited. After exposure to IPL, proparacaine hydrochloride eye drops were used again and the material was collected. The use of plastic products during sample preparation and experimentation was avoided to prevent contamination of the rouge. The steps performed for the collection of the materials were as follows: (1) the MG pressing method was used to squeeze out the secretions of the MGs with an MG expressor forceps – this is achieved by placing the thumb of one hand under the lower eyelid, squeezing the rim and rapidly pulling down, and squeezing out the secretion of the MG (the same method was used to remove the rouge from the upper eyelid); (2) a medical cotton swab was used to scrape the MG secretions, and the cotton swab was placed it in a cryotube and stored at −80°C until further analysis. The amount of rouge collected in this study was 1.77 ± 0.29 mg.

One-Dimensional LC-MS/MS

Liquid chromatography separation using CSH C18 column (1.7 μm, 2.1 × 100 mm, waters) was selected to perform reverse-phase chromatography. The lipid of meibum was redissolved in 200 μL 90% isopropanol or acetonitrile then centrifuged at 14,000 x g for 15 min, and finally, 3 μL of the sample was selected for injection. Solvent A: acetonitrile–water (6:4, v/v) with 0.1% formic acid and 0.1 Mm ammonium formate. Solvent B: acetonitrile–isopropanol (1:9, v/v) with 0.1% formic acid and

TABLE 1 | Clinical parameters before and after treatment of IPL in MGD ($n = 26$).

Clinical assessment	Before treatment	After treatment	T Value	*P* Value	
Age	48.89 ± 16.11	–	–	–	
Gender (Male/Female)	7/19	–	–	–	
OSDI	43.10 ± 15.55	24.78 ± 12.85	4.629	<0.001	***
TBUT(s)	3.19 ± 1.13	5.62 ± 1.81	−5.781	<0.001	***
TH	0.17 ± 0.08	0.21 ± 0.12	−1.386	0.172	
CR	1.38 ± 0.62	0.58 ± 0.44	5.399	<0.001	***
CF	1.00 ± 0.94	0.23 ± 0.43	3.801	<0.001	***
ML	1.04 ± 0.99	0.92 ± 1.01	0.417	0.679	
MG drop out	1.54 ± 0.86	1.54 ± 0.86	0.000	1	
MGE	1.31 ± 0.93	0.79 ± 0.53	2.474	0.017	*
Meibum quality	1.40 ± 0.85	0.73 ± 0.51	3.458	0.001	**

**P < 0.01, **P < 0.01, ***P < 0.001; data showed as mean ± standard deviation or n. OSDI, ocular surface disease index; TBUT, tear break-up time; TH, tear meniscus height; CR, redness of conjunctival inflammation; CF, corneal fluorescein staining; ML, marx line; MGE, meibomian gland expression.*

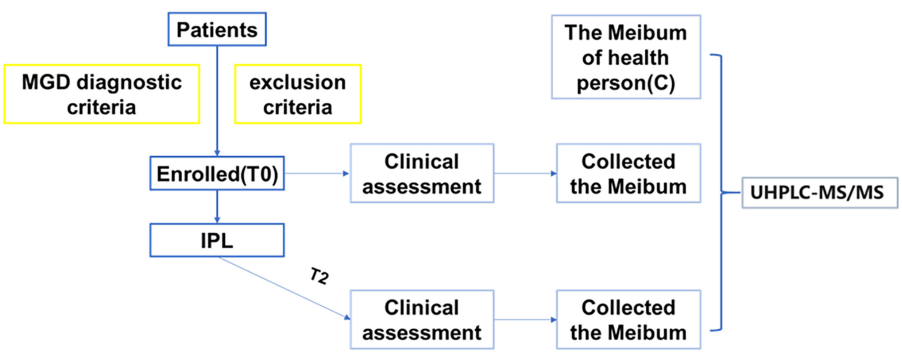

FIGURE 1 | A working diagram of data processing.

0.1 Mm ammonium formate. The initial mobile phase was 30% solvent B at a flow rate of 300 μL/min. It was held for 2 min and then linearly increased up to 100% solvent B in 23 min, followed by equilibrating at 5% solvent B for 10 min. Mass spectra were acquired by Q-Exactive Plus in positive and negative modes, respectively. ESI parameters were optimized and preset for all measurements as follows: source temperature, 300°C; capillary temperature, 350°C, the ion spray voltage was set at 3,000 V, S-Lens RF Level was set at 50%, and the scan range of the instruments was set at m/z 200–1800.

"Lipid Search" is a search engine for the identification of lipid species based on MS/MS math. Lipid Search contains more than 30 lipid classes and more than 1,500,000 fragment ions in the database. Both mass tolerance for precursor and fragment were set to 5 ppm.

Statistical Analysis

Data were analyzed using the SPSS version 22.0 (IBM Corp., Armonk, NY, USA) and R (version 4.0.2; package: corrplot version 0.90, psych version 2.1.9) software. Continuous intergroup variables were analyzed using an independent *t*-test, and pretreatment and continuous intragroup variables were analyzed with a paired *t*-test. Categorical intergroup variables were analyzed with the nonparametric Kruskal–Wallis test, and intragroup analysis of categorical variables was performed using the nonparametric Wilcoxon signed-rank test. Correlations between normally distributed values and nonnormally distributed values were analyzed with the linear Pearson's correlation coefficient and the Spearman's correlation coefficient, respectively. $p < 0.05$ denoted statistical significance.

RESULTS

Patient Demographics

A total of 26 patients' right eyes were enrolled in the study. We collected the meibum before the first treatment (T0) and the third treatment (T2). All enrolled patients completed the whole examination and treatment; there was no pain or any discomfort reported during the tests. All of the patients with MGD were asked to do the lipid analysis using LC-MS/MS. In addition, we also enrolled 10 volunteers who had no MGD diseases (the work plan is illustrated as follows) (**Figure 1**).

Tear Film and Ocular Surface Analysis

Following treatment with IPL, the ocular surface disease index (OSDI) was markedly decreased from 43.10 ± 15.55 to 24.78 ± 12.85 ($p < 0.01$). At the same time, the TBUT (s) increased following treatment from 3.19 ± 1.13 to 5.62 ± 1.81 ($p <$

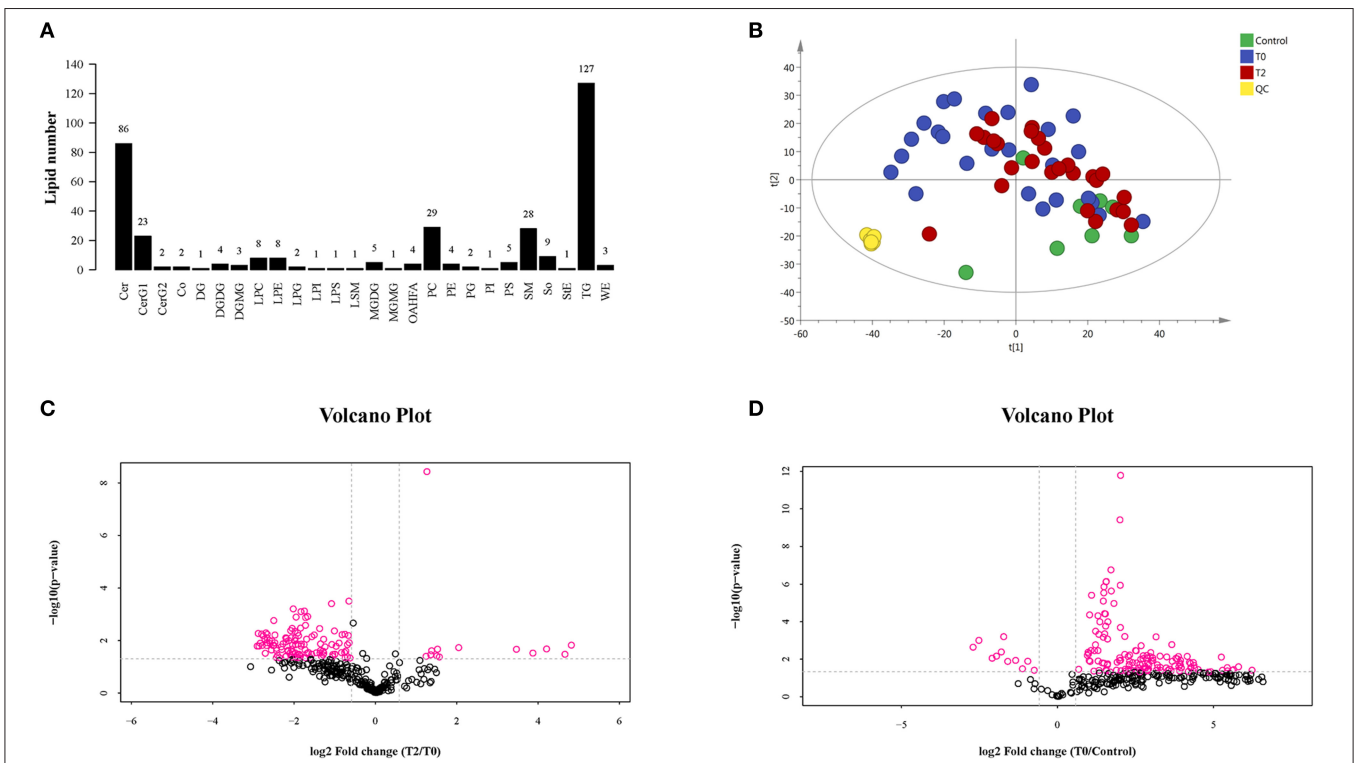

FIGURE 2 | The LC-MS/MS analysis of human meibum in normal control ($n = 10$), before the first treatment of IPL (T0, $n = 26$) and the third treatment (T2, $n = 26$). **(A)** The identification of the lipid species. **(B)** PCA diagram among T0 group, T2 group, control group, and QC group. There was a significant trend distinction between T0 and control groups. **(C,D)**, respectively). The volcano plot of the lipids' quality of T2 vs. T0 **(C)** and T0 vs. control **(D)**.

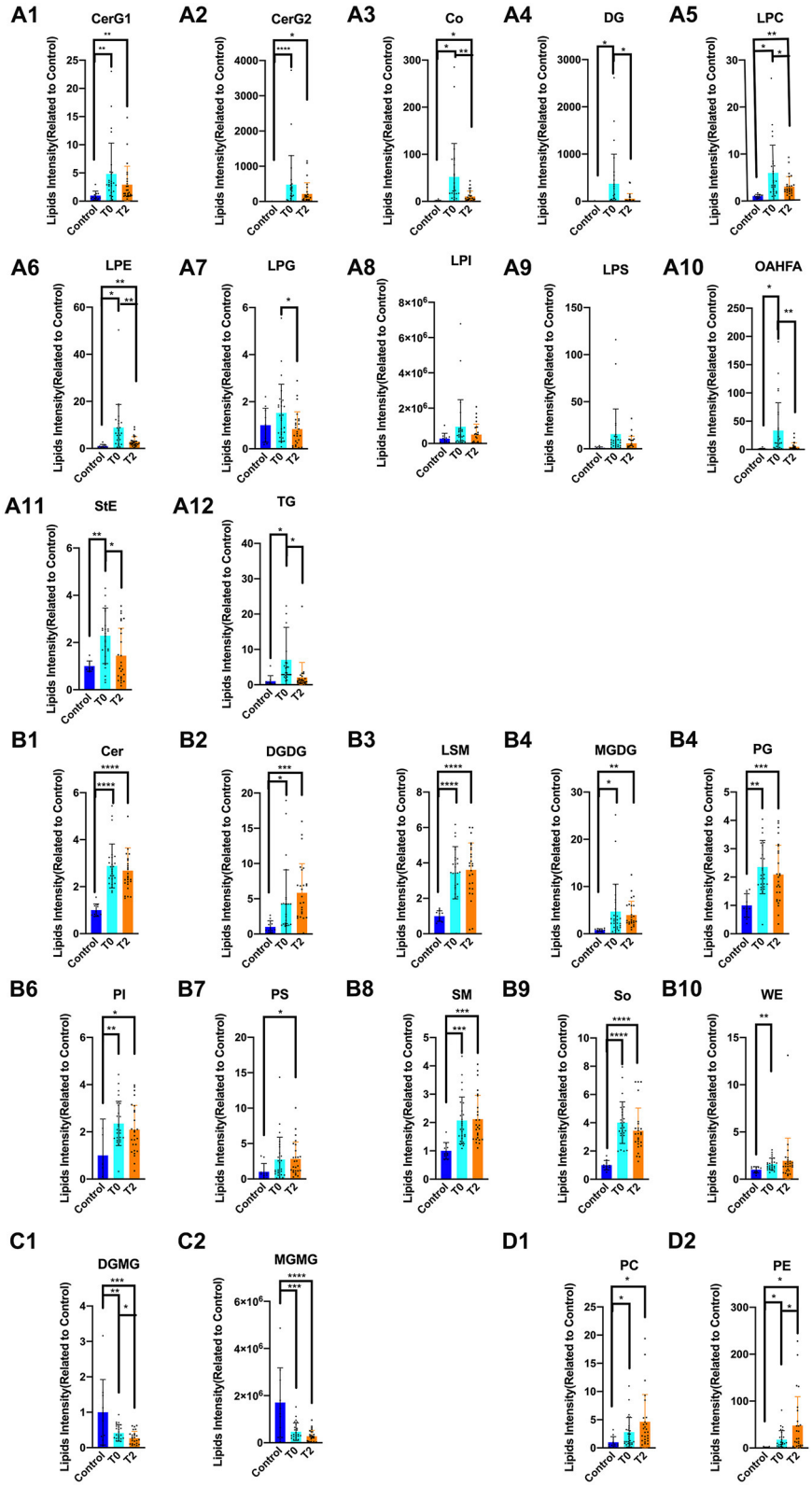

FIGURE 3 | The alternation of lipid compound involved in IPL treatment. $^{*}p < 0.05$, $^{**}p < 0.01$, $^{***}p < 0.001$, $^{****}p < 0.0001$. Control ($n = 10$), T0 ($n = 26$), T2 ($n = 26$). **(A1–A12)** The increased lipids in T0 of CerG1, CerG2, Co, DG, LPC, LPE, LPG, LPI, LPS, OAHFA, StE, and TG were decreased after treatment of IPL(T2). **(B1–B10)** There was no significant difference in Cer, DGDG, LSM, MGDG, PG, PI, PS, and SM, So, WE that increased in T0 and T2. **(C1–C2)** The decreased lipids in T0 of DGMG and MGMG could be reversed by treatment of IPL(T2). **(D1–D2)** Even more, the PC and PE were higher than T0 in T2.

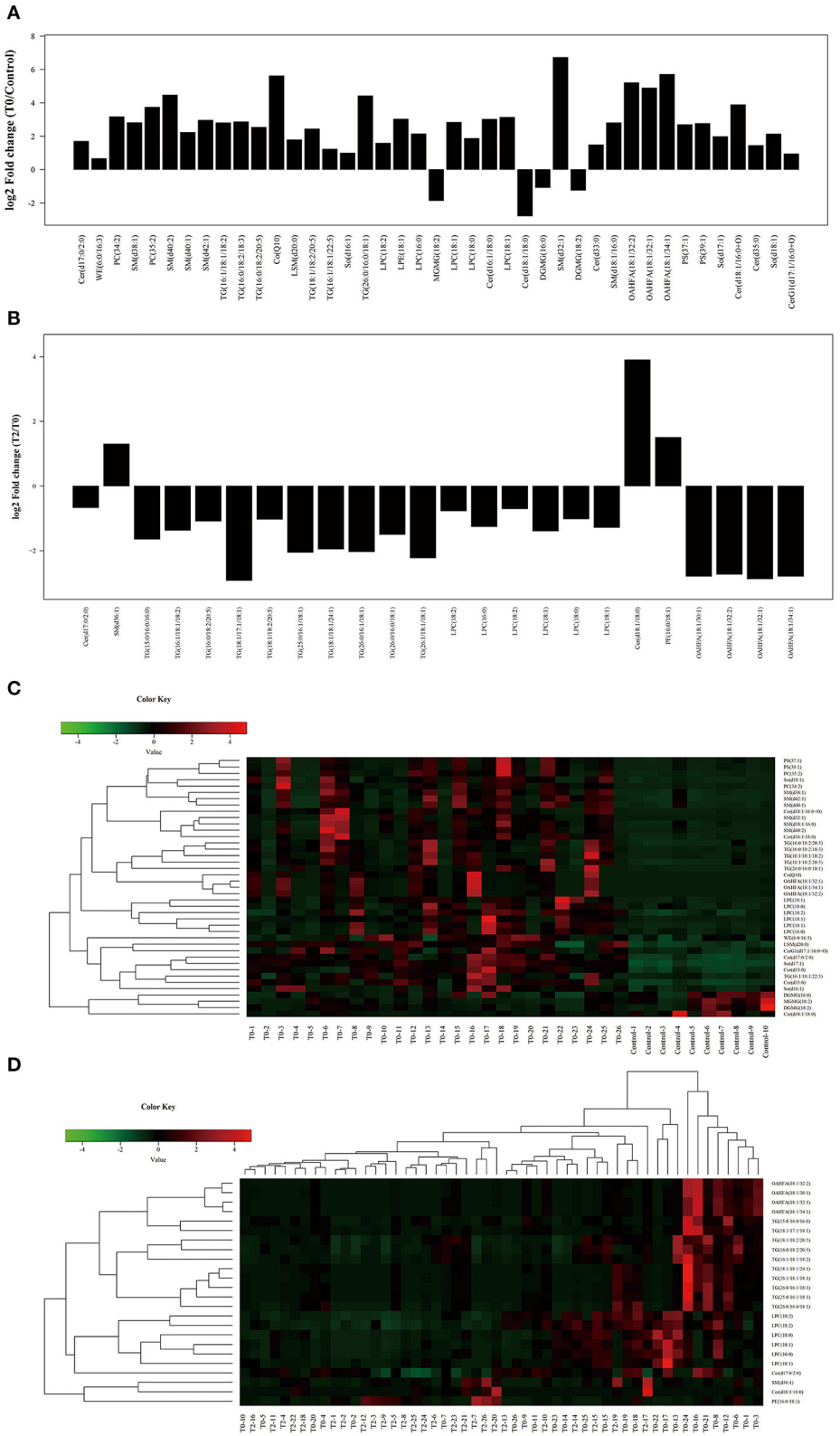

FIGURE 4 | Significant different subclasses of lipids involved in IPL treatment. The fold change **(A)** and heatmap **(C)** of T0 vs. C; the fold change **(B)** and heatmap **(D)** of T2 vs. T0. Control ($n = 10$), T0 ($n = 26$), T2 ($n = 26$).

0.001). The CF of corneal epithelium integration and the CR inflammation were markedly improved. The CF score decreased from 1.00 ± 0.94 to 0.23 ± 0.43 ($p < 0.001$), and the CR scores reduced from 1.38 ± 0.62 to 0.58 ± 0.44 ($p < 0.001$), respectively (**Table 1**).

Eyelid Margin Abnormalities

Our findings suggest that there was no statistically significant difference after the IPL treatment in terms of orifice abnormality and MG dropout (from 1.04 ± 0.99 to 0.92 ± 1.01, $p = 0.679$ and from 1.54 ± 0.86 to 1.54 ± 0.86, $p = 1$, respectively) (**Table 1**).

TABLE 2 | Significant different subclasses of lipids of T0($n = 26$) verse control ($n = 10$).

LipidIon	Class	CalMz	IonFormula	RT-(min)	Fold Change	P-value	VIP
SM(d32:1)+HCOO	SM	719.53	C38 H76 O8 N2 P1	8.743304	105.5802817	0.03955	1.27158
OAHFA(18:1/34:1)-H	OAHFA	785.74	C52 H97 O4	20.93825	52.16343297	0.03692	2.29603
Co(Q10)+NH4	Co	880.72	C59 H94 O4 N1	17.96348	49.2154925	0.03669	1.0111
OAHFA(18:1/32:2)-H	OAHFA	755.69	C50 H91 O4	18.67636	36.6853155	0.0444	2.04926
OAHFA(18:1/32:1)-H	OAHFA	757.71	C50 H93 O4	19.74312	29.63556255	0.04736	3.88388
SM(d40:2)+H	SM	785.65	C45 H90 O6 N2 P1	12.00555	21.94609662	0.03554	1.3621
TG(26:0/16:0/18:1)+Na	TG	995.9	C63 H120 O6 Na1	24.44222	21.32021673	0.02028	1.07358
Cer(d18:1/16:0+O)+H	Cer	554.51	C34 H68 O4 N1	10.187	14.87557017	0.01568	2.56661
PC(35:2)+H	PC	772.59	C43 H83 O8 N1 P1	10.84815	13.45758007	0.01122	1.40963
PC(34:2)+H	PC	758.57	C42 H81 O8 N1 P1	10.35652	9.044793221	0.02042	1.48086
LPC(18:1)+H	LPC	522.36	C26 H53 O7 N1 P1	2.829591	8.862523744	0.03903	1.58635
LPE(18:1)-H	LPE	478.29	C23 H45 O7 N1 P1	2.971951	8.196791624	0.0116	1.41347
Cer(d16:1/18:0)+HCOO	Cer	582.51	C35 H68 O5 N1	11.30124	8.162108672	0.00901	2.41341
SM(d42:1)+H	SM	815.7	C47 H96 O6 N2 P1	14.09983	7.808909475	0.00453	1.11772
TG(16:0/18:2/18:3)+Na	TG	875.71	C55 H96 O6 Na1	18.71938	7.301180438	0.0205	1.9029
LPC(18:1)+HCOO	LPC	566.35	C27 H53 O9 N1 P1	2.824801	7.164012181	0.00877	2.12477
SM(d38:1)+H	SM	759.64	C43 H88 O6 N2 P1	12.02927	7.023899481	0.0079	1.35097
SM(d18:1/16:0)+HCOO	SM	747.57	C40 H80 O8 N2 P1	9.977419	7.005964358	0.02223	2.06393
TG(16:1/18:1/18:2)+NH4	TG	872.77	C55 H102 O6 N1	19.68893	6.980513631	0.03026	1.53642
PS(39:1)-H	PS	830.59	C45 H85 O10 N1 P1	11.36284	6.821055558	0.03541	3.19895
PS(37:1)-H	PS	802.56	C43 H81 O10 N1 P1	10.3793	6.474225864	0.02929	1.56783
TG(16:0/18:2/20:5)+H	TG	877.73	C57 H97 O6	19.659	5.818026726	0.00493	2.28256
TG(18:1/18:2/20:5)+H	TG	903.74	C59 H99 O6	19.71597	5.444758925	0.00554	1.3387
SM(d40:1)+H	SM	787.67	C45 H92 O6 N2 P1	13.02854	4.693025458	0.01777	1.03408
LPC(16:0)+HCOO	LPC	540.33	C25 H51 O9 N1 P1	2.693533	4.427438179	0.0351	3.57942
So(d18:1)+H	So	300.29	C18 H38 O2 N1	2.422211	4.382913682	0.00565	2.80761
So(d17:1)+H	So	286.27	C17 H36 O2 N1	2.460979	3.940410295	3.91E-10	2.02106
LPC(18:0)+HCOO	LPC	568.36	C27 H55 O9 N1 P1	3.790138	3.64099302	0.03905	1.49809
LSM(d20:0)+H	LSM	495.39	C25 H56 O5 N2 P1	2.831587	3.444914731	1.08E-05	2.89417
Cer(d17:0/2:0)+H	Cer	330.3	C19 H40 O3 N1	1.913699	3.248423375	2.35E-06	1.85695
LPC(18:2)+H	LPC	520.34	C26 H51 O7 N1 P1	2.251227	2.988598263	0.00086	1.55151
Cer(d33:0)+H	Cer	526.52	C33 H68 O3 N1	9.731674	2.798888595	3.79E-05	1.15626
Cer(d35:0)+H	Cer	554.55	C35 H72 O3 N1	11.36469	2.720535667	8.07E-06	1.35036
TG(16:1/18:1/22:5)+H	TG	905.76	C59 H101 O6	15.60611	2.331510136	0.02129	1.30254
So(d16:1)+H	So	272.26	C16 H34 O2 N1	2.666427	1.985533979	0.01196	1.60794
CerG1(d17:1/16:0+O)+H	CerG1	702.55	C39 H76 O9 N1	9.514269	1.909466251	0.00627	1.18483
WE(6:0/16:3)+NH4	WE	352.32	H42 C22 O2 N1	3.006577	1.575320698	0.03507	1.08855
DGMG(16:0)+HCOO	DGMG	699.38	C32 H59 O16	2.678107	0.468996555	0.00695	1.61873
DGMG(18:2)+HCOO	DGMG	723.38	C34 H59 O16	2.225866	0.416667634	0.02013	2.13519
MGMG(18:2)+HCOO	MGMG	561.33	C28 H49 O11	2.625824	0.274625199	0.0003	1.38641
Cer(d18:1/18:0)+HCOO	Cer	610.54	C37 H72 O5 N1	12.32153	0.144934423	0.0018	1.9301

Comparison of 41 lipid subgroups between MGD group and control group. MGD, meibomian gland dysfunction; T0, before treatment.

TABLE 3 | Significant different subclasses of lipids of T2 ($n = 26$) verse T0 ($n = 26$).

LipidIon	Class	CalMz	IonFormula	RT-(min)	Fold Change	*P*-value	VIP
Cer(d18:1/18:0)+HCOO	Cer	610.5416	C37 H72 O5 N1	12.32153	15.03078	0.026831	3.35324
PE(16:0/18:1)-H	PE	716.5236	C39 H75 O8 N1 P1	11.40335	2.846096	0.021526	1.55677
SM(d36:1)+H	SM	731.6062	C41 H84 O6 N2 P1	11.06469	2.472157	0.033226	4.39805
Cer(d17:0/2:0)+H	Cer	330.3003	C19 H40 O3 N1	1.913699	0.628695	0.000317	1.16972
LPC(18:2)+HCOO	LPC	564.3307	C27 H51 O9 N1 P1	2.255877	0.61314	0.014431	1.04162
LPC(18:2)+H	LPC	520.3398	C26 H51 O7 N1 P1	2.251227	0.586953	0.005786	1.05027
LPC(18:0)+HCOO	LPC	568.362	C27 H55 O9 N1 P1	3.790138	0.494036	0.034213	1.26986
TG(18:1/18:2/20:5)+H	TG	903.7436	C59 H99 O6	19.71597	0.489044	0.006754	1.65819
TG(16:0/18:2/20:5)+H	TG	877.728	C57 H97 O6	19.659	0.470568	0.004624	1.1926
LPC(16:0)+HCOO	LPC	540.3307	C25 H51 O9 N1 P1	2.693533	0.418414	0.017479	3.33535
LPC(18:1)+H	LPC	522.3554	C26 H53 O7 N1 P1	2.829591	0.410042	0.03062	1.52317
TG(16:1/18:1/18:2)+NH4	TG	872.7702	C55 H102 O6 N1	19.68893	0.387629	0.013507	2.03988
LPC(18:1)+HCOO	LPC	566.3463	C27 H53 O9 N1 P1	2.824801	0.381895	0.003515	1.85389
TG(26:0/16:0/18:1)+Na	TG	995.8977	C63 H120 O6 Na1	24.44222	0.354542	0.018517	1.12173
TG(15:0/16:0/16:0)+NH4	TG	810.7545	C50 H100 O6 N1	21.12598	0.320491	0.027543	1.9067
TG(18:1/18:1/24:1)+NH4	TG	986.911	C63 H120 O6 N1	23.61661	0.259233	0.029449	1.11668
TG(26:0/16:1/18:1)+NH4	TG	988.9267	C63 H122 O6 N1	24.07609	0.244438	0.037562	1.01093
TG(25:0/16:1/18:1)+NH4	TG	974.911	C62 H120 O6 N1	23.85067	0.241359	0.035602	1.03776
TG(26:1/18:1/18:1)+NH4	TG	1014.942	C65 H124 O6 N1	24.10026	0.214039	0.027703	1.34062
OAHFA(18:1/32:2)-H	OAHFA	755.6923	C50 H91 O4	18.67636	0.150416	0.005079	2.50278
OAHFA(18:1/30:1)-H	OAHFA	729.6766	C48 H89 O4	18.52064	0.144494	0.007217	3.26419
OAHFA(18:1/34:1)-H	OAHFA	785.7392	C52 H97 O4	20.93825	0.144425	0.003703	2.80631
OAHFA(18:1/32:1)-H	OAHFA	757.7079	C50 H93 O4	19.74312	0.136615	0.004611	4.81245
TG(18:1/17:1/18:1)+NH4	TG	888.8015	C56 H106 O6 N1	21.16226	0.131759	0.016443	1.66444

Comparison of 24 lipid subgroups between T2 group and T0 group. T0, before treatment; T2, after treatment.

MGE and Meibum Quality

The scores of MGE and meibum quality were used to evaluate the quality and expressibility of the meibum. The MGE score and meibum quality score were significantly decreased (from 1.31 ± 0.93 to 0.79 ± 0.53, $p = 0.017$ and from 1.40 ± 0.85 to 0.73 ± 0.51, $p = 0.001$, respectively) (**Table 1**).

Lipid Classification and Kurtosis

A total of 323 lipid species were identified and most of them were rich in triglycerides (TG), ceramide (Cer), phosphatidylcholine (PC), sphingomyelin (SM), simple Glc series G1 (CerG1), sphingosine (SO), lysophosphatidylcholine (LPC), lysophosphatidylethanolamine (LPE), monogalactosyldiacylglycerol (MGDG), phosphatidylserine (PS), digalactosyldiacylglycerol (DGDG), and (O-acyl)-1-hydroxy fatty acid (OAHFA). More details can be seen in **Figure 2A**. The results of the principal component analysis (PCA) of the groups showed that there was an obvious distinguishing trend between T0 and control groups in lipid clusters (**Figure 2B**). When we compared the T2 to T0 and T0 to control, there were significant differences observed between the groups in lipid quality, as shown by the volcano plot **(Figures 2C,D)**. Moreover, when we compared the T2 to T0, most of the different lipids were decreased in the former; when we compared the T0 to the control group, most of the different lipids were increased in T0.

At the individual lipid compound level, the increased lipids in T0 (i.e., CerG1, CerG2, Co, DG, LPC, LPE, LPG, LPI, LPS, OAHFA, StE, and TG) were decreased following IPL treatment (T2) (**Figures 3A1–A12**). There were no significant differences in Cer, DGDG, LSM, MGDG, PG, PI, PS, SM, SO, and WE that increased in T0 and T2 (**Figures 3B1–B10**). The decrease in DGMG and MGMG in T0 could be reversed by IPL treatment (T2) (**Figures 3C1,C2**). Furthermore, the levels of PC and PE in T2 were higher than those measured in T0 (**Figures 3D1,D2**).

A total of 41 lipid species were significantly different in patients with MGD (T0) vs. healthy controls (**Figure 4A**). The difference between patients with MGD and controls included TG, SM, Cer, OAHFA, PC, DGMG, SO, PS, LPE, LSM, CerG1, CO, MGMG, and WE (**Table 2**). Following IPL treatment (T2), 24 lipid species were significantly different compared with T0: TG, LPC, OAHFA, Cer, SM, and PE (**Table 3**) (**Figure 4B**). The change in the lipid metabolic pattern was highly related to the improvement in the clinical index (**Figures 5**, **6**; **Table 5**). The correlation was rich in TBUT, CR, and meibum quality, and some lipids were crossrelated to them. Notably, 4 lipid clusters were significantly increased in T0, whereas they were decreased

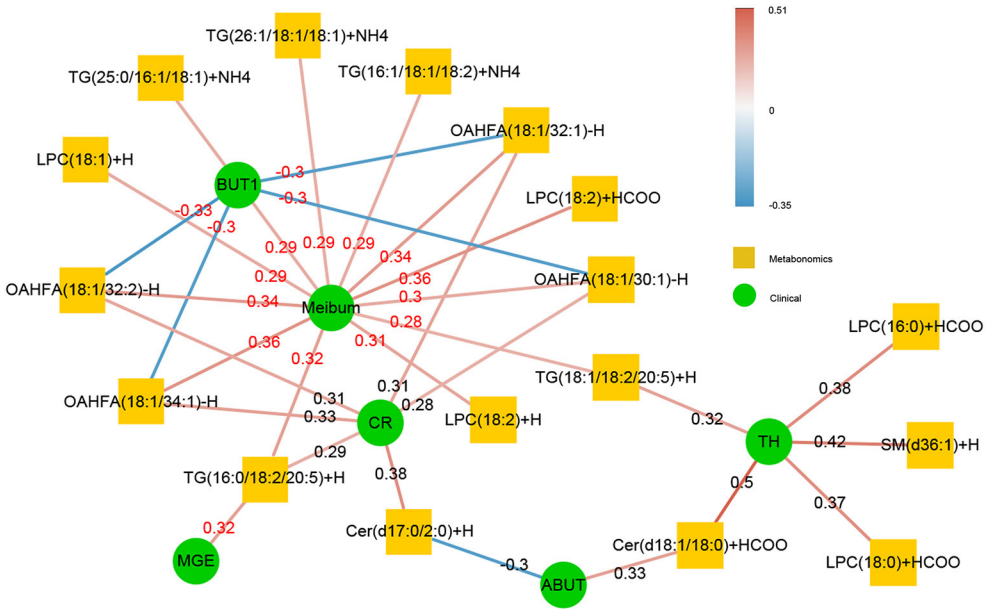

FIGURE 5 | The correlation of significant subclasses of lipids with the clinical syndrome. The change in the lipid metabolic was highly related to the improvement in the clinical index. The correlation was rich in TBUT, CR, and meibum quality, and some lipids were crossrelated to them. The green in the middle represents the clinical index data, and the orange in the outer circle is the differential metabolic lipid. The darker the color of the line was, the stronger the correlation was, and the number on the line was the *r*-value of its correlation coefficient. The red line indicated that there was a positive correlation between the two, whereas the blue line represented a negative correlation between the two.

following IPL treatment. The different lipids were OAHFA, LPC, TG, and Cer. More details can be seen in **Table 4**.

The results of correlation analysis between tear film lipid cluster components and ophthalmic clinical indexes showed that there was a significant correlation between SM and TH; TG and meibum; OAHFA and meibum, CR; LPC and meibum; and Cer and CR (all $p < 0.05$). Details can be found in **Figure 6**.

DISCUSSION

The finding of this study confirmed the therapeutic effect of IPL on MGD by symptoms and lipidomics analysis of the meibum. IPL treatment provides a novel approach that improves the management of MG diseases in a clinical setting, including improvement in the ocular surface health resulting from increasing tear production, stabilizing the tear film, improving corneal epithelial cell contacts, decreasing the conjunctival inflammation, and improving the quality and expressibility of the meibum from the MGs. Additionally, the lipids, such as LPC, OAHFA, TG, Cer, etc., were revealed alteration in patients with MGD after exposure to intense pulsed light (IPL) analyzed by lipidomics profiles. What is more, some of the lipids were highly related to the symptoms of MGD. These findings could be a valuable method to diagnose, prevent, and design personalized medical methods for MGD.

Intense pulsed light is a popular procedure for treating skin and ocular diseases. The mechanism of action of IPL systems is based on the principle of selective thermolysis, according to which certain targets, termed chromophores, are capable of absorbing and subsequently converting through nonradiative transfer the impinging light into heat energy. IPL treatment has been utilized for years in dermatological clinical practice (20, 21). Recently, this procedure was also applied in ophthalmology to treat MGD (22–24). Its use for this purpose stemmed from declines in DE symptoms noted in patients who underwent IPL treatment for facial rosacea. Previous research studies confirmed the efficacy of IPL treatment in relieving the symptoms and signs of MGD (23, 24). In our study, the patient's IPL treatment resulted in marked increases in the TBUT values. As previously reported, these rises occurred as a result of improved tear film stability and a reduction in the tear evaporation rate. These effects are in accord with our measurement of a significant increase in tear production. Furthermore, we found that the ocular surface health improved based on declines in bulbar redness and CF. All supported that IPL was performed as an effective treatment method for MGD.

It is understood that there is still a lack of specific reference data for evaluating the specific efficacy of IPL in the treatment of MGD. Through our study, we can quantitatively analyze the changes in lipid composition of the MG in patients with MGD, to infer its curative effect. We hypothesized that we could find the potential utility of novel biomarkers for predictive, preventive, and personalized medicine strategy for MGD through analysis of the alternation of the meibum lipidomics profile induced by IPL. The dysfunction of the MG

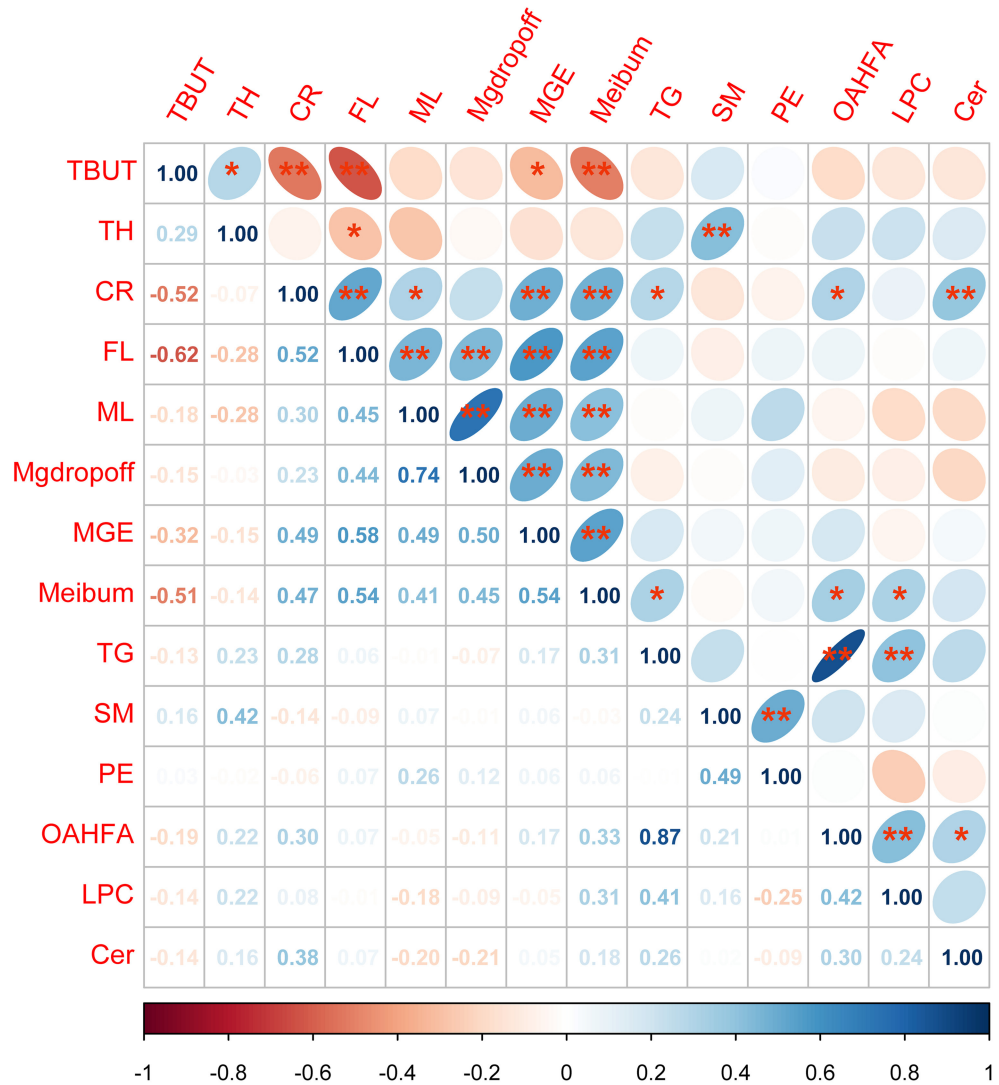

FIGURE 6 | Analysis of the correlation between tear film lipid clusters and ophthalmic clinical indexes. *$p < 0.05$; **$p < 0.01$ Spearman's correlation analysis between all lipid cluster components and ophthalmic clinical indicators, the lower-left corner number is the *r*-value of correlation, the darker the color, the stronger the correlation. The ellipse in the upper right corner facing to the left is a positive correlation while facing to the right is a negative correlation. Blue represented a positive correlation between the two indicators, whereas red represented a negative correlation between the two indicators.

was the initial factor of evaporative DE (9). Previous studies have demonstrated abnormal MGs, MG dropout, and abnormal keratosis in apolipoprotein E knockout mice. The corresponding microenvironmental cytokines all significantly changed. Studies showed that the increased expression of inflammatory factors such as IL-6 and TNF- α in acinar cells, the activation of NF- κ B signal pathway, and the enhancement of oxidative stress further simulated the histopathological, functional, and inflammatory changes in MGD (25). In addition, OAHFAs and their derivatives contribute to the formation of lipid polar gradients and participate in the connection between the tear lipid layer and the water layer to maintain tear film stability (26). LPC played an important role in maintaining the stability of tear film because of its chemical structure with both hydrophilic and lipophilic groups. These enzyme activities affected the regeneration of oxide membrane phospholipids and the maintenance of intracellular redox balance (27). Based on the effects of IPL treatment on the principal component analysis of patients with MGD, this procedure reversed several changes in the lipidomics profile toward patterns characteristic of those seen in healthy subjects. The moderate declines induced by IPL treatment in the MGD symptomology were associated with reversal of the hyperlipidemia in 12 of the 27 classes of lipids. It is possible that the restoration of the normal healthy profiles in this group of lipids contributed to the suppression of MGD symptomology (13). Of note, IPL treatment did not alter any of the other 15 classes of lipids changed by MGD. Furthermore, two sub classes (PC and PE) were higher than

TABLE 4 | Significant different subclasses of lipids of T0 ($n = 26$) verse control ($n = 10$) and T2 ($n = 26$) verse T0 ($n = 26$).

LipidIon	Class	CalMz	IonFormula	RT-(min)	T0 vs. control			T2 vs. T0		
					Fold change	*P*-value	VIP	Fold Change	*P*-value	VIP
OAHFA(18:1/34:1)-H	OAHFA	785.7392	C52 H97 O4	20.93825	52.16343297	0.036918	2.29603	0.14442499	0.003703	2.80631
OAHFA(18:1/32:1)-H	OAHFA	757.7079	C50 H93 O4	19.74312	29.63556255	0.047356	3.88388	0.136615378	0.004611	4.81245
OAHFA(18:1/32:2)-H	OAHFA	755.6923	C50 H91 O4	18.67636	36.6853155	0.044402	2.04926	0.150416143	0.005079	2.50278
LPC(18:1)+H	LPC	522.3554	C26 H53 O7 N1 P1	2.829591	8.862523744	0.039032	1.58635	0.410042149	0.03062	1.52317
LPC(18:0)+HCOO	LPC	568.362	C27 H55 O9 N1 P1	3.790138	3.64099302	0.039047	1.49809	0.494036433	0.034213	1.26986
LPC(18:1)+HCOO	LPC	566.3463	C27 H53 O9 N1 P1	2.824801	7.164012181	0.008767	2.12477	0.381895001	0.003515	1.85389
LPC(16:0)+HCOO	LPC	540.3307	C25 H51 O9 N1 P1	2.693533	4.427438179	0.035098	3.57942	0.418414154	0.017479	3.33535
LPC(18:2)+H	LPC	520.3398	C26 H51 O7 N1 P1	2.251227	2.988598263	0.000856	1.55151	0.586953112	0.005786	1.05027
TG(26:0/16:0/18:1)+Na	TG	995.8977	C63 H120 O6 Na1	24.44222	21.32021673	0.020276	1.07358	0.354541857	0.018517	1.12173
TG(18:1/18:2/20:5)+H	TG	903.7436	C59 H99 O6	19.71597	5.444758925	0.005544	1.3387	0.489043562	0.006754	1.65819
TG(16:0/18:2/20:5)+H	TG	877.728	C57 H97 O6	19.659	5.818026726	0.004927	2.28256	0.470568415	0.004624	1.1926
TG(16:1/18:1/18:2)+NH4	TG	872.7702	C55 H102 O6 N1	19.68893	6.980513631	0.030259	1.53642	0.387629187	0.013507	2.03988
Cer(d17:0/2:0)+H	Cer	330.3003	C19 H40 O3 N1	1.913699	3.248423375	2.35E-06	1.85695	0.628695394	0.000317	1.16972
Cer(d18:1/18:0)+HCOO	Cer	610.5416	C37 H72 O5 N1	12.32153	0.144934423	0.001796	1.9301	15.03077997	0.026831	3.35324

A number of 13 lipids were significantly increased in T0, whereas they were decreased following IPL treatment. The different lipids were OAHFA(18:1/34:1)-H($C_{52}H_{97}O_4$), OAHFA(18:1/32:1)-H($C_{50}H_{93}O_4$), OAHFA(18:1/32:2)-H($C_{50}H_{91}O_4$), LPC(18:1)+H($C_{26}H_{53}O_7N_1P_1$), LPC(18:0)+HCOO($C_{27}H_{55}O_9N_1P_1$), LPC(18:1)+HCOO ($C_{27}H_{53}O_9N_1P_1$), LPC(16:0)+HCOO($C_{25}H_{51}O_9N_1P_1$), LPC(18:2)+H($C_{26}H_{51}O_7$N1 P1), TG(26:0/16:0/18:1)+Na($C_{63}H_{120}O_6Na_1$), TG(18:1/18:2/20:5)+H($C_{59}H_{99}O_6$), TG(16:0/18:2/20:5)+H($C_{57}H_{97}O_6$), TG(16:1/18:1/18:2)+NH4 ($C_{55}H_{102}O_6N_1$), and Cer(d17:0/2:0)+H(C19 H40 O3 N1).

T0, before treatment; T2, after treatment.

those in the untreated MGD group. Collectively, these results indicate that IPL treatment cannot completely reverse MGD symptomology, which is in accord with the failure of this procedure to fully reverse all of the changes in the lipidomics profile induced by MGD. Despite the reversal of the changes in an appreciable number of lipid classes by IPL treatment, there was an appreciable number of insensitive lipid classes that could underlie the failure of the treatment to fully reverse all of the MGD symptomologies. Nevertheless, we found that the increases in 13 subclasses of lipids in MGD could be reversed by IPL. They were rich in OAHFA, LPC, TG, and Cer. These lipids may be the suitable markers for monitoring responses to IPL treatment. TBUT, CR, and meibum quality are three clinical indices that were vindicated as being relevant markers to assess IPL treatment efficacy. In a word, the lipidomics profile can be regarded as a promised method to evaluate the effectiveness of treatment of MGD. What is more, the changes in OAHFA, LPC, TG, and Cer represented that the IPL can significantly change the composition of lipidomics profile in subjects, thus significantly improving the clinical symptoms of patients with MGD.

Except for the omega-3, one of OAHFAs, dietary supplementation, most of the treatment strategies for MGD were symptomatic treatment. However, it was controversial about omega-3 dietary supplementation (28, 29). What is more, OAHFAs were detected decreased in MGD in our results and other researchers reported (30). Lam et al. reported that OAHFA level was positively correlated with TBUT, reduction in eye evaporation rate, and degree of eye discomfort; LPC also had a similar trend and this is consistent with our study (31). The results of thin-layer chromatography analysis showed that the content of phosphatidylinositol in tears of patients with MGD decreased significantly, but increased significantly after IPL treatment, which coincided with our results, and our study further confirmed that there was a significant positive correlation between LPC and meibum, so effectively increasing the content of LPC lipid components in tear film can improve their ocular symptoms (32). Our research shows that there is a strong correlation between OAHFA, LPC, and ML, FL, ABUT and other clinical indicators. Emerging treatment options for MGD should be developed. Based on our results, from the changes in lipidomics profile, the decrease taken of OAHFAs, TGs and LPCs may be a benefit for treating MGD.

However, this study has potential limitations. First of all, the sample size of this study was small, and we would further expand the scale of the study to verify the reliability of our conclusions. Moreover, adolescents and children were not included in the study group. Further studies should expand the sample size to obtain data for all ages. In addition, we will do further basic research on how the changes in lipid composition before and after IPL treatment affect the pathological mechanism of MGD and observe how IPL regulates the signal pathway of lipid composition changes.

CONCLUSIONS

In this study, we found that IPL treatment could reverse some of the MGD-induced hyperlipidemia. These changes alleviated some of the MGD symptomologies by stabilizing the tear film and

TABLE 5 | Analysis of the correlation between lipid composition and ophthalmic indexes.

Lipid composition	Ophthalmic index	Correlation coefficient	*P* value
Cer(d18:1/18:0)+HCOO	TH	0.504	0.000
SM(d36:1)+H	TH	0.422	0.002
LPC(16:0)+HCOO	TH	0.379	0.007
Cer(d17:0/2:0)+H	CR	0.376	0.007
LPC(18:0)+HCOO	TH	0.372	0.008
LPC(18:2)+HCOO	Meibum	0.363	0.010
OAHFA(18:1/34:1)-H	Meibum	0.357	0.011
OAHFA(18:1/32:2)-H	Meibum	0.342	0.015
OAHFA(18:1/32:1)-H	Meibum	0.339	0.016
OAHFA(18:1/32:2)-H	BUT1	−0.330	0.019
Cer(d18:1/18:0)+HCOO	ABUT	0.326	0.021
OAHFA(18:1/34:1)-H	CR	0.326	0.021
TG(16:0/18:2/20:5)+H	Meibum	0.324	0.022
TG(16:0/18:2/20:5)+H	MGE	0.323	0.022
TG(18:1/18:2/20:5)+H	TH	0.319	0.024
OAHFA(18:1/32:1)-H	CR	0.312	0.027
LPC(18:2)+H	Meibum	0.308	0.030
OAHFA(18:1/32:2)-H	CR	0.306	0.031
Cer(d17:0/2:0)+H	ABUT	−0.304	0.032
OAHFA(18:1/34:1)-H	BUT1	−0.304	0.032
OAHFA(18:1/30:1)-H	BUT1	−0.304	0.032
OAHFA(18:1/32:1)-H	BUT1	−0.303	0.032
OAHFA(18:1/30:1)-H	Meibum	0.295	0.037
LPC(18:1)+H	Meibum	0.294	0.039
TG(25:0/16:1/18:1)+NH4	Meibum	0.290	0.041
TG(16:1/18:1/18:2)+NH4	Meibum	0.290	0.041
TG(26:1/18:1/18:1)+NH4	Meibum	0.288	0.043
TG(16:0/18:2/20:5)+H	CR	0.287	0.043
OAHFA(18:1/30:1)-H	CR	0.283	0.046
TG(18:1/18:2/20:5)+H	Meibum	0.280	0.049

Significant correlation between ocular lipid composition and ophthalmic clinical indexes in descending order.

improving the ocular surface health. Therefore, IPL can be used as an effective regimen for the treatment of MGD. The pertinent lipid changes include LPC, OAHFA, TG, Cer, etc. in patients with MGD can be used as the biomarkers for taking personalized medical methods for MGD.

DATA AVAILABILITY STATEMENT

The raw data supporting the conclusions of this article will be made available by the authors, without undue reservation.

ETHICS STATEMENT

The studies involving human participants were reviewed and approved by Xinhua Hospital Affiliated to Medical College of Shanghai Jiao Tong University. The patients/participants provided their written informed consent to participate in this study.

AUTHOR CONTRIBUTIONS

HZ and S-NW carried out conceptualization. YS and L-YT involved in methodology. HZ, DX, and ZC provided resources. S-NW and JP performed visualization. HZ supervised the study. HZ contributed in funding acquisition. All authors have read and agreed to the published version of the manuscript.

FUNDING

This study was supported in part by the Medicine & Engineering Collaboration Research Fund of Shanghai Jiao Tong University (ZH2018QNB27). The funders have no role in the study design, data collection and analysis, decision on publishing, or preparation of the manuscript.

REFERENCES

1. Nelson JD, Shimazaki J. Benitez-del-Castillo JM, Craig JP, McCulley JP, Den S, et al. The international workshop on meibomian gland dysfunction: report of the definition and classification subcommittee. *Invest Ophthalmol Vis Sci.* (2011) 52:1930–7. doi: 10.1167/iovs.10-6997b
2. Hassanzadeh S, Varmaghani M, Zarei-Ghanavati S, Heravian Shandiz J, Azimi Khorasani A. Global prevalence of meibomian gland dysfunction: a systematic review and meta-analysis. *Ocul Immunol Inflamm.* (2021) 29:66–75. doi: 10.1080/09273948.2020.1755441
3. Zhang X, M VJ, Qu Y, He X, Ou S, Bu J, et al. Dry eye management: targeting the ocular surface microenvironment. *Int J Mol Sci.* (2017) 18:1398. doi: 10.3390/ijms18071398
4. Hagan S, Martin E. Enríquez-de-Salamanca A. Tear fluid biomarkers in ocular and systemic disease: potential use for predictive, preventive and personalised medicine. *EPMA J.* (2016) 7:15. doi: 10.1186/s13167-016-0065-3
5. Foulks GN, Bron AJ. Meibomian gland dysfunction: a clinical scheme for description, diagnosis, classification, and grading. *Ocul Surf.* (2003) 1:107–26. doi: 10.1016/S1542-0124(12)70139-8
6. Tomlinson A, Bron AJ, Korb DR, Amano S, Paugh JR, Pearce EI, et al. The international workshop on meibomian gland dysfunction: report of the diagnosis subcommittee. *Invest Ophthalmol Vis Sci.* (2011) 52:2006–49. doi: 10.1167/iovs.10-6997f
7. Ngo W, Gann D, Nichols JJ. Impact of the 2011 International Workshop on Meibomian Gland Dysfunction on clinical trial attributes for meibomian gland dysfunction. *Ocul Surf.* (2020) 18:27–30. doi: 10.1016/j.jtos.2019.10.003
8. Osae E A, Steven P, Redfern R, Hanlon S, Smith CW, Rumbaut RE, et al. Dyslipidemia and meibomian gland dysfunction: utility of lipidomics and experimental prospects with a diet-induced obesity mouse model. *Int J Mol Sci.* (2019) 20:3505. doi: 10.3390/ijms20143505
9. Bron AJ, Tiffany JM. The contribution of meibomian disease to dry eye. *Ocul Surf.* (2004) 2:149–65. doi: 10.1016/S1542-0124(12)70150-7

10. Butovich IA. The meibomian puzzle: combining pieces together. *Prog Retin Eye Res.* (2009) 28:483–98. doi: 10.1016/j.preteyeres.2009.07.002
11. Wojtowicz JC, Butovich IA, McCulley JP. Historical brief on composition of human meibum lipids. *Ocul Surf.* (2009) 7:145–53. doi: 10.1016/S1542-0124(12)70309-9
12. Nichols KK, Redfern RL, Jacob JT, Nelson JD, Fonn D, Forstot SL, et al. The TFOS International Workshop on Contact Lens Discomfort: report of the definition and classification subcommittee. *Invest Ophthalmol Vis Sci*. (2013) 54:Tfos14-9. doi: 10.1167/iovs.13-13074
13. Rong B, Tang Y, Tu P, Liu R, Qiao J, Song W, et al. Intense pulsed light applied directly on eyelids combined with meibomian gland expression to treat meibomian gland dysfunction. *Photomed Laser Surg.* (2018) 36:326–32. doi: 10.1089/pho.2017.4402
14. Gupta PK, Vora GK, Matossian C, Kim M, Stinnett S. Outcomes of intense pulsed light therapy for treatment of evaporative dry eye disease. *Can J Ophthalmol.* (2016) 51:249–53. doi: 10.1016/j.jcjo.2016.01.005
15. Vora GK, Gupta PK. Intense pulsed light therapy for the treatment of evaporative dry eye disease. *Curr Opin Ophthalmol.* (2015) 26:314–8. doi: 10.1097/ICU.0000000000000166
16. Yurttaser Ocak S, Karakus S, Ocak O B, Cakir A, Bolukbasi S, Erden B, et al. Intense pulse light therapy treatment for refractory dry eye disease due to meibomian gland dysfunction. *Int Ophthalmol.* (2020) 40:1135–41. doi: 10.1007/s10792-019-01278-3
17. Toyos R, McGill W, Briscoe D. Intense pulsed light treatment for dry eye disease due to meibomian gland dysfunction; a 3-year retrospective study. *Photomed Laser Surg.* (2015) 33:41–6. doi: 10.1089/pho.2014.3819
18. Tashbayev B, Yazdani M, Arita R, Fineide F, Utheim TP. Intense pulsed light treatment in meibomian gland dysfunction: a concise review. *Ocul Surf.* (2020) 18:583–94. doi: 10.1016/j.jtos.2020.06.002
19. Liu R, Rong B, Tu P, Tang Y, Song W, Toyos R, et al. Analysis of cytokine levels in tears and clinical correlations after intense pulsed light treating meibomian gland dysfunction. *Am J Ophthalmol.* (2017) 183:81–90. doi: 10.1016/j.ajo.2017.08.021
20. Paasch U, Schwandt A, Seeber N, Kautz G, Grunewald S, Haedersdal M. New lasers and light sources - old and new risks? *J Dtsch Dermatol Ges.* (2017) 15:487–96. doi: 10.1111/ddg.13238
21. Yi J, Hong T, Zeng H, Li P, Li P, Wang S, et al. A meta-analysis-based assessment of intense pulsed light for treatment of melasma. *Aesthetic Plast Surg.* (2020) 44:947–52. doi: 10.1007/s00266-020-01637-x
22. Wladis EJ, Aakalu VK, Foster JA, Freitag SK, Sobel RK, Tao JP, et al. Intense Pulsed Light for Meibomian Gland Disease: a report by the american academy of ophthalmology. *Ophthalmology.* (2020) 127:1227–33. doi: 10.1016/j.ophtha.2020.03.009
23. Craig JP, Chen YH, Turnbull PR. Prospective trial of intense pulsed light for the treatment of meibomian gland dysfunction. *Invest Ophthalmol Vis Sci.* (2015) 56:1965–70. doi: 10.1167/iovs.14-15764
24. Xue AL, Wang MTM, Ormonde SE, Craig JP. Randomised double-masked placebo-controlled trial of the cumulative treatment efficacy profile of intense pulsed light therapy for meibomian gland dysfunction. *Ocul Surf.* (2020) 18:286–97. doi: 10.1016/j.jtos.2020.01.003
25. Bu J, Wu Y, Cai X, Jiang N, Jeyalatha MV, Yu J, et al. Hyperlipidemia induces meibomian gland dysfunction. *Ocul Surf.* (2019) 17:777–86. doi: 10.1016/j.jtos.2019.06.002
26. Miyamoto M, Sassa T, Sawai M, Kihara A. Lipid polarity gradient formed by ω-hydroxy lipids in tear film prevents dry eye disease. *Elife*. (2020) 9:e53582. doi: 10.7554/eLife.53582.sa2
27. Wahlig S, Lovatt M, Mehta JS. Functional role of peroxiredoxin 6 in the eye. *Free Radic Biol Med.* (2018) 126:210–20. doi: 10.1016/j.freeradbiomed.2018.08.017
28. Al-Namaeh M. A systematic review of the effect of omega-3 supplements on meibomian gland dysfunction. *Ther Adv Ophthalmol.* (2020) 12:2515841420952188. doi: 10.1177/2515841420952188
29. Bhatt DL, Steg PG, Miller M, Brinton EA, Jacobson TA, Ketchum SB, et al. Cardiovascular risk reduction with icosapent ethyl for hypertriglyceridemia. *N Engl J Med.* (2019) 380:11–22. doi: 10.1056/NEJMoa1812792
30. Khanal S, Ngo W, Nichols K K, Wilson L, Barnes S, Nichols J J. Human meibum and tear film derived (O-acyl)-omega-hydroxy fatty acids in meibomian gland dysfunction. *Ocul Surf.* (2021) 21:118–28. doi: 10.1016/j.jtos.2021.05.009
31. Lam SM, Tong L, Duan X, Acharya UR, Tan JH, Petznick A, et al. Longitudinal changes in tear fluid lipidome brought about by eyelid-warming treatment in a cohort of meibomian gland dysfunction. *J Lipid Res.* (2014) 55:1959–69. doi: 10.1194/jlr.P051185
32. Suwal A, Hao JL, Zhou DD, Liu XF, Suwal R, Lu CW. Use of intense pulsed light to mitigate meibomian gland dysfunction for dry eye disease. *Int J Med Sci.* (2020) 17:1385–92. doi: 10.7150/ijms.44288

Conflict of Interest: The authors declare that the research was conducted in the absence of any commercial or financial relationships that could be construed as a potential conflict of interest.

Publisher's Note: All claims expressed in this article are solely those of the authors and do not necessarily represent those of their affiliated organizations, or those of the publisher, the editors and the reviewers. Any product that may be evaluated in this article, or claim that may be made by its manufacturer, is not guaranteed or endorsed by the publisher.

Copyright © 2022 Zhao, Wu, Shao, Xiao, Tang, Cheng and Peng. This is an open-access article distributed under the terms of the Creative Commons Attribution License (CC BY). The use, distribution or reproduction in other forums is permitted, provided the original author(s) and the copyright owner(s) are credited and that the original publication in this journal is cited, in accordance with accepted academic practice. No use, distribution or reproduction is permitted which does not comply with these terms.

frontiers in Neurology

ORIGINAL RESEARCH
published: 17 February 2022
doi: 10.3389/fneur.2022.821792

Characterization of a Novel Monoclonal Antibody for Serine-129 Phosphorylated α-Synuclein: A Potential Application for Clinical and Basic Research

*Weijin Liu[1], Qidi Zhang[1], Hao Xing[1], Ge Gao[1], Jia Liu[2], Yue Huang[3] and Hui Yang[1]**

[1] Department of Neurobiology, School of Basic Medical Sciences, Capital Medical University, Beijing Key Laboratory of Neural Regeneration and Repair, Beijing Key Laboratory on Parkinson's Disease, Key Laboratory for Neurodegenerative Disease of the Ministry of Education, Beijing Institute of Brain Disorders, Collaborative Innovation Center for Brain Disorders, Beijing, China, [2] Laboratory of Brain Disorders, Ministry of Science and Technology, Collaborative Innovation Center for Brain Disorders, Beijing Institute of Brain Disorders, Capital Medical University, Beijing, China, [3] China National Clinical Research Center for Neurological Diseases, Beijing Tiantan Hospital, Beijing, China

OPEN ACCESS

Edited by:
Yuzhen Xu,
Tongji University, China

Reviewed by:
Ning Zou,
Washington State University, United States
Jinyuan Ma,
Henry Ford Health System, United States

***Correspondence:**
Hui Yang
huiyang@ccmu.edu.cn

Specialty section:
This article was submitted to Neurological Biomarkers, a section of the journal Frontiers in Neurology

Received: *24 November 2021*
Accepted: *12 January 2022*
Published: *17 February 2022*

Citation:
Liu W, Zhang Q, Xing H, Gao G, Liu J, Huang Y and Yang H (2022) Characterization of a Novel Monoclonal Antibody for Serine-129 Phosphorylated α-Synuclein: A Potential Application for Clinical and Basic Research. Front. Neurol. 13:821792. doi: 10.3389/fneur.2022.821792

The Lewy bodies (LBs) are the pathological hallmark of Parkinson's disease (PD). More than 90% of α-synuclein (α-syn) within LBs is phosphorylated at the serine-129 residue [pSer129 α-syn (p-α-syn)]. Although various studies have revealed that this abnormally elevated p-α-syn acts as a pathological biomarker and is involved in the pathogenic process of PD, the exact pathophysiological mechanisms of p-α-syn are still not fully understood. Therefore, the development of specific and reliable tools for p-α-syn detection is important. In this study, we generated a novel p-α-syn mouse monoclonal antibody (C140S) using hybridoma technology. To further identify the characteristics of C140S, we performed several *in vitro* assays using recombinant proteins, along with *ex vivo* assays utilizing the brains of Thy1-SNCA transgenic (Tg) mice, the preformed fibril (PFF)-treated neurons, and the brain sections of patients with PD. Our C140S specifically recognized human and mouse p-α-syn proteins both *in vitro* and *ex vivo,* and similar to commercial p-α-syn antibodies, the C140S detected higher levels of p-α-syn in the midbrain of the Tg mice. Using immunogold electron microscopy, these p-α-syn particles were partly deposited in the cytoplasm and colocalized with the outer mitochondrial membrane. In addition, the C140S recognized p-α-syn pathologies in the PFF-treated neurons and the amygdala of patients with PD. Overall, the C140S antibody was a specific and potential research tool in the detection and mechanistic studies of pathogenic p-α-syn in PD and related synucleinopathies.

Keywords: **α-synuclein, Lewy bodies, Parkinson's disease, phosphorylation, phosphospecific antibody**

INTRODUCTION

Parkinson's disease (PD) is one of the most common movement disorders in the world. Characteristic pathological changes of PD include the formation of intracellular inclusions termed, "Lewy bodies" (LBs) and "Lewy neurites" (LNs) (1, 2). The major component of these inclusions is α-synuclein (α-syn). In normal physiological circumstances, α-syn is an "intrinsically disordered protein," that is highly dynamic in conformation (3). Under pathological conditions, misfolded α-syn can lead to the formation of different α-syn strains, which might have damaging effects within the neurons (1, 4). Despite intense research efforts, little is known about how α-syn abnormally aggregates and finally becomes the main component of LBs and LNs in the relevant brain regions. Moreover, pathological forms of α-syn can transfer from cell-to-cell in a prion-like manner, which might further contribute to the spread of α-syn pathology and promote the neurodegenerative process (5–7). While it is not clear what mechanisms regulate α-syn transmission, we still know little about the pathophysiological roles of the secreted α-syn.

It was reported that posttranslational modifications of α-syn, especially the phosphorylation of serine-129-site (pSer129 α-syn, p-α-syn), could regulate α-syn aggregation and toxicity in disease, and p-α-syn was also involved in the pathological propagation of α-syn. Previous experiments have revealed that approximately 90% of α-syn deposited in LBs was phosphorylated at serine-129 (pSer129 α-syn, p-α-syn), whereas only 4% was modified at this residue in the soluble components of normal brains (8, 9). Currently, it is unclear why extensive phosphorylation occurs in the pathological process of PD, and the role of p-α-syn remains controversial. Although some studies suggested that p-α-syn acted as a protective agent against α-syn aggregation and neurotoxicity (10, 11), others suggested that this abnormally elevated p-α-syn was crucial in mediating α-syn neurotoxicity and inclusion formation (12, 13). In addition to the above roles, p-α-syn also functions in cell-to-cell transmission of the pathological forms of α-syn. Phosphorylation at serine-129 was reported to induce the formation of distinct α-syn strains (14), and phosphorylated exogenous α-syn fibrils could exacerbate pathology and induce neuronal dysfunction in mice (15). A recent report also concluded that p-α-syn enhanced the interaction between α-syn fibrils and its receptors, which meant that p-α-syn could facilitate the spread of α-syn pathologies (16). Overall, the role of p-α-syn is relatively complicated, and further studies are still needed to reveal its exact mechanism involved in PD pathologies.

Currently, the development of specific and reliable antibodies for p-α-syn is of high importance. An increasing number of investigators have used p-α-syn antibodies to detect α-syn pathologies in multiple peripheral tissues and biofluids of patients with PD during the preclinical phase (17–19), which suggested the potential of p-α-syn as a diagnostic or progression biomarker for PD (20, 21). A series of p-α-syn antibodies has also been used to detect pathological α-syn inclusions in PD models, which facilitated the understanding of the pathogenesis of p-α-syn (22–24). However, the exact pathophysiological mechanisms of p-α-syn are still unclear, as there are no uniform approaches and antibodies for p-α-syn detection, and some p-α-syn antibodies can cross-react with nonspecific antigens (25–27). In the present study, we generated and identified a series of mouse monoclonal p-α-syn antibodies, and detected their specificities by comparing them with commercial antibodies. Then, we used the selected p-α-syn antibody to detect α-syn pathologies in the midbrains of Thy1-SNCA transgenic (Tg) mice, and used immunogold electron microscopy to detect the ultrastructural localization of p-α-syn. Next, we used C140S to recognize p-α-syn pathologies in the preformed fibril (PFF)-treated neurons and the brain sections of patients with PD. We then highlighted the potential applications of our p-α-syn antibody in the detection and mechanistic studies of p-α-syn in the related PD pathologies.

MATERIALS AND METHODS

Production of Monoclonal Antibodies to p-α-Syn

Generation of hybridoma cells was first performed. Briefly, human immunopeptides 1 (P1; Ac-CEAYEMP(pS)EGG-NH2; amino acids: 123–132 of p-α-syn) and peptides 2 (P2; Ac-EMP(pS)EEGYQDC-NH2; amino acids: 126–135 of p-α-syn) were emulsified with Freund's adjuvant and were repeatedly used to immunize female BALB/c mice subcutaneously. Spleen cells of mouse were selected and fused with Sp2/0 myeloma cells to generate the antibody-producing hybridomas, and 17 strains of hybridomas with satisfactory sensitivity were screened out using indirect enzyme-linked immunosorbent assays (ELISAs). We finally chose three candidate strains: C140S, C48S, and C54S for further detection. Each strain was intraperitoneally injected into female BALB/c-nu mice for antibody amplification. The collected ascites were then purified using Protein G-agarose affinity chromatography (Sigma-Aldrich; St. Louis, MO, USA).

Cloning, Expression, and Purification of Proteins

Full-length α-syn/β-syn cDNA was cloned into the pGEX-4T-1 expression vector and transformed into BL21 (DE3) competent cells (CB105-01; Tiangen, Beijing, China). GST-α-syn/β-syn was expressed after induction with 0.1 mM isopropyl-β-D-1-thiogalactopyranoside (IPTG). The purified recombinant protein

Abbreviations: α-syn, α-synuclein; AP, alkaline phosphatase; β-syn, β-synuclein; BCA, bicinchoninic acid; C, C-terminal domain of α-synuclein (residues 96–140); CBS, Coomassie Brilliant Blue staining; ELISA, enzyme-linked immunosorbent assay; h-α-syn, human α-synuclein; m-α-syn, mouse α-synuclein; MS, mass spectrometry; N, N-terminal domain of α-synuclein (N-α-syn, residues 1-60); ΔN, ΔN-terminal domain of α-synuclein; NAC, non-amyloid component, the central domain of α-synuclein (residues 61-95); p, phospho-group; p-α-syn, serine-129-site phosphorylated α-synuclein; PD, Parkinson's disease; PFF, preformed fibrils; PLK3, Polo-Like-Kinase 3; pNPP, p-nitrophenyl phosphate; KO, α-syn knock-out mice; R, rabbit; SD, standard deviation; SEM, standard error of the mean; TEM, transmission electron microscopy; Tg, Thy1-SNCA transgenic mice; ThT, thioflavin T; Wt, wild-type brood mice.

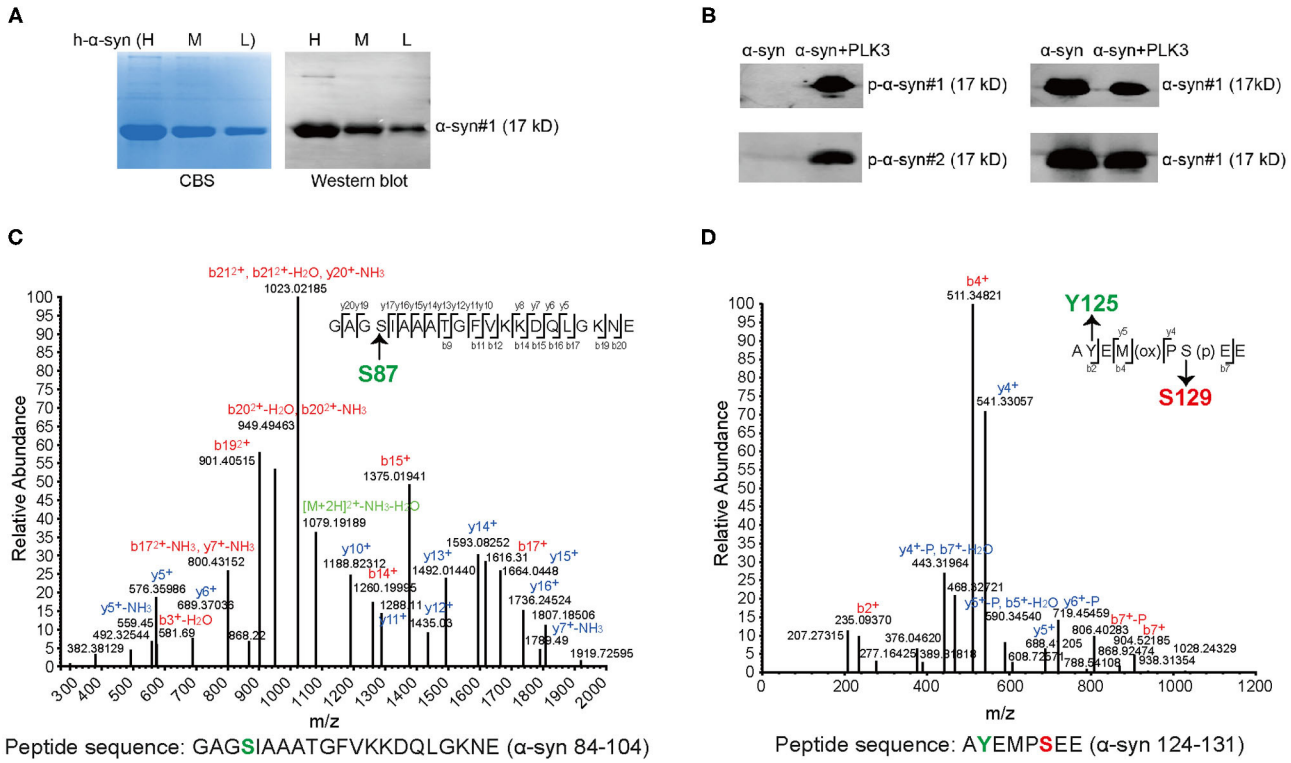

FIGURE 1 | Generation and characterization of recombinant p-α-syn protein *in vitro*. **(A)** Coomassie Brilliant Blue staining (CBS, left) and western blotting (right) of the purified recombinant h-α-syn from *E. Coli*. Three gradient elution with high concentration (H, 3 mg/mL)/moderate concentration (M, 2 mg/mL)/low concentration (L, 1 mg/mL) were analyzed. The h-α-syn was detected with α-syn#1 antibody (Santa Cruz Biotechnology, Santa Cruz, CA, USA). **(B)** Western blotting of 200 ng of recombinant h-α-syn in the absence or presence of Polo-Like-Kinase 3 (PLK3). The p-α-syn was probed with three anti-pSer129 α-syn antibodies (p-α-syn#1 and p-α-syn#2, left blot). The h-α-syn was detected with α-syn#1 antibody (right blot). **(C)** Representative mass spectrometry (MS) identification information of α-syn 84–104. GAGSIAAATGFVKKDQLGKNE (α-syn 84–104) was one of the digested peptides from the resultant p-α-syn (h-α-syn+PLK3). **(D)** Representative MS identification information of α-syn 124–131. AYEMPSEE (α-syn 124–131) was also a digested peptide from the resultant p-α-syn. Detailed MS information is represented in **Tables 2**, **3**. P, phospho-group.

was extracted from the bacterial lysate by combining with glutathione Sepharose^{TM} 4B (GE Health Life Sciences, US). The α-syn/β-syn was collected after digestion with human thrombin for 6 h at room temperature. The elution buffer, the phosphate-buffered saline (PBS) (140 mM NaCl, 2.7 mM KCl, 10 mM Na_2HPO_4, 1.8 mM KH_2PO_4, pH 7.3) for α-syn was changed into a working buffer (20 μM HEPES, 10 μM $MgCl_2$, 20 μM of dithiothreitol, pH 7.4) with a 10 kD molecular weight cut off filter (Millipore, Bedford, MA, USA). The purity of the collected α-syn was assessed with Coomassie Brilliant Blue staining and western blotting. The concentration of the α-syn/β-syn protein was tested with a bicinchoninic acid (BCA) Protein Assay Kit (Thermo Scientific Waltham, MA, USA). Aliquots of α-syn/β-syn were stored at −80°C.

Coomassie Brilliant Blue Staining

We used Coomassie Brilliant Blue staining to assess the purity of the recombinant h-α-syn. After electrophoresis, the gels were incubated with Bio-Safe Coomassie Stain (161-0786; Bio-Rad, Hercules, CA, USA) for 1 h at room temperature. The membranes were visualized in a Gel Doc^{TM} Imager system (Bio-Rad, CA, USA).

Preparation of p-α-Syn

To produce p-α-syn monomer, we used Polo-like-kinase 3 (PLK3), which was reported to phosphorylate α-syn at serine-129 *in vitro* (28). The reaction system consisted of 50 μL α-syn, 1.2 μL of PLK3 (Thermo Scientific, MA, USA), and 0.5 μL of adenosine triphosphate (ATP) (Sigma Aldrich, MO, USA). After incubation for 3 h in a 30°C water bath, the reaction was terminated by 25 mM ethylenediaminetetraacetic acid disodium salt (EDTA-Na_2). The resultant p-α-syn was verified with a p-α-syn antibody using western blotting. The phosphorylation state of α-syn was further identified by mass spectrum (Supported by proteomics platform, Institute of Genetics and Development Biology, Chinese Academy of Sciences). The p-α-syn monomer was then stored at −80°C.

Dot Blots

We used P1, P2, α-syn, p-α-syn, and β-syn to test the specificity of C140S, C48S, and C54S. Protein samples (250

TABLE 1 | Antibodies produced and used in this research.

Name	Species	Type	Immunopeptide sequence	Source
C140S	Mouse	Monoclonal	P1: Ac-CEAYEMP(pS)EGG-NH2, h p-α-syn 123-132	–
C48S	Mouse	Monoclonal	P2: Ac-EMP(pS)EEGYQDC-NH2, h p-α-syn 126-135	–
C54S	Mouse	Monoclonal	P1: Ac-CEAYEMP(pS)EGG-NH2, h p-α-syn 123-132	–
p-α-syn#1	Mouse	Monoclonal	h p-α-syn 124-134	Wako
p-α-syn#2	Rabbit	Monoclonal	h p-α-syn 100-140	Abcam
α-syn#1	Mouse	Monoclonal	-	Santa Cruz Biotechnology
α-syn#2	Rabbit	Monoclonal	h-α-syn 118-123	Abcam
α-syn#3	Rabbit	Monoclonal	surrounding Glu105 of m-α-syn	Cell Signaling technology

p, phospho-group; h, human; m, mouse.

TABLE 2 | The ion series of peptide AYEMPSEE (α-syn 124–131).

#1	b^+	b^{2+}	Sequence	y^+	y^{2+}	#2
1	72.04440	36.52584	A	–	–	8
2	235.10772	118.05750	Y	980.29551	490.65139	7
3	364.15032	182.57880	E	817.23219	409.11973	6
4	511.18573	256.09650	M-Oxidation	688.18959	344.59843	5
5	608.23850	304.62289	P	541.15417	271.08072	4
6	775.23686	388.12207	S-Phosphorylation	444.10140	222.55434	3
7	904.27946	452.64337	E	277.10304	139.05516	2
8	–	–	E	148.06044	74.53386	1

and 500 ng) were spotted onto nitrocellulose membranes. The membranes were incubated with 5% nonfat dried milk (Applygen Technology, Beijing, China) on a horizontal shaker for 1 h at room temperature. The blocking solution was then removed and replaced with primary antibodies. After incubation at 4°C overnight, the membranes were washed with Tween 20 in tris-buffered saline (TBST [2% TBS; 10 mM Tris-HCl, pH 7.5, 150 mM NaCl) for three times and incubated with alkaline phosphatase (AP) conjugated secondary antibody, mouse AP-IgG (E-2636; mAP-IgG; Sigma Aldrich, MO, USA), diluted at 1:1,000. BCIP/NBT (B3804, Sigma Aldrich, USA) was used to detect AP to reflect the immunoreactivity of C140S, C48S, and C54S.

Indirect Enzyme-Linked Immunosorbent Assays

Indirect ELISAs were conducted to verify the specificity of antibodies. A 96-well polystyrene plate (Corning, NY, USA) was coated with immunopeptides and antigens, at 100 μL/well, and incubated at 4°C overnight. Coating buffer [citrate-buffered saline (CBS), 200 mM $NaHCO_3$, pH 9.6] was used to dilute protein samples. The plate was then washed three times (5 min each) with PBST (0.2% Tween-20 in 0.01 M PBS), at 200 μL/well, and then incubated with 100 μL/well of 5% bovine serum albumin (BSA) (Sigma Aldrich, MO, USA) dissolved with PBST for 2 h at 37°C. After washing, 100 μL of detection antibody was added, and the plate was incubated for 2 h at 37°C. Next, the plate was washed and incubated at 37°C for 1 h with 100 μL/well of alkaline phosphatase (AP) conjugated secondary antibody (mouse AP-IgG, E-2636/rabbit AP-IgG, SA00002-2; Sigma Aldrich, MO, USA), diluted at 1:1,000. After being washed three times, each well-received 100 μL of enzyme-substrate p-nitrophenyl phosphate (pNPP; N1891; Sigma Aldrich, MO, USA) to react with AP-IgG. The reaction was allowed to proceed for 30 min at 37°C in a dark environment, after which the absorbance was read at 405 nm with a Multiskan MK3 microplate reader (Thermo Scientific, MA, USA).

Antibody Absorption Experiment

To test the specificity and affinity of C140S, a total of 5 μg h of p-α-syn protein was incubated with different concentrations of C140S antibody (3.2, 16, 80, 400 μg/mL) and control mouse IgG (m-IgG,16, 80 μg/mL) in a 200 μL of immunoprecipitation buffer system (0.5% Triton X-100, 10 mM Tris-HCl, pH 7.5, 150 mM NaCl, 2 mM EDTA-Na_2). The mixture was incubated with constant rotation for 12 h at 4°C. Protein G-Sepharose beads (P3296; 30 μL/tube; Sigma Aldrich, MO, USA) were added into the system and incubated for 6 h at room temperature. The antigen-antibody complex conjugated with Protein G was separated by centrifugation. The supernatant and the complex were then analyzed by western blotting.

Transmission Electron Microscopy

Transmission electron microscopy (TEM) was used to observe the morphology of PFF. These samples were diluted to 20 μg/mL with 0.01 M PBS and applied onto 200-mesh copper grids

TABLE 3 | The ion series of peptide GAGSIAAATGFVKKDQLGKNE (α-syn 84–104).

#1	b^+	b^{2+}	Sequence	y^+	y^{2+}	#2
1	58.02875	29.51801	G	–	–	22
2	129.06587	65.03657	A	2134.11399	1067.56063	21
3	186.08734	93.54731	G	2063.07687	1032.04207	20
4	273.11937	137.06332	S	2006.05540	1003.53134	19
5	386.20344	193.60536	I	1919.02337	960.01532	18
6	457.24056	229.12392	A	1805.93930	903.47329	17
7	528.27768	264.64248	A	1734.90218	867.95473	16
8	599.31480	300.16104	A	1663.86506	832.43617	15
9	700.36248	350.68488	T	1592.82794	796.91761	14
10	757.38395	379.19561	G	1491.78026	746.39377	13
11	904.45237	452.72982	F	1434.75879	717.88303	12
12	1003.52079	502.26403	V	1287.69037	644.34882	11
13	1131.61576	566.31152	K	1188.62195	594.81461	10
14	1259.71073	630.35900	K	1060.52698	530.76713	9
15	1374.73768	687.87248	D	932.43201	466.71964	8
16	1502.79626	751.90177	Q	817.40506	409.20617	7
17	1615.88033	808.44380	L	689.34648	345.17688	6
18	1672.90180	836.95454	G	576.26241	288.63484	5
19	1800.99677	901.00202	K	519.24094	260.12411	4
20	1915.03970	958.02349	N	391.14597	196.07662	3
21	2044.08230	1022.54479	E	277.10304	139.05516	2
22	–	–	E	148.06044	74.53386	1

(Agar Scientific, Essex, UK), which were pre-coated with Formvar. About 6 min later, the grids were blotted with a filter paper and negatively stained with 5% uranyl acetate for 3 min. Copper grids were then blotted and dried under infrared radiation for 24 h at 37°C. A JEM-2100 electron microscope (JEOL, Tokyo, Japan) was used to observe the protein structure.

Thioflavin T Post-Staining

The formation of α-syn fibrils was investigated by detecting the fluorescence intensity of Thioflavin T (ThT) in a diluted mixture of 5 μL × 3 mg/mL protein (monomeric h-α-syn and PFF) and 95 μL × 20 μM of ThT solution. Plates were sealed and incubated at room temperature with fluorescence measurements recorded every 30 min. Excitation and emission wavelengths were fixed at 440 and 485 nm, respectively.

Mice

Human α-syn (h-α-syn) overexpressing transgenic mice [017682; C57BL/6N-Tg (Thy1-SNCA) 15Mjff/J; hemizygotes] and wild-type (Wt) C57BL mice were purchased from the Jackson Laboratory, Bar Harbor, ME, USA. The α-syn knock-out (KO) mice (C57BL/129X1-Sncatm1Rosl/J) were purchased from the Model Animal Research Center of Nanjing University. The BALB/c, BALB-c/nu mice for antibody productions were bought from Vital River Laboratories (Beijing, China). All animals were housed at room temperature under a 12: 12 h light/dark cycle in the Laboratory Animal Center, Capital Medical University. Animal experiments conformed to the National Institutes of Health (NIH; Bethesda, MD, USA) guidelines for animal care and use. The animal study was reviewed and approved by the Institutional Animal Care and Use Committee. (Capital Medical University Animal Experiments and Experimental Animals Management Committee, AEEI-2014-031).

Western Blots

Western blotting was performed as previously described (29). Briefly, samples of recombinant protein (m-α-syn/m p-α-syn/h-α-syn/h p-α-syn, 200 ng/lane) and mice brain [midbrain/striatum/cortex homogenates; 30 μg/lane (α-syn detection), 100 μg/lane (p-α-syn detection)] were mixed with a loading buffer (250 mM Tris-HCl, pH 6.8, 30% glycerol, and 0.02% Bromophenol Blue) and then boiled at 95°C for 8 min. Proteins were separated by 12% sodium dodecyl sulfate-polyacrylamide gel electrophoresis. The gels were then transferred to polyvinylidene difluoride membranes (Millipore, MA, USA) at 2 mA/cm^2 for 90 min. The membranes were incubated with 0.4% paraformaldehyde (PFA) for 30 min and then washed three times with TBST. After being blocked with 5% skimmed milk for 1 h at room temperature, the membranes were incubated with primary antibodies overnight at 4°C. The membranes were then washed three times with TBST and incubated with fluorophore-conjugated secondary antibodies, including mouse 680 (926-68070; LI-COR Biosciences, Lincoln, NE, USA), mouse 800 (926-32210; LI-COR Biosciences, USA), rabbit 680 (926-68071; LI-COR Biosciences, NE,

TABLE 4 | Sensitivity of p-α-syn mouse monoclonal antibodies secreted from hybridomas.

Name	Volume (mL)	Theoretical sensitivity (ng)	Dilution ratio	Volume in use (μL)
C16S	0.1	0.05	1:500	10
C144S	0.1	0.05	1:500	10
C55D	0.15	5	1:100	50
C48S	**0.1**	**0.01**	**1:500**	**10**
C104S	0.1	0.25	1:250	20
C113D	0.15	0.01	1:500	10
C161S	0.1	0.05	1:500	10
C141D	0.15	5	1:100	50
C23S	0.15	0.05	1:500	10
C142S	0.1	0.01	1:500	10
C140S	**0.1**	**0.01**	**1:500**	**10**
C37S	0.1	0.05	1:500	10
C78S	0.1	0.01	1:500	10
C54S	**0.1**	**0.01**	**1:500**	**10**
C57D	0.1	5	1:100	50
C95D	0.1	5	1:100	50
C86S	0.1	1	1:200	25

Bold fonts indicate our selected monoclonal antibodies.

USA) and rabbit 800 (926-32211; LI-COR Biosciences, NE, USA), diluted at 1:10,000. After incubation with secondary antibodies for 1 h, the membranes were washed three times with TBST and visualized in an Odyssey imaging system (LI-COR Biosciences, NE, USA). Primary antibodies used in this study included C140S, p-α-syn#1 (pSyn#64; WAKO, Osaka, Japan), p-α-syn#2 (ab51253; Abcam, Cambridge, USA), α-syn#1 (Sc-69977; Santa Cruz, USA), α-syn#2 (ab138501, Abcam, Cambridge, UK), α-syn#3 (D37A6-4179, Cell Signaling Technology, Danvers, MA, USA), β-actin (66009-1-Ig; Proteintech, Chicago, IL, USA). The details are described in **Table 1**.

Immunofluorescence

Immunofluorescence assays were conducted as previously described (29). Briefly, the mice were perfused with 0.9% of NaCl in deep anesthesia. After the residual blood was removed, the circulatory system was perfused with 4% of PFA. The brain was removed and then was dehydrated and cryoprotected in 20 and 30% of sucrose solution for 24 h at 4°C, respectively, and then embedded with an optimum cutting temperature (OCT) reagent. The midbrain was cut into 30 μm-thick sections. These sections were immersed in PBST [0.3% Triton X-100 in 0.01 M PBS] for 10 min, followed by incubating in 10% goat serum (5,424; Cell Signaling Technology, MA, USA) for 60 min. C140S, p-α-syn#1 (Wako, Osaka, Japan) and α-syn#2 (Abcam, Cambridge, UK) antibodies were then incubated with sections for 24 h at 4°C. After being washed in PBST three times, the sections were incubated with secondary antibodies [A32744; mouse Alexa Fluor 594 (Invitrogen, Carlsbad, CA, USA), rabbit 488 (A32731; Invitrogen)] for 1 h at room temperature, followed by counterstaining with 4′,6-diamidino-2-phenylindole (D9542; diluted 1:2,000; Sigma-Aldrich, MO, USA) for 15 min. These sections were imaged with a confocal microscope (TCS 473 SP8, Leica, Solms, Germany) for examination.

PFF and Treatment

A microcentrifuge tube containing 100 μL recombinant h-α-syn (4 mg/mL) was sealed and incubated at 37°C under constant agitation at 1,000 rpm on an Eppendorf Thermomixer Comfort (Eppendorf AG, Hamburg, Germany) for 7 days. The PFFs were examined by TEM and ThT post-staining. The PFF treatment was performed as previously described (30). Primary mouse cortical neurons (wild-type mice) were cultured for 7 days before being treated with h-α-syn monomer and the sonicated-PFF (final concentration: 2 μg/mL). After a single h-α-syn or PFF application, the cells were maintained for 7 days. Neurons were fixed with 4% PFA, and were immersed in PBST [0.3% Triton X-100 in 0.01 M PBS] for 10 min, followed by incubating in 10% goat serum (5,424; Cell Signaling Technology, MA, USA) for 60 min. C140S and p-α-syn#1 (Wako, Osaka, Japan) antibodies were then incubated for immunofluorescence assays.

Immunohistochemistry of the Amygdala Tissues With p-α-Syn Antibodies

Sections (5 μm thick) of paraffin-embedded amygdala collected by the China National Clinical Research Center for Neurological Diseases (Beijing Tiantan Hospital) were processed for immunohistochemistry. Following dewaxing, hydration, and antigen retrieval, endogenous peroxidase activity was eliminated with 3% of H_2O_2 in PBS for 10 min. After washing in PBS, the sections were incubated with 10% goat serum followed by 0.3% TritonX-100 in PBS for 60 min, then incubated with C140S for 24 h at 4°C. For detection, primary antibodies, a biotinylated goat anti-mouse secondary antibody (PV9002; Zhongshan Golden Bridge Biotechnology, Beijing, China), and diaminobenzidine (ZLI-9017; Zhongshan Golden Bridge Biotechnology) were usedto detect the immunoreactivity. The sections were then counterstained with hematoxylin and imaged with a confocal microscope (TCS 473 SP8, Leica) for examination. The studies involving human participants were reviewed and approved by the IRB of Beijing Tiantan Hospital, Capital Medical University (KY2018-031-02).

Pre-Embedding Immunogold Electron Microscopy With p-α-Syn Antibodies

Mice were perfused with 0.9% of NaCl while in deep anesthesia. After the residual blood was removed, the circulatory system was perfused with 4% of PFA and 0.075% of glutaraldehyde (GA) in 0.1 M PB. The brain was removed and postfixed with 4% of PFA and 0.2% of GA for 8 h. The midbrain was cut into 50 μm-thick sections. These sections were permeabilized with PBST (0.3% Triton X-100 in 0.01 M PBS) for 1 h, followed by incubation with 5% of goat serum (5,425; Cell Signaling

Technology) for 1 h at room temperature. The C140S antibody was then incubated with the sections for 24 h at 4°C. After being washed with 1% bovine serum albumin (BSA)-PBST three times, the sections were incubated with secondary antibody conjugated to 1.4 nm gold particles [2002-0.5 mL; Nanogold-Fab goat anti-mouse IgG (H+L); Nanoprobes, Yaphank, NY, USA and 2004-0.5 mL; Nanogold-Fab goat anti-rabbit IgG (H+L); Nanoprobes], diluted 1:50 with 1% BSA-PBST, for 1 h at room temperature. After washing with 1% BSA-PBST three times, the sections were postfixed with 2% GA for 1 h. Silver enhancement (2013; Nanoprobes) was conducted for 5 min, followed by washing with deionized water three times. The immunogold-labeled midbrain sections were then re-embedded for ultrathin sectioning. We used a JEM-2100 electron microscope (JEOL, Tokyo, Japan) to analyze the ultrastructural localization of p-α-syn-specific immunolabeling in the ultrathin sections.

Statistical Analysis

Prism 8.0.1 software (GraphPad, La Jolla, CA, USA) was used for all statistical analyses. The presented results for each experiment were independently conducted at least three times. The data are expressed as the mean ± standard error of the mean (SEM). Differences of p-α-syn/α-syn levels in mice brain tissues or ThT post-staining between h-α-syn and PFF were evaluated using the unpaired *t*-test. Other data were examined by the One-way ANOVA and Tukey's multiple comparisons tests. In all cases, a value of $P < 0.05$ was considered statistically significant.

RESULTS

Generation and Characterization of Recombinant p-α-Syn Protein *in vitro*

To characterize the specificity of p-α-syn antibodies, we first prepared p-α-syn antigen *in vitro*. We prepared a recombinant p-α-syn protein using the kinase-catalyzed phosphorylation method (28). Recombinant human α-syn (h-α-syn; verified by Coomassie Brilliant Blue staining and western blotting; **Figure 1A**) was phosphorylated in the presence of Polo-Like-Kinase 3 (PLK3). To further determine whether phosphorylation of α-syn at serine-129 occurred, we used two approaches. First, we used two commercial pSer129 α-syn antibodies to recognize the resulting p-α-syn (p-α-syn#1 and p-α-syn#2). Western blot results (**Figure 1B**) showed p-α-syn positive bands (17 kD) in the "h-α-syn+PLK3" group, while the band was not detected in the "h-α-syn" group. In parallel, we analyzed the resultant p-α-syn using mass spectrometry (MS) to clearly define the phosphorylation sites of α-syn. The MS results (**Figures 1C,D**; **Tables 2**, **3**) showed that phosphorylation occurred specifically at amino acid 129 but not at amino acids 87 or 125. These results confirmed that PLK3 specifically phosphorylated α-syn at serine-129, and that we successfully prepared recombinant p-α-syn protein *in vitro*.

Preparation and Selection of Anti-p-α-Syn Mouse Monoclonal Antibodies

Because p-α-syn antibodies with high sensitivity and specificity are crucial for reliable detection, we first prepared and selected anti-p-α-syn mouse monoclonal antibodies peptides (**Table 1**). We immunized mice with two human p-α-syn peptides, P1 [Ac-CEAYEMP(pS)EGG-NH2; amino acids: 123-132] and P2 [Ac-EMP(pS)EEGYQDC-NH2; amino acids: 126-135]. Among the 17 strains of hybridomas (**Table 4**), C54S, C48S, and C140S obtained the highest sensitivities. To further test the specificity and affinity of these three p-α-syn antibodies, we conducted dot blot assays (**Figure 2A**) and indirect ELISAs (**Figures 2B–F**). The results showed that C54S and C140S exclusively bound to α-syn phosphorylated at the serine-129 residue (P1, P2, and p-α-syn) without cross-reactivity with α-syn and β-synuclein, and the results showed no difference from the commercial p-α-syn#1 antibody (targeted to amino acids 124–134 of p-α-syn). In contrast, C48S cross-reacted with α-syn (**Figure 1B**). Furthermore, compared to C54S and p-α-syn#1, C140S had much higher specificity toward p-α-syn (**Figure 2G**). Therefore, we chose C140S (IgG subclasses: IgG2b) for further characterization.

Specificity and Affinity of the C140S Antibody

It was verified that C140S had high specificity toward human p-α-syn (h p-α-syn), when using an indirect ELISA (**Figure 2D**). To further verify whether C140S recognized mouse p-α-syn (m p-α-syn), we prepared m p-α-syn and analyzed it with C140S. Western blotting (**Figure 3A**) and an indirect ELISA (**Figure 3B**) showed that C140S reacted with both h p-α-syn and m p-α-syn proteins. To further test the affinity of C140S toward p-α-syn, we conducted the following antibody absorption experiment, a brief summary of which is shown in the schematic diagram (**Figure 3C**). The results (**Supplementary Figures S2A,B**) showed that C140S, but not the control mouse IgG, specifically bound to p-α-syn, and as the additional amount of C140S increased, the enriched p-α-syn increased (**Supplementary Figures S2B,C**). Further experiments (**Figures 3D–F**) showed that the amount of p-α-syn (17 kD) in the supernatant decreased gradually with increasing concentrations of C140S, whereas p-α-syn in the complex increased gradually with the increasing concentrations of C140S. Complete depletion of p-α-syn in the supernatant was achieved when C140S concentration reached 400 μg/mL. Together, these results showed that C140S had high specificity and affinity for p-α-syn protein.

Comparative Immunoblotting of p-α-Syn Using C140S and p-α-Syn Commercial Antibodies

To better characterize the specificity of C140S, we compared C140S with commercially available p-α-syn antibodies, and analyzed their recognition patterns toward p-α-syn, both *in vitro* and *ex vivo*. First, we denatured and analyzed 200 ng of the m-α-syn/m p-α-syn/h-α-syn/h p-α-syn proteins with C140S

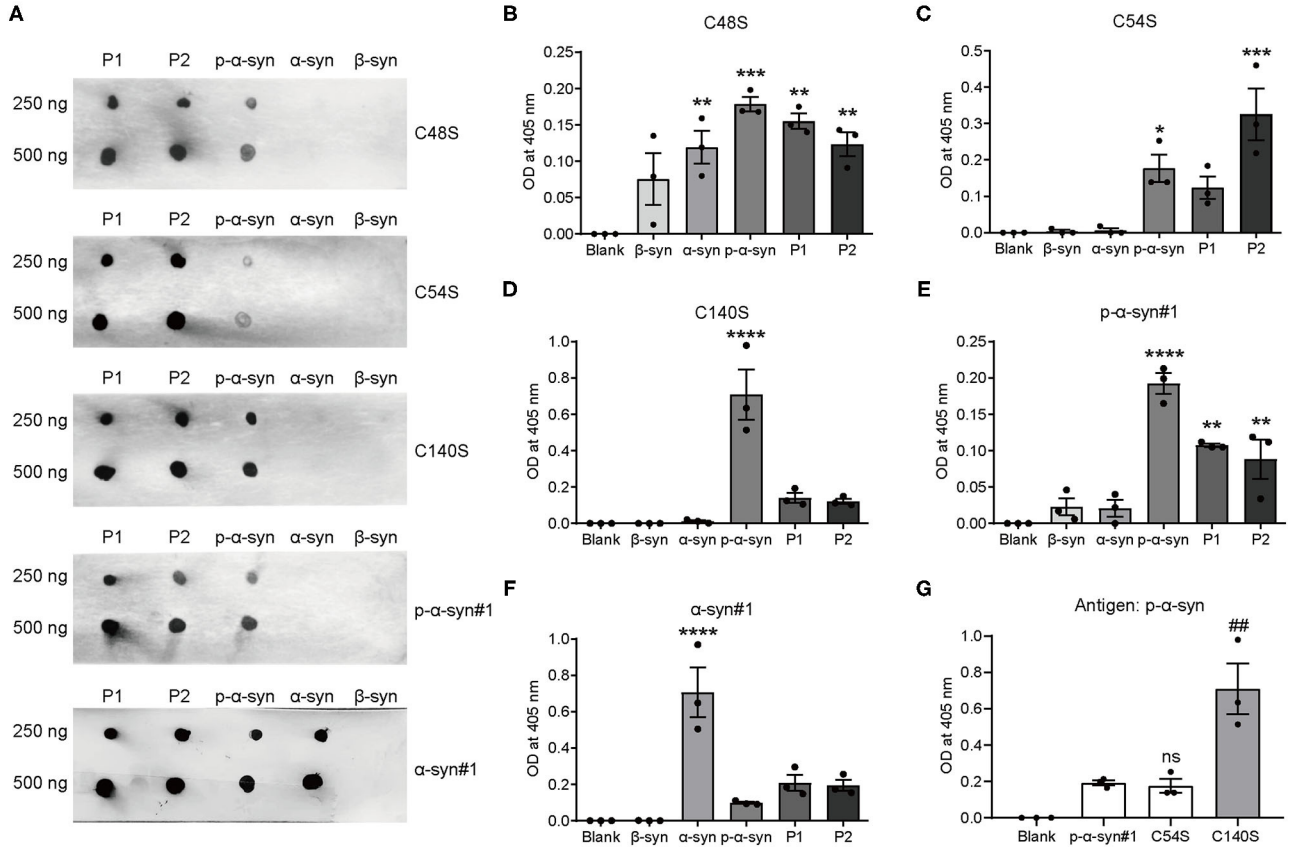

FIGURE 2 | Preparation and selection for anti-p-α-syn mouse monoclonal antibodies. **(A)** In total, 250 and 500 ng of immunopeptides 1 [P1; Ac-CEAYEMP(pS)EGG-NH2; amino acids: 123–132], peptides 2 [P2; Ac-EMP(pS)EEGYQDC-NH2; amino acids: 126–135], p-α-syn, α-syn, and β-syn human proteins were spotted onto nitrocellulose membranes, and then probed with antibodies. The p-α-syn was detected by three screened-out monoclonal antibodies, named as C140S (P1), C48S (P2), and C54S (P1). The p-α-syn#1 (Wako, Osaka, Japan, targeted to amino acids 124–134 of p-α-syn) was used as a positive control. The monoclonal α-syn#1 antibody (Santa Cruz Biotechnology) demonstrated equal loading of proteins. **(B–F)** Quantification of the absorbance differences among C140S, C48S, C54S, p-α-syn#1, and α-syn#1 when recognizing P1, P2, α-syn, p-α-syn, and β-syn (100 μg/mL) by indirect ELISA. **(G)** Quantification of the absorbance difference among C140S, C54S, and p-α-syn#1 when recognizing p-α-syn (100 μg/mL) in indirect ELISAs. The absorbance of plates was measured at 405 nm with a Multiskan MK3 microplate reader. The results are expressed as the mean ± standard error of the mean (SEM) (One-way ANOVA, Tukey's multiple comparisons test, $n = 3$). $^{*}P < 0.05$, $^{**}P < 0.01$, $^{***}P < 0.001$, $^{****}P < 0.0001$ *vs.* Blank; $^{\#\#}P < 0.01$ *vs.* p-α-syn#1. ns, no significance.

(**Figure 4A**), p-α-syn#1 (Wako, Osaka, Japan; **Figure 4B**), and p-α-syn#2 (Abcam, Cambridge, UK; **Figure 4C**). The western blot results showed that C140S specifically recognized m-p-α-syn/h p-α-syn rather than m-α-syn/h-α-syn, in a similar manner to p-α-syn#1 and p-α-syn#2 antibodies. We further demonstrated the specificity of C140S utilizing the brains of Thy1-SNCA transgenic (Tg) mice, which overexpressed h-α-syn driven by a broad neuronal promoter. We measured the expression level of α-syn using midbrain/striatum/cortex homogenates from 13-month-old Tg mice. Western blot results (**Figures 4D–F**; **Supplementary Figures S1A–C**) showed that α-syn was overexpressed to a moderate degree (two- to five-fold) in the brain regions examined in Tg mice when compared with their wild-type (Wt) littermates, indicating that this Tg mouse model could mimic the familial forms of PD. On this basis, we detected p-α-syn levels in the midbrain of Tg mice, using C140S and two commercially available p-α-syn antibodies (p-α-syn#1 and p-α-syn#2). Immunoblotting results of α-syn KO mice/Wt/Tg midbrains showed that C140S (**Figure 4G**) detected a band near the expected size of p-α-syn protein (17 kD), which was absent in the midbrain samples of KO mice, showing no differences with p-α-syn#1 (**Figure 4H**) and p-α-syn#2 (**Figure 4I**). It should be noted that these p-α-syn antibodies partially cross-reacted with other protein bands near 30–60 kD, which also existed in the KO mice. Moreover, we also found that the levels of p-α-syn (17 kD) were significantly increased in the midbrain homogenates of Tg mice (13-month-old), when compared to the controls (**Supplementary Figure S1D**). Based on these observations, we next used C140S to detect α-syn pathologies in the brains of Tg mice.

Immunofluorescence Staining of p-α-Syn in the Midbrain of Tg Mice

To test the synuclein pathological features in the midbrain of Tg mice, we prepared the midbrain sections from 13-month-old

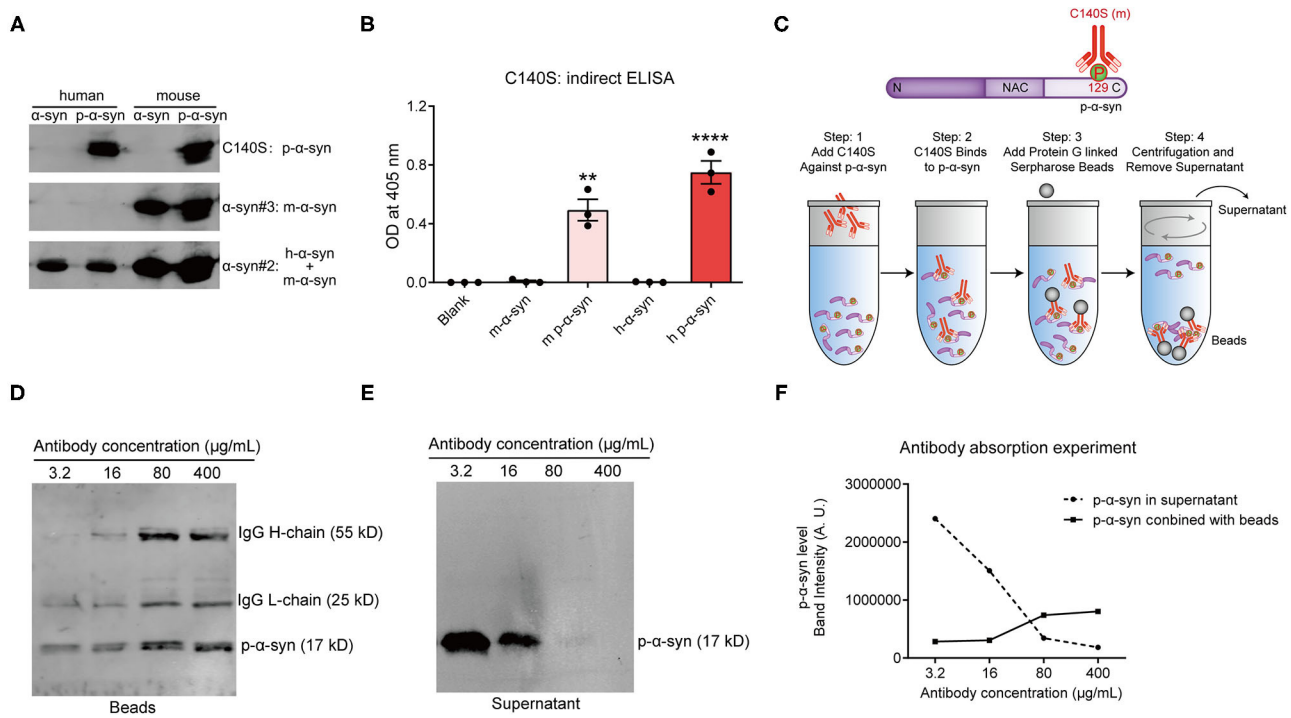

FIGURE 3 | Determining the specificity and affinity of C140S. **(A)** A total of 200 ng of human p-α-syn (h p-α-syn) and mouse p-α-syn (m p-α-syn) were prepared and probed by western blots with C140S. The α-syn#2 antibody (Abcam, Cambridge, UK) was used to detect human α-syn. The α-syn#3 antibody (CST) demonstrated an equal loading of mouse α-syn. **(B)** The affinity of C140S was assessed using indirect ELISAs on m-α-syn/m p-α-syn/h-α-syn/h p-α-syn protein (100 μg/mL) coated wells. The absorbance of plates was measured at 405 nm with a Multiskan MK3 microplate reader. The results are expressed as the mean ± standard error of the mean (SEM) (One-way ANOVA, Tukey's multiple comparisons test, $n = 3$). $^{**}P < 0.01$, $^{****}P < 0.0001$ *vs.* Blank. **(C)** The schematics of the antibody absorption experiment. N, N-terminal domain of α-syn (residues 1–60). NAC, non-amyloid component, is the central domain of α-syn (residues 61–95). C, C-terminal domain of α-syn (residues 96–140). P, phospho-group. m, mouse. According to the experimental schematics, 5 μg h of p-α-syn was incubated with different concentrations of C140S antibody (3.2, 16, 80, and 400 μg/mL). The protein G beads were added to conjugate with the antigen-antibody complex. The beads-antigen-antibody complex and supernatant were separated by centrifugation and examined using western bolts, shown in **(D,E)**. The p-α-syn was detected with p-α-syn#1 antibody (Wako, Osaka, Japan). **(F)** Quantification of the band intensities of p-α-syn in the beads-antigen-antibody complex **(D)** and supernatant **(E)**.

KO/Wt/Tg mice, and analyzed p-α-syn with C140S and p-α-syn#1 using immunofluorescence staining. **Figure 5A** shows that in the midbrain sections from α-syn KO mice, C140S did not produce a detectable signal. We also found that C140S produced a similar staining pattern to the commercial p-α-syn#1 antibody (**Figure 5B**). In addition, the level of p-α-syn was higher in Tg than in the Wt mice. Moreover, immunostaining results using high magnification showed that p-α-syn was mainly distributed in the cytoplasm, and that most of the p-α-syn was aggregated.

Immunogold Ultrastructural Observations of p-α-Syn in the Midbrain of Tg Mice

To determine the subcellular localization of p-α-syn aggregates, the Tg midbrain (13-months-old) was fixed and labeled with C140S and p-α-syn#2 for pre-embedding in the immunogold electron microscopy. The KO mice were also included as negative controls in the following tests. The results (**Figure 6A**) showed that the labels for C140S were specifically localized in the cytoplasm, and colocalized with the outer mitochondrial membrane, which was consistent with the results of p-α-syn#2 (**Figure 6B**). These results suggested that p-α-syn might play a role in the mitochondrial dysfunction.

Immunofluorescence Staining of p-α-Syn Pathological Inclusions in the PFF-Treated Neurons

It was reported that the addition of exogenous α-synuclein PFFs to primary neuronal cultures could induce the recruitment of endogenous α-synuclein to LB and LN-like aggregates (30–32). To further examine the pathological inclusions in the neurons induced by PFFs, we first generated PFFs by physically shaking monomeric h-α-syn. To prove that aggregation of α-syn occurred, PFFs were determined by negative-staining transmission electron microscopy (TEM). The results (**Figure 7A**) showed that α-syn aggregates were successfully formed in the PFF group. We also analyzed the fibrillar structure of PFFs using ThT post-staining. The results showed that the fluorescence of PFF aggregates was higher than α-syn monomers (**Figure 7B**). Together, the results showed that we successfully prepared PFF.

Primary mouse cortical neurons were prepared from E16-18 embryonic brains, and maintained for 7 days *in vitro*, following treatment with either phosphate-buffered saline (PBS) vehicle control, monomeric h-α-syn, or PFF, for 7 days. PFFs were sonicated to lengths of 40–120 nm (examined by TEM) before adding them into the medium. The results of p-α-syn immunofluorescence staining with C140S showed (**Figure 7C**) that when compared with monomeric h-α-syn treated cultures, the PFF-treated neurons showed higher levels of p-α-syn, with similar results also observed using p-α-syn#1 (**Figure 7D**). Notably, p-α-syn aggregates showed more punctate and serpentine structures within cell bodies stained with C140S (**Figure 6C**) while the p-α-syn#1-stained cells showed diffusely distributed p-α-syn (**Figure 7D**). Moreover, we also found the presence of p-α-syn aggregates in the nucleus of α-syn/PFF treated neurons, while nothing was detected in neurons treated with PBS.

C140S Detected p-α-Syn Histopathological Features in the Amygdala of Patients With PD

To further determine the ability of C140S to recognize disease-relevant pathological lesions in the post-mortem human brains, we obtained 5 μm thick amygdala sections from one patient with PD (male; 69-years-old; Braak PD stage V, collected by Beijing Tiantan Hospital), who was clinically diagnosed and pathologically confirmed with PD. We conducted immunohistochemistry using C140S, which showed that C140S recognized intracytoplasmic LBs and long thin LNs in these sections (**Figure 8A**), which was consistent with the results of p-α-syn#2 (**Figure 8B**).

DISCUSSION

The detection of p-α-syn heavily relies on the specificity of antibody. In the current study, we generated a series of mouse monoclonal p-α-syn antibodies, and selected the C140S antibody. The C140S reacted with the original immunopeptide P1 [Ac-CEAYEMP(pS)EGG-NH2; amino acids: 123–132], and also specifically recognized p-α-syn prepared *in vitro* and *ex vivo*, without cross-reacting with unphosphorylated α-syn and β-syn. Compared with commercial p-α-syn antibodies, in multiple experimental assays, C140S showed similar specificities toward p-α-syn. Therefore, we used C140S to examine α-syn pathologies in PFF-treated neurons, the midbrain of Thy1-SNCA transgenic mice, and in the amygdala of patients with PD. We also observed the ultrastructural localization of p-α-syn in mitochondria with C140S by immunogold electron-microscopy.

A widely used approach for the production of peptide antibodies is to immunize animals with a synthetic peptide, especially for raising antibodies against posttranslational modifications (33). In the current study, we used this experimental biology to generate a series of mouse monoclonal p-α-syn antibodies, and selected C48S, C54S, and C140S for further validation. Although the peptides we used for immunization were 11 amino acids (8–20 amino acids are recommended), we were still not sure whether C48S, C54S, and C140S antibodies could recognize the full-length p-α-syn antigens in denatured or native forms. Dot blot results (**Figure 2A**) showed that C48S, C54S, and C140S all recognized P1/P2 peptides, while compared to C48S and C54S, C140S showed better substrate recognition toward native full-length p-α-syn antigens. It was reported that the addition of a phosphate group to serine-129 altered intramolecular interactions with the C-terminus of α-syn (34). The environment, such as pH, calcium, and salt also affected the physiological structure of α-syn (3). In the present study, we prepared recombinant p-α-syn protein using the kinase-catalyzed phosphorylation method, and the reaction was performed in a working buffer. In contrast, P1/P2 peptides were dissolved in PBS. We proposed that phosphorylation reaction and the difference of solution might influence the secondary structure of p-α-syn. That might be the reason for the differential recognition of C48S and C54S toward P1/P2 peptides and p-α-syn.

Both western blotting and ELISA results showed that C140S specifically recognized m-p-α-syn/h p-α-syn rather than m-α-syn/h-α-syn, which showed no difference from the commercial p-α-syn#1 and p-α-syn#2 antibodies. We further tested the specificity of C140S in the midbrain of Tg mice by western blotting. Our prior results showed that aged Tg mice had higher levels of aggregated α-syn and p-α-syn in the soluble and insoluble components of the striatum (35). Consistent with these results, using C140S, we detected increased levels of p-α-syn (17 kD) in the midbrain of Tg mice (13-months-old). We also examined the histopathological features in the amygdala of patients with PD. Filamentous aggregates of p-α-syn were found in the axons and soma of neurons, which meant that C140S recognized intracytoplasmic LBs and long thin LNs. Taken together, the C140S showed relatively high specificity toward p-α-syn prepared both *in vitro* and *ex vivo*. Our present results showed that C140S specifically recognized full-length p-α-syn antigens (prepared *in vitro*) in native forms [Dot blot results (**Figure 2A**) and indirect ELISA results (**Figures 2D, 3B**)] and denatured forms [Western blot results (**Figures 3A, 4A**)]. Warranting caution, it was reported that different methods of preparing the tissues, such as different antigen retrieval methods and blocking agents might affect p-α-syn antibody performance. The p-α-syn#2 was found to detect an off-target higher-molecular weight protein unrelated to α-syn, but this protein was apparently not detected *via* immunohistochemistry or confocal approaches (27). Consistent with this, our immunofluorescence staining results (**Figure 5A**) showed that C140S and p-α-syn#1 specifically recognized p-α-syn antigens (mouse brain) in native forms, without cross-reaction with other brain proteins in α-syn KO mice. In contrast, western blot results showed that C140S and the other two commercial and p-α-syn#2 antibodies partially cross-reacted with denatured protein bands near 30–60 kD, which also existed in KO mice (**Figures 4G–I**). We considered the reason for this difference in the recognition of mouse brain in native forms and denatured forms might be due to the states or structural changes of brain proteins after heat-denatured in the presence of SDS and DTT. The denaturation of some proteins in the mouse brain results in the exposure of some similar epitopes,

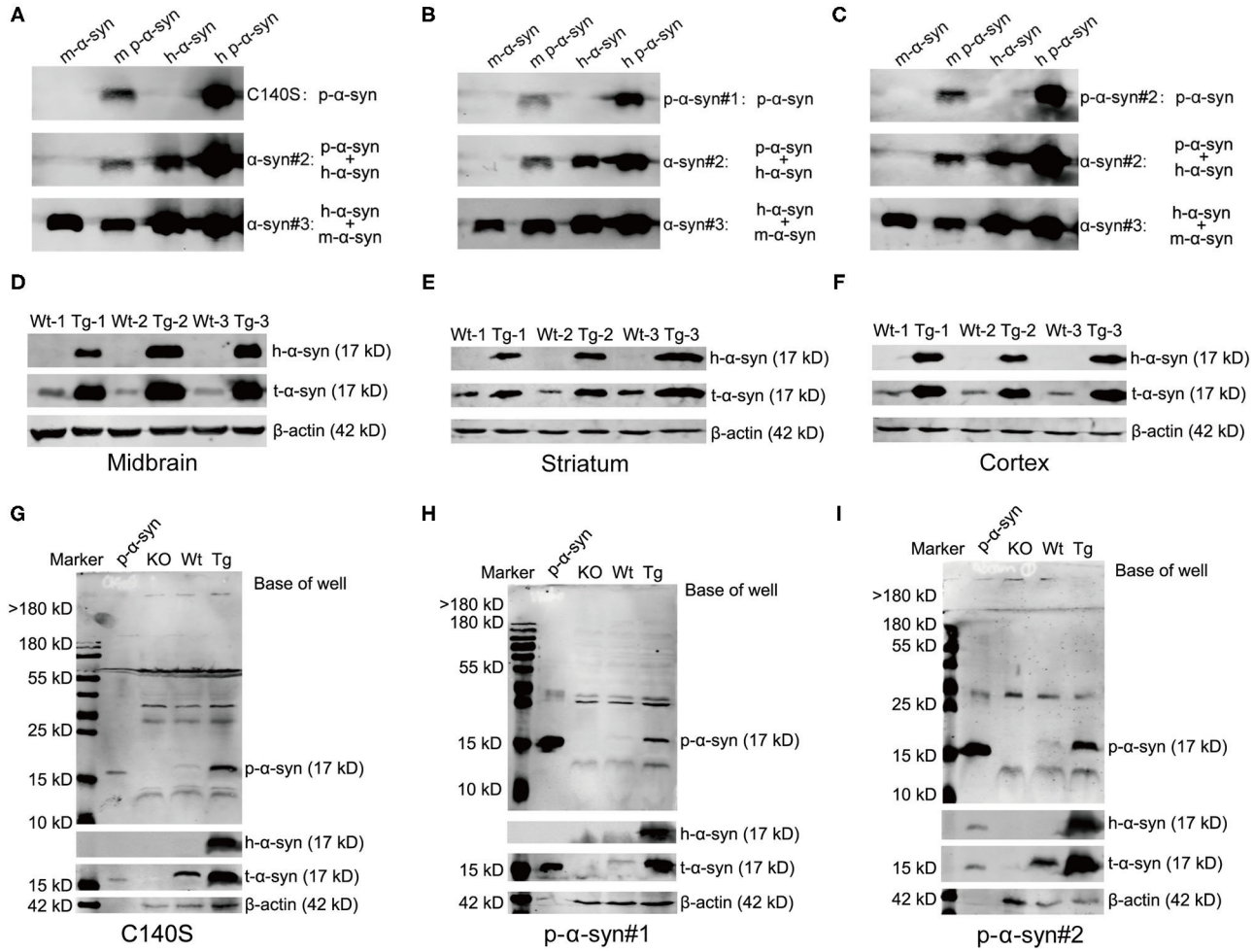

FIGURE 4 | Western blot results showed that C140S had similar recognition patterns as commercial p-α-syn antibodies. **(A–C)** Comparative immunoblotting of p-α-syn protein (prepared *in vitro*) between C140S, p-α-syn#1, and p-α-syn#1. A total of 200 ng m-α-syn/m p-α-syn/h-α-syn/h p-α-syn proteins were denatured and analyzed with C140S **(A)**, p-α-syn#1 [Wako, Osaka, Japan, **(B)**], and p-α-syn#2 [Abcam, Cambridge, UK, **(C)**]. The h-α-syn was detected with α-syn#2 antibody (Abcam, Cambridge, UK). The m-α-syn was detected with α-syn#3 antibody (CST). D-F. A total of 30 μg of brain homogenates of the midbrain **(D)**/the striatum **(E)**/the cortex **(F)** from wild-type brood (Wt)/Thy1-SNCA transgenic (Tg) mice were denatured and analyzed with h-α-syn and α-syn antibodies. **(G–I)** Comparative immunoblotting of mice midbrain between C140S, p-α-syn#1, and p-α-syn#2. 100 μg of midbrain homogenates from α-syn knock-out (KO)/Wt/Tg mice were denatured and analyzed with C140S **(G)**, p-α-syn#1 **(H)**, and p-α-syn#2 **(I)**. The h-α-syn was recognized by α-syn#2 antibody (Abcam, Cambridge, UK), and was used to show the successful overexpression of h-α-syn in the brain of Tg mice. The total α-syn level was detected with α-syn#1 antibody (Santa Cruz, CA, USA). The p-α-syn protein was added as a positive control. The KO mice were used as a negative control. β-actin (42 kD) was used as a loading and internal control to enable sample normalization. Mouse age: 13-months-old.

which might cause the cross-reaction of C140S, p-α-syn#1, and p-α-syn#2 antibodies. Previous studies had reported that the pSer473 neurofilament light epitope contained some sequence identity to pSer129 α-syn (26), we will further test whether C140S cross-react with pSer473 neurofilament light antigens in native forms and denatured forms. We also plan to excise, extract, and analyze these nonspecific bands in midbrain of α-syn KO mice by LC-MS/MS.

Even though a large number of studies have shown that aggregated α-syn partly localized to the mitochondria under pathological states, and α-syn accumulation and mitochondrial dysfunction have been implicated in the pathology of PD (36–41, 48), the mechanisms by which p-α-syn and mitochondrial proteins regulate each other to trigger mitochondrial dysfunction are poorly understood. Our p-α-syn electron microscopy immunogold results showed that p-α-syn partly localized to the mitochondria in the midbrain of 13-months-old Thy1-SNCA transgenic mice (**Figures 6A,B**), suggesting the possibility of direct interaction between p-α-syn and mitochondrial proteins. One previous study supports this possibility. They used the combination of peptide pulldown assays and mass spectrometry to identify the interaction

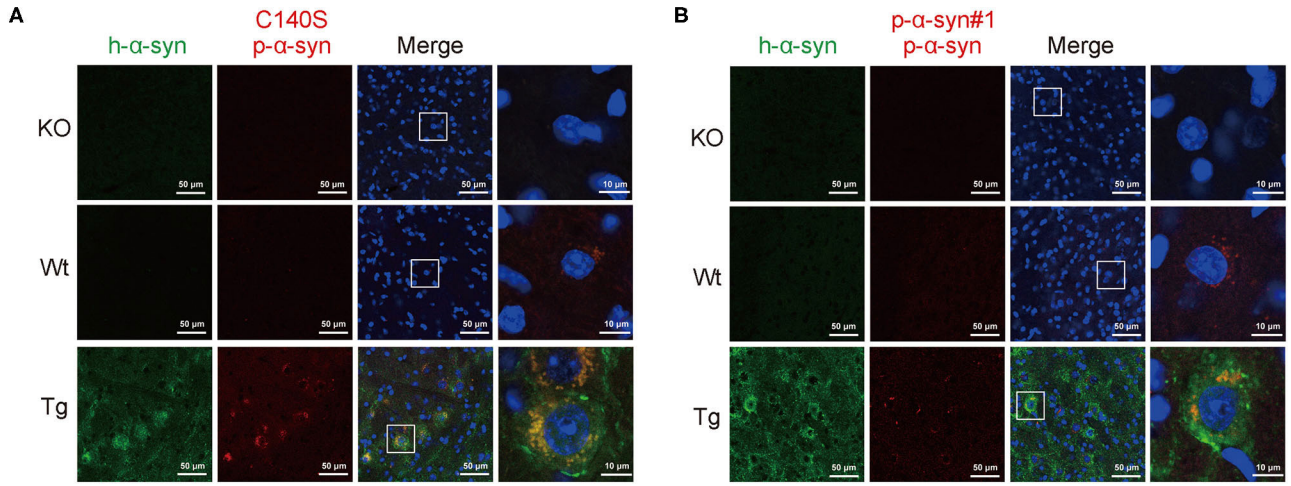

FIGURE 5 | Immunofluorescence staining of p-α-syn in the midbrain of Tg mice using C140S and p-α-syn#1. **(A,B)** The midbrain sections from α-syn knock-out (KO)/Wild-type brood (Wt)/Thy1-SNCA transgenic (Tg) mice were prepared and analyzed with C140S **(A)** and p-α-syn#1 **(B)**. The h-α-syn (green) recognized by α-syn#2 antibody (Abcam, Cambridge, UK) was used to show the successful overexpression of h-α-syn in the midbrain of Tg mice. Red color indicates p-α-syn staining (C140S) and blue color indicates nucleus. White squares, amplified area of midbrain section under low magnification. Scale bar, 50 μm (low magnification) and 10 μm (high magnification). Mouse age: 13-months-old.

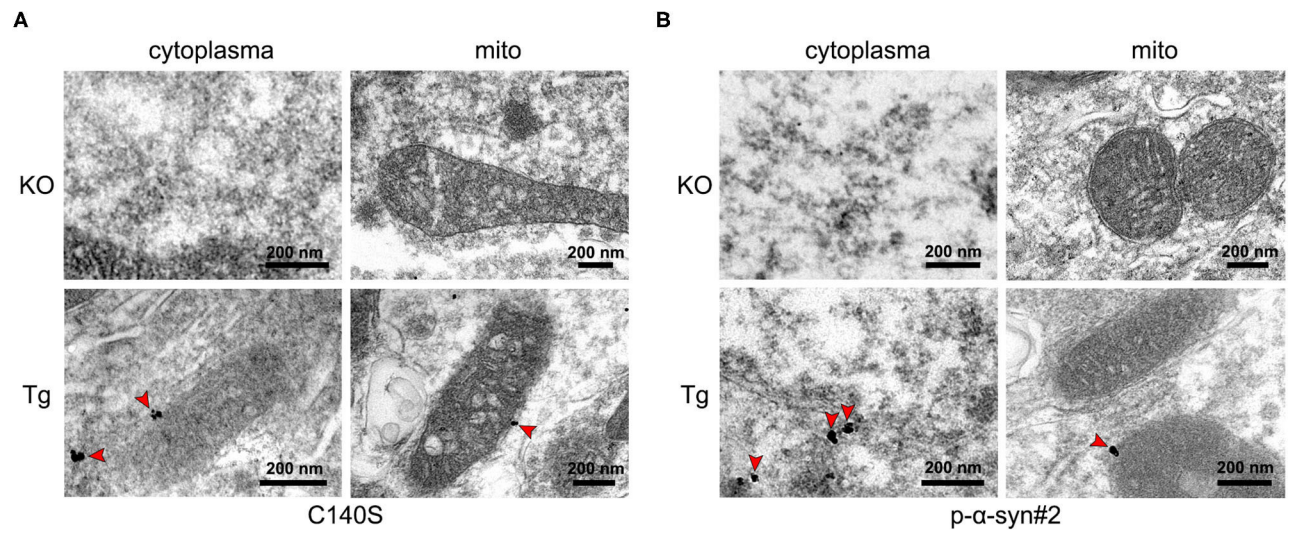

FIGURE 6 | Electron microscopy with immunogold labeling of p-α-syn in the midbrains of Tg mice using C140S and p-α-syn#2. **(A,B)** Immunogold labeling of C140S **(A)** and p-α-syn#2 **(B)** in the midbrain of α-syn knock-out (KO) mice and Thy1-SNCA transgenic (Tg) mice. The p-α-syn was specifically deposited in the cytoplasm, and colocalized with the outer mitochondrial membrane of Tg mice. Red arrow, the concentrated region of p-α-syn. Scale bar, 200 nm. Mice age: 13-months-old.

proteins of p-α-syn in the mouse brain synaptosomes, and found that the biotinylated pS129 peptides interacted with some mitochondrial proteins, such as solute carrier family 25 and serine-lactamase-like protein, LACTB (42). Another relevant study by Diego Grassi et al. showed that they discovered the existence of a phosphorylated α-syn species, and this type of p-α-syn aggregates was associated with mitochondria, and induced mitochondrial toxicity and fission, energetic stress, and mitophagy (43). Overall, the exact mechanism for these interactions between p-α-syn and mitochondrial proteins still needs more in-depth research. Additional studies will be necessary to identify the mitochondrial proteins that interacted with p-α-syn in the midbrain of Tg mice by Co-IP/MS, and to clarify the modulatory roles of p-α-syn in mitochondria.

Following the immunofluorescence staining experiments, we found an interesting phenomenon, monomeric h-α-syn, and PFF treatment caused α-syn pathology not only in the cytosol but also in the nucleus (**Figures 7C,D**). Despite being α-syn partially localized in the nucleus, the reason for its phosphorylation and abnormal aggregation in the nucleus under pathological

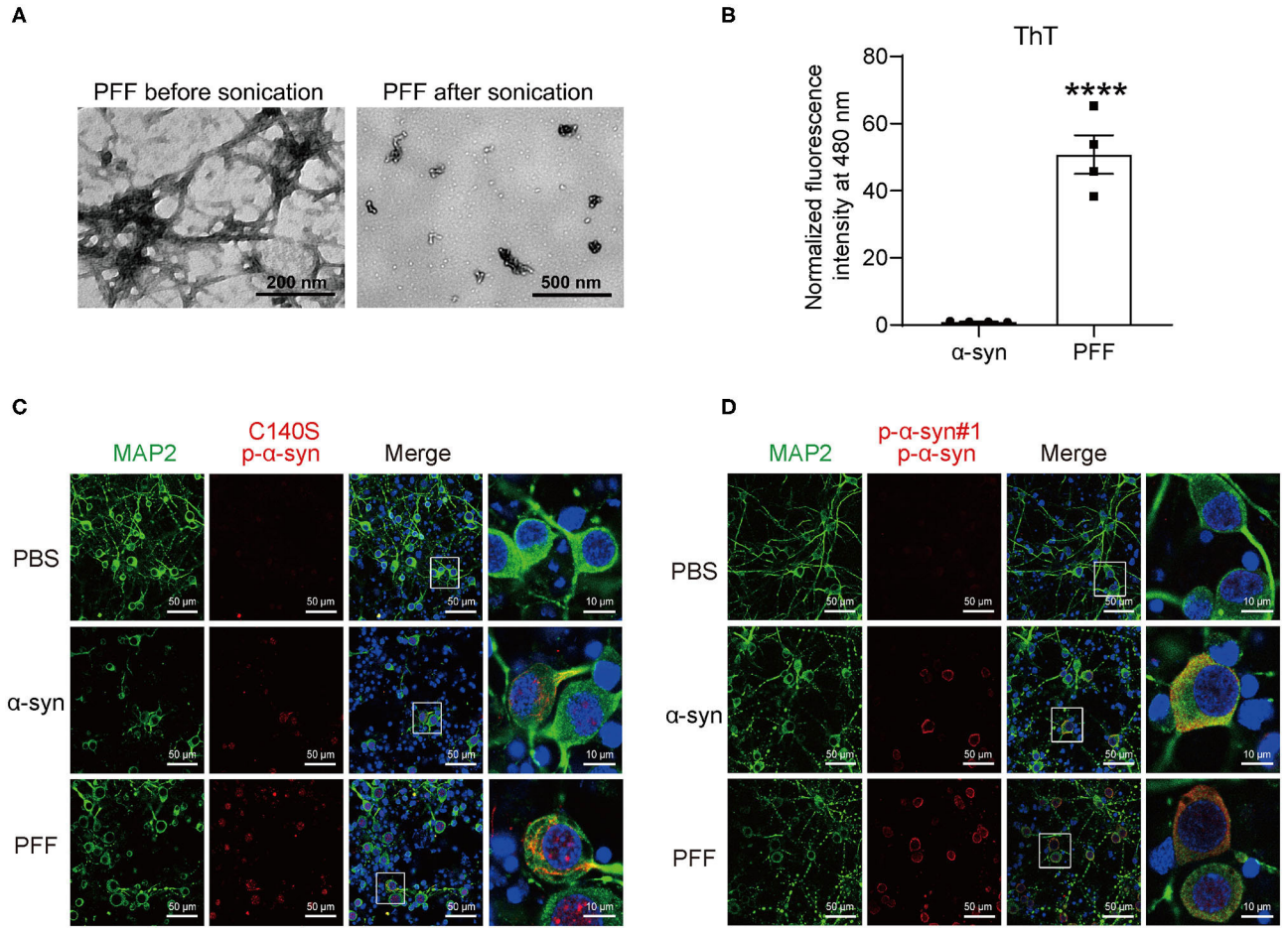

FIGURE 7 | Immunofluorescence staining of p-α-syn in primary neurons using C140S and p-α-syn#1. **(A)** Representative electron microscopy images of preformed fibrils (PFF, left) and the sonicated PFF (right). About 200 ng of PFF (before or after sonication) were applied onto 200-mesh copper grids. Scale bar, 200/500 nm. **(B)** Thioflavin T (ThT) post-staining of monomeric h-α-syn and PFF. **(C,D)** Immunofluorescence staining of p-α-syn in the cortical neurons of the primary mouse showed pathological inclusions. Primary neurons were treated with PBS, monomeric h-α-syn, and sonicated PFF, using C140S **(C)** and p-α-syn#1 **(D)**. Green color indicates microtubule-associated protein 2 (MAP2, green), red color indicates p-α-syn staining (C140S and p-α-syn#1), and blue color indicates nucleus. White squares, amplified area of neurons under low magnification. Scale bar, 50 μm (low magnification) and 10 μm (high magnification). The results are expressed as the mean ± standard error of mean (SEM) (unpaired *t*-test, $n = 4$). ****$P < 0.0001$ *vs.* α-syn.

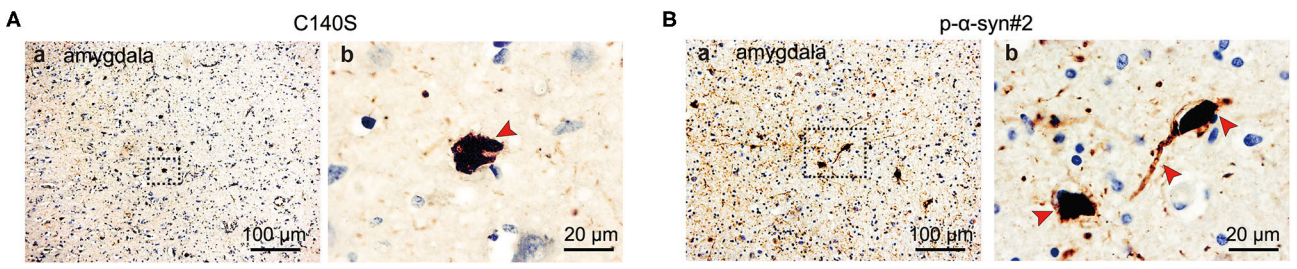

FIGURE 8 | Immunohistochemical staining of p-α-syn in the brain tissue of patients with PD using C140S and p-α-syn#2. Representative images of the immunoreactive structures detected with C140S **(A)** and p-α-syn#2 **(B)** in the amygdala of one patient with PD (male; 69 years old; Braak PD stage V). The brown color indicates p-α-syn staining (C140S and p-α-syn#2) and the blue color indicates hematoxylin (nucleus). Blank square (b), the amplified area of section in low magnification (a). Red arrow, the concentrated region of aggregated p-α-syn. Scale bar, 100 and 20 μm.

situations remains unclear (44, 45). Pinho et al. reported that the accumulation of α-syn species in the nucleus altered gene expression and reduced the toxicity of H4 cells, and the effect on gene expression and cytotoxicity was also modulated by phosphorylation on serine 129 site (46). A recent study also found an association between α-syn and DNA. Sydney E.Dent et al. used a combination of electrophoretic mobility shift assay and atomic force microscopy approaches, and found both α-syn and p-α-syn directly bind DNA within the major groove, and p-α-syn could induce the reductions in the ability of α-syn to bind and bend DNA, which meant that abnormally elevated p-α-syn might modulate DNA metabolism (47). Collectively, all these findings above support the potential modulatory roles of p-α-syn in the nucleus.

In summary, the best way to determine the role of p-α-syn is by using a highly specific antibody. We therefore generated and characterized a novel mouse monoclonal p-α-syn antibody named, C140S, in the present study, and a variety of validation assays were conducted to demonstrate the specificity of this antibody. The C140S could reliably detect α-syn pathologies in the cells and mice models of PD, and the brains from patients with PD. Overall, the antibody described herein should serve as a useful tool in the detection and mechanistic studies of pathogenic p-α-syn in PD and related pathologies.

DATA AVAILABILITY STATEMENT

The raw data supporting the conclusions of this article will be made available by the authors, without undue reservation.

ETHICS STATEMENT

The studies involving human participants were reviewed and approved by IRB of Beijing Tiantan Hospital, Capital Medical University (KY2018-031-02). The patients/participants provided their written informed consent to participate in this study. The animal study was reviewed and approved by Capital Medical University Animal Experiments and Experimental Animals Management Committee, AEEI-2014-031. Written informed consent was obtained from the individual(s) for the publication of any potentially identifiable images or data included in this article.

AUTHOR CONTRIBUTIONS

WL and HY conceived the manuscript. WL, QZ, and HX conducted experiments. WL wrote the manuscript. JL, GG, and HY reviewed the manuscript. YH kindly provided the brain sections of PD patients. HY was responsible for ensuring that the descriptions were accurate and agreed by authors.

FUNDING

This work was supported by the National Natural Science Foundation of China (No. 81870994), the National Natural Science Foundation of China (No. 82071417), and the National Key Plan for Scientific Research and Development of China (No. 2016YFC1306000).

SUPPLEMENTARY MATERIAL

The Supplementary Material for this article can be found online at: https://www.frontiersin.org/articles/10.3389/fneur.2022.821792/full#supplementary-material

Supplementary Figure S1 | Quantification of band intensities of α-syn and p-α-syn in the brains of Wt/Tg mice. **(A–C)** Quantification of the band intensities of α-syn levels in the midbrain **(A)**/striatum **(B)**/cortex **(C)** from wild-type brood (Wt) and Thy1-SNCA transgenic (Tg) mice (**Figures 4D–F**). **(D)** Quantification of the band intensities (17 kD) of p-α-syn levels in the midbrains of Wt and Tg mice (**Figures 4G–I**). The results are expressed as the mean ± standard error of mean (SEM) (unpaired *t*-test, $n = 3$–10). $^{*}P < 0.05$, $^{***}P < 0.001$ *vs.* Wt. Mice age: 13-months-old.

Supplementary Figure S2 | The specificity and affinity of C140S were confirmed by antibody absorption experiment. **(A,B)** A total of 5 μg h of p-α-syn was incubated with control mouse IgG (m-IgG) and C140S antibody (16 μg/mL). The protein G beads were added to conjugate with the antigen-antibody complex. The beads-antigen-antibody complex and supernatant were separated and examined using western bolts, shown in **(A,B)**. The p-α-syn was detected with p-α-syn#2 antibody (Abcam, Cambridge, UK), m-IgG was detected with fluorophore-conjugated secondary antibody mouse 680 (m680). **(C,D)** A total of 5 μg h of p-α-syn was incubated with m-IgG and C140S antibody (16, 80 μg/mL). The protein G beads were added to conjugate with the antigen-antibody complex. The beads-antigen-antibody complex was separated and examined using western bolts, shown in **(C,D)**. The p-α-syn was detected with p-α-syn#2 antibody (Abcam, Cambridge, UK), m-IgG was detected with m680. The p-α-syn protein was added as a positive control. Ab, Antibody.

REFERENCES

1. Goedert M, Spillantini MG, Del Tredici K, Braak H. 100 years of Lewy pathology. *Nat Rev Neurol.* (2013) 9:13–24. doi: 10.1038/nrneurol.2012.242
2. Fares MB, Jagannath S, Lashuel HA. Reverse engineering Lewy bodies: how far have we come and how far can we go? *Nat Rev Neurosci.* (2021) 22:111–31. doi: 10.1038/s41583-020-00416-6
3. Stephens AD, Zacharopoulou M, Kaminski Schierle GS. The cellular environment affects monomeric alpha-synuclein structure. *Trends Biochem Sci.* (2019) 44:453–66. doi: 10.1016/j.tibs.2018.11.005
4. Jankovic J, Sherer T. The future of research in Parkinson disease. *JAMA Neurol.* (2014) 71:1351–2. doi: 10.1001/jamaneurol.2014.1717
5. Guo JL, Lee VM. Cell-to-cell transmission of pathogenic proteins in neurodegenerative diseases. *Nat Med.* (2014) 20:130–8. doi: 10.1038/nm.3457
6. Lauwers E, Lalli G, Brandner S, Collinge J, Compernolle V, Duyckaerts C, et al. Potential human transmission of amyloid beta pathology: surveillance and risks. *Lancet Neurol.* (2020) 19:872–8. doi: 10.1016/S1474-4422(20)30238-6
7. Kovacs GG, Breydo L, Green R, Kis V, Puska G, Lorincz P, et al. Intracellular processing of disease-associated alpha-synuclein in the human brain suggests prion-like cell-to-cell spread. *Neurobiol Dis.* (2014) 69:76–92. doi: 10.1016/j.nbd.2014.05.020
8. Fujiwara H, Hasegawa M, Dohmae N, Kawashima A, Masliah E, Goldberg MS, et al. alpha-Synuclein is phosphorylated in synucleinopathy lesions. *Nat Cell Biol.* (2002) 4:160–4. doi: 10.1038/ncb748
9. Anderson JP, Walker DE, Goldstein JM, de Laat R, Banducci K, Caccavello RJ, et al. Phosphorylation of Ser-129 is the dominant pathological modification of alpha-synuclein in familial and sporadic Lewy body disease. *J Biol Chem.* (2006) 281:29739–52. doi: 10.1074/jbc.M600933200

10. Chen L, Feany MB. Alpha-synuclein phosphorylation controls neurotoxicity and inclusion formation in a Drosophila model of Parkinson disease. *Nat Neurosci.* (2005) 8:657–63. doi: 10.1038/nn1443
11. Paleologou KE, Schmid AW, Rospigliosi CC, Kim HY, Lamberto GR, Fredenburg RA, et al. Phosphorylation at Ser-129 but not the phosphomimics S129E/D inhibits the fibrillation of alpha-synuclein. *J Biol Chem.* (2008) 283:16895–905. doi: 10.1074/jbc.M800747200
12. Sato H, Arawaka S, Hara S, Fukushima S, Koga K, Koyama S, et al. Authentically phosphorylated alpha-synuclein at Ser129 accelerates neurodegeneration in a rat model of familial Parkinson's disease. *J Neurosci.* (2011) 31:16884–94. doi: 10.1523/JNEUROSCI.3967-11.2011
13. Colom-Cadena M, Pegueroles J, Herrmann AG, Henstridge CM, Munoz L, Querol-Vilaseca M, et al. Synaptic phosphorylated alpha-synuclein in dementia with Lewy bodies. *Brain.* (2017) 140:3204–14. doi: 10.1093/brain/awx275
14. Ma MR, Hu ZW, Zhao YF, Chen YX, Li YM. Phosphorylation induces distinct alpha-synuclein strain formation. *Sci Rep.* (2016) 6:37130. doi: 10.1038/srep37130
15. Karampetsou M, Ardah MT, Semitekolou M, Polissidis A, Samiotaki M, Kalomoiri M, et al. Phosphorylated exogenous alpha-synuclein fibrils exacerbate pathology and induce neuronal dysfunction in mice. *Sci Rep.* (2017) 7:16533. doi: 10.1038/s41598-017-15813-8
16. Zhang S, Liu YQ, Jia C, Lim YJ, Feng G, Xu E, et al. Mechanistic basis for receptor-mediated pathological alpha-synuclein fibril cell-to-cell transmission in Parkinson's disease. *Proc Natl Acad Sci USA*. (2021) 118:e2011196118. doi: 10.1073/pnas.2011196118
17. Tsukita K, Sakamaki-Tsukita H, Tanaka K, Suenaga T, Takahashi R. Value of in vivo alpha-synuclein deposits in Parkinson's disease: A systematic review and meta-analysis. *Mov Disord.* (2019) 34:1452–63. doi: 10.1002/mds.27794
18. Chahine LM, Beach TG, Brumm MC, Adler CH, Coffey CS, Mosovsky S, et al. In vivo distribution of alpha-synuclein in multiple tissues and biofluids in Parkinson disease. *Neurology.* (2020) 95:e1267–84. doi: 10.1212/WNL.0000000000010404
19. Hansson O. Biomarkers for neurodegenerative diseases. *Nat Med.* (2021) 27:954–63. doi: 10.1038/s41591-021-01382-x
20. Braak H, Del Tredici K, Bratzke H, Hamm-Clement J, Sandmann-Keil D, Rub U. Staging of the intracerebral inclusion body pathology associated with idiopathic Parkinson's disease (preclinical and clinical stages). *J Neurol.* (2002) 249:III/1–5. doi: 10.1007/s00415-002-1301-4
21. Braak H, Del Tredici K, Rub U, de Vos RA, Jansen Steur EN, Braak E. Staging of brain pathology related to sporadic Parkinson's disease. *Neurobiol Aging.* (2003) 24:197–211. doi: 10.1016/S0197-4580(02)00065-9
22. Mao X, Ou MT, Karuppagounder SS, Kam TI, Yin X, Xiong Y, et al. Pathological alpha-synuclein transmission initiated by binding lymphocyte-activation gene 3. *Science.* (2016) 353:aah3374. doi: 10.1126/science.aah3374
23. Luna E, Decker SC, Riddle DM, Caputo A, Zhang B, Cole T, et al. Differential alpha-synuclein expression contributes to selective vulnerability of hippocampal neuron subpopulations to fibril-induced toxicity. *Acta Neuropathol.* (2018) 135:855–75. doi: 10.1007/s00401-018-1829-8
24. Pediaditakis I, Kodella KR, Manatakis DV, Le CY, Hinojosa CD, Tien-Street W, et al. Modeling alpha-synuclein pathology in a human brain-chip to assess blood-brain barrier disruption. *Nat Commun.* (2021) 12:5907. doi: 10.1038/s41467-021-26066-5
25. Sacino AN, Brooks M, Thomas MA, McKinney AB, McGarvey NH, Rutherford NJ, et al. Amyloidogenic alpha-synuclein seeds do not invariably induce rapid, widespread pathology in mice. *Acta Neuropathol.* (2014) 127:645–65. doi: 10.1007/s00401-014-1268-0
26. Rutherford NJ, Brooks M, Giasson BI. Novel antibodies to phosphorylated alpha-synuclein serine 129 and NFL serine 473 demonstrate the close molecular homology of these epitopes. *Acta Neuropathol Commun.* (2016) 4:80. doi: 10.1186/s40478-016-0357-9
27. Delic V, Chandra S, Abdelmotilib H, Maltbie T, Wang S, Kem D, et al. Sensitivity and specificity of phospho-Ser129 alpha-synuclein monoclonal antibodies. *J Comp Neurol.* (2018) 526:1978–90. doi: 10.1002/cne.24468
28. Mbefo MK, Paleologou KE, Boucharaba A, Oueslati A, Schell H, Fournier M, et al. Phosphorylation of synucleins by members of the Polo-like kinase family. *J Biol Chem.* (2010) 285:2807–22. doi: 10.1074/jbc.M109.081950
29. Liu J, Liu W, Lu Y, Tian H, Duan C, Lu L, et al. Piperlongumine restores the balance of autophagy and apoptosis by increasing BCL2 phosphorylation in rotenone-induced Parkinson disease models. *Autophagy.* (2018) 14:845–61. doi: 10.1080/15548627.2017.1390636
30. Volpicelli-Daley LA, Luk KC, Lee VM. Addition of exogenous alpha-synuclein preformed fibrils to primary neuronal cultures to seed recruitment of endogenous alpha-synuclein to Lewy body and Lewy neurite-like aggregates. *Nat Protoc.* (2014) 9:2135–46. doi: 10.1038/nprot.2014.143
31. Luk KC, Kehm V, Carroll J, Zhang B, O'Brien P, Trojanowski JQ, et al. Pathological alpha-synuclein transmission initiates Parkinson-like neurodegeneration in nontransgenic mice. *Science.* (2012) 338:949–53. doi: 10.1126/science.1227157
32. Mahul-Mellier AL, Burtscher J, Maharjan N, Weerens L, Croisier M, Kuttler F, et al. The process of Lewy body formation, rather than simply alpha-synuclein fibrillization, is one of the major drivers of neurodegeneration. *Proc Natl Acad Sci USA.* (2020) 117:4971–82. doi: 10.1073/pnas.1913904117
33. Trier NH, Hansen PR, Houen G. Production and characterization of peptide antibodies. *Methods.* (2012) 56:136–44. doi: 10.1016/j.ymeth.2011.12.001
34. Stephens AD, Zacharopoulou M, Moons R, Fusco G, Seetaloo N, Chiki A, et al. Extent of N-terminus exposure of monomeric alpha-synuclein determines its aggregation propensity. *Nat Commun.* (2020) 11:2820. doi: 10.1038/s41467-020-16564-3
35. Tian H, Lu Y, Liu J, Liu W, Lu L, Duan C, et al. Leucine Carboxyl Methyltransferase Downregulation and Protein Phosphatase Methylesterase Upregulation Contribute Toward the Inhibition of Protein Phosphatase 2A by alpha-Synuclein. *Front Aging Neurosci.* (2018) 10:173. doi: 10.3389/fnagi.2018.00173
36. Aspholm EE, Matecko-Burmann I, Burmann BM. Keeping alpha-Synuclein at Bay: a more active role of molecular chaperones in preventing mitochondrial interactions and transition to pathological states? *Life.* (2020) 10:289. doi: 10.3390/life10110289
37. Burmann BM, Gerez JA, Matecko-Burmann I, Campioni S, Kumari P, Ghosh D, et al. Regulation of alpha-synuclein by chaperones in mammalian cells. *Nature.* (2020) 577:127–32. doi: 10.1038/s41586-019-1808-9
38. Haque ME, Akther M, Azam S, Kim IS, Lin Y, Lee YH, et al. Targeting alpha-synuclein aggregation and its role in mitochondrial dysfunction in Parkinson's disease. *Br J Pharmacol.* (2022) 179:23–45. doi: 10.1111/bph.15684
39. Nakamura K, Nemani VM, Azarbal F, Skibinski G, Levy JM, Egami K, et al. Direct membrane association drives mitochondrial fission by the Parkinson disease-associated protein alpha-synuclein. *J Biol Chem.* (2011) 286:20710–26. doi: 10.1074/jbc.M110.213538
40. Wang X, Becker K, Levine N, Zhang M, Lieberman AP, Moore DJ, et al. Pathogenic alpha-synuclein aggregates preferentially bind to mitochondria and affect cellular respiration. *Acta Neuropathol Commun.* (2019) 7:41. doi: 10.1186/s40478-019-0696-4
41. Malpartida AB, Williamson M, Narendra DP, Wade-Martins R, Ryan BJ. Mitochondrial Dysfunction and Mitophagy in Parkinson's Disease: From Mechanism to Therapy. *Trends Biochem Sci.* (2021) 46:329–43. doi: 10.1016/j.tibs.2020.11.007
42. McFarland MA, Ellis CE, Markey SP, Nussbaum RL. Proteomics analysis identifies phosphorylation-dependent alpha-synuclein protein interactions. *Mol Cell Proteomics.* (2008) 7:2123–37. doi: 10.1074/mcp.M800116-MCP200
43. Grassi D, Diaz-Perez N, Volpicelli-Daley LA, Lasmezas CI. Palpha-syn* mitotoxicity is linked to MAPK activation and involves tau phosphorylation and aggregation at the mitochondria.

Neurobiol Dis. (2019) 124:248–62. doi: 10.1016/j.nbd.2018.11.015
44. Huang Z, Xu Z, Wu Y, Zhou Y. Determining nuclear localization of alpha-synuclein in mouse brains. *Neuroscience.* (2011) 199:318–32. doi: 10.1016/j.neuroscience.2011.10.016
45. Davidi D, Schechter M, Elhadi SA, Matatov A, Nathanson L, Sharon R. alpha-Synuclein Translocates to the Nucleus to Activate Retinoic-Acid-Dependent Gene Transcription. *iScience.* (2020) 23:100910. doi: 10.1016/j.isci.2020.100910
46. Pinho R, Paiva I, Jercic KG, Fonseca-Ornelas L, Gerhardt E, Fahlbusch C, et al. Nuclear localization and phosphorylation modulate pathological effects of alpha-synuclein. *Hum Mol Genet.* (2019) 28:31–50. doi: 10.1093/hmg/ddy326
47. Dent SE, King DP, Osterberg VR, Adams EK, Mackiewicz MR, Weissman TA, et al. Phosphorylation of the aggregate-forming protein alpha-synuclein on serine-129 inhibits its DNA-bending properties. *J Biol Chem.* (2021) 101552. doi: 10.1016/j.jbc.2021.101552
48. Shaltouki A, Hsieh CH, Kim MJ, Wang X. Alpha-synuclein delays mitophagy and targeting Miro rescues neuron loss in Parkinson's models. *Acta Neuropathol.* (2018) 136:607–20. doi: 10.1007/s00401-018-1873-4

Conflict of Interest: The authors declare that the research was conducted in the absence of any commercial or financial relationships that could be construed as a potential conflict of interest.

Publisher's Note: All claims expressed in this article are solely those of the authors and do not necessarily represent those of their affiliated organizations, or those of the publisher, the editors and the reviewers. Any product that may be evaluated in this article, or claim that may be made by its manufacturer, is not guaranteed or endorsed by the publisher.

Copyright © 2022 Liu, Zhang, Xing, Gao, Liu, Huang and Yang. This is an open-access article distributed under the terms of the Creative Commons Attribution License (CC BY). The use, distribution or reproduction in other forums is permitted, provided the original author(s) and the copyright owner(s) are credited and that the original publication in this journal is cited, in accordance with accepted academic practice. No use, distribution or reproduction is permitted which does not comply with these terms.

frontiers in Neurology

ORIGINAL RESEARCH
published: 17 February 2022
doi: 10.3389/fneur.2022.834403

Gut Microbiota and Targeted Biomarkers Analysis in Patients With Cognitive Impairment

Shourong Lu[1], Ying Yang[1], Qiao Xu[1], Shuqiang Wang[2], Jie Yu[1], Bingshan Zhang[1], Zhuo Wang[1], Yunyun Zhang[3], Wenwei Lu[4]* and Kan Hong[1]**

[1] Department of Geriatric, The Affiliated Wuxi People's Hospital of Nanjing Medical University, Wuxi, China, [2] Department of Medicine, Wuxi Xin'an Community Health Service Center, Wuxi, China, [3] Department of General Practice, The Affiliated Wuxi People's Hospital of Nanjing Medical University, Wuxi, China, [4] State Key Laboratory of Food Science and Technology and School of Food Science and Technology, Jiangnan University, Wuxi, China

OPEN ACCESS

Edited by:
Yuzhen Xu,
Tongji University, China

Reviewed by:
Jiachao Zhang,
Hainan University, China
Mingqing He,
Soochow University, China

***Correspondence:**
Yunyun Zhang
zhangyunyun026133@126.com
Wenwei Lu
luwenwei@jiangnan.edu.cn
Kan Hong
lindashao99@163.com

Specialty section:
This article was submitted to Neurological Biomarkers, a section of the journal Frontiers in Neurology

Received: 13 December 2021
Accepted: 06 January 2022
Published: 17 February 2022

Citation:
Lu S, Yang Y, Xu Q, Wang S, Yu J, Zhang B, Wang Z, Zhang Y, Lu W and Hong K (2022) Gut Microbiota and Targeted Biomarkers Analysis in Patients With Cognitive Impairment. Front. Neurol. 13:834403. doi: 10.3389/fneur.2022.834403

Gut microbial alteration is closely associated with brain disorders including cognitive impairment (CI). Gut microbes have the potential to predicate the development of diseases. However, the gut microbial markers for CI remain to be elucidated. In this study, the gut microbial alterations were assessed using16S rRNA sequencing, and identified the gut microbial markers using a random forest model. The results showed that there were significant gut microbial differences between the control and CI groups based on beta diversity ($p < 0.002$). Patients with CI had higher abundances of Actinobacteria and Proteobacteria but lower proportions of Bcateroidetes and Firmicutes vs. that in the control group. Patients had 39 special genera and the control subjects had 11 special genera. Furthermore, 11 genera such as *Blautia*, *Roseburia*, and *Lactococcus* and 18 genera such as *Lactobacillus*, *Ruminococcus* 2, and *Akkermansia* were the differential taxa in the control and CI groups, respectively. Gene functions related to nutrient metabolisms were upregulated in patients with CI. This suggested that the huge differences in gut microbes between the two groups and gut microbiota had the potential to predicate the development of CI. Based on machine learning results, 15 genera such as *Lactobacillus, Bifidobacterium,* and *Akkermansia* were selected as the optimal marker set to predicate CI with an area under curve (AUC) value of 78.4%. The results revealed the gut microbial markers for CI and provided a potential diagnosis tool to prevent the development of CI in the elderly.

Keywords: cognitive impairment, gut microbiome, biomarkers, *Lactobacillus*, *Bifidobacterium*

INTRODUCTION

Cognitive impairment is closely associated with the development of psychiatric illnesses such as hypertension, depression, and Alzheimer's disease (1–3). Age is an important factor for cognitive impairment (CI) and there is increasing prevalence with the development of aging worldwide (4). Furthermore, educational degree, sleep disorder, and vitamin D intake are the risk factors for CI

in elderly people (5–7). In the elderly, gastrointestinal tract and brain functions are gradually declining, and these factors are inevitable challenges for them. CI is the high-risk factor for dementia in elderly people, 10–30% of patients with mild CI and 20–66% of them convert into dementia within 1 and 2–4 years, respectively (8, 9). Dementia is difficult to reverse and there are no effective ways to treat it (10). CI leads to a huge burden for family and society. Therefore, the early prevention of CI is a key window to reduce the prevalence of dementia in the elderly.

Gut microbial alteration is closely associated with the development of aging in the elderly and affects their physiology functions including CI. The "Gut-brain" axis has been reported to solve the function barrier related to the brain and suggests bacteria play a key role in the development of neurodevelopmental disorders (11). Bacterial species such as *Limosilactobacillus reuteri*, *Bifidobacterium pseudolongum*, and *Lactobacillus johnsonii* are reduced in the maternal high-fat-diet offspring and negatively affect offspring social behavior (12). *Verrucomicrobiaceae* and unclassified Firmicutes are increased but *Prevotellaceae* and *Erysipelotrichaceae* are decreased, and they affect the β-glucuronate and tryptophan metabolism in the patients with Parkinson's disease (13). These results suggest that gut microbiota and their metabolism influence deeply the brain function and manipulate the host's emotion and behavioral intentions. Fecal microbiota transplant from aged donor mice into young recipients leads to impaired spatial learning and memory (14). This implies that gut microbiota is an important cause to induce CI symptoms.

In recent years, microbial marker severs as a non-invasive diagnosis tool for some diseases such as hepatocellular carcinoma, colorectal cancer, and type 2 diabetes (15–17). Gut microbial marker has the potential to predict the development of CI and may be an effective target tool to prevent CI in the elderly. In this study, a total of 60 fecal samples were collected from the patients with CI and control subjects. Combined 16S rRNA sequencing with machine learning revealed microbial biomarkers that predicted the development of CI and provided a potential diagnosis tool to prevent CI for the elderly.

MATERIALS AND METHODS

Study Subjects

Patients ($n = 33$) with CI and controls ($n = 27$) aged more than 68 years were enrolled in the Xin'an community in Wuxi city. The study protocol was approved by the Ethics Committee of the Wuxi People's Hospital. Each subject provided written informed consent.

CI Assessment

Mini-mental state examination (MMSE) index was used to assess the mental state and degree of CI for the subjects (27–30, normal cognitive function; <27, CI). The activities of daily living (ADL) index was used to evaluate the ability of daily living in family and the community in the elderly people (100, self-care; >60, basically self-care; 41–60, need assistance; 21–40, rely on others; <20, completely dependent on others).

Baseline Clinical Characteristic Collection

Baseline clinical characteristics including gender, age, height, weight, education level, sleep duration, and occupation were collected during the clinical interview. Fecal samples were stored at −80°C until for use.

16S rRNA Amplicon Sequencing

Using the FastDNA Spin Kit (MP Biomedicals, Santa Ana, CA, USA), DNA was extracted for feces according to the instructions. The V3–V4 region was amplified with the primers (forward, 5′-CTCCTACGGGAGGCAGCA-3′; reverse, 5′-GGACTACHVGGGTWTCTAAT-3′). PCR products were purified by TIANgel Mini Purification Kit (TIANGEN, Beijing, China). After determination for DNA concentration and library construction, the amplified fragment was sequenced on an Illumina MiSeq PE300 platform (Illumina, Santiago, CA, USA). Sequencing results were analyzed using the QIIME2 pipeline. Non-metric multidimensional scaling (NMDS) was performed to evaluate change in beta diversity of gut microbiota based on the Bray-Curtis distance (18). Differential taxa were identified using the linear discriminant analysis effect size (LEfSe) (19). Phylogenetic investigation of communities by reconstruction of unobserved states (PICRUSt) was employed to predict the gene function of gut microbiota based on the Kyoto Encyclopedia of Genes and Genomes (KEGG) Orthology database between groups with and without CI (20). A random forest model was used to explore the microbial markers for CI (21). Sequence data were deposited in the Sequence Read Archive database as BioProject PRJNA789994.

Statistical Analysis

The SPSS software version 20 (Chicago, Illinois, USA) and R software version 4.0.5 (open access, https://www.r-project.org/) were used to perform statistical analysis. The comparison was performed using an unpaired *t*-test between the control and CI groups. A $p < 0.05$ was indicated statistically significant.

RESULTS

Baseline Characteristics of Subjects

In this trial, 33 patients with CI and 27 healthy controls were enrolled. As shown in **Figure 1**, there was no significant difference in gender, height, and weight between the two groups. Compared to the control group, patients with CI had lower MMSE and ADL indices but had higher age, education duration, and sleep duration per day in the CI group. Furthermore, patients in the CI group were all retirees but the farmer was the major occupation (74.07%) in the control group. The results showed that people with older age had a higher risk to suffer the CI symptoms although they had higher education duration and sleep duration in the CI group.

Alteration of Gut Microbial Diversity

To assess the alteration of gut microbial diversity including alpha and beta diversities in subjects, 16S ribosomal RNA sequencing was performed. For alpha diversity of gut microbes, there were no significant differences in evenness, observed_otus, and the

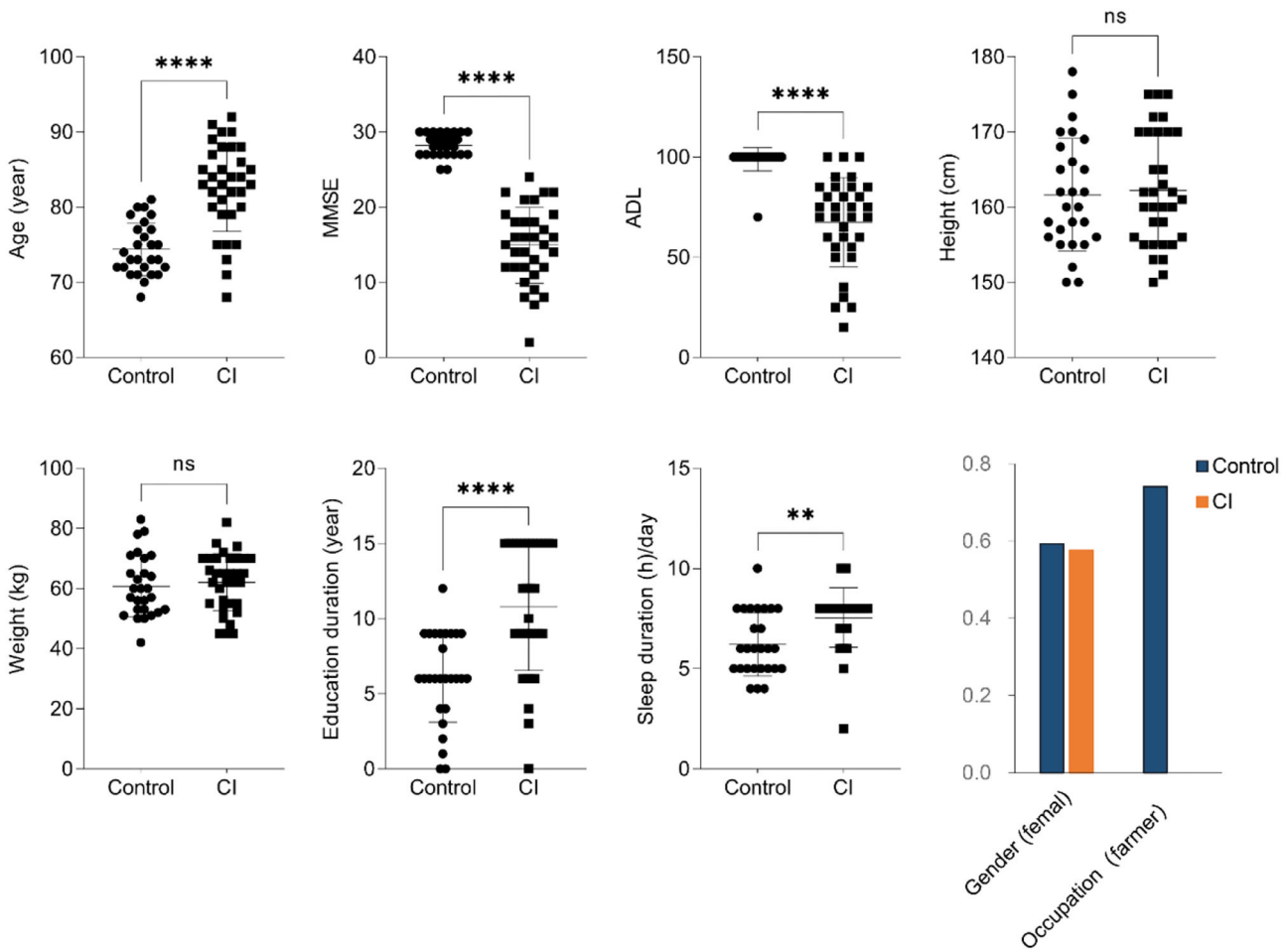

FIGURE 1 | Baseline clinical characteristics (unpaired *t*-test, ns, no significance, $^{**}p < 0.01$, $^{****}p < 0.0001$).

Shannon indices except for the faith_pd index (**Figure 2A**). Compared to the control group, the faith_pd index was significantly higher. Furthermore, there was a difference in the beta diversity of gut microbiota between the two groups [**Figure 2B**, stress = 0.25, $p < 0.002$, permutational multivariate ANOVA (PERMANOVA)], and the development of CI was associated with alterations of gut microbial composition. The results showed that alpha diversity of gut microbiota was no significant alteration between the two groups but beta diversity representing gut microbial structure and composition had remarkable changes in the CI group vs. the control group.

Changes in Gut Microbial Composition

At the phylum level, patients had shown higher abundances of Actinobacteria and Proteobacteria but lower proportions of Bacteroidetes and Firmicutes in the CI group vs. that in the control group (**Figure 3A**). There were no significant differences in the abundances of Verrucomicrobia and Tenericutes between the two groups. Fusobacteria was enriched in the control group but Euryarchaeota was higher in the CI group. At the genus level (relative abundance >0.005 in any group), *Bifidobacterium*, *Alistipes*, *Lactobacillus*, *Streptococcus*, (*Ruminococcus*) *torques* group, *Ruminococcus* 2, *Escherichia-Shigella*, and *Klebsiella* were enriched in the CI group (**Figure 3B**). The relative abundances of *Bacteroides*, *Prevotella* 9, *Lachnospiraceae*_g, *Anaerostipes*, *Fusicatenibacter*, *Lachnoclostridium*, *Roseburia*, *Tyzzerella* 4, (*Eubacterium*) *hallii* group, *Fusobacterium*, and *Akkermansia* were higher in the control group. Venn diagram showed that there were 121 common genera in both groups, 11 special genera, and 39 special genera in the control group and the CI group, respectively (**Figure 3C**). The results showed that there were significant differences in gut microbial composition between the two groups.

Differential Taxa Between Groups

To explore the differential taxa between the control and CI groups, LEfSe analysis was performed. The results showed that based on the alteration of relative abundances, 11 genera including *Blautia*, *Roseburia*, Fusicatenibacter, Anaerostipes, Phascolarctobacterium, Lachnospiraceae_g, RuminococcaceaeUCG_013, Paraprevotella, *Lactococcus*, Bilophila, and Tyzzerella 3 were

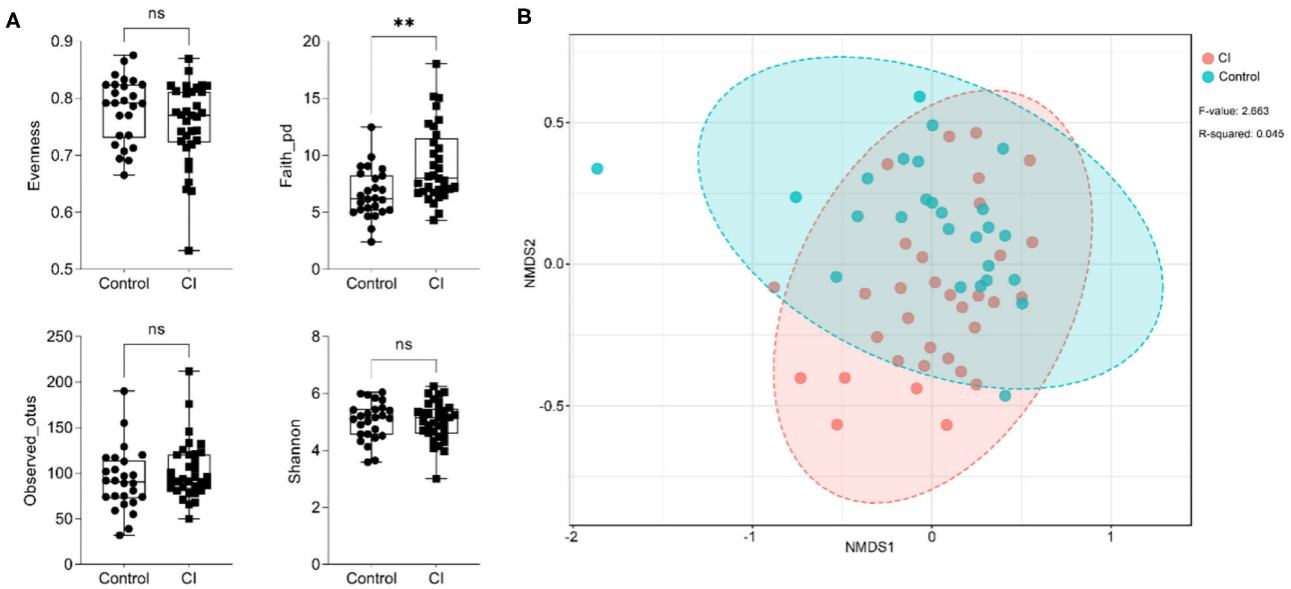

FIGURE 2 | Changes in the alpha and beta diversities of gut microbes. **(A)** Alteration of alpha diversity (unpaired *t*-test, ns, no significance, $^{**}p < 0.01$). **(B)** Beta diversity alteration based on non-metric multidimensional scaling (NMDS) analysis.

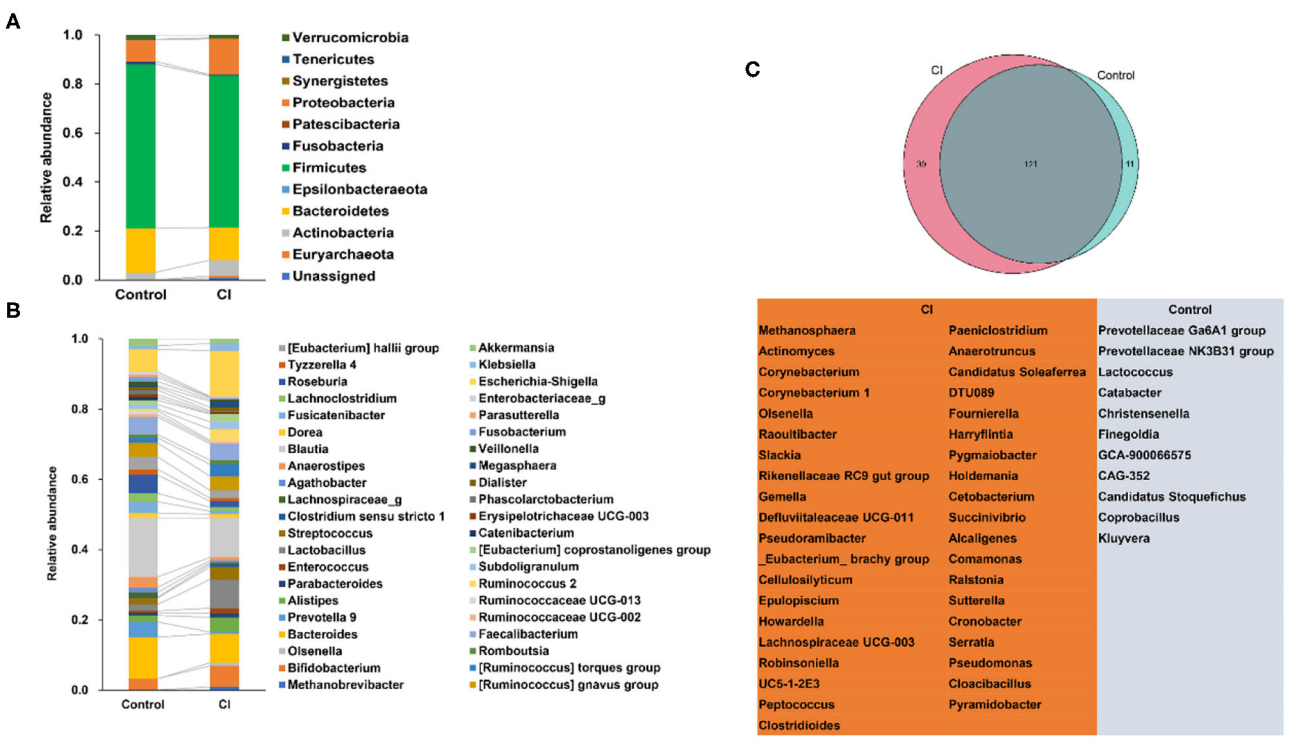

FIGURE 3 | Alterations of gut microbial composition. **(A)** Changes in gut microbes at the phylum level. **(B)** Changes in gut microbes at the genus level. **(C)** The special genera in the control and cognitive impairment (CI) groups.

enriched in the control group (**Figure 4A**). Hungatella, Desulfovibrio, RuminococcaceaeUCG_005, EC_Eubacterium_xylanophilumgroup, FamilyXIIIAD3011group, Sutterella, Slackia, ChristensenellaceaeR_7group, Eubacterium, RuminococcaeaeUCG_004, Butyricimonas, *Akkermansia*, Methanobrevibacter, Streptococcus, *Ruminococcus*2, and

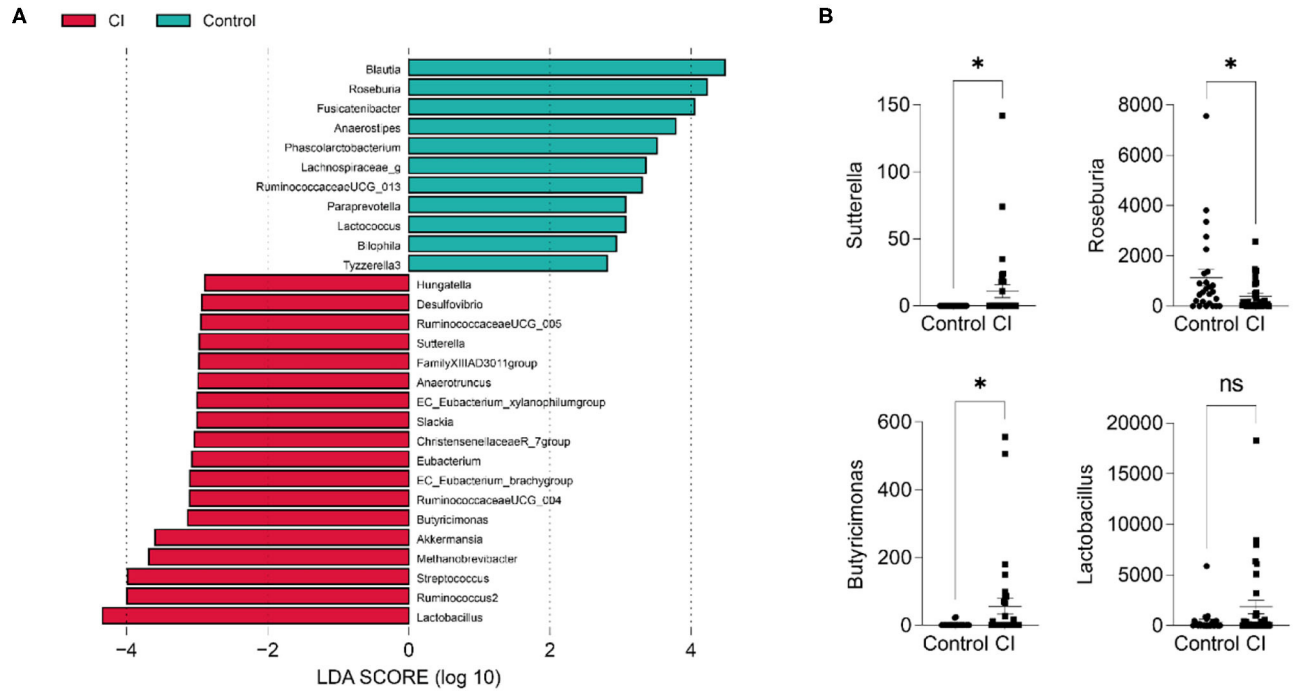

FIGURE 4 | Differential taxa in the control and CI groups. **(A)** Linear discriminant analysis effect size (LEfSe). **(B)** Comparisons of 4 genera between groups (unpaired t-test, ns, no significance, $^*p < 0.05$).

Lactobacillus were the differential taxa in the CI group. For instance, *Sutterella* and *Butyricimonas* were higher in the CI group and Roseburia was higher in the control group. *Lactobacillus* was enriched in the CI group than that in the control group although there was no significant statistical significance ($p > 0.05$, **Figure 4B**).

Gene Functions of Gut Microbiota Between Groups

Gut microbial alterations lead to differences in gene functions. Therefore, to evaluate the changes in gene functions of gut microbiota, PICRUSt analysis was performed based on gene function prediction. There were 33 gene functions with significant alterations in both groups (**Figure 5**, two-sided, Welch's *t*-test with Benjamini-Hochberg FDR multiple test correction). The abundances of photosynthesis proteins, photosynthesis, germination, oxidative phosphorylation, sporulation, cyanoamino acid metabolism, phenylpropanoid biosynthesis, bacterial chemotaxis, beta-lactam resistance, progesterone-mediated oocyte maturation, and antigen processing and presentation were upregulated in the control group. However, gene functions related to nutrient metabolisms such as glycolysis/gluconeogenesis, retinol metabolism, fatty acid metabolism, D-alanine metabolism, and pyruvate metabolism were upregulated in patients with CI. The results showed that gut microbial alteration induced significant differences in gene functions and this might be one of the causes for CI.

Identification of Microbial Markers for CI

To explore gut microbial markers for CI, a random forest classifier model was used to identify the control samples from CI samples. To detect unique microbial markers of CI, a random forest model between 27 healthy samples and 33 CI samples in the discovery phase. As shown in **Figure 6A**, 15 microbial markers such as *Lactobacillus, Bifidobacterium,* and *Akkermansia* were selected as the optimal marker set. An area under curve (AUC) value of 78.4% was received in the ROC curve based on these selected genera and implied a high diagnosis efficacy for patients with CI (**Figure 6B**). The results showed that 15 genera contained more information for CI predication and might be the microbial markers for CI.

DISCUSSION

In the present study, gut microbiota from the patients with CI and control subjects was comprised using 16S rRNA sequencing. Gut microbial microecology is important for maintaining physiological functions in the host and contributes to the regulation of immune responses. Dysbiosis of gut microbiota leads to changes in metabolisms and results in the onset of diseases, especially including central nervous system diseases (22). Many studies have shown that modulating gut microbiota has been considered an effective target to alleviate emotional and behavioral disorders, such as depression, stroke, and autism (23–25). The increase in *Fusobacterium* and reduction of short-chain fatty acids have been revealed to be associated with

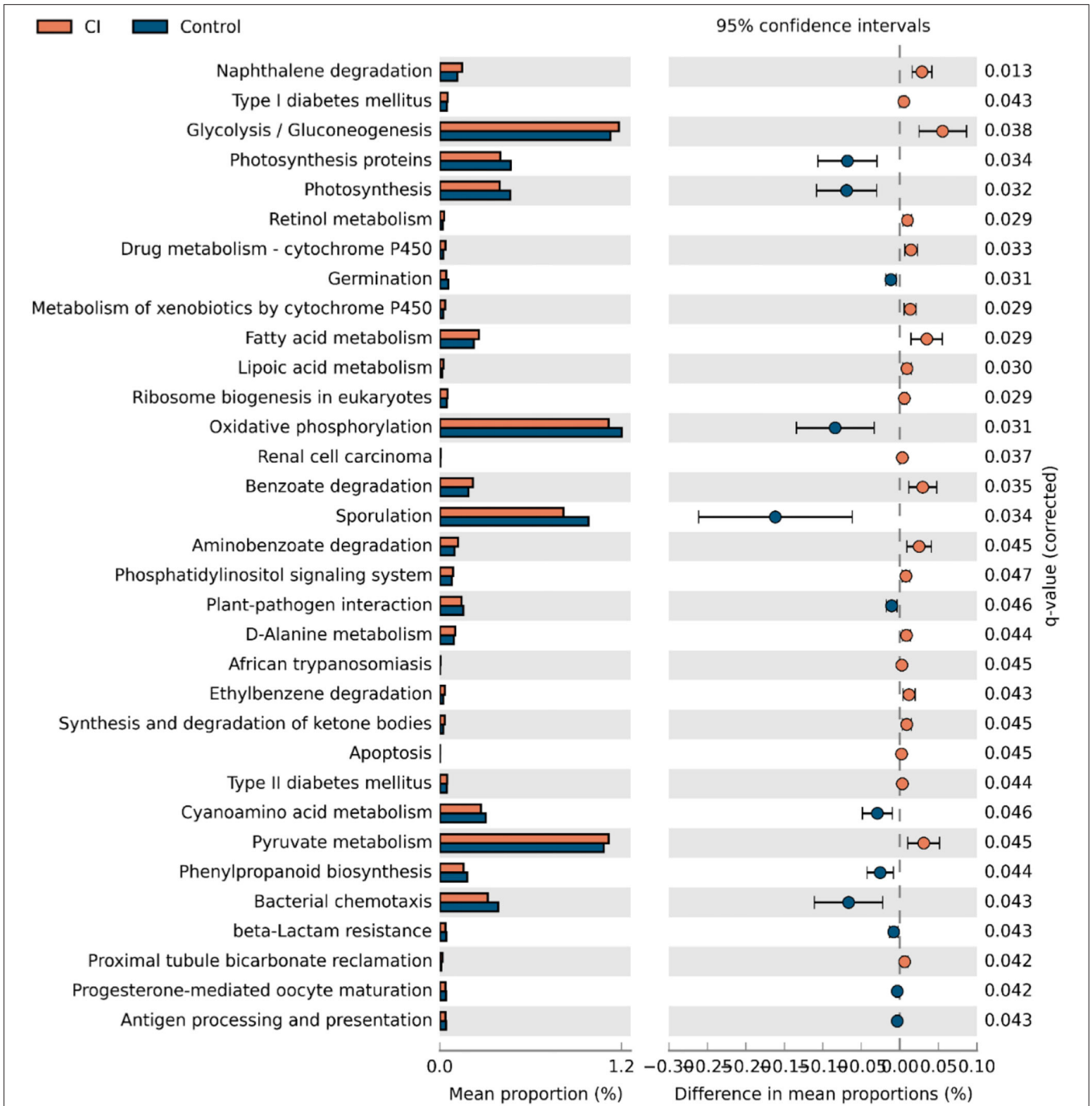

FIGURE 5 | Alterations of gene functions of gut microbiota.

post-stroke cognitive impairment (26), and this suggests the potential clinical diagnosis and treatment values of gut microbes for brain disorders.

Cognitive impairment (CI) is a common disease for the elderly, and the development of CI induces a decline in the ability of daily living to bring a huge burden to the family and society. Compared to the control group, patients with CI had a lower ADL and MMSE, although this might be partly attributed to the older age (**Figure 1**, $p < 0.001$). Furthermore, although in the CI group education duration was significantly higher than that in the control, that seemed to be no improvement for CI symptoms. Some studies have been shown education is negatively associated with CI performance, and more education duration time leads to an advantage of 0.2–0.4 *SD* in cognitive performance (27, 28).

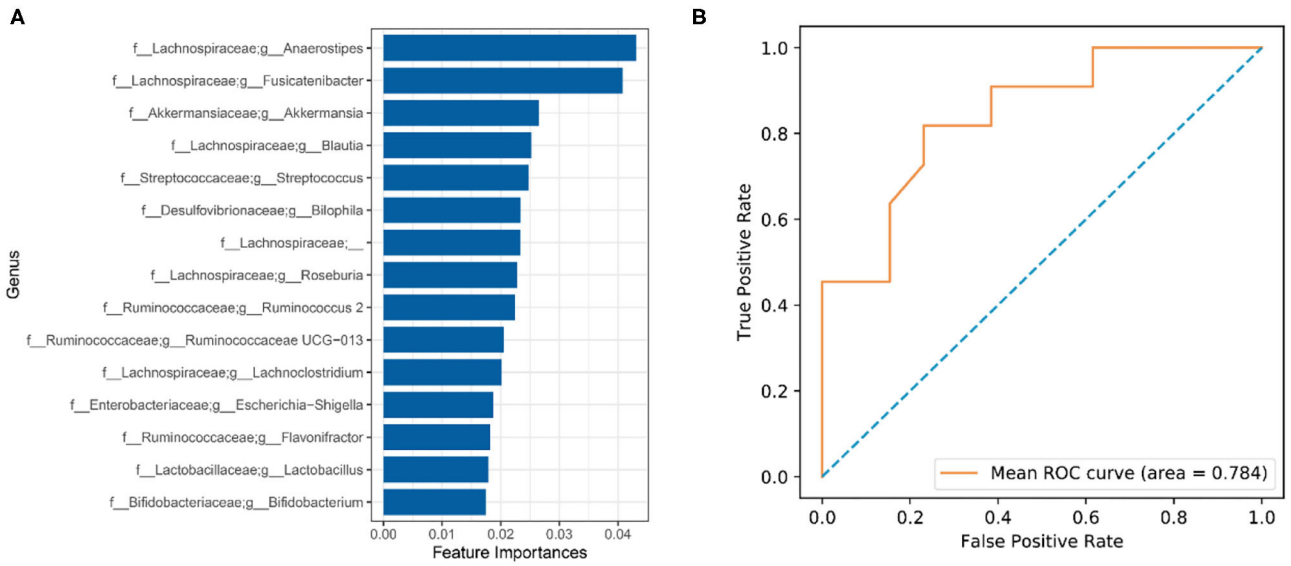

FIGURE 6 | Identification of gut microbial markers for CI by random forest model. **(A)** Microbial markers were predicated using a random forest model. **(B)** ROC curve evaluation.

Increasing evidence has demonstrated that sleep disturbance is closely associated with the development of CI in the elderly. Long sleep latency leads to a decrease in the chance of reversion to normal cognition but long sleep duration is related to the decline of risk for cognition (29). However, patients with CI in this study had a more sleep duration time vs. the control subjects (**Figure 1**). This might be associated with the deficiency of assessment for sleep-related parameters such as midsleep time, sleep latency, and daytime dysfunction in this trial. Sleep duration did not mean good sleep quality for subjects. The sleep-wake cycle is important for brain aging and is a potential way to improve CI symptoms (30). Therefore, these results suggested that the older age, the higher risk for CI it was, and it was not related to education duration under ignoring education degree.

There were differences in gut microbiota between the control and CI groups. In the CI group, the Faith_pd index was significantly higher than that in the control but other characteristics related to alpha diversity had no significant differences (**Figure 2A**). Furthermore, gut microbial beta diversity had a significant difference between the two groups ($p < 0.002$, **Figure 2B**) and this suggested that patients with CI had a distinct structure and composition of gut microbes. Actinobacteria and Proteobacteria were increased but Bacteroidetes and Firmicutes were reduced in the CI group (**Figure 3A**). Patients with Alzheimer's disease had an increase in the abundance of Bacteroidetes but decreases in Firmicutes (31). Furthermore, *Bifidobacterium*, *Alistipes*, *Lactobacillus*, *Streptococcus*, [*Ruminococcus*] *torques* group, *Ruminococcus* 2, *Escherichia-Shigella*, and *Klebsiella* were increased in the CI group (**Figure 3B**). The proportions of *Bifidobacterium*, *Butyricicoccus*, and *Clostridium XIVb* were negatively correlated with the presence of CI in patients with Parkinson's disease (32). This was not consistent with our results. *Lactobacillus* and *Bifidobacterium* are common beneficial bacteria and have been demonstrated to involve in the synthesis of neurotransmitters such as acetylcholine, serotonin, and gamma-aminobutyric acid (32). *Escherichia-Shigella* is a conditional pathogen and is related to some diseases such as intestinal disorder and CI. An increase in the proportion of *Escherichia-Shigella* has been revealed to be associated with a peripheral inflammatory state in patients with CI and brain amyloidosis (33). Furthermore, patients with post-stroke CI had higher abundances of Enterococcus, Bacteroides, and *Escherichia-Shigella* and a lower Faecalibacterium vs. patients with stroke (34). Venn diagram showed there were special taxa in the control and CI groups and displayed the distinct gut microbial composition from each other (**Figure 3C**). Therefore, based on the differences in gut microbial composition, microbial markers might be explored for CI in the elderly.

Linear discriminant analysis effect size (LEfSe) revealed the differential taxa including *Desulfovibrio*, *Sutterella*, *Eubacterium*, *Butyricimonas*, *Akkermansia*, *Streptococcus*, and *Lactobacillus* in the CI group (**Figure 4A**). Compared to the control group, *Sutterella*, *Butyricimonas*, and *Lactobacillus* significantly increased in the CI group. APOE4 is a risk factor for Alzheimer's disease and APOE4 carrier has an increased rate of cognitive decline. A study has shown the abundance of *Sutterella* was significantly increased in male EFAD transgenic mice (35). Compared to the patients with Parkinson's disease having normal cognition, the proportions of *Blautia* and *Ruminococcus* were reduced (36). Our results also showed a low abundance of *Blautia* in the CI group. In a cohort trial study, *Parabacteroides*, *Verrucomicrobia*, *Akkermansia*, *Butyricimonas*, *Veillonella*, *Odoribacter*, *Mucispirillum*, *Bilophila*, *Enterococcus*, and *Lactobacillus* were significantly enriched in patients with Parkinson's disease

than in controls (37), and some increased genera such as *Akkermansia*, *Butyricimonas*, and *Lactobacillus* were same to our findings.

We evaluated changes in gene functions of gut microbiota using PICRUSt analysis. The results showed that nutrient metabolisms such as glycolysis/gluconeogenesis, retinol metabolism, fatty acid metabolism, D-alanine metabolism, and pyruvate metabolism were upregulated in the CI group (**Figure 5**). The reduction of cognitive function is related to changes in brain glucose utilization (38). Compared to rats with normal cognition, significant differences in protein expression were demonstrated vs. the rats with CI and this was associated with the glycolysis/gluconeogenesis pathway. Supplement with ω-3 docosahexaenoic acid is an important way to prevent brain aging and the development of Alzheimer's disease (39), and thus increased fatty acid metabolism might be positively related to the development of CI. Furthermore, pyruvate has been reported to improve neuron survival and eliminate reactive oxygen species to alleviate CI symptoms in rats with Alzheimer's disease (40). Therefore, these studies were consistent with our findings, and upregulated metabolisms were positively related to CI symptoms. There were huge differences in gut microbial composition and gene functions, and thus gut microbiota had great potential to apply to microbial markers to diagnose the CI development. A random forest model was used to identify gut microbial markers for CI and the results showed that 15 genera were selected to predict the development of CI with an AUC value of 78.4% (**Figure 6**). Gut microbial markers have been applied to predict and diagnose early colorectal cancer and early hepatocellular carcinoma (15, 16). Prevention of CI is necessary for the elderly because it is difficult to reverse. Therefore, gut microbiota as a biomarker contributed to the diagnosis and prevention of CI in the elderly.

CONCLUSION

Collectively, the abnormal gut microbial composition is associated with CI. A random forest model reveals the gut microbial markers of CI, and they have the potential to predict the development of CI and prevent CI based on gut microbial sequencing for the elderly.

DATA AVAILABILITY STATEMENT

The datasets presented in this study can be found in online repositories. The names of the repository/repositories and accession number(s) can be found in the article/supplementary material.

ETHICS STATEMENT

The studies involving human participants were reviewed and approved by the Ethics of Clinical Experiments of the Wuxi People's Hospital (KS2019039). The patients/participants provided their written informed consent to participate in this study.

AUTHOR CONTRIBUTIONS

SL performed experiments and wrote the manuscript. YZ and WL performed the study conceptualization. YY and QX performed data analysis and interpretation. ZW and BZ performed the data curation. JY contributed to the data acquisition and supervision. SW performed the data validation. KH developed the experimental design and revised the manuscript. All authors contributed to the article and approved the submitted version.

FUNDING

This work was funded by the Young Project of the Wuxi Health Committee (Q201914), the Top Talent Support Program for Young and Middle-Aged People of Wuxi Health (BJ2020008), and the Major Project of the Wuxi Health Committee (Z202002).

ACKNOWLEDGMENTS

We thank the peer reviewers for their helpful comments on the manuscript.

REFERENCES

1. Iadecola C, Gottesman RF. Neurovascular and cognitive dysfunction in hypertension. *Circ Res.* (2019) 124:1025–44. doi: 10.1161/circresaha.118.313260
2. Ismail Z, Elbayoumi H, Fischer CE, Hogan DB, Millikin CP, Schweizer T, et al. Prevalence of depression in patients with mild cognitive impairment: a systematic review and meta-analysis. *JAMA Psychiatry.* (2017) 74:58–67. doi: 10.1001/jamapsychiatry.2016.3162
3. Bradburn S, Murgatroyd C, Ray N. Neuroinflammation in mild cognitive impairment and Alzheimer's disease: a meta-analysis. *Ageing Res Rev.* (2019) 50:1–8. doi: 10.1016/j.arr.2019.01.002
4. Eshkoor SA, Hamid TA, Mun CY, Ng CK. Mild cognitive impairment and its management in older people. *Clin Interv Aging.* (2015) 10:687–93. doi: 10.2147/cia.S73922
5. Iwashyna TJ, Ely EW, Smith DM, Langa KM. Long-term cognitive impairment and functional disability among survivors of severe sepsis. *JAMA.* (2010) 304:1787–94. doi: 10.1001/jama.2010.1553
6. Yaffe K, Laffan AM, Harrison SL, Redline S, Spira AP, Ensrud KE, et al. Sleep-disordered breathing, hypoxia, and risk of mild cognitive impairment and dementia in older women. *JAMA.* (2011) 306:613–9. doi: 10.1001/jama.2011.1115
7. Jorde R, Kubiak J, Svartberg J, Fuskevåg OM, Figenschau Y, Martinaityte I, et al. Vitamin D supplementation has no effect on cognitive performance after four months in mid-aged and older subjects. *J Neurol Sci.* (2019) 396:165–71. doi: 10.1016/j.jns.2018.11.020
8. Ward A, Tardiff S, Dye C, Arrighi HM. Rate of conversion from prodromal Alzheimer's disease to Alzheimer's dementia: a systematic review of the literature. *Dement Geriatr Cogn Dis Extra.* (2013) 3:320–32. doi: 10.1159/000354370

9. Brodaty H, Connors MH, Ames D, Woodward M. Progression from mild cognitive impairment to dementia: a 3-year longitudinal study. *Aust N Z J Psychiatry.* (2014) 48:1137–42. doi: 10.1177/0004867414536237
10. Tisher A, Salardini A, A. Comprehensive Update on Treatment of Dementia. *Semin Neurol.* (2019) 39:167–78. doi: 10.1055/s-0039-1683408
11. Cryan JF, O'Riordan KJ, Cowan CSM, Sandhu KV, Bastiaanssen TFS, Boehme M, et al. The microbiota-gut-brain axis. *Physiol Rev.* (2019) 99:1877–2013. doi: 10.1152/physrev.00018.2018
12. Buffington SA, Di Prisco GV, Auchtung TA, Ajami NJ, Petrosino JF, Costa-Mattioli M. Microbial reconstitution reverses maternal diet-induced social and synaptic deficits in offspring. *Cell.* (2016) 165:1762–75. doi: 10.1016/j.cell.2016.06.001
13. Bedarf JR, Hildebrand F, Coelho LP, Sunagawa S, Bahram M, Goeser F, et al. Functional implications of microbial and viral gut metagenome changes in early stage L-DOPA-naïve Parkinson's disease patients. *Genome Med.* (2017) 9:39. doi: 10.1186/s13073-017-0428-y
14. D'Amato A, Di Cesare Mannelli L, Lucarini E, Man AL, Le Gall G, Branca JJV, et al. Faecal microbiota transplant from aged donor mice affects spatial learning and memory via modulating hippocampal synaptic plasticity- and neurotransmission-related proteins in young recipients. *Microbiome.* (2020) 8:140. doi: 10.1186/s40168-020-00914-w
15. Ren Z, Li A, Jiang J, Zhou L, Yu Z, Lu H, et al. Gut microbiome analysis as a tool towards targeted non-invasive biomarkers for early hepatocellular carcinoma. *Gut.* (2019) 68:1014–23. doi: 10.1136/gutjnl-2017-315084
16. Yu J, Feng Q, Wong SH, Zhang D, Liang QY, Qin Y, et al. Metagenomic analysis of faecal microbiome as a tool towards targeted non-invasive biomarkers for colorectal cancer. *Gut.* (2017) 66:70–8. doi: 10.1136/gutjnl-2015-309800
17. Aasmets O, Lüll K, Lang JM, Pan C, Kuusisto J, Fischer K, et al. Machine learning reveals time-varying microbial predictors with complex effects on glucose regulation. *mSystems.* (2021) 6:e01191-20. doi: 10.1128/mSystems.01191-20
18. Lin D, Zheng X, Sanogo B, Ding T, Sun X, Wu Z. Bacterial composition of midgut and entire body of laboratory colonies of *Aedes aegypti* and *Aedes albopictus* from Southern China. *Parasit Vectors.* (2021) 14:586. doi: 10.1186/s13071-021-05050-4
19. Segata N, Izard J, Waldron L, Gevers D, Miropolsky L, Garrett WS, et al. Metagenomic biomarker discovery and explanation. *Genome Biol.* (2011) 12:R60. doi: 10.1186/gb-2011-12-6-r60
20. Langille MG, Zaneveld J, Caporaso JG, McDonald D, Knights D, Reyes JA, et al. Predictive functional profiling of microbial communities using 16S rRNA marker gene sequences. *Nat Biotechnol.* (2013) 31:814–21. doi: 10.1038/nbt.2676
21. Schepper JD, Collins F, Rios-Arce ND, Kang HJ, Schaefer L, Gardinier JD, et al. Involvement of the gut microbiota and barrier function in glucocorticoid-induced osteoporosis. *J Bone Miner Res.* (2020) 35:801–20. doi: 10.1002/jbmr.3947
22. Ma Q, Xing C, Long W, Wang HY, Liu Q, Wang RF. Impact of microbiota on central nervous system and neurological diseases: the gut-brain axis. *J Neuroinflammation.* (2019) 16:53. doi: 10.1186/s12974-019-1434-3
23. Valles-Colomer M, Falony G, Darzi Y, Tigchelaar EF, Wang J, Tito RY, et al. The neuroactive potential of the human gut microbiota in quality of life and depression. *Nat Microbiol.* (2019) 4:623–32. doi: 10.1038/s41564-018-0337-x
24. Spychala MS, Venna VR, Jandzinski M, Doran SJ, Durgan DJ, Ganesh BP, et al. Age-related changes in the gut microbiota influence systemic inflammation and stroke outcome. *Ann Neurol.* (2018) 84:23–36. doi: 10.1002/ana.25250
25. Fattorusso A, Di Genova L, Dell'Isola GB, Mencaroni E, Esposito S. Autism spectrum disorders and the gut microbiota. *Nutrients.* (2019) 11:521. doi: 10.3390/nu11030521
26. Liu Y, Kong C, Gong L, Zhang X, Zhu Y, Wang H, et al. The association of post-stroke cognitive impairment and gut microbiota and its corresponding metabolites. *J Alzheimers Dis.* (2020) 73:1455–66. doi: 10.3233/jad-191066
27. Lövdén M, Fratiglioni L, Glymour MM, Lindenberger U, Tucker-Drob EM. Education and cognitive functioning across the life span. *Psychol Sci Public Interest.* (2020) 21:6–41. doi: 10.1177/1529100620920576
28. Laditka SB, Laditka JN. More education may limit disability and extend life for people with cognitive impairment. *Am J Alzheimers Dis Other Demen.* (2014) 29:436–47. doi: 10.1177/1533317513518648
29. Suh SW, Han JW, Lee JR, Byun S, Kwon SJ, Oh SH, et al. Sleep and cognitive decline: a prospective nondemented elderly cohort study. *Ann Neurol.* (2018) 83:472–82. doi: 10.1002/ana.25166
30. Yaffe K, Falvey CM, Hoang T. Connections between sleep and cognition in older adults. *Lancet Neurol.* (2014) 13:1017–28. doi: 10.1016/s1474-4422(14)70172-3
31. Vogt NM, Kerby RL, Dill-McFarland KA, Harding SJ, Merluzzi AP, Johnson SC, et al. Gut microbiome alterations in Alzheimer's disease. *Sci Rep.* (2017) 7:13537. doi: 10.1038/s41598-017-13601-y
32. Qian Y, Yang X, Xu S, Wu C, Song Y, Qin N, et al. Alteration of the fecal microbiota in Chinese patients with Parkinson's disease. *Brain Behav Immun.* (2018) 70:194–202. doi: 10.1016/j.bbi.2018.02.016
33. Cattaneo A, Cattane N, Galluzzi S, Provasi S, Lopizzo N, Festari C, et al. Association of brain amyloidosis with pro-inflammatory gut bacterial taxa and peripheral inflammation markers in cognitively impaired elderly. *Neurobiol Aging.* (2017) 49:60–8. doi: 10.1016/j.neurobiolaging.2016.08.019
34. Huang Y, Shen Z, He W. Identification of gut microbiome signatures in patients with post-stroke cognitive impairment and affective disorder. *Front Aging Neurosci.* (2021) 13:706765. doi: 10.3389/fnagi.2021.706765
35. Maldonado Weng J, Parikh I, Naqib A, York J, Green SJ, Estus S, et al. Synergistic effects of APOE and sex on the gut microbiome of young EFAD transgenic mice. *Mol Neurodegener.* (2019) 14:47. doi: 10.1186/s13024-019-0352-2
36. Ren T, Gao Y, Qiu Y, Jiang S, Zhang Q, Zhang J, et al. Gut microbiota altered in mild cognitive impairment compared with normal cognition in sporadic Parkinson's disease. *Front Neurol.* (2020) 11:137. doi: 10.3389/fneur.2020.00137
37. Lin CH, Chen CC, Chiang HL, Liou JM, Chang CM, Lu TP, et al. Altered gut microbiota and inflammatory cytokine responses in patients with Parkinson's disease. *J Neuroinflammation.* (2019) 16:129. doi: 10.1186/s12974-019-1528-y
38. Freeman WM, VanGuilder HD, Bennett C, Sonntag WE. Cognitive performance and age-related changes in the hippocampal proteome. *Neuroscience.* (2009) 159:183–95. doi: 10.1016/j.neuroscience.2008.12.004
39. Román GC, Jackson RE, Gadhia R, Román AN, Reis J. Mediterranean diet: the role of long-chain ω-3 fatty acids in fish; polyphenols in fruits, vegetables, cereals, coffee, tea, cacao and wine; probiotics and vitamins in prevention of stroke, age-related cognitive decline, and Alzheimer disease. *Rev Neurol.* (2019) 175:724–41. doi: 10.1016/j.neurol.2019.08.005
40. Wang X, Hu X, Yang Y, Takata T, Sakurai T. Systemic pyruvate administration markedly reduces neuronal death and cognitive impairment in a rat model of Alzheimer's disease. *Exp Neurol.* (2015) 271:145–54. doi: 10.1016/j.expneurol.2015.06.008

Conflict of Interest: The authors declare that the research was conducted in the absence of any commercial or financial relationships that could be construed as a potential conflict of interest.

Publisher's Note: All claims expressed in this article are solely those of the authors and do not necessarily represent those of their affiliated organizations, or those of the publisher, the editors and the reviewers. Any product that may be evaluated in this article, or claim that may be made by its manufacturer, is not guaranteed or endorsed by the publisher.

Copyright © 2022 Lu, Yang, Xu, Wang, Yu, Zhang, Wang, Zhang, Lu and Hong. This is an open-access article distributed under the terms of the Creative Commons Attribution License (CC BY). The use, distribution or reproduction in other forums is permitted, provided the original author(s) and the copyright owner(s) are credited and that the original publication in this journal is cited, in accordance with accepted academic practice. No use, distribution or reproduction is permitted which does not comply with these terms.

frontiers in Neurology

ORIGINAL RESEARCH
published: 21 February 2022
doi: 10.3389/fneur.2022.823919

Brain Activity Changes in Slow 5 and Slow 4 Frequencies in Patients With Optic Neuritis: A Resting State Functional MRI Study

*Kai Yan[1], Wen-Qing Shi[2], Ting Su[3], Xu-Lin Liao[4], Shi-Nan Wu[2], Qiu-Yu Li[2], Jing Yu[5], Hui-Ye Shu[2], Li-Juan Zhang[2], Yi-Cong Pan[2] and Yi Shao[2]**

[1] Department of Radiology, Hangzhou TCM Hospital Affiliated to Zhejiang Chinese Medical University, Hangzhou, China, [2] Department of Ophthalmology, Jiangxi Centre of National Clinical Ophthalmology Institute, The First Affiliated Hospital of Nanchang University, Nanchang, China, [3] Department of Ophthalmology, Massachusetts Eye and Ear, Harvard Medical School, Boston, MA, United States, [4] Department of Ophthalmology and Visual Sciences, The Chinese University of Hong Kong, Hong Kong, Hong Kong SAR, China, [5] Department of Acupuncture and Moxibustion, Hangzhou TCM Hospital Affiliated to Zhejiang Chinese Medical University, Hangzhou, China

Objective: We used the amplitude of low-frequency fluctuation (ALFF) method to investigate spontaneous brain activity in patients with optic neuritis (ON) in specific frequency bands.

Data and Methods: A sample of 21 patients with ON (13 female and eight male) and 21 healthy controls (HCs) underwent functional magnetic resonance imaging (fMRI) scans in the resting state. We analyzed the ALFF values at different frequencies (slow-4 band: 0.027–0.073 Hz; slow-5 band: 0.01–0.027 Hz) in ON patients and HCs.

Results: In the slow-4 frequency range, compared with HCs, ON patients had apparently lower ALFF in the insula and the whack precuneus. In the slow-5 frequency range, ON patients showed significantly increased ALFF in the left parietal inferior and the left postcentral.

Conclusion: Our results suggest that ON may be involved in abnormal brain function and can provide a basis for clinical research.

Keywords: amplitude of low-frequency fluctuation, optic neuritis, resting state, functional magnetic resonance imaging, slow 5 and slow 4 frequencies

OPEN ACCESS

Edited by:
Yuzhen Xu,
Tongji University, China

Reviewed by:
Haijun Li,
Nanchang University, China
Ting Xue,
Inner Mongolia University of Science and Technology, China

***Correspondence:**
Yi Shao
freebee99@163.com

Specialty section:
This article was submitted to Neurological Biomarkers, a section of the journal Frontiers in Neurology

Received: *28 November 2021*
Accepted: *13 January 2022*
Published: *21 February 2022*

Citation:
Yan K, Shi W-Q, Su T, Liao X-L, Wu S-N, Li Q-Y, Yu J, Shu H-Y, Zhang L-J, Pan Y-C and Shao Y (2022) Brain Activity Changes in Slow 5 and Slow 4 Frequencies in Patients With Optic Neuritis: A Resting State Functional MRI Study. Front. Neurol. 13:823919. doi: 10.3389/fneur.2022.823919

INTRODUCTION

Optic neuritis (ON) refers to all inflammatory lesions of the optic nerve, usually manifesting as acute or subacute vision loss with or without orbital pain, eye rotation pain, visual field defects or other clinical symptoms, and is the most common neurological disease leading to visual loss in young and middle-aged adults (1). The causes of optic neuritis are thought to include demyelinating diseases of the central nervous system, infectious diseases and immune diseases. A survey found that ON was the second most damaging disease among patients under 50 years of age after glaucomatous optic neuropathy (2). Worldwide, the annual incidence of unilateral optic neuritis is (0.94–2.18)/100,000, of which the annual incidence in the United Kingdom is 1/100,000 and that in Japan is 1.6/100,000 (3, 4). ON occurs predominantly in people aged 20–50, with an average age of onset of 36 years, and more than 70% of patients are female (5). Evidence suggests that there are

racial and population differences in ON, which is more common among young, middle-aged, white females (6). Studies have shown that 80% of patients may have severe vision loss, and more than 60% of patients have monocular or binocular vision loss within 7.7 days after the first episode (7). The high incidence, young age of onset, high risk of blindness, and poor visual prognosis of ON have brought great physical and psychological burdens to patients and families, seriously affecting patients' quality of life. Its early diagnosis and treatment has become the focus of current research and the development of neuroimaging has provided a new method for the diagnosis of ON.

Magnetic resonance imaging (MRI) techniques have evolved rapidly to provide a non-invasive neuroimaging method that can assess functional and structural changes in the brain (8). Previous studies have demonstrated that synchronous brain activity is closely related to visual experience (9, 10). Resting state functional MRI (rsfMRI) was first proposed by Biswal (11) to assess consistent patterns of spontaneous fluctuation of blood oxygen level dependent (BOLD) signals during rest. These signals can be used to measure interhemispheric coordination (12).

The amplitude of low-frequency fluctuation is a widely used re-fMRI study method, which reflects the blood oxygen level-dependent (BOLD) signal of spontaneous neural activity in the low-frequency band (0.01–0.08 Hz) and can detect the intrinsic local activity of the brain. In recent years, domestic and international researchers have started to use sub-band ALFF analysis to study the correlation between neural activity and cognitive function in different neurological diseases by subdividing the frequency range of spontaneous brain activity, including slow-6 (0–0.01Hz), slow-5 (0.01–0.027Hz), slow-4 (0.027–0.073Hz), slow-3 (0.073–0.198Hz), slow-6 (0–0.01Hz), and slow-2 (0.198–0.250Hz). Among them, slow-2, 3 and 6 frequencies correspond to high frequency physiological noise interference, white matter signal and low frequency drift signal, respectively. And the study of slow-4 and slow-5 specific frequency bands can study the spatial distribution characteristics of brain regions with abnormal spontaneous functional activity in the brain in more depth, which in turn reduces the interference of noise in other frequency bands and increases the sensitivity of detecting abnormal activity in brain regions. RsfMRI and both functional and anatomic imaging have been applied to various ocular diseases (13–19).

The present study aims to determine whether spontaneous brain activity is related to the clinical characteristics of patients with ON. To detect the spontaneous brain activity of ON patients and healthy controls (HCs), we used the amplitude of low-frequency fluctuation (ALFF) technique to measure activity in different low frequency bands (slow 4 band: 0.027–0.073 Hz and slow 5 band: 0.01–0.027 Hz) and compared these between groups.

MATERIALS AND METHODS

Participants

This study included 21 ON patients (13 females and eight males) admitted to the Ophthalmology Department of the First Affiliated Hospital of Nanchang University (Nanchang, China). The selection criteria for all ON patients were: (1) the presence of eye pain related to acute vision loss; (2) nerve fiber damage and abnormal vision (**Figure 1**); (3) pupil block or abnormal visual evoked potential; (4) no other apparent cause of acute vision loss; (5) no medication taken before the examination; (6) no drug, alcohol, or tobacco addictions; and (7) no history of organ transplantation.

In addition, 21 age-matched HCs (13 females and eight males) were recruited. The inclusion criteria for HCs were as follows: (1) no abnormalities in brain parenchyma; (2) unilateral bare eye vision$\geq$1.0 (3) normal nervous system.

All participants are able to go through an MRI scan. We used logMAR (Logarithm of Mininal Angle Resolution) method to obtain the best-corrected visual acuity (BCVA) of both groups and mean hospital anxiety and depression scale (HADS) to get the association with ALFF values.

The study was approved by the ethics committee of the First Affiliated Hospital of Nanchang University, and all methods were applied in accordance with the Helsinki Declaration. The study design description was provided to the participants before they signed informed consent forms.

MRI Parameters

All subjects underwent MRI scans in a 3-Tesla scanner (Trio, Siemens, Munich, Germany). They are constrained to the inspection area of the instrument and their heads are secured to prevent movement during the scanning process. During examination, the subjects remained awake, closed their eyes, and relaxed while avoiding focused thought. All scans were conducted by the same imaging physician, who observed the subjects until the process was completed successfully. Routine brain localization and T1 and T2 sequences were performed first. The specific parameters were: repeat time (TR) = 1,900 ms; echo time (TE) = 2.26 ms, thickness =1.0 mm, gap = 0.5 mm, acquisition matrix = 256 × 256, field of view (FOV) = 250 mm × 250 mm, and reversal angle = 90°. No substantial brain lesions were identified in the scanning process. RsfMRI data were acquired using a gradient-recalled echo sequence. The specific parameters were: TR = 2,000 ms, TE = 30 ms, thickness = 4.0 mm, gap = 1.2 mm, acquisition matrix = 64 × 64, flip angle = 90°, FOV = 220 mm × 220 mm. Data were collected continuously at 240 time points, and the scanning range included the whole brain.

MRI Data Processing

Data were obtained from functional images using the MRIcro software package (www.MRIcro.com) after prefiltering. SPM8 (http://www.fil.ion.ucl.ac.uk/spm) and DPARSFA (http://rfmri.org/ DPARSF) software were used to preliminarily analyze data before conversion to the NIFTI format. During magnetization equilibration the first 10 time points were discarded. Subjects were excluded if they had 1.5 angular motion or more than 1.5 mm maximum shift in the x,

FIGURE 1 | Example of optic neuritis observed using a FC and FFA. FC, fundus camera; FFA, fluorescence fundus angiography.

TABLE 1 | Clinical characteristics of patients between ON and HC groups.

Characteristics	ON	HCs	*t*-value	*p*-values
Male/female	813	813	NA	NA
Age (years)	44.83 ± 10.71	45.83 ± 11.38	−0.222	0.821
Weight (kg)	57.08 ± 7.30	58.85 ± 5.85	−0.463	0.652
Height (cm)	160.81 ± 9.31	161.38 ± 6.28	−0.485	0.634
BMI (kg/m^2)	21.13 ± 1.62	21.17 ± 1.27	−0.056	0.963
Duration of ON (days)	4.67 ± 3.26	NA	NA	NA
Duration from onset of ON to rs-fMRI scan (days)	5.42 ± 2.94	NA	NA	NA
Best-corrected VA, right	0.25 ± 0.32*	1.30 ± 0.31	−8.138	<0.001
Best-corrected VA, left	0.85 ± 0.52*	1.28 ± 0.32	−2.481	<0.001

*Independent t-tests comparing the two groups (*P < 0.05) represented statistically significant differences). ON, optic neuritis; HCs, healthy controls; NA, not applicable; BMI, body mass index; rs-fMRI, resting-state functional magnetic resonance; VA, visual acuity.*

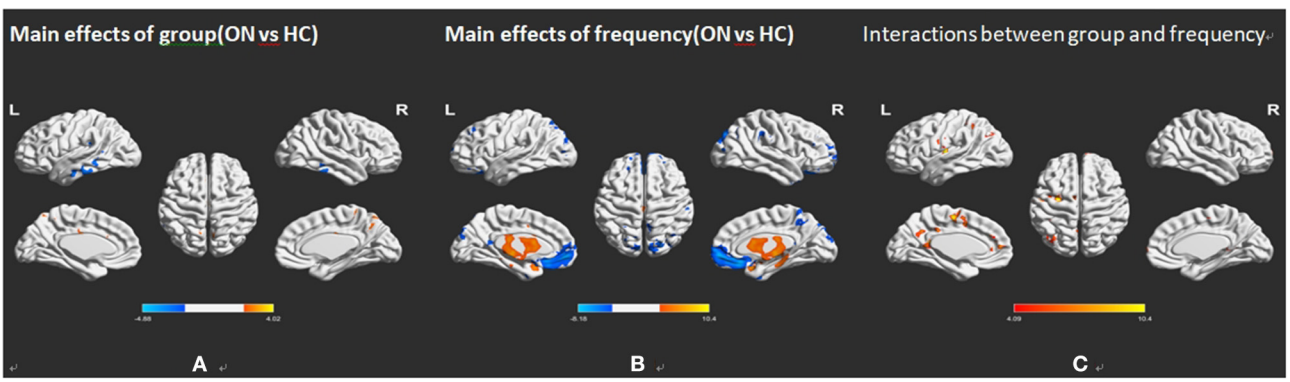

FIGURE 2 | Frequency-associated ALFF analyses between the ON and HC groups. **(A)** Main effects of group, **(B)** main effects of frequency band, and **(C)** their interactions, with Gaussian random field theory correction, voxel-level $P < 0.01$ and cluster-level $P < 0.05$. Compared with HC, red represents the brain areas with increased AlFF, and blue represents the brain areas with decreased AlFF in patients with ON. ALFF, amplitude of low-frequency fluctuation; ON, optic neuritis; L, left; HC, healthy control; R, right.

TABLE 2 | Frequency-associated ALFF differences, with Gaussian random field theory correction, voxel-level $P < 0.01$ and cluster-level $P < 0.05$.

Brain area	BA	Peak (MNI)			Peak voxels	*T*-value
		X	Y	Z		
Main effects of group						
Left cingulum ant	24	−6	10	20	89	13.11
Right cingulum ant	24	0	−12	30	83	23.11
Right cerebellum	/	18	−87	−45	800	13.67
Right temporal inf	20	45	−30	−21	117	10.02
Left temporal inf	21	−57	−12	−30	331	18.68
Left parietal inf	40	−54	−36	42	82	18.31
Main effects of frequency band						
Right rectus	11	9	27	−18	930	−1.88
Right occipital sup	19	24	−84	39	106	−6.2
Left caudate	24	−21	−36	12	3,044	10.4
Left temporal pole sup	38	−3	12	−24	145	7.08

ALFF, amplitude of low-frequency fluctuation; BA, Brodmann area; MNI, Montreal neurological institute.

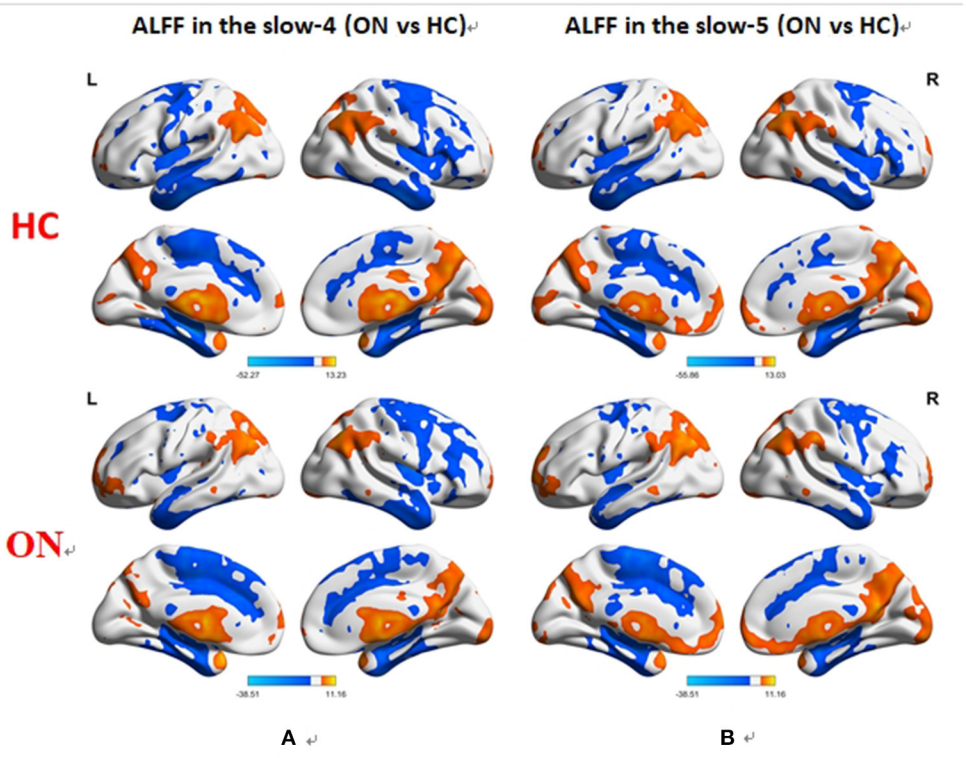

FIGURE 3 | Difference in the ALFF values in the brain between the ON and HC groups across slow-4 **(A)** and slow-5 **(B)** frequencies, with Gaussian random field theory correction, voxel-level $P < 0.01$ and cluster-level $P < 0.05$. Compared with HC, red represents the brain areas with increased AlFF, and blue represents the brain areas with decreased AlFF in patients with ON. ALFF, amplitude of low-frequency fluctuation; ON, optic neuritis; L, left; HC, healthy control; R, right.

y, or z direction during the fMRI examination. After the head motion correction, the fMRI images were spatially normalized to the Montreal Neurological Institute space criteria using the standard echo-planar imaging template and resampling the images at a resolution of 3 mm × 3 mm × 3 mm. On the basis of the above, the signals of slow-4 and slow-5 were extracted separately using band-pass filtering oscilloscope, and the ALFF values

TABLE 3 | In the slow-4 band (0.027–0.073 Hz), ALFF differences between the PHN and HC groups with Gaussian random field theory correction, voxel-level $P < 0.01$ and cluster-level $P < 0.05$.

Brain area	BA	Peak (MNI)			Peak voxels	*T*-value
		X	Y	Z		
ON<HCs						
Left insula	13	−39	−12	12	173	23.01
Left precuneus	31	−3	−54	33	111	12.67

ALFF, amplitude of low-frequency fluctuation; ON, optic neuritis; HCs, healthy controls; BA, Brodmann area; MNI, Montreal neurological institute.

TABLE 4 | In the slow-5 band (0.001–0.027 Hz), ALFF differences between the PHN and HC groups with Gaussian random field theory correction, voxel-level $P < 0.01$ and cluster-level $P < 0.05$.

Brain area	BA	Peak (MNI)			Peak voxels	*T*-value
		X	Y	Z		
ON>HCs						
Left parietal inf	40	−30	−48	54	109	18.68
Left postcentral	6	−33	−21	45	417	18.31

ALFF, amplitude of low-frequency fluctuation; ON, optic neuritis; HCs, healthy controls; BA, Brodmann area; MNI, Montreal neurological institute.

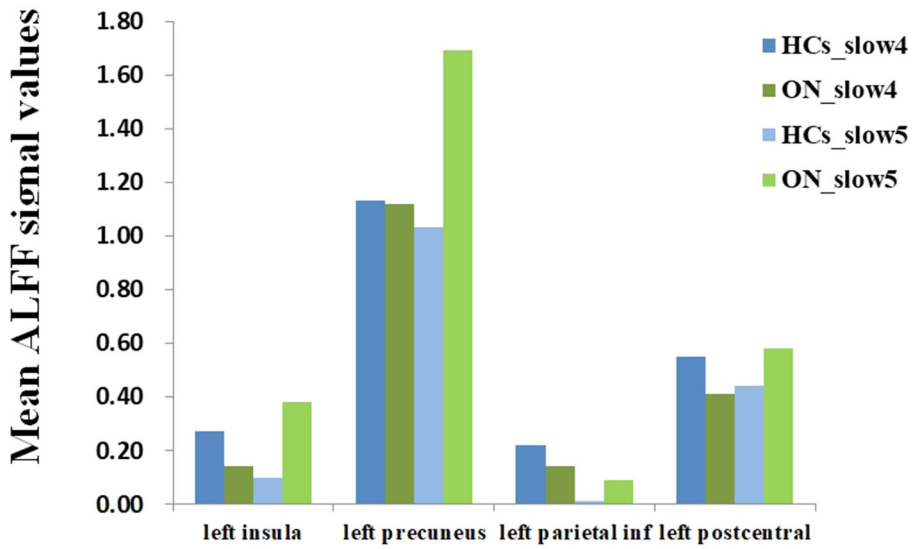

FIGURE 4 | The mean ALFF values of altered brain regions between the ON and HCs. ALFF, amplitude of low-frequency fluctuation; ON, optic neuritis; HCs, healthy controls.

were calculated and analyzed by REST software (http://sourceforge.net/projects/testing-fmri).

Statistical Analysis

Student's *t*-test was used to compare ALFF data between groups (20). A two-way analysis of variance and *post-hoc* tests were used to compare interaction s between groups and frequency bands. Based on Gaussian random field theory [$z > 2.3$, crowd >40 voxels, $P < 0.01$, false detection rate (FDR) corrected], we regulate the voxel offset ($P < 0.05$) as the statistical premise for comparisons.

Brain-Behavior Correlation Analysis

Pearson correlation analysis was used to look for associations between ALFF and clinical level using a threshold of $P < 0.05$ for statistical significance.

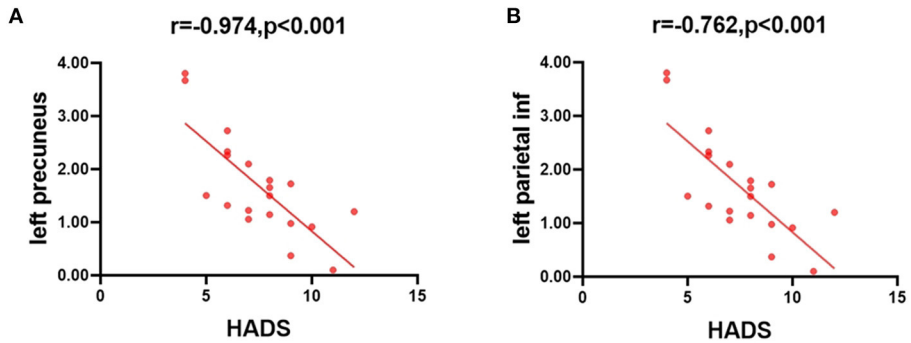

FIGURE 5 | Correlations between the mean ALFF values and the clinical behaviors. **(A)** The HADS scores showed a negative correlation with the ALFF value of the slow-4 band in the left precuneus ($r = -0.974$, $P < 0.001$), and **(B)** the HADS scores showed a negative correlation with the ALFF value of the slow-4 band in the left parietal inf ($r = -0.762$, $P < 0.001$). ALFF, amplitude of low-frequency fluctuation; HADS, hospital anxiety and depression scale.

TABLE 5 | Amplitude of low-frequency fluctuation method applied in ophthalmological diseases.

Reference	Disease
Huang et al. (13)	Primary angle-closure glaucoma
Tan et al. (14)	Congenital comitant strabismus
Li et al. (15)	Monocular blindness
Pan et al. (18)	Acute eye pain
Shi et al. (16)	Corneal ulcer
Kang et al. (17)	Retinal detachment
Wu et al. (19)	Retinal vein occlusion

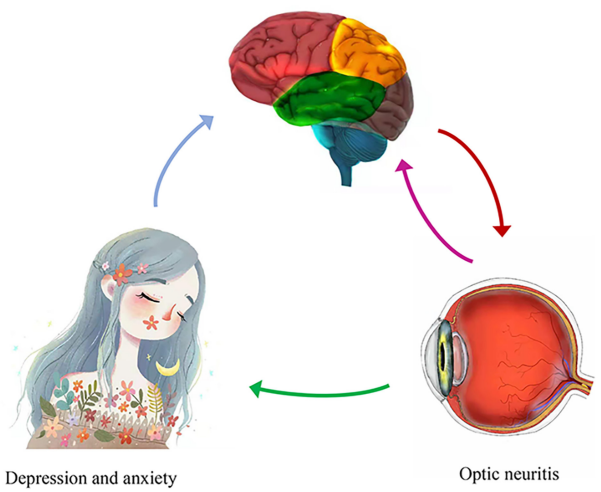

FIGURE 6 | Correlations between mean ALFF values and behavioral performance. Compared with the HCs, the ALFF value of the left precuneus was decreased in ON. And the patients with ON exhibited with more depression and anxiety. ALFF, amplitude of low-frequency fluctuation; HCs, healthy controls; ON, optic neuritis.

RESULTS

Clinical Characteristics of the Sample

No significant differences were found in age ($P = 0.821$), weight ($P = 0.652$), height ($P = 0.634$), or BMI ($P = 0.963$) between the two groups. Significant differences in best-corrected VA-right ($P < 0.001$) and best-corrected VA-left ($P < 0.001$) between the ON and HC groups. Details are shown in **Table 1**.

Changes in ALFF in Different Frequency Bands

As shown in **Figure 2A** and **Table 2**, he two-way repeated-measures ANOVA was applied to explore main effects between groups. There were apparently increased ALFF (ON > HCs) in the right cerebellum, the right temporal inferior (temporal inf), the left temporal inf, and the left parietal inferior (parietal inf) and remarkably decreased ALFF (ON < HCs) in the left cingulum anterior (cingulum ant) and the right cingulum ant in brain regions with a main effect of group.

In several brain regions (**Figure 2B**; **Table 2**), the ALFF differed significantly between frequency bands, including increased ALFF of the right rectus gyri (slow-5 > slow-4), right supraoccipital segment (right supraoccipital) and decreased ALFF (**Figure 2B**; **Table 2**). Slow-5 < slow-4 in left caudate and left temporal pole sup. No obvious interaction was found between groups and frequency bands (**Figure 2C**).

No bidirectional changes were detected by *post hoc t*-tests in ALFF across slow-4 and slow-5 frequencies. Significantly lower ALFF values were found in the left insula and the left precuneus in the slow-4 band, but significantly higher ALFF values in the left parietal inf and the left postcentral in the slow-5 band (**Figure 3**; **Tables 3**, **4**). The mean ALFF values between the ON patients and HCs are represented in **Figure 4**.

Correlation Analysis

In the patients with ON, the mean HADS scores negatively correlated with the ALFF values of the slow-4 band in the left precuneus ($r = -0.974$, $P < 0.001$), and in the left parietal inf ($r = -0.762$, $P < 0.001$) (**Figure 5**).

TABLE 6 | Brain regions alteration and its potential impact.

Brain regions	Experimental result	Brain function	Anticipated results
Insula	ON<HCs	Involved in consciousness, bodily impulses, and controlling and suppressing natural impulses	Abnormal activation of areas in the insula, diseases such as Alzheimer's disease and epilepsy
Precuneus	ON<HCs	Part of the default model network	Depression and anxiety
Parietal inf	ON>HCs	Part of the default model network, correlated with visual word recognition	Depression and anxiety, reflect compensation of the visual function
Postcentral	ON>HCs	Associated with information processing of tactile stimuli	Compensate the impairment of the sensorimotor dysfunction

ON, optic neuritis; HCs, healthy controls.

DISCUSSION

ALFF is a common clinical method reflecting the relationship between various clinical diseases and corresponding brain regions, as shown by many previous studies (**Table 5**).

Main Effect of the Groups

ALFF values were significantly higher in ON patients than HCs in the right cerebellum, the right temporal inf, the left temporal inf, and the left parietal inf, and lower than HCs in the left cingulum ant and the right cingulum ant.

The cerebellum is responsible for balance, cognitive tasks and motor control. We have shown using fMRI that the cerebellum is involved in cognition and memory (21). Previous studies have linked cerebellar dysfunction to schizophrenia (22), bipolar disorder (23), and depression (24) and demonstrated higher cerebellar activation in patients with primary progressive multiple sclerosis (MS) than in healthy controls (25–27). Similarly, we found that the ALFF value of the right cerebellum is higher in ON patients than in controls, which may reflect functional compensation for neural damage. In the resting state, the default model network (DMN) is continuously activated in the brain and is associated with many conscious activities (28–32). In about 20% of MS patients, ON is the most important clinical feature (33). Previous research has shown (34) that DMN connectivity of the anterior cingulate cortex of MS is weaker than in controls and that the converse is true in the posterior cingulate cortex, with relatively strong connectivity in MS. In line with these findings, the present study found decreased ALFF in patients with ON in the bilateral cingulum ant and left precuneus, and increased ALFF in the bilateral temporal inf and left parietal inf. ALFF may play vital roles in understanding functional reorganization in ON patients. Therefore, changes in the ALFF values of the bilateral cingulate gyrus and the left anterior gyrus may be explained by the DMN damage caused by ON, and the abnormalities of the bilateral temporal lobe and left parietal lobe inf may be related to the stability of the network.

Main Effect of Frequency Band

Higher ALFF was found at slow-5 than at slow-4 frequency range in the right rectus, and right occipital sup and the converse, with lower ALFF at slow-5 than at slow-4, in the left caudate and left temporal pole sup. Various neurophysiological mechanisms give rise to a range of oscillatory bands with a correspondingly wide range of physiological functions (35). Consistent with previous studies, we found abnormal amplitudes in the frontal, occipital and parietal cortex in ON (35), with the slow 4 range dominating the ventral prefrontal cortex (36).

Frequency-Dependent Alterations in ALFF in On Patients

We found bidirectional changes of ALFF both in the ON and HC groups across slow-4 and slow-5 frequency bands, providing new insight into frequency-dependent alterations of ON patients. Excessively secondary to ALFF decreased in insula and the punch precuneus gyrus in the slow-4 band, but ALFF values were seriously upper in the awaken parietal inf and the talk area over postcentral gyrus in the slow-5 band.

The insula is located in the depths of the lateral sulcus, (37) is anatomically related to the frontal, parietal, and temporal lobes (38) and plays vital roles in consciousness, bodily impulses, and in controlling and suppressing natural impulses (39, 40). Insular dysfunction has also been linked to diseases including Alzheimer's disease (41) and epilepsy (42). Previous studies have demonstrated abnormal activation of the insula in ON patients (43, 44). Based on these findings, we infer that ON may be involved in insula dysfunction.

Brain regions are associated with the DMN (45). It is increasingly evident that DMN vulnerability plays an important part in depression and anxiety (46). The present study found lower ALFF in the left precuneus in patients with ON which indicates that ON might lead to DMN damage (**Figure 6**).

The subparietal lobule participates in visual recognition (47). It is also related to diseases such as schizophrenia (48) and Alzheimer's disease (49). In our study, abnormality of left parietal atrial fibrillation in patients with ON may reflect compensation for abnormal visual function.

Located in the primary somatosensory cortex, the postcentral gyrus is associated with information processing triggered by tactile stimulation (50). The primary somatosensory cortex is involved in the perception of

pain (51). Previous research has demonstrated reduced white matter in the postcentral gyrus in patients with neuromyelitis optical (52). In addition, the sensorimotor system of patients with optic neuromyelitis is impaired (53). In the present study, we demonstrated increased ALFF values in the left postcentral gyrus in patients with ON, which may reflect compensation for sensorimotor dysfunction (**Table 6**).

LIMITATIONS

Our research has limitations. First, the sample size is relatively small. In addition, the correlation between clinical characteristics of ON and ALFF values require further investigation. Thus, we are looking forward to designing more experiments to further elucidate the underlying molecular mechanisms.

CONCLUSIONS

In summary, our study reveals abnormal spontaneous activities in regional brain areas in ON, and may provide insight into the underlying pathogenetic mechanism.

DATA AVAILABILITY STATEMENT

The raw data supporting the conclusions of this article will be made available by the authors, without undue reservation.

ETHICS STATEMENT

The study was approved by the Ethics Committee of the First Affiliated Hospital of Nanchang University, and all methods were applied in accordance with the Helsinki Declaration. The patients/participants provided their written informed consent to participate in this study. Written informed consent was obtained from the individual(s) for the publication of any potentially identifiable images or data included in this article.

AUTHOR CONTRIBUTIONS

KY, Y-CP, and W-QS performed the experiments and collected the data. TS, X-LL, and L-JZ designed the current study. S-NW, Q-YL, H-YS, JY, and YS given final approval of the version to be published. KY wrote the manuscript. All authors made substantial contributions to this research, read, and approved the final manuscript.

FUNDING

This research was supported by the National Natural Science Foundation of China (Nos. 81660158, 81160118, 81400372, 81460092, and 81500742), Natural Science research Foundation of Guangdong Province (Nos. 2017A030313614, 2017A020215187, and 2018A030313117), and Medical Science Foundation of Guangdong Province (No. A2016184).

REFERENCES

1. Beck RW, Gal RL. Treatment of acute optic neuritis: a summary of findings from the optic neuritis treatment trial. *Arch Ophthalmol.* (2008) 126:994–5. doi: 10.1001/archopht.126.7.994
2. Vedula SS, Brodney-Folse S, Gal RL, Beck R. Corticosteroids for treating optic neuritis. *Cochrane Database Syst Rev.* (2007) 24:CD001430. doi: 10.1002/14651858.CD001430.pub2
3. Wakakura M, Ishikawa S, Oono S, Tabuchi A, Kani K, Tazawa Y, et al. [Incidence of acute idiopathic optic neuritis and its therapy in Japan. Optic Neuritis Treatment Trial Multicenter Cooperative Research Group (ONMRG)]. *Nippon Ganka Gakkai Zasshi.* (1995) 99:93–7.
4. MacDonald BK, Cockerell OC, Sander JW, Shorvon SD. The incidence and lifetime prevalence of neurological disorders in a prospective community-based study in the UK. *Brain.* (2000) 123:665–76. doi: 10.1093/brain/123.4.665
5. Wilhelm H, Schabet M. The diagnosis and treatment of optic neuritis. *Dtsch Arztebl Int.* (2015) 112:616–25. doi: 10.3238/arztebl.2015.0616
6. Keltner JL, Johnson CA, Cello KE, Dontchev M, Gal RL, Beck RW, et al. Optic Neuritis Study, Visual field profile of optic neuritis: a final follow-up report from the optic neuritis treatment trial from baseline through 15 years. *Arch Ophthalmol.* (2010) 128:330–7. doi: 10.1001/archophthalmol.2010.16
7. Morrow MJ, Wingerchuk D. Neuromyelitis optica. *J Neuroophthalmol.* (2012) 32:154–66. doi: 10.1097/WNO.0b013e31825662f1
8. Brown HD, Woodall RL, Kitching RE, Baseler HA, Morland AB. Using magnetic resonance imaging to assess visual deficits: a review. *Ophthalmic Physiol Opt.* (2016) 36:240–65. doi: 10.1111/opo.12293
9. Foubert L, Bennequin D, Thomas MA, Droulez J, Milleret C. Interhemispheric synchrony in visual cortex and abnormal postnatal visual experience. *Front Biosci.* (2010) 15:681–707. doi: 10.2741/3640
10. Mima T, Oluwatimilehin T, Hiraoka T, Hallett M. Transient interhemispheric neuronal synchrony correlates with object recognition. *J Neurosci.* (2001) 21:3942–8. doi: 10.1523/JNEUROSCI.21-11-03942.2001
11. Biswal BB, Resting state fMRI: a personal history. *Neuroimage.* (2012) 62:938–44. doi: 10.1016/j.neuroimage.2012.01.090
12. Fox MD, Raichle ME. Spontaneous fluctuations in brain activity observed with functional magnetic resonance imaging. *Nat Rev Neurosci.* (2007) 8:700–11. doi: 10.1038/nrn2201
13. Huang X, Zhong YL, Zeng XJ, Zhou F, Liu XH, Hu PH, et al. Disturbed spontaneous brain activity pattern in patients with primary angle-closure glaucoma using amplitude of low-frequency fluctuation: a fMRI study. *Neuropsychiatr Dis Treat.* (2015) 11:1877–83. doi: 10.2147/NDT.S87596
14. Tan G, Huang X, Zhang Y, Wu AH, Zhong YL, Wu K, et al. A functional MRI study of altered spontaneous brain activity pattern in patients with congenital comitant strabismus using amplitude of low-frequency fluctuation. *Neuropsychiatr Dis Treat.* (2016) 12:1243–50. doi: 10.2147/NDT.S104756
15. Li Q, Huang X, Ye L, Wei R, Zhang Y, Zhong YL, et al. Altered spontaneous brain activity pattern in patients with late monocular blindness in middle-age using amplitude of low-frequency fluctuation: a resting-state functional MRI study. *Clin Interv Aging.* (2016) 11:1773–80. doi: 10.2147/CIA.S117292
16. Shi WQ, Wu W, Ye L, Jiang N, Liu WF, Shu YQ, et al. Altered spontaneous brain activity patterns in patients with corneal ulcer using amplitude of low-frequency fluctuation: an fMRI study. *Exp Ther Med.* (2019) 18:125–32. doi: 10.3892/etm.2019.7550
17. Kang HH, Shu YQ, Yang L, Zhu PW, Li D, Li QH, et al. Measuring abnormal intrinsic brain activities in patients with retinal detachment using amplitude of low-frequency fluctuation: a resting-state fMRI study. *Int J Neurosci.* (2019) 129:681–6. doi: 10.1080/00207454.2018.1554657
18. Pan ZM, Li HJ, Bao J, Jiang N, Yuan Q, Freeberg S, et al. Altered intrinsic brain activities in patients with acute eye pain using amplitude of low-frequency fluctuation: a resting-state fMRI study. *Neuropsychiatr Dis Treat.* (2018) 14:251–7. doi: 10.2147/NDT.S150051
19. Wu YY, Yuan Q, Li B, Lin Q, Zhu PW, Min YL, et al. Altered spontaneous brain activity patterns in patients with retinal vein occlusion indicated by the amplitude of low-frequency fluctuation: a functional magnetic resonance imaging study. *Exp Ther Med.* (2019) 18:2063–71. doi: 10.3892/etm.2019.7770

20. Gao L, Bai L, Zhang Y, Dai XJ, Netra R, Min Y, et al. Frequency-dependent changes of local resting oscillations in sleep-deprived brain. *PLoS ONE.* (2015) 10:e0120323. doi: 10.1371/journal.pone.0120323
21. Desmond JE, Fiez JA. Neuroimaging studies of the cerebellum: language, learning and memory. *Trends Cogn Sci.* (1998) 2:355–62. doi: 10.1016/S1364-6613(98)01211-X
22. Andreasen NC, Paradiso S, O'Leary DS. "Cognitive dysmetria" as an integrative theory of schizophrenia: a dysfunction in cortical-subcortical-cerebellar circuitry? *Schizophr Bull.* (1998) 24:203–18. doi: 10.1093/oxfordjournals.schbul.a033321
23. Baldacara L, Nery-Fernandes F, Rocha M, Quarantini LC, Rocha GG, Guimaraes JL, et al. Is cerebellar volume related to bipolar disorder? *J Affect Disord.* (2011) 135:305–9. doi: 10.1016/j.jad.2011.06.059
24. Bledsoe JC, Semrud-Clikeman M, Pliszka SR. Neuroanatomical and neuropsychological correlates of the cerebellum in children with attention-deficit/hyperactivity disorder–combined type. *J Am Acad Child Adolesc Psychiatry.* (2011) 50:593–601. doi: 10.1016/j.jaac.2011.02.014
25. Saini S, DeStefano N, Smith S, Guidi L, Amato MP, Federico A, et al. Altered cerebellar functional connectivity mediates potential adaptive plasticity in patients with multiple sclerosis. *J Neurol Neurosurg Psychiatry.* (2004) 75:840–6. doi: 10.1136/jnnp.2003.016782
26. Ceccarelli, Rocca MA, Valsasina P, Rodegher M, Falini A, Comi G, et al. Structural and functional magnetic resonance imaging correlates of motor network dysfunction in primary progressive multiple sclerosis. *Eur J Neurosci.* (2010) 31:1273–80. doi: 10.1111/j.1460-9568.2010.07147.x
27. Fox MD, Snyder AZ, Vincent JL, Corbetta M, Van Essen DC, Raichle ME. The human brain is intrinsically organized into dynamic, anticorrelated functional networks. *Proc Natl Acad Sci U S A.* (2005) 102:9673–8. doi: 10.1073/pnas.0504136102
28. Spreng RN, DuPre E, Selarka D, Garcia J, Gojkovic S, Mildner J, et al. Goal-congruent default network activity facilitates cognitive control. *J Neurosci.* (2014) 34:14108–14. doi: 10.1523/JNEUROSCI.2815-14.2014
29. Andreescu C, Wu M, Butters MA, Figurski J, Reynolds CF, 3rd, Aizenstein HJ. The default mode network in late-life anxious depression. *Am J Geriatr Psychiatry.* (2011) 19:980–3. doi: 10.1097/JGP.0b013e318227f4f9
30. Yao N, Shek-Kwan Chang R, Cheung C, Pang S, Lau KK, Suckling J, et al. The default mode network is disrupted in Parkinson's disease with visual hallucinations. *Hum Brain Mapp.* (2014) 35:5658–66. doi: 10.1002/hbm.22577
31. Vergara EF, Behrens MI. [Default mode network and Alzheimer's disease]. *Rev Med Chil.* (2013) 141:375–80. doi: 10.4067/S0034-98872013000300014
32. Meda SA, Ruano G, Windemuth A, O'Neil K, Berwise C, Dunn SM, et al. Multivariate analysis reveals genetic associations of the resting default mode network in psychotic bipolar disorder and schizophrenia. *Proc Natl Acad Sci U S A.* (2014) 111:E2066–75. doi: 10.1073/pnas.1313093111
33. Lee JY, Han J, Yang M, Oh SY. Population-based Incidence of Pediatric and Adult Optic Neuritis and the Risk of Multiple Sclerosis. *Ophthalmology.* (2020) 127:417–25. doi: 10.1016/j.ophtha.2019.09.032
34. Bonavita S, Gallo A, Sacco R, Corte MD, Bisecco A, Docimo R, et al. Distributed changes in default-mode resting-state connectivity in multiple sclerosis. *Mult Scler.* (2011) 17:411–22. doi: 10.1177/1352458510394609
35. Buzsaki G, Draguhn A. Neuronal oscillations in cortical networks. *Science.* (2004) 304:1926–9. doi: 10.1126/science.1099745
36. Zuo XN, Di Martino A, Kelly C, Shehzad ZE, Gee DG, Klein DF, et al. The oscillating brain: complex and reliable. *Neuroimage.* (2010) 49:1432–45. doi: 10.1016/j.neuroimage.2009.09.037
37. Mesulam MM, Mufson EJ. Insula of the old world monkey. III: Efferent cortical output and comments on function. *J Comp Neurol.* (1982) 212:38–52. doi: 10.1002/cne.902120104
38. Ebisch SJ, Bello A, Spitoni GF, Perrucci MG, Gallese V, Committeri G, et al. Emotional susceptibility trait modulates insula responses and functional connectivity in flavor processing. *Front Behav Neurosci.* (2015) 9:297. doi: 10.3389/fnbeh.2015.00297
39. Naqvi NH, Rudrauf D, Damasio H, Bechara A. Damage to the insula disrupts addiction to cigarette smoking. *Science.* (2007) 315:531–4. doi: 10.1126/science.1135926
40. Lerner, Bagic A, Hanakawa T, Boudreau EA, Pagan F, Mari Z, et al. Involvement of insula and cingulate cortices in control and suppression of natural urges. *Cereb Cortex.* (2009) 19:218–23. doi: 10.1093/cercor/bhn074
41. Hayata TT, Bergo FP, Rezende TJ, Damasceno A, Damasceno BP, Cendes F, et al. Cortical correlates of affective syndrome in dementia due to Alzheimer's disease. *Arq Neuropsiquiatr.* (2015) 73:553–60. doi: 10.1590/0004-282X20150068
42. Dylgjeri S, Taussig D, Chipaux M, Lebas A, Fohlen M, Bulteau C, et al. Insular and insulo-opercular epilepsy in childhood: an SEEG study. *Seizure.* (2014) 23:300–8. doi: 10.1016/j.seizure.2014.01.008
43. Toosy AT, Werring DJ, Bullmore ET, Plant GT, Barker GJ, Miller DH, et al. Functional magnetic resonance imaging of the cortical response to photic stimulation in humans following optic neuritis recovery. *Neurosci Lett.* (2002) 330:255–9. doi: 10.1016/S0304-3940(02)00700-0
44. Werring DJ, Bullmore ET, Toosy AT, Miller DH, Barker GJ, MacManus DG, et al. Recovery from optic neuritis is associated with a change in the distribution of cerebral response to visual stimulation: a functional magnetic resonance imaging study. *J Neurol Neurosurg Psychiatry.* (2000) 68:441–9. doi: 10.1136/jnnp.68.4.441
45. Liu Y, Li L, Li B, Feng N, Li L, Zhang X, et al. Decreased triple network connectivity in patients with recent onset post-traumatic stress disorder after a single prolonged trauma exposure. *Sci Rep.* (2017) 7:12625. doi: 10.1038/s41598-017-12964-6
46. Vicentini JE, Weiler M, Almeida SRM, de Campos BM, Valler L, Li LM. Depression and anxiety symptoms are associated to disruption of default mode network in subacute ischemic stroke. *Brain Imaging Behav.* (2017) 11:1571–80. doi: 10.1007/s11682-016-9605-7
47. Sliwinska MW, James A, Devlin JT. Inferior parietal lobule contributions to visual word recognition. *J Cogn Neurosci.* (2015) 27:593–604. doi: 10.1162/jocn_a_00721
48. Danivas V, Kalmady S, Arasappa R, Behere RV, Rao NP, Venkatasubramanian G, et al. Inferior parietal lobule volume and schneiderian first-rank symptoms in antipsychotic-naive schizophrenia: a 3-tesla MRI study. *Indian J Psychol Med.* (2009) 31:82–7. doi: 10.4103/0253-7176.63578
49. Reed TT, Pierce WM, Jr., Turner DM, Markesbery WR, D. Allan butterfield, proteomic identification of nitrated brain proteins in early Alzheimer's disease inferior parietal lobule. *J Cell Mol Med.* (2009) 13:2019–29. doi: 10.1111/j.1582-4934.2008.00478.x
50. Guic E, Carrasco X, Rodriguez E, Robles I, Merzenich MM. Plasticity in primary somatosensory cortex resulting from environmentally enriched stimulation and sensory discrimination training. *Biol Res.* (2008) 41:425–37. doi: 10.4067/S0716-97602008000400008
51. Kim W, Kim SK, Nabekura J. Functional and structural plasticity in the primary somatosensory cortex associated with chronic pain. *J Neurochem.* (2017) 141:499–506. doi: 10.1111/jnc.14012
52. Duan Y, Liu Y, Liang P, Jia X, Ye J, Dong H, et al. White matter atrophy in brain of neuromyelitis optica: a voxel-based morphometry study. *Acta Radiol.* (2014) 55:589–93. doi: 10.1177/0284185113501815
53. Liu Y, Duan Y, He Y, Wang J, Xia M, Yu C, et al. Altered topological organization of white matter structural networks in patients with neuromyelitis optica. *PLoS ONE.* (2012) 7:e48846. doi: 10.1371/journal.pone.0048846

Conflict of Interest: The authors declare that the research was conducted in the absence of any commercial or financial relationships that could be construed as a potential conflict of interest.

The reviewer HL declared a shared parent affiliation with several of the authors, W-QS, S-NW, Q-YL, H-YS, L-JZ, Y-CP and YS at the time of review.

Publisher's Note: All claims expressed in this article are solely those of the authors and do not necessarily represent those of their affiliated organizations, or those of the publisher, the editors and the reviewers. Any product that may be evaluated in this article, or claim that may be made by its manufacturer, is not guaranteed or endorsed by the publisher.

Copyright © 2022 Yan, Shi, Su, Liao, Wu, Li, Yu, Shu, Zhang, Pan and Shao. This is an open-access article distributed under the terms of the Creative Commons Attribution License (CC BY). The use, distribution or reproduction in other forums is permitted, provided the original author(s) and the copyright owner(s) are credited and that the original publication in this journal is cited, in accordance with accepted academic practice. No use, distribution or reproduction is permitted which does not comply with these terms.

frontiers in Neurology

ORIGINAL RESEARCH
published: 22 February 2022
doi: 10.3389/fneur.2022.806013

Correlation Between Blood Glucose Variability and Early Therapeutic Effects After Intravenous Thrombolysis With Alteplase and Levels of Serum Inflammatory Factors in Patients With Acute Ischemic Stroke

Yun Cai[1,2†], *Hongtao Zhang*[1†], *Qiang Li*[2] *and Peilan Zhang*[3*]

[1] *Clinical College of Neurology, Neurosurgery and Neurorehabilitation, Tianjin Medical University, Tianjin, China,* [2] *Department of Neurology, Affiliated Hospital of Hebei University, Baoding, China,* [3] *Department of Neurology, Tianjin Huanhu Hospital, Tianjin, China*

OPEN ACCESS

Edited by:
Jinming Han,
Capital Medical University, China

Reviewed by:
Xiangjian Xiao,
Hebei General Hospital, China
Xiaoyun Liu,
Second Hospital of Hebei Medical University, China

***Correspondence:**
Peilan Zhang
peilzhang1@163.com

†These authors have contributed equally to this work

Specialty section:
This article was submitted to Neurological Biomarkers, a section of the journal Frontiers in Neurology

Received: *31 October 2021*
Accepted: *24 January 2022*
Published: *22 February 2022*

Citation:
Cai Y, Zhang H, Li Q and Zhang P (2022) Correlation Between Blood Glucose Variability and Early Therapeutic Effects After Intravenous Thrombolysis With Alteplase and Levels of Serum Inflammatory Factors in Patients With Acute Ischemic Stroke. Front. Neurol. 13:806013. doi: 10.3389/fneur.2022.806013

Objective: To investigate the effects of blood glucose variability on early therapeutic effects after intravenous thrombolysis with alteplase and the levels of serum inflammatory factors in patients with acute ischemic stroke (AIS).

Methods: We enrolled AIS patients who received intravenous thrombolysis within 4.5 h of the onset of symptoms. Clinical data, including the National Institutes of Health Stroke Scale (NIHSS), glycosylated hemoglobin, mean blood glucose, standard deviation of blood glucose, mean amplitude of glycemic excursion, mean variation coefficient of blood glucose, interleukin-6 (IL-6), active matrix metalloproteinase-9 (MMP-9), tumor necrosis factor α (TNF-α), and hypersensitive C-reactive protein (hs-CRP) levels, were compared between a group who showed improvement (the improvement group) and a group who did not show improvement (the non-improvement group). Relevant factors for early neurological improvement after thrombolysis with alteplase were analyzed by using multivariate logistic regression models. A Pearson linear correlation analysis was also performed on blood glucose variation and inflammatory factor levels within the two groups.

Results: A total of 146 patients were included, 63 of which had early symptom improvement (43.15%). The diabetes ratio, atrial fibrillation ratio, baseline NHISS score, random blood glucose at admission, and glycosylated hemoglobin of patients in the improvement group were significantly lower than those in the non-improvement group ($P < 0.05$ in all cases). The mean blood glucose, standard deviation of blood glucose, mean amplitude of glycemic excursion, and mean blood glucose variation coefficients of patients in the improvement group were significantly lower than those in the non-improvement group ($P < 0.05$). Serum inflammatory factor levels, including IL-6, MMP-9, TNF-α and hs-CRP, were significantly lower in patients in the improvement group compared to patients in the non-improvement group ($P < 0.05$). Multivariate logistic

regression analysis showed that baseline NIHSS scores (OR = 1.28, 95% CI = 1.05–1.62, $P = 0.02$), glycosylated hemoglobin scores (OR = 2.57, 95% CI = 1.78–3.98, $P = 0.0005$), diabetes (OR = 13.10, 95% CI = 1.63∼131.45, $P = 0.021$), the mean amplitude of glycemic excursion (OR = 2.98, 95% CI = 1.92–5.00, $P < 0.0001$), and the mean variation coefficient of blood glucose (OR = 1.40, 95% CI = 1.26–1.60, $P = 0.0078$) were significantly correlated with early symptom improvement after thrombolysis. Pearson linear correlation analysis showed that the standard deviation of blood glucose, mean amplitude of glycemic excursion, and the mean variation coefficient of blood glucose were significantly positively correlated with IL-6, MMP-9, TNF-α and hs-CRP levels ($P < 0.01$).

Conclusions: Blood glucose variability is correlated with early neurological improvement after intravenous thrombolysis with alteplase in AIS patients. With the increase of blood glucose fluctuation range, the inflammatory response is enhanced, which affects the prognosis of patients.

Keywords: acute ischemic stroke, alteplase, thrombolytic therapy, blood glucose variability, inflammatory factors

Stroke is the disease with the highest incidence, disability, and mortality in China, with ischemic stroke accounting for 70% of disease burden. At present, the most effective treatment is intravenous thrombolytic therapy with recombinant tissue plasminogen activators (rt-PA) at early stages of the disease (<4.5 h) (1). Early improvement in neurological function after thrombolytic therapy is a marker of vascular recanalization and is independently predictive of good prognoses at 3 months. However, the efficacy of intravenous thrombolytic therapy is not always satisfactory. This may be due to many factors. Blood glucose and blood glucose variability are important risk factors for cardiovascular and cerebrovascular diseases, and blood glucose variation can induce the occurrence or aggravation of inflammatory responses. Recent studies have confirmed that blood glucose variability is an important prognostic factor that can independently predict death in critically ill patients. However, there is still no consensus about the influence of blood glucose variability on the effects of early thrombolytic therapy and inflammatory responses in AIS patients. Here, we studied AIS patients that were treated with intravenous thrombolytic therapy with alteplase. While strictly controlling for blood glucose levels and reducing the incidence of hypoglycemia, we evaluated the correlation between blood glucose variation levels, the early treatment effects of intravenous thrombolytic therapy with alteplase, and levels of serum inflammatory factors. We hope to guide effective blood glucose-based interventions, and to improve the therapeutic effects of intravenous thrombolysis in patients experiencing AIS.

PATIENTS AND METHOD

Patients

We included a total of 154 AIS patients who received intravenous thrombolysis with alteplase within 4.5 h of onset between August 2020 and June 2021. Among these patients, 8 cases were treated intravenously using bridging after intravenous thrombolysis, with a total of 146 cases eventually included in the final analysis.

Inclusion Criteria

(1) Age > 18. (2) Illness conformed to the "Guidelines for diagnosis and treatment of acute ischemic stroke 2018 in China". (3) Stroke symptom duration was ≥30 min, National Institutes of Health Stroke Scale (NIHSS) score between 4 and 25 points, with no significant improvement in symptoms before thrombolytic therapy. (4) The standard of intravenous thrombolysis was met within 4.5 h of onset. (5) The clinical data were detailed and complete. (6) Patients or their families agreed to the study and signed informed consent forms.

Exclusion Criteria

(1) Patients with a history of severe stroke and mRS scores >2 before onset. (2) Patients with a history of severe head trauma or stroke within the past 3 months. (3) Patients with intracranial hemorrhage. (4) Patients with active hemorrhage. (5) Patients with a history of seizures. (6) Patients with serious insufficiencies within important organs, including the heart, lungs, liver, kidneys, and others. (7) Patients with inflammatory conditions, including but not limited to connective tissue disease, vasculitis, infection, tumor and acute myocardial infarction. (8) Patients that had recently used anti-inflammatory drugs, including glucocorticoids, immunosuppressants, biologics and non-steroidal anti-inflammatory drugs (excluding low-dose aspirin and statins). (9)Patients with blood pressure higher than 185/110 mmHg (1 mmHg = 133.32 Pa) after antihypertensive therapy. (10) Patients with random blood glucose levels <2.7 mmol/L at admission. (11) Patients with oral anticoagulant therapy and INR >1.5. (12) Patients with platelets t < 100×10^9/L. (13) Cases where the time of onset was unknown. (14) Cases were intravenous thrombolysis was followed by endovascular bridging therapy. (15) Cases with incomplete

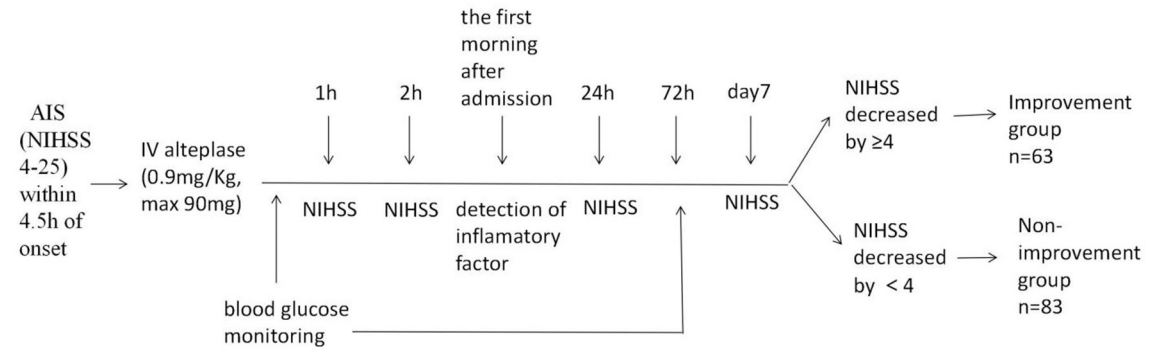

FIGURE 1 | Study schema. AIS, acute ischemic stroke; NIHSS, National Institutes of Health Stroke Scale; IV, intravenous.

clinical data. (16)Telephone or outpatient follow-up could not be completed.

This study was approved by the ethics committee of Tianjin Huanhu Hospital.

Methods

General Information Collection

Baseline data, including gender, age, hypertension, diabetes, hyperlipidemia, coronary heart disease, atrial fibrillation, prior stroke/transient ischemic attack (TIA), smoking history, drinking history, onset to treatment (OTT), and NIHSS score before thrombolysis, were collected for all patients.

Treatment

Lyophilized alteplase powder (specification: 20 and 50 mg) produced by the German company, Boehringer Ingelheim, was used. Alteplase was dissolved in 100 ml normal saline at a total dose of 0.9 mg/kg (maximum dose was 90 mg), 10% of which was intravenously injected within 1 min, and the other 90% of which was intravenously injected within 1 h. Brain CT or MRI examinations were performed 24 h after thrombolysis. Patients without cerebral hemorrhage were treated with anti-platelet aggregation drugs and neuroprotection. Patients after cerebral infarctions were treated with insulin hypoglycemia when blood sugar was more than 10.0 mmol/L, and when blood sugar was below 3.3 mmol/L, 10–20% glucose was administered orally or by injection. Patients who were unable to eat orally were given a nasal fluid diet, with their blood glucose levels closely monitored.

Observation Indicators

(1) Blood glucose monitoring: after admission, blood glucose was monitored every 4 h for 72 h using a Roche blood glucose meter. Then, the mean blood glucose (MBG), standard deviation of blood glucose (SDBG), mean amplitude of glycemic excursion (MAGE), and mean variation coefficient of blood glucose (MVCBG) were calculated. The last three indexes are used to measure the degree of variation in blood glucose levels. (2) Detection of inflammatory factors: in the morning following admission, 3 ml of fasting venous blood was extracted, and serum was separated. Interleukin-6 (IL-6), active matrix metalloproteinase-9 (MMP-9) and tumor necrosis factor α (TNF-α) were detected by enzyme-linked immunosorbent assay (ELISA), and the level of hypersensitive C-reactive protein (hs-CRP) were detected using scattering turbidimetry. (3) Efficacy evaluation: NIHSS scores were recorded at 1 h, 2 h, 24 h and 7 days after intravenous thrombolysis. Cases with NIHSS scores that decreased by ≥4 points 7 days after thrombolysis, or with neurological deficits that were completely resolved (i.e., NIHSS score = 0), were defined as having significant early improvement, as shown in **Figure 1**.

Case Grouping

Patients were divided into improvement and non-improvement groups based on whether neurological functioning improved in the early stages after thrombolytic therapy.

Statistical Analysis

Statistical analysis was carried out using SAS 9.4 statistical software. Data that conformed to normal distributions were expressed by mean ± standard deviation (SD) and assessed using t-tests. A rank sum test was also used for comparison for data that did not conform to normal distributions. Enumeration data were represented by frequency and rate (%), and assessed by a x^2 test. Multivariate Logistic stepwise regression analysis was performed for the factors with statistically significant differences in univariate analysis. The levels of blood glucose variability and inflammatory factors were compared between the two groups using Pearson linear correlation analysis. A $P < 0.05$ indicated a statistically significant difference.

RESULTS

Univariate Analysis of Baseline Data

There were 63 patients in the improvement group and 83 patients in the non-improvement group, including 2 patients with symptomatic intracerebral hemorrhage. The proportion of diabetes and atrial fibrillation in the non-improvement group was higher than that in the improvement group ($P < 0.05$). The baseline NHISS score of the non-improvement group was higher than that of the improvement group, the non-improvement group had higher random blood glucose levels at admission than the improvement group, and glycosylated hemoglobin in

TABLE 1 | Baseline data for the improvement group and non-improvement group.

Variable	Improvement group ($n = 63$)	Non-improvement group ($n = 83$)	t/Z/χ^2	P
Men (n, %)	38 (60.3%)	49 (59.0%)	0.024	0.876
Age (years, $\bar{x} \pm s$)	60.92 ± 11.88	64.10 ± 7.36	−1.868	0.065
Hypertension (n, %)	44 (69.8)	59 (71.1)	0.027	0.087
Diabetes (n, %)	15 (23.8)	34 (41.0)	4.727	0.030
Hyperlipidemia (n, %)	22 (34.9)	37 (44.6)	1.387	0.239
Coronary heart disease (n, %)	19 (30.2)	37 (44.6)	3.150	0.076
Atrial fibrillation (n, %)	11 (17.5)	33 (39.8)	8.458	0.004
Prior stroke/TIA (n, %)	16 (25.4)	19 (22.9)	0.123	0.725
Smoking history (n, %)	36 (57.1)	48 (57.8)	0.007	0.934
Drinking history (n, %)	23 (36.5)	31 (37.3)	0.011	0.917
Random blood glucose at admission (mmol/L, $\bar{x} \pm s$)	6.98 ± 1.30	7.51 ± 1.42	−2.331	0.021
Glycosylated hemoglobin (%, $\bar{x} \pm s$)	5.31 ± 1.00	6.37 ± 1.19	−5.835	0.000
Baseline NIHSS score ($\bar{x} \pm s$)	9.25 ± 3.67	11.01 ± 4.75	−2.525	0.013
OTT (min, $\bar{x} \pm s$)	169.37 ± 25.83	176.75 ± 23.74	−1.791	0.075

NIHSS, National Institutes of Health Stroke Scale; OTT, onset to treatment.

TABLE 2 | Comparison of blood glucose monitoring indexes.

Variable	Improvement group (n = 63)	Non-improvement group (n = 83)	t	P
MBG (mmol/L, $\bar{x} \pm s$)	7.65 ± 1.25	8.21 ± 1.04	19.3226	< 0.0001
SDBG (mmol/L, $\bar{x} \pm s$)	1.11 ± 0.41	1.65 ± 0.52	40.4752	< 0.0001
MAGE (%, $\bar{x} \pm s$)	2.16 ± 0.86	3.06 ± 1.08	25.0631	< 0.0001
MVCBG (%, $\bar{x} \pm s$)	14.32 ± 3.87	19.83 ± 4.55	42.9418	< 0.0001

MBG, mean blood glucose; SDBG, standard deviation of blood glucose; MAGE, mean amplitude of glycemic excursion; MVCBG, mean variation coefficient of blood glucose.

the non-improvement group was significantly higher than in the improvement group ($P < 0.05$; **Table 1**).

Comparison of Blood Glucose Monitoring Indexes

The MBG, SDBG, MAGE and MVCBG levels of patients in the improvement group were significantly lower than those in the non-improvement group ($P < 0.05$; **Table 2**).

Comparison of Inflammatory Factor Levels

Patients in the improvement group had significantly lower levels of serum inflammatory factors, including IL-6, MMP-9, TNF-α and hs-CRP, than patients in the non-improvement group ($P < 0.05$; **Table 3**).

TABLE 3 | Comparison of the levels of inflammatory factors.

Variable	Improvement group ($n = 63$)	Non-improvement group ($n = 83$)	t	P
TNF-α (ng/L, $\bar{x} \pm s$)	21.19 ± 4.11	28.45 ± 4.44	−10.099	0.000
IL-6 (μg/L, $\bar{x} \pm s$)	39.46 ± 2.53	44.33 ± 3.84	−9.229	0.000
MMP-9 (μg/L, $\bar{x} \pm s$)	117.75 ± 4.66	124.58 ± 4.45	−8.988	0.000
Hs-CRP (mg/L, $\bar{x} \pm s$)	4.25 ± 1.12	4.85 ± 1.26	−3.006	0.003

TNF-α, tumor necrosis factor α; IL-6, interleukin-6; MMP-9, active matrix metalloproteinase-9; Hs-CRP, hypersensitive C-reactive protein.

TABLE 4 | Multivariable analysis for early symptom improvement.

Factors	B	SE	OR	95%CI	p
Diabetes	2.57	1.11	13.10	(1.63, 131.45)	0.0210
Atrial fibrillation	−0.56	0.62	0.57	(0.16, 1.88)	0.3624
Random blood glucose	0.31	0.14	1.36	(1.05, 1.82)	0.7742
Glycosylated hemoglobin	0.94	0.20	2.57	(1.78, 3.98)	0.0005
Baseline NIHSS score	0.25	0.11	1.28	(1.05, 1.62)	0.0200
MBG	0.42	0.92	1.53	(0.21, 8.76)	0.6475
SDBG	−3.74	0.78	20.28	(7.05, 70.92)	0.9054
MAGE	−2.51	0.62	2.98	(1.92, 5.00)	<0.0001
MVCBG	−5.43	1.03	1.40	(1.26, 1.60)	0.0078

NIHSS, National Institutes of Health Stroke Scale; MBG, mean blood glucose; SDBG, standard deviation of blood glucose; MAGE, mean amplitude of glycemic excursion; MVCBG, mean variation coefficient of blood glucose.

Multivariate Logistic Regression Analysis

Variables with $P < 0.05$ in **Tables 1**, **2** (diabetes, atrial fibrillation, baseline NHISS scores, random blood glucose at admission, glycosylated hemoglobin, MBG, SDBG, MAGE, MVCBG) were selected for multivariate logistic regression analysis to analyze factors related to early symptom improvement. Results showed that baseline NIHSS scores, glycosylated hemoglobin, diabetes, MAGE, and MVCBG were significantly correlated with early symptom improvement after thrombolysis (**Table 4**).

Correlation Analysis of Blood Glucose Variability Indices and Inflammatory Factors

Pearson linear correlation analysis showed that the blood glucose variability indices, including SDBG, MAGE, and MVCBG, were significantly positively correlated with the inflammatory factors IL-6, MMP-9, TNF-α and hs-CRP ($P < 0.01$; **Table 5**).

DISCUSSION

Revascularization in patients with acute ischemic stroke has previously been associated with better outcomes. Early recovery of brain function has been considered to be an indicator of arterial recanalization and brain tissue reperfusion, and the relationship between vascular recanalization and early recovery of nerve function has been confirmed using multiple

TABLE 5 | Correlation analysis of blood glucose variability indices and inflammatory factors.

Blood glucose variability	MMP-9	TNF-α	IL-6	CRP
MVCBG	$r = 0.527$	$r = 0.576$	$r = 0.590$	$r = 0.439$
	$P < 0.01$	$P < 0.01$	$P < 0.01$	$P < 0.01$
MAGE	$r = 0.579$	$r = 0.637$	$r = 0.640$	$r = 0.580$
	$P < 0.01$	$P < 0.01$	$P < 0.01$	$P < 0.01$
SDBG	$r = 0.623$	$r = 0.678$	$r = 0.682$	$r = 0.602$
	$P < 0.01$	$P < 0.01$	$P < 0.01$	$P < 0.01$

MVCBG, mean variation coefficient of blood glucose; MAGE, mean amplitude of glycemic excursion; SDBG, standard deviation of blood glucose; MMP-9, active matrix metalloproteinase-9; TNF-α, tumor necrosis factor α; IL-6, interleukin-6; Hs-CRP, hypersensitive C-reactive protein.

examination methods, such as transcranial Doppler imaging (2), CT angiography, magnetic resonance angiography, or digital subtraction angiography (DSA), etc. In this study, baseline NIHSS scores, glycosylated hemoglobin, diabetes, MAGE, and MVCBG were associated with early improvement after intravenous thrombolysis with alteplase in patients with AIS. High baseline NIHSS scores, high glycosylated hemoglobin levels, a history of diabetes, and high blood glucose variability were risk factors for decreased vascular recanalization.

At present, a number of studies have reported that hyperglycemia and diabetes are associated with the low rate of recanalization and poor clinical outcomes in IV rt-PA-treated patients (3). Therefore, how to control blood glucose more effectively, or if lowering blood glucose level alone is sufficient, has become a research hotspot (4). Blood glucose variability (blood glucose fluctuation) is also known as blood glucose drift and refers to the tendency of blood glucose levels to fluctuate. Between peaks and troughs, these changes are considered to be a third type of dysglycemia, in addition to hypoglycemia and hyperglycemia. Blood glucose variability can lead to vascular endothelial cell apoptosis via oxidative stress and inflammatory responses. Patients with acute cerebral infarctions are prone to stress hyperglycemia, so blood glucose fluctuations are more obvious (5). However, blood glucose variability has been consistently overlooked in stroke studies exploring the association between glycemia and clinical outcomes (6), and there are currently limited studies which have evaluated the association between blood glucose variability and clinical outcomes of stroke. There are also few studies that have investigated intravenous thrombolytic therapy related to stroke (7). A retrospective study assessed GV as the range of glucose (maximum-minimum) in diabetic AIS patients (8). It showed that high GV was associated with adverse functional outcomes, even after adjusting for hyperglycemic measures or hypoglycemic events. In one study, 336 diabetic AIS patients were recruited within 72 h of stroke onset, and the mean amplitude of glycemic excursion was found to be associated with early neurological deterioration (9). A study evaluating the association between GV indices and clinical outcomes in acute stroke patients showed that greater GV might be related to decreased odds of neurological improvement during hospitalization (10). Furthermore, a recent study demonstrated that high GV values during the first 48-h after ischaemic stroke were associated with increased mortality (11). Patients treated with intravenous thrombolytic therapy and non-diabetic patients were included in this study. The results showed that the random blood glucose levels at admission, glycosylated hemoglobin, mean blood glucose levels and blood glucose variability indices (SDBG, MAGE, MVCBG) in the improvement group were lower than those in the non-improvement group. Differences in blood glucose variation, however, were more significant. We therefore suggest that blood glucose variability indices will better predict outcomes in AIS patients treated with intravenous alteplase thrombolysis, and that the sensitivity of MAGE and MVCBG is higher than that of SDBG.

The mechanism by which elevated blood glucose variability could lead to poor outcomes is not entirely clear. Some studies have confirmed that blood glucose fluctuation can induce the adhesion of inflammatory cytokines and vascular endothelial cells, aggravate body's inflammatory responses, and then affect the prognosis of patients with acute cerebral infarctions (12). Barbieri M et al. showed that both acute and chronic blood glucose fluctuations could induce inflammatory responses in T2DM patients. Compared with stable hyperglycemia, excessively large and frequent blood glucose fluctuations may cause more intense T2DM complications (13). Lowering the levels of blood glucose variability may reduce the levels of inflammatory factors, reduce the degree of neurological impairment in ACI patients, and improve their prognosis (14). TNF-α is one of the most important Th1 pro-inflammatory cytokines, and is considered a potential therapeutic target for acute stroke (15). As an important factor in the inflammatory response, Il-6 induces blood vessel damage during and following AIS (16). IL-6 can increase vascular endothelial permeability, improve coagulation factor activity, promote coagulation, and cause vascular dysfunction, which may ultimately lead to thrombosis and bleeding events (17). MMP-9 expression levels are low in normal brain tissue, but are increased after ischemic strokes. MMP-9 is involved in brain tissue injury through a number of mechanisms, including destruction of the blood-brain barrier (BBB), the promotion of inflammatory cell infiltration and inflammatory factor release, inducing nerve cell death and hemorrhage transformation of ischemic tissue (18, 19). C-reactive protein (CRP) is a sensitive acute reactive protein. Previous studies have shown that hs-CRP can predict the occurrence of ACI, and that the degree of neurological impairment in ACI patients is closely related to hs-CRP levels. Therefore, hs-CRP levels can indirectly indicate disease severity (20, 21).

Here, we selected four important inflammatory factors related to acute cerebral infarction as observation indicators, and found that their levels were significantly higher in the non-improvement group than in the improvement group. We therefore postulate that because IL-6, MMP-9, TNF-α and hs-CRP levels in AIS patients with high blood glucose variability who are treated with intravenous alteplase thrombolysis are significantly increased, the degree of inflammation is severe, which may lead to poor prognoses.

In summary, our study showed that blood glucose variability was significantly correlated with the early therapeutic effects of intravenous alteplase thrombolysis, as well as with the level of inflammatory factors in acute cerebral infarctions. If blood glucose fluctuates greatly, inflammatory reactions are obvious, and intravenous thrombolysis has a somewhat negligible effect. Thus, the reduction of blood glucose variability and inhibition of inflammatory responses has become a novel therapeutic mechanism for improving the prognosis of AIS patients. Clinicians should closely monitor and manage blood glucose variability in AIS patients. Blood glucose fluctuations should be controlled effectively, rather than by simply lowering blood glucose levels. Reducing blood glucose fluctuations may improve the prognosis of AIS patients treated with intravenous thrombolytic therapy.

Our study had some limitations. Since not all subjects were diabetic, fingernail blood glucose measurements were used to calculate blood glucose variability, rather than employing a continuous blood glucose monitoring method. In the future, we hope to apply a dynamic blood glucose monitoring system and obtain more accurate data. In addition, there is no widely accepted optimal index for blood glucose variability, leading to substantial reporting heterogeneity in relevant studies. Additionally, our sample size was small because this was a single-center study. A larger sample drawn from multiple centers would be useful for obtaining more reliable results in the future.

DATA AVAILABILITY STATEMENT

The original contributions presented in the study are included in the article/supplementary material, further inquiries can be directed to the corresponding author/s.

ETHICS STATEMENT

The studies involving human participants were reviewed and approved by the Ethics Committee of Tianjin Huanhu Hospital. The patients/participants provided their written informed consent to participate in this study.

AUTHOR CONTRIBUTIONS

YC and PZ: study conception, design, analysis and interpretation of data, and critical revision of the manuscript for important intellectual content. YC and HZ: acquisition of data and drafting of the manuscript. YC, PZ, HZ, and QL: statistical analysis. All authors contributed to the article and approved the submitted version.

REFERENCES

1. Powers WJ, Rabinstein AA, Ackerson T, Adeoye OM, Bambakidis NC, Becker K, et al. 2018 guidelines for the early management of patients with acute ischemic stroke: a guideline for healthcare professionals From the American Heart Association/American Stroke Association. *Stroke.* (2018) 49:e46–e110. doi: 10.1161/STR.0000000000000158
2. Eryildiz ES, Özdemir AÖ. Factors associated with early recovery after intravenous thrombolytic therapy in acute ischemic stroke. *Noro psikiyatri arsivi.* (2018) 55:80–3. doi: 10.29399/npa.22664
3. Saqqur M, Shuaib A, Alexandrov AV, Sebastian J, Khan K, Uchino K. The correlation between admission blood glucose and intravenous rt-PA-induced arterial recanalization in acute ischemic stroke: a multi-centre TCD study. *Int J Stroke.* (2015) 10:1087–92. doi: 10.1111/ijs.12517
4. Arnold M, Mattle S, Galimanis A, Kappeler L, Fischer U, Jung S, et al. Impact of admission glucose and diabetes on recanalization and outcome after intra-arterial thrombolysis for ischaemic stroke. *Int J Stroke.* (2014) 9:985–91. doi: 10.1111/j.1747-4949.2012.00879.x
5. Sun Y, Xu Y, Geng L. Caspase-3 inhibitor prevents the apoptosis of brain tissue in rats with acute cerebral infarction. *Exp Ther Med.* (2015) 10:133–138. doi: 10.3892/etm.2015.2462
6. Camara-Lemarroy CR. Glucose and stroke: what about glycemic variability. *J Neurol Sci.* (2017) 373:242–3. doi: 10.1016/j.jns.2017.01.015
7. Palaiodimou L, Lioutas VA, Lambadiari V, Paraskevas GP, Voumvourakis K, Tsivgoulis G. Glycemia management in acute ischemic stroke: current concepts and novel therapeutic targets. *Postgrad Med.* (2019) 131:423–37. doi: 10.1080/00325481.2019.1651206
8. Kim YS, Kim C, Jung KH, Kwon HM, Heo SH, Kim BJ, et al. Range of glucose as a glycemic variability and 3-month outcome in diabetic patients with acute ischemic stroke. *PLoS ONE.* (2017) 12:e0183894. doi: 10.1371/journal.pone.0183894
9. Hui J, Zhang J, Mao X, Li Z, Li X, Wang F, et al. The initial glycemic variability is associated with early neurological deterioration in diabetic patients with acute ischemic stroke. *Neurol Sci.* (2018) 39:1571–7. doi: 10.1007/s10072-018-3463-6
10. Palaiodimou L, Lioutas VA, Lambadiari V, Theodorou A, Themistocleous M, Aponte L, et al. Glycemic variability of acute stroke patients and clinical outcomes: a continuous glucose monitoring study. *Ther Adv Neurol Disord.* (2021) 14:17562864211045876. doi: 10.1177/17562864211045876 eCollection 2021.
11. Gutiérrez-Zúñiga R, Alonso de Leciñana M, Delgado-Mederos R, Gállego-Cullere J, Rodríguez-Yáñez M, Martínez-Zabaleta M, et al. Beyond hyperglycemia: glycaemic variability as a prognostic factor after acute ischemic stroke. *Neurologia.* (2020) 2020:S0213-4853(20)30272-3. doi: 10.1016/j.nrl.2020.06.018
12. Hobbs J, Tekes A, Klein J, Lemmon M, Felling RJ, Chavez-Valdez R. Acute paraplegia in a preterm infant with cerebral sinovenous thrombosis. *J Perinatol.* (2015) 35:460–2. doi: 10.1038/jp.2015.26
13. Chang C-M, Hsieh C-J, Huang J-C, Huang I-C. Acute and chronic fluctuations in blood glucose levels can increase oxidative stress in type 2 diabetes mellitus. *Acta Diabetol.* (2012) 49 Suppl 1:S171–7. doi: 10.1007/s00592-012-0398-x
14. Patgiri D, Pathak MS, Sharma *P*, Kutum T, Mattack N. Serum hsCRP: a novel marker for prediction of cerebrovascular accidents (Stroke). *J Clin Diagn Res.* (2014) 8:CC08–11. doi: 10.7860/JCDR/2014/10386.5302
15. Liu D-D, Chu S-F, Chen C, Yang *P*-F, Chen N-H, He X. Research progress in stroke-induced immunodepression syndrome (SIDS) and stroke-associated pneumonia (SAP). *Neurochem Int.* (2018) 114:42–54. doi: 10.1016/j.neuint.2018.01.002
16. Croci D, Nevzati E, Danura H, Schöpf S, Fandino J, Marbacher S, et al. The relationship between IL-6, ET-1 and cerebral vasospasm, in experimental rabbit subarachnoid hemorrhage. *J Neurosurg Sci.* (2019) 63:245–50. doi: 10.23736/S0390-5616.16.03876-5
17. Gu Y, Gutierrez J, Meier IB, Guzman VA, Manly JJ, Schupf N, et al. Circulating inflammatory biomarkers are related to cerebrovascular disease in older adults. *Neuroimmunol Neuroinflamm.* (2019) 6:e521. doi: 10.1212/NXI.0000000000000521, PMID:30568999

18. Li XF, Zhang XJ, Zhang C, Wang LN Li YR, Zhang Y, et al. Ulinastatin protects brain against cerebral ischemia/reperfusion injury through inhibiting MMP-9 and alleviating loss of ZO-1 and occludin proteins in mice. *Exp Neurol.* (2018) 302:68–74. doi: 10.1016/j.expneurol.2017.12.016
19. Hannocks MJ, Zhang X, Gerwien H, Chashchina A, Burmeister M, Korpos E, et al. The gelatinases, MMP-2 and MMP-9, as fine tuners of neuroinflammatory processes. *Matrix Biol.* (2019) 75–76:102–13. doi: 10.1016/j.matbio.2017.11.007
20. de Sousa Parreira J, Kallaur AP, Lehmann MF, Oliveira SR, Alfieri DF, Delongui F, et al. Tumor necrosis factor beta NcoI polymorphism (rs909253) is associated with inflammatory and metabolic markers in acute ischemic stroke. *Metab Brain Dis.* (2015) 30:159–67. doi: 10.1007/s11011-014-9584-6
21. Das S, Roy S, Kaul S, Jyothy A, Munshi A, CRP. gene (1059G>C) polymorphism and its plasma levels in ischemic stroke and hemorrhagic stroke in a south Indian population. *Inflammation.* (2014) 37:1683–88. doi: 10.1007/s10753-014-9897-y

Conflict of Interest: The authors declare that the research was conducted in the absence of any commercial or financial relationships that could be construed as a potential conflict of interest.

Publisher's Note: All claims expressed in this article are solely those of the authors and do not necessarily represent those of their affiliated organizations, or those of the publisher, the editors and the reviewers. Any product that may be evaluated in this article, or claim that may be made by its manufacturer, is not guaranteed or endorsed by the publisher.

Copyright © 2022 Cai, Zhang, Li and Zhang. This is an open-access article distributed under the terms of the Creative Commons Attribution License (CC BY). The use, distribution or reproduction in other forums is permitted, provided the original author(s) and the copyright owner(s) are credited and that the original publication in this journal is cited, in accordance with accepted academic practice. No use, distribution or reproduction is permitted which does not comply with these terms.

frontiers in Neurology

ORIGINAL RESEARCH
published: 08 March 2022
doi: 10.3389/fneur.2022.853930

Optical Coherence Tomography Angiography Biomarkers of Retinal Thickness and Microvascular Alterations in Sjogren's Syndrome

Ren Liu[1], Yan Wang[1], Qiuyu Li[2], Qiang Xia[1], Tian Xu[1], Ting Han[1], Shuang Cai[1], Shuilin Luo[1], Rui Wu[1] and Yi Shao[2]**

[1] Department of Rheumatology, The First Affiliated Hospital of Nanchang University, Nanchang, China, [2] Department of Ophthalmology, The First Affiliated Hospital of Nanchang University, Jiangxi Province Ocular Disease Clinical Research Center, Nanchang, China

Purpose: To investigate the differences of retinal thickness (RT) and superficial vascular density (SVD) between patients with Sjogren's syndrome (SS) and healthy controls (HCs) using optical coherence tomography angiography (OCTA).

Methods: Individuals with SS and healthy controls were enrolled ($n = 12$ per group). An en-face OCTA scan was performed on each eye. Images were segmented into 9 subregions and macular RT and SVD were measured and compared between the 2 groups.

Results: Visual acuity (VA) differed significantly between patients with SS (24 eyes) and controls (24 eyes) ($p < 0.001$). In patients with SS, inner RT was reduced in the inner superior region, outer RT was reduced in the outer nasal (ON) region, and full RT was reduced in the ON region compared with the control group ($p < 0.05$). RT was negatively correlated with serum IgG level in the outer and full retina at ON regions ($p < 0.05$). SVD in the inner nasal, ON, and inner temporal regions was significantly lower in patients with SS than in control subjects ($p < 0.05$). SVD was positively correlated with full RT in the ON region in patients with SS ($p < 0.05$). The areas under the receiver operating characteristic (ROC) curves for the diagnostic sensitivity of outer RT and full RT in the ON region for SS were 0.828 (95% *CI*: 0.709–0.947) and 0.839 (95% *CI*: 0.715–0.963), respectively.

Conclusions: In patients with SS, retinal thinning in the macular area—which affects vision—can also reflect the severity of dry eyes in SS and has clinical value for assisted imaging diagnosis.

Keywords: retinal thickness, Sjogren's syndrome, optical coherence tomography angiography, biomarker, vascular density

OPEN ACCESS

Edited by:
Yuzhen Xu,
Tongji University, China

Reviewed by:
Guanghui Liu,
Fujian Provincial People's Hospital, China
Guigang Li,
Huazhong University of Science and Technology, China

***Correspondence:**
Rui Wu
tcmclinic@163.com
Yi Shao
freebee99@163.com

Specialty section:
This article was submitted to Neurological Biomarkers, a section of the journal Frontiers in Neurology

Received: *13 January 2022*
Accepted: *09 February 2022*
Published: *08 March 2022*

Citation:
Liu R, Wang Y, Li Q, Xia Q, Xu T, Han T, Cai S, Luo S, Wu R and Shao Y (2022) Optical Coherence Tomography Angiography Biomarkers of Retinal Thickness and Microvascular Alterations in Sjogren's Syndrome. Front. Neurol. 13:853930. doi: 10.3389/fneur.2022.853930

INTRODUCTION

Sjogren's syndrome (SS) is a long-term diffuse connective tissue disease. The global prevalence rate is 61 people per 100,000 (1). The male-to-female ratio is between 1:9 and 1:10, and most patients are 30–60 years of age (2). The clinical manifestations of SS range from exocrine to systemic with multiple extraglandular involvement (3). Although SS is associated with

a lower incidence of visceral damage than systemic lupus erythematosus (SLE), the degree of disability is similar (4). Patients with SS often have physical and psychological disorders that reduce the social functioning and quality of life (5, 6). The symptomatology of SS overlaps with that of other systemic diseases, drug reactions, and viral infections. Thus, SS diagnosis and treatment represent a clinical challenge. In fact, the two-thirds of patients with SS are not correctly diagnosed initially (3, 7) and a diagnosis can take up to 10 years from initial symptom onset (8).

Since its discovery in the 1930s, the classification of SS has been continually updated. SS is suspected when the following symptoms are present: (1) constant and annoying dry eyes persisting for at least 3 months; (2) continual foreign body sensation in the eyes; (3) requiring the use of artificial tears $\geq$3 times a day; (4) feeling thirst every day for more than 3 months; and (5) a need to drink water to swallow solid food (9). The European League Against Rheumatism (EULAR) and American College of Rheumatology (ACR) issued classification standards for SS that included clinical and immune evaluations, with less emphasis placed on the eyes (10).

Among patients with SS, the incidences of xerophthalmia and thirst—the most common disease symptoms—were 44% and 39%, respectively (11). However, a study with a large sample size found that dry eye was much more common than dry mouth (12). Patients with SS often have ocular surface inflammation, such as eyelid swelling and corneal ulcer (8, 13–15); and ocular lesions in other parts of the eye such as optic neuritis (8), uveitis (16), and scleritis (17) have also been reported. Over one-third of patients with SS have extraglandular ocular manifestations and when these interfere with vision, patients are more likely to have fatal complications than those without such lesions (8). In patients with systemic autoimmune disorders, the choroid and retina may not only reflect ocular diseases but also indirect ocular injury (18). In SLE, retinopathy is an accurate reflection of disease activity in both recessive and dominant cases, and SLE patients with related retinopathy have a significantly lower survival rate than those without retinopathy (19). In SS, the significance of retinal changes is worth exploring.

There is currently no single clinical index or gold standard assay for the diagnosis and/or differentiation of SS, although a lip biopsy is useful (20). However, the invasiveness of the procedure precludes regular follow-up and monitoring. The main measure of disease activity in SS is the EULAR Patient Report Index (21), which includes just one eye-related assessment item. Optical coherence tomography angiography (OCTA) is a novel *in vivo* imaging technique that provides detailed morphologic and quantitative information on microvascular changes in the eye (22). OCTA can be used to show the microvascular structure in the macula and optic disk (23, 24), which can facilitate the diagnosis of diseases, such as Alzheimer's disease (25), diabetes (26), multiple sclerosis (27), and thyroid-related ophthalmopathy (28).

To date there have been no studies that have applied OCTA to the diagnosis of SS. In this study, we investigated the ocular status of patients with SS, and used OCTA to assess retinal thickness (RT) and vascular density (VD) in patients with SS compared with healthy controls.

MATERIALS AND METHODS

Subjects

This cross-sectional study was conducted at the Department of Ophthalmology and Rheumatology of The First Affiliated Hospital of Nanchang University (Nanchang, China) in 2020. Patients diagnosed with SS were recruited from the Outpatient Department of Rheumatism Immunology; and sex- and age-matched healthy normal subjects were recruited from the Ocular Disease Clinical Research Center. An ophthalmologist from the Medical Center evaluated the absence of abnormalities in the eyes of these subjects through clinical examination and OCTA imaging. All subjects were examined by the same retina specialist.

Inclusion and Exclusion Criteria

All patients were women and met the 2002 American European Consensus Group classification criteria for SS (9). The patients ranged in age from 18 to 66 years. None of the patients showed symptoms or the signs of retinal vasculitis, choroiditis, or optic neuritis. Patients with chorioretinopathy induced by hydroxychloroquine (HCQ) were excluded.

Other exclusion criteria were as follows: (1) autoimmune diseases other than SS; (2) systemic diseases, such as endocrine, cardiovascular, or nervous system disease affecting the eye or optic nerve; (3) retinopathy or choroidal disease (e.g., arteriovenous disease, glaucoma, or high intraocular pressure (IOP); (4) any history of eye surgery or trauma or eye tumor; (5) contraindications, allergies, or intolerance to local anesthetics or mydriatic drugs; (6) diseases that could affect fundus imaging; and (7) pregnant or lactating women.

Ethical Considerations

The study was conducted in accordance with the Helsinki Declaration and was approved by the hospital's ethics council (cdyfy2018026). Before signing the informed consent statement, all participants fully understood the research methods and objectives.

Clinical Examinations

All subjects underwent the following clinical and ophthalmic examinations: (1) Immunological information, such as antinuclear antibody, anti-SS-A antibody, anti-SS-B antibody, IgG, and complement and salivary gland biopsy findings (29); (2) analysis of C-reactive protein (CRP) level and erythrocyte sedimentation rate to assess the patient's inflammatory status; (3) EULAR SS disease activity index for disease activity (ESSDAI) (21); (4) examination of mental state using the Hospital Anxiety and Depression Scale (HADS) (30); (5) ocular measurements, such as visual acuity (VA) (Snellen chart), IOP (Goldmann tonometry), spherical equivalent, and keratoconjunctivitis sicca; and (6) OCTA.

Ocular Measurements

Tear breakup time (BUT): apply fluorescein sodium evenly on the ocular surface, observe the first tear film rupture point under cobalt blue light, and calculate the tear film rupture time. Less than 10 s is positive (31).

Ocular staining score (OSS): corneal fluorescein staining and conjunctival lysamine green staining were used for comprehensive evaluation. The ocular surface of each eye was divided into three parts: nasal conjunctiva, cornea, and temporal conjunctiva. The nasal and temporal conjunctiva were scored according to the number of conjunctival spots in the palpebral fissure area. An OSS score $\geq$3 was positive (9).

Schirmer's test (SIT): fold one end of 5 mm × 35 mm filter paper into right angle, put it into conjunctival sac after disinfection. The soaking length of filter paper is normally 15 mm/5 min and <5 mm/5min is positive (9).

Tear meniscus height (TMH): infrared light was used to focus and guide patients to blink. After white light shooting, the software (Keratograph 5M) was used to measure and record (32).

Optical Coherence Tomography Angiography

We used an RTVue Avanti XR system (Optovue, Fremont, CA) to perform OCTA imaging to simultaneously display retinal cross section and microvessels. The scanning speed is set as 70,000 a-scans/s, the axial resolution is 5 mm, the horizontal resolution is 22 μm, the central wavelength is 840 nm, and the bandwidth is 45 nm. The imaging time was 3.9 s. Five angiography was performed in 3 mm × 3 mm scanning mode, focusing on the fovea along the *X*-axis (216 A scans in total) and along the *Y*-axis (216 grating positions for each scan). At 216 y positions × 5 positions, we captured 1,080 B scans at 270 frames/s (33). By 4 volume scans, OCTA images of 3 mm × 3 mm were obtained: a total of 933,120 A scans (2 horizontal scans and 2 vertical scans). A 3 mm × 3 mm en-face OCTA angiographic image was calculated for each eye.

After scanning, each retina was segmented into nine early treatment diabetic retinopathy study (ETDRS) subregions, composed of three concentric round (0.5, 1.5, and 3 mm in radius), and their thickness was analyzed. Each story of the retina covers: (1) inner retina: from internal limiting membrane (ILM) to inner plexiform layer (IPL); (2) full retina: from ILM to retinal segment epithelium (RPE). We defined outer RT as the difference between full RT and inner RT. The vascular perfusion area as a percentage of the measured area was vascular density. Using the threshold method, vascular density was reckoned by creating two-dimensional en-face images of superficial retina (the layer between the vitreous retinal interface and the front boundary of the ganglion cell layer). Determine the value of the image block and assign it to each pixel perfusion (1) or background (0). The average value of the skeleton plate in the region of interest was scaled based on the pixel size (512 pixels/3 mm) to calculate vascular density from the center of the macula to the edge of the 3 mm × 3 mm brightness gradient image. Macular RT and superficial (S) VD were measured. All subjects used the right eye first. Data from the left eye were flipped to obtain a mirror image of the right eye. Left and right eye data were averaged and analyzed together (**Figure 1A**).

Statistical Analysis

The data were analyzed using SPSS version 22.0 (IBM Corp, Armonk, NY, USA) and GraphPad Prism version 8 (La Jolla, California, USA) are reported as mean ± SD. Independent-samples *t*-test, chi-square test, and Fisher's exact test were used to compare data between groups. The generalized estimation equation was employed to compare RT and SVD between SS eyes and control eyes and data were adjusted for known confounding variables to explain interocular correlation within subjects. The relationship between RT and systemic and ocular variables was analyzed using univariate and multivariate regression analyses. A linear correlation analysis was conducted between RT (full thickness, inner layer, and outer layer) and SVD in each group. To analyze the distinction between healthy and SS subjects, receiver operating characteristic (ROC) curves for RT (full, inner and outer) and SVD were plotted. The value of $p < 0.05$ was deemed statistically significant.

RESULTS

Subjects

There were 12 cases (24 eyes) in each group and all were women. The patients with SS and control subjects were comparable in the terms of age (the mean age of SS was 55.17 ± 9.68 years and the mean age of the control was 54.50 ± 9.25 years, $p = 0.808$). The mean time since diagnosis in the SS group was 3.92 ± 1.93 years, mean ESSDAI was 5.75 (range: 1–18), IgG was 16.11 ± 6.74 g/L, complement C3 was 0.85 ± 0.14 g/L, complement C4 was 0.21 ± 0.08 g/L. Patients with SS had a significantly higher HADS score than controls (8.08 ± 3.65 vs. 2.58 ± 0.97; $p < 0.001$) (**Table 1**).

The SS group had lower VA than the control group ($p < 0.001$) and had shorter BUT (4.67 ± 0.92 vs. 13.42 ± 1.50 s; $p < 0.001$), OSS (3.12 ± 1.90 vs. 0; $p < 0.0001$), lower SIT score (3.33 ± 1.86 vs. 12.92 ± 1.32 mm; $p < 0.001$), and lower TMH (0.15 ± 0.04 vs. 0.58 ± 0.12 mm; $p < 0.001$) (**Table 2**).

Macular RT

The subregional RT in the SS and control groups is shown in **Table 3**, **Figure 1B**. After adjusting for age, IOP, VA, and blood pressure (BP), inner RT was significantly lower in the SS group than in controls in the superior quadrant of the inner ring ($p = 0.022$) (**Figure 1C**). The other 3 regions of the inner ring (nasal, $p = 0.739$; inferior, $p = 0.115$; and temporal, $p = 0.841$), 4 regions of the outer ring (superior, $p = 0.348$; nasal, $p = 0.161$; inferior, $p = 0.513$; and temporal, $p = 0.472$), and foveal center ($p = 0.244$) did not differ significantly between groups.

Compared with healthy subjects, the outer RT of patients with SS was significantly lower in the outer nasal (ON) ($p < 0.001$) quadrants (**Figure 1D**). The other 3 regions of the outer ring (superior, $p = 0.493$; inferior, $p = 0.123$; and temporal, $p = 0.179$), the 4 regions of the inner ring (superior, $p = 0.118$; nasal, $p = 0.581$; inferior, $p = 0.228$; and temporal, $p = 0.302$),

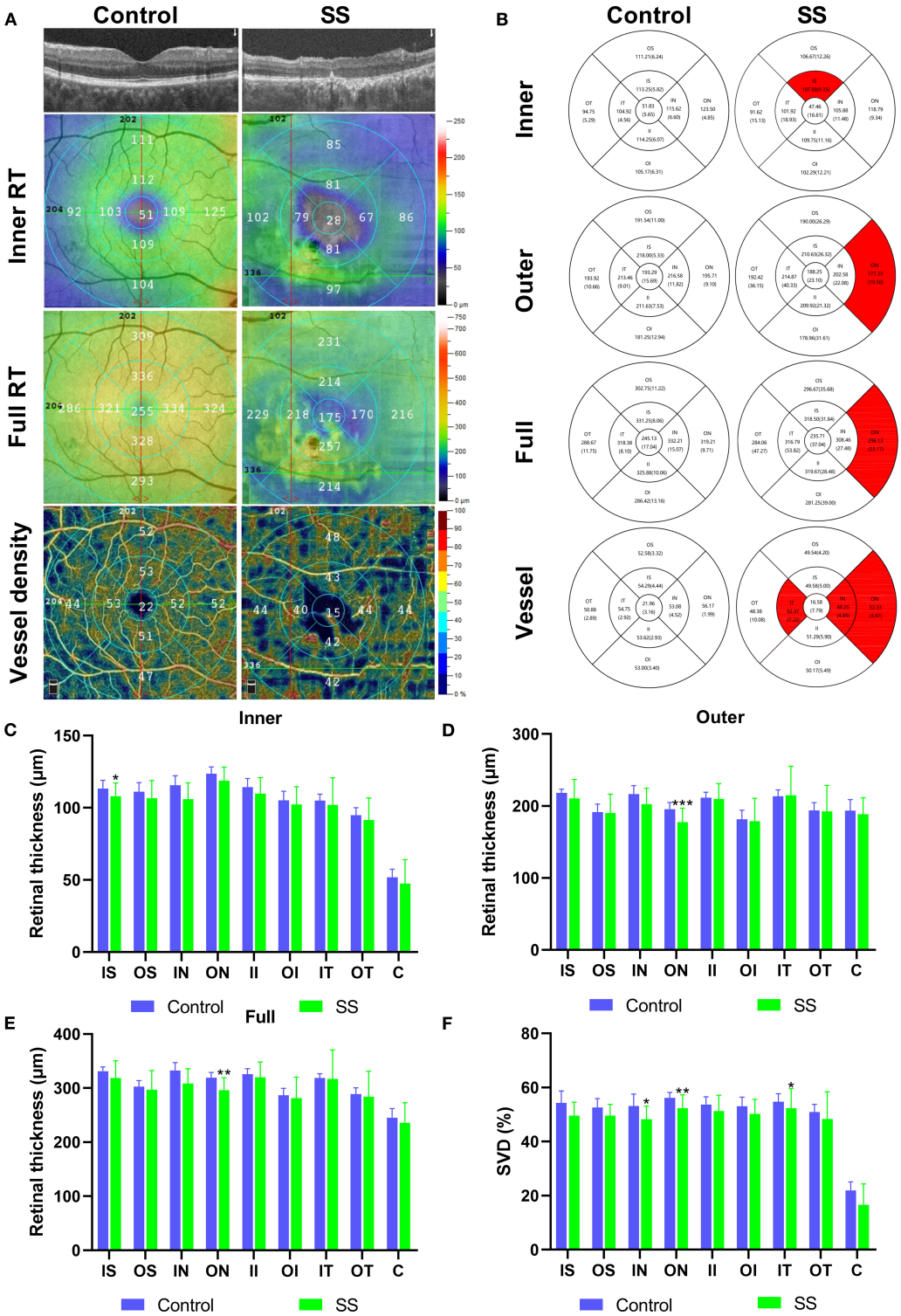

FIGURE 1 | The OCTA images and RT and SVD analysis of control and SS groups. **(A)** Cross-sectional view of RT in SS and health group used OCTA. The inner RT, full RT and SVD were measured by ETDRS. **(B)** The results of inner RT, outer RT, full RT and SVD in the SS and healthy group were compared. **(C–E)** Analysis of RT results in the SS and healthy group. The vertical coordinate is the value of RT, and the horizontal coordinate is the retinal subregions. **(F)** Analysis of SVD results in the SS and healthy group. The vertical coordinate is the value of SVD, and the horizontal coordinate is the retinal subregions. OCTA, optical coherence tomography angiography; SS, Sjogren's syndrome; RT, retinal thickness; SVD, superficial vessel density; ETDRS, early treatment of diabetic retinopathy study; IS, inner superior; OS, outer superior; IN, inner nasal; ON, outer nasal; II, inner inferior; OI, outer inferior; IT, inner temporal; OT, outer temporal; C center. * $p < 0.05$; ** $p < 0.01$; and *** $P < 0.001$.

TABLE 1 | General information of patients with SS and healthy subjects.

	SS (n = 12,24 eyes)	HC (n = 12,24 eyes)	t	P-value
Age (y)	55.17 ± 9.68	54.50 ± 9.25	−0.244	0.808[a]
Gender				
Female	12	12		1.0[b]
Duration of SS(y)	3.92 ± 1.93	N/A		
ESR (mm)	17.08 ± 8.43	N/A		
CRP (10mg/L)	2.73 ± 2.35	N/A		
ANA,n(%)	11(91.67)	N/A		
Anti SSA/Ro, n(%)	9(75.00)	N/A		
Anti SSB/La, n(%)	7(58.33)	N/A		
IgG (g/L)	16.11 ± 6.74	N/A		
C3 (g/L)	0.85 ± 0.14	N/A		
C4 (g/L)	0.21 ± 0.08	N/A		
ESSDAI—mean(range)	5.75(1-18)	N/A		
Salivary gland biopsy, *n* (%)	5(41.67)	N/A		
Focus Criteria + *n* (%)	2(40.00)	N/A		
Systolic blood pressure (mm Hg)	126.92 ± 5.60	123.08 ± 4.34	1.83	0.081[a]
Diastolic blood pressure (mm Hg)	78.67 ± 6.56	83.33 ± 6.82	1.671	0.109[a]
HADS	8.08 ± 3.65	2.58 ± 0.97	−7.139	**<0.001**[a]

Bold values indicates P < 0.05.
[a]*Independent t-test.*
[b]*Chi-square test.*
SS, Sjogren's syndrome; HC, healthy control; ANA, antinuclear antibody; ESR, erythrocyte sedimentation rate; CRP, C-reactive protein; ESSDAI, EULAR SS disease activity index for disease activity; HADS, hospital anxiety and Depression Scale; N/A, not applicable.

TABLE 2 | Ocular information of patients with SS and healthy subjects.

	SS (n = 12,24 eyes)	HC (n = 12,24 eyes)	P-value[a]
VA (logMAR)	0.20 ± 0.14	0.05 ± 0.07	**<0.001**
Spherical equivalent	1.75 ± 0.25	1.50 ± 0.50	0.891
Mean IOP (mm Hg)	14.63 ± 1.58	15.13 ± 1.61	0.357
BUT(s)	4.67 ± 0.92	13.42 ± 1.50	**<0.001**
OSS	3.12 ± 1.90	0	**<0.001**
SIT(mm)	3.33 ± 1.86	12.92 ± 1.32	**<0.001**
TMH(mm)	0.15 ± 0.04	0.58 ± 0.12	**<0.001**

Bold values indicates P < 0.05.
[a]*P-value was obtained with generalized estimating equation (both eyes of the subjects were included).*
SS, Sjogren's syndrome; HC, healthy control; VA, Visual acuity; IOP, intraocular pressure; BUT, Tear breakup time; OSS, Ocular staining score; SIT, Schirmer test; TMH, Tear meniscus height.

and foveal center ($p = 0.340$) showed no significant difference between groups.

The full RT in the nasal region of the outer ring was significantly thinner in patients with SS than in control subjects ($p = 0.007$) (**Figure 1E**). No significant differences between groups were observed in any of the other regions ($p > 0.05$).

In the univariate regression analysis, macular RT was negatively correlated with VA ($b = -14.237$, $p < 0.001$) but not with age, IOP, or BP. The multivariate regression analysis showed that advancing age ($b = -0.149$, $p = 0.030$) and poor VA ($b = -17.758$, $p = 0.002$) were significantly associated with thinner macular RT (**Table 4**).

Superficial Macular Retinal VD

Superficial VD at different retinal subregions in the SS and control groups is shown in **Table 5**, **Figure 1B**. After adjusting for age, IOP, VA, and BP, SVD was significantly lower in patients with SS than in controls on the nasal side (inner ring, $p = 0.010$ and outer ring, $p = 0.007$) and temporal region (inner ring, $p = 0.048$) (**Figure 1F**). In the SS group, SVD was negatively correlated with disease duration (−0.464) (**Figure 2A**).

ROC Curve Analysis of RT and SVD

Optical coherence tomography angiography data were analyzed to evaluate the specificity and sensitivity of RT and SVD as the diagnostic indicators of SS-related changes (**Figure 3**). Significant differences between groups were found in the inner superior (IS), outer ON, and full ON regions in the SS group. In the ON region, the area under the ROC curve for outer RT was 0.828 (95% *CI*: 0.709–0.947) and full RT was 0.839 (95% *CI*: 0.715–0.963), suggesting moderate to high diagnostic sensitivity for SS (**Figure 3A**).

Significant between-groups differences in SVD were found in the inner nasal (IN) and ON and inner temporal (IT) regions. The area under the SVD IN ROC curve was 0.806 (95% *CI*: 0.671–0.942), and the area under the SVD ON ROC curve was

TABLE 3 | Comparison of macular retinal thickness at different locations between patients with SS and healthy subjects.

Location	SS (n = 12,24 eyes)	HC (n = 12,24 eyes)	P-value[a]
Macular inner retinal thickness (μm, mean ± SD)			
IS	107.88 ± 9.35	113.25 ± 5.82	**0.022**
OS	106.67 ± 12.26	111.21 ± 6.24	0.348
IN	105.88 ± 11.48	115.62 ± 6.60	0.739
ON	118.79 ± 9.34	123.50 ± 4.85	0.161
II	109.75 ± 11.16	114.25 ± 6.07	0.115
OI	102.29 ± 12.21	105.17 ± 6.31	0.513
IT	101.92 ± 18.93	104.92 ± 4.56	0.841
OT	91.62 ± 15.13	94.75 ± 5.29	0.472
C	47.46 ± 16.61	51.83 ± 5.65	0.244
Macular outer retinal thickness (μm, mean ± sd)			
IS	210.63 ± 26.32	218.00 ± 5.33	0.118
OS	190.00 ± 26.29	191.54 ± 11.00	0.493
IN	202.58 ± 22.08	216.58 ± 11.82	0.581
ON	177.33 ± 19.50	195.71 ± 9.10	**<0.001**
II	209.92 ± 21.32	211.63 ± 7.53	0.228
OI	178.96 ± 31.61	181.25 ± 12.94	0.123
IT	214.87 ± 40.33	213.46 ± 9.01	0.302
OT	192.42 ± 36.15	193.92 ± 10.66	0.179
C	188.25 ± 23.10	193.29 ± 15.69	0.34
Macular full retinal thickness (μm, mean ± sd)			
IS	318.50 ± 31.84	331.25 ± 8.06	0.794
OS	296.67 ± 35.68	302.75 ± 11.22	0.25
IN	308.46 ± 27.48	332.21 ± 15.07	0.487
ON	296.13 ± 23.17	319.21 ± 9.71	**0.007**
II	319.67 ± 28.48	325.88 ± 10.06	0.878
OI	281.25 ± 39.00	286.42 ± 13.16	0.253
IT	316.79 ± 53.82	318.38 ± 8.10	0.521
OT	284.04 ± 47.27	288.67 ± 11.75	0.423
C	235.71 ± 37.04	245.13 ± 17.04	0.259

Bold values indicates P < 0.05.

[a]*Generalized estimating equation models were used to obtain P-values comparing mean inner,outer and full macular retinal thickness between SS patients and healthy subjects. Models were adjusted for age, intraocular pressure, acuity, blood pressure.*

SS, Sjogren's syndrome; HC, healthy control; IS, inner superior; OS, outer superior; IN, inner nasal; ON, outer nasal; II, inner inferior; OI, outer inferior; IT, inner temporal; OT, outer temporal; C, center.

0.752 (95% *CI*: 0.607–0.896), suggesting that SVD has moderate diagnostic sensitivity for SS (**Figure 3B**).

Relationship Between RT, SVD, IgG, and OSS

In patients with SS, full RT was correlated with SVD in the ON region ($r = 0.459$) (**Figure 4**), suggesting that retinal thinning is related to decreased VD in SS. The inner RT in the IS region of the SS group was negatively correlated with OSS (−0.431), implying that a thinner RT is related to the greater severity of xerophthalmia (**Figure 2B**). In patients with SS, negative correlations were found between RT and serum IgG level in the outer and full retina at ON regions (−0.564 and −0.467, respectively) (**Figure 2C**).

Relationship Between Disease Duration and HADS

A longer disease course in patients with SS was associated with a higher HADS index (0.897) (**Figure 2D**).

DISCUSSION

Sjogren's syndrome is characterized by exocrine gland involvement, abnormal proliferation of B lymphocytes, tissue infiltration of lymphocytes, and autoantibody production. The main clinical features dry eye, dry mouth, low fever, fatigue, and joint pain; about one-quarter of patients have visceral involvement. The risk of developing non-Hodgkin lymphoma is 40 times higher in patients with SS than in the general population (2). The EULAR and ACR issued a new classification standard for SS in 2016 (10) that emphasizes the pathologic features of the disease and the presence of autoantibodies; various indices corresponding to histology (labial gland biopsy), clinical indicators (SIT, OSS, and salivary flow rate), and immunology (anti–SS-A antibody) are stratified and weighted, and SS is diagnosed if the total score is ≥4. However, the lack of emphasis on the eyes in the assessment means that the significance of extraglandular changes in ophthalmic parameters are overlooked, although they are an important indicator of disease activity. We found that in the absence of clear ocular symptoms, patients in the SS group had significantly lower VA than healthy subjects, which has not been adequately addressed by other studies.

Sjogren's syndrome is referred as "benign lupus erythematosus" (34), which is another diffuse connective tissue disease associated with multiorgan damage; when the disease is active, the manifestations are similar to those of SLE and involve the vascular and nervous systems. The retina allows direct visualization of vascular changes (35) and provides a basis for early differentiation of patients with nervous system diseases (36). In our study, RT was calculated according to the ETDRS partition method and was found to be decreased in all areas of the retina in patients with SS, such as in the IS area of the inner retina, the ON area of the outer retina, and the ON area of the full-thickness retina. The results of the multiple regression analysis showed that visual impairment was associated with retinal thinning. This is in agreement with previous studies demonstrating that the ganglion cell inner plexiform and retinal nerve fiber layers were thinner in patients with SS compared with healthy subjects (37, 38). In healthy subjects, the inner RT is negatively correlated with age (39), which may be due to the loss of neurons, while the outer RT (especially RPE) may thicken with age (40). Our study found that full RT was negatively correlated with advancing age in patients with SS, this may need further longitudinal follow-up to confirm. The measurement of the full thickness of the retina in SS by OCTA has not yet been reported.

The choroidal blood supply is the most abundant in the body per unit weight and is therefore susceptible to inflammation in systemic diseases. Immune activation, autoantibody production, and impaired cellular immunity can damage the choroid. The activation of platelets and clotting pathways following vascular

TABLE 4 | Univariate and multivariate regression analyses of association between macular retinal thickness with demographic and ocular parameters in patients with SS.

Parameters	Univariate regression analysis Regression coefficient ($\beta \pm$ SE)	*P*-value[a]	Multivariate regression analysis Regression coefficient ($\beta \pm$ SE)	*P*-value[a]
Age (y)	−0.008 ± 0.044	0.861	−0.149 ± 0.069	**0.030**
VA (logMAR)	−14.237 ± 3.930	**<0.001**	−17.758 ± 5.841	**0.002**
Mean IOP (mm Hg)	0.204 ± 0.217	0.348	−0.013 ± 0.287	0.965
Systolic blood pressure (mm Hg)	−0.178 ± 0.114	0.120	−0.200 ± 0.110	0.070
Diastolic blood pressure (mm Hg)	0.108 ± 0.072	0.136	0.206 ± 0.127	0.105

Bold values indicates P < 0.05.
[a]P-value was obtained with generalized estimating equation.
SS, Sjogren's syndrome; HC, healthy control; VA, Visual acuity; IOP, intraocular pressure.

TABLE 5 | Comparison of superficial vessel density at different locations between patients with SS and healthy subjects.

Location (%, mean ± SD)	SS (*n* = 12,24eyes)	HC (*n* = 12,24eyes)	*P*-value[a]
IS	49.58 ± 5.00	54.29 ± 4.44	0.093
OS	49.54 ± 4.20	52.58 ± 3.32	0.825
IN	48.25 ± 4.85	53.08 ± 4.52	**0.01**
ON	52.33 ± 4.97	56.17 ± 1.99	**0.007**
II	51.29 ± 5.90	53.62 ± 2.93	0.214
OI	50.17 ± 5.49	53.00 ± 3.40	0.59
IT	52.37 ± 7.22	54.75 ± 2.92	**0.048**
OT	48.38 ± 10.08	50.88 ± 2.89	0.291
C	16.58 ± 7.79	21.96 ± 3.16	0.916

Bold values indicates P < 0.05. [a]Generalized estimating equation models were used to obtain P-values comparing mean superficial vessel density between SS patients and healthy subjects. Models were adjusted for age, intraocular pressure, acuity, blood pressure. SS, Sjogren's syndrome; HC, healthy control; IS, inner superior; OS, outer superior; IN, inner nasal; ON, outer nasal; II, inner inferior; OI, outer inferior; IT, inner temporal; OT, outer temporal; C, center.

injury can lead to intravascular microthrombosis. The resultant vascular lesions and intimal hyperplasia of small arterioles followed by lumen stenosis lead to tissue hypoxia and chronic ischemia (41). The choroid is particularly sensitive to subclinical disease activity. In SLE, changes in the choroid may reflect reversible nephropathy and neuropathy (42). Similar changes in the retina may have clinical value for SS.

The retina and brain originate from the same embryonic tissue and both have comparable metabolic activity. A decrease in retinal blood supply can lead to the death of retinal cells (43). The internal blood flow of the retina is mainly supplied by the central retinal artery with the contribution from choroid vessels. The choroid can increase the partial pressure of O_2 in the retina through the Root effect (44). When this occurs in the blood vessels supplying the retina, the resultant pathologic changes can affect the entire chorioretinal vascular network. Our study found that in patients with SS, the SVD showed a downward trend in all subregions with statistically significant decreases in the IN, ON, and IT regions. An increased neovascularization and the upregulation of vascular endothelial growth factor (VEGF)-A and its receptor VEGFR-2, which promote neovascularization, have been previously observed in the salivary glands of patients with SS (45), and angiogenesis is closely linked to the progression of SS (46). In contrast, we observed a decrease vascular density in the retina with increasing disease severity. Moreover, full RT was positively associated with SVD. Similar changes and associations have been reported in patients with diabetes (47) and Behcet's syndrome (18); alterations in microcirculation in these patients may precede clinically distinguishable retinopathy. We speculate that such subclinical changes exist in patients with SS. Retinal thinning was more obvious on the nasal side, while capillary loss was detected in the nasal and temporal regions. Choroidal capillary network lesions directly affect the blood supply to the outer retina; this can lead to chronic ischemia, especially of the photoreceptor layer and the death of rod cells and cone cells due to a decreased energy supply and loss of vision (43), which is supported by our findings (**Figure 5**).

The proliferation of peripheral B cells plays an important role in the development of SS. The overactivation of B cells is the main factor of hyperglobulinemia and autoantibody production (48, 49). At the same time, the disorder of peripheral B cell subsets exists in SS, such as the significant decrease of CD27 + memory B cells, the increase of CD27 initial B cells and CD19 + B cells (50), and the positive correlation between the number of CD19 + B cells and IgG serum level and hypergammaglobulinemia (51). In SLE, the deposition of IgG immune complex in retinal vascular wall is associated with retinal nerve fiber layer infarction and ganglion cell atrophy (52). In patients with glaucoma, the loss of retinal ganglion cells is accompanied by the accumulation of IgG autoantibodies on ganglion cell layer cells (53), and the deposition of IgG autoantibodies is accompanied by CD27 +/IgG + plasma cells, which occurs under pro-inflammatory conditions, the level of tumor necrosis factor-α (TNF-α), interleukin (IL)-6, and IL-8 were also increased (53). Immunity leads to antigen-specific and complex systemic immune responses, including the production of auto reactive antibodies against retinal and optic nerve epitopes with an increasing and time-dependent severity (53). Autoantibodies against a variety of retinal antigens have been reported, such as recoverin, α-Enolase, heat shock protein, arrestin, transducing protein, neurofilament protein, carbonic anhydrase II, and Tubby-related protein 1 (TULP1) (54). In our study, RT was found to be negatively correlated with IgG, indicating that RT may be affected by the abnormal immune

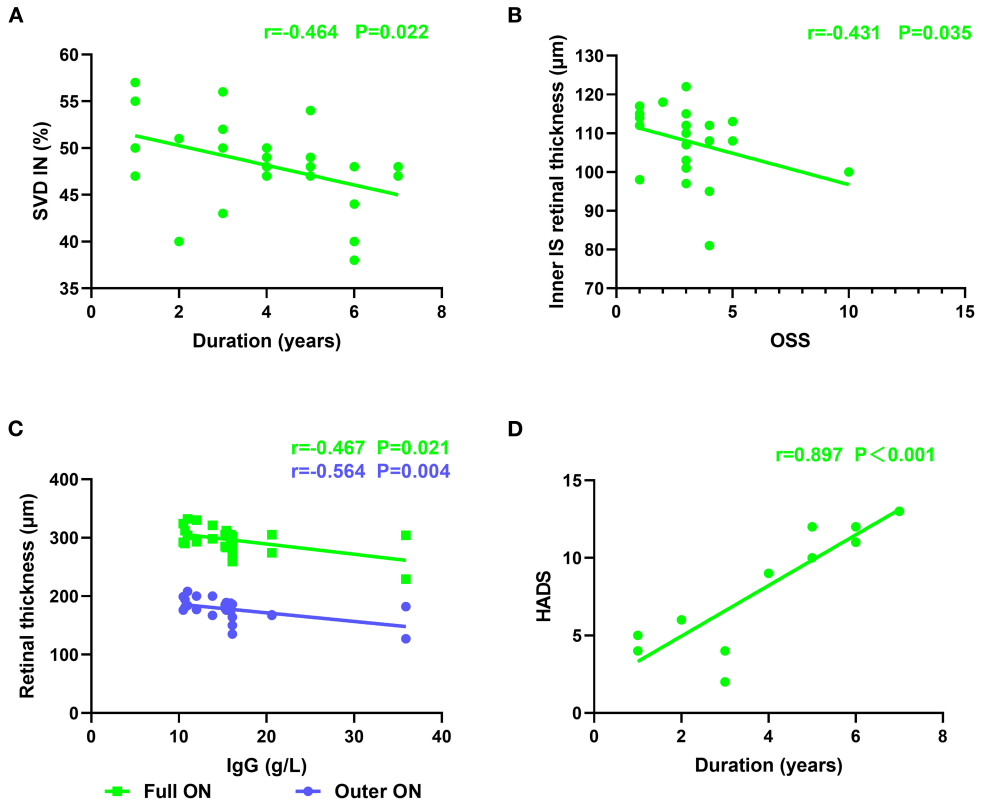

FIGURE 2 | Retinal thickness was correlated with serum IgG level and OSS. The correlation between the duration of disease and HADS, SVD. **(A)** Negative correlation was found between duration and SVD at IN region ($r = -0.464$, $p = 0.022$). The vertical coordinate is the value of SVD, and the horizontal coordinate is the duration. **(B)** Negative correlation was found between RT and OSS in the inner retina at IS region ($r = -0.431$, $p = 0.035$). The vertical coordinate is the value of RT, and the horizontal coordinate is the value of OSS. **(C)** Negative correlation was found between RT and serum IgG level in the outer retina at ON region ($r = -0.564$, $p = 0.004$). Negative correlation was found between RT and serum IgG level in the full retina at ON region ($r = -0.467$, $p = 0.021$). The vertical coordinate is the value of RT, and the horizontal coordinate is the value of IgG. **(D)** Positive correlation was found between duration and HADS ($r = 0.897$, $p < 0.001$). The vertical coordinate is the value of HADS, and the horizontal coordinate is the duration. SS, Sjogren's syndrome; OSS, ocular staining score; HADS, hospital anxiety and Depression Scale; RT, retinal thickness; SVD, superficial vessel density; IS, inner superior.

state of SS disease. The exact mechanism of vascular occlusion in autoimmune diseases is still unclear, however, some possible pathogenic mechanisms include immune complex deposition, complement activation with microvascular thrombosis, and the fibrinoid degeneration of vascular wall (55). This may also be the possible reason for the decrease of SVD in patients with SS, and indirectly lead to the thinning of RT.

In patients with SS, an imbalance in the ratio of type 1 to type 2 helper T cells (56) leads to excessive interferon-γ (57), IL-17 (58), IL-21 (59), and IL-22 (60) production, which creates an inflammatory microenvironment that can cause tissue damage. Goblet cells are the main cells responsible for eye lubrication and their secretory ability is an important indicator of eye surface health. The secretory function and proliferative capacity of goblet cells are inhibited by increased inflammatory cytokine levels, resulting in changes in the ocular surface and irregular tear secretion (61). The OSS, similar to SIT test and BUT, is a reliable and objective index of the degree of dryness of the eyes. Our results showed that with the worsening of dry eye, the SIT score and BUT decreased while OSS increased. Additionally, SIT, BUT, and TMH were reduced whereas OSS was significantly higher in patients with SS compared with control subjects while inner RT was negatively correlated with OSS, which indirectly reflected the degree of dryness of the eyes.

Mental health disorders are more common in patients with SS than in healthy individuals (62, 63). The prevalence of anxiety and depression in patients with SS in China is 33.8 and 36.9%, respectively (64). Anxiety and/or depression are associated with lower physical activity and treatment compliance, which can have adverse effects on the well-being of patients with SS and may increase the incidence rate of cardiovascular disease and exacerbate SS (65). In our study, patients with SS had a higher HADS score than control subjects, which was positively correlated with disease duration.

The results of the ROC curve analysis of outer and full RT in the ON region indicated that these parameters have diagnostic utility for SS. Early diagnosis and accurate evaluation are critical for the successful treatment and good prognosis. SS has variable clinical manifestations, disease course, and prognosis, and clinical symptomatology is often unrelated to the degree of gland destruction. Classification criteria are standardized tools for the selection of appropriately defined homogeneous

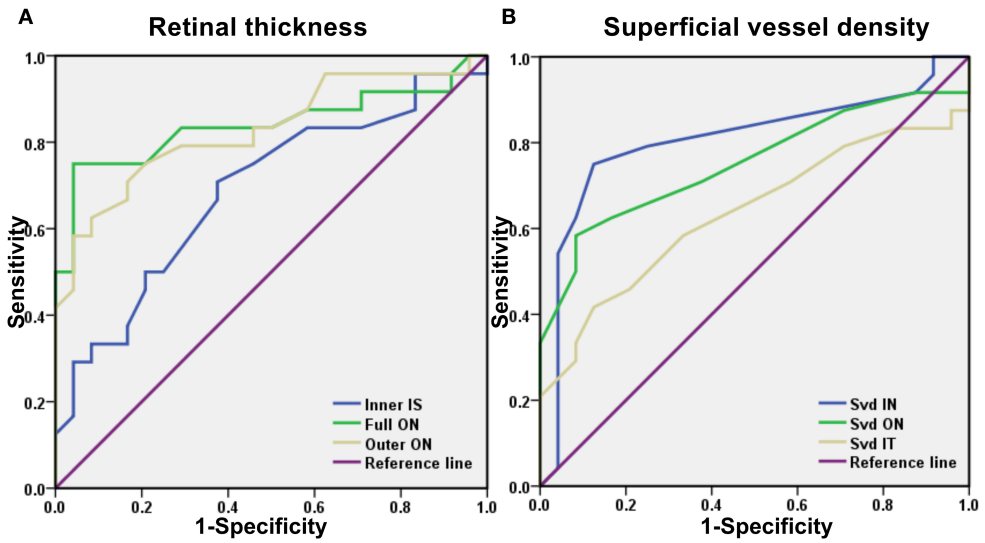

FIGURE 3 | A receiver operating characteristic (ROC) curve analysis of RT and SVD. **(A)** The area under the ROC curve were 0.688 (95% *CI* = 0.536–0.839) for inner IS, full ON 0.839 (95% *CI* = 0.715–0.963), outer ON 0.828 (95% *CI* = 0.709–0.947). **(B)** The area under the ROC curve were 0.806 (95% *CI* = 0.671–0.942) for SVD IN, SVD ON 0.752 (95% *CI* = 0.607–0.896), SVD IT 0.635 (95% *CI* = 0.473–0.798). ROC, receiver operating characteristic; CI, confidence interval; RT, retinal thickness; SVD, superficial vessel density; ON, outer nasal; IT, inner temporal; IS, inner superior; IN, inner nasal.

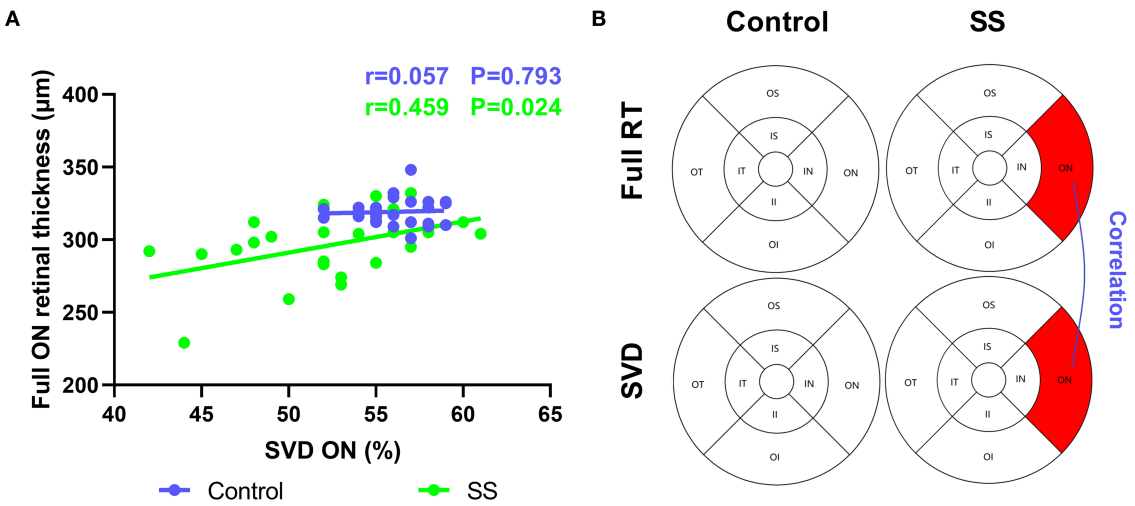

FIGURE 4 | Correlation between RT and SVD in normal and patients with SS. The vertical coordinate is the value of RT, and the horizontal coordinate is the value of SVD. **(A,B)** In the SS group, SVD was positively correlated with full RT at ON region ($r = 0.459$, $p = 0.024$). SS, Sjogren's syndrome; RT, retinal thickness; SVD, superficial vessel density; ON, outer nasal.

patient groups for research; however, they often fail to identify atypical individuals (20). OCTA is a noninvasive and convenient imaging method that can provide information on intraocular vascular network perfusion; RT measured by OCTA is a potential biomarker that can aid the diagnosis of SS. However, there is no previous report on the use of OCTA in patients with SS. So we did a preliminary study prudently. We set up a control group of healthy subjects in this study, so that we can distinguish SS from healthy people first through OCTA and then we will set up other control groups to test whether OCTA is helpful to distinguish SS from other diseases. At present, we are only exploring a possibility. We will conduct additional studies with larger samples to validate its diagnostic utility. At this stage, OCTA may be used in addition to the existing classification criteria.

This study had some limitations. First, given that patients with HCQ-induced retinochoroidosis were excluded, we did not consider the role of HCQ in SS in detail. Second, as the sample size was small, our findings require validation in a larger cohort before they can be translated into clinical practice. Due to the obvious gender bias of SS, the current study recruits female

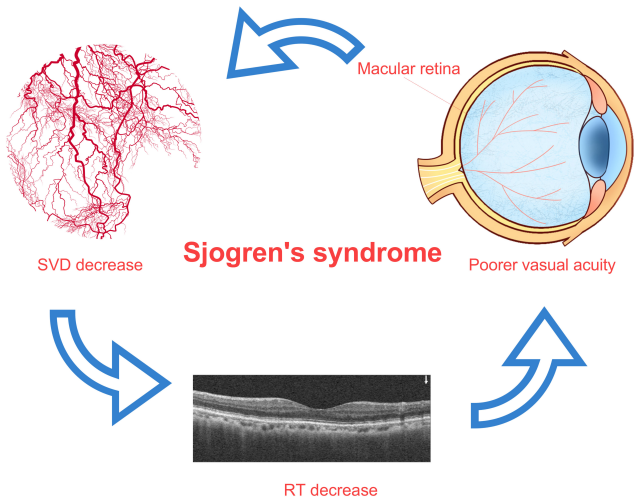

FIGURE 5 | Relationship among SVD decrease, RT thinning, and visual impairment in patients with SS. In patients with SS, the decrease of superficial retinal vascular density in macular area may lead to the decrease of retinal thickness in related areas, and the decrease of retinal thickness in macular area may lead to the decrease of vision. The macular area is marked on the image of eyeball, which indicates the decrease of superficial vascular density in this area. SS, Sjogren's syndrome; RT, retinal thickness; SVD, superficial vessel density.

patients. With the deepening of the study, we will include more cases, both male and female will be taken into account. Third, RT is affected by many factors (such as, age and spherical equivalent). We will consider the influence of related factors as much as possible in the future study.

CONCLUSIONS

We used OCTA to evaluate the significance of RT and SVD in SS, and found that the inner, outer, and full RT were thinner while SVD was decreased in the ON, IN, and IT regions of patients with SS compared with controls; additionally, RT is positively correlated with SVD and negatively related to IgG. Thus, retinal thinning in the macular area—which affects vision—can also reflect the severity of dry eyes in SS and has clinical value for assisted imaging diagnosis.

DATA AVAILABILITY STATEMENT

The datasets presented in this study can be found in online repositories. The name of the repository and accession number can be found below: Figshare, https://figshare.com/s/793657ff2e10765b6616.

ETHICS STATEMENT

The studies involving human participants were reviewed and approved by the Medical Ethics of the First Affiliated Hospital of Nanchang University (cdyfy2018026). Written informed consent for participation was not required for this study in accordance with the national legislation and the institutional requirements.

AUTHOR CONTRIBUTIONS

RL: writing the original draft and data analysis. YS: data analysis and editing. YW, QL, QX, TX, TH, SC, and SL: data collection. YS and RW: supervision and editing. All authors contributed to the article and approved the submitted version.

FUNDING

This research is supported by The Central Government Guides Local Science and Technology Development Foundation (20211ZDG02003); Key Research Foundation of Jiangxi Province (No: 20181BBG70004); Excellent Talents Development Project of Jiangxi Province (20192BCBL23020); Natural Science Foundation of Jiangxi Province (20181BAB205034); Grassroots Health Appropriate Technology Spark Promotion Plan Project of Jiangxi Province (No: 20188003); the Health Development Planning Commission Science Foundation of Jiangxi Province (No: 20201032); and the Health Development Planning Commission Science TCM Foundation of Jiangxi Province (No: 2018A060).

ACKNOWLEDGMENTS

The authors thank Department of Ophthalmology and Rheumatology of The First Affiliated Hospital of Nanchang University for the help during this study.

REFERENCES

1. Qin B, Wang J, Yang Z, Yang M, Ma N, Huang F, et al. Epidemiology of primary Sjögren's syndrome: a systematic review and meta-analysis. *Ann Rheum Dis.* (2015) 74:1983–9. doi: 10.1136/annrheumdis-2014-205375
2. Vivino FB. Sjogren's syndrome: Clinical aspects. *Clin Immunol (Orlando, Fla).* (2017) 182:48–54. doi: 10.1016/j.clim.2017.04.005
3. Stefanski AL, Tomiak C, Pleyer U, Dietrich T, Burmester GR, Dörner T. The Diagnosis and Treatment of Sjögren's Syndrome. *Dtsch Arztebl Int.* (2017) 114:354–61. doi: 10.3238/arztebl.2017.0354
4. Sutcliffe N, Stoll T, Pyke S, Isenberg DA. Functional disability and end organ damage in patients with systemic lupus erythematosus (SLE), SLE and Sjögren's syndrome (SS), and primary SS. *J Rheumatol.* (1998) 25:63–8.
5. Koh JH, Kwok SK, Lee J, Son CN, Kim JM, Kim HO, et al. Pain, xerostomia, and younger age are major determinants of fatigue in Korean patients with primary Sjögren's syndrome: a cohort study. *Scand J Rheumatol.* (2017) 46:49–55. doi: 10.3109/03009742.2016.1153142
6. Kotsis K, Voulgari PV, Tsifetaki N, Drosos AA, Carvalho AF, Hyphantis T. Illness perceptions and psychological distress associated with physical health-related quality of life in primary Sjögren's syndrome compared to systemic lupus erythematosus and rheumatoid arthritis. *Rheumatol Int.* (2014) 34:1671–81. doi: 10.1007/s00296-014-3008-0
7. Kassan SS, Moutsopoulos HM. Clinical manifestations and early diagnosis of Sjögren syndrome. *Arch Intern Med.* (2004) 164:1275–84. doi: 10.1001/archinte.164.12.1275

8. Akpek EK, Mathews P, Hahn S, Hessen M, Kim J, Grader-Beck T, et al. Ocular and systemic morbidity in a longitudinal cohort of Sjögren's syndrome. *Ophthalmology.* (2015) 122:56–61. doi: 10.1016/j.ophtha.2014.07.026
9. Vitali C, Bombardieri S, Jonsson R, Moutsopoulos HM, Alexander EL, Carsons SE, et al. Classification criteria for Sjögren's syndrome: a revised version of the European criteria proposed by the American-European Consensus Group. *Ann Rheum Dis.* (2002) 61:554–8. doi: 10.1136/ard.61.6.554
10. Shiboski CH, Shiboski SC, Seror R, Criswell LA, Labetoulle M, Lietman TM, et al. (2016 American College of Rheumatology/European League Against Rheumatism Classification Criteria for Primary Sjögren's Syndrome: a consensus and data-driven methodology involving three international patient cohorts. *Arthritis Rheumatol (Hoboken, NJ).* (2017) 69:35–45. doi: 10.1002/art.39859
11. Segal B, Bowman SJ, Fox PC, Vivino FB, Murukutla N, Brodscholl J, et al. Primary Sjögren's Syndrome: health experiences and predictors of health quality among patients in the United States. *Health Qual Life Outcomes.* (2009) 7:46. doi: 10.1186/1477-7525-7-46
12. Saldanha IJ, Petris R, Han G, Dickersin K, Akpek EK. Research Questions and Outcomes Prioritized by Patients With Dry Eye. *JAMA Ophthalmol.* (2018) 136:1170–9. doi: 10.1001/jamaophthalmol.2018.3352
13. Cohen KL. Sterile corneal perforation after cataract surgery in Sjögren's syndrome. *Br J Ophthalmol.* (1982) 66:179–82. doi: 10.1136/bjo.66.3.179
14. Gottsch JD, Akpek EK. Topical cyclosporin stimulates neovascularization in resolving sterile rheumatoid central corneal ulcers. *Trans Am Ophthalmol Soc.* (2000) 98:81–7; discussion 7–90.
15. Ou JI, Manche EE. Corneal perforation after conductive keratoplasty in a patient with previously undiagnosed Sjögren syndrome. *Arch Ophthalmol (Chicago, Ill: 1960).* (2007) 125:1131–2. doi: 10.1001/archopht.125.8.1131
16. Rosenbaum JT, Bennett RM. Chronic anterior and posterior uveitis and primary Sjögren's syndrome. *Am J Ophthalmol.* (1987) 104:346–52. doi: 10.1016/0002-9394(87)90223-6
17. Bamrolia NR, Arora R, Yadava U. Unusual presentation of a case of Sjogren's syndrome with neurological and ocular manifestation. *Cont Lens Anterior Eye.* (2012) 35:85–8. doi: 10.1016/j.clae.2011.10.002
18. Steiner M, Esteban-Ortega MDM, Muñoz-Fernández S. Choroidal and retinal thickness in systemic autoimmune and inflammatory diseases: a review. *Surv Ophthalmol.* (2019) 64:757–69. doi: 10.1016/j.survophthal.2019.04.007
19. Mukherjee B, Nair AG. Principles and practice of external digital photography in ophthalmology. *Indian J Ophthalmol.* (2012) 60:119–25. doi: 10.4103/0301-4738.94053
20. Jonsson R, Brokstad KA, Jonsson MV, Delaleu N, Skarstein K. Current concepts on Sjögren's syndrome - classification criteria and biomarkers. *Eur J Oral Sci.* (2018) 126 Suppl 1:37–48. doi: 10.1111/eos.12536
21. Seror R, Ravaud P, Bowman SJ, Baron G, Tzioufas A, Theander E, et al. EULAR Sjogren's syndrome disease activity index: development of a consensus systemic disease activity index for primary Sjogren's syndrome. *Ann Rheum Dis.* (2010) 69:1103–9. doi: 10.1136/ard.2009.110619
22. Chen M, Dai J, Gong L. Changes in retinal vasculature and thickness after small incision lenticule extraction with optical coherence tomography angiography. *J Ophthalmol.* (2019) 2019:3693140. doi: 10.1155/2019/3693140
23. Spaide RF, Klancnik JM. Jr, Cooney MJ. Retinal vascular layers imaged by fluorescein angiography and optical coherence tomography angiography. *JAMA Ophthalmol.* (2015) 133:45–50. doi: 10.1001/jamaophthalmol.2014.3616
24. Spaide RF, Fujimoto JG, Waheed NK, Sadda SR, Staurenghi G. Optical coherence tomography angiography. *Prog Retin Eye Res.* (2018) 64:1–55. doi: 10.1016/j.preteyeres.2017.11.003
25. Veverka KK, AbouChehade JE, Iezzi R., Pulido JS. NONINVASIVE GRADING OF RADIATION RETINOPATHY: the use of optical coherence tomography angiography. *Retina (Philadelphia, Pa).* (2015) 35:2400–10. doi: 10.1097/IAE.0000000000000844
26. Hasegawa N, Nozaki M, Takase N, Yoshida M, Ogura Y. New insights into microaneurysms in the deep capillary plexus detected by optical coherence tomography angiography in diabetic macular edema. *Invest Ophthalmol Vis Sci.* (2016) 57:Oct348-55. doi: 10.1167/iovs.15-18782
27. Wang X, Jia Y, Spain R, Potsaid B, Liu JJ, Baumann B, et al. Optical coherence tomography angiography of optic nerve head and parafovea in multiple sclerosis. *Br J Ophthalmol.* (2014) 98:1368–73. doi: 10.1136/bjophthalmol-2013-304547
28. Ye L, Zhou SS, Yang WL, Bao J, Jiang N, Min YL, et al. RETINAL MICROVASCULATURE ALTERATION IN ACTIVE THYROID-ASSOCIATED OPHTHALMOPATHY. *Endocr Pract.* (2018) 24:658–67. doi: 10.4158/EP-2017-0229
29. Kroese FGM, Haacke EA, Bombardieri M. The role of salivary gland histopathology in primary Sjögren's syndrome: promises and pitfalls. *Clin Exp Rheumatol.* (2018) 36 Suppl 112:222–33.
30. Mackenzie LJ, Carey ML, Sanson-Fisher RW, D'Este CA, Paul CL, Yoong SL. Agreement between HADS classifications and single-item screening questions for anxiety and depression: a cross-sectional survey of cancer patients. *Ann Oncol.* (2014) 25:889–95. doi: 10.1093/annonc/mdu023
31. Methodologies to diagnose and monitor dry eye disease: report of the Diagnostic Methodology Subcommittee of the International Dry Eye WorkShop (2007). *Ocular Surface.* (2007) 5:108–52. doi: 10.1016/S1542-0124(12)70083-6
32. Arita R, Yabusaki K, Hirono T, Yamauchi T, Ichihashi T, Fukuoka S, et al. Automated measurement of tear meniscus height with the kowa dr-1α tear interferometer in both healthy subjects and dry eye patients. *Invest Ophthalmol Vis Sci.* (2019) 60:2092–101. doi: 10.1167/iovs.18-24850
33. Kashani AH, Chen CL, Gahm JK, Zheng F, Richter GM, Rosenfeld PJ, et al. Optical coherence tomography angiography: a comprehensive review of current methods and clinical applications. *Prog Retin Eye Res.* (2017) 60:66–100. doi: 10.1016/j.preteyeres.2017.07.002
34. Diamond B. Systemic lupus erythematosus and Sjögren's syndrome. *Curr Opin Rheumatol.* (2007) 19:405. doi: 10.1097/BOR.0b013e3282b971f5
35. Md Noh UK, Zahidin AZ, Yong TK. Retinal vasculitis in systemic lupus erythematosus: an indication of active disease. *Clin Pract.* (2012) 2:e54. doi: 10.4081/cp.2012.e54
36. Karadag AS, Bilgin B, Soylu MB. Comparison of optical coherence tomographic findings between Behcet disease patients with and without ocular involvement and healthy subjects. *Arq Bras Oftalmol.* (2017) 80:69–73. doi: 10.5935/0004-2749.20170018
37. Arikan S, Gokmen F, Comez AT, Gencer B, Kara S, Akbal A. Evaluation of possible factors affecting contrast sensitivity function in patients with primary Sjögren's syndrome. *Arq Bras Oftalmol.* (2015) 78:150–3. doi: 10.5935/0004-2749.20150039
38. Yang JM, Sung MS, Ji YS, Heo H, Park SW. Analysis of clinical factors associated with retinal morphological changes in patients with primary Sjögren's syndrome. *PLoS ONE.* (2016) 11:e0157995. doi: 10.1371/journal.pone.0157995
39. Kerrigan-Baumrind LA, Quigley HA, Pease ME, Kerrigan DF, Mitchell RS. Number of ganglion cells in glaucoma eyes compared with threshold visual field tests in the same persons. *Invest Ophthalmol Vis Sci.* (2000) 41:741–8.
40. Staurenghi G, Sadda S, Chakravarthy U, Spaide RF. Proposed lexicon for anatomic landmarks in normal posterior segment spectral-domain optical coherence tomography: the IN•OCT consensus. *Ophthalmology.* (2014) 121:1572–8. doi: 10.1016/j.ophtha.2014.02.023
41. Ferreira CS, Beato J, Falcão MS, Brandão E, Falcão-Reis F, Carneiro Â M, et al. MANIFESTATIONS. *Retina (Philadelphia, Pa).* (2017) 37:529–35. doi: 10.1097/IAE.0000000000001193
42. Nguyen QD, Uy HS, Akpek EK, Harper SL, Zacks DN, Foster CS. Choroidopathy of systemic lupus erythematosus. *Lupus.* (2000) 9:288–98. doi: 10.1191/096120300680199024
43. Country MW. Retinal metabolism: a comparative look at energetics in the retina. *Brain Res.* (2017) 1672:50–7. doi: 10.1016/j.brainres.2017.07.025
44. Waser W, Heisler N. Oxygen delivery to the fish eye: root effect as crucial factor for elevated retinal PO2. *J Exp Biol.* (2005) 208:4035–47. doi: 10.1242/jeb.01874
45. Sisto M, Lisi S, Ingravallo G, Lofrumento DD, D'Amore M, Ribatti D. Neovascularization is prominent in the chronic inflammatory lesions of Sjögren's syndrome. *Int J Exp Pathol.* (2014) 95:131–7. doi: 10.1111/iep.12061
46. Rodrigues AR, Soares R. Inflammation in Sjögren's syndrome: cause or consequence? *Autoimmunity.* (2017) 50:141–50. doi: 10.1080/08916934.2017.1280027
47. Kim K, Kim ES, Kim DG, Yu SY. Progressive retinal neurodegeneration and microvascular change in diabetic retinopathy: longitudinal

study using OCT angiography. *Acta Diabetol.* (2019) 56:1275–82. doi: 10.1007/s00592-019-01395-6
48. Hershberg U, Meng W, Zhang B, Haff N, St Clair EW, Cohen PL, et al. Persistence and selection of an expanded B-cell clone in the setting of rituximab therapy for Sjögren's syndrome. *Arthritis Res Ther.* (2014) 16:R51. doi: 10.1186/ar4481
49. Zheng J, Huang Q, Huang R, Deng F, Yue X, Yin J, et al. B Cells Are Indispensable for a Novel Mouse Model of Primary Sjögren's Syndrome. *Front Immunol.* (2017) 8:1384. doi: 10.3389/fimmu.2017.01384
50. Ibrahem HM, B. cell dysregulation in primary Sjögren's syndrome: a review. *Jpn Dent Sci Rev.* (2019) 55:139–44. doi: 10.1016/j.jdsr.2019.09.006
51. Ishioka-Takei E, Yoshimoto K, Suzuki K, Nishikawa A, Yasuoka H, Yamaoka K, et al. Increased proportion of a CD38(high)IgD(+) B cell subset in peripheral blood is associated with clinical and immunological features in patients with primary Sjögren's syndrome. *Clin Immunol (Orlando, Fla).* (2018) 187:85–91. doi: 10.1016/j.clim.2017.10.008
52. Liu GY, Utset TO, Bernard JT. Retinal nerve fiber layer and macular thinning in systemic lupus erythematosus: an optical coherence tomography study comparing SLE and neuropsychiatric SLE. *Lupus.* (2015) 24:1169–76. doi: 10.1177/0961203315582285
53. Gramlich OW, Beck S, von Thun Und Hohenstein-Blaul N, Boehm N, Ziegler A, Vetter JM, et al. Enhanced insight into the autoimmune component of glaucoma: IgG autoantibody accumulation and pro-inflammatory conditions in human glaucomatous retina. *PLoS ONE.* (2013) 8:e57557. doi: 10.1371/journal.pone.0057557
54. Abazari A, Allam SS, Adamus G, Ghazi NG. Optical coherence tomography findings in autoimmune retinopathy. *Am J Ophthalmol.* (2012) 153:750–6, 6.e1. doi: 10.1016/j.ajo.2011.09.012
55. Yen YC, Weng SF, Chen HA, Lin YS. Risk of retinal vein occlusion in patients with systemic lupus erythematosus: a population-based cohort study. *Br J Ophthalmol.* (2013) 97:1192–6. doi: 10.1136/bjophthalmol-2013-303265
56. Mitsias DI, Tzioufas AG, Veiopoulou C, Zintzaras E, Tassios IK, Kogopoulou O, et al. The Th1/Th2 cytokine balance changes with the progress of the immunopathological lesion of Sjogren's syndrome. *Clin Exp Immunol.* (2002) 128:562–8. doi: 10.1046/j.1365-2249.2002.01869.x
57. Gliozzi M, Greenwell-Wild T, Jin W, Moutsopoulos NM, Kapsogeorgou E, Moutsopoulos HM, et al. A link between interferon and augmented plasmin generation in exocrine gland damage in Sjögren's syndrome. *J Autoimmun.* (2013) 40:122–33. doi: 10.1016/j.jaut.2012.09.003
58. Katsifis GE, Rekka S, Moutsopoulos NM, Pillemer S, Wahl SM. Systemic and local interleukin-17 and linked cytokines associated with Sjögren's syndrome immunopathogenesis. *Am J Pathol.* (2009) 175:1167–77. doi: 10.2353/ajpath.2009.090319
59. Scofield RH. IL-21 and Sjögren's syndrome. *Arthritis Res Ther.* (2011) 13:137. doi: 10.1186/ar3518
60. Ciccia F, Guggino G, Rizzo A, Ferrante A, Raimondo S, Giardina A, et al. Potential involvement of IL-22 and IL-22-producing cells in the inflamed salivary glands of patients with Sjogren's syndrome. *Ann Rheum Dis.* (2012) 71:295–301. doi: 10.1136/ard.2011.154013
61. Zoukhri D. Mechanisms involved in injury and repair of the murine lacrimal gland: role of programmed cell death and mesenchymal stem cells. *Ocul Surf.* (2010) 8:60–9. doi: 10.1016/S1542-0124(12)70070-8
62. Anyfanti P, Pyrpasopoulou A, Triantafyllou A, Triantafyllou G, Gavriilaki E, Chatzimichailidou S, et al. Association between mental health disorders and sexual dysfunction in patients suffering from rheumatic diseases. *J Sex Med.* (2014) 11:2653–60. doi: 10.1111/jsm.12672
63. Milin M, Cornec D, Chastaing M, Griner V, Berrouiguet S, Nowak E, et al. Sicca symptoms are associated with similar fatigue, anxiety, depression, and quality-of-life impairments in patients with and without primary Sjögren's syndrome. *Joint bone spine.* (2016) 83:681–5. doi: 10.1016/j.jbspin.2015.10.005
64. Koçer B, Tezcan ME, Batur HZ, Haznedaroglu S, Göker B, Irkeç C, et al. Cognition, depression, fatigue, and quality of life in primary Sjögren's syndrome: correlations. *Brain Behav.* (2016) 6:e00586. doi: 10.1002/brb3.586
65. Cui Y, Xia L, Li L, Zhao Q, Chen S, Gu Z. Anxiety and depression in primary Sjögren's syndrome: a cross-sectional study. *BMC Psychiatry.* (2018) 18:131. doi: 10.1186/s12888-018-1715-x

Conflict of Interest: The authors declare that the research was conducted in the absence of any commercial or financial relationships that could be construed as a potential conflict of interest.

Publisher's Note: All claims expressed in this article are solely those of the authors and do not necessarily represent those of their affiliated organizations, or those of the publisher, the editors and the reviewers. Any product that may be evaluated in this article, or claim that may be made by its manufacturer, is not guaranteed or endorsed by the publisher.

Copyright © 2022 Liu, Wang, Li, Xia, Xu, Han, Cai, Luo, Wu and Shao. This is an open-access article distributed under the terms of the Creative Commons Attribution License (CC BY). The use, distribution or reproduction in other forums is permitted, provided the original author(s) and the copyright owner(s) are credited and that the original publication in this journal is cited, in accordance with accepted academic practice. No use, distribution or reproduction is permitted which does not comply with these terms.

frontiers in Neurology

ORIGINAL RESEARCH
published: 08 March 2022
doi: 10.3389/fneur.2022.833922

Eucommia ulmoides Oliver-Tribulus terrestris L. Drug Pair Regulates Ferroptosis by Mediating the Neurovascular-Related Ligand-Receptor Interaction Pathway- A Potential Drug Pair for Treatment Hypertension and Prevention Ischemic Stroke

Qian Zhang[1], *Jie Yang*[2]*, *Chuanhua Yang*[2]*, *Xuesong Yang*[3] *and Yongzhi Chen*[2]

[1] Department of Science and Technology Office, The Affiliated Hospital of Shandong University of Traditional Chinese Medicine, Jinan, China, [2] Department of Cardiology, The Affiliated Hospital of Shandong University of Traditional Chinese Medicine, Jinan, China, [3] Department of Vascular Surgery, The Affiliated Hospital of Shandong University of Traditional Chinese Medicine, Jinan, China

OPEN ACCESS

Edited by:
Yuzhen Xu,
Tongji University, China

Reviewed by:
Bo Liu,
Shanghai Jiaotong University, China
Chao Xu,
The Second Affiliated Hospital of Shaanxi University of Traditional Chinese Medicine, China

***Correspondence:**
Jie Yang
yangjie@wanfeng.edu.bi
Chuanhua Yang
yangchuanhua@wanfeng.edu.bi

Specialty section:
This article was submitted to Neurological Biomarkers, a section of the journal Frontiers in Neurology

Received: 12 December 2021
Accepted: 08 February 2022
Published: 08 March 2022

Citation:
Zhang Q, Yang J, Yang C, Yang X and Chen Y (2022) Eucommia ulmoides Oliver-Tribulus terrestris L. Drug Pair Regulates Ferroptosis by Mediating the Neurovascular-Related Ligand-Receptor Interaction Pathway- A Potential Drug Pair for Treatment Hypertension and Prevention Ischemic Stroke. Front. Neurol. 13:833922. doi: 10.3389/fneur.2022.833922

Background: In this study, we used the network pharmacology approach to explore the potential disease targets of the *Eucommia ulmoides Oliver* (EUO)-*Tribulus terrestris* L. (TT) drug pair in the treatment of hypertension-associated neurovascular lesions and IS via the ferroptosis pathway.

Methods: We used the Traditional Chinese Medicine Systems Pharmacology Database and Analysis Platform to search for the key active compounds and targets of the drug pair. Based on the GeneCards database, the relevant targets for the drug pair were obtained. Then, we performed the molecular docking of the screened core active ingredients and proteins using the DAVID database and the R AutoDock Vina software. Based on the GSE22255 dataset, these screened target proteins were used to build random forest (RF) and support vector machine (SVM) models. Finally, a new IS nomogram prediction model was constructed and evaluated.

Results: There were 36 active compounds in the EUO-TT drug pair. CHRM1, NR3C1, ADRB2, and OPRD1 proteins of the neuroactive ligand-receptor interaction pathway interacted with the proteins related to the ferroptosis pathway. Molecular docking experiments identified 12 active ingredients of the drug pair that may tightly bind to those target proteins. We constructed a visual IS nomogram prediction model using four genes (CHRM1, NR3C1, ADRB2, and OPRD1). The calibration curve, DCA, and clinical impact curves all indicated that the nomogram model is clinically applicable and diagnostically capable. CHRM1, NR3C1, ADRB2,

and OPRD1, the target genes of the four effective components of the EUO-TT drug pair, were considered as risk markers for IS.

Conclusions: The active ingredients of EUO-TT drug pair may act on proteins associated with the neuroactive ligand-receptor interaction pathway to regulate ferroptosis in vascular neurons cells, ultimately affecting the onset and progression of hypertension.

Keywords: stroke, hypertension, *Eucommia ulmoides Oliver*, *Tribulus terrestris* L, ferroptosis, network pharmacology Taubert D

INTRODUCTION

Ischemic stroke (IS), one of the neurovascular disorders, is a common complication of hypertension, the second most common cause of death worldwide, and has become a major public health problem. Stroke affects approximately 15 million people worldwide each year, resulting in 5 million deaths and 5 million disabilities (1). A study based on the Global Burden of Disease, Injuries and Risk Factors (GDB2010) showed that stroke mortality has increased by 26% since 1990 (2). A prospective observational study of 61 populations worldwide (∼1 million people aged 40–89 years) found a positive association between stroke risk and blood pressure levels (3). The earliest appearances are changes in arterial elastic function and an increase in pressure wave conduction velocity. The continuous increase in blood pressure progressively damages the integrity of the vascular endothelium resulting in structural changes to the vessel wall. The higher the blood pressure level, the more severe the damage. There is a strong causal relationship between blood pressure levels and stroke morbidity and mortality. Although the effect of western medicine in the treatment of hypertension is precise, it is mainly based on the control of blood pressure. This treatment regimen has several disadvantages, such as high dependence on medicines, numerous side effects, and heavy economic burden due to long-term use. Chinese medicine has unique advantages in the prevention and treatment of hypertension and neurovascular related diseases since they target multiple pathways and are less toxic.

EUO is a living fossil plant. Recent studies have found more than a hundred compounds that can be extracted from EUO. Monomeric compounds and extracts of EUO have a wide range of pharmacological effects in the treatment of several diseases, including hypertension, hyperlipidemia, diabetes, and osteoporosis (4, 5). The active ingredients of EUO that are anti-hypertensive are divided into four major groups: lignans, phenylpropanoids, flavonoids, and cyclic enol ether terpenes. Among these, lignans are the most studied class of chemical compounds which may regulate nitric oxide levels, renin-angiotensin system, and direct arterial diastole (6). The lignans in EUO exert anti-hypertensive effects in spontaneously hypertensive rats (SHR), presumably by inhibiting aldose reductase (AR), inhibiting the Ang II-induced inflammation and oxidative stress signaling pathways, and preventing cardiovascular remodeling (7, 8). Moreover, lignans can protect against renal damage caused by hypertension (9). Other components of EUO, like phenylpropanoid caffeic acid, lowers the blood pressure by inducing nitric oxide synthase and promoting nitric oxide synthesis (10, 11). Further, quercetin, a flavonoid, has the effect of endothelium-dependent vasodilatation (11, 12). Thus, EUO contains a variety of anti-hypertensive components that may protect against hypertension-induced ischemic stroke.

Another Chinese medicine, TT, has been shown by modern pharmacological studies to be anti-hypertensive, diuretic, hypolipidemic, and anti-atherosclerotic. It also reduces left ventricular remodeling and improves cardiac function in the early post-myocardial infarction period (13–15). Phillips et al. studied the effects of the methanolic and aqueous extracts of TT on blood pressure and perfused mesenteric vascular bed in rats, and showed that TT resulted in a dose-related reduction in blood pressure of SHR (13). Further, Sharifi et al. found that TT lowers the blood pressure in hypertensive rat models by inhibiting the angiotensin-converting enzyme (16). Active components isolated from TT also exert anti-inflammatory effects by inhibiting inflammatory mediators and cytokines, including IL-6, IL-10, and TNF-α (17). Inflammation is one of the several pathogeneses of hypertension, and inflammatory factors such as IL-6 are involved in the development and progression of hypertension (18–20). Thus, the components of Tribulus terrestris L have a potential key role in the prevention and treatment of hypertension through several pathways.

Recent studies have found that treatment of ferroptosis may be an important means of preventing and improving the prognosis of patients with IS (21, 22). Ferroptosis is a novel form of cell death discovered by Dolma et al. (23). The main feature of ferroptosis is the iron ion-dependent accumulation of large amounts of lipid peroxides during cell death (24). P53, System Xc-, glutathione peroxidase 4 (GPX4), and Fe are the core components of the ferroptosis pathway. Moreover, ferroptosis-related genes are mainly involved in the oxidative stress response (25). Oxidative stress and associated oxidative damage may be the main cause of vascular injury and may be involved in hypertension, where increased utilization and/or decreased inactivation of reactive oxygen species (ROS) is key

Abbreviations: GPX4, glutathione peroxidase 4; FTH1, ferritin heavy polypeptide 1; PPI, protein-protein interaction; SHR, spontaneously hypertensive rats; TCMSP, traditional Chinese medicine systems pharmacology database and analysis platform; PPI, protein protein interaction; GO, gene ontology; KEGG, Kyoto encyclopedia of genes and genomes; OB, oral bioavailability; DL, drug-likeness.

to vasoconstriction dysfunction (26–28). GPX4 is a highly active antioxidant enzyme in the basal body that scavenges ROS and prevents oxidative stress. Hence, its decline, either by using a GPX4 inhibitor or knockdown of the GPX4 gene, is associated with the development of pre-eclampsia and a significant increase in intracellular ROS and lipid peroxidation, thereby inducing ferroptosis (29–31). Recent research has established a clear correlation between ferroptosis and hypertensive brain injury, indicating that increased blood pressure results in a large drop in GPX4 and GSH levels in brain tissue, resulting in iron overload. Excessive iron levels in the brain enhance oxidative stress and lipid peroxidation, finally resulting in brain damage (32). Further, hypertensive patients have decreased activity and expression of GPX (33). Inhibition of endothelial ferroptosis may help prevent endothelial cell apoptosis and calcification due to hypertension (34, 35). Thus, ferroptosis-related pathways may play a role in hypertension related vascular endothelial damage, but there is a lack of direct research to prove this.

In previous study, the ferroptosis of neuronal cells in hypertension is important for neurovascular diseases progression (22). This may be a critical mechanism for neurological mediation of the progression of hypertension. According to traditional Chinese medicine theory, the EUO-TT medication combination may help increase cerebrovascular health in hypertension patients, however further research is needed to confirm this idea. We hypothesize that the EUO-TT drug pair may aid in inhibiting ferroptosis in the hypertensive milieu, hence reducing hypertensive damage to the brain's endothelial cells. Treatment with the EUO-TT medication combination may help prevent and improve the prognosis of people with IS.

In this study, we used a network pharmacology approach to construct a "compound-target-disease" network through bioinformatics analysis to unravel the pharmacological basis and mechanism of action of the drug pair of EUO-TT in the treatment of hypertension-associated neurovascular lesions through the ferroptosis pathway. We believe that the findings of our study will provide a pharmacological basis for the clinical treatment of hypertension using Chinese medicine.

MATERIALS AND METHODS

Acquisition of Effective Compounds and Action Targets of EUO-TT

In this study, we searched for the chemical composition of EUO and TT through the pharmacology platform of the Chinese medicine network. We extracted the main active compounds of each medicine with the screening conditions of oral bioavailability $\geq$30% and drug-likeness $\geq$0.18 (36).

Prediction of Hypertension Disease Target

The hypertension-related targets were searched by MOL ID numbers (expressed as protein name) of compounds using the Traditional Chinese Medicine Systems Pharmacology Database and Analysis Platform (TCMSP). Further, the gene names corresponding to each target were searched by the Uniport database (37). Based on the GeneCards database, the relevant genes were searched by the keyword "hypertension" and intersected with the key active compounds of the pathway to obtain the relevant targets of the EUO-TT drug pair for the treatment of hypertension (38).

Protein-Protein Interaction (PPI) Network Construction and Key Target Screening

After importing the intersecting targets into the STRING database and restricting the study species to humans, we obtained the PPI network of EUO-TT drug pair acting on neuroactive ligand-receptor interaction pathway and ferroptosis pathway (39). The topological analysis of the PPI network was performed with the help of "Network Analyzer" in Cytoscape 3.7.1 software. The targets with degrees greater than the average of the degree of freedom, betweenness, and closeness were selected as key targets of the neuroactive ligand-receptor interaction pathway and ferroptosis pathway (39).

Construction and Analysis of the Neuroactive Ligand-Receptor Interaction Pathway-Ferroptosis Pathway Action Target Network

The active compounds and their targets in the neuroactive ligand-receptor interaction pathway were imported into Cytoscape 3.7.1 software, and the "STRING database" function was used to analyze the neuroactive ligand-receptor interaction pathway-ferroptosis pathway target network. The key compounds of EUO-Tribulus terrestris L drug pair mediating neuroactive ligand-receptor interaction pathway to coordinate ferroptosis pathway for the treatment of hypertension were screened based on compound-target connectivity.

Gene Ontology (GO) Functional Enrichment Analysis and Kyoto Encyclopedia of Genes and Genomes (KEGG) Pathway Analysis

In order to further understand the core target gene functions and the main pathways of action of EUO-Tribulus terrestris L in the treatment of hypertension, the drug-disease related targets were entered into the DAVID database (40). The species "homo sapiens" was selected, and a threshold value of adjust $p < 0.05$ was set for GO function enrichment and KEGG pathway analysis, of which results were visualized by R programming software (41, 42).

Molecular Docking

As described in previous studies, we molecularly docked the screened core active ingredient to the core protein to verify the interaction strength (43). The active ingredient structures were obtained from the PubChem database and the protein structures were obtained from the Protein Data Bank (PDB) (44, 45). The 3D structures of the active ingredients (mol2 format) were downloaded, and operations such as hydrogenation, charge addition, detection of ligand roots, and search and definition of rotatable bonds were performed with AutoDock. Molecular docking was performed using AutoDock Vina software, and the

results were optimized for mapping and further analysis with the help of Pymol software (46, 47). R software was used to analyze and thermogram small molecule bound amino acids.

Data Acquisition and Pre-processing

The GSE22255 dataset is an ischaemic stroke-related microarray dataset obtained from the GEO database (48). The dataset consisted of 20 IS patients and 20 age-matched controls. Analysis of variance was done using the "limma" package of R software (version 4.0.5) and the remove Barch effect function was used to remove batch effects. Gene expression was used for normalization analysis and *p*-values less than 0.05 were defined as significant differences.

Building Predictive Models

In short, the predictive model was constructed with reference to previous studies (49–53). With CHRM1, NR3C1, ADRB2, and OPRD1 as dependent variables and the presence or absence of IS as the dependent variable, the "pacman" package of R software was used to build random forest (RF) and support vector machine (SVM) models. A receiver operating characteristic (ROC) curve, reverse cumulative distribution of |residual|, and boxplots of |residual| were plotted to select the most appropriate model. Then, using the "mlbench" and "caret" programmes, the cross curve was plotted to identify the relevance of each element. Following that, the "rms" function was used to build the nomogram prediction model. Additionally, calibration curves, DCA curves, and clinical effect curves were developed to validate the model's predictive ability (54, 55).

RESULTS

Extraction of Effective Compounds and Action Targets of EUO-TT Drug Pair

The TCMSP analysis platform was used to search the main active ingredients of the EUO-TT drug pair. The active ingredients of each drug were screened and the targets of each compound were obtained according to the active ingredient "MOL ID". Among them, 25 active compounds were screened from EUO, 12 from TT, and one duplicate compound from both EUO and TT (MOL000422: kaempferol). We found 36 active compounds after de-weighting. Further, 30 compounds were found to correspond to 114 genes, and the gene names of each target were obtained from Uniprot (**Table 1**).

Enrichment Analysis of the Targets of Active Compounds in the EUO-TT Drug Pair

The potential target genes of the drugs were imported into the DAVID 6.8 database, the list of target genes was entered, the species was limited to "Homo sapiens", and the threshold was set to $P < 0.05$ for GO functional analysis and KEGG pathway enrichment analysis. The pathways and functional information with the top P-values in each type of process and pathways were selected, where smaller *P*-values and longer bar lengths indicated the strongest enrichment significance (**Figure 1A**). The top-ranked biological processes (BP), cellular components (CC), and molecular functions (MF) included: response to ammonium ion, cellular response to drug, response to xenobiotic stimulus, integral component of synaptic membrane, intrinsic component of postsynaptic membrane, integral component of postsynaptic membrane, adrenergic receptor activity, catecholamine binding, and G protein-coupled amine receptor activity. The top-ranked KEGG included: Folate biosynthesis, Calcium signaling pathway, AGE-RAGE signaling pathway in diabetic complications, and Neuroactive ligand-receptor interaction. Among them, the target genes of the EUO-TT drug pair were found to be significantly enriched in the neuroactive ligand-receptor interaction pathway. Therefore, we speculated that this drug pair may regulate the ferroptosis pathway by modulating the neuroactive ligand-receptor interaction pathway.

Potential Mechanism of Neuroactive Ligand-Receptor Interaction Pathway Mediated by the Active Compounds of EUO-TT Drug Pair for the Regulation of Ferroptosis

Since the target genes of the drug pair were significantly enriched in the neuroactive ligand-receptor interaction pathway, we completed the intersection analysis of the drug-neuroactive ligand-receptor interaction pathway, and 26 intersection targets were identified (**Figure 2A**). However, the drug-ferroptosis intersection analysis identified only two intersection targets (**Figure 2B**). We, therefore, hypothesized that the neuroactive ligand-receptor interaction pathway may be the direct targeting pathway of EUO-TT drug pair, while the ferroptosis pathway may be the indirect pathway. The STRING database was used for the PPI analysis of the 26 intersecting targets of the drug-neuroactive ligand-receptor interaction pathway and ferroptosis pathway proteins (from the KEGG database). The study species was set as "Homo sapiens" to obtain the PPI network of the drug pair (**Figure 1B**). We used the default parameters on the web page, and the file was saved in TSV format and imported into Cytoscape software for topological analysis of the PPI network. The nodes in **Figure 1B** were selected out in **Figure 2C**. Combined with the information on the degrees of freedom, degree, and centrality, the neuroactive ligand-receptor interaction pathway - ferroptosis pathway regulatory network was constructed (**Figure 2C**). The degree sizes of the proteins in the ferroptosis pathway were indicated by the size of the squares, and several proteins were found to be critical for the pathway, including GPX4, FTH1, TP53, SLC11A2, HMOX1, GCLM, STEAP3, SLC11A2, FTL, ATG7, and ATG5. Further, CHRM1, NR3C1, ADRB2, and OPRD1 in the neuroactive ligand-receptor interaction pathway were also found to interact with proteins related to the ferroptosis pathway. Among them, CHRM1 interacted with SLC3A2 and FTH1, NR3C1 interacted with TP53, ADRB2 interacted with PCBP2, and OPRD1 interacted with PCBP2. Therefore, CHRM1, NR3C1, ADRB2, OPRD1, FTH1, TP53, and PCBP2 were defined as the key proteins of the EUO-TT drug pair mediating ferroptosis through the neuroactive ligand-receptor interaction pathway.

TABLE 1 | Detailed information on active compounds from *Eucommia ulmoides Oliver* and *Tribulus terrestris* L.

Drug	MOL ID	Molecule name	OB	Drug-likeness
Eucommia ulmoides Oliver	MOL000073	ent-Epicatechin	48.96	0.24
Eucommia ulmoides Oliver	MOL000098	quercetin	46.43	0.28
Eucommia ulmoides Oliver	MOL000211	Mairin	55.38	0.78
Eucommia ulmoides Oliver	MOL000358	beta-sitosterol	36.91	0.75
Eucommia ulmoides Oliver	MOL000422	kaempferol	41.88	0.24
Eucommia ulmoides Oliver	MOL000443	Erythraline	49.18	0.55
Eucommia ulmoides Oliver	MOL002058	40957-99-1	57.20	0.62
Eucommia ulmoides Oliver	MOL004367	olivil	62.23	0.41
Eucommia ulmoides Oliver	MOL005922	Acanthoside B	43.35	0.77
Eucommia ulmoides Oliver	MOL006709	AIDS214634	92.43	0.55
Eucommia ulmoides Oliver	MOL007059	3-beta-Hydroxymethyllenetanshiquinone	32.16	0.41
Eucommia ulmoides Oliver	MOL007563	Yangambin	57.53	0.81
Eucommia ulmoides Oliver	MOL009007	Eucommin A	30.51	0.85
Eucommia ulmoides Oliver	MOL009009	(+)-medioresinol	87.19	0.62
Eucommia ulmoides Oliver	MOL009015	(–)-Tabernemontanine	58.67	0.61
Eucommia ulmoides Oliver	MOL009027	Cyclopamine	55.42	0.82
Eucommia ulmoides Oliver	MOL009029	Dehydrodiconiferyl alcohol 4,gamma'-di-O-beta-D-glucopyanoside_qt	51.44	0.40
Eucommia ulmoides Oliver	MOL009030	Dehydrodieugenol	30.10	0.24
Eucommia ulmoides Oliver	MOL009031	Epiquinidine	68.22	0.40
Eucommia ulmoides Oliver	MOL009038	GBGB	45.58	0.83
Eucommia ulmoides Oliver	MOL009042	Helenalin	77.01	0.19
Eucommia ulmoides Oliver	MOL009047	(+)-Eudesmin	33.29	0.62
Eucommia ulmoides Oliver	MOL009053	4-[(2S,3R)-5-[(E)-3-hydroxyprop-1-enyl]-7-methoxy-3-methylol-2,3-dihydrobenzofuran-2-yl]-2-methoxy-phenol	50.76	0.39
Eucommia ulmoides Oliver	MOL009055	hirsutin_qt	49.81	0.37
Eucommia ulmoides Oliver	MOL009057	liriodendrin_qt	53.14	0.80
Tribulus terrestris L.	MOL000354	isorhamnetin	49.60	0.31
Tribulus terrestris L.	MOL000359	sitosterol	36.91	0.75
Tribulus terrestris L.	MOL000422	kaempferol	41.88	0.24
Tribulus terrestris L.	MOL000483	Moupinamide	118.35	0.26
Tribulus terrestris L.	MOL008559	(2aR,2'R,4R,6aR,6bS,8aS,8bR,11aS,12aR,12bR)-4-((S)-2-(2,6-dimethylphenyl)propoxy)-5',5',6a,8a-tetramethyl-8-methylenedocosahydro-1H-spiro[pentaleno[2,1-a]phenanthrene-10,2'-pyran]	59.49	0.28
Tribulus terrestris L.	MOL008563	(3R,8S,9S,10R,13R,14R,17S)-17-((2S,5R)-5-ethyl-6-methylheptan-2-yl)-3-hydroxy-10,13-dimethyl-3,4,8,9,10,11,12,13,14,15,16,17-dodecahydro-1H-cyclopenta[a]phenanthren-7(2H)-one	40.93	0.79
Tribulus terrestris L.	MOL008567	(3R,7R,8S,9S,10S,13R,14S,17R)-17-((2R,5S)-5-ethyl-6-methylheptan-2-yl)-3,10-dimethyl-2,3,4,7,8,9,10,11,12,13,14,15,16,17-tetradecahydro-1H-cyclopenta[a]phenanthren-7-ol	34.21	0.76
Tribulus terrestris L.	MOL008568	(Z)-3-(3,4-dihydroxyphenyl)-N-[2-(4-hydroxyphenyl)ethyl]acrylamide	113.25	0.24
Tribulus terrestris L.	MOL008569	β-sitosterol-β-D-glucopyranoside	32.41	0.71
Tribulus terrestris L.	MOL008588	terrestriamide	114.09	0.29
Tribulus terrestris L.	MOL008590	(2aR,2'S,4R,4'R,5'S,6aS,6bS,8aS,8bR,9S,11aR,12aR,12bR)-4,4'-dihydroxy-5',6a,8a,9-tetramethylicosahydro-1H-spiro[pentaleno[2,1-a]phenanthrene-10,2'-pyran]-8(2H)-one	58.74	0.76
Tribulus terrestris L.	MOL008593	(2aR,5S,6aS,6bS,8aS,8bS,11aS,12aR,12bR)-10-isopentyl-6a,8a,9-trimethyl-2,2a,3,4,5,6,6a,6b,7,8,8a,8b,11a,12,12a,12b-hexadecahydro-1H-naphtho[2',1':4,5]indeno[2,1-b]furan-5-ol	39.21	0.84

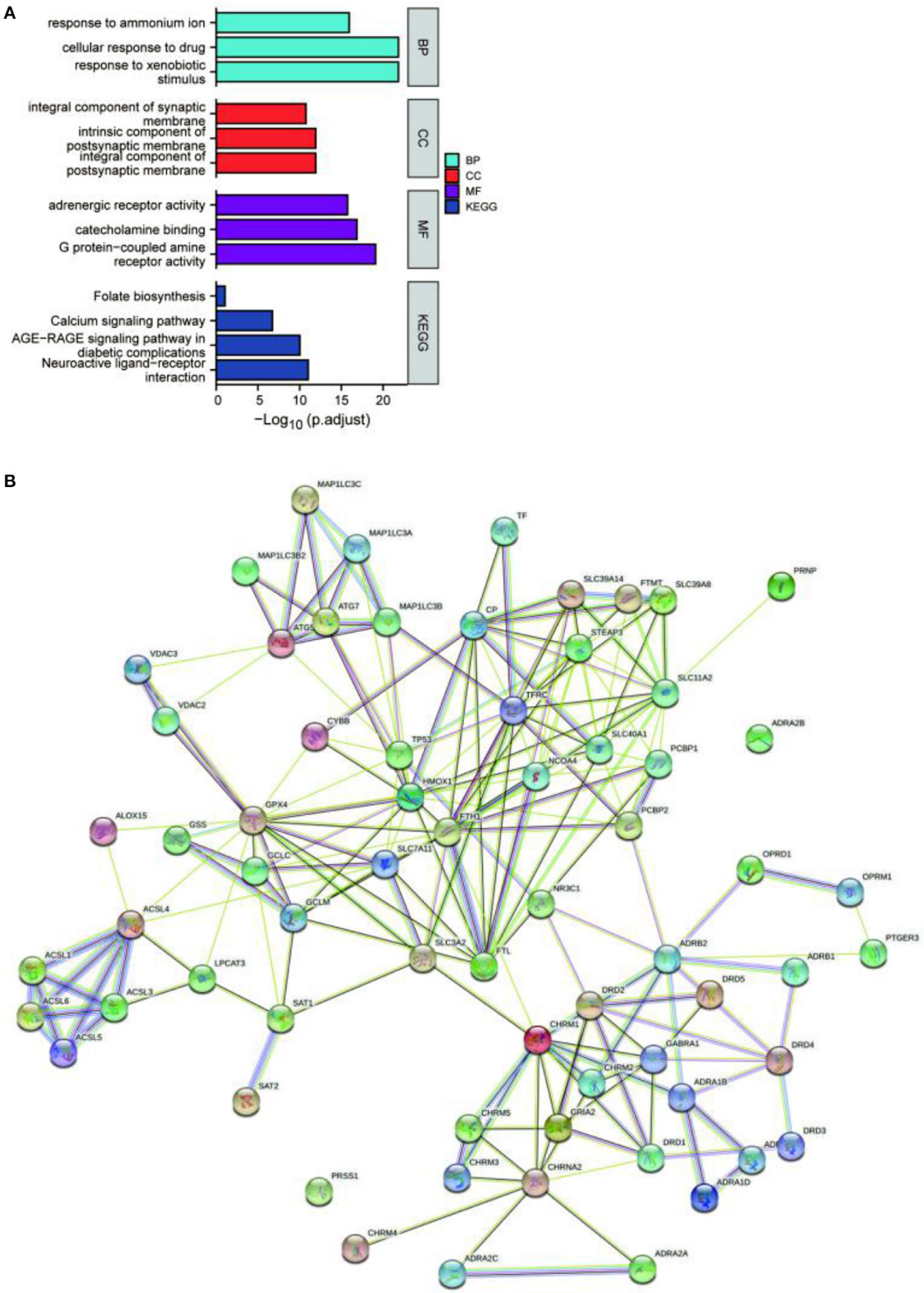

FIGURE 1 | Enrichment analysis and protein-protein interaction (PPI) network of the active compound targets of EUO-TT L. GO functional analysis and KEGG enrichment analysis of the active compound targets of EUO-TT L. drug pair **(A)**; PPI network analysis of the target genes of the neuroactive ligand-receptor interaction pathway, and the ferroptosis pathway mediated by the drug pair **(B)**.

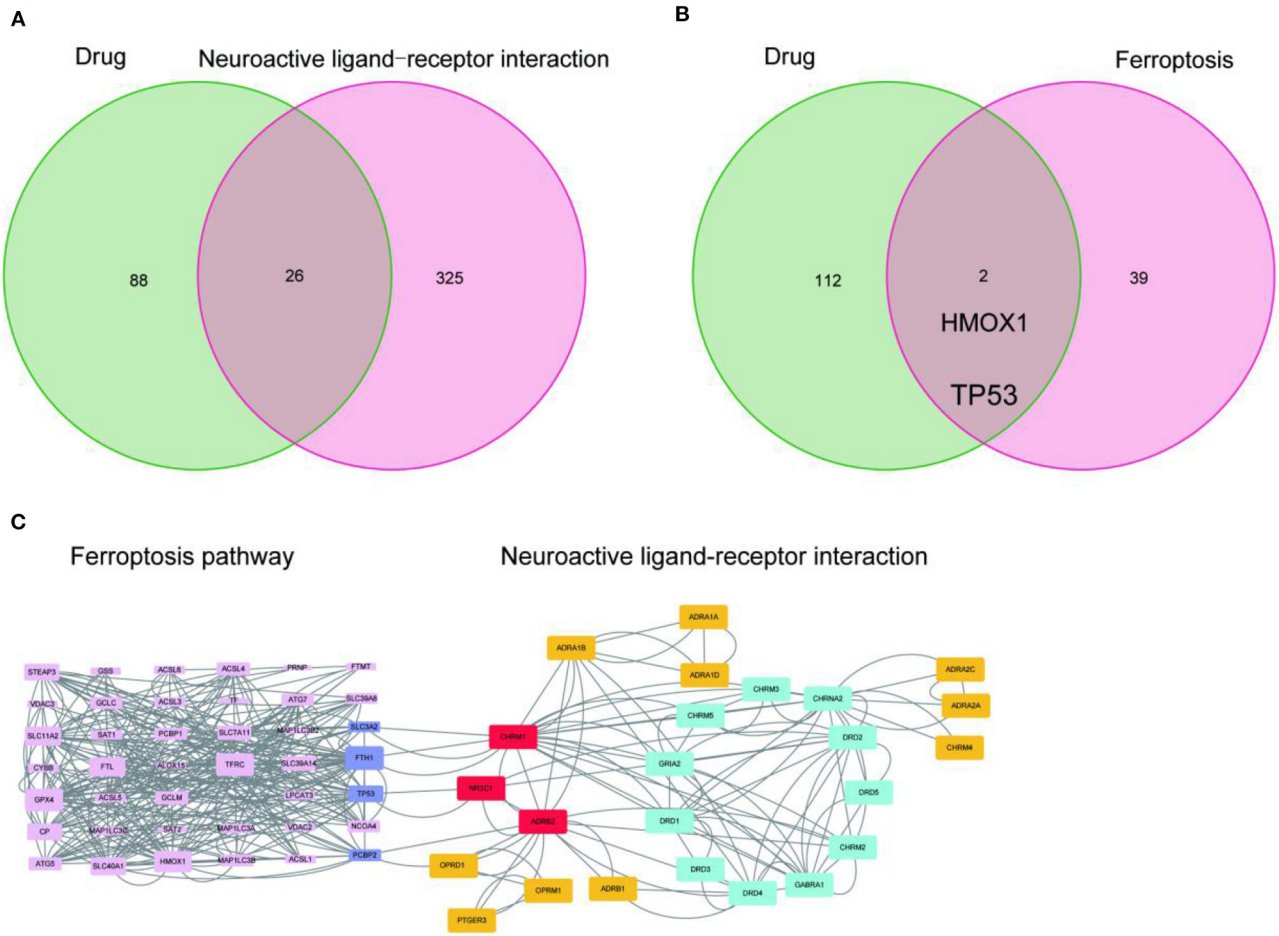

FIGURE 2 | Network analysis of the active compounds of EUO-TT L. mediating the neuroactive ligand-receptor interaction pathway regulating ferroptosis. Intersection analysis of drug-neuroactive ligand-receptor interaction pathway **(A)**; Intersection analysis of drug-ferroptosis pathway **(B)**; PPI network of neuroactive ligand-receptor interaction pathway - ferroptosis pathway **(C)**.

Active Ingredient-Pathway Target Network Construction and Analysis

The key proteins of the drug pair mediating ferroptosis were further used for enrichment analysis. The top-ranked BP, CC, and MF included: core promoter binding, G protein-coupled neurotransmitter receptor activity, neuropeptide binding, membrane raft, intrinsic component of the presynaptic membrane, integral component of the presynaptic membrane, G protein-coupled receptor signaling pathway coupled to cyclic nucleotide second messenger, adenylate cyclase-modulating G protein-coupled receptor signaling pathway, and phospholipase C-activating G protein-coupled receptor signaling pathway. The top-ranked KEGG included: Calcium signaling pathway, Ferroptosis, and Neuroactive ligand-receptor interaction (**Figure 3A**). Hence, the key proteins may be associated with cell membrane channels, cell signaling, ferroptosis, and the G-protein pathway. Further, Sankey plots were used to illustrate the regulatory network of drug-active ingredient-key targets of neuroactive ligand-receptor interaction pathway (**Figure 3B**). The "four target proteins with the highest values" refers to the neuroactive ligand-receptor interaction with the four most closely associated proteins in the ferroptosis pathway in the PPI network. Those four key target proteins of the neuroactive ligand-receptor interaction pathway may be regulated by 15 active ingredients of the EUO-TT drug pair.

Molecular Docking Verification Experiment

The 15 active ingredients and four target proteins with the highest values were screened according to the "drug-component-pathway-target" network, and molecular docking experiments were performed. Ultimately, 12 active ingredients were validated for potential target binding to these four proteins (**Table 2**). The results showed that the binding energy of docking of all proteins and the active ingredients were less than −5 kJ/mol, which indicates a tight binding between the ligand and receptor. The strongest protein-active ingredient bindings

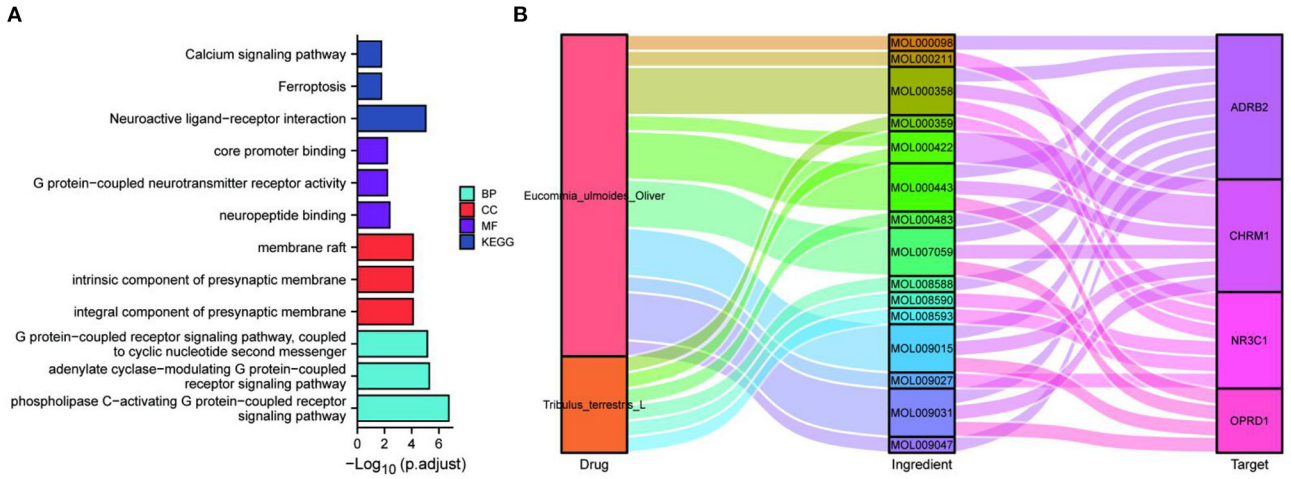

FIGURE 3 | Network construction and pathway analysis of the active ingredient-pathway targets. GO and KEGG enrichment analysis of the key proteins CHRM1, NR3C1, ADRB2, OPRD1, FTH1, TP53, and PCBP2 **(A)**; Sankey plots were used to demonstrate the drug-active ingredients-key neuroactive ligand-receptor interaction pathway targets regulatory network **(B)**.

TABLE 2 | Virtual docking of representative ingredients and proteins.

	ADRB2	CHRM1	NR3C1	OPRD1
Terrestriamide	−10			
Tabernemontanine	−9.7		−8.2	−9.4
Quercetin	−10.5			
Moupinamide	−9.9	−9.7	−7.8	−8.1
Mairin			−12.3	
kaempferol		−10		
Erythraline	−12.2	−11.4	−9.4	
Epiquinidine	−9.5	−11		−9
Cyclopamine	−17.1			
beta-sitosterol	−13.2	−13.7	−10.6	
3-Hydroxymethylenetanshinquinone	−8.6	−9.2		−9
(–)-Tabernemontanine	−9.6	−11.3		−9.5

Binging energy/(kcal/mol).

were as follows: ADRB2 and cyclopamine (−17.1 kJ/mol), CHRM1 and beta-sitosterol (−13.7 kJ/mol), and NR3C1 and mairin (−12.3 kJ/mol). OPRD1 bound to tabernemontanine (−9.4 kJ/mol), moupinamide (-8.1 kJ/mol), epiquinidine (−9 kJ/mol), 3-Hydroxymethylenetanshinquinone (−9 kJ/mol), and (–)- Tabernemontanine (−9.5 kJ/mol). In the molecular docking validation of ADRB2, CHRM1, NR3C1, and OPRD1 (**Figures 4**, **5**), valine, serine, and phenylalanine were found to be the key amino acids for the action of the active ingredients on ADRB2 (**Figure 4A**). Erythraline, quercetin, cyclopamine, moupinamide, terrestriamide, and beta-sitosterol had highly similar binding sites on ADRB2 (**Figure 4B**). Tyrosine was found to be the key amino acid for the action of the active ingredient on CHRM1 (**Figure 4C**). Kaempferol, beta-sitosterol, epiquinidine, (–)-tabememontanine, erythraline, and mouplinamide had highly similar binding sites on CHRM1 (**Figure 4D**). Lysine, arginine, and phenylalanine were found to be the key amino acids for the action of the active ingredient on NR3C1 (**Figure 5A**). Erythraline, moupinamide, beta-sitosterol, and mairin had highly similar binding sites on NR3C1 (**Figure 5B**). PHE was found to be the key amino acid for the action of the active ingredient on OPRD1 (**Figures 5C,D**).

Construction of IS Prediction Models Based on the Expression Profiles of CHRM1, NR3C1, ADRB2, and OPRD1

Person correlation analysis suggested that in the control group, OPRD1, ADRB2, and NR3C1 were positively correlated with each other, while CHRM1 was found to be negatively correlated with NR3C1 and ADRB2 (**Figure 6A**). And in the IS group, CHRM1 was found to be significantly and positively correlated with NR3C1 and OPRD1 (**Figure 6A**). The positions of the four genes CHRM1, NR3C1, ADRB2, and OPRD1 on the chromosomes are shown in a circular diagram (**Figure 6B**). To evaluate the predictive power of CHRM1, NR3C1, ADRB2, and OPRD1 for IS, RF and SVM models were constructed separately. The boxplot and cumulative distribution characteristics of the "residuals" indicate that the RF model has a lower residual distribution than the SVM model (**Figures 6C,D**). The variation of error in the random forest model with the number of "trees" included in the model is shown in **Figure 6E**. Based on the RF model, the importance of each feature was ranked from the largest to the smallest as OPRD1, CHRM1, NR3C1, and ADRB2 (**Figure 6F**).

The ROC curve analysis revealed that the AUC value of the RF model (AUC = 1.0) was higher than that of the SVM model (AUC = 0.845) (**Figure 6G**).

The Construction of a Nomogram Prediction Model, as Well as Its Risk Enrichment Characteristics

To create a visual model for IS prediction, we created a nomogram (**Figure 7A**) using the four identified genes (CHRM1, NR3C1, ADRB2, and OPRD1). According to the calibration curve, the IS positivity rate predicted by this nomogram was generally consistent with the actual positivity rate (**Figure 7B**). The DCA and clinical impact curves show that the nomogram model has good clinical application and diagnostic ability (**Figures 7C,D**). Based on the IS prediction model, all samples in the GSE22255 dataset were scored and divided into high-risk and low-risk groups based on their scores. Differential analysis was performed between the high-risk and low-risk groups. KEGG and GO enrichment were then performed and KEGG enrichment analysis revealed that yersinia infection, B cell receptor signaling pathway and autophagy (animal) were significantly associated with the risk score of this nomogram (**Figure 7E**). GO enrichment analysis revealed that the risk score of this nomogram was significantly associated with the enrichment of dendritic cell differentiation, aging, focal adhesion, overall composition of organelle membranes, protein serine/threonine/tyrosine kinase activity and manganese ion binding pathways (**Figure 7F**). Among them, dendritic cell differentiation and protein serine/threonine/tyrosine kinase activity and manganese ion binding were the most enriched (**Figure 7G**). Therefore, CHRM1, NR3C1, ADRB2, and OPRD1, the target genes of the four EUO-TT drug pair active ingredients, are considered to be risk markers for IS.

DISCUSSION

This study unraveled the mechanism of action of EUO-TT drug pair in the treatment of hypertension related endothelial injury through the ferroptosis pathway, providing a pharmacological basis for the clinical treatment of hypertension related cerebrovascular endothelial injury using Chinese medicine. CHRM1, NR3C1, ADRB2, and OPRD1, the target genes of the four active ingredients of the EUO-TT drug pair, were considered as risk markers for IS and a visual IS nomogram prediction model was constructed.

Network pharmacology was used to screen the active compounds of EUO-TT L. drug pair and found that the target genes were mainly enriched in the neuroactive ligand-receptor interaction pathway in this research. By constructing the PPI network of neuroactive ligand-receptor interaction pathway-ferroptosis, we found that CHRM1, NR3C1, ADRB2, OPRD1, FTH1, TP53, and PCBP2 were the main target genes of the drug pair. Through the regulatory network of the drug's active ingredients and their key targets in the neuroactive ligand-receptor interaction pathway, we found 15 active ingredients of the drug pair that were involved in the regulation of the key target proteins. Further, molecular docking experiments verified that 12 active ingredients of the drug pair were tightly bound to the target proteins. The expression profiles of CHRM1, NR3C1, ADRB2, and OPRD1 were used to construct IS prediction models. The residual distribution of the RF model was found to be lower than that of the SVM model, and the ROC curve suggested a higher prediction accuracy of the RF model. The RF model rated the genes in ascending order of importance: OPRD1, CHRM1, NR3C1, and ADRB2. Following that, the nomogram prediction model was constructed using the four selected genes (CHRM1, NR3C1, ADRB2, and OPRD1). However, only CHRM1, NR3C1, and OPRD1 were eventually included in the prediction model, as inclusion of these three components was sufficient to reliably predict prognosis in the logistic model. The calibration curve, DCA, and clinical effect curves all indicated that this nomogram model is clinically applicable and diagnostically capable. The enrichment of dendritic cell differentiation and protein serine/threonine/tyrosine kinase activity and manganese ion binding pathways was found to be the most correlated with the prediction results based on nomogram risk scores.

SLC3A2, FTH1, TP53, and PCBP2 are directly or indirectly associated with ferroptosis. SLC3A2 is a SystemXc- heavy chain subunit involved in the maintenance of a redox steady state (56, 57). When SystemXc- is blocked, glutamate and cystine cannot be exchanged, resulting in intracellular glutamate accumulation, reduced glutathione synthesis, and reduced GPX4 activity, which ultimately leads to ferroptosis (58). Further, the inhibition of SLC3A2, a ferroptosis suppressor gene, promotes ferroptosis in tumor and normal cells (57, 59), and hence, its upregulation is associated with poor prognosis of cancer (60). FTH1 (Ferritin heavy polypeptide 1) is an important component of ferritin. Ferritin degradation increases intracellular free iron content and can activate ferroptosis (61–63), while the overexpression of FTH1 can inhibit ferroptosis by impairing ferritinophagy (64). For instance, in the head and neck squamous cell carcinoma, FTH1 suppressed ferroptosis and led to the poor prognosis of the carcinoma (65). Further, FTH1 expression is downregulated in cells sensitive to ferroptosis relative to cells resistant to ferroptosis (66). p53 is an oncogene that regulates the cell cycle, induces apoptosis, and promotes DNA metabolism (67, 68). P53 may also regulate ferroptosis (69–72). Jiang et al. found that P53 inhibited SystemXc- activity and downregulated the expression of solute carrier family 7 member 11, which in turn induced cellular ferroptosis (70). P53 can also catalyse glutamate production by enhancing glutaminase 2 activity, thereby reducing the entry of cystine into cells, reducing glutathione synthesis, and inducing ferroptosis (73). In addition, P53 promotes cellular unsaturated fatty acid oxidation by enhancing the activation of spermidine/spermine N1-acetyltransferase 1, which also leads to cellular ferroptosis (71). Thus, P53 is closely related to ferroptosis. PCBP2 is a multifunctional adaptor protein of the Poly-binding family which is involved in iron metabolism and is an iron chaperone of ferritin (74). However, the specific binding sites of iron and ferritin on PCBP2 have not yet been identified (75). Iron and ROS are promoters and mediators of ferroptosis (76). Iron metabolic homeostasis and lipid peroxidation are crucial for the occurrence of cellular ferroptosis (77). A study

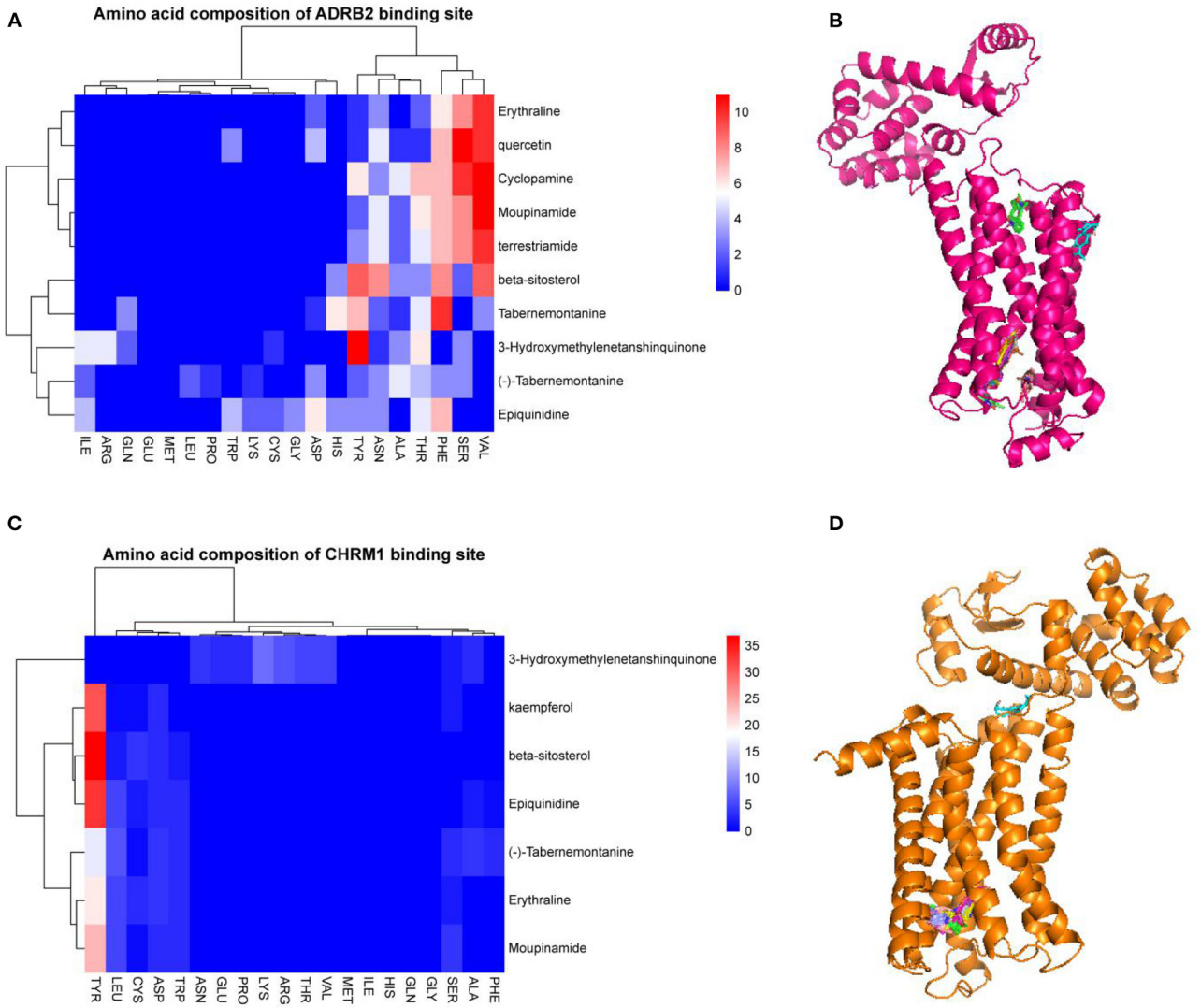

FIGURE 4 | Visualization of molecular docking validation of ADRB2 and CHRM1. Amino acid composition of ADRB2 binding site **(A)**; Bulk molecular docking map of ADRB2 **(B)**; Amino acid composition of CHRM1 binding site **(C)**; Bulk molecular docking map of CHRM1 **(D)**.

found that PCBP2 binding to severely oxidized RNA inhibited apoptosis induced by oxidative stress (78). Moreover, PCBP2 is one of the ferroptosis risk signature genes and can predict the prognosis of adrenocortical carcinoma in combination with the other five ferroptosis risk signature genes (79).

Similar to previous studies, we found that SLC3A2, FTH1, TP53, and PCBP2 were the ferroptosis pathway-associated proteins that interacted with CHRM1, NR3C1, ADRB2, and OPRD1. The NR3C1 protein regulates the genetic features involved in the P53 signaling pathway (80). Further, ADRB2 increases the protein levels of c-myc in pancreatic ductal adenocarcinoma cells through the recruitment of PCBP2 (81). Similarly, in this study, we found that NR3C1 interacted with TP53 andADRB2 interacted with PCBP2. In addition, this is the first study to show that CHRM1 interacted with SLC3A2 and FTH1, and OPRD1 interacted with PCBP2. These results indicated that CHRM1, NR3C1, ADRB2, and OPRD1 may influence the ferroptosis pathway by interacting with the key proteins related to ferroptosis. CHRM1, NR3C1, ADRB2, and OPRD1 were the target proteins related to the neuroactive ligand-receptor interaction pathway. Therefore, for the first time, we show that the neuroactive ligand-receptor interaction pathway may influence the process of ferroptosis through the interaction of its related proteins CHRM1, NR3C1, ADRB2, and OPRD1 with the key proteins of ferroptosis. We further showed that ADRB2 bound most tightly to cyclopamine; CHRM1 to beta-sitosterol; NR3C1 to mairin; OPRD1 to tabernemontanine, moupinamide, epiquinidine; and OPRD1 to tabernemontanine, moupinamide, epiquinidine, 3-Hydroxymethylenetanshinquinone, and (-)-Tabernemontanine. Beta-sitosterol has anti-inflammatory, anti-tumor, antioxidant, anti-hyperlipidemic, and antihypertensive effects (82–84), and

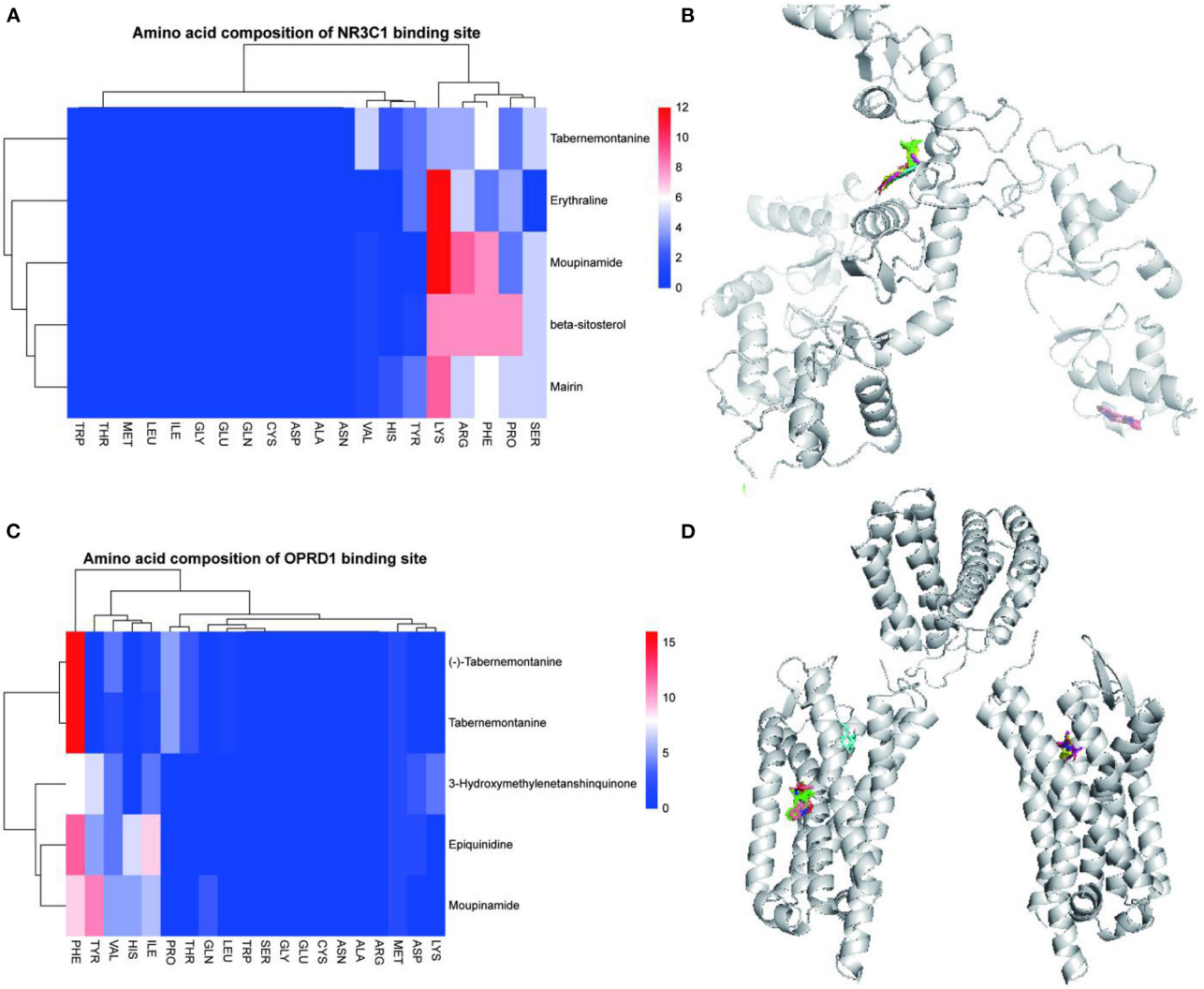

FIGURE 5 | Visualization of NR3C1 and OPRD1 molecular docking validation. Amino acid composition of NR3C1 binding site **(A)**; Bulk molecular docking map of NR3C1 **(B);** Amino acid composition of OPRD1 binding site **(C)**; Bulk molecular docking map of OPRD1 **(D)**.

moupinamide is also anti-inflammatory (85). Inflammatory processes are involved in the development of hypertension (86, 87). Therefore, it can be hypothesized that moupinamide has potential anti-hypertensive effects. Tanshinone was also found to have a protective effect against cardiac hypertrophy in SHRs (88). Tanshinone slowed the metabolism of the antihypertensive drug cloxacin by inhibiting CYP3A4/CYP2C9 activity (89). Further, the regulation of KV current by tanshinone reduced hypoxic pulmonary hypertension and inhibited hypoxia-induced pulmonary artery wall remodeling (90).

In this study, CHRM1, NR3C1, ADRB2, and OPRD1, the target genes of the four EUO-TT L. drug pair active ingredients, were considered as risk markers for IS. CHRM1 was found to be associated with muscarinic receptor-mediated anti-inflammatory mechanisms (91). Following IS, there is a decrease in B lymphocyte production, which may be related with aberrant NR3C1 expression (92). ADRB2, an apoptosis-related gene, was found to enhance the activity of BDNF/TrkB and cAMP/PKA signaling pathways leading to cellular ischemic injury (93). In addition, polymorphisms in the ADRB2 gene have been found to potentially contribute to a high risk of stroke (94). Common variants of OPRD1 have also been found to be associated with neurodegenerative diseases (95).

In the present study, the active ingredients of EUO-TT L., namely cyclopamine, beta-sitosterol, mairin, tabernemontanine, moupinamide, epiquinidine, and 3-Hydroxymethylenetanshinquinone, were found for the first time to target and bind neuroactive ligand-receptor interaction pathway-related proteins, which in turn regulated the process of cellular ferroptosis and ultimately affected the onset and progression of hypertension. There is a lack of previous studies confirming the association of the alkaloids tabernemontanine

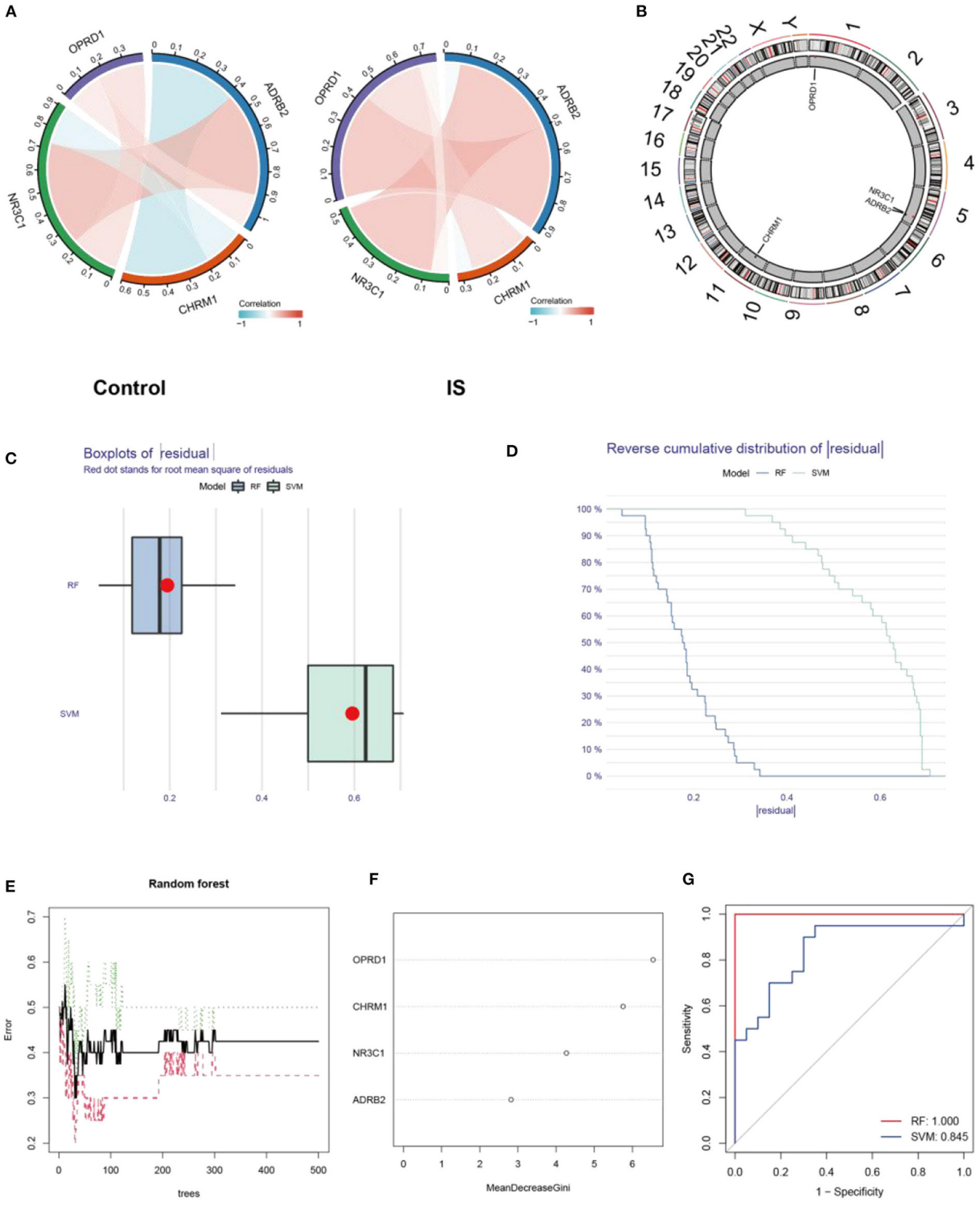

FIGURE 6 | Expression characterization and predictive power analysis of CHRM1, NR3C1, ADRB2, and OPRD1. Correlation analysis of CHRM1, NR3C1, ADRB2, and OPRD1 in the GSE22255 dataset in the control and IS groups, with red indicating positive correlation and blue indicating negative correlation **(A)**; The positions of the four genes CHRM1, NR3C1, ADRB2, and OPRD1 in the chromosome are shown in a circular diagram **(B)**; Boxplot of "residuals" in RF and SVM models **(C)**; Cumulative distribution characteristics of "residuals" in RF and SVM models **(D)**; The variation of error in the random forest model with the number of "trees" included in the model **(E)**; The genes are ranked according to their importance **(F)**; ROC curves reflecting the predictive power of RF and SVM models **(G)**.

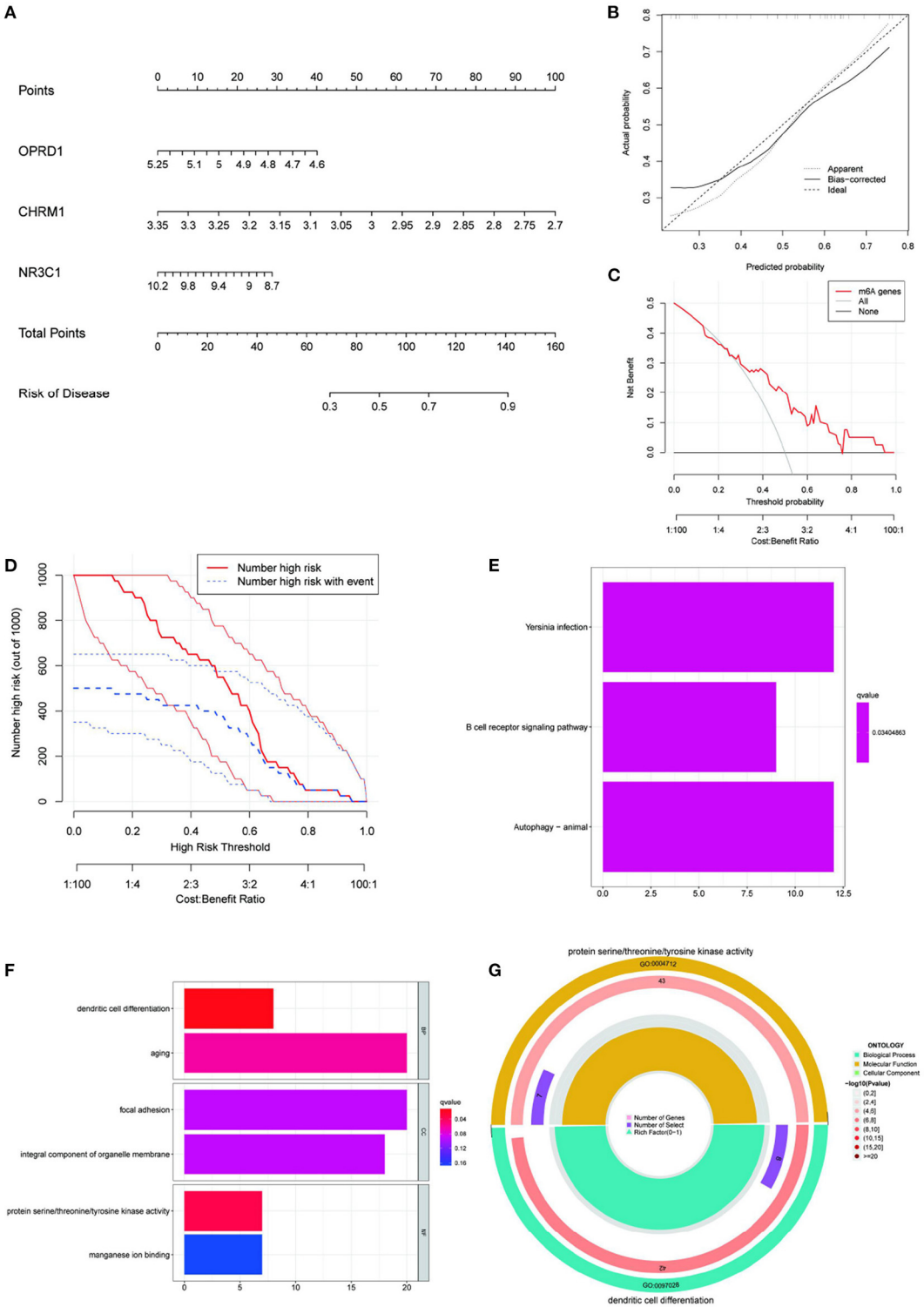

FIGURE 7 | Construction of nomogram prediction model and enrichment analysis based on this model. Construction an IS nomogram model based on the selected genes CHRM1, NR3C1, ADRB2, and OPRD1 **(A)**; Calibration curve showing the diagnostic power of the nomogram model **(B)**; DCA shows that the nomogram model has a good clinical application **(C)**; Clinical impact curves show high diagnostic power of the nomogram model **(D)**; KEGG **(E)** and GO **(F)** enrichment analysis of the genes included in this prediction model **(E,F)**; The most significant GO enrichment pathway associated with this predictive model **(G)**.

and epiquinidine, and the terpenoids cyclopamine, and mairin of EUO with hypertension, ferroptosis, and the neuroactive ligand-receptor interaction pathway. Hence, these pathways can be a new therapeutic target for the prevention and treatment of hypertension.

However, this study also has its shortcomings. The network pharmacology is based on the bioinformatics analysis of the database of herbal targets and disease genes, and thus lacks experimental validation. Hence, further experimental validation is needed to explore the mechanism of action of the drugs or their active ingredients. In addition, this study did not consider the selection of dosage in drug combination and the possible chemical reactions and changes of active ingredients in the process of concoction and decoction of herbal medicines. Furthermore, we also acknowledge that the current research in TCM for the treatment of endothelial injury in hypertension-related cerebrovascular disease is still limited, and therefore we suggest to provide more confirmation and discussion in the future.

CONCLUSIONS

The active ingredients of EUO-TT L. drug pair can act on proteins related to the neuroactive ligand-receptor interaction pathway, which may affect the process of cellular ferroptosis and potentially affect the progression of hypertension. CHRM1, NR3C1, ADRB2, and OPRD1, the target genes of the four EUO-TT L. drug pair active ingredients, were considered as risk markers for IS.

DATA AVAILABILITY STATEMENT

The original contributions presented in the study are included in the article/supplementary material, further inquiries can be directed to the corresponding author.

AUTHOR CONTRIBUTIONS

QZ: software, validation, formal analysis, data curation, and writing-original draft. JY: conceptualization, methodology, supervision, funding acquisition, and writing-review and editing. CY: methodology, conceptualization, project administration, and funding acquisition. XY: data curation and writing-review and editing. YC: software and data curation. All authors contributed to the article and approved the submitted version.

FUNDING

This work was supported by the National Natural Science Foundation of China (No. 81804061), Shandong Province Taishan Scholar Construction Project Funds No. 2018-35, and Ji'nan Science and Technology Project (No. 201805078).

ACKNOWLEDGMENTS

We would like to thank the reviewers for their valuable comments on our revisions. We thank Bullet Edits Limited for the linguistic editing and proofreading of the manuscript.

REFERENCES

1. Mirzaei H. Stroke in women: risk factors and clinical biomarkers. *J Cell Biochem.* (2017) 118:4191–202. doi: 10.1002/jcb.26130
2. Murray CJL, Vos T, Lozano R, Naghavi M, Flaxman AD, Michaud C, et al. Disability-adjusted life years (DALYs) for 291 diseases and injuries in 21 regions, 1990-2010: a systematic analysis for the Global Burden of Disease Study 2010. *Lancet.* (2012) 380:2197–223. doi: 10.1016/S0140-6736(12)61690-0
3. Lewington S, Clarke R, Qizilbash N, Peto R, Collins R, Prospective Studies Collaboration. Age-specific relevance of usual blood pressure to vascular mortality: a meta-analysis of individual data for one million adults in 61 prospective studies. *Lancet.* (2002) 360:1903–13. doi: 10.1016/S0140-6736(02)11911-8
4. Chen X, Sang X, Li S, Zhang S, Bai L. Studies on a chlorogenic acid-producing endophytic fungi isolated from Eucommia ulmoides Oliver. *J Ind Microbiol Biotechnol.* (2010) 37:447–54. doi: 10.1007/s10295-010-0690-0
5. Shao P, Zhang JF, Chen XX, Sun PL. Microwave-assisted extraction and purification of chlorogenic acid from by-products of Eucommia Ulmoides Oliver and its potential anti-tumor activity. *J Food Sci Technol.* (2015) 52:4925–34. doi: 10.1007/s13197-014-1571-8
6. Luo L, Wu W, Zhou Y, Yan J, Yang G, Ouyang D. Antihypertensive effect of Eucommia ulmoides Oliv. extracts in spontaneously hypertensive rats. *J Ethnopharmacol.* (2010) 129:238–43. doi: 10.1016/j.jep.2010.03.019
7. Gu J, Wang J-J, Yan J, Cui C-F, Wu W-H, Li L, et al. Effects of lignans extracted from Eucommia ulmoides and aldose reductase inhibitor epalrestat on hypertensive vascular remodeling. *J Ethnopharmacol.* (2011) 133:6–13. doi: 10.1016/j.jep.2010.08.055
8. Li Z-Y, Gu J, Yan J, Wang J-J, Huang W-H, Tan Z-R, et al. Hypertensive cardiac remodeling effects of lignan extracts from *Eucommia ulmoides* Oliv. Bark — A Famous Traditional Chinese Medicine. *Am J Chin Med.* (2013) 41:801–15. doi: 10.1142/S0192415X13500547
9. Li L, Yan J, Hu K, Gu J, Wang J-J, Deng X-L, et al. Protective effects of Eucommia lignans against hypertensive renal injury by inhibiting expression of aldose reductase. *J Ethnopharmacol.* (2012) 139:454–61. doi: 10.1016/j.jep.2011.11.032
10. Bhullar KS, Lassalle-Claux G, Touaibia M, Rupasinghe HPV. Antihypertensive effect of caffeic acid and its analogs through dual renin–angiotensin–aldosterone system inhibition. *Eur J Pharmacol.* (2014) 730:125–32. doi: 10.1016/j.ejphar.2014.02.038
11. Taubert D, Berkels R, Klaus W. Roesen R. Nitric oxide formation and corresponding relaxation of porcine coronary arteries induced by plant phenols: essential structural features. *J Cardiov Pharmacol.* (2002) 40:701–13. doi: 10.1097/00005344-200211000-00008
12. Pérez-Vizcaino F, Ibarra M, Cogolludo AL, Duarte J, Zaragozá-Arnáez F, Moreno L, et al. Endothelium-independent vasodilator effects of the flavonoid quercetin and its methylated metabolites in rat conductance and resistance arteries. *J Pharmacol Exp Ther.* (2002) 302:66–72. doi: 10.1124/jpet.302.1.66
13. Phillips OA, Mathew KT, Oriowo MA. Antihypertensive and vasodilator effects of methanolic and aqueous extracts of Tribulus terrestris in rats. *J Ethnopharmacol.* (2006) 104:351–5. doi: 10.1016/j.jep.2005.09.027
14. Guo Y, Shi D-Z, Yin H-J, Chen K-J. Effects of *Tribuli* saponins on ventricular remodeling after myocardial infarction in hyperlipidemic rats. *Am J Chin Med.* (2007) 35:309–16. doi: 10.1142/S0192415X07004837
15. Amin A, Lotfy M, Shafiullah M, Adeghate E. The protective effect of tribulus terrestris in diabetes. *Ann N Y Acad Sci.* (2006) 1084:391–401. doi: 10.1196/annals.1372.005
16. Sharifi AM, Darabi R, Akbarloo N. Study of antihypertensive mechanism of Tribulus terrestris in 2K1C hypertensive rats: Role of tissue ACE activity. *Life Sci.* (2003) 73:2963–71. doi: 10.1016/j.lfs.2003.04.002

17. Lee HH, Ahn E-K, Hong S-S, Oh JS. Anti-inflammatory effect of tribulusamide D isolated from Tribulus terrestris in lipopolysaccharide-stimulated RAW2647 macrophages. *Molec Med Rep.* (2017) 16:4421–8. doi: 10.3892/mmr.2017.7208
18. Harwani SC. Macrophages under pressure: the role of macrophage polarization in hypertension. *Transl Res.* (2018) 191:45–63. doi: 10.1016/j.trsl.2017.10.011
19. Zuccarella-Hackl C, von Känel R, Thomas L, Hauser M, Kuebler U, Widmer HR, et al. Macrophage superoxide anion production in essential hypertension: associations with biological and psychological cardiovascular risk factors. *Psychosom Med.* (2016) 78:750–7. doi: 10.1097/PSY.0000000000000324
20. Sesso HD, Jiménez MC, Wang L, Ridker PM, Buring JE, Gaziano JM. Plasma inflammatory markers and the risk of developing hypertension in men. *JAHA.* (2015) 4. doi: 10.1161/JAHA.115.001802
21. Fan J, Chen M, Cao S, Yao Q, Zhang X, Du S, et al. Identification of a ferroptosis-related gene pair biomarker with immune infiltration landscapes in ischemic stroke: a bioinformatics-based comprehensive study. *BMC Genomics.* (2022) 23:59. doi: 10.1186/s12864-022-08295-0
22. Luo M-Y, Su J-H, Gong S-X, Liang N, Huang W-Q, Chen W, et al. Ferroptosis: new dawn for overcoming the cardio-cerebrovascular diseases. *Front Cell Dev Biol.* (2021) 9:733908. doi: 10.3389/fcell.2021.733908
23. Dolma S, Lessnick SL, Hahn WC, Stockwell BR. Identification of genotype-selective antitumor agents using synthetic lethal chemical screening in engineered human tumor cells. *Cancer Cell.* (2003) 3:285–96. doi: 10.1016/S1535-6108(03)00050-3
24. Stockwell BR, Friedmann Angeli JP, Bayir H, Bush AI, Conrad M, Dixon SJ, et al. Ferroptosis: a regulated cell death nexus linking metabolism, redox biology, and disease. *Cell.* (2017) 171:273–85. doi: 10.1016/j.cell.2017.09.021
25. Zhang F, Liu H. Identification of ferroptosis-associated genes exhibiting altered expression in pulmonary arterial hypertension. *MBE.* (2021) 18:7619–30. doi: 10.3934/mbe.2021377
26. Dinh QN, Drummond GR, Sobey CG, Chrissobolis S. Roles of inflammation, oxidative stress, and vascular dysfunction in hypertension. *Biomed Res Int.* (2014) 2014:1–11. doi: 10.1155/2014/406960
27. Guzik TJ, Touyz RM. Oxidative stress, inflammation, and vascular aging in hypertension. *Hypertension.* (2017) 70:660–7. doi: 10.1161/HYPERTENSIONAHA.117.07802
28. Renna NF. Oxidative stress, vascular remodeling, and vascular inflammation in hypertension. *Int J Hypertens.* (2013) 2013:1–2. doi: 10.1155/2013/710136
29. Yuan H, Li X, Zhang X, Kang R, Tang D. Identification of ACSL4 as a biomarker and contributor of ferroptosis. *Biochem Biophys Res Commun.* (2016) 478:1338–43. doi: 10.1016/j.bbrc.2016.08.124
30. Mistry HD, Kurlak LO, Williams PJ, Ramsay MM, Symonds ME, Broughton Pipkin F. Differential expression and distribution of placental glutathione peroxidases 1, 3 and 4 in normal and pre-eclamptic pregnancy. *Placenta.* (2010) 31:401–8. doi: 10.1016/j.placenta.2010.02.011
31. Roland-Zejly L, Moisan V, St-Pierre I, Bilodeau J-F. Altered placental glutathione peroxidase mRNA expression in preeclampsia according to the presence or absence of labor. *Placenta.* (2011) 32:161–7. doi: 10.1016/j.placenta.2010.11.005
32. Yang J, Wang M, Wang S, Li G, Gao Y. Study on ferroptosis pathway that operates in hypertensive brain damage. *Clin Exp Hypertens.* (2020) 42:748–52. doi: 10.1080/10641963.2020.1783545
33. Redón J, Oliva MR, Tormos C, Giner V, Chaves J, Iradi A, et al. Antioxidant activities and oxidative stress byproducts in human hypertension. *Hypertension.* (2003) 41:1096–101. doi: 10.1161/01.HYP.0000068370.21009.38
34. Zhao L, Yang N, Song Y, Si H, Qin Q, Guo Z. Effect of iron overload on endothelial cell calcification and its mechanism. *Ann Transl Med.* (2021) 9:1658. doi: 10.21037/atm-21-5666
35. Lin X, Ouyang S, Zhi C, Li P, Tan X, Ma W, et al. Focus on ferroptosis, pyroptosis, apoptosis and autophagy of vascular endothelial cells to the strategic targets for the treatment of atherosclerosis. *Arch Biochem Biophys.* (2022) 715:109098. doi: 10.1016/j.abb.2021.109098
36. Di S, Han L, An X, Kong R, Gao Z, Yang Y, et al. In silico network pharmacology and in vivo analysis of berberine-related mechanisms against type 2 diabetes mellitus and its complications. *J Ethnopharmacol.* (2021) 276:114180. doi: 10.1016/j.jep.2021.114180
37. Ru J, Li P, Wang J, Zhou W, Li B, Huang C, et al. TCMSP: a database of systems pharmacology for drug discovery from herbal medicines. *J Cheminform.* (2014) 6:13. doi: 10.1186/1758-2946-6-13
38. Belinky F, Bahir I, Stelzer G, Zimmerman S, Rosen N, Nativ N, et al. Non-redundant compendium of human ncRNA genes in GeneCards. *Bioinformatics.* (2013) 29:255–61. doi: 10.1093/bioinformatics/bts676
39. Xu M, Ouyang T, Lv K, Ma X. Integrated WGCNA and PPI network to screen hub genes signatures for infantile hemangioma. *Front Genet.* (2021) 11:614195. doi: 10.3389/fgene.2020.614195
40. Dennis G, Sherman BT, Hosack DA, Yang J, Gao W, Lane HC, et al. Database for annotation, visualization, and integrated discovery. *Genome Biol.* (2003) 4:P3. doi: 10.1186/gb-2003-4-9-r60
41. Tanabe M, Kanehisa M. Using the KEGG database resource. *Curr Prot Bioinform.* (2012) 38. doi: 10.1002/0471250953.bi0112s38
42. Kang X, Chen Y, Yi B, Yan X, Jiang C, Chen B, et al. An integrative microenvironment approach for laryngeal carcinoma: the role of immune/methylation/autophagy signatures on disease clinical prognosis and single-cell genotypes. *J Cancer.* (2021) 12:4148–71. doi: 10.7150/jca.58076
43. Zhang W, Chao X, Wu J, Ma X, Yang Y, Wu Y, Lin J. Exploring the potential mechanism of guchang zhixie wan for treating ulcerative colitis by comprehensive network pharmacological approaches and molecular docking validation as well as cell experiments. *Chem Biodiversity.* (2021) 18. doi: 10.1002/cbdv.202000810
44. Trott O, Olson AJ. AutoDock Vina: Improving the speed and accuracy of docking with a new scoring function, efficient optimization, and multithreading. *J Comput Chem.* (2009) 31:455–61. doi: 10.1002/jcc.21334
45. O'Boyle NM, Banck M, James CA, Morley C, Vandermeersch T, Hutchison GR. Open babel: an open chemical toolbox. *J Cheminform.* (2011) 3:33. doi: 10.1186/1758-2946-3-33
46. Mooers BHM. Shortcuts for faster image creation in PyMOL. *Protein Sci.* (2020) 29:268–76. doi: 10.1002/pro.3781
47. Morris GM, Huey R, Lindstrom W, Sanner MF, Belew RK, Goodsell DS, et al. AutoDock4 and AutoDockTools4: Automated docking with selective receptor flexibility. *J Comput Chem.* (2009) 30:2785–91. doi: 10.1002/jcc.21256
48. Krug T, Gabriel JP, Taipa R, Fonseca BV, Domingues-Montanari S, Fernandez-Cadenas I, et al. TTC7B emerges as a novel risk factor for ischemic stroke through the convergence of several genome-wide approaches. *J Cereb Blood Flow Metab.* (2012) 32:1061–72. doi: 10.1038/jcbfm.2012.24
49. Jin X, Wang J, Ge L, Hu Q. Identification of immune-related biomarkers for sciatica in peripheral blood. *Front Genet.* (2021) 12:781945. doi: 10.3389/fgene.2021.781945
50. Wang Y, Dai G, Jiang L, Liao S, Xia J. Microarray analysis reveals an inflammatory transcriptomic signature in peripheral blood for sciatica. *BMC Neurol.* (2021) 21:50. doi: 10.1186/s12883-021-02078-y
51. Ying C, Guo C, Wang Z, Chen Y, Sun J, Qi X, et al. Prediction modeling based on the hospital for special surgery (hss) knee score for poor postoperative functional prognosis of elderly patients with patellar fractures. *Biomed Res Int.* (2021) 2021:1–10. doi: 10.1155/2021/6620504
52. Kang X, Chen B, Chen Y, Yi B, Yan X, Jiang C, et al. prediction modeling based on SNOT-22 score for endoscopic nasal septoplasty: a retrospective study. *PeerJ.* (2020) 8:e9890. doi: 10.7717/peerj.9890
53. Hu C, Li Q, Shou J, Zhang F-X, Li X, Wu M, et al. Constructing a predictive model of depression in chemotherapy patients with non-hodgkin's lymphoma to improve medical staffs' psychiatric care. *Biomed Res Int.* (2021) 2021:9201235. doi: 10.1155/2021/9201235
54. Van Calster B, Wynants L, Verbeek JFM, Verbakel JY, Christodoulou E, Vickers AJ, et al. Reporting and interpreting decision curve analysis: a guide for investigators. *Eur Urol.* (2018) 74:796–804. doi: 10.1016/j.eururo.2018.08.038
55. Olivieri AC, A. down-to-earth analyst view of rotational ambiguity in second-order calibration with multivariate curve resolution - a tutorial. *Anal Chim Acta.* (2021) 1156:338206. doi: 10.1016/j.aca.2021.338206
56. Lin C-H, Lin P-P, Lin C-Y, Lin C-H, Huang C-H, Huang Y-J, et al. Decreased mRNA expression for the two subunits of system xc–, SLC3A2 and SLC7A11, in WBC in patients with schizophrenia: Evidence in support of the hypo-glutamatergic hypothesis of schizophrenia. *J Psychiatr Res.* (2016) 72:58–63. doi: 10.1016/j.jpsychires.2015.10.007

57. Koppula P, Zhuang L, Gan B. Cystine transporter SLC7A11/xCT in cancer: ferroptosis, nutrient dependency, and cancer therapy. *Protein Cell.* (2021) 12:599–620. doi: 10.1007/s13238-020-00789-5
58. Sato M, Kusumi R, Hamashima S, Kobayashi S, Sasaki S, Komiyama Y, et al. The ferroptosis inducer erastin irreversibly inhibits system xc– and synergizes with cisplatin to increase cisplatin's cytotoxicity in cancer cells. *Sci Rep.* (2018) 8:968. doi: 10.1038/s41598-018-19213-4
59. Liu J, Xia X, Huang P. xCT: A critical molecule that links cancer metabolism to redox signaling. *Molec Therapy.* (2020) 28:2358–66. doi: 10.1016/j.ymthe.2020.08.021
60. Ren Z, Hu M, Wang Z, Ge J, Zhou X, Zhang G, et al. Ferroptosis-related genes in lung adenocarcinoma: prognostic signature and immune, drug resistance, mutation analysis. *Front Genet.* (2021) 12:672904. doi: 10.3389/fgene.2021.672904
61. Sun X, Ou Z, Chen R, Niu X, Chen D, Kang R, et al. Activation of the p62-Keap1-NRF2 pathway protects against ferroptosis in hepatocellular carcinoma cells: hepatobiliary malignancies. *Hepatology.* (2016) 63:173–84. doi: 10.1002/hep.28251
62. Hou W, Xie Y, Song X, Sun X, Lotze MT, Zeh HJ, et al. Autophagy promotes ferroptosis by degradation of ferritin. *Autophagy.* (2016) 12:1425–8. doi: 10.1080/15548627.2016.1187366
63. Gao M, Monian P, Pan Q, Zhang W, Xiang J, Jiang X. Ferroptosis is an autophagic cell death process. *Cell Res.* (2016) 26:1021–32. doi: 10.1038/cr.2016.95
64. Tian Y, Lu J, Hao X, Li H, Zhang G, Liu X, et al. FTH1 inhibits ferroptosis through ferritinophagy in the 6-OHDA model of Parkinson's disease. *Neurotherapeutics.* (2020) 17:1796–812. doi: 10.1007/s13311-020-00929-z
65. Hu Z-W, Wen Y-H, Ma R-Q, Chen L, Zeng X-L, Wen W-P, et al. Ferroptosis driver SOCS1 and suppressor FTH1 independently correlate with M1 and M2 macrophage infiltration in head and neck squamous cell carcinoma. *Front Cell Dev Biol.* (2021) 9:727762. doi: 10.3389/fcell.2021.727762
66. Yang WS, Stockwell BR. Synthetic lethal screening identifies compounds activating iron-dependent, nonapoptotic cell death in oncogenic-RAS-harboring cancer cells. *Chem Biol.* (2008) 15:234–45. doi: 10.1016/j.chembiol.2008.02.010
67. Wang X, Song H, Yu Q, Liu Q, Wang L, Liu Z, et al. Ad-p53 enhances the sensitivity of triple-negative breast cancer MDA-MB-468 cells to the EGFR inhibitor gefitinib. *Oncol Rep.* (2015) 33:526–32. doi: 10.3892/or.2014.3665
68. Vousden KH, Lu X. Live or let die: the cell's response to p53. *Nat Rev Cancer.* (2002) 2:594–604. doi: 10.1038/nrc864
69. Kang R, Kroemer G, Tang D. The tumor suppressor protein p53 and the ferroptosis network. *Free Radical Biol Med.* (2019) 133:162–8. doi: 10.1016/j.freeradbiomed.2018.05.074
70. Jiang L, Kon N, Li T, Wang S-J, Su T, Hibshoosh H, et al. Ferroptosis as a p53-mediated activity during tumour suppression. *Nature.* (2015) 520:57–62. doi: 10.1038/nature14344
71. Ou Y, Wang S-J, Li D, Chu B, Gu W. Activation of *SAT1* engages polyamine metabolism with p53-mediated ferroptotic responses. *Proc Natl Acad Sci USA.* (2016) 113:E6806–12. doi: 10.1073/pnas.1607152113
72. Li Y, Chen F, Chen J, Chan S, He Y, Liu W, et al. Disulfiram/copper induces antitumor activity against both nasopharyngeal cancer cells and cancer-associated fibroblasts through ROS/MAPK and ferroptosis pathways. *Cancers.* (2020) 12:138. doi: 10.3390/cancers12010138
73. Gao M, Monian P, Quadri N, Ramasamy R, Jiang X. Glutaminolysis and transferrin regulate ferroptosis. *Mol Cell.* (2015) 59:298–308. doi: 10.1016/j.molcel.2015.06.011
74. Leidgens S, Bullough KZ, Shi H, Li F, Shakoury-Elizeh M, Yabe T, et al. Each member of the Poly-r(C)-binding protein 1 (PCBP) family exhibits iron chaperone activity toward ferritin. *J Biol Chem.* (2013) 288:17791–802. doi: 10.1074/jbc.M113.460253
75. Yuan C, Chen M, Cai X. Advances in poly(rC)-binding protein 2: Structure, molecular function, and roles in cancer. *Biomed Pharmacother.* (2021) 139:111719. doi: 10.1016/j.biopha.2021.111719
76. Smith R, Tran K, Smith C, McDonald M, Shejwalkar P, Hara K. The role of the Nrf2/ARE antioxidant system in preventing cardiovascular diseases. *Diseases.* (2016) 4:34. doi: 10.3390/diseases4040034
77. Dixon SJ, Lemberg KM, Lamprecht MR, Skouta R, Zaitsev EM, Gleason CE, et al. Ferroptosis: an iron-dependent form of nonapoptotic cell death. *Cell.* (2012) 149:1060–72. doi: 10.1016/j.cell.2012.03.042
78. Ishii T, Igawa T, Hayakawa H, Fujita T, Sekiguchi M, Nakabeppu Y. PCBP1 and PCBP2 both bind heavily oxidized RNA but cause opposing outcomes, suppressing or increasing apoptosis under oxidative conditions. *J Biol Chem.* (2020) 295:12247–61. doi: 10.1074/jbc.RA119.011870
79. Chen X, Yan L, Jiang F, Lu Y, Zeng N, Yang S, et al. Identification of a ferroptosis-related signature associated with prognosis and immune infiltration in adrenocortical carcinoma. *Int J Endocrinol.* (2021) 2021:1–12. doi: 10.1155/2021/4654302
80. Xiao H, Ding Y, Gao Y, Wang L-M, Wang H, Ding L, et al. Haploinsufficiency of NR3C1 drives glucocorticoid resistance in adult acute lymphoblastic leukemia cells by down-regulating the mitochondrial apoptosis axis, and is sensitive to Bcl-2 blockage. *Cancer Cell Int.* (2019) 19:218. doi: 10.1186/s12935-019-0940-9
81. Wan C, Gong C, Zhang H, Hua L, Li X, Chen X, et al. β2-adrenergic receptor signaling promotes pancreatic ductal adenocarcinoma (PDAC) progression through facilitating PCBP2-dependent c-myc expression. *Cancer Lett.* (2016) 373:67–76. doi: 10.1016/j.canlet.2016.01.026
82. Alappat L, Valerio M, Awad AB. Effect of vitamin D and β-sitosterol on immune function of macrophages. *Int Immunopharmacol.* (2010) 10:1390–6. doi: 10.1016/j.intimp.2010.08.003
83. Awad AB, Chinnam M, Fink CS, Bradford PG. β-Sitosterol activates Fas signaling in human breast cancer cells. *Phytomedicine.* (2007) 14:747–54. doi: 10.1016/j.phymed.2007.01.003
84. Marahatha R, Gyawali K, Sharma K, Gyawali N, Tandan P, Adhikari A, et al. Pharmacologic activities of phytosteroids in inflammatory diseases: mechanism of action and therapeutic potentials. *Phytother Res.* (2021) 35:5103–24. doi: 10.1002/ptr.7138
85. Aswad M, Rayan M, Abu-Lafi S, Falah M, Raiyn J, Abdallah Z, et al. Nature is the best source of anti-inflammatory drugs: indexing natural products for their anti-inflammatory bioactivity. *Inflamm Res.* (2018) 67:67–75. doi: 10.1007/s00011-017-1096-5
86. Barbaro NR, de Araújo TM, Tanus-Santos JE, Anhê GF, Fontana V, Moreno H. Vascular damage in resistant hypertension: TNF-alpha inhibition effects on endothelial cells. *Biomed Res Int.* (2015) 2015:1–8. doi: 10.1155/2015/631594
87. Bautista LE, Vera LM, Arenas IA, Gamarra G. Independent association between inflammatory markers (C-reactive protein, interleukin-6, and TNF-α) and essential hypertension. *J Hum Hypertens.* (2005) 19:149–54. doi: 10.1038/sj.jhh.1001785
88. Feng J, Chen H-W, Pi L-J, Wang J, Zhan D-Q. Protective effect of tanshinone IIA against cardiac hypertrophy in spontaneously hypertensive rats through inhibiting the Cys-C/Wnt signaling pathway. *Oncotarget.* (2017) 8:10161–70. doi: 10.18632/oncotarget.14328
89. Wang R, Zhang H, Wang Y, Yu X, Yuan Y. Effects of salvianolic acid B and tanshinone IIA on the pharmacokinetics of losartan in rats by regulating the activities and expression of CYP3A4 and CYP2C9. *J Ethnopharmacol.* (2016) 180:87–96. doi: 10.1016/j.jep.2016.01.021
90. Zheng L, Liu M, Wei M, Liu Y, Dong M, Luo Y, et al. Tanshinone IIA attenuates hypoxic pulmonary hypertension via modulating KV currents. *Respir Physiol Neurobiol.* (2015) 205:120–8. doi: 10.1016/j.resp.2014.09.025
91. Rauly-Lestienne I, Heusler P, Cussac D, Lantoine-Adam F, de Almeida Cyrino FZG, Bouskela E. Contribution of muscarinic receptors to in vitro and in vivo effects of Ruscus extract. *Microvasc Res.* (2017) 114:1–11. doi: 10.1016/j.mvr.2017.05.005
92. Courties G, Frodermann V, Honold L, Zheng Y, Herisson F, Schloss MJ, et al. Glucocorticoids regulate bone marrow b lymphopoiesis after stroke. *Circ Res.* (2019) 124:1372–85. doi: 10.1161/CIRCRESAHA.118.314518
93. Gong J, Zhou F, Wang SXX, Xu J, Xiao F. Caveolin-3 protects diabetic hearts from acute myocardial infarction/reperfusion injury through β2AR, cAMP/PKA, and BDNF/TrkB signaling pathways. *Aging (Albany NY).* (2020) 12:14300–13. doi: 10.18632/aging.103469
94. Kumar A, Tripathi M, Srivastava MVP, Vivekanandhan S, Prasad K. Relationship between polymorphisms in beta−2 adrenergic receptor gene and ischemic stroke in North Indian Population: a hospital based case control study. *BMC Res Notes.* (2014) 7:396. doi: 10.1186/1756-0500-7-396

95. Roussotte FF, Jahanshad N, Hibar DP, Sowell ER, Kohannim O, Barysheva M, et al. A commonly carried genetic variant in the delta opioid receptor gene, OPRD1, is associated with smaller regional brain volumes: replication in elderly and young populations. *Hum Brain Mapp.* (2014) 35:1226–36. doi: 10.1002/hbm.22247

Conflict of Interest: The authors declare that the research was conducted in the absence of any commercial or financial relationships that could be construed as a potential conflict of interest.

Publisher's Note: All claims expressed in this article are solely those of the authors and do not necessarily represent those of their affiliated organizations, or those of the publisher, the editors and the reviewers. Any product that may be evaluated in this article, or claim that may be made by its manufacturer, is not guaranteed or endorsed by the publisher.

Copyright © 2022 Zhang, Yang, Yang, Yang and Chen. This is an open-access article distributed under the terms of the Creative Commons Attribution License (CC BY). The use, distribution or reproduction in other forums is permitted, provided the original author(s) and the copyright owner(s) are credited and that the original publication in this journal is cited, in accordance with accepted academic practice. No use, distribution or reproduction is permitted which does not comply with these terms.

frontiers | Frontiers in Neurology

ORIGINAL RESEARCH
published: 07 April 2022
doi: 10.3389/fneur.2022.885323

Serum Neuroglobin as a Potential Prognostic Biomarker for Cognitive Impairment After Intracerebral Hemorrhage

Yu Gao[1], *Bo Wang*[1], *Ye Miao*[2] *and Yu Han*[3]*

[1] Department of Cardiology, The First Affiliated Hospital of Jinzhou Medical University, Jinzhou, China, [2] Department of Neurosurgery, The First Affiliated Hospital of Jinzhou Medical University, Jinzhou, China, [3] Department of Emergency, The First Affiliated Hospital of Jinzhou Medical University, Jinzhou, China

Objective: Stroke is closely related to dementia, but there are few prospective studies on cognitive decline after stroke in patients with cerebral hemorrhage. Neuroglobin is an oxygen-binding protein mainly expressed in brain neurons. The aim of our current study was to determine whether neuroglobin could serve as a biomarker for cognitive prognosis in patients with intracerebral hemorrhage (ICH).

Methods: Three hundred and sixteen patients with ICH were consecutively enrolled in a prospective study. Baseline data such as age and gender of ICH patients on admission were recorded. Serum neuroglobin concentrations were determined by enzyme-linked immunosorbent assay (ELISA). All ICH patients 3 months after onset were divided into post-stroke cognitive impairment group (PSCI) and non-PSCI group according to MoCA assessment results.

Results: The PSCI and Non-PSCI groups had serum neuroglobin concentrations of (4.7 ± 0.9) and (7.5 ± 1.1) ng/ml, respectively, with a statistically significant difference between the two groups ($p < 0.05$). Age, gender, LDL, FBG, SBP, DBP, NHISS, and Hematoma volume were found to be adversely connected with MoCA ($p < 0.05$), while education, HDL, and serum neuroglobin were found to be positively correlated with MoCA ($p < 0.05$). After controlling for baseline data, regression analysis revealed that serum neuroglobin was remained an efficient biomarker for predicting cognitive performance in individuals with ICH ($p < 0.05$). The diagnostic accuracy of blood neuroglobin concentration for PSCI in ICH patients was 72.6%, the sensitivity was 67.4%, and the specificity was 75.5%, according to receiver operating characteristic (ROC) curve analysis.

Conclusions: Serum neuroglobin may serve as a potential biomarker to predict cognitive decline after ICH.

Keywords: intracranial hemorrhage, neuroglobin, post-stroke cognitive impairment, prognosis, biomarker

OPEN ACCESS

Edited by:
Yuzhen Xu,
Tongji University, China

Reviewed by:
Kai Wang,
Xuzhou Medical University, China
Yihong Ma,
Kumamoto University, Japan

***Correspondence:**
Yu Han
253668233@qq.com

Specialty section:
This article was submitted to Neurological Biomarkers, a section of the journal Frontiers in Neurology

Received: *27 February 2022*
Accepted: *14 March 2022*
Published: *07 April 2022*

Citation:
Gao Y, Wang B, Miao Y and Han Y (2022) Serum Neuroglobin as a Potential Prognostic Biomarker for Cognitive Impairment After Intracerebral Hemorrhage. Front. Neurol. 13:885323. doi: 10.3389/fneur.2022.885323

INTRODUCTION

Intracranial hemorrhage (ICH) is defined as any type of intracranial hemorrhage that kills neurons and pressures surrounding brain tissue, causing neurological impairments (1, 2). ICH accounts for 10–20% of all strokes and is the second most common subtype of stroke, with significant impairment or death as a result (3, 4). The prevalence of ICH varies greatly between countries and ethnic groups, with ICH in low- and middle-income countries being twice as common as in high-income countries (5). The incidence of ICH is 8–15% in Western countries such as the United States, United Kingdom and Australia, 18–24% in Japan and South Korea, and 14.9% in China (6–8). The average cost of initial hospitalization for ICH survivors was $28,360 and the first year after discharge was $16,035, with 8% requiring repeat hospitalizations and 41% unable to take care of themselves (9). The high morbidity, high cost, and disability rate of ICH make it an important factor restricting social and economic development, and the search for the potential etiology and biological targets of ICH has become an urgent need.

The globin isoform neuroglobin is found in both the central and peripheral neural systems (10). Thorsten Burmester et al. were the first to find it in 2000 (11). Its primary role is in maintaining cellular oxygen homeostasis and scavenging reactive oxygen species and nitrogen. It also improves brain tissue's oxygen supply capacity and protects it from hypoxic or ischemia damage, potentially lowering ischemic hypoxic brain injury (12, 13).

Cognitive impairment appears to be a common sequelae of (ICH) survivors, but effective prevention and treatment methods are still lacking (14, 15). Neuroglobin, as a potential neuroprotective protein discovered in recent years, is endowed with relatively broad application prospects (16). The goal of our research was to see if neuroglobin may be used as a biomarker for cognitive impairment following ICH.

METHODS

Study Population

Six hundred and thirty-seven patients with ICH were prospectively enrolled for screening and follow-up. The inclusion criteria for patients with cerebral hemorrhage were: within 24 h of onset, and confirmed ICH by cranial CT. The exclusion criteria for ICH patients were: pure intraventricular hemorrhage ($N = 11$), bleeding after trauma or tumor ($N = 79$), bleeding after trauma or tumor ($N = 79$), hemorrhage following a sinus thrombosis ($N = 7$), not survive the first 3 months ($N = 109$), prior dementia ($N = 63$), lost to follow-up ($N = 14$) and refuse MoCA inspection ($N = 23$). According to the inclusion and exclusion criteria, a total of 316 ICH patients were eventually included in the study. **Figure 1** depicts a detailed flowchart. Our study was approved by the local medical ethics committee, and the application of clinical data was with the permission of all participants or their families.

Baseline Data Collection

After enrolment, all ICH patients' baseline data were obtained. Age, gender, years of schooling, low density lipoprotein (LDL), high density lipoprotein (HDL), fasting plasma glucose (FBG), systolic blood pressure (SBP), diastolic blood pressure (DBP), National Institutes of Health Stroke Scale (NHISS), and Hematoma volumes were among the information collected. Statistical analysis of all baseline data was performed by professional personnel.

Serum Neuroglobin Concentration Determination

Within 24 h after the commencement of ICH, nurses drew venous blood from the patients. The venous blood was taken and left to sit at room temperature for 20 min before being centrifuged at high speed to extract serum. Serum was aliquoted and stored in a −80°C freezer. Purchased ELISA reagents from MyBioSource (San Diego, CA, USA) were used to detect serum neuroglobin concentrations. The specific experimental steps of ELISA refer to previous reports and product instructions (17).

MoCA Scale Evaluation

All ICH patients underwent cognitive function assessment 3 months after onset. The Montreal Cognitive Assessment (MoCA) is a worldwide cognitive screening tool founded in 1996 by Ziad Nasreddine in Montreal, Quebec. MoCA has a total score of 30 points, and the test content includes short-term memory, executive performance, attention, concentration, etc. (18). Compared with the well-known Mini Mental State Examination (MMSE), MoCA is a promising tool for the detection of mild cognitive impairment (MCI) and early Alzheimer's disease. The test is also being used in hospitals to decide whether to allow a patient to live alone or with a home assistant.

Statistical Analysis

Categorical variables are expressed as numbers, while continuous variables are expressed as mean and standard deviation (percent). The *t*-test and the chi-square test were used to compare continuous and categorical variables, respectively. The underlying etiologies affecting cognitive outcomes in patients with ICH were investigated using correlation and regression analysis. The predictive efficacy of serum neuroglobin levels for cognitive deterioration following ICH was assessed using a receiver operating characteristic (ROC) curve analysis. This study employed SPSS 22.0 (SPSS Inc., Chicago, IL, USA) for analysis, with p-values < 0.05 considered statistically significant.

RESULTS

Baseline Data

A total of 316 patients with cerebral hemorrhage were included in the study after screening. According to the MoCA score 3 months after ICH, ICH patients were separated into two groups: PSCI (MoCA 26) and non-PSCI (MoCA 26). **Table 1** summarizes the baseline data of all subjects. The statistical results revealed that there was no significant difference between the two groups in

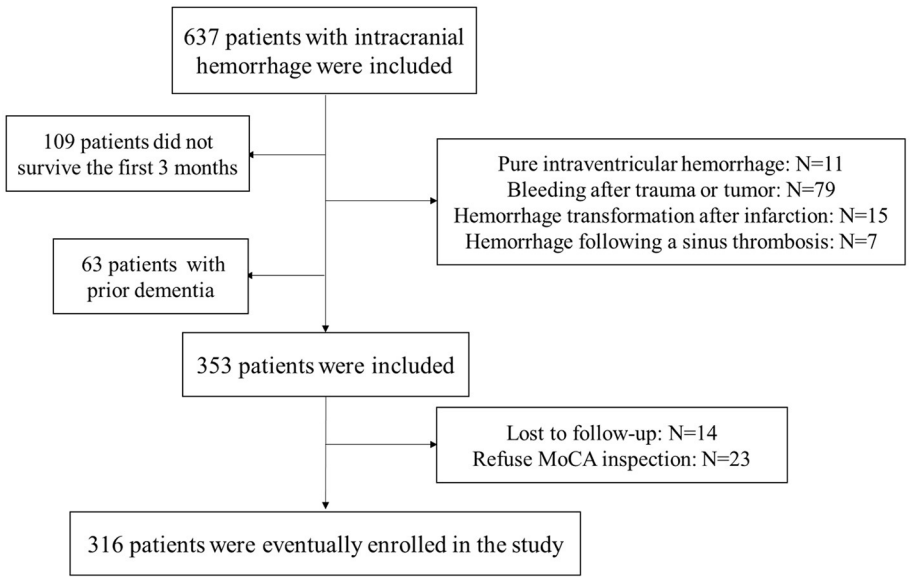

FIGURE 1 | Flow chart of the study. MoCA, Montreal Cognitive Assessment.

TABLE 1 | Baseline characteristics of ICH patients in the PSCI and non-PSCI groups.

	Non-PSCI group *N* = 124	PSCI group *N* = 192	*P*-value
Age, years	65.3 ± 8.2	65.7 ± 7.8	0.663
Gender, male/female	75/49	120/72	0.719
Education, years	10.1 ± 2.5	10.3 ± 2.1	0.444
LDL, mmol/L	2.37 ± 0.18	2.35 ± 0.14	0.269
HDL, mmol/L	1.12 ± 0.13	1.10 ± 0.09	0.107
FBG, mmol/L	6.14 ± 0.81	6.16 ± 0.87	0.838
SBP, mmHg	137.6 ± 11.2	137.1 ± 10.3	0.684
DBP, mmHg	84.5 ± 7.6	84.8 ± 7.0	0.719
NHISS, points	12.8 ± 2.4	13.2 ± 2.6	0.170
Hematoma (ml)	14.0 ± 6.7	14.4 ± 6.5	0.598
MoCA, points	27.1 ± 0.8	24.3 ± 1.2	<0.001
Neuroglobin, ng/ml	7.5 ± 1.1	4.7 ± 0.9	<0.001

LDL, low density lipoprotein; HDL, high density lipoprotein; FBG, fasting plasma glucose; SBP, systolic blood pressure; DBP, diastolic blood pressure; NHISS, National Institutes of Health Stroke Scale; MoCA, Montreal Cognitive Assessment.

terms of age, gender, years of education, LDL, HDL, FBG, SBP, DBP, NHISS, and hematoma volume ($p > 0.05$).

The MoCA scores of the PSCI and non-PSCI groups, on the other hand, were (24.3 ± 1.2) and (27.1 ± 0.8), respectively, with a statistically significant difference between the two groups ($p < 0.001$). Similarly, the PSCI and non-PSCI groups had blood neuroglobin concentrations of (4.7 ± 0.9) ng/ml and (7.5 ± 1.1) ng/ml, respectively, with a statistically significant difference between the two groups ($p < 0.001$). **Figure 2** shows a comparison of MoCA score and serum neuroglobin concentration.

Correlation Analysis

Correlation analysis showed that age, gender, LDL, FBG, SBP, DBP, NHISS and hematoma volume were negatively correlated with MoCA ($p < 0.05$), while education, HDL and serum neuroglobin were positively correlated with MoCA ($p < 0.05$). The specific correlation coefficients are shown in **Table 2**.

Regression Analysis

The results of the regression analysis are shown in **Table 3**. In Model 1, after adjusting for sex, age, and years of education, serum neuroglobin concentration was an independent risk predictor for PSCI ($\beta = 0.356$, $p < 0.001$). In Model 2, after further adjustment for LDL, HDL, FBG, SBP, and DBP, serum neuroglobin concentration was also an independent risk predictor for PSCI after ICH ($\beta = 0.329$, $p = 0.017$). In Model 2, after further adjustment for NHISS scores and Hematoma volumes, serum neuroglobin concentration was also an independent risk predictor for PSCI after ICH ($\beta = 0.311$, $p = 0.038$).

ROC Analysis

We used ROC analysis to determine the predictive value of serum neuroglobin concentration for PSCI following ICH, as shown in **Figure 3**. In the diagnosis of PSCI following ICH, serum neuroglobin concentration had a sensitivity, specificity, and accuracy of 67.4, 75.5, and 72.6%, respectively. For the diagnosis of poor prognosis in ICH, the threshold value for serum neuroglobin concentration was 5.9 ng/mL.

DISCUSSIONS

We investigated the value of serum neuroglobin in predicting cognitive impairment after ICH. Our study found that serum

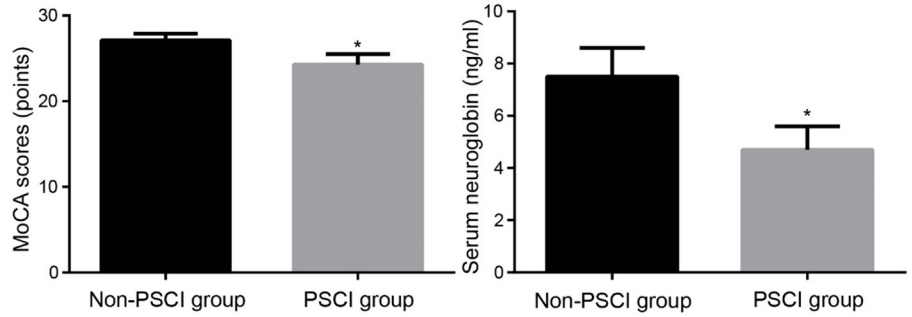

FIGURE 2 | Comparison of MoCA scores and serum neuroglobin concentrations between groups. MoCA, Montreal Cognitive Assessment; PSCI, post-stroke cognitive impairment. Compared to Non-PSCI group, $^{*}P < 0.05$.

TABLE 2 | Correlation analysis of MoCA scores with baseline characteristics.

	Spearman's correlation coefficient	*P*-values
Age, years	−0.142	<0.001
Gender, male/female	−0.205	0.036
Education, years	0.178	<0.001
LDL, mmol/L	−0.113	<0.001
HDL, mmol/L	0.164	<0.001
FBG, mmol/L	−0.193	<0.001
SBP, mmHg	−0.237	0.142
DBP, mmHg	−0.221	0.097
NHISS, points	−0.186	<0.001
Hematoma (ml)	−0.259	0.028
Neuroglobin, ng/ml	0.307	<0.001

MoCA, Montreal Cognitive Assessment; LDL, low density lipoprotein; HDL, high density lipoprotein; FBG, fasting plasma glucose; SBP, systolic blood pressure; DBP, diastolic blood pressure; NHISS, National Institutes of Health Stroke Scale.

TABLE 3 | Regression analysis of serum neuroglobin levels and MoCA scores.

	Regression coefficient	*P*-values
Model 1	0.356	<0.001
Model 2	0.329	0.017
Model 3	0.311	0.038

Model 1: adjusted for age, gender and education; Model 2: further adjusted for LDL, HDL, FBG, SBP and DBP; Model 3: further adjusted for NHISS scores and Hematoma volumes. MoCA, Montreal Cognitive Assessment; LDL, low density lipoprotein; HDL, high density lipoprotein; FBG, fasting plasma glucose; SBP, systolic blood pressure; DBP, diastolic blood pressure; NHISS, National Institutes of Health Stroke Scale.

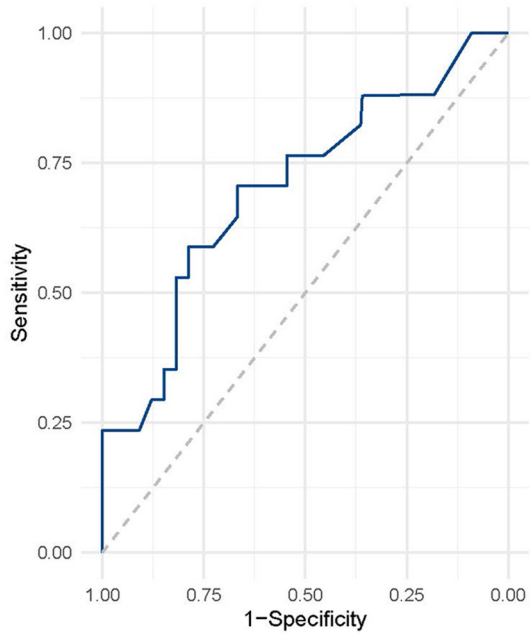

FIGURE 3 | ROC analysis of serum neuroglobin for predicting PSCI after ICH. ROC, receiver operating characteristic; ICH, intracranial hemorrhage.

neuroglobin concentrations were significantly lower in PSCI patients than in non-PSCI patients after ICH. Correlation regression analysis found that serum neuroglobin was an independent predictor of PSCI after ICH. Our further ROC analysis found that neuroglobin has high sensitivity and specificity in predicting PSCI after ICH, suggesting that it has a high value as a predictor of PSCI after ICH.

Neuroglobin is a monomeric hexametric heme protein with a molecular weight of 17 kda, belonging to the globin family, which is mainly expressed in neurons of the central and peripheral nervous systems (19, 20). Neuroglobin is a heme protein that is highly conserved during evolution, with more than 90% genetic sequence identity between humans and mice (21, 22). Neuroglobin is widely distributed in the human body, including the hippocampus, diencephalon, cerebral cortex, cerebellum, organs with endocrine functions, and retinal cells (23). Neuroglobin has a common 8 α-helix structure, and its main physiological function is to bind and transport oxygen, scavenge and detoxify reactive oxygen species (24). The heme prosthetic group of neuroglobin that transports oxygen is located between the fifth and sixth helices. Neuroglobin is

mainly expressed intracellularly, and it cannot pass through normal cell membranes and blood-brain barrier, which limits its application (25–27).

Neuroglobin has been found to have neuroprotective effects in recent years. The research of Professor Jin Kunlin's team showed that the neuroglobin level in the autopsy brain tissue of Alzheimer's disease patients increased compared with the normal control group (28). Italian scholars have found that the causative gene of Huntington's disease can damage the 17β-estradiol/neuroglobin signaling pathway, thereby affecting neuronal survival, suggesting that neuroglobin is involved in the pathogenic mechanism of Huntington's disease (29). In addition, the expression of neuroglobin present in the substantia nigra and striatum was upregulated in a mouse model of Parkinson's disease, suggesting that neuroglobin may be involved in the mechanism of its pathogenesis (30, 31). The above studies suggest that neuroglobin has a neuroprotective role in neurodegeneration. Another study showed that neuroglobin could be detected in multiple regions after cerebral infarction, and its expression was significantly increased in the ischemic penumbra (32). Based on the neuroprotective effect of neuroglobin, scientists developed a hyaluronic acid nanoparticle delivery system that can pass through the BBB (33), breaking through the application dilemma of neuroglobin to a certain extent.

The role of neuroglobin in hemorrhagic stroke has also received increasing attention. Cai et al.'s study showed that serum neuroglobin concentration on the second day after subarachnoid hemorrhage was closely related to poor prognosis, suggesting that it may be a potential biological target for predicting poor prognosis of subarachnoid hemorrhage (34). Another study showed that neuroglobin expression was significantly increased in the surrounding neurons of arteriovenous malformation and ICH patients and in the perihematoma area near cerebral hemorrhage, which may be involved in neuroprotection after brain injury (35). A recent study showed that early serum neuroglobin concentration predicts delayed cerebral ischemia in patients with aneurysmal subarachnoid hemorrhage (36). However, the role of neuroglobin in ICH remains poorly understood.

Our study is the first to demonstrate that serum neuroglobin is associated with PSCI after ICH. However, our study also has some limitations. First, we are a single-center study and include no normal controls; second, our main research object is the northern Han population in China, and the findings may not be applicable to other regions and ethnic groups; third, there is a lack of *in vitro* and *in vivo* studies on the neuroprotective mechanism of neuroglobin.

CONCLUSIONS

Serum neuroglobin concentration may be a potential biomarker for predicting PSCI after ICH. The correlation between serum neuroglobin and PSCI after ICH needs to be further studied, and the research results may provide new prospects for the prevention and treatment of PSCI after ICH.

DATA AVAILABILITY STATEMENT

The raw data supporting the conclusions of this article will be made available by the authors, without undue reservation.

ETHICS STATEMENT

The studies involving human participants were reviewed and approved by Ethics Committee of Jinzhou Medical University. The patients/participants provided their written informed consent to participate in this study.

AUTHOR CONTRIBUTIONS

YH designed this research and wrote the manuscript. YG, BW, and YM participated in experimental process and statistical analysis. All authors approved the submitted version.

REFERENCES

1. Miao Y, Zhang ZX, Feng X, Sun WM. IL-33 as a novel serum prognostic marker of intracerebral hemorrhage. *Oxidat Med Cell Long.* (2021) 2021:5597790. doi: 10.1155/2021/5597790
2. Sun W, Zhang Z, Feng X, Sui X, Miao Y. Serum neuropeptide Y: a potential prognostic marker of intracerebral hemorrhage. *Dis Mark.* (2021) 2021:7957013. doi: 10.1155/2021/7957013
3. An SJ, Kim TJ, Yoon B-W. Epidemiology, risk factors, and clinical features of intracerebral hemorrhage: an update. *J Stroke.* (2017) 19:3. doi: 10.5853/jos.2016.00864
4. Madangarli N, Bonsack F, Dasari R, Sukumari–Ramesh S. Intracerebral hemorrhage: blood components and neurotoxicity. *Brain Sci.* (2019) 9:316. doi: 10.3390/brainsci9110316
5. Ovbiagele B, Nguyen-Huynh MN. Stroke epidemiology: advancing our understanding of disease mechanism and therapy. *Neurotherapeutics.* (2011) 8:319–29. doi: 10.1007/s13311-011-0053-1
6. Murray CJ, Abraham J, Ali MK, Alvarado M, Atkinson C, Baddour LM, et al. The state of US health, 1990-2010: burden of diseases, injuries, and risk factors. *JAMA.* (2013) 310:591–606. doi: 10.1001/jama.2013.13805
7. World Health Organization. *The 2016 Global Status Report on Blood Safety and Availability*. Geneva: World Health Organization (2017).
8. Song J-P, Ni W, Gu Y-X, Wei Z, Chen L, Bin X, et al. Epidemiological features of nontraumatic spontaneous subarachnoid hemorrhage in China: a nationwide hospital-based multicenter study. *Chin Med J.* (2017) 130:776–81. doi: 10.4103/0366-6999.202729
9. Alkhachroum AM, Bentho O, Chari N, Kulhari A, Xiong W. Neuroscience step-down unit admission criteria for patients with intracerebral hemorrhage. *Clin Neurol Neurosurg.* (2017) 162:12–5. doi: 10.1016/j.clineuro.2017.09.002
10. Keller TS, Lechauve C, Keller AS, Brooks S, Weiss MJ, Columbus L, et al. The role of globins in cardiovascular physiology. *Physiol Rev.* (2022) 102:859–92. doi: 10.1152/physrev.00037.2020
11. Burmester T, Weich B, Reinhardt S, Hankeln T. A vertebrate globin expressed in the brain. *Nature.* (2000) 407:520–3. doi: 10.1038/35035093
12. Lopez IA, Acuna D, Shahram Y, Mowlds D, Ngan AM, Rungvivatjarus T, et al. Neuroglobin expression in the cochlea of rat pups exposed to chronic very mild carbon monoxide (25 ppm) in air during and after the prenatal period. *Brain Res.* (2010) 1327:56–68. doi: 10.1016/j.brainres.2010.02.078
13. Baez E, Echeverria V, Cabezas R, Ávila-Rodriguez M, Garcia-Segura LM, Barreto GE. Protection by neuroglobin expression in brain

pathologies. *Front Neurol.* (2016) 7:146. doi: 10.3389/fneur.2016.00146
14. Hostettler IC, Seiffge DJ, Werring DJ. Intracerebral hemorrhage: an update on diagnosis and treatment. *Expert Rev Neurotherap.* (2019) 19:679–94. doi: 10.1080/14737175.2019.1623671
15. Yuan M, Guo Y-S, Han Y, Gao Z-K, Shen XY, Bi X. Effectiveness and mechanisms of enriched environment in post-stroke cognitive impairment. *Behav Brain Res.* (2021) 410:113357. doi: 10.1016/j.bbr.2021.113357
16. Yu Z, Fan X, Lo EH, Wang X. Neuroprotective roles and mechanisms of neuroglobin. *Neurol Res.* (2009) 31:122–7. doi: 10.1179/174313209X389866
17. Zhang F, Hou G, Hou G, Wang C, Shi B, Zheng Y. Serum irisin as a potential biomarker for cognitive decline in vascular dementia. *Front Neurol.* (2021) 12:755046. doi: 10.3389/fneur.2021.755046
18. Wang Q, Wang K, Ma Y, Li S, Xu, Y. Serum galectin-3 as a potential predictive biomarker is associated with poststroke cognitive impairment. *Oxid Med Cell Long.* (2021) 2021:5827812. doi: 10.1155/2021/5827812
19. Ciccone L, Nencetti S, Socci S, Orlandini, E. Neuroglobin and neuroprotection: the role of natural and synthetic compounds in neuroglobin pharmacological induction. *Neural Regen Res.* (2021) 16:2353. doi: 10.4103/1673-5374.300981
20. Pore A, Bernhardt B, Kaur, K. Comparing components of neuroglobin with similar globins. *FASEB J.* (2021) 35:819. doi: 10.1096/fasebj.2021.35.S1.03819
21. Kugelstadt D, Haberkamp M, Hankeln T, Burmester T. Neuroglobin, cytoglobin, and a novel, eye-specific globin from chicken. *Biochem Biophys Res Commun.* (2004) 325:719–25. doi: 10.1016/j.bbrc.2004.10.080
22. Bocahut A, Derrien V, Bernad S, Sebban P, Sacquin-Mora S, Guittet E, et al. Heme orientation modulates histidine dissociation and ligand binding kinetics in the hexacoordinated human neuroglobin. *JBIC.* (2013) 18:111–22. doi: 10.1007/s00775-012-0956-2
23. Zhang C, Wang C, Deng M, Li L, Wang H, Fan M, et al. Full-length cDNA cloning of human neuroglobin and tissue expression of rat neuroglobin. *Biochem Biophys Res Commun.* (2002) 290:1411–9. doi: 10.1006/bbrc.2002.6360
24. Ascenzi P, di Masi A, Leboffe L, Fiocchetti M, Nuzzo MT, Brunori M, et al. Neuroglobin: from structure to function in health and disease. *Mol Aspects Med.* (2016) 52:1–48. doi: 10.1016/j.mam.2016.10.004
25. De Marinis E. *Neuroglobin: Molecular, Cellular and Biomedical Aspects*. Universitá degli studi Roma Tre (2011).
26. Papadopoulou LC, Tsiftsoglou AS. Transduction of human recombinant proteins into mitochondria as a protein therapeutic approach for mitochondrial disorders. *Pharm Res.* (2011) 28:2639–56. doi: 10.1007/s11095-011-0546-y
27. Singh N, Haldar S, Tripathi AK, Horback K, Wong J, Sharma D, et al. Brain iron homeostasis: from molecular mechanisms to clinical significance and therapeutic opportunities. *Antioxid Redox Signal.* (2014) 20:1324–63. doi: 10.1089/ars.2012.4931
28. Sun F, Mao X, Xie L, Greenberg DA, Jin K. Neuroglobin protein is upregulated in Alzheimer's disease. *J Alzheimer Dis.* (2013) 36:659–63. doi: 10.3233/JAD-130323
29. Nuzzo MT, Fiocchetti M, Totta P, Melone MAB, Cardinale A, Fusco FR, et al. Huntingtin polyQ mutation impairs the 17β-estradiol/neuroglobin pathway devoted to neuron survival. *Mol Neurobiol.* (2017) 54:6634–46. doi: 10.1007/s12035-016-0337-x
30. Mejía ME, Anaya ES, Gómez AM, Aldaco DM, Rivero MP, Bobadilla DH, et al. Presence of neuroglobin in cerebral areas of a murine model of Parkinson's disease. *J Neurol Sci.* (2019) 405:292–3. doi: 10.1016/j.jns.2019.10.1375
31. Ferrer I, Gómez A, Carmona M, Huesa G, Porta S, Riera-Codina M, et al. Neuronal hemoglobin is reduced in Alzheimer's disease, argyrophilic grain disease, Parkinson's disease, and dementia with Lewy bodies. *J Alzheimer Dis.* (2011) 23:537–50. doi: 10.3233/JAD-2010-101485
32. Jin K, Mao Y, Mao X, Xie L, Greenberg DA. Neuroglobin expression in ischemic stroke. *Stroke.* (2010) 41:557–9. doi: 10.1161/STROKEAHA.109.567149
33. Blanco S, Peralta S, Morales ME, Martínez-Lara E, Pedrajas JR, Castán HA, et al. Hyaluronate nanoparticles as a delivery system to carry neuroglobin to the brain after stroke. *Pharmaceutics.* (2020) 12:40. doi: 10.3390/pharmaceutics12010040
34. Cai H, Zheng S, Cai B, Yao P, Ding C, Chen F, et al. Neuroglobin as a novel biomarker for predicting poor outcomes in aneurysmal subarachnoid hemorrhage. *World Neurosurg.* (2018) 116:e258–65. doi: 10.1016/j.wneu.2018.04.184
35. Jin K, Mao X, Xie L, Greenberg DA. Neuroglobin expression in human arteriovenous malformation and intracerebral hemorrhage. *Intracerebral Hemorrhage Research*. (2011). 315–9. doi: 10.1007/978-3-7091-0693-8_52
36. Ding C, Kang D, Chen P, Wang Z, Lin Y, Wang D, et al. Early stage neuroglobin level as a predictor of delayed cerebral ischemia in patients with aneurysmal subarachnoid hemorrhage. *Brain Behav.* (2020) 10:e01547. doi: 10.1002/brb3.1547

Conflict of Interest: The authors declare that the research was conducted in the absence of any commercial or financial relationships that could be construed as a potential conflict of interest.

Publisher's Note: All claims expressed in this article are solely those of the authors and do not necessarily represent those of their affiliated organizations, or those of the publisher, the editors and the reviewers. Any product that may be evaluated in this article, or claim that may be made by its manufacturer, is not guaranteed or endorsed by the publisher.

Copyright © 2022 Gao, Wang, Miao and Han. This is an open-access article distributed under the terms of the Creative Commons Attribution License (CC BY). The use, distribution or reproduction in other forums is permitted, provided the original author(s) and the copyright owner(s) are credited and that the original publication in this journal is cited, in accordance with accepted academic practice. No use, distribution or reproduction is permitted which does not comply with these terms.

frontiers | Frontiers in Neurology

REVIEW
published: 11 April 2022
doi: 10.3389/fneur.2022.861714

Advances in the Role of Endothelial Cells in Cerebral Small Vessel Disease

*Tao Bai, Shijia Yu and Juan Feng**

Department of Neurology, Shengjing Hospital of China Medical University, China Medical University, Shen yang, China

Cerebral small vessel disease (CSVD) poses a serious socio-economic burden due to its high prevalence and severe impact on the quality of life of elderly patients. Pathological changes in CSVD mainly influence small cerebral arteries, microarteries, capillaries, and small veins, which are usually caused by multiple vascular risk factors. CSVD is often identified on brain magnetic resonance imaging (MRI) by recent small subcortical infarcts, white matter hyperintensities, lacune, cerebral microbleeds (CMBs), enlarged perivascular spaces (ePVSs), and brain atrophy. Endothelial cell (EC) dysfunction is earlier than clinical symptoms. Immune activation, inflammation, and oxidative stress may be potential mechanisms of EC injury. ECs of the blood–brain–barrier (BBB) are the most important part of the neurovascular unit (NVU) that ensures constant blood flow to the brain. Impaired cerebral vascular autoregulation and disrupted BBB cause cumulative brain damage. This review will focus on the role of EC injury in CSVD. Furthermore, several specific biomarkers will be discussed, which may be useful for us to assess the endothelial dysfunction and explore new therapeutic directions.

Keywords: cerebral small vessel disease (CSVD), endothelial cells (ECs), hypertension, blood-brain barrier, cognitive impairment, white matter hyperintensities (WMH)

OPEN ACCESS

Edited by:
Jinming Han,
Capital Medical University, China

Reviewed by:
Xuanting Li,
Capital Medical University, China
Jiachun Feng,
First Affiliated Hospital of Jilin University, China

***Correspondence:**
Juan Feng
juanfeng@cmu.edu.cn

Specialty section:
This article was submitted to Neurological Biomarkers, a section of the journal Frontiers in Neurology

Received: *25 January 2022*
Accepted: *09 March 2022*
Published: *11 April 2022*

Citation:
Bai T, Yu SJ and Feng J (2022) Advances in the Role of Endothelial Cells in Cerebral Small Vessel Disease. Front. Neurol. 13:861714. doi: 10.3389/fneur.2022.861714

INTRODUCTION

Cerebrovascular disease, one of the most important causes of neurological dysfunction, has become an urgent human health issue (1). Cerebral small vessel disease (CSVD) affects almost all people over 90, which is responsible for 45% of cases of dementia in the world (2). CSVD is caused by a disorder in perforating cerebral vessels, and most of the lesions are in cerebral white matter and deep gray matter (3). There is considerable evidence that vascular dysfunction is a fundamental change in CSVD. Vascular endothelial cells (ECs) form the luminal surface of all blood vessels and play an important role in maintaining vascular morphology and biological function (4). Recently, endothelial dysfunction has been considered as a key in the pathogenesis of CSVD and vascular dementia (VD). We focus on the decrease of cerebral blood flow (CBF) and the disruption of blood–brain barrier (BBB) during CSVD. Until now, there is a lack of effective prevention and treatment measures. A better comprehension of pathological mechanisms is beneficial for the investigation of diagnostic biomarkers and the development of treatment targets.

Arteriosclerosis-Related CSVD

Currently, CSVD is classified into six types according to its etiology (5): arteriosclerosis-related CSVD, amyloid-related CSVD, genetic CSVD (distinct from amyloid angiopathy), inflammatory/immunologically mediated CSVD, venous collagenosis, and other CSVDs. From

the pathological point of view, nongenetic CSVD is mainly divided into arteriosclerosis-related CSVD and amyloid-related CSVD (6), and the former CSVD is discussed in our study. However, for brevity, we will simply refer to it as CSVD. The aging of the population is closely related to the occurrence of CSVD, but the contribution of ethnicity in CSVD needs to be further confirmed by epidemiological studies (7, 8). CSVD increases the risk of acute stroke more than 2-fold (9), and its classical form is characterized by cognitive impairment or dementia, motor dysfunction, and psychobehavioral abnormalities. In addition, a typical pattern of cognitive impairment due to CSVD is an impaired executive function with the preservation of memory (5). In the acute phase, its clinical feature is acute stroke syndrome, including hemorrhage and infarction (10).

Currently, the opinion that CSVD is a local manifestation of systemic small vessel lesions in the brain is widely accepted (11), scholars have found that patients with CSVD were often accompanied by small vessel damage in other organs, including the kidney and retina (12, 13). The arterial walls demonstrated hyaline degeneration, leading to thickening and narrowing of the arteries eventually. Cerebral small vessel mainly involves the penetrating vessels <1 mm in diameter, including small arteries, micro-arteries, capillaries, and small veins (14). Typical lesions of CSVD were located in the thalamocortical loop and the corticospinal tracts, affecting the information-processing efficiency. Intracranial vessel wall lesions can be identified by 7T magnetic resonance imaging (MRI), but this technique is not yet widely available in clinical centers (15). Advances in imaging help us to check for indirect signs of CSVD on brain MRI. There are six categories of specific changes, including (16) recent small subcortical infarcts, white matter hyperintensity (WMH), lacune, cerebral microbleeds (CMB), enlarged perivascular spaces (ePVS), and brain atrophy. All of these changes may be the result of vascular dysfunction and vascular pathology. The MRI signal characteristics and typical manifestations of CSVD have been shown in **Table 1** and **Figure 1** (except brain atrophy).

Endothelial Cells

Vascular endothelium, a monolayer of ECs lining the interior walls of vessels, is an important tissue that regulates hemodynamic stability. ECs maintain the balance between coagulation and fibrinolysis and participate in vascular injury, inflammation, and repair (17). First, ECs are able to respond to hemodynamic changes *via* the release of vasoactive substances. For example, when shear stress increases, ECs release nitric oxide (NO), which mediates smooth muscle relaxation in blood vessels. This process begins with the upregulation of NO synthase in ECs (18). Second, ECs can secrete antiplatelet agents, including prostacyclin (PGI) and NO, which prevent platelet aggregation *via* increasing the cyclic adenosine monophosphate (cAMP) content in platelets (19). In addition, ECs can inactivate the clotting factors VIIIa and Va and suppress thrombosis with activation of the protein C/protein S pathway (20). Under the physiological state, ECs exhibit anticoagulant activities. Third, ECs express several innate immune receptors, including the toll-like receptor (TLR) family. When agonists bind to these receptors, the structure of adhesion molecules in ECs will change. This will increase vascular permeability, promote the production of inflammatory cytokines, recruit leukocytes, and reach a procoagulant state (21). Furthermore, ECs also play an important role in the process called angiogenesis, a physiological process by which new blood vessels grow from existing ones. During angiogenesis, activated ECs migrate toward the gradient of vascular endothelial growth factor (VEGF) under hypoxic conditions (22).

In the central nervous system, ECs mainly compose the structure of the neurovascular unit (NVU) and BBB (**Figure 2**). Nutrients transported *via* the blood supply ensure brain activities. However, researchers described for the first time that neuronal structures could influence brain blood flow (23), which regulated the supply of oxygen and nutrients (24). The NVU, a structure composed of neurons, interneurons, astrocytes, basal lamina covered with smooth muscle cells and pericytes, ECs, and an extracellular matrix, ensures the coupling relation between blood supply and neuronal demand (25, 26). ECs can interact with astrocytes and produce vasoactive factors (such as NO) to regulate vascular tone (27). Specifically, autoregulation maintains a nearly constant blood flow to the brain within the range of 50–160 mmHg (28), and hyperemia improves regional CBF by adjusting the changes in the activity of specific brain sectors (29), the phenomenon is called neurovascular coupling (NVC). In addition, complete BBB is the most important factor in maintaining brain tissue homeostasis, which prevents the entry of cells and molecules into brain tissue and eliminates masses formed in the brain by metabolic waste from the cerebral nerve. ECs anchored to each other by tight junctions or

TABLE 1 | Magnetic resonance imaging (MRI) characteristics related to cerebral small vessel disease (CSVD).

	Recent subcortical infarct	WMH	Lacune	ePVS	CMB
T1	↓	−/↓	↓	↓	−
T2	↑	↑	↑	↑	−
DWI	↑	−	−/↓	−	−
FLAIR	↑	↑	↓	↓	−
T2*- weighted GRE	−	↑	−(↓ if haemorrhage)	−	↓(SWI)
diameter	≤20mm	−	3–15mm	≤2mm	≤10mm

↑ : increased signal; − : iso-intense signal; ↓ : decreased signal.

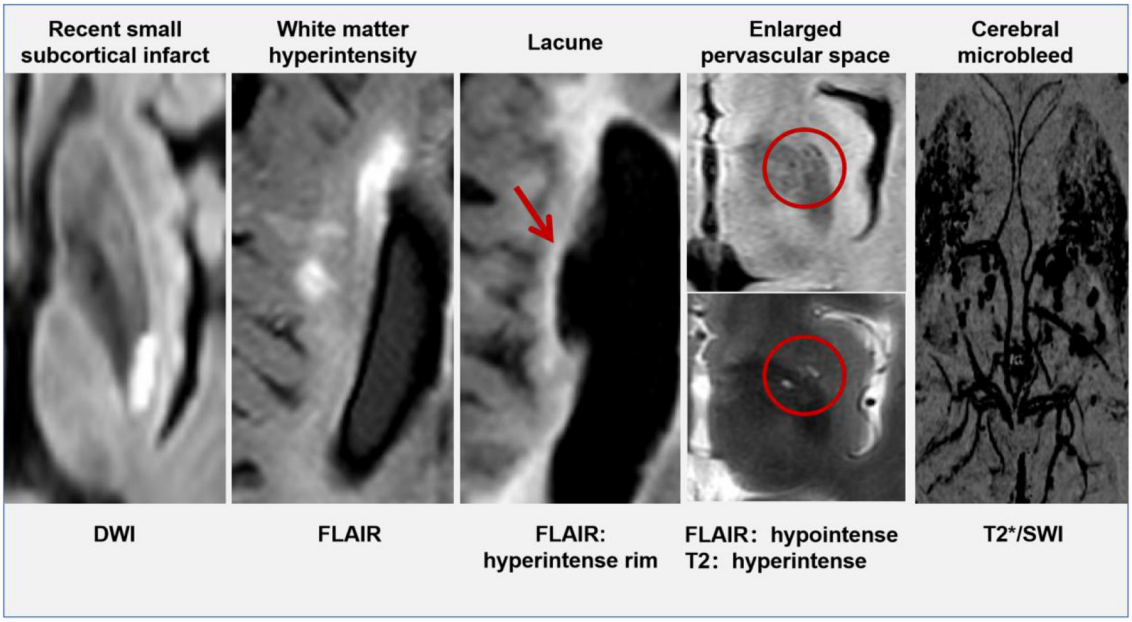

FIGURE 1 | The typical manifestation of cerebral small vessel disease (CSVD) on MRI.

adherens junction constitute the most important component of the BBB. Astrocytes and pericytes provide essential support for BBB function with additional contribution from the basement membrane and the glycocalyx (1).

Currently, a lot of studies have shown that vascular endothelial injury is a key pathological process in many vascular diseases, including CSVD (**Table 2**). In trials, endothelial dysfunction has been shown to be associated with lacunar cerebral infarction (38). An Australian study (39) further demonstrated that in cerebral white matter lesions, the function of ECs and the integrity of BBB were significantly reduced compared to that of normal brain tissue. In addition, the content of intracellular adhesion molecule-1 (ICAM-1) was significantly increased in the diseased region of white matter (40). When focusing on the altered cerebral hemodynamics, it can be found that impaired CBF regulation is widely available in CSVD (41). Furthermore, endothelial impairment is common in the population with atherosclerosis, hypertension, diabetes, and chronic kidney disease (42). Such people are at a higher risk of CSVD. However, the mechanisms has not yet elucidated. In summary, to unfold the nature of CSVD, this review focuses on the relationship between endothelial dysfunction and CSVD.

ETIOLOGIES OF AND RISK FACTORS FOR CSVD AND ENDOTHELIAL DYSFUNCTION

Similar to the cardiovascular risk factors associated with large vessel strokes and heart disease, common systemic vascular risk factors, such as hypertension, diabetes, hyperlipidemia, and hyperhomocysteinemia (43), also play an important role in CSVD. Such factors have been proven to be closely associated with WMH, lacune, and CMB. Among the many risk factors for CSVD, hypertension and age are the most important and independent ones (44). A study showed that EC integrity decreased with age, ultimately leading to an exponential decline in BBB function (45), which might be a potential reason for the high incidence of CSVD among the elderly population. With increasing age, other vascular risk factors further accelerate the development of CSVD (11). Compared to CSVD patients with normal blood pressure, those with hypertension exhibit more severe clinical manifestations and more obvious neuroimaging signs (46). Hypertension may induce microcirculatory change. Rajani et al. (32) also confirmed that EC injury caused by hypertension might be the earliest manifestation of CSVD in rats. Adequate antihypertensive medication contributes to a higher degree of microstructural integrity in cerebral white matter, providing the potential method to delay or prevent the emergence of WMH (47). Unsurprisingly, a recent meta-analysis showed that intensive blood pressure control could prevent the progression of WMH (48). It was found that there is a narrowing of the lumens in the arterioles, which suggested that arteriolosclerosis might be one of the complications associated with hypertension (49). In addition, hyperglycemia and smoking cause CSVD mainly *via* damage to vessel ECs. A study found that type 2 diabetes mellitus (T2DM) increased the risk for WMHs (50). NO produced by ECs plays an important role in blood flow regulation. While the endogenous NO synthase inhibitor, asymmetric dimethylarginine (ADMA), was shown to be significantly elevated in the plasma of patients with CSVD, the level of ADMA correlated with cognitive impairment in patients (51). Both elevated blood

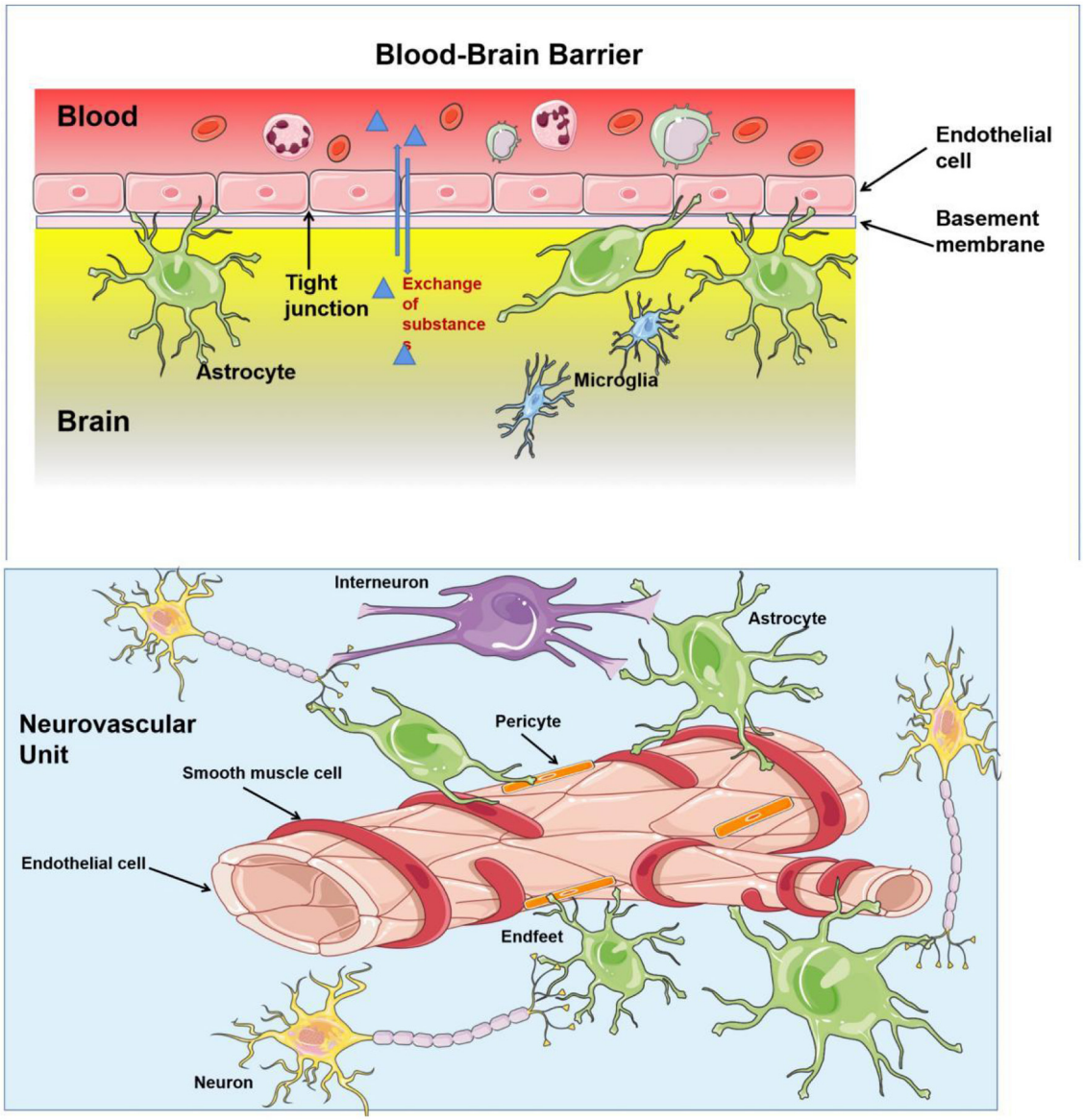

FIGURE 2 | The structure of blood–brain barrier (BBB) and neurovascular unit (NVU). BBB regulates substance influx and efflux to ensure a homeostatic environment for the brain function, which is composed by basement membrane, astrocytes, and endothelial cells (ECs) anchored to each others by tight junction. Neurones, interneurones, astrocytes, smooth muscular cells, pericytes, and ECs are important constituents of NVU, which provides a basic structure for NVC and regulates the cerebral blood flow (CBF).

glucose levels and smoking (52) can cause vasodilatory dysfunction by downregulating the expression of endothelial nitric oxide synthase (eNOS), which affects endothelium-dependent vasodilation. Furthermore, metabolic syndrome, a combination of abnormalities, including hypertension, T2DM, obesity, and dyslipidemia, is able to stimulate generalized inflammation and promote arteriolosclerosis (53). Insulin resistance (IR) increases the risk of metabolic syndrome. Interestingly, a high triglyceride–glucose (TyG) index (a marker of IR) has been shown to be associated with a higher prevalence and burden of CSVD (54).

As noted previously, the risk factors for atherosclerosis are very similar to those for CSVD. However, almost 90% of cerebral infarctions caused by intracranial atherosclerosis are larger than 2 cm in diameter, and large-artery atherosclerosis occasionally leads to lacunar stroke. In addition, the small perforating arterioles are thickened and stiff, with a reduced lumen size but not containing clots or occlusion. Thus, the pathology of CSVD is distinct from that of atherosclerosis, and the specific mechanisms are still unknown. Furthermore, Arntz et al. (55) conducted a follow-up study of young patients with transient ischemic attack or acute cerebral infarction for nearly 10 years. It was found that

TABLE 2 | Studies suggest that the injury to endothelial cells (ECs) is involved in the pathology of CSVD.

References	Year	Conclusion
Ashby et al. (30)	2021	ECs participate in the CSVD by regulating CBF
Quick et al. (31)	2021	Endothelial dysfunction do damage to BBB and cerebral white matter
Rajani et al. (32)	2018	Endothelial dysfunction is the initial feature of CSVD
Hainsworth et al. (33)	2015	The disruption of BBB caused by endothelial dysfuncion play an important role in the process of CSVD
Nezu et al. (34)	2015	Endothelial dysfunction positively correlates with the severity of WMH and microhemorrhage
Kimura et al. (35)	2012	Anti-endothelial cell antibodies play a role in CSVD
Hassan et al. (36)	2004	Hyperhomocysteinemia, an independent risk factor for CSVD, may play a role by mediating endothelial dysfunction
Leeuw et al. (37)	2002	Endothelial activation is associated with WMH

these patients developed CSVD 10–20 years earlier than controls and had more severe lesions. Patients with a history of stroke are more susceptible to cerebrovascular diseases because of their poor tolerance to vascular risk factors. Genetic predisposition may be a potential factor, which needs further investigation.

VASCULAR EC INJURY IN CSVD

In basilar ganglion, brain stem, centrum semiovale, and subcortical white matter, there are mutiple anastomoses between perforators from pial arteries and intracranial large arteries. The capillary bed composed of these terminal microarteries enables the actual exchange between the blood and the brain, which are diseased under the effect of vascular risk factors as we have discussed. In the 1960s, Fisher (56) performed an autopsy on a patient with lacunar cerebral infarction and first described the pathological features of CSVD in terms of vascular stenosis and hyalinosis, which were mainly found in arteries with a diameter of 40–150 μm. With the breakdown of the integrity of the vascular walls, these smaller arteries have thickened and narrowed (57). Meanwhile, vascular endothelial dysfunction is related to decreased CBF and impaired BBB (58, 59). Endothelial dysfunction is gradually being considered as the driving factor in the development of CSVD (31, 37) (**Figure 3**).

CBF Dysregulation in CSVD

Stable CBF ensures a sufficient supply of nutrients and elimination of metabolic waste. Dramatic changes in CBF will result in ischemia or hemorrhage (60), and impaired cerebrovascular hemodynamics is associated with the loss of the structural integrity of cerebral white matter (61).

The neurovascular unit is important in the blood circulation of the brain (4), which provides a basic structure for NVC (**Figure 2**). In patients with CSVD, an altered adaptive response of the cerebral microvasculature has been found (62). The regulation of CBF depends on intact vascular endothelial structure and function (30). Pericytes have also been shown to play an important role in vasoconstriction. The loss of pericytes severely affects NVC and impairs cerebral vascular autoregulation (63). In summary, the modes of endothelium-derived blood flow regulation include chemical control of CBF, cell–cell interactions, second messenger signaling, and endothelial response to physical forces and inflammatory factors (30). Endothelial injury may alter this adaptation of blood supply to the local energy needs of the brain. In addition, cerebrovascular ECs are sensitive to elevated shear forces and hypoperfusion, which further affect microcirculation regulation due to endothelial dysfunction. This vicious circle aggravates the ischemic–hypoxic brain injury. Anatomically, the deep white matter of the bilateral cerebral hemispheres is supplied by terminal branches of small vessels from two sources, making it extremely fragile to this chronic hypoperfusion. Sustained and intermittent hypoxia causes damage to white matter fiber tracks of the brain resulting in corresponding clinical symptoms, which may be precursors or predictors of dementia (64).

In addition, a few studies have shown reduced CBF in the white matter of patients with CSVD, and the CBF is lower in subjects with more WMH (65, 66). More significantly, researchers confirmed the presence of decreased CBF in the normal-appearing white matter surrounding WMH. This area, termed the CBF penumbra, may be associated with future WMH expansion (67).

The Function of BBB in CSVD

The blood-brain barrier is made up of ECs, pericytes and astrocytes, which regulates the exchange of substances between the brain and the blood. While ECs tightly regulate this exchange across the BBB (30). In addition to the reduction of CBF, BBB failure also plays an equally important role in the pathological process of CSVD (33). Classical vascular risk factors, salt toxicity, inflammation/infection, and altered hemodynamics can damage the BBB (68).

Via dynamic contrast-enhanced MRI, a larger volume with BBB leakage in WMH and cortical gray matter could be found in patients with CSVD (69), and the compromised BBB integrity was associated with total MRI CSVD burden (70). Interestingly, Wong et al. (59) confirmed by functional MRI that BBB permeability was higher in the normal appearing white matter surrounding WMH than in other normal white matter, suggesting that increased BBB permeability might precede the onset of WMH. Researchers also suggested the altered BBB permeability in the normal white matter might be an early indicator of CSVD, which signified a poor prognosis (71, 72). Another study added to mounting evidence that the integrity of BBB was associated with the severity of WMH (39).

White matter hyperintensity pathology might link to the decline of information processing speed (73). Besides, cognitive function descending of patients with CSVD was associated with the degree of BBB leakage at baseline, especially in executive function (74). BBB leakage leads to local microhemorrhage and reduced distal blood flow, which intensifies regional ischemia and hypoxia in the brain. What is more, the leakage and deposition

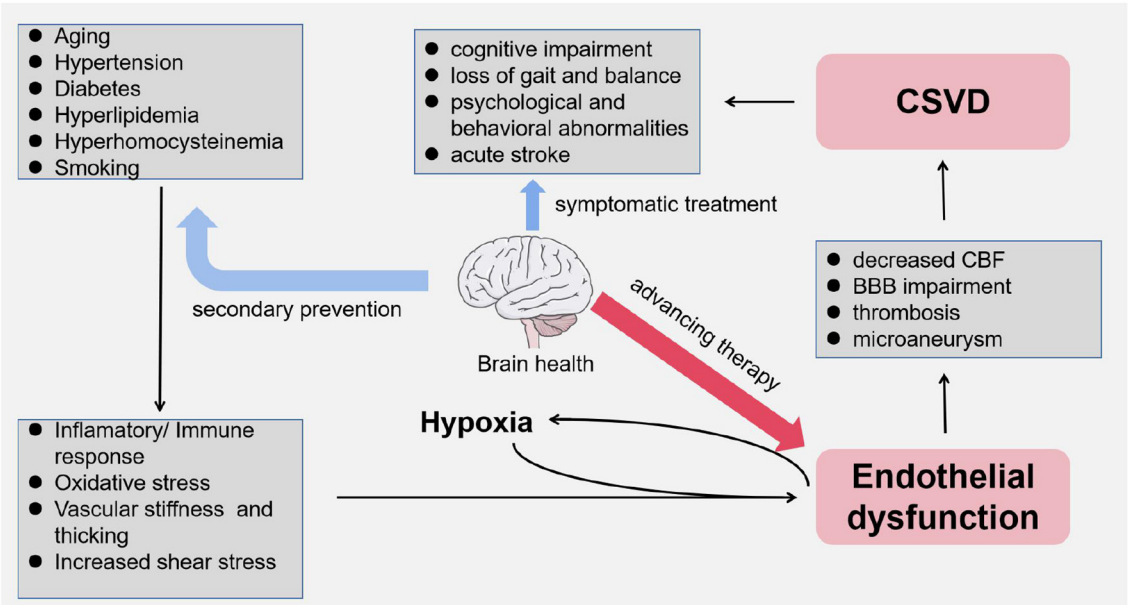

FIGURE 3 | Graphic abstract of this review.

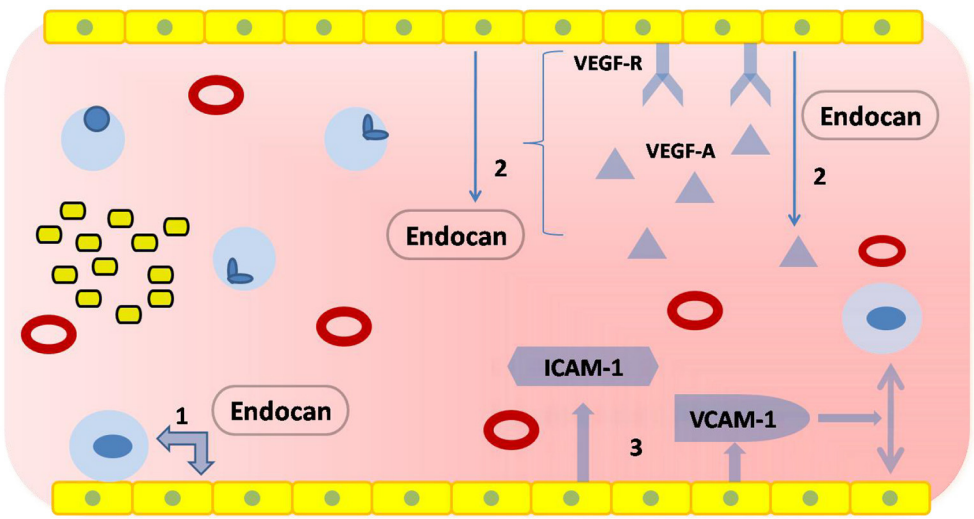

FIGURE 4 | Physiological functions of Endocan. The yellow squares at the upper or lower edges represent ECs, which form vascular endothelium by tight junctions; the red hollow circles represent red blood cells; the light blue circles represent leukocytes; the yellow squares with black borders represent platelets. (1) Endocan regulates the interaction between ECs and leukocytes. (2) Endocan promotes the expression of vascular endothelial growth factor-A (VEGF-A) and enhances the binding of VEGF-A to its receptors. The activation of a VEGF signaling pathway contributes to the production of Endocan. (3) Endocan promotes the release of pro-inflammatory substances.

of hematogenous material can lead to perivascular edema (75), which injuries brain cells and leads to demyelination as observed in WMH. Unfortunately, whether BBB breakdown is the starting point of CSVD remains to be studied.

At the same time, it was found that local low CBF was significantly negatively correlated with the permeability of BBB (57). On one hand, it is possible that the low shear stress caused by hypoperfusion leads to the downregulation expression of tight junctions, which results in larger intercellular space and increased material permeation (76). On the other hand, hypoxia may, to some extent, induce the increase of vascular permeability adaptively, allowing more nutrients to enter the brain parenchyma (77). However, the interaction between the two in CSVD and whether they jointly

contribute to disease progression remains to be elucidated by further studies.

Potential Mechanisms of ECs Injury

Endothelial cell injury includes two important pathophysiological processes: EC overactivation and EC dysfunction. Endothelial activation refers to the alterations in the expression, structure, and distribution of endothelial tight junctions responding to a variety of pathological conditions, and ECs turn to an abnormal pro-inflammatory and pro-thrombotic phenotype (78). EC dysfunction is mainly reflected in the imbalance between biomolecules produced by the endothelium that contribute to vasodilation and vasoconstriction, which leads to a series of pathological changes, such as vasoconstriction, leukocyte aggregation, platelet activation, and thrombosis (79). As we have discussed earlier, increased vascular shear stress and ischemic–hypoxic injury both lead to endothelial dysfunction; however, pathological responses, including immune activation, inflammation, and oxidative stress, may be potential mechanisms for EC injury, which ultimately leads to the development of CSVD.

Produced by many different cellular processes, reactive oxygen species (ROS) are the mediators of demyelination and disruption of the BBB. ROS have strong oxidant effects and are able to induce the accumulation and extravasation of leukocytes and trigger the innate immune response. Indeed, several vascular risk factors, such as hypertension, diabetes, smoking, hyperhomocysteinemia, and infections, can promote excess ROS levels. The imbalance between ROS and the antioxidant defense system will cause endothelial injury (80). Homocysteine (HCY) has been shown to promote oxidative injury to the endothelium (81), and total HCY level correlates with CSVD MRI burden (43). In addition, it is believed that smoking-induced oxidative stress can also be a triggering factor that disrupts endothelial integrity (82).

A few experts pointed out that inflammatory factors play an important role in the pathogenesis of CSVD, and patients with ischemic or hemorrhagic lesions on brain MRI have a different distribution of inflammatory markers in their plasma (83). Pro-inflammatory cytokines induce ECs to secrete adhesion molecules and chemokines, recruit immune cells, and generate a waterfall-like inflammatory response, which further impairs the function of endothelium and BBB. In innate immune responses, monocytes activate inflammatory polarization pathways and produce ROS, while macrophages infiltrate the vascular wall, causing smooth muscle cell proliferation and blood vessel remodeling (84). In addition, both cytokines and neopterin secreted by mononuclear macrophages are able to impair BBB by acting directly on the endothelium (85). Neopterin can promote the interaction between EC adhesion molecules and leukocytes, perhaps through the kappa-B pathway (86). In addition, neopterin is able to induce the production of C-reactive protein in the liver, which further generates systemic vascular inflammation (85). In fact, it has been confirmed that adaptive immune responses also participate in the process of endothelial injury. A previous study suggested that aggregated T-cells can attack vascular endothelium directly and decrease CBF (87). Various anti-EC antibodies were detected in the serum of patients with CSVD (35), suggesting that the activation of B-cells might play a role in pathophysiological processes and, to some extent, confirming widespread endothelial dysfunction in CSVD.

ECS IN THE DIAGNOSIS AND TREATMENT OF CSVD

Diagnostic Strategies

The autoregulation of cerebral blood flow is the most important feature of cerebral microcirculation. Endothelial injury, the critical part of vascular dysfunction, can be evaluated by flow-mediated dilatation (FMD) of the brachial artery or digital reactive hyperemia index in peripheral arterial tonometry (88, 89). However, these devices have not become popular in clinical practice for various reasons. Thankfully, new techniques, such as digital pulse amplitude tonometry and passive leg movement technique, are on the way (90, 91). In addition, taking BBB leakage into consideration may be helpful in diagnosing CSVD. Another study showed that markers of vascular inflammation and endothelial injury were significantly elevated in blood samples from patients with hypertension-induced CSVD (30). And, it has been found that BBB leakage could be reflected by slow-wave activity during sleep, which could be another biomarker of CSVD (92). However, circulating biomarkers are the ones that provide us with the most opportunities to assess endothelial function (**Table 3**). These biomolecules are mainly related to endothelial injury and activation (131), including ICAM-1, vascular cell adhesion molecule-1 (VCAM-1), the soluble fraction of von Willebrand factor (vWF), and endothelium-derived exosomes (109, 132). However, most of them are still limited to the laboratory. Previous longitudinal research found that ICAM levels and baseline WMH load were independent predictors of WMH progression (98). Abnormally increased ADMA levels are associated with endothelial dysfunction and the risk of silent brain infarcts (93). Patients with CSVD had higher levels of ADMA in their blood. Matrix metalloproteinase-9 (MMP-9) regulates the metabolism of an extracellular matrix, which is an important component of the blood vessel wall. The levels of MMP-9 were determined to be significantly elevated in patients with WMH (41). In addition, it was confirmed that EC-specific molecule-1 reflected endothelial injury with increased specificity and sensitivity (110). This molecule, also known as Endocan (92), is a soluble dermatopoietin sulfate proteoglycan (DSPG) secreted mainly by ECs. Other studies found that higher levels of Endocan contributed to the production of proinflammatory substances, such as lipopolysaccharide, tumor necrosis factor-α, and interleukins-1β (111). It was hypothesized that Endocan exerted its biological effects through several mechanisms (**Figure 4**):

① Involve in endothelial activation by regulating the interaction between ECs and leukocytes (133).
② Act on the VEGF signaling pathway to mediate the inflammatory response (134): on one hand, Endocan promotes the expression of VEGF-A and enhances the binding of VEGF-A to its receptors. This process alters

TABLE 3 | Potential biomarkers of endothelial injury.

Biomolecule	Function	Test	Variation	Conclusion	References
asymmetric dimethylarginine (ADMA)	NO synthase inhibitor	ELISA	↑	causing endothelial dysfunction by blocking the activity of endogenous NO synthase	(93, 94)
VCAM-1	inducing the interactions between leukocytes and endothelium	ELISA	↑	higher expression of VCAM-1 is related with endothelial activation	(82, 95, 96)
ICAM-1	inducing the interactions between leukocytes and endothelium; participating in the substance transmembrane transportation	ELISA	↑	higher expression of ICAM-1 is related with endothelial activation	(82, 97–99)
myeloperoxidase (MPO)	involved in the impairment of tissues and inflammation	ELISA	↑	MPO can cause endothelil injury and dysfunction	(100)
Claudin-5	maintaining the structure of tight junction	ELISA	↑	Decreased Claudin-5 level are associated with the disruption of BBB integrity	(101, 102)
matrix metalloproteinase-2/9 (MMP-2/MMP-9)	degrading the components of extracellular matrix	gelatin zymography	↑	Increased MMP-2/MMP-9 level are associated with the disruption of BBB integrity	(103–105)
endothelin-1 (ET-1)	regulating vasoconstriction	ELISA	↑	Excess ET-1 causes pathological vasoconstriction	(106)
vWF	facilitating clotting and the adhesion of platelets	ELISA;gelatin zymography;Immunoelectrophoresis	↑	Injured ECs release polymeric vWF, further causing vascular dysfunction	(106–108)
endothelial microparticles (EMPs)	involved in the intercellular communication	flow cytometry; atomic force microscope; electron microscope	↑	Activated ECs release specific EMPs into the bloodstream	(92, 93, 98, 109–117)
Endoglin (CD105)	involved in the angiogenesis, vasodilation, and inflammation	ELISA; Western blot	↑	Increased Endoglin worsen inflammation and weak the relaxation response of the vessel	(118–123)
Endocan (ESM-1)	inducing the interactions between leukocytes and endothelium; regulating the vascular function	ELISA	↑	Injured ECs release Endocan into the bloodstream, which promotes the infiltrating of leucocytes	(124–127)
micRNA	participating in various kinds of endothelial function	PCR	↑/↓	Several micRNAs expressed specifically by ECs can suggest the endothelial dysfunction	(128–130)

↑:increased expression level; ↓:decreased expression level.

vascular permeability; on the other hand, activation of the VEGF signaling pathway contributes to the production of Endocan.

③ Promote the release of proinflammatory substances from ECs, including ICAM-1 and VCAM-1 (135).

In contrast to blood biomarkers, there are a few studies assessing biomarkers of CSVD or endothelial dysfunction using cerebrospinal fluid (CSF) samples. Elevated albumin and other serum proteins have been found in the CSF of patients with VD (42). An increased albumin CSF/serum ratio, though not specific, may be useful in reflecting BBB dysfunction. In addition, the CSF level of ICAM-1 and VCAM-1 were higher in diabetics with cerebral vascular injury (136), but the correlation between adhesion molecules in CSF and CSVD is still unknown. Further studies are needed to search for CSF biomarkers of CSVD.

Currently, several methodological issues prevent clinical practice, and the replication of these results is indispensable. On one hand, the distribution of biomolecules in different populations is also with heterogeneity and complexity, and the variability of labs or measuring approaches will induce a great measurement error. On the other hand, changes in peripheral blood biomarkers may not be able to fully reflect the degree of cerebral tissue damage and the state of brain function, and the content of biological molecules may be influenced by various physiological or pathological conditions. In addition, it may be more reliable to assess endothelial function by monitoring changes of a set of molecules rather than a single molecule.

Therapeutic Directions

The goal of treating CSVD is to prevent stroke, delay cognitive decline, improve gait, and resolve psychological abnormalities. According to the lesion changes revealed by MRI, doctors can observe the curative effect (137). Currently, clinical interventions for CSVD are mainly limited to health management of risk factors. Tight blood pressure control may be beneficial in preventing or delaying the onset of CSVD. It is important to note that blood pressure variability (BPV) comes to be valued in treatment. In addition, low-dose rosuvastatin (a kind of lipid lower agents) may be a reasonable therapy for CSVD (138). In a recent study, the results suggested that nimodipine (a kind of antihypertensive medications) combined with rosuvastatin was safe and effective in treating mild cognitive impairment in

patients with CSVD (139). Apart from the routine drug therapy, healthy lifestyles, such as smoking cessation, low-salt diet, and exercise, may help to halt or delay the progression of CSVD. Antiplatelet therapy is one of the most important measures in the treatment of cerebrovascular disorders. Due to hemodynamic fluctuations in the cerebral microcirculation and impaired BBB, patients with CSVD have a higher risk of bleeding during the application of antithrombotic drugs, especially in patients with more microhemorrhage foci (140). Something else we need to be careful about is the higher prevalence of aspirin resistance in patients with CSVD (141). Unfortunately, donepezil and memantine, which are commonly used to improve cognitive function, have little effect on the cognitive impairment caused by CSVD.

Endothelial dysfunction, the keystone of this article, is a key in the pathological process of CSVD. Therefore, the treatment of ECs is expected to be a breakthrough. The concept of "endothelial therapy" was proposed in the late 1990s. The therapy was aimed to prevent and repair EC injury and was mainly involved in the treatment of cardiovascular diseases (142). A study (32) has confirmed that reversal of endothelial dysfunction could reduce the cerebral white matter damage in CSVD rats, providing a basic theory for subsequent clinical applications.

Firstly, a healthy lifestyle may be beneficial to endothelial health. A study found that the Mediterranean diet could modulate endothelial function, even in those with severe endothelial dysfunction (143). In addition, aerobic exercise training was considered to provide the same benefit (144). Secondly, existing drugs may be effective in protecting ECs. For example, it has been found that metformin may exert protective effects in preventing endothelial dysfunction (106). Carvedilol, a nonselective beta- and alpha-receptor antagonist, was found to have the antioxidative potential *in vitro* (145). Anti-inflammation and anti-oxidation agents may play a positive role in endothelial health. However, more randomized controlled trials and experimental studies are needed to confirm the above conclusions, and whether these interventions are effective in delaying the progression of CSVD needs to be further clarified. What is more, new therapeutic strategies targeting endothelial repair are worth investigating. Several cytokines or molecules may be useful in endothelial repair. Scholars have found that granulocyte colonystimulating factor (G-CSF) had protective effects on endothelial impairment and WM injury in CSVD. G-CSF promoted the expression of VEGF and downregulated the level of MMP-9, thus repairing the cerebral vascular endothelium (146). Endothelial progenitor cells (EPCs) are capable of repairing injured endothelium, thus providing promising therapy to treat CSVD (147). In addition, several plant extracts have also been shown to be potential for alleviating the EC injury (148, 149). The pharmacological functions of these natural substances mainly include lessening oxidative injury, decreasing EC apoptosis, and reducing the inflammation response. In addition, the therapeutic potential of endothelium-specific microRNAs for the treatment of EC dysfunction is attracting attention (150), and antibodies against the endothelium may be a target for immunotherapy in the future.

CONCLUSION

This review focuses on the function of ECs, particularly their pathological changes in the process of CSVD. We hold the opinion that ECs are culprits and victims during CSVD at the same time. Increased shear stress or hypoxia causes EC dysfunction. More importantly, endothelial activation enhances the inflammatory response and immune reaction, leading to BBB leakage and impaired cerebral blood supply. In addition, reduced endothelial NO synthesis and the pro-thrombotic state exacerbate the ischemic brain damage.

In summary, it is important to continue to deepen our knowledge of endothelial dysfunction to understand the nature of CSVD. Identification of endothelial-specific markers will be useful for both laboratory studies and clinical trials. And, it certainly makes sense to therapeutically target ECs during CSVD.

AUTHOR CONTRIBUTIONS

TB reviewed the literature and designed and drafted this manuscript. SY revised the manuscript. JF was involved in the design and revision of the manuscript. All authors contributed to this article and approved the submitted version.

FUNDING

The study was financially supported by grants from the National Natural Science Foundation of China (81771271) and the Outstanding Scientific Fund of Shengjing Hospital (M0475) awarded to JF.

REFERENCES

1. Feigin VL, Roth GA, Naghavi M, Parmar P, Krishnamurthi R, Chugh S, et al. Global burden of diseases, injuries and risk factors study 2013 and stroke experts writing group. global burden of stroke and risk factors in 188 countries, during 1990-2013: a systematic analysis for the global burden of disease study 2013. *Lancet Neurol.* (2016) 15:913–24. doi: 10.1016/S1474-4422(16)30073-4
2. Mok V, Wong A, Tang WK, Lam WW, Fan YH, Richards PS, et al. Determinants of prestroke cognitive impairment in stroke associated with small vessel disease. *Dement Geriatr Cogn Disord.* (2005) 20:225–30. doi: 10.1159/000087310
3. Wardlaw JM, Smith C, Dichgans M. Small vessel disease: mechanisms and clinical implications. *Lancet Neurol.* (2019) 18:684–96. doi: 10.1016/S1474-4422(19)30079-1
4. De Silva TM, Faraci FM. Contributions of aging to cerebral small vessel disease. *Annu Rev Physiol.* (2020) 82:275–95. doi: 10.1146/annurev-physiol-021119-034338
5. Litak J, Mazurek M, Kulesza B, Szmygin P, Litak J, Kamieniak P, et al. Cerebral small vessel disease. *Int J Mol Sci.* (2020) 21:9729. doi: 10.3390/ijms21249729
6. Cuadrado-Godia E, Dwivedi P, Sharma S, Ois Santiago A, Roquer Gonzalez J, Balcells M, et al. Cerebral small vessel disease: a review focusing on pathophysiology, biomarkers, and machine learning strategies. *J Stroke.* (2018) 20:302–20. doi: 10.5853/jos.2017.02922

7. Cannistraro RJ, Badi M, Eidelman BH, Dickson DW, Middlebrooks EH, Meschia JF, et al. small vessel disease: a clinical review. *Neurology.* (2019) 92:1146–56. doi: 10.1212/WNL.0000000000007654
8. Castello JP, Pasi M, Abramson JR, Rodriguez-Torres A, Marini S, Demel S, et al. Contribution of racial and ethnic differences in cerebral small vessel disease subtype and burden to risk of cerebral hemorrhage recurrence. *Neurology.* (2021) 96:e2469–80. doi: 10.1212/WNL.0000000000011932
9. Debette S, Markus HS. The clinical importance of white matter hyperintensities on brain magnetic resonance imaging: systematic review and meta-analysis. *BMJ.* (2010) 341:c3666. doi: 10.1136/bmj.c3666
10. Wardlaw JM, Smith C, Dichgans M. Mechanisms of sporadic cerebral small vessel disease: insights from neuroimaging. *Lancet Neurol.* (2013) 12:483–97. doi: 10.1016/S1474-4422(13)70060-7
11. Thompson CS, Hakim AM. Living beyond our physiological means: small vessel disease of the brain is an expression of a systemic failure in arteriolar function: a unifying hypothesis. *Stroke.* (2009) 40:e322–30. doi: 10.1161/STROKEAHA.108.542266
12. Yang S, Cai J, Lu R, Wu J, Zhang M, Zhou X. Association between serum cystatin c level and total magnetic resonance imaging burden of cerebral small vessel disease in patients with acute lacunar stroke. *J Stroke Cerebrovasc Dis.* (2017) 26:186–91. doi: 10.1016/j.jstrokecerebrovasdis.2016.09.007
13. Xiao L, Lan W, Sun W, Dai Q, Xiong Y, Li L, et al. Chronic kidney disease in patients with lacunar stroke: association with enlarged perivascular spaces and total magnetic resonance imaging burden of cerebral small vessel disease. *Stroke.* (2015) 46:2081–6. doi: 10.1161/STROKEAHA.114.008155
14. Pantoni L. Cerebral small vessel disease: from pathogenesis and clinical characteristics to therapeutic challenges. *Lancet Neurol.* (2010) 9:689–701. doi: 10.1016/S1474-4422(10)70104-6
15. Zwartbol MH, van der Kolk AG, Kuijf HJ, Witkamp TD, Ghaznawi R, Hendrikse J, et al. Intracranial vessel wall lesions on 7T MRI and MRI features of cerebral small vessel disease: The SMART-MR study. *J Cereb Blood Flow Metab.* (2021) 41:1219–28. doi: 10.1177/0271678X20958517
16. Wardlaw JM, Smith EE, Biessels GJ, Cordonnier C, Fazekas F, Frayne R, et al. STandards for ReportIng Vascular changes on nEuroimaging (STRIVE v1). Neuroimaging standards for research into small vessel disease and its contribution to ageing and neurodegeneration. *Lancet Neurol.* (2013) 12:822–38. doi: 10.1016/S1474-4422(13)70124-8
17. Sturtzel C. Endothelial cells. *Adv Exp Med Biol.* (2017) 1003:71–91. doi: 10.1007/978-3-319-57613-8_4
18. Xiao Z, Zhang Z, Ranjan V, Diamond SL. Shear stress induction of the endothelial nitric oxide synthase gene is calcium-dependent but not calcium-activated. *J Cell Physiol.* (1997) 171:205–11. doi: 10.1002/(SICI)1097-4652(199705)171:2<205::AID-JCP11>3.0.CO;2-C
19. de Graaf JC, Banga JD, Moncada S, Palmer RM, de Groot PG, Sixma JJ. Nitric oxide functions as an inhibitor of platelet adhesion under flow conditions. *Circulation.* (1992) 85:2284–90. doi: 10.1161/01.CIR.85.6.2284
20. Krüger-Genge A, Blocki A, Franke RP, Jung F. Vascular endothelial cell biology: an update. *Int J Mol Sci.* (2019) 20:4411. doi: 10.3390/ijms20184411
21. Khakpour S, Wilhelmsen K, Hellman J. Vascular endothelial cell Toll-like receptor pathways in sepsis. *Innate Immun.* (2015) 21:827–46. doi: 10.1177/1753425915606525
22. Gerhardt H, VEGF. and endothelial guidance in angiogenic sprouting. *Organogenesis.* (2008) 4:241–6. doi: 10.4161/org.4.4.7414
23. Roy CS, Sherrington CS. On the Regulation of the Blood-supply of the Brain. *J Physiol.* (1890) 11:85–158.17. doi: 10.1113/jphysiol.1890.sp000321
24. Keramidas ME, Kounalakis SN, Eiken O, Mekjavic IB. Carbon monoxide exposure during exercise performance: muscle and cerebral oxygenation. *Acta Physiol (Oxf).* (2012) 204:544–54. doi: 10.1111/j.1748-1716.2011.02363.x
25. Harder DR, Zhang C, Gebremedhin D. Astrocytes function in matching blood flow to metabolic activity. *News Physiol Sci.* (2002) 17:27–31. doi: 10.1152/physiologyonline.2002.17.1.27
26. Kim KJ, Filosa JA. Advanced in vitro approach to study neurovascular coupling mechanisms in the brain microcirculation. *J Physiol.* (2012) 590:1757–70. doi: 10.1113/jphysiol.2011.222778
27. Muoio V, Persson PB, Sendeski MM. The neurovascular unit - concept review. *Acta Physiol (Oxf).* (2014) 210:790–8. doi: 10.1111/apha.12250
28. Duchemin S, Boily M, Sadekova N, Girouard H. The complex contribution of NOS interneurons in the physiology of cerebrovascular regulation. *Front Neural Circuits.* (2012) 6:51. doi: 10.3389/fncir.2012.00051
29. Gordon GR, Mulligan SJ, MacVicar BA. Astrocyte control of the cerebrovasculature. *Glia.* (2007) 55:1214–21. doi: 10.1002/glia.20543
30. Ashby JW, Mack JJ. Endothelial control of cerebral blood flow. *Am J Pathol.* (2021) 191:1906–16. doi: 10.1016/j.ajpath.2021.02.023
31. Quick S, Moss J, Rajani RM, Williams A, A. Vessel for change: endothelial dysfunction in cerebral small vessel disease. *Trends Neurosci.* (2021) 44:289–305. doi: 10.1016/j.tins.2020.11.003
32. Rajani RM, Quick S, Ruigrok SR, Graham D, Harris SE, Verhaaren BFJ, et al. Reversal of endothelial dysfunction reduces white matter vulnerability in cerebral small vessel disease in rats. *Sci Transl Med.* (2018) 10:eaam9507. doi: 10.1126/scitranslmed.aam9507
33. Hainsworth AH, Oommen AT, Bridges LR. Endothelial cells and human cerebral small vessel disease. *Brain Pathol.* (2015) 25:44–50. doi: 10.1111/bpa.12224
34. Nezu T, Hosomi N, Aoki S, Kubo S, Araki M, Mukai T, et al. Endothelial dysfunction is associated with the severity of cerebral small vessel disease. *Hypertens Res.* (2015) 38:291–7. doi: 10.1038/hr.2015.4
35. Kimura A, Sakurai T, Yamada M, Koumura A, Hayashi Y, Tanaka Y, et al. Anti-endothelial cell antibodies in patients with cerebral small vessel disease. *Curr Neurovasc Res.* (2012) 9:296–301. doi: 10.2174/156720212803530726
36. Hassan A, Hunt BJ, O'Sullivan M, Bell R, D'Souza R, Jeffery S, et al. Homocysteine is a risk factor for cerebral small vessel disease, acting via endothelial dysfunction. *Brain.* (2004) 127:212–9. doi: 10.1093/brain/awh023
37. de Leeuw FE, de Kleine M, Frijns CJ, Fijnheer R, van Gijn J, Kappelle LJ. Endothelial cell activation is associated with cerebral white matter lesions in patients with cerebrovascular disease. *Ann N Y Acad Sci.* (2002) 977:306–14. doi: 10.1111/j.1749-6632.2002.tb04831.x
38. Pretnar-Oblak J, Sabovic M, Pogacnik T, Sebestjen M, Zaletel M. Flow-mediated dilatation and intima-media thickness in patients with lacunar infarctions. *Acta Neurol Scand.* (2006) 113:273–7. doi: 10.1111/j.1600-0404.2006.00578.x
39. Young VG, Halliday GM, Kril JJ. Neuropathologic correlates of white matter hyperintensities. *Neurology.* (2008) 71:804–11. doi: 10.1212/01.wnl.0000319691.50117.54
40. Fernando MS, Simpson JE, Matthews F, Brayne C, Lewis CE, Barber R, et al. MRC cognitive function and ageing neuropathology study group. White matter lesions in an unselected cohort of the elderly: molecular pathology suggests origin from chronic hypoperfusion injury. *Stroke.* (2006) 37:1391–8. doi: 10.1161/01.STR.0000221308.94473.14
41. Yu C, Lu W, Qiu J, Wang F, Li J, Wang L. Alterations of the whole cerebral blood flow in patients with different total cerebral small vessel disease burden. *Front Aging Neurosci.* (2020) 12:175. doi: 10.3389/fnagi.2020.00175
42. Furuta A, Ishii N, Nishihara Y, Horie A. Medullary arteries in aging and dementia. *Stroke.* (1991) 22:442–6. doi: 10.1161/01.STR.22.4.442
43. Cao Y, Su N, Zhang D, Zhou L, Yao M, Zhang S, et al. Correlation between total homocysteine and cerebral small vessel disease: a Mendelian randomization study. *Eur J Neurol.* (2021) 28:1931–8. doi: 10.1111/ene.14708
44. Gyanwali B, Shaik MA, Tan BY, Venketasubramanian N, Chen C, Hilal S. Risk factors for and clinical relevance of incident and progression of cerebral small vessel disease markers in an asian memory clinic population. *J Alzheimers Dis.* (2019) 67:1209–19. doi: 10.3233/JAD-180911
45. Farrall AJ, Wardlaw JM. Blood-brain barrier: ageing and microvascular disease–systematic review and meta-analysis. *Neurobiol Aging.* (2009) 30:337–52. doi: 10.1016/j.neurobiolaging.2007.07.015
46. Pavlovic AM, Pekmezovic T, Trajkovic JZ, Tomic G, Cvitan E, Sternic N. Increased risk of cognitive impairment and more severe brain lesions in hypertensive compared to non-hypertensive patients with cerebral small vessel disease. *J Clin Hypertens (Greenwich).* (2018) 20:1260–5. doi: 10.1111/jch.13357
47. Gons RA, de Laat KF, van Norden AG, van Oudheusden LJ, van Uden IW, Norris DG, et al. Hypertension and cerebral diffusion tensor imaging in small vessel disease. *Stroke.* (2010) 41:2801–6. doi: 10.1161/STROKEAHA.110.597237

48. Lai Y, Jiang C, Du X, Sang C, Guo X, Bai R, et al. Effect of intensive blood pressure control on the prevention of white matter hyperintensity: Systematic review and meta-analysis of randomized trials. *J Clin Hypertens (Greenwich).* (2020) 22:1968–73. doi: 10.1111/jch.14030
49. Kang CK, Park CA, Lee H, Kim SH, Park CW, Kim YB, et al. Hypertension correlates with lenticulostriate arteries visualized by 7T magnetic resonance angiography. *Hypertension.* (2009) 54:1050–6. doi: 10.1161/HYPERTENSIONAHA.109.140350
50. Tamura Y, Araki A. Diabetes mellitus and white matter hyperintensity. *Geriatr Gerontol Int.* (2015) 15 Suppl 1:34–42. doi: 10.1111/ggi.12666
51. Gao Q, Fan Y, Mu LY, Ma L, Song ZQ, Zhang YN. S100B and ADMA in cerebral small vessel disease and cognitive dysfunction. *J Neurol Sci.* (2015) 354:27–32. doi: 10.1016/j.jns.2015.04.031
52. Chen R, Ovbiagele B, Feng W. Diabetes and stroke: epidemiology, pathophysiology, pharmaceuticals and outcomes. *Am J Med Sci.* (2016) 351:380–6. doi: 10.1016/j.amjms.2016.01.011
53. Ighodaro ET, Abner EL, Fardo DW, Lin AL, Katsumata Y, Schmitt FA, et al. Risk factors and global cognitive status related to brain arteriolosclerosis in elderly individuals. *J Cereb Blood Flow Metab.* (2017) 37:201–16. doi: 10.1177/0271678X15621574
54. Nam KW, Kwon HM, Jeong HY, Park JH, Kwon H, Jeong SM. High triglyceride-glucose index is associated with subclinical cerebral small vessel disease in a healthy population: a cross-sectional study. *Cardiovasc Diabetol.* (2020) 19:53. doi: 10.1186/s12933-020-01031-6
55. Arntz RM, van den Broek SM, van Uden IW, Ghafoorian M, Platel B, Rutten-Jacobs LC, et al. Accelerated development of cerebral small vessel disease in young stroke patients. *Neurology.* (2016) 87:1212–9. doi: 10.1212/WNL.0000000000003123
56. Fisher CM. Lacunar strokes and infarcts: a review. *Neurology.* (1982) 32:871–6. doi: 10.1212/WNL.32.8.871
57. Bailey EL, Smith C, Sudlow CL, Wardlaw JM. Pathology of lacunar ischemic stroke in humans–a systematic review. *Brain Pathol.* (2012) 22:583–91. doi: 10.1111/j.1750-3639.2012.00575.x
58. Faraci FM. Watching small vessel disease grow. *Circ Res.* (2018) 122:810–2. doi: 10.1161/CIRCRESAHA.118.312762
59. Wong SM, Jansen JFA, Zhang CE, Hoff EI, Staals J, van Oostenbrugge RJ, et al. Blood-brain barrier impairment and hypoperfusion are linked in cerebral small vessel disease. *Neurology.* (2019) 92:e1669–77. doi: 10.1212/WNL.0000000000007263
60. Lockhart CJ, Hamilton PK, Quinn CE, McVeigh GE. End-organ dysfunction and cardiovascular outcomes: the role of the microcirculation. *Clin Sci (Lond).* (2009) 116:175–90. doi: 10.1042/CS20080069
61. Purkayastha S, Fadar O, Mehregan A, Salat DH, Moscufo N, Meier DS, et al. Impaired cerebrovascular hemodynamics are associated with cerebral white matter damage. *J Cereb Blood Flow Metab.* (2014) 34:228–34. doi: 10.1038/jcbfm.2013.180
62. Huneau C, Benali H, Chabriat H. Investigating human neurovascular coupling using functional neuroimaging: a critical review of dynamic models. *Front Neurosci.* (2015) 9:467. doi: 10.3389/fnins.2015.00467
63. Brown R, Benveniste H, Black SE, Charpak S, Dichgans M, Joutel A, et al. Understanding the role of the perivascular space in cerebral small vessel disease. *Cardiovasc Res.* (2018) 114:1462–73. doi: 10.1093/cvr/cvy113
64. Wolters FJ, Zonneveld HI, Hofman A, van der Lugt A, Koudstaal PJ, Vernooij MW, et al. Heart-Brain Connection Collaborative Research Group. Cerebral perfusion and the risk of dementia: a population-based study. *Circulation.* (2017) 136:719–28. doi: 10.1161/CIRCULATIONAHA.117.027448
65. O'Sullivan M, Lythgoe DJ, Pereira AC, Summers PE, Jarosz JM, Williams SC, et al. Patterns of cerebral blood flow reduction in patients with ischemic leukoaraiosis. *Neurology.* (2002) 59:321–6. doi: 10.1212/WNL.59.3.321
66. Shi Y, Thrippleton MJ, Makin SD, Marshall I, Geerlings MI, de Craen AJM, et al. Cerebral blood flow in small vessel disease: a systematic review and meta-analysis. *J Cereb Blood Flow Metab.* (2016) 36:1653–67. doi: 10.1177/0271678X16662891
67. Promjunyakul N, Lahna D, Kaye JA, Dodge HH, Erten-Lyons D, Rooney WD, et al. Characterizing the white matter hyperintensity penumbra with cerebral blood flow measures. *Neuroimage Clin.* (2015) 8:224–9. doi: 10.1016/j.nicl.2015.04.012
68. Ihara M, Yamamoto Y. Emerging evidence for pathogenesis of sporadic cerebral small vessel disease. *Stroke.* (2016) 47:554–60. doi: 10.1161/STROKEAHA.115.009627
69. Zhang CE, Wong SM, van de Haar HJ, Staals J, Jansen JF, Jeukens CR, et al. Blood-brain barrier leakage is more widespread in patients with cerebral small vessel disease. *Neurology.* (2017) 88:426–32. doi: 10.1212/WNL.0000000000003556
70. Li Y, Li M, Zuo L, Shi Q, Qin W, Yang L, et al. Compromised blood-brain barrier integrity is associated with total magnetic resonance imaging burden of cerebral small vessel disease. *Front Neurol.* (2018) 9:221. doi: 10.3389/fneur.2018.00221
71. Wardlaw JM, Doubal FN, Valdes-Hernandez M, Wang X, Chappell FM, Shuler K, et al. Blood-brain barrier permeability and long-term clinical and imaging outcomes in cerebral small vessel disease. *Stroke.* (2013) 44:525–7. doi: 10.1161/STROKEAHA.112.669994
72. Huisa BN, Caprihan A, Thompson J, Prestopnik J, Qualls CR, Rosenberg GA. Long-term blood-brain barrier permeability changes in binswanger disease. *Stroke.* (2015) 46:2413–8. doi: 10.1161/STROKEAHA.115.009589
73. Freeze WM, Jacobs HIL, de Jong JJ, Verheggen ICM, Gronenschild EHBM, Palm WM, et al. White matter hyperintensities mediate the association between blood-brain barrier leakage and information processing speed. *Neurobiol Aging.* (2020) 85:113–22. doi: 10.1016/j.neurobiolaging.2019.09.017
74. Kerkhofs D, Wong SM, Zhang E, Uiterwijk R, Hoff EI, Jansen JFA, et al. Blood-brain barrier leakage at baseline and cognitive decline in cerebral small vessel disease: a 2-year follow-up study. *Geroscience.* (2021) 43:1643–52. doi: 10.1007/s11357-021-00399-x
75. Low A, Mak E, Rowe JB, Markus HS, O'Brien JT. Inflammation and cerebral small vessel disease: A systematic review. *Ageing Res Rev.* (2019) 53:100916. doi: 10.1016/j.arr.2019.100916
76. Cucullo L, Hossain M, Puvenna V, Marchi N, Janigro D. The role of shear stress in Blood-Brain Barrier endothelial physiology. *BMC Neurosci.* (2011) 12:40. doi: 10.1186/1471-2202-12-40
77. Stanimirovic DB, Friedman A. Pathophysiology of the neurovascular unit: disease cause or consequence? *J Cereb Blood Flow Metab.* (2012) 32:1207–21. doi: 10.1038/jcbfm.2012.25
78. Liao JK. Linking endothelial dysfunction with endothelial cell activation. *J Clin Invest.* (2013) 123:540–1. doi: 10.1172/JCI66843
79. Dhananjayan R, Koundinya KS, Malati T, Kutala VK. Endothelial dysfunction in type 2 diabetes mellitus. *Indian J Clin Biochem.* (2016) 31:372–9. doi: 10.1007/s12291-015-0516-y
80. Grochowski C, Litak J, Kamieniak P, Maciejewski R. Oxidative stress in cerebral small vessel disease. *Role of reactive species Free Radic Res.* (2018) 52:1–13. doi: 10.1080/10715762.2017.1402304
81. Xi H, Zhang Y, Xu Y, Yang WY, Jiang X, Sha X, et al. Caspase-1 inflammasome activation mediates homocysteine-induced pyrop-apoptosis in endothelial cells. *Circ Res.* (2016) 118:1525–39. doi: 10.1161/CIRCRESAHA.116.308501
82. Golbidi S, Edvinsson L, Laher I. Smoking and endothelial dysfunction. *Curr Vasc Pharmacol.* (2020) 18:1–11. doi: 10.2174/1573403X14666180913120015
83. Shoamanesh A, Preis SR, Beiser AS, Vasan RS, Benjamin EJ, Kase CS, et al. Inflammatory biomarkers, cerebral microbleeds, and small vessel disease: Framingham heart study. *Neurology.* (2015) 84:825–32. doi: 10.1212/WNL.0000000000001279
84. Liberale L, Dallegri F, Montecucco F, Carbone F. Pathophysiological relevance of macrophage subsets in atherogenesis. *Thromb Haemost.* (2017) 117:7–18. doi: 10.1160/TH16-08-0593
85. Rouhl RP, Damoiseaux JG, Lodder J, Theunissen RO, Knottnerus IL, Staals J, et al. Vascular inflammation in cerebral small vessel disease. *Neurobiol Aging.* (2012) 33:1800–6. doi: 10.1016/j.neurobiolaging.2011.04.008
86. Cirillo P, Pacileo M, DE Rosa S, Calabrò P, Gargiulo A, Angri V, et al. Neopterin induces pro-atherothrombotic phenotype in human coronary endothelial cells. *J Thromb Haemost.* (2006) 4:2248–55. doi: 10.1111/j.1538-7836.2006.02125.x
87. Senchenkova EY, Russell J, Kurmaeva E, Ostanin D, Granger DN. Role of T lymphocytes in angiotensin II-mediated

microvascular thrombosis. *Hypertension.* (2011) 58:959–65. doi: 10.1161/HYPERTENSIONAHA.111.173856
88. Bonetti PO, Pumper GM, Higano ST, Holmes DR Jr, Kuvin JT, Lerman A. Noninvasive identification of patients with early coronary atherosclerosis by assessment of digital reactive hyperemia. *J Am Coll Cardiol.* (2004) 44:2137–41. doi: 10.1016/j.jacc.2004.08.062
89. Kitta Y, Obata JE, Nakamura T, Hirano M, Kodama Y, Fujioka D, et al. Persistent impairment of endothelial vasomotor function has a negative impact on outcome in patients with coronary artery disease. *J Am Coll Cardiol.* (2009) 53:323–30. doi: 10.1016/j.jacc.2008.08.074
90. Hamburg NM, Benjamin EJ. Assessment of endothelial function using digital pulse amplitude tonometry. *Trends Cardiovasc Med.* (2009) 19:6–11. doi: 10.1016/j.tcm.2009.03.001
91. Gifford JR, Richardson RS. CORP: Ultrasound assessment of vascular function with the passive leg movement technique. *J Appl Physiol.* (2017) 123:1708–20. doi: 10.1152/japplphysiol.00557.2017
92. Semyachkina-Glushkovskaya O, Postnov D, Penzel T, Kurths J. Sleep as a novel biomarker and a promising therapeutic target for cerebral small vessel disease: a review focusing on alzheimer's disease and the blood-brain barrier. *Int J Mol Sci.* (2020) 21:6293. doi: 10.3390/ijms21176293
93. Pikula A, Böger RH, Beiser AS, Maas R, DeCarli C, Schwedhelm E, et al. Association of plasma ADMA levels with MRI markers of vascular brain injury: Framingham offspring study. *Stroke.* (2009) 40:2959–64. doi: 10.1161/STROKEAHA.109.557116
94. Notsu Y, Nabika T, Bokura H, Suyama Y, Kobayashi S, Yamaguchi S, et al. Evaluation of asymmetric dimethylarginine and homocysteine in microangiopathy-related cerebral damage. *Am J Hypertens.* (2009) 22:257–62. doi: 10.1038/ajh.2008.346
95. Mokotedi L, Millen AME, Mogane C, Gomes M, Woodiwiss AJ, Norton GR, et al. Associations of inflammatory markers and vascular cell adhesion molecule-1 with endothelial dysfunction in collagen-induced arthritis. *Eur J Pharmacol.* (2019) 865:172786. doi: 10.1016/j.ejphar.2019.172786
96. Lalor PF, Sun PJ, Weston CJ, Martin-Santos A, Wakelam MJ, Adams DH. Activation of vascular adhesion protein-1 on liver endothelium results in an NF-kappaB-dependent increase in lymphocyte adhesion. *Hepatology.* (2007) 45:465–74. doi: 10.1002/hep.21497
97. Hlubocká Z, Umnerová V, Heller S, Peleska J, Jindra A, Jáchymová M, et al. Circulating intercellular cell adhesion molecule-1, endothelin-1 and von Willebrand factor-markers of endothelial dysfunction in uncomplicated essential hypertension: the effect of treatment with ACE inhibitors. *J Hum Hypertens.* (2002) 16:557–62. doi: 10.1038/sj.jhh.1001403
98. Markus HS, Hunt B, Palmer K, Enzinger C, Schmidt H, Schmidt R. Markers of endothelial and hemostatic activation and progression of cerebral white matter hyperintensities: longitudinal results of the Austrian Stroke Prevention Study. *Stroke.* (2005) 36:1410–4. doi: 10.1161/01.STR.0000169924.60783.d4
99. Hassan A, Hunt BJ, O'Sullivan M, Parmar K, Bamford JM, Briley D, et al. Markers of endothelial dysfunction in lacunar infarction and ischaemic leukoaraiosis. *Brain.* (2003) 126:424–32. doi: 10.1093/brain/awg040
100. Vita JA, Brennan ML, Gokce N, Mann SA, Goormastic M, Shishehbor MH, et al. Serum myeloperoxidase levels independently predict endothelial dysfunction in humans. *Circulation.* (2004) 110:1134–9. doi: 10.1161/01.CIR.0000140262.20831.8F
101. Bailey EL, Wardlaw JM, Graham D, Dominiczak AF, Sudlow CL, Smith C. Cerebral small vessel endothelial structural changes predate hypertension in stroke-prone spontaneously hypertensive rats: a blinded, controlled immunohistochemical study of 5- to 21-week-old rats. *Neuropathol Appl Neurobiol.* (2011) 37:711–26. doi: 10.1111/j.1365-2990.2011.01170.x
102. Nitta T, Hata M, Gotoh S, Seo Y, Sasaki H, Hashimoto N, et al. Size-selective loosening of the blood-brain barrier in claudin-5-deficient mice. *J Cell Biol.* (2003) 161:653–60. doi: 10.1083/jcb.200302070
103. Gheissari A, Meamar R, Abedini A, Roomizadeh P, Shafiei M, Samaninobandegani Z, et al. Association of matrix metalloproteinase-2 and matrix metalloproteinase-9 with endothelial dysfunction, cardiovascular disease risk factors and thrombotic events in children with end-stage renal disease. *Iran J Kidney Dis.* (2018) 12:169–77.
104. Loso J, Lund N, Avanesov M, Muschol N, Lezius S, Cordts K, et al. Serum biomarkers of endothelial dysfunction in fabry associated cardiomyopathy. *Front Cardiovasc Med.* (2018) 5:108. doi: 10.3389/fcvm.2018.00108
105. Kim Y, Kim YK, Kim NK, Kim SH, Kim OJ, Oh SH. Circulating matrix metalloproteinase-9 level is associated with cerebral white matter hyperintensities in non-stroke individuals. *Eur Neurol.* (2014) 72:234–40. doi: 10.1159/000362876
106. Nafisa A, Gray SG, Cao Y, Wang T, Xu S, Wattoo FH, et al. Endothelial function and dysfunction: Impact of metformin. *Pharmacol Ther.* (2018) 192:150–62. doi: 10.1016/j.pharmthera.2018.07.007
107. Lip GY, Blann A. von Willebrand factor: a marker of endothelial dysfunction in vascular disorders? *Cardiovasc Res.* (1997) 34:255–65. doi: 10.1016/S0008-6363(97)00039-4
108. Constans J, Conri C. Circulating markers of endothelial function in cardiovascular disease. *Clin Chim Acta.* (2006) 368:33–47. doi: 10.1016/j.cca.2005.12.030
109. Gaudet A, Chenevier-Gobeaux C, Parmentier E, Delobel JE, Dubucquoi S, Mathieu D, et al. Endocan is a stable circulating molecule in ICU patients. *Clin Biochem.* (2017) 50:870–7. doi: 10.1016/j.clinbiochem.2017.04.011
110. Leite AR, Borges-Canha M, Cardoso R, Neves JS, Castro-Ferreira R, Leite-Moreira A. Novel biomarkers for evaluation of endothelial dysfunction. *Angiology.* (2020) 71:397–410. doi: 10.1177/0003319720903586
111. Sarrazin S, Adam E, Lyon M, Depontieu F, Motte V, Landolfi C, et al. Endocan or endothelial cell specific molecule-1 (ESM-1): a potential novel endothelial cell marker and a new target for cancer therapy. *Biochim Biophys Acta.* (2006) 1765:25–37. doi: 10.1016/j.bbcan.2005.08.004
112. Jung KH, Chu K, Lee ST, Park HK, Bahn JJ, Kim DH, et al. Circulating endothelial microparticles as a marker of cerebrovascular disease. *Ann Neurol.* (2009) 66:191–9. doi: 10.1002/ana.21681
113. Werner N, Wassmann S, Ahlers P, Kosiol S, Nickenig G. Circulating CD31+/annexin V+ apoptotic microparticles correlate with coronary endothelial function in patients with coronary artery disease. *Arterioscler Thromb Vasc Biol.* (2006) 26:112–6. doi: 10.1161/01.ATV.0000191634.13057.15
114. Hu SS, Zhang HG, Zhang QJ, Xiu RJ. Small-size circulating endothelial microparticles in coronary artery disease. *PLoS ONE.* (2014) 9:e104528. doi: 10.1371/journal.pone.0104528
115. Brodsky SV, Zhang F, Nasjletti A, Goligorsky MS. Endothelium-derived microparticles impair endothelial function in vitro. *Am J Physiol Heart Circ Physiol.* (2004) 286:H1910–5. doi: 10.1152/ajpheart.01172.2003
116. Song R, Chou YI, Kong J, Li J, Pan B, Cui M, et al. Association of endothelial microparticle with NO, eNOS, ET-1, and fractional flow reserve in patients with coronary intermediate lesions. *Biomarkers.* (2015) 20:429–35. doi: 10.3109/1354750X.2015.1094140
117. McCarthy EM, Wilkinson FL, Parker B, Alexander MY. Endothelial microparticles: Pathogenic or passive players in endothelial dysfunction in autoimmune rheumatic diseases? *Vascul Pharmacol.* (2016) 86:71–6. doi: 10.1016/j.vph.2016.05.016
118. La Sala L, Pujadas G, De Nigris V, Canivell S, Novials A, Genovese S, et al. Oscillating glucose and constant high glucose induce endoglin expression in endothelial cells: the role of oxidative stress. *Acta Diabetol.* (2015) 52:505–12. doi: 10.1007/s00592-014-0670-3
119. Ikemoto T, Hojo Y, Kondo H, Takahashi N, Hirose M, Nishimura Y, et al. Plasma endoglin as a marker to predict cardiovascular events in patients with chronic coronary artery diseases. *Heart Vessels.* (2012) 27:344–51. doi: 10.1007/s00380-011-0163-z
120. Vitverova B, Blazickova K, Najmanova I, Vicen M, Hyšpler R, Dolezelova E, et al. Soluble endoglin and hypercholesterolemia aggravate endothelial and vessel wall dysfunction in mouse aorta. *Atherosclerosis.* (2018) 271:15–25. doi: 10.1016/j.atherosclerosis.2018.02.008
121. Blázquez-Medela AM, García-Ortiz L, Gómez-Marcos MA, Recio-Rodríguez JI, Sánchez-Rodríguez A, López-Novoa JM, et al. Increased plasma soluble endoglin levels as an indicator of cardiovascular alterations in hypertensive and diabetic patients. *BMC Med.* (2010) 8:86. doi: 10.1186/1741-7015-8-86

122. Santibanez JF, Letamendia A, Perez-Barriocanal F, Silvestri C, Saura M, Vary CP, et al. Endoglin increases eNOS expression by modulating Smad2 protein levels and Smad2-dependent TGF-beta signaling. *J Cell Physiol.* (2007) 210:456–68. doi: 10.1002/jcp.20878
123. Rathouska J, Jezkova K, Nemeckova I, Nachtigal P. Soluble endoglin, hypercholesterolemia and endothelial dysfunction. *Atherosclerosis.* (2015) 243:383–8. doi: 10.1016/j.atherosclerosis.2015.10.003
124. Rocha SF, Schiller M, Jing D, Li H, Butz S, Vestweber D, et al. Esm1 modulates endothelial tip cell behavior and vascular permeability by enhancing VEGF bioavailability. *Circ Res.* (2014) 115:581–90. doi: 10.1161/CIRCRESAHA.115.304718
125. Musialowska D, Zbroch E, Koc-Zorawska E, Musialowski P, Malyszko J. Endocan Concentration in patients with primary hypertension. *Angiology.* (2018) 69:483–9. doi: 10.1177/0003319717736158
126. Balamir I, Ates I, Topcuoglu C, Turhan T. Association of endocan, ischemia-modified albumin, and hsCRP levels with endothelial dysfunction in type 2 diabetes mellitus. *Angiology.* (2018) 69:609–16. doi: 10.1177/0003319717740781
127. Altintas N, Mutlu LC, Akkoyun DC, Aydin M, Bilir B, Yilmaz A, et al. Effect of CPAP on new endothelial dysfunction marker, endocan, in people with obstructive sleep apnea. *Angiology.* (2016) 67:364–74. doi: 10.1177/0003319715590558
128. Fernández-Hernando C, Suárez Y. MicroRNAs in endothelial cell homeostasis and vascular disease. *Curr Opin Hematol.* (2018) 25:227–36. doi: 10.1097/MOH.0000000000000424
129. Nemecz M, Alexandru N, Tanko G, Georgescu A. Role of MicroRNA in endothelial dysfunction and hypertension. *Curr Hypertens Rep.* (2016) 18:87. doi: 10.1007/s11906-016-0696-8
130. Santulli G. MicroRNAs and endothelial (Dys) function. *J Cell Physiol.* (2016) 231:1638–44. doi: 10.1002/jcp.25276
131. Poggesi A, Pasi M, Pescini F, Pantoni L, Inzitari D. Circulating biologic markers of endothelial dysfunction in cerebral small vessel disease: a review. *J Cereb Blood Flow Metab.* (2016) 36:72–94. doi: 10.1038/jcbfm.2015.116
132. Arrebola-Moreno AL, Laclaustra M, Kaski JC. Noninvasive assessment of endothelial function in clinical practice. *Rev Esp Cardiol (Engl Ed).* (2012) 65:80–90. doi: 10.1016/j.rec.2011.10.004
133. Canpolat U, Kocyigit D, Yildirim A. Role of endothelial dysfunction and endocan in atherosclerosis: point of origin or end point? *Angiology.* (2020) 71:477. doi: 10.1177/0003319716654627
134. Sun H, Zhang H, Li K, Wu H, Zhan X, Fang F, et al. ESM-1 promotes adhesion between monocytes and endothelial cells under intermittent hypoxia. *J Cell Physiol.* (2019) 234:1512–21. doi: 10.1002/jcp.27016
135. Lee W, Ku SK, Kim SW, Bae JS. Endocan elicits severe vascular inflammatory responses in vitro and in vivo. *J Cell Physiol.* (2014) 229:620–30. doi: 10.1002/jcp.24485
136. Janelidze S, Hertze J, Nägga K, Nilsson K, Nilsson C. Swedish BioFINDER Study Group, et al. Increased blood-brain barrier permeability is associated with dementia and diabetes but not amyloid pathology or APOE genotype. *Neurobiol Aging.* (2017) 51:104–12. doi: 10.1016/j.neurobiolaging.2016.11.017
137. Bath PM, Wardlaw JM. Pharmacological treatment and prevention of cerebral small vessel disease: a review of potential interventions. *Int J Stroke.* (2015) 10:469–78. doi: 10.1111/ijs.12466
138. Ji T, Zhao Y, Wang J, Cui Y, Duan D, Chai Q, et al. Effect of low-dose statins and apolipoprotein e genotype on cerebral small vessel disease in older hypertensive patients: a subgroup analysis of a randomized clinical trial. *J Am Med Dir Assoc.* (2018) 19:995–1002.e4. doi: 10.1016/j.jamda.2018.05.025
139. Zhang J, Liu N, Yang C. Effects of rosuvastatin in combination with nimodipine in patients with mild cognitive impairment caused by cerebral small vessel disease. *Panminerva Med.* (2019) 61:439–43. doi: 10.23736/S0031-0808.18.03475-4
140. SPS3 Investigators, Benavente OR, Hart RG, McClure LA, Szychowski JM, Coffey CS, et al. Effects of clopidogrel added to aspirin in patients with recent lacunar stroke. *N Engl J Med.* (2012) 367:817–25. doi: 10.1056/NEJMoa1204133
141. Staszewski J, Piusińska-Macoch R, Skrobowska E, Brodacki B, Macek K, Stepień A. Aspirin resistance: risk factors and prognostic significance in patients with cerebral small vessel disease. *Ann Clin Lab Sci.* (2018) 48:45–54. doi: 10.1016/j.pjnns.2017.11.005
142. Barton M. Prevention and endothelial therapy of coronary artery disease. *Curr Opin Pharmacol.* (2013) 13:226–41. doi: 10.1016/j.coph.2013.05.005
143. Yubero-Serrano EM, Fernandez-Gandara C, Garcia-Rios A, Rangel-Zuñiga OA, Gutierrez-Mariscal FM, Torres-Peña JD, et al. Mediterranean diet and endothelial function in patients with coronary heart disease: an analysis of the CORDIOPREV randomized controlled trial. *PLoS Med.* (2020) 17:e1003282. doi: 10.1371/journal.pmed.1003282
144. Pedralli ML, Marschner RA, Kollet DP, Neto SG, Eibel B, Tanaka H, et al. Different exercise training modalities produce similar endothelial function improvements in individuals with prehypertension or hypertension: a randomized clinical trial Exercise, endothelium and blood pressure. *Sci Rep.* (2020) 10:7628. doi: 10.1038/s41598-020-64365-x
145. Fahlbusch SA, Tsikas D, Mehls C, Gutzki FM, Böger RH, Frölich JC, et al. Effects of carvedilol on oxidative stress in human endothelial cells and healthy volunteers. *Eur J Clin Pharmacol.* (2004) 60:83–8. doi: 10.1007/s00228-004-0729-0
146. Tuo M, Xiao Y, Xu Y, Wang L, Wei X, Zhang L. Role of granulocyte-colony stimulating factor in the protection of cerebral vascular endothelium, white matter, and cognition. *Curr Neurovasc Res.* (2019) 16:425–32. doi: 10.2174/1567202616666191029115113
147. Li J, Ma Y, Miao XH, Guo JD Li DW. Neovascularization and tissue regeneration by endothelial progenitor cells in ischemic stroke. *Neurol Sci.* (2021) 42:3585–93. doi: 10.1007/s10072-021-05428-3
148. Li MT, Ke J, Guo SF, Wu Y, Bian YF, Shan LL, et al. The protective effect of quercetin on endothelial cells injured by hypoxia and reoxygenation. *Front Pharmacol.* (2021) 12:732874. doi: 10.3389/fphar.2021.732874
149. Lu YW, Hao RJ, Wei YY Yu GR. The protective effect of harpagoside on angiotensin II (Ang II)-induced blood-brain barrier leakage in vitro. *Phytother Res.* (2021) 35:6241–54. doi: 10.1002/ptr.7269
150. Chamorro-Jorganes A, Araldi E, Suárez Y. MicroRNAs as pharmacological targets in endothelial cell function and dysfunction. *Pharmacol Res.* (2013) 75:15–27. doi: 10.1016/j.phrs.2013.04.002

Conflict of Interest: The authors declare that the research was conducted in the absence of any commercial or financial relationships that could be construed as a potential conflict of interest.

Publisher's Note: All claims expressed in this article are solely those of the authors and do not necessarily represent those of their affiliated organizations, or those of the publisher, the editors and the reviewers. Any product that may be evaluated in this article, or claim that may be made by its manufacturer, is not guaranteed or endorsed by the publisher.

Copyright © 2022 Bai, Yu and Feng. This is an open-access article distributed under the terms of the Creative Commons Attribution License (CC BY). The use, distribution or reproduction in other forums is permitted, provided the original author(s) and the copyright owner(s) are credited and that the original publication in this journal is cited, in accordance with accepted academic practice. No use, distribution or reproduction is permitted which does not comply with these terms.

frontiers | Frontiers in Neurology

ORIGINAL RESEARCH
published: 11 April 2022
doi: 10.3389/fneur.2022.852013

hsa-miR-518-5p/hsa-miR-3135b Regulates the REL/SOD2 Pathway in Ischemic Cerebral Infarction

*Boyan Zhao and Xiaofan Jiang**

Department of Neurosurgery, Xijing Hospital, Fourth Military Medical University, Xi'an, China

Objectives: Ischemic cerebral infarction (ICI) is a fatal neurovascular disorder. A bioinformatics approach based on single-cell and bulk RNA-seq analyses was applied to investigate the pathways and genes involved in ICI and study the expression profile of these genes.

Methods: First, the aberrantly regulated "small-molecule ribonucleic acids" [microRNA (miRNAs)] and messenger RNAs (mRNAs) were analyzed using transcriptome data from the ischemic brain infarction dataset of the Gene Expression Omnibus (GEO) database. In mouse cerebrovascular monocytes, the single-cell regulatory network inference and clustering (SCENIC) workflow was used to identify key transcription factors (TFs). Then, the two miRNA-TF-mRNA interaction networks were constructed. Moreover, the molecular complex detection (MCODE) extracted the core sub-networks and identified the important TFs within these sub-networks. Finally, whole blood samples were collected for validation of the expression of critical molecules in ICI.

Results: We identified four cell types and 266 regulons in mouse cerebrovascular monocytes using SCENIC analysis. Moreover, 112 differently expressed miRNAs and 3,780 differentially expressed mRNAs were identified. We discovered potential biomarkers in ICI by building a miRNA-TF-mRNA interaction network. The hsa-miR-518-5p/hsa-miR-3135b/REL/SOD2 was found to play a potential role in ICI progression. The expression of REL and superoxide dismutase 2 (SOD2) was significantly elevated in the ICI group in the clinical cohort ($P < 0.05$). Furthermore, a REL expression was elevated in endothelial cells and fibroblasts at the single-cell level, indicating that REL is a cell-specific regulon. Functional enrichment analyses revealed that REL is primarily engaged in neurotransmitter activity and oxidative phosphorylation.

Conclusions: Our research uncovered novel biomarkers for ICI of neurovascular disease. The hsa-miR-518-5p/hsa-miR-3135b may regulate the REL/SOD2 pathway in ICI progression.

Keywords: neurovascular, ischemic stroke (IS), scRNA-seq, regulatory network, REL

OPEN ACCESS

Edited by:
Yuzhen Xu,
Tongji University, China

Reviewed by:
Zhongcheng Xie,
University of South China, China
Chen Chen,
The First Affiliated Hospital of Soochow University, China

***Correspondence:**
Xiaofan Jiang
xd7ravd@163.com;
xiaofan-jiang@seu.edu.mk

Specialty section:
This article was submitted to Neurological Biomarkers, a section of the journal Frontiers in Neurology

Received: *10 January 2022*
Accepted: *24 February 2022*
Published: *11 April 2022*

Citation:
Zhao B and Jiang X (2022) hsa-miR-518-5p/hsa-miR-3135b Regulates the REL/SOD2 Pathway in Ischemic Cerebral Infarction. Front. Neurol. 13:852013. doi: 10.3389/fneur.2022.852013

INTRODUCTION

Stroke is a common and fatal neurovascular disease that has high morbidity and mortality rates worldwide, accounting for ∼17 million new cases annually (1–5). Ischemic stroke (IS) accounts for 80% of all stroke cases (6). Multiple emboli blocking the intracerebral arteries result in irreversible functional deficiencies in local brain tissue, eventually leading to ischemia and hypoxic necrosis (7, 8). Ischemic cerebral infarction (ICI) is a fatal neurovascular disorder (9). Due to its complexity, the molecular pathways underlying the development of ICI are not well-known at the transcriptome level. Exploring the regulatory network of signaling pathways is critical to understanding the mechanism by which ICI develops and to developing effective strategies for preventing and treating ICI.

Single-cell RNA sequencing (scRNA-seq) is a technique for obtaining whole-transcriptome expression profiles at the single-cell level. It is based on the amplification of microscopic whole-transcriptome RNA from isolated individual cells and subsequent high-throughput sequencing to elucidate the molecular regulatory mechanisms underlying specific biological processes and disease pathogenesis (10). In recent years, the scRNA-seq has gradually gained traction in the disciplines of oncology, microbiology, and neuroscience (11–13). In addition to studying changes in gene expression patterns at the population level, the scRNA-seq can be used to study single-cell gene expression, thus, resolving any bias arising due to cellular heterogeneity. Therefore, scRNA-seq is particularly well-suited for studying highly heterogeneous cell populations, such as neural cells (14, 15). Using scRNA-seq, Gate et al. showed that the T-cell receptor (TCR) signaling pathway is activated in CD8+ terminally differentiated effector cells (TEMRA) in the cerebrospinal fluid of patients with Alzheimer's disease, indicating that these cells contribute to the onset of neurological symptoms through their cytotoxic role (16). Vanlandewijck et al. used scRNA-seq to conduct a transcriptional investigation of the constituent cell types of the cerebral vasculature and discovered that endothelial cells, pericytes, and fibroblasts are implicated in the formation of neurovascular disease lesions. In this study, we attempted to address the dearth of molecular studies on cerebrovascular cell types and to establish the groundwork for future research on the molecular pathways underlying cerebrovascular disorders (17). The single-cell regulatory network infeAbegail Floresrence and clustering (SCENIC) is a computational approach for identifying cell states and constructing gene regulatory networks from scRNA-seq data (18). The SCENIC can be used to identify critical transcription factors (TFs) involved in the pathophysiology of ICI.

Apart from single-cell technology, various bioinformatics techniques have emerged as important tools to study complex biological phenomena. The "small-molecule ribonucleic acids" [microRNA (miRNAs)] are a class of non-coding, endogenous single-stranded RNA molecules composed of 20–24 nucleotides that regulate the expression of target genes in various physiological and pathological processes (19). The miRNAs serve as molecular markers for early diagnosis and prognosis, as well as therapeutic targets for ICI (20–23). The miR-PC-5P-12969 inhibits the production of amyloid and promotes IS (24). In acute ICI, the serum miR-124 and other miRs are inhibited, resulting in neuroinflammation and brain damage (25). Additionally, miRNAs can contribute to ICI by modulating TFs. Atherosclerosis (AS) has a significant role in the pathophysiology of ICI (26). Li et al. showed that miR-NA-663 governs the phenotypic metamorphosis of human vascular smooth muscle cells by adversely regulating the expression of its downstream TF, Jun B (27). The miRNA-23b can reduce vascular smooth muscle cell proliferation and migration, and the TF FoxO4 may be a direct target of miRNA-23b (28). Thus, the miRNAs play a critical role in the development of AS by controlling the proliferation, differentiation, and function of vascular smooth muscle cells *via* TF regulation, potentially altering the course of ICI. Therefore, single-cell sequencing is critical for identifying miRNA-TF-gene regulatory networks involved in ICI progression, which may reveal novel gene targets and molecular markers for ICI diagnosis and therapy.

In this study, we analyzed bulk RNA-seq, as well as scRNA-seq data, to identify a miRNA-TF-mRNA regulatory network that may be vital to ICI progression. Our research aimed to uncover novel biomarkers for ICI of neurovascular disease. The findings of this study may provide new avenues for the prevention and treatment of IS, as well as strategies to improve patient outcomes.

METHODS

Data Acquisition

First, the ICI dataset was retrieved from the Gene Expression Omnibus (GEO) database. The GEO database is a repository of raw data, including transcriptomic data from published studies. From the GSE16561 dataset, transcriptomic data was acquired from whole blood samples of 39 patients with ICI, and 24 healthy individuals (29). Moreover, transcriptomic data from 24 control blood samples were collected from the GSE55937 dataset (30). The GSE98816, an scRNA-seq collection, contains transcriptomic information of 3,186 cells derived from mouse cerebrovascular tissue (17). Then, the expression of differentially expressed TFs in mouse cerebrovascular tissue was analyzed based on bulk RNA-seq data. Finally, to validate the expression of differentially expressed genes (DEGs) identified from bioinformatics analyses, whole blood samples were collected from 24 patients with ICI and 22 healthy individuals at our institution and were subjected to differential gene expression analysis. The inclusion criteria are: patients with ischemic cerebral infarction met the diagnostic criteria; patients with cerebral infarction were confirmed by imaging and the onset of the disease did not exceed 48 h; and informed consent was provided and signed by the patients. The exclusion criteria are: severe liver and kidney damage; cardiac diseases such as myocardial infarction and heart failure; acute complications of diabetes mellitus; acute infection combined with malignancy; and cerebral hemorrhage or cardiogenic cerebral embolism. This

Abbreviations: AS, atherosclerosis; IS, ischemic stroke; scRNA-seq, single-cell RNA-sequencing; SCENIC, single-cell regulatory network inference and clustering; SOD2, superoxide dismutase 2; TF, transcription factor.

study was approved by the Institutional Ethics Review Board of The Xijing Hospital. Informed written consent was obtained from all the patients. The following statistical criteria were used for comparing differences between the two groups: $^{*}P < 0.05$, $^{**}P < 0.01$, and $^{***}P < 0.001$.

scRNA-seq Analysis

The GSE98816, a scRNA-seq collection, was used for scRNA-seq analysis. The cells isolated from mouse cerebrovascular tissue were clustered and annotated to facilitate subsequent analysis of transcriptional regulation patterns in different cell populations. Like previous research, the R package Seurat (v. 4.0) was used to perform quality control on the scRNA-seq data, as well as data reduction, cell clustering, and cell annotation (31–33). After identifying highly variable genes using the "FindVariableFeatures" function, the principal component analysis (PCA) was performed to extract gene expression features from scRNA-seq data. The principal components (PCs) that account for the majority of the true signal were identified using JackStraw and Elbow plots. Then, cells were grouped according to these selected PCs. Cell clustering was performed using uniform manifold approximation and projection (UMAP). In the cell clustering results, the characteristic genes were identified for each cell cluster. Cell annotation was performed using SingleR (v. 1.0), and marker genes were annotated based on the results of previous studies (34, 35).

SCENIC Analysis and Gene Regulatory Network Construction

Core TFs in scRNA-seq were obtained using the SCENIC method. The SCENIC is a computational approach for identifying cell states and constructing gene regulatory networks from scRNA-seq data (34). The SCENIC was used to analyze the significant TFs in each cell population after acquiring the annotation information and tissue origin of each cell. First, a gene co-expression network was constructed using data from a gene expression matrix of mouse cerebrovascular cells. Subsequently, from this gene co-expression network, the "RcisTarget" package in R was used to identify TF-mRNA regulatory networks with direct regulatory linkages, and these TFs were classified as regulons. Finally, a regulon activity score (RAS) was calculated for each cell corresponding to each regulon, which represents the regulatory activity of the associated regulon in each cell. Subsequently, these newly discovered regulons were used for further analysis.

Differential Analysis and Identification of miRNA-mRNA Interactions

To identify genes that are dysregulated in IS, the "linear model" function of the "limma" package in R was used to compare the expression of mRNAs and miRNAs between the ICI and healthy control (HC) groups (36, 37). Differentially expressed mRNAs (DEmRNAs) and miRNAs (DEmiRNAs) were selected according to $P < 0.05$. Subsequently, the miRWalk (<http://mirwalk.umm.uni-heidelberg.de/>) open-source platform was used to identify DEmiRNA-DEmRNA networks.

Identification of Molecular Interaction Networks and Core Regulons

First, the TF-target gene pairs present in the miRNA-mRNA network were predicted using the TRRUST (v2) database, followed by the identification of the key TFs in the network (38). Then, the core regulons were derived by conducting an intersection analysis on these major TFs, and the regulons were identified by SCENIC analysis. Finally, a network of interactions between miRNAs, TFs (regulons), and mRNAs were constructed. Protein-protein interaction (PPI) networks were visualized using Cityscape (v. 3.9), with all proteins corresponding to the nodes in this network. Furthermore, the Molecular Complex Detection (MCODE) plug-in was used to investigate and generate the core sub-networks of the gene interaction network (degree cutoff = 2, node score cutoff = 0.2, and maximum depth = 100).

Gene Set Enrichment Analysis

To understand the function of the DEGs, the "clusterProfiler" package in R was used for functional enrichment analysis, including the Kyoto Encyclopedia of Genes and Genomes (KEGG) and Gene Ontology (GO) analyses (39). In contrast, the gene set enrichment analysis (GSEA) was performed to analyze the functional pathways involved in the screening of dysregulated regulons in patients with ICI (40). The reference gene set "c2.cp.v7.2.symbols.gmt [Curated]" was obtained from MSigDB Collections (https://www.gsea-msigdb.org/gsea/msigdb/), and *P*-values were calculated using a random sample swap ($n = 1{,}000$). The threshold for screening functional pathways was set as follows: false discovery rate (FDR) <0.25 and adjusted *P*-value <0.05.

Quantitative Real-Time PCR

The total RNA was extracted from whole blood samples using TRIzol reagent (Invitrogen) according to the manufacturer's instructions. The RNA was reverse-transcribed to complementary DNA (cDNA) using a cDNA synthesis kit (K1622; Fermentas, Waltham, MA), following the manufacturer's instructions. Finally, quantitative real-time PCR (qRT-PCR) was performed using an ABI 7500 real-time PCR system (Applied Biosystems, CA, USA), and amplification was performed using SYBR Green (Prime Script RT Master Mix, Takara, Tokyo, Japan). The Glyceraldehyde-3-phosphate dehydrogenase (*GAPDH*) gene was used as an internal reference gene for the normalization of gene expression levels. As with previous research, the following gene-specific primers were used: *GAPDH*, forward: 5′-AGAAGGTGGTGAAGCAGGC-3′ and reverse: 5′-TCCACCACCCAGTTGCTG-3′; *REL*, forward: 5′-GAATCAATCCATTCAATGTCCC-3′ and reverse: 5′-AAGAGCAGTCGTCAAATTACC-3′; *SOD2*, forward: 5′-GACAAACCTCAGCCCTAACG-3′ and reverse: 5′-CGTCAGCTTCTCCTTAAACTTG-3′ (41, 42). The gene expression levels were calculated using the $2^{-\Delta\Delta CT}$ method and normalized to the mRNA levels of *GAPDH*.

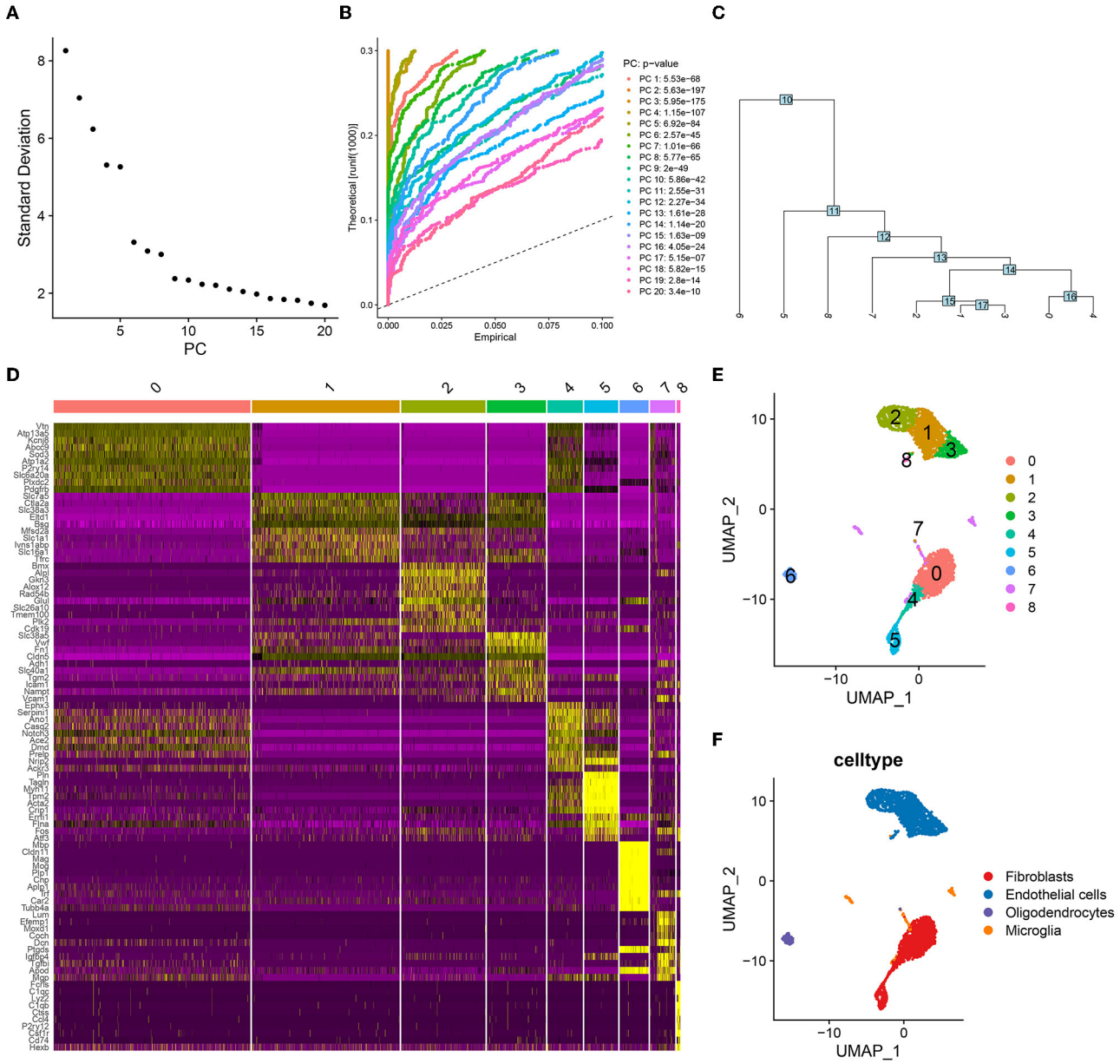

FIGURE 1 | Cell clustering and annotation processes in single-cell analysis. **(A)** The top twenty principal components (PCs) were ranked according to the extent of the explanatory difference between them. According to the calculation, several PCs between 10 and 20 may cover all features of ICI. Here, 15 PCs are selected for the following round of investigation. **(B)** The top 20 PCs were found to be significantly enriched for features with low P-values. **(C)** A tree was constructed during the cell-clustering phase and nine distinct cell clusters were obtained. **(D)** The heat map shows the significant differences in the expression of marker genes in these nine cell clusters. **(E)** UMAP visualized the distribution of nine cell clusters. **(F)** These four cell clusters were annotated as fibroblasts, endothelial cells, oligodendrocytes and microglia, respectively.

Statistical Analysis

Statistical analysis and graphing were performed using R software (version 4.0.2). Gene regulatory networks based on SCENIC analysis were constructed using the pySCENIC (v. 0.11) package in Python. The Pearson's correlation analysis was performed to calculate the correlation between two measured variables. Statistical significance was set at $P < 0.05$.

RESULTS

Single-Cell Data Filtering and Cell Fractionation

First, we filtered the mouse cerebrovascular scRNA-seq data according to a set threshold (i.e., traits expressed in a minimum of 3 cells and cells with a minimum of 500 traits expressed were screened for inclusion in the study). A total of 3,186 cells

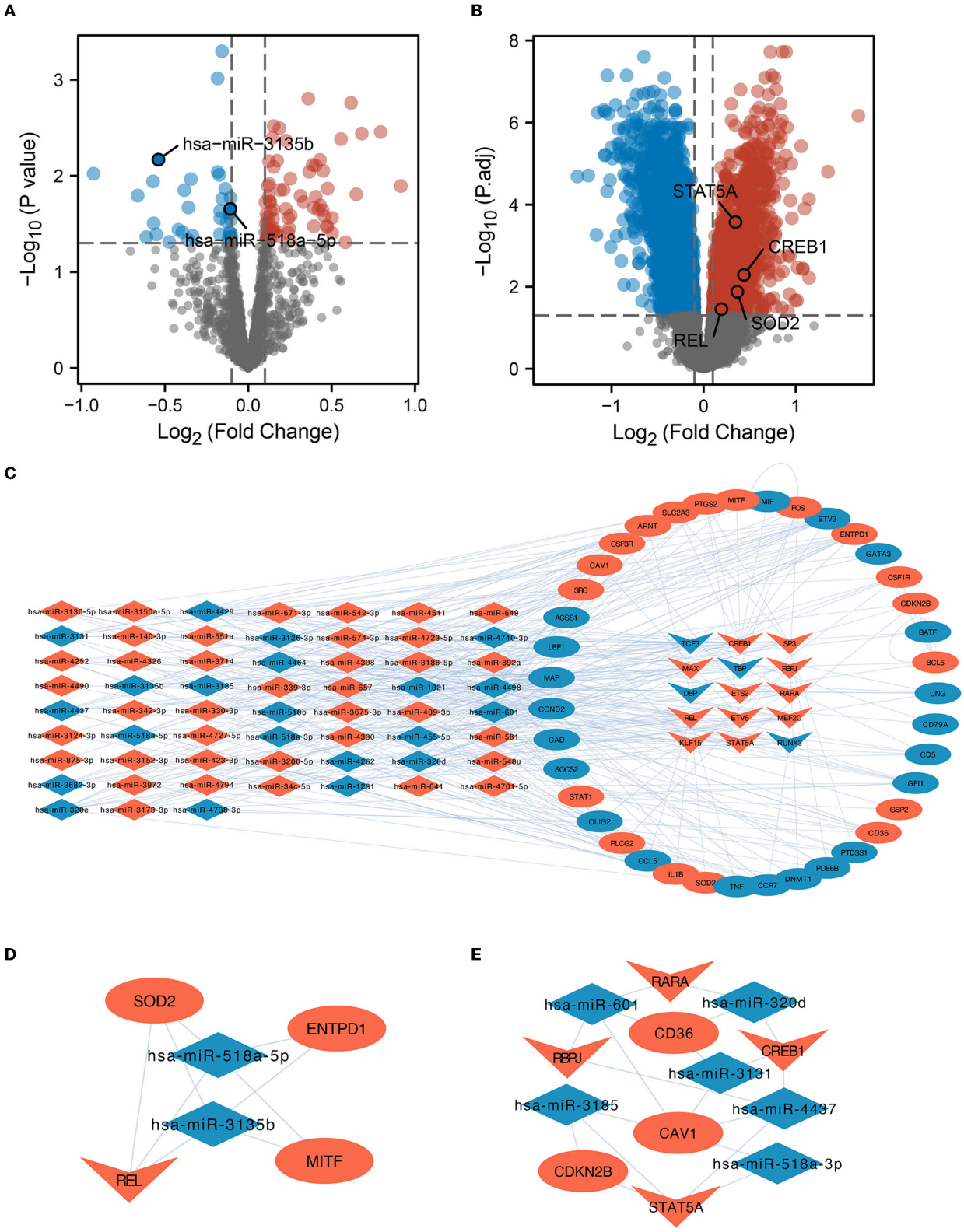

FIGURE 2 | Variance analysis and PPI network construction. **(A)** A map of differentially expressed micro RNAs (DEmiRNAs) in the form of a volcano. The important miRNAs were identified and tagged. **(B)** Differentially expressed messenger RNA (DE-mRNA) volcano map. The diagram labels important transcription factors (TFs)

(Continued)

FIGURE 2 | and genes in the protein-protein interaction (PPI) sub-network. **(C)** Network investigation of miRNA-TF-gene connections. The network diagram depicts the connections between dysregulated miRNAs, TFs, and target genes. Dysregulated microRNAs are represented by the diamond, dysregulated genes are represented by the oval, and transcription factors are represented by the inner quadrilateral. Increased regulation is shown by the color red, whilst lower regulation is indicated by the color blue. **(D)** REL is the core TF in the PPI network. Subnetwork 1 of PPI and REL/superoxide dismutase 2 (SOD2) was regulated by the hsa-miR-518a-5p and hsa-miR-3135b microRNAs. **(E)** RARA, CREB1, RBPJ, and STAT5A were shown to be the most critical TFs in PPI Subnetwork 2.

were obtained for subsequent analysis. We estimated the top 2,000 DEGs and analyzed their expression patterns using PCA. The top 10–20 PCs were selected (**Figure 1A**). The JackStraw plot also verified that the top 20 PCs were enriched in most of the features with low *P*-values (**Figure 1B**). Fifteen PCs were selected for further clustering analysis, the results of which revealed nine-cell clusters (**Figure 1C**). The expression of the marker genes for these nine-cell clusters is depicted as a heat map in **Figure 1D**. The UMAP diagram depicts the clustering of these nine-cell clusters (**Figure 1E**). Based on the results of singleR and cell markers, the cell types were further classified as fibroblasts, endothelial cells, oligodendrocytes, and microglia (**Figure 1F**). Subsequently, we used SCENIC to identify 266 regulons, as well as the accompanying gene regulatory networks in four cell groups.

miRNA-TF-mRNA Interactions Analysis

Bulk RNAs were analyzed for differences in their expression between the ICI and HC groups based on GSE16561 and GSE55937. We found 73 upregulated and 39 downregulated miRNAs (**Figure 2A**), as well as 1,496 upregulated and 2,284 downregulated mRNAs, based on the filtering conditions (**Figure 2B**). Moreover, we found 11,525 DEmiRNA-DEmRNA interaction pairs using the prediction results of the miRWalk database. Based on the prediction results of the TRRUST database and the 266 regulons identified by SCENIC analysis, we identified 20 regulons and their corresponding target genes. Finally, the identified DEmiRNAs, DETFs, and DE gene mRNAs were used to build the miRNA-TF-gene interaction network (**Figure 2C**). Using MCODE, two key sub-networks (**Figures 2D,E**) were identified in this network. The REL was identified as the key TF in sub-network 1, while *SOD2* was identified as a target gene of REL (**Figure 2D**). Therefore, the hsa-miR-518a-5p and hsa-miR-3135b were found to control the expressions of *REL* and *SOD2*. Furthermore, TFs [Retinoic Acid Receptor Alpha (RARA), Recombination Signal Binding Protein For Immunoglobulin Kappa J Region (RBPJ), CAMP Responsive Element Binding Protein 1 (CREB1), and Signal Transducer and Activator of Transcription 5A (STAT5A)] and microRNAs (hsa-miR-601, hsa-miR-320d, hsa-miR-3131, hsa-miR-4437, hsa-miR-518-3p, and hsa-miR-3185) co-regulate mRNAs (CD36, CAV1, and CDKN2B) in sub-network 2 (**Figure 2E**). Here, potential mechanisms of ICI are uncovered based on miRNA-TF-mRNA integration analysis.

Functional Pathways Enriched in the Core Network

Next, enrichment analysis of mRNAs in sub-networks 1 and 2 was conducted to investigate the pathways involved in the core sub-network. The findings revealed that the ICI group had increased functions and pathways involved in viral oncogenesis, DNA-binding transcriptional activator activity, transcription factor complex, and myeloid cell differentiation (**Figure 3A**). Then, we performed a functional enrichment analysis of the downstream target genes of the transcription factor REL based on the findings of SCENIC prediction. The findings revealed that the downstream molecules of *REL* were mostly enriched in the functional pathways of the actin cytoskeleton, positive control of muscle tissue development, eicosanoid biosynthetic process, and mitotic nuclear division regulation (**Figure 3B**). The results of the above enrichment analysis exemplify the potential functions and pathways enriched by these TFs and guide the way for further research.

Expression of REL in Mouse Cerebrovascular Cells

We analyzed the expression of key regulons in the gene interaction network in mouse cerebrovascular cells. Firstly, TFs in endothelial cells and fibroblasts were sorted for presentation according to the regulon specificity score (RSS) (**Figures 4A,B**). The t-Distributed Stochastic Neighbor Embedding (tSNE) plots in **Figures 4C,D** show the distribution of REL expression in endothelial cells and fibroblasts. Furthermore, the expression of *REL* is presented in the tSNE plot (**Figure 4E**). **Figure 4F** depicts the motifs of the downstream target genes of *REL*. The results revealed that REL is highly expressed in both endothelial cells and fibroblasts. However, *REL* is potentially regulated by hsa-miR-518-5p/hsa-miR-3135b (**Figure 2D**). We concluded that hsa-miR-518-5p/hsa-miR-3135b-regulated *REL*/*SOD2* plays a potential role in ICI progression.

Expression of REL/SOD2 in Clinical Cohorts

The qRT-PCR was performed on blood samples from ICI and HC to further validate the results of the bioinformatic analysis in a clinical cohort. The expressions of *REL* and *SOD2* were significantly higher in the ICI group than in the HC group ($P < 0.05$) (**Figure 5A**). Additionally, results of PCA revealed a positive correlation between *SOD2* and *REL* expressions ($r = 0.325$, $P = 0.027$) (**Figure 5B**). These findings confirm that *REL* and *SOD2* are dysregulated in the ICI group.

GSEA in Samples With Upregulated *REL* Expression

The GSEA was performed to further explore the pathways associated with *REL* expression. The results revealed

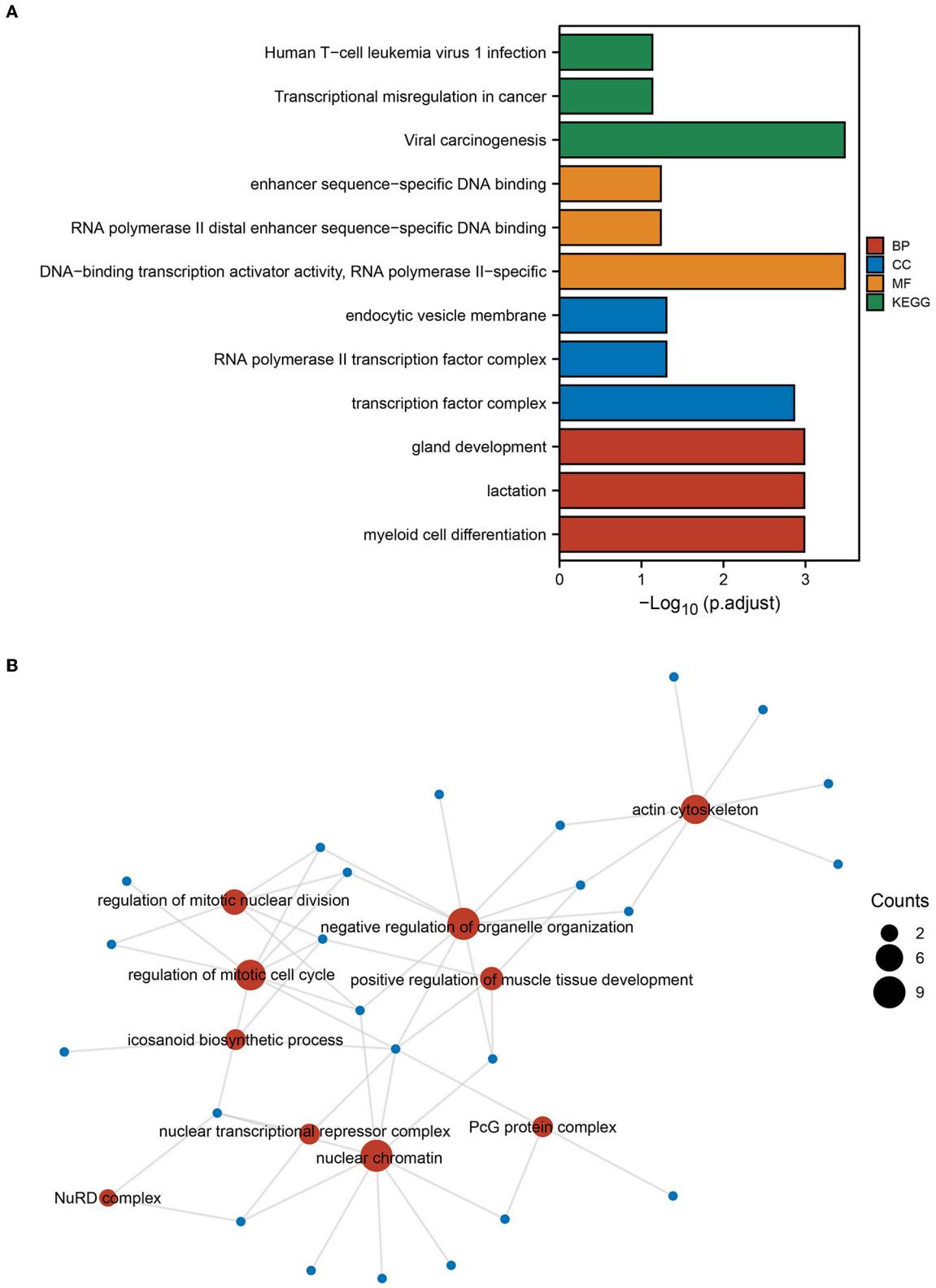

FIGURE 3 | GO and KEGG enrichment analysis. **(A)** Gene Ontology (GO) and Kyoto Encyclopedia of Genes and Genomes (KEGG) enrichment analysis of genes from PPI subnetwork 1 and subnetwork 2 gene. **(B)** Based on the results of the single-cell regulatory network inference and clustering (SCENIC) analysis, GO functional enrichment analysis was performed for genes downstream of the transcription factor REL. The size of the dot indicates the number of genes.

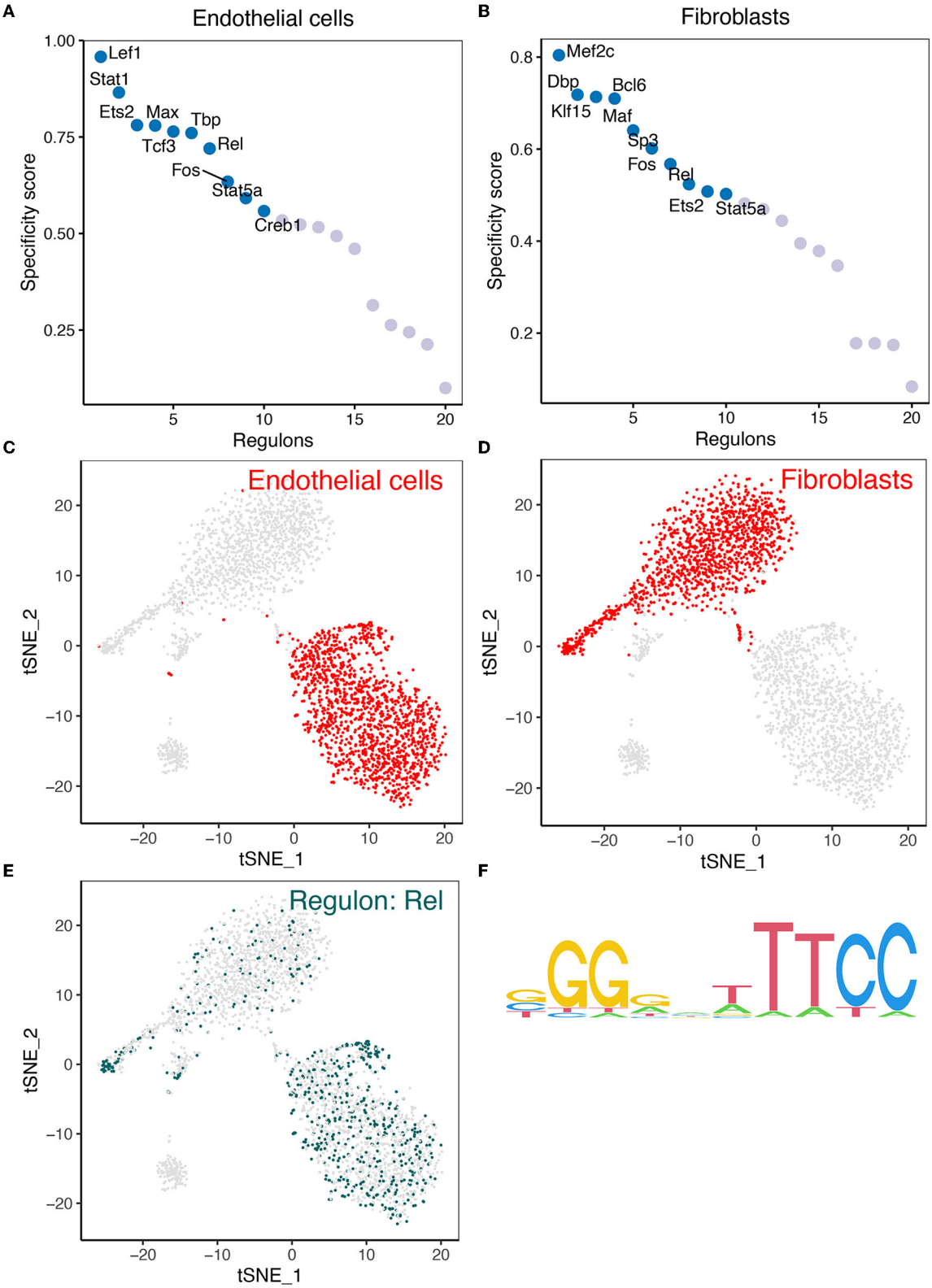

FIGURE 4 | The findings of the SCENIC investigation of REL. **(A)** The regulon specificity score was used to rate the various regulators in endothelial cells. **(B)** The regulon specificity score was used to rank the various regulators in fibroblasts. **(C)** In the tSNE map, endothelial cells are visible. **(D)** Fibroblasts are visualized in the tSNE map. **(E)** *REL* was discovered to be significantly expressed in endothelial cells and fibroblasts. As can be seen, endothelial cells have greater levels of REL expression than fibroblasts. **(F)** Base distribution in REL-functioning motifs.

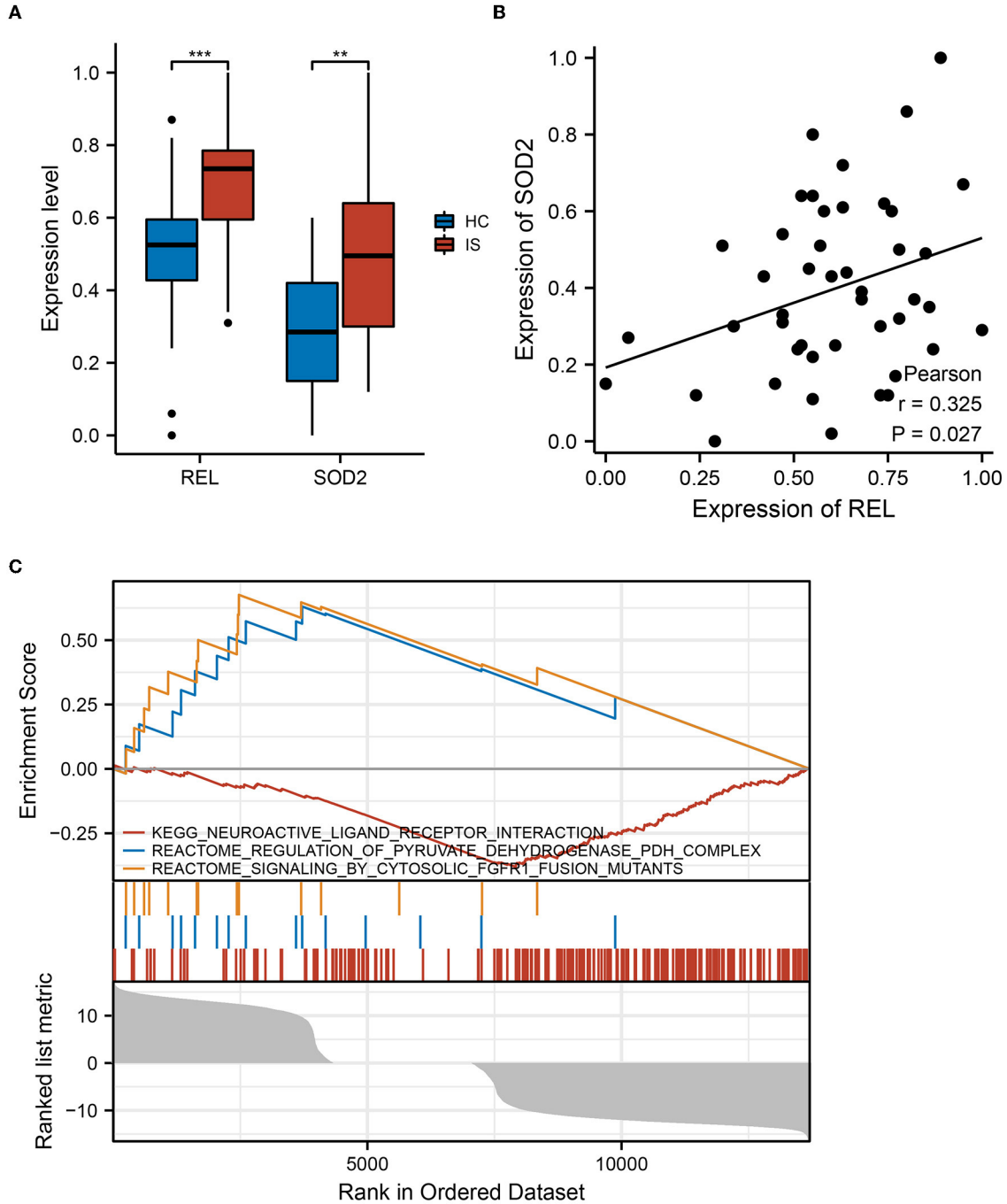

FIGURE 5 | REL and SOD2 expression in clinical cohorts. **(A)** There was a substantial difference in REL and SOD2 expression between the healthy controls (HC) and Ischaemic cerebral infarction (ICI) groups. The ICI group had greater levels of REL and SOD2 expression than the HC group, and the results were statistically significant ($P = 0.05$). **means the p-value is less than 0.01, ***means the p-value is less than 0.001. **(B)** Pearson correlation analysis revealed a strong positive correlation between SOD2 and REL expression ($r = 0.325$, $P = 0.027$). **(C)** In samples with high REL expression, gene set enrichment analysis (GSEA) reveals up- and downregulated functional pathways.

that neuroactive ligand-receptor interaction and pyruvate dehydrogenase (PDH) complex regulation pathways were upregulated in samples with increased *REL* expression, but the cytosolic Fibroblast growth factor receptor 1 (FGFR1) fusion mutant signaling pathway was downregulated (**Figure 5C**). These findings imply that REL may be associated with the

action of numerous neurotransmitters and their receptors, thus, affecting neurological and psychiatric symptoms. Additionally, REL may be involved in changes in oxidative phosphorylation, which is associated with ICI.

DISCUSSION

The major miRNA-TF-mRNA regulatory network in the ICI was investigated employing a bioinformatic approach that integrated single-cell analysis with bulk RNA-seq data. This study uncovered novel biomarkers for ICI of neurovascular disease. The hsa-miR-518-5p/hsa-miR-3135b/REL/SOD2 was identified as a potential player in ICI progression. The expression of the key molecules was also validated in clinical samples and at the single-cell level.

In this study, we first tried to construct two miRNA-TF-mRNA interaction networks and then found that REL was the key transcription factor. A miRNA-TF-mRNA interaction network was established and then two major sub-networks from this network were constructed. We also uncovered novel biomarkers for ICI of neurovascular disease. The hsa-miR-518-5p/(hsa-miR-3135b)/REL/SOD2 was identified as a key pathway involved in the course of ICI in sub-network 1. The RARA, CREB1, RBPJ, and STAT5A were identified as TFs involved in ICI progression in another network sub-network (sub-network 2). The REL and SOD2 expression were higher in the ICI group than in the clinical cohort. The REL expression was also enhanced in endothelial cells and fibroblasts at the single-cell level, indicating that it is a cell-specific regulon. Functional enrichment analyses revealed that REL is implicated in neurotransmitter activity and oxidative phosphorylation pathways.

No previous study has elucidated the direct role of miRNA-518 and miR-3135b in ICI. The hsa-miRNA-518 and its target gene Early growth response factor 1 (*EGR1*) are implicated in the regulation of cell proliferation, death, and angiogenesis (43). The *EGR1* serves as a pro-inflammatory factor in experimental animal models and is implicated in post-ischemic inflammation, inflammation-induced blood-brain barrier (BBB) dysfunction, and ischemic brain injury, suggesting that it plays a role in ICI progression (44–47). The peroxisome proliferator-activated receptor alpha (*PPAR*) mRNA may also be targeted by miR-518 (48). The PPAR suppresses the expression of the pro-inflammatory factor EGR1, which is important for lipid homeostasis and inflammation (44, 49). In a model of experimental IS, the PPARic stroke exped the (ul13) infarct volume (43, 44). The miR-518 may play a role in the evolution of ICI by regulating PPAR and EGR1. Human endothelial cells exposed to acrolein, an unsaturated aldehyde capable of generating oxidative stress and inflammation, showed higher expression of miR-518 (50). As a result, we postulate that miRNA-518 is implicated in IS-related inflammation and vascular endothelial dysfunction. In individuals with severe hypertension, miR-3135b expression was found to be dramatically increased (51, 52). Additionally, miR-3135b is linked to coronary artery calcification and is an excellent marker for the diagnosis of obstructive coronary artery disease (53). In contrast, diabetes, hypertension, atherosclerosis, and other metabolic disorders are all risk factors for ICI (26, 54–56). As a result, we postulate that miR-3135b has a role in ICI as well. Moreover, based on the increased expression of REL and SOD2 in patients with ICI compared to healthy controls, we postulated that hsa-miR-518-5p and hsa-miR-3135b were downregulated in ICI. The hsa-miR-518-5p and hsa-miR-3135b, which are differentially expressed in IS, are implicated in ICI progression *via* the regulation of the core TF, REL, and its target gene *SOD2* in the ICI regulatory network. Therefore, based on our study and previous studies showing the significance of miR-518 and miR-3135b in IS-related pathogenic processes, we suggest that both may affect the development of ICI through various pathways.

The miRNAs can form gene regulatory networks by targeting TFs (57). The miRNAs may contribute significantly to the development of AS by controlling the proliferation, differentiation, and function of vascular smooth muscle cells through TF regulation, thereby affecting the course of ICI (26–28). Similar to previous findings, the current study showed that hsa-miR-518-5p and hsa-miR-3135b regulate the expression of their target gene *SOD2* by targeting the core TF REL, which forms the key regulatory network for ICI development. In this study, REL and SOD2 were highly expressed in patients with cerebral infarction at the bulk RNA, single-cell RNA, and clinical levels. Previous research indicates that v-rel reticuloendotheliosis viral oncogene homolog A (RELA) may enhance inflammatory responses and apoptosis in cerebral hemorrhage, however, c-REL may exert the opposite effect (58). Additionally, RELA, RELB, and c-REL, all of which are involved in the production of pro-inflammatory cytokines, are related to NF-κB-mediated inflammatory disorders (59). Inhibition of NF-κB activation prevented cerebral ischemia/reperfusion injury in rats (60). Inflammation is a risk factor for ICI and is associated with poor patient prognosis (61, 62). Therefore, we postulate that REL may affect the course of ICI and, hence, affect patient prognosis. Similarly, one study discovered that SOD2 is a mitochondrial enzyme with increased mRNA expression in patients with type 2 diabetes mellitus and those with Parkinson's disease (63). The SOD2 is involved in a variety of biological processes, including inflammation, glucose metabolism, and lipid metabolism, all of which contribute to the development of ICI (64–66). In this study, *SOD2* was identified as a target gene of REL in the ICI gene regulatory network. We found that REL might be involved in the activity of various neurotransmitters and their receptors, which may affect neurological and psychiatric symptoms. Therefore, we postulate that REL and ROS contribute significantly to ICI progression.

Along with the major sub-network hsa-miR-518-5p/hsa-miR-3135b/REL/SOD2, we identified a sub-network containing the transcription factors RARA, CREB1, RBPJ, and STAT5A. Previous studies have found that activation of RARA can exert neuroprotective effects after ischemic brain injury. Tanka et al. found a significant increase in phosphorylated CREB levels in the peri-infarct region after focal cerebral ischemia (67). The RBPJ is an important transcription factor of the

Notch signaling pathway (68). Activation of the Notch signaling pathway is associated with atherogenesis and inflammatory responses, which are risk factors for ICI (26, 69, 70). After cerebral ischemia, activated STAT5 could improve the hypoxia tolerance of neurons and inhibit apoptosis, as well as participate in the protective effect of brain tissue (71). Similar to previous studies, we found that RARA, CREB1, RBPJ, and STAT5A may be critical transcription factors implicated in the development of ICI.

We studied the miRNA-TF-gene interaction network (hsa-miR-518-5p/hsa-miR-3135b regulates the REL/SOD2 pathway), which may play a critical role in ICI progression. Our research uncovered novel biomarkers for ICI of neurovascular disease. The findings of this shed light on the mechanism of ICI development and are expected to facilitate the identification of novel targets and therapeutic strategies for the treatment of ICI. There are certain limitations to the present study. In the future, the sample size for inclusion in the study should be further expanded. Since the findings of this study are mostly based on bioinformatic analysis, the identified signaling pathways still require experimental validation, including elucidation of their mechanisms of action, *in vitro* and *in vivo*.

CONCLUSION

Our research uncovered novel biomarkers for ICI of neurovascular disease. The REL/SOD2 pathway is important in the formation of ICI as a key network route and may be regulated by hsa-miR-518-5p/hsa-miR-3135b. This study's findings provide insight on the potential relevance of the REL/SOD2 pathway in IS, paving the way for additional research into ICI mechanisms.

DATA AVAILABILITY STATEMENT

Publicly available datasets were analyzed in this study. This data can be found here: National Center for Biotechnology Information (NCBI) Gene Expression Omnibus (GEO), https://www.ncbi.nlm.nih.gov/geo/, GSE16561, GSE55937 and GSE98816.

ETHICS STATEMENT

The studies involving human participants were reviewed and approved by the Institutional Ethics Review Board of the Xijing Hospital. Written informed consent to participate in this study was provided by the patient/participants' or patient/participants legal guardian/next of kin.

AUTHOR CONTRIBUTIONS

BZ: software, validation, formal analysis, data curation, and writing—original draft. XJ: conceptualization, methodology, supervision, writing—review and editing, and project administration. Both authors contributed to the article and approved the submitted version.

ACKNOWLEDGMENTS

We would like to express our sincere gratitude to all patients who participated in this study.

REFERENCES

1. Guo M, Wang X, Zhao Y, Yang Q, Ding H, Dong Q, et al. Ketogenic diet improves brain ischemic tolerance and inhibits NLRP3 inflammasome activation by preventing Drp1-mediated mitochondrial fission and endoplasmic reticulum stress. *Front Mol Neurosci.* (2018) 11:86. doi: 10.3389/fnmol.2018.00086
2. Zhao B, Shi Q, Zhang Z, Wang S, Wang X, Wang H. Protective effects of paeonol on subacute/chronic brain injury during cerebral ischemia in rats. *Exp Ther Med.* (2018) 15:3836–46. doi: 10.3892/etm.2018.5893
3. Zheng Z, Liu S, Wang C, Wang C, Tang D, Shi Y, et al. Association of genetic polymorphisms in CASP7 with risk of ischaemic stroke. *Sci Rep.* (2019) 9:18627. doi: 10.1038/s41598-019-55201-y
4. Bonita R, Mendis S, Truelsen T, Bogousslavsky J, Toole J, Yatsu F. The global stroke initiative. *Lancet Neurol.* (2004) 3:391–3. doi: 10.1016/S1474-4422(04)00800-2
5. Weinstein JR, Koerner IP, Möller T. Microglia in ischemic brain injury. *Fut Neurol.* (2010) 5:227–46. doi: 10.2217/fnl.10.1
6. Shang Y, Chen L, Toborek M, Yu G. Diffuse optical monitoring of repeated cerebral ischemia in mice. *Opt Express.* (2011) 19:20301. doi: 10.1364/OE.19.020301
7. Favate AS, Younger DS. Epidemiology of ischemic stroke. *Neurol Clin.* (2016) 34:967–80. doi: 10.1016/j.ncl.2016.06.013
8. Benjamin EJ, Virani SS, Callaway CW, Chamberlain AM, Chang AR, Cheng S, et al. Heart disease and stroke statistics-−2018 update: a report from the American Heart Association. *Circulation.* (2018) 137:e67–492. doi: 10.1161/CIR.0000000000000558
9. Zhang Q, Zhang L, Yang X, Wan Y, Jia J. The effects of exercise preconditioning on cerebral blood flow change and endothelin-1 expression after cerebral ischemia in rats. *J Stroke Cerebrovasc Dis.* (2014) 23:1696–702. doi: 10.1016/j.jstrokecerebrovasdis.2014.01.016
10. Tang F, Barbacioru C, Wang Y, Nordman E, Lee C, Xu N, et al. mRNA-Seq whole-transcriptome analysis of a single cell. *Nat Methods.* (2009) 6:377–82. doi: 10.1038/nmeth.1315
11. Alberter B, Klein CA, Polzer B. Single-cell analysis of CTCs with diagnostic precision: opportunities and challenges for personalized medicine. *Expert Rev Mol Diagn.* (2016) 16:25–38. doi: 10.1586/14737159.2016.1121099
12. Martijn J, Schulz F, Zaremba-Niedzwiedzka K, Viklund J, Stepanauskas R, Andersson SGE, et al. Single-cell genomics of a rare environmental alphaproteobacterium provides unique insights into Rickettsiaceae evolution. *ISME J.* (2015) 9:2373–85. doi: 10.1038/ismej.2015.46
13. Lake BB, Chen S, Sos BC, Fan J, Kaeser GE, Yung YC, et al. Integrative single-cell analysis of transcriptional and epigenetic states in the human adult brain. *Nat Biotechnol.* (2018) 36:70–80. doi: 10.1038/nbt.4038
14. Fuzik J, Zeisel A, Máté Z, Calvigioni D, Yanagawa Y, Szabó G, et al. Integration of electrophysiological recordings with single-cell RNA-seq data identifies neuronal subtypes. *Nat Biotechnol.* (2016) 34:175–83. doi: 10.1038/nbt.3443
15. Johnson MB, Walsh CA. Cerebral cortical neuron diversity and development at single-cell resolution. *Curr Opin Neurobiol.* (2017) 42:9–16. doi: 10.1016/j.conb.2016.11.001
16. Gate D, Saligrama N, Leventhal O, Yang AC, Unger MS, Middeldorp J, et al. Clonally expanded CD8 T cells patrol the cerebrospinal fluid in Alzheimer's disease. *Nature.* (2020) 577:399–404. doi: 10.1038/s41586-019-1895-7

17. Vanlandewijck M, He L, Mäe MA, Andrae J, Ando K, Del Gaudio F, et al. A molecular atlas of cell types and zonation in the brain vasculature. *Nature.* (2018) 554:475–80. doi: 10.1038/nature25739
18. Aibar S, González-Blas CB, Moerman T, Huynh-Thu VA, Imrichova H, Hulselmans G, et al. SCENIC: single-cell regulatory network inference and clustering. *Nat Methods.* (2017) 14:1083–6. doi: 10.1038/nmeth.4463
19. Reddy PH, Tonk S, Kumar S, Vijayan M, Kandimalla R, Kuruva CS, et al. A critical evaluation of neuroprotective and neurodegenerative MicroRNAs in Alzheimer's disease. *Biochem Biophys Res Communic.* (2017) 483:1156–65. doi: 10.1016/j.bbrc.2016.08.067
20. Vijayan M, Reddy PH. Peripheral biomarkers of stroke: focus on circulatory microRNAs. *Biochim Biophys Acta.* (2016) 1862:1984–93. doi: 10.1016/j.bbadis.2016.08.003
21. Selvamani A, Williams MH, Miranda RC, Sohrabji F. Circulating miRNA profiles provide a biomarker for severity of stroke outcomes associated with age and sex in a rat model. *Clin Sci.* (2014) 127:77–89. doi: 10.1042/CS20130565
22. Ryu CS, Oh SH, Lee KO, Park HS, An HJ, Lee JY, et al. MiR-10a, 27a, 34b/c, and 300 polymorphisms are associated with ischemic stroke susceptibility and post-stroke mortality. *Life.* (2020) 10:309. doi: 10.3390/life10120309
23. Lidong D, Zhanghong X, Huawu M, Xiaofang H, Junhua G, Kaifu K, et al. Ischemia modified albumin and miR-126 play important role in diagnosis of posterior circulation transient ischemic attack and prediction of secondary cerebral infarction. *Neurol India.* (2021) 69:75–80. doi: 10.4103/0028-3886.310100
24. Vijayan M, Kumar S, Yin X, Zafer D, Chanana V, Cengiz P, et al. Identification of novel circulatory microRNA signatures linked to patients with ischemic stroke. *Hum Mol Genet.* (2018) 27:2318–29. doi: 10.1093/hmg/ddy136
25. Liu Y, Zhang J, Han R, Liu H, Sun D, Liu X. Downregulation of serum brain specific microRNA is associated with inflammation and infarct volume in acute ischemic stroke. *J Clin Neurosci.* (2015) 22:291–5. doi: 10.1016/j.jocn.2014.05.042
26. Mujaj B, Bos D, Muka T, van der Lugt A, Ikram MA, Vernooij MW, et al. Antithrombotic treatment is associated with intraplaque haemorrhage in the atherosclerotic carotid artery: a cross-sectional analysis of The Rotterdam Study. *Eur Heart J.* (2018) 39:3369–76. doi: 10.1093/eurheartj/ehy433
27. Li P, Zhu N, Yi B, Wang N, Chen M, You X, et al. MicroRNA-663 regulates human vascular smooth muscle cell phenotypic switch and vascular neointimal formation. *Circ Res.* (2013) 113:1117–27. doi: 10.1161/CIRCRESAHA.113.301306
28. Iaconetti C, De Rosa S, Polimeni A, Sorrentino S, Gareri C, Carino A, et al. Down-regulation of miR-23b induces phenotypic switching of vascular smooth muscle cells *in vitro* and *in vivo*. *Cardiovasc Res.* (2015) 107:522–33. doi: 10.1093/cvr/cvv141
29. Barr TL, Conley Y, Ding J, Dillman A, Warach S, Singleton A, et al. Genomic biomarkers and cellular pathways of ischemic stroke by RNA gene expression profiling. *Neurology.* (2010) 75:1009–14. doi: 10.1212/WNL.0b013e3181f2b37f
30. Jickling GC, Ander BP, Zhan X, Noblett D, Stamova B, Liu D. microRNA expression in peripheral blood cells following acute ischemic stroke and their predicted gene targets. *PLoS ONE.* (2014) 9:e99283. doi: 10.1371/journal.pone.0099283
31. Stuart T, Butler A, Hoffman P, Hafemeister C, Papalexi E, Mauck WM, et al. comprehensive integration of single-cell data. *Cell.* (2019) 177:1888–902.e21. doi: 10.1016/j.cell.2019.05.031
32. Lin W, Wang Y, Chen Y, Wang Q, Gu Z, Zhu Y. Role of calcium signaling pathway-related gene regulatory networks in ischemic stroke based on multiple WGCNA and single-cell analysis. *Oxid Med Cell Longev.* (2021) 2021:1–35. doi: 10.1155/2021/8060477
33. Chen Y, Sun Y, Xu Y, Lin W-W, Luo Z, Han Z, et al. Single-cell integration analysis of heterotopic ossification and fibrocartilage developmental lineage: endoplasmic reticulum stress effector Xbp1 transcriptionally regulates the notch signaling pathway to mediate fibrocartilage differentiation. *Oxid Med Cell Longev.* (2021) 2021:1–29. doi: 10.1155/2021/7663366
34. Lin W-W, Xu L-T, Chen Y-S, Go K, Sun C, Zhu Y-J. Single-cell transcriptomics-based study of transcriptional regulatory features in the mouse brain vasculature. *Biomed Res Int.* (2021) 2021:1–15. doi: 10.1155/2021/7643209
35. Wu J, Qin J, Li L, Zhang K, Chen Y, Li Y, et al. Roles of the immune/methylation/autophagy landscape on single-cell genotypes and stroke risk in breast cancer microenvironment. *Oxid Med Cell Longev.* (2021) 2021:1–32. doi: 10.1155/2021/5633514
36. Ritchie ME, Phipson B, Wu D, Hu Y, Law CW, Shi W, et al. Limma powers differential expression analyses for RNA-sequencing and microarray studies. *Nucleic Acids Res.* (2015) 43:e47. doi: 10.1093/nar/gkv007
37. Feng W, Yang J, Song W, Xue Y. Crosstalk between Heart Failure and Cognitive Impairment via hsa-miR-933/RELB/CCL21 Pathway. *Biomed Res Int.* (2021) 2021:1–16. doi: 10.1155/2021/2291899
38. Han H, Cho J-W, Lee S, Yun A, Kim H, Bae D, et al. TRRUST v2: an expanded reference database of human and mouse transcriptional regulatory interactions. *Nucleic Acids Res.* (2018) 46:D380–6. doi: 10.1093/nar/gkx1013
39. Yu G, Wang L-G, Han Y, He Q-Y. clusterProfiler: an R package for comparing biological themes among gene clusters. *OMICS J Integrat Biol.* (2012) 16:284–7. doi: 10.1089/omi.2011.0118
40. Subramanian A, Tamayo P, Mootha VK, Mukherjee S, Ebert BL, Gillette MA, et al. Gene set enrichment analysis: a knowledge-based approach for interpreting genome-wide expression profiles. *Proc Natl Acad Sci.* (2005) 102:15545–50. doi: 10.1073/pnas.0506580102
41. Williamson-Reisdorph CM, Quindry TS, Tiemessen KG, Cuddy J, Hailes W, Slivka D, et al. Blood oxidative stress and post-exercise recovery are unaffected byhypobaric and hypoxic environments. *J Sports Sci.* (2021) 39:1356–65. doi: 10.1080/02640414.2021.1872960
42. Mohammadi SM, Mohammadnejad D, Hosseinpour Feizi AA, Movassaghpour AA, Montazersaheb S, Nozad Charoudeh H. Inhibition of c-REL using siRNA increased apoptosis and decreased proliferation in pre-B ALL blasts: therapeutic implications. *Leuk Res.* (2017) 61:53–61. doi: 10.1016/j.leukres.2017.08.012
43. Yang W, Lu Z, Zhi Z, Liu L, Deng L, Jiang X, et al. High-throughput transcriptome-Seq and small RNA-Seq reveal novel functional genes and microRNAs for early embryonic arrest in humans. *Gene.* (2019) 697:19–25. doi: 10.1016/j.gene.2018.12.084
44. Li Y-Y, Guo J-H, Liu Y-Q, Dong J-H, Zhu C-H. PPARγ activation-mediated Egr-1 inhibition benefits against brain injury in an experimental ischaemic stroke model. *J Stroke Cerebrovasc Dis.* (2020) 29:105255. doi: 10.1016/j.jstrokecerebrovasdis.2020.105255
45. Yan S-F, Fujita T, Lu J, Okada K, Shan Zou Y, Mackman N, et al. Egr-1, a master switch coordinating upregulation of divergent gene families underlying ischemic stress. *Nat Med.* (2000) 6:1355–61. doi: 10.1038/82168
46. Okada M, Fang Yan S, Pinsky DJ. Peroxisome proliferator-activated receptor-γ (PPAR-γ) activation suppresses ischemic induction of Egr-1 and its inflammatory gene targets. *FASEB J.* (2002) 16:1861–8. doi: 10.1096/fj.02-0503com
47. Tureyen K, Brooks N, Bowen K, Svaren J, Vemuganti R. Transcription factor early growth response-1 induction mediates inflammatory gene expression and brain damage following transient focal ischemia. *J Neurochem.* (2008) 105:1313–24. doi: 10.1111/j.1471-4159.2008.05233.x
48. Peyrou M, Ramadori P, Bourgoin L, Foti M. PPARs in liver diseases and cancer: epigenetic regulation by microRNAs. *PPAR Res.* (2012) 2012:1–16. doi: 10.1155/2012/757803
49. Zhao C, Zhang T, Shi Z, Ding H, Ling X. MicroRNA-518d regulates PPARα protein expression in the placentas of females with gestational diabetes mellitus. *Mol Med Rep.* (2014) 9:2085–90. doi: 10.3892/mmr.2014.2058
50. Lee SE, Yang H, Son GW, Park HR, Cho J-J, Ahn H-J, et al. Identification and characterization of MicroRNAs in acrolein-stimulated endothelial cells: implications for vascular disease. *Biochip J.* (2015) 9:144–55. doi: 10.1007/s13206-015-9303-3
51. Shi J, Ren Y, Liu Y, Cheng Y, Liu Y. Circulating miR-3135b and miR-107 are potential biomarkers for severe hypertension. *J Hum Hypertens.* (2021) 35:343–50. doi: 10.1038/s41371-020-0338-0
52. Wang F, Li Z, Zhao M, Ye W, Wu H, Liao Q, et al. Circulating miRNAs miR-574-5p and miR-3135b are potential metabolic regulators for serum lipids and blood glucose in gestational diabetes mellitus. *Gynecol Endocrinol.* (2021) 37:665–71. doi: 10.1080/09513590.2021.1908990
53. Liu W, Ling S, Sun W, Liu T, Li Y, Zhong G, et al. Circulating microRNAs correlated with the level of coronary artery calcification in symptomatic patients. *Sci Rep.* (2015) 5:16099. doi: 10.1038/srep16099

54. Naito H, Hosomi N, Kuzume D, Nezu T, Aoki S, Morimoto Y, et al. Increased blood pressure variability during the subacute phase of ischemic stroke is associated with poor functional outcomes at 3 months. *Sci Rep*. (2020) 10:811. doi: 10.1038/s41598-020-57661-z
55. Kissela BM, Khoury J, Kleindorfer D, Woo D, Schneider A, Alwell K, et al. Epidemiology of ischemic stroke in patients with diabetes. *Diabetes Care*. (2005) 28:355–9. doi: 10.2337/diacare.28.2.355
56. Boden-Albala B, Sacco RL, Lee H-S, Grahame-Clarke C, Rundek T, Elkind MV, et al. Metabolic syndrome and ischemic stroke risk: northern Manhattan study. *Stroke*. (2008) 39:30–5. doi: 10.1161/STROKEAHA.107.496588
57. Alves-Junior L, Niemeier S, Hauenschild A, Rehmsmeier M, Merkle T. Comprehensive prediction of novel microRNA targets in *Arabidopsis thaliana*. *Nucleic Acids Res.* (2009) 37:4010–21. doi: 10.1093/nar/gkp272
58. Zhang Z-L, Song Y, Li F, Huang Q-B. Bimodal distribution of nuclear factor-κB activation and expression of subunits in experimental models of intracerebral hemorrhage *in vivo*. *J Stroke Cerebrovasc Dis.* (2019) 28:821–9. doi: 10.1016/j.jstrokecerebrovasdis.2018.11.028
59. Sun J, Huang P, Liang J, Li J, Shen M, She X, et al. Cooperation of Rel family members in regulating Aβ1-40-mediated pro-inflammatory cytokine secretion by retinal pigment epithelial cells. *Cell Death Dis.* (2017) 8:e3115. doi: 10.1038/cddis.2017.502
60. Deng Y, Xiong D, Yin C, Liu B, Shi J, Gong Q. Icariside II protects against cerebral ischemia–reperfusion injury in rats via nuclear factor-κB inhibition and peroxisome proliferator-activated receptor up-regulation. *Neurochem Int*. (2016) 96:56–61. doi: 10.1016/j.neuint.2016.02.015
61. Mo Y, Sun Y-Y, Liu K-Y. Autophagy and inflammation in ischemic stroke. *Neural Regen Res.* (2020) 15:1388. doi: 10.4103/1673-5374.274331
62. Wu KK, Kuo C-C, Yet S-F, Lee C-M, Liou J-Y. 5-methoxytryptophan: an arsenal against vascular injury and inflammation. *J Biomed Sci.* (2020) 27:79. doi: 10.1186/s12929-020-00671-w
63. Santiago JA, Scherzer CR, Potashkin JA. Network analysis identifies SOD2 mRNA as a potential biomarker for Parkinson's Disease. *PLoS ONE.* (2014) 9:e109042. doi: 10.1371/journal.pone.0109042
64. Schramm F, Kern A, Barthel C, Nadaud S, Meyer N, Jaulhac B, et al. Microarray analyses of inflammation response of human dermal fibroblasts to different strains of Borrelia burgdorferi Sensu Stricto. *PLoS ONE.* (2012) 7:e40046. doi: 10.1371/journal.pone.0040046
65. Kang L, Dai C, Lustig ME, Bonner JS, Mayes WH, Mokshagundam S, et al. Heterozygous SOD2 deletion impairs glucose-stimulated insulin secretion, but not insulin action, in high-fat–fed mice. *Diabetes.* (2014) 63:3699–710. doi: 10.2337/db13-1845
66. Singh BK, Kumar A, Ahmad I, Kumar V, Patel DK, Jain SK, et al. Oxidative stress in zinc-induced dopaminergic neurodegeneration: implications of superoxide dismutase and heme oxygenase-1. *Free Rad Res.* (2011) 45:1207–22. doi: 10.3109/10715762.2011.607164
67. Tanaka K, Nagata E, Suzuki S, Dembo T, Nogawa S, Fukuuchi Y. Immunohistochemical analysis of cyclic AMP response element binding protein phosphorylation in focal cerebral ischemia in rats. *Brain Res.* (1999) 818:520–6. doi: 10.1016/s0006-8993(98)01263-3
68. Lake RJ, Tsai P-F, Choi I, Won K-J, Fan H-Y. RBPJ, the major transcriptional effector of notch signaling, remains associated with chromatin throughout mitosis, suggesting a role in mitotic bookmarking. *PLoS Genet*. (2014) 10:e1004204. doi: 10.1371/journal.pgen.1004204
69. Liu Z-J, Tan Y, Beecham GW, Seo DM, Tian R, Li Y, et al. Notch activation induces endothelial cell senescence and pro-inflammatory response: implication of Notch signaling in atherosclerosis. *Atherosclerosis.* (2012) 225:296–303. doi: 10.1016/j.atherosclerosis.2012.04.010
70. Meng L, Bai Z, He S, Mochizuki K, Liu Y, Purushe J, et al. The notch ligand DLL4 defines a capability of human dendritic cells in regulating Th1 and Th17 differentiation. *JI.* (2016) 196:1070–80. doi: 10.4049/jimmunol.1501310
71. Harrison DA. The JAK/STAT pathway. *Cold Spring Harbor Perspect Biol.* (2012) 4:a011205. doi: 10.1101/cshperspect.a011205

Conflict of Interest: The authors declare that the research was conducted in the absence of any commercial or financial relationships that could be construed as a potential conflict of interest.

Publisher's Note: All claims expressed in this article are solely those of the authors and do not necessarily represent those of their affiliated organizations, or those of the publisher, the editors and the reviewers. Any product that may be evaluated in this article, or claim that may be made by its manufacturer, is not guaranteed or endorsed by the publisher.

Copyright © 2022 Zhao and Jiang. This is an open-access article distributed under the terms of the Creative Commons Attribution License (CC BY). The use, distribution or reproduction in other forums is permitted, provided the original author(s) and the copyright owner(s) are credited and that the original publication in this journal is cited, in accordance with accepted academic practice. No use, distribution or reproduction is permitted which does not comply with these terms.

frontiers | Frontiers in Neurology

ORIGINAL RESEARCH
published: 14 April 2022
doi: 10.3389/fneur.2022.860124

Association of Blood Pressure Within 6 h After Endovascular Thrombectomy and Functional Outcomes in Ischemic Stroke Patients With Successful Recanalization

Xuening Zhang[1], Ting Cui[1], Qiange Zhu[2], Changyi Wang[3,4], Anmo Wang[1], Yuan Yang[1], Shucheng Li[1], Fayun Hu[1†] and Bo Wu[1*†]*

[1] Department of Neurology, West China Hospital, Sichuan University, Chengdu, China, [2] Second Department of Neurology, Shaanxi Provincial People's Hospital, Xi'an, China, [3] Department of Rehabilitation Medicine Center, West China Hospital, Sichuan University, Chengdu, China, [4] Key Laboratory of Rehabilitation Medicine in Sichuan Province, West China Hospital, Sichuan University, Chengdu, China

Background and Purpose: Blood pressure in the days following endovascular thrombectomy (EVT) can influence functional outcomes of patients who have suffered an acute ischemic stroke, but whether the same is true of blood pressure during the first few hours after EVT is unclear.

Methods: Several blood pressure parameters were retrospectively analyzed in acute ischemic stroke patients who underwent EVT at West China Hospital from March 2016 to December 2019. Baseline blood pressure, speed of blood pressure reduction, postoperative blood pressure, degree of blood pressure reduction, and quality of blood pressure management were evaluated during the first 24 h after EVT. We explored whether these parameters during different time windows correlated significantly with patients' modified Rankin Scale (mRS) score at 90 days.

Results: Analysis of 163 patients showed that poor functional outcome (mRS scores 3–6) correlated significantly with higher postoperative blood pressure and worse blood pressure management during the first 6 h after EVT. Postoperative systolic blood pressure at 37 min after EVT was significantly higher in patients with poor outcome (141 mmHg) than in those with good outcome (mRS scores 0–2; 122 mmHg, $p = 0.006$), and systolic pressure >136 mmHg at this time point was associated with a significantly higher risk of poor outcome, before and after adjusting for other risk factors (adjusted OR 0.395, 95% CI 0.20–0.79).

Conclusions: Among acute ischemic patients who successfully undergo recanalization, adequate blood pressure management during the first 30–40 min after EVT may be important for ensuring good 90-day functional outcomes.

Keywords: brain ischemia, cerebral Infarction, stroke, endovascular procedures, thrombectomy, cerebral revascularization, blood pressure, hypertension

OPEN ACCESS

Edited by:
Yuzhen Xu,
Tongji University, China

Reviewed by:
Jie Pan,
People's Hospital of Hangzhou Medical College, China
Longfei Wu,
Capital Medical University, China
Michael Abraham,
University of Kansas Medical Center, United States

***Correspondence:**
Fayun Hu
hufayun2006@163.com
Bo Wu
dr.bowu@hotmail.com

† These authors have contributed equally to this work and share last authorship

Specialty section:
This article was submitted to Neurological Biomarkers, a section of the journal Frontiers in Neurology

Received: *22 January 2022*
Accepted: *02 March 2022*
Published: *14 April 2022*

Citation:
Zhang X, Cui T, Zhu Q, Wang C, Wang A, Yang Y, Li S, Hu F and Wu B (2022) Association of Blood Pressure Within 6 h After Endovascular Thrombectomy and Functional Outcomes in Ischemic Stroke Patients With Successful Recanalization. Front. Neurol. 13:860124. doi: 10.3389/fneur.2022.860124

INTRODUCTION

Since its description in 2015, endovascular thrombectomy (EVT) has become a standard method for treating large-vessel acute ischemic stroke within 6 h of onset (1), and large clinical trials suggest that it remains effective even when performed up to 24 h after onset (2, 3). How blood pressure management before and after EVT affects patient outcomes remains uncertain, which makes it difficult to optimize such management.

Several studies have suggested that lower blood pressure during 24 h after EVT is associated with a better prognosis (4–6), but we are unaware of studies examining whether blood pressure sooner after EVT is also important. This is an important question, given that the blood pressure of most acute ischemic stroke patients stabilizes at 6–8 h after EVT (7).

Therefore, we performed a retrospective observational study to explore whether blood pressure parameters during the first 6 h after EVT significantly influence functional outcomes.

METHODS

Study Population

Medical records were retrospectively examined for acute ischemic stroke patients who underwent EVT at West China Hospital from March 2016 to December 2019. Follow-up information was derived from a database we set up prospectively since 2016 for all ischemic stroke patients admitted to West China Hospital and underwent reperfusion. Patients were considered eligible for the present study if they were older than 18 years, underwent emergency EVT for acute ischemic stroke affecting the anterior circulation [including the internal carotid artery (ICA), middle cerebral artery (MCA), and anterior cerebral artery (ACA)], and underwent successful recanalization after EVT [defined as the modified Thrombolysis in Cerebral Infarction score (mTICI) $\geq$2b]. Patients were excluded if blood pressure data were missing for any of the following time points: on admission, every hour during the first 6 h after EVT, and every 2 h until 24 h after EVT. Patients were also excluded if computed tomography (CT) data were unavailable within 24 h after EVT, or if the modified Rankin Scale (mRS) score at 90 days after EVT was unknown.

This study was approved by the Institutional Review Board of West China Hospital, which waived the requirement for written informed consent because, at the time of treatment, patients or their legal guardians gave informed oral consent for the patient's anonymized medical data to be analyzed and published for research purposes.

Procedures and Treatment

Patient eligibility for EVT was determined based on established clinical guidelines (8). Vasopressors or the antihypertensives urapidil hydrochloride or nicardipine hydrochloride were injected at the attending physician's discretion to control blood pressure. The blood pressure target of patients during the first 24 h after EVT in this study was 120 mmHg, which reflects the standard practice at our hospital for acute ischemic stroke patients who successfully undergo recanalization.

Blood Pressure Parameters

BP values at set points were measured non-invasively. Based on the blood pressure information, we calculated parameters reflecting 5 aspects of blood pressure profiles: (1) baseline BP level: including admission SBP and the first postoperative SBP (FPO SBP). FPO SBP was the SBP value patients on their first measurement when they returned to the ward after EVT; (2) postoperative BP level: including mean SBP and minimum SBP; (3) degree of BP reduction: including FPO SBP-mean SBP, FPO SBP-minimum SBP (FPO SBP-mean SBP)/FPO SBP and (FPO SBP-minimum SBP)/FPO SBP; (4) velocity of BP reduction: indicated by the time from FPO SBP to the minimum SBP record during the first 6 h after EVT; (5) BP management quality: including maximum SBP and the time below 120 and 140 mmHg. The threshold of 140 mmHg was chosen because several studies have proposed it as a target blood pressure during the first 24 h after EVT for patients with successful recanalization (9–11).

Time points of measurements were divided into intervals of 0.5 h. Measurements for the abovementioned parameters, excluding baseline blood pressure and speed of BP reduction, were categorized into the following four intervals after EVT: 1–6, 7–12, 13–18, and 19–24 h.

Outcomes and Covariates

The primary study outcome was the mRS score at 90 days, which was determined through telephone interviews with patients or their legal guardians. Good outcome was defined as mRS scores 0–2, while poor outcome was defined as mRS scores 3–6. The secondary study outcome was intracerebral hemorrhage (ICH) which may have occurred during hospitalization and malignant cerebral edema (defined as the development of clinical signs of herniation, including a decrease in consciousness and/or anisocoria), accompanied by prominent imaging evidence of brain swelling (i.e., midline shift of brain structure or effacement of basal cisterns).

We collected data on numerous covariates to adjust for their potential influence in our analyses and thereby isolate the influence of blood pressure at different times after EVT. Covariates included age; sex; history of hypertension, diabetes, coronary heart disease, cardiac dysfunction, and atrial fibrillation; pre-EVT laboratory findings, such as fasting blood glucose, low-density lipoprotein, prothrombin time, and international normalized ratio; Alberta Stroke Program Early Computed Tomography Score (ASPECTS) on pre-EVT computed tomography; score on the National Institutes of Health Stroke Scale (NIHSS) at admission; occluded segment; prior treatment with intravenous alteplase; time from onset to puncture (OTP); postoperative hypotension, underwent decompressive craniectomy and postoperative residual moderate to severe stenosis.

Statistical Analysis

Continuous data were expressed as mean $\pm$ standard deviation if normally distributed, or as median (interquartile range, IQR) otherwise. Categorical data were expressed as n (%). The

normality of data distribution was assessed using the Shapiro-Wilk test. Analyses were conducted initially across all patients for whom covariate data were complete. Differences between patients with poor or good outcome and between patients with or without intracerebral hemorrhage were assessed for significance using a chi-squared test in the case of categorical data, Student's *t* test in the case of normally distributed continuous data, or the Mann-Whitney U test in the case of skewed continuous data.

Variables with a $p < 0.1$ in univariate analysis were entered into two logistic regression models: Model 1 adjusted for gender, fasting blood glucose, and NIHSS; Model 2 adjusted for age and ASPECTS. Multiple imputation was used to fill in missing values. Stratified analysis was performed based on whether systolic blood pressure at admission was <140 or ≥140 mmHg, patients had ICA occlusion or not, time from onset to thrombectomy was ≤6h, and patients had cardiac dysfunction or not. We set the systolic blood pressure threshold at 140 mmHg because a previous study found that systolic pressures higher than this value were associated with higher mRS score (9).

We also performed four analyses to examine closely the potential relationship between the first postoperative systolic blood pressure and the primary study outcome. First, we created a generalized additive model to describe how the 90-day mRS score varied with first postoperative systolic blood pressure. Second, we created a linear regression model to describe how the risk of poor functional outcome changed with increasing first postoperative systolic blood pressure. Third, we determined the first postoperative systolic blood pressure that best predicted good or poor functional outcome based on receiver operating characteristic curves and the Youden index. Fourth, we dichotomized first postoperative systolic blood pressure values at the cut-off values and assessed the association of each group of values with functional outcome using the chi-squared test and the abovementioned logistic regression models.

All regressions and imputations were conducted using SPSS for Windows (version 26.0; IBM, Chicago, IL, USA). Data were plotted and Student tests were performed using GraphPad Prism for Windows (version 8.01; GraphPad Software, San Diego, CA, USA). Generalized additive modeling was conducted using R (version 4.1). Differences were considered significant at a level of $\alpha = 0.05$.

RESULTS

Characteristics of the Study Population

Of the 206 consecutive patients reviewed for enrollment, 163 were included in the final analysis (**Figure 1**). The median age of the 163 patients was 69 years (IQR 59–78) and mean NIHSS was 15 (SD 5) (**Table 1**). One-third of patients (49, 30.1%) had ICA occlusion. All patients underwent EVT under general anesthesia.

Just over half of patients (90, 55.2%) had poor functional outcome at 90 days. These patients were older and showed more severe infarction reflected in a lower rate of ASPECTS > 6 and higher NIHSS score than patients with good functional outcome.

Associations of Functional Outcome With Various Blood Pressure Parameters During the First 24 h After EVT

Patients who experienced good or poor functional outcomes did not differ significantly in systolic blood pressure at admission (141 ± 24 vs. 149 ± 27 mmHg, $p = 0.072$, **Table 2**). In contrast, those with poor functional outcome showed significantly higher systolic blood pressure at the first postoperative measurement (141 vs. 122 mmHg, $p = 0.006$), which was taken an average of 37 min (95%CI 34–40) after EVT.

During the first 6 h after EVT, patients with poor functional outcomes showed significantly higher postoperative blood pressure, in terms of mean SBP ($p = 0.023$) and minimum SBP ($p = 0.011$) (**Table 2**). Those patients also showed worse quality of blood pressure management, reflected in significantly higher maximum SBP ($p = 0.005$) and shorter time when SBP was below 140 mmHg ($p = 0.025$). During the other time windows analyzed during the first 24 h after EVT, patients who experienced good or poor functional outcomes did not differ significantly in any of the blood pressure parameters except the degree of blood pressure reduction (**Table 2**).

Consistent with these results, logistic regression Model 1 showed significant correlations of functional outcome with the first postoperative measurement of systolic blood pressure as well as minimum and maximum values of systolic blood pressure during the first 6 h after EVT. However, the significance did not remain when adjusted for age and ASPECT in Model 2 (**Supplementary Table 1**).

When we dichotomized patients based on whether the first postoperative measurement of systolic blood pressure was <140 or ≥140 mmHg, we found that none of the other blood pressure parameters correlated significantly with the functional outcome in both subgroups (data not shown). Among the subgroups of patients with ICA occlusion, time from onset to puncture (<6h), or without cardiac dysfunction, good functional outcome significantly correlated with lower FPO BP, lower postoperative blood pressure, and better quality of blood pressure management during the first 6 h. Among patients without ICA occlusion, functional outcome correlated significantly with maximum and minimum systolic blood pressures during the first 6 h. Among patients with admission SBP ≥140 mmHg, good functional outcome correlated significantly with lower FPO BP and lower maximum SBP during the first 6 h (**Supplementary Table 2**). Our additional comparison of patients with or without ICA occlusion showed that the two subgroups did not differ significantly in systolic blood pressure at admission or the first postoperative measurement, nor in mean or maximum systolic blood pressures during any time windows within the first 24 h after EVT (data not shown).

Further Analysis of the Association Between Functional Outcome and the First Postoperative Measurement of Systolic Blood Pressure

A generalized additive model showed that an increase in the first postoperative measurement of systolic blood pressure was

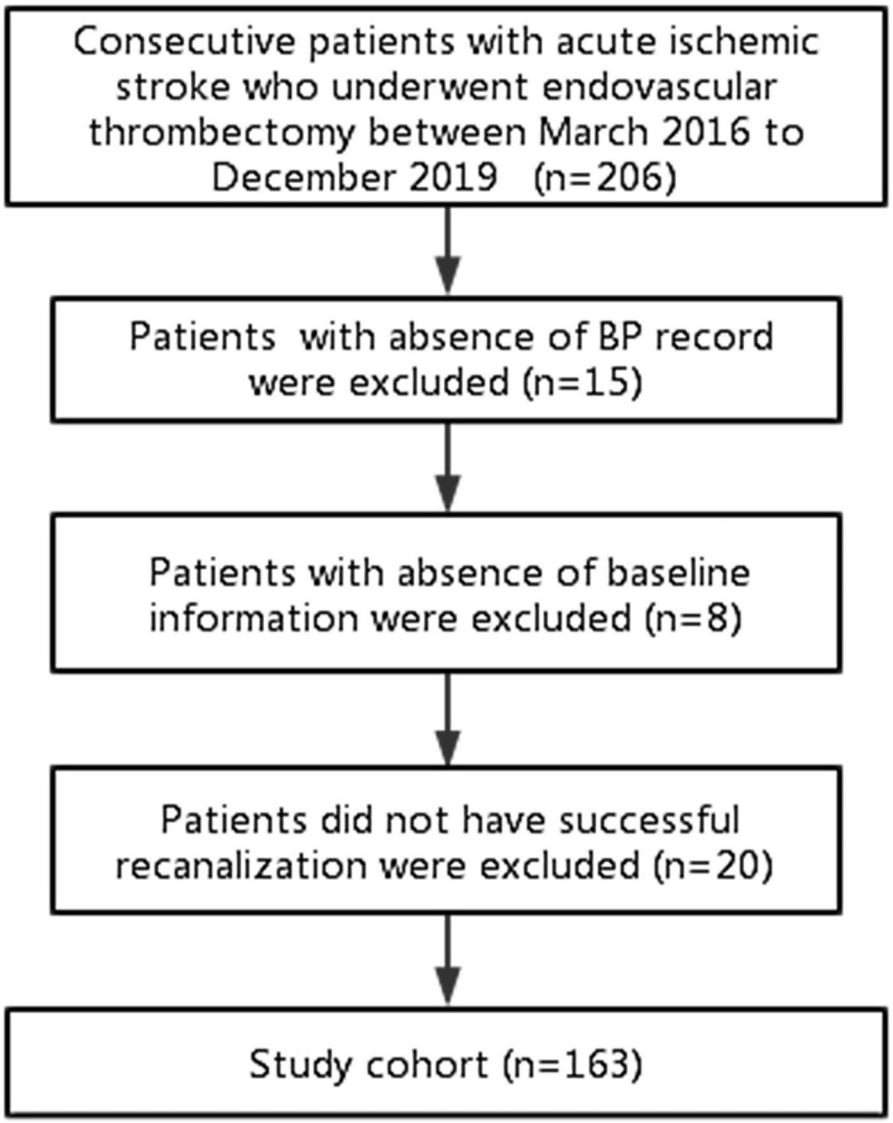

FIGURE 1 | Flowchart of patient inclusion.

associated with poor functional outcomes (**Figure 2A**). In fact, each 10-mmHg increase in this measurement, as long as it remained below 160 mmHg, raised the risk of poor outcome in a linear fashion ($\beta = 0.073$, $p = 0.004$, $R^2 = 0.91$; **Figure 2B**). The Youden index identified a value of 136 mmHg as able to discriminate between patients who experienced good or poor functional outcomes. The area under the receiver operating characteristic curve was 0.63 (95%CI 0.54–0.71, $p = 0.006$), sensitivity was 57%, and specificity was 67%.

Significant correlation of higher FPO BP dichotomized at 136 mmHg and poor functional outcome was shown in both univariate analysis ($p = 0.004$; OR 2.55; 95%CI 1.34–4.85) and logistic regression (model 1 $p = 0.009$, OR 0.395; 95%CI 0.20–0.79; model 2 $p = 0.329$, OR 0.69; 95%CI 0.32–1.46) (**Figure 3**). Patients with first postoperative systolic blood pressure above 136 mmHg had significantly higher postoperative blood pressure and worse quality of blood pressure management during the first 6 h after EVT (**Supplementary Table 3**). Their systolic blood pressure also took significantly longer to fall from the first postoperative level to the minimum level during the first 6 h.

Associations of Intracerebral Hemorrhage and Baseline Characteristics or Various Blood Pressure Parameters During the First 24 h After EVT

Of the 163 patients we included, 61 patients (37%) had ICH during hospitalization. These patients were more likely to suffer malignant cerebral edema and have lower ASPECTS, higher NIHSS score and higher fasting blood

TABLE 1 | Baseline characteristics of study population compared between patients with good and poor functional outcome (mRS 0–2 vs. 3–6).

	Total number	90-day mRS			Missing (good/poor)
		Good, *n* (%)	Poor, *n* (%)	*p*-value (unadjusted)	
Number of patients	163	73 (44.8)	90 (55.2)		
Patient characteristics					
Age, y, median (IQR)	69 (59–78)	63 (53–74)	74 (64–80)	**<0.001**	
Female	74 (0.45)	25 (0.34)	49 (0.54)	**0.012**	
ASPECTS 6–10	103 (68.2)	57 (86.4)	46 (54.1)	**<0.001**	7/5
NIHSS score (mean ± SD)	15 ± 5	13 ± 6	17 ± 5	**<0.001**	1/0
Previous use of IV thrombolysis	56 (34.4)	27 (37.0)	29 (32.2)	0.638	
OTP [mean (SD)]	4.64 (1.11)	4.58 (0.99)	4.69 (1.21)	0.56	3/5
Postoperative hypotension	12 (7.4)	3 (4.1)	9 (10.0)	0.258	
Decompressive craniectomy	4 (2.5)	1 (1.4)	3 (3.4)	0.76	
Malignant cerebral edema	23 (14.1)	2 (2.7)	21 (23.3)	**<0.001**	
Postoperative residual stenosis (moderate or severe)	25 (15.6)	11 (15.5)	14 (15.7)	1	
ICH during hospitalization	61 (37.4)	20 (27.4)	41 (45.6)	**0.026**	
Medical history					
Hypertension	80 (49.1)	33 (45.2)	47 (52.2)	0.463	
Diabetes mellitus	32 (19.6)	10 (13.7)	22 (24.4)	0.129	
Coronary heart disease	24 (14.7)	10 (13.7)	14 (15.6)	0.912	
Cardiac dysfunction	44 (27.0)	18 (24.7)	26 (28.9)	0.669	
Atrial fibrillation	75 (46.0)	29 (39.7)	46 (51.1)	0.196	
Laboratory index					
Fasting blood glucose, median (IQR)	7.3 (6.3–9)	6.9 (6.1–8.3)	7.5 (6.7–9.6)	**0.012**	0/1
LDL, median (IQR)	2.4 (1.9–2.9)	2.7 (2.1–2.9)	2.4 (1.9–3)	0.201	0/1
PT, median (IQR)	11.5 (10.8–12.4)	11.4 (10.8–12.4)	11.7 (10.9–12.3)	0.597	0/2
INR, median (IQR)	1.01 (0.97–1.10)	1.02 (0.95–1.09)	1.01 (0.97–1.11)	0.344	0/2
Occluded segment					
ICA	49 (30.1)	18 (24.7)	31(34.4)	0.237	
M1	71 (43.6)	33 (45.2)	38 (42.2)	0.823	
M2	36 (22.1)	20 (27.4)	16 (17.8)	0.2	
Other*	9 (5.5)	2 (2.7)	7 (7.8)	0.291	

mRS, modified Rankin scale; IQR, interquartile range; ASPECT, alberta stroke program early CT score; NIHSS, national institute of health stroke Scale; SD, standard deviation; IV, intravenous; OTP, time from onset to puncture; ICH, intracerebral hemorrhage; PT, prothrombin time; INR, international normalized ratio; ICA, internal carotid artery; M(segment), middle cerebral artery; A(segment), anterior cerebral artery.

**A1/A2/M3 occlusion. Bold values means p-values ≤ 0.05.*

glucose than patients without ICH (**Supplementary Table 4**). As data showed in **Supplementary Table 5**, no significant association was found between blood pressure parameters and intracerebral hemorrhage.

DISCUSSION

Our analysis of acute ischemic stroke patients who underwent EVT found that higher blood pressure within 6 h after the procedure correlated with worse functional outcomes at 90 days, particularly in patients with ICA occlusion or without cardiac dysfunction. In particular, using various approaches, we demonstrated an association between blood pressure within 30–40 min after EVT and functional outcome. Increasing blood pressure at this early time point correlated with increasing mRS score at 90 days, and blood pressure of 136 mmHg at this time point predicted reasonably well which patients later experienced poor or good functional outcome. Our study suggests that blood pressure should be adequately managed early after EVT to ensure good outcomes.

Differences in blood pressure parameters, especially postoperative blood pressure, between patients with good or poor functional outcomes were larger during the first 6 h after EVT than during other time windows within the first 24 h. Our results are consistent with previous studies reporting that clinical outcomes were significantly associated with mean blood pressure (12) or maximum systolic blood pressure (13) during the first 6 h after EVT. The importance of adequate blood pressure immediately after EVT may have several explanations. One is that cerebral autoregulation may be injured during the acute phase of ischemic stroke, leading to dysregulation of blood pressure (5, 14, 15). The effects of such dysregulation may be exacerbated by the large fluctuations in perfusion soon after recanalization. A second explanation may be that blood pressure

TABLE 2 | Associations between BP parameters and functional outcomes (mRS 0–2 vs. 3–6).

		90-day mRS				Missing (good/poor)
		Total	Good (74)	Poor (109)	*p*-value (unadjusted)	
Baseline BP level						
Admission SBP (mean ± SD)		145 ± 26	141 ± 24	149 ± 27	0.072	0/5
FPO SBP [median (IQR)]		133 (112–152)	122 (107–148)	141 (117–155)	**0.006**	
Postoperative BP level						
Mean SBP (mean ± SD)	A	128 ± 14	125 ± 14	130 ± 14	**0.023**	
	B	121 ± 14	120 ± 14	122 ± 13	0.212	
	C	121 ± 14	121 ± 15	122 ± 13	0.685	
	D	123 ± 15	122 ± 15	125 ± 16	0.253	
Minimum SBP (mean ± SD)	A	110 ± 13	107 ± 12	112 ± 14	**0.011**	
	B	112 ± 14	112 ± 13	113 ± 14	0.626	
	C	111 ± 14	111 ± 14	111 ± 14	0.888	
	D	114 ± 15	112 ± 15	114 ± 16	0.402	
BP reduction degree						
FPO SBP-Mean SBP (mean ± SD)	A	6 ± 21	3 ± 20	9 ± 21	0.055	
	B	13 ± 29	8 ± 28	17 ± 30	0.059	
	C	13 ± 29	7 ± 28	18 ± 28	**0.020**	
	D	11 ± 28	6 ± 27	15 ± 28	**0.050**	
FPO SBP-Minimum SBP (mean ± SD)	A	24 ± 25	21 ± 24	27 ± 26	0.136	
	B	22 ± 30	16 ± 28	27 ± 31	**0.028**	
	C	23 ± 29	17 ± 28	28 ± 30	**0.011**	
	D	21 ± 30	16 ± 27	26 ± 31	**0.026**	
(FPO SBP-Mean SBP)/FPO SBP (mean ± SD)	A	0.02 ± 0.15	−0.01 ± 0.15	0.04 ± 0.14	**0.041**	
	B	0.06 ± 0.20	0.03 ± 0.20	0.09 ± 0.20	0.064	
	C	0.06 ± 0.20	0.02 ± 0.21	0.10 ± 0.19	**0.017**	
	D	0.05 ± 0.19	0.02 ± 0.20	0.08 ± 0.19	**0.045**	
(FPO SBP-Minimum SBP)/FPO SBP (mean ± SD)	A	0.16 ± 0.14	0.14 ± 0.14	0.17 ± 0.14	0.155	
	B	0.13 ± 0.20	0.09 ± 0.19	0.16 ± 0.20	**0.032**	
	C	0.14 ± 0.19	0.10 ± 0.19	0.17 ± 0.19	**0.011**	
	D	0.13 ± 0.20	0.09 ± 0.19	0.16 ± 0.20	**0.030**	
Velocity of BP reduction						
Time from FPO to the minimum SBP A (h)		2.5 (1.0-5.0)	2.5 (0.5-4.5)	3.0 (1.1-5.0)	0.104	
BP management quality median (mean)						
Time under 120 mmHg (h)	A	2 (2.52)	2.5 (2.79)	2 (2.29)	0.119	
	B	3 (3.11)	3 (3.24)	3 (3.01)	0.430	
	C	3 (3.6)	3 (4.15)	3 (3.14)	0.628	
	D	2 (2.84)	4 (3.12)	2 (2.61)	0.290	
Time under 140 mmHg (h)	A	5 (4.61)	6 (4.89)	5 (4.38)	**0.025**	
	B	6 (5.33)	6 (5.45)	6 (5.23)	0.564	
	C	6 (5.39)	6 (5.37)	6 (5.41)	0.805	
	D	6 (5.15)	6 (5.18)	6 (5.12)	0.548	
Maximum SBP (mean ± SD)	A	152 ± 25	146 ± 23	157 ± 25	**0.005**	
	B	131 ± 16	129 ± 15	133 ± 16	0.099	
	C	131 ± 16	129 ± 16	132 ± 15	0.144	
	D	132 ± 16	129 ± 17	134 ± 16	**0.046**	

mRS, modified Rankin scale; BP, blood pressure; SBP, systolic blood pressure; SD, standard deviation; FPO SBP, the first postoperative SBP; h, hours; A, 0–6 h following procedural; B, 7–12 h following procedural; C, 13–18 h following procedural; D, 19–24 h following procedural. Bold values means p-values ≤ 0.05.

soon after EVT may rise above preoperative levels but then decrease over the next several hours until stabilizing (6, 7). Blood pressure fluctuations may be more damaging when blood pressure is already high, which may help explain why functional outcomes can be so sensitive to blood pressure management early after EVT. Third, our previous study revealed that the

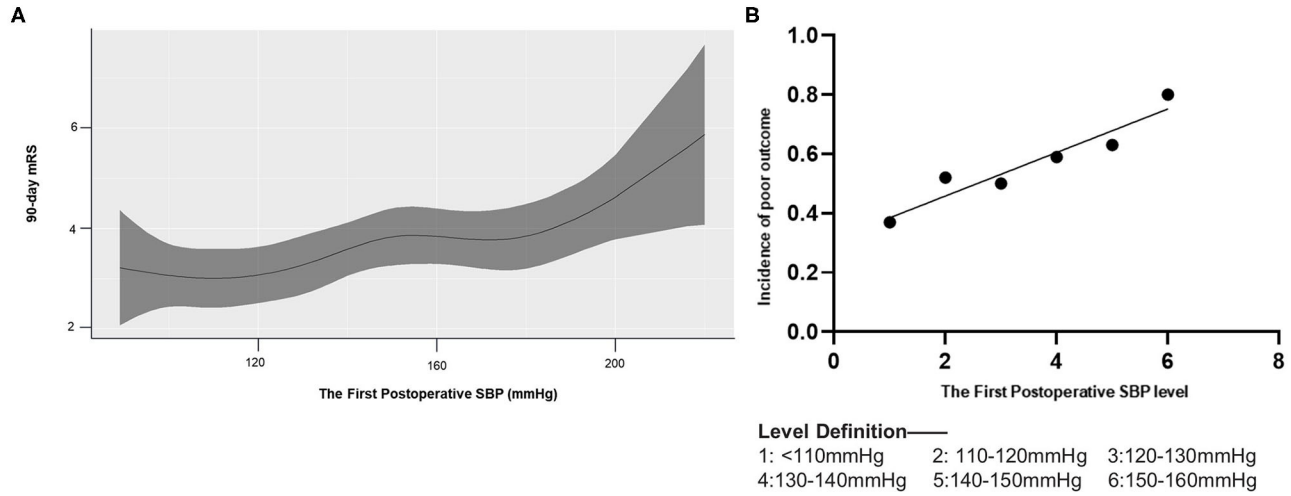

FIGURE 2 | Association of 90-day mRS and the first postoperative SBP. mRS, modified Rankin Scale. **(A)** A generalized additive model with the line shows predictive values of 90-day mRS score according to the first postoperative SBP (the shade represents 95% CI of them). **(B)** Linear regression model for the first postoperative SBP and the incidence of poor outcome (mRS 3–6).

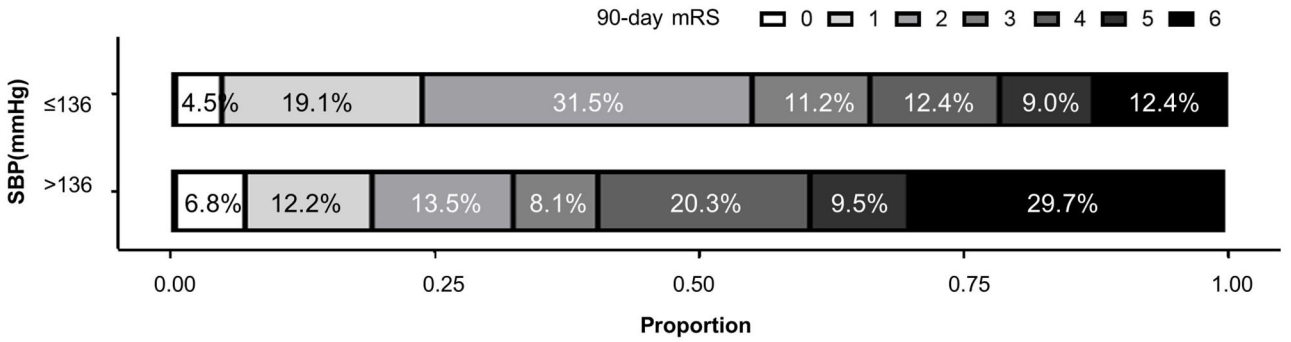

FIGURE 3 | Distributions of 90-day modified Rankin Scale (mRS) in patients with different first postoperative SBP values.

extent of cerebral hyperdensities after EVT on postinterventional non-contrast-enhanced CT correlated with malignant brain edema (16). Whether early blood pressure parameters after EVT had an impact on postinterventional cerebral hyperdensities need more evidence.

To the best of our knowledge, this is the first study to report a potential association between blood pressure at 30–40 min after EVT and clinical outcomes. When patients were stratified according to whether systolic blood pressure at this time point was above or below 130 or 140 mmHg, no other blood pressure parameters showed significant associations with functional outcome. This implies that the various correlations of other blood pressure parameters with functional outcome reflect the influence of systolic blood pressure at 30–40 min. Consistent with this idea, we found that pressures at this time point that was below 160 mm were linearly associated with the risk of poor functional outcome. In our sample, a pressure of 136 mmHg predicted well whether our patients experienced good or poor outcomes at 90 days.

In our study, patients with higher systolic blood pressure at the first postoperative measurement had higher mean, minimum and maximum blood pressures, and they were at higher risk of poor mRS score at 90 days. This is consistent with previous reports that higher blood pressure can lead to poor functional outcomes in acute ischemic stroke patients (6, 9–11, 17, 18). These observations lead us to recommend strictly controlling blood pressure during the first 6 h or at least the first 24 h after EVT based on the first postoperative measurement of blood pressure.

Our subgroup analyses revealed that blood pressure parameters correlated significantly with functional outcomes in patients with ICA occlusion, but not in those without such occlusion. We originally thought that this result might reflect that ICA occlusion correlates with higher blood pressure at admission, but we did not detect such a correlation when we compared blood pressure between subgroups with or without occlusion. Therefore, other mechanisms may be responsible. One possibility is that ICA occlusion is associated with poor collateral

circulation (19). Poor collateral circulation may compromise the body's ability to compensate for ICA occlusion, rendering tissues and vessels more sensitive to changes in perfusion.

LIMITATION

Given the retrospective design of our study, we didn't collect blood pressure data 30–40 mins after EVT, which made it difficult to analyze and demonstrate the accuracy of the blood pressure profile at the early stage. Besides, we did we have data on NIHSS after EVT, so we could not explore the potential influence of symptomatic intracerebral hemorrhage on functional outcomes. All our patients underwent EVT while under general anesthesia, so our results may not be generalizable to those who undergo the procedure with local anesthesia, with or without conscious sedation. The type of anesthesia is known to affect blood pressure (20–22).

CONCLUSION

Blood pressure of acute ischemic stroke patients during the first 6 h after EVT can significantly influence functional outcomes at 90 days. In fact, blood pressure at 30–40 min after the procedure may be independently associated with outcomes, highlighting the need to carefully manage blood pressure early after EVT.

DATA AVAILABILITY STATEMENT

The raw data supporting the conclusions of this article will be made available by the authors, without undue reservation.

ETHICS STATEMENT

The studies involving human participants were reviewed and approved by Ethics Committee on Biomedical Research, West China Hospital of Sichuan University. Written informed consent for participation was not required for this study in accordance with the national legislation and the institutional requirements.

AUTHOR CONTRIBUTIONS

XZ: design of the study, methodology, data analysis, and article writing. TC: data collection and trimming. QZ: literature search and data collection. CW: data analysis direction. AW, YY, and SL: data collection. FH: direction of the study. BW: direction of the study and funding. All authors contributed to the article and approved the submitted version.

FUNDING

This study was supported by National Natural Science Foundation of China (82071320 and 81870937) and 1.3.5 Project for Disciplines of Excellence, West China Hospital, Sichuan University (No. ZYGD18009).

SUPPLEMENTARY MATERIAL

The Supplementary Material for this article can be found online at: https://www.frontiersin.org/articles/10.3389/fneur.2022.860124/full#supplementary-material

REFERENCES

1. Campbell BC, Mitchell PJ, Kleinig TJ, Dewey HM, Churilov L, Yassi N, et al. Endovascular therapy for ischemic stroke with perfusion-imaging selection. *N Engl J Med.* (2015) 372:1009–18. doi: 10.1056/NEJMoa1414792
2. Nogueira RG, Jadhav AP, Haussen DC, Bonafe A, Budzik RF, Bhuva P, et al. Thrombectomy 6 to 24 hours after stroke with a mismatch between deficit and infarct. *N Engl J Med.* (2018) 378:11–21. doi: 10.1056/NEJMoa1706442
3. Leslie-Mazwi TM, Hamilton S, Mlynash M, Patel AB, Schwamm LH, Lansberg MG, et al. DEFUSE 3 non-DAWN patients. *Stroke.* (2019) 50:618–25. doi: 10.1161/STROKEAHA.118.023310
4. Mistry EA, Mistry AM, Nakawah MO, Khattar NK, Fortuny EM, Cruz AS, et al. Systolic blood pressure within 24 hours after thrombectomy for acute ischemic stroke correlates with outcome. *J Am Heart Assoc.* (2017) 6:e006167. doi: 10.1161/JAHA.117.006167
5. Goyal N, Tsivgoulis G, Pandhi A, Chang JJ, Dillard K, Ishfaq MF, et al. Blood pressure levels post mechanical thrombectomy and outcomes in large vessel occlusion strokes. *Neurology.* (2017) 89:540–7. doi: 10.1212/WNL.0000000000004184
6. Mistry EA, Sucharew H, Mistry AM, Mehta T, Arora N, Starosciak AK, et al. Blood pressure after endovascular therapy for ischemic stroke (BEST): a multicenter prospective cohort study. *Stroke.* (2019) 50:3449–55. doi: 10.1161/STROKEAHA.119.026889
7. Mazighi M, Richard S, Lapergue B, Sibon I, Gory B, Berge J, et al. Safety and efficacy of intensive blood pressure lowering after successful endovascular therapy in acute ischaemic stroke (BP-TARGET): a multicentre, open-label, randomised controlled trial. *Lancet Neurol.* (2021) 20:265–74. doi: 10.1016/S1474-4422(20)30483-X
8. Powers WJ, Rabinstein AA, Ackerson T, Adeoye OM, Bambakidis NC, Becker K, et al. 2018 guidelines for the early management of patients with acute ischemic stroke: a guideline for healthcare professionals from the American Heart Association/American Stroke Association. *Stroke.* (2018) 49:e46–e110. doi: 10.1161/STR.0000000000000158
9. Cernik D, Sanak D, Divisova P, Kocher M, Cihlar F, Zapletalova J, et al. Impact of blood pressure levels within first 24 hours after mechanical thrombectomy on clinical outcome in acute ischemic stroke patients. *J Neurointerv Surg.* (2019) 11:735–9. doi: 10.1136/neurintsurg-2018-014548
10. Chang JY, Han MK. Postthrombectomy systolic blood pressure and clinical outcome among patients with successful recanalization. *Eur Neurol.* (2019) 81:216–22. doi: 10.1159/000502519
11. Choi KH, Kim JM, Kim JH, Kim JT, Park MS, Choi SM, et al. Optimal blood pressure after reperfusion therapy in patients with acute ischemic stroke. *Sci Rep.* (2019) 9:5681. doi: 10.1038/s41598-019-42240-8
12. Chu HJ, Lin CH, Chen CH, Hwang YT, Lee M, Lee CW, et al. Effect of blood pressure parameters on functional independence in patients with acute ischemic stroke in the first 6 hours after endovascular thrombectomy. *J Neurointerv Surg.* (2020) 12:937–41. doi: 10.1136/neurintsurg-2019-015412
13. Samuels N, van de Graaf RA, van den Berg CAL, Uniken Venema SM, Bala K, van Doormaal PJ, et al. Blood pressure in the first 6 hours following endovascular treatment for ischemic stroke is associated with outcome. *Stroke.* (2021) 52:3514–22. doi: 10.1161/STROKEAHA.120.033657
14. Chen H, Su Y, He Y, Zhang Y, Sun Y, Fan L, et al. Controlling blood pressure under transcranial doppler guidance after endovascular treatment in patients with acute ischemic stroke. *Cerebrovasc Dis.* (2020) 49:160–9. doi: 10.1159/000506855

15. Petersen NH, Silverman A, Strander SM, Kodali S, Wang A, Sansing LH, et al. Fixed compared with autoregulation-oriented blood pressure thresholds after mechanical thrombectomy for ischemic stroke. *Stroke.* (2020) 51:914–21. doi: 10.1161/STROKEAHA.119.026596
16. Wang C, Zhu Q, Cui T, Wang L, Yang T, Hao Z, et al. Early prediction of malignant edema after successful recanalization in patients with acute ischemic stroke. *Neurocrit Care.* (2021). doi: 10.1007/s12028-021-01380-4
17. Anadani M, Orabi MY, Alawieh A, Goyal N, Alexandrov AV, Petersen N, et al. Blood pressure and outcome after mechanical thrombectomy with successful revascularization. *Stroke.* (2019) 50:2448–54. doi: 10.1161/STROKEAHA.118.024687
18. Anadani M, Orabi Y, Alawieh A, Chatterjee A, Lena J, Al Kasab S, et al. Blood pressure and outcome post mechanical thrombectomy. *J Clin Neurosci.* (2019) 62:94–9. doi: 10.1016/j.jocn.2018.12.011
19. Liu D, Nie X, Pan Y, Yan H, Pu Y, Wei Y, et al. Adverse outcomes associated with higher mean blood pressure and greater blood pressure variability immediately after successful embolectomy in those with acute ischemic stroke, and the influence of pretreatment collateral circulation status. *J Am Heart Assoc.* (2021) 10:e019350. doi: 10.1161/JAHA.120.019350
20. Valent A, Maïer B, Chabanne R, Degos V, Lapergue B, Lukaszewicz A-C, et al. Anaesthesia and haemodynamic management of acute ischaemic stroke patients before, during and after endovascular therapy. *Anaesth Crit Care Pain Med.* (2020) 39:859–70. doi: 10.1016/j.accpm.2020.05.020
21. Oliveira RSSd, Ciarlariello VB, Martins HNF, Lobato MDS, Miranda RCAN, Freitas FFMd, et al. Blood pressure behavior during mechanical thrombectomy and drugs used for conscious sedation or general anesthesia. *Arq Neuropsiquiatr.* (2021) 79:660–5. doi: 10.1590/0004-282X-ANP-2020-0243
22. Samuels N, van de Graaf RA, van den Berg CAL, Nieboer D, Eralp I, Treurniet KM, et al. Blood pressure during endovascular treatment under conscious sedation or local anesthesia. *Neurology.* (2021) 96:e171–e81. doi: 10.1212/WNL.0000000000011006

Conflict of Interest: The authors declare that the research was conducted in the absence of any commercial or financial relationships that could be construed as a potential conflict of interest.

Publisher's Note: All claims expressed in this article are solely those of the authors and do not necessarily represent those of their affiliated organizations, or those of the publisher, the editors and the reviewers. Any product that may be evaluated in this article, or claim that may be made by its manufacturer, is not guaranteed or endorsed by the publisher.

Copyright © 2022 Zhang, Cui, Zhu, Wang, Wang, Yang, Li, Hu and Wu. This is an open-access article distributed under the terms of the Creative Commons Attribution License (CC BY). The use, distribution or reproduction in other forums is permitted, provided the original author(s) and the copyright owner(s) are credited and that the original publication in this journal is cited, in accordance with accepted academic practice. No use, distribution or reproduction is permitted which does not comply with these terms.

frontiers | Frontiers in Neurology

ORIGINAL RESEARCH
published: 26 April 2022
doi: 10.3389/fneur.2022.796339

Caveolin-1 Promoted Collateral Vessel Formation in Patients With Moyamoya Disease

Jinbing Zhao, Zhiqiang Yu, Yanping Zhang, Cheng Qiu, Guangxu Zhang, Lijiu Chen, Shengxue He and Jun Ma**

Nanjing Comprehensive Stroke Center, Affiliated Nanjing Brain Hospital, Nanjing Medical University, Nanjing, China

Background: Caveolin-1 (Cav-1) plays pivotal roles in the endothelial function and angiogenesis postischemia. Moyamoya disease (MMD) is characterized by progressive artery stenosis with unknown etiology. We aim to determine whether serum Cav-1 levels of patients with MMD were associated with collateral vessel formation after bypass surgery.

Methods: We studied serum Cav-1 levels of 130 patients with MMD (16 with *RNF213* p.R4810K mutation and 114 without *RNF213* p.R4810K mutation), 15 patients with acute stroke, and 33 healthy controls. Cerebral perfusion and collateral circulation were evaluated preoperation and at 6 months after operation using pseudocontinuous arterial spin labeling MRI (pCASL-MRI) and digital subtraction angiography (DSA), respectively. Endothelial expression of Cav-1 was verified in the superficial temporal artery (STA) wall of patients with MMD by immunofluorescence double staining. We also investigated whether overexpression of Cav-1 affects cell migration and tube formation using human microvascular endothelial cells (HMECs).

Results: The serum Cav-1 level of patients with MMD intermediated between the stroke group and healthy controls and it was enhanced after the bypass surgery (681.87 ± 311.63 vs. 832.91 ± 464.41 pg/ml, $p = 0.049$). By 6 months after bypass surgery, patients with MMD with better collateral compensation manifested higher postoperative/preoperative Cav-1 ratio (rCav-1) than bad compensation patients. Consistently, cerebral blood flow (CBF) determined by pCASL-MRI ($nCBF_{MCA}$ ratio) was positively in line with rCav-1 ratio ($r = 0.8615$, $p < 0.0001$). Cav-1 was expressed in the endothelial cells of the STA vessels of patients with MMD. Overexpression of Cav-1 by plasmid transfection in HMECs promoted tube formation and cell migration.

Conclusion: This study indicated that Cav-1 may be a potential driver to promote angiogenesis and collateral formation after bypass surgery in patients with MMD, providing a better understanding of MMD pathophysiology and potential non-surgical targets of MMD.

Keywords: moyamoya disease, caveolin-1, collateral circulation, bypass surgery, stenosis

OPEN ACCESS

Edited by:
Wen-Jun Tu,
Chinese Academy of Medical Sciences and Peking Union Medical College, China

Reviewed by:
Peter Vajkoczy,
Charité University Medicine Berlin, Germany
Peicong Ge,
Capital Medical University, China

****Correspondence:***
Jun Ma
majun_njmu@163.com
Jinbing Zhao
zhaojb@njmu.edu.cn

Specialty section:
This article was submitted to Neurological Biomarkers, a section of the journal Frontiers in Neurology

Received: *16 October 2021*
Accepted: *24 March 2022*
Published: *26 April 2022*

Citation:
Zhao J, Yu Z, Zhang Y, Qiu C, Zhang G, Chen L, He S and Ma J (2022) Caveolin-1 Promoted Collateral Vessel Formation in Patients With Moyamoya Disease. Front. Neurol. 13:796339. doi: 10.3389/fneur.2022.796339

INTRODUCTION

Moyamoya disease (MMD) is a chronic progressive cerebrovascular disease with bilateral or unilateral distal internal carotid artery (ICA), middle cerebral artery (MCA), and anterior cerebral artery (ACA) stenosis or occlusion, accompanied by the formation of hazy vessels at the base of the brain. Owing to the stenosis of ICA, patients typically present with transient ischemia attack and infarction, while aberrant formation of basicranial hazy vessels leads to cerebral hemorrhage. In clinic, bypass surgery is a main option to restore cerebral perfusion for MMD (1), although it entails the possibility of perioperative complications and long-term insufficient collateral growth. Currently, there is no pharmaceutical treatment to prevent MMD progression (2). In theory, the outgrowth of preformed collateral vessels is the most important endogenous rescue system to cope with the chronic cerebral hypoperfusion (3). Therefore, the concept of therapeutic stimulating collateral vessel growth is supposed to be an effective remedy for patients with MMD.

Caveolin-1 (Cav-1) is a small concave protein, particularly abundant in endothelial cells, smooth muscle cells, fibroblasts, and epithelial cells (4). Cav-1 may promote angiogenesis and collateralization in ischemic stroke (5) and limb ischemia (6). On the other hand, Cav-1 recruited endothelial progenitor cells from the bone marrow to circulation, creating favorable conditions for vasculogenesis (7). Therefore, Cav-1 is predicted to be a possible target of MMD. Recent studies demonstrated that serum Cav-1 level was positively associated with the ICA diameter of MMD, indicating that Cav-1 may take part in ICA stenosis and occlusion (8). The Ring Finger Protein 213 (*RNF213*) gene was identified as the strongest susceptibility gene for MMD in the East Asian countries such as Japan (9). Bang et al. showed that the presence of the *RNF213* variant was associated with Cav-1 level, showing that the *RNF213* mutant patients with MMD have lower Cav-1 levels (10). These studies aroused our interest in studying the role of Cav-1 in angiogenesis of MMD in Chinese population. However, there is still lacking studies concerning the association between serum Cav-1 and the collateral formation of MMD. Additionally, whether compensative collateral network formation and cerebral perfusion after bypass surgery are associated with serum Cav-1 is unknown.

Conventional angiography such as digital subtraction angiography (DSA) is the mainstay to visualize the degree of artery lumen stenosis and the collateral vessels of MMD. Additionally, territory-specific perfusion measured by cerebral blood flow (CBF) imaging also plays a determine role in disease severity and whether to choose bypass surgery or not. Pseudocontinuous arterial spin labeling (pCASL) is a non-invasive MR perfusion imaging technique, which is a feasible way to access CBF changes in patients with MMD (11, 12). pCASL with multiple postlabeling delay (PLD) could provide more accurate CBF measurements because of the severe intracranial arterial stenosis and occlusion.

In this study, we investigated serum Cav-1 levels preoperation and 6 months postoperation and correlated Cav-1 levels with collateral compensation and CBF, with the purpose to find a better understanding of MMD pathophysiology and potential non-surgical targets of MMD. Furthermore, we proved the expression of Cav-1 in human artery and the function of that in *in-vitro* experiment. We hypothesized that enhanced postoperative expression of Cav-1 could be positively correlated with collateral formation and cerebral perfusion.

METHODS

Patients

We prospectively recruited 130 patients with MMD (16 patients with *RNF213* mutation and 114 patients without *RNF213* mutation), 15 patients with acute stroke, and 33 healthy controls from the Nanjing Brain Hospital and Nanjing Drum Tower Hospital between January 2016 and May 2021. The diagnosis of MMD was based on the distal ICA or MCA/ACA stenosis and a hazy network of basal collaterals evaluated by DSA. Enrolled criterions of patients with MMD were as follows: (1) Adult patients with MMD; (2) All the patients underwent DSA examination and met the diagnostic criteria recommended by the Japan Research Committee on the Pathology and Treatment of Spontaneous Occlusion of the Circle of Willis in 2012; and (3) A written consent signed by the patients for the use of serum samples for biomarker examinations and other clinical data including DSA and MRI data. Patients with surgical contraindications were excluded. All the enrolled patients underwent unilateral superficial temporal artery-middle cerebral artery (STA-MCA) anastomosis and encephalo-duro-myo-synangiosis (EDMS). For patients with MMD with ischemic symptoms, bypass operations were performed at least 1 month after acute ischemia onset; for patients with MMD with cerebral hemorrhage, bypass operations were performed at least 2 months after bleeding absorption. Therefore, serum taken from patients with MMD was 1 or 2 months after acute cerebrovascular event. The STA samples were collected during the surgery. In the operation, the STA should be trimmed to an adequate length before anastomosed to M4 cortical artery and the trimmed STA arteries were collected as samples. In the control group, patients with temporal epilepsy underwent anterior temporal lobectomy or selective amygdalohippocampectomy and the STA trunk or branches under the incision were collected as samples for the control group. Patients with age-matched ischemic stroke (7 days within stroke onset) and healthy controls were recruited. This study was conducted in accordance with the Declaration of Helsinki and approved by the Ethics Committee of Nanjing Brain Hospital. Each patient signed a written consent.

Blood Biomarkers for Caveolin-1

Serum samples were collected uniformly on the second day after patient admission. Among 130 patients with MMD, 55 patients provided the serum preoperatively and 6 months postoperatively. The other 75 patients only provided the serum preoperatively. Peripheral fresh blood samples were drawn out in coagulation tubes and serum was collected after centrifugation with 1,500 g for 10 min. Serum Cav-1 was quantified using the Cav-1 ELISA Kit (Catalog No. E0214h; EIAAB, Wuhan, China) according to the manufacturer's instructions. All the samples were run

in duplicate. All the ELISA plates were read at the absorbance of 450 nm using the Tecan Spark 10M Microplate Reader (Tecan, Switzerland).

Identification of the Ring Finger Protein 213 Mutation

The *RNF213* mutation analysis was performed by PCR amplification. The genomic DNA was extracted from peripheral blood leukocyte using the DNA Purification Kit (Promega, Madison, USA). Specific primers were designed according to the genomic sequence data of the *RNF213*, which was obtained from the National Center for Biotechnology Information website (http://www.ncbi.nlm.nih.gov/). The primers were designed as follows: *RNF213* p.R4810K F: TCTCGCAGCCAGTCTCAAAG and *RNF213* p.R4810K R: AGAGGGAGGTGCTTTTCAGC.

Polymerase chain reaction was performed using the ABI PRISM BigDye Terminator Cycle Sequencing Kit and the products were analyzed by the ABI 310 Genetic Analyzer (Applied Biosystems, California, USA).

Human Microvascular Endothelial Cells Cultures and Plasmid Transfection

Human microvascular endothelial cells (HMECs) were grown in Dulbecco's Modified Eagle's Medium (DMEM) with 10% fetal bovine serum (FBS) maintained at 37°C in 5% CO_2 atmosphere. HMECs were transfected with Cav-1 overexpression plasmid or vector CMV-MCS-IRES-EGFP-SV40-neomycin by lipofectamine 3000 (Thermo Fisher Scientific, USA) according to the manufacturer's protocols. Plasmid mixtures were added to the HMECs and incubated at 37°C in 5% CO_2 for 6 h and then altered to fresh DMEM/5% FBS media. 24 h later, transfection efficiency was verified by Olympus IX73. Then, transfected HMECs were used to the following experiments.

Capillary-Like Tubule Formation Assay and Wound Scratch Assay

BD Matrigel Basement Membrane Matrix (Corning, USA) was diluted 1:1 in the cultured media. Then, 96-well plates were precoated with 50 μl diluted mixture per well for 30 min at 37°C. HMECswere transfected with Cav-1 or vector plasmids for 24 h as described above. Then, cells were digested with trypsin and seeded at a density of 15,000 cells per well in the endothelial cell medium (ECM) (ScienCell Research Laboratories, USA) in Matrigel-coated plates and incubated at 37°C for a period of 20 h. The formation of capillary-like tubular structures was captured using an Olympus IX70 microscope and assessed with Image J version 1.8.0 software. Wound scratch assay was performed on confluent layers of transfected HMECs. 24 h after plasmid transfection, cells were seeded into 24-well cell culture plate confluently and were incubated for 24 h to allow them to adhere. Migration was initiated by scratching wound with the 10 μl pipette tip followed by two washes with DMEM media. Images of migration were taken immediately and 14 h after scratch.

Magnetic Resonance Images and Cerebral Blood Flow Measurements

Cerebral blood flow of patients with MMD was investigated using pCASL sequence of 3.0-Tesla MR scanner (Discovery MR750, GE Healthcare, USA). Each raw ASL scan had a 3-dimensional fast gradient and spin-echo readout module with background suppression. Besides, we applied different postlabeling delays (PLDs) of pCASL scan for more accurate evaluation of cerebral perfusion. The standard and long PLDs were set as 1,525 and 2,525 ms, respectively. Quantitative measurement of regional CBF values was acquired by a recommended equation (13). Regions of interest (ROIs) were drawn over the MCA territory (CBF_{MCA}) at the level of basal ganglia and ventricular roof (14–16). ROI within cerebellum (CBF_{CbII}) was set as control because of its hemodynamic stability in MMD (17). Thus, normalized CBF ratios adjusted to the cerebellum ($nCBF_{MCA} = CBF_{MCA}/CBF_{CbII}$) were calculated to minimize the known inhomogeneous perfusion effect.

Clinical Evaluation Scales

Collateral formations were graded by two independent experienced neurosurgeons. Preoperative angiographic stages of MMD by DSA were categorized into I to VI according to Suzuki and Takaku's Scale (18). Matsushima Clinical scale represents the clinical manifestations of each patient (19). Briefly, Type I: Transient ischemic attacks (TIAs) or episodes of reversible ischemic neurological deficit (RIND) occurring less than twice a month and with a normal CT appearance. Type II: Episodes of TIA or RIND occurring at least twice a month, with normal CT findings and neurological examination. Type III: Repeated TIAs or RINDs, with low density areas present on CT or with permanent focal neurological deficits. Type IV: Permanent focal neurological impairment secondary to cerebral infarction, followed by recurrent TIAs or RINDs or rarely repeated episodes of cerebral infarction. Type V: Neurological deficits due to cerebral infarction, followed by repeated episodes of cerebral infarction. Type VI: Intracerebral hemorrhage and other symptoms.

Then, DSA follow-ups were scheduled at 6 months after surgery to evaluate collateral revascularization. Revascularization assessments were conducted according to postoperative angiographic grading, as described previously (20). Briefly, Level 0: No obvious neoangiogenesis was found; level 1: collateral formation covering less than one-third of MCA territory; level 2: one-third to two-thirds of MCA territory; and level 3: collateral formation from external carotid artery system covering more than two-thirds of MCA territory. Based on this criterion, levels 0 and 1 were further defined as "bad compensation," while levels 2 and 3 were defined as "good compensation."

Immunofluorescence

The STA vessels were fixed in 4% paraformaldehyde for 24 h and sliced by Leica slicer. Cryostat sections were washed twice in phosphate-buffered saline (PBS) and blocked with 2% bovine serum albumin (BSA) for 1 h. Sections were incubated sequentially with the primary antibodies for double immunofluorescent staining. Staining for Cav-1 and CD31

TABLE 1 | The clinical properties of patients from healthy controls (CNT), MMD groups, and acute stroke group.

	MMD (RNF213 WT)	MMD (RNF213 Mu)	Acute Stroke	Control	*P*
Cases	114 (87.69%)	16 (12.31%)	15	33	
Age (y)	48.52 ± 10.57	41.06 ± 14.91	55.13 ± 16.47	46.67 ± 7.30	0.149
Sex (F/M)	52/62	8/8	6/9	16/17	0.861
Hypertension	48 (42.11%)	6 (37.5%)	12 (80%)	6 (18.18%)	<0.001
Diabetes mellitus	22 (19.30%)	4 (25%)	8 (53.33%)	0	<0.001
Hyperlipemia	4 (3.51%)	0	2 (13.33%)	0	0.079
Initial presentation					
Headache	30 (26.32%)	3 (18.75%)	0	5 (15.15%)	0.731
Dizzy	38 (33.33%)	4 (25%)	0	5 (15.15%)	0.504
TIA	10 (8.77%)	2 (12.5%)	0	0	0.983
Stroke	51 (44.74%)	10 (62.5%)	15 (100%)	0	0.182
Hemorrhage	34 (29.82%)	2 (12.5%)	0	0	0.249
Post-operative complications					
Acute stroke	8 (7.02%)	1 (6.25%)	-	-	1.000
ICH	2 (1.75%)	1 (6.25%)	-	-	0.328
Hemodynamic disorders	26 (22.81%)	2 (12.5%)	-	-	0.520
Seizures	10 (8.77%)	0	-	-	0.611
Wound complication	2 (1.75%)	0	-	-	1.000
Caveolin-1 (pg/ml)	581.56 ± 357.63	487.63 ± 259.70	891.27 ± 489.38	221.52 ± 131.63	

MMD, moyamoya; RNF, Ring Finger Protein; WT, wild type; Mu, mutation; TIA, transient ischemic attack; ICH, intracerebral hemorrhage.

was performed first at 4°C overnight with rabbit monoclonal antibody to caveolin-1 (1:200; Abcam) and mouse monoclonal antibody to CD31 (1:500; Abcam), respectively. Sections were then washed in PBS three times for 10 min each time, followed by incubation with 594-conjugated donkey antirabbit immunoglobulin G (IgG) (1:500; Invitrogen, USA) and 488-conjugated donkey antimouse IgG (1:500; Invitrogen, USA) at 37°C for 1.5 h in the dark. Finally, 4',6-diamidino-2-phenylindole (DAPI) was used to stain the cell nuclei for 2 min at room temperature. After washed 5 times with PBS for 5 min each time, the slides were mounted and covered. Images were examined using Olympus IX70 microscope (Tokyo, Japan).

Western Blotting

Twenty four hours after transfection, HMECs were lysed for detecting the expression of Cav-1. Briefly, 50 μg protein extracted from cell lyses was loaded to each lane, separated by 12% SDS-polyacrylamide gel electrophoresis (SDS-PAGE) and transferred to polyvinylidene difluoride (PVDF) membrane. The membranes were blocked with 5% non-fat milk and incubated overnight at 4°C with primary antibodies [rabbit antihuman caveolin-1, 1:1,000 dilution, Abcam, USA; rabbit antihuman glyceraldehyde 3-phosphate dehydrogenase (GAPDH), 1:2,000 dilution, Abcam, USA] and then incubated for 2 h with secondary antibodies. Membranes were developed by enhanced chemiluminescence (ECL) system.

Statistical Analysis

All the statistical analyses were performed with SPSS version 26.0 (IBM Incorporation, Chicago, USA) and GraphPad Prism version 8.0 (GraphPad Software, San Diego, USA). Qualitative parameters of the different groups were analyzed by the Student's *t*-test and one-way or two-way ANOVA. Categorical variables and non-Gaussian distribution data were assessed by non-parametric tests such as the non-parametric Spearman's correlation analysis. The receiver operating characteristic (ROC) curve was run for testing the sensitivity and specificity for serum Cav-1 at different cutoff values. All the data were expressed as mean ± SD and $p < 0.05$ was set as statistically significant difference.

RESULTS

Characterizations of Enrolled Patients

A total of 130 patients with MMD, 15 patients with acute stroke, and 33 age-matched healthy controls were enrolled in this study. The baseline features of patients are given in **Table 1**. Generally, in the MMD group, 16/130 (12.31%) patients were the *RNF213* mutation. Patients with MMD frequently presented with ischemic stroke (46.92%), hemorrhage (27.69%), dizziness (32.30%), headache (25.38%), and transient ischemic attack (TIA) (9.23%). All the enrolled patients with MMD underwent bypass surgery after diagnosis. The postoperative complications frequently occurred during the first 2 weeks, including hemodynamic disorders (28/130), acute postoperative seizure (10/130), acute stroke (9/130), intracerebral hemorrhage (3/130), and wound complication (2/130). Most patients recovered during the follow-up period and only two patients suffered from moderate disability. The average Cav-1 levels of patients with MMD (without the *RNF213* mutation) was 581.56

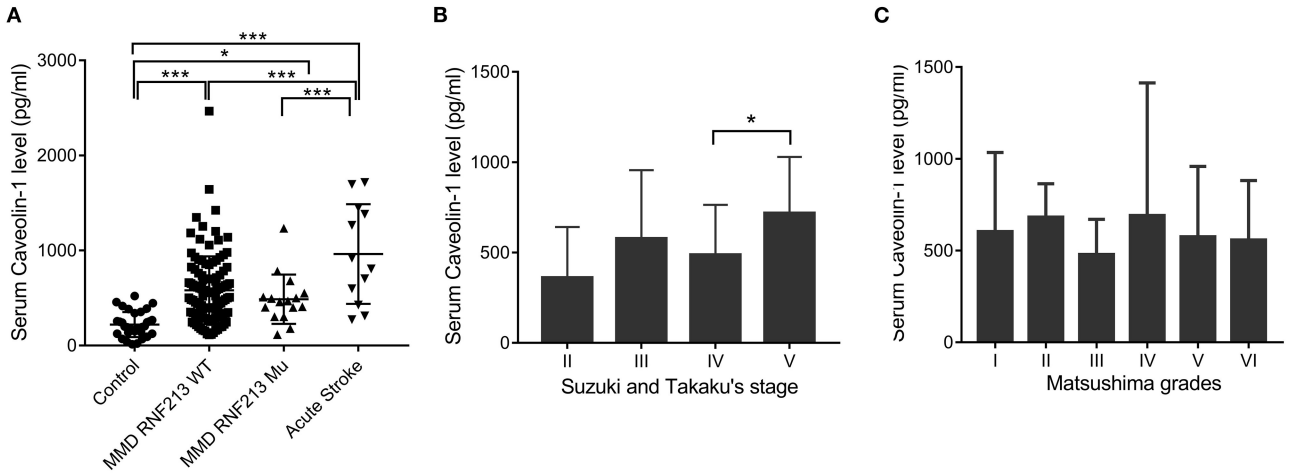

FIGURE 1 | Serum caveolin-1 (Cav-1) levels in patients with moyamoya disease (MMD), acute stroke, and healthy controls. **(A)** Serum Cav-1 levels of patients with MMD [with or without the Ring Finger Protein 213 (*RNF213*) mutation], age-matched controls, and patients with acute stroke. **(B)** Serum Cav-1 levels of patients with MMD categorized by Suzuki and Takaku's stages. Stage V demonstrated higher Cav-1 levels than patients in stage IV. **(C)** Serum Cav-1 levels of patients with MMD categorized by the Matsushima grades. *$p < 0.05$, ***$p < 0.001$. WT, wild type; Mu, mutation.

± 357.63 pg/ml, which was much higher than age-matched controls (221.52 ± 131.63 pg/ml, $p < 0.001$), but lower than the acute stroke group (891.27 ± 489.38 pg/ml, $p < 0.001$, **Figure 1A**). Additionally, there was no statistical difference of serum Cav-1 levels between the patients with the *RNF213* mutation and without the *RNF213* mutation (487.63 ± 259.70 vs. 581.56 ± 357.63 pg/ml, $p = 0.7176$, **Figure 1A**).

Serum Caveolin-1 Is Associated With Collateral Circulation Determined by Digital Subtraction Angiography

Among patients with MMD, Cav-1 level differs by angiographic features. Generally, there were 2, 74, 36, and 18 patients belonging to grades II, III, IV, and V by Suzuki and Takaku's Scale, respectively. Interestingly, patients in grade V, who were characterized with better spontaneous collateral formations, demonstrated higher Cav-1 levels than patients in grade IV (717.93 ± 311.79 vs. 487.74 ± 276.2 pg/ml, $p < 0.05$, **Figure 1B**). Cav-1 levels did not differ by clinical presentation scale—the Matsushima scale. The Matsushima scale VI reflects a group of patients with MMD with hemorrhage or other atypical symptoms, while the Matsushima scale I-V reflects patients with recurrent stroke or TIA (**Figure 1C**).

Preoperative and 6 months postoperative serum Cav-1 were detected in 55 patients with MMD and the baseline information is given in **Table 2**. By DSA grading, 5 patients were graded 0, 8 patients were graded 1, 9 patients were graded 2, and the rest 33 patients were graded 3. Therefore, there are 13 cases in the bad compensation group (DSA grades 0–1) and 42 cases in the good compensation group (DSA grades 2–3), respectively. We found that the Cav-1 levels increased obviously after surgery (preoperative 681.87 ± 311.63 vs. postoperative 832.91 ± 464.41 pg/ml, $F = 3.981$, $p = 0.049$), while the absolute Cav-1 levels did not show any statistical difference between the "bad compensation" and "good compensation" groups ($F = 0.187$, $P = 0.666$) by two-way ANOVA. Furthermore, the change of Cav-1 was analyzed. ΔCav-1 was defined as postoperative serum Cav-1 subtracted the preoperative serum Cav-1. We carefully assessed the revascularization by DSA after bypass surgery. Notably, good compensation patients presented much higher ΔCav-1 than the bad compensation group ($p < 0.01$, **Figure 2B**), so did postoperative/preoperative Cav-1 ratio (rCav-1, $p < 0.05$, **Figure 2A**). By the Spearman's correlation analysis, we observed that both the ΔCav-1 and rCav-1 were positively correlated with the collateral compensation ($r = 0.3586$, $p = 0.0072$; $r = 0.3784$, $p = 0.0044$, respectively, **Figures 2C,D**). Besides, the area under the ROC curve for rCav-1 was 0.841 ($p < 0.0001$). The rCav-1 cutoff value of 1.02 yields good sensitivity at 71.4% and specificity at 84.6% (**Figures 2E,F**). Therefore, higher postoperative/preoperative Cav-1 ratios indicated better collateral formation after bypass for patients with MMD.

Serum Caveolin-1 Is Associated With Cerebral Blood Flow Determined by Pseudocontinuous Arterial Spin Labeling MRI

The CBF is calculated as ml/100 g/min, indicating the volume of blood (ml) that circulates through 100 g brain parenchyma in 1 min. By pCASL-MRI, mean absolute CBF values in MCA territory of the anastomosed hemisphere were 33.70 ± 9.21 and 40.48 ± 9.16 ml/100 g/min at pre- and postoperative follow-up time points, respectively ($p < 0.001$). The pCASL-MRI changes of one typical patient with MMD underwent the left STA-MCA anastomosis and EDMS are shown in **Figure 3**. We observed the profound hypoperfusion signal of the left MCA territory from

the raw and color CBF maps at PLD 1,525 ms (**Figures 3A,B**) and 2,525 ms (**Figures 3C,D**) before bypass surgery. By 6 months after bypass surgery, cerebral perfusion was improved by pCASL-MRI re-evaluation (**Figures 3G–J**), which was verified by DSA with abundant collateral formation in the left hemisphere (**Figures 3E,K**).

A total of 15 patients with MMD with detailed preoperative and postoperative clinical data (including serum Cav-1 levels, DSA, and pCASL images) were recruited for statistics. To minimize the inhomogeneous perfusion effect, we used normalized CBF ratio ($nCBF_{MCA}$ ratio = Postoperative/Preoperative $nCBF_{MCA}$) for further analysis. The rCav-1 had strong positive relationship with the $nCBF_{MCA}$ ratio in both the regular PLD (1,525 ms, $r = 0.8615$, $p < 0.0001$) and long PLD (2,525 ms, $r = 0.5915$, $p = 0.0428$) by the Spearman's correlation analysis (**Figures 3F,L**). These trends supported higher serum Cav-1 ratios that represented improved CBF and cerebral perfusion after bypass surgery.

Caveolin-1 Overexpression Promotes Endothelial Cell Migration and Capillary-Like Tube Formation

We further determined whether endothelial cells could express Cav-1 in patients with MMD. The STA tissue samples of patients with MMD were stained with Cav-1 (**Figure 4A**), CD31 (**Figure 4B**) and 4',6-diamidino-2-phenylindole (DAPI, **Figure 4C**). As shown in **Figure 4D**, Cav-1 was mainly located in the intima and media of the STA. CD31 positive cells co-expressed Cav-1, indicating endothelial cells could express Cav-1 (**Figure 4D**). Then, we investigated Cav-1 functions in cultured HMECs. The cultured HMECs were dealt with empty vector (**Figure 5A**) and Cav-1 overexpression plasmid vector (**Figure 5B**) for 24 h before the following two assays. The green signals represented successful transfection and the enhanced expression of Cav-1 after transfection was confirmed by Western blotting (**Figure 5C**). Transfecting Cav-1 accelerated tubule formation, leading to a dramatic 1.83-fold increase in the number of capillary-like tubular structures ($p < 0.01$, **Figures 5D,E,I**). Consistently, tube branch length of the Cav-1 transfection group was 1.34-fold of that in the control group ($p < 0.01$, **Figures 5D–F**). Next, we assessed the effect of Cav-1 on endothelial cell migration by wound scratch assay. HMECs migration in the Cav-1 overexpression group and the control group was analyzed at 0 and 14 h after cell scratching. As shown in **Figures 5G–L**, HMECs in the Cav-1 overexpression group demonstrated reduced scratching gap compared to the cells in the control group ($p < 0.01$). The results demonstrated that Cav-1 promoted the migration of endothelial cells.

TABLE 2 | The clinical properties of 55 MMD patients with both preoperative and postoperative serum Cav-1.

	Good compensation	Bad compensation	*P*
Cases	42 (76.36%)	13 (23.64%)	
Age (y)	44.50 ± 12.21	52.92 ± 5.97	0.002
Sex (F/M)	22/20	6/7	0.695
Hypertension	13 (30.95%)	8 (61.54%)	0.098
Diabetes mellitus	7 (16.67%)	1 (7.69%)	0.725
Hyperlipemia	1 (2.38%)	0	1.000
Initial presentation			
Headache	11 (26.19%)	5 (38.46%)	0.616
Dizzy	14 (33.33%)	2 (15.38%)	0.370
TIA	4 (9.52%)	0	0.562
Stroke	16 (38.10%)	2 (15.38%)	0.235
Hemorrhage	14 (33.33%)	6 (46.15%)	0.610
Post-operative complications			
Acute stroke	1 (2.38%)	0	1.000
ICH	1 (2.38%)	0	1.000
Hemodynamic disorders	10 (23.81%)	3 (23.08%)	1.000
Seizures	3 (7.14%)	0	1.000
Wound complication	0	0	
RNF213 mutation	6 (14.29%)	1 (7.69%)	0.883
DSA grading(0/1/2/3)	0/0/9/33	5/8/0/0	<0.001
Caveolin-1 (pg/ml)			
Preoperative	642.89 ± 298.40	807.81 ± 332.07	0.096
Postoperative	890.09 ± 493.13	648.16 ± 302.10	0.101
ΔCav-1	247.21 ± 64.41	−159.64 ± 68.65	0.002
rCav-1	1.67 ± 1.23	0.85 ± 0.28	0.021

MMD, moyamoya disease; TIA, transient ischemic attack; ICH, intracerebral hemorrhage. RNF, Ring Finger Protein; ΔCav-1, post-operative serum Cav-1 subtracts the pre-operative serum Cav-1; rCav-1, post-operative/pre-operative Cav-1 ratio.

DISCUSSION

To summarize our findings, the serum Cav-1 level of patients with MMD intermediated between the stroke group and healthy controls and it was enhanced after the bypass surgery. Patients with MMD with better collateral compensation manifested higher postoperative/preoperative Cav-1 ratio (rCav-1) than bad compensation patients. The rCav-1 cutoff value of 1.02 yield good sensitivity (71.4%) and specificity (84.6%) in determining good or bad compensation. Consistently, CBF determined by pCASL-MRI ($nCBF_{MCA}$ ratio) was positively in line with postoperative/preoperative Cav-1 ratio. Cav-1 could be expressed in the endothelial cells of the STA vessels of patients with MMD. Overexpression of Cav-1 by plasmid transfection in HMECs promoted tube formation and cell migration. This study indicated that Cav-1 could be a potential driver to promote angiogenesis and collateral formation of patients with MMD.

Moyamoya disease is an idiopathic cerebrovascular disease with unknown etiologies. Multiple factors involving genetic, inflammatory, and angiogenic aspects covalently contributed to MMD pathogenesis (2, 21). The *RNF213* has been confirmed to be a high susceptibility gene for MMD in East Asian populations. It is reported that p.R4810K mutation of the *RNF213* gene is about 13% in Chinese Han population (22) and 80% in sporadic patients with MMD of Japan (9, 23). Consistent with previous literatures, the incidence of the *RNF213* p.R4810K mutation is about 12.3% (16/130) in this study. One study from the Korea cohort demonstrated that the *RNF213* mutant

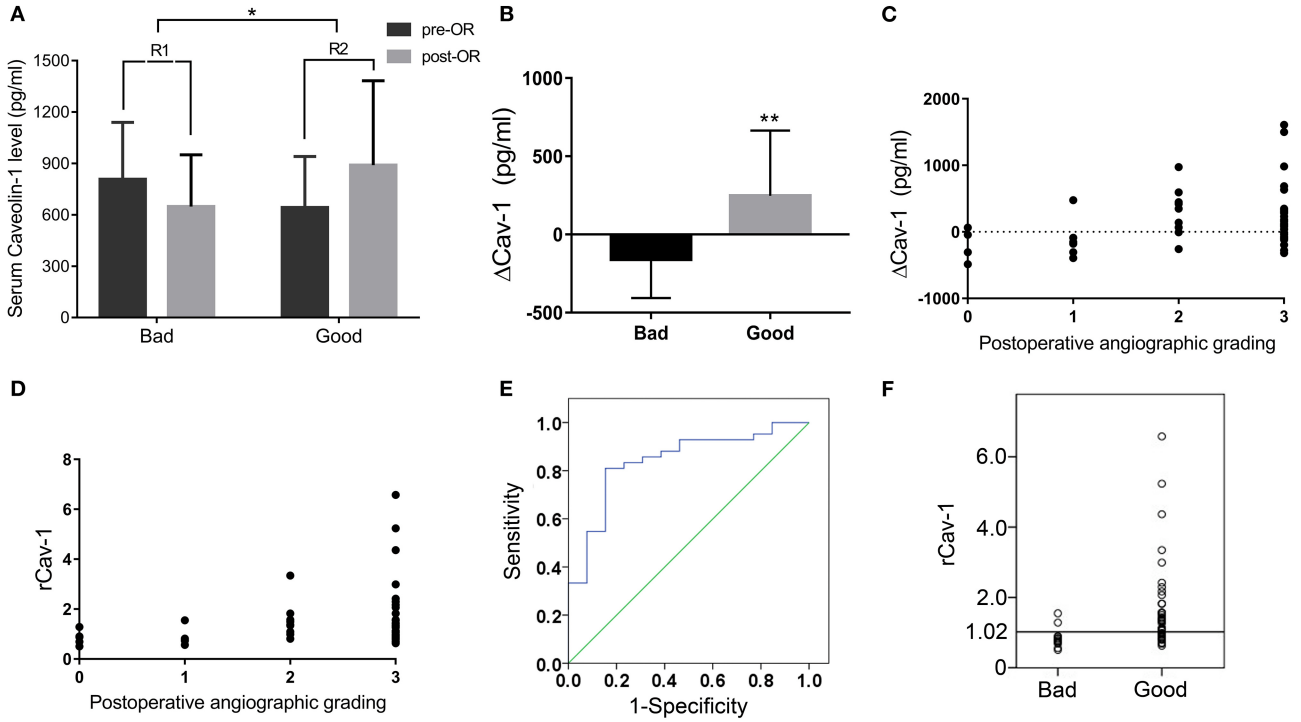

FIGURE 2 | Serum Cav-1 increase after operation indicated good collateral circulation by digital subtraction angiography (DSA). **(A)** Preoperative and 6 months postoperative serum Cav-1 levels in both the bad and good compensation groups. The rCav-1 increased in the good compensation group (R2) and differed considerably from the bad compensation group (R1). **(B)** The ΔCav-1 value in the bad and good compensation groups, respectively. **(C,D)** ΔCav-1 and rCav-1 were positively correlated with the postoperative angiographic grading by the Spearman's correlation analysis ($r = 0.3586$, $p = 0.0072$; $r = 0.3784$, $p = 0.0044$, respectively). **(E,F)** The receiver operating characteristic (ROC) curve and cutoff value of rCav-1 in the bad and good compensation groups. The area under the curve was 0.841 ($p < 0.0001$), and the rCav-1 cutoff value was set at 1.02 with sensitivity at 71.4% and specificity at 84.6%. ΔCav-1: postoperative serum Cav-1 subtracted preoperative serum Cav-1; rCav-1: postoperative/preoperative Cav-1 ratio; *$p < 0.05$, **$p < 0.01$.

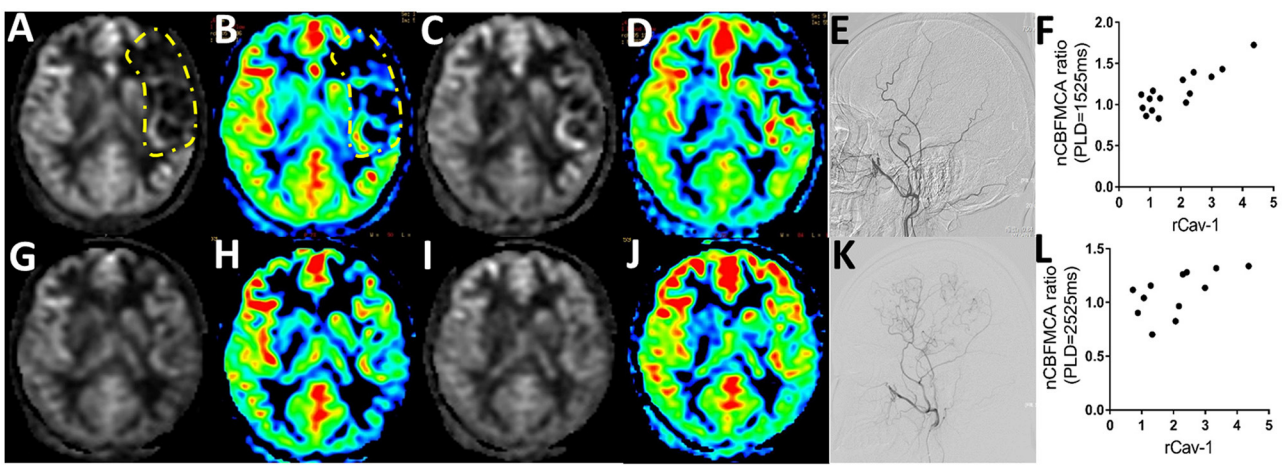

FIGURE 3 | Serum Cav-1 was associated with cerebral blood flow (CBF) determined by arterial spin labeling MRI (ASL-MRI). **(A)** 24-year-old female patient was hospitalized for right hand numbness and diagnosed as MMD. The raw and color preoperative CBF maps by regular postlabeling delay (PLD) **(A,B)** and long PLD pseudocontinuous ASL (pCASL) imaging **(C,D)** demonstrated the hypoperfusion of middle cerebral artery (MCA) territory (circled by yellow lines). The CBF improved obviously in 6 months postoperative pCASL scanning with regular PLD **(G,H)** and long PLD **(I,J)**. The collaterals from the left external carotid artery before and after bypass surgery were shown in **(E,K)** by DSA. The rCav-1 had a strong positive relationship with the $nCBF_{MCA}$ ratio in both the regular ($r = 0.8615$, $p < 0.0001$, **(F)**) and long PLD ($r = 0.5915$, $p = 0.0428$, **(L)**) by Spearman analysis. $nCBF_{MCA}$ ratio, postoperative/preoperative $nCBF_{MCA}$; $nCBF_{MCA}$, CBF of MCA territory/CBF of ipsilateral cerebellum; rCav-1, postoperative/preoperative Cav-1.

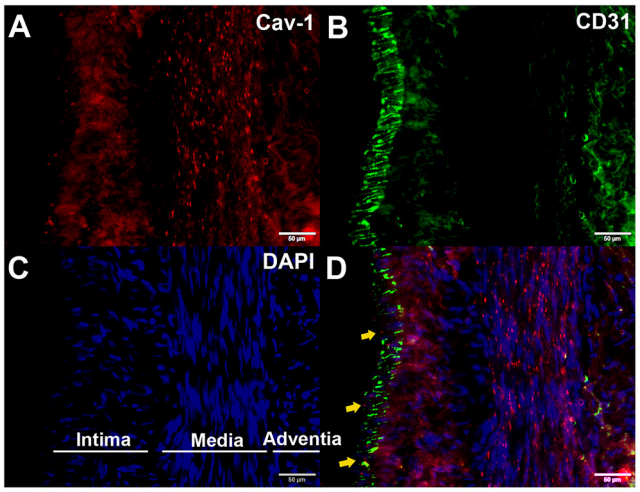

FIGURE 4 | Enhanced expression of Cav-1 in the superficial temporal artery (STA) of patients with MMD. The STA samples from patients with MMD were stained with Cav-1 (red, **A**), CD31 (green, **B**), and 4',6-diamidino-2-phenylindole (DAPI) (blue, **C**). Cav-1 was mainly located in the intima and media of the STA (yellow arrows, **(D)**). Scale bar = 50 μm.

patients with MMD were associated with lower serum Cav-1 levels (10), while another study of Chung (8) did not find any difference between the *RNF213* mutant and non-mutant groups, which is similar with the results of this study. This discrepancy may be caused by racial difference or statistical bias due to insufficient sample sizes. The *RNF213* global knockout mice demonstrated similar Cav-1 level with wild-type mice in endothelial cells of lung tissue (24). The correlation between the *RNF213* and Cav-1 does not come into consensus and needs further study. In our Chinese cohort, the serum Cav-1 level of patients with MMD intermediated between the stroke group and healthy controls. Our result is consistent with previous studies showing that serum Cav-1 level of patients with acute stroke is much higher than patients with MMD (8) and age-matched healthy controls (25). Whether the serum Cav-1 comes from is currently unknown. Studies from mouse ischemic stroke model demonstrated that Cav-1 immunoreactivity is significantly and specifically increased in the endothelial cells in the infarcted area 24 h post-MCA occlusion (MCAO). Serum Cav-1 is positively correlated with Cav-1 immunoreactivity of the brain (26). Accumulating evidence pointed out that Cav-1 was expressed in human brain microvascular endothelial cells and smooth muscle cells (8, 27). In this study, we observed the expression of Cav-1 in endothelial cells and smooth muscle cells in patients with MMD. Therefore, it is possible that serum Cav-1 may be derived from vessel wall. However, this hypothesis needs further investigation.

Although we observed the serum alternation of Cav-1 in patients with MMD, clinical significance of Cav-1 is still unknown. Preliminary study reported that patients with MMD with higher baseline Cav-1 level was positively associated with larger ICA diameter (8). MCA or ICA diameter was not a staging parameter in Suzuki and Takaku's grades. Suzuki and Takaku's grades are sensitive to categorize the collateral establishment. During the progression of Suzuki and Takaku's stages IV–V, abnormal smoking-like vessels begin to decrease, while good collateral circulation gradually develops. In this cross-sectional study, baseline serum Cav-1 levels in the stage V group were higher than that in the stage IV group, which provided a hint that Cav-1 may take part in the progression of collateral branch formation. Nevertheless, the level of Cav-1 among each grade may be a comprehensive result of multiple factors, including negative remodeling and collateral formation. Combined STA-MCA anastomosis and encephalo-duro-myo-synangiosis surgery (EDMS) is considered to be the optimal therapy for patients with MMD (1). All our enrolled patients received bypass surgery. This longitudinal study initially applied Cav-1 detection during the anastomosis follow-up period. It beared noting that patients with better Cav-1 expression indicated good collateral circulation compensation. Currently, DSA is still the "gold standard" for evaluating the severity of moyamoya angiopathy and the revascularization after bypass surgery (28). Among the promising non-invasive imaging options, ASL enables CBF evaluation by magnetically labeling the protons of inflows in feeding arteries. Pseudocontinuous ASL with multiple PLDs offers more accurate information compared to ASL with a single standard PLD (29, 30). With the application of DSA and pCASL with two PLDs, this study demonstrated that good post-/preoperative Cav-1 ratio was positively correlated with the establishment of collateral circulation and cerebrovascular perfusion improvement. The rCav-1 cutoff value of 1.02 yields good sensitivity (71.4%) and specificity (84.6%) in determining good or bad compensation after bypass surgery. PET/single-photon emission CT (SPECT) was considered to be a gold standard for estimating brain perfusion. However, those perfusion studies cannot be performed frequently due to the cost, contrast use, and radiation dose. ASL-MRI is a non-invasive and could be repetitively performed examination, which enables us to estimate brain perfusion frequently over a long-term follow-up period in MMD. Studies comparing SPECT and ASL-MRI addressed a strong correlation coefficient in patients with MMD (31). Recent studies in patients with steno-occlusive disease demonstrated that higher test-retest reliability led to better ASL sensitivity than SPECT for postoperative ΔCBF, suggesting that ASL-MRI may be better than SPECT for postoperative re-evaluation. Additionally, ASL with postlabeling delay of 2,333 ms presented higher reliability and sensitivity to ΔCBF (32). In this study, we evaluated CBF_{MCA} ratio (postoperative/preoperative $nCBF_{MCA}$) in both the regular PLD (1,525 ms) and long PLD (2,525 ms), which was reliable and feasible. These findings indicated that serum Cav-1 in MMD could be a promising biomarker used to determine the collateral circulation after bypass surgery.

Besides MMD, serum level of Cav-1 has been reported in other cerebrovascular disease. In acute ischemic stroke, lower serum Cav-1 level is associated with the presence of microbleeds (33) and predicts symptomatic bleeding after thrombolytic therapy (25). In our MMD cohort, 65 patients

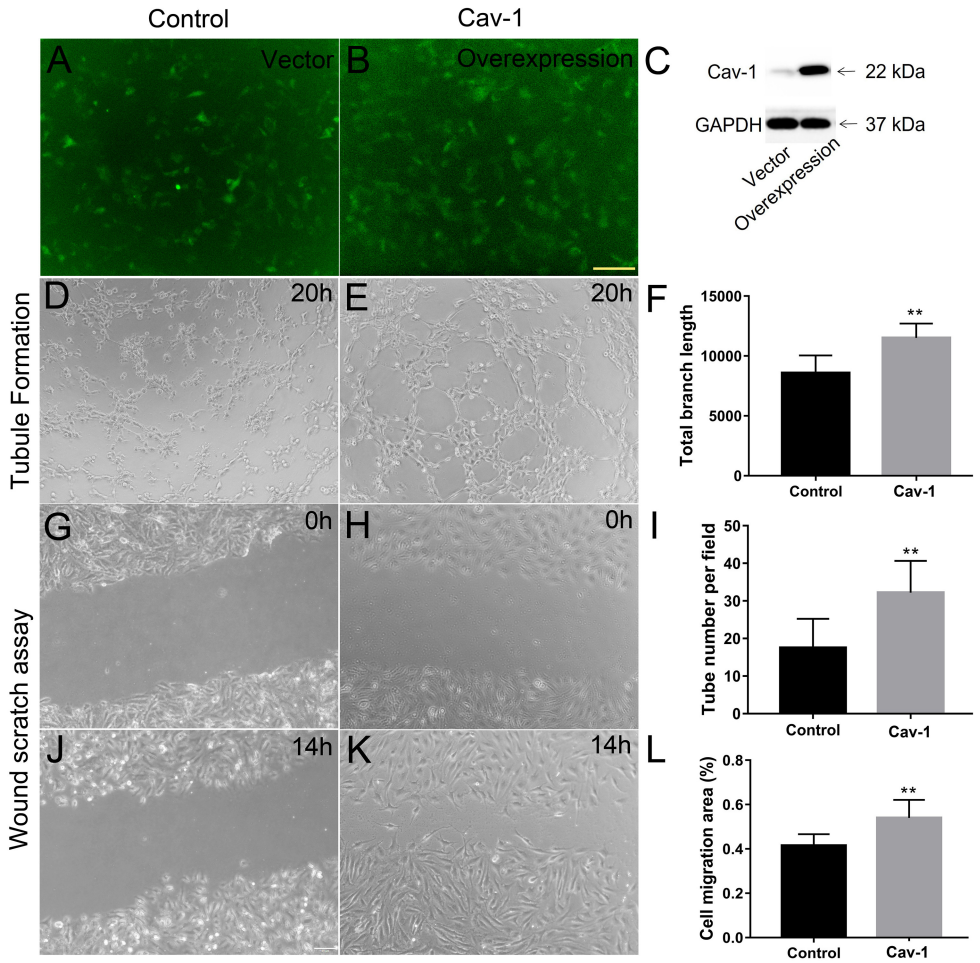

FIGURE 5 | Cav-1 overexpression promotes endothelial cell proliferation and capillary-like tube formation. The cultured human microvascular endothelial cells (HMECs) were dealt with empty vector **(A)** and Cav-1 overexpression plasmid vector **(B)** for 24 h. before the following two assays (green signals represented successful transfection) and the enhanced expression of Cav-1 after transfection was confirmed by Western blotting **(C)**. The capillary-like tube formation assay **(D,E)** was evaluated at 20 h after HMECs reseeded and the total branch length and tube numbers in per field were calculated **(F,I)**. Wound scratching assay of HEMCs was assessed at 0 **(G,H)** and 14 h **(J,K)** after scratching by the 10 μl pipette tip for both the groups. The residual area after scratching was calculated to evaluate the cell migration ability **(L)**. $^{**}p < 0.01$; scale bar = 100 μm.

were enrolled in the Matsushima scale VI group, which reflected a group of patients with MMD with intracranial hemorrhage or other atypical symptoms such as headache and dizziness. However, we did not observe patients with MMD in the Matsushima scale VI presented with lower Cav-1. Though the serum Cav-1 levels of patients with acute ischemic stroke were tremendously higher than the control group and the MMD group, patients with recurrent episode of ischemia or infarction (the Matsushima scale I–V) were comparable with that in patients in the Matsushima scale VI.

Histological investigations of the STA revealed apparently fibrocellular thickening intima (34–36), indicating an involvement of extracranial arteries of MMD. Moreover, the STA is relatively easy to obtain during surgery. In EDMS, the deep temporal artery (DTA) and middle meningeal artery (MMA) must be protected because of their vigorous revascularization ability after surgery. So, the tissue samples of DTA and MMA were uneasy to obtain and the STA was abundant for further immunohistochemical staining with Cav-1 antibody. We observed Cav-1 signals in the endothelial cells of intima. Except in the intima, we also detected Cav-1 expression in the smooth muscle cells of media layer, which is supposed to function in the negative remodeling of MMD arteries (8). It is widely accepted that Cav-1 was abundantly expressed in endothelial and smooth muscle cells from previous studies (37). Overexpression of Cav-1 in HMECs accelerated the capillary-like tube formation and cell migration in this study, which is consistent with previous study by Chung et al. (8). In endothelium-specific Cav-1-KO mice, angiogenesis in both

the isolated aortic ring assay and hindlimb ischemia animal model was impaired (38). Similarly, in systemic Cav-1-KO mice, disrupted endothelial network formation was found in a hindlimb ischemia model (6). Mechanically, as a key structural protein of caveolae domains, Cav-1 compartmentalized endothelial nitric oxide synthase (eNOS) and exerted a tonic inhibition of eNOS activity, while excess eNOS activity secondary to Cav-1 deletion impaired endothelial angiogenesis (39). On the other hand, Cav-1 also appears to be a critical regulator of vascular endothelial growth factor (VEGF)-mediated angiogenesis by anchoring VEGF receptor (VEGFR) in the caveolae (6, 40).

There are some limitations, which should be pointed out when interpreting the results. First, in this study, we only enrolled patients with MMD who needed bypass surgery. Patients of Suzuki and Takaku's grades I and VI were excluded and only two patients of grade II were included. Patients selected under these criteria may be unable to represent the overall MMD population. Second, low mutation rate of the *RNF213* gene in Chinese Han population and the relatively small number of patients with preoperative and postoperative data weakening the strength of our conclusions. We proposed that further studies could be conducted to confirm our results, utilizing broader sample sizes, multicenter cooperation, and longer follow-up periods. Third, the number of control patients is much smaller than the MMD group, which may lead to statistical bias.

Taken together, this study demonstrated that the serum Cav-1 level of patients with MMD intermediated between the stroke group and healthy controls. The elevation of Cav-1 after bypass surgery plays an important role in the establishment of collateral circulation in patients with MMD.

DATA AVAILABILITY STATEMENT

The raw data supporting the conclusions of this article will be made available by the authors, without undue reservation.

ETHICS STATEMENT

The studies involving human participants were reviewed and approved by Ethics Committee of Nanjing Brain Hospital. The patients/participants provided their written informed consent to participate in this study.

AUTHOR CONTRIBUTIONS

JZ and JM designed this study. JZ and YZ wrote this manuscript. JZ and ZY revised the manuscript. ZY and CQ performed MRI and collected data. GZ and LC performed experiments and analyzed data. SH and JM recruited the patients. All authors contributed to the article and approved the submitted version.

FUNDING

This study was supported by the National Natural Science Foundation of China (Grant No. 81301049), the Natural Science Foundation of Jiangsu Province of China (Grant No. BK20130085), Jiangsu Provincial Medical Youth Talent (QNRC2016048), and the Training Project for Young Talents of Nanjing Brain Hospital.

ACKNOWLEDGMENTS

We thank Dr. Meijuan Zhang for providing some control and stroke serum samples from the Nanjing Drum Tower Hospital.

REFERENCES

1. Zhao J, Liu H, Zou Y, Zhang W, He S. Clinical and angiographic outcomes after combined direct and indirect bypass in adult patients with moyamoya disease: A retrospective study of 76 procedures. *Exp Ther Med.* (2018) 15:3570–6. doi: 10.3892/etm.2018.5850
2. Bang OY, Fujimura M, Kim S-K. The pathophysiology of Moyamoya disease: an update. *J Stroke.* (2016) 18:12–20. doi: 10.5853/jos.2015.01760
3. Cho WS, Kim JE, Kim CH, Ban SP, Kang HS, Son YJ, et al. Long-term outcomes after combined revascularization surgery in adult moyamoya disease. *Stroke.* (2014) 45:3025–31. doi: 10.1161/STROKEAHA.114.005624
4. Liu J, Wang XB, Park DS, Lisanti MP. Caveolin-1 expression enhances endothelial capillary tubule formation. *J Biol Chem.* (2002) 277:10661–8. doi: 10.1074/jbc.M110354200
5. Pang Q, Zhao Y, Chen X, Zhao K, Zhai Q, Tu F. Apigenin protects the brain against Ischemia/Reperfusion injury via Caveolin-1/VEGF In Vitro and In Vivo. *Oxid Med Cell Longev.* (2018) 2018:7017204. doi: 10.1155/2018/7017204
6. Sonveaux P, Martinive P, DeWever J, Batova Z, Daneau G, Pelat M, et al. Caveolin-1 expression is critical for vascular endothelial growth factor-induced ischemic hindlimb collateralization and nitric oxide-mediated angiogenesis. *Circ Res.* (2004) 95:154–61. doi: 10.1161/01.RES.0000136344.27825.72
7. Sbaa E, Dewever J, Martinive P, Bouzin C, Frerart F, Balligand JL, et al. Caveolin plays a central role in endothelial progenitor cell mobilization and homing in SDF-1-driven postischemic vasculogenesis. *Circ Res.* (2006) 98:1219–27. doi: 10.1161/01.RES.0000220648.80170.8b
8. Chung J-W, Kim DH, Oh MJ, Cho YH, Kim EH, Moon GJ, et al. Cav-1 (Caveolin-1) and Arterial remodeling in adult Moyamoya Disease. *Stroke.* (2018) 49:2597–604. doi: 10.1161/STROKEAHA.118.021888
9. Kamada F, Aoki Y, Narisawa A, Abe Y, Komatsuzaki S, Kikuchi A, et al. A genome-wide association study identifies RNF213 as the first Moyamoya disease gene. *J Hum Genet.* (2011) 56:34–40. doi: 10.1038/jhg.2010.132
10. Bang OY, Chung JW, Kim SJ, Oh MJ, Kim SY, Cho YH, et al. Caveolin-1, Ring finger protein 213, and endothelial function in Moyamoya disease. *Int J Stroke.* (2016) 11:999–1008. doi: 10.1177/1747493016662039
11. Noguchi T, Kawashima M, Nishihara M, Hirai T, Matsushima T, Irie H. Arterial spin-labeling MR imaging in Moyamoya disease compared with clinical assessments and other MR imaging findings. *Eur J Radiol.* (2013) 82:e840–7. doi: 10.1016/j.ejrad.2013.08.040
12. Zhang J, Xia C, Liu Y, Qian W, Peng W, Liu K, et al. Comparative study of MR mTI-ASL and DSC-PWI in evaluating cerebral hemodynamics of patients with Moyamoya disease. *Medicine.* (2018) 97:e12768. doi: 10.1097/MD.0000000000012768
13. Alsop DC, Detre JA, Golay X, Gunther M, Hendrikse J, Hernandez-Garcia L, et al. Recommended implementation of arterial spin-labeled perfusion MRI for clinical applications: a consensus of the ISMRM perfusion study group and the European consortium for ASL in dementia. *Magn Reson Med.* (2015) 73:102–16. doi: 10.1002/mrm.25197

14. Lin YH, Kuo MF, Lu CJ, Lee CW, Yang SH, Huang YC, et al. Standardized MR perfusion scoring system for evaluation of sequential perfusion changes and surgical outcome of Moyamoya Disease. *AJNR Am J Neuroradiol.* (2019) 40:260–6. doi: 10.3174/ajnr.A5945
15. Barber PA, Demchuk AM, Zhang J, Buchan AM. Validity and reliability of a quantitative computed tomography score in predicting outcome of hyperacute stroke before thrombolytic therapy. ASPECTS Study Group. Alberta Stroke Programme Early CT Score. *Lancet.* (2000) 355:1670–4. doi: 10.1016/S0140-6736(00)02237-6
16. Kim JJ, Fischbein NJ, Lu Y, Pham D, Dillon WP. Regional angiographic grading system for collateral flow: correlation with cerebral infarction in patients with middle cerebral artery occlusion. *Stroke.* (2004) 35:1340–4. doi: 10.1161/01.STR.0000126043.83777.3a
17. Kraemer M, Karakaya R, Matsushige T, Graf J, Albrecht P, Hartung HP, et al. Efficacy of STA-MCA bypass surgery in moyamoya angiopathy: long-term follow-up of the Caucasian Krupp Hospital cohort with 81 procedures. *J Neurol.* (2018) 265:2425–33. doi: 10.1007/s00415-018-9031-4
18. Suzuki J, Takaku A. Cerebrovascular "moyamoya" disease. Disease showing abnormal net-like vessels in base of brain. *Arch Neurol.* (1969) 20:288–99. doi: 10.1001/archneur.1969.00480090076012
19. Matsushima Y, Aoyagi M, Niimi Y, Masaoka H, Ohno K. Symptoms and their pattern of progression in childhood moyamoya disease. *Brain Dev.* (1990) 12:784–9. doi: 10.1016/S0387-7604(12)80007-6
20. Matsushima T, Inoue T, Suzuki SO, Fujii K, Fukui M, Hasuo K. Surgical treatment of moyamoya disease in pediatric patients–comparison between the results of indirect and direct revascularization procedures. *Neurosurgery.* (1992) 31:401–5. doi: 10.1097/00006123-199209000-00003
21. Weng L, Cao X, Han L, Zhao H, Qiu S, Yan Y, et al. Association of increased Treg and Th17 with pathogenesis of moyamoya disease. *Sci Rep.* (2017) 7:3071. doi: 10.1038/s41598-017-03278-8
22. Wu Z, Jiang H, Zhang L, Xu X, Zhang X, Kang Z, et al. Molecular analysis of RNF213 gene for moyamoya disease in the Chinese Han population. *PLoS ONE.* (2012) 7:e48179. doi: 10.1371/journal.pone.0048179
23. Liu W, Morito D, Takashima S, Mineharu Y, Kobayashi H, Hitomi T, et al. Identification of RNF213 as a susceptibility gene for moyamoya disease and its possible role in vascular development. *PloS ONE.* (2011) 6:e22542. doi: 10.1371/journal.pone.0022542
24. Kobayashi H, Kabata R, Kinoshita H, Morimoto T, Ono K, Takeda M, et al. Rare variants in RNF213, a susceptibility gene for moyamoya disease, are found in patients with pulmonary hypertension and aggravate hypoxia-induced pulmonary hypertension in mice. *Pulm Circ.* (2018) 8:2045894018778155. doi: 10.1177/2045894018778155
25. Castellanos M, van Eendenburg C, Gubern C, Kadar E, Huguet G, Puig J, et al. Low levels of Caveolin-1 predict symptomatic bleeding after thrombolytic therapy in patients with Acute Ischemic Stroke. *Stroke.* (2018) 49:1525–7. doi: 10.1161/STROKEAHA.118.020683
26. Gubern-Merida C, Comajoan P, Huguet G, Garcia-Yebenes I, Lizasoain I, Moro MA, et al. Cav-1 protein levels in serum and infarcted brain correlate with hemorrhagic volume in a mouse model of Thromboembolic Stroke, Independently of rt-PA Administration. *Mol Neurobiol.* (2022) 59:1320–32. doi: 10.1007/s12035-021-02644-y
27. Yang MC, Zhang HZ, Wang Z, You FL, Wang YF. The molecular mechanism and effect of cannabinoid-2 receptor agonist on the blood-spinal cord barrier permeability induced by ischemia-reperfusion injury. *Brain Res.* (2016) 1636:81–92. doi: 10.1016/j.brainres.2016.01.047
28. Shi Z, Ma G, Zhang D. Haemodynamic analysis of adult patients with moyamoya disease: CT perfusion and DSA gradings. *Stroke Vasc Neurol.* (2021) 6:41–7. doi: 10.1136/svn-2019-000317
29. Wang R, Yu S, Alger JR, Zuo Z, Chen J, Wang R, et al. Multi-delay arterial spin labeling perfusion MRI in moyamoya disease–comparison with CT perfusion imaging. *Eur Radiol.* (2014) 24:1135–44. doi: 10.1007/s00330-014-3098-9
30. Woods JG, Chappell MA, Okell TW. Designing and comparing optimized pseudo-continuous Arterial Spin Labeling protocols for measurement of cerebral blood flow. *Neuroimage.* (2020) 223:117246. doi: 10.1016/j.neuroimage.2020.117246
31. Noguchi T, Kawashima M, Irie H, Ootsuka T, Nishihara M, Matsushima T, et al. Arterial spin-labeling MR imaging in moyamoya disease compared with SPECT imaging. *Eur J Radiol.* (2011) 80:e557–62. doi: 10.1016/j.ejrad.2011.01.016
32. Amemiya S, Takao H, Watanabe Y, Takei N, Ueyama T, Kato S, et al. Reliability and sensitivity to longitudinal CBF changes in Steno-Occlusive diseases: ASL Versus (123) I-IMP-SPECT. *J Magn Reson Imaging.* (2021). doi: 10.1002/jmri.27996
33. Zhang J, Zhu W, Xiao L, Cao Q, Zhang H, Wang H, et al. Lower Serum Caveolin-1 is associated with cerebral microbleeds in patients with Acute Ischemic Stroke. *Oxid Med Cell Longev.* (2016) 2016:9026787. doi: 10.1155/2016/9026787
34. Aoyagi M, Fukai N, Yamamoto M, Matsushima Y, Yamamoto K. Development of intimal thickening in superficial temporal arteries in patients with moyamoya disease. *Clin Neurol Neurosurg.* (1997) 99:S213–7. doi: 10.1016/S0303-8467(97)00046-2
35. Aoyagi M, Fukai N, Yamamoto M, Nakagawa K, Matsushima Y, Yamamoto K. Early development of intimal thickening in superficial temporal arteries in patients with moyamoya disease. *Stroke.* (1996) 27:1750–4. doi: 10.1161/01.STR.27.10.1750
36. Sun SJ, Zhang JJ, Li ZW, Xiong ZW, Wu XL, Wang S, et al. Histopathological features of middle cerebral artery and superficial temporal artery from patients with moyamoya disease and enlightenments on clinical treatment. *J Huazhong Univ Sci Technolog Med Sci.* (2016) 36:871–5. doi: 10.1007/s11596-016-1677-5
37. Ramirez CM, Zhang X, Bandyopadhyay C, Rotllan N, Sugiyama MG, Aryal B, et al. Caveolin-1 regulates atherogenesis by attenuating low-density lipoprotein transcytosis and vascular inflammation independently of endothelial nitric oxide synthase activation. *Circulation.* (2019) 140:225–39. doi: 10.1161/CIRCULATIONAHA.118.038571
38. Ito A, Shiroto T, Godo S, Saito H, Tanaka S, Ikumi Y, et al. Important roles of endothelial caveolin-1 in endothelium-dependent hyperpolarization and ischemic angiogenesis in mice. *Am J Physiol Heart Circ Physiol.* (2019) 316:H900–H10. doi: 10.1152/ajpheart.00589.2018
39. Morais C, Ebrahem Q, Anand-Apte B, Parat M-O. Altered angiogenesis in Caveolin-1 gene-deficient mice is restored by ablation of endothelial nitric oxide synthase. *Am J Pathol.* (2012) 180:1702–14. doi: 10.1016/j.ajpath.2011.12.018
40. Labrecque L, Royal I, Surprenant DS, Patterson C, Gingras D, Beliveau R. Regulation of vascular endothelial growth factor receptor-2 activity by caveolin-1 and plasma membrane cholesterol. *Mol Biol Cell.* (2003) 14:334–47. doi: 10.1091/mbc.e02-07-0379

Conflict of Interest: The authors declare that the research was conducted in the absence of any commercial or financial relationships that could be construed as a potential conflict of interest.

Publisher's Note: All claims expressed in this article are solely those of the authors and do not necessarily represent those of their affiliated organizations, or those of the publisher, the editors and the reviewers. Any product that may be evaluated in this article, or claim that may be made by its manufacturer, is not guaranteed or endorsed by the publisher.

Copyright © 2022 Zhao, Yu, Zhang, Qiu, Zhang, Chen, He and Ma. This is an open-access article distributed under the terms of the Creative Commons Attribution License (CC BY). The use, distribution or reproduction in other forums is permitted, provided the original author(s) and the copyright owner(s) are credited and that the original publication in this journal is cited, in accordance with accepted academic practice. No use, distribution or reproduction is permitted which does not comply with these terms.

frontiers | Frontiers in Neurology

REVIEW
published: 03 May 2022
doi: 10.3389/fneur.2022.895316

MicroRNA-Based Diagnosis and Therapeutics for Vascular Cognitive Impairment and Dementia

Weijie Zhai†, *Meng Zhao*†, *Guimei Zhang, Zicheng Wang, Chunxiao Wei and Li Sun**

Department of Neurology and Neuroscience Center, The First Hospital of Jilin University, Jilin University, Changchun, China

Vascular cognitive impairment and dementia (VCID) is a neurodegenerative disease that is recognized as the second leading cause of dementia after Alzheimer's disease (AD). The underlying pathological mechanism of VCID include crebromicrovascular dysfunction, blood-brain barrier (BBB) disruption, neuroinflammation, capillary rarefaction, and microhemorrhages, etc. Despite the high incidence of VCID, no effective therapies are currently available for preventing or delaying its progression. Recently, pathophysiological microRNAs (miRNAs) in VCID have shown promise as novel diagnostic biomarkers and therapeutic targets. Studies have revealed that miRNAs can regulate the function of the BBB, affect apoptosis and oxidative stress (OS) in the central nervous system, and modulate neuroinflammation and neurodifferentiation. Thus, this review summarizes recent findings on VCID and miRNAs, focusing on their correlation and contribution to the development of VCID pathology.

Keywords: apoptosis, blood-brain barrier, miRNAs, neuroinflammation, neurodifferentiation, oxidative stress, vascular cognitive impairment, dementia

OPEN ACCESS

Edited by:
Yuzhen Xu,
Tongji University, China

Reviewed by:
Yunpeng Cao,
The First Affiliated Hospital of China Medical University, China
Zhe Wang,
Dalian Medical University, China

***Correspondence:**
Li Sun
sunli99@jlu.edu.cn

†*These authors have contributed equally to this work and share first authorship*

Specialty section:
This article was submitted to Neurological Biomarkers, a section of the journal Frontiers in Neurology

Received: *13 March 2022*
Accepted: *28 March 2022*
Published: *03 May 2022*

Citation:
Zhai W, Zhao M, Zhang G, Wang Z, Wei C and Sun L (2022) MicroRNA-Based Diagnosis and Therapeutics for Vascular Cognitive Impairment and Dementia. Front. Neurol. 13:895316. doi: 10.3389/fneur.2022.895316

INTRODUCTION

Vascular cognitive impairment and dementia (VCID) is a term that ranges from mild cognitive impairment (MCI) to vascular dementia (VaD) and encompasses a continuum of cognitive disorders with cerebrovascular pathology (1). With an increase in the human lifespan, the number of individuals over the age of 60 in 2,050 is projected to be 2 billion (2), which will increase the demand for research on neurodegenerative diseases, especially those associated with aging. Age-related cerebrovascular factors are becoming recognized as a hallmark of VCID; thus, the number of patients affected by VCID is expected to exponentially increase in the upcoming decades (3) and be responsible for approximately 30% of the aging population living with dementia in Asia and developing countries (4).

VCID and dementia is a subtype of dementia affected by multiple factors, such as low educational attainment, female sex, stroke, and lifestyle (5). Current theories of the pathologies of VCID include cerebromicrovascular dysfunction, blood–brain barrier (BBB) disruption, neuroinflammation, capillary rarefaction, and microhemorrhages (3). However, none of the available pharmacological or preventative treatments decrease the development and progression of VCID. Improving our understanding of microRNAs (miRNAs) has provided strong epidemiological and experimental evidence that miRNAs are crucial for neuronal differentiation,

survival, and activity (6). By inhibiting messenger RNA (mRNA) translation or promoting its degradation, miRNAs can regulate the expression levels of proteins and ultimately affect disease progression (7, 8). In the central nervous system (CNS), miRNAs can modulate the tight junctions of the BBB, affect the proliferation and differentiation of neuronal cells, and participate in the occurrence and development of neuroinflammation and oxidative stress (OS), resulting in neurodegenerative diseases and cognitive impairment and indicating that miRNAs have a more extensive influence on various brain diseases.

Biomarkers found in the CNS are typically present at relatively low concentrations in the BBB. The miRNAs are mainly transported within liposomes, high-density lipoproteins (HDLs), exosomes, and proteins that can protect them from degradation (9). Therefore, miRNAs are relatively stable compared to other biomarkers, and it is easy to monitor changes in their expression. Compared with Alzheimer's disease (AD), VCID is preventable and curable, suggesting that advanced diagnoses and reliable risk assessments will provide patients with more promising clinical outcomes. This review provides an up-to-date assessment of the role of miRNAs in VCID, from the series of depression of the BBB, apoptosis and OS, neuroinflammation, and neurodifferentiation (**Figure 1**).

DEVELOPMENT AND FUNCTION OF miRNAs

miRNAs are small non-coding RNAs of approximately 18–21 nucleotides that regulate gene expression by targeting mRNAs *via* cleavage and translational repression (10). The biogenesis of miRNAs starts with pri-miRNAs, which are transcribed by RNA polymerase II and converted into mature miRNA by RNase III enzymes such as Drosha and Dicer (11). Mature miRNAs leave the nucleus and are then combined with the Argonaute protein (AGO) or targeted mRNAs. It is understood that miRNAs can participate in and regulate molecular expression by interacting with 3′ untranslated regions (3′-UTRs) to post-transcriptionally affect the expression of target mRNA (11). Complete or partial function of miRNAs is also based on 3′-UTRs of target mRNAs (12). Several studies have shown that miRNAs may serve as novel therapeutic agents. While a single miRNA could target hundreds of mRNAs and influence the expression of genes involved in a functional interacting pathway (13), synergetic miRNAs share a common transcriptional regulatory mechanism on the levels of sequence, secondary structure, and transcriptional regulation (12). Depending on the construction of these miRNA–mRNA functional synergetic networks (MFSNs), the central role of these synergetic miRNAs can be analyzed in complex diseases (3). To further apply miRNAs in disease diagnosis and therapy, considerable research has been conducted to characterize their pathophysiological function.

The ability of miRNAs to target multiple genes within the signaling pathway makes them a promising target for modulation, and powerful regulators of cellular activities, such as cell differentiation, development, and apoptosis (14); synaptic homeostasis and plasticity processes (15); and angiogenesis in endothelial cells (ECs) (16) in CNS. In CNS, functional neurons are specialized and persistently renew the information required for constant neuronal adaptation to environmental clues (17), and the value of miRNAs has been recognized, especially for neural cells. As non-protein-coding molecules, miRNAs could modulate the function of tight junction proteins, ECs, astrocytes, and pericytes of BBB (18, 19), which help maintain the microenvironment of neural cells. To protect neural cells from apoptosis and OS, miRNAs can regulate the signaling pathway involved in modulating the proliferation or differentiation of cells (7, 20). Using public databases, such as the Gene Ontology (GO) annotation and Kyoto Encyclopedia of Genes and Genomes (KEGG) pathway enrichment analyses, the principles of miRNA–mRNA interactions in signaling pathways were further characterized and provide a novel insight into the mechanisms of disease progression (21).

miRNAs AND VCID

miRNAs and BBB Dysfunction

As the most important protector of neurons in the brain, BBB exists between the blood microcirculation system and the brain parenchyma (19) to restrict the invasion of toxic substances, immune cells, and pathogens, playing an irreplaceable role in maintaining CNS homeostasis and proper function (22). Tight junctions constructed by ECs form the basic BBB structure, along with the basement membrane (BM), astrocytes, and pericytes, that contribute to the support and regulatory function of the BBB (23). However, the structural and functional integrity of the BBB is easily degraded by neuroinflammation, age-related degeneration, and other risk factors, which contribute to the onset and progression of cerebrovascular changes and neurodegenerative pathologies (24, 25).

Scientists have made great efforts to understand the molecular structure and pathological changes in the BBB, and have found that, compared with other cytokines, exosomes enriched with proteins and miRNAs can be easily released into the extracellular space, with functions ranging from blood coagulation to cell-to-cell communication (26). Ischemia is one of the most pathological processes of VCID that results in BBB dysfunction *via* inflammation or OS under the regulation of miRNAs and other factors (27, 28). A recent study showed that circular RNA DLGAP4 (circDLGAP4), which is an endogenous sponge of miR-143, *via* regulating the tight-junction protein and mesenchymal cell marker to inhibit the endothelial–mesenchymal transition, circDLGAP4 can significantly attenuate infarct areas and BBB damage, and is proposed to partially decrease the incidence of dementia (29). The miR-132 could target matrix metalloproteinase 9 (MMP-9) and dysregulate its expression, acting protection role in reducing the degradation of tight-junction proteins VE-cadherin and β-catenin to maintain the integrity of BBB (30). In addition, miR-9-5p can also mitigate BBB damage by activating the Hedgehog pathway and inhibiting the nuclear factor (NF)-κB/MMP-9 pathway (31). As mentioned earlier, ECs form the basic structure of the BBB. Of note, miR-126 participates in the maintenance of BBB integrity by regulating the functional status of ECs and attenuating BBB disruption

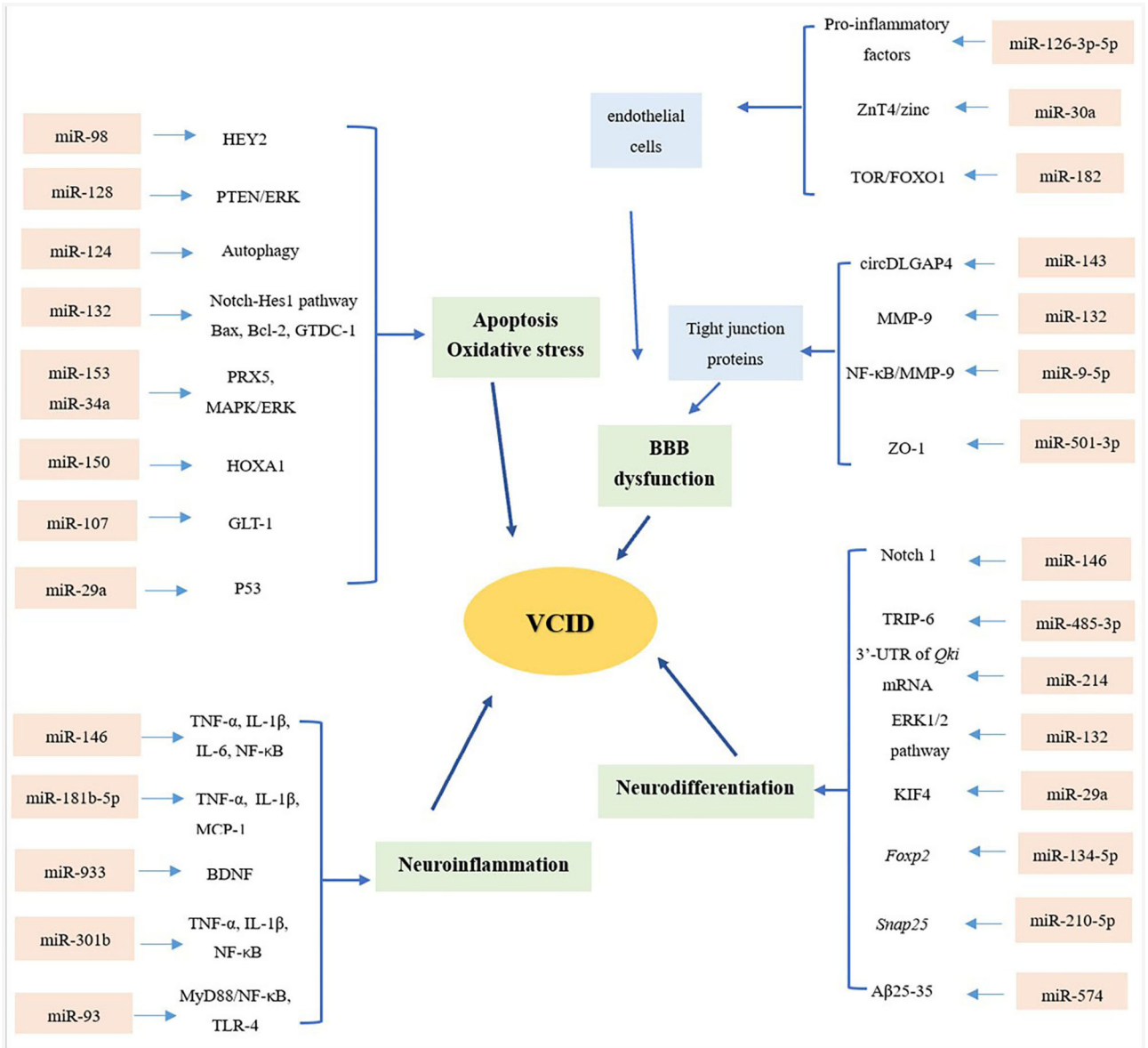

FIGURE 1 | Overview of miRNAs and mechanisms of VCID. From the aspects of blood–brain barrier (BBB) dysfunction, apoptosis and oxidative stress, neuroinflammation and neurodifferentiation, microRNAs (miRNAs) playing multiple roles in the pathology of vascular cognitive impairment and dementia (VCID), providing a novel sight and promising targets in the diagnosis and treatment of VCID.

by suppressing pro-inflammatory cytokines (32). It has been certificated that both *in vivo* and *in vitro*, miR-98 and miR-126-3p/-5p could significantly reduce the brain infract volume and improved behavioral outcomes (27, 32). Moreover, tumor necrosis factor alpha (TNF-α) modulates cerebral tight junctions and affects the BBB *via* the regulation of laudin-5 and tight-junction protein 1 (ZO-1) through the TNF-α-miR-501-3p–ZO-1 axis, resulting in working memory deficits and white matter lesions (33). In addition, it was found that overexpression of miR-Let7A does not only prevent brain endothelial (bEnd.3) cell death and inhibit pro-inflammatory responses but also protects tight-junction proteins from degradation under high-glucose conditions, indicating that miR-Let7A may be a novel solution for controlling BBB degradation, especially in patients with concomitant diabetes mellitus (DM) (34). Furthermore, exact mechanisms of how miRNAs affect the BBB integrity and ECs function have also been carried out, and miR-30a and miR-182 could modulate BBB permeability, tight-junction protein loss, and ECs apoptosis *via* ZnT4/zinc signaling pathway and mTOR/FOXO1 pathway, respectively (35, 36). Further study of complex physiological processes between miRNAs and BBB, and how to apply these mechanisms in clinic treatment are warranted.

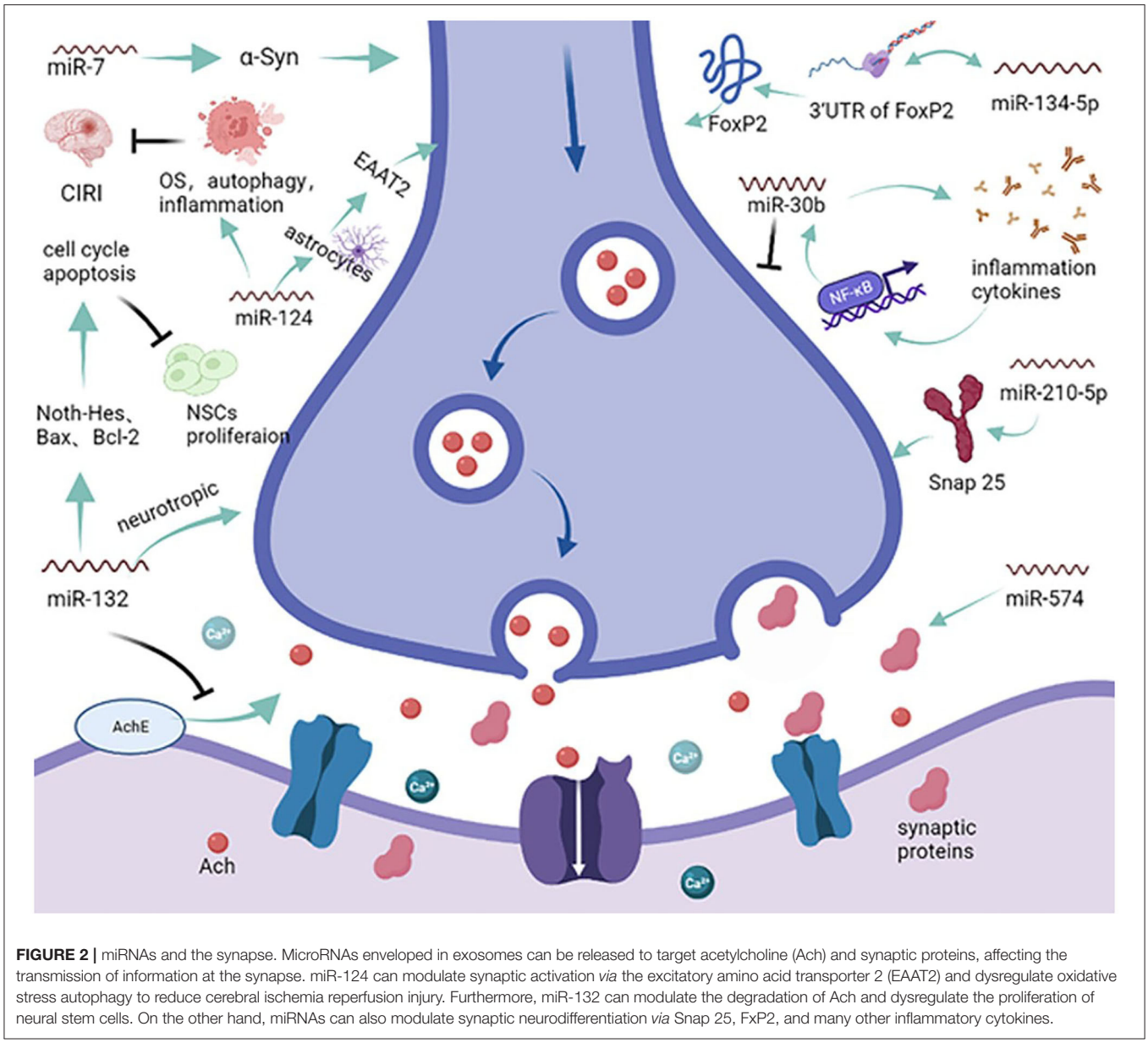

FIGURE 2 | miRNAs and the synapse. MicroRNAs enveloped in exosomes can be released to target acetylcholine (Ach) and synaptic proteins, affecting the transmission of information at the synapse. miR-124 can modulate synaptic activation *via* the excitatory amino acid transporter 2 (EAAT2) and dysregulate oxidative stress autophagy to reduce cerebral ischemia reperfusion injury. Furthermore, miR-132 can modulate the degradation of Ach and dysregulate the proliferation of neural stem cells. On the other hand, miRNAs can also modulate synaptic neurodifferentiation *via* Snap 25, FxP2, and many other inflammatory cytokines.

miRNAs and Apoptosis/Oxidative Stress

Abnormal apoptosis is a prerequisite for endothelial and neuronal cell damage, resulting in the onset and progression of VCID (37). Additionally, synergistic and additive interactions between apoptosis and other signaling pathways add to the symptoms of VCID. Dementia caused by multiple infarcts implies that if strokes are prevented, so is the VCID that results from cerebral infarcts (38). Identifying pathways that predominantly include miRNAs during apoptosis will contribute to a better understanding of the functional overlap across diseases. As one of the most abundant miRNAs in brain tissue, miR-124a can be transported into astrocytes through neuronal exosomes, significantly increasing the expression of protein excitatory amino acid transporter 2 (EAAT2, rodent analog GLT1) and modulating synaptic activation (**Figure 2**) (39). However, the exact role of miR-124 has not been systematically elucidated. In age-related ischemic encephalopathy (IE), miR-124 can improve the effects of cerebral ischemic reperfusion injury (CIRI) by regulating OS, autophagy, and neuroinflammation but plays a negative role in synaptic plasticity and axonal growth *via* apoptosis (40). A greater understanding of miR-124 will open new avenues for further intervention in VCID. Increasing evidence suggests that cognitive decline in the early stages of neurodegenerative diseases, such as VCID, is a consequence of changes in synaptic structure and function (15). Based on analyses using online tools and a luciferase reporter assay, miR-132 was shown to protect acetylcholine (Ach) from degradation by most fast enzymes like acetylcholinesterase (ACHE) found

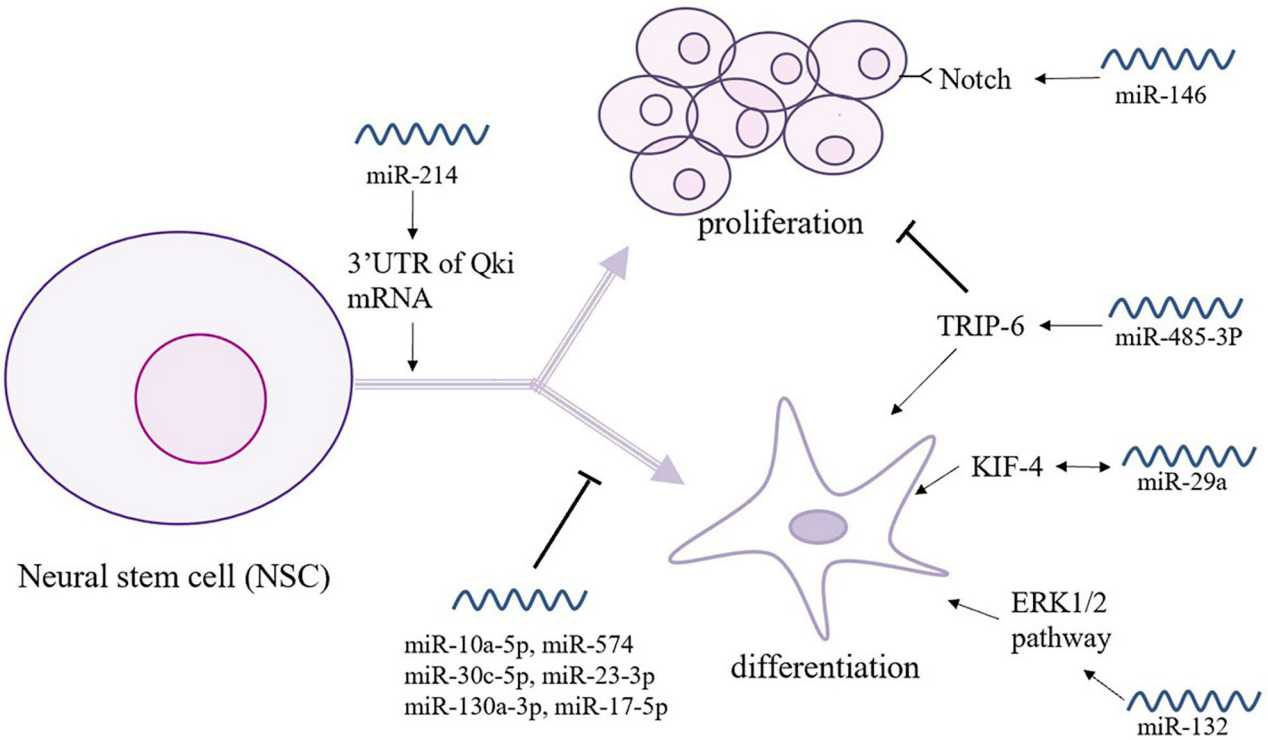

FIGURE 3 | The relationship between miRNAs and neural stem cells (NSCs). NSCs play a key role in brain homeostasis and repair and show intrinsic pleiotropic properties. Thus, the intimate connections between NSCs and miRNAs are under study. As shown here, miR-146 and miR-585-3p play an opposite role in the proliferation and differentiation of NSCs. Moreover, a great number of miRNAs participates in the self-renewal and gene expression of NSCs.

in the body, and that miR-132 could also exert favorable effects on CNS neurons *via* brain-derived neurotrophic factors (BDNF) (41). In contrast, another report showed that miR-132 negatively regulates neural stem cell (NSC) proliferation by affecting the cell cycle and apoptosis through the Notch-Hes1 pathway, Bax, Bcl-2, and glycosyl transferase-like domain containing−1 (GTDC-1), which could induce neural cell apoptosis and tau phosphorylation (**Figure 2**) (20, 42). Due to the complexity of miRNAs, the key miRNA in these types of pathways and the construction of a shared-miRNA network is imperative. Previous studies have investigated the implications of α-synuclein (α-Syn), especially in inducing mitochondrial fragmentation, OS, and autophagy, which could promote neuronal cell death after stroke. It has been reported that treatment with miR-7 mimics greatly reduces the post-ischemic induction of α-Syn, significantly decreases the lesion volume, and improves motor and cognitive functional recovery (43). In addition, miR-153 and miR-34a have confirmed roles in protecting neural cells from death and apoptosis by upregulating peroxiredoxin 5 (PRX5) and MAPK/ERK signaling pathways, respectively, reducing the cell cycle and leading to a reduction in cell proliferation (44, 45), which could ultimately mitigate the pathology of dementia. Moreover, compared with the miR-150 mimic negative group, miR-150 overexpression significantly aggravated cell apoptosis by inhibiting the expression of homeobox (HOX) A1, which aggravates hippocampal neuronal apoptosis and cognitive impairment (46).

In addition to apoptosis, OS is also considered as one of the significant events in the pathological cascade of dementia, causing mitochondrial dysfunction and protein misfolding (47). Many studies in this field have shown that there is a mutual correlation between OS and miRNAs, and OS affects the expression of miRNAs, which have a counteracting effect on genes involved in OS (6). In the CNS, ECs play an irreplaceable role in protecting the cerebrovascular system from conditions, such as OS erosion, inflammation, and diabetes; however, OS has been predicted to predispose neurons to death in both direct and indirect ways (6, 48). Attenuating OS responsiveness could specifically limit the risk factors of cerebrovascular disease and improve endothelial homeostasis in vascular depression and VCID (49). The miR-107c and miR-29a could target glutamate transporter-1 (GLT-1) to modulate excitotoxicity in the CNS; miR-107c could target GLT-1 directly to evaluate the glutamate accumulation and neuronal excitotoxicity, whereas miR-29a mainly acts on p53 upregulated modulator of apoptosis (PUMA), which could attenuate OS and protect neurons from dementia caused by ischemic injury (50). The miR-128 is enriched in the CNS and easily detected in circulating lymphocytes and can inhibit neuronal damage caused by oxygen and glucose deprivation/reoxygenation (OGD/R) *via* the PTEN and ERK

pathways (51). The correlation between miR-124 level and lesion size on CT indicated that miR-124 could be released from damaged brain tissue in patients who died within 3 months after suffering from a stroke (52). In contrast, by binding to the regulatory factor X1 (*RFX1*) mRNA, miR-124 could increase the expression of *RFX1*, resulting in the suppression of apolipoprotein E (APOE) and cellular amyloid beta (Aβ) in microglia, which could undermine the cognitive behavior of dementia (53). Another area of research in this field tracked the expression level of miRNAs in 45 patients with MCI and AD; notably, miR-146a and miR-181a were significantly upregulated in patients with MCI who later converted to AD, which was related to Aβ and APOE ε4 allele presence (54). This indicates that miRNAs can also be an indicator of disease progression, providing an insight in disease prediction. Furthermore, according to the measurement of OS-related proteins, superoxide dismutase and Na^+, K^+, and ATP, Chen et al. found that miR-98 could bind to the enhancer of split (Hes) related with the YRPW motif protein 2 (HEY2) to inhibit the production of Aβ and improve OS and mitochondrial dysfunction, providing a novel basis for targeted therapy for dementia (55).

miRNAs and Neuroinflammation

Dynamic changes in miRNAs regulate the expression of genes involved in cognitive processes such as learning and executive abilities. Although the pathophysiology of VCID remains largely unknown, considerable efforts have been focused on neuroinflammation. Neuroinflammation is a hallmark of many neurological disorders, and pro-inflammatory or anti-inflammatory miRNAs within CNS signaling pathways can greatly aggravate or mitigate the pathological consequences of neurodegenerative diseases (56, 57). It has been reported that anti-inflammatory miRNAs (miR-21, miR-124, and miR-146a) and pro-inflammatory miRNAs (miR-27b, miR-155, and miR-326) regulate neuroinflammation by down or upregulating endogenous levels of immune receptors such as toll-like receptors (TLRs) or misfolded proteins that accumulate in the extracellular space (58). Related experiments conducted in BV-2 microglial cells and mice showed that miR-146 could suppress the release of pro-inflammatory factors [TNF-α, interleukin (IL)-1β, and IL-6] and the expression of mRNA in targeted cells; the upregulation of miR-146 could not only suppress the NF-κB pathway and microglial activation in the hippocampus but also promote hippocampus-dependent learning and memory capability (59). In addition to miR-146, mouse model and bioinformatics studies confirmed that miR-181b-5p can repress the expression of pro-inflammatory mediators such as TNF-α, IL-1β, and monocyte chemoattractant protein (MCP)-1. Injection of an miR-181b-5p mimic into the hippocampus of mice significantly improved cognition (60). Moreover, middle cerebral artery occlusion (MCAO)-induced behavioral disability and microglial activation in the brain were greatly improved and inhibited by miRNA-210-LNA (miR-210 inhibitor) post-treatment, providing new insight into the molecular basis of a novel therapeutic strategy (61). As the cholesterol metabolite, 27-hydroxycholesterol (27-OHC), induces discrete or directional inflammatory factors in microvascular endothelial cells (human microvascular endothelial cells, HMVECs) and increases the expression of miR-933 and inflammatory cytokines, which are elevated in plasma from dementia patients, more than that, *via* facilitates permeability and directional secretion from ECs into the brain, miR-933 may act as a paracrine inhibitor of neuronal BDNF, which provides a useful neuroprotective properties (62). These results show how miRNA functions in neuroinflammation and VCID progression, providing a novel insight on possible VCID interventions.

Before VCID occurs, a sustained pro-inflammatory environment brought about by NF-κB leads to chronic reactive astrogliosis, undermining the white matter (WM) (63). By interacting with NF erythroid 2-related factor 2 (Nrf2), NF-κB can fine-tune the cellular oxidative and inflammatory balance and participate in multiple pathologies in VCID, such as restoration of endothelial function and neurovascular coupling, reduction of amyloidopathy, and protection of WM integrity (64). To further implement miRNAs in disease mechanisms, counter intervention between miRNAs and NF-κB is ongoing. With advances in understanding that acupuncture can alleviate cognitive degeneration in VCID, in rats treated with acupuncture, TLR-4 was greatly dysregulated, accompanied by a decrease in miR-93 and MyD88/NF-κB signaling pathway activation (65). Furthermore, miR-301b accelerated cognitive impairment in mice with depression-like behavior; overexpression of miR-301b activated the NF-κB signaling pathway and aggravated inflammation in hippocampus, which accompanied the release of TNF-α, IL-1β, and many other cytokines (66).

miRNAs and Neurodifferentiation

Vascular cognitive impairment and dementia typically refers to patients with both stroke and cognitive impairment. Recent studies have highlighted the roles of cerebrovascular injury, white matter tract integrity, microinfarcts, and secondary neurodegeneration in the development of VCID. The miRNAs modulate multiple biological functions, such as cell fate determination and differentiation. It has been found that the onset of cognitive impairment is accompanied by the senescence, loss, and neurogenesis decline of hippocampal neural stem cells (H-NSCs). Interestingly, embryonic stem cell-derived small extracellular vesicles (ESC-sEVs) can alleviate senescence and recover the compromised proliferation and differentiation capacity of H-NSCs *via* miR-17-5p, miR-18a-5p, miR-21-5p, and miR-29a-3p, which can inhibit the mammalian target of rapamycin complex 1 (mTORC1) activation (67).

Over the past 20 years, stem cell technology has become an increasingly helpful in the investigation and treatment of neurodegenerative diseases. NSCs participate in brain homeostasis and repair and show pleiotropic intrinsic properties, making them a promising candidate for the treatment of dementia (**Figure 3**) (68). Indeed, Notch signaling encodes a highly conserved cell-surface receptor that affects cell processes such as cell differentiation, cell apoptosis, and cell proliferation. In serum-free medium, miR-146 significantly promoted NSC proliferation by targeting the Notch 1 pathway but reduced the

differentiation efficiency of glial cells (69). However, miR-485-3p has the complete opposite effect; miR-485-3p can reduce proliferation but can promote the differentiation of NSCs by decreasing TRIP-6 activity (70). Following the criteria and moderated *t*-statistics, miR-10a-5p was shown to attenuate the self-renewal of undifferentiated NSCs; however, similar to miR-574, miR-30c-5p, miR23-3p, miR130a-3p, and miR-17-5p miRNA families were predicted to decrease the expression of several genes associated with the differentiation of neurons, synapse formation, and neurite outgrowth (71). The miR-214 not only affects the differentiation of NSCs but also plays a key role that helps maintain the balance between proliferation and differentiation by binding the 3′-UTR of *Qki* mRNA, affecting downstream its signal transmission (72). Additionally, miR-132 is significantly overexpressed in differentiating NSCs and is accompanied by the activation of the ERK1/2 pathway, and it promotes glial cell differentiation *via* Mecp2 expression (20). During the process of neurodifferentiation, the level of miR-29a in plasma shows a time-dependent increase similar to that of Kruppel-like factor 4 (KlF4), which suggests that the regulation of miR-29a occurs through the KlF4 signaling pathway (73). This mechanism suggests that KIF4 may be used to promote miR-29a and provides a novel possibility for the treatment of VCID (73).

A widely accepted theory is that memory deficiency associated with cognitive impairment results from synaptic dysfunction. Another focus of research in this field is the investigation of the correlation between miRNAs and synaptic proteins (**Figure 2**). It has been found that miR-134-5p can act on Forkhead box P2 (*Foxp2*) mRNA to affect its level of expression; however, silencing *Foxp2* minimizes the effect of miR-134-5p on synaptic protein loss, which may prevent the development of cognitive impairment, especially in vocal learning (74). In addition, by comparing the expression level of miR-30b in APP transgenic (TG) and wild-type (WT) mice, miR-30b was significantly upregulated in TG mice, causing synaptic and cognitive dysfunction (75). Indeed, miR-30b is triggered by pro-inflammatory cytokines through NF-κB signaling, suggesting a feedback loop in the process of dementia. More specifically, real-time reverse transcription polymerase chain reaction (RT-PCR) revealed that overexpression of miR-210-5p can decrease the number of synapses in primary hippocampal neurons by targeting synaptosomal-associated protein, 25 kDa (*Snap25*) (76). In experimental trials that used APP/PS1 mice and WT mice, miR-574 could lower neuritin and synaptic protein expression in primary hippocampal neurons *via* targeting Aβ25-35, resulting aggravation of cognitive dysfunction in APP/PS1 mice compared with WT mice (77).

THE PERSPECTIVE OF miRNAs IN THE DIAGNOSIS AND TREATMENT OF VCID

As the second most common cause of cognitive impairment, patients with VCID will be up to 150 million in 2,050. VCID has drawn the attention of researchers because it is preventable and curable; however, some neuroprotective agents have been reported to attenuate but not cure symptoms. Risk factors of VCID including protective factors, such as higher education, occupation and social networks, and others, increase the risk of dementia (38). According to the National Institute for Neurological Disorders and Stroke-Association International pour la Recherché et l'Enseignement en Neurosciences (NINDS-AIREN), the basic features of VCID include (1) acute impairment of memory and at least two other cognitive domains, (2) neuroimaging evidence of cerebrovascular lesions, and (3) evidence for a temporal relationship between stroke and cognitive loss (78). In recent years, miRNAs are regarded as cost-effective and non-invasive biomarkers in disease diagnosis and therapy response monitoring (79). Additionally, miRNAs are easily detected in biofluids like plasma and cerebrospinal fluid (CSF) due to their unique biological characteristics (15), which can provide biological and clinical breakthroughs.

To gain a better understanding of how miRNAs could support both diagnosis and therapy, studies of clinical patients and biological experiments have been conducted. Validation studies revealed that four miRNAs (miR-409-3p, miR-502-3p, miR-486-5p, and miR-451a) are potentially valuable biomarkers for identifying VCID with relatively high sensitivity and specificity (80). Moreover, combined receiver operating characteristic curve analysis of seven miRNAs revealed an area under the curve (AUC) of 0.64 with a sensitivity of 55.5% and specificity of 65.7%, whereas plasma miR-409-3p, miR-502-3p, miR-486-5p, and miR-451a could differentiate patients with VCID from healthy controls (80). To improve the diagnosis and anti-diastole level of dementia, the value of miRNAs in differential diagnosis protocols was determined. Through the measurement of miRNA expression levels in MCI, VCID, AD, and Parkinson's disease with dementia (PDD), miR-1, miR-384, and miR-19b-3p were identified as good diagnostic biomarkers and provided a novel insight in disease prevention (81, 82). Another study comparing different miRNAs expressed in AD, MCI, and healthy controls found that miR-455-3p, miR-4668-5p, miR-3613-3p, and miR-4674 were upregulated, whereas miR-6722 was downregulated in AD and MCI compared with healthy controls (83). More research is warranted concerning the clinical consequences of VCID and expression changes of miRNAs, especially in disease diagnosis and prediction (**Table 1**).

A large number of fundamental experiments have been conducted to gain a better understanding of their signaling pathways and the post-transcriptional mechanisms of miRNAs. Comparison of astrocytic and microglial activation, WM damage, water channels, and glymphatic dysfunction in mice with miR-126 deletion (miR-126 $EC^{-/-}$), and control (miR-126 flox/flox), miR-126 $EC^{-/-}$mice showed significantly decreased cerebral blood flow (CBF) and increased inflammation that was accompanied by poor performance and cognitive deficits (84). As a vasoconstrictor factor, endothelin-1 (ET-1) was increased in the plasma of patients after stroke and in the CSF of patients with VCID (86). An miR-125a inhibitor substantially upregulated the expression of ET-1, whereas miR-125a and the presence of the rs12976445 minor allele polymorphism downregulated the delivery of ET-1 to ECs (87). These results suggested that

TABLE 1 | Changes in miRNAs expression level and its role in disease diagnostics.

miRNAs	Source	Expression level	Diagnosis	Reference
miR-409-3p	Plasma	Down	Discrimination diagnosis	(80)
miR-502-3p		Up		
miR-486-5p		Up		
miR-451a		Up		
miR-1	Exosome	Down	AD, VaD, or PDD	(81), (82)
miR-384		Up		
miR-19b-3p		Down		
miR-455-3p	Serum	Up	AD, MCI, or healthy	(83)
miR-4668-5p		Up		
miR-3613-3p		Up		
miR-4674		Up		
miR-126	Mouse serum	Down	Neuroinflammation, water channel and glymphatic dysfunction	(84)
miR-191	Mice	Up	Apoptosis and proliferation dysregulation	(85)

miR-125a, ET-1, and rs12976445 have a promising potential as pathological solutions for post-stroke dementia.

Apoptosis and proliferation have been implicated in many diseases, confirming the negative correlation between miRNAs and cognitive impairment. It is known that miR-191 can aggravate apoptosis and misregulate proliferation and migration; *in vivo* studies have shown that applying an miR-191 antagomir significantly attenuated infarction volume by mechanically targeting vascular endothelial zinc finger 1 (*VEZF1*) transcript (85). In addition, miR-196a and LRIG3 enhanced learning and memory by ameliorating injury to hippocampal neurons *via* the PI3K/Akt pathway (88). Although these studies represent only the tip of the iceberg, they provide a novel insight into the multiple miRNAs that can intervene in signaling pathway function and affect the outcomes of patients with different forms of dementia and cognitive impairment.

Various treatments and interventions have been reported to be effective for dementia; however, no therapeutic cures are currently available. According to previous reports, symptomatic and alternative therapies are effective; however, antipsychotic treatment is less satisfactory (89). For VCID caused by vascular factors that may be mixed with AD pathological changes, more attention should be focused on therapeutic agents for synaptic protection, anti-pathologic therapeutics, and effective management of vascular risk factors (90). However, acupuncture is a promising alternative therapy and may be an underlying TLR4 inhibitor for VCID (65). Preclinical experiments indicate the advantages of remote ischemic conditioning (RIC) for decreasing the recurrence of ischemic stroke, and repetitive treatments with RIC in patients for 6 months show satisfactory outcomes, especially in neuropsychological assessments (91). Currently, therapeutics based on miRNAs are mainly focused on miRNA mimics and inhibitors (antagomirs), respectively, to adjust the expression level of target genes (92). Mice with transient middle cerebral artery occlusion showed that pre- or post-ischemic treatment with an miR-7 mimic decreased lesion volume and improved motor and cognitive functional recovery (43). Biomarkers can aid in early diagnosis before the pathology occurs, limiting disease progression, and potentially indicating patient response to the treatment. Thus, refining the use of biomarkers will allow dementia treatment to enter the era of precision medicine (93).

CONCLUSION

This is an exciting time for miRNAs research because of the recent advancement and identification of miRNA genes, their expression patterns, and their regulatory targets in diseases such as VCID, AD, and other neurodegenerative diseases. The mechanisms discussed in this review provide *prima facie* evidence for the mutual effects of miRNAs on the pathogenesis of VCID. A vast number of miRNAs play roles in the mutual regulation in genes and proteins, and it has been reported that high- or low-expression level of miRNAs can improve or impair the pathological progress of diseases. Hence, we have highlighted the roles of miRNAs in the modulation of VCID. However, the clear interventions of miRNAs and VCID are still poorly reported, and further studies in this area are expected to emphasize the pathways and mechanisms that could improve disease and help develop VCID therapies.

AUTHOR CONTRIBUTIONS

WZ and MZ organized the content of the entire manuscript, wrote the sections, and were responsible for the figures. GZ, ZW, CW, and LS contributed substantially to the conception and design of the work. All authors read and approved the final manuscript.

FUNDING

This study was supported by the grant provided by the Major Chronic Disease Program of the Ministry of Science and Technology of China (No. 2018YFC1312301) and the General Program of the National Natural Science Foundation of China (No. 82071442), The First Hospital of Jilin University, China.

ACKNOWLEDGMENTS

We would like to thank Editage (https://www.editage.cn) for English language editing.

REFERENCES

1. Nguyen DH, Cunningham JT, Sumien N. Estrogen receptor involvement in vascular cognitive impairment and vascular dementia pathogenesis and treatment. *Geroscience.* (2021) 43:159–66. doi: 10.1007/s11357-020-00263-4
2. Wortmann M. Dementia: a global health priority - highlights from an adi and world health organization report. *Alzheimers Res Ther.* (2012) 4:40. doi: 10.1186/alzrt143
3. Balasubramanian P, DelFavero J, Ungvari A, Papp M, Tarantini A, Price N, et al. Time-restricted feeding (Trf) for prevention of age-related vascular cognitive impairment and dementia. *Aging Res Rev.* (2020) 64:101189. doi: 10.1016/j.arr.2020.101189
4. Wolters FJ, Ikram MA. Epidemiology of vascular dementia. *Arterioscler Thromb Vasc Biol.* (2019) 39:1542–9. doi: 10.1161/ATVBAHA.119.311908
5. van der Flier WM, Skoog I, Schneider JA, Pantoni L, Mok V, Chen CLH, et al. Vascular cognitive impairment. *Nat Rev Dis Primers.* (2018) 4:18003. doi: 10.1038/nrdp.2018.3
6. Konovalova J, Gerasymchuk D, Parkkinen I, Chmielarz P, Domanskyi A. Interplay between micrornas and oxidative stress in neurodegenerative diseases. *Int J Mol Sci.* (2019) 20:23. doi: 10.3390/ijms20236055
7. Juzwik CA. S SD, Zhang Y, Paradis-Isler N, Sylvester A, Amar-Zifkin A, et al. Microrna dysregulation in neurodegenerative diseases: a systematic review. *Prog Neurobiol.* (2019) 182:101664. doi: 10.1016/j.pneurobio.2019.101664
8. Correia de Sousa M, Gjorgjieva M, Dolicka D, Sobolewski C, Foti M. Deciphering mirnas' action through mirna editing. *Int J Mol Sci.* (2019) 20:24. doi: 10.3390/ijms20246249
9. Tili E, Mezache L, Michaille JJ, Amann V, Williams J, Vandiver P, et al. Microrna 155 up regulation in the cns is strongly correlated to down's syndrome dementia. *Ann Diagn Pathol.* (2018) 34:103–9. doi: 10.1016/j.anndiagpath.2018.03.006
10. Wang F, Niu G, Chen X, Cao F. Molecular imaging of micrornas. *Eur J Nucl Med Mol Imaging.* (2011) 38:1572–9. doi: 10.1007/s00259-011-1786-0
11. Lee YS, Dutta A. Micrornas in cancer. *Annu Rev Pathol.* (2009) 4:199–227. doi: 10.1146/annurev.pathol.4.110807.092222
12. Bartel DP. Micrornas: genomics, biogenesis, mechanism, and function. *Cell.* (2004) 116:281–97. doi: 10.1016/S0092-8674(04)00045-5
13. Lu TX, Rothenberg ME. Microrna. *J Allergy Clin Immunol.* (2018) 141:1202–7. doi: 10.1016/j.jaci.2017.08.034
14. Saliminejad K, Khorram Khorshid HR, Soleymani Fard S, Ghaffari SH. An overview of micrornas: biology, functions, therapeutics, analysis methods. *J Cell Physiol.* (2019) 234:5451–65. doi: 10.1002/jcp.27486
15. Siedlecki-Wullich D, Minano-Molina AJ, Rodriguez-Alvarez J. Micrornas as early biomarkers of alzheimer's disease: a synaptic perspective. *Cells.* (2021) 10:1. doi: 10.3390/cells10010113
16. Tiwari A, Mukherjee B, Dixit M. Microrna key to angiogenesis regulation: mirna biology and therapy. *Curr Cancer Drug Targets.* (2018) 18:266–77. doi: 10.2174/1568009617666170630142725
17. Wu J, He J, Tian X, Luo Y, Zhong J, Zhang H, et al. Microrna-9-5p alleviates blood-brain barrier damage and neuroinflammation after traumatic brain injury. *J Neurochem.* (2020) 153:710–26. doi: 10.1111/jnc.14963
18. Toyama K, Spin JM, Mogi M, Tsao PS. Therapeutic perspective on vascular cognitive impairment. *Pharmacol Res.* (2019) 146:104266. doi: 10.1016/j.phrs.2019.104266
19. Almutairi MM, Gong C, Xu YG, Chang Y, Shi H. Factors controlling permeability of the blood-brain barrier. *Cell Mol Life Sci.* (2016) 73:57–77. doi: 10.1007/s00018-015-2050-8
20. Chen D, Hu S, Wu Z, Liu J, Li S. The role of mir-132 in regulating neural stem cell proliferation, differentiation and neuronal maturation. *Cell Physiol Biochem.* (2018) 47:2319–30. doi: 10.1159/000491543
21. Liu B, Li J, Cairns MJ. Identifying mirnas, targets and functions. *Brief Bioinform.* (2014) 15:1–19. doi: 10.1093/bib/bbs07
22. Ma F, Zhang X, Yin KJ. Micrornas in central nervous system diseases: a prospective role in regulating blood-brain barrier integrity. *Exp Neurol.* (2020) 323:113094. doi: 10.1016/j.expneurol.2019.113094
23. Van Dyken P, Lacoste B. Impact of metabolic syndrome on neuroinflammation and the blood-brain barrier. *Front Neurosci.* (2018) 12:930. doi: 10.3389/fnins.2018.00930
24. Goodall EF, Leach V, Wang C, Cooper-Knock J, Heath PR, Baker D, et al. Age-associated mrna and mirna expression changes in the blood-brain barrier. *Int J Mol Sci.* (2019) 20:12. doi: 10.3390/ijms20123097
25. Daneman R, Prat A. The blood-brain barrier. *Cold Spring Harb Perspect Biol.* (2015) 7:a020412. doi: 10.1101/cshperspect.a020412
26. Chakraborty C, Sharma AR, Sharma G, Bhattacharya M, Lee SS. Micrornas: possible regulatory molecular switch controlling the bbb microenvironment. *Mol Ther Nucleic Acids.* (2020) 19:933–6. doi: 10.1016/j.omtn.2019.12.024
27. Bernstein DL, Zuluaga-Ramirez V, Gajghate S, Reichenbach NL, Polyak B, Persidsky Y, et al. Mir-98 reduces endothelial dysfunction by protecting blood-brain barrier (Bbb) and improves neurological outcomes in mouse ischemia/reperfusion stroke model. *J Cereb Blood Flow Metab.* (2020) 40:1953–65. doi: 10.1177/0271678X19882264
28. Vasudeva K, Munshi A. Mirna dysregulation in ischaemic stroke: focus on diagnosis, prognosis, therapeutic and protective biomarkers. *Eur J Neurosci.* (2020) 52:3610–27. doi: 10.1111/ejn.14695
29. Bai Y, Zhang Y, Han B, Yang L, Chen X, Huang R, et al. Circular rna dlgap4 ameliorates ischemic stroke outcomes by targeting mir-143 to regulate endothelial-mesenchymal transition associated with blood-brain barrier integrity. *J Neurosci.* (2018) 38:32–50. doi: 10.1523/JNEUROSCI.1348-17.2017
30. Zuo X, Lu J, Manaenko A, Qi X, Tang J, Mei Q, et al. Microrna-132 attenuates cerebral injury by protecting blood-brain-barrier in mcao mice. *Exp Neurol.* (2019) 316:12–9. doi: 10.1016/j.expneurol.2019.03.017
31. O'Carroll D, Schaefer A. General principals of mirna biogenesis and regulation in the brain. *Neuropsychopharmacology.* (2013) 38:39–54. doi: 10.1038/npp.2012.87
32. Pan J, Qu M, Li Y, Wang L, Zhang L, Wang Y, et al. Microrna-126-3p/-5p overexpression attenuates blood-brain barrier disruption in a mouse model of middle cerebral artery occlusion. *Stroke.* (2020) 51:619–27. doi: 10.1161/STROKEAHA.119.027531
33. Toyama K, Spin JM, Deng AC, Huang TT, Wei K, Wagenhauser MU, et al. Microrna-Mediated therapy modulating blood-brain barrier disruption improves vascular cognitive impairment. *Arterioscler Thromb Vasc Biol.* (2018) 38:1392–406. doi: 10.1161/ATVBAHA.118.310822
34. Song J, Yoon SR, Kim OY. Mir-Let7a controls the cell death and tight junction density of brain endothelial cells under high glucose condition. *Oxid Med Cell Longev.* (2017) 2017:6051874. doi: 10.1155/2017/6051874
35. Wang P, Pan R, Weaver J, Jia M, Yang X, Yang T, et al. Microrna-30a regulates acute cerebral ischemia-Induced blood-brain barrier damage through znt4/Zinc pathway. *J Cereb Blood Flow Metab.* (2021) 41:641–55. doi: 10.1177/0271678X20926787
36. Zhang T, Tian C, Wu J, Zhang Y, Wang J, Kong Q, et al. Microrna-182 exacerbates blood-brain barrier (Bbb) disruption by downregulating the mtor/Foxo1 pathway in cerebral ischemia. *FASEB J.* (2020) 34:13762–75. doi: 10.1096/fj.201903092R
37. Wang XX, Zhang B, Xia R, Jia QInflammation Y. Apoptosis and autophagy as critical players in vascular dementia. *Eur Rev Med Pharmacol Sci.* (2020) 24:9601–14. doi: 10.26355/eurrev_202009_23048
38. Iadecola C, Duering M, Hachinski V, Joutel A, Pendlebury ST, Schneider JA, et al. Vascular cognitive impairment and dementia: jacc scientific expert panel. *J Am Coll Cardiol.* (2019) 73:3326–44. doi: 10.1016/j.jacc.2019.04.034
39. Morel L, Regan M, Higashimori H, Ng SK, Esau C, Vidensky S, et al. Neuronal exosomal mirna-dependent translational regulation of astroglial glutamate transporter glt1. *J Biol Chem.* (2013) 288:7105–16. doi: 10.1074/jbc.M112.410944
40. Liu X, Feng Z, Du L, Huang Y, Ge J, Deng Y, et al. The potential role of microrna-124 in cerebral ischemia injury. *Int J Mol Sci.* (2019) 21:1. doi: 10.3390/ijms21010120
41. Yang FW, Wang H, Wang C, Chi GN. Upregulation of acetylcholinesterase caused by downregulation of microrna-132 is responsible for the development of dementia after ischemic stroke. *J Cell Biochem.* (2020) 121:135–41. doi: 10.1002/jcb.28985
42. Liu DY, Zhang L. Microrna-132 promotes neurons cell apoptosis and activates tau phosphorylation by targeting gtdc-1 in alzheimer's disease. *Eur Rev Med Pharmacol Sci.* (2019) 23:8523–32.
43. Kim T, Mehta SL, Morris-Blanco KC, Chokkalla AK, Chelluboina B, Lopez M, et al. The microrna mir-7a-5p ameliorates ischemic

brain damage by repressing alpha-synuclein. *Sci Signal*. (2018) 11:560. doi: 10.1126/scisignal.aat4285
44. Li GF Li ZB, Zhuang SJ Li GC. Inhibition of microrna-34a protects against propofol anesthesia-Induced neurotoxicity and cognitive dysfunction via the mapk/Erk signaling pathway. *Neurosci Lett.* (2018) 675:152–9. doi: 10.1016/j.neulet.2018.03.052
45. Xu C, Wang C, Meng Q, Gu Y, Wang Q, Xu W, et al. Mir153 promotes neural differentiation in the mouse hippocampal ht22 cell line and increases the expression of neuronspecific enolase. *Mol Med Rep*. (2019) 20:1725–35. doi: 10.3892/mmr.2019.10421
46. Wei C, Xu X, Zhu H, Zhang X, Gao Z. Promotive role of microrna150 in hippocampal neurons apoptosis in vascular dementia model rats. *Mol Med Rep*. (2021) 23:4. doi: 10.3892/mmr.2021.11896
47. Nunomura A, Perry Rna G. and Oxidative Stress in Alzheimer's Disease: Focus on Micrornas. *Oxid Med Cell Longev*. (2020) 2020:2638130. doi: 10.1155/2020/2638130
48. Gocmez SS, Sahin TD, Yazir Y, Duruksu G, Eraldemir FC, Polat S, et al. Resveratrol prevents cognitive deficits by attenuating oxidative damage and inflammation in rat model of streptozotocin diabetes induced vascular dementia. *Physiol Behav*. (2019) 201:198–207. doi: 10.1016/j.physbeh.2018.12.012
49. Luca M, Luca A. Oxidative stress-Related endothelial damage in vascular depression and vascular cognitive impairment: beneficial effects of aerobic physical exercise. *Oxid Med Cell Longev*. (2019) 2019:8067045. doi: 10.1155/2019/8067045
50. Khoshnam SE, Winlow W, Farbood Y, Moghaddam HF, Farzaneh M. Emerging roles of micrornas in ischemic stroke: as possible therapeutic agents. *J Stroke*. (2017) 19:166–87. doi: 10.5853/jos.2016.01368
51. Liu P, Han Z, Ma Q, Liu T, Wang R, Tao Z, et al. Upregulation of microrna-128 in the peripheral blood of acute ischemic stroke patients is correlated with stroke severity partially through inhibition of neuronal cell cycle reentry. *Cell Transplant*. (2019) 28:839–50. doi: 10.1177/0963689719846848
52. Rainer TH, Leung LY, Chan CPY, Leung YK, Abrigo JM, Wang D, et al. Plasma mir-124-3p and mir-16 concentrations as prognostic markers in acute stroke. *Clin Biochem*. (2016) 49:663–8. doi: 10.1016/j.clinbiochem.2016.02.016
53. Feng CZ, Yin JB, Yang JJ, Cao L. Regulatory factor x1 depresses apoe-Dependent abeta uptake by mirna-124 in microglial response to oxidative stress. *Neuroscience*. (2017) 344:217–28. doi: 10.1016/j.neuroscience.2016.12.017
54. Ansari A, Maffioletti E, Milanesi E, Marizzoni M, Frisoni GB, Blin O, et al. Mir-146a and mir-181a are involved in the progression of mild cognitive impairment to alzheimer's disease. *Neurobiol Aging*. (2019) 82:102–9. doi: 10.1016/j.neurobiolaging.2019.06.005
55. Chen FZ, Zhao Y, Chen HZ. Microrna-98 reduces amyloid beta-Protein production and improves oxidative stress and mitochondrial dysfunction through the notch signaling pathway via hey2 in alzheimer's disease mice. *Int J Mol Med*. (2019) 43:91–102. doi: 10.3892/ijmm.2018.3957
56. Slota JA, Booth SA. Micrornas in neuroinflammation: implications in disease pathogenesis, biomarker discovery and therapeutic applications. *Non-coding RNA*. (2019) 5:2. doi: 10.3390/ncrna5020035
57. Nuzziello N, Liguori M. The microrna centrism in the orchestration of neuroinflammation in neurodegenerative diseases. *Cells*. (2019) 8:10. doi: 10.3390/cells8101193
58. Gaudet AD, Fonken LK, Watkins LR, Nelson RJ, Popovich PG. Micrornas: roles in regulating neuroinflammation. *Neuroscientist*. (2018) 24:221–45. doi: 10.1177/1073858417721150
59. Chen L, Dong R, Lu Y, Zhou Y, Li K, Zhang Z, et al. Microrna-146a protects against cognitive decline induced by surgical trauma by suppressing hippocampal neuroinflammation in mice. *Brain Behav Immun*. (2019) 78:188–201. doi: 10.1016/j.bbi.2019.01.020
60. Lu Y, Xu X, Dong R, Sun L, Chen L, Zhang Z, et al. Microrna-181b-5p attenuates early postoperative cognitive dysfunction by suppressing hippocampal neuroinflammation in mice. *Cytokine*. (2019) 120:41–53. doi: 10.1016/j.cyto.2019.04.005
61. Huang L, Ma Q, Li Y, Li B, Zhang L. Inhibition of microrna-210 suppresses pro-Inflammatory response and reduces acute brain injury of ischemic stroke in mice. *Exp Neurol*. (2018) 300:41–50. doi: 10.1016/j.expneurol.2017.10.024
62. Dias IHK, Brown CL, Shabir K, Polidori MC, Griffiths HR. Mirna 933 expression by endothelial cells is increased by 27-hydroxycholesterol and is more prevalent in plasma from dementia patients. *J Alzheimers Dis*. (2018) 64:1009–17. doi: 10.3233/JAD-180201
63. Saggu R, Schumacher T, Gerich F, Rakers C, Tai K, Delekate A, et al. Astroglial nf-Kb contributes to white matter damage and cognitive impairment in a mouse model of vascular dementia. *Acta Neuropathol Commun*. (2016) 4:76. doi: 10.1186/s40478-016-0350-3
64. Yang T, Zhang F. Targeting transcription factor nrf2 (Nuclear factor erythroid 2-related factor 2) for the intervention of vascular cognitive impairment and dementia. *Arterioscler Thromb Vasc Biol*. (2021) 41:97–116. doi: 10.1161/ATVBAHA.120.314804
65. Wang L, Yang JW, Lin LT, Huang J, Wang XR, Su XT, et al. Acupuncture attenuates inflammation in microglia of vascular dementia rats by inhibiting mir-93-mediated tlr4/Myd88/Nf-Kappab signaling pathway. *Oxid Med Cell Longev*. (2020) 2020:8253904. doi: 10.1155/2020/8253904
66. Tang CZ, Zhang DF, Yang JT, Liu QH, Wang YR, Wang WS. Overexpression of microrna-301b accelerates hippocampal microglia activation and cognitive impairment in mice with depressive-like behavior through the nf-Kappab signaling pathway. *Cell Death Dis*. (2019) 10:316. doi: 10.1038/s41419-019-1522-4
67. Hu G, Xia Y, Zhang J, Chen Y, Yuan J, Niu X, et al. Esc-Sevs rejuvenate senescent hippocampal nscs by activating lysosomes to improve cognitive dysfunction in vascular dementia. *Adv Sci (Weinh)*. (2020) 7:1903330. doi: 10.1002/advs.201903330
68. Boese AC, Hamblin MH, Lee JP. Neural stem cell therapy for neurovascular injury in alzheimer's disease. *Exp Neurol*. (2020) 324:113112. doi: 10.1016/j.expneurol.2019.113112
69. Xiao WZ, Lu AQ, Liu XW, Li Z, Zi Y, Wang ZW. Role of mirna-146 in proliferation and differentiation of mouse neural stem cells. *Biosci Rep*. (2015) 35:5. doi: 10.1042/BSR20150088
70. Gu J, Shao R, Li M, Yan Q, Hu H. Mir-485-3p modulates neural stem cell differentiation and proliferation via regulating trip6 expression. *J Cell Mol Med*. (2020) 24:398–404. doi: 10.1111/jcmm.14743
71. Kumar S, Curran JE, DeLeon E, Leandro AC, Howard TE, Lehman DM, et al. Role of mirna-Mrna interaction in neural stem cell differentiation of induced pluripotent stem cells. *Int J Mol Sci*. (2020) 21:19. doi: 10.3390/ijms21196980
72. Shu P, Fu H, Zhao X, Wu C, Ruan X, Zeng Y, et al. Microrna-214 modulates neural progenitor cell differentiation by targeting quaking during cerebral cortex development. *Sci Rep*. (2017) 7:8014. doi: 10.1038/s41598-017-08450-8
73. Gao Y, Qiao H, Zhong T, Lu Z, Hou Y. Microrna29a promotes the neural differentiation of rat neural stem/progenitor cells by targeting klf4. *Mol Med Rep*. (2020) 22:1008–16. doi: 10.3892/mmr.2020.11177
74. Ragusa M, Bosco P, Tamburello L, Barbagallo C, Condorelli AG, Tornitore M, et al. Mirnas plasma profiles in vascular dementia: biomolecular data and biomedical implications. *Front Cell Neurosci*. (2016) 10:51. doi: 10.3389/fncel.2016.00051
75. Song Y, Hu M, Zhang J, Teng ZQ, Chen C, A. novel mechanism of synaptic and cognitive impairments mediated via microrna-30b in alzheimer's disease. *EBioMedicine*. (2019) 39:409–21. doi: 10.1016/j.ebiom.2018.11.059
76. Ren Z, Yu J, Wu Z, Si W, Li X, Liu Y, et al. Microrna-210-5p contributes to cognitive impairment in early vascular dementia rat model through targeting snap25. *Front Mol Neurosci*. (2018) 11:388. doi: 10.3389/fnmol.2018.00388
77. Li F, Wei G, Bai Y, Li Y, Huang F, Lin J, et al. Microrna-574 is involved in cognitive impairment in 5-month-Old app/Ps1 mice through regulation of neuritin. *Brain Res*. (2015) 1627:177–88. doi: 10.1016/j.brainres.2015.09.022
78. Kalaria RN. Neuropathological diagnosis of vascular cognitive impairment and vascular dementia with implications for alzheimer's disease. *Acta Neuropathol*. (2016) 131:659–85. doi: 10.1007/s00401-016-1571-z
79. Ghoreishy A, Khosravi A, Ghaemmaghami A. Exosomal microrna and stroke: a review. *J Cell Biochem*. (2019) 120:16352–61. doi: 10.1002/jcb.29130
80. Prabhakar P, Chandra SR, Christopher R. Circulating micrornas as potential biomarkers for the identification of vascular dementia due to cerebral small vessel disease. *Age Aging*. (2017) 46:861–4. doi: 10.1093/ageing/afx090
81. Yang TT, Liu CG, Gao SC, Zhang Y, Wang PC. The serum exosome derived microrna-135a,−193b, and−384 were potential alzheimer's disease biomarkers. *Biomed Environ Sci*. (2018) 31:87–96. doi: 10.3967/bes2018.011

82. Swarup V, Hinz FI, Rexach JE, Noguchi KI, Toyoshiba H, Oda A, et al. Identification of evolutionarily conserved gene networks mediating neurodegenerative dementia. *Nat Med.* (2019) 25:152–64. doi: 10.1038/s41591-018-0223-3
83. Kumar S, Vijayan M, Reddy PH. Microrna-455-3p as a potential peripheral biomarker for alzheimer's disease. *Hum Mol Genet.* (2017) 26:3808–22. doi: 10.1093/hmg/ddx267
84. Yu P, Venkat P, Chopp M, Zacharek A, Shen Y, Ning R, et al. Role of microrna-126 in vascular cognitive impairment in mice. *J Cereb Blood Flow Metab.* (2019) 39:2497–511. doi: 10.1177/0271678X18800593
85. Du K, Zhao C, Wang L, Wang Y, Zhang KZ, Shen XY, et al. Mir-191 inhibit angiogenesis after acute ischemic stroke targeting vezf1. *Aging (Albany NY).* (2019) 11:2762–86. doi: 10.18632/aging.101948
86. Nakajima M, Morimoto S, Takamoto S, Kitano S, Fukuo K, Onishi T, et al. endothelin-1 in cerebrospinal fluid in elderly patients with hypertension and dementia. *Hypertension.* (1994) 24:97–100. doi: 10.1161/01.HYP.24.1.97
87. Tiedt S, Prestel M, Malik R, Schieferdecker N, Duering M, Kautzky V, et al. Rna-Seq identifies circulating mir-125a-5p, mir-125b-5p, and mir-143-3p as potential biomarkers for acute ischemic stroke. *Circ Res.* (2017) 121:970–80. doi: 10.1161/CIRCRESAHA.117.311572
88. Yang K, Feng S, Ren J, Zhou W. Upregulation of microrna-196a improves cognitive impairment and alleviates neuronal damage in hippocampus tissues of alzheimer's disease through downregulating lrig3 expression. *J Cell Biochem.* (2019) 120:17811–21. doi: 10.1002/jcb.29047
89. Perng CH, Chang YC, Tzang RF. The treatment of cognitive dysfunction in dementia: a multiple treatments meta-Analysis. *Psychopharmacology (Berl).* (2018) 235:1571–80. doi: 10.1007/s00213-018-4867-y
90. Sun MK. Potential therapeutics for vascular cognitive impairment and dementia. *Curr Neuropharmacol.* (2018) 16:1036–44. doi: 10.2174/1570159X15666171016164734
91. Liao Z, Bu Y, Li M, Han R, Zhang N, Hao J, et al. Remote ischemic conditioning improves cognition in patients with subcortical ischemic vascular dementia. *BMC Neurol.* (2019) 19:206. doi: 10.1186/s12883-019-1435-y
92. Sun P, Liu DZ, Jickling GC, Sharp FR, Yin KJ. Microrna-Based therapeutics in central nervous system injuries. *J Cereb Blood Flow Metab.* (2018) 38:1125–48. doi: 10.1177/0271678X18773871
93. Rosenberg GA. Binswanger's disease: biomarkers in the inflammatory form of vascular cognitive impairment and dementia. *J Neurochem.* (2018) 144:634–43. doi: 10.1111/jnc.14218

Conflict of Interest: The authors declare that the research was conducted in the absence of any commercial or financial relationships that could be construed as a potential conflict of interest.

Publisher's Note: All claims expressed in this article are solely those of the authors and do not necessarily represent those of their affiliated organizations, or those of the publisher, the editors and the reviewers. Any product that may be evaluated in this article, or claim that may be made by its manufacturer, is not guaranteed or endorsed by the publisher.

Copyright © 2022 Zhai, Zhao, Zhang, Wang, Wei and Sun. This is an open-access article distributed under the terms of the Creative Commons Attribution License (CC BY). The use, distribution or reproduction in other forums is permitted, provided the original author(s) and the copyright owner(s) are credited and that the original publication in this journal is cited, in accordance with accepted academic practice. No use, distribution or reproduction is permitted which does not comply with these terms.

frontiers | Frontiers in Neurology

ORIGINAL RESEARCH
published: 09 May 2022
doi: 10.3389/fneur.2022.886246

Expression and Potential Biomarkers of Regulators for M7G RNA Modification in Gliomas

Zhen Chen[1†], *Zhe Zhang*[1†], *Wei Ding*[2], *Jie-hui Zhang*[2], *Zi-long Tan*[1], *Yu-ran Mei*[1], *Wei He*[1*] *and Xiao-jing Wang*[1,3*]

[1] Department of Neurosurgery, The Second Affiliated Hospital of Nanchang University, Nanchang, China, [2] Yifeng County People's Hospital, Yichun City, China, [3] Department of Neurology, The First Affiliated Hospital of Anhui Medical University, Hefei, China

Gliomas are the most frequent primary malignant brain tumors of the central nervous system, causing significant impairment and death. There is mounting evidence that N7 methylguanosine (m7G) RNA dysmethylation plays a significant role in the development and progression of cancer. However, the expression patterns and function of the m7G RNA methylation regulator in gliomas are yet unknown. The goal of this study was to examine the expression patterns of 31 critical regulators linked with m7G RNA methylation and their prognostic significance in gliomas. To begin, we systematically analyzed patient clinical and prognostic data and mRNA gene expression data from The Cancer Genome Atlas (TCGA) and the Gene Expression Omnibus (GEO) databases. We found that 17 key regulators of m7G RNA methylation showed significantly higher expression levels in gliomas. We then divided the sample into two subgroups by consensus clustering. Cluster 2 had a poorer prognosis than cluster 1 and was associated with a higher histological grade. In addition, cluster 2 was significantly enriched for cancer-related pathways. Based on this discovery, we developed a risk model involving three m7G methylation regulators. Patients were divided into high-risk and low-risk groups based on risk scores. Overall survival (OS) was significantly lower in the high-risk group than in the low-risk group. Further analysis showed that the risk score was an independent prognostic factor for gliomas.

Keywords: N7-methylguanosine, gliomas, epigenetics, prognostic signature, bioinformatics

OPEN ACCESS

Edited by:
Yuzhen Xu,
Tongji University, China

Reviewed by:
Shu-Ping Zhou,
Ningbo College of Health Sciences, China
Hao-Cheng Qin,
Fudan University, China

***Correspondence:**
Xiao-jing Wang
wangxiaojing0729@163.com
Wei He
hewei1456@sina.com

[†]These authors have contributed equally to this work and share first authorship

Specialty section:
This article was submitted to Neurological Biomarkers, a section of the journal Frontiers in Neurology

Received: *28 February 2022*
Accepted: *11 April 2022*
Published: *09 May 2022*

Citation:
Chen Z, Zhang Z, Ding W, Zhang J-h, Tan Z-l, Mei Y-r, He W and Wang X-j (2022) Expression and Potential Biomarkers of Regulators for M7G RNA Modification in Gliomas. Front. Neurol. 13:886246. doi: 10.3389/fneur.2022.886246

INTRODUCTION

Gliomas square measure the foremost frequent primary central systema nervosum tumors in humans, accounting for 30% of all primary brain tumors and 81% of malignant brain tumors (1). Due to their unique biology and clinical properties, gliomas are a highly varied group of brain tumors. Traditionally, gliomas subtypes and grades were determined primarily by histological characteristics. However, this classification technique does not adequately replicate the tumor's heterogeneity, is subject to subjectivity and disagreement among neuropathologists, falls short of precisely forecasting disease course, and cannot be used to guide treatment in a reliable manner (2). Despite advancements in surgical procedures and clinical regimens, high-grade gliomas therapy remains difficult and is associated with poor therapeutic effectiveness and overall survival (3). As a

result, it is critical to develop innovative and trustworthy molecular signs for prognostic prediction in order to improve the dismal outcomes of patients with gliomas.

Currently, RNA methylation is a widespread post-transcriptional modification found in eukaryotes, prokaryotes (4, 5), and a few archaea (6). As with epigenetic modifications at the DNA and protein levels, these posttranscriptional RNA modifications, included N1-methyladenosine, N7-methylguanosine (m7G), 5-Methylcytidine (m5C), pseudouridine, N6-methyladenosine (m6A), and2-O-methylation (7), can be dynamically and reversibly regulated by specific enzymes (8). Among these, m7G, or guanosine methylation at position N7, is a highly conserved RNA modification found in tRNA, rRNA, mRNA 5′cap, and internal mRNA regions, where it plays a vital role in regulating RNA processing, metabolism, and function (9).

RNA modifications are required for the metabolism of RNA, the regulation of gene expression, and the development of human diseases such as cancer. Recent research demonstrates that various RNA modifications play critical roles in cancer. For instance, when overexpressed, METTL3, an m6A "writer" that modifies a large subset of messenger RNAs, is carcinogenic (10). Lan et al. demonstrated that KIAA1429 is significantly expressed in hepatocellular carcinoma and is linked with poor prognosis (11). Deposition of m5C by NSUN2 and mcm5s2U alteration at tRNA nucleotide position 34 play crucial roles in cancer. Increased levels of m1A, which are linked to hTrm6p/hTrm61p, were found to be linked to an increased risk of urinary bladder cancer (12). In eukaryotes, METTL1 and WDR4 form a methyltransferase complex that catalyzes the m7G modification of tRNAs (13). Dai et al. discovered that silencing METTL1 or WDR4 in human intrahepatic cholangiocarcinoma cell lines resulted in the loss of typical malignant transformation markers such as stalled cell proliferation, increased apoptosis, reduced colony formation, and migration, and decreased tumor formation in xenografted mice (14). These studies demonstrate that abnormal RNA modifications can have an effect on tumor initiation and progression. Additionally, methylation of RNA has been shown to have a key role in gliomas. Recent studies have reported that m6A RNA methylation regulators are critical in maintaining glioma stem cells and radioresistance and have a potential role in prognostic and therapeutic strategy development (15). However, there is a dearth of thorough studies examining the expression of m7G RNA methylation regulators in gliomas, their role in malignant progression, and their prognostic relevance.

The expression of 31 major regulators of m7G RNA modification in gliomas was assessed in this work using transcriptome data from The Cancer Genome Atlas (TCGA) database. Additionally, by using consensus clustering, glioma patients were classified into two clusters based on the expression of regulators of m7G RNA modification, and the two clusters had dramatically different prognoses. Additionally, a signature incorporating three selected m7G RNA methylation regulators was developed to stratify glioma prognosis.

MATERIALS AND METHODS

Data Collection

RNA-sequencing transcriptome data and clinical data on patients with glioma were extracted from the TCGA database (https://portal.gdc.cancer.gov/; until January 2022). A total of 698 glioma patients and 5 normal surrounding tumor tissues were used for further investigation. We downloaded 31 m7G methylation-related genes from the Gene Set Enrichment Analysis (GSEA) database (http://www.gsea-msigdb.org/gsea/index.jsp), including DCP2, DCPS, NUDT1, NUDT10, NUDT11, NUDT16, NUDT16L1, NUDT3, NUDT4, NUDT4B, NUDT5, NUDT7, AGO2, CYFIP1, CYFIP2, EIF4E, EIF4E1B, EIF4E2, EIF4E3, GEMIN5, LARP1, NCBP1, NCBP2, NCBP3, EIF3D, EIF4A1, EIF4G3, IFIT5, LSM1, NCBP2L, and SNUPN (collect and download from GSEA). The expression data for these 31 genes were retrieved for further investigation from the TCGA gliomas group. External validation was performed using an independent cohort (GSE4412) encompassing glioma samples with associated gene expression and survival data collected from the Gene Expression Omnibus (GEO) database (http://www.ncbi.nlm.nih.gov/geo).

Bioinformatics Analysis

The Wilcoxon test was utilized to identify genes encoding m7G RNA methylation regulators that were differentially expressed across gliomas and normal tissues. The following criteria were used to determine significance: A false discovery rate (FDR) of <0.05 and an absolute Fold change (FC) >1.5 are required. The expression of these m7G-related genes was then visualized using a vioplot in 698 Glioma patients and five normal neighboring samples. We used Spearman correlation analysis in R (https://www.r-project.org/, version R 4.1.2) to determine the relationship between m7G RNA methylation regulators. The packages of "limma," "ggplot2," "pheatmap" and "corrplot" were used in these analyses.

To evaluate the relation between the expression of m7G RNA methylation regulators and glioma prognosis, the glioma tissues were grouped into two distinct subgroups exploitation the R package "ConsensusClusterPlus." Then, principal component analysis (PCA) was used to validate the categorization findings using the "ggplot2" and "limma" packages.

To assess survival between subgroups, a survival curve was produced using the Kaplan–Meier analysis log-rank test. The Chi-square tests were used to compare the differences in clinical parameters between the two clusters. Functional annotation of differentially expressed genes in two clusters using Kyoto Encyclopedia of Genes and Genomes (KEGG) and Gene Ontology (GO) analysis. The link between m7G-related genes and overall survival (OS) was evaluated using univariate Cox regression models. Subsequently, to minimize overfitting, To eliminate highly associated genes, we utilized the "glment" package to perform least absolute shrinkage and selection operator (LASSO) Cox regression. Finally, a risk profile consisting of three m7G regulatory genes was found. To calculate a risk score, we multiplied the gene expression

by the LASSO Cox regression coefficient. Patients with glioma were then categorized into low- or high-risk groups based on median risk scores. Kaplan–Meier analysis was performed using the "Survival" software. The accuracy of the model for prognostic prediction was determined using receiver operating characteristic (ROC) curves. Clinicopathological characteristics were compared between low- and high-risk groups using the Chi-square test and displayed using a heatmap.

We utilized the GSE4412 dataset from GEO to evaluate the predictive usefulness of this three-m7G-regulatory-gene risk profile. We adopted this cutoff criterion to categorize patients as low- or high-risk. Following that, the prognostic value was determined using Kaplan–Meier survival analysis and receiver operating characteristic curve analysis. Moreover, to use the "rms" package, we used the risk score of three m7G-regulatory genes to predict survival in patients with glioma. All of the R packages listed before were downloaded from http://www.bioconductor.org.

Statistical Analysis

All statistical analyses were conducted using R software (version 4.1.2).

RESULTS

Identification of Glioma-Specific m7G RNA Modification Regulators

The differentially expressed 17 m7G regulatory genes were analyzed in Glioma ($n = 698$) and surrounding tissues ($n = 5$). The heatmap demonstrated unequivocally that the majority of these m7G regulatory genes were differently expressed across glioma and normal tissues (**Figure 1A**). NUDT1, DCPS, NUDT5, EIF3D, NCBP2, CYFIP1, LSM1, GEMIN5, IFIT5, NCBP1, EIF4E, EIF4G3, LARP1, EIF4E3, CYFIP2, NCBP2L, and EIF4E1B expression levels were significantly different between the glioma group and normal group. The relevant heat map and box-plot of these differential genes are shown, respectively, in **Figures 1B,C**.

Clusters of Glioma Patients Identified by Consensus Clustering Based on m7G RNA Modification Regulators

Based on the similarity of expression of the m7G RNA methylation regulators, $k = 2$ seemed to be the best cluster to divide these samples into two clusters, i.e., clusters 1 and 2 (**Figures 2A–D**). Furthermore, the expression of most m7G RNA modification regulators in cluster 1 was greater than in cluster 2 (**Figure 2E**). Cluster 1 was strongly linked with high grade ($p < 0.001$) and high age ($p < 0.05$). However, gender was not shown to be a major factor (**Figure 2E**). Thus, the consensus clustering results suggested a strong correlation between the expression pattern of m7G RNA modification regulators and the malignant state of glioma. As a consequence, cluster 2 has a significantly lower OS than cluster 1 ($p < 0.001$) (**Figure 2F**). To validate the clustering results, we used PCA and t-SNE to examine these two clusters further. The PCA and t-SNE plots revealed a significant difference between clusters 1 and 2 (train: **Figures 3A,C**; test: **Figures 3B,D**).

To explore the biological processes associated with m7G RNA methylation regulators in gliomas, functional annotation of differentially expressed genes in clusters 1 and 2 was performed using GO and KEGG analysis. In the TCGA group, according to the KEGG analysis, the differential genes were primarily enriched in "Phagosome," "Focal adhesion," "Staphylococcus aureus infection," "GABAergic synapse," "Complement and coagulation cascades Leishmaniasis," "Viral myocarditis," "Amoebiasis," "Nicotine addiction," "ECM-receptor interaction," "AGE-RAGE signaling pathway in diabetic complications Type I diabetes mellitus" (**Figures 4A,C,E**). In the GSE4412 group, the KEGG analysis revealed that the differential genes were primarily enriched in "GABAergic synapse," "Morphine addiction," "Nicotine addiction," "Glutamatergic synapse," "Synaptic vesicle cycle," "Type I diabetes mellitus," "Phagosome," "Insulin secretion," "Retrograde endocannabinoid signaling," "Neuroactive ligand-receptor interaction" (**Figures 4B,D,F**). In the TCGA group, the GO analysis revealed that the differential genes were primarily enriched in "Regulation of trans-synaptic signaling," "Synapse organization," "Modulation of chemical synaptic transmission," "Learning or memory," "Cognition," "Extracellular matrix organization," "Extracellular structure organization," "External encapsulating structure organization," "Wound healing," "Regulation of synaptic plasticity" (**Figures 5A,C,E**). In the GSE4412 group, the GO analysis revealed that the differential genes were primarily enriched in "Modulation of chemical synaptic transmission," "Regulation of trans–synaptic signaling," "Synapse organization," "Vesicle–mediated transport in synapse," "Synaptic vesicle cycle," "Regulation of synaptic plasticity," "Neurotransmitter transport," "Learning or memory," "Regulation of membrane potential," "Cognition" (**Figures 5B,D,F**).

Development of a Predictive Risk Model Based on m7G Regulator Gene Expression Profiles and Validation Using the GEO Database

Given the high correlation between m7G RNA methylation regulators and glioma patient prognosis. Combined with the results of the TCGA and GSE4412 datasets, three genes (NUDT7, NUDT11, CYFIP2) were chosen for the development of the risk model (**Figure 6A**), along with the related LASSO method coefficients (**Figures 6B,C**). The univariate Cox regression analysis of these genes showed that NUDT7, NUDT11, and CYFIP2 are all protective factors with a hazard ratio (HR) of less than 1 for the OS of glioma patients. To evaluate the prognostic value of this three-gene signature model, glioma patients were separated into low- and high-risk groups based on their median risk score. Survival analysis revealed that patients with a high-risk score had a lower OS than patients with a low-risk score (**Figure 6D**). The ROC curve analysis showed that the AUC for 1-, 3-, and 5-year OS was 0.783, 0.807, and 0.763, respectively. The above results indicated the risk model has good discrimination for the outcome of patients with glioma

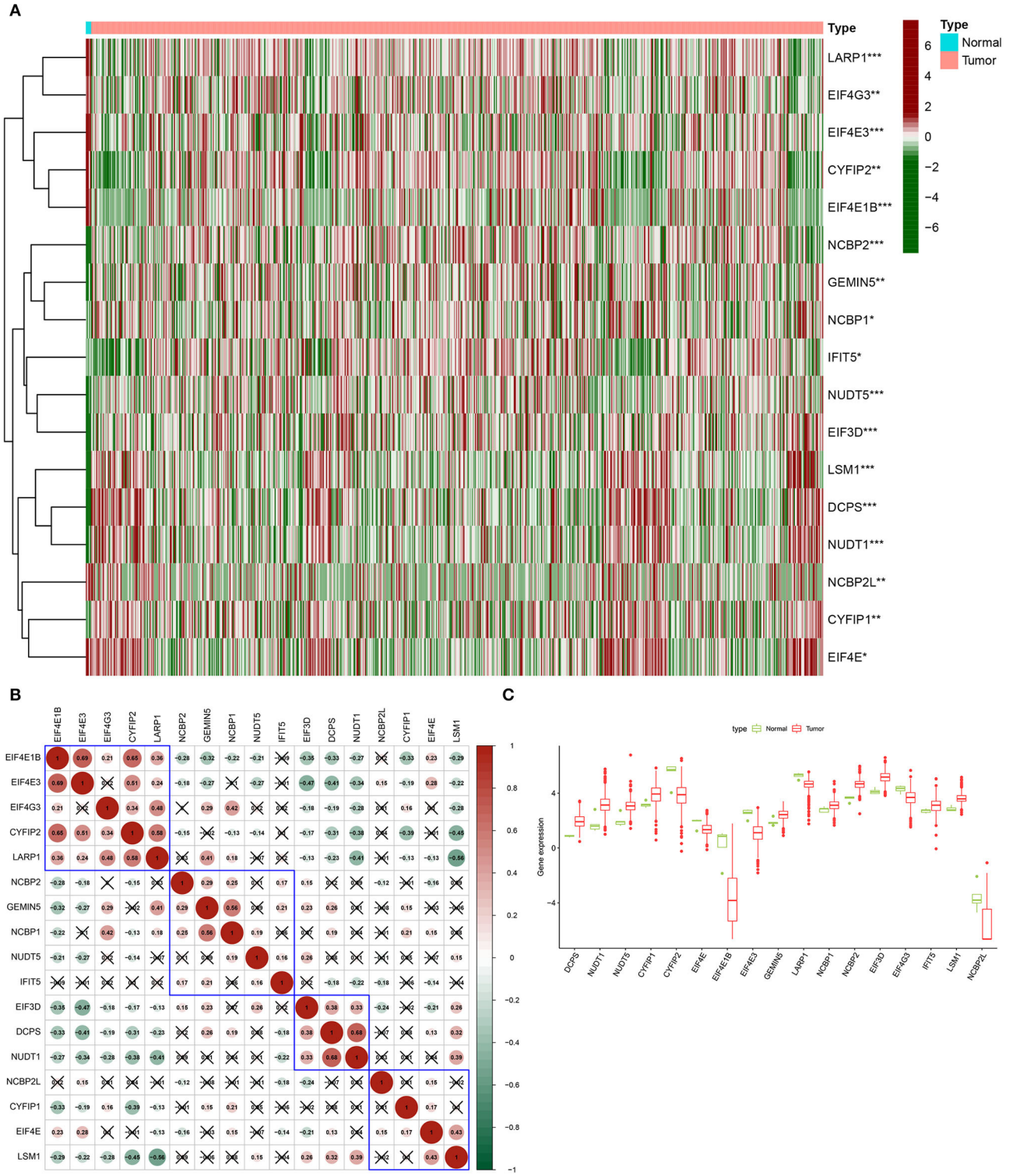

FIGURE 1 | Expression of m7G methylation regulators in glioma tissues and normal tissues. **(A)** Heat map showing 17 m7G RNA methylation regulators expressed at different levels between the two samples (Red for high expression level, green for low expression level. $*p < 0.05$, $**p < 0.01$, $***p < 0.001$). **(B)** Spearman correlation analysis of 17 m7G RNA methylation regulators in gliomas (Red for positive correlation, green for negative correlation). **(C)** Violplot visualizes the expression levels of 17 m7G RNA methylation regulators in two samples.

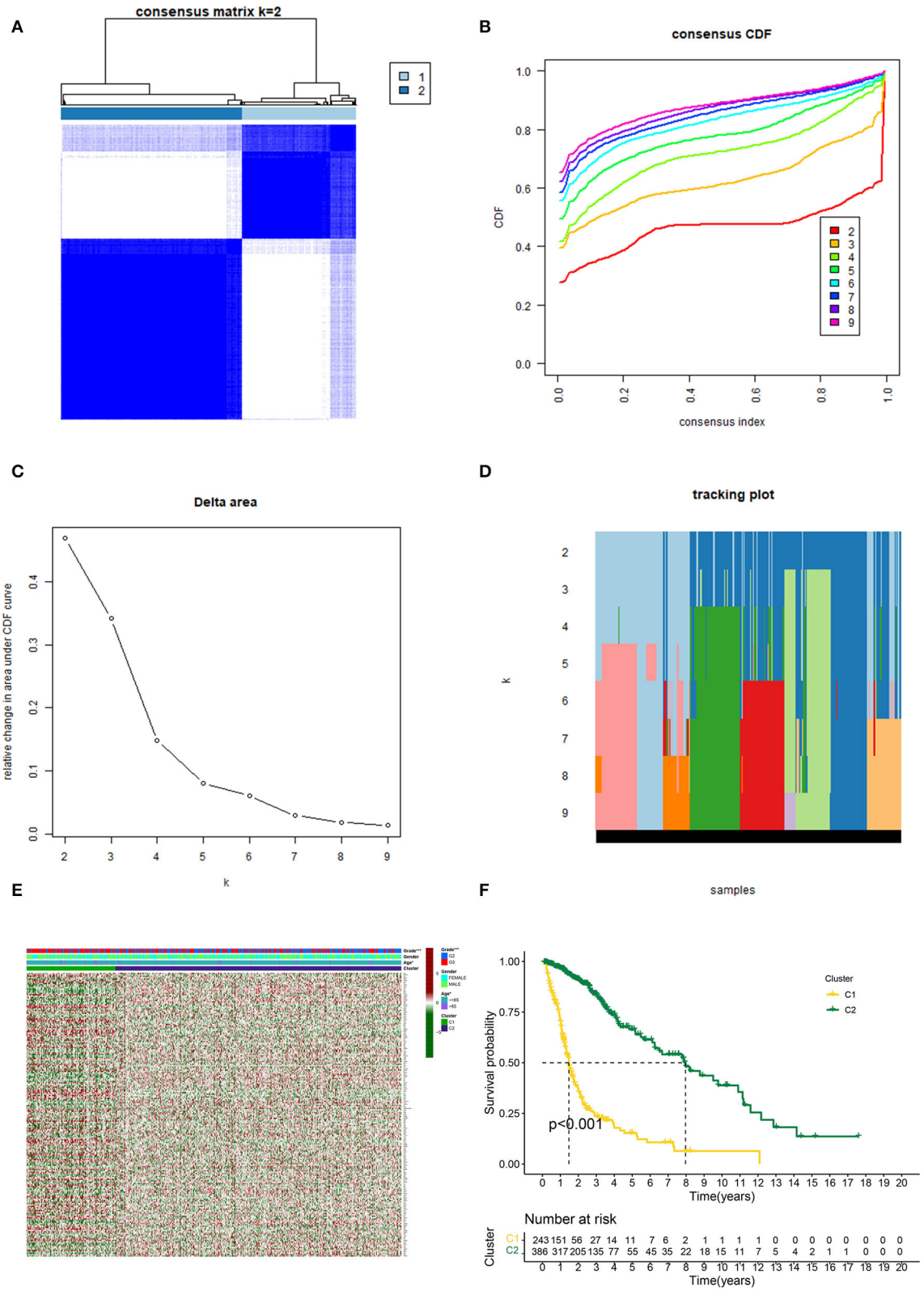

FIGURE 2 | Consistent cluster analysis of gliomas. **(A)** Consensus clustering matrix with $k = 2$. **(B)** Cumulative distribution function (CDF) for consistent clustering at $k = 2$–9. **(C)** For $k = 2$–9, the relative change in the area under the CDF curve. **(D)** Sample distribution for $k = 2$–9. **(E)** Heatmap and clinicopathologic characteristics of the two clusters established by the consensus expression of the m7G RNA methylation regulators (Red for high expression level, green for low expression level). **(F)** Comparison of Kaplan–Meier OS rates for overall survival (OS) curves in the two clusters (*$p < 0.05$, ***$p < 0.001$).

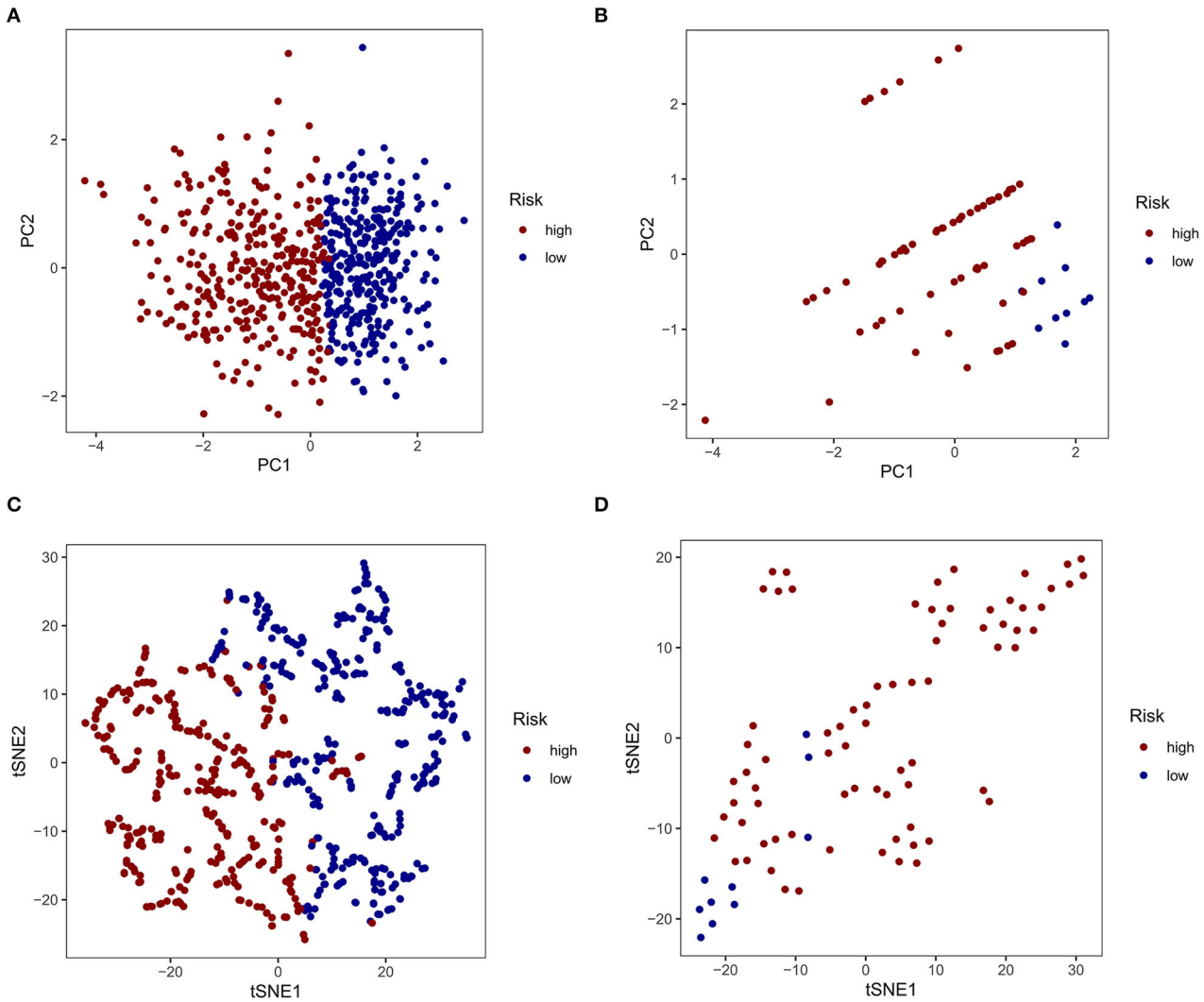

FIGURE 3 | Principal component analysis (PCA) and t-distributed stochastic neighbor embedding (t-SNE) analysis. **(A, C)** PCA and t-SNE analysis of Clusters 1 and 2 from the TCGA database. **(B, D)** PCA and t-SNE analysis of Clusters 1 and 2 from the GEO database.

(**Figure 7A**). Additionally, as illustrated in **Figure 7C**, the risk score distribution of glioma patients was displayed. The survival status of each patient was represented by a dot plot (**Figure 7E**). A heatmap was created to show the expression of three prognostic genes in high- and low-risk groups (**Figure 8C**). Above the heatmap, clinical importance was also shown. To verify the predictive discrimination of the gene signature; we used the GEO data (GSE4412) to assess the prognostic utility of the three-gene signature in new files for survival prediction. The area under the curve (AUC) for the ROC curves for 1, 3, and 5 year OS was 0.573, 0.705, and 0.656, respectively (**Figure 7B**). Additionally, as illustrated in **Figure 7D**, the risk score distribution of glioma patients was displayed. The survival status of each patient was represented by a dot plot in **Figure 7F**.

Univariate and multivariate Cox regression analysis to determine the prognostic value in m7G methylation regulator based on clinical information on gliomas in the TCGA database. By univariate analysis, trigene risk score, age, and grading were all significantly associated with OS in patients with glioma (**Figure 8A**). To determine whether the trigene risk score was an independent prognostic factor for glioma independent of other clinical factors, these factors were included in a multivariate Cox regression analysis, which showed that all three gene risk scores, age, and grade were independently associated with OS in glioma patients (**Figure 8B**).

DISCUSSION

Despite recent breakthroughs in glioma treatment, effective glioma therapy remains an unmet medical need, as current treatments, which often include a mix of surgical intervention (tumor excision), radiotherapy, and chemotherapy, do not

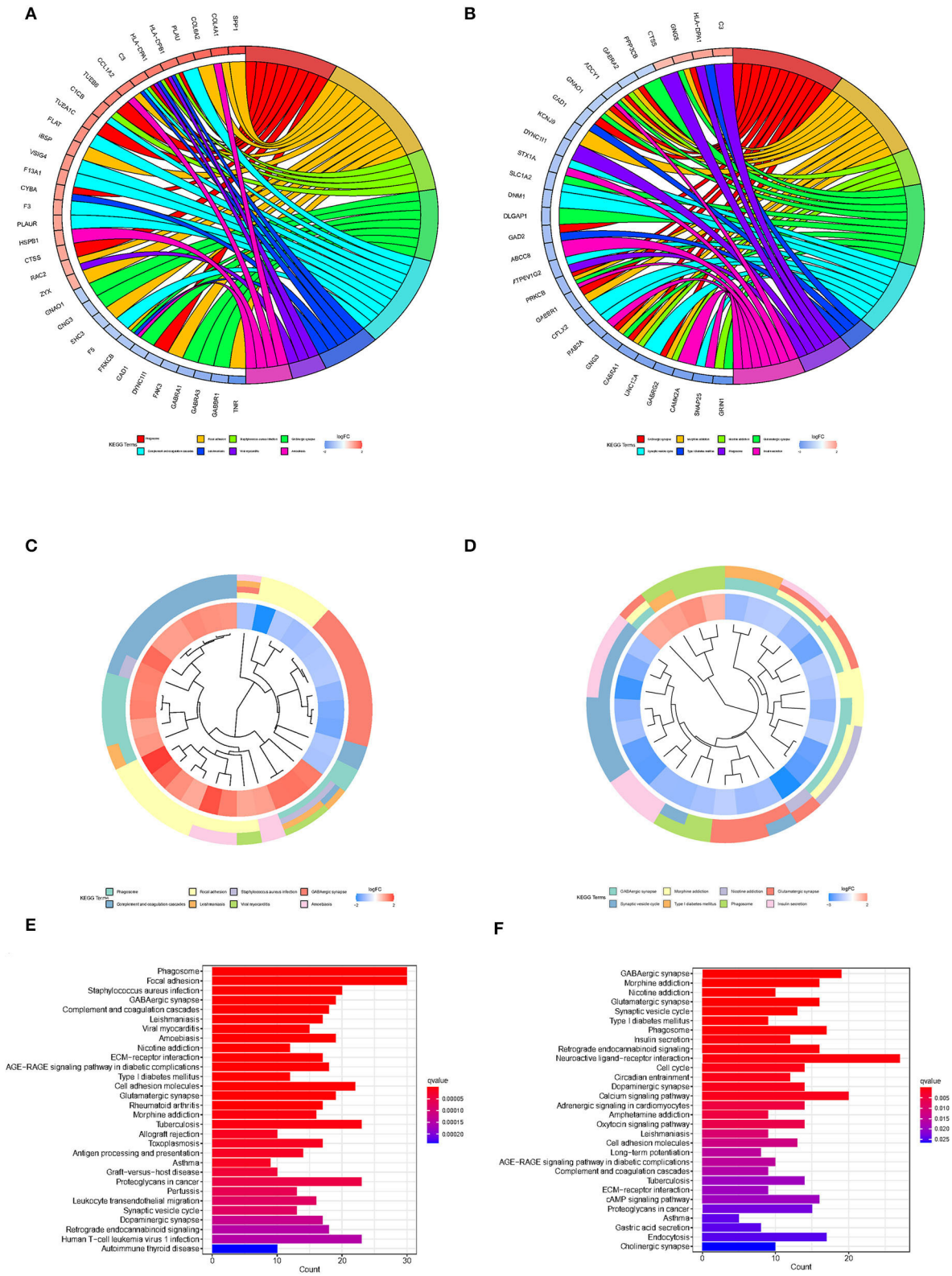

FIGURE 4 | Analyses of differentially expressed genes between two clusters using the Kyoto Encyclopedia of Genes and Genomes (KEEG). **(A, C, E)** KEGG analysis for functional annotation of differentially expressed genes in two clusters of the TCGA database. **(B, D, F)** KEGG analysis for functional annotation of differentially expressed genes in two clusters of the GSE4412 data sets.

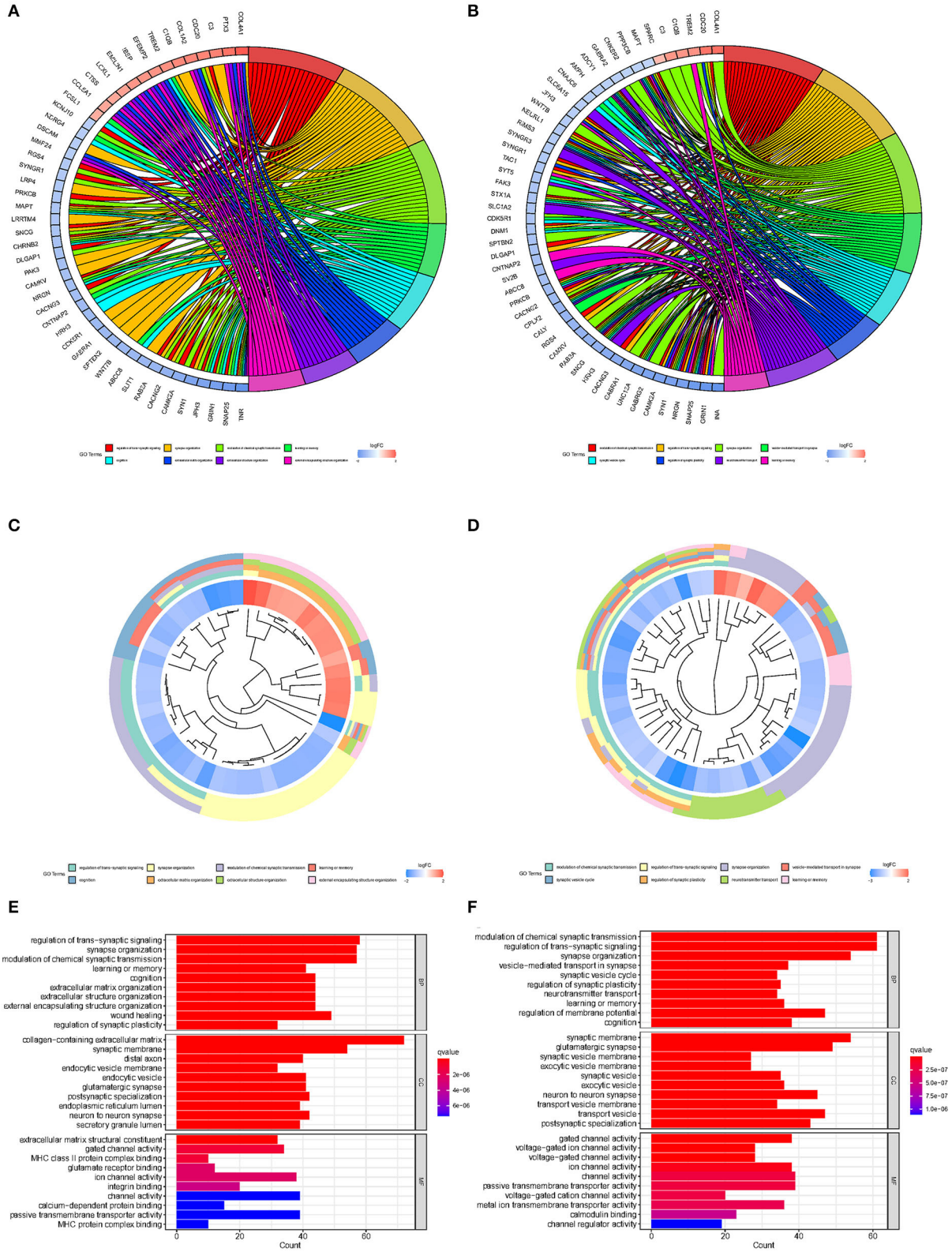

FIGURE 5 | Analyses of differentially expressed genes between two clusters using the Gene ontology (GO). **(A, C, E)** GO analysis for functional annotation of differentially expressed genes in two clusters of the TCGA database. **(B, D, F)** GO analysis for functional annotation of differentially expressed genes in two clusters of the GSE4412 datasets.

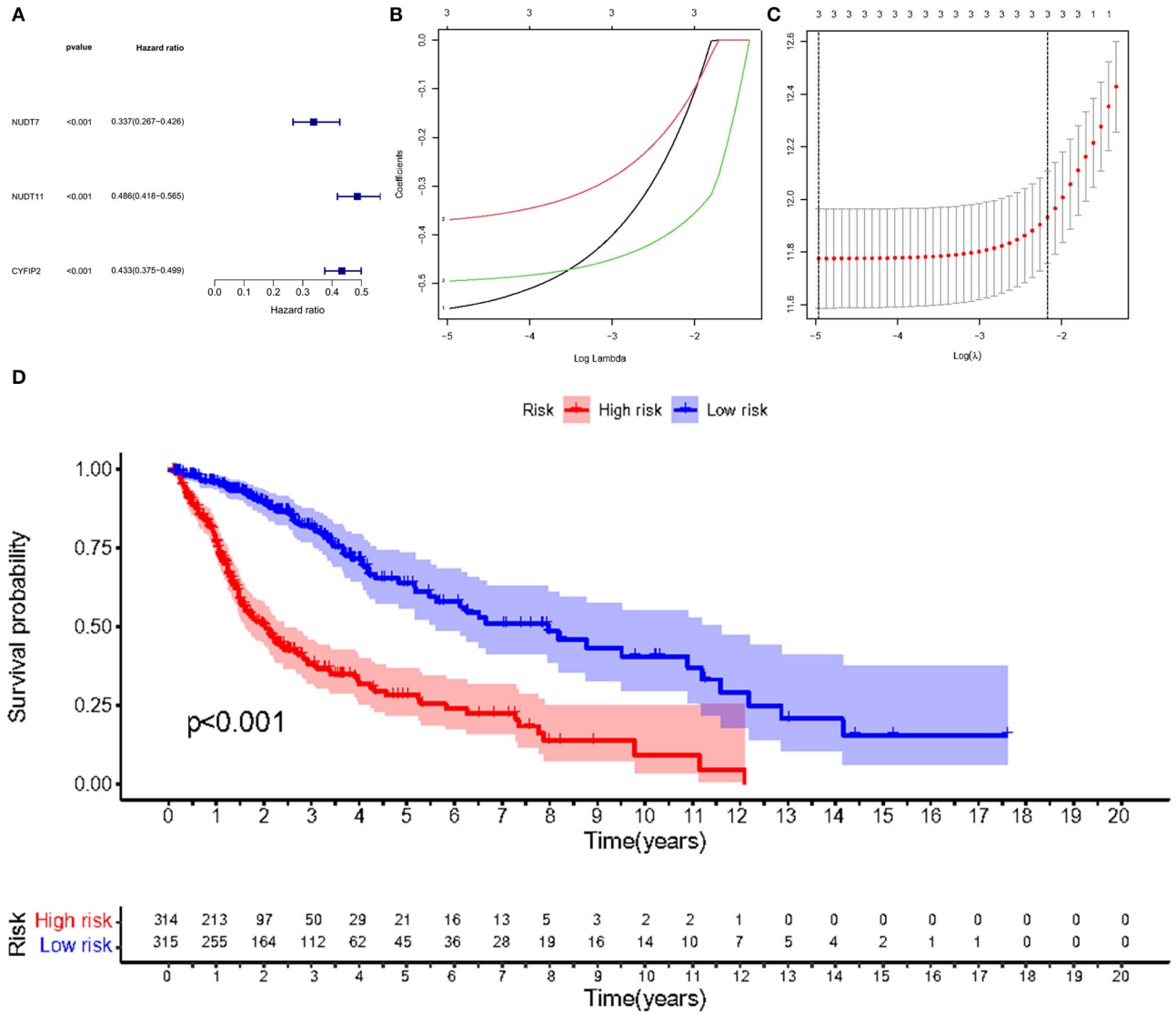

FIGURE 6 | Risk signature with three m7G RNA methylation regulators. **(A)** Univariate Cox regression analysis of the m7G RNA methylation regulators. **(B, C)** LASSO regression analysis was used to calculate the coefficients of the three m7G RNA methylation regulators. **(D)** Glioma patients were divided into low- and high-risk groups based on the median risk score.

achieve satisfying results. The prognosis for patients remains poor, with a median OS of approximately 15 months for those with the most aggressive grade IV glioblastomas (16). According to the WHO, cellularity, mitotic activity, nuclear atypia, vascularity, and necrosis are used to grade (17). This classification method has some limitations, including a lack of consistency, which results in a high rate of inter- and even intra-observer variability, and a lack of prognostic precision (18, 19). As a result, there is an urgent need to understand the molecular mechanisms driving glioma formation.

Traditional molecular techniques, which have mostly focused on structural changes in genes such as point mutations, gene deletions, and rearrangements, have provided vital insights into the glioma-genesis process as well as the diagnostic, prognostic, and predictive power of these tumors (20). For the past few years, understanding the role of epigenetic modifications in the development of human tumors has added critical pieces to the gliomagenesis puzzle and will result in the discovery of novel prognostic biomarkers and therapeutic techniques. DNA methylation and histone alterations are two of the most well-studied epigenetic changes in gliomas, and they are both associated with an increased risk of cancer (21, 22). Recently, RNA methylation has been found to be another way to control your DNA. RNA has been revealed to have over 170 chemical modifications, which play important roles in many cellular processes (23, 24). Among them, m7G, the

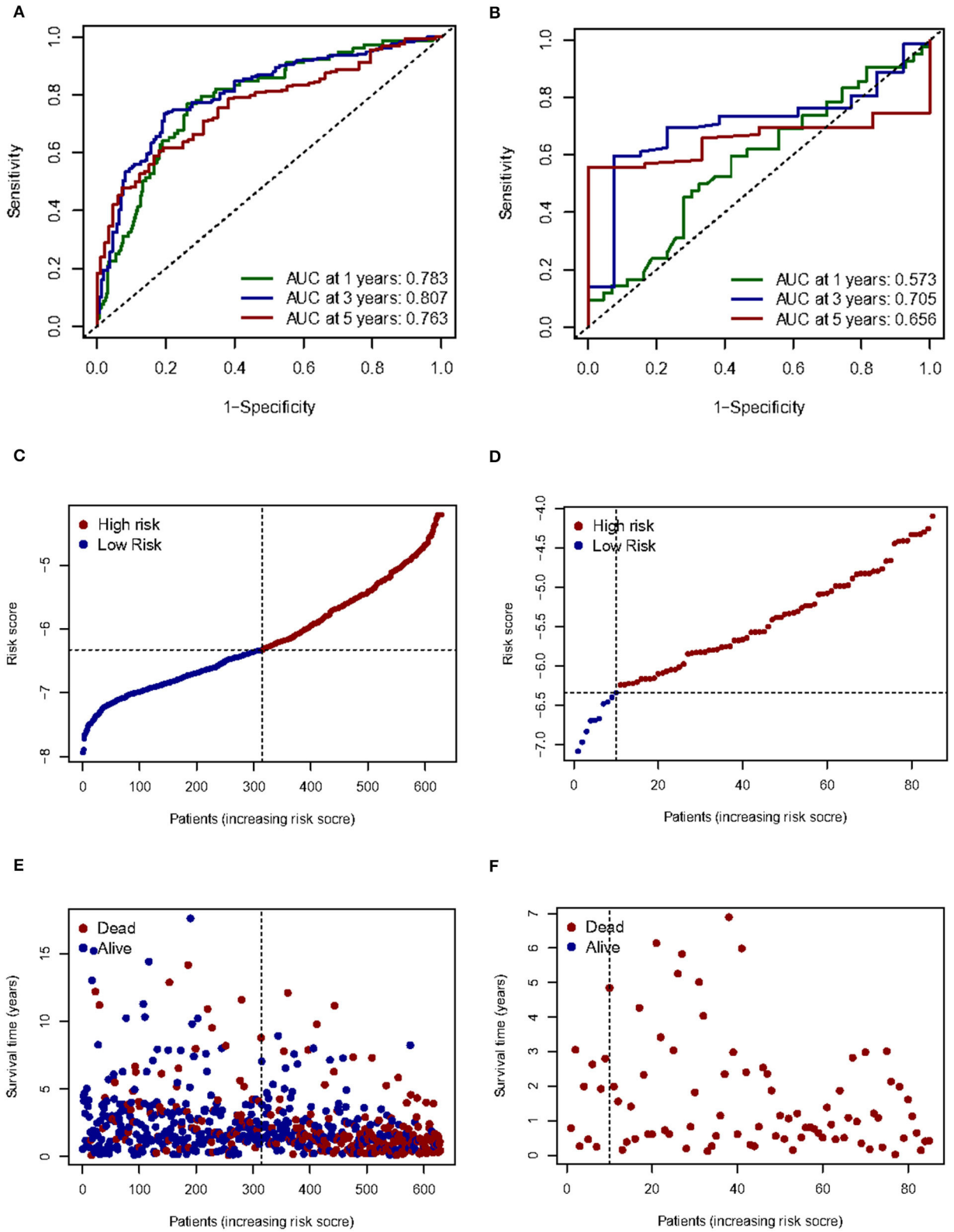

FIGURE 7 | Prognostic value of three m7G RNA methylation regulators. **(A, B)** In the TCGA and GEO databases, the receiver operating characteristic (ROC) curves demonstrate the risk scores' predictive ability for patient survival at 1, 3, and 5 years. **(C,D)** Distribution of risk scores for glioma patients. **(E,F)** Survival status of each patient.

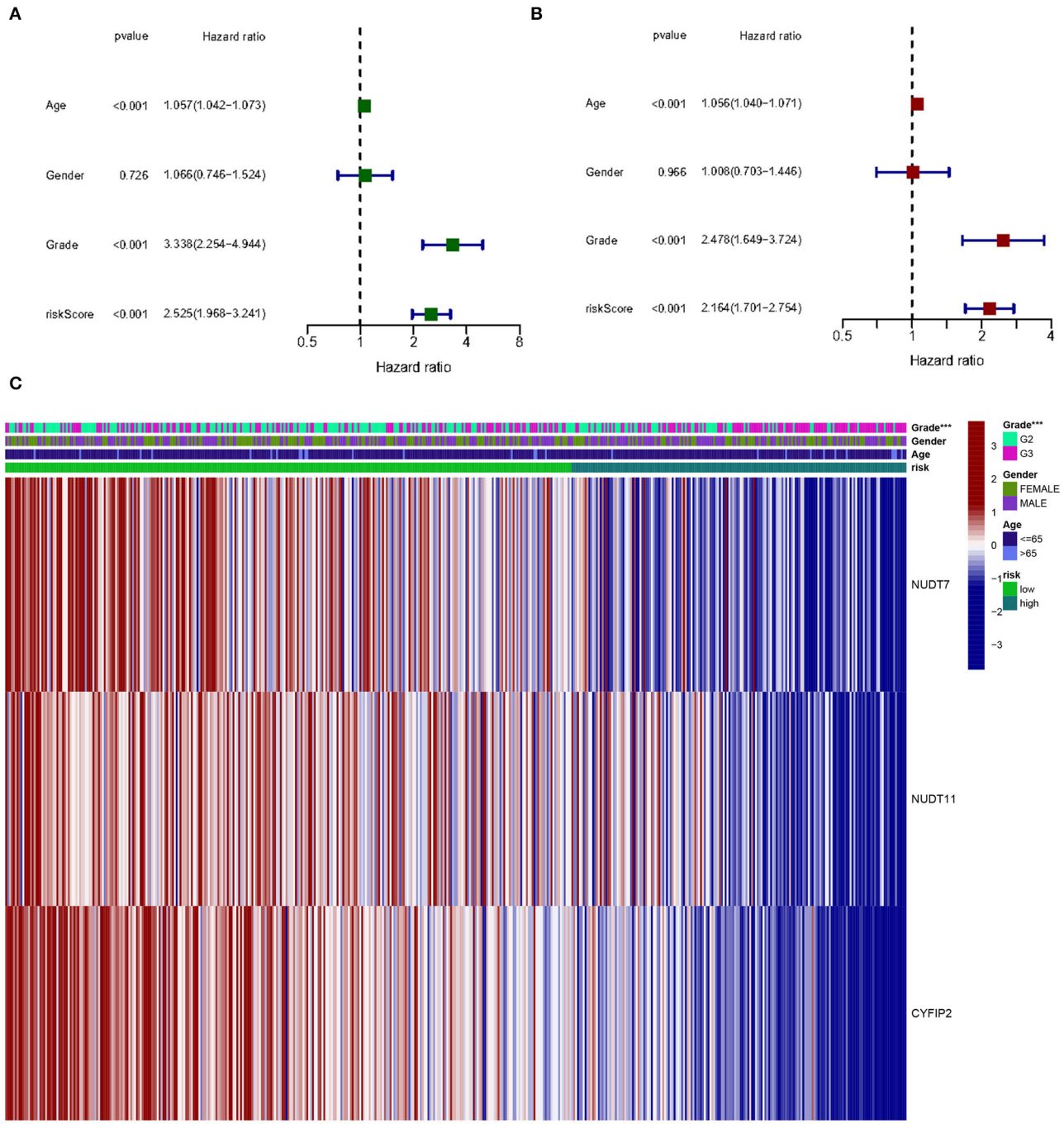

FIGURE 8 | The effect of a risk score on the prognosis of patients with gliomas. **(A)** Univariate Cox regression analysis of three-gene risk score, age, and grade. **(B)** Multivariate Cox regression analysis of three-gene risk score, age, and grade (***$p < 0.001$). **(C)** Heat map shows the distribution of the expression of three m7G RNA-modifying regulators and clinicopathological features in high- and low-risk populations.

most prevalent RNA cap modification, is co-transcribed with the 5′ cap during the earliest phases of transcription and prior to subsequent RNA processing processes (25). The m7G capping is a positively charged RNA modification that is required for gene expression, protein synthesis, and transcript stabilization. It has been discovered that m7G cap alteration can influence practically every part of the mRNA life cycle (26). The m7G RNA alteration was also discovered in tRNA

(27) and rRNA (28), and its presence has been linked to a variety of illnesses. In humans, for example, a mutation in the methyltransferase complex WDR4 has been associated with primordial dwarfism, a condition marked by facial dysmorphism, brain malformation, and severe encephalopathy with convulsions (29). Because of the widespread use of RNA-seq and microarray techniques, which offer significant potential for the development of innovative diagnostics, risk score methods based on multiple gene signatures are increasingly being utilized to forecast human cancer prognosis (30). In the current investigation, we found that the expression of regulators of m7G RNA methylation was strongly associated with the malignancy and prognosis of gliomas. Using three m7G RNA modification regulators, we produced a predictive signature. Fortunately, the risk score was capable of independently predicting the fate of glioma patients. As a result, the risk signature identified in this study may aid clinicians in performing more accurate customized survival forecasts.

Previous research has established that the expression levels of the METTL1 and WDR4 components of the tRNA m7G methyltransferase complex are dramatically increased in human cancer samples and are negatively linked with patient prognosis. For example, Yang et al. found that overexpression of METTL1 inhibited colon cancer progression by regulating the let-7e miRNA/high mobility group AT-hook 2 axis in a m7G dependent manner (31). Chen, Z. et al. found that m7G tRNA modification and its catalase METTL1 and WDR4 proteins were significantly upregulated in hepatocellular carcinoma and inversely correlated with patient survival (32). Orellana et al. established a link between higher METTL1/WDR4 complex expression and elevated m7G tRNA levels and malignancy and poor survival in a variety of human malignancies, including glioblastomas, breast tumors, and acute myelogenous leukemias, among others (33), m7G methylation can selectively boost the translation of specific cell cycle regulating and carcinogenic mRNAs that are enriched in corresponding m7G-tRNA cognate codons, thereby buffering against ribosome stopping, which can result in translation inhibition *via* ribosome collisions (34). However, no research on m7G methylation in gliomas has been conducted. In this investigation, we compared the expression of all m7G RNA methylation regulators in glioma and normal tissues. The results indicated that tumor tissues expressed considerably more m7G regulatory genes than normal tissues. Additionally, we divided patients with glioma into subgroups based on their gene expression profiles. The consensus clustering results indicated a strong correlation between the expression pattern of m7G RNA methylation regulators and the gliomas malignancy. Based on previous findings, the reason may be related to the up-or down-regulation of specific m7G RNA methylation regulators associated with mis-regulated RNAs in tumors.

The m7G RNA methylation regulators were also linked to the biological processes and signaling pathways involved in the malignant development of gliomas, according to this study. According to current research, the main biological processes and signaling pathways associated with m7G methylation in cancer are RNA metabolism, embryonic stem cell self-renewal and differentiation (13), tumor immunity (35), vascular development (36), FGF/TGF-β/Wnt pathway (37), WNT/β-catenin pathway (38), MAPK/ERK pathway (39), and so on. Here, we conducted KEGG and GO analysis on differentially expressed genes. The KEGG analysis revealed that the differential genes were primarily enriched in "Phagosome," "Focal adhesion," "*Staphylococcus aureus* infection," "GABAergic synapse," "Complement and coagulation cascades Leishmaniasis," "Viral myocarditis," "Amoebiasis," "Nicotine addiction," "ECM-receptor interaction," "AGE-RAGE signaling pathway in diabetic complications Type I diabetes mellitus," "Morphine addiction," "Glutamatergic synapse," "Synaptic vesicle cycle," "Type I diabetes mellitus," "Insulin secretion," "Retrograde endocannabinoid signaling," "Neuroactive ligand-receptor interaction". The GO analysis revealed that the differential genes were primarily enriched in "Regulation of trans-synaptic signaling," "Synapse organization," "Modulation of chemical synaptic transmission," "Learning or memory," "Cognition," "Extracellular matrix organization," "Extracellular structure organization," "External encapsulating structure organization," "Wound healing," "Regulation of synaptic plasticity," "Vesicle-mediated transport in synapse," "Synaptic vesicle cycle," "Neurotransmitter transport," "Regulation of membrane potential." According to the data collected, we discovered that the expression of m7G RNA methylation regulators in gliomas is associated significantly with biological processes such as extracellular matrix formation, response to hypoxia, inflammatory response, synaptic vesicle regulation, and others, as well as signaling pathways such as AGE-RAGE signaling pathway, ECM receptor interaction, and others.

To further investigate the effect of m7G RNA methylation regulators on glioma prognosis. After performing Cox univariate and LASSO Cox regression analyses, we selected three genes (NUDT7, NUDT11, and CYFIP2) to construct a risk score model that stratified glioma patients into low- and high-risk groups. The results showed that NUDT7, NUDT11, and CYFIP2 were all protective factors for OS in glioma patients. Survival analysis revealed that patients with high-risk scores had worse OS. Finally, we established a prognosis model consisting of these three m7G RNA methylation regulators. Cox regression analysis showed that the risk score can independently predict the prognosis of gliomas. These findings suggest that NUDT7, NUDT11, and CYFIP2 are promising gliomas prognostic biomarkers. Notably, the expression and potential role of NUDT7, NUDT11, and CYFIP2 in cancer are becoming increasingly important. NUDT7 and NUDT11 are both hydrolases that belong to the peroxisomal nudix family of enzymes (40, 41). Mutations of NUDT7 have been described in colorectal cancer, inhibition of Nudt7 may contribute to the progression of Kras ^{G12D} colorectal cancer through upregulation of Wnt/β-catenin signaling and palmitic acid accumulation (42). Genetic and functional analyses showed that when NUDT11 was inhibited, colony formation of tumor-associated cell phenotypes was significantly reduced and their proliferation/survival capacity was compromised (43). Therefore, genetic alterations in m7G regulatory factors may contribute to the pathogenesis of glioma in conjunction with dysregulation of peroxisome lipid metabolism. CYFIP2, a member of the

cytoplasmic FMR1-interacting protein family (44). It has been reported that inhibition of CYFIP2 increased cell growth and resistance to chemotherapy in gastric cancer through activating the Akt signal (45). In addition, Saller et al. reported CYFIP2 as a candidate p53 target gene in H1299 lung cancer cells (46), and Jackson et al. verified in DLD1 colorectal adenocarcinoma cells that CYFIP2 can act as a p53-inducible gene to promote apoptosis in colorectal adenocarcinoma cells (47). Also, Tong et al. found that CYFIP2 expression was decreased in clear cell renal cell carcinoma and was associated with poorer clinicopathological parameters of clear cell renal cell carcinoma patients (48). CYFIP2 activates the cell death program to inhibit the proliferation of tumor cells, indicating that CYFIP2 is a potent tumor suppressor. In this study, we demonstrate for the first time that the risk scores of NUDT7, NUDT11, and CYFIP2 can be used as independent prognostic factors for gliomas.

Nevertheless, we acknowledge several limitations in this study worth mentioning. Since our data are derived from the TCGA and GEO databases, further experimental evidence is required to corroborate our findings. And the sample size for the normal and tumor groups varied significantly, which may impair the credibility of the results. In addition, the mechanisms underlying the aberrant expression and up- or down-regulation of m7G RNA methylation regulator in gliomas require further studies to validate.

In conclusion, our study demonstrates the expression of m7G RNA methylation regulator in gliomas and its association with clinical characteristics. Notably, prognostic models generated by three m7G methylation-regulated gene risk scores independently predicted the prognosis of glioma patients. These findings provide a new insight into the underlying mechanism of m7G modification in tumorigenesis and the development of gliomas.

DATA AVAILABILITY STATEMENT

The datasets presented in this study can be found in online repositories. The names of the repository/repositories and accession number(s) can be found in the article/**Supplementary Material**.

ETHICS STATEMENT

Ethical review and approval was not required for the study on human participants in accordance with the local legislation and institutional requirements. Written informed consent from the patients/participants or patients/participants' legal guardian/next of kin was not required to participate in this study in accordance with the national legislation and the institutional requirements.

AUTHOR CONTRIBUTIONS

ZC, ZZ, WH, and X-jW conceived and designed the experiments. WD, J-hZ, and Z-lT collected the data. ZC and ZZ analyzed the data. WH and X-jW wrote the article. Z-lT and Y-rM conducted quality control on the articles and guided the submission. All authors read and approved the final manuscript.

FUNDING

This study was supported by the Project of Youth Project of Jiang xi Provincial Department of Education (GJJ200244).

SUPPLEMENTARY MATERIAL

The Supplementary Material for this article can be found online at: https://www.frontiersin.org/articles/10.3389/fneur.2022.886246/full#supplementary-material

REFERENCES

1. Schwartzbaum JA, Fisher JL, Aldape KD, Wrensch M. Epidemiology and molecular pathology of glioma. *Nat Clin Pract Neurol.* (2006) 2:494–503, 1–516. doi: 10.1038/ncpneuro0289
2. Masui K, Mischel PS, Reifenberger G. Molecular classification of gliomas. *Handb Clin Neurol.* (2016) 134:97–120. doi: 10.1016/B978-0-12-802997-8.00006-2
3. Luo C, Xu S, Dai G, Xiao Z, Chen L, Liu Z. Tumor treating fields for high-grade gliomas. *Biomed Pharmacother.* (2020) 127:110193. doi: 10.1016/j.biopha.2020.110193
4. Chen Y, Wang J, Xu D, Xiang Z, Ding J, Yang X, et al. M(6)a mrna methylation regulates testosterone synthesis through modulating autophagy in leydig cells. *Autophagy.* (2021) 17:457–75. doi: 10.1080/15548627.2020.1720431
5. Courtney DG, Tsai K, Bogerd HP, Kennedy EM, Law BA, Emery A, et al. Epitranscriptomic addition of m(5)c to hiv-1 transcripts regulates viral gene expression. *Cell Host Microbe.* (2019) 26:217–27. doi: 10.1016/j.chom.2019.07.005
6. Edmonds CG, Crain PF, Gupta R, Hashizume T, Hocart CH, Kowalak JA, et al. Posttranscriptional modification of trna in thermophilic archaea (archaebacteria). *J Bacteriol.* (1991) 173:3138–48. doi: 10.1128/jb.173.10.3138-3148.1991
7. Motorin Y, Helm M. Rna nucleotide methylation: 2021 update. *Wiley Interdiscip Rev RNA.* (2022) 13:e1691. doi: 10.1002/wrna.1691
8. Yang Y, Chen YS, Sun BF, Yang YG. rna methylation: regulations and mechanisms. *Yi Chuan.* (2018) 40:964–76. doi: 10.16288/j.yczz.18-175
9. Ramanathan A, Robb GB, Chan SH. Mrna capping: biological functions and applications. *Nucleic Acids Res.* (2016) 44:7511–26. doi: 10.1093/nar/gkw551
10. Zeng C, Huang W, Li Y, Weng H. Roles of mettl3 in cancer: mechanisms and therapeutic targeting. *J Hematol Oncol.* (2020) 13:117. doi: 10.1186/s13045-020-00951-w
11. Cheng X, Li M, Rao X, Zhang W, Li X, Wang L, et al. Kiaa1429 regulates the migration and invasion of hepatocellular carcinoma by altering m6a modification of id2 mrna. *Onco Targets Ther.* (2019) 12:3421–8. doi: 10.2147/OTT.S180954
12. Shi L, Yang XM, Tang DD, Liu G, Yuan P, Yang Y, et al. Expression and significance of m1a transmethylase, htrm6p/htrm61p and its related gene htrm6/htrm61 in bladder urothelial carcinoma. *Am J Cancer Res.* (2015) 5:2169–79.
13. Lin S, Liu Q, Lelyveld VS, Choe J, Szostak JW, Gregory RI. Mettl1/wdr4-mediated m(7)g trna methylome is required for normal mrna translation and embryonic stem cell self-renewal and differentiation. *Mol Cell.* (2018) 71:244–55. doi: 10.1016/j.molcel.2018.06.001
14. Dai Z, Liu H, Liao J, Huang C, Ren X, Zhu W, et al. N(7)-methylguanosine trna modification enhances oncogenic mrna translation and promotes intrahepatic cholangiocarcinoma progression. *Mol Cell.* (2021) 81:3339–55. doi: 10.1016/j.molcel.2021.07.003

15. Chai RC, Wu F, Wang QX, Zhang S, Zhang KN, Liu YQ, et al. M(6)a rna methylation regulators contribute to malignant progression and have clinical prognostic impact in gliomas. *Aging (Albany NY).* (2019) 11:1204–25. doi: 10.18632/aging.101829
16. Stupp R, Mason WP, van den Bent MJ, Weller M, Fisher B, Taphoorn MJ, et al. Radiotherapy plus concomitant and adjuvant temozolomide for glioblastoma. *N Engl J Med.* (2005) 352:987–96. doi: 10.1056/NEJMoa043330
17. Louis DN, Ohgaki H, Wiestler OD, Cavenee WK, Burger PC, Jouvet A, et al. The 2007 who classification of tumours of the central nervous system. *Acta Neuropathol.* (2007) 114:97–109. doi: 10.1007/s00401-007-0243-4
18. Coons SW, Johnson PC, Scheithauer BW, Yates AJ, Pearl DK. Improving diagnostic accuracy and interobserver concordance in the classification and grading of primary gliomas. *Cancer Am Cancer Soc.* (1997) 79:1381–93. doi: 10.1002/(sici)1097-0142(19970401)79:7<1381::aid-cncr16>3.0.co;2-w
19. Sledzinska P, Bebyn MG, Furtak J, Kowalewski J, Lewandowska MA. Prognostic and predictive biomarkers in gliomas. *Int J Mol Sci.* (2021) 22:10373. doi: 10.3390/ijms221910373
20. Kreth S, Thon N, Kreth FW. Epigenetics in human gliomas. *Cancer Lett.* (2014) 342:185–92. doi: 10.1016/j.canlet.2012.04.008
21. Chai RC, Liu YQ, Zhang KN, Wu F, Zhao Z, Wang KY, et al. A novel analytical model of mgmt methylation pyrosequencing offers improved predictive performance in patients with gliomas. *Mod Pathol.* (2019) 32:4–15. doi: 10.1038/s41379-018-0143-2
22. Aoki K, Natsume A. Overview of dna methylation in adult diffuse gliomas. *Brain Tumor Pathol.* (2019) 36:84–91. doi: 10.1007/s10014-019-00339-w
23. Boccaletto P, Machnicka MA, Purta E, Piatkowski P, Baginski B, Wirecki TK, et al. Modomics: a database of rna modification pathways. 2017 update. *Nucleic Acids Res.* (2018) 46:D303–7. doi: 10.1093/nar/gkx1030
24. Wu X, Wei Z, Chen K, Zhang Q, Su J, Liu H, et al. M6acomet: large-scale functional prediction of individual m(6)a rna methylation sites from an rna co-methylation network. *BMC Bioinformatics.* (2019) 20:223. doi: 10.1186/s12859-019-2840-3
25. Cowling VH, Cole MD. Myc regulation of mrna cap methylation. *Genes Cancer.* (2010) 1:576–9. doi: 10.1177/1947601910378025
26. Song B, Tang Y, Chen K, Wei Z, Rong R, Lu Z, et al. M7ghub: deciphering the location, regulation and pathogenesis of internal mrna n7-methylguanosine (m7g) sites in human. *Bioinformatics.* (2020) 36:3528–36. doi: 10.1093/bioinformatics/btaa178
27. Guy MP, Phizicky EM. Two-subunit enzymes involved in eukaryotic post-transcriptional trna modification. *RNA Biol.* (2014) 11:1608–18. doi: 10.1080/15476286.2015.1008360
28. Siepel A, Bejerano G, Pedersen JS, Hinrichs AS, Hou M, Rosenbloom K, et al. Evolutionarily conserved elements in vertebrate, insect, worm, and yeast genomes. *Genome Res.* (2005) 15:1034–50. doi: 10.1101/gr.3715005
29. Sauna ZE, Kimchi-Sarfaty C. Understanding the contribution of synonymous mutations to human disease. *Nat Rev Genet.* (2011) 12:683–91. doi: 10.1038/nrg3051
30. Wang Y, Zhang Q, Gao Z, Xin S, Zhao Y, Zhang K, et al. A novel 4-gene signature for overall survival prediction in lung adenocarcinoma patients with lymph node metastasis. *Cancer Cell Int.* (2019) 19:100. doi: 10.1186/s12935-019-0822-1
31. Liu Y, Zhang Y, Chi Q, Wang Z, Sun B. Methyltransferase-like 1 (mettl1) served as a tumor suppressor in colon cancer by activating 7-methyguanosine (m7g) regulated let-7e mirna/hmga2 axis. *Life Sci.* (2020) 249:117480. doi: 10.1016/j.lfs.2020.117480
32. Chen Z, Zhu W, Zhu S, Sun K, Liao J, Liu H, et al. Mettl1 promotes hepatocarcinogenesis via m(7) g trna modification-dependent translation control. *Clin Transl Med.* (2021) 11:e661. doi: 10.1002/ctm2.661
33. Orellana EA, Liu Q, Yankova E, Pirouz M, De Braekeleer E, Zhang W, et al. Mettl1-mediated m(7)g modification of arg-tct trna drives oncogenic transformation. *Mol Cell.* (2021) 81:3323–38. doi: 10.1016/j.molcel.2021.06.031
34. Katsara O, Schneider RJ. M(7)g trna modification reveals new secrets in the translational regulation of cancer development. *Mol Cell.* (2021) 81:3243–5. doi: 10.1016/j.molcel.2021.07.030
35. Zhang M, Song J, Yuan W, Zhang W, Sun Z. Roles of rna methylation on tumor immunity and clinical implications. *Front Immunol.* (2021) 12:641507. doi: 10.3389/fimmu.2021.641507
36. Deng Y, Zhou Z, Ji W, Lin S, Wang M. Mettl1-mediated m(7)g methylation maintains pluripotency in human stem cells and limits mesoderm differentiation and vascular development. *Stem Cell Res Ther.* (2020) 11:306. doi: 10.1186/s13287-020-01814-4
37. Van Camp JK, Beckers S, Zegers D, Van Hul W. Wnt signaling and the control of human stem cell fate. *Stem Cell Rev Rep.* (2014) 10:207–29. doi: 10.1007/s12015-013-9486-8
38. Chen B, Jiang W, Huang Y, Zhang J, Yu P, Wu L, et al. N(7)-methylguanosine trna modification promotes tumorigenesis and chemoresistance through wnt/beta-catenin pathway in nasopharyngeal carcinoma. *Oncogene.* (2022) 41:2239–2253. doi: 10.1038/s41388-022-02250-9
39. Deng Y, Zhou Z, Lin S, Yu B. Mettl1 limits differentiation and functioning of epcs derived from human-induced pluripotent stem cells through a mapk/erk pathway. *Biochem Biophys Res Commun.* (2020) 527:791–8. doi: 10.1016/j.bbrc.2020.04.115
40. Leslie NR, McLennan AG, Safrany ST. Cloning and characterisation of haps1 and haps2, human diadenosine polyphosphate-metabolising nudix hydrolases. *BMC Biochem.* (2002) 3:20. doi: 10.1186/1471-2091-3-20
41. Hunt MC, Tillander V, Alexson SE. Regulation of peroxisomal lipid metabolism: the role of acyl-coa and coenzyme a metabolizing enzymes. *Biochimie.* (2014) 98:45–55. doi: 10.1016/j.biochi.2013.12.018
42. Song J, Park S, Oh J, Kim D, Ryu JH, Park WC, et al. Nudt7 loss promotes kras(g12d) crc development. *Cancers (Basel).* (2020) 12:576. doi: 10.3390/cancers12030576
43. Grisanzio C, Werner L, Takeda D, Awoyemi BC, Pomerantz MM, Yamada H, et al. Genetic and functional analyses implicate the nudt11, hnf1b, and slc22a3 genes in prostate cancer pathogenesis. *Proc Natl Acad Sci U S A.* (2012) 109:11252–7. doi: 10.1073/pnas.1200853109
44. Schenck A, Bardoni B, Moro A, Bagni C, Mandel JL. A highly conserved protein family interacting with the fragile x mental retardation protein (fmrp) and displaying selective interactions with fmrp-related proteins fxr1p and fxr2p. *Proc Natl Acad Sci U S A.* (2001) 98:8844–9. doi: 10.1073/pnas.151231598
45. Jiao S, Li N, Cai S, Guo H, Wen Y. Inhibition of cyfip2 promotes gastric cancer cell proliferation and chemoresistance to 5-fluorouracil through activation of the akt signaling pathway. *Oncol Lett.* (2017) 13:2133–40. doi: 10.3892/ol.2017.5743
46. Saller E, Tom E, Brunori M, Otter M, Estreicher A, Mack DH, et al. Increased apoptosis induction by 121f mutant p53. *EMBO J.* (1999) 18:4424–37. doi: 10.1093/emboj/18.16.4424
47. Jackson RN, Cho YJ, Stein S, Liang P. Cyfip2, a direct p53 target, is leptomycin-b sensitive. *Cell Cycle.* (2007) 6:95–103. doi: 10.4161/cc.6.1.3665
48. Tong J, Meng X, Lv Q, Yuan H, Li W, Xiao W, et al. The downregulation of prognosis- and immune infiltration-related gene cyfip2 serves as a novel target in ccrcc. *Int J Gen Med.* (2021) 14:6587–99. doi: 10.2147/IJGM.S335713

Conflict of Interest: The authors declare that the research was conducted in the absence of any commercial or financial relationships that could be construed as a potential conflict of interest.

Publisher's Note: All claims expressed in this article are solely those of the authors and do not necessarily represent those of their affiliated organizations, or those of the publisher, the editors and the reviewers. Any product that may be evaluated in this article, or claim that may be made by its manufacturer, is not guaranteed or endorsed by the publisher.

Copyright © 2022 Chen, Zhang, Ding, Zhang, Tan, Mei, He and Wang. This is an open-access article distributed under the terms of the Creative Commons Attribution License (CC BY). The use, distribution or reproduction in other forums is permitted, provided the original author(s) and the copyright owner(s) are credited and that the original publication in this journal is cited, in accordance with accepted academic practice. No use, distribution or reproduction is permitted which does not comply with these terms.

frontiers | Frontiers in Neurology

ORIGINAL RESEARCH
published: 17 May 2022
doi: 10.3389/fneur.2022.877801

Intracranial Aneurysms Induced by *RUNX1* Through Regulation of *NFKB1* in Patients With Hypertension-An Integrated Analysis Based on Multiple Datasets and Algorithms

Yang Li[1†], *Zhen Zhang*[2†] *and Donghua Liu*[3*]

[1] Department of Neurosurgery, The First People's Hospital of Yinchuan, Yinchuan, China, [2] Department of Neurosurgery, The Affiliated Yantai Yuhuangding Hospital of Qingdao University, Yantai, China, [3] Department of Neurosurgery, The Second People's Hospital of Yinchuan, Yinchuan, China

Objective: The purpose of this study was to identify potential therapeutic targets by examining the hub genes contributing to progression of intracranial aneurysm (IA) in patients with hypertension.

Methods: The bulk RNA sequencing (RNA-seq) datasets of hypertension and IA were obtained from the Gene Expression Omnibus (www.ncbi.nlm.nih.gov/geo) database. These data were then used to calculate disease-related differentially expressed genes (DEGs) at the individual level. An scRNA-seq dataset of patients with abdominal aortic aneurysms (AAA) was used to analyze monocyte/macrophage-related DEGs. On the basis of the DEG data related to monocytes and macrophages, a TF-genes network has been developed. Hub genes and core sub-networks have also been identified. Furthermore, the key genes have been validated in an external cohort.

Results: From combined monocyte and macrophage-derived DEGs from abdominal aortic aneurysms, five hub DEGs were detected, including *IFI30, SERPINE1, HMOX1, IL24*, and *RUNX1*. A total of 57 genes were found in the IA bulk RNA-seq dataset. A support vector machine-recursive feature elimination algorithm (SVM-RFE) was applied to further screen the seven genes (*RPS4Y1, DDX3Y, RUNX1, CLEC10A, PLAC8, SLA, and LILRB3*). *RUNX1* was the hub gene that regulated *NFKB1* in the monocyte/macrophage-related network. And *RUNX1* is implicated in IA progression by regulating hematopoietic stem cell differentiation and abnormal platelet production, according to gene set enrichment analysis.

Conclusion: Among patients with hypertension, *RUNX1* in monocytes and macrophages was associated with a higher risk of IA through its regulation of *NFKB1*.

Keywords: intracranial aneurysm (IA), hypertension, monocytes/macrophages, Runx1, NFKB1

OPEN ACCESS

Edited by:
Yuzhen Xu,
Tongji University, China

Reviewed by:
Yu Zeng,
Second Affiliated Hospital of Guangdong Medical University, China
Xinbing Liu,
Changxing People's Hospital, China
Yang Jie,
Second Affiliated Hospital of Shandong University of Traditional Chinese Medicine, China

***Correspondence:**
Donghua Liu
DhuaL@mau.edu.mk

[†]*These authors have contributed equally to this work*

Specialty section:
This article was submitted to Neurological Biomarkers, a section of the journal Frontiers in Neurology

Received: *17 February 2022*
Accepted: *22 April 2022*
Published: *17 May 2022*

Citation:
Li Y, Zhang Z and Liu D (2022) Intracranial Aneurysms Induced by RUNX1 Through Regulation of NFKB1 in Patients With Hypertension-An Integrated Analysis Based on Multiple Datasets and Algorithms. Front. Neurol. 13:877801. doi: 10.3389/fneur.2022.877801

INTRODUCTION

Intracranial aneurysm (IA) is a cerebrovascular disease caused by the limited dilation of cerebral arteries (1). Its incidence is approximately 3.2%, and it is higher in women than in men (2–4). IA ruptures and bleeding are associated with high morbidity rates and mortality rates (5). Subarachnoid hemorrhage (SAH) results from an IA rupture or bleeding, and accounts for 70–85% of all spontaneous SAHs (6). In addition, IA can induce intracerebral or subdural hematoma (7, 8). Hypertension is a common risk factor for IA as well as an independent risk factor for IA rupture (9–11). IA poses a significant risk to patients with hypertension. Therefore, IA progression in this patient group should be prevented.

The role played by monocytes/macrophages in the pathogenesis of IA has been demonstrated in recent studies. Development of IA involves complex pathophysiological processes, such as endothelial inflammatory responses triggered by altered hemodynamics and genetic factors (12, 13). Changes in cerebral artery hemodynamics can trigger a prolonged and excessive inflammatory response in the vessel wall, leading to the development, growth, and rupture of IA (13). Cell death in the vessel wall and destruction of the extracellular matrix can occur as a result of this chronic inflammation caused by the recruitment of monocytes/macrophages (14). During inflammation, monocytes can infiltrate the vessels and become macrophages, which modulates the immune response (15). Macrophages of the M1 type can release cytokines to increase the inflammatory response and recruit further macrophages (16). It is also possible for M1-type macrophages to remodel the blood vessels in addition to releasing cytokines (17). By inhibiting macrophage recruitment and accumulation in the vessel wall of individuals with IA, the incidence and size of IA in animal models will be significantly reduced (18). Monocytes and macrophages play an important role in IA pathogenesis, but the mechanism is not known.

Cells are the basic unit of life, which can communicate via two distinct pathways (paracrine and autocrine) to regulate metabolism, differentiation, and other biological functions (19). Monocytes and macrophages in a hypertensive microenvironment may cause IA through scRNA-seq analysis. The rapid development of single-cell sequence technologies has allowed previous studies to collect gene expression data at the single-cell level in recent years (20–24). The analysis of single cells can identify the mechanisms of cellular interactions and is essential for establishing the molecular regulation of diseases at the microscopic level (25–28). Single-cell RNA sequencing analysis revealed that megakaryocytes and a few monocyte subpopulations may significantly elevate cytokine levels in patients with severe coronavirus disease 2019 (29). We hypothesized that single-cell analysis could provide insight into possible mechanisms underlying the development of hypertension-induced IA.

Abbreviations: AAA, Abdominal aortic aneurysm; IA, Intracranial aneurysm; *RUNX1,* Runt-related transcription factor 1; SAH, Subarachnoid hemorrhage, SVM-RFE, Support Vector Machines–Recursive Feature Elimination algorithm.

This study examined hub genes that contribute to IA progression among patients with hypertension and identified potential therapeutic targets for preventing and reducing the risk of IA, thereby lowering the risk of neurovascular diseases including cerebral hemorrhage.

METHODS

Data Acquisition

First, the Gene Expression Omnibus (GEO) database was searched for IA-related bulk and single-cell RNA-seq datasets. To investigate the possible role of hypertension in IA development, the keyword "Hypertension" was retrieved from the GEO dataset to obtain HT-related datasets. The filtering criteria for the datasets were as follows: First, bulk RNA-seq datasets were derived from human samples, and each dataset contained at least 10 samples. Second, single-cell RNA-seq datasets were assigned as the control design. Transcriptomic data from the peripheral blood mononuclear cells (PBMCs) of 11 patients with hypertension and 10 healthy controls (HCs) were collected from the GSE75360 dataset to analyze hypertension-related differentially expressed genes (DEGs) according to the set conditions (30). The mRNA transcriptomic data from 44 IA samples and 16 HC samples of the intracranial cortical artery from the GSE122897 dataset were used to analyze IA-related DEGs. The GSE13353 dataset contains 11 ruptured and 8 unruptured intracranial aneurysm samples, and this dataset was used as an external validation cohort in this study (31). To assess the transcription of AI-related genes at the single-cell level, we included a single-cell RNA-seq dataset (Gene Expression Omnibus accession no. GSE166676) with four cases of abdominal aortic aneurysm (AAA) and two cases of non-aneurysmal control (NAC) among patients with atherosclerotic occlusive disease after a cautious examination (32). The single-cell RNA sequencing (scRNA-seq) dataset contains transcriptomic data from 14,088 cells. All analyses and plots were created using R (version 4.0.2). Differences between groups were assessed using the Wilcoxon rank-sum test.

Quality Control and Data Merging of ScRNA-Seq Data

First, the R package Seurat (version 4.0) was used for the quality control of scRNA-seq data from AAA and NAC samples (33). The metrics used for quality control included the number of gene signatures detected in each cell, total RNA count, and proportion of mitochondrial and hemoglobin genes expressed. High-quality data from the scRNA-seq dataset were screened by removing cells containing < 200 or $> 2{,}500$ genes as well as cells with $> 10\%$ of mitochondrial genes. Finally, we obtained 9,796 cells for subsequent analysis. The "SelectIntegrationFeatures" function was then used to identify the top 2,000 highly variable genes shared among the six samples. Further, the "FindIntegrationAnchors" function was then used to find the anchors from the highly variable genes. Finally, by applying the "IntegrateData" function, the scRNA-seq data from the six samples were combined for subsequent dimension reduction and clustering analysis.

Dimensionality Reduction, Clustering, and Annotation of scRNA-seq Data

The uniform manifold approximation and projection (UMAP) algorithm was used to analyze and visualize cell clustering (34). The top 30 principal components (PCs) were selected to further perform UMAP and clustering analysis. We first used SingleR (version 1.4) to predict the cell types of individual cell clusters (35). The Database of Immune Cell Expression (DICE) and Monaco Immune Cell Data were selected as the reference datasets to predict the types of immune cells in the IA single-cell dataset. Then, the cell type predictions were manually validated against the marker molecules of immune cells from the CellMarker (http://biocc.hrbmu.edu.cn/CellMarker/index.jsp) website to complete the final cell annotation.

Extraction and Differential Analysis of Target Cell Populations

According to a literature review, monocytes/macrophages play an essential role in IA progression (36). Therefore, we further included monocytes/macrophages for subsequent analysis. First, the RNA transcripts of all genes in the monocytes/macrophages between the AAA and NAC groups were subjected to differential expression analysis. Two approaches were used to identify DEGs between the two groups. The first approach applied the "FindMarker" function to identify DEGs between the two cell populations. The other approach used DESeq2 to the constructed pseudo-bulk RNA data after establishing the pseudo-bulk RNA-seq data for differential expression analysis. DEGs identified with these two approaches were combined as monocyte/macrophage-related DEGs.

Differential Analysis of Bulk RNA and Identification of Shared DEGs

Based on the type of bulk RNA-seq data, the limma or edgeR package was used for differential expression analysis. We applied the limma package for the differential analysis of FPKM-type RNA data and obtained IA-related DEGs (37). The R package "edgeR" was used to identify hypertension-related DEGs and to perform the differential analysis of count-type RNA data (38). DEGs were screened with a threshold of $P < 0.05$. Subsequently, we performed intersection analysis of IA-related DEGs, hypertension-related DEGs, and monocyte/macrophage-related DEGs to obtain shared DEGs, which were considered as genes of interest (GOIs).

Support Vector Machines–Recursive Feature (SVM-RFE) Elimination Model Construction and Variable Selection

Intersection analysis of IA-related DEGs and monocyte/macrophage-related DEGs revealed 57 shared DEGs. Then, using the bulk RNA-seq data for IA, we incorporated these 57 genes into the Support Vector Machines–Recursive Feature Elimination (SVM–RFE) model to predict the incidence of IA. This model can be applied to select the optimal number of variables that must be included in the model and can yield the most relevant variables for classification prediction (39).

TF-Gene Network Construction and Functional Pathway Enrichment Analysis

To explore the significant TF regulatory network in monocytes/macrophages, we applied the TRRUST (version 2.0) database to predict the TF–gene pairs corresponding to monocyte/macrophage-related DEGs (40). Cytoscape (version 3.9) was used to visualize this TF–gene network, and the Molecular Complex Detection plug-in was further used to identify the core sub-networks in this network (degree cutoff = 2, node score cutoff = 0.2, and max depth = 100).

To explore the potential pathways involved in DEGs, we used the clusterProfiler R package for Kyoto Encyclopedia of Genes and Genomes and Gene Ontology (GO) analysis as previous research (41, 42). Gene Set Enrichment Analysis (GSEA) was applied to analyze the functional pathways of enrichment of core genes at the individual and cellular levels. The "c2.cp.v7.2.symbols.gmt [Curated]" gene set downloaded from MSigDB Collections (https://www.gsea-msigdb.org/gsea/msigdb/) was used as the reference gene set. The filtering threshold for differences in functional pathways was set at $P < 0.05$ (43).

RESULTS

Quality Control and Annotation Results for scRNA-seq Data

First, we performed quality control on the scRNA-seq data of arterial tissue. The **Figure 1A** shows the distribution of total NRA counts, the number of gene signatures, and the proportion of mitochondrial gene expression and hemoglobin-related gene expression in cells before filtration. Following the pre-defined filtering conditions, 9,796 cells were included in the subsequent analysis (**Figure 1B**). UMAP showed that each cell cluster overlapped between the two groups and between the six samples. Therefore, data integration eliminated the batch effect (**Figures 1C,D**). Data were reduced in dimension and clustered into 21 cell clusters (**Figure 2A**). **Figures 2B,C** show four and eight cell clusters annotated using the DICE and Monaco reference datasets, respectively. Among them, monocytes had a relatively large overlap between the two annotation methods. Subsequently, we applied cellular annotation with nine cellular marker genes from CellMarker, which were consistently expressed between the two groups (**Figure 2D**). **Figures 3A,B** illustrate the expression of these nine cell markers within each cluster of cells. Among them, CSF1R was used to annotate monocytes/macrophages, CD14 to annotate monocytes, CD68 to annotate macrophages, CD3D and CD2 to annotate T cells, PRF1, and KLRF1 to annotate NK cells, ITGAX to annotate dendritic cells, and CD19 to annotate B cells. Finally, four cell types were annotated by combining the cell annotation results of SingleR and CellMarker, including T cells, B cells, NK cells, and monocytes/macrophages (**Figure 3C**). A significant difference in the percentage of T cells was observed between the AAA and NAC groups (p 0.05) (**Figure 3D**). In

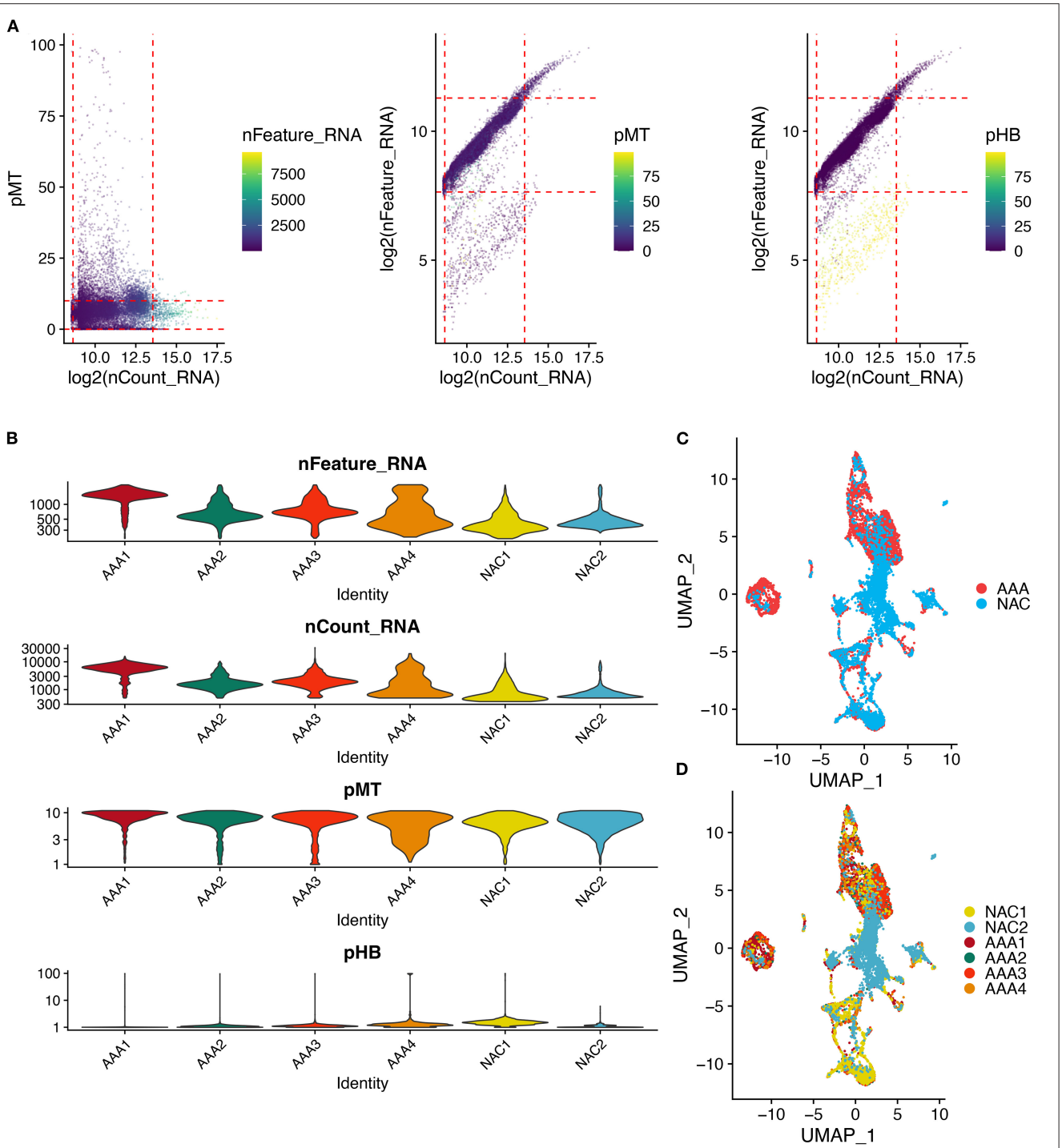

FIGURE 1 | Quality control and cell clustering of single cell data. **(A)** Scatter plot of quality control metrics for scRNA-seq data. The red dashed line represents the threshold used to filter out high quality transcriptomic data. pMT: percent of mitochondrial counts; pHB: percent of hemoglobin RNA counts. **(B)** Violin plots showing the distribution of cell characteristics after quality control. **(C,D)**. UMAPs show the results of cell clustering based on the top 30 principal components, color coded by **(C)** tissue type, or **(D)** patient.

addition, the proportion of monocytes/macrophages differed significantly between samples in the AAA group. Thus, monocytes/macrophages might be involved in the different stages of IA progression.

Results of Differential and Intersection Analyses

In total, 2,102 monocytes/macrophages were extracted and used for differential analysis between the AAA and NAC

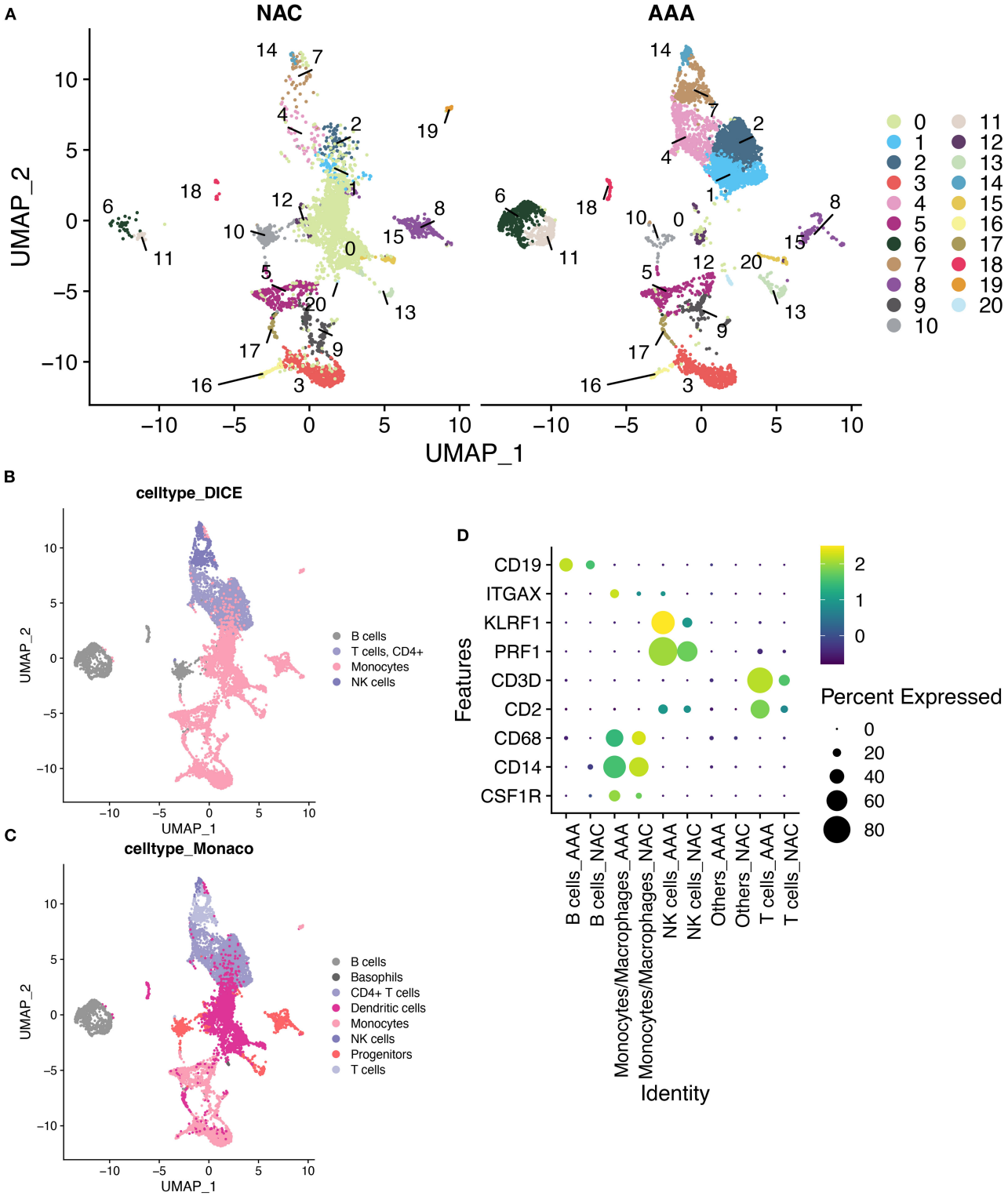

FIGURE 2 | SingleR annotation of cell clusters. **(A)** The UMAPs show a distribution of 21 cell clusters in the AAA and NAC groups, respectively. **(B)**. Application of cell annotation to the DICE reference dataset.DICE: Database of Immune Cell Expression (/eQTLs/Epigenomics). **(C)** Cell annotation using Monaco Immune Cell Data. **(D)** Heat map showing good concordance in the expression of cellular marker genes between AAA and NAC groups.

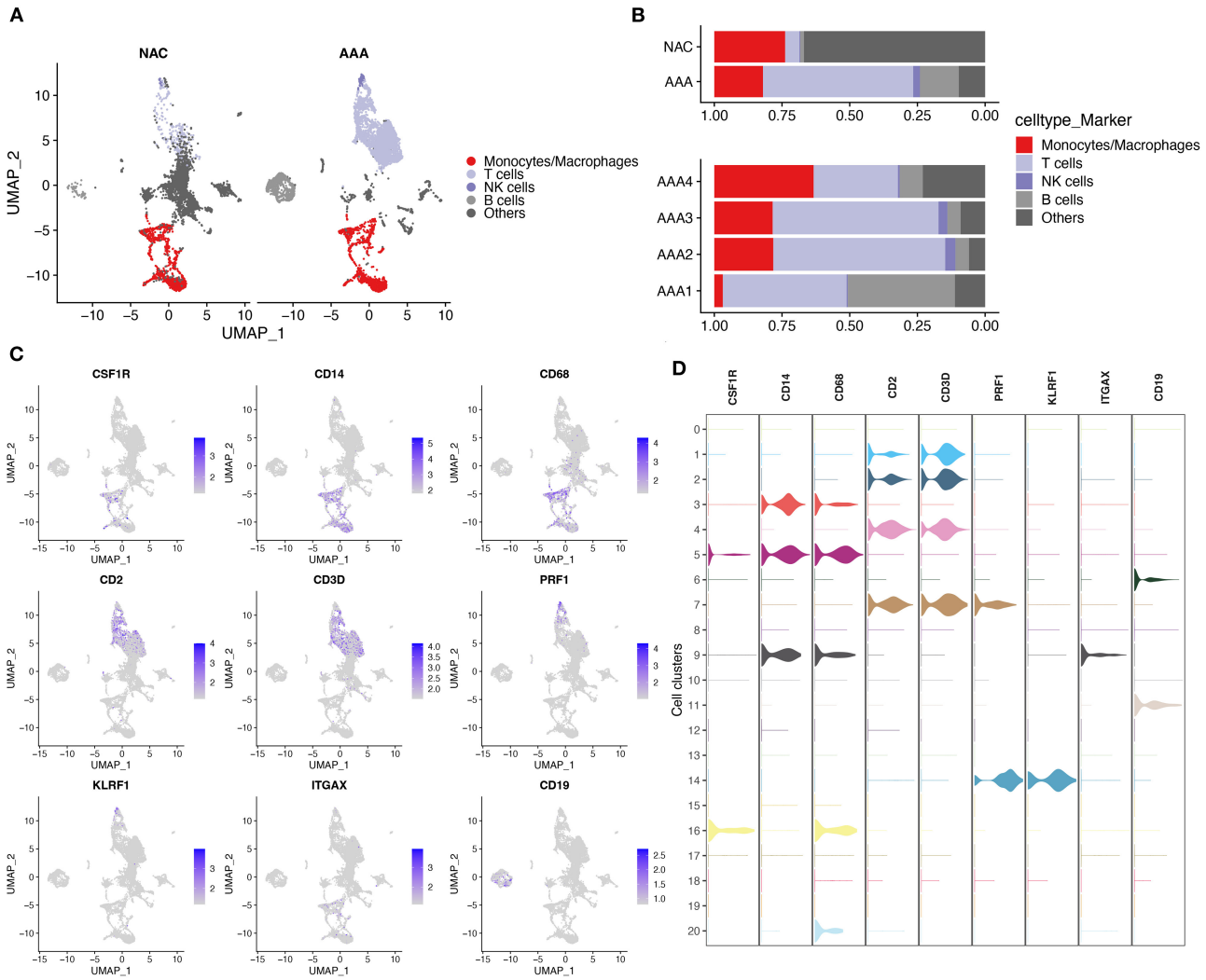

FIGURE 3 | Cell annotation in conjunction with CellMarker. **(A)** UMAPs show the results of applying the marker genes in CellMaker to annotate cells. **(B)** The bars depict the percentage of each cell type in each tissue type and patient. **(C)** UMAPs show the expression of cellular marker genes in cells. **(D)** Violin diagram depicting cell marker gene expression in each cell cluster.

groups. Further, DESeq2 and FindMarker identified 419 and 539 DEGs, respectively, with a total of 869 genes after removal of intersections. Then, 2,550 and 3,079 DEGs were identified from the bulk RNA-seq data of HT and IA, respectively. These genes of interest (GOIs) were annotated in the volcano map (**Figures 4A,B**). The top 20 upregulated and downregulated DEGs in AAA identified by FindMarker and DESeq2, respectively, are shown in **Figures 4C,D**. To further explore the functional pathways that are jointly dysregulated in hypertension and IA, GO function enrichment analysis of the 95 DEGs common to HT and IA was performed. **Figures 4E,F** show the pathways that are jointly upregulated and downregulated in hypertension and IA, respectively. Finally, cross-tabulation analysis revealed that five GOIs, including *IFI30, SERPINE1, HMOX1, IL24,* and *RUNX1*, were found to be associated with hypertension, IA, and monocytes/macrophages (**Figure 4G**). And the differential expression of *IFI30, SERPINE1, HMOX1, IL24,* and *RUNX1* were shown in the volcano plot (**Figures 4A,B**).

SVM–RFE Analysis of the Expression Distribution of Hub Genes in the Bulk RNA of IA

In total, 57 genes were identified as shared DEGs in monocytes/macrophages from AAA and IA (**Figure 4G**). These DEGs were then further screened by applying SVM–RFE to the bulk RNA-seq dataset from IA. The variable screening results of the SVM–RFE algorithm showed that the IA prediction model constructed from seven gene features (*RPS4Y1, DDX3Y, RUNX1, CLEC10A, PLAC8, SLA,* and *LILRB3*) had the highest accuracy (**Figure 5A**), with an area under the curve (AUC) of 0.862 (**Figure 5B**). This seven-gene SVM model was validated by ROC analysis with the GSE13353 dataset as an external cohort

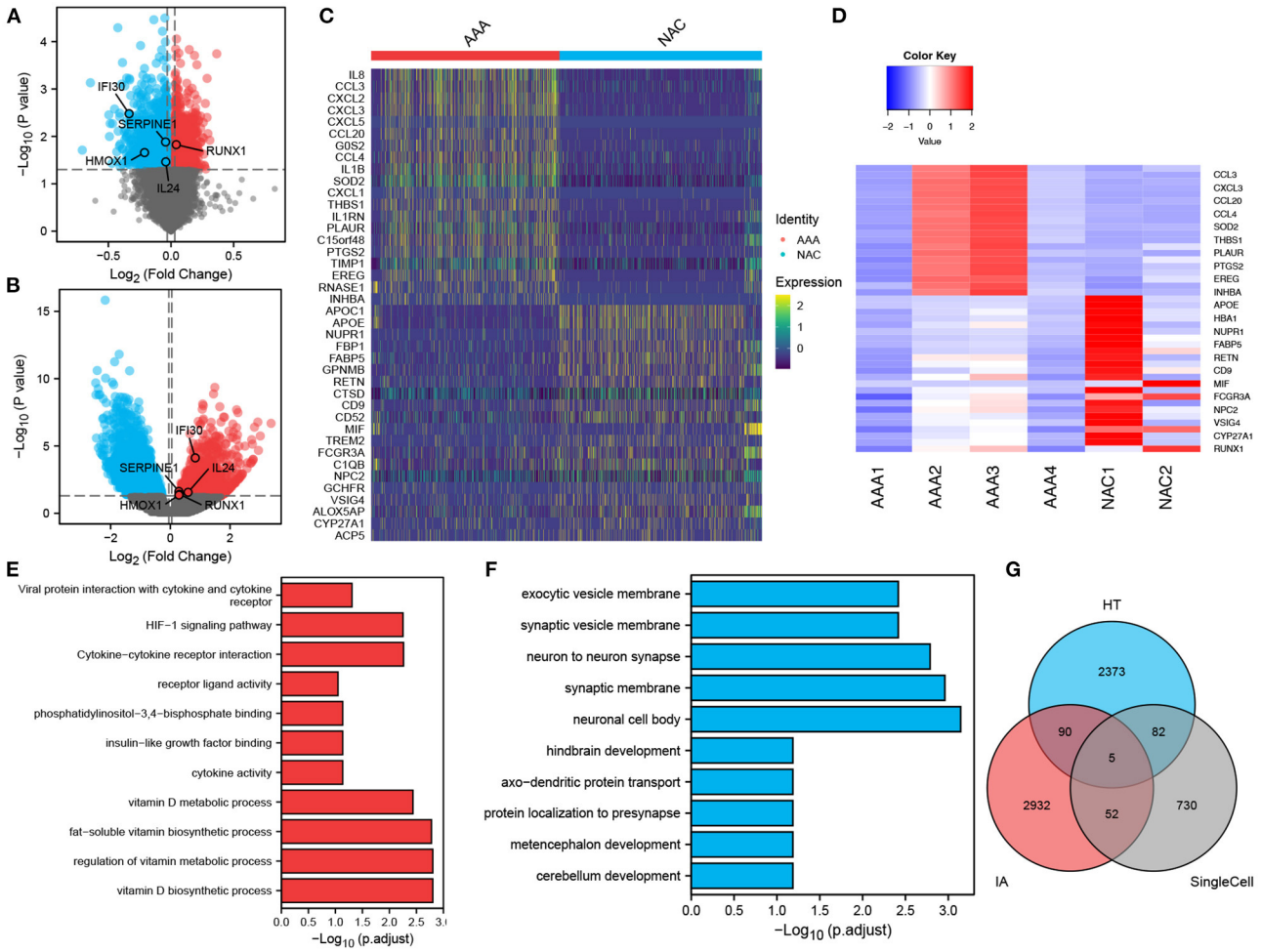

FIGURE 4 | Differentially expressed genes and intersection analysis. **(A,B)** Volcano plots showing the results of tests for differentially expressed genes in **(A)** HT, and **(B)** IA, respectively, and the differences in expression of GOIs are marked in the plots. **(C,D)**. Differentially expressed genes in monocytes/macrophages obtained by applying **(C)** FindMarker, or **(D)** DEGs. **(E,F)** Differential gene-enriched (E) up-regulation pathway and (F) down-regulation pathway shared in HT and IA. **(G)** Intersection analysis of HT-associated DEGs, IA-associated DEGs and monocytes/macrophages-associated DEGs revealed five GOIs.

(AUC: 0.812) (**Figure 5C**). **Figures 5D,E** depict the ROC curves for each of the seven genes (AUC: 0.601–0.817). The above studies suggest that these genes (*RPS4Y1, DDX3Y, RUNX1, CLEC10A, PLAC8, SLA,* and *LILRB3*) can predict the prevalence of IA. **Figure 5F** depicts the expression distribution of these seven genes in the bulk RNA of IA. By analyzing the heat map, *RUNX1, CLEC10A, PLAC8, SLA*, and *LILRB3* were found to be highly expressed in IA, while *RPS4Y1* and *DDX3Y* were lowly expressed in IA.

RUNX1 As a Hub Gene in IA Progression Determined via Network Analysis and Intersection Analysis

We analyzed and constructed the TF regulatory network in monocytes and macrophages (**Figure 6A**). In addition, the intersection analysis of the seven genes and five GOIs used to build the IA prediction model revealed that *RUNX1* was the hub gene (**Figure 6B**). In the PPI network, *RUNX1* was responsible for regulating four downstream molecules. According to the core sub-network of this PPI network, *NFKB1*, regulated by *RUNX1*, is the hub gene of the entire network (**Figure 6C**). Therefore, *RUNX1* was identified as a hub gene in the IA process by network analysis and crossover analysis.

Correlation Between *RUNX1* and IA Progression

We performed GSEA analysis of monocytes/macrophages in the single cell dataset. GSEA showed phospholipase C-mediated cascade FGFR4, dopaminergic neurogenesis, and RHO GTPases activate PAKs were downregulated in monocytes/macrophages upregulated with *RUNX1* (**Figure 6D**). Based on GSE122897, GSEA was also further performed to explore the functional pathways enriched for *RUNX1* at the individual level (**Figure 7**). Moreover, it revealed that in

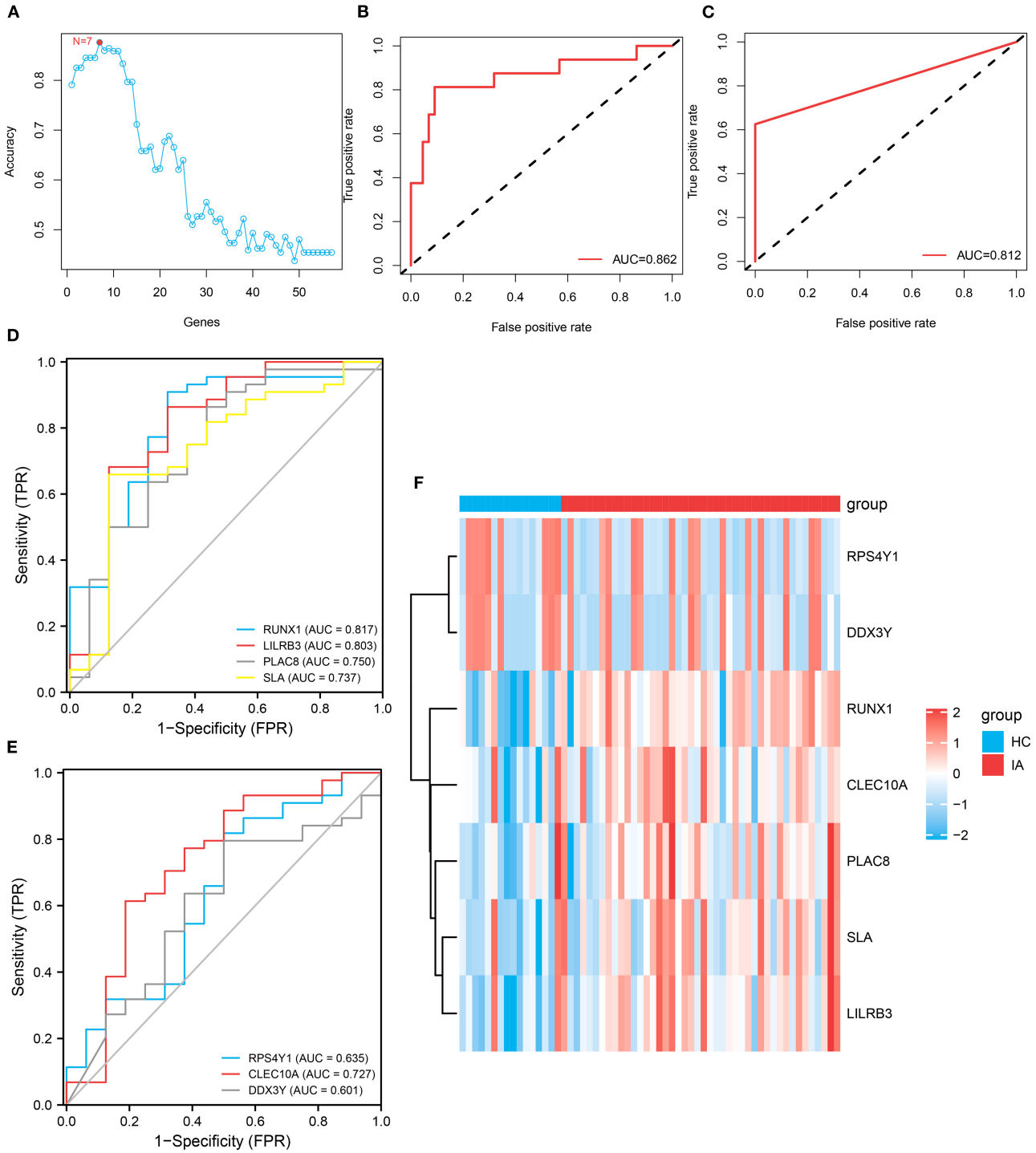

FIGURE 5 | Construction and variable selection of the intracranial aneurysm prediction model using the Support Vector Machines–Recursive Feature Elimination (SVM–RFE) algorithm. **(A)** Broken line graph of the number of genes identified using the SVM–RFE model and the accuracy of the model. Hence, the highest accuracy can be achieved using the SVM model constructed from seven genes. **(B)** Receiver operating characteristic (ROC) curve based on the SVM model constructed from these seven genes, with an area under the curve (AUC) value of 0.862. **(C)** Validation of this seven-gene SVM model by ROC analysis with an external cohort. **(D,E)** ROC curves showing the AUCs of *RUNX1*, *LILRB3, PLAC8, SLA, RPS4Y1, CLEC10A,* and *DDX3Y*. **(F)** Heatmap depicts the expression distribution of these seven genes in the bulk RNA of IA.

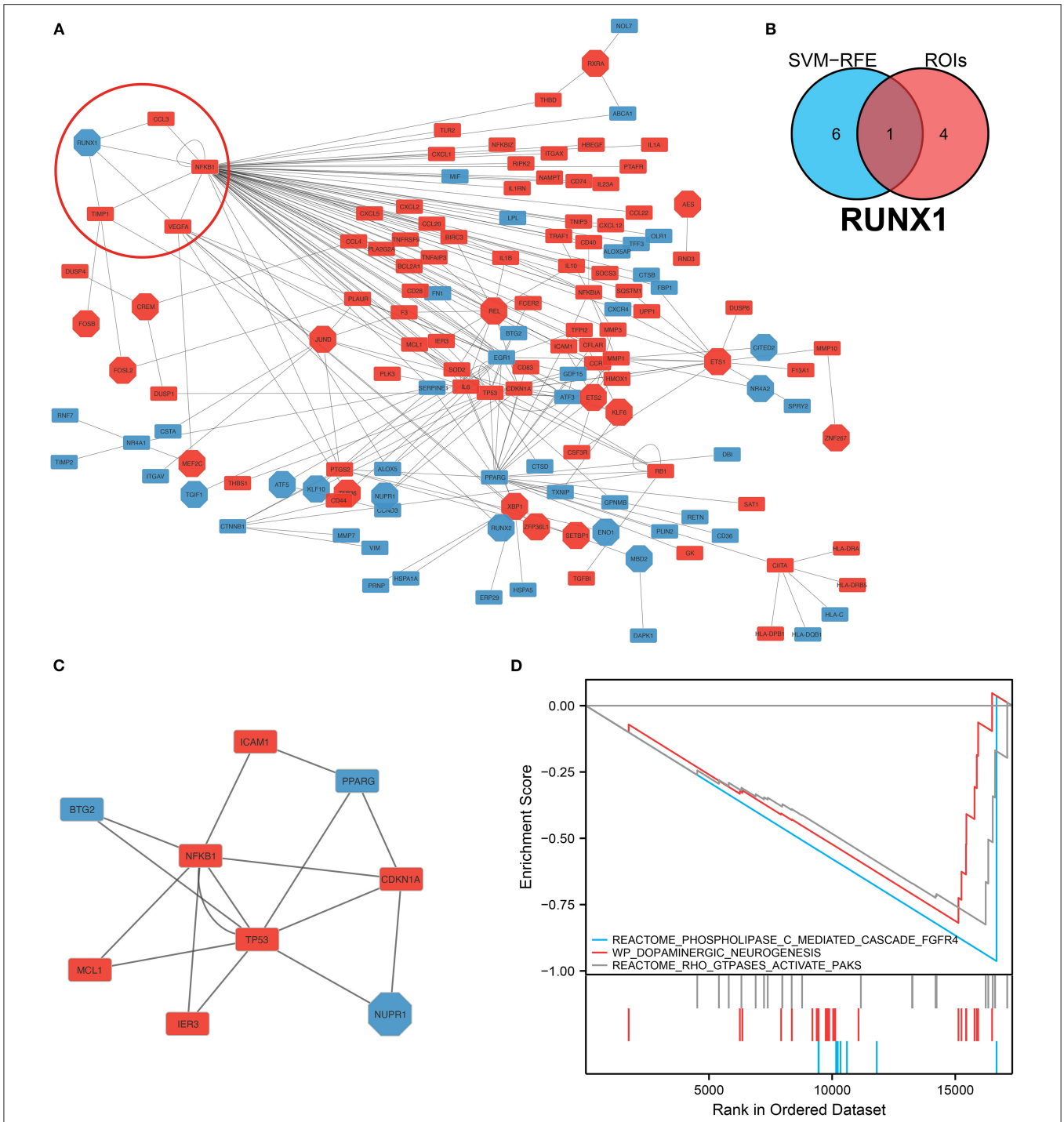

FIGURE 6 | Construction of the protein–protein interaction network and hub gene screening. **(A)** TF-mRNA protein–protein interaction network in monocytes/macrophages. The red circles denote the *RUNX1* and target genes. **(B)** Intersection analysis of the seven genes screened using the SVM–RFE model, and these five regions of interest yielded the hub gene *RUNX1*. **(C)** Sub-protein–protein interaction network showing that *NFKB1*, which is regulated by *RUNX1*, is the hub gene in this PPI network. **(D)** Gene Set Enrichment Analysis of *RUNX1* at the single-cell level.

samples with upregulated *RUNX1* expression, nonalcoholic fatty liver disease, oxidative phosphorylation, *RUNX1* regulates the transcription of genes involved in the differentiation of HSCs and those involved in megakaryocyte differentiation, and platelet function pathway *RUNX1* regulates genes involved in megakaryocyte differentiation and platelet function. Therefore, *RUNX1* plays a complex role in IA progression. Further, it might be involved in IA progression via the regulation of HSC differentiation and platelet production and might play a potential regulatory role in oxidative phosphorylation.

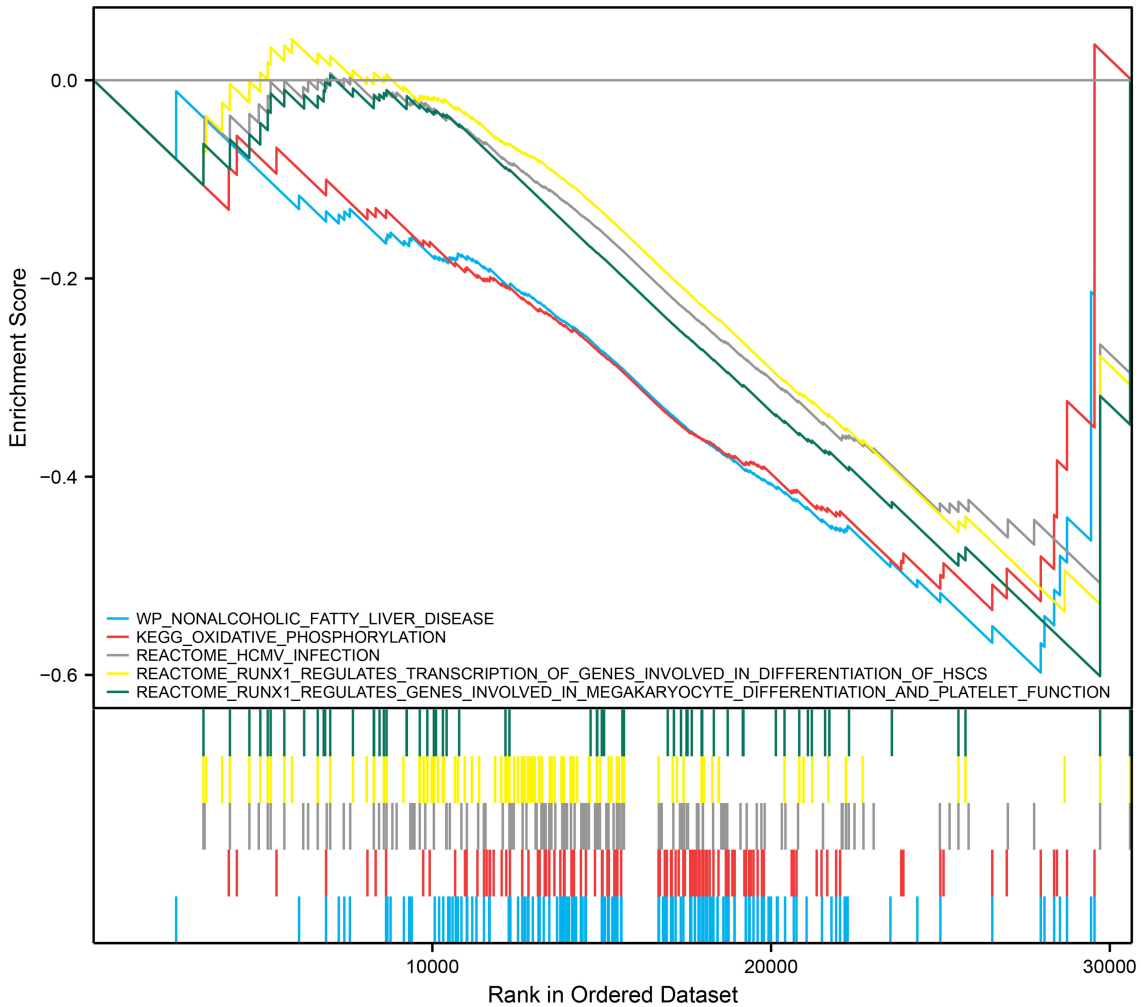

FIGURE 7 | *RUNX1* GSEA at the bulk RNA level.

DISCUSSION

From cellular data, it is evident that *RUNX1* contributes to the development of IA via its role in regulating *NFKB1* in monocytes/macrophages within the hypertensive microenvironment. GSEA revealed that *RUNX1* was associated with IA progression by regulating hematopoietic stem cell differentiation and platelet production.

In this study, scRNA-seq data were used to examine the transcriptional patterns of IA at the single-cell level. The risk mRNAs of IA were screened, and predictive models were established using the combined bulk RNA-seq data. Further, the IA-related TF-gene regulatory network was constructed. *RUNX1* was identified as the hub gene, and it regulated four genes. And *NFKB1* was found to be regulated by *RUNX1*. This finding was consistent with that of previous studies showing that NF-κB was involved in IA progression (44, 45). And we first identified the mechanism at the single-cell level.

RUNX1 was significantly expressed in the IA group ($P < 0.001$). GSEA revealed that phospholipase C-mediated cascade FGFR4, dopaminergic neurogenesis, and RHO GTPases activate PAKs were downregulated in monocytes/macrophages cells where *RUNX1* was upregulated. Thus, *RUNX1* plays a complex role in IA progression, possibly via the regulation of hematopoietic stem cell differentiation and platelet production. *RUNX1* might be a hub gene between hypertension, IA, and DEGs in monocytes. Previous studies have found that *RUNX1* is involved in hypertension progression to some extent. Further, it is an important hematopoietic transcription factor associated with thrombocytopenia and impaired platelet activation response and is correlated with vascular disease progression (46). *RUNX1* is involved in endothelial cells and hematopoietic processes, thereby affecting endothelial function and inflammatory changes, and the abnormal expression of *RUNX1* can induce hypertension (47). An experimental study has shown that the inhibition of *RUNX1* expression decreases pulmonary hypertension progression in mice (47). In addition, it reduces vascular remodeling and macrophage recruitment, which play essential roles in hypertension progression (48, 49). Hypertension is a significant risk factor for IA progression.

The role of *RUNX1* identified in related studies may be relevant to IA. *RUNX1* is involved in regulating endothelial cell function and is a key transcriptional regulator of the conversion of endothelial to hematopoietic cells (47, 50). An early feature of IA is endothelial cell dysfunction and degeneration (51). Lilly et al. found that SOX7 interacted with *RUNX1* at the protein level and inhibited the transcriptional activity of *RUNX1*, thereby regulating the conversion of endothelial to hematopoietic cells and maintaining arterial endothelium stability (52). *RUNX1* can directly or indirectly regulate signal transduction pathways such as the TGF-β signaling pathway and the Wnt signaling pathway (53). TGF-β is associated with cerebral edema after subarachnoid hemorrhage and can be used as a prognostic indicator (54). Therefore, *RUNX1* in the TGF-β signaling pathway may be correlated with the progression and prognosis of IA. Based on the functions played by *RUNX1* in the progression of hypertension and IA, we hypothesized that *RUNX1* promotes hypertension progression combined with IA.

A population-wide genomic study showed that *NFKB1* is a susceptibility gene for primary hypertension (54). *NFKB1* is involved in hypertension progression by affecting vascular endothelial function via the regulation of downstream NOS3 gene expression (55). It also promotes oxidative stress injury in gestational hypertensive mice, which contributes to hypertension pathogenesis (56–58). In addition, NF-κB is involved in the IA progression via several pathways. The activation of NF-κB in signaling pathways upregulates MCP-1 expression and participates in the apoptotic process in vascular smooth muscle cells. This phenomenon further reduces the elasticity of the cerebral vascular wall, making it less able to adapt to altered hemodynamics, promotes IA progression, and increases the risk of rupture (59–61). NF-κB elevates the transcription of various pro-inflammatory genes such as *COX-2, CCL-2, MMP,* and *iNOS*, and the inflammatory response is involved in the progression and rupture of IA (62, 63). Moreover, macrophage infiltration and NF-κB activation are reduced if macrophages are specifically absent or in the mutants of the NF-κB inhibitory protein. To the best of our knowledge, this study first identified the role of *RUNX1* in monocytes/macrophages at the single-cell level in IA progression among patients with hypertension via the regulation of *NFKB1*.

The purpose of this study was to investigate the potential mechanisms of IA induction by monocytes and macrophages in the hypertensive microenvironment at the single-cell level using bioinformatics. *RUNX1* and its regulated *NFKB1* were identified as hub genes. *RUNX1* may play a role in the progression of IA by regulating abnormalities in hematopoietic stem cell differentiation and platelet production. Identification of these two genes is an important step in understanding IA mechanisms in patients with hypertension. Moreover, it can facilitate further research about potential targets for preventing and reducing the risk of IA in patients with hypertension. There was no single-cell dataset available for IA assessment; therefore, the single-cell dataset (GSE166676) for AAA assessment was used instead. The dataset should be expanded in the future. Finally, neither cellular nor animal tests were conducted to investigate the signaling pathways of the identified hub genes. Further work is required to corroborate these findings.

CONCLUSION

RUNX1 in monocytes/macrophages is associated with the development of IA via the expression of *NFKB1* among patients with hypertension. This potential role can lay the foundation for the further identification of molecular mechanisms underlying IA progression in patients with hypertension and can provide data about treatment targets in IA among patients with hypertension.

DATA AVAILABILITY STATEMENT

Publicly available datasets were analyzed in this study. This data can be found here: National Center for Biotechnology Information (NCBI) Gene Expression Omnibus (GEO), https://www.ncbi.nlm.nih.gov/geo/, GSE75360 data set and GSE122897.

ETHICS STATEMENT

Ethical review and approval was not required for the study on human participants in accordance with the local legislation and institutional requirements. Written informed consent from the patients/participants or patients/participants' legal guardian/next of kin was not required to participate in this study in accordance with the national legislation and the institutional requirements.

AUTHOR CONTRIBUTIONS

YL: software, validation, formal analysis, data curation, and writing—original draft. ZZ: software, validation, formal analysis, supervision, data curation, and writing—original draft. DL: conceptualization, methodology, supervision, writing—review and editing, and project administration. All authors contributed to the article and approved the submitted version.

FUNDING

This work was funded by Project of Ningxia Medical University (XZ2021025 to YL). This work was also supported by the Natural Science Foundation of Shandong Province (A study on the mechanism of temporal lobe epilepsy comorbid anxiety based on negative emotional information processing in amygdala activation and changes in the effective link of brain function. No. ZR2019BH043).

SUPPLEMENTARY MATERIAL

The Supplementary Material for this article can be found online at: https://www.frontiersin.org/articles/10.3389/fneur.2022.877801/full#supplementary-material

REFERENCES

1. Bo L, Wei B, Wang Z, Li C, Gao Z, Miao Z. Bioinformatic analysis of gene expression profiling of intracranial aneurysm. *Mol Med Report*. (2017) 17:3473–80. doi: 10.3892/mmr.2017.8367
2. Vlak MH, Algra A, Brandenburg R, Rinkel GJ. Prevalence of unruptured intracranial aneurysms, with emphasis on sex, age, comorbidity, country, and time period: a systematic review and meta-analysis. *Lancet Neurol*. (2011) 10:626–36. doi: 10.1016/S1474-4422(11)70109-0
3. Thompson BG, Brown RD, Amin-Hanjani S, Broderick JP, Cockroft KM, Connolly ES, et al. Guidelines for the management of patients with unruptured intracranial aneurysms: a Guideline for healthcare professionals from the american heart association/American stroke association. *Stroke*. (2015) 46:2368–400. doi: 10.1161/STR.0000000000000070
4. Tada Y, Makino H, Furukawa H, Shimada K, Wada K, Liang EI. et al. Roles of estrogen in the formation of intracranial aneurysms in ovariectomized female mice. *Neurosurgery*.. (2014) 75:690–5. doi: 10.1227/NEU.0000000000000528
5. Jiranukool J, Thiarawat P, Galassi W. Prevalence of intracranial aneurysms among acute ischemic stroke patients. *Surgical Neurol Int*. (2020) 11:341. doi: 10.25259/SNI_506_2020
6. De Backer A. Handbook of neurosurgery. *Acta Chirurgica Belgica*. (2016) 116:269. doi: 10.1080/00015458.2016.1229422
7. Niemann DB, Wills AD, Maartens NF, Kerr RSC, Byrne JV, Molyneux AJ. Treatment of intracerebral hematomas caused by aneurysm rupture: coil placement followed by clot evacuation. *J Neurosurg*. (2003) 99:843–7. doi: 10.3171/jns.2003.99.5.0843
8. Zacharia BE, Hickman ZL, Grobelny BT, DeRosa P, Kotchetkov I, Ducruet AF, et al. Epidemiology of aneurysmal subarachnoid hemorrhage. *Neurosurg Clin N Am*. (2010) 21:221–33. doi: 10.1016/j.nec.2009.10.002
9. Long A, Bui HT, Barbe C, Henni AH, Journet J, Metz D, et al. Prevalence of abdominal aortic aneurysm and large infrarenal aorta in patients with acute coronary syndrome and proven coronary stenosis: a prospective monocenter study. *Ann Vasc Surg*. (2010) 24:602–8. doi: 10.1016/j.avsg.2009.12.010
10. Joviliano EE, Ribeiro MS, Tenorio EJ, MicroRNAs R. Current concepts on the pathogenesis of abdominal aortic aneurysm. *Braz J Cardiovasc Surg*. (2017) 32: 215–24. doi: 10.21470/1678-9741-2016-0050
11. Adewunmi T. A review on the effects of sleep duration on hypertension. *Life Res*. (2020) 3:39. doi: 10.53388/life2020-0125-303
12. Dietrich P. Genetischer einfluss bei intrakraniellen aneurysmen. *Radiologe*. (2020) 60:329–33. doi: 10.1007/s00117-020-00663-9
13. Kataoka H, Yagi T, Ikedo T, Imai H, Kawamura K, Yoshida K, et al. Histopathological changes in the early phase of the development of an intracranial aneurysm. Neurol Med Chir(Tokyo). (2020) 60:319–28. doi: 10.2176/nmc.st.2020-0072
14. Ikedo T, Minami M, Kataoka H, Hayashi K, Nagata M, Fujikawa R, et al. Dipeptidyl peptidase-4 inhibitor anagliptin prevents intracranial aneurysm growth by suppressing macrophage infiltration and activation. *JAHA*. (2017) 6:4777. doi: 10.1161/JAHA.116.004777
15. Muhammad S, Chaudhry SR, Dobreva G, Lawton MT, Niemelä M, Hänggi D. Vascular macrophages as therapeutic targets to treat intracranial aneurysms. *Front Immunol*. (2021) 12:630381. doi: 10.3389/fimmu.2021.630381
16. Liu Y, Fang S, Li X, Feng J, Du J, Guo L, et al. Aspirin inhibits lPS-induced macrophage activation via the nF-κB pathway. *Sci Rep*. (2017) 7:11549. doi: 10.1038/s41598-017-10720-4
17. Shao L, Qin X, Liu J, Jian Z, Xiong X, Liu R. Macrophage polarization in cerebral aneurysm: perspectives and potential targets. *J Immunol Res*. (2017) 2017:1–7. doi: 10.1155/2017/8160589
18. Aoki T, Saito M, Koseki H, Tsuji K, Tsuji A, Murata K, et al. Macrophage imaging of cerebral aneurysms with ferumoxytol: an exploratory study in an animal model and in patients. *J Stroke Cerebrovasc Dis*. (2017) 26:2055–64. doi: 10.1016/j.jstrokecerebrovasdis.2016.10.026
19. Maruoka M, Kedashiro S, Ueda Y, Mizutani K, Takai Y. Nectin-4 co-stimulates the prolactin receptor by interacting with sOCS1 and inhibiting its activity on the jAK2-STAT5a signaling pathway. *J Biol Chem*. (2017) 292:6895–909. doi: 10.1074/jbc.M116.769091
20. Efremova M, Vento-Tormo M, Teichmann SA, Vento-Tormo R. CellPhoneDB: inferring cell–cell communication from combined expression of multi-subunit ligand–receptor complexes. *Nat Protoc*. (2020) 15:1484–506. doi: 10.1038/s41596-020-0292-x
21. Jin S, Guerrero-Juarez CF, Zhang L, Chang I, Ramos R, Kuan C-H, et al. Analysis of cell-cell communication using cellchat. *Nat Commun*. (2021) 12:1088. doi: 10.1038/s41467-021-21246-9
22. Zhao X, Yang J, Yang C. The neuronal transcription factor creb3l1 potential upregulates ntrk2 in the hypertensive microenvironment to promote vascular smooth muscle cell-neuron interaction and prevent neurons from ferroptosis: a bioinformatic research of scRNA-seq data. *DIS MARKERS*. 11:8339759. doi: 10.1155/2022/8339759
23. Chen Y, Sun Y, Xu Y, Lin W-W, Luo Z, Han Z, et al. Single-cell integration analysis of heterotopic ossification and fibrocartilage developmental lineage: endoplasmic reticulum stress effector xbp1 transcriptionally regulates the notch signaling pathway to mediate fibrocartilage differentiation. *Oxid Med Cel Longev*. (2021) 2021:1–29. doi: 10.1155/2021/7663366
24. Lin W, Wang Y, Chen Y, Wang Q, Gu Z, Zhu Y. Role of calcium signaling pathway-Related gene regulatory networks in ischemic stroke based on multiple wGCNA and single-cell analysis. *Oxid Med Cel Longev*. (2021) 2021:1–35. doi: 10.1155/2021/8060477
25. Liu X, Gao W, Liu W. Identification of kLF6/PSGs and nPY-Related uSF2/CEACAM transcriptional regulatory networks via spinal cord bulk and single-Cell rNA-Seq analysis. *Dis Markers*. (2021) 2021:1–21. doi: 10.1155/2021/2826609
26. Kumar MP, Du J, Lagoudas G, Jiao Y, Sawyer A, Drummond DC, et al. Analysis of single-Cell rNA-Seq identifies cell-cell communication associated with tumor characteristics. *Cell Reports*. (2018) 25:1458–68.e4. doi: 10.1016/j.celrep.2018.10.047
27. Murray LMA, Krasnodembskaya AD. Concise review: intercellular communication via organelle transfer in the biology and therapeutic applications of stem cells. *Stem Cells*. (2019) 37:14–25. doi: 10.1002/stem.2922
28. Garofalo M, Villa A, Crescenti D, Marzagalli M, Kuryk L, Limonta P, et al. and cross-species tropism of cancer-derived extracellular vesicles. *Theranostics*.. (2019) 9:5681–93. doi: 10.7150/thno.34824
29. Ren X, Wen W, Fan X, Hou W, Su B, Cai P, et al. COVID-19 immune features revealed by a large-scale single-cell transcriptome atlas. *Cell*. (2021) 184:1895–913.e19. doi: 10.1016/j.cell.2021.01.053
30. Dluzen DF, Noren Hooten N, Zhang Y, Kim Y, Glover FE, Tajuddin SM, et al. Racial differences in microRNA and gene expression in hypertensive women. *Sci Rep*. (2016) 6:35815. doi: 10.1038/srep35815
31. Kurki MI, Häkkinen S-K, Frösen J, Tulamo R, von und zu Fraunberg M, Wong G, et al. Upregulated signaling pathways in ruptured human saccular intracranial aneurysm wall: an emerging regulative role of toll-Like receptor signaling and nuclear factor-κB, hypoxia-Inducible factor-1A, and eTS transcription factors. *Neurosurgery*. (2011) 68:1667–76. doi: 10.1227/NEU.0b013e318210f001
32. Davis FM, Tsoi LC, Melvin WJ, denDekker A, Wasikowski R, Joshi AD, et al. Inhibition of macrophage histone demethylase jMJD3 protects against abdominal aortic aneurysms. *J Exp Med*. (2021) 218:e20201839. doi: 10.1084/jem.20201839
33. Stuart T, Butler A, Hoffman P, Hafemeister C, Papalexi E, Mauck WM, et al. Comprehensive integration of single-vcell data. *Cell*. (2019) 177:1888–902.e21. doi: 10.1016/j.cell.2019.05.031
34. Becht E, McInnes L, Healy J, Dutertre C-A, Kwok IWH, Ng LG, et al. Dimensionality reduction for visualizing single-cell data using uMAP. *Nat* Biotechnol. (2018) 37:38–44. doi: 10.1038/nbt.4314
35. Aran D, Looney AP, Liu L, Wu E, Fong V, Hsu A, et al. Reference-based analysis of lung single-cell sequencing reveals a transitional profibrotic macrophage. *Nat Immunol*. (2019) 20:163–72. doi: 10.1038/s41590-018-0276-y
36. Raffort J, Lareyre F, Clément M, Hassen-Khodja R, Chinetti G, Mallat Monocytes Z. Macrophages in abdominal aortic aneurysm. *Nat Rev Cardiol*.. (2017) 14:457–71. doi: 10.1038/nrcardio.2017.52
37. Ritchie ME, Phipson B, Wu D, Hu Y, Law CW, Shi W, et al. limma powers differential expression analyses for rNA-sequencing and microarray studies. *Nucleic Acids Res*. (2015) 43:e47. doi: 10.1093/nar/gkv007
38. Robinson MD, McCarthy DJ, Smyth GK. edgeR: a bioconductor package for differential expression analysis of digital gene expression data. *Bioinformatics*. (2010) 26:139–40. doi: 10.1093/bioinformatics/btp616

39. Huang M-L, Hung Y-H, Lee WM, Li RK, Jiang B-R. SVM-RFE based feature selection and taguchi parameters optimization for multiclass sVM classifier. *Sci World J*. (2014) 2014:795624. doi: 10.1155/2014/795624
40. Han H, Cho J-W, Lee S, Yun A, Kim H, Bae D, et al. TRRUST v2: an expanded reference database of human and mouse transcriptional regulatory interactions. *Nucleic Acids Re.s*. (2018) 46:D380–6. doi: 10.1093/nar/gkx1013
41. Yu G, Wang L-G, Han Y, He Q-Y. clusterProfiler: an r Package for comparing biological themes among gene clusters. *OMICS J Integr Biol*. (2012) 16:284–7. doi: 10.1089/omi.2011.0118
42. Lu L, Kang X, Yi B, Jiang C, Yan X, Chen B, et al. Exploring the mechanism of yiqi qingre ziyin method in regulating neuropeptide expression for the treatment of atrophic rhinitis. *Disease Mar*. (2022) 2022:1–12. doi: 10.1155/2022/4416637
43. Subramanian A, Tamayo P, Mootha VK, Mukherjee S, Ebert BL, Gillette MA, et al. Gene set enrichment analysis: a knowledge-based approach for interpreting genome-wide expression profiles. *PNAS*. (2005) 102:15545–50. doi: 10.1073/pnas.0506580102
44. Sun X, Zheng X, Zhang X, Zhang Y, Luo G. Exosomal microRNA-23b-3p from bone marrow mesenchymal stem cells maintains t helper/Treg balance by downregulating the pI3k/Akt/NF-κB signaling pathway in intracranial aneurysm. *Brain Research Bulletin*. (2020) 165:305–15. doi: 10.1016/j.brainresbull.2020.09.003
45. Aoki T, Fr?sen J, Fukuda M, Bando K, Shioi G, Tsuji K, et al. Prostaglandin e [[sb]]2[[/s]] –EP2–NF-κB signaling in macrophages as a potential therapeutic target for intracranial aneurysms. *Sci Signal*. (2017) 10:eaah6037. doi: 10.1126/scisignal.aah6037
46. Mao G, Songdej N, Voora D, Goldfinger LE, Del Carpio-Cano FE, Myers RA, et al. Transcription factor *rUNX*1 regulates platelet *pCTP*. (Phosphatidylcholine transfer protein) : implications for cardiovascular events: differential effects of *rUNX*1 variants. *Circulation*. (2017) 136:927–39. doi: 10.1161/CIRCULATIONAHA.116.023711
47. Chen MJ, Yokomizo T, Zeigler BM, Dzierzak E, Speck NA. *RUNX*1 is required for the endothelial to haematopoietic cell transition but not thereafter. *Nature*. (2009) 457:887–91. doi: 10.1038/nature07619
48. Jeong E-M, Pereira M, So E-Y, Wu KQ, Del Tatto M, Wen S, et al. Targeting *rUNX*1 as a novel treatment modality for pulmonary arterial hypertension. *Cardiovasc Res*. (2022) 00:1. doi: 10.1093/cvr/cvac001
49. Luo F, Wu Y, Ding Q, Yuan Y, Jia W. Rs884225 polymorphism is associated with primary hypertension by compromising interaction between epithelial growth factor receptor. (EGFR) and miR-214. *J Cell Mol Med*. (2021) 25:3714–23. doi: 10.1111/jcmm.15976
50. Kurokawa M. AML1/*RUNX*1 as a versatile regulator of hematopoiesis: regulation of its function and a role in adult hematopoiesis. *Int J Hematol*. (2006) 84:136–12. doi: 10.1532/IJH97.06070
51. Liu P, Shi Y, Fan Z, Zhou Y, Song Y, Liu Y, et al. Inflammatory smooth muscle cells induce endothelial cell alterations to influence cerebral aneurysm progression via regulation of integrin and vEGF expression. *Cell Transplant*. (2019) 28:713–22. doi: 10.1177/0963689718815824
52. Lilly AJ, Costa G, Largeot A, Fadlullah MZH, Lie-A-Ling M, Lacaud G, et al. Interplay between sOX7 and *rUNX*1 regulates hemogenic endothelial fate in the yolk sac. *Development*. (2016) 1:140970. doi: 10.1242/dev.140970
53. Bae S-C, Kolinjivadi AM, Ito Y. Functional relationship between p53 and rUNX proteins. *J Mol Cell Biol*. (2019) 11:224–30. doi: 10.1093/jmcb/mjy076
54. Douglas MR, Daniel M, Lagord C, Akinwunmi J, Jackowski A, Cooper C, et al. High cSF transforming growth factor levels after subarachnoid haemorrhage: association with chronic communicating hydrocephalus. *J Neurol Neurosurg Psychiatry*. (2009) 80:545–50. doi: 10.1136/jnnp.2008.155671
55. Park J-Y, Farrance IKG, Fenty NM, Hagberg JM, Roth SM, Mosser DM, et al. NFKB1 promoter variation implicates shear-induced nOS3 gene expression and endothelial function in prehypertensives and stage i hypertensives. *Am J Physiol Heart Circ Physiol*. (2007) 293:H2320–7. doi: 10.1152/ajpheart.00186.2007
56. Guo Y, Liu Z, Wang M. *NFKB*1-mediated downregulation of microRNA-106a promotes oxidative stress injury and insulin resistance in mice with gestational hypertension. *Cytotechnology*. (2021) 73:115–26. doi: 10.1007/s10616-020-00448-x
57. Baradaran A, Nasri H, Rafieian-Kopaei M. Oxidative stress and hypertension: possibility of hypertension therapy with antioxidants. *J Res Med Sci*. (2014) 19:358–67.
58. Gryszczyńska B, Budzyń M, Begier-Krasińska B, Osińska A, Boruczkowski M, Kaczmarek M, et al. Association between advanced glycation end products, soluble rAGE receptor, endothelium dysfunction. evaluated by circulating endothelial cells and endothelial progenitor cells in patients with mild and resistant hypertension. *IJMS*. (2019) 20:3942. doi: 10.3390/ijms20163942
59. Staarmann B, Smith M, Prestigiacomo CJ. Shear stress and aneurysms: a review. *Neurosurgical Focus*. (2019) 47:E2. doi: 10.3171/2019.4.FOCUS19225
60. Chalouhi N, Atallah E, Jabbour P, Patel PD, Starke RM, Hasan D. Aspirin for the prevention of intracranial aneurysm rupture. *Neurosurgery*. (2017) 64:114–8. doi: 10.1093/neuros/nyx299
61. Chu C, Xu G, Li X, Duan Z, Tao L, Cai H, et al. Sustained expression of mCP-1 induced low wall shear stress loading in conjunction with turbulent flow on endothelial cells of intracranial aneurysm. *J Cell Mol Med*. (2021) 25:110–9. doi: 10.1111/jcmm.15868
62. Yoshida K, Uwano I, Sasaki M, Takahashi O, Sakai N, Tsuruta W, et al. Small unruptured aneurysm verification-prevention effect against growth of cerebral aneurysm study using statin. *Neurol Med Chir*(*Tokyo*). (2021) 61:442–51. doi: 10.2176/nmc.oa.2021-0017
63. Fisher CL, Demel SL. Non-steroidal anti-Inflammatory drugs: a potential pharmacological treatment for intracranial aneurysm. *Cerebrovasc Dis Extra*. (2019) 9:31–45. doi: 10.1159/000499077

Conflict of Interest: The authors declare that the research was conducted in the absence of any commercial or financial relationships that could be construed as a potential conflict of interest.

Publisher's Note: All claims expressed in this article are solely those of the authors and do not necessarily represent those of their affiliated organizations, or those of the publisher, the editors and the reviewers. Any product that may be evaluated in this article, or claim that may be made by its manufacturer, is not guaranteed or endorsed by the publisher.

Copyright © 2022 Li, Zhang and Liu. This is an open-access article distributed under the terms of the Creative Commons Attribution License (CC BY). The use, distribution or reproduction in other forums is permitted, provided the original author(s) and the copyright owner(s) are credited and that the original publication in this journal is cited, in accordance with accepted academic practice. No use, distribution or reproduction is permitted which does not comply with these terms.

frontiers | Frontiers in Neurology

ORIGINAL RESEARCH
published: 24 May 2022
doi: 10.3389/fneur.2022.879444

Brain Activity in Different Brain Areas of Patients With Dry Eye During the Female Climacteric Period According to Voxel-Based Morphometry

Meng-Yan Hu†, Li-Juan Zhang†, Min Kang†, Yi-Cong Pan, Qian-min Ge, Qiu-yu Li, Lin Yang, Chong-Gang Pei and Yi Shao**

Department of Ophthalmology, The First Affiliated Hospital of Nanchang University, Jiangxi Province Ocular Disease Clinical Research Center, Nanchang, China

OPEN ACCESS

Edited by:
Yuzhen Xu,
Tongji University, China

Reviewed by:
Yingying Shi,
University of Miami Health System, United States
Wensi Tao,
University of Miami Health System, United States

***Correspondence:**
Chong-Gang Pei
peichonggang11@163.com
Yi Shao
freebee99@163.com

†*These authors share first authorship*

Specialty section:
This article was submitted to Neurological Biomarkers, a section of the journal Frontiers in Neurology

Received: *19 February 2022*
Accepted: *26 April 2022*
Published: *24 May 2022*

Citation:
Hu M-Y, Zhang L-J, Kang M, Pan Y-C, Ge Q-m, Li Q-y, Yang L, Pei C-G and Shao Y (2022) Brain Activity in Different Brain Areas of Patients With Dry Eye During the Female Climacteric Period According to Voxel-Based Morphometry. Front. Neurol. 13:879444. doi: 10.3389/fneur.2022.879444

We aim to investigate potential morphological alterations of the brain in female climacteric patients with dry eye (DE) and their relationship to behavioral performances. Twenty-five female patients with DE disease during the female climacteric period and 25 age and education-matched healthy controls (HCs) underwent magnetic resonance imaging. Imaging data were analyzed using voxel-based morphometry (VBM) to identify group differences in DE patients and HCs. Compared with HCs, patients with DE during the female climacteric period had significantly decreased VBM in the Putamen_L, Thalamus_R, Precuneus_L, Frontal_Sup_R, Cingulum_Mid_L, and Frontal_Mid_L. There was increased VBM in the Temporal_Pole_Sup_R, Precentral_R and Insula_L. Receiver operating characteristic curve analysis indicated that the VBM method has clear potential for diagnosis of DE patients during the climacteric period. Correlation analysis found a negative correlation between the VBM values of the Putamen_L and the anxiety score (AS) and depression score (DS), a positive correlation was found between VBM values of the Temporal_Pole_Sup_R and AS. Moreover, VBM values in the Cingulum_Mid_L were positively correlated with AS and DS. These results revealed abnormal spontaneous activity in the brain regions of patients with DE during the climacteric period, which may indicate underlying pathological mechanisms. These results may help to advance clinical treatments.

Keywords: voxel-based morphometry, magnetic resonance imaging, gray matter density, dry eye disease, climacteric period

INTRODUCTION

Dry eye (DE) is a term used for a variety of diseases with eye surface tissue damage caused by an abnormal quantity or quality of tears or tear film instability caused by dynamic abnormalities. Eye discomfort is the main complaint and, in some severe cases, visual impairment may occur. Generally, DE can be divided into two types: insufficient tear production and excessive tear evaporation. The former is caused by lacrimal gland dysfunction, which has been termed aqueous tear deficiency (ATD). The latter mainly refers to meibomian gland dysfunction (MGD). DE is more prevalent in women than men and the incidence increases with age (1, 2). According to an epidemiological study, 11.3% of people more than 50 years old were diagnosed with DE, and that

percentage increased to 22.8% in women more than 75 years old (1). Since DE not only causes visual impairment, which directly affects daily living, it also brings sociopsychological problems that reduce the quality of life. The increased need for therapy and reduced incomes due to decreasing productivity makes DE a cause of economic burdens (1–5).

The climacteric period, also known as menopause, refers to a period of time that correlates with the age-related decline in ovarian hormone production, usually starting at the ages of 49 to 52 years. Although statements about the climacteric period have been made in the medical literature for centuries, a scientific approach to understanding the climacteric years is a young branch of medicine (6). As mentioned above, DE is more prevalent in females, especially at the age of menopause. This is mainly because of hormonal disorders. Decreased hormonal levels may reduce production of tear film components (7). Several studies have suggested that hormone replacement therapy may have benefits in DE patients during the female climacteric period (8, 9). AlAwlaqi and Hammadeh showed an increased risk of DE symptoms in women taking hormone replacement therapy (10). Thus, the specific mechanism of hormonal disorders and DE remains unclear.

In recent years, research on the clinical diagnosis, treatment, and pathological development of ophthalmic diseases has increasingly proliferated with medical imaging technology. Voxel-based morphometry (VBM), as a new method of magnetic resonance imaging (MRI) analysis, can be used to quantitatively analyze alterations in the density and volume of white and gray matter using each individual voxel in magnetic resonance images, thus reflecting the anatomical structure differences in corresponding regions (11). This may provide an entirely new way to explore neuropathological changes with eye diseases. The VBM technique has already been used widely in many ophthalmic diseases, such as retinal detachment, monocular blindness, concomitant strabismus, optic neuritis, and acute eye pain, as well as other neurogenic diseases (**Table 1**). In our study, we aimed to determine whether structural changes exist in certain brain regions of female patients with DE during the climacteric period compared to healthy controls (HCs).

TABLE 1 | VBM method applied in ophthalmologic and neurogenic diseases.

	Author	Year	Disease
VBM method applied in ophthalmologic and neurogenic disease			
Ophthalmologic Disease	Li et al. (12)	2020	retinal detachment
	Shi et al. (13)	2019	monocular blindness
	Ouyang et al. (14)	2017	comitant strabismus
	Huang et al. (11)	2016	optic neuritis
	Lan et al. (15)	2019	acute eye pain
Neurogenic Disease	González-Ortiz et al. (16)	2021	epilepsy
	Ting et al. (17)	2015	Alzheimer disease
	Ågren et al. (18)	2021	essential tremor
	Xuan et al. (19)	2019	Parkinson disease

MATERIALS AND METHODS

Subjects

Twenty-five female patients with DE during the female climacteric period were recruited. Inclusive criteria were as follows: 1) primary DE diagnosed by an experienced ophthalmologist; 2) no menstruation for at least 12 months and met the criteria of climacteric period judged by the gynecologist; and 3) not treated with any drugs or had stopped treatment for at least 2 weeks before recruitment. Exclusive criteria were as follows: 1) conjunctival scarring, atresia, or complete atrophy of the lacrimal gland and accessory lacrimal glands; 2) other obvious abnormalities of the conjunctiva, cornea, or iris; 3) pregnant or nursing women; 4) history of mental health disorders, diabetes, cerebral infarction, or cardiovascular diseases; 5) history of addictions (alcohol and/or drugs); 6) abnormality of the brain parenchyma as shown by MRI; and 7) contraindication for MRI scanning.

Twenty-five female HCs were also enrolled. Their average age and educational level were similar to the participants in the DE group. All HCs met the following criteria: 1) best-corrected visual acuity >1.0; 2) no organic ocular diseases; 3) no menstruation for at least 12 months and met the criteria of climacteric period judged by the gynecologist; 4) no abnormalities of the brain parenchyma or visual pathway on head MRI scans; 5) no drug or alcohol addiction; 6) no mental illness or cerebral diseases, and 7) no contraindications for MRI.

The study was authorized by the Ethics Committee of the First Affiliated Hospital of Nanchang University. All participants were offered an explanation of the standard operation procedure (SOP) for MRI scans and signed the consent form. All the protocols in the study followed the Declaration of Helsinki and conformed to the principles of medical ethics.

Administration of the Hospital Anxiety and Depression Scale (HADS)

The HADS was used to quantitatively assess anxiety and depression (20). For participants who were illiterate or were unable to read due to visual impairment, an investigator read the questionnaire aloud. For all participants, an investigator verbally explained the purpose of the questionnaire and its confidential nature. We calculated the anxiety score (AS) and depression score (DS) separately.

Structural MRI Parameters

A 3T MR scanner (Siemens, Munich, Germany) with a 12-channel head coil was used to perform MRI scanning. We acquired high-resolution T1-weighted functional images using a magnetization-prepared rapid gradient echo (MP-RAGE) sequence covering the entire brain. The detailed parameters were as follows: 176 slices with section thickness of 1.0 mm; echo time = 2.26 ms; repetition time = 1,900 ms; and field of view = 215 × 230 mm. The scanning procedure was carried out for all participants by the same experienced radiologist and no participants were excluded.

Image Processing

For data acquisition and processing, MRIcron (http://www.nitrc.org/projects/mricron) was employed to classify functional data and eliminate incomplete data. The structural images were processed with a voxel-based morphometry toolbox (VBM8, dbm.neuro.uni-jena.de/vbm8) on a statistical parameter map (SPM8; http://www.fil.ion.ucl.ac.uk). All procedures were carried out using MATLAB7.9.0 software (The MathWorks, Natick, MA). Based on VBM8, individual brains were divided into gray matter (GM), white matter (WM), and cerebrospinal fluid (CSF). More details were presented in a previous study (13).

Processing of Data

Using the SPM8 toolkit, we applied general linear model analysis (GLM) to investigate the differences in GM and WM between DE patients and HCs after controlling for age. $P < 0.05$ was considered statistically significant, and Gaussian random field (GRF) theory correction was used for multiple comparisons (minimum z >2.3). To generate a colored map, significant voxels were superimposed on the normalization of three-dimensional magnetization, fast acquisition gradient echo sequences (3DT1WIs). Area analysis of gray matter changes was performed at the voxel threshold setting as 20 neighboring voxels.

Using REST1.8 software (www.resting-fmri.Sourceforge.net), distinct brain regions were defined as regions of interest (ROIs). We then used receiver operating characteristic (ROC) curves for each ROI to explore the relationship between mean outcomes and clinical features in different regions of the brain.

Statistical Analysis

We used two-sample *t*-tests to compare VBM values at the ROIs between the DE and HCs groups with age as covariates to control for these factors. ROC curves were also used to assess sensitivity of the discrimination between mean VBM values in the two groups. In addition, Pearson's correlation analysis was applied to VBM and HADS scores. SPSS version 19.0 statistical software for Windows (SPSS, IBM Corp, USA) was used to analyze the data, and GraphPad Prism 8.0 software (the GraphPad Software, Inc. La Jolla, CA) was applied for figure generation. * meant the *P*-value was <0.05 and was considered statistically significant in all cases.

RESULTS

Demographics and Visual Measurements

The best-corrected visual acuity was significantly decreased in both eyes of DE patients, compared with HCs ($p = 0.034$, right eyes; $p = 0.032$, left eyes.) No significant differences were found in weight ($p = 0.892$) or age ($p = 0.854$) between the DE patients and HCs (**Table 2**).

TABLE 2 | Clinical characteristics of patients in the DE and HC groups.

Characteristics	DE	HCs	*t*-value	*P* -values
Age(years)	56.76 ± 10.16	57.12 ± 11.68	−0.319	0.854
Weight(kg)	58.64 ± 7.91	59.12 ± 6.75	−0.462	0.892
Handedness(left/right)	0/25	0/25	NA	NA
Duration of DE (mons)	34.32 ± 13.11	NA	NA	NA
Best-corrected VA, right	0.75 ± 0.33*	1.17 ± 0.69	−3.142	0.034
Best-corrected VA, left	0.67 ± 0.24*	1.21 ± 0.46	−2.169	0.032

*Independent t-tests comparing the two groups (*P < 0.05) showed statistically significant differences.*

DE, dry eye; HCs, healthy controls; NA, not applicable; VA, visual acuity.

VBM Values and Brain Regions

Compared to HCs, DE patients had significantly increased VBM in the Temporal_Pole_Sup_R ($t = -4.1164$), Precentral_R ($t = -27.6921$) and Insula_L ($t = -4.6003$), decreased VBM values in the Putamen_L ($t = 7.5285$), Thalamus_R ($t = 5.4554$), Precuneus_L ($t = 6.5564$), Frontal_Sup_R ($t = 9.7716$), Cingulum_Mid_L ($t = 12.6833$) and Frontal_Mid_L (t = 7.7449; **Figures 1**, **2**, **Table 3**).

3.3. ROC Curve Analysis

The area under the ROC curves were 0.548 for the Precuneus_L ($p = 0.562$; 95% CI: 0.385–0.711); 0.415 for the Putamen_L ($p = 0.308$; 95% CI: 0.253–0.577); 0.525 for the Frontal_Sup_R ($p = 0.764$; 95% CI: 0.360–0.690); 0.518 for the Frontal_Mid_L ($p = 0.826$; 95% CI: 0.353–0.683); 0.545 for the Thalamus_R ($p = 0.589$; 95% CI: 0.381–0.709); and 0.590 for the Cingulum_Mid_L ($p = 0.280$; 95% CI: 0.428–0.752; **Figure 3A**). The area under the ROC curves were 0.532 for the Insula_L ($p = 0.704$; 95% CI: 0.367–0.696); 0.585 for the Precentral_R ($p = 0.308$; 95% CI: 0.423–0.747); and 0.517 for the Temporal_Pole_Sup_R ($p = 0.841$; 95% CI: 0.351–0.682; **Figure 3B**).

Correlation Analysis of the VBM Values and Clinical Measurements in DE Patients

Mean VBM values in the Cingulum_Mid_L of DE patients were positively correlated with the AS (r = 0.2371, $p = 0.0136$) and DS (r = 0.2135, $p = 0.0200$). The mean VBM values in the Putamen_L of DE patients were negatively correlated with the AS (r = 0.3956, $p = 0.0008$) and DS (r = 0.3770, $p = 0.0011$). The mean VBM values in the Temporal_Pole_Sup_R of DE patients were positively correlated with the AS (r = 0.2190, $p = 0.0183$; **Figure 4**). No correlation was found between the duration of the disease and VBM values in any of the brain regions.

DISCUSSION

This is the first study that investigated changes in brain regions in DE patients during the female climacteric period using a VBM approach. In our study, compared to HCs, significantly decreased VBM values was found in the left putamen, right thalamus, left precuneus, right superior frontal lobe, left middle cingulum, and left middle frontal lobe. Meanwhile, increased VBM values were found in the right superior temporal pole, and right precentral and left insula (**Figure 5**). ROC curve analysis indicated the potential role of the VBM method for diagnosing DE patients during the climacteric period. Correlation analysis suggested a correlation between the VBM values of certain brain regions in DE patients and their HADS score, but no correlation was found

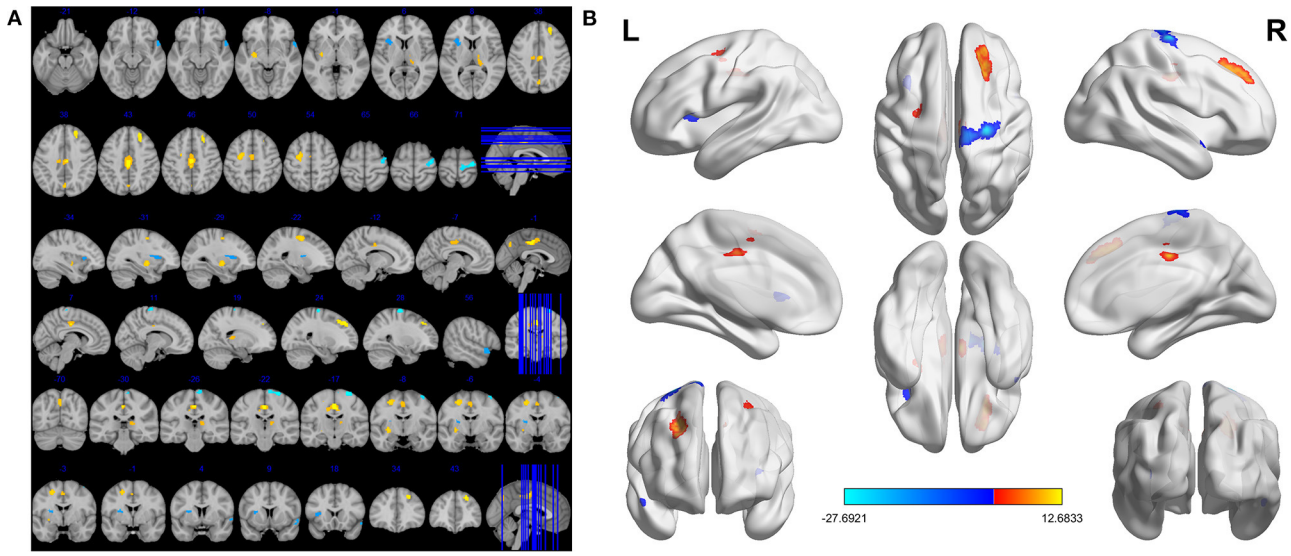

FIGURE 1 | Significant differences in VBM values between DE patients and HCs. The brain regions with different VBM values were the Precuneus_L, Putamen_L, Frontal_Sup_R, Frontal_Mid_L, Thalamus_R, Cingulum_Mid_L, Insula_L, Precentral_R, Temporal_Pole_Sup_R **(A)**. The read areas denote higher fALFF brain regions and blue areas denote lower fALFF brain regions **(B)**.

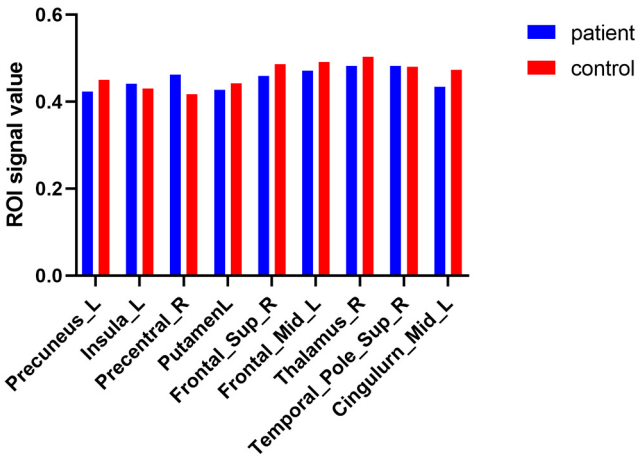

FIGURE 2 | The average VBM values of DE patients and HCs. Compared with HCs, DE patients had significantly decreased VBM values in the left putamen, right thalamus, left precuneus, right superior frontal lobe, left middle cingulum and left middle frontal lobe; increased VBM in the right superior temporal_pole, right precentral area, and left insula lobe.

TABLE 3 | Brain areas with significantly different VBM values between the groups.

Brain areas (DE vs HCs)	BA	MNI coordinates			Voxels number	T-value
		X	Y	Z		
Temporal_Pole_Sup_R	38	54	16	−12	98	−4.1164
Putamen_L	/	−30	−10	−4	130	7.5285
Insula_L	13	−26	−2	16	83	−4.6003
Thalamus_R	/	16	−22	8	122	5.4554
Precuneus_L	7	0	−70	38	108	6.5564
Frontal_Sup_R	8	24	40	42	194	9.7716
Cingulum_Mid_L	24	0	−18	46	513	12.6833
Frontal_Mid_L	6	−26	−8	52	209	7.7449
Precentral_R	6	26	−20	70	265	−27.6921

The statistical threshold was set at voxels with $p < 0.01$ for multiple comparisons using Gaussian random field corrections.
MNI, Montreal Neurological Institute; BA, Brodmann's area.

between the duration of the disease and VBM values. Namely, the VBM values of the Putamen_L were negatively correlated with the AS and DS, while a positive correlation was found between VBM values in the Temporal_Pole_Sup_R and the AS. Moreover, VBM values in the Cingulum_Mid_L of DE patients were positively correlated with the AS and DS.

The precuneus is the posterior part of the medial parietal cortex (21). Recent functional imaging findings suggested that the precuneus may participate in visuo-spatial imagery and other highly integrated works (22). The precuneus may also be responsible for self-consciousness (23). In our study, lower VBM values of the Precuneus_L were found in DE patients compared to HCs, suggesting that visual impairment secondary to DE may be correlated with changes in the precuneus lobe.

The thalamus is located in the diencephalon and is comprised of four parts (24). It is a vital relay center for both sensory and motor mechanisms and has several important functions, including sensory and motor functions, sleeping, and emotions (22). Basilious summarized 32 studies and concluded that the prevalence of depression and anxiety are much higher in DE patients (25). In another study, DE patients showed sleep quality reduction (26). In addition, menopausal women with sexual

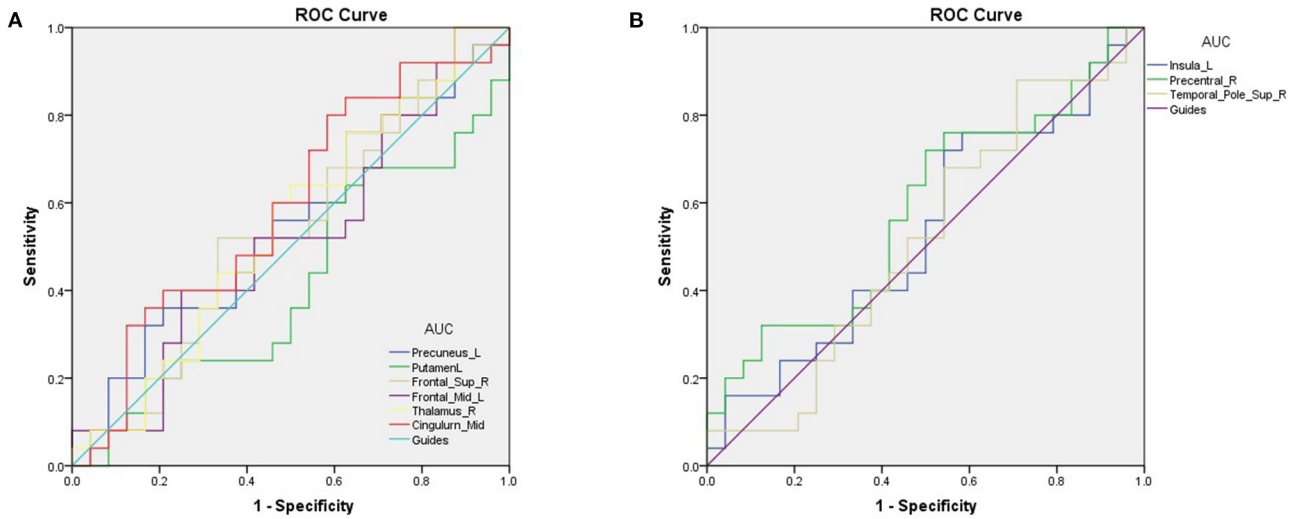

FIGURE 3 | ROC curve analysis of the mean VBM values for altered brain regions. **(A)** The areas under the ROC curve were 0.548 for Precuneus_L ($p = 0.562$; 95% CI: 0.385–0.711); Putamen_L 0.415, ($p = 0.308$; 95% CI: 0.253–0.577); Frontal_Sup_R 0.525, ($p = 0.764$; 95% CI: 0.360–0.690); Frontal_Mid_L 0.518, ($p = 0.826$; 95% CI: 0.353–0.683); Thalamus_R 0.545, ($p = 0.589$; 95% CI: 0.381–0.709); Cingulum_Mid_L 0.590, ($p = 0.280$; 95% CI: 0.428–0.752). **(B)** The areas under the ROC curve were 0.532 for the Insula_L ($p = 0.704$; 95% CI: 0.367–0.696); 0.585 for the Precentral_R ($p = 0.308$; 95% CI: 0.423–0.747) and 0.517 for the Temporal_Pole_Sup_R ($p = 0.841$; 95% CI: 0.351–0.682). AUC, area under the curve; ROC, receiver operating characteristic.

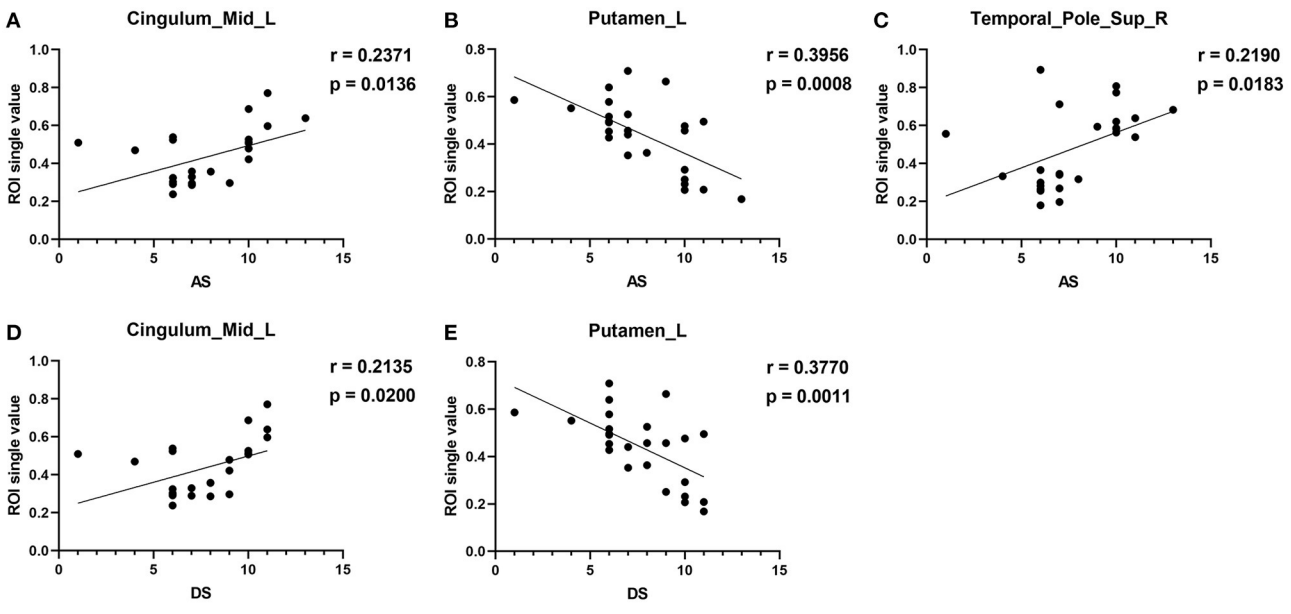

FIGURE 4 | Correlation between the VBM values of the brain regions and HADS. In the DE group, the VBM values of the Cingulum_Mid_L showed a positive correlation with the AS [$r = -0.2371$, $p = 0.0136$, **(A)**] and DS [$r = 0.2135$, $p = 0.0200$, **(D)**]. Mean VBM values in the Putamen_L of DE patients were negatively correlated with the AS [$r = 0.3956$, $p = 0.0008$, **(B)**] and DS [$r = 0.3770$, $p = 0.0011$, **(E)**]. Mean VBM values in the Temporal_Pole_Sup_R of DE patients were positively correlated with AS **(C)** [$r = 0.2190$, $p = 0.0183$].

dysfunction also reported a higher prevalence of depression and anxiety (27), as well as sleeping disorders (28). In the present study, the VBM values of Thalamus_R were obviously decreased in DE patients compared to HCs, which corresponded with emotional changes (depression and anxiety) and sleep disorders in DE patients during menopause.

The putamen is part of the lentiform nucleus, which constitutes part of the basal ganglia with other nuclei (29). The putamen is mainly responsible for learning and motor control, as well as cognitive function (30, 31). Kuru found putamen abnormalities in patients with various motor and cognitive dysfunctions (32). In our study, the VBM values of

Putamen_L in DE patients were lower and negatively correlated with HADS scores, indicating that these patients may have cognitive disfunction or movement disorders.

The frontal lobe is located anteriorly to the central sulcus and superiorly to the lateral sulcus. The external part of the frontal lobe is divided into three large surfaces (33). In recent years, the middle frontal gyrus (MFG) has been suggested to be part of the language network (34). In addition, Carter's research indicated the role of MFG in stress and cognitive functions (35). The superior frontal gyrus (SFG) has been linked to depression, cognition, and attention (36). Chang and his colleagues found SFG abnormalities in patients with depression (37). Thus, dysfunction of the frontal lobe may result in emotional and cognitive problems. In fact, we found VBM values declined in the frontal lobe, which was in accordance with our previous study (38).

The temporal lobe is a complex region. It has diverse cortical functions. Abnormal activation of these brain regions may cause epilepsy, schizophrenia, and amnesia (39). The insular cortex is buried inside the lateral sulcus of the brain (40). It can be divided into four functional parts with motor, olfactogustatory, socioemotional, and cognitive functions (41). The precentral gyrus is located on the lateral surface of the frontal lobe. It is involved in controlling voluntary motor movement (42). Another study found a correlation between decreased FA values in the precentral gyrus and age processing (43). Brain region alternation and its potential impact was summarized in **Table 4**. In this study, we demonstrated increased VBM values in the above brain regions in DE patients during menopause. Abnormal activity in these brain regions may be correlated with some excessive symptoms of DE patients, such as anxiety. Given that other functionally-similar brain regions showed contradictory low VBM values, compensation mechanisms may also exist in these brain regions.

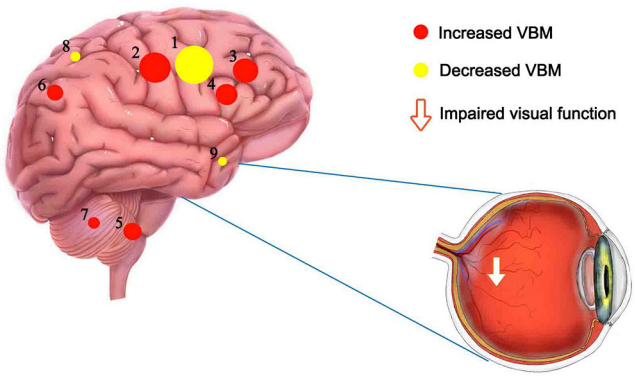

FIGURE 5 | Mean VBM values of altered brain regions. Compared to HC subjects, the VBM values of the following regions were decreased to various extents: 6- Precuneus_L (t = 6.5564), 5- Putamen_L (t = 7.5285), 3- Frontal_Sup_R (t = 9.7716), 4- Frontal_Mid_L (t = 7.7449), 7-Thalamus_R (t = 5.4554), 2- Cingulum_Mid_L (t = 12.6833). Compared with the HCs, the VBM values of the following regions were increased to various extents: 8-Insula_L (t = −4.6003), 1- Precentral_R (t = −27.6921), 9- Temporal_Pole_Sup_R (t = −4.1164). HCs, healthy controls; BA, Brodmann's area.

A variety of systemic comorbidities has been reported in patients with DE and other ocular diseases, such as problems with memory, depression, cognition, and sleep (44). More severe organic symptoms, sensory and sensorimotor neuropathies, and movement disorders have also been reported (45). We believe that these symptoms may be related to changes in the VBM values of the brain regions mentioned above. Our research demonstrated that the clinical symptoms of DE patients were indeed associated with brain dysfunctions. Thus, we offer two assumptions: 1) DE causes emotional instability, which aggravates endocrine disorders and makes menopausal symptoms more obvious; and 2) abnormal endocrine function in menopause leads to poor lacrimal gland function, meibomian gland dysfunction, and then finally develops to DE.

There are some limitations in our study. First, DE can be divided into many different types, and our sample size was not large enough to subdivide patients into subgroups. Larger sample MRI studies may help increase understanding of the explicit changes in brain activity and DE at different ages or in different categories. Second, both DE and the climacteric period may cause psychological problems, thus impacting brain activity. Whether brain activity changes are secondary to DE, further aggravate symptoms of the climacteric period, or that the climacteric period caused brain activity changes and then contributes to DE remains unknown. In the future, larger more in-depth studies may help to address this question.

TABLE 4 | Brain region alternations and their potential impact.

Brain regions	Experimental result	Brain function	Anticipated results
Temporal_Pole_Sup_R	DE > HC	electro physiologic networks, language	Schizophrenia, epilepsy, anterograde amnesia
Putamen_L	DE < HC	learning and motor control	Eye movements, learning problems
Insula_L	DE > HC	socioemotional, sensorimotor, processing, cognitive functions	Depression, cognitive activity disorder
Thalamus_R	DE < HC	sensory and motor function, attention, memory, speech, and emotion	Tremor, sleep disorder, depression, etc.
Precuneus_L	DE < HC	visuo-spatial imagery, episodic memory retrieval, self-consciousness	Visual impairment, amnesia
Frontal_Sup_R	DE < HC	Cognitive, emotional, pain, and behavioral management	Irritability, mood swings, depression, etc.
Cingulum_Mid_L	DE < HC	Executive functions, attention and memory	depression, pain, and anxiety
Frontal_Mid_L	DE < HC	Key parts of word processin	Cognitive activity disorder
Precentral_R	DE > HC	voluntary motor movement, aging process	Eye movements, climacteric period

CONCLUSIONS

In conclusion, our study found significant abnormalities in certain brain regions in patients with DE during the climacteric period. ROC analyses indicated high accuracy of the VBM method for diagnosing DE patients. In the future, further investigations are needed to form a comprehensive understanding of the neuropathological mechanisms of DE.

DATA AVAILABILITY STATEMENT

The raw data supporting the conclusions of this article will be made available by the authors, without undue reservation.

ETHICS STATEMENT

The studies involving human participants were reviewed and approved by the committee for medical ethics of the First Affiliated Hospital of Nanchang University. The patients/participants provided their written informed consent to participate in this study.

AUTHOR CONTRIBUTIONS

M-YH, YS, and C-GP designed the current study. MK, M-YH, and L-JZ recruited healthy controls. MK, Y-CP, and L-JZ performed MRI scanning. LY, Q-mG, and Q-yL collected and analyzed the data. M-YH wrote the manuscript. All the authors read and approved the final manuscript.

FUNDING

This research was supported by Key Research Foundation of Jiangxi Province (Nos. 20203BBG73059 and 20181BBG70004), Excellent Talents Development Project of Jiangxi Province (20192BCBL23020), Health Development Planning Commission Science Foundation of Jiangxi Province (20175115), and Education Department Youth Scientific Research Foundation (GJJ160122).

REFERENCES

1. Farrand KF, Fridman M, Stillman IO, Schaumberg DA. Prevalence of diagnosed dry eye disease in the united states among adults aged 18 years and older. *Am J Ophthalmol.* (2017) 182:90–8. doi: 10.1016/j.ajo.2017.06.033
2. Pflugfelder SC. Prevalence, burden, and pharmacoeconomics of dry eye disease. *Am J Manag Care.* (2008) 14:S102–106.
3. Dalzell MD. Dry eye: prevalence, utilization, economic implications. *Manag Care.* (2003) 12:9–13.
4. O'Neil EC, Henderson M, Massaro-Giordano M, Bunya VY. Advances in dry eye disease treatment. *Curr Opin Ophthalmol.* (2019) 30:166–78. doi: 10.1097/ICU.0000000000000569
5. Patel VD, Watanabe JH, Strauss JA, Dubey AT. Work productivity loss in patients with dry eye disease: an online survey. *Curr Med Res Opin.* (2011) 27:1041–8. doi: 10.1185/03007995.2011.566264
6. Takahashi TA, Johnson KM. Menopause. *Med Clin North Am.* (2015) 99:521–34. doi: 10.1016/j.mcna.2015.01.006
7. Peck T, Olsakovsky L, Aggarwal S. Dry eye syndrome in menopause and perimenopausal age group. *J Midlife Health.* (2017) 8:51–4. doi: 10.4103/jmh.JMH_41_17
8. Jensen AA, Higginbotham EJ, Guzinski GM, Davis IL, Ellish NJ, A. survey of ocular complaints in postmenopausal women. *J Assoc Acad Minor Phys.* (2000) 11:44–9.
9. Metka M, Enzelsberger H, Knogler W, Schurz B, Aichmair H. Eye manifestations as climacteric symptom. *Geburtshilfe Frauenheilkd.* (1991) 51:143–5. doi: 10.1055/s-2007-1023691
10. AlAwlaqi A, Hammadeh M. Examining the relationship between hormone therapy and dry-eye syndrome in postmenopausal women: a cross-sectional comparison study. *Menopause.* (2016);23:550–5. doi: 10.1097/GME.0000000000000570
11. Huang X, Zhang Q, Hu PH, Zhong YL, Zhang Y, Wei R, et al. White and gray matter volume changes and correlation with visual evoked potential in patients with optic neuritis: a Voxel-Based morphometry study. *Med Sci Monit.* (2016) 22:1115–23. doi: 10.12659/MSM.897837
12. Li B, Liu YX Li HJ, Yuan Q, Zhu PW, Ye L, et al. Reduced gray matter volume in patients with retinal detachment: evidence from a voxel-based morphometry study. *Acta Radiol.* (2020) 61:395–403. doi: 10.1177/0284185119861898
13. Shi WQ, He Y, Li QH, Tang LY Li B, Lin Q, et al. Central network changes in patients with advanced monocular blindness: a voxel-based morphometric study. *Brain Behav.* (2019) 9:e01421. doi: 10.1002/brb3.1421
14. Ouyang J, Yang L, Huang X, Zhong YL, Hu PH, Zhang Y, et al. The atrophy of white and gray matter volume in patients with comitant strabismus: evidence from a voxel-based morphometry study. *Mol Med Rep.* (2017) 16:3276–82. doi: 10.3892/mmr.2017.7006
15. Lan DY, Zhu PW, He Y, Xu QH, Su T, Li B, et al. Gray matter volume changes in patients with acute eye pain: a Voxel-Based morphometry study. *Transl Vis Sci Technol.* (2019) 8:1. doi: 10.1167/tvst.8.1.1
16. Gonzalez-Ortiz S, Medrano S, Capellades J, Vilas M, Mestre A, Serrano L, et al. Voxel-based morphometry for the evaluation of patients with pharmacoresistant epilepsy with apparently normal mRI. *J Neuroimaging.* (2021) 31:560–8. doi: 10.1111/jon.12849
17. Ting WK, Fischer CE, Millikin CP, Ismail Z, Chow TW, Schweizer TA. Grey matter atrophy in mild cognitive impairment / early alzheimer disease associated with delusions: a voxel-based morphometry study. *Curr Alzheimer Res.* (2015) 12:165–72. doi: 10.2174/1567205012666150204130456
18. Agren R, Awad A, Blomstedt P, Fytagoridis A. Voxel-Based morphometry of cerebellar lobules in essential tremor. *Front Aging Neurosci.* (2021) 13:667854. doi: 10.3389/fnagi.2021.667854
19. Xuan M, Guan X, Huang P, Shen Z, Gu Q, Yu X, et al. Different patterns of gray matter density in early- and middle-late-onset parkinson's disease: a voxel-based morphometry study. *Brain Imaging Behav.* (2019) 13:172–9. doi: 10.1007/s11682-017-9745-4
20. Snaith RP. The hospital anxiety and depression scale. *Health Qual Life Outcomes.* (2003) 1:29. doi: 10.1186/1477-7525-1-29
21. Cavanna AE, Trimble MR. The precuneus: a review of its functional anatomy and behavioural correlates. *Brain.* (2006) 129:564–83. doi: 10.1093/brain/awl004
22. Cunningham SI, Tomasi D, Volkow NStructural D. and functional connectivity of the precuneus and thalamus to the default mode network. *Hum Brain Mapp.* (2017) 38:938–56. doi: 10.1002/hbm.23429
23. Cavanna AE. The precuneus and consciousness. *CNS Spectr.* (2007) 12:545–52. doi: 10.1017/S1092852900021295
24. Herrero MT, Barcia C, Navarro JM. Functional anatomy of thalamus and basal ganglia. *Childs Nerv Syst.* (2002) 18:386–404. doi: 10.1007/s00381-002-0604-1
25. Han SB, Yang HK, Hyon JY, Wee WR. Association of dry eye disease with psychiatric or neurological disorders in elderly patients. *Clin Interv Aging.* (2017) 12:785–92. doi: 10.2147/CIA.S137580

26. Magno MS, Utheim TP, Snieder H, Hammond CJ, Vehof J. The relationship between dry eye and sleep quality. *Ocul Surf.* (2021) 20:13–9. doi: 10.1016/j.jtos.2020.12.009
27. Tavoli A, Tavoli Z, Effatpanah M, Montazeri prevalence and associated risk factors for sexual dysfunction among postmenopausal women: a study from Iran. *Womens Midlife Health*. (2021) 7:10. doi: 10.1186/s40695-021-00069-0
28. Abdelaziz EM, Elsharkawy NB, Mohamed SM. Efficacy of internet-based cognitive behavioral therapy on sleeping difficulties in menopausal women: a randomized controlled trial. *Perspect Psychiatr Care.* (2021). doi: 10.1111/ppc.13005
29. Ghandili M, Putamen S. *Munakomi Neuroanatomy*. Treasure Island, FL: StatPearls (2021).
30. Hamada I. Role of the putamen in voluntary movement. *No To Shinkei.* (1994) 46:723–30.
31. Vinas-Guasch N, Wu YJ. The role of the putamen in language: a meta-analytic connectivity modeling study. *Brain Struct Funct.* (2017) 222:3991–4004. doi: 10.1007/s00429-017-1450-y
32. Kuru S, Kato T, Sakai M, Konagaya M, Sobue G, Matsuoka Y. Familial parkinsonism with the abnormalities in putamen on MRI. *Rinsho Shinkeigaku.* (2000) 40:741–5.
33. Catani M. The anatomy of the human frontal lobe. *Handb Clin Neurol.* (2019) 163:95–122. doi: 10.1016/B978-0-12-804281-6.00006-9
34. Hazem SR, Awan M, Lavrador JP, Patel S, Wren HM, Lucena O, et al. Middle frontal gyrus and area 55b: perioperative mapping and language outcomes. *Front Neurol.* (2021) 12:646075. doi: 10.3389/fneur.2021.646075
35. Carter RM, O'Doherty JP, Seymour B, Koch C, Dolan RJ. Contingency awareness in human aversive conditioning involves the middle frontal gyrus. *Neuroimage.* (2006) 29:1007–12. doi: 10.1016/j.neuroimage.2005.09.011
36. Tops M, Boksem MA, A. potential role of the inferior frontal gyrus and anterior insula in cognitive control, brain rhythms, event-related potentials. *Front Psychol.* (2011) 2:330. doi: 10.3389/fpsyg.2011.00330
37. Chang CC Yu SC, McQuoid DR, Messer DF, Taylor WD, Singh K, et al. Reduction of dorsolateral prefrontal cortex gray matter in late-life depression. *Psychiatry Res.* (2011) 193:1–6. doi: 10.1016/j.pscychresns.2011.01.003
38. Yu K, Guo Y, Ge QM, Su T, Shi WQ, Zhang LJ, et al. Altered spontaneous activity in the frontal gyrus in dry eye: a resting-state functional mRI study. *Sci Rep.* (2021) 11:12943. doi: 10.1038/s41598-021-97182-x
39. Lehman VT, Black DF, Bernstein MA, Welker KM. Temporal lobe anatomy: eight imaging signs to facilitate interpretation of mRI. *Surg Radiol Anat.* (2016) 38:433–43. doi: 10.1007/s00276-015-1582-9
40. Uddin LQ, Nomi JS, Hebert-Seropian B, Ghaziri J, Boucher structure and function of the human insula. *J Clin Neurophysiol.* (2017) 34:300–6. doi: 10.1097/WNP.0000000000000377
41. Kurth F, Zilles K, Fox PT, Laird AR, Eickhoff SB, A. link between the systems: functional differentiation and integration within the human insula revealed by meta-analysis. *Brain Struct Funct.* (2010) 214:519–34. doi: 10.1007/s00429-010-0255-z
42. Sharan AD, Rosenow JM, Turbay M, Testerman R, Rezai AR. Precentral stimulation for chronic pain. *Neurosurg Clin N Am.* (2003) 14:437–44. doi: 10.1016/S1042-3680(03)00014-7
43. Zhou L, Tian N, Geng ZJ, Wu BK, Dong LY, Wang MR. Diffusion tensor imaging study of brain precentral gyrus and postcentral gyrus during normal brain aging process. *Brain Behav.* (2020) 10:e01758. doi: 10.1002/brb3.1758
44. Delalande S, de Seze J, Fauchais AL, Hachulla E, Stojkovic T, Ferriby D, et al. Neurologic manifestations in primary sjogren syndrome: a study of 82 patients. *Medicine (Baltimore).* (2004) 83:280–91. doi: 10.1097/01.md.0000141099.53742.16
45. Margaretten M. Neurologic manifestations of primary sjogren syndrome. *Rheum Dis Clin North Am.* (2017) 43:519–29. doi: 10.1016/j.rdc.2017.06.002

Conflict of Interest: The authors declare that the research was conducted in the absence of any commercial or financial relationships that could be construed as a potential conflict of interest.

Publisher's Note: All claims expressed in this article are solely those of the authors and do not necessarily represent those of their affiliated organizations, or those of the publisher, the editors and the reviewers. Any product that may be evaluated in this article, or claim that may be made by its manufacturer, is not guaranteed or endorsed by the publisher.

Copyright © 2022 Hu, Zhang, Kang, Pan, Ge, Li, Yang, Pei and Shao. This is an open-access article distributed under the terms of the Creative Commons Attribution License (CC BY). The use, distribution or reproduction in other forums is permitted, provided the original author(s) and the copyright owner(s) are credited and that the original publication in this journal is cited, in accordance with accepted academic practice. No use, distribution or reproduction is permitted which does not comply with these terms.

frontiers | Frontiers in Neurology

ORIGINAL RESEARCH
published: 25 May 2022
doi: 10.3389/fneur.2022.878947

miR-17-5p/*HOXA7* Is a Potential Driver for Brain Metastasis of Lung Adenocarcinoma Related to Ferroptosis Revealed by Bioinformatic Analysis

*Quanfang Chen, Qingyun Pan, Han Gao, Yingju Wang and Xiaoning Zhong**

Department of Respiratory Medicine, First Affiliated Hospital of Guangxi Medical University, Nanning, China

Objectives: Present study aims to identify the essential mRNAs responsible for the development of brain neurovascular-related metastases (BNM) among lung adenocarcinoma (LUAD) patients. Further, we attempted to predict brain metastases more accurately and prevent their development in LUAD patients.

Methods: Transcriptome data analysis was used to identify differentially expressed mRNAs (DEMs) associated with brain metastasis, and thereby the ferroptosis index (FPI) is calculated using a computational model. Meanwhile, the DEmRNAs linked with FPI, and brain metastasis were derived by the intersection of these two groups of DEMs. We also constructed a ceRNA network containing these DEmRNAs, identifying the *HCP5* /hsa-miR-17-5p/*HOXA7* axis for analysis. Further, a clinical cohort was employed to validate the regulatory roles of molecules involved in the ceRNA regulatory axis.

Results: Here we report the development of a ceRNA network based on BNM-associated DEMs and FPI-associated DEmRNAs which includes three core miRNAs (hsa-miR-338-3p, hsa-miR-429, and hsa-miR-17-5p), three mRNAs (*HOXA7*, *TBX5*, and *TCF21*), and five lncRNAs (*HCP5, LINC00460*, *TP53TG1*). Using gene set enrichment analysis (GSEA) and survival analysis, the potential axis of *HCP5* /hsa-miR-17-5p/*HOXA7* was further investigated. It is found that *HOXA7* and ferroptosis index are positively correlated while inhibiting tumor brain metastasis. It may be that *HCP5* binds competitively with miR-17-5p and upregulates *HOXA7* to increase iron death limiting brain cancer metastases

Conclusions: The expression of both *HOXA7* and *HCP5* is positively correlated with FPI, indicating a possible link between ferroptosis and BNM. According to the results of our study, the ferroptosis-related ceRNA *HCP5* /hsa-miR-17-5p/*HOXA7* axis may contribute to the development of BNM in LUAD patients.

Keywords: *HCP5*, hsa-miR-17-5p, *HOXA7*, lung adenocarcinoma, ferroptosis, neurovascular, brain metastasis, biomarker

OPEN ACCESS

Edited by:
Yuzhen Xu,
Tongji University, China

Reviewed by:
Peng-fei Liu,
First Affiliated Hospital of Harbin Medical University, China
Tingyuan Lang,
Chongqing University, China

****Correspondence:***
Xiaoning Zhong
uhk3807@163.com

Specialty section:
This article was submitted to Neurological Biomarkers, a section of the journal Frontiers in Neurology

Received: *18 February 2022*
Accepted: *03 May 2022*
Published: *25 May 2022*

Citation:
Chen Q, Pan Q, Gao H, Wang Y and Zhong X (2022) miR-17-5p/HOXA7 Is a Potential Driver for Brain Metastasis of Lung Adenocarcinoma Related to Ferroptosis Revealed by Bioinformatic Analysis. Front. Neurol. 13:878947. doi: 10.3389/fneur.2022.878947

INTRODUCTION

Lung adenocarcinoma (LUAD) is the most common histological subtype of non-small cell lung cancer (NSCLC) which frequently occurs in peripheral lung tissue while accounting for approximately 70% of NSCLC and 40% of lung tumors (1–4). There has been an increase in LUAD morbidity and mortality rates worldwide in recent years (5–7). LUAD patients have an extremely low average survival rate (8, 9). In some studies, it has been estimated that there are 90,000 LAUD cases and around 8,00,000 LUAD deaths worldwide each year (10, 11). The 5-year survival rate for LUAD is <20% even though treatment options have evolved in recent times (12, 13). Such a low survival rate for LUAD patients may be attributed to its high infiltration and metastasis rates (14). Metastasis of LUAD often occurs in the brain, where the incidence and prognosis are poor, which poses a significant risk to the patients' health (15, 16). This suggests that brain metastases are a significant cause of treatment failure and death in patients with LUAD. Hence, to improve LUAD patients' prognosis, it is critical to identify biomarkers associated with brain metastases (17).

It has been demonstrated that ferroptosis plays a significant regulatory role in the treatment of many diseases, including cardiovascular, kidney, and oncological disorders (18–21). A ferroptosis process has been observed to influence tumor growth in oncological diseases and its role is expected to be exploited as an anti-cancer therapy target (22, 23). Ferroptosis is associated with the development of NSCLC and inducing ferroptosis may improve the therapeutic potential of NSCLC (24, 25). Some studies suggest that ferroptosis in lung cancer is regulated by USP35, which is thought to affect the growth and progression of the disease and may represent a new therapeutic target (22). Furthermore, ferroptosis appears to enhance the antitumor effects of conventional chemotherapy and radiotherapy (26–28). However, an exact mechanism of action for ferroptosis in LUAD brain metastases is still unknown.

Additionally, the ceRNA network is involved in regulating multiple tumor types (29–32). Several studies have shown that the ceRNA network has an association with lung cancer prognosis and NSCLC cell proliferation (33, 34). There was previously a finding that lincRNA00494 as ceRNA suppresses the proliferation of non-small cell lung cancer cells by regulating SRCIN1 expression (33). Studies have also shown that ceRNA regulatory networks can be used to construct models for assessing the prognosis of patients with malignancies (35). Thus, ferroptosis-related ceRNA may be a good candidate for the identification of new biomarkers in lung cancer diagnosis and prognosis (36).

The major focus of our study was to identify the major mRNAs involved in the development of BNM among LUAD patients and to explore the potential of the ceRNA regulation network for identifying new biomarkers. In addition, this research also intended to uncover any possible therapeutic target to monitor and improve the risk of BNM in LUAD patients with the possibility to extend their survival period.

Abbreviations: TCGA, the cancer genome atlas; GEO, gene expression omnibus (GEO); LUAD, lung adenocarcinoma; BM, brain metastasis; nM-LUAD, LUAD without metastasis; ceRNA, competing endogenous RNAs; DE-mRNAs, differentially expressed mRNAs; DE-miRNAs, differentially expressed microRNAs; DE-lncRNAs, differentially expressed lncRNAs; FPI, ferroptosis Potential Index; GO, gene ontology; GSEA, gene set enrichment analysis; KEGG, kyoto encyclopedia of genes and genomes; K-M, kruskal-wallis; OS, overall survival; qRT-PCR, quantitative reverse transcription PCR.

METHODS

Data Download

Due to the lack of BNM information in The Cancer Genome Atlas (TCGA, accessible at https://portal.gdc.cancer.gov/) project, we downloaded the transcriptome profile of LUAD brain neurovascular-related metastases (BNMs) from GSE141685 in the Gene Expression Omnibus (GEO) database (37). This BNM-LUAD dataset is containing bulky RNA sequencing (RNA-seq) data from surgically resected brain metastases of 6 LUAD patients. To investigate the potential molecules and pathways involved in LUAD brain metastasis, we have compared the BNM-LUAD bulk RNA-seq data with nM-LUAD (LUAD with no metastasis) bulk RNA-seq data of 384 patients from the TCGA database. From the TCGA database, we also downloaded miRNA sequences and clinical characterization data on nM-LUAD. In addition, the raw transcript RNA-seq data from the BNM-LUAD dataset were stored in Sequence Read Archive (SRA) file format and downloaded locally for subsequent RNA-seq analysis.

Data Preparation and Recruitment of Patients

The Kallisto software was used to quantify transcript abundance on bulk RNA-seq data (38). The transcripts per million (TPM) units of gene expression are included in the quantitative results of the transcriptome data and the log (TPM+1) for gene expression is calculated. In the next step, we applied the "ComBat" function from the limma package to remove the batch effect and pooling of data (39). To validate the findings of this study, an independent cohort of LUAD patients was also utilized. The Institutional Ethics Review Board of The First Affiliated Hospital of Guangxi Medical University has approved this study and informed written consent was also obtained from all the patients. We randomly collected and then examined 29 tumor tissue samples from the First Affiliated Hospital of Guangxi Medical University where this cohort was enrolled as a clinical cohort. A combination of diagnostic imaging and histology is used to better understand the clinical diagnosis. To obtain tumor tissue samples, surgical excision was used, and excess tumor tissues were collected only after a confirmed pathological diagnosis.

Identification of FPI-Related Genes

In the TCGA nM-LUAD dataset, we used the GSVA package to calculate the enrichment scores of ferroptosis-related gene sets (including *ACSL4, ALOX15, COQ10A, COQ10B, FDFT1, GPX4, HMGCR, SLC3A2, SLC7A11, NFE2L2, NOX1, NOX3, NOX4, and NOX5*). This followed the ferroptosis index (FPI) calculation by applying the standardized method as described previously (40, 41). These FPI scores are used to quantify the likelihood of ferroptosis of cells within a tumor or tissue and

based on median FPI scores, nM-LUAD patients are divided into high and low FPI groups. We next performed differential expression analyses for lncRNAs, miRNAs, and mRNAs between the low and high FPI groups with the limma package ($p < 0.05$). These differentially expressed mRNAs (DEMs) were defined as ferroptosis-related or FPI-related mRNAs (including FPI-related DEmRNAs, DEmiRNAs, and DElncRNAs). As described previously by utilizing the clusterProfiler R package the FPI-associated DEmRNAs are used for functional pathway analysis including the Kyoto Encyclopedia of Genes and Genomes (KEGG) and gene ontology (GO) (42–44).

Identification of Brian Metastasis-Related Genes

In this study, a significance level of $p < 0.05$ was set as the cut-off criterion. We have also performed a differential expression analysis between the BNM and no metastasis groups using the "limma" package. The calculated DEMs were named BNM-related mRNAs which are associated with the development of BNM in LUAD.

Identification of Genes Potentially Regulated by Identified FPI-Related miRNAs

We performed intersection analysis studies while including FPI-related DEmRNAs and BNM-related DEmRNAs that may play a crucial role in ferroptosis and brain metastases. Firstly, the miRcode database confirmed a relationship between delncRNAs and demiRNAs (45, 46). After that, we used miRWalk (http://mirwalk.umm.uni-heidelberg.de/) to identify shared DEmiRNAs and DEmRNAs between FPI and BNM (47). As a result, ceRNA networks were constructed based on DElncRNA-DEmiRNA interaction pairs and DEmiRNA-DEmiRNA interaction pairs.

Identification of Genes as the Target of FPI-Related miRNAs Associates to FPI, Brain Metastasis, and FPI-Related miRNAs

The correlation analysis was used to screen possible lncRNA-miRNA and miRNA-mRNA interaction pairs further. A Cox regression analysis was conducted on the molecules in these interaction pairs to predict the probability of survival of LUAD patients after 1, 3, and 6 years. To quantify and predict the survival rates of LUAD patients, the time-dependent receiver operating characteristic curve (ROC) and area under the curve (AUC) were used. We used the "survival" R package to analyze survival data and the "survminer" R package to visualize the data. A Pearson's method and linear regression analysis were then performed to determine the correlation between the variables. The "ggplot2" package was used to plot the heat map and scatter plots of the statistical tests.

Gene Set Enrichment Analysis

GSEA (Gene Set Enrichment Analysis) is a bioinformatics technique for exploring a specific set of functional genes (48, 49). Two groups are generated depending on the expression level of the target gene and critical pathway analysis was then conducted using GSEA. We used the reference dataset "c2.cp.v7.2.symbols.gmt [Curated]" for the enrichment analysis. All adjusted p-values <0.05 were considered significantly enriched.

Quantitative Reverse Transcription PCR (qRT-PCR)

To quantify the abundance of mRNAs and miRNAs in samples, the total RNA was extracted from cells using Trizol reagent (Invitrogen) and quantified using Nanodrop (Thermo Scientific, Waltham, USA). The expression of miRNAs was determined by stem-loop qPCR (Taq-Man) as mentioned previously as a reference. We conducted a qPCR on the cDNA template with TB GreenTM Premix Ex TaqTM II (Takara; RR820A) to determine the levels of mRNA. In addition, qPCR primer sets for miRNAs as well as mRNAs were obtained from RiboBio while mRNA qPCR primers have been synthesized by Sangon (Shanghai, China), as described in previous studies (50). For the relative quantification of gene expression levels, the CT method was performed in triplicates while GAPDH or U6 are included as internal controls.

Statistical Methods

Statistical analyses were performed using R software (version 4.0.2). The Kaplan-Meier method was used, and survival curves were plotted for survival analyses. Unless otherwise stated, $p < 0.05$ was found to be significant.

RESULTS

DEGs Related to Ferroptosis Index in LUAD

The flow chart of this study is shown in **Figure 1.** We calculated the probability of ferroptosis based on the core mRNAs associated with ferroptosis and it was termed the ferroptosis index (FPI) (40). According to their median FPI values, 384 LUAD patients without metastasis (nM-LUAD) in the TCGA-LUAD project were classified into high or low FPI groups. We then identified 5,958 DEmRNAs, 2,380 lncRNAs, and 68 DEmiRNAs to analyze the differences between the low and high FPI groups (**Figures 2A–C**). It has been proposed that these dysregulated mRNAs are associated with ferroptosis and are known as FPI-related mRNAs. The DEmRNAs that were upregulated in the low FPI group were enriched in RNA splicing, stereocilium, presynaptic active zone, and RNA polymerase complex (**Figure 2D**). Conversely, pathways that were downregulated in the low FPI group included collagen–containing extracellular matrix, positive regulators of cell adhesion, focal adhesion, and cell adhesion molecule binding (**Figure 2E**). The analysis described above can identify the mRNAs associated with FPI in LUAD, as well as their possible functions.

Identification of Shared DEmRNAs and Construction of ceRNA Network

To identify DEmRNAs shared with both FPI and BNM, the differential analysis between BNM-LUAD and nM-LUAD revealed 154 BNM-related DEmRNAs. Then, the intersection analysis of BNM-related DEmRNAs and FPI-related DEmRNAs

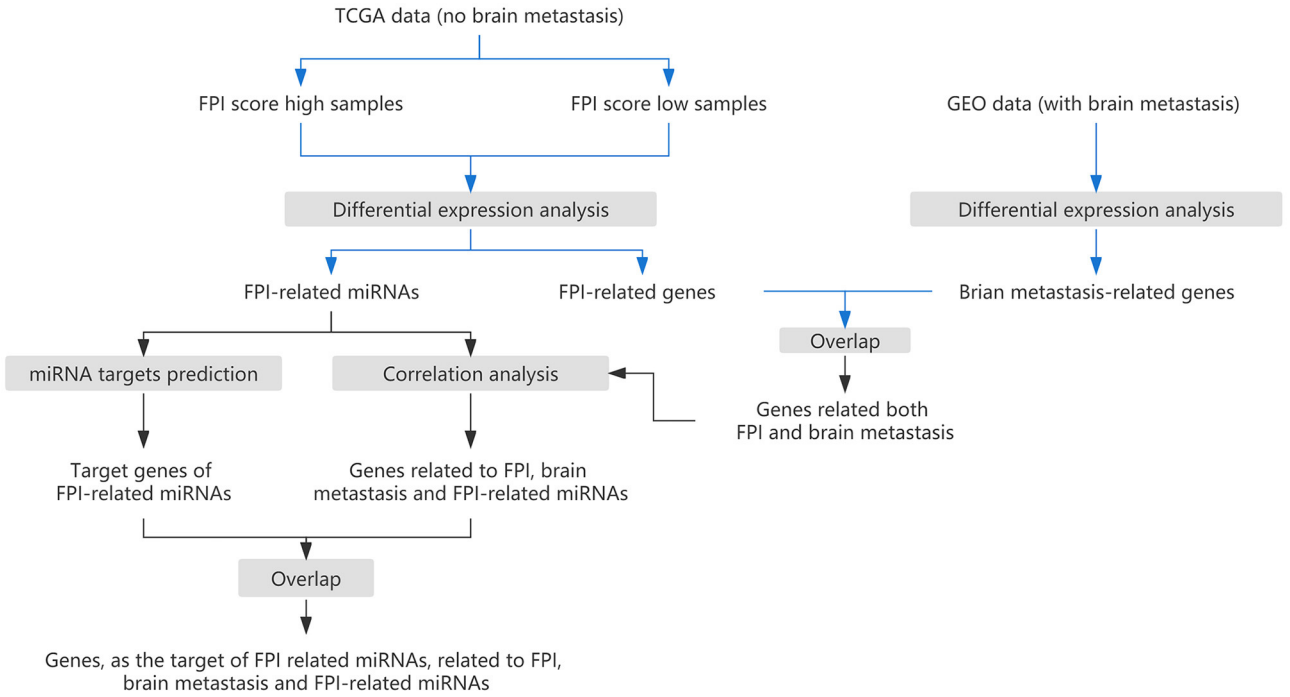

FIGURE 1 | The research strategy for this study.

identified 46 downregulated 44 mRNAs that are common to both brain metastases and ferroptosis (**Figures 3A,B**). BNM-LUAD downregulated 44 out of the 46 shared mRNAs. Downregulated mRNAs were mostly found to be enriched in leukocyte-mediated cytotoxicity MHC protein complexes, segment specification, HMG box domain binding, allograft rejection, and graft-vs.-host diseases (**Figure 3C**). Immunologically-related pathways may likely be downregulated in patients with LUAD, contributing to brain metastases.

Based on these 44 DEmRNAs [RT1], we constructed a ceRNA network (**Figure 3D**). The DElncRNAs and DEmiRNAs in the network were derived from DEMs related to FPI. The ceRNA network consists of three core miRNAs (hsa-miR-338-3p, hsa-miR-429, and hsa-miR-17-5p), three mRNAs (*HOXA7*, *TBX5*, and *TCF21*), and five lncRNAs (*HCP5, LINC00460*, *TP53TG1*, RGS5, and MAGI2-AS3).

Identification of Potential *HCP5*/hsa-miR-17-5p/*HOXA7* Pathways From the ceRNA Network

Based on the constructed ceRNA network, we performed correlation analysis to identify potential pathways. An analysis of the correlation between these 11 dysregulated molecules is depicted in **Figure 4A**. Significant correlations ($p < 0.01$) were observed between the mRNA and miRNA groups. The heat map in **Figure 4B** shows the expression of these 11 dysregulated molecules in LUAD. The correlation studies identified the *HCP5* /hsa-miR-17-5p/*HOXA7* axes associated with ferroptosis and BNM from the ceRNA network (**Figures 4C,D**). There was a negative correlation between the expression of *HCP5* and hsa-miR-17-5p (Pearson r = −0.13, p 0.05). Also, the expression of hsa-miR-17-5p and *HOXA7* exhibited a negative correlation (Pearson r = −0.17, p 0.01). Additionally, we found a positive correlation between FPI and HXOA7 and *HCP5* ($p < 0.01$), as well as a negative correlation between FPI and hsa-miR-17-5p ($p < 0.05$). *HCP5* overexpression was also linked to a superior primary therapy outcome, suggesting that it may improve the prognosis of LUAD patients (**Table 1**). Thus, ceRNA *HCP5* /hsa-miR-17-5p/*HOXA7* may play a role in the development of LUAD.

Correlation of *HCP5,* hsa-miR-17-5p, and *HOXA7* With LUAD Prognosis and FPI

To further evaluate the effect of *HCP5* /hsa-miR-17-5p/*HOXA7* in LUAD, ROC curves and analysis of differential expression were used to examine the relationship between *HCP5,* hsa-miR-17-5p, and *HOXA7* and LUAD prognosis and FPI. In ROC analysis, *HCP5* (AUC = 0.596, 95% CI: 0.534-0.657), *HOXA7* (AUC = 0.617, 95% CI: 0.556–0.678) and hsa-miR-17-5p (AUC = 0.575, 95% CI: 0.512–0.637) significantly predicted low FPI scores (**Figures 5A–C**). In addition, time-dependent ROC curves indicated that *HCP5,* HSA-miR-17-5p, and *HOXA7* might be associated with the survival of LUAD patients (**Figures 5D,E**). In addition, there was a statistically significant difference in the expression levels of *HCP5, HOXA7*, and hsa-miR-17-5p between the high and low FPI groups (**Figure 5G**). The potential *HCP5* /hsa-miR-17-5p/*HOXA7* axis is therefore thought to be related to ferroptosis.

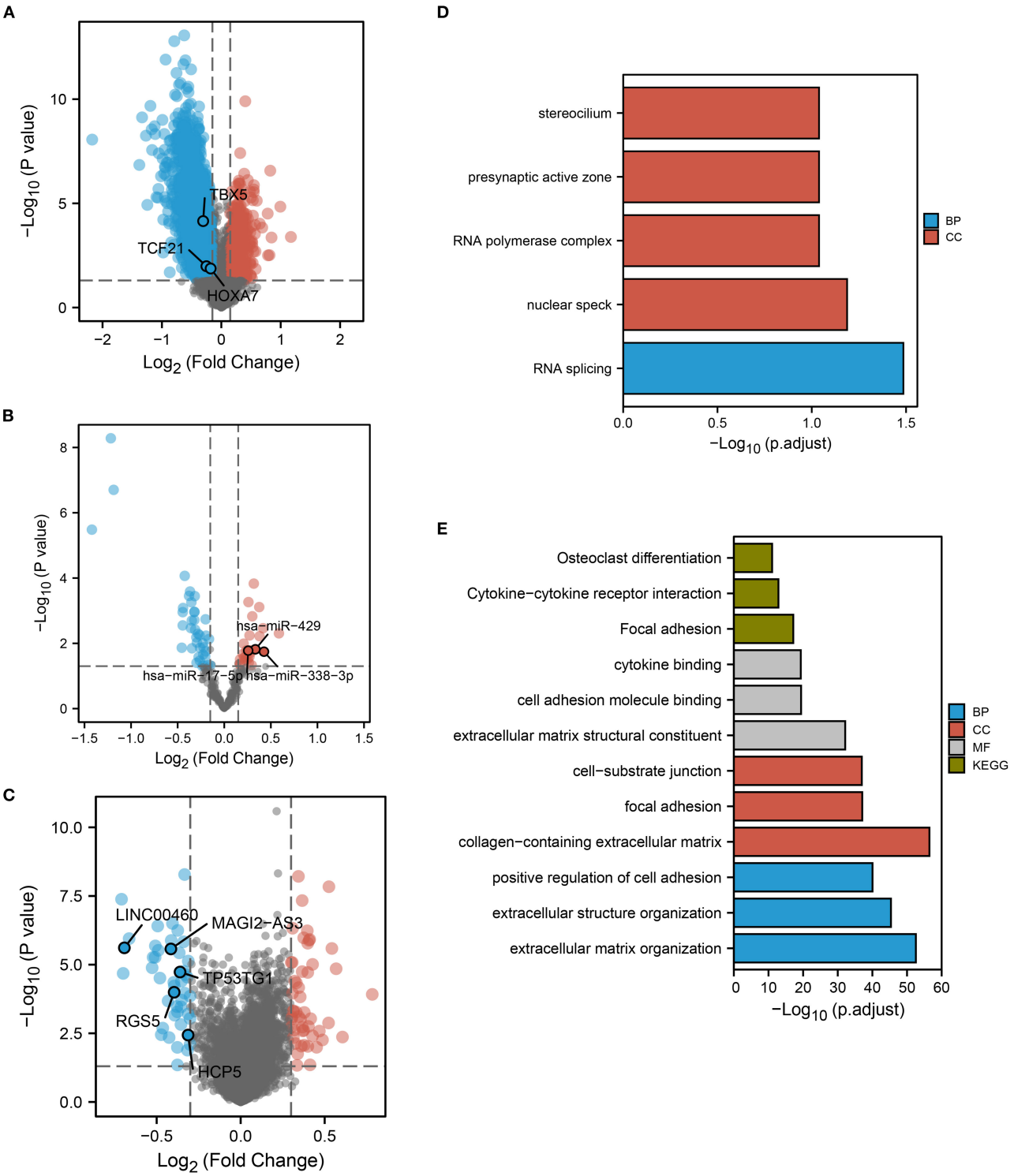

FIGURE 2 | FPI-related DEGs and functional pathway analysis. Volcano plots showed FPI-related **(A)** DEmRNAs, **(B)** DEmiRNAs, and **(C)** DElncRNAs. The plots show the predicted RNAs in ceRNA networks. Red dots indicate upregulated genes in low FPI groups. The low FPI fraction group **(D)** upregulated **(E)** downregulated GO and KEGG pathways.

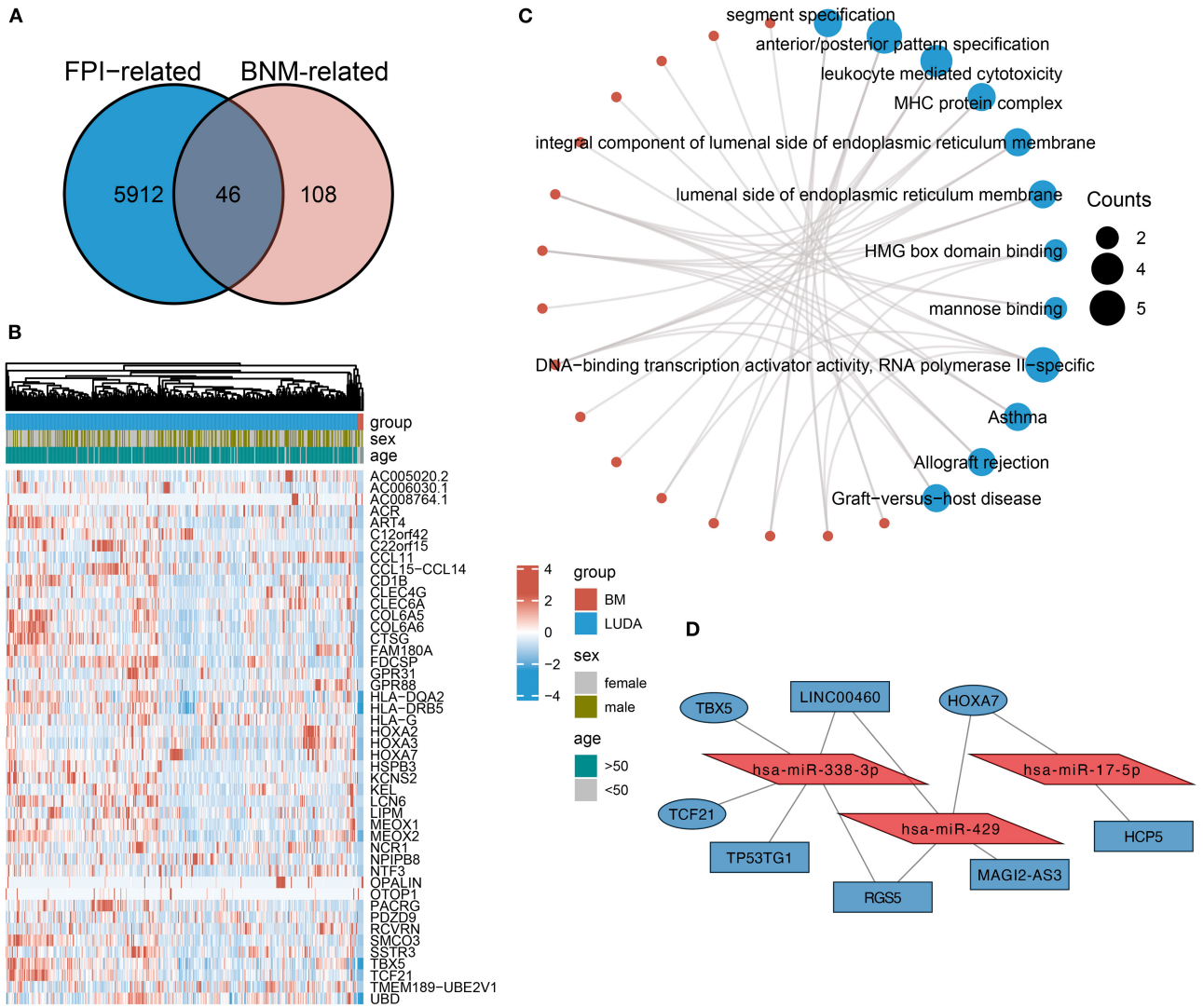

FIGURE 3 | An intersection analysis of FPI- and BM-associated DEmRNAs, and the construction of ceRNA networks. **(A)** Venn plot showed 46 shared DEmRNAs among FPI- and BNM-associated DEmRNAs. In BNM and the low FPI group, 44 of these shared DEmRNAs were downregulated. **(B)** Expression of genes shared by brain metastases and non-metastases. **(C)** The functional pathways of the shared DEmRNAs downregulated in BNM. **(D)** Construction of ceRNA networks based on the shared DEmRNAs.

Clinical Correlation Analysis of *HCP5*, hsa-miR-17-5p, and *HOXA7*

To explain the potential effectiveness of the *HCP5* /hsa-miR-17-5p/*HOXA7* axis in LUAD at the clinical level, we performed qRT-PCR using available tumor samples from 29 LUAD patients. The expression of *HCP5* and *HOXA7* correlated positively in clinical samples (**Figure 6A**; Pearson r = 0.45, $p = 0.014$), while hsa-miR-17-5p correlated negatively with *HCP5* (**Figure 6B**; Pearson r = −0.39, $p = 0.037$) as well as *HOXA7* (**Figure 6C**; Pearson $r = -0.548$, $p = 0.002$). Furthermore, *HOXA7* expression and hsa-miR-17-5p expression were negatively related. In this study, lncRNA *HCP5* was found to act as an "RNA sponge" to sequester hsa-miR-17-5p, thereby decreasing the effects of hsa-miR-17-5p on the target *HOXA7* mRNA.

Functional Analysis of *HCP5* and *HOXA7*

Using GSEA, we determined the relationship between pathway activation and inhibition when *HCP5* and *HOXA7* expression levels were high and low, respectively. The GSEA indicated that the tumor samples with elevated *HOXA7* expression downregulated miRNA targets in ECM and membrane receptors, as well as metastatic brain tumor pathways, while the apoptosis pathway was upregulated (**Figure 6D**). Additionally, the tumor samples with elevated *HCP5* expression downregulated miRNA targets in ECM and membrane receptors, metastatic brain tumors, as well as and miRNA regulation of the p53 pathway in prostate cancer (**Figure 6E**). Therefore, increased levels of *HOXA7* and *HCP5* were associated with the downregulation of tumor brain metastasis. Additionally, the expression of *HOXA7*

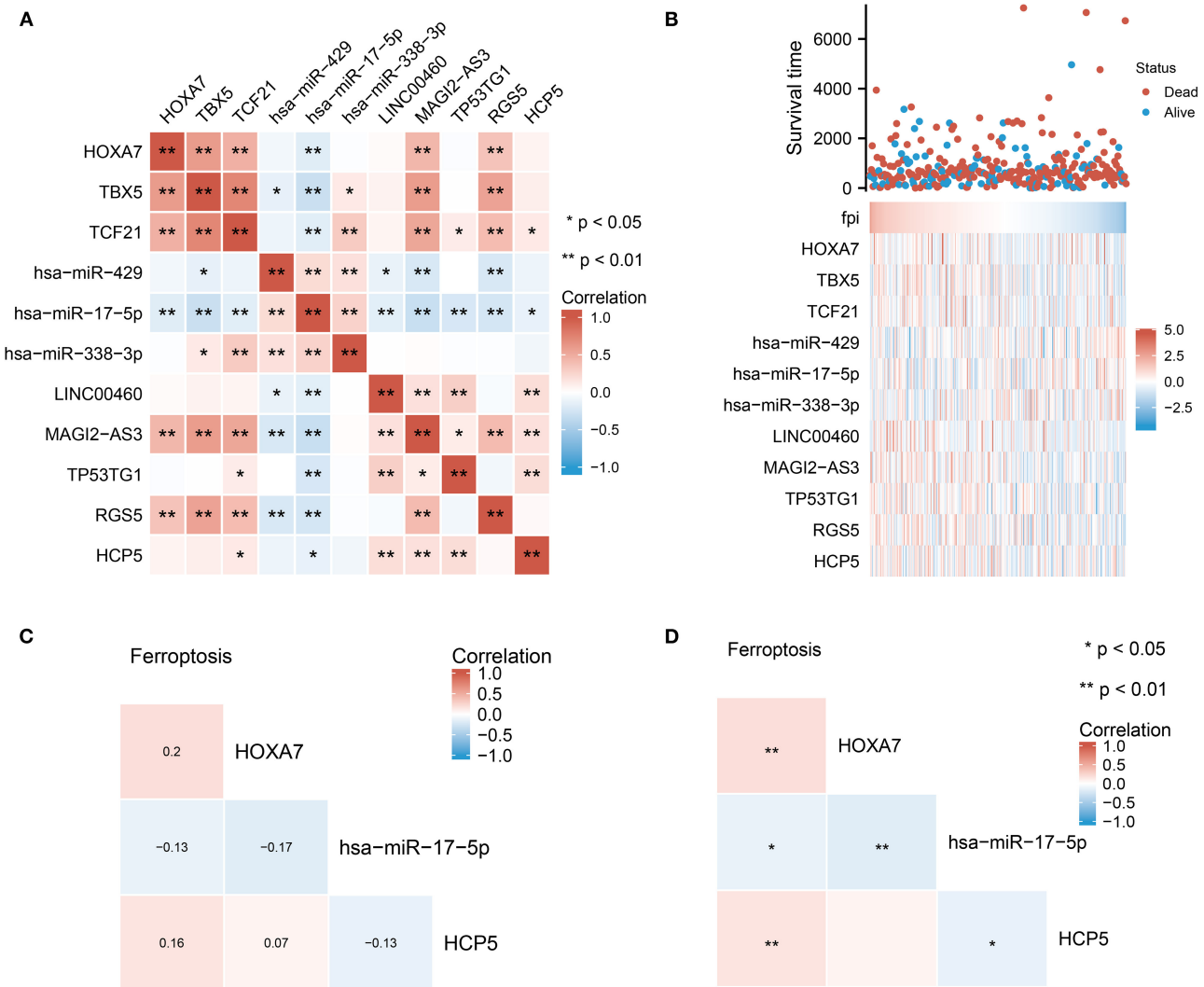

FIGURE 4 | Identification of potential *HCP5* /hsa-miR-17-5p/*HOXA7* pathways from the ceRNA network. **(A)** Correlation analysis of each element in the ceRNA network. **(B)** FPI and the expression of individual elements in the *HCP5* /hsa-miR-17-5p/*HOXA7* pathway have statistically significant connections. **(C,D)** Ferroptosis is significantly linked to each molecule in the *HCP5* /hsa-miR-17-5p/*HOXA7* pathway; **(C)** shows the correlation coefficients and **(D)** shows the statistical differences.

and *HCP5* was positively correlated with FPI, indicating a strong relationship between ferroptosis and BNM.

DISCUSSION

According to this study, BNM and ferroptosis are linked in LUAD. It has been observed that the ferroptosis-related ceRNA *HCP5*/hsa-miR-17-5p/*HOXA7* axis may play an important role in the development of BNM in LUAD.

We examined the BNM-related DEMs in LUAD with and without metastatic tumors. In addition, we investigated DEmRNAs associated with FPI in LUAD patients without metastatic tumors between high and low FPI. Furthermore, the intersection studies identified DEmRNAs shared between BMogenesis and ferroptosis. Based on intersection analysis, a ceRNA network associated with BNM and ferroptosis was constructed. The *HCP5*/hsa-miR-17-5p/*HOXA7* axis is thought to play a central role in the ceRNA regulatory network of LUAD. In a clinical cohort, we validated the *HCP5* /hsa-miR-17-5p/*HOXA7* axis and confirmed our bioinformatic findings.

Previous studies suggest that *HOXA7* participates in the pathogenesis of LUAD, providing a new target for the early treatment of LUAD (51). In brain tumors, *HOXA7* is involved in glioma progression and affects patient prognosis (52). However, there is a lack of research on the role of *HOXA7* in the brain metastasis of lung cancer. Several studies have demonstrated that *HOXA7* is involved in tumor metastasis, suggesting that *HOXA7* expression is different in different types of cancer.

TABLE 1 | The relation between HCP5 expression levels and LUAD clinicopathological features.

Characteristic	Low expression of HCP5 ($n = 267$)	High expression of HCP5 ($n = 268$)	*p*-value
Age, *n* (%)			0.187
<=65	135 (26.2%)	120 (23.3%)	
>65	122 (23.6%)	139 (26.9%)	
Gender, *n* (%)			0.022
Female	129 (24.1%)	157 (29.3%)	
Male	138 (25.8%)	111 (20.7%)	
Smoker, *n* (%)			0.139
No	31 (6%)	44 (8.4%)	
Yes	229 (44%)	217 (41.7%)	
Race, *n* (%)			0.371
Asian	2 (0.4%)	5 (1.1%)	
Black or African American	31 (6.6%)	24 (5.1%)	
White	204 (43.6%)	202 (43.2%)	
T stage, *n* (%)			0.172
T1	77 (14.5%)	98 (18.4%)	
T2	152 (28.6%)	137 (25.8%)	
T3	29 (5.5%)	20 (3.8%)	
T4	9 (1.7%)	10 (1.9%)	
N stage, *n* (%)			0.379
N0	176 (33.9%)	172 (33.1%)	
N1	43 (8.3%)	52 (10%)	
N2	40 (7.7%)	34 (6.6%)	
N3	0 (0%)	2 (0.4%)	
M stage, *n* (%)			0.621
M0	185 (47.9%)	176 (45.6%)	
M1	11 (2.8%)	14 (3.6%)	
Pathologic stage, *n* (%)			0.681
Stage I	144 (27.3%)	150 (28.5%)	
Stage II	62 (11.8%)	61 (11.6%)	
Stage III	46 (8.7%)	38 (7.2%)	
Stage IV	11 (2.1%)	15 (2.8%)	
Primary therapy outcome, *n* (%)			0.005
Progressive disease	45 (10.1%)	26 (5.8%)	
Stable disease	20 (4.5%)	17 (3.8%)	
Partial response	0 (0%)	6 (1.3%)	
Complete response	159 (35.7%)	173 (38.8%)	
Residual tumor, *n* (%)			0.172
R0	180 (48.4%)	175 (47%)	
R1	6 (1.6%)	7 (1.9%)	
R2	0 (0%)	4 (1.1%)	

HOXA1 has diverse effects on tumor progression depending on the type of malignancy. By downregulating *HOXA7* and promoting cell migration and invasion, miR-196a plays a pro-cancer role in colorectal cancer (53). It has been shown that *HOXA7* expression is elevated in metastatic hepatocellular carcinoma, enhancing the metastasis of hepatocellular carcinoma, and is associated with a poor prognosis for patients (54). Also, *HOXA7* is upregulated in the ceRNA network in oral squamous cell carcinoma, increasing the invasion and migration of oral cancer cells (55). Our study is the first to investigate the role of *HOXA7* in brain metastasis in LUAD. In patients with brain metastases, *HOXA7* expression has been observed to be downregulated. Downregulation of *HOXA7* can lead to tumors becoming more likely to metastasize to the brain, which may be associated with a poor prognosis in patients who have brain metastases. Our findings showed a positive correlation between *HOXA7* and the ferroptosis index, suggesting *HOXA7* may promote ferroptosis. Some studies have revealed that negative regulation of ferroptosis can lead to increased resistance to chemotherapy in lung cancer patients with brain metastases (56). In addition, the promotion of ferroptosis inhibited brain metastasis in HER2-positive breast cancer (57). Thus, we hypothesized that *HOXA7* downregulation promotes LUAD brain metastasis, which may be related to ferroptosis induced by *HOXA7*.

Li et al. demonstrated that miR-17-5p is highly expressed in LUAD and is associated with patient prognosis as a novel marker for clinical diagnosis of NSCLC (58, 59). Moreover, miR-17-5p is a direct target of metastasis-associated LUAD transcript 1 (MALAT1) (60). Additionally, miR-17-5p has been shown to directly target MALT1 (metastasis-associated LUAD transcript 1). A study has shown that increased MALAT1 expression promotes brain metastasis in lung cancer and correlates with patient survival (61). Additionally, miR-17-5p is also involved in brain metastasis of other cancers (62). It is therefore thought that miR-17-5p promotes LUAD brain metastasis, and this may be due to the inhibition of ferroptosis. Even though no studies have indicated a link between miR-17-5p and ferroptosis, some studies have found that miR-17-5p can resist lung cancer cell apoptosis (63). In the present study, miR-17-5p has been observed to negatively regulate *HOXA7*, thus possibly promoting LUAD brain metastasis. According to our correlation analysis, miR-17-5p promotes LUAD brain metastasis by inhibiting ferroptosis and negatively targeting *HOXA7*.

HCP5 affects tumor progression differently depending on the type of malignancies. Several studies have explored the relationship between *HCP5* and metastasis and prognosis in cancer (64). It was reported by Jiang et al. that *HCP5* was highly expressed in tumor tissues of LUAD patients and contributed to epithelial-mesenchymal transition (EMT) of LUAD cells, tumor growth, and metastasis, and was positively correlated with poor patient prognosis (65). Brain metastasis associated with lung cancer is also attributed to EMT (61, 66). We observed that patients with high *HCP5* expression had a lower prognosis than those with low *HCP5*. We found, however, that *HCP5* may regulate *HOXA7* by binding to miR-17-5p and inhibiting LUAD brain metastasis by adsorbing miR-17-5p, indicating a different mechanism of action for *HCP5* to affect LUAD brain metastasis. Furthermore, our study revealed a positive correlation between *HCP5* and ferroptosis index, suggesting that *HCP5* may promote ferroptosis. Cancer metastasis is promoted by *HCP5* through EMT in several tumor diseases (65, 67). Ferroptosis is enhanced

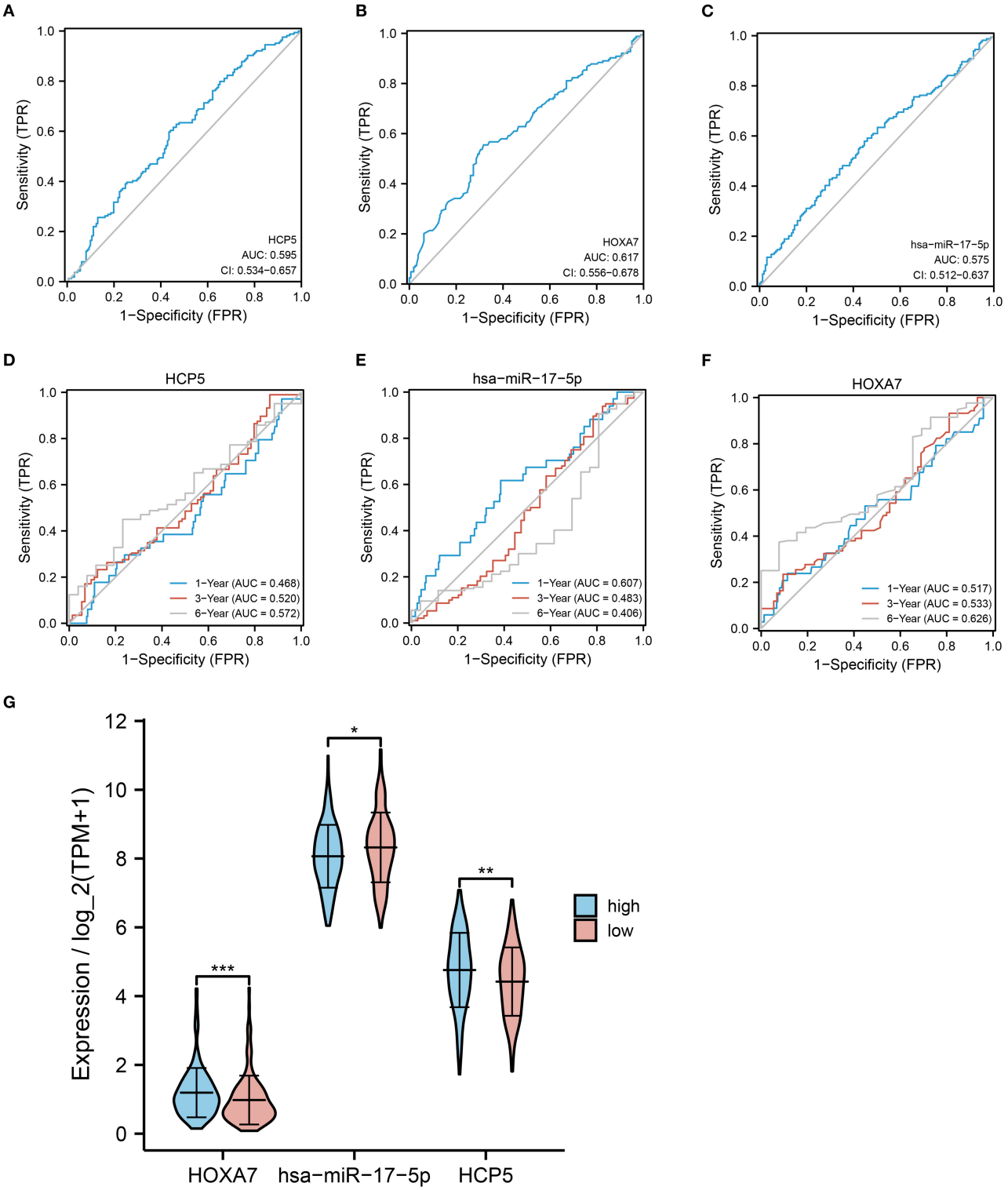

FIGURE 5 | Correlation between *HCP5*, hsa-miR-17-5p, and *HOXA7* with LUAD prognosis and FPI. **(A–C)** ROC curves predicting high or low FPI scores for **(A)** *HCP5,* **(B)** *HOXA7*, **(C)** hsa-miR-17-5p. **(D–F)** ROC curves for predicting 1-, 3-, and 6-year survival rates. **(G)** Comparison of the expression of *HCP,* hsa-miR-17-5p, and *HOXA7* in high and low FPI groups. **P* < 0.05, ***P* < 0.01, and ****P* < 0.001.

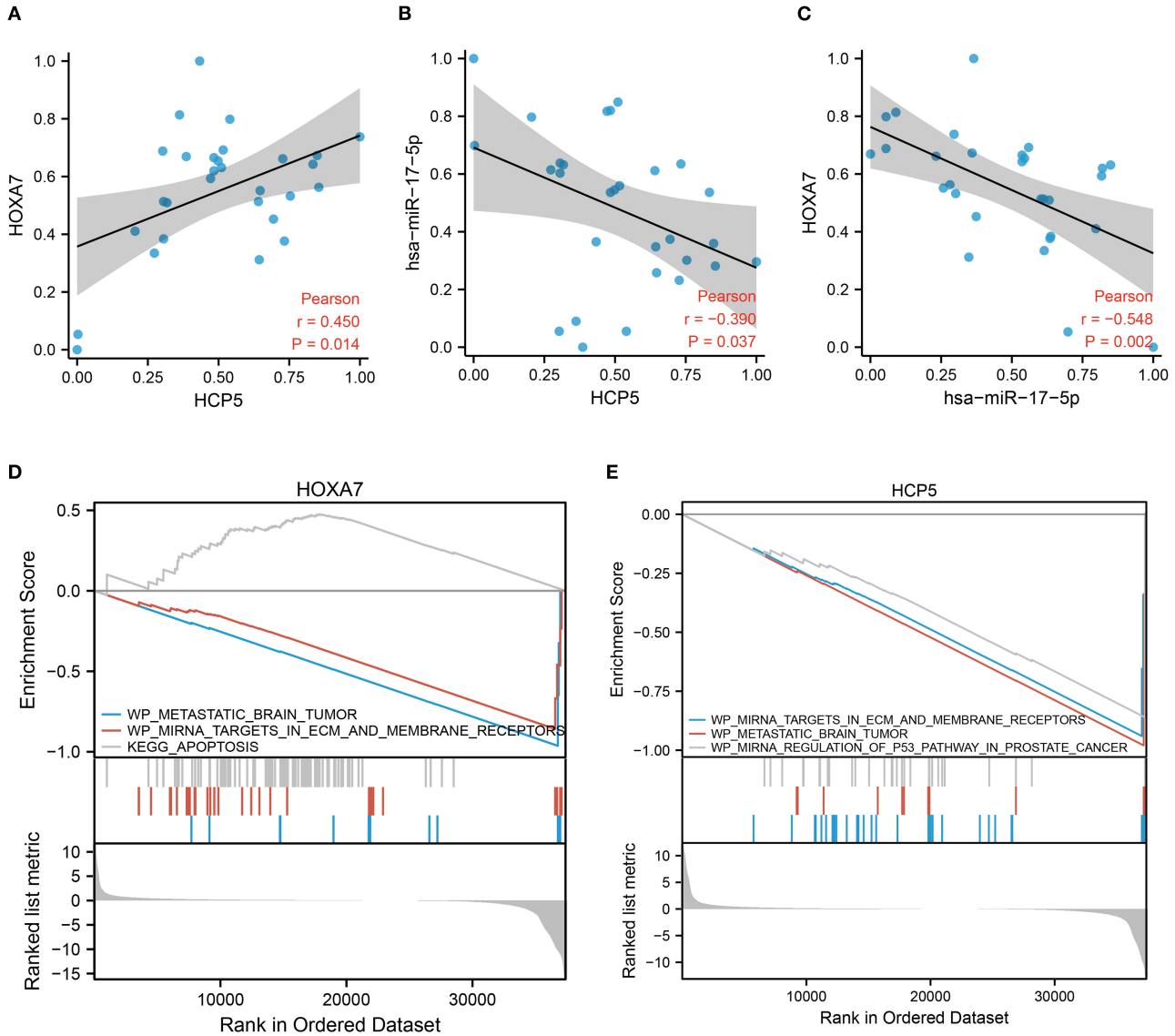

FIGURE 6 | Validation of the *HCP5* /hsa-miR-17-5p/*HOXA7* pathway using GSEA and correlation analysis. **(A)** A positive correlation between the expression of *HOXA7* and *HCP5* in clinical cohort samples (Pearson $r = 0.45$, $p = 0.014$). **(B)** The expression of hsa-miR-17-5p and *HCP5* was negatively correlated ($r = -0.39$, $p = 0.037$). **(C)** The expression of *HOXA7* and hsa-miR-17-5p was negatively correlated (Pearson $r = -0.548$, $p = 0.002$). **(D,E)** GSEA demonstrates pathways involving *HOXA7* and *HCP5*.

by the induction of EMT in cancer cells (68). We, therefore, proposed that *HCP5* promotes ferroptosis and inhibits LUAD brain metastasis by upregulating *HOXA7* through adsorption of miR-17-5p.

We can speculate that dysregulation of *HCP5* expression in LUAD patients may lead to tumor brain metastasis by downregulating *HOXA7* by affecting miR-17-5p. Therefore, a decrease in *HOXA7* expression may promote the development of brain metastases. In the present study, *HOXA7* levels were significantly lower in the BNM group than in the metastasis-free group. According to GSEA, elevated *HOXA7* and *HCP5* were linked to a decreased incidence of brain metastasis in tumors and may affect brain metastasis by regulating cell membrane surface receptors. In addition, the expression of both *HOXA7* and *HCP5* was positively correlated with FPI, suggesting a strong correlation between ferroptosis and tumor brain metastasis. The study demands further investigation to explore the relationship between brain tumors and ferroptosis.

The study was limited by the small number of subjects, including clinical study, and the lack of *in vitro* cell-based validation. We plan to further validate the ceRNA *HCP5* /hsa-miR-17-5p/*HOXA7* axis' effect on LUAD BNM from basic experiments and clinical samples in our future studies.

CONCLUSION

In conclusion, bioinformatics and clinical studies have demonstrated a correlation between the expression of *HOXA7* and *HCP5*. It may be possible to link ferroptosis to tumor neurovascular brain metastasis from correlation studies. Moreover, our study demonstrated that the ferroptosis-related ceRNA *HCP5* /hsa-miR-17-5p/*HOXA7* axis may play an essential role in LUAD BNM.

DATA AVAILABILITY STATEMENT

Publicly available datasets were analyzed in this study. This data can be found here: National Institute of Health (NIH), National Cancer Institute (NCI), The Cancer Genome Atlas (TCGA) Program, https://portal.gdc.cancer.gov/ and TCGA-LUAD and National Center for Biotechnology Information (NCBI), Gene Expression Omnibus (GEO), https://www.ncbi.nlm.nih.gov/geo/, GSE141685.

ETHICS STATEMENT

Ethical review and approval was not required for the study on human participants in accordance with the local legislation and institutional requirements. Written informed consent from the patients/participants or patients/participants' legal guardian/next of kin was not required to participate in this study in accordance with the national legislation and the institutional requirements.

AUTHOR CONTRIBUTIONS

QC, QP, and HG performed the data collection and analyses. QC and XZ analyzed and interpreted the results. QC, YW, and XZ drafted and reviewed the manuscript. All authors read and approved the final manuscript.

ACKNOWLEDGMENTS

We thank the reviewers for their outstanding contribution to the improvement of this manuscript. We thank Bullet Edits Limited for the linguistic editing and proofreading of the manuscript.

SUPPLEMENTARY MATERIAL

The Supplementary Material for this article can be found online at: https://www.frontiersin.org/articles/10.3389/fneur.2022.878947/full#supplementary-material

REFERENCES

1. Motono N, Funasaki A, Sekimura A, Usuda K, Uramoto H, et al. Prognostic value of epidermal growth factor receptor mutations and histologic subtypes with lung adenocarcinoma. *Med Oncol*. (2018) 35:22. doi: 10.1007/s12032-018-1082-y
2. Dong Y, Yang W, Wang J, Zhao J, Qiang Y, Zhao Z, et al. MLW-gcForest: a multi-weighted gcForest model towards the staging of lung adenocarcinoma based on multi-modal genetic data. *BMC Bioinformatics*. (2019) 20:578. doi: 10.1186/s12859-019-3172-z
3. Zhang W, Shen Y, Feng G: Predicting the survival of patients with lung adenocarcinoma using a four-gene prognosis risk model. *Oncol Lett*. (2019). doi: 10.3892/ol.2019.10366
4. Du J, Zhang G, Qiu H, Yu H, Yuan W. The novel circular RNA circ-CAMK2A enhances lung adenocarcinoma metastasis by regulating the miR-615-5p/fibronectin 1 pathway. *Cell Mol Biol Lett*. (2019) 24:72. doi: 10.1186/s11658-019-0198-1
5. Jemal A, Siegel R, Ward E, Hao Y, Xu J, Thun MJ. Cancer statistics, 2017. *CA: A Cancer J Clin*. (2017) 67:7–30. doi: 10.3322/caac.21387
6. Jemal, Bray F, Center MM, Ferlay J, Ward E, Forman. Global cancer statistics. *CA: A Cancer J Clin*. (2011) 61:69–90. doi: 10.3322/caac.20107
7. Sun F, Huang Y, Yang X, Zhan C, Xi J, Lin Z, et al. Solid component ratio influences prognosis of GGO-featured IA stage invasive lung adenocarcinoma. *Cancer Imaging*. (2020) 20:87. doi: 10.1186/s40644-020-00363-6
8. Hirsch FR, Scagliotti GV, Mulshine JL, Kwon R, Curran Jr WJ, Wu YL, et al. Lung cancer: current therapies and new targeted treatments. *The Lancet*. (2017) 389:299–311. doi: 10.1016/S0140-6736(16)30958-8
9. Yu Z, Zhu X, Li Y, Liang M, Liu M, Liu Z, et al. Circ-HMGA2 (hsa_circ_0027446) promotes the metastasis and epithelial-mesenchymal transition of lung adenocarcinoma cells through the miR-1236-3p/ZEB1 axis. *Cell Death Dis*. (2021) 12:313. doi: 10.1038/s41419-021-03601-2
10. Ferlay J, Soerjomataram I, Dikshit R, Eser S, Mathers C, Rebelo M, et al. Cancer incidence and mortality worldwide: sources, methods and major patterns in Globocan 2012: Globocan (2012). *Int. J. Cancer*. (2015) 136:E359–E386. doi: 10.1002/ijc.29210
11. Zheng H, Huang Q, Huang S, Yang X, Zhu T, Wang W, et al. Senescence inducer Shikonin ROS-dependently suppressed lung cancer progression. *Front. Pharmacol*. (2018) 9:519. doi: 10.3389/fphar.2018.00519
12. Chen Z, Fillmore CM, Hammerman PS, Kim CF, Wong KK. Non-small-cell lung cancers: a heterogeneous set of diseases. *Nat Rev Cancer*. (2014) 14:535–46. doi: 10.1038/nrc3775
13. Walter JE, Heuvelmans MA, de Jong PA, Vliegenthart R, van Ooijen PM, Peters RB, et al. Occurrence and lung cancer probability of new solid nodules at incidence screening with low-dose CT: analysis of data from the randomised, controlled NELSON trial. *Lancet Oncol*. (2016) 17:907–16. doi: 10.1016/S1470-2045(16)30069-9
14. Walter JE, Heuvelmans MA, de Jong PA, Vliegenthart R, van Ooijen PM, Peters RB, et al. Comprehensive profiling reveals distinct microenvironment and metabolism characterization of lung adenocarcinoma. *Front. Genet*. (2021) 12:619821. doi: 10.3389/fgene.2021.619821
15. Ning M, Chunhua M, Rong J, Yuan L, Jinduo L, Bin W, et al. Diagnostic value of circulating tumor cells in cerebrospinal fluid. *Open Medicine*. (2016) 11:21–4. doi: 10.1515/med-2016-0005
16. Ning M, Chunhua M, Rong J, Yuan L, Jinduo L, Bin W, et al. Clinical efficacy and safety evaluation of pemetrexed combined with radiotherapy in treatment of patients with lung adenocarcinoma brain metastasis. *Oncol Lett*. (2019). doi: 10.3892/ol.2019.9894
17. Kawabe T, Phi JH, Yamamoto M, Kim DG, Barfod BE, Urakawa Y. Treatment of brain metastasis from lung cancer. In: Kim, D.G. and Lunsford, L.D. (eds.) *Progress in Neurol Surg*. (2012):148–155. *KARGER*, Basel. doi: 10.1159/000331188
18. Fang X, Wang H, Han D, Xie E, Yang X, Wei J, et al. Ferroptosis as a target for protection against cardiomyopathy. *Proc Natl Acad Sci USA*. (2019) 116:2672–80. doi: 10.1073/pnas.1821022116
19. Friedmann Angeli JP, Schneider M, Proneth B, Tyurina YY, Tyurin VA, Hammond VJ, et al. Inactivation of the ferroptosis regulator Gpx4 triggers acute renal failure in mice. *Nat Cell Biol*. (2014) 16:1180–91. doi: 10.1038/ncb3064
20. Liang C, Zhang X, Yang M, Dong X. Recent progress in ferroptosis inducers for cancer therapy. *Adv Mater*. (2019) 31:1904197. doi: 10.1002/adma.201904197

21. Qiu C, Zhang X, Huang B, Wang S, Zhou W, Li C, et al. Disulfiram, a ferroptosis inducer, triggers lysosomal membrane permeabilization by up-regulating ROS in glioblastoma. *OTT*. (2020) 13:10631–40. doi: 10.2147/OTT.S272312
22. Tang Z, Jiang W, Mao M, Zhao J, Chen J, Cheng N. Deubiquitinase USP35 modulates ferroptosis in lung cancer via targeting ferroportin. *Clin Translat Med*. (2021) 11:4. doi: 10.1002/ctm2.390
23. Hassannia B, Vandenabeele P, Berghe TV. Targeting ferroptosis to iron out cancer. *Cancer Cell*. (2019) 35:830–49. doi: 10.1016/j.ccell.2019.04.002
24. Li G, Yang J, Zhao G, Shen Z, Yang K, Tian L, et al. Dysregulation of ferroptosis may involve in the development of non-small-cell lung cancer in Xuanwei area. *J Cell Mol Med*. (2021) 25:2872–84. doi: 10.1111/jcmm.16318
25. Tang X, Ding H, Liang M, Chen X, Yan Y, Wan N, et al. Curcumin induces ferroptosis in non-small-cell lung cancer via activating autophagy. *Thorac Cancer*. (2021) 12:1219–1230. doi: 10.1111/1759-7714.13904
26. Lu B, Chen XB, Ying MD, He QJ, Cao J, Yang B. The role of ferroptosis in cancer development and treatment response. *Front Pharmacol*. (2018) 8:992.. doi: 10.3389/fphar.2017.00992
27. Lei G, Zhang Y, Koppula P, Liu X, Zhang J, Lin SH, et al. The role of ferroptosis in ionizing radiation-induced cell death and tumor suppression. *Cell Res*. (2020) 30:146–162. doi: 10.1038/s41422-019-0263-3
28. Ye LF, Chaudhary KR, Zandkarimi F, Harken AD, Kinslow CJ, Upadhyayula PS, et al. Higgins, Radiation-induced lipid peroxidation triggers ferroptosis and synergizes with ferroptosis inducers. *ACS Chem Biol*. 15:469–84. (2020). doi: 10.1021/acschembio.9b00939
29. Hu H, Liu S, Chu A, Chen J, Xing C, Jing J. Comprehensive analysis of ceRNA network of ERCC4 in colorectal cancer. *PeerJ*. (2021) 9:e12647. doi: 10.7717/peerj.12647
30. Jia X, Meng W, Zhang L, Jia Y, Shi Y, Tong Z. Construction of differentially expressed Her-2 related lncRNA-mRNA-miRNA ceRNA network in Her-2 positive breast cancer. *Transl Cancer Res TCR*. (2020) 9:2527–33. doi: 10.21037/tcr.2020.03.34
31. Wang Y, Zhang F, Wu D, Wang Q, Nie L, Yu J. A novel circ_0099999/miR-330-5p/FSCN1 ceRNA crosstalk in pancreatic cancer. *Autoimmunity*. (2021) 54:471–82. doi: 10.1080/08916934.2021.1963958
32. Chu A, Liu J, Yuan Y, Gong Y. Comprehensive analysis of aberrantly expressed ceRNA network in gastric cancer with and without *H.pylori* infection. *J. Cancer*. (2019) 10:853–63. doi: 10.7150/jca.27803
33. Dong J, Li B, Lin D, Lu D, Liu C, Lu X, et al. LincRNA00494 suppresses non-small cell lung cancer cell proliferation by regulating SRCIN1 expression as a ceRNA. *Front Oncol*. 10:79 (2020). doi: 10.3389/fonc.2020.00079
34. Cao Q, Dong Z, Liu S, An G, Yan B, Lei L. Construction of a metastasis-associated ceRNA network reveals a prognostic signature in lung cancer. *Cancer Cell Int*. (2020) 20:208. doi: 10.1186/s12935-020-01295-8
35. Xu J, Ling T, Dai S, Han S, Ding K. Constructing the ceRNA regulatory network and combining immune cells to evaluate prognosis of colon cancer patients. *Front Cell Dev Biol*. (2021) 9:686844. doi: 10.3389/fcell.2021.686844
36. Zhao Y, Ma S, Cui Z, Li S, Chen Y, Yin Y, et al. The relationship between LncRNAs and lung adenocarcinoma as well as their ceRNA network. (2021) *CBM*. 31:165–176. doi: 10.3233/CBM-203078
37. Shih DJ, Nayyar N, Bihun I, Dagogo-Jack I, Gill CM, Aquilanti E, et al. Genomic characterization of human brain metastases identifies drivers of metastatic lung adenocarcinoma. *Nat Genet*. (2020) 52:371–377. doi: 10.1038/s41588-020-0592-7
38. Bray NL, Pimentel H, Melsted P, Pachter L. Near-optimal probabilistic RNA-seq quantification. *Nat Biotechnol*. (2016) 34:525–527. doi: 10.1038/nbt.3519
39. Ritchie ME, Phipson B, Wu DI, Hu Y, Law CW, Shi W, et al. limma powers differential expression analyses for RNA-sequencing and microarray studies. *Nucleic Acids Res*. (2015) 43:e47. doi: 10.1093/nar/gkv007
40. Liu Z, Zhao Q, Zuo ZX, Yuan SQ, Yu K, Zhang Q, et al. Systematic analysis of the aberrances and functional implications of ferroptosis in cancer. *iScience*. (2020) 23:101302. doi: 10.1016/j.isci.2020.101302
41. Chen C, Zhao J, Liu JN, Sun C. Mechanism and role of the neuropeptide LGI1 Receptor ADAM23 in regulating biomarkers of ferroptosis and progression of esophageal cancer. *Dis Markers*. (2021) 2021:9227897. doi: 10.1155/2021/9227897
42. Yu G, Wang LG, Han Y, He QY. Clusterprofiler: an R package for comparing biological themes among gene clusters. *OMICS: A J Integrative Biol*. (2012) 16:284–287. doi: 10.1089/omi.2011.0118
43. Sun C, Ma S, Chen Y, Kim NH, Kailas S, Wang Y, et al. Diagnostic value, prognostic value, and immune infiltration of LOX family members in liver cancer: bioinformatic analysis. *Front. Oncol*. (2022) 12:843880. doi: 10.3389/fonc.2022.843880
44. Lu L, Kang X, Yi B, Jiang C, Yan X, Chen B, et al. Exploring the mechanism of Yiqi Qingre Ziyin method in regulating neuropeptide expression for the treatment of atrophic rhinitis. *Disease Markers*. (2022) 2022:1–12. doi: 10.1155/2022/4416637
45. Jeggari A, Marks DS, Larsson E. miRcode: a map of putative microRNA target sites in the long non-coding transcriptome. *Bioinformatics*. (2012) 28:2062–2063. doi: 10.1093/bioinformatics/bts344
46. Huang J, Liang X, Cai. A potential cerna network for neurological damage in preterm infants. *BioMed Research International*. (2021) 2021:2628824. doi: 10.1155/2021/2628824
47. Sticht C, De La Torre C, Parveen A, Gretz N. miRWalk: An online resource for prediction of microRNA binding sites. *PLoS ONE*. (2011) 3:e0206239. doi: 10.1371/journal.pone.0206239
48. Subramanian A, Tamayo P, Mootha VK, Mukherjee S, Ebert BL, Gillette MA et al. Gene set enrichment analysis: A knowledge-based approach for interpreting genome-wide expression profiles. *Procee Nat Academy Sci*. (2005) 102:15545–50. doi: 10.1073/pnas.0506580102
49. Chen Y, Sun Y, Xu Y, Lin WW, Luo Z, Han Z, et al. Single-cell integration analysis of heterotopic ossification and fibrocartilage developmental lineage: endoplasmic reticulum stress effector xbp1 transcriptionally regulates the notch signaling pathway to mediate fibrocartilage Differentiation."*Oxidative Medicine and Cellular Longevity*. (2021) 2021:1–29. doi: 10.1155/2021/7663366
50. Luo Z, Sun Y, Qi B, Lin J, Chen Y, Xu Y, et al. Human bone marrow mesenchymal stem cell-derived extracellular vesicles inhibit shoulder stiffness via let-7a/Tgfbr1 axis. *Bioact Mat*. (2022) 17:S2452199X22000226. doi: 10.1016/j.bioactmat.2022.01.016
51. Kang JU. Characterization of amplification patterns and target genes on the short arm of chromosome 7 in early-stage lung adenocarcinoma. *Mol Med Reports*. (2013) 8:1373–1378. doi: 10.3892/mmr.2013.1686
52. Li B, McCrudden CM, Yuen HF, Xi X, Lyu P, Chan KW, et al. CD133 in brain tumor: the prognostic factor. *Oncotarget*. (2017) 8:11144–59. doi: 10.18632/oncotarget.14406
53. Schimanski CC, Frerichs K, Rahman F, Berger M, Lang H, Galle PR, et al. High miR-196a levels promote the oncogenic phenotype of colorectal cancer cells. *WJG*. (2009) 15:2089. doi: 10.3748/wjg.15.2089
54. Tang B, Qi G, Sun X, Tang F, Yuan S, Wang Z, etal. HOXA7 plays a critical role in metastasis of liver cancer associated with activation of Snail. *Mol Cancer*. (2016) 15:57. doi: 10.1186/s12943-016-0540-4
55. Chen H, Zhang Y, Wu K, Qiu X. CircVAPA promotes the proliferation, migration and invasion of oral cancer cells through the miR-132/HOXA7 axis. *J Int Med Res*. (2021) 49:030006052110132. doi: 10.1177/03000605211013207
56. Liu W, Zhou Y, Duan W, Song J, Wei S, Xia S et al. Glutathione peroxidase 4-dependent glutathione high-consumption drives acquired platinum chemoresistance in lung cancer-derived brain metastasis. *Clin Translat Med*. (2021) 11:517. doi: 10.1002/ctm2.517
57. Nagpal A, Redvers RP, Ling X, Ayton S, Fuentes M, Tavancheh E, et al. Neoadjuvant neratinib promotes ferroptosis and inhibits brain metastasis in a novel syngeneic model of spontaneous HER2+ve breast cancer metastasis. *Breast Cancer Res*. (2019) 21:94. doi: 10.1186/s13058-019-1177-1
58. Li J, Li Z, Zhao S, Song Y, Si L, Wang X. Identification key genes, key miRNAs and key transcription factors of lung adenocarcinoma. *J Thorac Dis*. (2020) 12:1917–1933. doi: 10.21037/jtd-19-4168
59. Zhang Y, Zhang Y, Yin Y, Li S. Detection of circulating exosomal miR-17-5p serves as a novel non-invasive diagnostic marker for non-small cell lung cancer patients. *Pathol - Res Prac*. (2019) 215:152466. doi: 10.1016/j.prp.2019.152466
60. Wei S, Wang K, Huang X, Tang W, Zhao Z, Zhao Z. Knockdown of the lncRNA MALAT1 alleviates lipopolysaccharide-induced A549 cell injury by

targeting the miR-17-5p/FOXA1 axis. *Mol Med Report*. (2019) 20:2021–9. doi: 10.3892/mmr.2019.10392
61. Shen L, Chen L, Wang Y, Jiang X, Xia H, Zhuang Z. Long noncoding RNA MALAT1 promotes brain metastasis by inducing epithelial-mesenchymal transition in lung cancer. *J Neurooncol*. (2015) 121:101–108. doi: 10.1007/s11060-014-1613-0
62. Global Analysis of miRNA–mRNA interaction network in breast cancer with brain metastasis. *AR*. (2017) 37, no. 8,. doi: 10.21873/anticanres.11841
63. Matsubara H, Takeuchi T, Nishikawa E, Yanagisawa K, Hayashita Y, Ebi H, et al. Apoptosis induction by antisense oligonucleotides against miR-17-5p and miR-20a in lung cancers overexpressing miR-17-92. *Oncogene*. (2007) 26:6099–105. doi: 10.1038/sj.onc.1210425
64. Hu SP, Ge MX, Gao L, Jiang M, Hu KW. LncRNA HCP5 as a potential therapeutic target and prognostic biomarker for various cancers: a meta-analysis and bioinformatics analysis. *Cancer Cell Int*. (2021) 21:686. doi: 10.1186/s12935-021-02404-x
65. Jiang L, Wang R, Fang LI, Ge X, Chen L, Zhou M, et al. HCP5 is a SMAD3-responsive long non-coding RNA that promotes lung adenocarcinoma metastasis via miR-203/SNAI axis. *Theranostics*. (2019) 9:2460–74. doi: 10.7150/thno.31097
66. Chen JH, Zhou LY, Xu S, Zheng YL, Wan YF, Hu CP. Overexpression of lncRNA HOXA11-AS promotes cell epithelial–mesenchymal transition by repressing miR-200b in non-small cell lung cancer. *Cancer Cell Int*. (2017) 17:64. doi: 10.1186/s12935-017-0433-7
67. Gao M, Liu L, Yang Y, Li M, Ma Q, Chang Z. LncRNA HCP5 induces gastric cancer cell proliferation, invasion, and EMT processes through the miR-186-5p/WNT5A Axis Under Hypoxia. *Front.Cell Dev. Biol*. (2021) 9:663654. doi: 10.3389/fcell.2021.663654
68. Lee J, You JH, Kim MS, Roh JL. Epigenetic reprogramming of epithelial-mesenchymal transition promotes ferroptosis of head and neck cancer. *Redox Biology*. (2020) 101697. doi: 10.1016/j.redox.2020.101697

Conflict of Interest: The authors declare that the research was conducted in the absence of any commercial or financial relationships that could be construed as a potential conflict of interest.

Publisher's Note: All claims expressed in this article are solely those of the authors and do not necessarily represent those of their affiliated organizations, or those of the publisher, the editors and the reviewers. Any product that may be evaluated in this article, or claim that may be made by its manufacturer, is not guaranteed or endorsed by the publisher.

Copyright © 2022 Chen, Pan, Gao, Wang and Zhong. This is an open-access article distributed under the terms of the Creative Commons Attribution License (CC BY). The use, distribution or reproduction in other forums is permitted, provided the original author(s) and the copyright owner(s) are credited and that the original publication in this journal is cited, in accordance with accepted academic practice. No use, distribution or reproduction is permitted which does not comply with these terms.

frontiers | Frontiers in Neurology

ORIGINAL RESEARCH
published: 26 May 2022
doi: 10.3389/fneur.2022.893624

15-Hydroxyprostaglandin Dehydrogenase Is a Predictor of Stroke-Associated Pneumonia

Yunfei Xu[1,2,3,4], *Haoduo Qiao*[1,2,3,4], *Shun Yang*[1], *Lin Zhou*[1,2,3,4], *Yao Zhao*[1,2,3,4], *Qing Xu*[1,2,3,4], *Shuying Miao*[4,5], *Dun Yuan*[1]*, *Jie Zhao*[1]* and *Ying Liu*[1,2,3,4]*

[1] Department of Pathophysiology, Xiangya School of Medicine, Central South University, Changsha, China, [2] Department of Neurosurgery, Xiangya Hospital, Central South University, Changsha, China, [3] Sepsis Translational Medicine Key Lab of Hunan Province, Central South University, Changsha, China, [4] China-Africa Research Center of Infectious Diseases, Central South University, Changsha, China, [5] Department of Pathology, Nanjing Drum Tower Hospital, Nanjing University Medical School, Nanjing, China

OPEN ACCESS

Edited by:
Wen-Jun Tu,
Chinese Academy of Medical Sciences and Peking Union Medical College, China

Reviewed by:
Erming Zeng,
Nanchang University, China
Li Zhou,
Chinese Academy of Medical Sciences and Peking Union Medical College, China

***Correspondence:**
Ying Liu
liu1977ying@126.com
Jie Zhao
steelzj@csu.edu.cn
Dun Yuan
yuandunlp@hotmail.com

Specialty section:
This article was submitted to Neurological Biomarkers, a section of the journal Frontiers in Neurology

Received: 10 March 2022
Accepted: 27 April 2022
Published: 26 May 2022

Citation:
Xu Y, Qiao H, Yang S, Zhou L, Zhao Y, Xu Q, Miao S, Yuan D, Zhao J and Liu Y (2022) 15-Hydroxyprostaglandin Dehydrogenase Is a Predictor of Stroke-Associated Pneumonia. Front. Neurol. 13:893624. doi: 10.3389/fneur.2022.893624

Background and Purpose: Stroke is a serious fatal and disabling disease. Stroke-associated pneumonia (SAP) is the most common complication of stroke, which may further aggravate the stroke. The prevention and early prediction of SAP is a key clinical strategy. 15-hydroxyprostaglandin dehydrogenase (15-PGDH) is involved in pneumonia, while its relationship with SAP has yet to be determined. Therefore, we investigated the predictive value of 15-PGDH for SAP and visualized their relationship.

Methods: Stroke patients were recruited and divided into SAP group and Non-SAP group. Baseline demographic and clinical data were obtained from the medical record system, blood samples were collected to detect relevant variables and 15-PGDH levels. Patient characteristics were compared with a t-test. Binary logistic regression analysis was performed to determine the predictive value of 15-PGDH for SAP. Restricted cubic splines (RCS) were performed to visualize the relationship between 15-PGDH and SAP risk. Finally, the SAP patient characteristics between the severe group and mild group were compared.

Results: 50 patients were enrolled and divided into SAP group ($n = 26$) and Non-SAP group ($n = 24$). 15-PGDH in the SAP group was lower than that in the Non-SAP group (0.258 ± 0.275 vs. 0.784 ± 0.615, $p = 0.025$). Binary logistic regression analysis revealed that the lower 15-PGDH, the higher the risk of SAP (OR = 0.04, 95%CI, 0.010–0.157, $p < 0.001$). The RCS model showed the L-shaped relationship between 15-PGDH and SAP.

Conclusions: In stroke patients, serum 15-PGDH is a valuable biomarker for predicting SAP. There is an L-shaped relationship between the level of 15-PGDH and the risk of SAP.

Keywords: 15-PGDH, stroke, pneumonia, PGE2, predictor

INTRODUCTION

Stroke is a common acute cerebrovascular disease, which is the second leading cause of death and the third-leading cause of death and disability combined globally (1). The high mortality rate of stroke is largely attributable to its complications. Stroke-associated pneumonia (SAP) is the most common complication of stroke, occurring most often within the first week in 8.6% to 14.3% of stroke patients (2–4). Stroke activates inflammatory cascades in the brain, such as the excessive release of cytokines, then stimulates the central immune system to produce anti-inflammatory signals. Subsequently, the efferent vagus nerve is activated and inhibits cytokine production, ultimately leading to the suppression of systemic immunity. Stroke-induced immunosuppression increases the susceptibility of stroke patients to infection, accompanied by decreased pulmonary clearance and impaired secretion drainage caused by the alteration in tracheal endothelia after stroke, ultimately leading to the occurrence of SAP (5–7). At the same time, risk factors such as stroke severity, advanced age, hypertension, and smoking history also contribute to the occurrence of SAP (8, 9). SAP further increases the severity of the stroke, lengthens hospital stay, increases financial burden, worsens the functional outcome, and increases patient mortality (9, 10). Prevention and early diagnosis or prediction of SAP is an important clinical strategy. However, current methods are less specific and sensitive, making the early diagnosis of SAP become a big difficulty (3, 11). There is still great value in exploring the early markers of SAP.

Prostaglandin E2 (PGE2) is a key mediator of inflammation, its elevation is a response to inflammation (12). 15-hydroxyprostaglandin dehydrogenase (15-PGDH) is the sole degradation enzyme of PGE2 by oxidizing it to inactive 15-keto PGE2 (13). The decrease of 15-PGDH can lead to an increase in PGE2, which has been observed in stroke (14). Meanwhile, 15-PGDH is generally identified as a tumor suppressor, such as lung cancer, breast cancer, colorectal cancer, etc (15–17). In addition, 15-PGDH is also involved in lipopolysaccharide-induced acute kidney injury, pulmonary fibrosis, tissue repair, and other pathological processes (18–20). Interestingly, a previous study reported that in pulmonary infection caused by pseudomonas aeruginosa, inhibition of PGE2 overproduction shows a protective effect, in part by raising the level of 15-PGDH (21). However, no report has revealed the level of 15-PGDH in SAP and the relationship between 15-PGDH and SAP. Therefore, we will determine the relationship between 15-PGDH and SAP, and determine whether it can be used as an early marker to predict SAP and provide a basis for early diagnosis of SAP.

Abbreviations: 15-PGDH, 15-hydroxyprostaglandin dehydrogenase; AUC, area under the curve; COPD, chronic obstructive pulmonary disease; CI, confidence interval; CT, computerized tomography; ELISA, enzyme-linked immunosorbent assay; GCS, Glasgow coma score; IQR, interquartile range; MRI, magnetic resonance imaging; OR, odds ratio; PGE2, prostaglandin E2; PSI, pneumonia severity index; RBC, red blood cell; RCS, restricted cubic splines; ROC, receiver operating characteristic; SAP, stroke-associated pneumonia; WBC, white blood cell.

METHODS

Patients Selection

This was a retrospective study, all the patients with hemorrhagic stroke or ischemic stroke were recruited from the Department of Neurosurgery, Xiangya Hospital, Central South University between February 2019 to June 2021. This research was approved by the ethics committee of the Xiangya Hospital of Central South University and the human ethics identification number is 2021101119. All participants involved in this study provided written informed consent.

The inclusion criteria of stroke patients were as follows: (1) age≥18 years; (2) stroke onset within 48 h; (3) acute stroke confirmed by brain magnetic resonance imaging (MRI) or brain computerized tomography (CT). The exclusion criteria were as follows: (1) active infection or pneumonia before admission; (2) patients treated with nonsteroidal anti-inflammatory drugs; (3) patients with incomplete clinical records. Besides, the diagnosis of SAP was performed by two experienced neurologists based on the modified Centers for Disease Control and Prevention criteria of hospital- acquired pneumonia (22), assisted with clinical and laboratory parameters of respiratory infection and was confirmed by chest X-ray or CT (23).

54 Patients Were Recruited, 4 Patients Were Excluded, and 50 Patients Were Included in This Study. Further, 26 Patients Were Diagnosed in the SAP Group and 24 Patients Were Diagnosed in the Non-SAP Group (**Figure 1**). The SAP Group Was Evaluated by Pneumonia Severity Index (PSI) for Severity and Was Divided Into Severe Group (PSI>90) and the Mild Group (PSI≤90) (24).

Clinical Characteristics and Laboratory Data Collection

Baseline demographic and clinical data were obtained from the medical record system, mainly including age, sex, risk factors or past medical history such as history of smoking and drinking, hypertension, hyperlipidemia, coronary heart disease, chronic obstructive pulmonary disease (COPD), diabetes mellitus, and nephropathy, as well as ICU admission, hospitalization time, stroke subtype. Glasgow coma score (GCS) was used to assess the severity of stroke at admission. Blood samples were collected the morning after admission and tested for the counts of white blood cell (WBC), red blood cell (RBC), hemoglobin, platelets, neutrophils, and lymphocytes. Further, after SAP diagnosis, PSI was used to assess the severity of SAP.

Measurement of 15-PGDH

Blood samples were collected the morning after admission. After centrifugation at 2000 g for 10 min, serum was isolated and frozen at −80°C for later measurement. A Human 15-PGDH/HPGD enzyme-linked immunosorbent assay (ELISA) kit (Cat No. ELH-15PGDH-1, RayBiotech) was used to detect the levels of serum 15-PGDH. Detect and calculate the results according to the instructions of the kit.

Statistical Analysis

All statistical analyses were performed using Statistical Package for the Social Sciences version 26 (SPSS) and R (version 4.1.2).

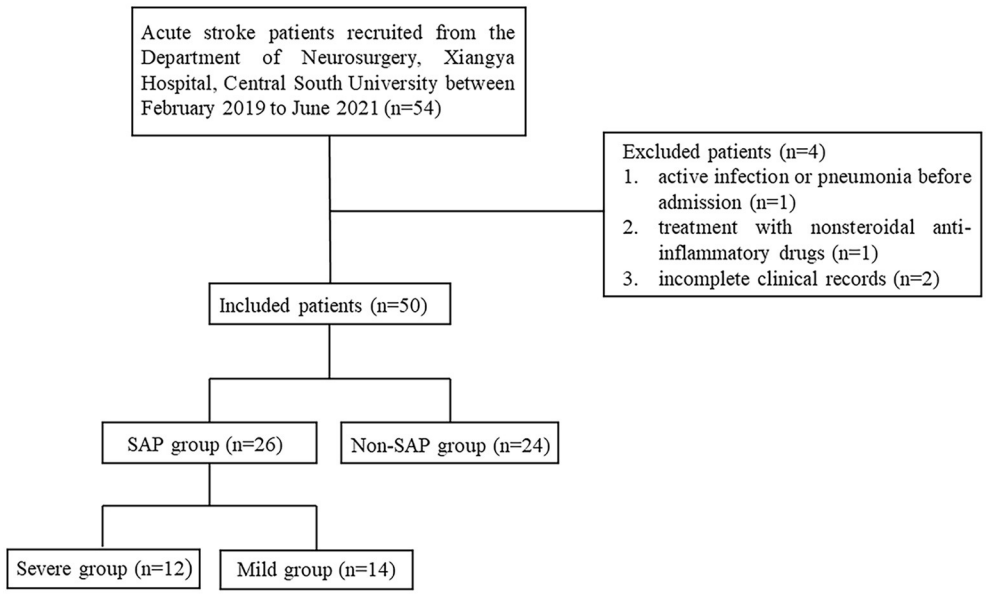

FIGURE 1 | Flowchart of case recruitment. SAP, stroke-associated pneumonia; PSI, pneumonia severity index.

TABLE 1 | Patient characteristics with SAP and Non-SAP with stroke.

Variables	SAP ($n = 26$)	Non-SAP ($n = 24$)	*p*-value
Age, y, mean (SD)	59.2 (11.2)	55 (11.2)	0.011
Sex, male (%)	14 (53.8)	10 (41.7)	0.389
Smoking (%)	10 (38.5)	3 (12.5)	0.037
Drinking (%)	6 (23.1)	2 (8.3)	0.155
Hypertension (%)	15 (57.7)	13 (54.2)	0.802
Hyperlipidemia (%)	2 (7.7)	2 (8.3)	0.934
Coronary heart disease (%)	4 (15.4)	1 (4.2)	0.187
COPD (%)	2 (7.7)	2 (8.3)	0.934
Diabetes mellitus (%)	2 (7.7)	3 (12.5)	0.571
Nephropathy (%)	7 (26.9)	3 (12.5)	0.203
Hemorrhagic stroke (%)	18 (69.2)	14 (58.3)	0.423
GCS, median (IQR)	7.5 (6.3)	11.0 (4.0)	0.029
WBC, 10^9/L	11.7 (6.4)	8.3 (2.3)	0.034
RBC, 10^9/L	3.67 (0.73)	3.76 (0.87)	0.676
Hemoglobin, g/L	117.8 (30.2)	115.0 (28.8)	0.739
Thrombocytes, 10^9/L	176.2 (63.3)	229.7 (104.7)	0.032
Lymphocytes, 10^9/L	1.03 (0.53)	1.26 (0.77)	0.021
Neutrophil, 10^9/L	8.90 (6.30)	6.93 (3.38)	0.012
ICU admission (%)	24 (92.3)	19 (79.2)	0.181
hospitalization time, d, median (IQR)	17.00 (18.00)	12.00 (9.25)	0.039
15-PGDH, ng/mL	0.258 (0.275)	0.784 (0.615)	0.025

SAP, stroke-associated pneumonia; SD, standard deviation; COPD, chronic obstructive pulmonary disease; GCS, Glasgow coma scale; IQR, interquartile range; WBC, white blood cell; RBC, red blood cell; ICU, intensive care unit; 15-PGDH, 15-hydroxyprostaglandin dehydrogenase.

TABLE 2 | Factors contributed to SAP by the multivariate analysis.

Variables	OR	95%CI	*p*-value
Age	1.057	1.026–1.090	<0.001
Smoking	4.375	2.124–9.010	<0.001
GCS	0.754	0.658–0.864	<0.001
WBC	1.283	1.128–1.459	<0.001
Thrombocytes	0.992	0.988–0.996	<0.001
15-PGDH	0.04	0.010–0.157	<0.001
Neutrophil	1.088	1.015–1.166	0.017
Lymphocytes	0.575	0.354-–0.933	0.025

SAP, stroke-associated pneumonia; GCS, Glasgow coma scale; WBC, white blood cell; 15-PGDH, 15-hydroxyprostaglandin dehydrogenase; OR, odds ratio; 95%CI, 95% confidence interval.

Normally distributed continuous variables were presented as the mean ± standard deviation, while other continuous variables were presented as the median and interquartile range (IQR). Continuous variables were analyzed by *t*-test or the Mann–Whitney U-test. Classified data were presented as percentages and analyzed by the chi-square test or Fisher exact test. Binary Logistic regression analysis was used to confirm the contribution of risk factors to SAP occurrence. The receiver operating characteristic (ROC) curve was used to determine the discrimination ability of 15-PGDH levels to predict SAP. The area under the curve (AUC) was determined from the ROC curve analysis. Restricted cubic splines (RCS) with four knots were performed to visualize the relationship between 15-PGDH and SAP risk. All statistical analyses were two-sided and $p<0.05$ was set to be a statistical difference.

RESULTS

Patient Characteristics

From February 2019 to June 2021, 54 stroke patients were recruited from the Department of Neurosurgery, Xiangya

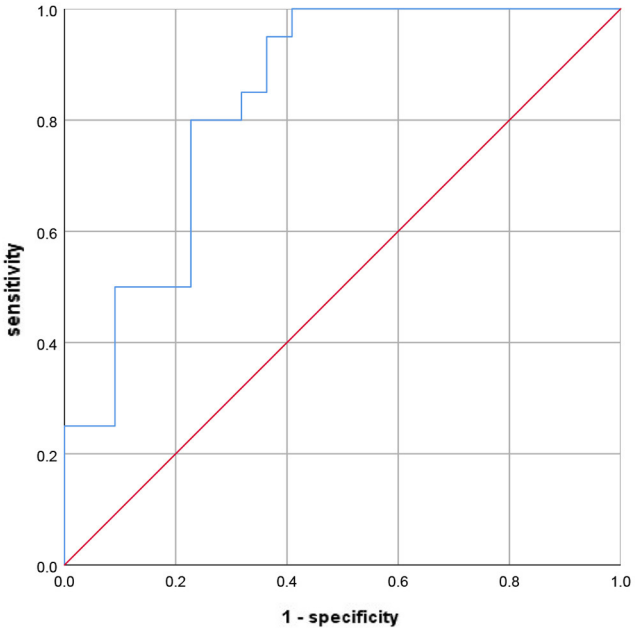

FIGURE 2 | The ROC curve to evaluate the diagnostic value of 15-PGDH for SAP. ROC, receiver operating characteristic; SAP, stroke-associated pneumonia; 15-PGDH, 15-hydroxyprostaglandin dehydrogenase.

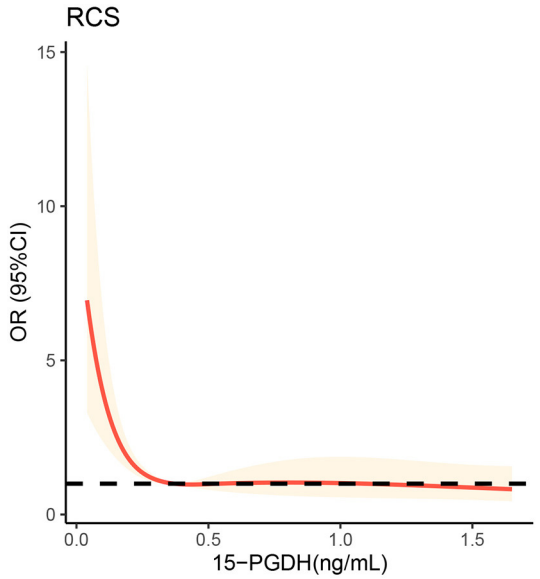

FIGURE 3 | Restricted cubic spline analysis to evaluate the association between serum 15-PGDH levels and risk of SAP. SAP, stroke-associated pneumonia; OR, odds ratio; 95%CI, 95% confidence interval; 15-PGDH, 15-hydroxyprostaglandin dehydrogenase.

Hospital, Central South University. While 4 patients were excluded, 1 patient due to active infection or pneumonia before admission, 1 patient due to treatment with non-steroidal anti-inflammatory drugs, and 2 patients due to incomplete clinical records. Finally, 50 patients were included in the study. Twenty Six patients were assigned to the SAP group (52%) and 24 to the Non-SAP group (48%). Further, according to PSI, the SAP group was further divided into severe group ($n = 12$) and mild group ($n = 14$). These results were summarized in **Figure 1**.

As shown in **Table 1**, age ($p = 0.011$), smoking ($p = 0.037$), the counts of WBC ($p = 0.034$) and neutrophils ($p = 0.012$) and hospitalization time ($p = 0.039$) in SAP group were significantly higher than those in Non-SAP group, and GCS score ($p = 0.029$), the counts of thrombocytes ($p = 0.032$) and lymphocytes ($p = 0.021$) in SAP group were significantly lower than those in Non-SAP group. While other variables including sex, drinking, hypertension, hyperlipidemia, coronary heart disease, COPD, diabetes mellitus, nephropathy, stroke type, the counts of RBC and hemoglobin were not statistically different. Notably, the level of 15-PGDH ($p = 0.025$) in the SAP group was significantly lower than that in the Non-SAP group, indicating that there may be some relationship between 15-PGDH and SAP, which is what we will analyze next.

15-PGDH Is Valuable to Predict SAP

A binary logistic regression analysis was performed to determine which variables could be potential for predicting SAP. As shown in **Table 2**, higher age (OR = 1.057, 95%CI = 1.026–1.090, $p < 0.001$), smoking (OR = 4.375, 95%CI = 2.214–9.010, $p < 0.001$), WBC (OR = 1.283, 95%CI = 1.128–1.459, $p < 0.001$), neutrophil (OR = 1.088, 95%CI = 1.015–1.166, $p = 0.017$) and lower GCS (OR = 0.754, 95%CI = 0.658–0.864, $p < 0.001$), thrombocytes (OR = 0.992, 95%CI = 0.988–0.996, $p < 0.001$), lymphocytes (OR = 0.575, 95%CI = 0.354–0.933, $p = 0.025$) were risk factors of SAP.

Notably, lower 15-PGDH (OR = 0.040, 95%CI = 0.010–0.157, $p < 0.001$) was also a risk factor for SAP. Further, according to the ROC curve in **Figure 2**, the AUC of 15-PGDH for predicting SAP was 0.836, 95%CI = 0.751–0.922, $p < 0.001$. Besides, the

TABLE 3 | Patient characteristics with severe SAP and mild SAP.

Variables	Severe group ($n = 12$)	Mild group ($n = 14$)	*p*-value
Age, y, mean (SD)	64.9 (9.7)	53.5 (9.8)	<0.001
Sex, male (%)	7 (58.3)	7 (50.0)	0.671
Smoking (%)	5 (41.7)	5 (35.7)	0.756
Drinking (%)	3 (25.0)	3 (21.4)	0.829
Hypertension (%)	8 (66.7)	6 (42.9)	0.225
Nephropathy (%)	4 (33.3)	3 (21.4)	0.495
GCS, median (IQR)	7.5 (3.5)	9.0 (3.0)	0.376
WBC, 10^9/L	12.2 (7.9)	9.3 (4.2)	0.017
Thrombocytes, 10^9/L	155.9 (47)	193.5 (68.8)	0.002
Lymphocytes, 10^9/L	0.98 (0.53)	1.06 (0.34)	0.391
Neutrophil, 10^9/L	10.4 (8.2)	7.5 (4.1)	0.018
Hospitalization time, d, median (IQR)	21 (24.5)	20 (12.5)	0.786

SAP, stroke-associated pneumonia; SD, standard deviation; GCS, Glasgow coma scale; IQR, interquartile range; WBC, white blood cell.

optimal cutoff value of 15-PGDH for SAP was 0.186 ng/mL, with a specificity of 100% and a sensitivity of 59.1%.

To further visualize the relationship between 15-PGDH and SAP risk, restricted cubic spline was next performed. As shown in the **Figure 3**, the lowest level of 15-PGDH represented the highest risk of SAP. With the increase of 15-PGDH, the risk of SAP decreases continuously. In particular, 0.37 ng/ mL was a point of interest. When it was lower than 0.37 ng/ mL, the risk of SAP increased sharply with the decrease of 15-PGDH, while when it was higher than 0.37 ng/ mL, the risk of SAP increased relatively gentle.

Patient Characteristics With Severe SAP and Mild SAP

According to PSI, the SAP group was further divided into severe group ($n = 12$) and mild group ($n = 14$). There were some differences between the two groups in terms of patient characteristics in **Table 3**. Patients in the severe group observed higher age ($p < 0.001$), WBC count ($p = 0.017$) and neutrophils count ($p = 0.018$) than those in the mild group.

DISCUSSION

Two important findings are presented in this study. First, lower serum 15-PGDH increases the risk of SAP in stroke patients. Second, there is an L-shaped relationship between 15-PGDH and SAP risk. Once 15-PGDH is lower than the critical value, SAP risk will be significantly increased.

Stroke is an acute neurovascular disease with high morbidity, mortality and disability. SAP is the most common complication of stroke, usually manifests within 7 days after the onset of stroke (3). The complication of SAP further aggravates the severity of stroke, prolonged hospitalization, worsen the prognosis, and increase mortality (6, 10). The occurrence of SAP increases the difficulty of stroke treatment. Therefore, the prevention and early prediction or diagnosis of SAP should not be ignored in the treatment of stroke patients. Our study demonstrates that advanced age, smGoking, higher WBC and neutrophils, and lower GCS, thrombocytes, and lymphocytes are all risk factors for SAP. In addition, previous studies have found that dysphagia (25), aspiration (26), invasive treatments, antacids, hypertension, diabetes, pulmonary diseases and so on are also risk factors for SAP (27). Prevention and early diagnosis of so many risk factors are an important part of stroke and SAP management.

Inflammation-related indicators are the most important predictive markers of SAP and contribute greatly to the early diagnosis of SAP. Monocyte to lymphocyte ratio (28), neutrophil to lymphocyte ratio (24) and platelet to lymphocyte ratio (29) have been proven to be valuable predictors of SAP markers. PGE2 is an important inflammatory mediator involved in many inflammatory processes. As the degradation enzyme of PGE2, 15-PGDH is potential to become one predictive marker of SAP. In our study, serum 15-PGDH level in patients with SAP were significantly lower than those without SAP. Binary logistic regression analysis proved that low 15-PGDH was a risk factor for SAP. With an AUC of 0.836, 15-PGDH is undoubtedly a valuable predictor of SAP. Furthermore, RCS visualizes the relationship between 15-PGDH and SAP risk as L-shaped, which may contribute significantly to the prediction and treatment of SAP. It should be noted that the 15-PGDH concentration of 0.37 ng/mL is a critical threshold. When 15-PGDH is lower than 0.37 ng/mL, its decrease will sharply increase the risk of SAP, while when higher than 0.37 ng/mL, this trend is very gentle. Therefore, when assessing the risk of SAP, on the premise of avoiding the reduction of 15-PGDH, it is more important to ensure that 15-PGDH should not be lower than 0.37 ng/mL, which may be critical for SAP prevention.

Admittedly, there are some limitations to our research. First, since our study is a retrospective study, it is difficult to draw a causal relationship between 15-PGDH and SAP, which requires further verification by subsequent studies. Second, we did not collect enough patients, which may lead to partial results bias. For example, the incidence of SAP was higher than previously reported. Third, although we compared the characteristics of SAP patients in the severe group and mild group, it is unclear whether the level of 15-PGDH is predictive of the severity of SAP. Furthermore, we did not analyze patients with different stroke types separately, and there may be some different findings.

CONCLUSION

In stroke patients, serum 15-PGDH is a valuable biomarker for predicting SAP. There is an L-shaped relationship between the level of 15-PGDH and the risk of SAP. Once lower than 0.37 ng/mL, the risk of SAP will increase rapidly.

DATA AVAILABILITY STATEMENT

The original contributions presented in the study are included in the article/supplementary material, further inquiries can be directed to the corresponding authors.

ETHICS STATEMENT

The studies involving human participants were reviewed and approved by the Ethics Committee of the Xiangya Hospital of Central South University. The patients/participants provided their written informed consent to participate in this study.

AUTHOR CONTRIBUTIONS

DY, YL, and JZ designed and directed the project. SY collected clinical samples. HQ collected baseline demographic and clinical data. YX, LZ, YZ, and QX performed the experiments. YX wrote the manuscript.

FUNDING

This work was supported by the National Natural Science Foundation of China (Nos. 82172147, 81571880, 81373147, 30901555, 30972870, and 81360080), Natural Science Foundation of Hunan Province (2021JJ30900 and 2016JJ2157), and the

Fundamental Research Funds for the Central Universities of Central South University (2020zzts222). All funding bodies were involved in the study design, collection, analysis, interpretation of data, and writing the manuscript.

ACKNOWLEDGMENTS

We thank the patients for granting permission to publish this information.

REFERENCES

1. Global, regional, and national burden of stroke and its risk factors, 1990-2019: a systematic analysis for the global burden of disease study 2019. *Lancet Neurol.* 2021 20:795–820. doi: 10.1016/S1474-4422(21)00252-0
2. Cugy E, Sibon I. Stroke-Associated pneumonia risk score: validity in a French stroke unit. *J Stroke Cerebrovasc Dis.* (2017) 26:225–9. doi: 10.1016/j.jstrokecerebrovasdis.2016.09.015
3. Kishore AK, Vail A, Chamorro A, Garau J, Hopkins SJ, Di Napoli M, et al. How is pneumonia diagnosed in clinical stroke research? a systematic review and meta-analysis. *Stroke.* (2015) 46:1202–9. doi: 10.1161/STROKEAHA.114.007843
4. Chen Y, Yang H, Wei H, Chen Y, Lan M. Stroke-associated pneumonia: a bibliometric analysis of worldwide trends from 2003 to 2020. *Medicine (Baltimore).* (2021) 100:e27321. doi: 10.1097/MD.0000000000027321
5. Johnston KC Li JY, Lyden PD, Hanson SK, Feasby TE, Adams RJ, et al. Medical and neurological complications of ischemic stroke: experience from the RANTTAS trial. *RANTTAS Investigators Stroke.* (1998) 29:447–53. doi: 10.1161/01.str.29.2.447
6. Finlayson O, Kapral M, Hall R, Asllani E, Selchen D, Saposnik G. Risk factors, inpatient care, and outcomes of pneumonia after ischemic stroke. *Neurology.* (2011) 77:1338–45. doi: 10.1212/WNL.0b013e31823152b1
7. Faura J, Bustamante A, Miró-Mur F, Montaner J. Stroke-Induced immunosuppression: implications for the prevention and prediction of post-stroke infections. *J Neuroinflammation.* (2021) 18:127. doi: 10.1186/s12974-021-02177-0
8. Suda S, Aoki J, Shimoyama T, Suzuki K, Sakamoto Y, Katano T, et al. Stroke-associated infection independently predicts 3-month poor functional outcome and mortality. *J Neurol.* (2018) 265:370–5. doi: 10.1007/s00415-017-8714-6
9. Teh WH, Smith CJ, Barlas RS, Wood AD, Bettencourt-Silva JH, Clark AB, et al. Impact of stroke-associated pneumonia on mortality, length of hospitalization, and functional outcome. *Acta Neurol Scand.* (2018) 138:293–300. doi: 10.1111/ane.12956
10. Smith CJ, Bray BD, Hoffman A, Meisel A, Heuschmann PU, Wolfe CD, et al. Can a novel clinical risk score improve pneumonia prediction in acute stroke care? *a* UK multicenter cohort study. *J Am Heart Assoc.* (2015) 4:e001307. doi: 10.1161/JAHA.114.001307
11. Warusevitane A, Karunatilake D, Sim J, Smith C, Roffe C. Early diagnosis of pneumonia in severe stroke: clinical features and the diagnostic role of C-reactive protein. *PLoS ONE.* (2016) 11:e0150269. doi: 10.1371/journal.pone.0150269
12. Mahesh G, Anil Kumar K, Reddanna P. Overview on the discovery and development of anti-inflammatory drugs: should the focus be on synthesis or degradation of PGE(2)? *J Inflamm Res.* (2021) 14:253–63. doi: 10.2147/JIR.S278514
13. Shin MK, Koh Y, Vázquez-Rosa E, Cintrón-Pérez C, Markowitz S, Pieper AA. Inhibition of 15-hydroxyprostaglandin dehydrogenase protects a mouse model of Alzheimer's disease without affecting amyloid pathology. *Alzheimers Dement.* (2021) 17 (Suppl. 3):e052500. doi: 10.1002/alz.052500
14. Xu Y, Liu Y, Li K, Miao S, Lv C, Wang C, et al. Regulation of PGE(2) pathway during cerebral ischemia reperfusion injury in Rat. *Cell Mol Neurobiol.* (2021) 41:1483–96. doi: 10.1007/s10571-020-00911-5
15. Wang W, Yang C, Deng H. Overexpression of 15-hydroxyprostaglandin dehydrogenase inhibits A549 lung adenocarcinoma cell growth via inducing cell cycle arrest and inhibiting epithelial-mesenchymal transition. *Cancer Manag Res.* (2021) 13:8887–900. doi: 10.2147/CMAR.S331222
16. Volpato M, Cummings M, Shaaban AM, Abderrahman B, Hull MA, Maximov PY, et al. Downregulation of 15-hydroxyprostaglandin dehydrogenase during acquired tamoxifen resistance and association with poor prognosis in ERα-positive breast cancer. *Explor Target Antitumor Ther.* (2020) 1:355–71. doi: 10.37349/etat.2020.00021
17. Zhang S, Liu J, Yang M, Fan D, Gao J, Liu X, et al. Single nucleotide polymorphism rs2555639 in 15-PGDH and colorectal cancer metastasis. *J buon.* (2019) 24:1507–11.
18. Miao S, Lv C, Liu Y, Zhao J, Li T, Wang C, et al. Pharmacologic blockade of 15-PGDH protects against acute renal injury induced by LPS in mice. *Front Physiol.* (2020) 11:138. doi: 10.3389/fphys.2020.00138
19. Smith JNP, Witkin MD, Jogasuria AP, Christo KF, Raffay TM, Markowitz SD, et al. Therapeutic targeting of 15-PGDH in murine pulmonary fibrosis. *Sci Rep.* (2020) 10:11657. doi: 10.1038/s41598-020-68336-0
20. Palla AR, Ravichandran M, Wang YX, Alexandrova L, Yang AV, Kraft P, et al. Inhibition of prostaglandin-degrading enzyme 15-PGDH rejuvenates aged muscle mass and strength. *Science.* (2021) 371:abc8059. doi: 10.1126/science.abc8059
21. Mao YX, Xu JF, Seeley EJ, Tang XD, Xu LL, Zhu YG, et al. Adipose tissue-derived mesenchymal stem cells attenuate pulmonary infection caused by pseudomonas aeruginosa via inhibiting overproduction of prostaglandin E2. *Stem Cells.* (2015) 33:2331–42. doi: 10.1002/stem.1996
22. Smith CJ, Kishore AK, Vail A, Chamorro A, Garau J, Hopkins SJ, et al. Diagnosis of stroke-associated pneumonia: recommendations from the pneumonia in stroke consensus group. *Stroke.* (2015) 46:2335–40. doi: 10.1161/STROKEAHA.115.009617
23. Shi G, Li M, Zhou R, Wang X, Xu W, Yang F, et al. Procalcitonin related to stroke-associated pneumonia and clinical outcomes of acute ischemic stroke after IV rt-PA treatment. *Cell Mol Neurobiol.* (2021). doi: 10.1007/s10571-020-01031-w
24. Nam KW, Kim TJ, Lee JS, Kwon HM, Lee YS, Ko SB, et al. High neutrophil-to-lymphocyte ratio predicts stroke-associated pneumonia. *Stroke.* (2018) 49:1886–92. doi: 10.1161/STROKEAHA.118.021228
25. Eltringham SA, Kilner K, Gee M, Sage K, Bray BD, Smith CJ, et al. Factors associated with risk of stroke-associated pneumonia in patients with dysphagia: a systematic review. *Dysphagia.* (2020) 35:735–44. doi: 10.1007/s00455-019-10061-6
26. Hannawi Y, Hannawi B, Rao CP, Suarez JI, Bershad EM. Stroke-associated pneumonia: major advances and obstacles. *Cerebrovasc Dis.* (2013) 35:430–43. doi: 10.1159/000350199
27. Liu DD, Chu SF, Chen C, Yang PF, Chen NH, He X. Research progress in stroke-induced immunodepression syndrome (SIDS) and stroke-associated pneumonia (SAP). *Neurochem Int.* (2018) 114:42–54. doi: 10.1016/j.neuint.2018.01.002
28. Cheng HR, Song JY, Zhang YN, Chen YB, Lin GQ, Huang GQ, et al. High monocyte-to-lymphocyte ratio is associated with stroke-associated pneumonia. *Front Neurol.* (2020) 11:575809. doi: 10.3389/fneur.2020.575809
29. Altintas O, Altintas MO, Tasal A, Kucukdagli OT, Asil T. The relationship of platelet-to-lymphocyte ratio with clinical outcome and final infarct core

in acute ischemic stroke patients who have undergone endovascular therapy. *Neurol Res.* (2016) 38:759–65. doi: 10.1080/01616412.2016.1215030

Conflict of Interest: The authors declare that the research was conducted in the absence of any commercial or financial relationships that could be construed as a potential conflict of interest.

Publisher's Note: All claims expressed in this article are solely those of the authors and do not necessarily represent those of their affiliated organizations, or those of the publisher, the editors and the reviewers. Any product that may be evaluated in this article, or claim that may be made by its manufacturer, is not guaranteed or endorsed by the publisher.

Copyright © 2022 Xu, Qiao, Yang, Zhou, Zhao, Xu, Miao, Yuan, Zhao and Liu. This is an open-access article distributed under the terms of the Creative Commons Attribution License (CC BY). The use, distribution or reproduction in other forums is permitted, provided the original author(s) and the copyright owner(s) are credited and that the original publication in this journal is cited, in accordance with accepted academic practice. No use, distribution or reproduction is permitted which does not comply with these terms.

frontiers | Frontiers in Neurology

ORIGINAL RESEARCH
published: 01 June 2022
doi: 10.3389/fneur.2022.881190

Decreased Macular Retinal Thickness in Patients With Pterygium

Feng Wang[1†], Li Qi Liu[2†], Rong Bin Liang[2†], Li Juan Zhang[2], Hui Ye Shu[2], Xu Lin Liao[3], Yi Cong Pan[2], Jie Li Wu[4], Ting Su[4,5] and Yi Shao[2]*

[1] Department of Ophthalmology, Meizhou Pepole's Hospital, Meizhou, China, [2] Department of Ophthalmology, First Affiliated Hospital of Nanchang University, Nanchang, China, [3] Department of Ophthalmology and Visual Sciences, The Chinese University of Hong Kong, Shatin, Hong Kong SAR, China, [4] Department of Ophthalmology, Xiang'an Hospital of Xiamen University, Xiamen, China, [5] Department of Ophthalmology, Massachusetts Eye and Ear Infirmary, Harvard Medical School, Boston, MA, United States

Purpose: To explore alterations in macular retinal thickness (RT) and analyze correlation between macular RT and pterygium area, length in pterygium patients.

Methods: Totally 13 patients with pterygium (left eye) and 13 healthy controls (left eye) were recruited. OCTA was applied to scan each eye to generate three-dimensional images. Based on the Early Treatment Diabetic Retinopathy Study (ETDRS) method, each image was divided into nine subregions for the ETDRS: central (C); inner superior (IS); outer superior (OS); inner nasal (IN); outer nasal (ON); inner inferior (II); outer inferior (OI); inner temporal (IT); and outer temporal (OT). The macular RT in each subregion was measured. Furthermore, the correlation between RT and the area, length of pterygium was analyzed.

Results: The visual acuity of pterygium patient was different from that of the control ($P < 0.05$). Besides, decreased intraretinal thickness of the IN and ON, increased intraretinal thickness of OT, decreased extraretinal thickness of OT, IN, ON, OS, and decreased retinal full layer thickness of medial superior, OS, IN, ON, and II subregions in pterygium group were observed. There was a negative correlation between RT of the IN and ON subregions and the length of pterygium ($r = -0.5803$ and $r = -0.6013$, $P = 0.0376$ and $P = 0.0297$). The RT of IN subregion was negatively correlated with pterygium area ($r = -0.5844$, $P = 0.0359$). According to the receiver operating characteristic analysis, in the ON subregion, the areas under the curve of the inner retinal thickness, outer retinal thickness and the whole retinal thickness were 1.0 (95% CI: 1.0), 0.882 (95% CI: 0.715 and 0.963), and 1.0 (95% CI: 1.0). The smallest area under the curve of retinal thickness in OT subregion was 0.018 (95% CI: 0–0.059).

Conclusion: RT of pterygium patients was significantly decreased, and the main alterations occurred in the temporal side suggesting there might exist retinal structural alterations in pterygium.

Keywords: pterygium, optical coherence tomography angiography, macular, retinal thickness, examine

OPEN ACCESS

Edited by:
Yuzhen Xu,
Tongji University, China

Reviewed by:
Qinxiang Zheng,
Wenzhou Medical University, China
He Wang,
Xuzhou Medical University, China

***Correspondence:**
Yi Shao
freebee99@163.com

[†]These authors have contributed equally to this work

Specialty section:
This article was submitted to Neurological Biomarkers, a section of the journal Frontiers in Neurology

Received: *22 February 2022*
Accepted: *28 April 2022*
Published: *01 June 2022*

Citation:
Wang F, Liu LQ, Liang RB, Zhang LJ, Shu HY, Liao XL, Pan YC, Wu JL, Su T and Shao Y (2022) Decreased Macular Retinal Thickness in Patients With Pterygium. Front. Neurol. 13:881190. doi: 10.3389/fneur.2022.881190

INTRODUCTION

Pterygium is an ocular disorder occurring on the surface of the eye. The main characteristic is the pterygoid growth which could invade the limbus and conjunctiva on the adjacent cornea (1). The prevalence of pterygium ranges from 3 to 19.5% (2); although it typically occurs in the lateral nasal position, it occasionally develops in both directions (3). The pathogenesis of pterygium is currently unclear; however, research suggests that environmental factors, especially ultraviolet radiation (UV), play an important part (3, 4). Surgical resection is the only effective treatment for pterygium. However, depending on the technology used, the risk of recurrence can be as high as 89% (3). Therefore, the long-term efficacy of surgery is debatable. Corneal irregularity has an important influence on maintaining good eyesight after surgery. The improvement will not be evident in the early postoperative period. Hence, the evaluation of visual function has important clinical significance in determining whether surgery should be performed (5). Nevertheless, the human fundus macular area is responsible for almost the entire vision of humans and contains the highest distribution of visual (6) and retinal ganglion cells.

Recent studies have shown that changes in the anterior segment can also cause changes in macular structure. Zhang et al. (7) found that in the unilateral congenital cataract patients, the results of OCTA recorded after cataract surgery revealed increased vascular density and retinal thickness (RT), compared with that recorded before surgery. These findings suggested that the refractive axis became transparent after alleviating visual deprivation in the affected eyes would increase the light stimulation to fundus and change the structure. This increases the amount of light signal stimulation that enters the eye. Srujana et al. (8) used OCT to analyze 67 cases of keratoconus (129 eyes) and 87 cases of non-keratoconus (174 eyes). The average RT of the central fovea and macular area of keratoconus patients was lager than that of the control. They hypothesized that macular changes may be related to broader eye structural disorders of patients with keratoconus or optimization of the compensation mechanism of corneal irregular vision. Extension of pterygium beyond 2.2 mm results in obvious corneal astigmatism (9). Corneal astigmatism (mainly regular) or direct invasion of the visual axis will lead to visual problems (10). As a non-invasive *in vivo* imaging technique, OCTA can display morphological and quantitative information regarding fudus alterations in detail (11), including microvascular system of the retina and choroid (12), which is helpful to diagnose of myopia (13), microvascular changes in macular area after Phacoemulsification (14), glaucoma (15), thyroid-associated ophthalmology (TAO) (16) etc. Thus far, OCTA has not been used to study whether macular area changes is related to pterygium or not. In this study, we used OCTA to analyze the macular retina of all subjects and investigate changes of RT. The correlation between macular RT and pterygium length and area in patients with pterygium was also evaluated.

MATERIALS AND METHODS

Research Subjects

This retrospective cross-sectional study was carried out at The First Affiliated Hospital of Nanchang University (Nanchang, China) in 2021. All subjects were recruited from the Outpatient Department and examined by the same retina specialist and divided into two groups. Patients diagnosed with pterygium belong to the experimental group and healthy subjects matched for sex and age with no ocular or systemic disease constitute the control.

Recruitment Criteria

A total of 26 subjects, including 13 patients with primary pterygium in the left eye (pterygium group; aged 40–52 years; mean age: 46 ± 3 years) and 13 healthy individuals (control group; 13 left eyes; mean age: 45 ± 4 years) were recruited. The clinical condition score was evaluated using the NOSPECS classification, and inflammation score would be determined through the 7-point Clinical Activity Score. The control group included healthy subjects without ocular abnormalities according to clinical examination at the medical center and the OCTA imaging examination did not display any disorder.

Inclusion criteria (1) Patient who was diagnosed with pterygium in left eye for the first time (2) The primary pterygiod growth occurred in the nasal side; (3) A medical history of 7 months to 20 years, with an average of 8.77 ± 5.94 years; (4) pterygium invasion toward the corneal limbus is almost 2.0–7.0 mm; (5) binocular visual acuity was in the normal range (without anisometropia >2 D); (6) the intraocular pressure ranged from 10 to 21 mmHg; (7) Fundus examination did not display obvious abnormality.

Exclusion condition (1) the medical history of ocular trauma and surgery; (2) drug treatment or radiotherapy within the recent 14 days; (3) anterior abnormality, such as corneal diseases (including patients who wear corneal contact lens, pseudopterygium and fibromyalgia), glaucoma, cataract; (4) retinal abnormality, such as highly myopic, maculopathy and retinal detachment (5) systemic diseases which can affect ocular vasculature, such as diabetes, hypertension, nephropathy; (6) patients with amblyopia; (7) patients with systemic diseases such as autoimmune diseases and nervous diseases; (8) pregnancy and lactating women; (9) Pupil dilation and patients who are sensitive to mydriatic. The general condition of the patients and condition of pterygium are shown in **Table 1**.

Ethical Considerations

The study was carried out in accordance with the principles of the Helsinki Declaration seriously and was approved by the Medical Ethics Committee of Nanchang University. Before the consent forms were signed, all subjects had comprehended the objectives and methods.

Clinical Examinations

Volunteers completed the following testings.

(1) Slit lamp examination. The anterior segment of the eye was examined by Slit lamp microscopy including ocular surface inflammation, cataract with severe intraocular astigmatism, the pterygium size;

(2) Optometry. Obtain corrected binocular visual acuity of all participants by standard logarithmic visual acuity chart;

(3) Intraocular pressure (IOP). Measure intraocular pressure by transpalpebral diatom tonometer (TDT,

TABLE 1 | Demographic characteristics and clinical findings of patients with Pterygium and HCs.

Condition	Pterygium	HC	t	*p*-Value*
Age(years)	46 ± 3	45 ± 4	0.40	0.69
Sex(male/female)	2/11	2/11	N/A	>0.99
uncorrected visual acuity	0.6 ± 0.1	0.9 ± 0.1	0.39	0.04*
Best-corrected visual acuity	0.7 ± 0.1	1 ± 1	0.35	0.04*
SE-L(diopter)	1.15 ± 1.00	1.25 ± 0.75	0.19	0.83
Astigmatism -L(diopter)AL(mm)	2.75 ± 0.75 23.53	1.25 ± 0.5023.72	4.17 0.12	0.03*0.89
SSI	9 ± 1	9 ± 1	N/A	>0.99
The course of pterygium(years)	8.77 ± 5.94	/	/	/
The Length of pterygium(mm)	5.24 ± 0.89	/	/	/
The height of pterygium(mm)	5.84 ± 1.20	/	/	/
The area of pterygium(mm)	16.62 ± 5.72	/	/	/
Heart rate(beats/min)	70 ± 6	69 ± 7	−0.13	0.98
Systolic blood pressure(mm Hg)	124 ± 6	123 ± 10	−0.25	0.89
Diastolic blood pressure(mmHg)	82 ± 7	83 ± 6	−0.12	0.73
Mean intra-ocular pressure(mmHg)	15 ± 2	14 ± 3	−0.25	0.81

**P < 0.05 Independent t-tests comparing two groups.*
HC, healthy control; N/A, not applicable; L, left; SE, Spherical equivalent; AL, axial length; SSI, Signal strength Index.

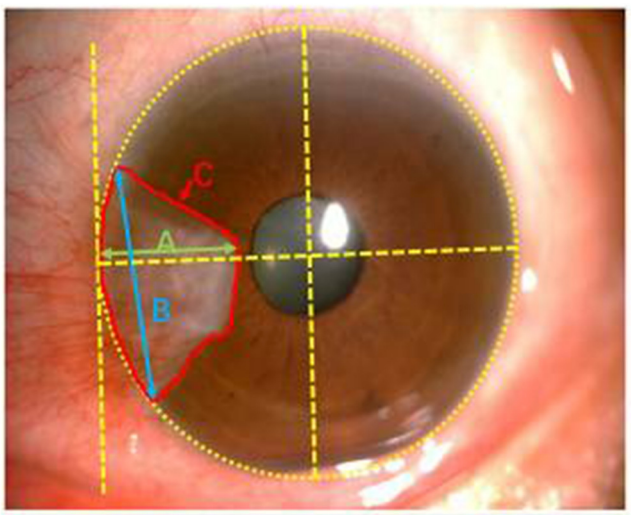

FIGURE 1 | Note clinical photographic imaging using Zeiss slit lamp mounted camera and nihimage J software to measure the size of pterygium. Green, blue and red lines depict length (A), height (B) and area (C), respectively.

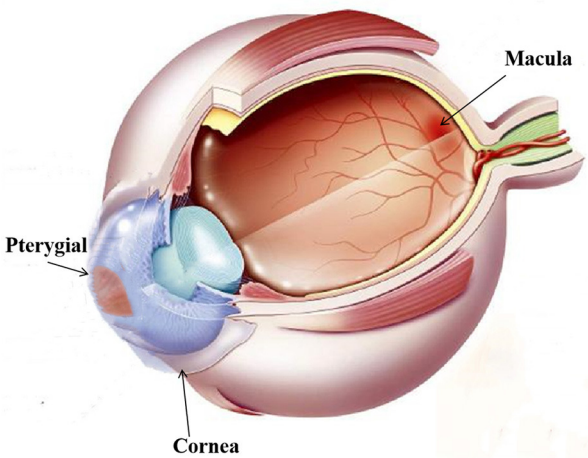

FIGURE 2 | Illustration of the pterygium and macular retinal thickness area: As shown in the figure, see the pterygium of the nasal limbus of the left eye and the macula of the fundus.

BiCOM, Long Beach, NY, USA) for 3 times and calculatethe average values. IOP recorded of both eyes are in the normal range. The D-value between the different measurements of the same one was ≤3 mmHg.

(4) Calculate the size of pterygium by ImageJ software (WayneRasband,NIH,USA). The horizontal distance between corneal limbus and pterygium head is length. The distance between upper and lower point where pterygium grows into the limbus is the height, and coverage of pterygium to cornea is the area (**Figure 1**) (17). Measure the length (A), height (B) and area (C) of each meat for 5 times, and calculate the average.

OCTA Imaging

We used RTVue Avanti XR system to performed OCTA imaging and display both the cross-section of the retina and microvasculature. The scanning speed was set at 70,000 A-scans/s; the axial resolution was 5 mm; the horizontal resolution was 22 μm; the central wavelength was 840 nm; and the bandwidth was 45 nm. The imaging time was 3.9 s. Five angiograms were performed in the 3 × 3 mm scan mode,

focusing on the fovea along the x axis (total: 216 A-scans) and along the y axis (216 raster positions per scan). At 216 y positions ×5 positions, we captured 1,080 B-scans at a speed of 270 frames (33 frames) pers. Following four volume scans, 6 × 6 mm OCTA images were obtained. Also, the 3 × 3 mm macular retinal image of each eye was obtained. According to the ETDRS, retina of each eye was divided into 9 subregions. Three cercles concentriques composed them. The radii were set at 0.5, 1.5 and 3 mm, respectively. These subregions whose thickness was analyzed were as follows: outer superior (OS); outer temporal (OT); outer nasal (ON); outer inferior (OI); inner superior (IS); inner temporal (IT); inner nasal (IN); inner inferior (II) and central (C); Each retinal layer includes the inner retina and the full-year retina. The relationship between pterygium and the retinal fovea is illustrated in **Figure 2**. The partition of macular retinal area is shown in **Figures 3A–C**.

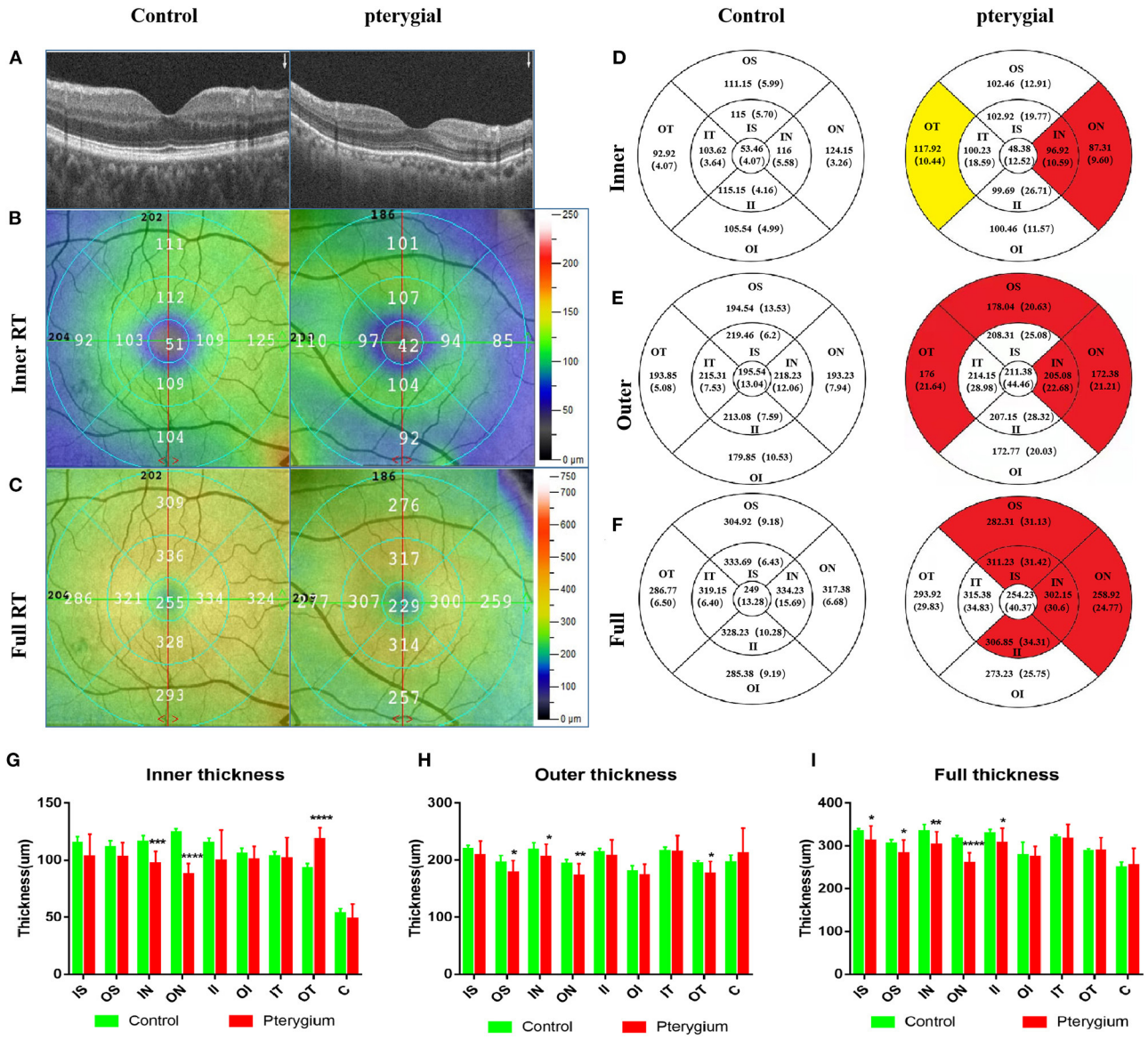

FIGURE 3 | OCTA images and RT analysis of the control group and pterygium group. **(A)** RT cross sections of the control group and pterygium group measured by OCTA. **(B)** Internal RT was measured with ETDRS. **(C)** Complete RT measurement diagram. **(D)** Internal RT measurement results of the control group and pterygium group (red area indicates the area with significant decrease in retinal thickness, yellow area indicates the area with significant increase in retinal thickness, $P < 0.05$). **(E)** External RT measurements in the control group and pterygium group **(F)** complete RT measurements. **(G–I)** Analysis of retinal thickness results in the control group and pterygium group. OCTA, optical coherence tomography angiography; RT, retinal thickness; ETDRS, early treatment of diabetic retinopathy study; IS, inner superior; OS, outer superior; IN, inner nasal; ON, outer nasal; II, inner inferior; OI, outer inferior; IT, inner temporal; OT, outer temporal; C, center. $^{*}P < 0.05$; $^{**}P < 0.01$; $^{***}P < 0.001$; $^{****}P < 0.0001$.

Statistical Analysis

All data were analyzed by statistical software package (statistica, v7.1; StatSoft, Inc, Tulsa, OK, USA) and medcalc software (V10; medcalc software, mariakerke, Belgium). Continuous variables are proposed to be expressed as mean ± standard deviation (SD). RT of each subregion among each group was analyzed by One Way ANOVA. The difference between two group was access from minimum significant difference by a specific test. $P < 0.05$ was statistically significant. Graphpad prism 7.0 was used to analyzed the correlation between retinal thickness and the length, width and area of pterygium. Use Graphpad prism 7.0 to analyze the relation between RT and pterygium size, and the Receiver Operator Characteristic (ROC) curves of retinal thickness in the retinal epithelium was plotted by SPSS 23.0 (IBM Corp, Armonk, NY, USA) to differentiate between patients with pterygium and healthy subjects.

RESULTS

Macular Retinal Thickness

Regional retinal thicknesses of the experimental and the control is shown in **Table 2**. The internal RT in the IN and ON subregions of patient were lower than that recorded in the control ($P = 0.0001$, $P < 0.0001$, respectively). The internal RT of the OT subregion in the patient with pterygium was higher than that recorded in the healthy ($P < 0.0001$) (**Figures 3D,G**). Three other domains of the inner loop (superior part: $P = 0.0703$; lower part: $P = 0.0673$; temporal part: $P = 0.6463$, respectively), two subregions of the outer loop (superior part: $P = 0.0547$; lower part: $P = 0.1543$, respectively), C subregions ($P = 0.1921$) were not distinctly different when comparing those two groups.

The external retinal thicknesses in the IN, ON, OT, and OS subregions of pterygium were lower than that measured in the healthy ($P = 0.0268$, $P = 0.0062$, $P = 0.0180$, P 0.0454)

TABLE 2 | Comparison of macular retinal thickness at different locations between patients with Pterygium and health controls.

Location	Pterygium (n = 13,13 eyes)	HC (n = 13,13 eyes)	p-Value[a]
Macular inner retinal thickness (μm, mean ± SD)			
IS	115.00 ± 5.70	102.92 ± 19.77	0.0703
OS	111.15 ± 5.99	102.92 ± 19.77	0.0547
IN	116.00 ± 5.58	96.92 ± 10.59	**0.0001**
ON	124.15 ± 3.26	87.31 ± 9.60	**<0.0001**
II	115.15 ± 4.16	99.69 ± 26.71	0.0673
OI	105.54 ± 4.99	100.46 ± 11.57	0.1543
IT	103.62 ± 3.64	100.23 ± 18.59	0.6463
OT	92.92 ± 4.07	117.92 ± 10.44	**<0.0001**
C	53.46 ± 4.07	48.38 ± 12.52	0.1921
Macular outer retinal thickness (μm, mean ± SD)			
IS	219.46 ± 6.20	208.31 ± 25.08	0.1366
OS	194.54 ± 13.53	178.04 ± 20.08	**0.0454**
IN	218.23 ± 12.06	205.08 ± 22.68	**0.0268**
ON	193.23 ± 7.94	172.38 ± 21.21	**0.0062**
II	213.08 ± 7.59	207.15 ± 28.32	0.4172
OI	179.85 ± 10.53	172.77 ± 20.03	0.2649
IT	215.31 ± 7.53	214.15 ± 28.98	0.8775
OT	193.85 ± 5.08	176.00 ± 21.64	**0.0180**
C	195.54 ± 13.04	211.38 ± 44.46	0.2837
Macular full retinal thickness (μm, mean ± SD)			
IS	333.69 ± 6.43	311.23 ± 31.42	**0.0398**
OS	304.92 ± 9.18	311.23 ± 31.42	**0.0283**
IN	334.23 ± 15.69	302.15 ± 30.6	**0.0014**
ON	317.38 ± 6.68	258.92 ± 24.77	**<0.0001**
II	328.23 ± 10.28	306.85 ± 34.31	**0.0363**
OI	285.38 ± 9.19	273.23 ± 25.75	0.1476
IT	319.15 ± 6.40	315.38 ± 314.83	0.6908
OT	286.77 ± 6.50	293.92 ± 29.83	0.4465
C	249.00 ± 13.28	254.23 ± 34.31	0.6825

Bold values indicates P < 0.05.

[a]*Generalized estimating equation models were used to obtain P-values comparing mean inner, outer and full macular retinal thickness between Pterygium patients and healthy subjects. Models were adjusted for age, intraocular pressure, acuity, blood pressure.*

HC, healthy control; IS, inner superior; OS, outer superior; IN, inner nasal; ON, outer nasal;II, inner inferior; OI, outer inferior; IT, inner temporal; OT, outer temporal; C, center.

(**Figures 3E,H**). The other three subregions of the inner loop (temporal part: $P = 0.8775$; lower part: $P = 0.4172$; superior part: $P = 0.1366$), one subregion of the outer ring (lower part: $P = 0.2649$), C subregion ($P = 0.2837$) were not distinctly different when comparing those two groups.

The full-layer retinal thickness of the IN, ON, IS, II, and OS subregions in the pterygium group was lower than that noted in the control ($P = 0.0014$, $P < 0.0001$, $P = 0.0398$, $P = 0.0363$, $P = 0.0283$, respectively) (**Figures 3F,I**). One other subregion of the inner ring (nose: $P = 0.0283$), two subregions of the outer ring (lower part: $P = 0.1476$; temporal: $P = 0.4465$), and the foveal center ($P = 0.6825$) were not distinctly different between when comparing those two groups.

ROC Curve Analysis of RT

Use OCTA results to evaluate the sensitivity and specificity of RT to changed anterior segments of pterygium patients (**Figure 4**). In ON subregion, the areas under the curve of the inner retinal thickness, outer retinal thickness and the whole retinal thickness were 1.0 (95% CI: 1.0), 0.882 (95% CI: 0.715–0.963), and 1.0 (95% CI: 1.0). It suggested medium to high specificity and sensitivity in pterygium diagnosis (**Figure 4**). In the IN area, the areas under the curve of external retinal thickness and full retinal thickness were 0.973 (95% CI: 0.916–1.0), 0.698 (95% CI: 0.491–0.905), and 0.852 (95% CI: 1.0), respectively. That indicated medium to high specificity and sensitivity in pterygium diagnosis (**Figure 4**). The minimum area under the ROC curve of retinal thickness in OT area was 0.018 (95% CI: 0–0.059), indicating low diagnostic specificity and sensitivity for pterygium, with high possibility for false positive results (**Figure 4**).

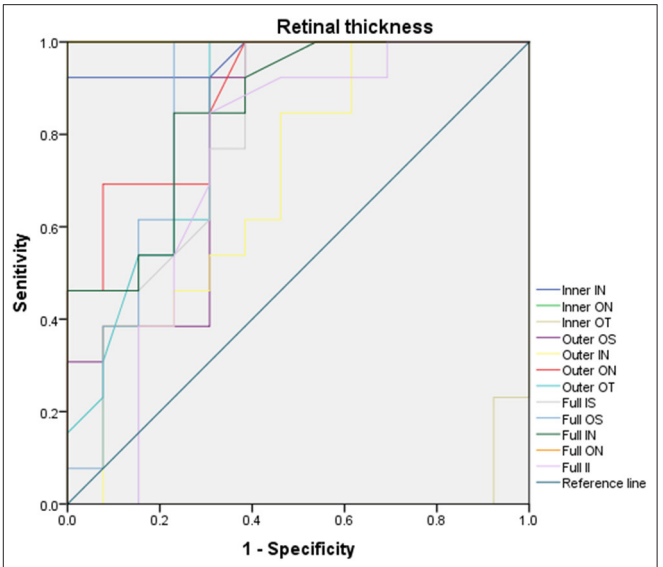

FIGURE 4 | ROC curve analysis of RT. In ON subregion, the areas under the curve of the inner retinal thickness, outer retinal thickness and the whole retinal thickness were 1.0 (95% CI: 1.0), 0.882 (95% CI: 0.715–0.963), and 1.0 (95% CI: 1.0). In the IN area, the areas under the curve of external retinal thickness and full retinal thickness were 0.973 (95% CI: 0.916–1.0), 0.698 (95% CI: 0.491–0.905), and 0.852 (95% CI: 1.0), respectively, the minimum area under ROC curve of RT in OT area is 0.018 [95% confidence interval (CI): 0–0.059]. ROC, receiver operating characteristic; CI, confidence interval; RT, retinal thickness; IS, inner superior; OS, outer superior;IN, inner nasal; ON, outer nasal; II, inner inferior; OI, outer inferior; IT, inner temporal; OT, outer temporal; C, center.

Correlation Between Retinal Thickness and Length and Area of Pterygium

There was a negative correlation between RT of the IN and ON subregions and the length of pterygium ($r = -0.5803$ and $r = -0.6013$, $P = 0.0376$ and $P = 0.0297$), indicating that a lower RT was associated with longer pterygium (**Figures 5A,B**). In the pterygium group, RT in the IN region was in a negative correlation with pterygium area ($r = 0.5844$, $P = 0.0359$). This revealed that lower RT is related to larger pterygium (**Figure 5C**).

DISCUSSION

In this study by using the OCTA approach, our data revealed significant alterations in RT of patients with pterygium. According to ROC curve, the inner, the outer, and full-layer retinal thickness of the IN and ON regions of patients with pterygium exhibited high sensitivity and specificity, whereas the ON region showed low sensitivity and specificity of the approach. These findings indicated that the RT of individuals with pterygium was distinctly decreased, and alterations mainly occurred on the temporal side. At the same time the area and length of pterygium were in a negative correlation with retinal thickness. This is the first time to investigate retinal thickness alterations in pterygium patients. The research provides a potential way to assess the progression of pterygium according to the changed retinal thickness. Also, it may indicate the natural etiology of pterygium at the retinal level.

However, it is unclear whether the alterations in RT occurs due to alterations in the anterior segment, which occures prior to these alterations or accompanied by alterations in the anterior segment. Nevertheless, we hypothesized several possible mechanisms underlying the alterations. This alteration in RT may be related to the retinal movement of photoreceptors, similar to those observed in animal models of visual deprivation. Liang et al. (18) used opaque occluders to cover one eye of hatchling chicks reared for 1, 2 or 4 weeks to expound the pathogenesis of deprivation myopia. Thinner retina and choroid existed in all deprived eyes. Thicker cone inner segments, rod outer segments, damaged cone outer segment made their distal tips can attach to the RPE basement membrane or depress the nucleus. In this study, the visual acuity of subjects with pterygium was decreased (**Table 1**). We hypothesized the "rod-push" mechanism induces thinner retina with poor vision. Pterygium may cover the cornea on the nasal side, resulting in thickening of the corneal tissue. The decrease in the thickness of the temporal retina may occur as a compensatory response to corneal alterations and prevent the overall structural disorder of the eye. Feng et al. (19) indicated total macular volume could increase after corneal refractive surgery while Lasik should not influence fundus. Therefore, according to OCTA scans, alterations in the optical

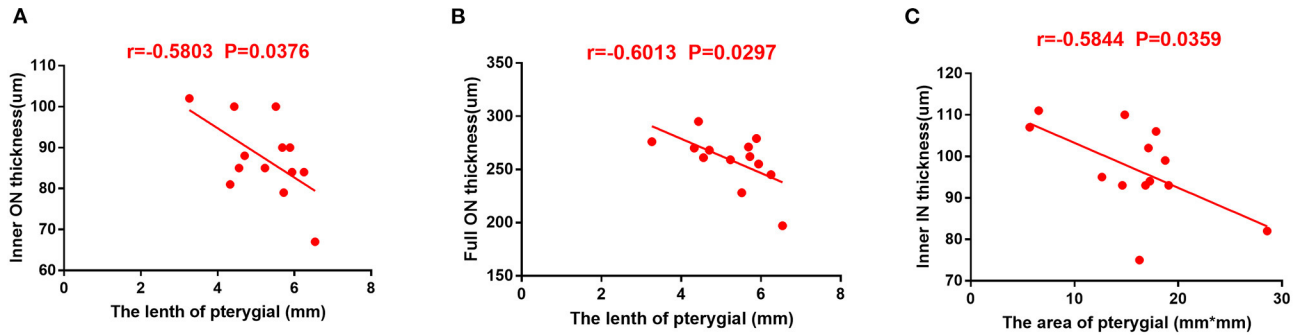

FIGURE 5 | The correlation between RT and pterygium length and area in patients with pterygium. **(A)** RT in ON area of internal retina was in a negative correlation with the length of pterygium ($r = -0.5803$, $P = 0.0376$). **(B)** RT in ON region of the complete retina was in a negative correlation with area of pterygium ($r = -0.6013$, $P = 0.0297$). **(C)** Total retinal RT is negatively correlated with pterygium area ($r = -0.5844$, $P = 0.0359$). RT, retinal thickness; IN, inner nasal; ON, outer nasal.

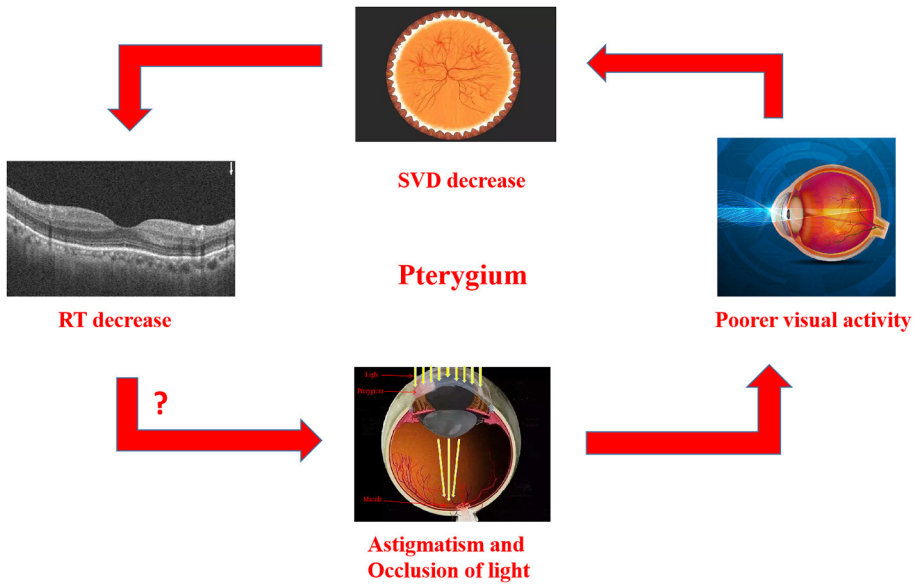

FIGURE 6 | Relationship between RT thinning in patients with Pterygium, and there is also a correlation between RT thinning and visual impairment. In Pterygium group, astigmatism and occlusion of light may lead to the decrease of vision., SVD in macular and RT in related areas. The macular area is marked on the image of eyeball, which reveals the decrease of SVD and RT in this area. RT, retinal thickness; SVD, superficial vessel density.

surface of the eye may lead to retina changes. Longer length and larger area of pterygium will result in more compensation for the apparent volume of the retina and lower thickness of the temporal retina. This is consistent with our study results, implying a compensation mechanism in the eye, through which alterations in one component might impact other components.

Another possible reason for alterations in RT is a decrease in the amount of light. It is reported that cataract could block 18–40% of different wavelengths of light (20). Zhou et al. (21) found that macular vascular density increased after cataract surgery. Although some studies have shown that inflammation after cataract surgery is a potential pathogenic factor for fundus alterations after cataract surgery (22), inflammation itself cannot last for prolonged periods of time. The investigators suggested that higher light levels could induce retinal metabolism and angiogenesis; this process can be taken as postoperative phototoxicity and explain why age-related macular degeneration is more common in intraocular lens eye (23). Similarly, pterygium on the side of the nose will also block light. Nevertheless, whether the decrease in light will also lead to a decrease in the activity and metabolic needs of photoreceptor cells in the retina, thereby resulting in a decrease in blood flow (24), will still need further investigations.

In our previous study, there was also a decrease in vascular density (VD) in temporal subregion of pterygium (25). Retina and brain exhibit similar metabolic activities because they derive from the same embryonic tissue. The lack of blood supply could induce retinal cell apoptosis (26). A reduction in the blood supply

to the temporal side of the retina may lead to not only chronic ischemia, but also the death of rods and cones due to reduced energy supply and loss of vision (26). Thus, all these alterations lead to a decrease in RT. which is supported by our findings. Our results also demonstrated that alterations in the internal and panretinal thickness of the ON subregion were in a distinctly negative correlation with length of pterygiod growth while the intraretinal thickness of the IN subregion was in a distinctly negative correlation with the area. Han et al. (27) reported that the corneal astigmatism caused by pterygium was more correlated with the length than with width and area. Mohammad-Salih and Sharif (9) reported the corneal astigmatism was most correlated with the dilatation of pterygium, then the whole area This is consistent with our results showing the length and area of pterygium have the greatest impact on corneal astigmatism, which thus affects vision and further leads to alterations in fundus RT. On the other hand, as light vision is done by cone cells, reducing light leads to a decrease of cellular activity. While the location of the ON subregion is shown to be closest to the central fovea, the consistency in location supports that the decrease in light may reduce macular blood vessel density. Accordingly, a larger size or longer length of pterygium, will result in more light block, thus lead to more significant alterations, which further confirms our results (**Figure 6**).

Certain shortcoming existed in this research. First of all, the sample size was not large. And then, the optometry of pterygium patients was lower than that of healthy individuals (**Table 1**). This might be explained that pterygium could cause corneal alterations (28), thus leading to poor visual acuity. Besides, the large pterygium will invades the pupil area; thus result in a decrease in visual acuity. Therefore, the effect of alteration in RT on visual acuity warrants further investigation. In addition, in this study, we obtained false positive results of increased thickness of the retina in the nasal OT subregion of patients with pterygium. As a non-invasive technique, OCT could use light to scan retina or anterior segment and obtain image according to the interference with backscatter or reflectance (29). While, depend on the enface and depth-encoded slabs, OCTA technology can display flowing image of retinal and choroidal vascular plexus, which would be indistinct with previous imaging mode (30). However, OCTA also has its own shortcomings, e.g., Opaque medium limits OCTA examination and lead to signal abnormality because light source is the foundation of the technology. Significant astigmatism also affects the assessment of RT and results in signal attenuation and shadow artifacts (12). Hence, we speculate this may be related to pterygium, which blocks the light on the side of the nose. Consequently, motion artifacts or measurement errors occur, resulting in an increase in the thickness of the retina in the measured OT area.

CONCLUSION

In summary, the RT of patients with pterygium is decreased than that of healthy individuals, and the main alteration is observed in the temporal side. The results show that, there are important differences in the posterior segment of pterygium as well as the anterior segment. Therefore, macular alterations may be related to broader eye structural disorders in patients with pterygium or the optimization of the compensation mechanism of irregular corneal vision and light occlusion in patients with pterygium. However, it is unclear whether these alterations occur before or as a result of the development of pterygium. Further investigation is warranted to repeat the present findings and determine their clinical importance.

DATA AVAILABILITY STATEMENT

The original contributions presented in the study are included in the article/supplementary material, further inquiries can be directed to the corresponding author.

ETHICS STATEMENT

This study confirmed to the Declaration of Helsinki and had formal approval from the Medical Ethics Committee of the First Affiliated Hospital of Nanchang University. The patients/participants provided their written informed consent to participate in this study. Written informed consent was obtained from the individual(s) for the publication of any potentially identifiable images or data included in this article.

AUTHOR CONTRIBUTIONS

FW: acquisition, analysis, interpretation of data, and drafting the article. LL: acquisition and interpretation of data. RL: acquisition and analysis of data. LZ, HS, and XL: literature revision and data discussion. YP: acquisition of data. JW: literature revision. TS: data discussion. YS: conception, design of the study, and supervised the work. All authors critically revised the manuscript for important intellectual property and approved the final version to be submitted.

FUNDING

This work was supported by National Natural Science Foundation (No: 82160195); Central Government Guides Local Science and Technology Development Foundation (No: 20211ZDG02003); Key Research Foundation of Jiangxi Province (Nos: 20181BBG70004 and 20203BBG73059); Excellent Talents Development Project of Jiangxi Province (No: 20192BCBL23020); Natural Science Foundation of Jiangxi Province (No: 20181BAB205034); Grassroots Health Appropriate Technology "Spark Promotion Plan" Project of Jiangxi Province (No: 20188003); Health Development Planning Commission Science Foundation of Jiangxi Province (Nos: 20201032 and 202130210); Health Development Planning Commission Science TCM Foundation of Jiangxi Province (Nos: 2018A060 and 2020A0087). Research and Cultivation Project of Guang-dong Meizhou people's Hospital (PY-2021060).

REFERENCES

1. Shahraki T, Arabi A, Feizi S. Pterygium: an update on pathophysiology, clinical features, and management. *Ther Adv Ophthalmol.* (2021) 13. doi: 10.1177/25158414211020152
2. Rezvan F, Khabazkhoob M, Hooshmand E, Yekta A, Saatchi M, Hashemi H. Prevalence and risk factors of pterygium: a systematic review and meta-analysis. *Surv Ophthalmol.* (2018) 63:719–35. doi: 10.1016/j.survophthal.2018.03.001
3. Hovanesian JA, Starr CE, Vroman DT, Mah FS, Gomes J, Farid M, et al. Surgical techniques and adjuvants for the management of primary and recurrent pterygia. *J Cataract Refract Surg.* (2017) 43:405. doi: 10.1016/j.jcrs.2017.03.002
4. Fonseca EC, Rocha EM, Arruda GV. Comparison among adjuvant treatments for primary pterygium: a network meta-analysis. *Br J Ophthalmol.* (2018) 102:748–56. doi: 10.1136/bjophthalmol-2017-310288
5. Ono T, Mori Y, Nejima R, Lee J, Miyata K. Long-term changes and effect of pterygium size on corneal topographic irregularity after recurrent pterygium surgery. *Sci Rep.* (2020) 10:8398. doi: 10.1038/s41598-020-65376-4
6. Provis JM, Penfold PL, Cornish EE, Sandercoe TM, Madigan MC. Anatomy and development of the macula: specialisation and the vulnerability to macular degeneration. *Clin Exp Optom.* (2005) 88:269–81. doi: 10.1111/j.1444-0938.2005.tb06711.x
7. Zhang W, Hu H, Cheng H, Liu Q, Yuan D. Evaluation of the changes in vessel density and retinal thickness in patients who underwent unilateral congenital cataract extraction by OCTA. *Clin Ophthalmol.* (2020) 14:4221–8. doi: 10.2147/OPTH.S286372
8. Srujana S, Amirul I, Sanj W, Mark D, Baird PN. Assessment of macular parameter changes in patients with keratoconus using optical coherence tomography. *J Ophthalmol.* (2015) 2015:1–6. doi: 10.1155/2015/245953
9. Mohammad-Salih AK, Sharif A. Analysis of pterygium size and induced corneal astigmatism. *Cornea.* (2008) 27:434. doi: 10.1097/ICO.0b013e3181656448
10. Garg P, Sahai A, Shamshad MA, Tyagi L, Singhal Y, Gupta S. A comparative study of preoperative and postoperative changes in corneal astigmatism after pterygium excision by different techniques. *Indian J Ophthalmol.* (2019) 67:1036–9. doi: 10.4103/ijo.IJO_1921_18
11. Chen M, Dai J, Gong L. Changes in retinal vasculature and thickness after small incision lenticule extraction with optical coherence tomography angiography. *J Ophthalmol.* (2019) 2019:1–7. doi: 10.1155/2019/3693140
12. Spaide RF, Klancnik JM, Cooney MJ. Retinal vascular layers imaged by fluorescein angiography and optical coherence tomography angiography. *JAMA Ophthalmol.* (2015) 133:45–50. doi: 10.1001/jamaophthalmol.2014.3616
13. Wang T, Li H, Zhang R, Yu Y, Xiao X, Wu C. Evaluation of retinal vascular density and related factors in youth myopia without maculopathy using OCTA. *Sci Rep.* (2021) 11:15361. doi: 10.1038/s41598-021-94909-8
14. Liu J, Liu Q, Yu H, Xia Y, Zhang H, Geng C, et al. Microvascular changes in macular area after phacoemulsification and its influencing factors assessed by optical coherence tomography angiography. *Ther Clin Risk Manag.* (2021) 17:405–14. doi: 10.2147/TCRM.S309679
15. Cornelius A, Pilger D, Riechardt A, Reitemeyer E, Rubsam A, Winterhalter S, et al. Macular, papillary and peripapillary perfusion densities measured with optical coherence tomography angiography in primary open angle glaucoma and pseudoexfoliation glaucoma. *Graefes Arch Clin Exp Ophthalmol.* (2021) 260:957–65. doi: 10.1007/s00417-021-05321-x
16. Ye L, Zhou SS, Yang WL, Bao J, Jiang N, Min YL, et al. Retinal microvasculature alteration in active thyroidassociated ophthalmopathy. *Endocr Pract.* (2018) 24:658–67. doi: 10.4158/EP-2017-0229
17. Tang Y, Qian D, Wei L, Du Y, Zhu X. Influences of the three-dimensional parameters of pterygium on corneal astigmatism and the intraocular lens power calculation. *Sci Rep.* (2020) 10:5017. doi: 10.1038/s41598-020-61959-3
18. Liang H, Crewther DP, Crewther SG, Barila AM. A role for photoreceptor outer segments in the induction of deprivation myopia. *Vision Res.* (1995) 35:1217–25. doi: 10.1016/0042-6989(94)00241-D
19. Feng L, Burns SA, Shao L, Yang Y. Retinal measurements using time domain OCT imaging before and after myopic lasik. *Ophthalmic Physiol Opt.* (2012) 32:222–7. doi: 10.1111/j.1475-1313.2012.00905.x
20. Artigas JM, Adelina F, Amparo N, Adriana F, Cristina A. spectral transmission of the human crystalline lens in adult and elderly persons: color and total transmission of visible light. *Invest Ophthalmol Vis Sci.* (2012) 53:4076–84. doi: 10.1167/iovs.12-9471
21. Zhou Y, Zhou M, Wang Y, Ben S, Gao M, Zhang S, et al. Short-term changes in retinal vasculature and layer thickness after phacoemulsification surgery. *Curr Eye Res.* (2020) 45:31–7. doi: 10.1080/02713683.2019.1649703
22. Kim SJ, Flach AJ, Jampol LM. Nonsteroidal anti-inflammatory drugs in ophthalmology. *Curr Eye Res.* (2010) 55:108–33. doi: 10.1016/j.survophthal.2009.07.005
23. Yilmaz T, Karci AA, Yilmaz I, Yilmaz A, Yildirim Y, Sakalar YB. Long-term changes in subfoveal choroidal thickness after cataract surgery. *Med Sci Monit.* (2016) 22:1566–70. doi: 10.12659/MSM.898714
24. Libre PE. Intraoperative light toxicity: a possible explanation for the association between cataract surgery and age-related macular degeneration. *Am J Ophthalmol.* (2003) 136:961. doi: 10.1016/S0002-9394(03)00906-1
25. Wang F, Shu H-Y, Liao X-L, Liang R-B, Li Q-Y, Zhang L-J, et al. Decreased retinal microvasculature densities in pterygium. *Int J Ophthalmol.* (2021) 14:1858–67. doi: 10.18240/ijo.2021.12.08
26. Country MW. Retinal metabolism: a comparative look at energetics in the retina. *Brain Res.* (2017) 1672:50–7. doi: 10.1016/j.brainres.2017.07.025
27. Han SB, Jeon HS, Kim M, Lee SJ, Wee WR. Quantification of astigmatism induced by pterygium using automated image analysis. *Cornea.* (2016) 35:370–6. doi: 10.1097/ICO.0000000000000728
28. Mootha VV, Pingree M, Jaramillo J. Pterygia with deep corneal changes. *Cornea.* (2004) 23:635–8. doi: 10.1097/01.ico.0000121701.74077.78
29. Huang D, Swanson EA, Lin CP, Schuman JS, Stinson WG, Chang W, et al. Optical coherence tomography. *Science.* (1991) 254:1178–81. doi: 10.1126/science.1957169
30. de Carlo TE, Romano A, Waheed NK, Duker JS. A review of optical coherence tomography angiography (OCTA). *Int J Retina Vitreous.* (2015). doi: 10.1186/s40942-015-0005-8

Conflict of Interest: The authors declare that the research was conducted in the absence of any commercial or financial relationships that could be construed as a potential conflict of interest.

Publisher's Note: All claims expressed in this article are solely those of the authors and do not necessarily represent those of their affiliated organizations, or those of the publisher, the editors and the reviewers. Any product that may be evaluated in this article, or claim that may be made by its manufacturer, is not guaranteed or endorsed by the publisher.

Copyright © 2022 Wang, Liu, Liang, Zhang, Shu, Liao, Pan, Wu, Su and Shao. This is an open-access article distributed under the terms of the Creative Commons Attribution License (CC BY). The use, distribution or reproduction in other forums is permitted, provided the original author(s) and the copyright owner(s) are credited and that the original publication in this journal is cited, in accordance with accepted academic practice. No use, distribution or reproduction is permitted which does not comply with these terms.

frontiers | Frontiers in Neurology

ORIGINAL RESEARCH
published: 02 June 2022
doi: 10.3389/fneur.2022.905069

Clinical Features and Influencing Factors for the Prognosis of Patients With Sudden Deafness

Wei Lin[1†], *Gaoyun Xiong*[1†], *Kailei Yan*[2], *Wumin Yu*[3], *Xiaoxing Xie*[1], *Ze Xiang*[4], *Jian Wu*[5], *Yanping Ge*[1*] and *Ying Wang*[6*]

[1] Department of Otolaryngology, Tongde Hospital of Zhejiang Province, Hangzhou, China, [2] The Second Clinical Medical College, Zhejiang Chinese Medical University, Hangzhou, China, [3] Basic Medical College, Zhejiang Chinese Medical University, Hangzhou, China, [4] Zhejiang University School of Medicine, Hangzhou, China, [5] Department of Clinical Laboratory, The Affiliated Suzhou Hospital of Nanjing Medical University, Suzhou Municipal Hospital, Gusu School, Nanjing Medical University, Suzhou, China, [6] Department of Infection Management, The Affiliated Suzhou Hospital of Nanjing Medical University, Suzhou Municipal Hospital, Gusu School, Nanjing Medical University, Suzhou, China

Backgrounds: Studies on risk factors influencing the prognosis of patients with sudden onset deafness are lacking.

Methods: From March 2018 to March 2021, 500 patients, from the Tongde Hospital in Zhejiang Province, with sudden onset deafness were enrolled. We collected clinical information from the hospital medical records, including certain demographic characteristics, information related to sudden-onset deafness, and laboratory parameters. Univariate and multivariate analyses were performed to determine independent prognostic risk factors for patients with sudden deafness. Additionally, we also employed orthogonal partial least squares discriminant analysis (OPLS-DA) to analyze the data of these enrolled patients.

Results: The baseline clinical characteristics of the enrolled patients were analyzed. Based on their prognoses, the included patients were divided into the overall effective and ineffective groups. Between these two groups, the univariate and multivariate analyses were performed. Age, type of hearing curve at the initial diagnosis, acute phase, and sudden deafness site were found to be independently associated with the prognoses of patients with sudden deafness (all $P < 0.05$). Through the OPLS-DA, the sudden deafness site was found to be an indicator with the highest predictive power.

Conclusions: Age, type of hearing curve at the initial diagnosis, acute phase, and sudden deafness site were all independently correlated with the prognoses of patients with sudden deafness and, therefore, need to be emphasized.

Keywords: clinical characteristics, risk factors, treatment effects, prognosis, sudden deafness

OPEN ACCESS

Edited by:
Yuzhen Xu,
Tongji University, China

Reviewed by:
Sicong Zhang,
Cixi People's Hospital, China
Sheng LI,
Quzhou City People's Hospital, China

***Correspondence:**
Ying Wang
wangy830224@sina.com
Yanping Ge
13858077335@163.com

[†]These authors have contributed equally to this work

Specialty section:
This article was submitted to Neurological Biomarkers, a section of the journal Frontiers in Neurology

Received: *26 March 2022*
Accepted: *09 May 2022*
Published: *02 June 2022*

Citation:
Lin W, Xiong G, Yan K, Yu W, Xie X, Xiang Z, Wu J, Ge Y and Wang Y (2022) Clinical Features and Influencing Factors for the Prognosis of Patients With Sudden Deafness. Front. Neurol. 13:905069. doi: 10.3389/fneur.2022.905069

INTRODUCTION

Sudden deafness, also known as idiopathic sudden deafness, refers to sudden and unexplained sensorineural hearing loss (1). In recent times, the incidence of sudden deafness is on the rise (2). Although large sample epidemiological data are lacking, the incidence of sudden deafness has been increasing in China in recent years (3). The incidence of sudden deafness in the United States

ranges from 5 to 27 people per 100,000, and approximately 66,000 new cases are reported annually (4). The incidence of sudden deafness in Japan was 27.5 persons per 100,000 in 2001, and it shows an increasing year-on-year trend (5). The incidence reported in the German guidelines for sudden deafness in 2004 was 20 per 100,000, which increased to 160–400 per 100,000 per year in 2011 (6).

The etiology and pathophysiological mechanism underlying sudden deafness remains unclear. Local and systemic factors may lead to sudden onset deafness (7, 8). Common causes include vascular diseases, viral infection, autoimmune diseases, and so on (9). Mental tension, pressure, mood swings, irregular life, and sleep disorders also underlie the main causes of sudden onset deafness (10, 11). Currently, the recognized pathogenesis includes inner ear vasospasm, stria vascular dysfunction, vascular embolism or thrombosis, membrane labyrinth hydrops, and hair cell injury (12, 13).

The clinical manifestations of patients with sudden onset deafness include sudden hearing loss, tinnitus, ear fullness, dizziness, hyperacusis, and paresthesia around the ear (14, 15). Some patients even face psychological symptoms, such as anxiety and sleep disorder, which affect their quality of life (16, 17). Nowadays, several prognostic factors may affect the prognoses of patients with sudden onset deafness. Several previous studies have focused on the factors influencing different diseases from multiple perspectives (18–20). Nevertheless, the research on risk factors influencing the prognosis of patients with sudden onset deafness is incomplete. Therefore, we examined the independent risk factors for the treatment of patients with sudden deafness in a clinical cohort to provide new directions and insights into the treatment and prognosis of sudden deafness.

PATIENTS AND METHODS

Patients

From March 2018 to March 2021, 500 patients who met the inclusion criteria for sudden deafness were enrolled at the Tongde Hospital in Zhejiang Province. Inclusion criteria for sudden deafness were as follows (21): (1) sensorineural hearing loss occurred suddenly within 72 h, with hearing loss of $\geq$ 20 dBHL in at least two adjacent frequencies, mostly unilateral, and a few cases could occur bilaterally or sequentially; (2) no clear etiology was found, including systemic or local factors; (3) patients may be accompanied by tinnitus, ear fullness, and paresthesia around the ear; and (4) patients may be accompanied by dizziness, nausea, and vomiting. Exclusion criteria were as follows: (1) patients who did not meet the above inclusion criteria; (2) those with organic lesions of the middle ear; (3) cases of sudden deafness and pregnant women suffering from systemic diseases, such as hypertension and diabetes; and (4) patients considered with the possibility of the posterior cochlear space-occupying lesion as evidenced by magnetic resonance imaging (MRI) of the skull or middle inner ear, or computed tomography (CT) scan of the temporal bone.

The following treatment methods were adopted in this study: antiviral drug ribavirin liquid injection, glucocorticoid oral prednisone, nerve adenosine triphosphate (ATP) oral nutrition, low molecular dextran, B vitamins, and other comprehensive treatment regimens; simultaneous oxygen therapy during infusion therapy, children under the age of 14, according to the weight-adjusted doses. After treatment for 7 days, bone-air conduction pure tone audiometry results were reviewed and compared with those before treatment.

Based on the curative effect grading standard of sudden deafness, hearing curative effects were evaluated as follows (21): recover: the average hearing threshold of the damaged frequency was completely restored to normal, or reached the level of the healthy ear; significantly effective: the average hearing threshold of damaged frequencies improved by $\geq$ 30dB; effective: the average hearing threshold of damaged frequencies improved by $\geq$ 15dB; and ineffective: the average hearing threshold of damaged frequencies improved by $<$ 15dB. Recovery, significantly effective, and effective were considered as the overall efficacy of the treatment.

We collected clinical information from the hospital medical records, including certain demographic characteristics, information related to sudden deafness, and laboratory parameters. This study design was approved by the Ethics Committee of the Tongde Hospital, Zhejiang Province (approval number: KTSC2019132). Informed consents were obtained from patients or their families.

Data Analysis

Statistical analyses were performed using GraphPad Prism 9 and SIMCA. Univariate and multivariate analyses were used to determine independent risk indicators for the prognoses of sudden onset deafness patients. Data for all samples were analyzed using the Statistical Software SIMCA (Version 14.1.0.2047, 64-bit, MKS Umetrics, Umea, Sweden) for orthogonal partial least squares discriminant analysis (OPLS-DA). $P < 0.05$ was considered statistically significant.

RESULTS

Clinical Characteristics of Enrolled Patients

A total of 500 patients with sudden onset deafness were enrolled in our study. **Table 1** shows the baseline clinical characteristics of these included patients. The average age was 40 years. The age distribution of patients ranged between 30 and 54 years. Of the 500 patients with sudden onset deafness, 261 were males and 239 were females. According to the types of the hearing curve, flat type deafness was present in 52 patients, low-mid frequency decline type deafness in 187 patients, high-mid frequency decline type deafness in 157 patients, and total deafness in 104 patients. A total of 385 patients were in the acute phase within 3 weeks; the remaining 115 patients were not. Notably, none of the patients in this cohort had a family or genetic history of sudden onset deafness.

All patients underwent laboratory tests. Based on the results of the patients' examination, the average level of total bilirubin level was 12.40 (9.60–16) μmol/L, and the level of indirect bilirubin level was 9.95 (7.70–12.80) μmol/L, the total protein level was 73.40 (69.72–76.90) g/L, and the albumin level was

TABLE 1 | Clinical characteristics of enrolled patients with sudden deafness.

Variables	Sudden deafness patients ($n = 500$)
Age (year)	40.00 (30.00–54.00)
Male (%)	261 (52.20)
Females (%)	239 (47.80)
Initially diagnosed hearing curve types	
Flat type deafness (%)	52 (10.40)
Low-mid frequency decline type deafness (%)	187 (37.40)
High-mid frequency decline type deafness (%)	157 (31.40)
Total deafness (%)	104 (20.80)
Acute phase (%)	385 (77.00)
Non-Acute phase (%)	115 (23.00)
Total bilirubin (μmol/L)	12.40 (9.60–16.00)
Indirect bilirubin (μmol/L)	9.95 (7.70–12.80)
Total protein (g/L)	73.40 (69.72–76.90)
Albumin (g/L)	45.00 (42.30–47.20)
Family history (%)	0
Genetic history (%)	0
Sudden deafness site	
Unilateral (%)	380 (76.00)
Bilateral (%)	120 (24.00)
Vertigo (%)	79 (15.80)
Tinnitus (%)	380 (76.00)
Hyperbaric oxygen treatment (%)	312 (62.40)

45 (42.30–47.20) g/L. Approximately 76% of these patients had unilateral, while 24% had bilateral sudden onset deafness. Moreover, 79 patients developed vertigo. About 380 patients presented symptoms of tinnitus. A total of 312 patients received hyperbaric oxygen treatment, while the remaining did not.

Univariate and Multivariate Analyses of the Prognostic Risk Factors for Patients With Sudden Deafness

To determine the prognostic risk factors for patients with sudden onset deafness, 117 patients in our cohort were divided into the recovery, significantly effective, effective, and ineffective groups according to the observed treatment effects. A total of 110 patients were in the recovery group, 45 in the significantly effective group, 45 in the effective group, and 323 in the ineffective group. Patients in the recovery, significantly effective, and effective groups were considered to show overall effective treatment. Therefore, univariate and multivariable analyses for the prognostic risk factors were performed between the overall effective and ineffective groups (**Table 2**). Through univariate analysis, age, type of hearing curve at the initial diagnosis, acute phase, total protein level, albumin level, sudden deafness site, and hyperbaric oxygen treatment were found to be the significant risk factors for poor prognosis of patients with sudden onset deafness. Subsequently, the multivariable analysis was performed for these risk factors, and age, type of hearing curve at the initial diagnosis, acute phase, and sudden deafness site were found to be independently associated with prognoses of patients with sudden deafness (all $P < 0.05$).

OPLS-DA

To further rank and assess the risk factors for poor prognosis of patients with sudden deafness, the OPLS-DA method was used. According to the results of OPLS-DA, differences could be clearly distinguished between patients with sudden deafness in the overall effective and ineffective groups (**Figures 1A,B**). In addition, sudden deafness site was an indicator with the highest predictive power (**Figures 1C,D**).

DISCUSSION

Sudden deafness is a common emergency in otorhinolaryngology. The incidence ratio in males and females is similar, and, most frequently, comprises unilateral onset. Since the etiology and pathogenesis remain unclear, the clear clinical cause underlying sudden deafness is known in approximately 10% of these patients. It is difficult to evaluate the curative effects and prognoses due to the lack of standardized specific treatment and the presence of several influencing factors. Although sudden deafness shows a self-healing tendency, some patients recover to varying degrees. However, a poor prognosis is seen in some patients. Therefore, this present study focused on identifying the independent risk factors affecting the prognoses of patients with sudden deafness.

A total of 500 patients with sudden onset deafness with an average age of 40 years were enrolled. The age distribution ranged from 30 to 54 years. Among the patients enrolled in this study, 261 were males and 239 were females. According to the hearing curve types, 52 patients showed flat type deafness, 187 patients had low-mid frequency decline type deafness, 157 had high-mid frequency decline type deafness, and 104 patients had total deafness. Three hundred eighty five patients were in the acute phase within 3 weeks, while 115 were not. Notably, none of the patients in the cohort had a family or genetic history of sudden onset deafness. All included patients underwent laboratory tests. Based on these results, the total bilirubin level was 12.40 (9.60–16) μmol/L and the indirect bilirubin level was 9.95 (7.70–12.80) μmol/L. The level of total protein was 73.40 (69.72–76.90) g/L, and the level of albumin was 45 (42.30–47.20) g/L. In addition, 76% of these patients showed unilateral sudden deafness, while 24% had bilateral sudden deafness. A total of 79 patients developed vertigo, while 380 patients presented with symptoms of tinnitus. A total of 312 patients received hyperbaric oxygen treatment, while the remaining 188 patients did not receive it.

To determine the prognostic risk factors for patients with sudden deafness, 177 patients were divided into recovery, significantly effective, effective, and ineffective groups according to the outcomes of treatment received by patients with sudden deafness. Recovery, significantly effective, and effective were

TABLE 2 | Univariate and multivariate analysis in the overall effective and ineffective groups.

Variables	Overall effective group (n = 177)	Ineffective group (n =323)	P	Univariate analysis		Multivariate analysis	
				OR (95% CI)	P	OR (95% CI)	P
Age (year)	34.00 (26.00–44.00)	45.00 (33.00–59.00)	<0.001	1.044(1.029–1.058)	<0.001	1.037(1.020–1.053)	<0.001
Males (%)	99 (55.93)	162 (50.15)	0.216	0.793 (0.549–1.146)	0.217		
Initially diagnosed hearing curve types			<0.001	1.484 (1.209–1.821)	<0.001	1.325 (1.057–1.660)	0.015
Flat type deafness (%)	19 (10.73)	33 (10.22)					
Low-mid frequency decline type deafness (%)	101 (57.06)	86 (26.63)					
High-mid frequency decline type deafness (%)	22 (12.43)	135 (41.80)					
Total deafness (%)	35 (19.77)	69 (21.36)					
Acute phase (%)	164 (92.66)	221 (68.42)	<0.001	0.172 (0.093–0.317)	<0.001	0.224 (0.118–0.424)	<0.001
Total bilirubin (μmol/L)	12.50 (9.55–16.20)	12.40 (9.60–15.70)	0.596	1.006 (0.984–1.028)	0.620		
Indirect bilirubin (μmol/L)	9.90 (7.65–12.90)	10.00 (7.70–12.60)	0.703	0.998 (0.965–1.033)	0.927		
Total protein (g/L)	73.85 ± 5.38	72.81 ± 5.57	0.044	0.966 (0.934–0.999)	0.044		
Albumin (g/L)	45.50 (42.75–47.70)	44.60 (42.00–47.00)	0.012	0.934 (0.886–0.985)	0.012		
Vertigo (%)	21 (11.86)	58 (17.96)	0.074	1.626 (0.950–2.781)	0.076		
Tinnitus (%)	135 (76.27)	245 (75.85)	0.916	0.977 (0.636–1.502)	0.916		
Sudden deafness site			<0.001	5.202 (2.918–9.272)	<0.001	3.447(1.856–6.402)	<0.001
Unilateral (%)	162 (91.53)	218 (67.49)					
Bilateral (%)	15 (8.47)	105 (32.51)					
Hyperbaric oxygen treatment (%)	100 (56.50)	212 (65.63)	0.044	1.471 (1.010–2.141)	0.044		

considered as overall effective. Univariate and multivariate analyses for risk factors were performed between the overall effective and ineffective groups. In univariate analysis, age, type of hearing curve at the initial diagnosis, acute phase, total protein level, albumin level, sudden deafness site, and hyperbaric oxygen treatment were identified as the risk factors for poor prognosis in patients with sudden deafness. Multivariate risk factor analysis was then performed. Based on these results, age, type of hearing curve at the initial diagnosis, acute phase, and sudden deafness site were all found to be independently associated with the prognosis of patients with sudden deafness (all P <.05). Among them, the older were the patients, the worse was the prognosis, mainly due to the vulnerability of the auditory system and other physical conditions that can exacerbate deafness (22). Additionally, sudden deafness site was also considered an important factor that influenced the prognosis of patients with sudden deafness, consistent with the results of several previous studies (23, 24). Therefore, these factors should be emphasized during the treatment of patients with sudden deafness, which would be conducive to their better treatment and prognosis.

To further rank and evaluate the risk factors affecting the prognosis of patients with sudden deafness, the OPLS-DA method was used for analysis. Based on the results, the difference between patients in the overall effective and ineffective groups could be distinguished. Moreover, sudden deafness site was considered to be an indicator with the highest predictive power. It was speculated that patients with bilateral sudden deafness may have a poorer prognosis than those with unilateral sudden deafness.

However, there are limitations to this study. First, the sample size of patients with sudden deafness needs to be increased to validate the above conclusions. Second, the patients in this study all came from the same hospital, which may contribute to certain regional deviations. Finally, the statistics of some clinical parameters in patients with sudden deafness were incomplete, and more clinical data are needed to evaluate the independent risk factors that may lead to poor prognoses of sudden onset deafness.

CONCLUSION

In conclusion, age, type of hearing curve at the initial diagnosis, acute phase, and sudden deafness site were independently correlated with the prognosis of patients with sudden deafness (all $P < 0.05$). Notably, sudden deafness site was an indicator with the highest predictive power. These factors should be considered during the treatment of patients with sudden deafness. Our finding may thus provide better clinical guidance for the treatment and prognosis of patients with sudden deafness.

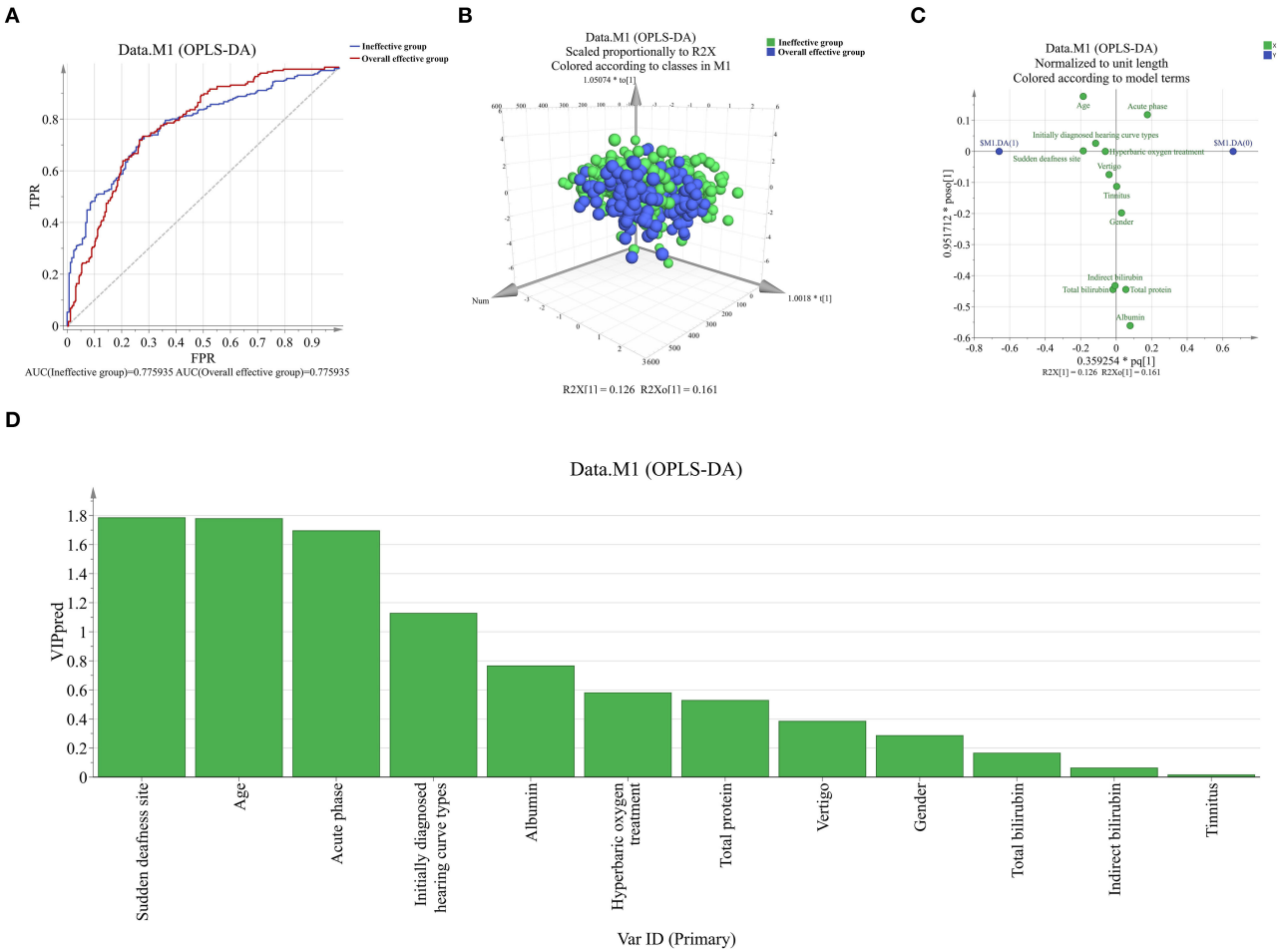

FIGURE 1 | Orthogonal partial least squares discriminant analysis (OPLS-DA) assessed the ability of risk factors to predict the prognosis of patients with sudden deafness **(A,B)**. Through OPLS-DA, patients in the overall effective group could be unambiguously distinguished from patients in the ineffective group; **(C,D)**. Sudden deafness site was considered as the top 1 indicator with highest predictive capability.

DATA AVAILABILITY STATEMENT

The raw data supporting the conclusions of this article will be made available by the authors, without undue reservation.

ETHICS STATEMENT

The studies involving human participants were reviewed and approved by the Ethics Committee of the Tongde Hospital, Zhejiang Province (approval number: KTSC2019132). The patients/participants provided their written informed consent to participate in this study.

AUTHOR CONTRIBUTIONS

WL and GX: guarantor of this work. KY, WY, and XX: data collection. YG and YW: statistical analysis and manuscript writing. ZX and JW: critical revision of the manuscript. All authors contributed to the article and approved the submitted version.

FUNDING

This study was funded by grants from Zhejiang basic public welfare research plan (LGC22H130001) and Zhejiang traditional Chinese medicine science and technology plan (20212A036).

REFERENCES

1. Young Y-H. Contemporary review of the causes and differential diagnosis of sudden sensorineural hearing loss. *Int J Audiol.* (2020) 59:243–53. doi: 10.1080/14992027.2019.1689432
2. World Health Organization. *Addressing the Rising Prevalence of Hearing Loss*. Geneva: World Health Organization. (2018). Available online at: https://apps.who.int/iris/handle/10665/260336
3. Lai D, Zhong J, Lu T. Pu J-M. Patient education in sudden sensorineural hearing loss: knowledge, attitude/belief, and practice findings among

otolaryngologists and otologists in China *Patient Educ Couns.* (2019) 102:93–8. doi: 10.1016/j.pec.2018.08.022
4. Chandrasekhar SS, Tsai Do BS, Schwartz SR, Bontempo LJ, Faucett EA, Finestone SA, et al. Clinical practice guideline: sudden hearing loss (update). *Otolaryngol Head Neck Surg.* (2019) 161(Suppl. 1):S1–45. doi: 10.1177/0194599819859883
5. Alexander TH, Harris JP. Incidence of sudden sensorineural hearing loss. *Otol Neurotol.* (2013) 34:1586–9. doi: 10.1097/MAO.0000000000000222
6. Michel O. The revised version of the german guidelines "Sudden Idiopathic Sensorineural Hearing Loss." *Laryngorhinootolog.* (2011) 90:290–3. doi: 10.1055/s-0031-1273721
7. Suckfüll M. Perspectives on the pathophysiology and treatment of sudden idiopathic sensorineural hearing loss. *Dtsch Arztebl Int.* (2009) 106:669. doi: 10.3238/arztebl.2009.0669
8. Sun XM, Zhuang SM, Xiao ZW, Luo JQ, Long Z, Lan LC, et al. Autoimmune thyroiditis in patients with sudden sensorineural hearing loss. *Laryngoscope Investig Otolaryngol.* (2022) 7:571–7. doi: 10.1002/lio2.755
9. Hung W-C, Lin K-Y, Cheng P-W, Young Y-H. Sudden deafness: a comparison between age groups. *Int J Audiol.* (2021) 60:911–6. doi: 10.1080/14992027.2021.1900611
10. Jin L, Fan K, Tan S, Liu S, Wang Y, Yu S. Analysis of the characteristics of outpatient and emergency diseases in the department of otolaryngology during the "Covid-19" pandemic. *Sci Prog.* (2021) 104:00368504211036319. doi: 10.1177/00368504211036319
11. Stachler RJ, Chandrasekhar SS, Archer SM, Rosenfeld RM, Schwartz SR, Barrs DM, et al. Clinical practice guideline: sudden hearing loss. Otolaryngol Head Neck Surg. (2012) 146(Suppl. 3):S1–35. doi: 10.1177/0194599819859885
12. Chen J, He J, Luo J, Zhong S. Association of aenac P. Ala663thr gene polymorphism with sudden sensorineural hearing loss. *Front Genetics.* (2021) 12:659517. doi: 10.3389/fgene.2021.659517
13. Acipayam H, Koçak HE, Elbistanli MS. Sudden sensorineural hearing loss. *Excursus Hearing Loss.* (2018):71.
14. Conte G, Di Berardino F, Mastrapasqua RF, Casale S, Scola E, Capaccio P, et al. Prognostic value of early magnetic resonance imaging patterns in sudden hearing loss. *Audiol Neurootol.* (2022) 27:64–74. doi: 10.1159/000515153
15. Fife TD, Tourkevich R. Tinnitus, hyperacusis, otalgia, and hearing loss. *Continuum (Minneap Minn).* (2021) 27:491–525. doi: 10.1212/CON.0000000000000961
16. Yuan Y, Wang H, Chen Q, Xie C, Li H, Lin L, et al. Illness experience and coping styles of young and middle-aged patients with sudden sensorineural hearing loss: a qualitative study. *BMC Health Serv Res.* (2021) 21:1–10. doi: 10.1186/s12913-021-06763-z
17. Sun B, Liu L, Ren X, Wang Z. Psychological state of patients with sudden deafness and the effect of psychological intervention on recovery. *J Int Med Res.* (2020) 48:0300060520957536. doi: 10.1177/0300060520957536
18. Wu J, Guo Y, Lu X, Huang F, Lv F, Wei D, et al. Th1/Th2 Cells and associated cytokines in acute hepatitis E and related acute liver failure. *J Immunol Res.* (2020) 2020:1–8. doi: 10.1155/2020/6027361
19. Wang L, Wu J, Song S, Chen H, Hu Y, Xu B, et al. Plasma exosome-derived sentrin sumo-specific protease 1: a prognostic biomarker in patients with osteosarcoma. *Front Oncol.* (2021) 11:296. doi: 10.3389/fonc.2021.625109
20. Wu J, Shi C, Sheng X, Xu Y, Zhang J, Zhao X, et al. Prognostic nomogram for patients with hepatitis E virus-related acute liver failure: a multicenter study in China. J Clin Transl Hepatol. (2021) 9:828. doi: 10.14218/JCTH.2020.00117
21. Chinese M. Guideline of diagnosis and treatment of sudden deafness. *Zhonghua Er Bi Yan Hou Tou Jing Wai Ke Za Zhi.* (2015) 50:443–7.
22. Golmohammadi R, Darvishi E. The combined effects of occupational exposure to noise and other risk factors– a systematic review. *Noise Health.* (2019) 21:125. doi: 10.4103/nah.NAH_4_18
23. Oh J-H, Park K, Lee SJ, Shin YR, Choung Y-H. Bilateral vs. unilateral sudden sensorineural hearing loss. Otolaryngol Head Neck Surg. (2007) 136:87–91. doi: 10.1016/j.otohns.2006.05.015
24. Metrailer AM, Babu SC. Management of sudden sensorineural hearing loss. *Curr Opin Otolaryngol Head Neck Surg.* (2016) 24:403–6. doi: 10.1097/MOO.0000000000000287

Conflict of Interest: The authors declare that the research was conducted in the absence of any commercial or financial relationships that could be construed as a potential conflict of interest.

Publisher's Note: All claims expressed in this article are solely those of the authors and do not necessarily represent those of their affiliated organizations, or those of the publisher, the editors and the reviewers. Any product that may be evaluated in this article, or claim that may be made by its manufacturer, is not guaranteed or endorsed by the publisher.

Copyright © 2022 Lin, Xiong, Yan, Yu, Xie, Xiang, Wu, Ge and Wang. This is an open-access article distributed under the terms of the Creative Commons Attribution License (CC BY). The use, distribution or reproduction in other forums is permitted, provided the original author(s) and the copyright owner(s) are credited and that the original publication in this journal is cited, in accordance with accepted academic practice. No use, distribution or reproduction is permitted which does not comply with these terms.

frontiers | Frontiers in Neurology

ORIGINAL RESEARCH
published: 02 June 2022
doi: 10.3389/fneur.2022.886329

Hypoxia- and Inflammation-Related Transcription Factor SP3 May Be Involved in Platelet Activation and Inflammation in Intracranial Hemorrhage

Ding Wan[1,2†], *Jin Feng*[1†], *Peng Wang*[2], *Zhenxing Yang*[1] *and Tao Sun*[1,2*]

[1] *Department of Neurosurgery, General Hospital of Ningxia Medical University, Yinchuan, China,* [2] *Ningxia Key Laboratory of Craniocerebral Diseases, Ningxia Medical University, Yinchuan, China*

The purpose of this study was to identify the biomarkers implicated in the development of intracranial hemorrhage (ICH) and potential regulatory pathways. In the transcriptomic data for patients with ICH, we identified DEmiRNAs and DEmRNAs related to hypoxia, inflammation, and their transcription factors (TFs). An ICH-based miRNA-TF-mRNA regulatory network was thus constructed, and four biomarkers (*TIMP1*, *PLAUR*, *DDIT3*, and *CD40*) were screened for their association with inflammation or hypoxia by machine learning. Following this, SP3 was found to be a transcription factor involved in hypoxia and inflammation, which regulates *TIMP1* and *PLAUR*. From the constructed miRNA-TF-mRNA regulatory network, we identified three axes, hsa-miR-940/RUNX1/TIMP1, hsa-miR-571/SP3/TIMP1, and hsa-miR-571/SP3/PLAUR, which may be involved in the development of ICH. Upregulated *TIMP1* and *PLAUR* were validated in an independent clinical cohort 3 days after ICH onset. According to Gene Set Enrichment Analysis (GSEA), SP3 was discovered to be important in interleukin signaling and platelet activation for hemostasis. Transcription factor SP3 associated with hypoxia or inflammation plays an important role in development of ICH. This study provides potential targets for monitoring the severity of inflammation and hypoxia in patients with ICH.

Keywords: ICH, hypoxia, inflammation, SP3, biomarkers, cerebrovascular disease

OPEN ACCESS

Edited by:
Yuzhen Xu,
Tongji University, China

Reviewed by:
Xinbing Liu,
Changxing People's Hospital, China
Pengpai Zhang,
Shanghai Jiao Tong University, China

****Correspondence:***
Tao Sun
umc9402321@163.com

[†]These authors have contributed equally to this work

Specialty section:
This article was submitted to Neurological Biomarkers, a section of the journal Frontiers in Neurology

Received: *28 February 2022*
Accepted: *27 April 2022*
Published: *02 June 2022*

Citation:
Wan D, Feng J, Wang P, Yang Z and Sun T (2022) Hypoxia- and Inflammation-Related Transcription Factor SP3 May Be Involved in Platelet Activation and Inflammation in Intracranial Hemorrhage. Front. Neurol. 13:886329. doi: 10.3389/fneur.2022.886329

INTRODUCTION

Intracranial hemorrhage (ICH) is a condition characterized by bleeding from the brain parenchyma caused by the rupture of blood vessels in the brain, which leads to compression of the surrounding nerve tissue, disruption of the brain function, and triggering of disorders (1). ICH can be triggered by various factors, such as trauma, hypertension, and infection (2, 3). ICH accounts for 10–15% of strokes and is its most lethal subtype (4–8). The formation of a hematoma from ICH can severely disrupt tracts, leading to various dysfunctions and threatening patients' lives, which makes ICH highly disabling and mortal (4). More than 1 million people are affected by ICH each year (9). The mortality rate for patients with ICH range from 30 to 50% at 1 month and 54% at 1 year (10, 11). The unprecedented virus (COVID-19) have also been identified as potential risk factors for ICH (12). Patients with ICH need to be diagnosed and treated early and accurately in order to achieve the best possible outcome.

Neuronal apoptosis, inflammation, oxidative stress, edema formation, and the breakdown of the blood–brain barrier all contribute to ICH development (13, 14). ICH is not only pathologically characterized by inflammation, but it also causes secondary damage to the brain (15, 16). Inflammatory injury can damage the vascular endothelium and, thus, is involved in ICH development (17, 18). The infiltrating leukocytes can release pro-inflammatory factors, which further damage the blood–brain barrier, thereby worsening the secondary brain injury after ICH development (19–21). Meanwhile, hypoxia can be activated through oxidative stress mechanisms, which in turn are involved in the developmental mechanisms of ICH (14, 22). Therefore, we hypothesize that inflammation and hypoxia play important roles in ICH pathogenesis; however, the molecular mechanisms involved are not yet clear.

Because inflammation is involved in secondary damage after ICH, the degree of inflammation can be used to predict the prognosis of patients with ICH (21, 23, 24). Some indicators of inflammation, such as the neutrophil-to-lymphocyte ratio, have been shown to be useful in predicting the prognosis of patients with ICH, and they are predictive of a good outcome (25). Brain tissue can become hypoxic from ICH, causing irreversible damage (26). Genes associated with hypoxia or inflammation, as well as their pathways of action, play an important role in the development and progression of ICH. ICH development is involved in the Nrf2/HO-1 signaling pathway, according to the previous studies (27). KLF6 acts as a transcription factor that mediates SIRT5 inhibition of the Nrf2/HO-1 signaling pathway, which in turn exacerbates neuronal apoptosis and oxidative stress after ICH development (28). KLF6 plays a crucial role in the inflammatory and hypoxic response (27). Inflammation and hypoxia dramatically impact the survival and quality of life of patients with ICH. Thus, identifying the degree of inflammation and hypoxia in ICH is essential for monitoring the prognosis of patients with ICH.

Recent developments in bioinformatics, including the availability of considerable RNA sequencing data resources, have provided a direction for disease diagnosis and treatment (29–32). Gene expression profiles associated with inflammation or hypoxia can be obtained from RNA sequencing data. This study was designed to examine the genes and pathways that are potentially involved in inflammation during ICH.

METHODS

Data Downloaded From the GEO Database

The GEO database was searched for intracerebral hemorrhage-related RNA transcriptomic datasets based on the following keywords: "intracerebral haemorrhage" and "brain haemorrhage". Exclusion criteria were set as follows: (1) transcriptomic data from animal models or knockout animals; (2) brain hemorrhage caused by vascular malformations, aneurysms, etc.; and (3) drug experiments designed. A dataset containing mixed plasma samples from 15 patients with ICH and eight healthy controls (GSE43618 dataset) was filtered based on the filtering criteria (33). Peripheral blood mRNA transcriptomic data were obtained from GSE125512 for 11 patients with ICH at the onset and 3 days after onset (34). These two datasets were used to identify differentially expressed miRNAs (DEmiRNAs) and differentially expressed mRNAs (DEmRNAs). These DEmRNAs were derived from an analysis of differences between peripheral blood transcriptome expression profiles 3 days after and at ICH onset. The transcriptome data were log-2 transformed with different unit formats, and de-batching between samples was performed. Finally, we collected peripheral blood samples from 20 patients with an ICH and 17 healthy control volunteers in order to validate the genes related to inflammation and hypoxia identified by the bioinformatics analysis. Included patients must meet the following criteria: (1) experience acute cerebral hemorrhage within 3 days; (2) have clear diagnostic imaging and laboratory results; (3) have no vascular malformations, coagulation disorders, or other causes of bleeding; and (4) be free of malignant tumors and other serious diseases. Ethics approval for this study was obtained from the General Hospital of Ningxia Medical University. All the participants provided written informed consent.

Inflammation or Hypoxia-Associated Gene Sets

In order to select a broad list of candidate gene sets for inflammation- and hypoxia-related genes, we searched the Kyoto Encyclopedia of Genes and Genomes (KEGGs) database (www.kegg.jp). Furthermore, the PubMed and Web of Science databases were searched for inflammation- or hypoxia-related gene complements. Ultimately, a total of 50 hypoxia-related genes and 200 inflammation-related genes were identified. These genes are mainly involved in inflammatory or hypoxic response processes during disease development.

Analysis of Variances

First, the limma R package was used to identify DEGs, including DEmiRNAs and DEmRNAs, in the occurrence of ICH (35). We identified mRNAs that are up- and down-regulated in patients with ICH 3 days after cerebral hemorrhage compared with those at the onset of cerebral hemorrhage using differential expression analysis of the peripheral blood transcriptome. DEGs were filtered using $p < 0.05$ as the threshold. Data were then filtered by genes using Perl (https://www.perl.org/) to obtain dysregulated genes associated with inflammation or with hypoxia and the corresponding gene expression matrix.

Biological Functional Pathway Analysis

Functional pathway analysis of up- or down-regulated DEmRNAs using the Kyoto Encyclopedia of Genes and Genomes (KEGGs) and Gene Ontology (GO). GO terminology is described in three parts: biological processes (BPs), cellular components (CCs), and molecular functions (MFs). The clusterProfiler R package was used to complete GO and KEGG analysis as previous research (36, 37). Further, GSEA is used to analyze functional pathways of dysregulated biology involving key genes (38). Selected functional pathways for differential analysis are referenced from "c2.cp.v7.2.symbols.gmt [Curated]" in MSigDB collections (https://www.gsea-msigdb.org/gsea/msigdb/) gene set. The threshold used to identify dysfunctional

pathways was set at a false discovery rate of <0.25 and adjusted p of <0.05.

Construction of miRNA–TF–mRNA Network

According to the previous study, the miRNA–TF–mRNA network was constructed (39–42). First, TF–mRNA relationship pairs were predicted in DEmRNAs using the TRRUST (v2) database (43), where mRNAs were associated with hypoxia or inflammation. To explore regulatory relationships between DEmiRNAs and DEmRNAs (including TFs), miRWalk was used (http://mirwalk.umm.uni-heidelberg.de/>). R software was used to match the interrelationships between DEmiRNAs and DEmRNAs. Among the predicted miRNA–mRNA molecular pairs, only those with opposite regulatory directions were subjected to further analysis. Furthermore, Cytoscape was used to visualize the entire miRNA–TF–mRNA interaction network and to identify the hub genes in the network based on the number of connections in each node (44).

Machine Learning

Intelligent machines are converging with advancing biotechnologies to shape the future of medicine (45). Machine learning is used to screen genes associated with the progression of ICH. Support Vector Machine–Recursive Feature Elimination (SVM–RFE) was used to investigate genes associated with hypoxia and inflammation (46). SVM is excellent at handling small datasets and shows good classification performance. Redundant genes are filtered using the iterative algorithm of SVM–RFE, resulting in genes highly correlated with the outcome. Furthermore, the least absolute shrinkage and selection operator (LASSO) is used for gene screening. As previous research, LASSO analysis was performed using the "glmnet" R package (42, 47). ROC curves were used to assess the predictive ability of core genes to distinguish between patients with ICH at different progression stages, thereby testing their reliability for the outcome prediction. Principle component analysis and t-distributed stochastic neighbor embedding (t-SNE) (48) were used to demonstrate the ability of screened core genes to classify patients with ICH at different developmental stages. The R package "Rtsne" was used to implement the t-SNE algorithm based on non-linear dimensionality reduction.

Quantitative qRT-PCR

Total RNA was extracted using TRIzol (TaKaRa Bio, Shiga, Japan) and reverse-transcribed into cDNA using PrimeScript RT Master Mix (TaKaRa Bio, Shiga, Japan). According to the manufacturer's instructions, Real-time PCR was performed using SYBR Green PCR Master Mix (Takara). Using GAPDH as a reference, the $2^{-\Delta\Delta Ct}$ method was applied for the relative quantification of core gene expression levels and normalized.

Statistical Analysis

All the drawings are performed using the R software (version 4.0.5). The "VennDiagram" R package is used to create a Venn diagram to present the results of the gene intersection analysis. Spearman's correlation test was used to assess the correlation between key genes, and correlation coefficients of >0.3 were considered to be co-expression relationships. Differential analysis of gene expression between the two groups was performed using the Wilcoxon rank-sum test. Unless otherwise indicated, $p < 0.05$ was considered a statistically significant difference.

RESULTS

Neutrophils Play an Important Role in ICH Development

To obtain biomarkers and pathways associated with the occurrence or progression of ICH, we performed a differential expression analysis. First, 46 DEmiRNAs were identified by differential analysis between ICH and healthy control (HC) (**Figure 1A**). Based on the transcriptomic data obtained from the peripheral blood of ICH at different development stages, 914 DEmRNAs were identified. Compared to the onset of ICH, 444 genes were upregulated and 470 genes were downregulated 3 days after the onset of ICH (**Figure 1B**). These up- and downregulated genes were then subjected to separate functional pathway analyses. The main pathways shown to be upregulated in ICH by GO and KEGG included neutrophil-mediated immunity, secretory granule lumen, cell adhesion molecule binding, and regulation of actin cytoskeleton (**Figure 1C**). In addition, the pathways enriched by the downregulated genes contained RNA splicing, nuclear speck, Herpes simplex virus 1 infection, and condensed chromosome (**Figure 1D**). These results suggest that neutrophils play an important role in the development of ICH.

Identification of Differentially Expressed Genes Associated With Inflammation or Hypoxia

To explore the possible role of inflammation- or hypoxia-related genes in ICH development, we further screened the inflammation- and hypoxia-related genes separately in the DEmRNAs. We identified 15 genes associated with hypoxia; their relative expression between ICHs is shown in **Figure 2A**. The number of genes related to inflammation was 16 (**Figure 2B**). The corresponding heat map showed a clear boundary between hypoxia or inflammation-related DEGs in patients with different stages of ICH. This suggests that the genes associated with hypoxia or inflammation play an important role in ICH development.

PPI Network Shows SP3 as a Hub Gene and May Be Associated With Hypoxia and Inflammation

From all the DEmRNAs, eight differentially expressed transcription factors (DETFs) were identified, which can regulate some of these genes in DEGs associated with hypoxia or inflammation. Furthermore, 10 DEmiRNAs were predicted to potentially act on these DEmRNAs (or DETFs) associated with hypoxia or inflammation. And the relationship pairs between these DEmiRNAs and DEmRNAs (including DETFs) were constructed as an miRNA–TF–mRNA interaction network (**Figure 2C**). From this molecular interaction network, SP3 was identified as the hub gene in the network, as it has the

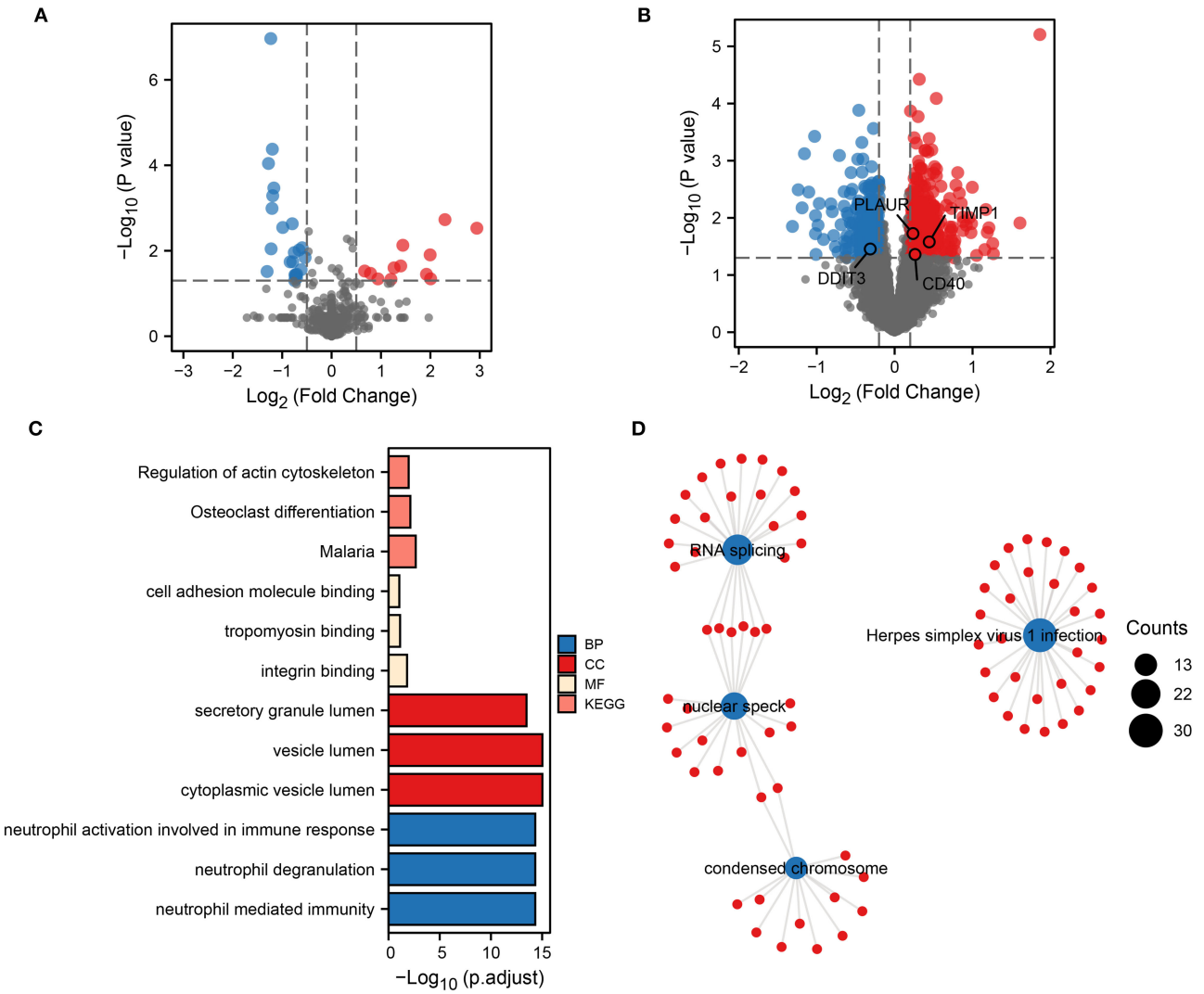

FIGURE 1 | Biological functional pathways of DEGs. Volcano plot showing DEmiRNAs **(A)** and DEmRNAs **(B)**. Red represents upregulated genes, and blue represents downregulated genes. Upregulated **(C)** and downregulated **(D)** biological functional pathways enriched by DEGs.

highest number of linkages (**Figure 2D**). From the constructed molecular interaction network, we further identified a possible correlation between *SP3* and *TIMP1* and *PLAUR*. *TIMP1* is an inflammation-related gene, while *PLAUR* is a gene associated with hypoxia and inflammation. Therefore, the hub gene *SP3* might be a transcription factor associated with hypoxia and inflammation.

Thirteen Important Genes Obtained From Machine Learning Screening

To evaluate the genes associated with hypoxia or inflammation that are closely related to ICH development, SVM–RFE and LASSO analyses were applied to screen DEGs. SVM–RFE showed minimal error in outcome prediction when all 31 hypoxia- or inflammation-related DEmRNAs were selected (**Figure 3A**). In a subsequent analysis, the Lasso analysis identified 13 hypoxia- or inflammation-related genes that were strongly associated with ICH development (**Figure 3B**). **Figure 3C** shows the co-expression network of these 13 genes, and *TIMP1* and *PLAUR* were found to be co-expressed with several genes. Moreover, PCA and tSNE visualizations demonstrate that these 13 genes can be used to distinguish patients with ICH at different stages (**Figures 3D,E**).

Venn Analysis Identified Four DEGs Associated With Inflammation or Hypoxia

An intersection analysis of hypoxia- or inflammation-related DEGs obtained from machine learning and PPI networks was performed, and four core inflammation- or hypoxia-related DEGs (*TIMP1*, *PLAUR*, *DDIT3*, and *CD40*) were identified (**Figure 4A**). The relative expression profiles of these four core genes in patients with ICH are

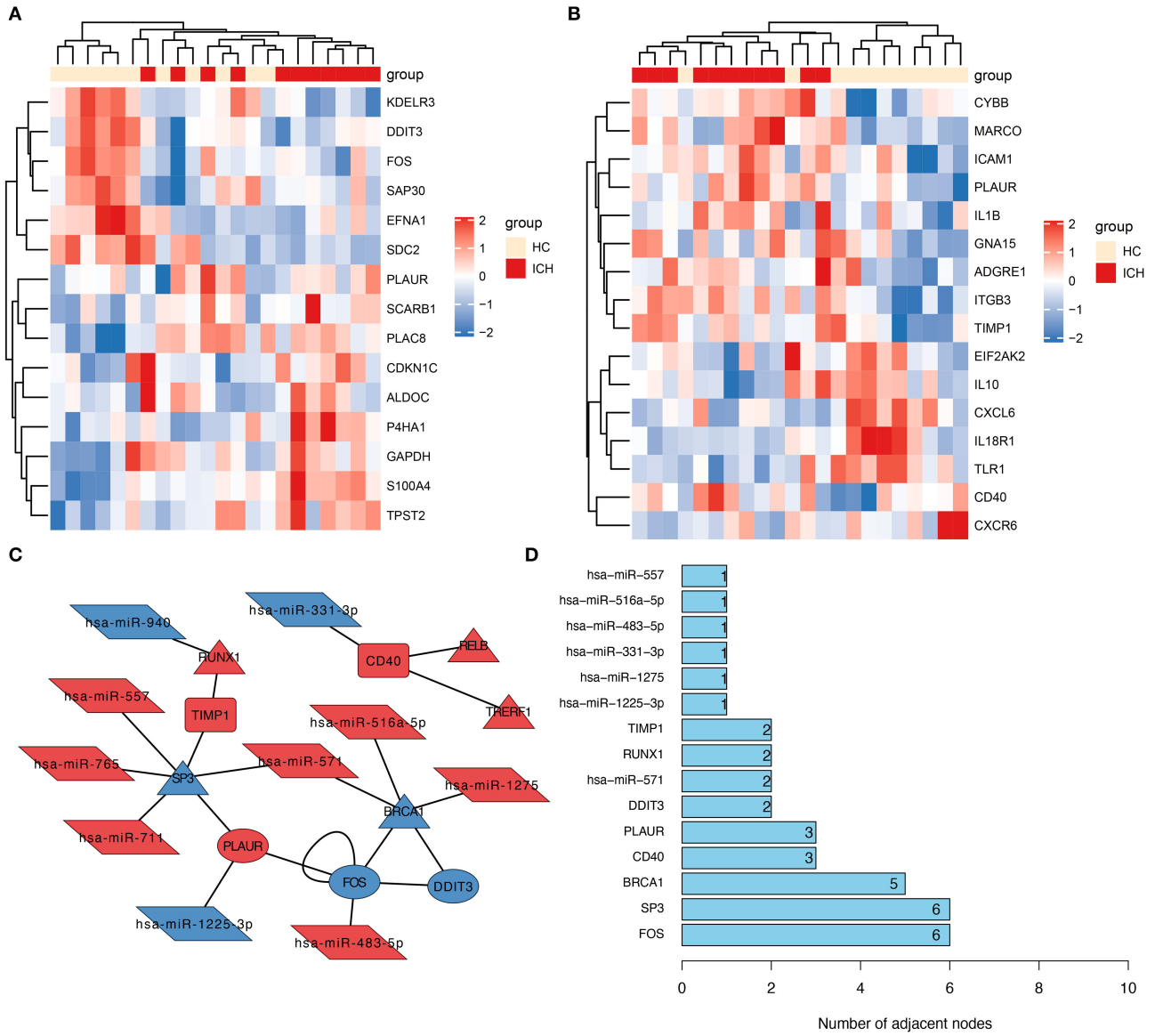

FIGURE 2 | Construction of molecular interactions networks. Heat map showing hypoxia- **(A)** and inflammation-related **(B)** DEGs in patients with ICH. The depth of the color was used to indicate the intensity of gene expression. **(C)** The constructed miRNA–TF–mRNA network. Each node represents a gene and each edge represents a gene interaction. Triangle represents transcription factors, parallelogram represents miRNAs, ellipse represents hypoxia-related genes, and the round rectangle represents inflammation-related genes. **(D)** Number of junctions between individual genes in this miRNA–TF–mRNA network.

shown in **Figure 4B**. The ROC curves for *PLAUR* (AUC = 0.777), *DDIT3* (AUC = 0.669), *CD40* (AUC = 0.727), and *TIMP1* (AUC = 0.719) for the different stages of ICH development are shown in **Figures 4C–F**, respectively, indicating their moderate predictive power. PCA and tSNE visualization showed that patients with different stages of ICH can be distinguished based on these four genes (*TIMP1*, *PLAUR*, *DDIT3*, and *CD40*) (**Figures 4G,H**). Therefore, four biomarkers (TIMP1, PLAUR, DDIT3, and CD40) were screened for their association with inflammation or hypoxia by machine learning.

Transcription Factors and Corresponding miRNAs That Regulate *TIMP1*

In the regulatory network, we discover that RUNX1 and SP3 may act as transcriptional regulators of *TIMP1* (**Figure 2C**). RUNX1 is regulated by hsa-miR-940, and SP3 is regulated by hsa-miR-571 (which has the most junctions). The magnitudes of the fold change values for hsa-miR-940 and hsa-miR-571 are shown in **Figure 5A**. The relative ranking of the fold change values for *TIMP1*, *PLAUR*, *DDIT3*, and *CD40* are shown in **Figure 5B**. Further correlation analysis showed a positive correlation between *RUNX1* and *TIMP1* ($r = 0.24$, **Figure 5C**) and a negative

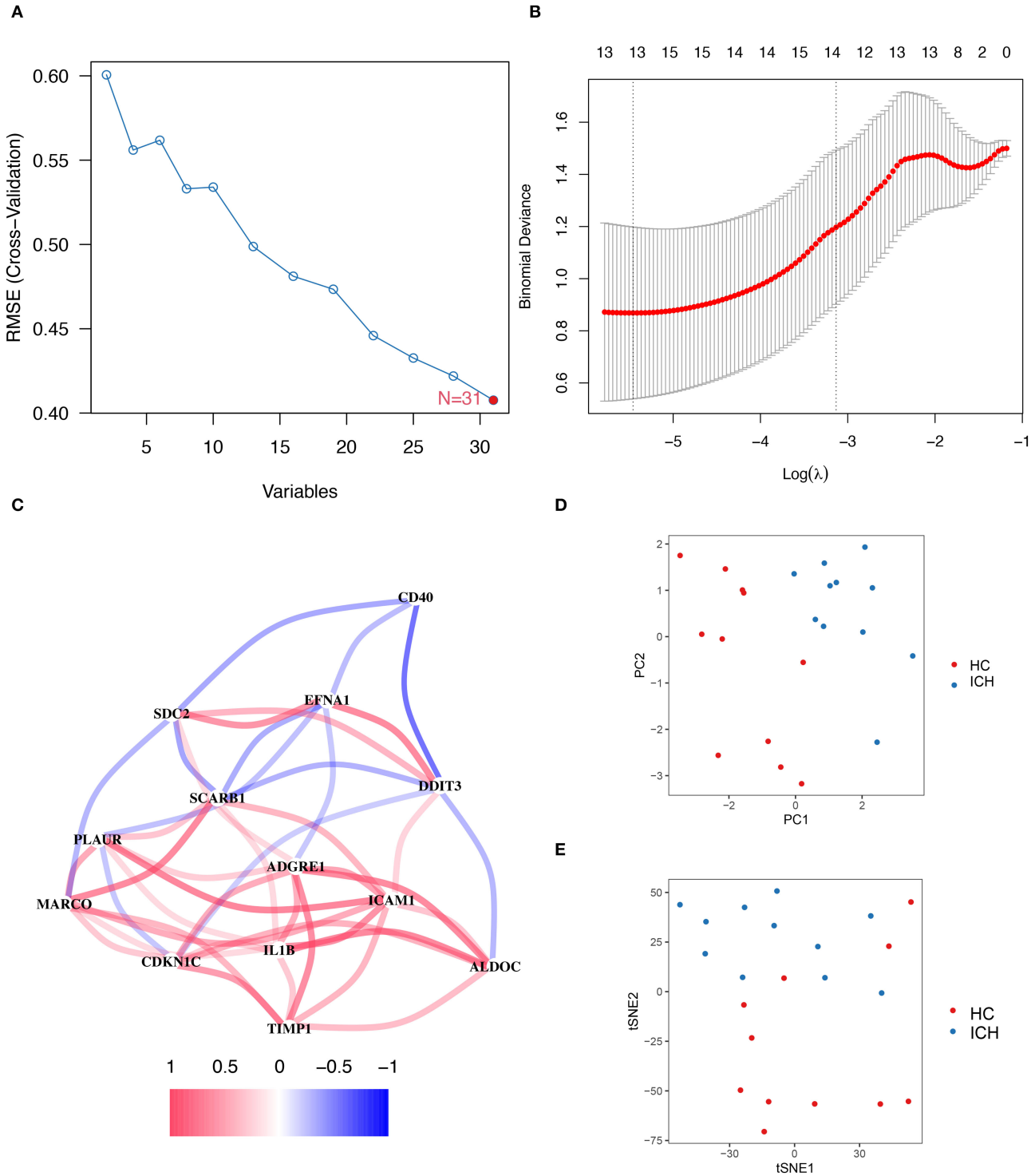

FIGURE 3 | SVM–RFE and LASSO regression analysis results. **(A)** On a line graph the prediction accuracy of each variable included in the model is displayed. And the SVM–RFE screening process showed the smallest errors were obtained when all 31 genes were included in the model. **(B)** The LASSO analysis resulted in a final screening of 13 genes. **(C)** Correlation linkage maps of hypoxia- and inflammation-related genes using machine learning. **(D)** PCA shows that the visualization of data based on PC1 and PC2 can be clearly distinguish between patients with ICH at different stages. **(E)** Visualizes the ability to distinguish patients with ICH at different stages of development by tSNE method.

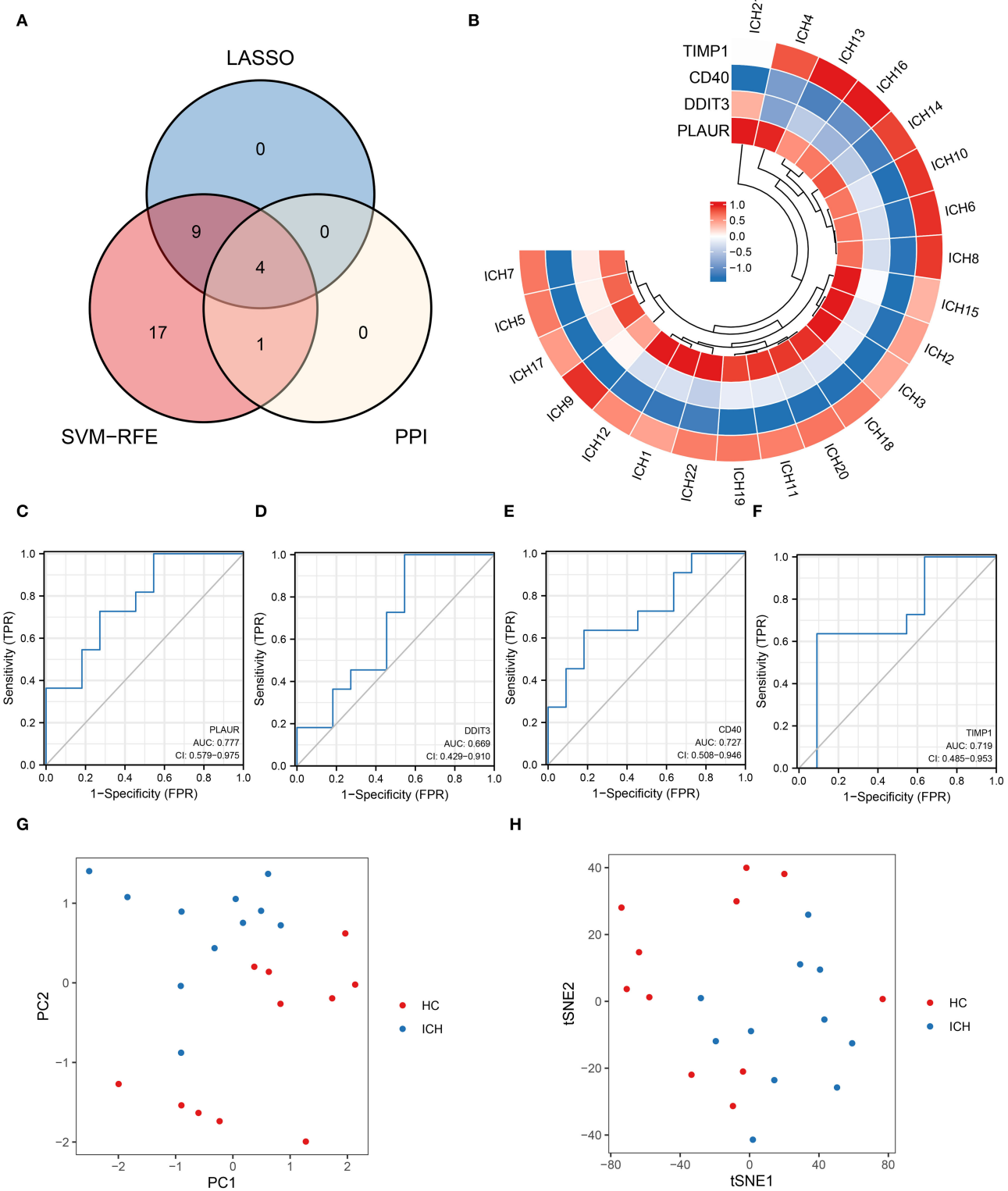

FIGURE 4 | Four key genes obtained from the cross-tabulation analysis. **(A)** The Venn diagram shows that four core genes are shared in the PPI network, SVM–RFE, and LASSO. **(B)** Relative expression profiles of these four core genes in all the patients. **(C)** PALUR, **(D)** DDIT3, **(E)** CD40, and **(F)** the ability of TIMP1 to differentiate between patients with ICH at different development stages. **(G)** PCA and **(H)** tSNE visualization showing the ability to discriminate between patients with ICH at different development stages.

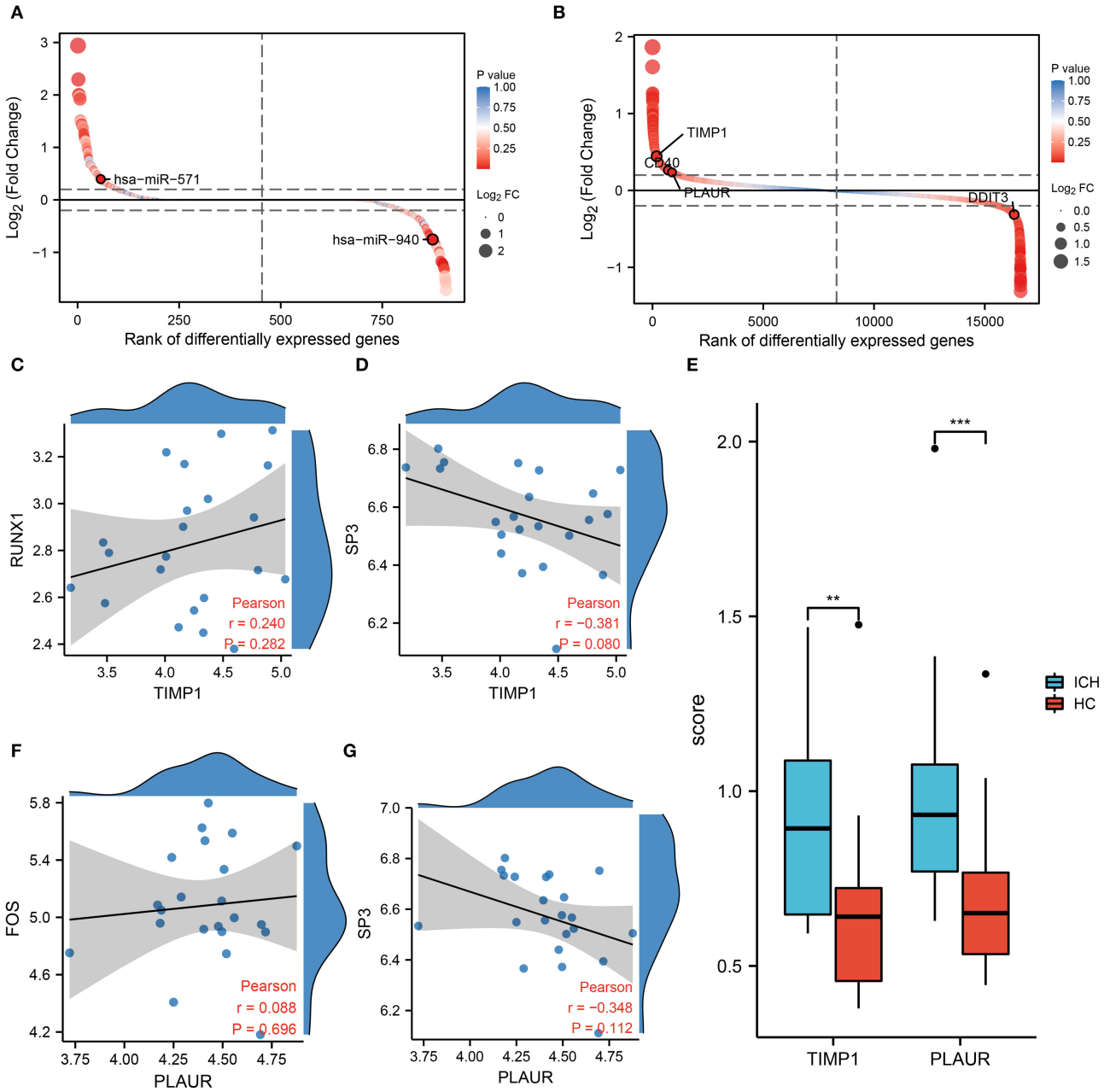

FIGURE 5 | Results of co-expression analysis of four core genes. DEmiRNAs **(A)** DEmRNAs **(B)** are arranged by $\log_2$ (Fold Change). **(C)** Correlation analysis between *RUNX1* and the inflammation-associated gene *TIMP1*. **(D)** Correlation analysis between *SP3* and the inflammation-associated gene *TIMP1*. **(E)** PCR showed differential expression of *TIMP1* and *PLAUR* between the HC and ICH groups. **(F)** Correlation analysis between FOS and PLAUR. **(G)** Correlation analysis between SP3 and PLAUR.

correlation between *SP3* and *TIMP1* ($r = -0.381$, **Figure 5D**). Although there was no statistically significant difference, more cellular research are needed. Therefore, we further predicted two miRNA–TF–mRNA axes around the inflammation-related gene TIMP1, namely, hsa-miR-940/RUNX1/*TIMP1* and hsa-miR-571/SP3/TIMP1 (**Figure 2C**). Validation in an independent clinical cohort showed statistically significant differences in *TIMP1* expression between ICH and HC ($p < 0.01$, **Figure 5E**).

Transcription Factors and Corresponding miRNAs That Regulate PLAUR

In the molecular interaction network (**Figure 2C**), the transcription factors of the hypoxia-related gene *PLAUR* were SP3 and FOS. SP3 also exhibited a regulatory effect on the inflammation-related gene *TIMP3*. Based on a condition of >0.3 correlation coefficient, we found no co-expression between *FOS* and *PLAUR* ($r = 0.08$, $p = 0.282$, **Figure 5F**), while

there was some negative correlation between *SP3* and *PLAUR* ($r = -0.348$, **Figure 5G**). Therefore, we identified SP3 as a key hypoxia- and inflammation-related transcription factor. In addition, hsa-miR-571/SP3/*PLAUR* was constructed around *SP3* and *PLAUR* as an axis miRNA-TF-mRNA (**Figure 2C**). There was a significant difference in *PLAUR* expression between ICH and HC based on the data from an independent clinical cohort ($p < 0.01$, **Figure 5E**).

SP3 Is Involved in Leukocyte- and Platelet-Related Physiological Processes

We performed GSEA analysis of the transcription factors SP3 and RUNX1 to explore the pathways in which they might be involved. GSEA showed that the signaling by interleukins, hemostasis, platelet activation signaling and aggregation, and mitotic prometaphase pathways were upregulated in patients with ICH with SP3 downregulation (**Figure 6A**). In patients with ICH with elevated RUNX1 expression, elastic fiber formation was downregulated, while the transcriptional regulation of the granulopoiesis pathway was upregulated (**Figure 6B**). The aforementioned results indicate that SP3 may be involved in interleukin signaling and platelet activation for hemostasis, while RUNX1 may be involved in granulopoiesis after ICH onset.

TIMP1 Is Associated With Platelets and Angiogenesis

In patients with ICH with *PLAUR* upregulation, mitotic prometaphase and cell cycle checkpoints were downregulated, while interferon signaling and hippoyap signaling pathway were upregulated (**Figure 6C**). In patients with ICH with elevated expression of *TIMP1*, the platelet activation signaling and aggregation, insulin signaling pathway, and angiogenesis pathways were upregulated (**Figure 6D**). *PLAUR* and *TIMP1* were both upregulated 3 days after ICH onset. Therefore, it is hypothesized that *PLAUR*, a hypoxia and inflammation-related gene, may be involved in upregulating the interferon signaling pathway and hippo pathway, while *TIMP1* may be involved in platelet activation and aggregation, activating insulin signaling pathways, and promoting angiogenesis.

DISCUSSION

Four hypoxia- or inflammation-related biomarkers (*TIMP1*, *PLAUR*, *DDIT3,* and *CD40*) were identified in this study. Among them, SP3 might act as a transcriptional regulator for *TIMP1* and *PLAUR*. A bioinformatics approach was used to predict the possible roles of the three hypoxia- and inflammation-related miRNA–TF–mRNA axes (hsa-miR-940/RUNX1/*TIMP1*, hsa-miR-571/SP3/*TIMP1*, and hsa-miR-571/SP3/*PLAUR*) in ICH development. Independent clinical cohort studies have validated upregulation of *TIMP1* and *PLAUR* expression after the onset of ICH. In addition, GSEA was used to analyze the functions of *SP3*, *RUNX1*, *TIMP1*, and *PLAUR*.

TIMP1 and *PLAUR* have been identified in the previous studies as involved in the progression of ICH. Matrix metalloproteinases (MMPs) are the most important degrading enzymes in the pathogenesis of ICH (49), during extracellular matrix reconstruction and blood–brain barrier disruption (50). TIMP1 is a major endogenous inhibitor of MMP-9 and was found to be significantly more expressed in the serum of patients with ICH than in normal controls in a study of the Chinese Han patients with ICH (51). TIMP-1 expression is also associated with early mortality in ICH as its potential biomarker for predicting mortality (52). The urokinase-type fibrinogen activator encoded by the *PLAUR* gene plays an important role in the development of cortical neural circuits and in brain tissue remodeling after brain injury (53, 54). Thus, *PLAUR* can be related to the prognosis of patients with ICH. In this study, *TIMP1* and *PLAUR* were upregulated 3 days after the onset of ICH compared with that before the onset. Previous studies have found that TIMP1 is associated with primary sarcopenia, colon cancer progression and metastasis, and some infectious diseases (55–57). We found that TIMP1 is involved in platelet activation and aggregation, insulin signaling pathway activation, and angiogenesis. The upregulation of *TIMP1* can therefore affect recovery, regression, and progression of the patients with ICH by affecting both platelet function and angiogenesis. And *PLAUR* is associated as an inflammation-related gene with diseases or processes, such as asthma, myocardial infarction, and reduced lung function (58–60). TIMP1 and PLAUR are involved in inflammation and hypoxia-related progression in ICH. MMP-9 is expressed in inflamed tissues and is involved in the inflammatory process (61). TIMP-1 is a natural inhibitor of MMP-9 (62). Thus, TIMP-1 might play a role in the inflammatory response by inhibiting MMP-9. After inflammation occurs, PLAUR binds to PLAU and activates plasminogen to plasmin, promoting inflammatory cell migration and activation and matrix metallopeptidase (MMP) activation, thereby participating in the inflammatory response (60, 63–65). In addition, PLAUR can be regulated by the hypoxia-inducible factor HIF-1 to play a role in the hypoxia-related mechanisms of the disease (66). In this study, TIMP1 and PLAUR upregulation in ICH was validated in an independent cohort, which confirms the involvement of TIMP1 and PLAUR in ICH development.

In this study, we found that both *TIMP1* and *PLAUR* are regulated by SP3, a transcription factor associated with both hypoxia and inflammation. Hypoxia has long been found to downregulate SP3 (67). The SP transcription factor family can be involved in the regulation of hypoxic gene expression in the hippocampus through a mechanism mediated by oxidative stress during hypoxia (68). In addition, SP3 is involved in the molecular regulatory mechanism of hypoxia-inducible factor 1α (69). Following inflammatory stimuli, SP3 and NF–κB interact to regulate inflammatory gene expression (70). SP3 is also involved in LPS-induced cellular inflammation (71). In patients with concomitant SP3 downregulation, signaling by interleukins, hemostasis, platelet activation signaling and aggregation, and mitotic prometaphase pathways were upregulated. These pathways suggest that downregulated SP3 is involved in interleukin signaling, platelet activation, and hemostasis. Therefore, SP3 downregulation might influence the progression and regression of ICH by affecting the degree of

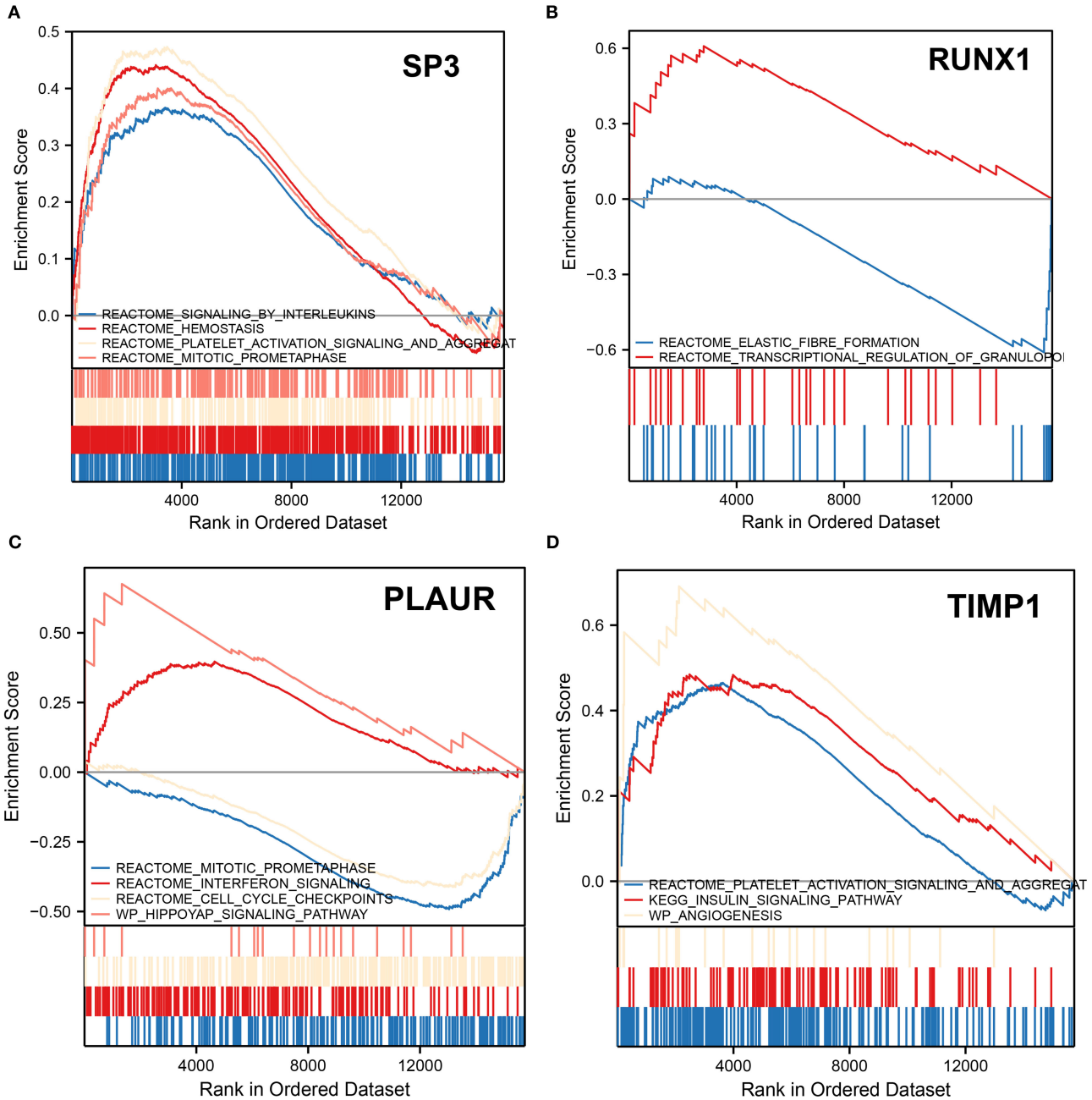

FIGURE 6 | Gene set enrichment analysis. **(A)** GSEA shows altered pathways in samples with downregulated SP3. **(B)** GSEA shows altered pathways in samples with upregulated RUNX1. **(C)** GSEA shows altered pathways in samples upregulated by PLAUR. **(D)** GSEA shows altered pathways in samples with TIMP1 upregulation. The upward peaks of the curve represent the upward adjustment pathway, while the downward peaks represent the downward adjustment pathway.

platelet activation as well as the level of inflammation, ultimately affecting the prognosis and quality of life of patients.

The miRNA–TF–mRNA network identified hsa-miR-571 as the pivotal miRNA regulating SP3. Previous studies have found that miR-571 functions in DNA replication and genomic stability (72). miR-571 is involved in the inflammatory process in cirrhosis (73), and can regulate the activation of human stem stellate cells (74) by mediating the Notch3 signaling pathway (75). However, there is a lack of studies on the relationship between miR-571 and SP3. In this study, we found the first evidence suggesting that hsa-miR-571 regulated the level of inflammation and platelet activation in ICH by regulating SP3 translation. And hsa-miR-571/SP3/TIMP1 and hsa-miR-571/SP3/PLAUR are two miRNA-TF-mRNAs involved in ICH development.

TIMP1 and PLAUR were differentially expressed in ICH and were upregulated 3 days after the onset of ICH. The upregulation of TIMP1 might have influenced the outcome of patients with ICH by affecting the platelet function and angiogenesis. PLAUR, in turn, was involved in the upregulation of the interferon signaling pathway and the hippo pathway. The hypoxia- and inflammation-related transcription factor SP3 was involved in the regulation of TIMP1 and PLAUR. SP3 might have influenced the progression of ICH by affecting the degree of platelet activation and the inflammation level. These findings provide potential targets for the diagnosis, treatment, and regression of ICH in order to monitor the severity of inflammation and hypoxia in patients with ICH. Although clinical samples were used for validating the study results, the number of clinical samples was small and the strength of validation needs improvement. Bioinformatic findings will need to be validated in the relevant cell lines as well as ICH animal models in the future. In addition to investigate the relationship between SP3 and its counterparts hsa-miR-571, *TIMP1*, and *PLAUR*, more research is needed to identify the role of SP3 in ICH.

CONCLUSION

The hsa-miR-940/RUNX1/TIMP1, hsa-miR-571/SP3/TIMP1, and hsa-miR-571/SP3/PLAUR play important roles in ICH development. The hypoxia- and inflammation-related transcription factor SP3 might be involved in platelet activation in ICH through the regulation of TIMP1/PLAUR, as well as in inflammatory regulation.

DATA AVAILABILITY STATEMENT

The original contributions presented in the study are included in the article/**Supplementary Material**, further inquiries can be directed to the corresponding author/s.

ETHICS STATEMENT

The studies involving human participants were reviewed and approved by General Hospital of Ningxia Medical University's Ethics Committee. The patients/participants provided their written informed consent to participate in this study.

AUTHOR CONTRIBUTIONS

DW, JF, PW, ZY, and TS performed the data curation and analysis. DW, JF, and TS analyzed and interpreted the results. TS drafted and reviewed the manuscript. All authors read and approved the final manuscript.

ACKNOWLEDGMENTS

The authors thank all the patients and staff who participated in this study.

SUPPLEMENTARY MATERIAL

The Supplementary Material for this article can be found online at: https://www.frontiersin.org/articles/10.3389/fneur.2022.886329/full#supplementary-material

REFERENCES

1. Choy KW, Tsai AP-Y, Lin PB-C, Wu M-Y, Lee C, Alias A, et al. The role of urocortins in intracerebral hemorrhage. *Biomolecules.* (2020) 10:96. doi: 10.3390/biom10010096
2. Aguilar MI, Brott TG. Update in intracerebral hemorrhage. *Neurohospitalist.* (2011) 1:148–59. doi: 10.1177/1941875211409050
3. Cho S-M, Lee T, Starling RC, Thompson NR, Uchino K. The impact of infection and elevated INR in LVAD-associated intracranial hemorrhage: a case-crossover study. *ASAIO J.* (2019) 65:545–9. doi: 10.1097/MAT.0000000000000887
4. Sun L, Zhang K, Zhai W, Li H, Shen H, Yu Z, et al. TAR DNA binding protein-43 loss of function induced by phosphorylation at S409/410 blocks autophagic flux and participates in secondary brain injury after intracerebral hemorrhage. *Front Cell Neurosci.* (2018) 12:79. doi: 10.3389/fncel.2018.00079
5. Chen S, Yang Q, Chen G, Zhang JH. An update on inflammation in the acute phase of intracerebral hemorrhage. *Transl Stroke Res.* (2015) 6:4–8. doi: 10.1007/s12975-014-0384-4
6. Leclerc JL, Santiago-Moreno J, Dang A, Lampert AS, Cruz PE, Rosario AM, et al. Increased brain hemopexin levels improve outcomes after intracerebral hemorrhage. *J Cereb Blood Flow Metab.* (2018) 38:1032–46. doi: 10.1177/0271678X16679170
7. Zhai W, Chen D, Shen H, Chen Z, Li H, Yu Z, et al. A1 adenosine receptor attenuates intracerebral hemorrhage-induced secondary brain injury in rats by activating the P38-MAPKAP2-Hsp27 pathway. *Mol Brain.* (2016) 9:66. doi: 10.1186/s13041-016-0247-x
8. Mao L, Li P, Zhu W, Cai W, Liu Z, Wang Y, et al. Regulatory T cells ameliorate tissue plasminogen activator-induced brain haemorrhage after stroke. *Brain.* (2017) 140:1914–1931. doi: 10.1093/brain/awx111
9. An SJ, Kim TJ, Yoon B-W. Epidemiology, risk factors, and clinical features of intracerebral hemorrhage: an update. *J Stroke.* (2017) 19:3–10. doi: 10.5853/jos.2016.00864
10. Jiang C, Wang Y, Hu Q, Shou J, Zhu L, Tian N, et al. Immune changes in peripheral blood and hematoma of patients with intracerebral hemorrhage. *FASEB j.* (2020) 34:2774–91. doi: 10.1096/fj.201902478R
11. Al-Mufti F, Thabet AM, Singh T, El-Ghanem M, Amuluru K, Gandhi CD. Clinical and radiographic predictors of intracerebral hemorrhage outcome. *Intervent Neurol.* (2018) 7:118–36. doi: 10.1159/000484571
12. Adewunmi T, Modinat A, Lois H. A systematic review on the neurological manifestations of COVID-19. *Life Res.* (2020) 3:158. doi: 10.53388/life2020-1014-303
13. Iniaghe LO, Krafft PR, Klebe DW, Omogbai EKI, Zhang JH, Tang J. Dimethyl fumarate confers neuroprotection by casein kinase 2 phosphorylation of Nrf2 in murine intracerebral hemorrhage. *Neurobiol Dis.* (2015) 82:349–58. doi: 10.1016/j.nbd.2015.07.001
14. Wei C-C, Kong Y-Y, Li G-Q, Guan Y-F, Wang P, Miao C-Y. Nicotinamide mononucleotide attenuates brain injury after intracerebral hemorrhage by activating Nrf2/HO-1 signaling pathway. *Sci Rep.* (2017) 7:717. doi: 10.1038/s41598-017-00851-z
15. Bi Y, Huan Y, Cai W, Wang X, Liang Z, Liu Z, et al. Mild hypothermia in combination with minimally invasive evacuation of hematoma reduces inflammatory damage in patients via the nuclear factor-κB pathway. *Exp Ther Med.* (2014) 8:1717–22. doi: 10.3892/etm.2014.2012
16. Wilkinson DA, Pandey AS, Thompson BG, Keep RF, Hua Y, Xi G. Injury mechanisms in acute intracerebral hemorrhage. *Neuropharmacology.* (2018) 134:240–8. doi: 10.1016/j.neuropharm.2017.09.033

17. Yenari MA, Han HS. Neuroprotective mechanisms of hypothermia in brain ischaemia. *Nat Rev Neurosci.* (2012) 13:267–78. doi: 10.1038/nrn3174
18. Cai PY, Bodhit A, Derequito R, Ansari S, Abukhalil F, Thenkabail S, et al. Vagus nerve stimulation in ischemic stroke: old wine in a new bottle. *Front Neurol.* (2014) 5:107. doi: 10.3389/fneur.2014.00107
19. Keep RF, Xiang J, Ennis SR, Andjelkovic A, Hua Y, Xi G, Hoff JT. Blood-brain barrier function in intracerebral hemorrhage. In: Zhou L-F, Chen X-C, Huang F-P, Xi G, Keep RF, Hua Y, et al. editors. *Cerebral Hemorrhage. Acta Neurochirurgica Supplementum*. Vienna: Springer Vienna (2008). p. 73–7.
20. Joice SL, Mydeen F, Couraud P-O, Weksler BB, Romero IA, Fraser PA, et al. Modulation of blood–brain barrier permeability by neutrophils: in vitro and in vivo studies. *Brain Res.* (2009) 1298:13–23. doi: 10.1016/j.brainres.2009.08.076
21. Yu Z, Zheng J, Guo R, Ma L, You C, Li H. Prognostic impact of leukocytosis in intracerebral hemorrhage: a PRISMA-compliant systematic review and meta-analysis. *Medicine.* (2019) 98:e16281. doi: 10.1097/MD.0000000000016281
22. Mohammadi H, Shamshirian A, Eslami S, Shamshirian D, Ebrahimzadeh MA. Magnesium sulfate attenuates lethality and oxidative damage induced by different models of hypoxia in mice. *BioMed Res Int.* (2020) 2020:1–8. doi: 10.1155/2020/2624734
23. Zhou Y, Wang Y, Wang J, Anne Stetler R, Yang Q-W. Inflammation in intracerebral hemorrhage: from mechanisms to clinical translation. *Progress Neurobiol.* (2014) 115:25–44. doi: 10.1016/j.pneurobio.2013.11.003
24. Brunswick AS, Hwang BY, Appelboom G, Hwang RY, Piazza MA, Connolly ES. Serum biomarkers of spontaneous intracerebral hemorrhage induced secondary brain injury. *J Neurol Sci.* (2012) 321:1–10. doi: 10.1016/j.jns.2012.06.008
25. Lattanzi S, Cagnetti C, Provinciali L, Silvestrini M. Neutrophil-to-lymphocyte ratio predicts the outcome of acute intracerebral hemorrhage. *Stroke.* (2016) 47:1654–57. doi: 10.1161/STROKEAHA.116.013627
26. Liu Y, Zhang J, Zan J, Zhang F, Liu G, Wu A. Lidocaine improves cerebral ischemia-reperfusion injury in rats through cAMP/PKA signaling pathway. *Exp Ther Med.* (2020) 20:495–9. doi: 10.3892/etm.2020.8688
27. Kim G, Ng HP, Chan ER, Mahabeleshwar GH. Kruppel-like factor 6 promotes macrophage inflammatory and hypoxia response. *FASEB J.* (2020) 34:3209–23. doi: 10.1096/fj.201902221R
28. Sun J, Cai J, Chen J, Li S, Liao X, He Y, et al. Krüppel-like factor 6 silencing prevents oxidative stress and neurological dysfunction following intracerebral hemorrhage via sirtuin 5/Nrf2/HO-1 axis. *Front Aging Neurosci.* (2021) 13:646729. doi: 10.3389/fnagi.2021.646729
29. Zhao X, Yang J, Yang C. The neuronal transcription factor Creb3l1 potential upregulates Ntrk2 in the hypertensive microenvironment to promote vascular smooth muscle cell-neuron interaction and prevent neurons from ferroptosis: a bioinformatic research of scRNA-seq data. *Dis Markers*. (2022) 2022:8339759. doi: 10.1155/2022/8339759
30. Lin W, Wang Y, Chen Y, Wang Q, Gu Z, Zhu Y. Role of calcium signaling pathway-related gene regulatory networks in ischemic stroke based on multiple WGCNA and single-cell analysis. *Oxid Med Cell Longevity.* (2021) 2021:1–35. doi: 10.1155/2021/8060477
31. Sun C, Ma S, Chen Y, Kim NH, Kailas S, Wang Y, et al. Diagnostic value, prognostic value, and immune infiltration of LOX family members in liver cancer: bioinformatic analysis. *Front Oncol.* (2022) 12:843880. doi: 10.3389/fonc.2022.843880
32. Mei S, Li Y, Kang X. Prognostic and functional analysis of NPY6R in uveal melanoma using bioinformatics. *Disease Markers.* (2022) 2022:1–14. doi: 10.1155/2022/4143447
33. Guo D, Liu J, Wang W, Hao F, Sun X, Wu X, et al. Alteration in abundance and compartmentalization of inflammation-related miRNAs in plasma after intracerebral hemorrhage. *Stroke.* (2013) 44:1739–42. doi: 10.1161/STROKEAHA.111.000835
34. Walsh KB, Zhang X, Zhu X, Wohleb E, Woo D, Lu L, et al. Intracerebral hemorrhage induces inflammatory gene expression in peripheral blood: global transcriptional profiling in intracerebral hemorrhage patients. *DNA Cell Biol.* (2019) 38:660–9. doi: 10.1089/dna.2018.4550
35. Ritchie ME, Phipson B, Wu D, Hu Y, Law CW, Shi W, et al. Limma powers differential expression analyses for RNA-sequencing and microarray studies. *Nucleic Acids Res.* (2015) 43:e47. doi: 10.1093/nar/gkv007
36. Yu G, Wang L-G, Han Y, He Q-Y. clusterProfiler: an r package for comparing biological themes among gene clusters. *OMICS J Integrative Biol.* (2012) 16:284–7. doi: 10.1089/omi.2011.0118
37. Lu L, Kang X, Yi B, Jiang C, Yan X, Chen B, et al. Exploring the mechanism of Yiqi Qingre Ziyin method in regulating neuropeptide expression for the treatment of atrophic rhinitis. *Dis Mark.* (2022) 2022:1–12. doi: 10.1155/2022/2056837
38. Subramanian A, Tamayo P, Mootha VK, Mukherjee S, Ebert BL, Gillette MA, et al. Gene set enrichment analysis: a knowledge-based approach for interpreting genome-wide expression profiles. *Proc Natl Acad Sci.* (2005) 102:15545–50. doi: 10.1073/pnas.0506580102
39. Feng W, Yang J, Song W, Xue Y. Crosstalk between heart failure and cognitive impairment via hsa-miR-933/RELB/CCL21 pathway. *BioMed Res Int.* (2021) 2021:1–16. doi: 10.1155/2021/2291899
40. Sun Y, Wang H, Li Y, Liu S, Chen J, Ying H. miR-24 and miR-122 negatively regulate the transforming growth factor-β/Smad signaling pathway in skeletal muscle fibrosis. *Mol Ther Nucleic Acids.* (2018) 11:528–37. doi: 10.1016/j.omtn.2018.04.005
41. Chen Y, Sun Y, Xu Y, Lin W-W, Luo Z, Han Z, et al. Single-cell integration analysis of heterotopic ossification and fibrocartilage developmental lineage: endoplasmic reticulum stress effector Xbp1 transcriptionally regulates the notch signaling pathway to mediate fibrocartilage differentiation. *Oxid Med Cell Longevity.* (2021) 2021:1–29. doi: 10.1155/2021/8302831
42. Hu C, Li Q, Shou J, Zhang F, Li X, Wu M, et al. Constructing a predictive model of depression in chemotherapy patients with non-Hodgkin's lymphoma to improve medical staffs' psychiatric care. *BioMed Res Int.* (2021) 2021:9201235. doi: 10.1155/2021/9201235
43. Han H, Cho J-W, Lee S, Yun A, Kim H, Bae D, et al. TRRUST v2: an expanded reference database of human and mouse transcriptional regulatory interactions. *Nucleic Acids Res.* (2018) 46:D380–6. doi: 10.1093/nar/gkx1013
44. Cline MS, Smoot M, Cerami E, Kuchinsky A, Landys N, Workman C, et al. Integration of biological networks and gene expression data using Cytoscape. *Nat Protoc.* (2007) 2:2366–82. doi: 10.1038/nprot.2007.324
45. Moingeon P. Artificial intelligence and the future of medicine: a multidimensional analysis. *Life Res.* (2021) 4:3. doi: 10.53388/life2021-0103-301
46. Huang M-L, Hung Y-H, Lee WM, Li RK, Jiang B-R. SVM-RFE based feature selection and Taguchi parameters optimization for multiclass SVM classifier. *Sci World J.* (2014) 2014:795624. doi: 10.1155/2014/795624
47. Liu Z, Li C. A predictive model for the risk of cognitive impairment in patients with gallstones. *BioMed Res Int.* (2021) 2021:3792407. doi: 10.1155/2021/3792407
48. Cieslak MC, Castelfranco AM, Roncalli V, Lenz PH, Hartline DK. t-Distributed stochastic neighbor embedding (t-SNE): a tool for eco-physiological transcriptomic analysis. *Mar Genomics.* (2020) 51:100723. doi: 10.1016/j.margen.2019.100723
49. Wu S, Guo T, Qi W, Li Y, Gu J, Liu C, et al. Curcumin ameliorates ischemic stroke injury in rats by protecting the integrity of the blood-brain barrier. *Exp Ther Med.* (2021) 22:783. doi: 10.3892/etm.2021.10215
50. Simão F, Ustunkaya T, Clermont AC, Feener EP. Plasma kallikrein mediates brain hemorrhage and edema caused by tissue plasminogen activator therapy in mice after stroke. *Blood.* (2017) 129:2280–90. doi: 10.1182/blood-2016-09-740670
51. Wang H-X, Yang Q-D, Liu B-Q, Zhang L, Ma M-M, Hu Z-Y, et al. TIMP-1 polymorphisms in a Chinese Han population with intracerebral hemorrhage. *Int J Neurosci.* (2014) 124:61–7. doi: 10.3109/00207454.2013.823604
52. Lorente L, Martín MM, Ramos L, Argueso M, Cáceres JJ, Solé-Violán J, et al. High serum tissue inhibitor of matrix metalloproteinase-1 levels and mortality in patients with spontaneous intracerebral hemorrhage. *World Neurosurg.* (2020) 134:e476–80. doi: 10.1016/j.wneu.2019.10.106
53. Levi M, Moons L, Bouché A, Shapiro SD, Collen D, Carmeliet P. Deficiency of Urokinase-type plasminogen activator–mediated plasmin generation impairs vascular remodeling during hypoxia-induced pulmonary hypertension in mice. *Circulation.* (2001) 103:2014–20. doi: 10.1161/01.CIR.103.15.2014
54. Liu Z, Zhang R, Chen X, Yao P, Yan T, Liu W, et al. Identification of hub genes and small-molecule compounds related to intracerebral hemorrhage with bioinformatics analysis. *PeerJ.* (2019) 7:e7782. doi: 10.7717/peerj.7782

55. Suzan V, Yavuzer H, Bag Soytas R, Bektan Kanat B, Arman P, Emiroglu Gedik T, et al. The relationship between primary sarcopenia and SARC-F, serum MMP9, TIMP1 levels, and MMP9/TIMP1 ratio in the geriatric patients. *Eur Geriatr Med.* (2021) 12:1229–35. doi: 10.1007/s41999-021-00519-y
56. Song G, Xu S, Zhang H, Wang Y, Xiao C, Jiang T, et al. TIMP1 is a prognostic marker for the progression and metastasis of colon cancer through FAK-PI3K/AKT and MAPK pathway. *J Exp Clin Cancer Res.* (2016) 35:148. doi: 10.1186/s13046-016-0427-7
57. Fan C, Zhang X, Zhang P, Zhao J, Shen H, Zhang Y, et al. LPS stimulation during HCV infection induces MMP/TIMP1 imbalance in macrophages. *J Med Microbiol.* (2020) 69:759–766. doi: 10.1099/jmm.0.001185
58. Barton SJ, Koppelman GH, Vonk JM, Browning CA, Nolte IM, Stewart CE, et al. PLAUR polymorphisms are associated with asthma, PLAUR levels, and lung function decline. *J Allergy Clin Immunol.* (2009) 123:1391–400.e17. doi: 10.1016/j.jaci.2009.03.014
59. Xu J, Li W, Bao X, Ding H, Chen J, Zhang W, et al. Association of putative functional variants in the *PLAU* gene and the *PLAUR* gene with myocardial infarction. *Clin Sci.* (2010) 119:353–9. doi: 10.1042/CS20100151
60. Egervall K, Rosso A, Elmståhl S. Association between cardiovascular disease- and inflammation-related serum biomarkers and poor lung function in elderly. *Clin Proteom.* (2021) 18:23. doi: 10.1186/s12014-021-09329-7
61. Nuti E, Rossello A, Cuffaro D, Camodeca C, Van Bael J, van der Maat D, et al. Bivalent inhibitor with selectivity for trimeric MMP-9 amplifies neutrophil chemotaxis and enables functional studies on MMP-9 proteoforms. *Cells.* (2020) 9:1634. doi: 10.3390/cells9071634
62. Li Y-Q, Liu R, Xue J-H, Zhang Y, Gao D-F, Wu X-S, et al. Effects of monocyte-endothelium interactions on the expression of type IV collagenases in monocytes. *Exp Ther Med.* (2015) 9:527–32. doi: 10.3892/etm.2014.2109
63. Mondino A, Blasi F. uPA and uPAR in fibrinolysis, immunity and pathology. *Trends Immunol.* (2004) 25:450–5. doi: 10.1016/j.it.2004.06.004
64. Thunø M, Macho B, Eugen-Olsen J. suPAR: the molecular crystal ball. *Dis Markers.* (2009) 27:157–72. doi: 10.1155/2009/504294
65. Stewart CE, Sayers I. Characterisation of urokinase plasminogen activator receptor variants in human airway and peripheral cells. *BMC Mol Biol.* (2009) 10:75. doi: 10.1186/1471-2199-10-75
66. Knyazev E, Maltseva D, Raygorodskaya M, Shkurnikov M. HIF-Dependent NFATC1 activation upregulates ITGA5 and PLAUR in intestinal epithelium in inflammatory bowel disease. *Front Genet.* (2021) 12:791640. doi: 10.3389/fgene.2021.791640
67. Discher DJ, Bishopric NH, Wu X, Peterson CA, Webster KA. Hypoxia regulates β-enolase and pyruvate kinase-M promoters by modulating Sp1/Sp3 binding to a conserved GC element. *J Biol Chem.* (1998) 273:26087–93. doi: 10.1074/jbc.273.40.26087
68. Hota SK, Hota KB, Prasad D, Ilavazhagan G, Singh SB. Oxidative-stress-induced alterations in Sp factors mediate transcriptional regulation of the NR1 subunit in hippocampus during hypoxia. *Free Radical Biol Med.* (2010) 49:178–91. doi: 10.1016/j.freeradbiomed.2010.03.027
69. Duval E, Bouyoucef M, Leclercq S, Baugé C, Boumédiene K. Hypoxia inducible factor 1 alpha down-regulates type i collagen through Sp3 transcription factor in human chondrocytes: HIF-1 alpha down regulates COL1A1 through Sp3. *IUBMB Life.* (2016) 68:756–63. doi: 10.1002/iub.1539
70. Carver BJ, Plosa EJ, Stinnett AM, Blackwell TS, Prince LS. Interactions between NF-κB and SP3 connect inflammatory signaling with reduced FGF-10 expression. *J Biol Chem.* (2013) 288:15318–25. doi: 10.1074/jbc.M112.447318
71. Zheng C, Li D, Zhan W, He K, Yang H. Downregulation of SENP1 suppresses LPS-induced macrophage inflammation by elevating Sp3 SUMOylation and disturbing Sp3-NF-κB interaction. *Am J Transl Res.* (2020) 12:7439–48.
72. Zhang Y, Li Z, Hao Q, Tan W, Sun J, Li J, et al. The Cdk2–c-Myc–miR-571 axis regulates DNA replication and genomic stability by targeting geminin. *Cancer Res.* (2019) 79:4896–910. doi: 10.1158/0008-5472.CAN-19-0020
73. Roderburg C, Mollnow T, Bongaerts B, Elfimova N, Vargas Cardenas D, Berger K, et al. Micro-RNA profiling in human serum reveals compartment-specific roles of miR-571 and miR-652 in liver cirrhosis. *PLoS ONE.* (2012) 7:e32999. doi: 10.1371/journal.pone.0032999
74. Preusse M, Theis FJ, Mueller NS. miTALOS v2: analyzing tissue specific microRNA function. *PLoS ONE.* (2016) 11:e0151771. doi: 10.1371/journal.pone.0151771
75. Cong S, Liu Y, Li Y, Chen Y, Chen R, Zhang B, et al. MiR-571 affects the development and progression of liver fibrosis by regulating the Notch3 pathway. *Sci Rep.* (2021) 11:21854. doi: 10.1038/s41598-021-00638-3

Conflict of Interest: The authors declare that the research was conducted in the absence of any commercial or financial relationships that could be construed as a potential conflict of interest.

Publisher's Note: All claims expressed in this article are solely those of the authors and do not necessarily represent those of their affiliated organizations, or those of the publisher, the editors and the reviewers. Any product that may be evaluated in this article, or claim that may be made by its manufacturer, is not guaranteed or endorsed by the publisher.

Copyright © 2022 Wan, Feng, Wang, Yang and Sun. This is an open-access article distributed under the terms of the Creative Commons Attribution License (CC BY). The use, distribution or reproduction in other forums is permitted, provided the original author(s) and the copyright owner(s) are credited and that the original publication in this journal is cited, in accordance with accepted academic practice. No use, distribution or reproduction is permitted which does not comply with these terms.

frontiers | Frontiers in Neurology

ORIGINAL RESEARCH
published: 09 June 2022
doi: 10.3389/fneur.2022.909828

MicroRNAs Promote the Progression of Sepsis-Induced Cardiomyopathy and Neurovascular Dysfunction Through Upregulation of NF-kappaB Signaling Pathway-Associated HDAC7/ACTN4

Qiancheng Luo[1†], *Hanning Ma*[2†], *Enwei Guo*[1], *Lin Yu*[1], *Ling Jia*[1], *Bingyu Zhang*[1], *Gang Feng*[1] *and Rui Liu*[1*]

[1] Department of Critical Care Medicine, Shanghai Pudong New Area Gongli Hospital, Shanghai, China, [2] Department of Emergency Medicine, General Hospital of Ningxia Medical University, Shanghai, China

OPEN ACCESS

Edited by:
Yuzhen Xu,
Tongji University, China

Reviewed by:
Bo Liu,
Shanghai Jiao Tong University, China
Zhihu Zhao,
Tianjin Hospital, China
Ning Wang,
Shanghai Jiao Tong University, China

***Correspondence:**
Rui Liu
ru194904@163.com

[†]These authors have contributed equally to this work

Specialty section:
This article was submitted to Neurological Biomarkers, a section of the journal Frontiers in Neurology

Received: 31 March 2022
Accepted: 03 May 2022
Published: 09 June 2022

Citation:
Luo Q, Ma H, Guo E, Yu L, Jia L, Zhang B, Feng G and Liu R (2022) MicroRNAs Promote the Progression of Sepsis-Induced Cardiomyopathy and Neurovascular Dysfunction Through Upregulation of NF-kappaB Signaling Pathway-Associated HDAC7/ACTN4. Front. Neurol. 13:909828. doi: 10.3389/fneur.2022.909828

Introduction: The objective of this study was to determine the NF-kappaB pathway, hub genes, and transcription factors (TFs) in monocytes implicated in the progression of neurovascular-related sepsis-induced cardiomyopathy (SIC) as well as potential miRNAs with regulatory functions.

Methods : Sepsis-induced cardiomyopathy—and heart failure (HF)-related differentially expressed genes (DEGs) between SIC and HF groups were identified separately by differential analysis. In addition, DEGs and differentially expressed miRNAs (DEmiRNAs) in monocytes between sepsis and the HC group were identified. Then, common DEGs in SIC, HF, and monocyte groups were identified by intersection analysis. Based on the functional pathways enriched by these DEGs, genes related to the NF-kB-inducing kinase (NIK)/NF-kappaB signaling pathway were selected for further intersection analysis to obtain hub genes. These common DEGs, together with sepsis-related DEmiRNAs, were used to construct a molecular interplay network and to identify core TFs in the network.

Results : A total of 153 upregulated genes and 25 downregulated genes were obtained from SIC-, HF-, and monocyte-related DEGs. Functional pathway analysis revealed that the upregulated genes were enriched in NF-κB signaling pathway. A total of eight genes associated with NF-κB signaling pathway were then further identified from the 178 DEGs. In combination with sepsis-related DEmiRNAs, HDAC7/ACTN4 was identified as a key transcriptional regulatory pair in the progression of SIC and in monocyte regulation. hsa-miR-23a-3p, hsa-miR-3175, and hsa-miR-23b-3p can regulate the progression of SIC through the regulation of HDAC7/ACTN4. Finally, gene set enrichment analysis (GSEA) suggested that HDAC7/ACTN4 may be associated with apoptosis in addition to the inflammatory response.

Conclusion : hsa-miR-23a-3p, hsa-miR-3175, and hsa-miR-23b-3p are involved in SIC progression by regulating NF-κB signaling signaling pathway-related HDAC7/ACTN4 in monocytes and cardiac tissue cells. These mechanisms may contribute to sepsis-induced neurovascular damage.

Keywords: neurovascular, biomarkers, HDAC7, ACTN4, microRNA, NF-kappaB (NF-κB), sepsis-induced cardiomyopathy (SIC)

INTRODUCTION

Sepsis is a life-threatening organ dysfunction resulting from a dysregulated response of the organism to infection (1). Cardiac dysfunction caused by sepsis is defined as sepsis-induced cardiomyopathy (SIC) (2). The incidence and progression of SIC involve inflammatory responses, mitochondrial disorders, and metabolic changes (3). Impaired cardiac function occurs in approximately 60% of patients with septic shock within 3 days of admission (4). Patients with SIC have a poor prognosis and high morbidity and mortality rates (5). The mortality rate for patients with sepsis without cardiovascular compromise is 20% (6). However, the mortality rate increases for patients with SIC (7, 8). Severe toxic symptoms cause abnormal energy metabolism and myocardial damage in patients with sepsis, induce myocardial cell dysfunction, and eventually lead to severe events such as HF, which may endanger the patient's life (9–11). In recent years, SIC has also been found to cause dysfunction of the vascular nerve unit, which can lead to neurovascular dysfunction (12, 13). However, there is a lack of biomarkers and studies on the association of SCI with neurovascular diseases.

Researchers have found that the degree of cardiac dysfunction is a major factor in predicting mortality and morbidity in sepsis (14). The growing body of research confirms that signaling between the brain and circulatory system is essential to maintaining homeostasis during sepsis (15, 16). In patients with sepsis, endotoxin damages the cardiac and nervous systems (17). Endotoxins activate neutrophils excessively in sepsis, resulting in abnormal activation of the NF-kappaB signaling pathway; this interferes with the signaling communication between the brain and the immune system, contributing to vascular nerve damage associated with sepsis (12, 15). NF-kappaB-related signaling pathways are activated in the cardio-cerebral system; however, their molecular biological mechanisms need to be further elucidated (18). The NF-kappaB pathway can specifically block the proinflammatory and proapoptotic signaling caused by sepsis in the heart and brain, which can save other organs from the negative effects of sepsis (18, 19). Investigating the process of SIC and SIC-related neurovascular damage in the presence of the NF-kappaB-related signaling pathway is the focus of this study.

Abbreviations: SIC, Sepsis-induced cardiomyopathy; GEO, Gene Expression Omnibus; DEGs, Differentially expressed genes; DEmiRNAs, Differentially expressed microRNAs; DEmRNAs, Differentially expressed mRNAs; GO, Gene Ontology; KEGG, Kyoto Encyclopedia of Genes and Genomes; GSEA, Gene set enrichment analysis; scRNA-seq, Single-cell RNA sequencing.

The activation of NF-kappaB signaling pathways is closely associated with monocytes in SIC (20). Monocytes are involved in various biological pathways that are crucial for the progression and prognosis of a disease. In addition, these pathways play a key role in the onset and progression of SIC. Monocytes are crucial regulators of inflammation. In response to inflammatory stimuli, monocytes are activated and migrate to the sites of inflammation to participate in the progression of inflammation (21). The inflammatory response causes upregulation of gene expression to trigger a massive release of inflammatory factors such as interleukin (IL)-6 and tumor necrosis factor (TNF)-α, leading to the incidence of SIC (2). Monocytes are also involved in oxidative stress (22). Intracellular over-activation of oxidative stress plays an important role in SIC (23). There are two immune responses in the course of sepsis, a hyperinflammatory response and immunosuppression (24). Death in patients with sepsis often occurs in the late immunosuppressive phase of the disease. The low expression of monocyte human leukocyte antigen-DR (mHLA-DR) is a universally recognized marker of an immunosuppressed state and is widely used in the treatment of sepsis (25–27). Therefore, identification of altered pathways in SIC and monocytes is essential to monitor the prognosis of patients with SIC.

microRNAs play a crucial regulatory role in the progression of various diseases (28–31). A study found that miR-21-3p is involved in the onset and progression of SIC (32). The miR-144-3p/NF-kB signaling pathway can regulate SIC injury (33). Furthermore, miR-133a-3p, miR-23b, and miR-155 are associated with SIC, suggesting that miRNA is a potential target for SIC therapy (34). In addition, miRNAs play a role in inflammation, oxidative stress, and apoptosis (35, 36), and these processes are also involved in SIC progression (37, 38).

Advancements in bioinformatics have enabled in-depth research into disease diagnosis and treatment from the perspective of big biological data (39–42). A large number of gene expression profiles can be easily obtained from RNA-sequencing (RNA-seq) data (43–46). High-throughput-based gene sequencing and functional pathway analysis allow bulk access to differentially expressed genes (DEGs) to examine the key pathways involved in disease progression (47, 48). This study aimed to identify the key pathways, hub genes, and TFs in monocytes and potential miRNAs with regulatory functions involved in the progression of SIC. In addition, we aimed to screen for targets and related neurovascular damage mechanism associated with the progression, diagnosis, treatment, and recurrence of SIC to monitor risks and eventually improve the prognosis of patients with SIC.

MATERIALS AND METHODS

Data Acquisition and Pre-Processing

First, the keywords "Sepsis," "Sepsis-induced cardiomyopathy (SIC)," "Septic cardiomyopathy (SCM)," and "Heart failure (HF)" were searched in the Gene Expression Omnibus (GEO) database. Datasets were filtered for bioinformatic analyses according to the following criteria: (1) data collected from human tissues; (2) single-cell RNA-sequencing (scRNA-seq) data; (3) sepsis and healthy control data; and (4) inclusion of at least 3 samples per group in the bulk RNA-seq transcriptome dataset. The GSE94717 (49), GSE101639, GSE79962 (50), and GSE167363 (51) datasets were eventually included. GSE94717 and GSE101639 contain miRNA transcript data obtained from the blood samples of 15 (12 patients with sepsis and 3 healthy controls) and 9 (6 patients with sepsis and 3 healthy controls) subjects, respectively (49). These datasets were used to screen for sepsis-related DEmiRNAs. GSE79962 is a dataset consisting of mRNA transcript data obtained from the heart tissue samples of 51 subjects (20 patients with HF, 11 healthy controls and 20 patients with SIC). Transcriptomic data from the GSE79962 dataset were used to identify SIC- and HF-related (differentially expressed genes) DEGs (50). Finally, to explore disease-related gene transcription patterns at the single-cell level, we obtained scRNA-seq data of 5 subjects (2 healthy controls and 3 patients with sepsis) from the GSE167363 dataset for differential analysis of gene expression at the single-cell level (51).

Quality Control and Integration of ScRNA-Seq Data

As described in previous studies, RNA-seq data obtained from a total of 31,909 single cell from 5 samples were subjected to quality control using the "Seurat" package (52–55). The inclusion criteria for cells were as follows: (1) samples with 200–6,000 DEGs; (2) RNA counts > 1,000; (3) mitochondrial gene expression < 20%; and (4) hemoglobin-related gene expression < 1% (51). In addition, the inclusion criteria for cell characteristics were set as expression in at least 3 cells. A total of 30,091 cells and 20,597 characteristics were included in the subsequent single-cell analysis. Finally, the scRNA-seq data were integrated using the "SCTransform" function.

Cell Clustering and Annotation

After integration of the scRNA-seq data, the "RunPCA" and "RunUMAP" functions were used to extract characteristics and reduce the dimensionality of single-cell transcripts. The "FindNeighbors" function was used to cluster the cells based on the default top 30 principal components (PCs), and the uniform manifold approximation and projection (UMAP) was used to visualize the cell clusters (56). Subsequently, the SingleR (version: 1.4) R package was used for cell cluster annotation based on the Monaco reference dataset (36). We calculated the number of cell types in each category as a percentage of the total number of cells in each sample.

Differential Analysis of DEGs

At the level of scRNA-seq, monocytes were isolated to calculate monocyte-related DEGs in patients with sepsis (SP group) and healthy controls (HC group). The "FindMarker" function was used to identify monocyte-related DEGs, and the "ComBat" function was used to remove batch effects from different datasets before calculating DEmiRNAs. At the level of bulk-RNA analysis, the "limma" R package was used to identify SIC-related DEGs in the SIC and HC groups, HF-related DEGs in the HF and HC groups, and sepsis-related DEmiRNAs in the SP and HC groups at the individual level (57). p-Value < 0.05 was set as the threshold for DEG identification, and fold change values were used to identify upregulated and downregulated DEGs.

Intersection Analysis

After identifying monocyte-, SIC-, and HF-related DEGs, intersection analysis was performed to identify common DEGs. Specifically, the analysis was performed separately for upregulated and downregulated DEGs, yielding co-upregulated or co-downregulated DEGs associated with monocytes, SICs, and HFs. Finally, the "VennDiagram" R package (https://cran.r-project.org/web/packages/VennDiagram/index.html) was used to draw a Venn diagram to present the results of the intersection analysis.

Functional Pathway Analysis and Gene Set Enrichment Analysis

Common DEGs were subjected to the functional pathway analysis to identify pathways in which these dysregulated genes may be involved. The Kyoto Encyclopedia of Genes and Genomes (KEGG) and Gene Ontology (GO) analyses were performed using the "clusterProfiler" R package (58). GO terms are classified as biological process (BP), cellular component (CC), and molecular function (MF). We performed functional pathway analyses for co-upregulated and co-downregulated DEGs separately. Based on the "c2.cp.v7.2.symbols.gmt [Curated]" reference gene set, gene set enrichment analysis (GSEA) was performed to identify functional pathways enriched by the hub genes as reported in previous studies (55, 59).

Downloading of Genes Associated With NF-κB Signaling Pathway

The results of the functional pathway analysis suggested that the NF-kB-inducing kinase pathway (NIK)/NF-kappaB signaling pathway (GO: 0038061) was upregulated in the monocytes of patients with sepsis, SIC, and HF. Therefore, we further retrieved and collected a list of 144 genes associated with this pathway from the Molecular Signatures Database (MSigDB) (59–62). Genes in this gene set were subjected to intersection analysis with common DEGs to obtain DEGs associated with NF-κB signaling pathway.

Construction of a Molecular Interaction Network

From TRRUST (v2), a list of TF and target genes with corresponding expression levels was downloaded and used to predict TF-target gene pairs in DEGs. Then, miRWalk (<http://mirwalk.umm.uni-heidelberg.de/>), based on the identified

sepsis-related DEmiRNAs, was used to identify predicted TF-target gene pairs (63). Among the predicted miRNA–mRNA interaction pairs, only those molecular pairs that were dysregulated in the opposite direction were retained. We then visualized the molecular interaction network using Cytoscape 3.5.1 based on these predicted TF-target genes and miRNA–mRNA pairs (64).

Receiver Operating Characteristic Curve Analysis

The receiver operating characteristic (ROC) curve tool was used to assess the diagnostic capability of hub genes. In the horizontal and vertical coordinates of the curve, sensitivity was set on the y-axis, whereas "1-specificity" (i.e., false-positive rate) was set on the x-axis. Thereafter, the area under the ROC curve (AUC) was calculated to quantify the diagnostic capability. As an indicator of diagnostic capability, the AUC value should be usually between 1.0 and 0.5, with a value closer to 1.0, indicating a more accurate diagnosis. In addition, the ROC curve was plotted using the "pROC" package (65).

Statistical Analysis

In this study, statistical analyses were performed and graphical plots were created using R (version 4.0.2). All tests were two-sided, and a p-value < 0.05 was considered significant.

RESULTS

Quality Control and Integration of Single-Cell Data

The distribution of key cell features, including feature counts, RNA counts, percentage of mitochondria (pMT), and percentage of hemoglobin (pHB), before quality control of the single-cell data, is shown in **Figure 1A**. Subsequently, the single-cell data were filtered with reference to the filtering conditions set in the original study from which the scRNA-seq data were obtained (**Figure 1B**) (51). The distribution of features of the filtered single-cell data is shown in **Figures 1C–F**. Subsequently, scRNA-seq data from five samples were integrated. Finally, UMAP showed that the batch effects among the five samples were removed, and the single-cell data were well integrated (**Figures 1G,H**). With the above quality control process, the quality of the data was assessed and low-quality cells were removed.

Seven Cell Types Identified by Cell Clustering and Annotation

To examine the effects of optimal resolution on single-cell clustering, a range of resolution gradient values was selected (**Figure 2A**). Based on the relationship between the number of clusters and resolution, a final resolution of 0.3 was selected for clustering, which resulted in 11 cell clusters (**Figure 2B**). The distribution of RNA features, RNA count, and pMT in these 11 cell clusters is shown in **Figure 2C**. The features of different cell clusters were different, suggesting possible heterogeneity among the clusters. Subsequently, using the Monaco reference dataset, these cell clusters were identified as seven major cell populations, including monocytes, natural killer (NK) cells, T cells, B cells, dendritic cells, CD4+ T cells, and CD8+ cells (**Figure 2D**). The proportion of monocytes fluctuated from 22.82 to 49.65% in the five samples (**Figure 2E**). In the SP group, there were more monocytes than in the HC group (37.5 vs. 24.9%, respectively).

Common DEGs Associated With Monocytes, SICs, and HFs

The differential expression analysis of DEGs associated with monocytes between the SP and HC groups yielded 4,429 upregulated and 380 downregulated DEGs (**Figure 3A**), which were named monocyte-related DEGs. SIC- and HF-related DEGs are shown in volcano plots (**Figures 3B,C**). The Venn diagram showed that a total of 153 genes were co-upregulated (**Figure 3D**) and 25 genes were co-downregulated in the monocyte, SIC, and HF groups (**Figure 3E**). These common DEGs were identified as hub genes involved in the progression of SIC. In addition, they were found to be dysregulated in monocytes during the onset and progression of sepsis. Therefore, these dysregulated genes may be the hub genes involved in the progression of SIC.

DEGs Associated With NF-κB Signaling Pathway

The functional pathway analysis showed that the identified co-upregulated genes were mainly enriched in NF-κB signaling pathway and pathways related to the regulation of cell shape (**Figure 4A**). The co-downregulated genes were mainly enriched in pathways associated with proteasome, Parkinson's disease, and pertussis (**Figure 4B**). Among these pathways, NF-κB signaling pathway is associated with various biological processes including immunity, inflammation, stress response, B-cell development, and lymphoid organogenesis. The intersection analysis of common DEGs and genes associated with NF-κB signaling pathway revealed eight dysregulated genes (e.g., *ACTN4*, *DICER1*, *DLG1*, *HDAC7*, *NFAT5*, *PPP4C*, *TERF2IP,* and *TRIM44*) (**Figure 4C**). The expression of these eight genes among the SIC, HF, and HC groups is shown in **Figure 4D**. These genes were upregulated in both SIC and HF groups, suggesting that they may be the hub genes involved in the progression of SIC *via* NF-κB signaling pathway.

Role of HDAC7/ACTN4 Regulation in Monocytes in the Progression of SIC

To examine the molecular regulatory network that may play a crucial role in the progression of SIC, a molecular interaction network was constructed for sepsis-related DEmiRNAs and NF-κB signaling pathway-related DEGs. In this regulatory network, HDAC7 was found to be the transcriptional regulator of ACTN4. **Figure 5A** shows the expression profiles of 11 DEmiRNAs that may regulate ACTN4 and HDAC7. The results revealed 11 hub miRNAs, which, along with the HDAC7/ACTN4 regulatory pair, constitute the key molecular interaction network involved in SIC progression (**Figure 5B**). A total of four miRNAs had negative regulatory effects on HDAC7, whereas seven miRNAs had negative regulatory effects on ACTN4. The p-values and fold change distributions of the differential analysis

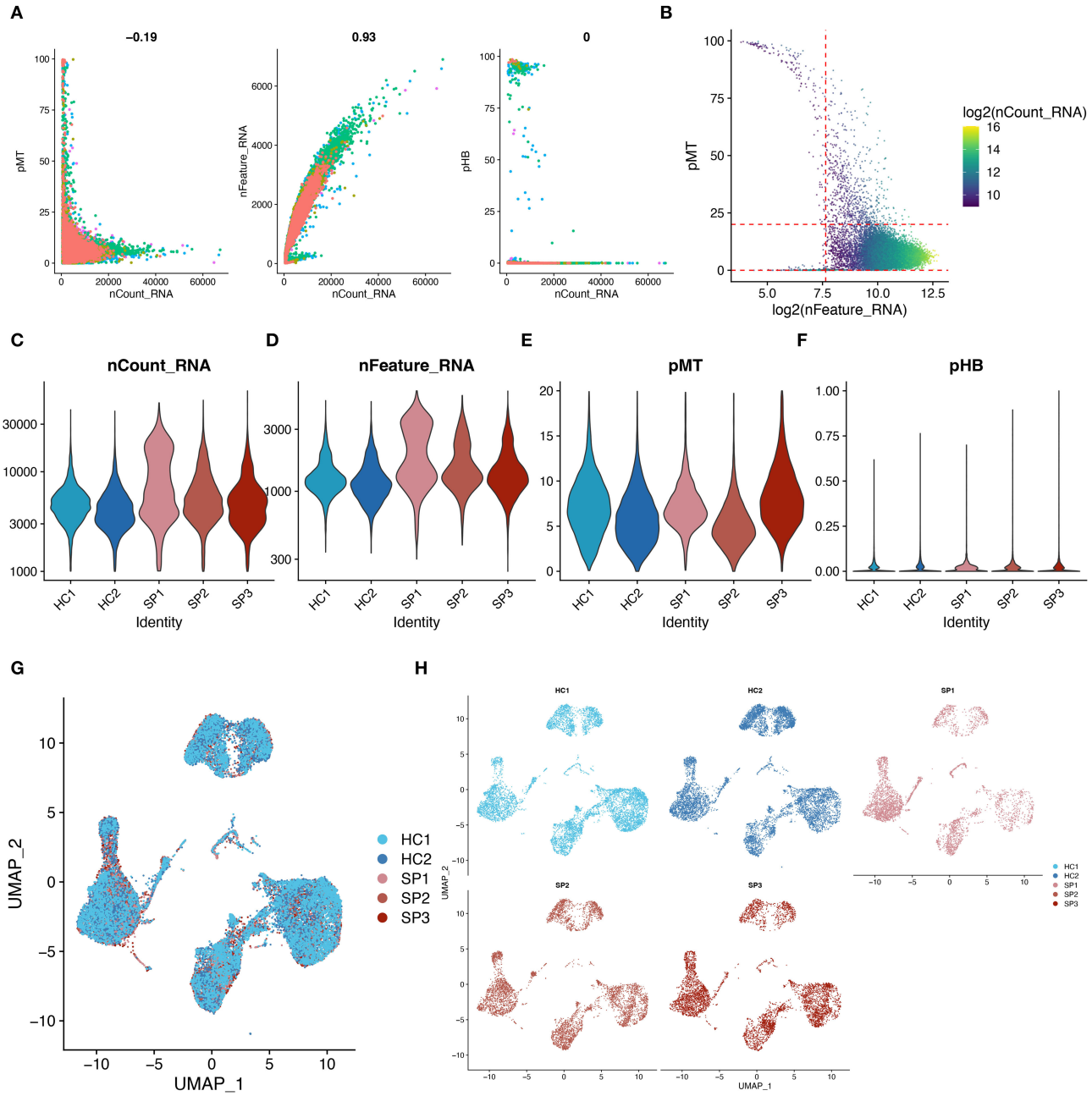

FIGURE 1 | Quality control and data integration of single-cell datasets. **(A)** Scatter plot showing the relationship between cell characteristics in the single-cell data before data filtering. **(B)** Scatter plot showing the relationship between cell characteristics, mitochondrial proportions (pMT), and RNA counts. The red line represents the threshold used in performing cell mass filtering. **(C–F)** Violin plots showing the distribution of cellular features in each sample after data filtering. **(G,H)** UMAP showing the overlaps and distribution of single-cell data after integration. These plots show the removal of batch effects.

of HDAC7 and ACTN4 were shown in the volcano plot (**Figures 3B,C**). In addition, UMAP showed that the expression of HDAC7 and ACTN4 in blood was mainly concentrated in monocytes (**Figure 5C**) and was higher in the SP group than in the HC group (**Figures 3A**, **5D**). Therefore, we hypothesized that HDAC7/ACTN4 regulation in monocytes may play a crucial role in the progression and recurrence of SIC.

Establishment of an MiRNA–TF–MRNA Regulatory Axis With ACTN4/HDAC7 as the Core

Based on the HDAC7/ACTN4 regulatory pair, three significant DEmiRNAs regulating HDAC7, including hsa-miR-23a-3p, hsa-miR-3175, and hsa-miR-23b-3p, were further identified

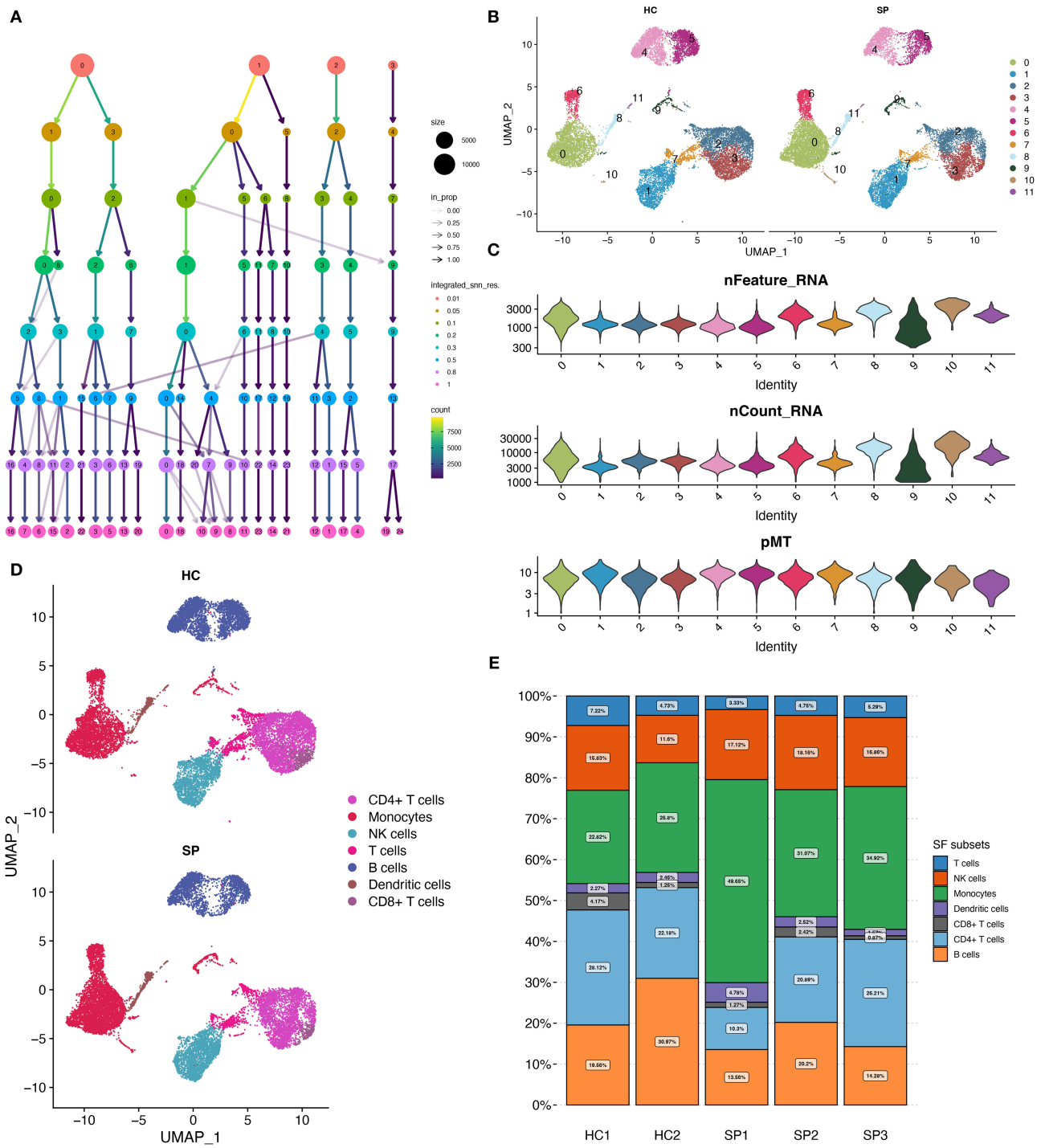

FIGURE 2 | Cell clustering and annotation. **(A)** Diagram showing the cell clustering process. **(B)** UMAP showing the distribution of cell clusters, 0–11 indicate different subgroups of cells. **(C)** Cellular characteristics exhibited by each cell cluster. **(D)** UMAP showing the annotated cell types in HC and SP. **(E)** Relative proportion of each cell type between the five samples.

(**Figure 6B**). The AUC values of HDAC7 and ACTN4 as the biomarkers for SIC diagnosis were 0.859 and 0.755, respectively (**Figures 6C,D**). For the diagnosis of HF/HC group, the AUC values for HDAC7 and ACTN4 were 0.809 and 0.705, respectively (**Figures 6E,F**). These results suggest that HDAC7 and ACTN4 have good predictive ability for the diagnosis of SIC and HF. Finally, three potential miRNAs regulating HDAC7 were identified with HDAC7/ACTN4 as

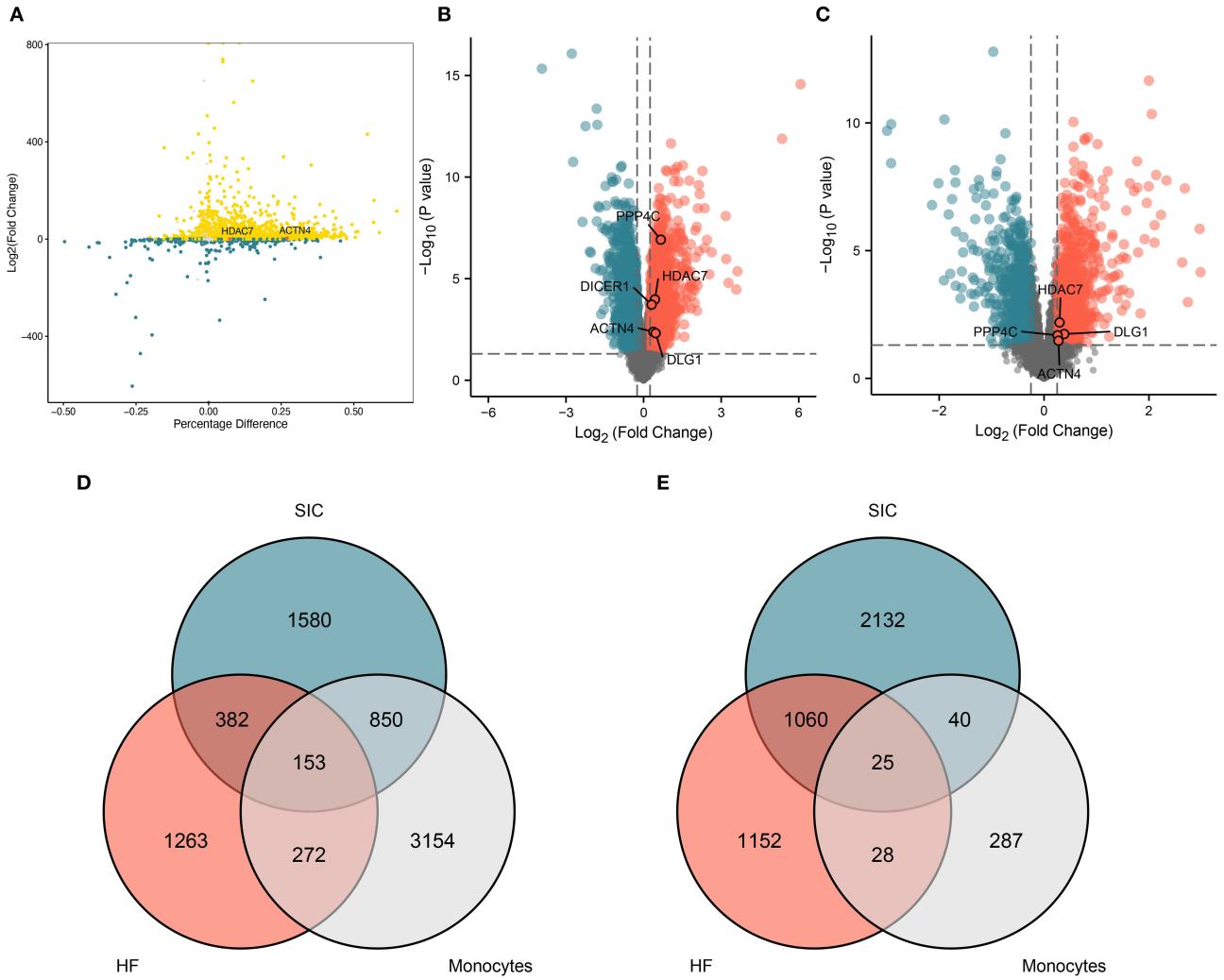

FIGURE 3 | Genes co-differentially expressed. **(A)** The differentially expressed genes associated with monocytes in sepsis. **(B)** Volcano plot showing differentially expressed genes associated with SIC. **(C)** Volcano plot showing differentially expressed genes associated with HF. **(D,E)** Venn diagram showing the identified differentially expressed genes which are either **(D)** upregulated or **(E)** downregulated and are common in septic monocytes, heart failure, and septic cardiomyopathy; **(D,E)** shows 153 and 25 shared genes, respectively.

the core, and the corresponding miRNAs–HDAC7-ACTN4 axis was established.

Role of HDAC7/ACTN4 in Inflammatory Response and Apoptosis

Gene set enrichment analysis was performed to examine the potential role of dysregulated HDAC7 in the progression of SIC based on the bulk RNA transcript data of patients with sepsis. The results showed that the neutrophil degranulation, IL signaling, VEGFA–VEGFR2 signaling, and apoptosis modulation pathways were upregulated in samples with upregulated HDAC7 (**Figure 6G**). In samples with elevated ACTN4 expression levels, the interleukin signaling, neutrophil degranulation, and apoptosis modulation pathways were also upregulated (**Figure 6H**). Therefore, in addition to the inflammatory response, HDAC7/ACTN4 upregulation may also be involved in several pathways including apoptosis. Alterations in these pathways may be associated with the progression of SIC and HF, thus affecting patient prognosis.

DISCUSSION

In this study, bioinformatic analyses revealed the neurovascular-related NF-κB signaling pathway as the main pathway enriched by SIC-, HF-, and monocyte-related DEGs. NF-κB signaling pathway and genes in this pathway were screened from the enriched functional pathways. In addition, HDAC7 and ACTN4 were identified as the key genes involved in the progression of SIC *via* NF-κB signaling pathway. hsa-miR-23a-3p, hsa-miR-3175, and hsa-miR-23b-3p were identified as the possible regulators

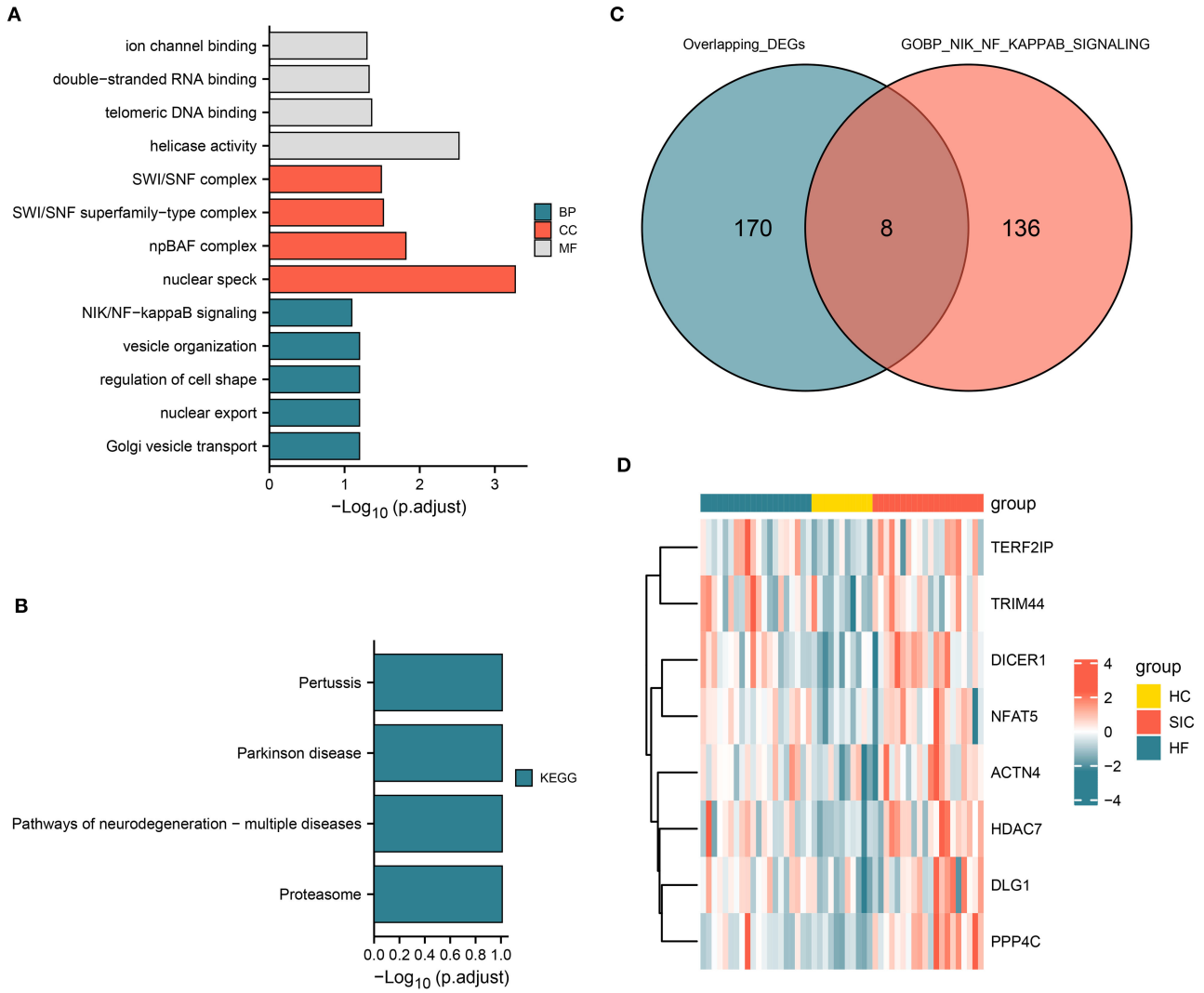

FIGURE 4 | Functional pathway analysis and genes associated with the NIK/NF-kappa B signaling pathway. **(A)** Pathways associated with upregulated genes; molecular function (MF), cellular component (CC), and biological process (BP). **(B)** Pathways related to upregulated and downregulated genes. **(C)** Intersection of the differentially expressed genes and genes involved in the NIK/NF-kappa B signaling pathway. **(D)** Heatmap showing the intersecting genes in each group.

of SIC progression, which act by regulating HDAC7/ACTN4. Finally, HDAC7 and ACTN4 were subjected to GSEA, which suggested that HDAC7/ACTN4 were involved in apoptosis as well as inflammation.

A previous study found that the NF-kB signaling pathway regulates SIC injury (33). In the early stages of sepsis, bacterial stimulation can cause significant changes in the NF-kB-inducing kinase (NIK) pathway (66). The inflammatory factor IL-33 can increase pyroptosis levels in macrophages and mortality in septic mice by activating the NF-kB signaling pathway (67). Moreover, NF-kB affects the inflammatory process in various diseases such as asthma and kidney diseases (68–70). In addition, oxidative stress generated by NF-kB-induced iNOS and COX-2 signaling pathways can impair myocardial function in patients with sepsis (71, 72). NF-kB mediates the transcription of several proinflammatory genes and induces the release of inflammatory factors such as ILs and TNF-α, which leads to myocardial dysfunction and accelerates the progression of SIC (73). Drugs targeting NF-kB inhibition can help to improve cardiac function in patients with SIC and hence improve their prognosis (73). Therefore, NF-kB pathway-related genes may play a crucial role in the onset and progression of SIC. Dysregulated monocytes may produce large amounts of inflammatory cytokines, resulting in widespread inflammation, organ failure, and even death (51). Furthermore, monocytes are involved in the release of inflammatory mediators (24). Circulating monocytes in HF are also pathologically activated through enhanced NF-κB activity (74–76). Therefore, monocytes are closely associated with the progression of SIC and the onset of HF.

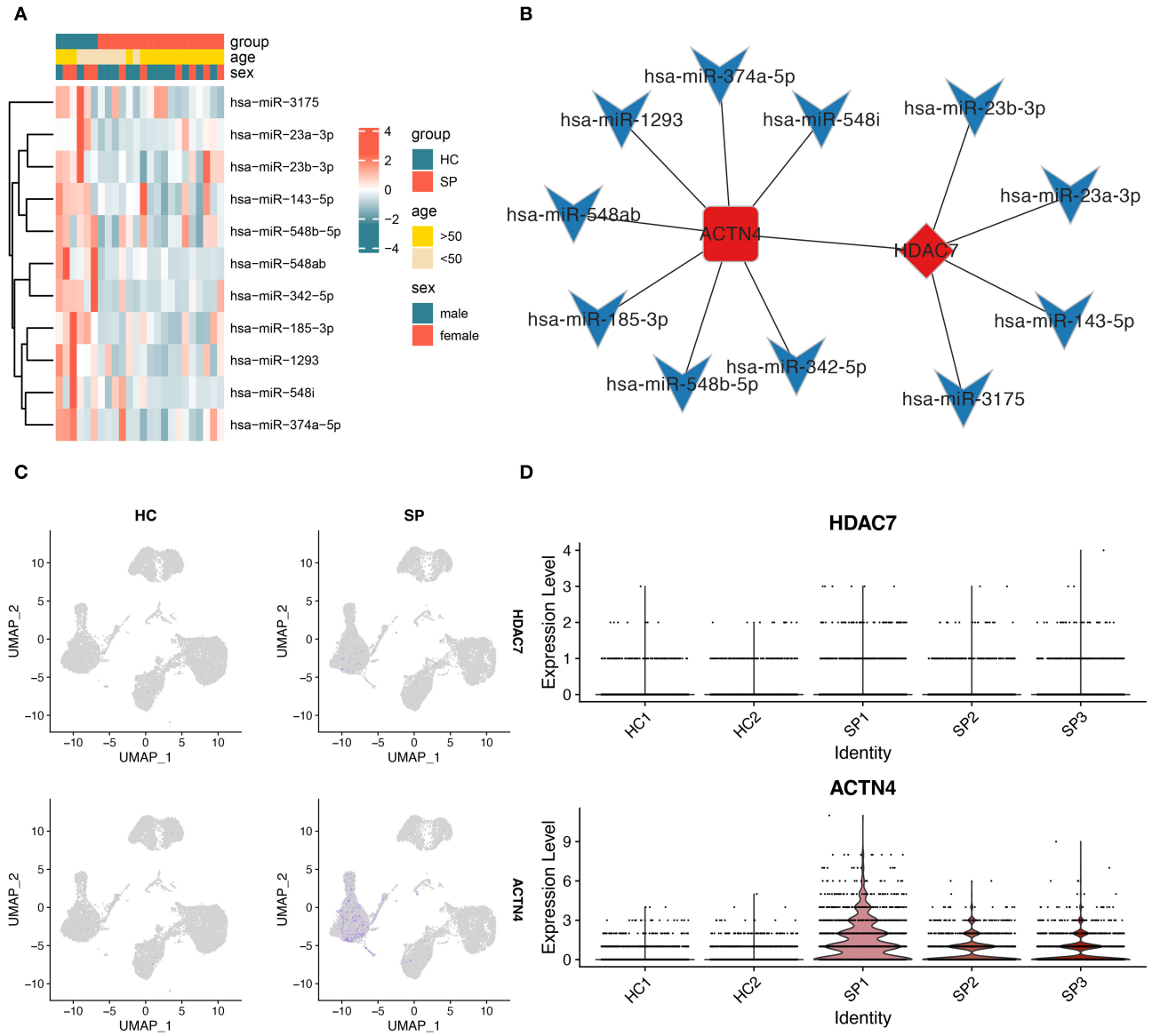

FIGURE 5 | Construction of the molecular interaction network. **(A)** Heatmap showing the expression of miRNAs in the molecular interaction network between HC and SP groups. **(B)** Molecular interaction network showing HDAC7 as the core TF and *ACTN4* as the gene regulated by HDAC7. The diamond represents TFs, the round rectangle represents mRNAs, the V-shaped icon represents miRNAs, red bars indicate upregulated genes, and blue bars indicate downregulated genes. **(C)** Figure showing the expression of *HDAC7* and *ACTN4* between HC and SP groups. **(D)** Expression distribution of HDAC7 and ACTN4 between individual samples in single-cell data analysis.

In this study, HDAC7 and ACTN4 were identified, for the first time, as the hub genes involved in the progression of SIC *via* NF-κB signaling pathway. In addition, HDAC7/ACTN4 was upregulated in monocytes in patients with sepsis. A previous study reported a significant elevation in HDAC7 mRNA expression in the monocytes of patients with coronary artery disease (77). In addition, mCRP-treated monocytes have upregulated ACTN4 (78). The extracellular ACTN4-derived fragment has monocyte chemotactic activity and can promote monocyte maturation (79). Monocytes are involved in various biological processes such as inflammatory responses, oxidative stress, and immunosuppression (21, 25, 58), and these processes also influence the progression of SIC (23, 24, 37, 38, 59). We hypothesized that NF-κB-induced upregulation of HDAC7/ACTN4 in monocytes may be associated with the progression of SIC.

Studies reporting on the role of HDAC7/ACTN4 in sepsis or SIC are limited. However, a previous study found that HDAC7 is involved in the regulation of apoptosis (80). The enzymatic activity of HDAC7 is essential for TLR-induced production of

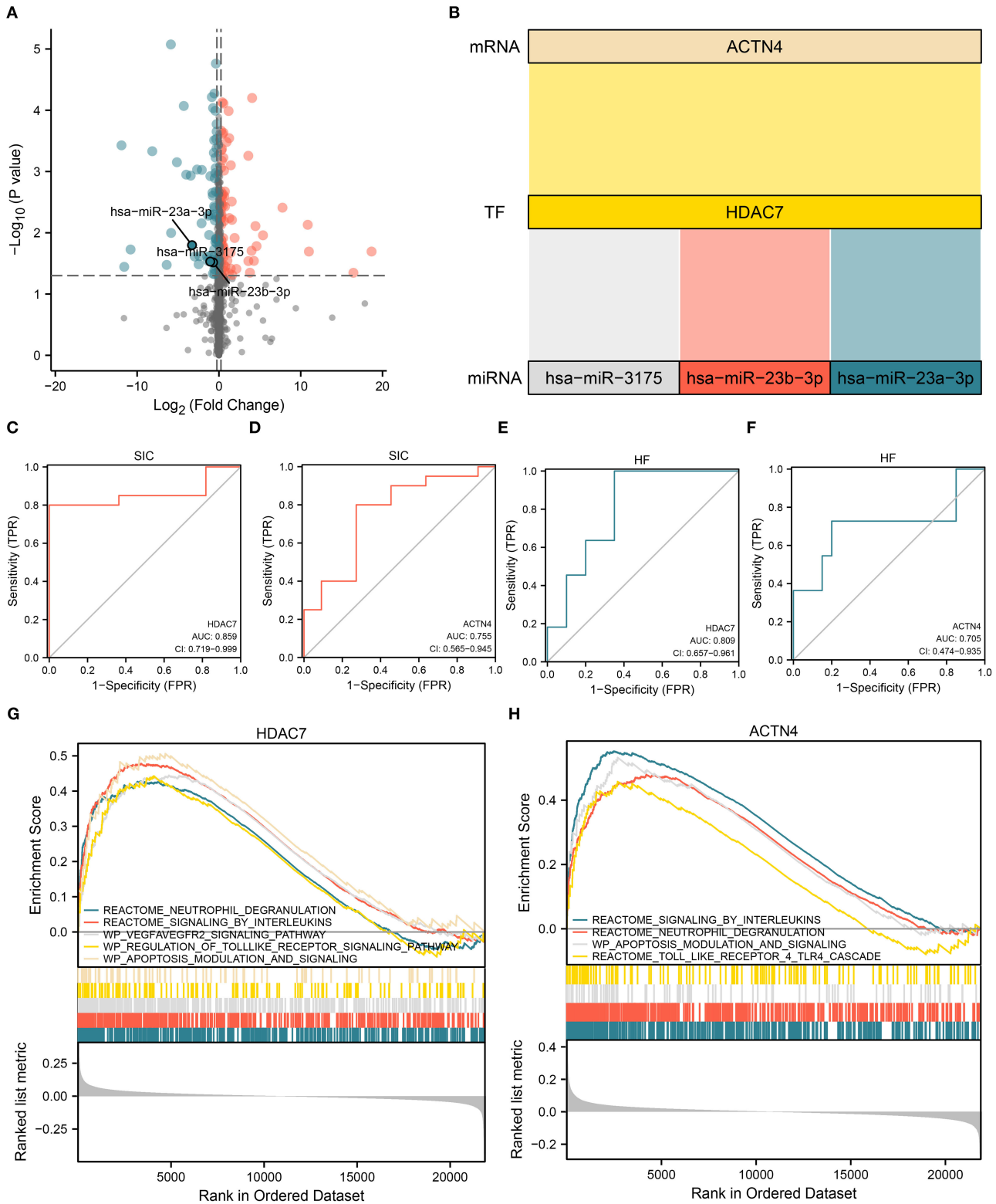

FIGURE 6 | Establishment of the miRNA/TF/mRNA axis and gene set enrichment analysis (GSEA). **(A)** Volcano plot showing the differential expression of miRNAs that regulate TF in molecular interaction networks. **(B)** Sankey diagram showing the core miRNA/TF/mRNA regulatory axis. **(C,D)** ROC curves showing the ability of **(C)** HDAC7 (AUC:0.859) and **(D)** ACTN4 (AUC:0.755) to distinguish between SIC and HC. **(E,F)** ROC curves showing the ability of **(E)** HDAC7 (AUC:0.809) and **(F)** ACTN4 (AUC:0.705) to distinguish between HF and HC. **(G,H)** GSEA results for **(G)** HDAC7 and **(H)** ACTN4.

inflammatory mediators and is involved in the inflammatory response (81). ACTN4 is involved in the inflammatory or immune response in the lungs (82). ACTN4 phosphorylation also mediates cell injury (83). Inflammatory response and apoptosis are involved in the progression of SIC (23, 37, 38). Similar to previous studies, the hub genes identified in this study, HDAC7 and ACTN4, were found to be associated with the inflammatory response.

By regulating the translation of HDAC7, hsa-miR-23a-3p, hsa-miR-3175, and hsa-miR-23b-3p may influence the inflammatory response in SIC and the extent of apoptosis. miR-23a-3p is one of the abundant miRNAs in the myocardial tissue, which attenuates apoptosis in myocardial cells during ischaemia–reperfusion injury (84). It is closely related to the incidence of myocardial lesions and HF (85). Downregulation of miR-23a-3p expression in acute HF promotes polarization of macrophages toward the repair phenotype (86). In addition, miR-23a-3p reduces superoxide dismutase-induced oxidative stress injury (49). Oxidative stress is an important biological process in the progression of SIC (23). miR-23b inhibits SIC progression by attenuating the inflammatory response, suppressing apoptosis, and blocking NF-κB activation and is a potential target for SIC therapy (34). Previous studies on miR-3175 have focused on tumors (87, 88). However, miR-3175 is also involved in oxidative damage of cells (89). Based on the results of this study, we hypothesized that hsa-miR-23a-3p, hsa-miR-3175, and hsa-miR-23b-3p play a regulatory role in the progression of SIC by interfering with HDAC7/ACTN4 in monocytes and cardiac tissue cells.

The neutrophil degranulation, IL signaling, VEGFA–VEGFR2 signaling, and apoptosis modulation pathways were upregulated in samples with elevated HDAC7 expression levels. These results suggest that in addition to the inflammatory response, upregulation of HDAC7/ACTN4 may also be involved in some apoptosis-related pathways. A previous study also reported the involvement of apoptosis in the progression of SIC (90). Therefore, HDAC7/ACTN4 may be involved in pathways related to inflammatory response and apoptosis, thus influencing the recovery, recurrence, and progression of SIC and affecting the prognosis of patients with SIC. SIC-, HF-, and monocyte-related DEGs are enriched in NF-κB signaling pathway. Moreover, hsa-miR-23a-3p, hsa-miR-3175, and hsa-miR-23b-3p may influence SIC progression by regulating HDAC7/ACTN4. These hub genes, TFs, and miRNAs may be the potential targets related to the progression, treatment, and recurrence of SIC. In addition, they can be used to monitor the risk of SIC and to improve the prognosis of patients with SIC. However, the results of this study were not validated in clinical samples, and relevant cellular and animal experiments were lacking. Moreover, we did not examine the relationship between HDAC7/ACTN4 and corresponding miRNAs in SIC further. Further studies are required to investigate the regulatory role of HDAC7/ACTN4 in the progression of SIC.

CONCLUSION

Sepsis-induced cardiomyopathy in blood mononuclear cells and cardiac tissue cells is stimulated by serum levels of biomarkers (hsa-miR-23a-3p, hsa-miR-317, and hsa-miR-23b-3), which alter neurovascular-related HDAC7/ACTN4 signaling pathways linked to the NF-κB pathway. This study investigated the underlying mechanisms of neurovascular dysfunction associated with SIC and sepsis.

DATA AVAILABILITY STATEMENT

The original contributions presented in the study are included in the article/supplementary material, further inquiries can be directed to the corresponding author.

ETHICS STATEMENT

Ethical review and approval was not required for the study on human participants in accordance with the local legislation and institutional requirements. Written informed consent from the patients/participants or patients/participants legal guardian/next of kin was not required to participate in this study in accordance with the national legislation and the institutional requirements.

AUTHOR CONTRIBUTIONS

QL: software, validation, formal analysis, data curation, reviewing and editing, and writing—original draft. RL: conceptualization, methodology, supervision, funding acquisition, writing, reviewing, and editing. HM: methodology, conceptualization, project administration, funding acquisition, and software. EG: conceptualization, project administration and data curation. LY: software, data curation, and supervision. LJ and GF: data curation, writing, reviewing and editing, and data curation. BZ: methodology, supervision, funding acquisition, and data curation. All authors contributed to the article and approved the submitted version.

FUNDING

The study was funded by Clinical Characteristic Discipline Construction Project of Shanghai Pudong New Area Health Commission (PWYts2021-17).

ACKNOWLEDGMENTS

The authors wish to thank all the patients and staff who participated in this study.

REFERENCES

1. Yin J, Chen Y, Huang J, Yan L, Kuang Z, Xue M, et al. Prognosis-related classification and dynamic monitoring of immune status in patients with sepsis: a prospective observational study. *World J Emerg Med.* (2021) 12:185. doi: 10.5847/wjem.j.1920-8642.2021.03.004
2. Xie J, Zhang L, Fan X, Dong X, Zhang Z, Fan W. MicroRNA-146a improves sepsis-induced cardiomyopathy by regulating the TLR-4/NF-κB signaling pathway. *Exp Ther Med*. (2019) 18:779–85. doi: 10.3892/etm.2019.7657
3. Li J, Ning B, Wang Y, Li B, Qian J, Ren H, et al. The prognostic value of left ventricular systolic function and cardiac biomarkers in pediatric severe sepsis. *Medicine.* (2019) 98:e15070. doi: 10.1097/MD.0000000000015070
4. Vieillard-Baron A, Caille V, Charron C, Belliard G, Page B. Jardin F. Actual incidence of global left ventricular hypokinesia in adult septic shock. *Crit Care Med.* (2008) 36:1701–6. doi: 10.1097/CCM.0b013e318174db05
5. Jeong HS, Lee TH, Bang CH, Kim J-H, Hong SJ. Risk factors and outcomes of sepsis-induced myocardial dysfunction and stress-induced cardiomyopathy in sepsis or septic shock: a comparative retrospective study. *Medicine.* (2018) 97:e0263. doi: 10.1097/MD.0000000000010263
6. Jia L, Wang Y, Wang Y, Ma Y, Shen J, Fu Z, et al. Heme Oxygenase-1 in macrophages drives septic cardiac dysfunction via suppressing lysosomal degradation of inducible nitric oxide synthase. *Circ Res.* (2018) 122:1532–44. doi: 10.1161/CIRCRESAHA.118.312910
7. Flierl MA, Rittirsch D, Huber-Lang MS, Sarma JV, Ward PA. Molecular events in the cardiomyopathy of sepsis. *Mol Med.* (2008) 14:327–36. doi: 10.2119/2007-00130.Flierl
8. Hollenberg SM, Singer M. Pathophysiology of sepsis-induced cardiomyopathy. *Nat Rev Cardiol.* (2021) 18:424–34. doi: 10.1038/s41569-020-00492-2
9. Seymour CW, Liu VX, Iwashyna TJ, Brunkhorst FM, Rea TD, Scherag A, et al. Assessment of clinical criteria for sepsis: for the third international consensus definitions for sepsis and septic shock (Sepsis-3). *JAMA*. (2016) 315:762. doi: 10.1001/jama.2016.0288
10. Liu M, Shehu M, Herrold E, Cohen H. Prognostic value of initial elevation in cardiac troponin I level in critically Ill patients without acute coronary syndrome. *Crit Care Nurse.* (2015) 35:e1–e10. doi: 10.4037/ccn2015300
11. Fleischmann C, Scherag A, Adhikari NKJ, Hartog CS, Tsaganos T, Schlattmann P, et al. Assessment of global incidence and mortality of hospital-treated sepsis. current estimates and limitations. *Am J Respir Crit Care Med.* (2016) 193:259–72. doi: 10.1164/rccm.201504-0781OC
12. Gu M, Mei X-L, Zhao Y-N. Sepsis and cerebral dysfunction: BBB damage, neuroinflammation, oxidative stress, apoptosis and autophagy as key mediators and the potential therapeutic approaches. *Neurotox Res.* (2021) 39:489–503. doi: 10.1007/s12640-020-00270-5
13. Huffman WJ, Subramaniyan S, Rodriguiz RM, Wetsel WC, Grill WM, Terrando N. Modulation of neuroinflammation and memory dysfunction using percutaneous vagus nerve stimulation in mice. *Brain Stimul.* (2019) 12:19–29. doi: 10.1016/j.brs.2018.10.005
14. Suzuki T, Suzuki Y, Okuda J, Kurazumi T, Suhara T, Ueda T, et al. Sepsis-Induced cardiac dysfunction and β-adrenergic blockade therapy for sepsis. *J intensive care.* (2017) 5:22. doi: 10.1186/s40560-017-0215-2
15. Elenkov IJ, Wilder RL, Chrousos GP, Vizi ES. The sympathetic nerve–an integrative interface between two supersystems: the brain and the immune system. *Pharmacol Rev.* (2000) 52:595–638.
16. Hoover DB. Cholinergic modulation of the immune system presents new approaches for treating inflammation. *Pharmacol Ther.* (2017) 179:1–16. doi: 10.1016/j.pharmthera.2017.05.002
17. Brown GC. The endotoxin hypothesis of neurodegeneration. *J Neuroinflammation.* (2019) 16:180. doi: 10.1186/s12974-019-1564-7
18. Brown M A. NF-kB action in sepsis: the innate immune system and the heart. *Front Biosci.* (2004) 9:1201. doi: 10.2741/1304
19. Wu KK, Kuo C-C, Yet S-F, Lee C-M, Liou J-Y. 5-methoxytryptophan: an arsenal against vascular injury and inflammation. *J Biomed Sci.* (2020) 27:79. doi: 10.1186/s12929-020-00671-w
20. Qiu P, Liu Y, Zhang J. Review: the role and mechanisms of macrophage autophagy in sepsis. *Inflammation.* (2019) 42:6–19. doi: 10.1007/s10753-018-0890-8
21. Mitchell JW, Baik N, Castellino FJ, Miles LA. Plasminogen inhibits TNFα-induced apoptosis in monocytes. *Blood.* (2006) 107:4383–90. doi: 10.1182/blood-2005-07-2872
22. Gunawardhana LP, Gibson PG, Simpson JL, Benton MC, Lea RA, Baines KJ. Characteristic DNA methylation profiles in peripheral blood monocytes are associated with inflammatory phenotypes of asthma. *Epigenetics.* (2014) 9:1302–16. doi: 10.4161/epi.33066
23. L'Heureux M, Sternberg M, Brath L, Turlington J, Kashiouris MG. Sepsis-Induced cardiomyopathy: a comprehensive review. *Curr Cardiol Rep*. (2020) 22:35. doi: 10.1007/s11886-020-01277-2
24. Assinger A, Schrottmaier WC, Salzmann M, Rayes J. Platelets in sepsis: an update on experimental models and clinical data. *Front Immunol.* (2019) 10:1687. doi: 10.3389/fimmu.2019.01687
25. Leijte GP, Rimmelé T, Kox M, Bruse N, Monard C, Gossez M, et al. Monocytic HLA-DR expression kinetics in septic shock patients with different pathogens, sites of infection and adverse outcomes. *Crit Care.* (2020) 24:110. doi: 10.1186/s13054-020-2830-x
26. van der Poll T, van de Veerdonk FL, Scicluna BP, Netea MG. The immunopathology of sepsis and potential therapeutic targets. *Nat Rev Immunol.* (2017) 17:407–20. doi: 10.1038/nri.2017.36
27. Venet F, Monneret G. Advances in the understanding and treatment of sepsis-induced immunosuppression. *Nat Rev Nephrol.* (2018) 14:121–37. doi: 10.1038/nrneph.2017.165
28. Wang J, Chen J, Sen S. MicroRNA as Biomarkers and diagnostics: MicroRNAs as biomarkers for diagnostics. *J Cell Physiol.* (2016) 231:25–30. doi: 10.1002/jcp.25056
29. Saliminejad K, Khorram Khorshid HR, Soleymani Fard S, Ghaffari SH. An overview of microRNAs: biology, functions, therapeutics, and analysis methods. *Journal Cellular Physiology.* (2019) 234:5451–65. doi: 10.1002/jcp.27486
30. Sun Y, Wang H, Li Y, Liu S, Chen J, Ying H. miR-24 and miR-122 negatively regulate the transforming growth factor-β/Smad signaling pathway in skeletal muscle fibrosis. *Molecular Therapy - Nucleic Acids.* (2018) 11:528–37. doi: 10.1016/j.omtn.2018.04.005
31. Lin J, Luo Z, Liu S, Chen Q, Liu S, Chen J. Long non-coding RNA H19 promotes myoblast fibrogenesis via regulating the miR-20a-5p-Tgfbr2 axis. *Clin Exp Pharmacol Physiol.* (2021) 48:921–31. doi: 10.1111/1440-1681.13489
32. Shao M, Yu M, Zhao J, Mei J, Pan Y, Zhang J, et al. miR-21-3p regulates AGE/RAGE signaling and improves diabetic atherosclerosis. *Cell Biochem Funct.* (2020) 38:965–75. doi: 10.1002/cbf.3523
33. Wei J-L, Wu C-J, Chen J-J, Shang F-T, Guo S-G, Zhang X-C, et al. LncRNA NEAT1 promotes the progression of sepsis-induced myocardial cell injury by sponging miR-144-3p. *Eur Rev Med Pharmacol Sci.* (2020) 24:851–61. doi: 10.26355/eurrev_202001_20069
34. Cao C, Zhang Y, Chai Y, Wang L, Yin C, Shou S, et al. Attenuation of sepsis-induced cardiomyopathy by regulation of MicroRNA-23b is mediated through targeting of MyD88-mediated NF-κB activation. *Inflammation.* (2019) 42:973–86. doi: 10.1007/s10753-019-00958-7
35. Bai X, Zhou Y, Chen P, Yang M, Xu J. MicroRNA-142-5p induces cancer stem cell-like properties of cutaneous squamous cell carcinoma via inhibiting PTEN. *J Cell Biochem.* (2018) 119:2179–88. doi: 10.1002/jcb.26379
36. Zhou J, Shuang O, Li J, Cai Z, Wu C, Wang W. miR-34a alleviates spinal cord injury via TLR4 signaling by inhibiting HMGB-1. *Exp Ther Med*. (2018) 17:1912–18 doi: 10.3892/etm.2018.7102
37. Peng S, Xu J, Ruan W, Li S, Xiao F. PPAR- γ activation prevents septic cardiac dysfunction via inhibition of apoptosis and necroptosis. *Oxid Med Cell Longev.* (2017) 2017:1–11. doi: 10.1155/2017/8326749
38. Xu J, Lin C, Wang T, Zhang P, Liu Z, Lu C. Ergosterol attenuates LPS-induced myocardial injury by modulating oxidative stress and apoptosis in rats. *Cell Physiol Biochem.* (2018) 48:583–92. doi: 10.1159/000491887
39. Gauthier J, Vincent AT, Charette SJ, Derome N. A brief history of bioinformatics. *Brief Bioinform.* (2019) 20:1981–96. doi: 10.1093/bib/bby063
40. Mirza B, Wang W, Wang J, Choi H, Chung NC, Ping P. Machine learning and integrative analysis of biomedical big data. *Genes.* (2019) 10:87. doi: 10.3390/genes10020087
41. Zhao X, Yang J, Yang C. The Neuronal Transcription Factor Creb3l1 Potential Upregulates Ntrk2 in the Hypertensive Microenvironment to Promote

Vascular Smooth Muscle Cell-Neuron Interaction and Prevent Neurons from Ferroptosis: A Bioinformatic Research of scRNA-seq Data. *Dis Markers.* (2022) 2022:8339759. doi: 10.1155/2022/8339759
42. Chen D, Li D. A potential miRNA-mRNA network for dementia and hernia crosstalk. *Biomed Res Int.* (2021) 2021:4324068. doi: 10.1155/2021/4324068
43. Stark R, Grzelak M, Hadfield J. RNA sequencing: the teenage years. *Nat Rev Genet.* (2019) 20:631–56. doi: 10.1038/s41576-019-0150-2
44. Hwang B, Lee JH, Bang D. Single-Cell RNA sequencing technologies and bioinformatics pipelines. *Exp Mol Med.* (2018) 50:1–14. doi: 10.1038/s12276-018-0071-8
45. Zhang P, Liu B. Integrative bioinformatics analysis reveals that infarct-mediated overexpression of potential miR-662/CREB1 pathway-induced neuropeptide VIP is associated with the risk of atrial fibrillation: a correlation analysis between myocardial electrophysiology and neuroendocrine. *Dis Markers.* (2021) 2021:1–17. doi: 10.1155/2021/8116633
46. Shi Q, Yan X, Wang J, Zhang X. Collagen family genes associated with risk of recurrence after radiation therapy for vestibular schwannoma and pan cancer analysis. *Dis Markers.* (2021) 2021:1–15. doi: 10.1155/2021/7897994
47. Wang TT, Abelson S, Zou J, Li T, Zhao Z, Dick JE, et al. High efficiency error suppression for accurate detection of low-frequency variants. *Nucleic Acids Res.* (2019) 47:e87–e87. doi: 10.1093/nar/gkz474
48. Li R, Wang L, Wang X, Geng R, Li N, Liu X. Identification of hub genes associated with outcome of clear cell renal cell carcinoma. *Oncol Lett*. (2020) 19:2846–60. doi: 10.3892/ol.2020.11389
49. Ge Q-M, Huang C-M, Zhu X-Y, Bian F, Pan S-M. Differentially expressed miRNAs in sepsis-induced acute kidney injury target oxidative stress and mitochondrial dysfunction pathways. *PLoS ONE.* (2017) 12:e0173292. doi: 10.1371/journal.pone.0173292
50. Matkovich SJ, Al Khiami B, Efimov IR, Evans S, Vader J, Jain A, et al. Mann DL. Widespread down-regulation of cardiac mitochondrial and sarcomeric genes in patients with sepsis*. *Crit Care Med.* (2017) 45:407–14. doi: 10.1097/CCM.0000000000002207
51. Qiu X, Li J, Bonenfant J, Jaroszewski L, Mittal A, Klein W, et al. Dynamic changes in human single-cell transcriptional signatures during fatal sepsis. *J Leukoc Biol.* (2021) 110:1253–68. doi: 10.1002/JLB.5MA0721-825R
52. Stuart T, Butler A, Hoffman P, Hafemeister C, Papalexi E, Mauck WM, Hao Y, Stoeckius M, Smibert P, Satija R. Comprehensive integration of single-cell data. *Cell*. (2019) 177:1888–1902.e21. doi: 10.1016/j.cell.2019.05.031
53. Yip SH, Sham PC, Wang J. Evaluation of tools for highly variable gene discovery from single-cell RNA-seq data. *Brief Bioinform.* (2019) 20:1583–9. doi: 10.1093/bib/bby011
54. Lin W, Wang Y, Chen Y, Wang Q, Gu Z, Zhu Y. Role of calcium signaling pathway-related gene regulatory networks in ischemic stroke based on multiple WGCNA and single-cell analysis. *Oxid Med Cell Longev.* (2021) 2021:1–35. doi: 10.1155/2021/8060477
55. Chen Y, Sun Y, Xu Y, Lin W-W, Luo Z, Han Z, et al. Single-Cell integration analysis of heterotopic ossification and fibrocartilage developmental lineage: endoplasmic reticulum stress effector Xbp1 transcriptionally regulates the notch signaling pathway to mediate fibrocartilage differentiation. *Oxid Med Cell Longev.* (2021) 2021:1–29. doi: 10.1155/2021/7663366
56. Becht E, McInnes L, Healy J, Dutertre C-A, Kwok IWH, Ng LG, Ginhoux F, Newell EW. Dimensionality reduction for visualizing single-cell data using UMAP. *Nat Biotechnol.* (2019) 37:38–44. doi: 10.1038/nbt.4314
57. Ritchie ME, Phipson B, Wu D, Hu Y, Law CW, Shi W, et al. limma powers differential expression analyses for RNA-sequencing and microarray studies. *Nucleic Acids Res.* (2015) 43:e47. doi: 10.1093/nar/gkv007
58. Yu G, Wang L-G, Han Y, He Q-Y. ClusterProfiler: an R Package for comparing biological themes among gene clusters. *OMICS: J Integrative Biol.* (2012) 16:284–7. doi: 10.1089/omi.2011.0118
59. Subramanian A, Tamayo P, Mootha VK, Mukherjee S, Ebert BL, Gillette MA, et al. Gene set enrichment analysis: a knowledge-based approach for interpreting genome-wide expression profiles. *Proc Nat Acad Sci.* (2005) 102:15545–50. doi: 10.1073/pnas.0506580102
60. Xiao G, Fong A, Sun S-C. Induction of p100 Processing by NF-κB-inducing kinase involves docking IκB Kinase α (IKKα) to p100 and IKKα-mediated phosphorylation. *J Biol Chem.* (2004) 279:30099–105. doi: 10.1074/jbc.M401428200
61. Xiao G, Harhaj EW, Sun S-C. NF-κB-Inducing kinase regulates the processing of NF-κB2 p100. *Mol Cell.* (2001) 7:401–9. doi: 10.1016/S1097-2765(01)00187-3
62. Liberzon A, Subramanian A, Pinchback R, Thorvaldsdottir H, Tamayo P. Mesirov JP. Molecular signatures database (MSigDB) 30. *Bioinformatics.* (2011) 27:1739–40. doi: 10.1093/bioinformatics/btr260
63. Han H, Cho J-W, Lee S, Yun A, Kim H, Bae D, et al. TRRUST v2: an expanded reference database of human and mouse transcriptional regulatory interactions. *Nucleic Acids Res.* (2018) 46:D380–6. doi: 10.1093/nar/gkx1013
64. Cline MS, Smoot M, Cerami E, Kuchinsky A, Landys N, Workman C, et al. Integration of biological networks and gene expression data using cytoscape. *Nat Protoc.* (2007) 2:2366–82. doi: 10.1038/nprot.2007.324
65. Robin X, Turck N, Hainard A, Tiberti N, Lisacek F, Sanchez J-C, et al. pROC: an open-source package for R and S+ to analyze and compare ROC curves. *BMC Bioinformatics.* (2011) 12:77. doi: 10.1186/1471-2105-12-77
66. Anirudhan A, Paramasivam P, Murugesan R, Ahmed SSSJ. Temporal changes of NF-κB signaling pathway genes in bacterial stimulated whole blood- a host mechanism associated with sepsis. *Microb Pathog.* (2020) 147:104415. doi: 10.1016/j.micpath.2020.104415
67. Ke J, Cai G. Effect of IL-33 on pyroptosis of macrophages in mice with sepsis via NF-κB/p38 MAPK signaling pathway. *Acta Cir Bras.* (2021) 36:e360501. doi: 10.1590/acb360501
68. Song I-H, Jung K-J, Lee T-J, Kim J-Y, Sung E-G, Bae YC, et al. Mesenchymal stem cells attenuate adriamycin-induced nephropathy by diminishing oxidative stress and inflammation via downregulation of the NF-kB: MSCs attenuate ADR-induced nephropathy. *Nephrology.* (2018) 23:483–92. doi: 10.1111/nep.13047
69. Wei D, Guo X, Lin L, Lin M, Gong Y, Ying B, et al. Effects of angelicin on ovalbumin (OVA)-induced airway inflammation in a mouse model of asthma. *Inflammation.* (2016) 39:1876–82. doi: 10.1007/s10753-016-0423-2
70. Zhao W, Sun Z, Wang S, Li Z, Zheng L. Wnt1 participates in inflammation induced by lipopolysaccharide through upregulating scavenger receptor A and NF-kB. *Inflammation.* (2015) 38:1700–6. doi: 10.1007/s10753-015-0147-8
71. Spasojević I, Obradović B, Spasić S. Bench-to-bedside review: neonatal sepsis - redox processes in pathogenesis. *Crit Care.* (2012) 16:221. doi: 10.1186/cc11183
72. Wink DA, Hines HB, Cheng RYS, Switzer CH, Flores-Santana W, Vitek MP, et al. Nitric oxide and redox mechanisms in the immune response. *J Leukoc Biol.* (2011) 89:873–91. doi: 10.1189/jlb.1010550
73. Lee S-Y, Hsin L-W, Su M-J, ChangChien C-C, Ku H-C. A novel isoquinoline derivative exhibits anti-inflammatory properties and improves the outcomes of endotoxemia. *Pharmacological Reports.* (2019) 71:1281–8. doi: 10.1016/j.pharep.2019.06.015
74. Prabhu SD, Chandrasekar B, Murray DR, Freeman GL. β-Adrenergic blockade in developing heart failure: effects on myocardial inflammatory cytokines, nitric oxide, and remodeling. *Circulation.* (2000) 101:2103–9. doi: 10.1161/01.CIR.101.17.2103
75. Frantz S, Stoerk S, Ok S, Wagner H, Angermann CE, Ertl G, et al. Effect of chronic heart failure on nuclear factor kappa B in peripheral leukocytes. *Am J Cardiol.* (2004) 94:671–3. doi: 10.1016/j.amjcard.2004.05.041
76. Hamid T, Guo SZ, Kingery JR, Xiang X, Dawn B, Prabhu SD. Cardiomyocyte NF-κB p65 promotes adverse remodelling, apoptosis, and endoplasmic reticulum stress in heart failure. *Cardiovasc Res.* (2011) 89:129–38. doi: 10.1093/cvr/cvq274
77. Li Xiao LX, Yu Cao YC, Yang Wang YW, Xin Lai XL, Ke-Qin Gao K-QG, Pei Du PD, Bi-Kui Zhang B-KZ, Su-Jie Jia S-JJ. Aberrant histone modifications of global histone and MCP-1 promoter in CD14+ monocytes from patients with coronary artery disease. *Pharmazie*. (2018) 73:202–206. doi: 10.1691/ph.2018.7342
78. Eisenhardt SU, Habersberger J, Oliva K, Lancaster GI, Ayhan M, Woollard KJ, et al. proteomic analysis of C-reactive protein stimulated THP-1 monocytes. *Proteome Sci.* (2011) 9:1. doi: 10.1186/1477-5956-9-1
79. Magdolen U, Schroeck F, Creutzburg S, Schmitt M, Magdolen V. Non-muscle α-actinin-4 interacts with plasminogen activator inhibitor type-1 (PAI-1). *Biol Chem*. (2004) 385:801–8. doi: 10.1515/BC.2004.105
80. Nie X, Jia W, Li X, Pan X, Yin R, Liu N, et al. FBXW7 induces apoptosis in glioblastoma cells by regulating HDAC7. *Cell Biol Int.* (2021) 45:2150–8. doi: 10.1002/cbin.11668

81. Ramnath D, Das Gupta K, Wang Y, Abrol R, Curson JEB, Lim J, et al. The histone deacetylase Hdac7 supports LPS-inducible glycolysis and Il-1β production in murine macrophages via distinct mechanisms. *J Leukocyte Bio.* (2022) 111:327–36. doi: 10.1002/JLB.2MR1021-260R
82. Shi Y, Zhao T, Yang X, Sun B, Li Y, Duan J. Sun Z. PM25-induced alteration of DNA methylation and RNA-transcription are associated with inflammatory response and lung injury. *Sci Total Environ.* (2019) 650:908–21. doi: 10.1016/j.scitotenv.2018.09.085
83. Feng D, Kumar M, Muntel J, Gurley SB, Birrane G, Stillman IE, et al. Phosphorylation of ACTN4 leads to podocyte vulnerability and proteinuric glomerulosclerosis. *JASN.* (2020) 31:1479–95. doi: 10.1681/ASN.2019101032
84. Ma M, Dai J, Tang H, Xu T, Yu S, Si L, et al. MicroRNA-23a-3p Inhibits mucosal melanoma growth and progression through targeting adenylate cyclase 1 and attenuating cAMP and MAPK pathways. *Theranostics.* (2019) 9:945–60. doi: 10.7150/thno.30516
85. Bukauskas T, Mickus R, Cereskevicius D, Macas A. Value of serum miR-23a, miR-30d, and miR-146a biomarkers in ST-elevation myocardial infarction. *Med Sci Monit.* (2019) 25:3925–32. doi: 10.12659/MSM.913743
86. Kain V, Ingle KA, Rajasekaran NS, Halade GV. Activation of EP4 receptor limits transition of acute to chronic heart failure in lipoxygenase deficient mice. *Theranostics.* (2021) 11:2742–54. doi: 10.7150/thno.51183
87. Huang H, Qing X, Zhou Q, Li H, Hu Z. Silencing of microRNA−3175 represses cell proliferation and invasion in prostate cancer by targeting the potential tumor-suppressor *SCN4B*. *Kaohsiung J Med Sci.* (2021) 37:20–6. doi: 10.1002/kjm2.12292
88. Xia G, Li X, Chen F, Shao Z. LncRNA LINC00520 Predicts poor prognosis and promotes progression of lung cancer by inhibiting MiR-3175 expression. *CMAR. Volume.* (2020) 12:5741–8. doi: 10.2147/CMAR.S250631
89. Chen J, Liang J, Zhen Y-F, Chang L, Zhou Z, Shen X. DCAF1-targeting microRNA-3175 activates Nrf2 signaling and inhibits dexamethasone-induced oxidative injury in human osteoblasts. *Cell Death Dis.* (2021) 12:1024. doi: 10.1038/s41419-021-04300-8
90. Zhu X, Sun M, Guo H, Lu G, Gu J, Zhang L, et al. Verbascoside protects from LPS-induced septic cardiomyopathy via alleviating cardiac inflammation, oxidative stress and regulating mitochondrial dynamics. *Ecotoxicol Environ Saf.* (2022) 233:113327. doi: 10.1016/j.ecoenv.2022.113327

Conflict of Interest: The authors declare that the research was conducted in the absence of any commercial or financial relationships that could be construed as a potential conflict of interest.

Publisher's Note: All claims expressed in this article are solely those of the authors and do not necessarily represent those of their affiliated organizations, or those of the publisher, the editors and the reviewers. Any product that may be evaluated in this article, or claim that may be made by its manufacturer, is not guaranteed or endorsed by the publisher.

Copyright © 2022 Luo, Ma, Guo, Yu, Jia, Zhang, Feng and Liu. This is an open-access article distributed under the terms of the Creative Commons Attribution License (CC BY). The use, distribution or reproduction in other forums is permitted, provided the original author(s) and the copyright owner(s) are credited and that the original publication in this journal is cited, in accordance with accepted academic practice. No use, distribution or reproduction is permitted which does not comply with these terms.

frontiers | Frontiers in Neurology

BRIEF RESEARCH REPORT
published: 14 June 2022
doi: 10.3389/fneur.2022.881528

Detection of Vascular Notch3 Deposits in Unfixed Frozen Skin Biopsy Sample in CADASIL

Akihiko Ueda[1], Makoto Nakajima[1], Yohei Misumi[1], Keiichi Nakahara[1], Satoru Shinriki[2], Masayoshi Tasaki[1,3], Hirotaka Matsui[2] and Mitsuharu Ueda[1]*

[1] Department of Neurology, Kumamoto University, Kumamoto, Japan, [2] Department of Molecular Laboratory Medicine, Graduate School of Medical Sciences, Kumamoto University, Kumamoto, Japan, [3] Department of Biomedical Laboratory Sciences, Graduate School of Health Sciences, Kumamoto University, Kumamoto, Japan

This study aimed to evaluate the utility of immunohistochemical staining of vascular Notch3 deposits in biopsied unfixed frozen skin samples from patients with suspected cerebral autosomal dominant arteriopathy with subcortical infarcts and leukoencephalopathy (CADASIL). We analyzed vascular Notch3 deposits in unfixed frozen skin biopsy samples obtained from 43 patients with suspected CADASIL by immunohistochemistry using antibodies against the extracellular domain (ECD) of Notch3. We also sequenced the *NOTCH3* gene in all patients, as well as evaluated their symptoms and neuroimages. We found granular Notch3 ECD deposits in the vessel walls of unfixed frozen skin biopsy samples in 10 of the 43 suspected patients with CADASIL. All 10 cases with skin Notch3 ECD deposits also carried reported pathogenic variants in the *NOTCH3* gene associated with CADASIL. *NOTCH3* variants of unknown significance were found in the other four patients without vascular Notch3 ECD or granular osmiophilic material deposits in biopsied skin samples. The remaining 29 cases without vascular Notch3 ECD deposits did not have variants in the *NOTCH3* gene. Immunohistochemical evaluation of vascular Notch3 ECD deposits in unfixed frozen biopsied skin samples may be useful for detecting Notch3 deposits in CADASIL.

Keywords: CADASIL, Notch3 deposits, *NOTCH3* variants, skin biopsy, immunohistochemistry

OPEN ACCESS

Edited by:
Jinming Han,
Capital Medical University, China

Reviewed by:
Akitoshi Takeda,
Osaka City University, Japan
Kenya Nishioka,
Juntendo University, Japan
Kelly Young,
University of Michigan, United States

****Correspondence:***
Akihiko Ueda
akihiko-shima@k4.dion.ne.jp

Specialty section:
This article was submitted to Neurological Biomarkers, a section of the journal Frontiers in Neurology

Received: *22 February 2022*
Accepted: *16 May 2022*
Published: *14 June 2022*

Citation:
Ueda A, Nakajima M, Misumi Y, Nakahara K, Shinriki S, Tasaki M, Matsui H and Ueda M (2022) Detection of Vascular Notch3 Deposits in Unfixed Frozen Skin Biopsy Sample in CADASIL. Front. Neurol. 13:881528. doi: 10.3389/fneur.2022.881528

INTRODUCTION

Cerebral autosomal dominant arteriopathy with subcortical infarcts and leukoencephalopathy (CADASIL) is a hereditary cerebrovascular disease caused by mutations in *NOTCH3* (1). Migraine, stroke recurrence, and cognitive decline are typical symptoms of CADASIL. Diffuse white matter lesions containing lesions in the temporal pole are characteristic findings of brain magnetic resonance imaging (MRI) in CADASIL. Genetic analysis of *NOTCH3* is required for the definitive diagnosis of CADASIL. Most patients with CADASIL have cysteine-related variants in *NOTCH3* that lead to an odd number of cysteine residues in epidermal growth factor-like repeats (EGFr) in the Notch3 extracellular domain (ECD). The occurrence of granular osmiophilic material (GOM) and Notch3 ECD deposits have been detected in brain vessels in CADASIL (2, 3).

For the diagnosis of CADASIL, simpler and less invasive detection of vascular Notch3 ECD deposits in the skin is a feasible alternative for detecting vascular pathogenic changes in the brain. Formalin-fixed paraffin-embedded (FFPE) sections, a standard method

to fix biopsied samples, have previously been used for the immunohistochemical detection of vascular Notch3 deposits (4–7). However, immunohistochemical detection using FFPE samples has failed to detect Notch3 deposits due to structural alterations during tissue processing. In contrast, unfixed frozen tissue sections, in which the structural conformation of Notch3 ECD is considerably retained, maybe better for the detection of vascular Notch3 ECD deposits in patients with CADASIL (8).

In this retrospective case series, we evaluated the usefulness of immunohistochemical staining for the detection of vascular Notch3 ECD deposits using unfixed frozen skin biopsy samples obtained from 43 patients with suspected CADASIL.

MATERIALS AND METHODS

Subjects

We consulted 380 patients who were suspected of developing CADASIL based on MRI T2 hyperintense lesions in periventricular white matter, deep white matter, and temporal pole white matter each attending doctor between 2008 and 2018 at Kumamoto University Hospital. We enrolled 43 suspected patients with CADASIL with informed consent, who agreed to participate in this study, for the investigation of the diagnostic utility of immunohistochemical detection of vascular Notch3 ECD deposits in the skin of these patients. We did not include patients with CADASIL reported in the previous study (8).

Skin Biopsy Samples

We obtained 0.8 × 1.5 cm of skin biopsy samples from the upper arm of the 43 patients with suspected CADASIL. The biopsied skin samples were equally divided into three parts. The first part was fixed in 4% paraformaldehyde solution with 2.5% glutaraldehyde in 0.1-M sodium cacodylate buffer for electron microscopic analysis. The second part was rapidly frozen in isopentane and cooled in nitro liquid to prepare unfixed frozen sections for immunohistochemical staining of vascular Notch3 ECD deposits. The third part was fixed in 4% paraformaldehyde in phosphate buffer solution (PBS) for standard histopathological examinations.

Immunohistochemical Staining of Vascular Notch3 ECD Deposits

For immunohistochemical staining of vascular Notch3 ECD deposits, we used 10-μm unfixed frozen skin sections. The sections were stained with rabbit antisera against Notch3 ECD (amino acid residues 1,555–1,569), which was prepared according to a previous study (9), overnight at 4°C. The sections were then washed with PBST for 3 h or more. To decrease the non-specific reaction of the primary antibodies, we prolonged the time of washing the sections in this step. The sections were then incubated with horseradish peroxidase (HRP)-conjugated goat secondary antibodies against rabbit immunoglobulin (Agilent, Santa Clara, CA, United States) for 2 h. Then, the sections were washed five times in phosphate-buffered saline with Tween20 (PBST). The sections were then incubated with 0.3 mg/ml diaminobezidine (Dojin Laboratories, Kumamoto, Japan), 0.65 mg/ml of sodium azide, and 100 μl of 30% hydrogen peroxide for 2 min, and counterstained with Victoria blue to visualize the internal elastic lamina.

Electron Microscopy

Electron microscopy was performed as previously described (10). Briefly, the samples were post-fixed in buffered osmium tetroxide, dehydrated in ascending grades of ethanol, and embedded in Epon. Semi-thin sections were cut and stained with toluidine blue to select arteries of the appropriate size for thin sectioning. Thin sections were double-stained with uranyl acetate and lead citrate, and examined by transmission electron microscopy (TH 7700, HITACHI, Tokyo).

Genetic Analysis and Clinical Presentations

We sequenced the *NOTCH3* gene in the 43 patients with suspected CADASIL using a next-generation sequencing panel as follows. We had designed a screening panel of genes for use with the Illumina TruSeq Custom Amplicon platform (Illumina, Inc., San Diego, CA, United States). The panel includes amplicons defining all coding exons of the 27 genes whose mutations are known to cause cerebral small vessel diseases including *NOTCH3*. Sequencing was performed using the MiSeq (Illumina, Inc.). The obtained sequences were aligned to the reference genome (GRCh37hg19) using MiSeq Reporter software (Illumina, Inc.). The generated virtual contact file (VCF) files containing variant calls were reviewed and further filtered. The clinical significance of the *NOTCH3* variants detected in the patients was assessed using ClinVar (https://www.ncbi.nlm.nih.gov/clinvar/). Pathogenicity of *NOTCH3* variants was predicted using PolyPhen-2 (http://genetics.bwh.harvard.edu/pph2/index.shtml) and MutationTaser2021 (https://www.genecascade.org/MutationTaster2021/#transcript). We analyzed the frequencies of each *NOTCH3* variant using the Human Genetic Variation Database (HGVD) (https://www.hgvd.genome.med.kyoto-u.ac.jp/about.html) for the Japanese population and the Genome Aggregation Database (gnomAD) (https://gnomad.broadinstitute.org/) for the general population. Symptoms and MRI findings using the Fazekas scale for white matter lesions were also evaluated.

RESULTS

Vascular Notch3 ECD Deposits in Patients With and Without *NOTCH3* Mutations

Vascular Notch3 ECD deposits in unfixed frozen skin sections were visualized as granular dots in the arterial walls by immunohistochemical staining in 10 of the 43 patients with suspected CADASIL (**Figures 1A–F**, **Table 1**). Although amounts of granular Notch3 deposits were slightly different among patients with CADASIL, we found Notch3 deposits

Abbreviations: CADASIL, cerebral autosomal dominant arteriopathy with subcortical infarcts and leukoencephalopathy; EGFr, epidermal growth factor-like repeats; ECD, extracellular domain; GOM, granular osmiophilic material; FFPE, formalin-fixed paraffin-embedded sections; PBS, phosphate buffer solution; HRP, horseradish peroxidase; DAB, diaminobenzidine.

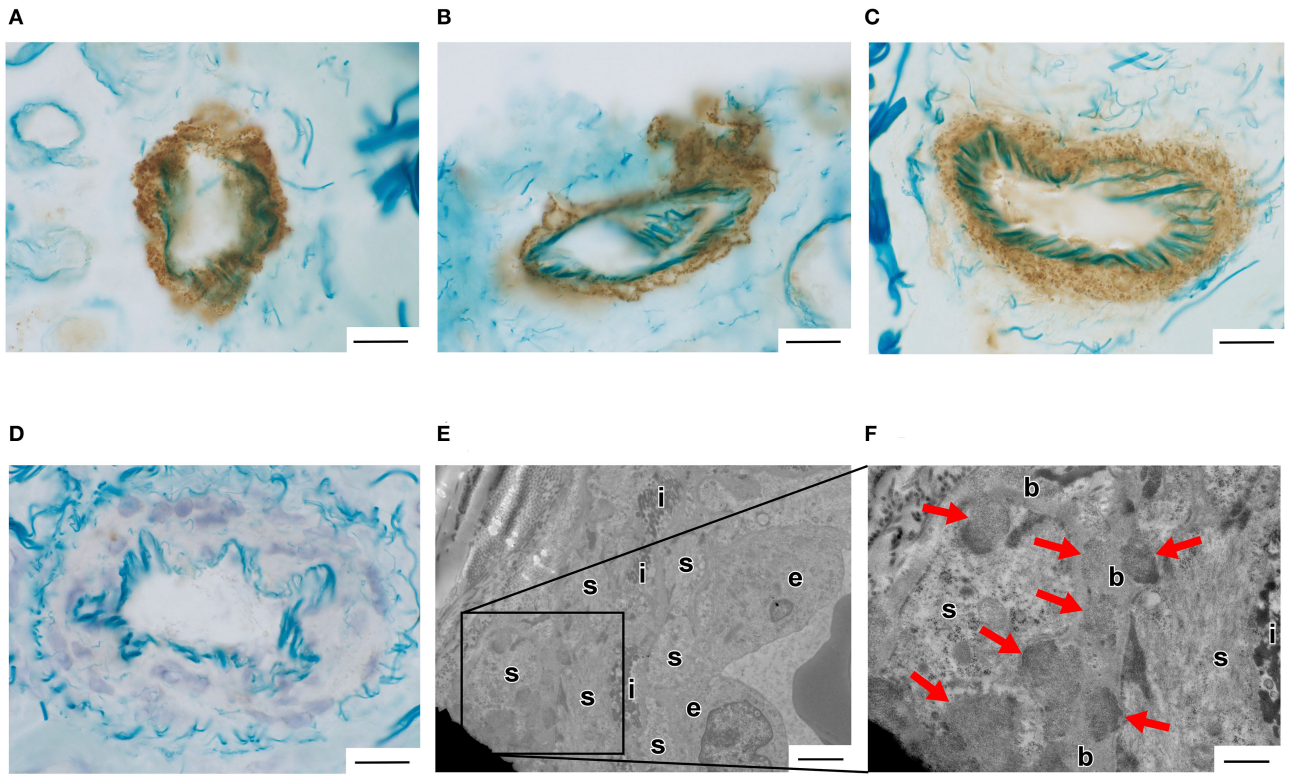

FIGURE 1 | (A–D) Vascular Notch3 ECD deposits were detected by immunohistochemical staining using anti-Notch3 ECD antibodies in an unfixed frozen skin biopsy sample obtained from a patient with cerebral autosomal dominant arteriopathy with subcortical infarcts and leukoencephalopathy (CADASIL). **(A)** Case 2 with the pathogenic *NOTCH3* p.Arg110Cys variant. **(B)** Case 6 with the pathogenic *NOTCH3* p.Trp1003Cys variant. **(C)** Case 9 with the pathogenic *NOTCH3* p.Tyr1021Cys variant. **(D)** Case 35 with the likely benign variants of *NOTCH3* p.Arg75Gln (**Table 1**). Bars = 20 μm. **(E,F)** Vascular granular osmiophilic material (GOM) deposits were detected by electron microscopic analysis in a biopsied skin sample obtained from a patient with CADASIL (Case 9 with the pathogenic *NOTCH3* p.Tyr1021Cys variant, **Table 1**). Arrows indicate GOM deposits. e, endothelial cells; s, smooth muscle cells; i, internal elastic lamina; b, basal lamina. **(E)** Bar = 2 μm. **(F)** Bar = 400 nm.

in all the arterioles. We detected Notch3 deposits in 8 (62%) of 13 patients with lesions in the temporal pole and 2 (7%) of 30 patients without lesions in the temporal pole (**Table 2**). We detected Notch3 deposits in 10 (34%) of 29 patients with Fazekas grade 3 white matter lesions and did not find them in 13 patients with Fazekas grade 1–2 white matter lesions (**Table 2**). GOM deposits were observed by electron microscopy (**Figures 1E,F**). The location and morphological features of the vascular Notch3 ECD and the GOM deposits were similar. We found Notch3 ECD deposits in all the three randomly selected CADASIL cases with GOM deposits (**Table 1**). Moreover, sequencing revealed that all 10 patients with vascular Notch3 ECD deposits had pathogenic or likely pathogenic variants of *NOTCH3*, such as p.Arg110Cys, p.Tyr258Cys, p Cys408Arg, p.Cys516Phe, p. Trp1003Cys, and p.Tyr1021Cys, which are reportedly associated with CADASIL (**Table 1**). *NOTCH3* p.Arg110Cys and p.Tyr258Cys variants are located in Notch3 EGFr domains 1–6 (case 2 and 10), and *NOTCH3* p.Cys408Arg, p.Cys516Phe, p.Trp1003Cys, and p.Tyr1021Cys variants are located in Notch3 EGFr domains 7–34 (cases 1 and 3–9). We did not find significant correlations between the degree of Notch3 deposits and *NOTCH3* mutation location. Based on the ClinVar database, the *NOTCH3* p.Arg75Gln variant is "likely benign." The other five variants, such as p.Thr900Pro, p.Leu989Arg, p.Cys1372Gly, p Glu1373Gly, p.Ala1649Thr, and p.Gly1650Ser, were not found in the ClinVar database. According to PolyPhen-2 and MutationTaser2021, p.Leu989Arg, p.Ala1649Thr, and p.Gly1650Ser were predicted to be "benign" and p.Thr900Pro, p.Cys1372Gly, and p Glu1373Gly were predicted to be "probably damaging" and "deleterious" (**Table 1**).

Four of the 33 patients without vascular Notch3 ECD or GOM deposits in skin biopsy samples (cases 12, 25, 26, and 35) (**Table 1**) had *NOTCH3* variants of unknown significance, such as p.Arg75Gln, p.Thr900Pro, p.Leu989Arg, p.Cys1372Gly, p Glu1373Gly, and p.Gly1650Ser. The remaining 29 patients without vascular Notch3 ECD deposits did not have any *NOTCH3* variants. We also investigated vascular GOM deposits in 16 of the 29 patients and found no GOM deposits in any of the 16 patients without vascular Notch3 ECD deposits or *NOTCH3* variants (**Table 1**).

TABLE 1 | Skin vascular Notch3 ECD deposits and *NOTCH3* variants in 43 patients with suspected CADASIL.

Case no.	Age	Sex	Skin vascular Notch3 ECD deposits	Skin vascular GOM deposits	*NOTCH3* variants	EGFr domain no.	ClinVar	PolyPhen-2	MutationTaster2021	HGVD (allele frequency in the Japanese population)	gnomAD (allele frequency in the global population)	Fazekas grades	Lesions in the temporal pole	Clinical findings	Family history of stroke
1	61	F	+	NA	p.Trp1003Cys	26	Likely pathogenic	Probably damaging	Deleterious	Unknown	Unknown	3	+	Stroke	+
2	62	F	+	NA	p.Arg110Cys	2	Pathogenic	Probably damaging	Deleterious	Unknown	0.000004	3	+	Stroke	+
3	51	F	+	+	p.Trp1003Cys	26	Likely pathogenic	Probably damaging	Deleterious	Unknown	Unknown	3	+	Dizziness, hemorrhage	+
4	41	M	+	+	p.Cys408Arg	10	NA	Probably damaging	Deleterious	Unknown	Unknown	3	+	Migraine	+
					p.Cys1410Tyr	NA (LNR1)	NA	Probably damaging	Deleterious	Unknown	Unknown				
5	45	M	+	NA	p.Trp1003Cys	26	Likely pathogenic	Probably damaging	Deleterious	Unknown	Unknown	3	+	Stroke	+
					p.Ala1649Thr	NA	NA	Benign	Benign	Unknown	Unknown				
6	48	M	+	NA	p.Trp1003Cys	26	Likely pathogenic	Probably damaging	Deleterious	Unknown	Unknown	3	+	Depression	+
7	42	M	+	NA	p.Trp1003Cys	26	Likely pathogenic	Probably damaging	Deleterious	Unknown	Unknown	3	+	Stroke	+
8	68	M	+	NA	p.Cys516Phe	13	Pathogenic	Probably damaging	Deleterious	Unknown	Unknown	3	–	Cognitive decline	–
9	50	M	+	+	p.Tyr1021Cys	26	Pathogenic	Probably damaging	Deleterious	Unknown	Unknown	3	+	Stroke	+
10	54	F	+	NA	p.Tyr258Cys	6	Pathogenic	Probably damaging	Deleterious	Unknown	Unknown	3	–	Stroke, cognitive decline	–
11	51	M	–	–	–	NA	NA	NA	NA	NA	NA	3	–	Stroke, cognitive decline	+
12	47	M	–	–	p.Leu989Arg	25	NA	Benign	Benign	Unknown (0.00030 in 8.3KJPN*)	Unknown	3	–	Cognitive decline	–
13	54	M	–	–	–	NA	NA	NA	NA	NA	NA	3	–	Headache, Stroke, cognitive decline	+
14	46	M	–	–	–	NA	NA	NA	NA	NA	NA	3	–	Cognitive decline	–

(Continued)

TABLE 1 | Continued

Case no.	Age	Sex	Skin vascular Notch3 ECD deposits	Skin vascular GOM deposits	*NOTCH3* variants	EGFr domain no.	ClinVar	PolyPhen-2	MutationTaster2021	HGVD (allele frequency in the Japanese population)	gnomAD (allele frequency in the global population)	Fazekas grades	Lesions in the temporal pole	Clinical findings	Family history of stroke
15	43	M	–	NA	–	NA	NA	NA	NA	NA	NA	1	–	Cerebral hemorrhage	–
16	49	M	–	NA	–	NA	NA	NA	NA	NA	NA	3	+	Cognitive decline	–
17	44	F	–	–	–	NA	NA	NA	NA	NA	NA	3	+	Headache, stroke, cognitive decline	+
18	58	F	–	NA	–	NA	NA	NA	NA	NA	NA	3	–	Cognitive decline	+
19	57	M	–	NA	–	NA	NA	NA	NA	NA	NA	3	–	Stroke	+
20	66	F	–	NA	–	NA	NA	NA	NA	NA	NA	3	+	Headache	+
21	48	M	–	NA	–	NA	NA	NA	NA	NA	NA	2	–	Headache, stroke, MCI	+
22	56	F	–	NA	–	NA	NA	NA	NA	NA	NA	2	–	Mood disorder	+
23	49	M	–	NA	–	NA	NA	NA	NA	NA	NA	3	–	Cognitive decline	–
24	55	M	–	NA	–	NA	NA	NA	NA	NA	NA	3	+	Asymptomatic stroke	–
25	56	F	–	–	p.Cys1372Gly	34	NA	Probably damaging	Deleterious	Unknown	Unknown	2	–	Migraine	–
					p.Gly1650Ser	NA	NA	Benign	Benign	Unknown	Unknown				
26	55	F	–	–	p.Cys1372Gly	34	NA	Probably damaging	Deleterious	Unknown	Unknown	2	–	Cognitive decline	–
					p.Thr900Pro	23	NA	Probably damaging	Deleterious	Unknown	Unknown (0.000004in TOPMed**)				
					p Glu1373Gly	34	NA	Probably damaging	Deleterious	Unknown	Unknown				
27	35	M	–	NA	–	NA	NA	NA	NA	NA	NA	3	–	Migraine, stroke	+
28	55	F	–	–	–	NA	NA	NA	NA	NA	NA	3	–	Asymptomatic aneurism	+
29	62	M	–	–	–	NA	NA	NA	NA	NA	NA	3	–	Brain hemorrhage	–
30	60	M	–	NA	–	NA	NA	NA	NA	NA	NA	3	–	Stroke	+

(Continued)

TABLE 1 | Continued

Case no.	Age	Sex	Skin vascular Notch3 ECD deposits	Skin vascular GOM deposits	*NOTCH3* variants	EGFr domain no.	ClinVar	PolyPhen-2	MutationTaster2021	HGVD (allele frequency in the Japanese population)	gnomAD (allele frequency in the global population)	Fazekas grades	Lesions in the temporal pole	Clinical findings	Family history of stroke
31	67	M	–	–	–	NA	NA	NA	NA	NA	NA	3	–	Stroke, Cognitive decline	+
32	67	F	–	–	–	NA	NA	NA	NA	NA	NA	3	–	Cognitive decline	–
33	49	F	–	–	–	NA	NA	NA	NA	NA	NA	2	+	MCI	–
34	61	M	–	–	–	NA	NA	NA	NA	NA	NA	3	–	Stroke, cognitive decline	+
35	38	F	–	–	p.Arg75Gln	1	Likely benign	Probably damaging	Benign	Unknown	Unknown	2	–	Migraine	–
36	42	F	–	NA	–	NA	NA	NA	NA	NA	NA	1	–	Dizziness	–
37	31	M	–	NA	–	NA	NA	NA	NA	NA	NA	NA	–	Headache	+
38	45	F	–	–	–	NA	NA	NA	NA	NA	NA	2	–	Stroke	+
39	50	F	–	–	–	NA	NA	NA	NA	NA	NA	2	–	MCI, mood disorder	+
40	53	F	–	–	–	NA	NA	NA	NA	NA	NA	2	–	Migraine	–
41	53	F	–	–	–	NA	NA	NA	NA	NA	NA	3	–	Stroke	+
42	56	M	–	–	–	NA	NA	NA	NA	NA	NA	2	–	MCI	–
43	63	M	–		–	NA	NA	NA	NA	NA	NA	2	–	Asymptomatic	–

EGFr, epidermal growth factor like repeats; gnomAD, the Genome Aggregation Database; GOM, granular osmiophilic material; HGVD, the Human Genetic Variation Database; MCI, mild cognitive impairment; NA, not available. [*] *Tadaka et al., 3.5KJPNv2: an allele frequency panel of 3,552 Japanese individuals including the X chromosome.* ***Hum Genome Var*** *(2019) 6:28.* [**] *TOPMed ("https://topmed.nhlbi.nih.gov/").*

TABLE 2 | Number of patients with and without skin Notch3 deposits among patients with suspected CADASIL.

	Total number	Skin Notch3 positive	Skin Notch3 negative
Patients with pathogenic *NOTCH3* variants associated with CADASIL	10	10 (100%)	0 (0%)
Patients with *NOTCH3* variants of unknown significance	4	0 (0%)	4 (100%)
Patients without *NOTCH3* variants	29	0 (0%)	29 (100%)
Patients with lesions in the temporal pole	13	8 (62%)	5 (38%)
Patients without lesions in the temporal pole	30	2 (7%)	28 (93%)
Patients with Fazekas grade 3 white matter lesions	29	10 (34%)	19 (66%)
Patients with Fazekas grade 1–2 white matter lesions	13	0 (0%)	13 (100%)

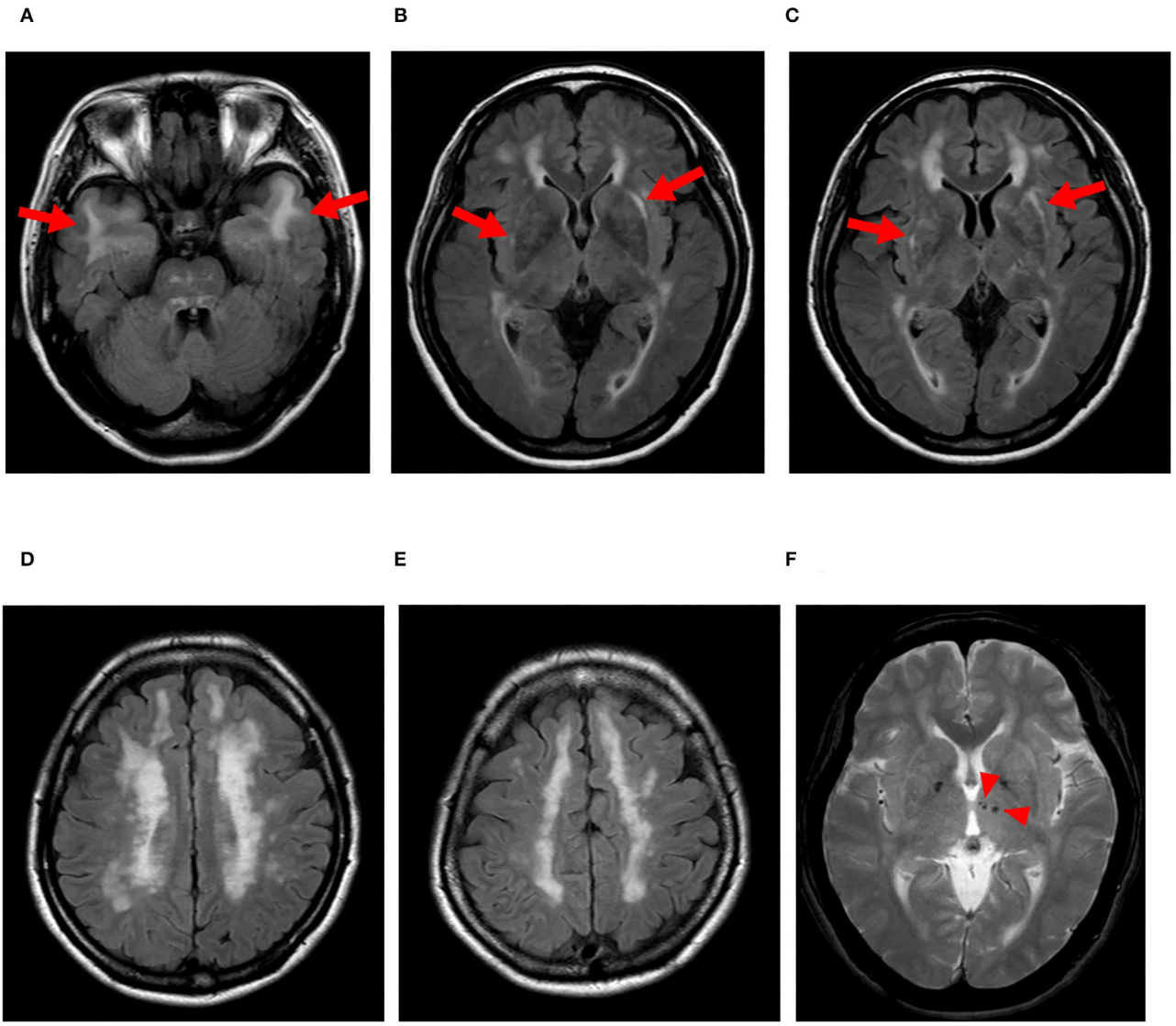

FIGURE 2 | Representative MRI findings of CADASIL. Case 2 with the pathogenic *NOTCH3* p.Arg110Cys variant. **(A–E)** FLAIR images, **(F)** T2-star weighted image. **(A)** Arrows indicate lesions in the temporal pole. **(B,C)** Arrows indicate lesions in the extra capsule of the putamen, and **(F)** arrowheads indicate microbleeds.

Brain MRI Findings in Patients With and Without Vascular Notch3 ECD Deposits

We found lesions in the temporal pole on MRI (**Figure 2**) and a family history of stroke in eight of the 10 (80%) patients with vascular Notch3 ECD deposits. Two patients (cases 8 and 10) with vascular Notch3 ECD deposits had neither lesion in the temporal pole on MRI nor a family history of stroke (**Table 1**). In contrast, 5 of the 33 (15%) patients without vascular Notch3 ECD deposits (cases 16, 17, 20, 24, and 33) had lesions in the temporal pole. No *NOTCH3* variants were found in these five patients (**Table 1**).

DISCUSSION

In this case series study of 43 patients with suspected CADASIL, we detected vascular Notch3 ECD deposits in all 10 patients by immunohistochemical staining using unfixed frozen biopsied samples, which were confirmed to have pathogenic *NOTCH3* variants causing CADASIL. In contrast, conventional immunohistochemical staining using FFPE tissue samples fails to detect vascular Notch3 deposits in 5–15% of patients with CADASIL with pathogenic variants in *NOTCH3* (4–6). Therefore, unfixed frozen biopsied tissue samples may be more suitable than FFPE-biopsied tissue samples for the detection of vascular Notch3 ECD deposits in the skin.

Patients with CADASIL carrying pathogenic *NOTCH3* variants, which were mostly associated with cysteine replacement (11), located in the EGFr domains 7–34, reportedly showed milder phenotypes than those with *NOTCH3* variants located in the EGFr domains 1–6 (12). In addition, Gravesteijn et al. (13) recently reported that the amount of vascular Notch3 ECD and GOM deposits in the skin in patients with CADASIL with *NOTCH3* variants in EGFr 7–34 was lesser than that in those with *NOTCH3* variants in EGFr 1–6. In this case series study, we successfully detected vascular Notch3 ECD deposits in patients with CADASIL with both milder *NOTCH3* EGFr 7–34 variants and typical severe *NOTCH3* EGFr 1–6 variants by immunohistochemical staining using unfixed frozen biopsied skin samples (**Table 1**). Therefore, immunohistochemical staining using unfixed frozen biopsied skin samples seems to be suitable for detecting Notch3 deposits in CADASIL regardless of the amount of Notch3 ECD deposits.

Detecting Notch3 and GOM deposits are thought to be helpful for the diagnosis of CADASIL. Brain MRI findings reportedly varied considerably between patients with CADASIL and were dependent on the *NOTCH3* genotype (14). While the involvement of the anterior temporal pole and external capsule may be helpful for the diagnosis of CADASIL, these MRI findings were reportedly not sufficient for accurate diagnosis of CADASIL (14). Skin biopsy is less invasive than brain biopsy to directly confirm pathogenic Notch3 and GOM deposits in patients with suspected CADASIL. In this study, 10 of 43 cases were identified as positive of staining of Notch3 and/or GOM. We believe that skin biopsy is useful especially for detecting Notch3 deposits in patients with CADASIL with *NOTCH3* variants of unknown significance, while skin biopsy may not be essential for the diagnosis of patients with CADASIL with typical *NOTCH3* variants and typical MRI findings in the daily clinical practice.

This study is limited in that it had a small sample size. Large-scale studies including more patients with CADASIL with other genotypes are needed to determine the sensitivity and specificity of this immunohistochemical method in differentiating between CADASIL and other cerebral small vessel diseases.

CONCLUSION

Immunohistochemical staining of vascular Notch3 ECD deposits in unfixed frozen skin sections may be useful over conventional immunohistochemical staining for detecting Notch3 deposits in CADASIL.

DATA AVAILABILITY STATEMENT

The raw data supporting the conclusions of this article will be made available by the authors, without undue reservation.

ETHICS STATEMENT

This study was approved by the Human genome Ethics Committee of Kumamoto University. The patients/participants provided their written informed consent to participate in this study.

AUTHOR CONTRIBUTIONS

AU drafted the manuscript, devised the study concept and design, collected data, and performed the pathological examinations. SS and HM performed the gene analysis. MN, KN, MT, and YM revised the manuscript. MU revised the manuscript, devised the study concept and design, and supervised the study. All authors have contributed to the manuscript and approved the submitted version.

FUNDING

This study was funded by a grant-in-aid for research on intractable diseases from the Japanese Ministry of Health, Labor, and Welfare (Grant No. 21FC1007).

ACKNOWLEDGMENTS

We would like to thank Editage (www.editage.com) for English language editing.

REFERENCES

1. Joutel A, Vahedi K, Corpechot C, Troesch A, Chabriat H, Vayssière C, et al. Strong clustering and stereotyped nature of *notch3* mutations in patients with CADASIL. *Lancet.* (1997) 350:1511–5. doi: 10.1016/S0140-6736(97)08083-5
2. Esters ML, Chimowitz MI, Awad IA, McMahon JT, Furlan AJ, Ratiff NB. Sclerosing vasculopathy of the central nervous system in nonelderly patients. *Arch Neurol.* (1991) 46:631–6. doi: 10.1001/archneur.1991.00530180087022
3. Joutel A, Andreux F, Gaulis S, Domenga V, Cecillon M, Battail N, et al. The ectodomain of the Notch 3 receptor accumulates within the cerebrovascular of patients with CADASIL. *J Clin Invest.* (2000) 105:597–605. doi: 10.1172/JCI8047
4. Joutel A, Favrole P, Labauge P, Chabriat H, Lescoat C, Andreux F, et al. Skin biopsy immunostaining with a Notch3 monoclonal antibody for CADASIL diagnosis. *Lancet.* (2001) 358:2049–51. doi: 10.1016/S0140-6736(01)07142-2
5. Lesnik Oberstein SA, van Duinen SG, van den Boom R, Maat-Schieman ML, van Buchem MA, van Houwelingen HC, et al. Evaluation of diagnostic Notch3 immunostaining in CADASIL. *Acta Neuropathol.* (2003) 106:107–11. doi: 10.1007/s00401-003-0701-6
6. Ampuero I, Alegre-Abarrategui J, Rodal I, España A, Raquel Ros SJLL, et al. On the diagnosis of CADASIL. *J Alzhemer's Dis.* (2009) 17:787–94. doi: 10.3233/JAD-2009-1112
7. Tikka S, Mykkänen K, Junna M, Bergholm R, Pöyhönen M, Baumann M, et al. Diagnosing Vascular Dementia by Skin Biopsy-Uniqueness of CADASIL. In: Khopkar U, editor. *Skin Biopsy-Perspectives*. London: Intechopen (2011).
8. Ueda A, Ueda M, Nagatoshi A, Hirano T, Ito T, Arai N, et al. Genotypic and phenotypic spectrum of CADASIL in Japan: the experience at a referral center in Kumamoto university From 1997 to 2014. *J Neurol.* (2015) 262:1828–36. doi: 10.1007/s00415-015-7782-8
9. Yamamoto Y, Craggs LJ, Watanabe A, Booth T, Attems J, Low RW, et al. Brain microvascular accumulation and distribution of the Notch3 ectodomain and granular osmiophilic material in CADASIL. *J Neuropathol Exp Neurol.* (2013) 72:416–31. doi: 10.1097/NEN.0b013e31829020b5
10. Tikka S, Mykkänen K, Ruchoux MM, Bergholm R, Junna M, Pöyhönen M, et al. Congruence between Notch3 mutations and GOM in 131 patients with CADASIL. *Brain.* (2009) 132:933–9. doi: 10.1093/brain/awn364
11. Matsushima T, Conedera S, Tanaka R, Li Y, Yoshino H, Funayama M, et al. Genotype-phenotype correlations of cysteine replacement in CADASIL. *Neurobiol Aging.* (2017) 169:e7–169. doi: 10.1016/j.neurobiolaging.2016.10.026
12. Rutten JW, Van Eijsden BJ, Duering M, Jouvent E, Opherk C, Pantoni L, et al. The effect of Notch3 pathogenic variant position on CADASIL disease severity: Notch3 EGFr 1–6 pathogenic variant are associated with a more severe phenotype and lower survival compared with EGFr 7–34 pathogenic variant. *Genet Med.* (2019) 21:676–82. doi: 10.1038/s41436-018-0088-3
13. Gravesteijn G, Hack RJ, Mulder AA, Cerfontaine MN, van Doorn R, Hegeman IM, et al. Notch3 variant position is associated with Notch3 aggregation load in CADASIL vasculature. *Neuropathol Appl Neurobiol.* (2022) 48:e12751. doi: 10.1111/nan.12751
14. Schoemaker D, Quiroz YT, Torrico-Teave H, Arboleda-Velasquez JF. Clinical and research applications of magnetic resonance imaging in the study of CADASIL. *Neurosci Lett.* (2019) 698:173–9. doi: 10.1016/j.neulet.2019.01.014

Conflict of Interest: The authors declare that the research was conducted in the absence of any commercial or financial relationships that could be construed as a potential conflict of interest.

Publisher's Note: All claims expressed in this article are solely those of the authors and do not necessarily represent those of their affiliated organizations, or those of the publisher, the editors and the reviewers. Any product that may be evaluated in this article, or claim that may be made by its manufacturer, is not guaranteed or endorsed by the publisher.

Copyright © 2022 Ueda, Nakajima, Misumi, Nakahara, Shinriki, Tasaki, Matsui and Ueda. This is an open-access article distributed under the terms of the Creative Commons Attribution License (CC BY). The use, distribution or reproduction in other forums is permitted, provided the original author(s) and the copyright owner(s) are credited and that the original publication in this journal is cited, in accordance with accepted academic practice. No use, distribution or reproduction is permitted which does not comply with these terms.

frontiers | Frontiers in Neurology

REVIEW
published: 14 June 2022
doi: 10.3389/fneur.2022.854605

Neuroimaging Markers of Chronic Eye Diseases and Their Application Values

*Chen-Yu Yu†, Rong Huang†, Shi-Qi Li† and Yi Shao**

Department of Ophthalmology, Jiangxi Province Ocular Disease Clinical Research Center, The First Affiliated Hospital of Nanchang University, Nanchang, China

In recent years, the impact of various chronic eye diseases on quality of life has become increasingly apparent. Therefore, it is particularly important to control the progress of chronic diseases at an early stage. Many studies have used neuroimaging methods to explore the effects of chronic eye diseases on the brain, and to identify changes in brain function that may act as markers for early diagnosis and treatment. This article reviews the clinical application of different techniques of functional magnetic resonance imaging in chronic eye diseases.

Keywords: magnetic resonance imaging, chronic eye diseases, markers, neurology, application

OPEN ACCESS

Edited by:
Yuzhen Xu,
Tongji University, China

Reviewed by:
Benito de Celis Alonso,
Meritorious Autonomous University of Puebla, Mexico
He Wang,
Xuzhou Medical University, China
Yuan Liu,
University of Miami Health System, United States

***Correspondence:**
Yi Shao
freebee99@163.com

†These authors have contributed equally to this work

Specialty section:
This article was submitted to Neurological Biomarkers, a section of the journal Frontiers in Neurology

Received: *14 January 2022*
Accepted: *11 May 2022*
Published: *14 June 2022*

Citation:
Yu C-Y, Huang R, Li S-Q and Shao Y (2022) Neuroimaging Markers of Chronic Eye Diseases and Their Application Values. Front. Neurol. 13:854605. doi: 10.3389/fneur.2022.854605

APPLICATION OF ALFF IN CHRONIC EYE DISEASES

As a resting-state functional magnetic resonance imaging (MRI) analysis tool, the amplitude of low-frequency fluctuation (ALFF) has high accuracy and repeatability and does not require definition of regions of interest (ROI) in advance. By calculating the root mean square of the blood oxygen level dependent (BOLD) signal power spectrum at low frequencies (0.01HZ−0.08HZ), the neuronal activity in different brain regions is expressed and is an indicator of spontaneous neuronal activity (1). The value of ALFF technology in detecting brain neuron activity has been confirmed in previous experiments (2). Changes in ALFF value reflect disease progression, in part and are widely used in the diagnosis and monitoring of eye diseases. ALFF markers for chronic eye disease are shown in **Table 1**, where the middle frontal gyrus (MFG) features prominently. However, changes in ALFF values at the MFG have implications that vary with disease. For example, in patients with monocular blindness (5) and neovascular glaucoma (10), ALFF changes at the MFG are related to visual perception impairment or compensation, while similar changes in diabetic vitreous hemorrhage (9) indicate visual motor disorder, and in strabismic amblyopia (7), diabetic retinopathy and nephropathy (8) they may indicate a tendency toward anxiety and depression.

APPLICATION OF DC IN CHRONIC EYE DISEASES

Voxel-wise degree centrality (DC) is another commonly used technique in resting state functional MRI technology. It assesses functional connectivity within the brain by measuring the topological structure of brain functional connectors at voxel level, and provides the correlation between different nodes and the importance of each node in the network structure (11). The degree of direct functional connection between two nodes can be expressed by DC values. A high DC value indicates a higher degree of direct connection between the node and other nodes. A change in DC values indicates a change in connectivity between the node and the network and clearly shows the state of each node (12). This method can be used to find any changes in brain functional connectivity in

chronic ocular disease, and the changemay be an important marker for disease detection. Chronic diseases and their corresponding DC value markers are shown in **Table 2**.

APPLICATION OF REHO IN CHRONIC EYE DISEASES

Regional homogeneity (ReHo) is a widely used analytical method in resting state MRI, and plays an important role in exploring changes in local synchronization of voxels in brain regions (16). The analysis of ReHo is based on the measurement of voxels, and is used to measure the synchronization of adjacent regions based on the similarity between the time series of a given voxel and its nearest adjacent time series (calculated by the Kendall consistency coefficient of BOLD time series) (17). The coherence and centrality of regional brain activity are closely related to the ReHo values. ReHo is usually calculated in the low frequency range (0.01Hz–0.1Hz). Like ALFF, ReHo does not need a priori definition of ROI and can provide information about the activity of the whole brain. ReHo has been widely used in various studies to explore the local synchronization of spontaneous fMRI signals. In addition, the ReHo method is used in many studies of chronic eye diseases. Altered ReHo values can be used as a marker to monitor progress of various diseases, as shown by **Table 3**. ReHo measures at the inferior temporal gyrus (ITG) and the right cuneus (RC) are common markersfor chronic eye disease. The significantly increased ReHo values of the ITG in concomitant exotropia (23) and monocular blindness (20) indicated the compensatory mechanism of visual function. In monocular blindness, the ReHo values of RC decrease significantly, indicating the interruption of synchronous neural activity. The RC also showed a decreased ReHo value in diabetic retinopathy (22), reflecting vision-related dysfunction in this area. In patients with anisometropic amblyopia (18), a clear increase in RC was related to the compensatory mechanism of eye movement.

TABLE 1 | Application of ALFF in chronic eye diseases.

Disease	Year	Increased ALFF values	Decreased ALFF values
High myopia (3)	2016	BMCC, LposCG, LpreCU/IPL	RITG/MTG, LMTG, LIFG/PT, RIFG/PT/IS, RMFG, RIPL
Diabetic retinopathy (4)	2016	BOG, RLG, preCU	RP/ACL, RPG, RFG, RSTG, RIPG, RAG
Monocular blindness (5)	2016	RMFG, LMFG, LSMG	LCAL, RMG, RC, LPCG/PCL
Congenital comitant strabismus (6)	2016	BCPL, LAG	BMFG
Strabismus with amblyopia (7)	2018	RSFG, RPC, LC, BPCG	LCPL, LT, RT, LMFG
Diabetic retinopathy and nephropathy (8)	2019	BCPL, LITG	BMFG, RSTG, RMFG, LMFG, BP, LIPL
Vitreous hemorrhage (9)	2020	RCPL, LCPL, LCPL/LLG, BSFG/LPG	RMFG, RIFG, RMFG/LAC, RSFG, RSFG/MFG, LMFG
Neovascular glaucoma (10)	2020	RSFG, LMFG	RC, RMOG, RP, LCG, LMFG

RITG/MTG, right inferior and middle temporal gyrus; LMTG,left middle temporal gyrus; LIFG/PT, left Inferior frontal gyrus/putamen; RIFG/PT/IS, right inferior frontal gyrus/putamen/insula; RMFG, right middle frontal gyrus; RIPL, right inferior parietal lobule; BMCC, bilateral midcingulate cortex; LposCG, left postcentral gyrus; LpreCU/IPL, left precuneus/inferior parietal lobule; BOG, bilateral occipital gyrus; RLG, right lingual gyrus; RP/ACL, right posterior/anterior cerebellar lobe; RPG, right parahippocampal gyrus; RFG, right fusiform gyrus; RSTG, right superior temporal gyrus; RIPG, right inferior parietal gyrus; RAG, right angular gyrus; LAG, left angular gyrus; LSMG, left supramarginal gyrus; RC, right cuneus; LC, left cuneus; LCAL, left cerebellum anterior lobe; LPCG/PCL, left precentral gyrus/paracentral lobule; BCPL, bilateral cerebellum posterior lobe; RSFG, right superior frontal gyrus; RPC, right precuneus; BPCG, bilateral precentral gyrus; LCPL, left cerebellum posterior lobe; LT, left thalamus; RT, right thalamus; LITG, left Inferior frontal gyrus; BP, bilateral precuneus; LLG, left lingual gyrus; LPG, left postcentral gyrus; LAC, left anterior cingulate;RP, right precuneus; RMOG, bilateral middle occipital gyrus; LCG, left cingulate gyrus.

APPLICATION OF FC IN CHRONIC EYE DISEASES

Functional connectivity (FC) is a seed-based or ROI-based functional connection, in which areas functionally related to activities in the seed area may be found (24). In seed-based analysis, cross-correlation is calculated between the time series of the seed and the rest of the brain to assess the activity of the selected brain region. Functional connections may be considered as brain areas which have been activated similarly, indicating that they have a similar role in brain functional activity. Physiologically, the relevant brain regions may not be directly connected by nerve fibers, but the connectivity matrix shows connection strength and range including indirect connections. Flexibility and sensitivity of this technique has resulted in it being widely used in the study of various brain functional diseases (25). The FC value indicates the intensity of activity and may be used to mark changes in brain functional activity caused by disease. Application of the FC method as a marker in brain functional activity of chronic ophthalmopathy is shown in **Table 4**.

APPLICATION OF VBM IN CHRONIC EYE DISEASES

Voxel-based morphometry (VBM) is an MRI whole-brain analysis technique for measuring density and volume changes of gray and white matter at the voxel level, and is used to enhance understanding of the anatomical structure of the brain (30). In contrast with some other resting MRI techniques, VBM has no preset region of interest, it detects changes in neural activity across all parts of the brain, and is an objective measure so is minimally influenced by subjective factors. The VBM approach filters the white and gray matter areas with statistically significant activity by comparing the processed MRI images (31), and can

TABLE 2 | Application of DC in chronic eye diseases.

Disease	Year	Increased DC values	Decreased DC values
Comitant exotropic strabismus (13)	2018	RSTG, BAC, LIPL	RCPL, RIFG, RMFG, RSPL/SI
Diabetic nephropathy and retinopathy (14)	2019	BP	RITG, LSG
Monocular blindness (15)	2019	LITG, BMFG	BC/V1/V2

RSTG, right superior temporal gyrus; BAC, bilateral anterior cingulate; LIPL, left inferior parietal lobule; RCPL, right cerebellum posterior lobe; RMFG, right middle frontal gyrus; RSTG, right superior temporal gyrus; RIFG, right inferior frontal gyrus; BP, bilateral precuneus; LSG, left subcallosal gyrus; RITG, right inferior temporal gyrus; LITG, left inferior temporal gyrus; BMFG, Bilateral medial frontal gyrus; BC, Bilateral cuneus; V1, primary visual cortex, V2, secondary visual cortex.

TABLE 3 | Application of ReHo in chronic eye diseases.

Disease	Year	Increased ReHo values	Decreased ReHo values
Anisometropic amblyopia (18)	2012	RINS/PUT, LSTG, LperCG, LFG, RMOG	RC, LMPC, LIFG, LC
Comitant strabismus (19)	2016	RITG/RFG/RCAL, RLG, BCG	_
Monocular blindness (20)	2017	RITG, RFMO, LPC/LP, LMFG	RRG, RC, RAC, RLOC
Strabismus and amblyopia (21)	2019	LLG, RMOG/RP, BAC, LMOG, BPG	LIFG
Diabetic retinopathy (22)	2019	RCPL, LCPL	RAC, RC, BP, LMFG
Constant exotropia (23)	2019	RV2	LBA47

RINS/PUT, right insula and putamen; LSTG, left superior temporal gyrus; LperCG, left precentral gyrus; LFG, left fusiform gyrus; LMPC, left media prefrontal cortex; LIFG, left inferior frontal gyrus; RITG, right inferior temporal gyrus; LITG, left inferior temporal gyrus; RFG, right fusiform gyrus; RCAL, right cerebellum anterior lobe; RLG, right lingual gyrus; BCG, bilateral cingulate gyrus; RRG, right rectal gyrus; RFMO, right frontal middle orbital ; LPC, left posterior cingulate; LP, left precuneus; RP, right precuneus; BP, bilateral precuneus; LMFG, left middle frontal gyrus; RMFG, right middle frontal gyrus; RRG, right rectal gyrus; RC, right cuneus; RAC, right anterior cingulate; RLOC, right lateral occipital cortex; LLG, left lingual gyrus; RMOG, right middle occipital gyrus; LMOG, left middle occipital gyrus; BAC, bilateral anterior cingulate; RAC, right anterior cingulate; BPG, bilateral precentral gyrus; RCPL, right cerebellum posterior lobe; lCPL, left cerebellum posterior lobe; RV2, right secondary visual cortex; LBA47, left Brodmann area 47; RC, right cerebellum; LC, left cerebellum.

TABLE 4 | Application of FC in chronic eye diseases.

Disease	Year	Increased FC values	Decreased FC values
Anisometropic amblyopia (26)	2013	Lpost, LPL/MFG	BC, BIPL/AL, LMFL/PreG
Comitant exotropia (27)	2018	_	LLG/CPL, RMOG, LPreG/PG, RIPL/PG
Comitant Strabismus (28)	2019	PPVC, BA19, BA6	_
Neovascular Glaucoma (29)	2020	BMFG	LP, BC
Strabismus (30)	2021	BC, BC/RLG, LIOG, RMOG	LP/PG, RI/RO, LPG, BPL/PG/RPG/LPG

LPostG, left postcentral gyrus; LPL/MFG, left paracentral lobule and the middle frontal gyrus; BC, bilateral cerebellum; BIPL/AL, bilateral inferior parietal lobe and the angular lobe; LMFL/PreG, left middle frontal lobe and the precentral gyrus; LLG/CPL, left lingual gyrus/cerebellum posterior lobe; RMOG, right middle occipital gyrus; LPreG/PG, left precentral gyrus/postcentral gyrus; RIPL/PG, right inferior parietal lobule/postcentral gyrus; BMFG, bilateral middle frontal gyrus; LP, left precuneus; BC, bilateral cuneus; RLG, right lingual gyrus; LIOG, left inferior occipital gyrus; RI/RO, right insula and rolandic operculum; RPG, right postcentral gyrus; PPVC, posterior primary visual cortex; BA, Brodmann area.

TABLE 5 | Application of VBM in chronic eye diseases.

Disease	Year	Altered WMV values	Altered GMV values
Adult strabismus (32)	2004	_	OEF, PEF, PEF, SEF, PFC, SR
Amblyopia (33)	2005	_	C/PC, MPOJ, LPOJ, VTC
Comitant strabismus (34)	2017	LMTG, RMTG, RP, RPC	LMTP, LCPL, RPCC, LC, RPC
Monocular blindness (35)	2019	-_	RSM, RI, LI, RAC, LMOG, RIPL

C/PC, calcarine and paracalcarine cortex; MPOJ, medial parietal-occipital junction; LPOJ, lateral parietal-occipital junction; VTC, ventral temporal cortex; WMV , white matter volume; GMV, grey matter volume; LMTG, left middle temporal gyrus; RMTG, right middle temporal gyrus; RP, right precuneus; RPC, right premotor cortex; LMTP, left middle temporal pole; LCPL, left cerebellum posterior lobe; RPCC, right posterior cingulate cortex; LC, left cuneus; RSM, right supra marginal; RI, right insular cortex; LI, left insular cortex; RAC, right anterior cingulate; LMOG, left middle occipital gyrus; RIPL, right inferior parietal lobe; OEF, occipital eye field; PEF, parietal eye field; FEF, frontal eye field; SEF, supplementary eye field; PFC, prefrontal cortex; SR, subcortical regions.

be used to detect pathological changes of brain function caused by disease. Changes of this kind have been found to accompany progression of many ophthalmic diseases, as shown in **Table 5**.

APPLICATION OF VMHC IN CHRONIC EYE DISEASES

Voxel-mirrored homotopic connectivity (VMHC) is a new resting-state FC analysis method to measure the functional connection between hemispheres (36). This method can detect abnormal functional activity in local brain areas and changes of functional connection and synchronization of neural activity between corresponding regions in bilateral cerebral hemispheres at rest, which shows that the degree of separation of cerebral hemispheres is its outstanding advantage. The normal human brain generally has the characteristic of high synchronization of spontaneous nerve activity in homotopic regions between hemispheres. Many studies have confirmed that this characteristic may be generally destroyed in patients with chronic eye diseases, suggesting that hemispheric dysfunction

TABLE 6 | Application of VMHC in chronic eye diseases.

Disease	Year	Increased VMHC values	Decreased VMHC values
Early blindness (37)	2017	_	PVC, VAC, SAC
Monocular blindness (38)	2018	LI, LMFG	LC/C/LG, RC/C/LG, RPMC/PSC, RSPL
Comitant exotropia (39)	2018	STG, MFG	PreG, IPL, SPL
Diabetic retinopathy and nephropathy (40)	2020	_	BMTG, BMOG, BMFG

LC/C/LG, left cuneus/calcarine/lingual gyrus; LI, left insula; LMFG, left middle frontal gyrus; RC/C/LG, right cuneus/calcarine/lingual gyrus; RPMC/PSC, right primary motor cortex (M1)/primary somatosensory cortex (S1); RSPL, right superior parietal lobule; BMFG, bilateral medial frontal gyrus; STG, superior temporal gyrus; PreG, precentral gyrus; IPL, inferior parietal lobule; SPL, superior parietal lobule; BMOG, bilateral middle occipital gyrus; BMTG, bilateral medial frontal gyrus; PVC, primary visual cortex; VAC, visual association cortex; SAC, somatosensory association cortex.

plays an important role in brain dysfunction in patients with chronic eye diseases. Using VMHC, this loss of synchrony has been demonstrated in patients with diseases of this kind, as shown in **Table 6**.

APPLICATION OF OTHER TECHNIQUES IN CHRONIC EYE DISEASES

The fractional amplitude of low-frequency fluctuation (fALFF) provides a measure of inherent spontaneous brain activity (41). Measurement of fALFF values need to be carried out within a specified frequency range, and spontaneous brain activity can be expressed by the measurement of cerebral blood flow at the amplitude of low frequency oscillation (0.01–0.08 Hz) (42). The fALFF technique has the advantages of high sensitivity and specificity and is non-invasive, so it is widely used in brain functional activity imaging. Diffusion tensor imaging (DTI) is a widely used MRI method, which describes the diffusion direction of water as average diffusion coefficient (MD; diffusion within voxels) and fractional anisotropy (FA) (43). The overall extent of water diffusion may also be displayed. On the basis of eigenvalues ($\lambda 1$, $\lambda 2$, $\lambda 3$) of diffusion tensor, scalar values ranging from 0 to 1 can be obtained. These are the FA values, which measure the overall directionality of water diffusion and the complexity of cytoskeleton structure, of great significance to the movement of water inside and outside of cells (44). Changes in direction of water diffusion help understand the pathological changes of myelin and other related brain tissues. On this basis, some studies have explored the application of DTI in eye diseases, and the value of DTI as a marker in the diagnosis of diseases. Arterial spin labeling (ASL) is a new technology developed on the basis of magnetic resonance perfusion imaging, which has high accuracy and is non-invasive. It can detect blood flow changes reflecting pathological changes in various regions of the brain. The ASL method has been successfully applied to trace the changes of local blood flow in eye diseases and is beneficial to disease diagnosis. **Table 7** shows the application of fALFF, DTI and ASL methods in chronic eye diseases.

TABLE 7 | Application of other techniques in chronic eye diseases.

Disease	Year	fALFF	
		Increased fALFF values	Decreased fALFF values
Monocular blindness (45)	2020	LP, RPI, LPI	LAC
Neovascular glaucoma (46)	2021	LP	RRO, LAC, RC
Disease	Year	DTI	
		Increased DTI values	Decreased DTI values
Amblyopia (47)	2013	PC	_
Comitant strabismus (48)	2016	LSTG	BMFG, RGP/B, BP
Disease	Year	ASL	
		Increased ASL values	Decreased ASL values
Comitant exophoria (49)	2018	RHP, BMFG/ACC, LIFG, RIFG, LSFG, BMCC, RMFG, RPL	_

LP, left precuneus; RPI, right inferior parietal lobes; LPI, left inferior parietal lobes; LAC, left anterior cingulate; RRO, right rolandic operculum; RC, right caudate; LSTG, left superior temporal gyrus; BMFG, bilateral medial frontal gyrus; RGP/B, right globus pallidus/brainstem; BP, bilateral precuneus; RHP, right parahippocampal; ACC, anterior cingulate cortex; LIFG, left inferior frontal gyrus; RIFG, right inferior frontal gyrus; LSFG, left superior frontal gyrus; BMCC, bilateral medial cingulate cortex; RPL, right paracentral lobule; PC, prechiasmatic region.

Summary and Future Prospects

In summary, each magnetic resonance imaging technique has its own characteristics. To summarize the above, both ALFF and fALFF show regional differences in the brain, with high accuracy and repeatability, and do not need to pre-define regions of interest (ROI) (1), while fALFF makes improvements in noise reduction on the basis of ALFF (50); DC is more sensitive to showing the changes of connectivity in the brain network structure and the state changes of each node, so as to show the correlation of each network structure (11, 12); Both ReHo and FC can show the temporal distribution of voxels in brain functional regions (17, 25). ReHo focuses on describing the consistency within regions, while FC focuses on describing the synchronization between regions, but neither of them directly describes the intensity of brain activity in a certain region, that is, activity detection cannot be carried out. VMHC, as a new static FC analysis method, is more sensitive to the changes of functional synchronization between the two hemispheres of the brain (36). VBM focuses on exploring the changes of brain anatomy (51); DTI has irreplaceable advantages in understanding the complex cytoskeleton structure and other fine structures of the brain (43);

ASL can track the changes of local blood flow in eye diseases and improve the accuracy of diagnosis.

In recent years, MRI has been increasingly widely used to explore disease-related changes in brain activity and functional connections. It provides a useful imaging index for understanding the mechanism and monitoring the progress of pathological changes in disease. Its role as a disease marker has been confirmed in many studies. Most chronic eye diseases are characterized by occult and chronic progression, which easily leads to missed diagnosis and misdiagnosis. Using MRI, changes in spontaneous brain activity which occur with eye diseases may be detected at an early stage and monitored, and then accurately locate the brain region where lesions occur, and combine clinical symptoms based on the consistent physiological functions of different brain regions to improve the accuracy of diagnosis, aiding both early diagnosis and treatment of chronic eye diseases. However, the application of magnetic resonance imaging as a marker in chronic eye diseases has some limitations, since physiological and hardware-related factors may affect the experimental results. In addition, due to overlapping functions of different brain regions, it may not be possible to accurately locate the affected areas of the diseased brain. Despite these limitations, MRI technology has great potential and scope to provide indicators of onset and progression of chronic eye diseases. With the continuous progress of technology, MRI technology will usher in a broader range of applications, increasing the scope for exploration of chronic eye diseases.

AUTHOR CONTRIBUTIONS

C-YY was responsible for the writing of the manuscript. RH was responsible for data analysis and the later submission. S-QL was responsible for collecting and screening the data. YS was responsible for the revision of the paper. All authors contributed to the article and approved the submitted version.

FUNDING

The Central Government Guides Local Science and Technology Development Foundation (20211ZDG02003); Key Research Foundation of Jiangxi Province (No: 20181BBG70004); Excellent Talents Development Project of Jiangxi Province (20192BCBL23020); Natural Science Foundation of Jiangxi Province (20181BAB205034); Grassroots Health Appropriate Technology Spark Promotion Plan Project of Jiangxi Province (No: 20188003); Health Development Planning Commission Science Foundation of Jiangxi Province (No: 20201032); Health Development Planning Commission Science TCM Foundation of Jiangxi Province (No: 2018A060).

REFERENCES

1. Zuo XN, Di Martino A, Kelly C, Shehzad ZE, Gee DG, Klein DF, et al. The oscillating brain: complex and reliable. *Neuroimage.* (2010) 49:1432–45. doi: 10.1016/j.neuroimage.2009.09.037
2. Logothetis NK, Pauls J, Augath M, Trinath T, Oeltermann A. Neurophysiological investigation of the basis of the fMRI signal. *Nature.* (2001) 412:150–7. doi: 10.1038/35084005
3. Huang X, Zhou FQ, Hu YX, Xu XX, Zhou X, Zhong YL, et al. Altered spontaneous brain activity pattern in patients with high myopia using amplitude of low-frequency fluctuation: a resting-state fMRI study. *Neuropsychiatr Dis Treat.* (2016) 12:2949–56. doi: 10.2147/NDT.S118326
4. Wang ZL, Zou L, Lu ZW, Xie XQ, Jia ZZ, Pan CJ, et al. Abnormal spontaneous brain activity in type 2 diabetic retinopathy revealed by amplitude of low-frequency fluctuations: a resting-state fMRI study. *Clin Radiol.* (2017) 72:340.e1–7. doi: 10.1016/j.crad.2016.11.012
5. Li Q, Huang X, Ye L, Wei R, Zhang Y, Zhong YL, et al. Altered spontaneous brain activity pattern in patients with late monocular blindness in middle-age using amplitude of low-frequency fluctuation: a resting-state functional MRI study. *Clin Interv Aging.* (2016) 11:1773–80. doi: 10.2147/CIA.S117292
6. Tan G, Huang X, Zhang Y, Wu AH, Zhong YL, Wu K, et al. A functional MRI study of altered spontaneous brain activity pattern in patients with congenital comitant strabismus using amplitude of low-frequency fluctuation. *Neuropsychiatr Dis Treat.* (2016) 12:1243–50. doi: 10.2147/NDT.S104756
7. Min YL, Su T, Shu YQ, Liu WF, Chen LL, Shi WQ, et al. Altered spontaneous brain activity patterns in strabismus with amblyopia patients using amplitude of low-frequency fluctuation: a resting-state fMRI study. *Neuropsychiatr Dis Treat.* (2018) 14:2351–9. doi: 10.2147/NDT.S171462
8. Wang Y, Shao Y, Shi WQ, Jiang L, Wang XY, Zhu PW, et al. The predictive potential of altered spontaneous brain activity patterns in diabetic retinopathy and nephropathy. *EPMA J.* (2019) 10:249–59. doi: 10.1007/s13167-019-00171-4
9. Shi WQ, Tang LY, Lin Q, Li B, Jiang N, Zhu PW, et al. Altered spontaneous brain activity patterns in diabetic patients with vitreous hemorrhage using amplitude of lowfrequency fluctuation: a restingstate fMRI study. *Mol Med Rep.* (2020) 22:2291–9. doi: 10.3892/mmr.2020.11294
10. Peng ZY, Liu YX Li B, Ge QM, Liang RB Li QY, et al. Altered spontaneous brain activity patterns in patients with neovascular glaucoma using amplitude of low-frequency fluctuations: a functional magnetic resonance imaging study. *Brain Behav.* (2021) 1:e02018. doi: 10.1002/brb3.2018
11. Wu GR, Stramaglia S, Chen H, Liao W, Marinazzo D. Mapping the voxel-wise effective connectome in resting state FMRI. *PLoS ONE.* (2013) 8:e73670. doi: 10.1371/journal.pone.0073670
12. Xu QH Li QY, Yu K, Ge QM, Shi WQ Li B, et al. Altered brain network centrality in patients with diabetic optic neuropathy: a resting-state fmri study. *Endocr Pract.* (2020). doi: 10.4158/EP-2020-0045
13. Tan G, Dan ZR, Zhang Y, Huang X, Zhong YL, Ye LH, et al. Altered brain network centrality in patients with adult comitant exotropia strabismus: A resting-state fMRI study. *J Int Med Res.* (2018) 46:392–402. doi: 10.1177/0300060517715340
14. Wang Y, Jiang L, Wang XY, Chen W, Shao Y, Chen QK, et al. Evidence of altered brain network centrality in patients with diabetic nephropathy and retinopathy: an fMRI study using a voxel-wise degree centrality approach. *Ther Adv Endocrinol Metab.* (2019) 10:2042018819865723. doi: 10.1177/2042018819865723
15. Huang X, Li HJ, Peng DC, Ye L, Yang QC, Zhong YL, et al. Altered brain network centrality in patients with late monocular blindness: a resting-state fMRI study. *Arch Med Sci.* (2019) 15:1301–7. doi: 10.5114/aoms.2019.87133
16. Zang Y, Jiang T, Lu Y, He Y, Tian L. Regional homogeneity approach to fMRI data analysis. *Neuroimage.* (2004) 22:394–400. doi: 10.1016/j.neuroimage.2003.12.030
17. Tononi G, McIntosh AR, Russell DP, Edelman GM. Functional clustering: identifying strongly interactive brain regions in neuroimaging data. *Neuroimage.* (1998) 7:133–49. doi: 10.1006/nimg.1997.0313
18. Lin X, Ding K, Liu Y, Yan X, Song S, Jiang T. Altered spontaneous activity in anisometropic amblyopia subjects: revealed by resting-state FMRI. *PLoS ONE.* (2012) 7:e43373. doi: 10.1371/journal.pone.0043373
19. Huang X, Li SH, Zhou FQ, Zhang Y, Zhong YL, Cai FQ, et al. Altered intrinsic regional brain spontaneous activity in patients with comitant strabismus: a resting-state functional MRI study. *Neuropsychiatr Dis Treat.* (2016) 12:1303–8. doi: 10.2147/NDT.S105478

20. Huang X, Ye CL, Zhong YL, Ye L, Yang QC Li HJ, et al. Altered regional homogeneity in patients with late monocular blindness: a resting-state functional MRI study. *Neuroreport.* (2017) 28:1085–91. doi: 10.1097/WNR.0000000000000855
21. Shao Y, Li QH Li B, Lin Q, Su T, Shi WQ, et al. Altered brain activity in patients with strabismus and amblyopia detected by analysis of regional homogeneity: a restingstate functional magnetic resonance imaging study. *Mol Med Rep.* (2019) 19:4832–40. doi: 10.3892/mmr.2019.10147
22. Liao XL, Yuan Q, Shi WQ Li B, Su T, Lin Q, et al. Altered brain activity in patients with diabetic retinopathy using regional homogeneity: a resting-state fmri study. *Endocr Pract.* (2019) 25:320–7. doi: 10.4158/EP-2018-0517
23. Shi H, Wang Y, Liu X, Xia L, Chen Y, Lu Q, et al. Cortical alterations by the abnormal visual experience beyond the critical period: a resting-state fMRI study on constant exotropia. *Curr Eye Res.* (2019) 44:1386–92. doi: 10.1080/02713683.2019.1639767
24. Maldjian JA, Davenport EM, Whitlow CT, Graph theoretical analysis of resting-state MEG data: Identifying interhemispheric connectivity and the default mode. *Neuroimage*. (2014). 96:88–94. doi: 10.1016/j.neuroimage.2014.03.065
25. Su T, Yuan Q, Liao XL, Shi WQ, Zhou XZ, Lin Q, et al. Altered intrinsic functional connectivity of the primary visual cortex in patients with retinal vein occlusion: a resting-state fMRI study. *Quant Imaging Med Surg.* (2020) 10:958–69. doi: 10.21037/qims.2020.03.24
26. Ding K, Liu Y, Yan X, Lin X, Jiang T. Altered functional connectivity of the primary visual cortex in subjects with amblyopia. *Neural Plast.* (2013) 2013:612086. doi: 10.1155/2013/612086
27. Zhu PW, Huang X, Ye L, Jiang N, Zhong YL, Yuan Q, et al. Altered intrinsic functional connectivity of the primary visual cortex in youth patients with comitant exotropia: a resting state fMRI study. *Int J Ophthalmol.* (2018) 11:668–73.
28. Yan X, Wang Y, Xu L, Liu Y, Song S, Ding K, et al. Altered functional connectivity of the primary visual cortex in adult comitant strabismus: a resting-state functional MRI study. *Curr Eye Res.* (2019) 44:316–23. doi: 10.1080/02713683.2018.1540642
29. Wu YY, Wang SF, Zhu PW, Yuan Q, Shi WQ, Lin Q, et al. Altered intrinsic functional connectivity of the primary visual cortex in patients with neovascular glaucoma: a resting-state functional magnetic resonance imaging study. *Neuropsychiatr Dis Treat.* (2020) 16:25–33. doi: 10.2147/NDT.S228606
30. Yu K, Lin Q, Ge QM Yu CY, Li QY, Pan YC, et al. Measuring functional connectivity in patients with strabismus using stationary functional magnetic resonance imaging: a resting-state network study. *Acta Radiol.* (2021) 10:284185120983978. doi: 10.1177/0284185120983978
31. Ashburner J, Friston KJ. Voxel-based morphometry–the methods. *Neuroimage.* (2000) 11:805–21. doi: 10.1006/nimg.2000.0582
32. Chan ST, Tang KW, Lam KC, Chan LK, Mendola JD, Kwong KK. Neuroanatomy of adult strabismus: a voxel-based morphometric analysis of magnetic resonance structural scans. *Neuroimage.* (2004) 22:986–94. doi: 10.1016/j.neuroimage.2004.02.021
33. Mendola JD, Conner IP, Roy A, Chan ST, Schwartz TL, Odom JV, et al. Voxel-based analysis of MRI detects abnormal visual cortex in children and adults with amblyopia. *Hum Brain Mapp.* (2005) 25:222–36. doi: 10.1002/hbm.20109
34. Ouyang J, Yang L, Huang X, Zhong YL, Hu PH, Zhang Y, et al. The atrophy of white and gray matter volume in patients with comitant strabismus: evidence from a voxel-based morphometry study. *Mol Med Rep.* (2017) 16:3276–82. doi: 10.3892/mmr.2017.7006
35. Shi WQ, He Y, Li QH, Tang LY Li B, Lin Q, et al. Central network changes in patients with advanced monocular blindness: a voxel-based morphometric study. *Brain Behav.* (2019) 9:e01421. doi: 10.1002/brb3.1421
36. Zuo XN, Kelly C, Di Martino A, Mennes M, Margulies DS, Bangaru S, et al. Growing together and growing apart: regional and sex differences in the lifespan developmental trajectories of functional homotopy. *J Neurosci.* (2010) 30:15034–43. doi: 10.1523/JNEUROSCI.2612-10.2010
37. Hou F, Liu X, Zhou Z, Zhou J, Li H. Reduction of interhemispheric functional brain connectivity in early blindness: a resting-state fMRI study. *Biomed Res Int.* (2017) 2017:6756927. doi: 10.1155/2017/6756927
38. Shao Y, Bao J, Huang X, Zhou FQ, Ye L, Min YL, et al. Comparative study of interhemispheric functional connectivity in left eye monocular blindness versus right eye monocular blindness: a resting-state functional MRI study. *Oncotarget.* (2018) 9:14285–95. doi: 10.18632/oncotarget.24487
39. Zhang Y, Zhu PW, Huang X, Ma MY, Shi WQ, Tao Q. Alternations of interhemispheric functional connectivity in patients with comitant exotropia: a resting state fMRI study. *Int J Clin Exp Med.* (2018) 10:10966–73. Available online at: http://210.35.251.113/s/us/e-century/G.https/web/journal_search.php?journal=ijcem&q=Alternations%20of%20interhemispheric%20functional%20connectivity%20in%20patients%20with%20comitant%20exotropia%3A%20a%20resting%20state%20fMRI%20study
40. Wang Y, Wang X, Chen W, Shao Y, Zhou J, Chen Q, et al. Brain function alterations in patients with diabetic nephropathy complicated by retinopathy under resting state conditions assessed by voxel-mirrored homotopic connectivity. *Endocr Pract.* (2020) 26:291–8. doi: 10.4158/EP-2019-0355
41. Guo Z, Liu X, Li J, Wei F, Hou H, Chen X, et al. Fractional amplitude of low-frequency fluctuations is disrupted in Alzheimer's disease with depression. *Clin Neurophysiol.* (2017) 128:1344–9. doi: 10.1016/j.clinph.2017.05.003
42. Zou QH, Zhu CZ, Yang Y, Zuo XN, Long XY, Cao QJ, et al. An improved approach to detection of amplitude of low-frequency fluctuation (ALFF) for resting-state fMRI: fractional ALFF. *J Neurosci Methods.* (2008) 172:137–41. doi: 10.1016/j.jneumeth.2008.04.012
43. Beaulieu C. The basis of anisotropic water diffusion in the nervous system - a technical review. *NMR Biomed.* (2002) 15:435–55. doi: 10.1002/nbm.782
44. Pierpaoli C, Basser PJ. Toward a quantitative assessment of diffusion anisotropy. *Magn Reson Med.* (1996) 36:893–906. doi: 10.1002/mrm.1910360612
45. Fang JW Yu YJ, Tang LY, Chen SY, Zhang MY, Sun T, et al. Abnormal fractional amplitude of low-frequency fluctuation changes in patients with monocular blindness: a functional magnetic resonance imaging (MRI) study. *Med Sci Monit.* (2020) 26:e926224. doi: 10.12659/MSM.926224
46. Zhang YQ, Peng MY, Wu SN, Yu CY, Chen SY, Tan SW, et al. Fractional amplitude of low-frequency fluctuation in patients with neovascular glaucoma: a resting-state functional magnetic resonance imaging study. *Quant Imaging Med Surg.* (2021) 10:855. doi: 10.21037/qims-20-855
47. Gümüstas S, Altintas Ö, Anik Y, Kaya A, Altintas L, Inan N, et al. Anterior visual pathways in amblyopia: quantitative assessment with diffusion tensor imaging. *J Pediatr Ophthalmol Strabismus.* (2013) 50:369–74. doi: 10.3928/01913913-20131125-04
48. Huang X, Li HJ, Zhang Y, Peng DC, Hu PH, Zhong YL, et al. Microstructural changes of the whole brain in patients with comitant strabismus:evidence from a diffusion tensor imaging study. *Neuropsychiatr Dis Treat.* (2016) 12:2007–14. doi: 10.2147/NDT.S108834
49. Huang X, Zhou S, Su T, Ye L, Zhu PW, Shi WQ, et al. Resting cerebral blood flow alterations specific to the comitant exophoria patients revealed by arterial spin labeling perfusion magnetic resonance imaging. *Microvasc Res.* (2018) 120:67–73. doi: 10.1016/j.mvr.2018.06.007
50. Wallis I, Ellis L, Suh K, Pfenninger KH, et al. Immunolocalization of a neuronal growth-dependent membrane glycoprotein. *J Cell Biol.* (1985) 101:1990–8. doi: 10.1083/jcb.101.5.1990
51. Palaniyappan L, Maayan N, Bergman H, Davenport C, Adams CE, Soares-Weiser K. Voxel-based morphometry for separation of schizophrenia from other types of psychosis in first episode psychosis. *Cochrane Database Syst Rev.* (2015) 8:CD011021. doi: 10.1002/14651858.CD011021.pub2

Conflict of Interest: The authors declare that the research was conducted in the absence of any commercial or financial relationships that could be construed as a potential conflict of interest.

Publisher's Note: All claims expressed in this article are solely those of the authors and do not necessarily represent those of their affiliated organizations, or those of the publisher, the editors and the reviewers. Any product that may be evaluated in this article, or claim that may be made by its manufacturer, is not guaranteed or endorsed by the publisher.

Copyright © 2022 Yu, Huang, Li and Shao. This is an open-access article distributed under the terms of the Creative Commons Attribution License (CC BY). The use, distribution or reproduction in other forums is permitted, provided the original author(s) and the copyright owner(s) are credited and that the original publication in this journal is cited, in accordance with accepted academic practice. No use, distribution or reproduction is permitted which does not comply with these terms.

frontiers | Frontiers in Neurology

ORIGINAL RESEARCH
published: 15 June 2022
doi: 10.3389/fneur.2022.889518

Admission Serum Calcium Level and Short-Term Mortality After Acute Ischemic Stroke: A Secondary Analysis Based on a Norwegian Retrospective Cohort

Yuzhao Lu[1], *Xin Ma*[2], *Kiarash Tazmini*[3], *Ming Yang*[4]*, *Xiaobing Zhou*[1]* and *Yang Wang*[1,5]*

[1] Department of Neurosurgery, The First Affiliated Hospital of Nanchang University, Nanchang University, Nanchang, China, [2] Department of Thoracic Surgery, Jingshan Union Hospital of Huazhong University of Science and Technology, Wuhan, China, [3] Department of Endocrinology, Morbid Obesity and Preventive Medicine, Faculty of Medicine, Oslo University Hospital, Oslo, Norway, [4] Department of Neurosurgery, Central Theater General Hospital of Chinese PLA, Wuhan, China, [5] Department of Neurosurgery, Beijing Chaoyang Hospital, Capital Medical University, Beijing, China

OPEN ACCESS

Edited by:
John Zhang,
Loma Linda University, United States

Reviewed by:
Yan Fan,
Liaocheng People's Hospital, China
Tao-Hsin Tung,
Taizhou Hospital of Zhejiang Province Affiliated to Wenzhou Medical University, China

***Correspondence:**
Ming Yang
yangmingwh2021@163.com
Xiaobing Zhou
xiaobingzhou1234@163.com
Yang Wang
wangyang6877@163.com

Specialty section:
This article was submitted to Neurological Biomarkers, a section of the journal Frontiers in Neurology

Received: 04 March 2022
Accepted: 09 May 2022
Published: 15 June 2022

Citation:
Lu Y, Ma X, Tazmini K, Yang M, Zhou X and Wang Y (2022) Admission Serum Calcium Level and Short-Term Mortality After Acute Ischemic Stroke: A Secondary Analysis Based on a Norwegian Retrospective Cohort. Front. Neurol. 13:889518. doi: 10.3389/fneur.2022.889518

Background: Disturbed serum calcium levels are related to the risk of stroke. However, previous studies exploring the correlation between serum calcium and the clinical outcome of ischemic stroke (IS) have shown inconsistent results.

Object: The study aimed to investigate the relationship between admission serum calcium and 30-day mortality in patients with IS.

Methods: A total of 876 IS patients from a Norwegian retrospective cohort were included for secondary analysis. The exposure variable and the primary outcome were albumin-corrected serum calcium (ACSC) at baseline and all-cause mortality within 30 days after the first admission, respectively. Multivariable logistic regression analysis was used to estimate the risk of 30-day mortality according to ACSC levels. Moreover, the potential presence of a non-linear relationship was evaluated using two-piecewise linear regression with a smoothing function and threshold level analysis. The stability of the results was evaluated by unadjusted and adjusted models.

Results: The result of multiple regression analysis showed that ACSC at baseline was positively associated with the incidence of 30-day mortality after adjusting for the potential confounders (age, gender, serum glucose, hypertension, atrial fibrillation/atrial flutter, renal insufficiency, heart failure, chronic obstructive pulmonary disease, pneumonia, paralysis, and aphasia) (OR = 2.43, 95% CI 1.43–4.12). When ACSC was translated into a categorical variable, the ORs and 95% CIs in the second to the fourth quartile vs. the first quartile were 1.23 (0.56, 2.69), 1.16 (0.51, 2.65), and 2.13 (1.04, 4.38), respectively (*P* for trend = 0.03). Moreover, the results of two-piecewise linear regression and curve-fitting revealed a linear relationship between ACSC and 30-day mortality.

Conclusion: ACSC is positively associated with 30-day mortality in IS patients, and the relationship between them is linear.

Keywords: serum calcium, albumin-corrected serum calcium, association, ischemic stroke, 30-day mortality, baseline

INTRODUCTION

Stroke can cause a low quality of life for patients and their families, as well as a great burden and loss for society due to high rates of disability and mortality (1). Ischemic stroke (IS), which is the main subtype of stroke, accounts for about 60–80% (1) of all stroke cases according to the latest evidence. Given this, early risk stratification after acute IS may contribute to improving clinical decision-making.

Calcium is the most abundant mineral in the human body (2), widely taking part in various crucial physiological processes including signal transduction, maintenance of the stability of the cell membrane, coagulation process, movement of the smooth muscle or skeletal muscle, and endocrine function (3, 4). Serum calcium level in a normal physiological situation is strictly controlled to remain within a narrow range (5). Moreover, dyscalcemia has been demonstrated to be related to the risk of cardiovascular and cerebrovascular diseases (6–8).

To date, a limited amount of studies have addressed the association between serum calcium levels and IS outcomes, with conflicting results (9–13). In these studies, both low (10) and high levels (12) of serum calcium have been reported to correlate with poor outcomes of IS. One study reported a U shape association between serum calcium levels and in-hospital all-cause mortality (11). Furthermore, Asian and North American patients were the main subjects in previous studies, which failed to consider European populations. However, not only do the incidence rate and morbidity of stroke vary in different populations (14), in addition to the calcium metabolism (15).

Serum calcium is susceptible to serum albumin levels (16) and albumin-corrected serum calcium (ACSC) calculated according to the classic formula (17) is increasingly used in place of serum calcium in many clinical studies (10–13). Therefore, this study was designed to assess the correlation between ACSC and 30-day mortality in IS patients based on a Norwegian retrospective cohort.

METHODS

Data Source

Initial data were downloaded from the public database "DRYAD" (www.datadryad.org). In this database, Tazmini et al. (18) authorized the use of their data in the DRYAD database. Thus, this secondary research based on the raw data for a different research hypothesis was permitted. In addition, the original corresponding author, Kiarash Tazmini, was listed as a co-author with their consent for the contribution of their team in data collection and making their data publicly available.

The original research was a single-center retrospective cohort study that included 31,966 unique patients (62,991 registered admission information) who visited the emergency department of the Diakonhjemmet Hospital in Oslo (Norway) from 2010 to 2015. In this study, a total of 974 visits (admission information) with a principal diagnosis of IS (ICD-10, I63) were selected from the raw cohort according to the International Classification of Diseases 10th revision (ICD-10). The raw data included information on multiple hospitalizations for the same patient, but only the first one for each patient was considered in this study. A total of 886 unique IS patients were identified according to their first admission information after excluding the second or subsequent admissions. Subsequently, 10 patients were excluded for missing ACSC information ($n = 5$) or wrong death information ($n = 5$). Ultimately, 876 IS patients were included (**Figure 1**).

The original research was approved by the Norwegian Regional Committee for Medical and Health Research Ethics South East as a quality study, which did not require ethical approval (19). Informed consent was also not necessary because all the data were anonymously processed (19). Thus, separate ethical approval was not required for this secondary analysis. Finally, this study complied with the Helsinki Declaration.

All the laboratory indicators were taken from the first laboratory results after admission. Serum calcium (mmol/L), serum-albumin (g/L), serum-sodium (mmol/L), serum-potassium (mmol/L), serum-glucose (mmol/L), serum-phosphate (mmol/L), and serum-magnesium (mmol/L) were recorded in the original data.

The ACSC levels in the previous study were calculated according to a standard formula and the epidemiological data of the northern European population (20). And the calculation formula is as follows: ACSC = measured serum-calcium level + 0.020 × (41.3–serum-albumin) where 41.3 g/L is the albumin median (19). The unit of ACSC and serum calcium was converted to mg/dl.

Co-morbidities

Secondary diagnostic information was used to identify co-morbidities including diabetes (ICD-10: E10-E14), hypertension (ICD-10: I10), hyperlipemia (ICD-8: E78), atrial fibrillation/atrial flutter (ICD-10: I48), heart failure (ICD-10: I50), renal insufficiency (ICD-10: N18), chronic obstructive pulmonary disease (ICD-10: J42–44), coronary heart disease (ICD-10: I25), chronic obstructive pulmonary disease (ICD-10: J42–44), cancer (ICD-10: C0-C9, Z51.0-3), malnutrition (ICD-10: E40-E46), and pneumonia (ICD-10: J98, J69, J11-18). Moreover, common complications associated with strokes such as paralysis (ICD-10: G80-G83), epilepsy (ICD-10: G40), cognitive disorder (ICD-10: F06), and aphasia (ICD-10: F80, R47) were also considered. All the above-mentioned co-morbidities were processed into categorical variables to facilitate the statistical analysis.

Outcome

The primary outcome was all-cause mortality within 30 days after the first admission.

Missing Data

The missing data of covariates of all 876 patients, in the final analysis, are shown in **Table 1**. Serum-phosphate and serum-magnesium were missing a large portion of information and were thus converted into categorical variables to address the lower statistical power and potential bias caused by excluding missing

Abbreviations: IS, ischemic stroke; ACSC, albumin-corrected serum calcium; COPD, chronic obstructive pulmonary disease; CHD, coronary heart disease.

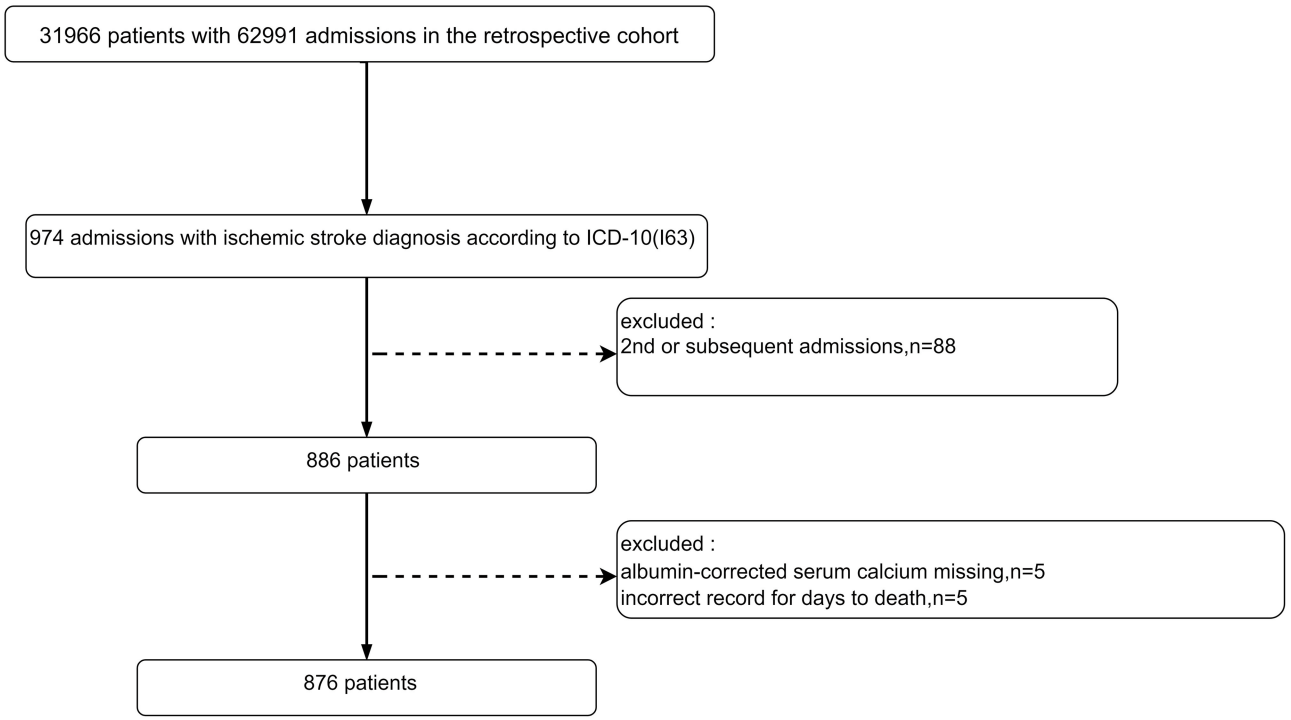

FIGURE 1 | Flowchart of screening the study population.

data. Dummy variables were used to identify the missing values of the covariate (21).

Multiple imputations based on five replications and a chained equation approach in the R MI procedure were used to deal with missing data (22). Moreover, a comparison between primary data and interpolation data was performed for the sensitivity analysis. The result is shown in **Supplementary Figure 2** and **Supplementary Table 1**.

Statistical Analysis

Statistical analysis was performed using EmpowerStats (www.empowerstats.com, X&Y Solutions, Inc., Boston, MA) and the statistical software package R (http://www.R-project.org, The R Foundation).

Mean ± standard or median (interquartile range) were used to describe continuous variables and categorical variables were expressed as percentages. One-way ANOVA test for continuous variables with normal distribution, Kruskal–Wallis *H*-test for continuous variables with skewed distribution, and chi-square tests (or Fisher's exact test) for categorical variables were used to analyze differences between or among groups.

Multiple logistic regression analysis was used to assess the specific relationships between the exposure (ACSC) and outcome (30-day mortality); odds ratio (OR) and 95% confidence interval (CI) were used to evaluate the risk.

Four models were built to control for the effect of confounding factors: (1) crude model, i.e., unadjusted. (2) Model I, which was adjusted for age and gender. (3) Model II, which was adjusted for age, gender, serum glucose, atrial fibrillation/atrial flutter, renal insufficiency, heart failure, chronic obstructive pulmonary disease, cancer, pneumonia, paralysis, and aphasia. Covariates were included as potential confounders in the final models if they changed the estimates of admission albumin-corrected serum calcium on 30-day mortality by more than 10% or were significantly associated with 30-day mortality (23); gender as a basic variable was also included in the fully adjusted model. (4) Model III, which was additionally adjusted for serum-phosphate tertiles, serum-magnesium tertiles, cognitive disorder, and epilepsy based on Model II (In Model III, the potential influence of missing variables and clinical significance of the other two neurological complications were considered).

A two-piecewise linear regression model and curve fitting were used to examine the potential linear relationship and threshold effect.

Sensitivity Analysis

ACSC quartiles were also used to test the stability of multiple regression results, and the linear tests were performed by assigning medians to each ACSC quartile as a continuous variable in the models (24).

An *E*-value was used to explore the potential of unmeasured confounding between ACSC and 30-day mortality. The *E*-value was defined as the required magnitude for an unmeasured confounder to overturn the observed association between ACSC and 30-day mortality (25).

TABLE 1 | Baseline characteristics of the patients according to quartiles of ACSC level.

ACSC (mg/dl)	Quantile1	Quantile 2	Quantile 3	Quantile 4	*P*-value
N = 876	209	223	206	238	
Age (years)	75.09 ± 13.53	76.91 ± 12.61	76.77 ± 11.83	79.91 ± 10.61	0.002
Gender (male), *n* (%)	119 (56.94%)	108 (48.43%)	95 (46.12%)	75 (31.51%)	<0.001
Serum-sodium (mmol/L, mean ± SD) (1 missing)	139.19 ± 3.99	139.66 ± 3.23	139.59 ± 3.01	139.26 ± 3.89	0.6
Serum-glucose (mmol/L, mean ± SD)	6.82 ± 2.33	6.77 ± 2.09	6.85 ± 2.12	7.19 ± 2.32	0.01
Serum-potassium (mmol/L) (3 missing)	4.11 ± 0.44	4.14 ± 0.43	4.12 ± 0.40	4.17 ± 0.45	0.4
Serum-phosphate (mmol/L) tertiles, *n* (%)					0.1
Tertile 1 (≤0.97)	25 (11.96%)	18 (8.07%)	28 (13.59%)	28 (11.76%)	
Tertile 2 (0.98–1.12)	20 (9.57%)	24 (10.76%)	26 (12.62%)	24 (10.08%)	
Tertile 3 (≥1.13)	22 (10.53%)	20 (8.97%)	29 (14.08%)	40 (16.81%)	
Not recorded	142 (67.94%)	161 (72.20%)	123 (59.71%)	146 (61.34%)	
Serum-magnesium (mmol/L) tertiles, *n* (%)					0.02
Tertile 1 (≤0.78)	23 (11.00%)	11 (4.93%)	29 (14.08%)	39 (16.39%)	
Tertile 1 (0.79–0.84)	22 (10.53%)	28 (12.56%)	25 (12.14%)	23 (9.66%)	
Tertile 1 (≥0.85)	28 (13.40%)	24 (10.76%)	29 (14.08%)	32 (13.45%)	
Not recorded	136 (65.07%)	160 (71.75%)	123 (59.71%)	144 (60.50%)	
Diabetes, *n* (%)	15 (7.18%)	19 (8.52%)	21 (10.19%)	20 (8.40%)	0.7
Hyperlipemia, *n* (%)	3 (1.44%)	4 (1.79%)	12 (5.83%)	15 (6.30%)	0.008
Hypertension, *n* (%)	52 (24.88%)	56 (25.11%)	61 (29.61%)	71 (29.83%)	0.5
Atrial fibrillation/atrial flutter, *n* (%)	56 (26.79%)	57 (25.56%)	50 (24.27%)	67 (28.15%)	0.8
Heart failure, *n* (%)	4 (1.91%)	7 (3.14%)	7 (3.40%)	8 (3.36%)	0.8
Renal insufficiency, *n* (%)	6 (2.87%)	11 (4.93%)	10 (4.85%)	13 (5.46%)	0.6
COPD, *n* (%)	1 (0.48%)	6 (2.69%)	4 (1.94%)	1 (0.42%)	0.1
CHD, *n* (%)	11 (5.26%)	11 (4.93%)	14 (6.80%)	9 (3.78%)	0.6
Cancer, *n* (%)	3 (1.44%)	4 (1.79%)	3 (1.46%)	7 (2.94%)	0.6
Malnutrition, *n* (%)	6 (2.87%)	3 (1.35%)	1 (0.49%)	9 (3.78%)	0.08
Dehydration, *n* (%)	9 (4.31%)	9 (4.04%)	7 (3.40%)	9 (3.78%)	1.0
Pneumonia, *n* (%)	6 (2.87%)	12 (5.38%)	9 (4.37%)	13 (5.46%)	0.5
Paralysis, *n* (%)	15 (7.18%)	24 (10.76%)	16 (7.77%)	31 (13.03%)	0.1
Epilepsy, *n* (%)	4 (1.91%)	0 (0.00%)	2 (0.97%)	2 (0.84%)	0.2
Cognitive disorder, *n* (%)	3 (1.44%)	8 (3.59%)	4 (1.94%)	13 (5.46%)	0.07
Aphasia, *n* (%)	18 (8.61%)	17 (7.62%)	9 (4.37%)	19 (7.98%)	0.3
30-day mortality	13 (6.22%)	20 (8.97%)	16 (7.77%)	36 (15.13%)	0.008

All data in the ACSC subgroups are expressed as mean ± SD or number (%). ACSC: quantile 1: ≤9.26 mg/dl; quantile 2: 9.30–9.50 mg/dl; quantile 3: 9.54–9.74 mg/dl, and quantile 4: ≥9.78 mg/dl. ACSC, albumin-corrected serum calcium; COPD, chronic obstructive pulmonary disease; CHD, coronary heart disease.

RESULTS

Baseline Characteristics of Participants

The average age of participants was 77.26 ± 12.26 (34–100) years and 54.68% were female. The baseline characteristics and co-morbidities of participants are listed in **Table 1** by ACSC quartiles. Age, gender, serum-glucose, serum-magnesium (tertiles), hyperlipemia, and 30-day mortality of the ACSC quartile groups were statistically different (all $p < 0.05$).

Univariate Analysis Related to 30-Day Mortality

The outcome of 30-day mortality was chosen as a dependent variable, and univariate analysis was used to investigate which independent variable was related to 30-day mortality. The results indicated that age (OR = 1.08, 95% CI 1.05–1.11), ACSC (OR = 2.38, 95% CI 1.50–3.78), serum-glucose (OR = 1.11, 95% CI 1.03–1.21), hypertension (yes vs. no: OR = 0.54, 95% CI 0.30–0.97), heart failure (yes vs. no: OR = 6.46, 95% CI 2.83–14.74), renal insufficiency (yes vs. no: OR = 3.91, 95% CI 1.87–8.14), pneumonia (yes vs. no: OR = 7.41, 95% CI 3.76–14.61) and aphasia (yes vs. no: OR = 2.39, 95% CI 1.22–4.68) were all associated with 30-day mortality (**Table 2**).

Multivariate Logistic Regression Analysis of ACSC and 30-Day Mortality

ACSC was chosen as the independent variable and 30-day mortality as the dependent variable in the multiple regression equation. Other variables were used as covariates to adjust the model to prove the stability of the results, and four models were built. No covariates were adjusted in the crude model and the

TABLE 2 | Univariate analysis related to 30-day mortality.

Variables	Statistics	OR (95% CI)	*p*-value
Age (year)	77.26 ± 12.26	1.08 (1.05, 1.11)	<0.0001
Gender			
Male	397 (45.32%)	Reference	
Female	479 (54.68%)	1.34 (0.85, 2.12)	0.2
ACSC (mg/dL)	9.56 ± 0.43	2.38 (1.50, 3.78)	0.0002
Serum-sodium (mmol/L)	139.42 ± 3.56	1.05 (0.98, 1.12)	0.2
Serum-glucose (mmol/L)	6.91 ± 2.22	1.11 (1.03, 1.21)	0.01
Serum-potassium (mmol/L)	4.13 ± 0.43	1.40 (0.84, 2.32)	0.2
Serum-phosphate (mmol/L) tertiles, *n* (%)			
Tertile 1 (≤0.97)	99 (11.30%)	Reference	
Tertile 2 (0.98–1.12)	94 (10.73%)	1.60 (0.65, 3.95)	0.3
Tertile 3 (≥1.13)	111 (12.67%)	1.44 (0.60, 3.50)	0.4
Not recorded	572 (65.30%)	0.94 (0.44, 1.97)	0.9
Serum-magnesium (mmol/L) tertiles, *n* (%)			
Tertile 1 (≤0.78)	102 (11.64%)	Reference	
Tertile 2 (0.79–0.84)	98 (11.19%)	1.05 (0.41, 2.63)	0.9
Tertile 3 (≥0.85)	113 (12.90%)	1.63 (0.71, 3.74)	0.3
Not recorded	563 (64.27%)	0.86 (0.42, 1.76)	0.7
Diabetes, *n* (%)			
No	801 (91.44%)	Reference	
Yes	75 (8.56%)	0.79 (0.33, 1.89)	0.6
Hyperlipemia, *n* (%)			
No	842 (96.12%)	Reference	
Yes	34 (3.88%)	-	§
Hypertension, *n* (%)			
No	637 (72.72%)	Reference	
Yes	239 (27.28%)	0.54 (0.30, 0.97)	0.04
Atrial fibrillation/atrial flutter, *n* (%)			
No	646 (73.74%)	Reference	
Yes	230 (26.26%)	1.52 (0.94, 2.45)	0.08
Heart failure, *n* (%)			
No	850 (97.03%)	Reference	
Yes	26 (2.97%)	6.46 (2.83, 14.74)	<0.0001
Renal insufficiency, *n* (%)			
No	835 (95.32%)	Reference	
Yes	40 (4.57%)	3.91 (1.87, 8.14)	0.0003
Chronic obstructive pulmonary disease (%)			
No	864 (98.63%)	Reference	
Yes	12 (1.37%)	3.18 (0.84, 11.98)	0.09
Coronary heart disease, *n* (%)			
No	831 (94.86%)	Reference	
Yes	45 (5.14%)	1.17 (0.45, 3.06)	0.7
Cancer, *n* (%)			
No	859 (98.06%)	Reference	
Yes	17 (1.94%)	2.03 (0.57, 7.21)	0.3
Malnutrition, *n* (%)			
No	857 (97.83%)	Reference	
Yes	19 (2.17%)	1.10 (0.25, 4.83)	0.9
Dehydration, *n* (%)			
No	842 (96.12%)	Reference	
Yes	34 (3.88%)	0.90 (0.27, 3.00)	0.9
Pneumonia, *n* (%)			
No	836 (95.66%)	Reference	
Yes	40 (4.57%)	7.41 (3.76, 14.61)	<0.0001
Paralysis, *n* (%)			
No	790 (90.18%)	Reference	
Yes	86 (9.82%)	1.78 (0.94, 3.36)	0.08
Epilepsy, *n* (%)			
No	868 (99.09%)	Reference	
Yes	8 (0.91%)	-	§
Cognitive disorder, *n* (%)			
No	848 (96.80%)	Reference	
Yes	28 (3.20%)	0.34 (0.05, 2.51)	0.3
Aphasia, *n* (%)			
No	813 (92.81%)	Reference	
Yes	63 (7.19%)	2.39 (1.22, 4.68)	0.01

Data are expressed as OR (95% CI) p-value. ACSC, albumin-corrected serum calcium.
§The model failed because of the small sample size.

result showed that ACSC was independently associated with 30-day mortality (OR = 2.38, 95% CI 1.50–3.78). The result in the Model I also revealed that ACSC was independently related to 30-day mortality (OR = 2.52, 95% CI 1.52–4.18) after adjusting for age and gender. Moreover, the result was similar in the Model II adjusted for covariates such as age, gender, serum glucose, hypertension, atrial fibrillation/atrial flutter, renal insufficiency, heart failure, chronic obstructive pulmonary disease, pneumonia, paralysis, and aphasia (OR = 2.43, 95% CI 1.43–4.12). In Model III which additionally adjusted for serum-phosphate tertiles, serum-magnesium tertiles, cognitive disorder, and epilepsy based

on Model II, the result was also robust (OR = 2.77, 95% CI 1.59–4.84) (**Table 3**).

Sensitivity Analysis

The results of the linear trend tests of the four models all showed that higher ACSC quartile groups were significantly related to an increased risk of 30-day mortality. And the *p*-values for the trends in the crude model, Model I, Model II, and Model III were 0.002, 0.01, 0.03, and 0.02, respectively (**Table 3**).

An *E*-value was calculated to assess the sensitivity to unmeasured confounding. The primary findings were stable unless an unmeasured confounder existed and was highly positively related to ACSC (OR $\geq$ 4.29) and 30 day-mortality (OR $\geq$ 4.29).

Curve Fitting and Two-Piecewise Linear Regression Model of ACSC and 30-Day Mortality

Curve fitting and two-piecewise linear regression analysis were used to investigate a potential non-linear association between ACSC and 30-day mortality. The result of curve fitting adjusted for age, gender, serum glucose, hypertension, atrial fibrillation/atrial flutter, renal insufficiency, heart failure, chronic obstructive pulmonary disease, pneumonia, cognitive disorder, epilepsy, paralysis, and aphasia showed a curve that continued to rise (**Figure 2**), and the results for the other three models were the same (**Supplementary Figure 1**). Furthermore, despite two different effective sizes based on the demarcation point (9.6 mg/dl) of the curve fitting was observed in the two-piecewise linear regression analysis adjusted according to Model II, the *p*-value for the likelihood ratio test was 0.7 (**Table 4**).

The other three models showed similar results and the *p*-values for the likelihood ratio test were all >0.05 (**Table 4**). Thus, no threshold effect was observed according to the demarcation point, indicating that the relationship between ACSC and 30-day mortality was linear.

DISCUSSION

This study revealed an appreciable positive association between ACSC and 30-day mortality in IS patients. The relevant results were also significant after adjustment of the three different models with potential confounding factors. ACSC was then translated into a categorical variable (quartile) to analyze the sensitivity of the results, and the results were stable (OR values gradually increased significantly, from the second to the fourth quartile, and the values of p for trend were <0.05 in the four models). Furthermore, the results of curve fitting and the two-piecewise linear regression model revealed a stable linear relationship.

Despite the pivotal role of calcium ions in neuronal damage after ischemic events having been demonstrated as early as 1998 (26), few studies have focused on the correlation between baseline serum calcium and the clinical outcome in patients with IS. In a retrospective cohort study involving 173 IS patients, Buck et al. (9) explored between admission serum calcium and infarct volumes on diffusion-weighted imaging and their results revealed that high serum calcium levels were related to small cerebral infarct area and good outcomes. The study of Buck et al. (9) adjusted for serum glucose, blood pressure, co-morbidities, and stroke subtype in the final model, but serum albumin which might affect the serum calcium level was not considered. However, another study based on the Virtual International Stroke Trials Archive demonstrated that elevated 72–96-h serum calcium levels are related to 3-month functional outcome, but earlier (<4.5 h) serum calcium is not associated with the functional outcome (10). The result revealed that serum calcium levels can reflect a secondary epiphenomenon of stroke. However, the variation of intra-individual calcium levels, in reality, is ∼2% (27), and the transportation of extracellular into neuronal cells would not significantly alter serum calcium levels. In 2010, an Israeli clinical study including 784 patients revealed that too high and too low serum calcium levels were both correlated with long-term mortality in female stroke patients (11). Moreover, a Korean cohort study that included 1915 IS patients showed that elevated admission ACSC levels are related to a short-time functional outcome and long-term mortality in IS patients (12). Admission serum calcium and ACSC were both included in the analysis, and the results of ACSC showed a significantly increased risk of all-cause death with the ACSC level elevating, but there were no positive results for serum calcium. Given the physiologic characteristic that more than 50% of calcium ions are combined with albumin and the difficulty for the measurement of ionized calcium in clinical practice, ACSC might be a better parameter than serum calcium to assess the effect of calcium. Most recently, a China national stroke cohort study demonstrated a high risk of long-term mortality of IS patients in the top quartile group of ACSC levels, with no statistical difference between patients of different genders (13).

Heterogeneity between the various study populations may have led to the inconsistency in the findings. Epidemiologic evidence showed that the incidence and mortality of stroke differed in various populations (14), in addition to calcium metabolism in different ethnicity (15). It was noteworthy that the relationship between serum calcium level and risk of stroke in Swedish and Korean populations also showed opposite results (7, 8). This study added evidence of the correlation between ACSC and clinical outcomes in IS patients from a different populations. Compared with other countries at a similar economical level, Nordic countries were with cold climate (28), short sunshine time (29), and plant-based diet pattern (30) which may impact the vitamin-D intake and serum calcium level. However, due to the nature of a retrospective study, the ethnicity, diet, climate, and environment of the selected sample group could not be included in the analysis. Prospective, large sample size studies that included these population characteristics are required in the future to accurately explore the risk range of serum calcium for Norwegian IS patients. In addition, due to the raw data of this study are from a large emergency cohort, ACSC may have a broad application prospect for IS patients admitted to emergency departments especially in primary or smaller Emergency Departments as a brief blood biomarker that could be quickly obtained at admission. Moreover, the causality

TABLE 3 | Multivariate regression analysis of ACSC and 30-day mortality.

Exposure	Crude model	Mode I	Mode II	Model III
ACSC (continuous)	2.38 (1.50, 3.78)	2.52 (1.52, 4.18)	2.43 (1.43, 4.12)	2.77 (1.59, 4.84)
ACSC quartiles				
Quantile 1	Reference	Reference	Reference	Reference
Quantile 2	1.49 (0.72, 3.07)	1.38 (0.66, 2.90)	1.23 (0.56, 2.69)	1.22 (0.56, 2.69)
Quantile 3	1.27 (0.59, 2.71)	1.25 (0.57, 2.70)	1.16 (0.51, 2.65)	1.17 (0.51, 2.67)
Quantile 4	2.69 (1.38, 5.22)	2.32 (1.17, 4.63)	2.13 (1.04, 4.38)	2.21 (1.07, 4.56)
P for trend	0.002	0.01	0.03	0.02

Data are expressed as OR (95% CI) p-value. ACSC, albumin-corrected serum calcium (mg/dl); ACSC, quantile 1: ≤9.26 mg/dl; quantile 2: 9.30–9.50 mg/dl; Quantile 3: 9.54–9.74 mg/dl, and quantile 4: ≥9.78 mg/dl.

Crude model: not adjusted.

Mode I: adjusted for age and gender.

Mode II: adjusted for age, gender, serum glucose, atrial fibrillation/atrial flutter, renal insufficiency, heart failure, chronic obstructive pulmonary disease, cancer, pneumonia, paralysis, and aphasia.

Model III: adjusted for age, gender, serum glucose, serum-phosphate tertiles, serum-magnesium tertiles, atrial fibrillation/atrial flutter, renal insufficiency, heart failure, chronic obstructive pulmonary disease, cancer, pneumonia, paralysis, aphasia, cognitive disorder, and epilepsy.

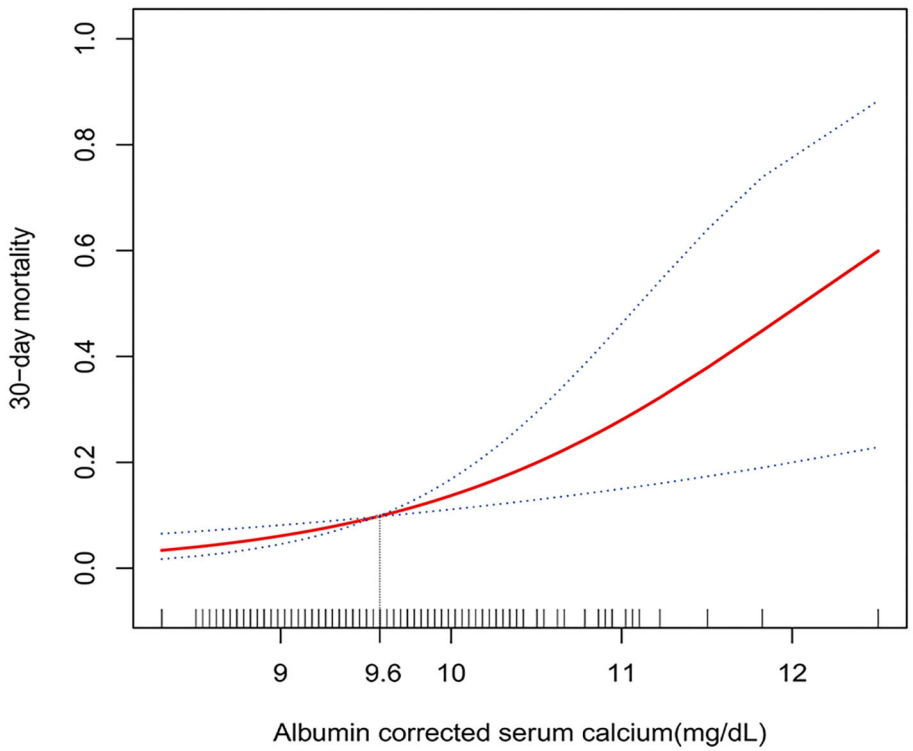

FIGURE 2 | Multivariate adjusted smooth curve-fitting for association between ACSC and 30-day mortality. Same confounder factors as in model III: age, gender, serum glucose, serum-phosphate tertiles, serum-magnesium tertiles, atrial fibrillation/atrial flutter, renal insufficiency, heart failure, chronic obstructive pulmonary disease, cancer, pneumonia, paralysis, aphasia, cognitive disorder, and epilepsy, were adjusted. The red line represents the best-fit line, and the blue lines are 95% CIs. The potential demarcation point was 9.6 mg/dl according to the smoothing spline plots.

of admission serum calcium level and short-term mortality could not be determined in this study. If future studies can demonstrate that admission elevated serum calcium cause increased mortality, clinical treatment including intravenous rehydration, enhancing kidney clearance of calcium (loop diuretics, calcitonin, and haemodialysis), calcium channel blocker, and limiting calcium and Vitamin D supplementation, might be beneficial to improve ischemic stroke patient outcomes.

The results of this study were compatible with the results of the previous study on the Chinese cohort (13). This study revealed that higher baseline ACSC levels were associated with 30-day mortality in IS patients. After processing ACSC as a

TABLE 4 | Two-piecewise linear regression analysis for ACSC and 30-day mortality.

ACSC (mg/dL)	Crude model	Model I	Model II	Model III
<9.6	2.97 (0.85, 10.35)	2.21 (0.62, 7.88)	1.90 (0.51, 7.16)	2.03 (0.52, 7.83)
≥9.6	2.18 (1.14, 4.17)	2.63 (1.30, 5.31)	2.62 (1.26, 5.47)	3.17 (1.47, 6.84)
P-value for likelihood ratio test	0.7	0.8	0.7	0.6

Data are expressed as OR (95% CI) p-value, ACSC, albumin-corrected serum calcium (mg/dl).
Crude model: not adjusted.
Model I: adjusted for age and gender.
Model II: adjusted for age, gender, serum glucose, atrial fibrillation/atrial flutter, renal insufficiency, heart failure, chronic obstructive pulmonary disease, cancer, pneumonia, paralysis, and aphasia.
Model III: adjusted for age, gender, serum glucose, serum-phosphate tertiles, serum-magnesium tertiles, atrial fibrillation/atrial flutter, renal insufficiency, heart failure, chronic obstructive pulmonary disease, cancer, pneumonia, paralysis, aphasia, cognitive disorder, and epilepsy.

categorical variable (quartiles), our results demonstrated that the top quartile group of ACSC levels most significantly increased the 30-day mortality. This result was also in agreement with the recent study from China (13), whose outcome is 1-year mortality (top quartile group, HR = 1.56, fully adjusted model). Moreover, previous studies had also demonstrated potential correlations between low serum calcium levels and cerebral infarct volume and short-term functional outcome, and U-shape relationship between baseline serum calcium and long-term mortality were shown by Appel et.al. Thus, we used curve fitting and the two-piecewise linear regression analyses to more accurately explore the relationship in this study. The results illustrated a linear relationship without threshold effect between ACSC level and 30-day mortality in IS patients, unlike the non-linear result of a previous study from the study of Appel et al. (11). In addition to differences in study populations, the study by Appel et al. (11) included both ischemic and hemorrhagic stroke patients, and different mediating mechanisms between serum calcium and mortality may account for their results, but this possibility needs to be verified by further studies.

Although extant studies demonstrated that high serum calcium levels were significantly associated with the risk of stroke (7) and clinical outcomes (12, 13), the pathophysiological mechanisms remain undefined. Previous studies revealed the key role of serum calcium in the promotion of vascular calcification, which is a complex process including the promotion of osteogenic/chondrogenic differentiation, vesicle release, cell apoptosis, loss of inhibitors, and extracellular matrix degradation (31, 32), leading to atherosclerosis. Thus, elevated serum calcium levels may accelerate the process of atherosclerosis, cardio-cerebrovascular calcification, and plaque rupture which has been associated with poor clinical outcomes (33–35). In addition, calcium ion is a crucial intracellular messenger, and plays a key role in neuronal damage and cell death (26). Furthermore, mitochondrial damage caused by high calcium concentration may be another mechanism (36). Moreover, recent research has shown that calcium ions could affect the cortical spreading depolarization after ischemic injury by regulating microglia activity (37). The association between elevated extracellular serum calcium levels and microglial calcium overload leading to cortical spreading depolarizations may explain the relationship between serum calcium levels and poor IS outcome. However, the inconsistent results of different studies suggested that there were more complicated mechanisms are needed to explain the effects of different ranges of serum calcium on all-cause mortality for IS patients, and the specific mechanisms need to be further studied.

This study has several advantages. First, the results of univariate analysis, regression coefficient change, and previous literature were used to select the covariates. Second, curve fitting and two-piecewise linear regression were used to explore a potential non-linear relationship, as shown in a previous study. Third, one crude model and four models adjusted with potential variables were used to test the stability of the results. Finally, ACSC was taken as a continuous variable and categorical variable into the multiple regression equation to avoid the contingency of the analysis, and the sensitivity analysis and trend test were used.

However, the following limitations exist. First, owing to the retrospective nature of this study, the non-inclusion of patients with missing ACSC information or wrong death information would lead to selection bias. Thus, the baseline information between the included group and the excluded group was compared, and the results showed no significant differences between the groups (**Supplementary Table 2**). Second, even though the ACSC level was calculated according to the standard formula, since the relationship between serum albumin and serum calcium could be more complex in the disease state, in addition to some studies having underlined that this formula could overestimate calcium levels (38, 39), further studies are needed to explore the actual relationship among serum calcium, serum albumin, and 30-day mortality. Though first-time laboratory results at admission, which are more likely to reflect the initial state of the patient at the onset, were used, it would be better to examine the dynamic changes in ACSC in future studies to understand the potential mechanism of the associations. Because of the retrospective study design, we could not confirm the time of blood collection, which will influence the ACSC level. Thus, further prospective studies with predesigned identical examination times are required. Third, the presence of unmeasured confounders could not be excluded. Since the secondary analysis originated from a retrospective cohort, variables that were not collected could not be adjusted. *E*-value was used to explore the potential for unmeasured confounding between ACSC and 30-day mortality

and the result showed that an unmeasured confounder was unlikely to explain the entirety of the mortality effect. Pre-stroke medications such as calcium and vitamin D supplements might affect the level of admission to ACSC, and patients with chronic comorbidities were more likely to have a medication history. A stratification analysis was performed on comorbidity and non-comorbidity subgroups, revealing that the results remained stable in both subgroups. This means that the results remain stable even in the non-comorbidity patients who may be less likely to take medication before stroke (**Supplementary Table 3**). In addition, given that the medication treatment in the hospital would tend to a bias toward the null, it is postulated that the unmeasured confounding of medication treatment in the hospital might underestimate the observed effect. Neurological function (NIHSS score or Norwegian trial Scandinavian Stroke Scale), IS subtypes, and functional status before stroke are important information to evaluate the outcome of stroke patients. Therefore, common complications associated with neurological function including paralysis, epilepsy, cognitive disorder, and aphasia were additionally adjusted, and the results were also robust after adjustment (Model III). Moreover, some studies have revealed a negative association between serum calcium at the baseline and admission neurological function (9, 40). Therefore, adjustment for the neurological function tends to elevate the estimated effect. Finally, the participants in this study were represented by the Norwegian population, and the findings could not necessarily apply to other populations.

CONCLUSIONS

Admission albumin-corrected serum calcium in ischemic stroke patients was positively correlated with 30-day mortality, and the relationship between them was almost linear.

DATA AVAILABILITY STATEMENT

The datasets used in this study are publicly available and can be accessed via the database www.Datadryad.org.

ETHICS STATEMENT

The original research was approved by the Norwegian Regional Committee for Medical and Health Research Ethics South East as a quality study, which did not need ethical approval. Thus, our secondary analysis based on this original research did not require separate ethical approval. This research was performed according to the Declaration of Helsinki. All data was processed anonymously and therefore written informed consent from the patients/participants was not required for this study in accordance with the national legislation and the institutional requirements.

AUTHOR CONTRIBUTIONS

Conceptualization and methodology: YL and XM. Data source: KT. Software and writing—original draft preparation: YL. Visualization: XM. Writing—reviewing and editing: YW, MY, and XZ. All authors listed have read and approved the manuscript.

FUNDING

This study was supported by the National Natural Science Foundation of China (No. 81960330) (http://www.nsfc.gov.cn) and Jiangxi Provincial Department of Science and Technology (Grant Numbers: 20202BABL206053, 20192BAB205045, and 20161BBI90018).

ACKNOWLEDGMENTS

The authors specially thank the other authors of the original study. They and KT completed the whole study and shared their data selflessly and kindly (19). They are [the rankings and institutions of these researchers are ranked according to the original reference (19)]: Professor Ståle H. Nymo (Department of Internal Medicine, Diakonhjemmet Hospital, Oslo, Norway), Professor William E. Louch (Institute of Experimental Medical Research, Oslo University Hospital, Ullevål and University of Oslo, Oslo, Norway; Center for Heart Failure Research, University of Oslo, Oslo, Norway), Professor Anette H. Ranhoff (Department of Internal Medicine, Diakonhjemmet Hospital, Oslo, Norway; Department of Clinical Science, University of Bergen, Bergen, Norway), and Professor Erik Øie (Department of Internal Medicine, Diakonhjemmet Hospital, Oslo, Norway; Department of Clinical Science, University of Bergen, Bergen, Norway). The authors are also grateful to Professor Xinglin Chen and Professor Changzhong Chen (Statistical consultant, X&Y Solution, lnc. Boston MA) for their assistance in statistics. Finally, YL would like to especially thank his daughter (Mrs. Yanli Lu) and other family members for their encouragement and kind support.

SUPPLEMENTARY MATERIAL

The Supplementary Material for this article can be found online at: https://www.frontiersin.org/articles/10.3389/fneur.2022.889518/full#supplementary-material

REFERENCES

1. GBD 2019 Stroke Collaborators. Global, regional, and national burden of stroke and its risk factors, 1990-2019: a systematic analysis for the Global Burden of Disease Study 2019. *Lancet Neurol.* (2021) 20:795–820. doi: 10.1016/S1474-4422(21)00252-0
2. Baird GS. Ionized calcium. *Clin Chim Acta.* (2011) 412:696–701. doi: 10.1016/j.cca.2011.01.004
3. Kraft MD. Phosphorus and calcium: a review for the adult nutrition support clinician. *Nutr Clin Pract.* (2015) 30:21–33. doi: 10.1177/0884533614565251
4. Santulli G, Marks AR. Essential roles of intracellular calcium release channels in muscle, brain, metabolism, and aging. *Curr Mol*

Pharmacol. (2015) 8:206–22. doi: 10.2174/1874467208666150507105105
5. Walsh J, Gittoes N, Selby P, Society for Endocrinology Endocrine Emergency Guidance. Emergency management of acute hypercalcaemia in adult patients. *Endocr Connect.* (2016) 5:G9–11. doi: 10.1530/EC-16-0055
6. Reid IR, Gamble GD, Bolland MJ. Circulating calcium concentrations, vascular disease and mortality: a systematic review. *J Intern Med.* (2016) 279:524–40. doi: 10.1111/joim.12464
7. Rohrmann S, Garmo H, Malmstrom H, Hammar N, Jungner I, Walldius G, et al. Association between serum calcium concentration and risk of incident and fatal cardiovascular disease in the prospective AMORIS study. *Atherosclerosis.* (2016) 251:85–93. doi: 10.1016/j.atherosclerosis.2016.06.004
8. Dibaba DT, Xun P, Fly AD, Bidulescu A, Tsinovoi CL, Judd SE, et al. Calcium intake and serum calcium level in relation to the risk of ischemic stroke: findings from the REGARDS study. *J Stroke.* (2019) 21:312–23. doi: 10.5853/jos.2019.00542
9. Buck BH, Liebeskind DS, Saver JL, Bang OY, Starkman S, Ali LK, et al. Association of higher serum calcium levels with smaller infarct volumes in acute ischemic stroke. *Arch Neurol.* (2007) 64:1287–91. doi: 10.1001/archneur.64.9.1287
10. Ovbiagele B, Starkman S, Teal P, Lyden P, Kaste M, Davis SM, et al. Serum calcium as prognosticator in ischemic stroke. *Stroke.* (2008) 39:2231–6. doi: 10.1161/STROKEAHA.107.513499
11. Appel SA, Molshatzki N, Schwammenthal Y, Merzeliak O, Toashi M, Sela BA, et al. Serum calcium levels and long-term mortality in patients with acute stroke. *Cerebrovasc Dis.* (2011) 31:93–9. doi: 10.1159/000321335
12. Chung JW, Ryu WS, Kim BJ, Yoon BW. Elevated calcium after acute ischemic stroke: association with a poor short-term outcome and long-term mortality. *J Stroke.* (2015) 17:54–9. doi: 10.5853/jos.2015.17.1.54
13. Zhang JF, Meng X, Jing J, Pan Y, Wang YL, Zhao XQ, et al. Serum calcium and long-term outcome after ischemic stroke: results from the China National stroke registry III. *Atherosclerosis.* (2021) 325:24–9. doi: 10.1016/j.atherosclerosis.2021.03.030
14. Tsai CF, Thomas B, Sudlow CL. Epidemiology of stroke and its subtypes in Chinese vs. white populations: a systematic review. *Neurology.* (2013) 81:264–72. doi: 10.1212/WNL.0b013e31829bfde3
15. Andersen S, Noahsen P, Rex KF, Fleischer I, Albertsen N, Jorgensen ME, et al. Serum 25-hydroxyvitamin D, calcium and parathyroid hormone levels in Native and European populations in Greenland. *Br J Nutr.* (2018) 119:391–7. doi: 10.1017/S0007114517003944
16. Bushinsky DA, Monk RD. Electrolyte quintet: calcium. *Lancet.* (1998) 352:306–11. doi: 10.1016/S0140-6736(97)12331-5
17. Payne RB, Little AJ, Williams RB, Milner JR. Interpretation of serum calcium in patients with abnormal serum proteins. *Br Med J.* (1973) 4:643–6. doi: 10.1136/bmj.4.5893.643
18. Tazmini K, Nymo SH, Louch WE, Ranhoff AH, Oie E. Data from: electrolyte imbalances in an unselected population in an emergency department: a retrospective cohort study. *Dryad Dataset.* (2019). doi: 10.5061/dryad.f3h26j3
19. Tazmini K, Nymo SH, Louch WE, Ranhoff AH, Oie E. Electrolyte imbalances in an unselected population in an emergency department: a retrospective cohort study. *PLoS ONE.* (2019) 14:e215673. doi: 10.1371/journal.pone.0215673
20. Rustad P, Felding P, Franzson L, Kairisto V, Lahti A, Martensson A, et al. The nordic reference interval project 2000: recommended reference intervals for 25 common biochemical properties. *Scand J Clin Lab Invest.* (2004) 64:271–84. doi: 10.1080/00365510410006324
21. Vetter C, Devore EE, Wegrzyn LR, Massa J, Speizer FE, Kawachi I, et al. Association between rotating night shift work and risk of coronary heart disease among women. *JAMA.* (2016) 315:1726–34. doi: 10.1001/jama.2016.4454
22. Bernhardt PW. Model validation and influence diagnostics for regression models with missing covariates. *Stat Med.* (2018) 37:1325–42. doi: 10.1002/sim.7584
23. Bjerregaard LG, Pedersen DC, Mortensen EL, Sorensen T, Baker JL. Breastfeeding duration in infancy and adult risks of type 2 diabetes in a high-income country. *Matern Child Nutr.* (2019) 15:e12869. doi: 10.1111/mcn.12869
24. Park SY, Freedman ND, Haiman CA, Le Marchand L, Wilkens LR, Setiawan VW. Association of coffee consumption with total and cause-specific mortality among nonwhite populations. *Ann Intern Med.* (2017) 167:228–35. doi: 10.7326/M16-2472
25. Haneuse S, VanderWeele TJ, Arterburn D. Using the E-value to assess the potential effect of unmeasured confounding in observational studies. *JAMA.* (2019) 321:602–3. doi: 10.1001/jama.2018.21554
26. Kristian T, Siesjo BK. Calcium in ischemic cell death. *Stroke.* (1998) 29:705–18. doi: 10.1161/01.STR.29.3.705
27. Valero-Politi J, Ginard-Salva M, Gonzalez-Alba JM. Annual rhythmic and non-rhythmic biological variation of magnesium and ionized calcium concentrations. *Clin Chem Lab Med.* (2001) 39:45–9. doi: 10.1515/CCLM.2001.011
28. Nafstad P, Skrondal A, Bjertness E. Mortality and temperature in Oslo, Norway, 1990-1995. *Eur J Epidemiol.* (2001) 17:621–7. doi: 10.1023/A:1015547012242
29. Moan J, Baturaite Z, Juzeniene A, Porojnicu AC. Vitamin D, sun, sunbeds and health. *Public Health Nutr.* (2012) 15:711–5. doi: 10.1017/S1368980011002801
30. Kehoe L, Walton J, Flynn A. Nutritional challenges for older adults in Europe: current status and future directions. *Proc Nutr Soc.* (2019) 78:221–33. doi: 10.1017/S0029665118002744
31. Yang H, Curinga G, Giachelli CM. Elevated extracellular calcium levels induce smooth muscle cell matrix mineralization *in vitro*. *Kidney Int.* (2004) 66:2293–9. doi: 10.1111/j.1523-1755.2004.66015.x
32. Reynolds JL, Joannides AJ, Skepper JN, McNair R, Schurgers LJ, Proudfoot D, et al. Human vascular smooth muscle cells undergo vesicle-mediated calcification in response to changes in extracellular calcium and phosphate concentrations: a potential mechanism for accelerated vascular calcification in ESRD. *J Am Soc Nephrol.* (2004) 15:2857–67. doi: 10.1097/01.ASN.0000141960.01035.28
33. Bugnicourt JM, Leclercq C, Chillon JM, Diouf M, Deramond H, Canaple S, et al. Presence of intracranial artery calcification is associated with mortality and vascular events in patients with ischemic stroke after hospital discharge: a cohort study. *Stroke.* (2011) 42:3447–53. doi: 10.1161/STROKEAHA.111.618652
34. Pelisek J, Eckstein HH, Zernecke A. Pathophysiological mechanisms of carotid plaque vulnerability: impact on ischemic stroke. *Arch Immunol Ther Exp.* (2012) 60:431–42. doi: 10.1007/s00005-012-0192-z
35. Magdic J, Cmor N, Kaube M, Hojs FT, Hauer L, Sellner J, et al. Intracranial vertebrobasilar calcification in patients with ischemic stroke is a predictor of recurrent stroke, vascular disease, and death: a case-control study. *Int J Environ Res Public Health.* (2020) 17:13. doi: 10.3390/ijerph17062013
36. Nicholls DG. A role for the mitochondrion in the protection of cells against calcium overload? *Prog Brain Res.* (1985) 63:97–106. doi: 10.1016/S0079-6123(08)61978-0
37. Liu L, Kearns KN, Eli I, Sharifi KA, Soldozy S, Carlson EW, et al. Microglial calcium waves during the hyperacute phase of ischemic stroke. *Stroke.* (2021) 52:274–83. doi: 10.1161/STROKEAHA.120.032766
38. Pfitzenmeyer P, Martin I, D'Athis P, Grumbach Y, Delmestre MC, Blonde-Cynober F, et al. A new formula for correction of total calcium level into ionized serum calcium values in very elderly hospitalized patients. *Arch Gerontol Geriatr.* (2007) 45:151–7. doi: 10.1016/j.archger.2006.10.006
39. Byrnes MC, Huynh K, Helmer SD, Stevens C, Dort JM, Smith RS, et al. comparison of corrected serum calcium levels to ionized calcium levels among critically ill surgical patients. *Am J Surg.* (2005) 189:310–4. doi: 10.1016/j.amjsurg.2004.11.017

40. Guven H, Cilliler AE, Koker C, Sarikaya SA, Comoglu SS. Association of serum calcium levels with clinical severity of acute ischemic stroke. *Acta Neurol Belg.* (2011) 1 11:45–9.

Conflict of Interest: The authors declare that the research was conducted in the absence of any commercial or financial relationships that could be construed as a potential conflict of interest.

Publisher's Note: All claims expressed in this article are solely those of the authors and do not necessarily represent those of their affiliated organizations, or those of the publisher, the editors and the reviewers. Any product that may be evaluated in this article, or claim that may be made by its manufacturer, is not guaranteed or endorsed by the publisher.

Copyright © 2022 Lu, Ma, Tazmini, Yang, Zhou and Wang. This is an open-access article distributed under the terms of the Creative Commons Attribution License (CC BY). The use, distribution or reproduction in other forums is permitted, provided the original author(s) and the copyright owner(s) are credited and that the original publication in this journal is cited, in accordance with accepted academic practice. No use, distribution or reproduction is permitted which does not comply with these terms.

frontiers | Frontiers in Neurology

ORIGINAL RESEARCH
published: 20 June 2022
doi: 10.3389/fneur.2022.889106

Role of Ultrasound Imaging in the Prediction of *TRIM67* in Brain Metastases From Breast Cancer

Zhidong Xuan, Ting Ma, Yue Qin and Yajie Guo*

Department of Ultrasound, Cangzhou Central Hospital, Cangzhou, China

Objectives: Ultrasound (US) imaging is a relatively novel strategy to monitor the activity of the blood–brain barrier, which can facilitate the diagnosis and treatment of neurovascular-related metastatic tumors. The purpose of this study was to investigate the clinical significance of applying a combination of US imaging outcomes and the associated genes. This was performed to construct line drawings to facilitate the prediction of brain metastases arising from breast cancer.

Methods: The RNA transcript data from The Cancer Genome Atlas (TCGA) database was obtained for breast cancer, and the differentially expressed genes (DEGs) associated with tumor and brain tumor metastases were identified. Subsequently, key genes associated with survival prognosis were subsequently identified from the DEGs.

Results: Tripartite motif-containing protein 67 (*TRIM67*) was identified and the differential; in addition, the survival analyses of the TCGA database revealed that it was associated with brain tumor metastases and overall survival prognosis. Applying independent clinical cohort data, US-related features (microcalcification and lymph node metastasis) were associated with breast cancer tumor metastasis. Furthermore, ultrasonographic findings of microcalcifications showed correlations with *TRIM67* expression. The study results revealed that six variables [stage, *TRIM67*, tumor size, regional lymph node staging (N), age, and HER2 status] were suitable predictors of tumor metastasis by applying support vector machine–recursive feature elimination. Among these, US-predicted tumor size correlated with tumor size classification, whereas US-predicted lymph node metastasis correlated with tumor N classification. The *TRIM67* upregulation was accompanied by upregulation of the integrated breast cancer pathway; however, it leads to the downregulation of the miRNA targets in ECM and membrane receptors and the miRNAs involved in DNA damage response pathways.

Conclusions: The *TRIM67* is a risk factor associated with brain metastases from breast cancer and it is considered a prognostic survival factor. The nomogram constructed from six variables—stage, *TRIM67*, tumor size, N, age, HER2 status—is an appropriate predictor to estimate the occurrence of breast cancer metastasis.

Keywords: breast cancer, brain metastases, ultrasonography, TRIM67, biomarkers

OPEN ACCESS

Edited by:
Yuzhen Xu,
Tongji University, China

Reviewed by:
Junming Xu,
Shanghai General Hospital, China
Chao Deng,
Shanghai Jiao Tong University, China

****Correspondence:***
Ting Ma
mating5058@163.com

Specialty section:
This article was submitted to Neurological Biomarkers, a section of the journal Frontiers in Neurology

Received: *03 March 2022*
Accepted: *16 May 2022*
Published: *20 June 2022*

Citation:
Xuan Z, Ma T, Qin Y and Guo Y (2022) Role of Ultrasound Imaging in the Prediction of TRIM67 in Brain Metastases From Breast Cancer. Front. Neurol. 13:889106. doi: 10.3389/fneur.2022.889106

INTRODUCTION

Brain metastases (BM) have gradually become the most common malignancy of the central nervous system, with 20–40% of patients with cancer developing BM (1, 2). Primarily, BM arises from tumors in the lungs and the breast; however, they are observed at other sites as well (3). Annually, the global incidence of BM has progressively increased and is associated with a poor prognosis. The overall survival varies from 3 to 25 months depending on tumor type and subtype, BM has become a clinically important disease that poses a remarkable threat to human health (2, 4). An estimated 30–50% of patients with metastatic breast cancer (MBC) develop BM (5, 6). The development of BM depends on the action of neurovascular units (NVU), thereby emphasizing the unique and close relationship between the vessels and cells in the brain (7). Brain endothelial cells (BECs) occupy a central position in the NVU and they are regulated by neuronal cells in the formation and maintenance of the blood–brain barrier. Tumor cells must overcome the tightly connected endothelial barrier of BECs to ensure the occurrence of BM (8). Breast cancer (BRCA) is a relatively common type of tumor that leads to the formation of neurovascular metastases and has a very poor prognosis; furthermore, its presence is a notable health risk for patients with cancer (9, 10). Identifying neurovascular metastases from brain tumors is essential for monitoring the prognosis of patients with breast cancer.

Understanding ultrasound (US) signals related to neurovascular tissues in disease conditions will be instrumental in elucidating disease mechanisms and identifying potential diagnostic and treatment targets (11). Ultrasound examinations expose the patient to considerably low levels of radiation, and the test itself is non-invasive and reproducible. Considering this, US examinations are a common and convenient modality in the management of breast cancer (12). Previously, several studies have examined the role of US imaging in the identification of breast cancer metastasis and prognosis. Ultrasound imaging has a suitable degree of sensitivity and specificity in diagnosing breast cancer metastasis to axillary lymph nodes (13). Tumors diagnosed *via* breast US have better prognostic features in terms of size and lymphovascular invasion (14). Furthermore, the formation of microcalcifications affected the growth and infiltration of breast cancer and is associated with disease prognosis in patients (15). Ultrasonography can provide a multidirectional, multi-angle sweep of microcalcified breast cancer lesions; this feature is more widely used in the screening and diagnosis of microcalcifications in breast cancer (16). In addition, ultrasonographic observation of lesion blood flow grading correlated with positive ER expression of the estrogen receptor, which can indirectly indicate the sensitivity of breast cancer to treatment (17, 18). However, neurovascular metastases in breast cancer were closely related to gene expression characteristics, and the items examined *via* breast US imaging alone were biased as they do not adequately reflect this.

The recent developments in bioinformatics have facilitated the diagnosis and treatment of the disease with the help of large-scale biological data (19–22). The considerable amount of RNA sequencing data and the increasing number of prognostic factors and therapeutic targets identified have considerably aided in the examination of the mechanisms related to cancer development and clinical treatment (23, 24). One study used RNA sequencing to probe the cellular origin and evolution of breast cancer in *BRCA1* mutant carriers (25). Additionally, bioinformatics has reportedly been used to identify differentially expressed genes (DEGs) associated with breast cancer metastasis and provide potential therapeutic targets for metastatic breast cancer (26). Bioinformatics data combined with imaging findings can also play a crucial role in breast cancer diagnosis and prognosis. Breast US imaging combined with plasma miR-21 and miR-27a significantly improves the diagnostic efficiency of breast cancer, thereby facilitating early clinical intervention (27). We believe that a combination of US imaging and transcriptional profiling can predict the risk of cerebral neurovascular metastases in patients with breast cancer.

In this study, we aimed to investigate the genes associated with the development of neurovascular BM in patients with breast cancer and to explore the role of ultrasonography in the examination of tumor metastases. Furthermore, this was performed to identify potential diagnostic and therapeutic targets/features to monitor and improve the risk of BM in patients with breast cancer and to extend their life expectancy.

METHODS

Clinical Information and TCGA Data Acquisition

We retrospectively analyzed patients with surgically confirmed breast cancer who presented themselves to our hospital between August 2015 and March 2021. The following cases were excluded in this study: (1) cases of male breast cancer; (2) cases where the elapsed time between surgery and US was more than 2 weeks; (3) cases with incomplete clinical information; (4) cases with unilateral multiple foci; and (5) cases with primary malignancy at a different site. Using the above exclusion criteria, a total of 97 breast cancer patients with adequate follow-up were finally screened. Postoperative pathological staging was based on the American Joint Committee on Cancer (AJCC) TNM staging criteria for breast cancer. Informed consent was obtained from all patients. Consent was also obtained from the Ethics Committee of Cangzhou Central Hospital. The Cancer Genome Atlas (TCGA; https://portal.gdc.cancer.gov/) project database was searched for 1,041 breast invasive carcinoma (BRCA) patient samples consisting of 60 tumors with non-brain metastasis (nBM–BRCA), 4 tumors with brain metastasis (BM–BRCA), and 977 tumors without distant brain metastasis (nDM–BRCA). Transcriptome data were downloaded in transcripts per million (TPM) unit format and were log-transformed.

Abbreviations: TCGA, The Cancer Genome Atlas; BRCA, Breast invasive carcinoma; BM, Brain metastasis; nDM–BRCA, BRCA with no distance metastasis; nBM–BRCA, BRCA with non-brain metastasis; TPM, Transcripts per million; DE–mRNAs, Differentially expressed mRNAs; DEGs, Differentially expressed genes; GSEA, Gene Set Enrichment Analysis; KM, Kruskal–Wallis; OS, Overall survival; qRT-PCR, Quantitative Reverse Transcription-PCR.

Tumor Features Evaluation by Ultrasonography

Sonography was performed using a Siemens-2000 color Doppler diagnostic US machine with a probe frequency of 7–15 Hz. Different clinical features were analyzed using US including tumor size, microcalcification status, blood flow grading, and lymph node metastases. The longest measured diameter of a lesion in any section scan was considered as the size of the primary tumor. The size (<1-mm in diameter), number, and distribution of calcified spots were used as bases to determine the status of microcalcifications in breast cancer. Blood flow was graded into four levels according to Adler blood flow grading: Grade 0, no blood flow in the tumor lesion; Grade I, little blood flow, i.e., one or two spots of blood flow (<1-mm in diameter) are visible; Grade II, moderate blood flow, i.e., one main vessel or several small vessels visible; Grade III, significant blood flow, i.e., four or more vessels visible (28). Ultrasound was used to assess axillary lymph node metastases by (1) high-frequency US sonograph showing a lymph node thickness of more than 3 mm or a solid axillary hypoechogenicity, or (2) color flow imaging showing abundant blood flow within the lymph nodes.

Logistic Regression Analysis

To explore the relationship between tumor features and metastasis, logistics regression was used to determine the predictive power of the observed tumor features from the sonographs in relation to tumor metastasis (29, 30). The purpose of using logistic regression in this step is not to train diagnostic classifiers, but to test for multivariate differences. First, univariate logistics regression was used to analyze the general clinical and US-related features of the patients, with the relevant characteristics screened at $p < 0.05$ level of significance. Then, the screened US and clinical characteristics were subjected to multivariate logistic regression analysis. The odds ratio (OR) and 95% confidence interval (95% CI) for each variable were assessed as statistical indicators. The variables with a significance level of $p < 0.05$ in both univariate and multifactorial logistic regression analyses were considered as independent predictors of tumor metastasis.

Bioinformatics Analysis

Distant metastases- and BM-associated differentially expressed genes (DEGs) were identified through the differential analysis of transcriptomic data from tumor tissue samples using the limma package (31). The DEGs were filtered based on a threshold value of $p < 0.05$. Subsequently, intersection analysis of DM- and BM-associated DEGs was performed to identify genes that were differentially expressed in both DM and BM. From the obtained gene list, survival analysis was employed to further screen for prognosis-related genes.

Quantitative Reverse Transcription-PCR

Quantitative RT-PCR (qRT-PCR) was used to quantify the RNA expression levels of key genes present in tumor samples collected after surgical resection. The total RNA was extracted using the mirVana™ miRNA isolation kit (Ambion) according to the manufacturer's protocol. The harvested total RNA was reverse transcribed to cDNA using RevertAid first strand cDNA synthesis kit (Thermo Scientific™, USA). The qRT-PCR was performed using SYBR® Green Realtime PCR master mix (Toyobo, Japan) on ABI 7500 real-time PCR system (Applied Biosystems, CA, USA). Using GAPDH as the reference gene, the $2^{-\Delta\Delta CT}$ method was used for the relative quantification of gene expression levels. In the final conclusion, gene expression levels were reported as the fold-change (FC) relative to the reference.

Support Vector Machine–Recursive Feature Elimination

To screen for features associated with tumor metastases, an exploratory analysis of the patient's general characteristics, US-related features, postoperative pathological features and key genes was applied support vector machine–recursive feature elimination (SVM–RFE) (32). In supervised machine learning, support vector machines (SVMs) are often used for non-linear classification. In addition, SVM showed good performance in processing data sets with small sample sizes (30, 33, 34). Support vector machine–recursive feature elimination filtered the variables of the prediction results by iteratively removing redundant feature variables. Using a cross-validation approach, the root mean squared error (RMSE) parameter was used to assess the predictive performance of the model and to screen for the best combination of variables. The entire dataset was divided into a training set and a test set in a ratio of 7:3. The training set was used for feature selection and model training, and the test set was used for testing the model. The area under curve (AUC) of the receiver operating characteristic curve (ROC) was also applied to assess the predictive performance of the model; pROC curves are plotted using the "pROC" package.

Nomogram Construction

A principal component analysis (PCA) was applied to further extract features from the SVM–RFE that reflect tumor metastasis in order to determine whether they provided adequate information for classification. To develop predictive models for these characteristics, multivariate logistic regression was applied. Decision curve analysis (DCA) assesses the usefulness and safety of clinical prediction models by calculating the net benefit ratio for different threshold probabilities. To facilitate clinical use, a visualization tool was constructed by applying the "rms" to the nomogram of this clinical prediction model. Calibration curves are used to assess the agreement between predicted probabilities and actual outcomes.

Survival Analysis

For BRCA patients, Kaplan–Meier (KM) curves were used to calculate the probability of overall survival (OS) at 1, 3, and 5 years. Cox regression analysis was used to perform a difference-in-difference test analysis of the survival curves between the two groups. The time-dependent ROC and area under the curve (AUC) values were used to quantify the predictive performance of the target gene for survival in BRCA patients (35). Survival data were analyzed using "survival" package, and visualization was carried out using survminer R package.

Gene Set Enrichment Analysis

Analysis of functional pathways dysregulated in TCGA–BRCA tumor samples with dysregulated genes using Gene Set Enrichment Analysis (GSEA) as the previous researches (36–39). The pathways in the analysis were annotated using the "c2.cp.v7.2.symbols.gmt [Curated]" gene set from MSigDB Collections (https://www.gsea-msigdb.org/gsea/msigdb/). Package clusterProfiler was used to calculate the statistical significance of the enrichment of functional pathways (40). The threshold of statistical significance for functional pathway enrichment was set at adjusted $p < 0.05$.

Statistical Analysis

All statistical analyses and figures were obtained using the R (version 4.0.2) software. In the statistical analysis of patients' baseline data, the Pearson's Chi-squared test or Fisher's exact test was used to test the count data. Differences in the measurements between the two groups were determined using the Wilcoxon rank–sum test or unpaired *t*-test. Correlation analysis was performed using the Spearman method. The results from these statistical analyses were plotted using the "ggplot2" package. Computed *p*-values of <0.05 were considered to be statistically significant.

RESULTS

Baseline Patients' Information

Among the 97 patients with breast cancer enrolled in the clinical cohort study, distant metastases (DM) developed and did not develop in 34 and 63, respectively. The clinical baseline information, postoperative pathological features, and US features of the patients with breast cancer are summarized in **Table 1**. Patients with breast cancer with and without DM showed significant differences in terms of TNM stage, metastasized staging (M), tumor size staging (T), regional lymph node staging (N), HER2, tumor size, microcalcification, Adler blood flow grading, and prediction of lymph node metastasis. No statistically significant differences were observed in terms of age, menopausal status, tumor location, histology, ER, and PR. However, microcalcifications confirmed by preoperative US, higher blood flow grading, and lymph node metastases may indicate a higher risk of DM.

Ultrasound Predicts BRCA Metastasis

Typically, the logistics model is used to screen for risk factors associated with the poor outcomes. In this section, we have included only general clinical features and ultrasonography-related features for analysis to explore the ability of preoperative ultrasonography and diagnosis to assess the likelihood of DM in patients with tumors. Results of logistic regression analysis to screen the predictors associated with DM are presented in **Table 2**. Univariate logistic analysis showed that tumor size in US imaging ($p = 0.015$), microcalcification ($p < 0.001$), Adler blood flow grading ($p = 0.003$), and lymph node metastasis ($p = 0.001$) were significantly associated with the occurrence of DM in patients with breast cancer. Further multivariate logistic regression analysis showed that microcalcification ($p = 0.02$) and

TABLE 1 | Baseline characteristics of patients in the clinical cohort.

Characteristic	Metastasis		*P*
	Yes	No	
N	34	63	
Age, mean ± *SD*	59.29 ± 12.38	55.87 ± 11.86	0.185
Menopause, *n* (%)			0.413
Premenopause	9 (9.3%)	18 (18.6%)	
Perimenopause	5 (5.2%)	4 (4.1%)	
Postmenopause	20 (20.6%)	41 (42.3%)	
Location, *n* (%)			0.756
Left	17 (17.5%)	35 (36.1%)	
Right	17 (17.5%)	28 (28.9%)	
Histology, *n* (%)			0.712
Infiltrating ductal carcinoma	20 (20.6%)	41 (42.3%)	
Infiltrating lobular carcinoma	8 (8.2%)	14 (14.4%)	
Others	6 (6.2%)	8 (8.2%)	
Stage, *n* (%)			<0.001**
Stage I	0 (0%)	11 (11.3%)	
Stage II	6 (6.2%)	41 (42.3%)	
Stage III	20 (20.6%)	11 (11.3%)	
Stage IV	8 (8.2%)	0 (0%)	
M, *n* (%)			<0.001**
M0	26 (26.8%)	63 (64.9%)	
M1	8 (8.2%)	0 (0%)	
N, *n* (%)			<0.001**
N0	1 (1%)	30 (30.9%)	
N1	15 (15.5%)	23 (23.7%)	
N2	10 (10.3%)	7 (7.2%)	
N3	8 (8.2%)	3 (3.1%)	
T, *n* (%)			0.007**
T1	3 (3.1%)	19 (19.6%)	
T2	19 (19.6%)	37 (38.1%)	
T3	10 (10.3%)	6 (6.2%)	
T4	2 (2.1%)	1 (1%)	
ER, *n* (%)			0.592
Negative	10 (10.3%)	14 (14.4%)	
Positive	24 (24.7%)	49 (50.5%)	
PR, *n* (%)			0.166
Negative	17 (17.5%)	21 (21.6%)	
Positive	17 (17.5%)	42 (43.3%)	
HER2, *n* (%)			<0.001**
Negative	17 (17.5%)	53 (54.6%)	
Positive	17 (17.5%)	10 (10.3%)	
TRIM67, median (IQR)	−0.08 (−0.52, 0)	−0.41 (−0.94, −0.02)	0.021*
US examination			
Size/mm, median (IQR)	33 (24.12, 53.88)	27.3 (17.7, 38.4)	0.013*
Microcalcification, *n* (%)			<0.001**
No	5 (5.2%)	35 (36.1%)	
Yes	29 (29.9%)	28 (28.9%)	
Adler blood flow grading, *n* (%)			0.005**
0–I	9 (9.3%)	37 (38.1%)	
II–III	25 (25.8%)	26 (26.8%)	
Lymph node metastasis, *n* (%)			<0.001**
No	3 (3.1%)	29 (29.9%)	
Yes	31 (32%)	34 (35.1%)	

Ultrasound examination include tumor size calculation, microcalcification, altered blood grading, and lymph node metastasis prediction.
*$p < 0.05$, **$p < 0.01$.

TABLE 2 | Univariate and multivariate logistics regression analysis with US-related variables.

Variables	Univariate logistic regression			Multivariate logistic regression		
	OR	95% CI	*p*	OR	95% CI	*p*
Age[#]	1.02	0.99, 1.06	0.185			
Premenopause						
Perimenopause	0.39	0.09, 1.63	0.194			
Postmenopause	0.4	0.08, 1.86	0.243			
Location (Left)						
Right	1.25	0.54, 2.9	0.601			
Size[#]	1.04	1.01, 1.07	0.015*	1.02	0.98, 1.05	0.366
Microcalcification (No)						
Yes	7.25	2.66, 23.51	<0.001**	5.1	1.38, 22.33	0.02*
Adler blood flow grading (I–II)						
II–III	3.95	1.63, 10.26	0.003**	0.97	0.25, 3.39	0.957
Lymph node metastasis (No)						
Yes	8.81	2.78, 39.39	0.001**	6.19	1.71, 30.79	0.011*

[#]*Continuous variable; CI, confidence interval.*
**p < 0.05, **p < 0.01.*

lymph node metastasis ($p = 0.011$) were independent predictors of DM.

The *TRIM67* Expression Correlates With BM and DM

We performed differential expression analysis of the RNA transcript data between the two groups at the tumor tissue level. Differential analysis of The Cancer Genome Atlas (TCGA) data and patients with breast cancer with and without DM revealed 3,759 DEGs, which were identified as DM-associated DEGs (**Figure 1A**). Similarly, 2,029 BM-associated DEGs were identified between the BM and nBM groups (**Figure 1B**), and Cox analysis revealed 1,727 survival-associated DEGs. Cross-tabulation analysis subsequently showed that four genes—*TRIM67*, SFXN2, CEL, and IGKV6-21—were associated with DM, BM, and survival outcomes. Additionally, *TRIM67* expression was significantly different between the DM and nDM groups ($p = 0.021$) and between the BM and nBM groups ($p = 0.007$) (**Figures 1C,D**). Therefore, *TRIM67* was used for further analysis.

Ultrasonography and *TRIM67* Expression

To investigate whether US can assess *TRIM67* expression, an exploratory analysis of the relationship between US findings and *TRIM67* was performed. The results showed a significant difference between microcalcifications and *TRIM67* expression in the US findings ($p = 0.027$). The *TRIM67* expression was higher in the group with microcalcifications than in the group without microcalcifications (**Figure 2A**). the *TRIM67* expression showed no significant differences from Adlerian blood flow grading, lymph node metastasis prediction, and tumor size (**Figures 2B–D**). However, the results appeared to imply that a higher blood flow grading, positive lymph node metastasis prediction, and larger tumor size correlated with a higher *TRIM67* expression.

The SVM–RFE Shows Variables Associated With Prognosis

The general patient characteristics, the ultrasonographic information, the postoperative pathological information, and the predictive power of *TRIM67* in tumor metastasis were assessed using SVM–RFE. The results showed that the model had the lowest RMSE (**Figure 3A**) when six variables (stage, *TRIM67*, tumor size, N, age, and HER2 status) were included in the SVM model. The receiver operating characteristic (ROC) curves of *TRIM67* [area under ROC curve (AUC), 0.643], tumor size (AUC, 0.654), and age (AUC, 0.580) for the prediction of tumor metastasis are shown in **Figure 3B**, indicating their general predictive ability. The AUCs of the multifactor logistic regression model constructed by combining the above six characteristics were 0.917, 0.865, and 0.912 for the training group, test group, and all groups, respectively (**Figure 3C**). The clinical prediction model showed an acceptable predictive power for tumor metastasis. **Table 3** shows the coefficients for these six variables in the clinical prediction model. A positive correlation was found between the probability of tumor metastasis and stages III–IV, *TRIM67*, size, N1–N3, and positive HER2. The DCA of the clinical prediction model in the training, test, and overall groups is shown in **Figure 3D**, demonstrating the large clinical range of the model.

Construction of a Clinical Prediction Model for Tumor Metastasis

Developing a predictive model has the potential to be useful in clinical practice is our aim. First, the correction curves showed a good degree of agreement between the predicted outcomes of this constructed clinical prediction model and the patients' perceptions of the true outcomes (**Figure 4A**). Subsequently, the PCA analysis showed that patients with breast cancer with and without tumor metastases could be differentiated according to the variables used in the model (**Figure 4B**). Ultimately, based on a multivariate logistic regression model, the nomogram was prepared to facilitate its use in clinical settings (**Figure 4C**). Nomograms are composed of selected feature variables and their corresponding scores. The total score was obtained by summing the corresponding scores for each variable before converting it directly to obtain the probability of tumor metastasis. Therefore, the nomogram ensures that a patient's likelihood of developing metastases can easily be assessed by using important clinical features, preoperative US findings, and postoperative pathological information.

Relationship Between *TRIM67* and US and Postoperative Pathology

Variables in the clinical prediction model have been discussed further in this section. The tumor size observed on US

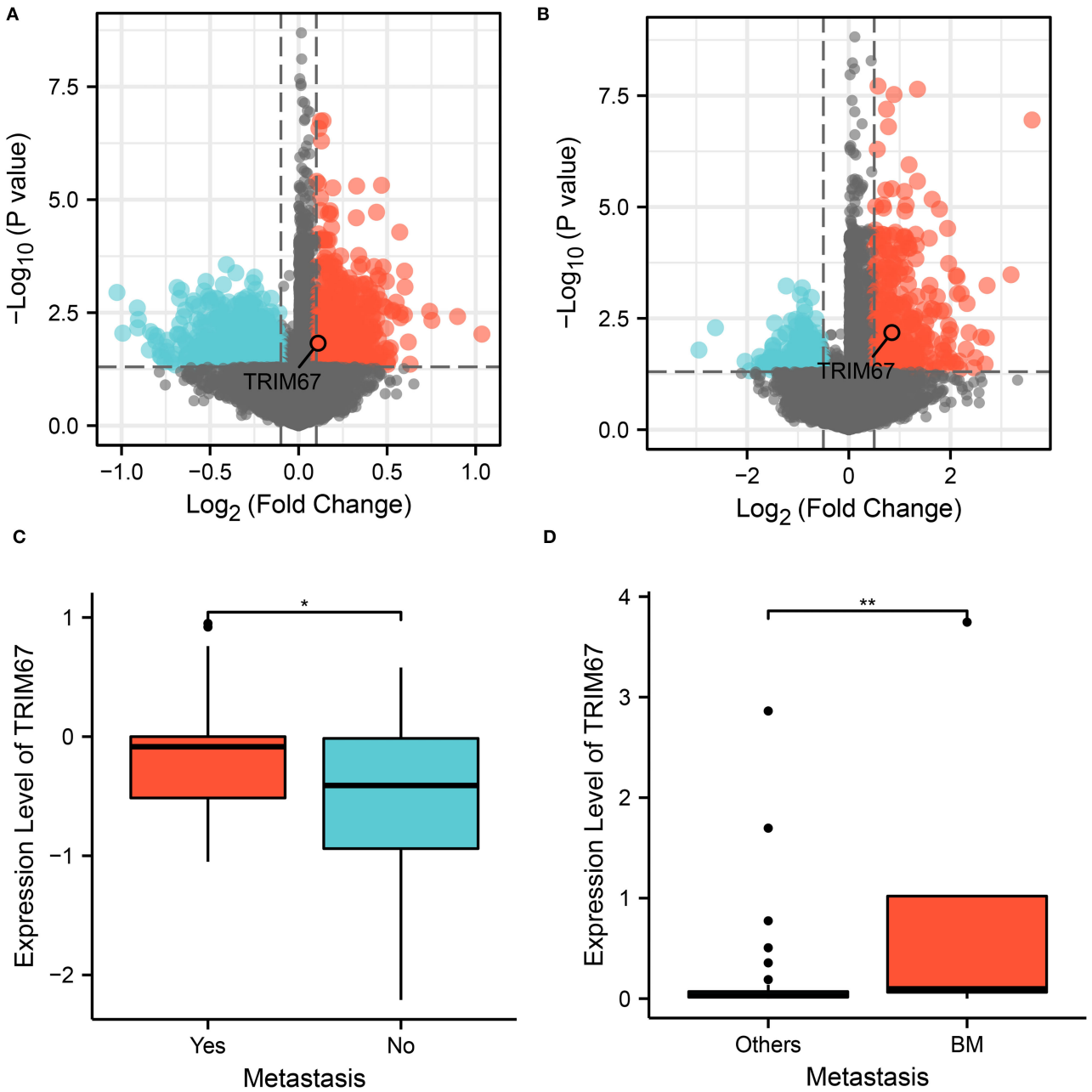

FIGURE 1 | Analysis of variance showed that *TRIM67* was upregulated in both DM and BM. **(A)** Volcano plot showing differentially expressed genes between the DM and nDM groups, where *TRIM67* was found to be upregulated in DM; **(B)** Differential expression analysis between BM and nBM groups showed that *TRIM67* was upregulated in BM; **(C)** There was a statistically significant difference in *TRIM67* expression between the DM and nDM groups ($p = 0.021$); **(D)** There was a statistically significant difference in *TRIM67* expression between the BM and nBM groups ($p = 0.007$).

examinations appeared to correlate with the T stage in the TNM classification (**Figure 5A**). Furthermore, the distribution of N grades in the TNM grading showed significant differences between the US-predicted lymph node metastasis group and the US-predicted non-lymphoid node metastasis group ($p < 0.05$, **Figure 5B**). These results demonstrated that, in the clinical prediction model, the tumor size measured using US reflects the T-staging of the tumor, whereas the N-staging corresponds to the lymph node metastasis predicted by US. This illustrated the important role of ultrasonography in predicting the development of tumor metastases in patients with breast cancer. In addition, normal and tumor tissues showed different *TRIM67* expression levels (**Figure 5C**). Additionally, significant differences in *TRIM67* expression were identified between

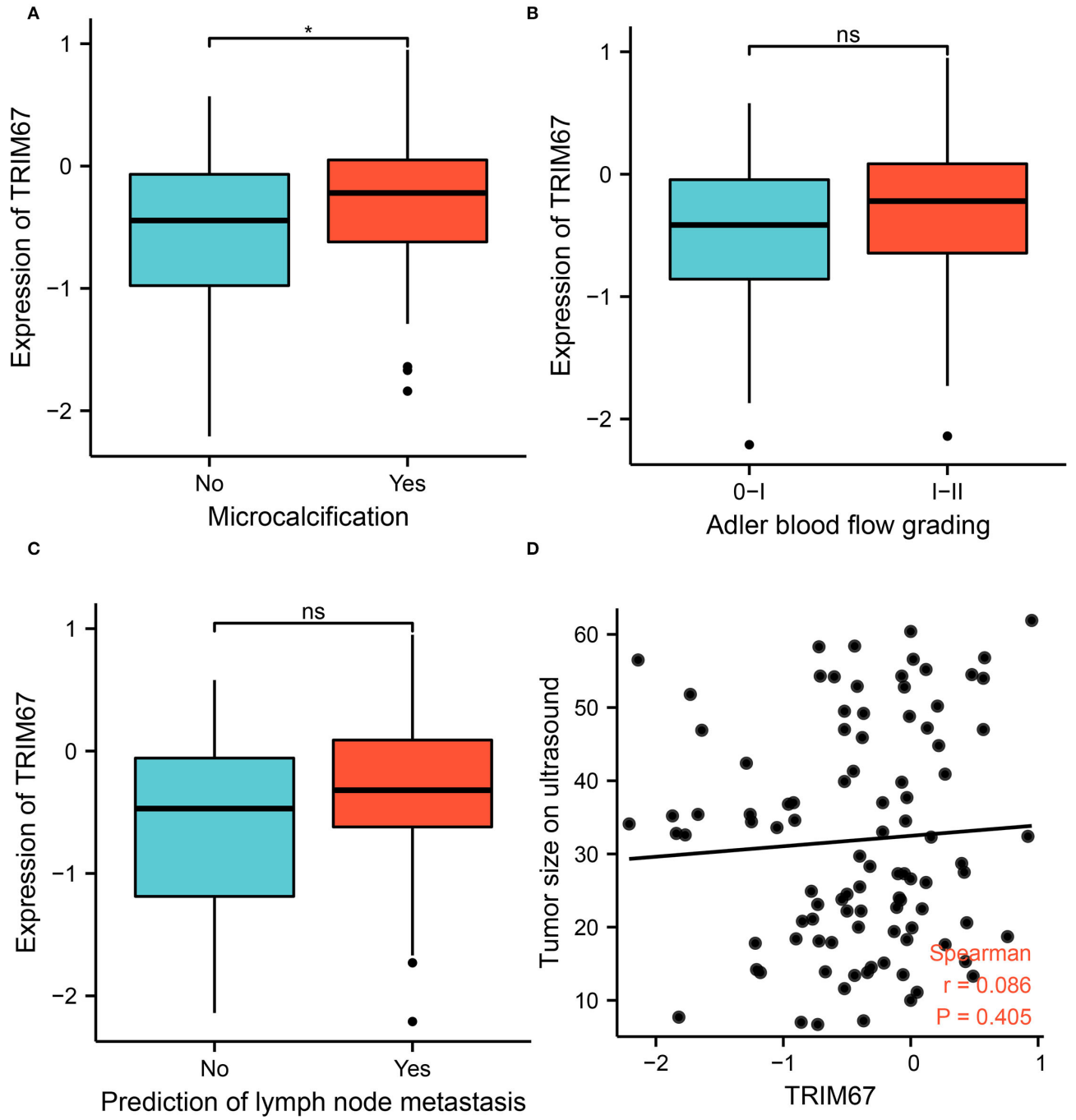

FIGURE 2 | Relationship between US-related features and *TRIM67* expression. **(A)** Microcalcifications in tumor tissue correlated with *TRIM67* expression ($p = 0.027$); **(B,C)** The bar graph shows the relationship between Adler blood flow grading and lymph node metastasis in relation to differential expression of *TRIM67*; **(D)** Correlation analysis of tumor size on US and *TRIM67* expression.

T1, T2, T3, and T4 (**Figure 5D**). Therefore, T staging can reflect *TRIM67* expression to some extent. The abovementioned results demonstrated the complex interrelationship between ultrasonography-related features, postoperative pathological grading, and *TRIM67* expression.

Elevated *TRIM67* Suggests a Poor Prognosis

The KM curve for *TRIM67* is shown in **Figure 6A**. Median overall survival time from the initial diagnosis of breast cancer was significantly shorter in the high *TRIM67* group than

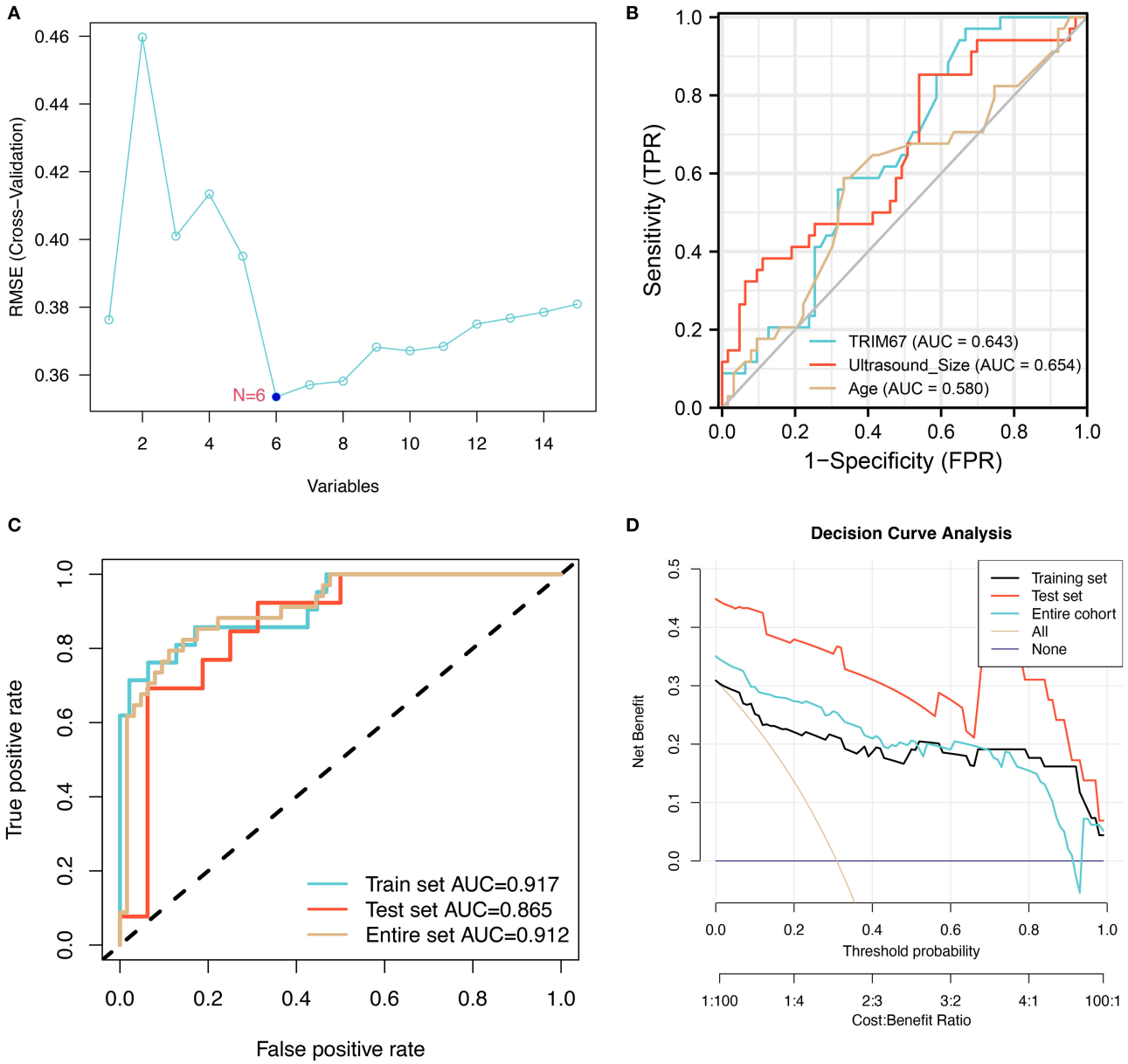

FIGURE 3 | The training process and performance evaluation of SVM-RFE models. **(A)** The variable screening process showed the smallest RMSE for the model when six variables were selected; **(B)** The ROCs show the predictive power of *TRIM67*, tumor size, and age on tumor metastasis in a selection of six variables; **(C)** The ROC shows the predictive power of a logistic regression model combining six indicators for tumor metastasis; **(D)** The DCA suggested that the clinical prediction model has a good range of clinical use in the training, test, and overall groups.

in the low *TRIM67* group (9.6 vs. 12.2 years, respectively, $p = 0.031$). Univariate Cox analysis showed a statistical difference between *TRIM67* expression and survival outcome ($p = 0.032$, HR = 1.42, 95% CI: 1.03–1.95). The ROC curves showed that the predicted AUC of *TRIM67* for overall survival at 1, 3, and 5 years were 0.543, 0.570, and 0.556, respectively (**Figure 6B**). These results suggested that elevated *TRIM67* was associated with a poor prognosis in patients with breast cancer.

Pathways Enriched by Concomitant *TRIM67* Upregulation in BM

To further explore the possible functional pathways involved in *TRIM67* in BM in patients with breast cancer, we used RNA sequencing data from patients with breast cancer who developed distant tumor metastasis in TCGA for Gene Set Enrichment Analysis (GSEA). The results showed that in *TRIM67*-upregulated tumors, the integrated breast cancer pathway was upregulated, whereas the miRNA targets in ECM

TABLE 3 | Included variables of the nomogram-based model.

Variables	β	Odds ratio (95% CI)	p
(Intercept)	−4.220	0.01 (0–0.15)	0.003**
Stage (III–IV vs. I–II)	2.380	10.81 (2.98–47.76)	0.001**
TRIM67	1.240	3.46 (1.13–13.77)	0.047*
Size	0.020	1.02 (0.97–1.07)	0.478
Age (>50 vs. <50, years)	0.240	1.28 (0.33–5.08)	0.721
N (N1–3 vs. N0)	1.910	6.76 (0.96–138.87)	0.098
HER2 (Positive vs. Negative)	1.530	4.62 (1.27–19.14)	0.025*

β, *the regression coefficient; CI, confidence interval.*
*$p < 0.05$, **$p < 0.01$.

and membrane receptors and miRNAs involved in DNA damage response pathways were downregulated (**Figure 6C**). The *TRIM67* upregulation appeared to accompany the upregulation of the pathways related to breast cancer. In addition, *TRIM67* upregulation may be associated with the downregulation of certain miRNA-regulated functional pathways, including the role of membrane receptors targeted by miRNAs and their response in the DNA damage response. Alterations in these pathways may be associated with the development of BM in patients with breast cancer, and ultimately affect patient OS.

DISCUSSION

Ultrasound imaging is a new strategy for monitoring the activity of the blood–brain barrier, which can facilitate the diagnosis and treatment of metastatic tumors related to neurovascular tissues. In this study, we explored the possible role of US as well as *TRIM67* in the development of BM in breast cancer through a retrospective clinical cohort study and bioinformatics analysis. The *TRIM67* was identified as a factor associated with neurovascular metastasis, tumor metastasis, and prognostic survival in brain tumors in bioinformatics analysis of TCGA and breast cancer.

The *TRIM67* expression was correlated with microcalcifications on ultrasonography. Following this, we incorporated TRIM67 expression data, general clinical information, postoperative pathology, and US-related characteristics and screened six variables (stage, *TRIM67*, tumor size, N, age, and HER2 status) with the SVM–RFE method, which could predict the likelihood of tumor metastasis. Of these six features, tumor size measured using US correlates with the T classification of the tumor, whereas lymph node metastasis was predicted by US correlated with the N classification.

In this study, *TRIM67* was upregulated in patients with BM from breast cancer and DM. The previous studies on *TRIM67* in tumors have demonstrated that the *TRIM67* protein functions differently in different tumors. The *TRIM67* was reportedly downregulated in colorectal cancer and *TRIM67* inhibited tumor proliferation and metastasis (41, 42). The *TRIM67* promoted the progression of non-small cell lung cancer through the Notch pathway, including promoting cell proliferation, migration, and EMT (43). However, upregulation of *TRIM67* expression increased apoptosis in non-small cell lung cancer cells (44). Although the relationship between *TRIM67* and tumors remains unclear, all studies mentioned above reported that *TRIM67* was associated with tumor size, lymph node metastasis, tumor stage, and disease prognosis (41–43). Similar to the previous studies, we observed that *TRIM67* was associated with BM in breast cancer and was a risk factor for a poor prognosis. Microcalcifications on US findings correlated with *TRIM67* expression, and a higher blood flow grade, positive prediction of lymph node metastasis, and larger tumor size corresponded with higher *TRIM67* expression. In *TRIM67* upregulated tumors, the integrated breast cancer pathway was upregulated, whereas miRNA targets in ECM and membrane receptors and the miRNAs involved in DNA damage response pathways were downregulated. Therefore, these pathways may play an important role in the metastasis of breast cancer.

Microcalcification is an important early sign of breast cancer and its early diagnosis depends on the identification of suspected microcalcifications (45–47). The morphology and distribution of microcalcifications can be used to differentiate between benign and malignant lesions (48, 49). The previous studies have observed the presence of an association between microcalcifications and lymph node metastasis and prognosis in breast cancer (50, 51). BMP-2 is closely associated with microcalcification (50). The BMP signaling affects the invasiveness of breast cancer tumor cells (52). Similar to the previous studies, we observed that microcalcification and lymph node metastasis measured using US examinations were independent risk factors for distant tumor metastasis based on preoperative US. Ultrasound has been widely used to detect lymph node metastases in breast cancer. Ultrasound and needle biopsy of suspected lymph nodes could effectively identify the presence of lymph node metastases from breast cancer (53). Therefore, it is our understanding that microcalcification and lymph node metastasis play an important role in predicting breast cancer metastasis. In this study, *TRIM67* was associated with tumor microcalcification, and ultrasonography may reflect changes in *TRIM67* to some extent by monitoring the status of microcalcifications. The *TRIM67* expression is associated with DM in breast cancer; therefore, US combined with examination of *TRIM67* expression may have a better predictive function in breast cancer metastases.

The six variables screened by SVM–RFE were used to construct clinical prediction models. Using the nomogram, we can easily assess the likelihood of tumor metastasis in patients with breast cancer using important clinical features, preoperative US findings, and postoperative pathological information. Tumor size measured *via* US examination reflects the T-grade of the tumor, whereas the N-grade corresponds to the lymph node metastases predicted by US. Similar findings have been observed in the previous studies on the relationship between US and clinicopathological features of breast cancer. Li et al. reported that the pathological grading of breast cancer correlated with the shape of the tumor measured using US (54). Lamb et al. found that the grade and infiltration of breast cancer correlated with the echogenicity and tumor margin measured by US (55). This highlighted the important role of ultrasonography in

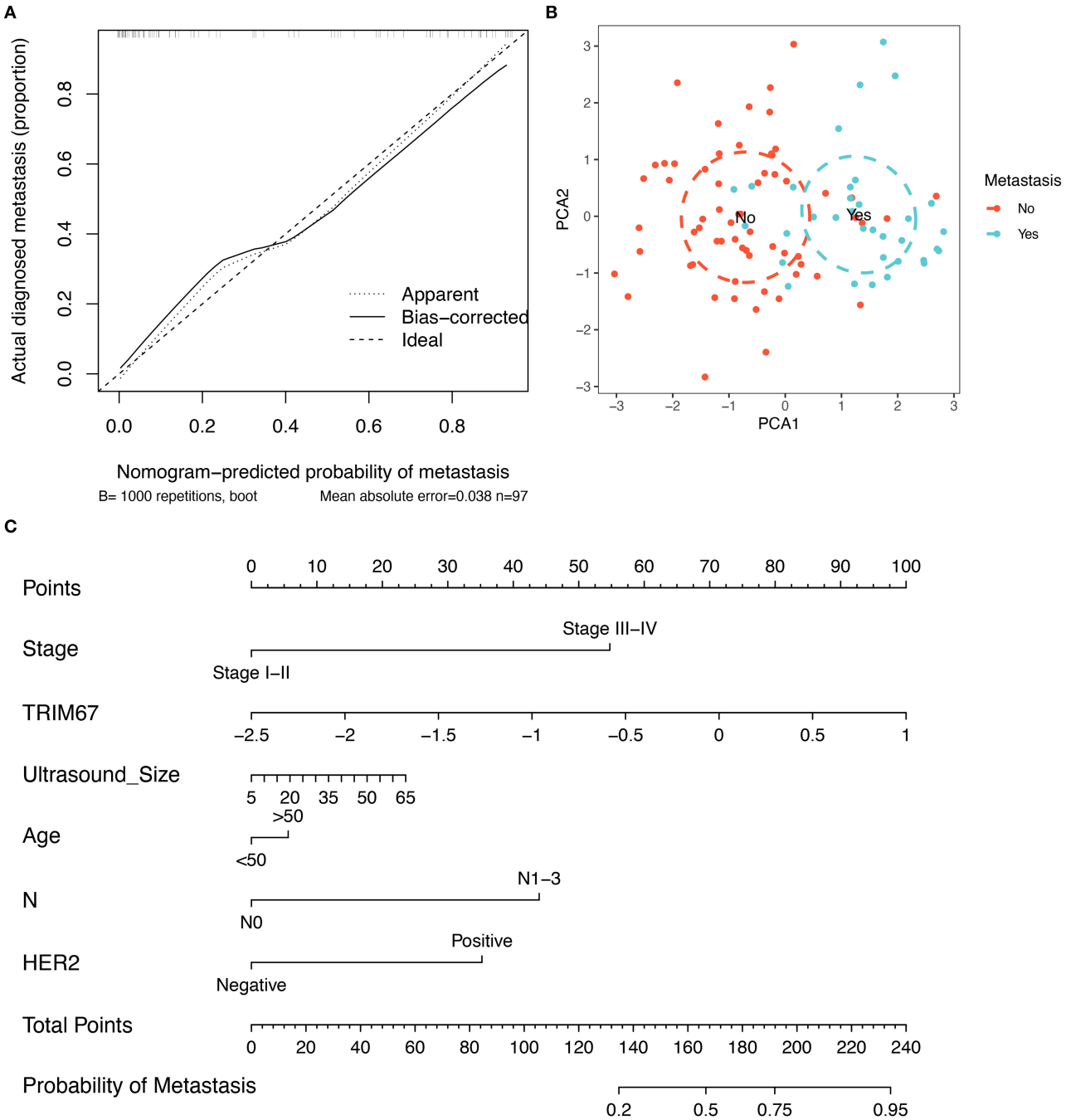

FIGURE 4 | Construction of a clinical prediction model for tumor metastasis. **(A)** The correction curves show that the predicted outcomes of this clinical prediction model are in good agreement with the true outcomes of the patients; **(B)** The PCA visualization demonstrates the efficacy of using the six variables to differentiate patients with breast cancer who developed tumor metastases; **(C)** The nomogram, constructed based on a clinical prediction model, allows an assessment of the likelihood of tumor metastasis based on these six variables.

predicting the development of tumor metastases in patients with breast cancer.

Upregulation of *TRIM67* was accompanied by upregulation of the pathways associated with breast cancer. In addition, the upregulation of *TRIM67* may be associated with the downregulation of certain miRNA-regulated functional pathways, including the role of membrane receptors targeted by miRNAs and response in the DNA damage response. Alterations in these pathways may be associated with the development of BM in patients with breast cancer and ultimately affect their OS.

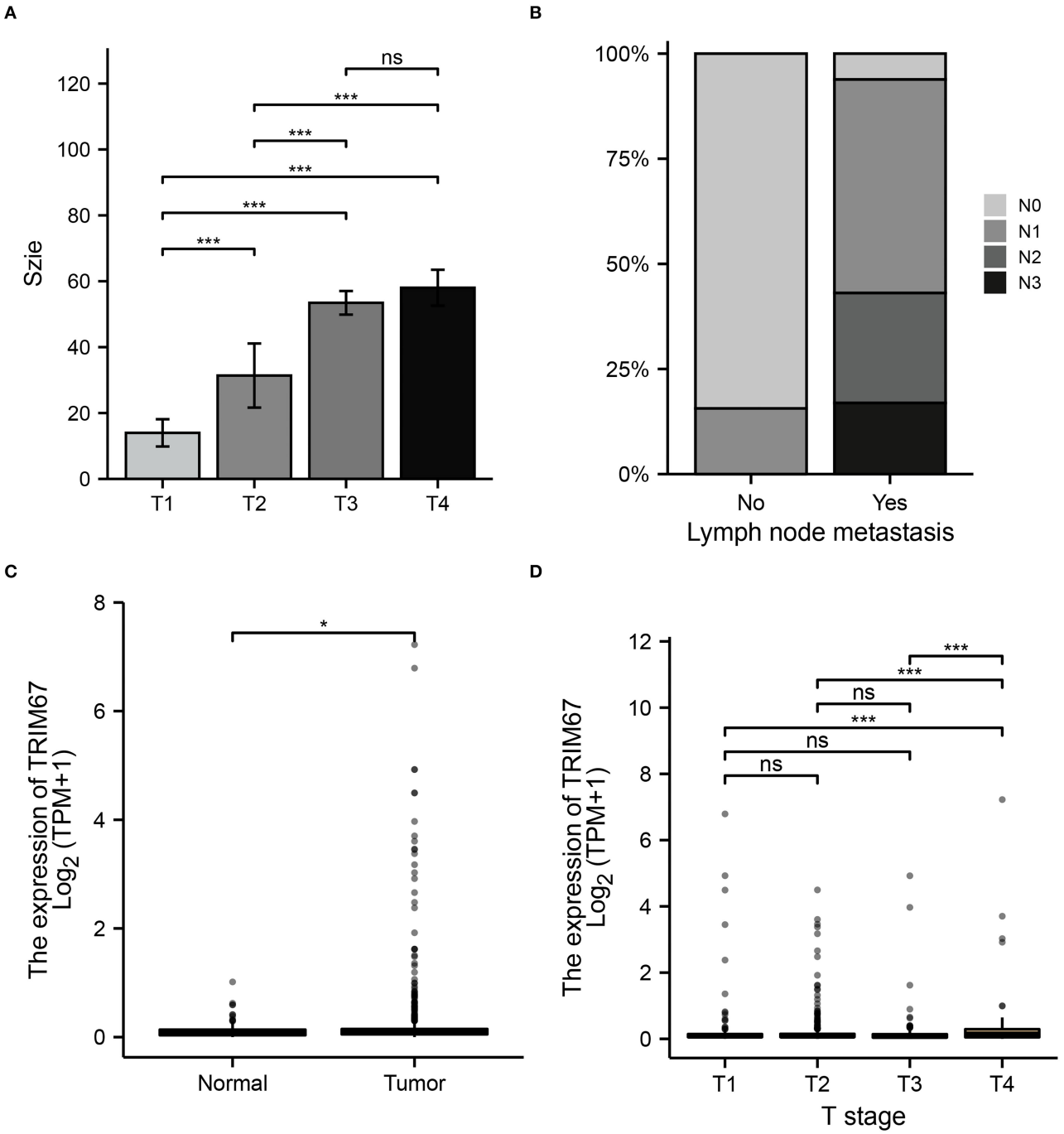

FIGURE 5 | Relationship between preoperative ultrasonography and *TRIM67* and postoperative pathological features. **(A)** The bar chart shows a correlation between the T-grading of the tumor and the size of the tumor as measured using preoperative US; **(B)** There was a correlation between US-predicted lymph node metastasis and the N grade of the tumor; **(C)** There were differences in *TRIM67* expression between normal and tumor tissues; **(D)** There were differences in *TRIM67* expression between different tumor T-grades.

In the future, further in-depth studies are warranted to address the relationship between the role of US and related molecules in breast cancer.

There are some limitations to this study. Patients with BM from breast cancer were not compared to patients without BM as a separate group in the clinical study population. We

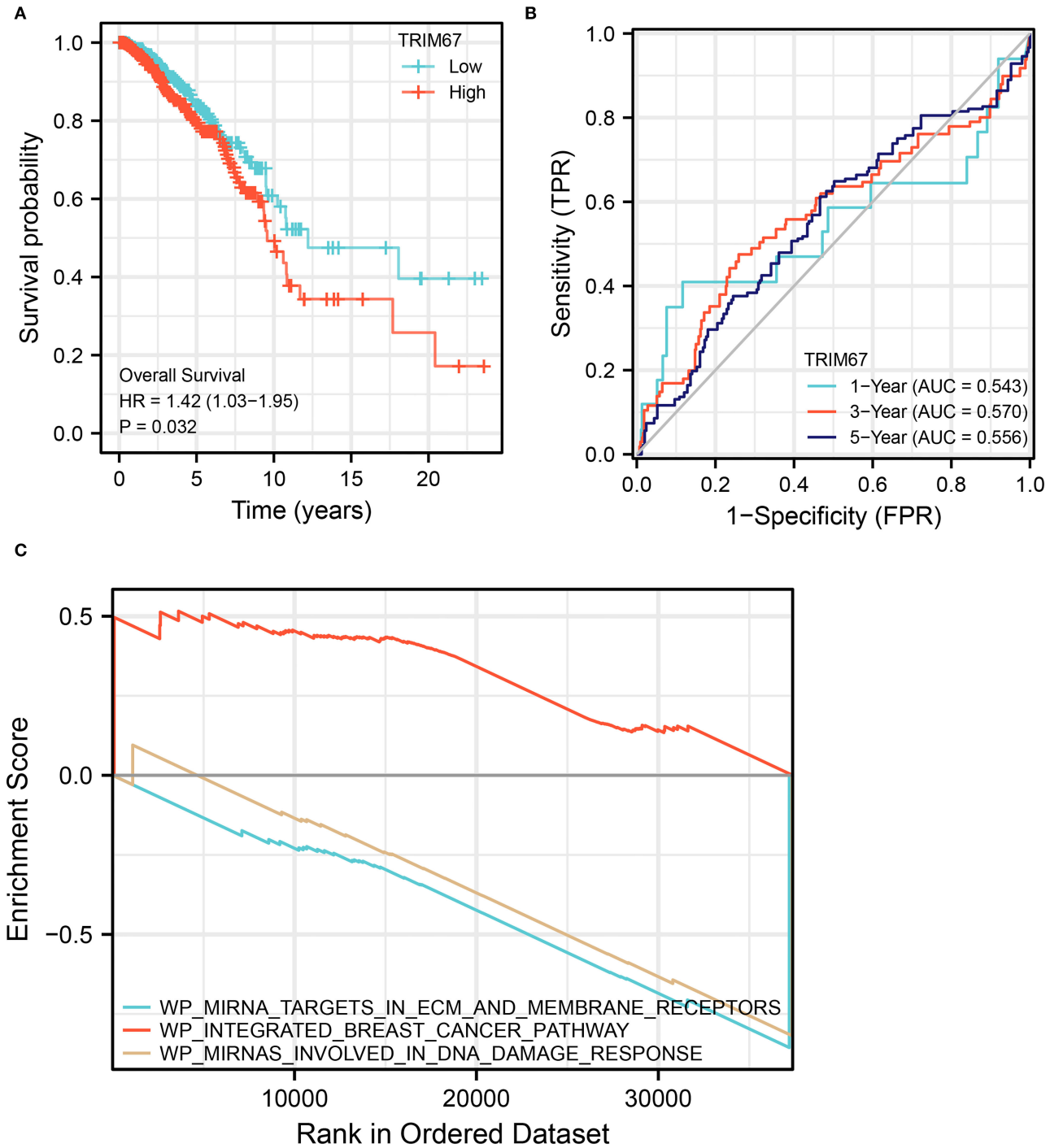

FIGURE 6 | Survival analysis and GSEA for *TRIM67*. **(A)** KM curves showed significant differences ($p = 0.032$) in survival curves between high and low *TRIM67* groups for patients with breast cancer; **(B)** ROC shows the predictive power of *TRIM67* for overall survival at 1, 3, and 5 years; **(C)** GSEA shows the functional pathways that are enriched when *TRIM67* is upregulated.

aim to expand the sample size for further detailed analysis in the future. Additionally, we will further investigate the mechanism of *TRIM67* in breast cancer metastasis at the basic experimental level.

CONCLUSION

Several risk factors were examined in this study associated with BRCA brain metastases. Ultrasound and its prediction of

TRIM67 play an important predictive role in neurovascular-related metastases from breast cancer. The nomogram of six variables—stage, *TRIM67*, tumor size, N, age, and HER2 status—were biomarkers of the likelihood of breast cancer metastasis.

DATA AVAILABILITY STATEMENT

The original contributions presented in the study are included in the article/supplementary material, further inquiries can be directed to the corresponding authors.

ETHICS STATEMENT

The studies involving human participants were reviewed and approved by the Ethics Committee of Cangzhou Central Hospital. The patients/participants provided their written informed consent to participate in this study.

AUTHOR CONTRIBUTIONS

ZX, TM, YQ, and YG performed the data curation and analysis. ZX and TM analyzed and interpreted the results. ZX drafted and reviewed the manuscript. TM provided funding. All authors read and approved the final manuscript.

ACKNOWLEDGMENTS

The authors wish to thank all patients and staff who participated in this study.

REFERENCES

1. Badakhshi H, Engeling F, Budach V, Ghadjar P, Zschaeck S, Kaul D. Are prognostic indices for brain metastases of melanoma still valid in the stereotactic era? *Radiat Oncol.* (2018) 13:3. doi: 10.1186/s13014-017-0951-4
2. Kotecki N, Lefranc F, Devriendt D, Awada A. Therapy of breast cancer brain metastases: challenges, emerging treatments and perspectives. *Ther Adv Med Oncol.* (2018) 10:175883591878031. doi: 10.1177/1758835918780312
3. Tao J, Gao Z, Huang R, Li H. Therapeutic effect of combined hyperbaric oxygen and radiation therapy for single brain metastasis and its influence on osteopontin and MMP-9. *Exp Ther Med.* (2018) 17:465–471. doi: 10.3892/etm.2018.6930
4. Taillibert S, Le Rhun É. Épidémiologie des lésions métastatiques cérébrales. *Cancer Radiothér.* (2015) 19:3–9. doi: 10.1016/j.canrad.2014.11.001
5. Garcia-Alvarez A, Papakonstantinou A, Oliveira M. Brain metastases in HER2-positive breast cancer: current and novel treatment strategies. *Cancers.* (2021) 13:2927. doi: 10.3390/cancers13122927
6. Brosnan EM, Anders CK. Understanding patterns of brain metastasis in breast cancer and designing rational therapeutic strategies. *Ann Transl Med.* (2018) 6:163. doi: 10.21037/atm.2018.04.35
7. Iadecola C. The neurovascular unit coming of age: a journey through neurovascular coupling in health and disease. *Neuron.* (2017) 96:17–42. doi: 10.1016/j.neuron.2017.07.030
8. Haskó J, Fazakas C, Molnár K, Mészáros Á, Patai R, Szabó G, et al. Response of the neurovascular unit to brain metastatic breast cancer cells. *Acta Neuropathol Commun.* (2019) 7:133. doi: 10.1186/s40478-019-0788-1
9. Arnold J, Schattschneider J, Blechner C, Krisp C, Schlüter H, Schweizer M, et al. Tubulin Tyrosine Ligase Like 4 (TTLL4) overexpression in breast cancer cells is associated with brain metastasis and alters exosome biogenesis. *J Exp Clin Cancer Res.* (2020) 39:205. doi: 10.1186/s13046-020-01712-w
10. Patil A, Sherbet GV. Therapeutic approach to the management of HER2-positive breast cancer metastatic to the brain. *Cancer Lett.* (2015) 358:93–9. doi: 10.1016/j.canlet.2014.12.026
11. Liebner S, Dijkhuizen RM, Reiss Y, Plate KH, Agalliu D, Constantin G. Functional morphology of the blood–brain barrier in health and disease. *Acta Neuropathol.* (2018) 135:311–36. doi: 10.1007/s00401-018-1815-1
12. Wu G-G, Zhou L-Q, Xu J-W, Wang J-Y, Wei Q, Deng Y-B, et al. Artificial intelligence in breast ultrasound. *WJR.* (2019) 11:19–26. doi: 10.4329/wjr.v11.i2.19
13. Zhang Y-N, Wang C-J, Xu Y, Zhu Q-L, Zhou Y-D, Zhang J, et al. Sensitivity, specificity and accuracy of ultrasound in diagnosis of breast cancer metastasis to the axillary lymph nodes in Chinese patients. *Ultrasound Med Biol.* (2015) 41:1835–41. doi: 10.1016/j.ultrasmedbio.2015.03.024
14. Gutierrez Blanco C, Evans EB, Porter AJ. Breast cancer diagnosis in a specialised breast clinic: are cancers detected by ultrasound alone less aggressive? *J Med Imaging Radiat Oncol.* (2019) 63:40–6. doi: 10.1111/1754-9485.12826
15. Alsheh Ali M, Eriksson M, Czene K, Hall P, Humphreys K. Detection of potential microcalcification clusters using multivendor for-presentation digital mammograms for short-term breast cancer risk estimation. *Med Phys.* (2019) 46:1938–46. doi: 10.1002/mp.13450
16. Relea A, Alonso JA, González M, Zornoza C, Bahamonde S, Viñuela BE, et al. Utilidad del artefacto Doppler de centelleo de color (twinkle) en la detección ecográfica de microcalcificaciones mamarias. *Radiología.* (2018) 60:413–23. doi: 10.1016/j.rx.2018.04.004
17. Zhao X, Yang X, Fu L, Yu K. Associations of estrogen receptor, progesterone receptor, human epidemic growth factor Receptor-2 and Ki-67 with ultrasound signs and prognosis of breast cancer patients. *CMAR.* (2021) 13:4579–86. doi: 10.2147/CMAR.S276422
18. Yan J, Liu X-L, Han L-Z, Xiao G, Li N-L, Deng Y-N, et al. Relation between Ki-67, ER, PR, Her2/neu, p21, EGFR, and TOP II-α expression in invasive ductal breast cancer patients and correlations with prognosis. *Asian Pac J Cancer Prev.* (2015) 16:823–9. doi: 10.7314/APJCP.2015.16.2.823
19. Canzoneri R, Lacunza E, Abba MC. Genomics and bioinformatics as pillars of precision medicine in oncology. *Medicina.* (2019) 79:587–92.
20. Kang X, Chen Y, Yi B, Yan X, Jiang C, Chen B, et al. An integrative microenvironment approach for laryngeal carcinoma: the role of immune/methylation/autophagy signatures on disease clinical prognosis and single-cell genotypes. *J Cancer.* (2021) 12:4148–71. doi: 10.7150/jca.58076
21. Sun C, Ma S, Chen Y, Kim NH, Kailas S, Wang Y, et al. Diagnostic value, prognostic value, and immune infiltration of LOX family members in liver cancer: bioinformatic analysis. *Front Oncol.* (2022) 12:843880. doi: 10.3389/fonc.2022.843880
22. Lois H. New advances in immunotherapy for prostate cancer. *Life Res.* (2019) 2:152. doi: 10.53388/life2019-1025-302
23. Du Y, Miao W, Jiang X, Cao J, Wang B, Wang Y, et al. The epithelial to mesenchymal transition related gene calumenin is an adverse prognostic factor of bladder cancer correlated with tumor microenvironment remodeling, gene mutation, and ferroptosis. *Front Oncol.* (2021) 11:683951. doi: 10.3389/fonc.2021.683951
24. An N, Yang X. Identification of prognostic genes through expression differentiation during metastatic process in lung adenocarcinoma. *Sci Rep.* (2017) 7:11119. doi: 10.1038/s41598-017-11520-6
25. Hu L, Su L, Cheng H, Mo C, Ouyang T, Li J, et al. Single-cell RNA sequencing reveals the cellular origin and evolution of breast cancer in *BRCA1* mutation carriers. *Cancer Res.* (2021) 81:2600–11. doi: 10.1158/0008-5472.CAN-20-2123
26. Wang L, Mo C, Wang L, Cheng M. Identification of genes and pathways related to breast cancer metastasis in an integrated cohort. *Eur J Clin Invest.* (2021) 51:e13525. doi: 10.1111/eci.13525
27. Li M, Li Q, Yin Q, Wang Y, Shang JM, Wang LH. Evaluation of color Doppler ultrasound combined with plasma miR-21 and miR-27a in the diagnosis of breast cancer. *Clin Transl Oncol.* (2021) 23:709–17. doi: 10.1007/s12094-020-02501-9

28. Adler DD, Carson PL, Rubin JM, Quinn-Reid D. Doppler ultrasound color flow imaging in the study of breast cancer: Preliminary findings. *Ultrasound Med Biol.* (1990) 16:553–9. doi: 10.1016/0301-5629(90)90020-D
29. Min Y, Huang Y, Wei M, Wei X, Chen H, Wang X, et al. Preoperatively predicting the central lymph node metastasis for papillary thyroid cancer patients with Hashimoto's Thyroiditis. *Front Endocrinol.* (2021) 12:713475. doi: 10.3389/fendo.2021.713475
30. Ying C, Guo C, Wang Z, Chen Y, Sun J, Qi X, et al. A prediction modeling based on the Hospital for Special Surgery (HSS) knee score for poor postoperative functional prognosis of elderly patients with patellar fractures. *Biomed Res Int.* (2021) 2021:6620504. doi: 10.1155/2021/6620504
31. Ritchie ME, Phipson B, Wu D, Hu Y, Law CW, Shi W, et al. limma powers differential expression analyses for RNA-sequencing and microarray studies. *Nucleic Acids Res.* (2015) 43:e47. doi: 10.1093/nar/gkv007
32. Huang M-L, Hung Y-H, Lee WM, Li RK, Jiang B-R. SVM-RFE based feature selection and Taguchi parameters optimization for multiclass SVM classifier. *ScientificWorldJournal.* (2014) 2014:795624. doi: 10.1155/2014/795624
33. Bhadra S, Kumar CJ. An insight into diagnosis of depression using machine learning techniques: a systematic review. *Curr Med Res Opin.* (2022) 38:749–71. doi: 10.1080/03007995.2022.2038487
34. Hu C, Li Q, Shou J, Zhang F-X, Li X, Wu M, et al. Constructing a predictive model of depression in chemotherapy patients with Non-Hodgkin's Lymphoma to improve medical staffs' psychiatric care. *Biomed Res Int.* (2021) 2021:9201235. doi: 10.1155/2021/9201235
35. Blanche P, Dartigues J-F, Jacqmin-Gadda H. Estimating and comparing time-dependent areas under receiver operating characteristic curves for censored event times with competing risks. *Stat Med.* (2013) 32:5381–97. doi: 10.1002/sim.5958
36. Subramanian A, Tamayo P, Mootha VK, Mukherjee S, Ebert BL, Gillette MA, et al. Gene set enrichment analysis: a knowledge-based approach for interpreting genome-wide expression profiles. *Proc Natl Acad Sci.* (2005) 102:15545–50. doi: 10.1073/pnas.0506580102
37. Mei S, Li Y, Kang X. Prognostic and functional analysis of NPY6R in Uveal Melanoma using bioinformatics. *Dis Markers.* (2022) 2022:4143447. doi: 10.1155/2022/4143447
38. Lin W, Wang Y, Chen Y, Wang Q, Gu Z, Zhu Y. Role of calcium signaling pathway-related gene regulatory networks in ischemic stroke based on multiple WGCNA and single-cell analysis. *Oxid Med Cell Longev.* (2021) 2021:8060477. doi: 10.1155/2021/8060477
39. Chen Y, Sun Y, Xu Y, Lin W-W, Luo Z, Han Z, et al. Single-cell integration analysis of heterotopic ossification and fibrocartilage developmental lineage: endoplasmic reticulum stress effector Xbp1 transcriptionally regulates the notch signaling pathway to mediate fibrocartilage differentiation. *Oxid Med Cell Longev.* (2021) 2021:7663366. doi: 10.1155/2021/7663366
40. Yu G, Wang L-G, Han Y, He Q-Y. clusterProfiler: an R package for comparing biological themes among gene clusters. *OMICS.* (2012) 16:284–7. doi: 10.1089/omi.2011.0118
41. Liu Y, Wang G, Jiang X, Li W, Zhai C, Shang F, et al. *TRIM67* inhibits tumor proliferation and metastasis by mediating *MAPK11* in Colorectal Cancer. *J Cancer.* (2020) 11:6025–37. doi: 10.7150/jca.47538
42. Wang S, Zhang Y, Huang J, Wong CC, Zhai J, Li C, et al. TRIM67 activates p53 to suppress colorectal cancer initiation and progression. *Cancer Res.* (2019) 79:4086–98. doi: 10.1158/0008-5472.CAN-18-3614
43. Jiang J, Ren H, Xu Y, Wudu M, Wang Q, Liu Z, et al. *TRIM67* promotes the proliferation, migration, and invasion of non-small-cell lung cancer by positively regulating the notch pathway. *J Cancer.* (2020) 11:1240–9. doi: 10.7150/jca.38286
44. Liu R, Chen Y, Shou T, Hu J, Chen J, Qing C. TRIM67 promotes NF-κB pathway and cell apoptosis in GA-13315-treated lung cancer cells. *Mol Med Rep.* (2019) 20:2936–44. doi: 10.3892/mmr.2019.10509
45. Nalawade YV. Evaluation of breast calcifications. *Indian J Radiol Imaging.* (2009) 19:282–6. doi: 10.4103/0971-3026.57208
46. Gerasimova-Chechkina E, Toner BC, Batchelder KA, White B, Freynd G, Antipev I, et al. Loss of Mammographic tissue homeostasis in invasive lobular and ductal breast carcinomas vs. benign lesions. *Front Physiol.* (2021) 12:660883. doi: 10.3389/fphys.2021.660883
47. Lai C-J, Shaw CC, Geiser W, Chen L, Arribas E, Stephens T, et al. Comparison of slot scanning digital mammography system with full-field digital mammography system: comparison of slot scanning digital mammography system with full-field digital mammography system. *Med Phys.* (2008) 35:2339–46. doi: 10.1118/1.2919768
48. Burnside ES, Ochsner JE, Fowler KJ, Fine JP, Salkowski LR, Rubin DL, et al. Use of microcalcification descriptors in BI-RADS 4th edition to stratify risk of malignancy. *Radiology.* (2007) 242:388–95. doi: 10.1148/radiol.2422052130
49. Liu J, Huang L. Image-guided vacuum-assisted breast biopsy in the diagnosis of breast microcalcifications. *J Int Med Res.* (2018) 46:2743–53. doi: 10.1177/0300060518770577
50. Zhang L, Hao C, Wu Y, Zhu Y, Ren Y, Tong Z. Microcalcification and BMP-2 in breast cancer: correlation with clinicopathological features and outcomes. *OTT.* (2019) 12:2023–33. doi: 10.2147/OTT.S187835
51. Zheng K, Tan J-X, Li F, Wei Y-X, Yin X-D, Su X-L, et al. Relationship between mammographic calcifications and the clinicopathologic characteristics of breast cancer in Western China: a retrospective multi-center study of 7317 female patients. *Breast Cancer Res Treat.* (2017) 166:569–82. doi: 10.1007/s10549-017-4406-2
52. Ren J, Wang Y, Ware T, Iaria J, ten Dijke P, Zhu H-J. Reactivation of BMP signaling by suboptimal concentrations of MEK inhibitor and FK506 reduces organ-specific breast cancer metastasis. *Cancer Lett.* (2020) 493:41–54. doi: 10.1016/j.canlet.2020.07.042
53. Afzal S, Masroor I, Munir A, Idress R, Khan P, Khan S. Preoperative ultrasound-guided core biopsy of axillary nodes for staging of clinically negative axilla in breast cancer patients – A pilot study. *Cureus.* (2020) 12:e6718. doi: 10.7759/cureus.6718
54. Li J, Zhang K, Shi Z, Zhang X, Xie J, Liu J, et al. Triple-negative invasive breast carcinoma: the association between the sonographic appearances with clinicopathological feature. *Sci Rep.* (2018) 8:9040. doi: 10.1038/s41598-018-27222-6
55. Lamb PM, Perry NM, Vinnicombe SJ, Wells CA. Correlation between ultrasound characteristics, mammographic findings and histological grade in patients with invasive ductal carcinoma of the breast. *Clin Radiol.* (2000) 55:40–4. doi: 10.1053/crad.1999.0333

Conflict of Interest: The authors declare that the research was conducted in the absence of any commercial or financial relationships that could be construed as a potential conflict of interest.

Publisher's Note: All claims expressed in this article are solely those of the authors and do not necessarily represent those of their affiliated organizations, or those of the publisher, the editors and the reviewers. Any product that may be evaluated in this article, or claim that may be made by its manufacturer, is not guaranteed or endorsed by the publisher.

Copyright © 2022 Xuan, Ma, Qin and Guo. This is an open-access article distributed under the terms of the Creative Commons Attribution License (CC BY). The use, distribution or reproduction in other forums is permitted, provided the original author(s) and the copyright owner(s) are credited and that the original publication in this journal is cited, in accordance with accepted academic practice. No use, distribution or reproduction is permitted which does not comply with these terms.

frontiers | Frontiers in Neurology

ORIGINAL RESEARCH
published: 22 June 2022
doi: 10.3389/fneur.2022.893401

Associations of Abdominal Visceral Fat Content and Plasma Adiponectin Level With Intracranial Atherosclerotic Stenosis: A Cross-Sectional Study

Fei-Hong Wang[1†], Long-Yan Meng[1†], Tong-Ya Yu[1], Yan Tan[1], Hui Quan[1], Jia-Yu Hu[1], Qing-Ke Bai[2], Jun-Chao Xie[1*] and Yan-Xin Zhao[1*]*

[1] Department of Neurology, Shanghai Tenth People's Hospital, Tongji University School of Medicine, Shanghai, China, [2] Department of Neurology, Pudong New Area People's Hospital, Shanghai, China

Background: Abdominal obesity and adipocytokines are closely related to atherosclerosis, and adiponectin level is considered one of the important clinical indicators. This study aimed to analyze the associations of abdominal visceral fat content and adiponectin level with intracranial atherosclerotic stenosis (ICAS).

Methods: A total of 186 patients were enrolled in this study. Patients were distributed into ICAS and non-ICAS by the degree of artery stenosis. Plasma adiponectin levels and the ratio of visceral adipose tissue (VAT) to subcutaneous adipose tissue (SAT) were measured. The related factors of intracranial atherosclerotic stenosis were determined using multivariable logistic regression analysis.

Results: The VAT/SAT ratio (OR, 26.08; 95% CI, 5.92–114.83; $p < 0.001$) and adiponectin (OR, 0.61; 95% CI, 0.44–0.84; $p = 0.002$) were found to be the independent predictors of ICAS in a multivariable logistic regression analysis. The prevalence of ICAS increased (T1: 27.4%; T2: 50.0%; T3: 75.8%) as the VAT/SAT ratio tertile increased ($p < 0.001$). The prevalence of ICAS decreased (T1: 72.6%; T2: 54.8%; T3: 25.8%) as the adiponectin tertile increased ($p < 0.001$). In ROC curves analysis, VAT/SAT ratio had a sensible accuracy for the prediction of ICAS. The optimal cut-off value of VAT/SAT ratio to predict ICAS in this study was 1.04 (AUC: 0.747; $p < 0.001$; sensitivity: 67.4%; specificity: 74.7%). The optimal adiponectin cutoff was 3.03 ug/ml (AUC: 0.716; $p < 0.001$; sensitivity:75.8%; specificity: 61.5%).

Conclusion: Higher VAT/SAT ratio and lower plasma adiponectin levels were closely related to the increased risk of intracranial atherosclerotic stenosis.

Keywords: intracranial atherosclerotic stenosis, abdominal obesity, visceral adipose, adiponectin, stroke

OPEN ACCESS

Edited by:
Wen-Jun Tu, Chinese Academy of Medical Sciences and Peking Union Medical College, China

Reviewed by:
Sofya Pchelina, Petersburg Nuclear Physics Institute (RAS), Russia
Wen-Song Yang, First Affiliated Hospital of Chongqing Medical University, China

***Correspondence:**
Qing-Ke Bai
zhaozhenguo1@sina.com
Jun-Chao Xie
xiejunchao_sh@126.com
Yan-Xin Zhao
zhao_yanxin@126.com

[†]These authors have contributed equally to this work

Specialty section:
This article was submitted to Neurological Biomarkers, a section of the journal Frontiers in Neurology

Received: *10 March 2022*
Accepted: *25 May 2022*
Published: *22 June 2022*

Citation:
Wang F-H, Meng L-Y, Yu T-Y, Tan Y, Quan H, Hu J-Y, Bai Q-K, Xie J-C and Zhao Y-X (2022) Associations of Abdominal Visceral Fat Content and Plasma Adiponectin Level With Intracranial Atherosclerotic Stenosis: A Cross-Sectional Study. Front. Neurol. 13:893401. doi: 10.3389/fneur.2022.893401

INTRODUCTION

Ischemic stroke caused by intracranial atherosclerotic stenosis is frequent in the Asian, African–American, and Hispanic populations (1). Large artery intracranial occlusive disease (LAICOD) has become the most common subtype of stroke in the world (2). Stroke is the leading cause of death in China, with a high recurrence rate (3). ICAS is an important predictor of stroke and its recurrence (4, 5). Looking for the relevant factors of ICAS is of great significance for the prediction and early intervention of stroke.

Several studies previously investigated traditional risk factors associated with ICAS including sex, age, metabolic syndrome (MetS), hyperlipidemia, hypertension, diabetes, smoking, and hyperhomocysteinemia (6). Lipid metabolism disorders including elevated low-density lipoprotein cholesterol (LDL-C) and cholesterol levels are the most important modifiable factors for increased risk of recurrent stroke and ICAS-related vascular events (4). Obesity is closely related to cardiovascular events (7). However, little is known about the relationship between obesity and intracranial atherosclerosis. Several obesity-related parameters, such as waist circumference, body mass index (BMI), and waist to hip ratio (WHR) have shown a weaker correlation with intracranial atherosclerosis (8). Abdominal obesity may be more likely to cause atherosclerosis than systemic obesity (9). Measurement of central obesity, especially VAT, may be more closely related to intracranial atherosclerosis. The increase of visceral fat and the decrease of subcutaneous fat accumulation may be positively correlated to atherosclerosis (10). Adiponectin, secreted by adipocytes, is a unique adipokine that has anti-inflammatory, antioxidant, anti-atherosclerotic effects and also a significant inhibitory effect on obesity (11–13). A recent study showed that the adiponectin-transfected endothelial progenitor cells protected T2DM rats from cerebral ischemia-reperfusion injury by increasing angiogenesis (14). Previous reports have shown that the levels of circulating adiponectin are reduced in patients with obesity, T2DM, coronary artery diseases, carotid artery stenosis, and atherosclerotic plaques (15, 16). However, there are few investigations on the relationship between adiponectin and intracranial atherosclerosis. Therefore, this study aimed to investigate the relationship between visceral fat, adiponectin, and intracranial atherosclerosis.

METHODS

Study Design and Participants

This was a single-center cross-sectional study with 226 consecutive patients recruited from September 2018 to June 2019 at Shanghai Tenth People's Hospital. Patients were admitted if they satisfied the following conditions: Age $\geq$ 45 years, complete abdominal non-enhanced CT (NECT), and CT angiography (CTA)/magnetic resonance angiography (MRA) of cerebral arteries. If the patient was $<$ 45 years old, had acute cerebral infarction, missed key clinical data, had a history of severe abdominal organ disease or previous abdominal surgery, they would be excluded. All patients gave their informed permission. Gender, age, smoking history, low-density lipoprotein cholesterol, diabetes, hypertension, and coronary heart disease were acquired as baseline characteristics of classical cerebrovascular risk factors. The patients fasted overnight and had 5 ml venous blood drawn the next morning. Within 4 h after anticoagulation with 2% EDTA, the blood was centrifuged at 3,000 rpm for 15 min. Plasma was kept at -80°C in a refrigerator. An enzyme-linked immunosorbent assay (ELISA) kit from MultiSciences in China was used to determine the concentration of plasma adiponectin. Self-reported history of hypertension, use of anti-hypertensive medication before admission, and the diagnosis of hypertension after discharge are all considered hypertension. Diabetes mellitus (DM) was identified as a self-reported history of diabetes, diabetes medication, a glycated hemoglobin level of more than 7%, or a diabetes diagnosis at discharge. Smokers were defined as those who smoked for 6 months and had more than one cigarette per day, while heavy drinkers were defined as those whose average daily alcohol consumption was 2 units for men or 1 unit for women (17). For statistical purposes, we referred to some relevant references (18–20) and defined tertiles for adiponectin and VAT/SAT ratio separately as follows: T1, low-adiponectin (0.83–2.09 ug/ml); T2, middle-adiponectin (2.10–3.41 ug/ml); T3, high- adiponectin (3.42–6.38ug/ml); T1, low-VAT/SAT (0.30–0.84); T2, middle-VAT/SAT (0.85–1.13); T3, high-VAT/SAT (1.14–2.06).

Radiological Imaging

A 16-section NECT (uCT 510, United Imaging Healthcare) was used to perform abdominal CT images (120 kVp, 100 mAs, 5 mm slide thickness). The intracranial arteries were examined using computed tomography angiography (CTA) to see whether there were any atherosclerotic lesions. Participants with renal insufficiency or a contraindication to contrast agents had their cerebral arteries examined with MRA to see if they had atherosclerotic stenosis. MRA was done using a 3.0T Verio Scanner (Siemens, Erlangen, Germany).

The cerebral atherosclerotic stenosis of each major intracranial artery was examined by two professional radiologists who were not given any personal information about the individuals. If a conflict arises, it is handled by consultation. Severe stenosis occurs when the lumen diameter of an intracranial artery is decreased by 50%. A stenosis of 50% or more in the large intracranial arteries, including intracranial segments of the internal carotid artery (ICA), anterior cerebral artery (ACA), middle cerebral artery (MCA), posterior cerebral artery (PCA), basilar artery (BA), and intracranial segments of vertebral artery (VA) was classified as the ICAS. The warfarin–aspirin symptomatic intracranial disease (WASID) study criteria were used to measure intracranial artery stenosis. The percentage of stenosis in an intracranial artery was calculated using the following formula: the percentage of intracranial atherosclerotic stenosis $=$ {1–[(diameter of narrowest segment)/(diameter of normal segment)]} $\times$ 100%, where the diameter of the narrowest segment is the diameter of the artery at the site of the most severe stenosis, and diameter of the normal segment is the diameter of the proximal normal artery (21).

Measurements of the Abdominal Adipose-Relevant Parameters

The abdominal circumference was measured at the level of the navel. At the level of the navel, ImageJ 1.52a (National Institute of Health, USA) was used to calculate VAT, SAT, and total adipose tissue (TAT) (22). The attenuation threshold was −190 to −30 Hu. The region of interest (ROI) for subcutaneous adipose was drawn along the outline of the abdominal skin, and ROI for visceral adipose was drawn along the inner edge of the abdominal muscles and the anterior edge of the spine, and then the full pixel area within the attenuation of the region of interest was measured. TAT was calculated by VAT plus SAT (23). The VAT/SAT ratio was determined using these two parameters. The liver/spleen (L/S) attenuation ratio <1 was used to characterize non–alcoholic fatty liver disease (NAFLD). Regions of interest with an area of over 2 cm^2 were placed at different axial levels of the liver, while the spleen was in the same axial image correspondingly, vessels and biliary structures in the liver were avoided (22).

Statistical Analysis

We used the χ^2 test and Fisher's exact categorical variables test, as well as independent samples t-tests or Mann-Whitney U tests, depending on the distribution of continuous variables, to perform univariate analyses of demographic characteristics, vascular risk factors, laboratory indices, and imaging characteristics of patients in the ICAS and non-ICAS groups. The mean ± standard deviation or median with interquartile range is used to represent continuous variables. The Shapiro–Wilk test was employed to determine the distribution's normality. After examining standard cerebrovascular risk variables in the study, multivariable logistic regression analysis was used to discover

TABLE 1 | Clinical characteristics and abdominal adipose-relevant parameters of patients.

Variable	Total (*n* = 186)	Non-ICAS (*n* = 091)	ICAS (*n* = 95)	*P* value
Age (year)	67.19 ± 8.68	66.73 ± 8.31	67.64 ± 9.04	0.472
Male, *n* (%)	110 (59.1)	45 (49.4)	65 (68.4)	0.009
TAT area (cm^2)	341.66 ± 96.57	333.16 ± 95.26	349.80 ± 97.62	0.241
VAT area (cm^2)	169.72 ± 56.97	154.27 ± 52.30	184.53 ± 57.58	<0.001
SAT area (cm^2)	171.94 ± 53.91	178.89 ± 56.74	165.27 ± 50.45	0.086
VAT/SAT ratio	1.02 ± 0.31	0.89 ± 0.25	1.15 ± 0.30	<0.001
BMI (kg/ cm^2)	24.80 ± 2.01	24.65 ± 2.01	24.95 ± 2.02	0.309
Abdominal circumference (cm)	89.26 ± 10.57	87.69 ± 10.61	90.77 ± 10.37	0.046
NAFLD, *n* (%)	54 (29)	18 (19.8)	36 (37.9)	0.007
Smoking, *n* (%)	64 (34.4)	25 (27.5)	39 (41.1)	0.051
Drinking, *n* (%)	38 (20.4)	17 (18.7)	21 (22.1)	0.563
Diabetes mellitus, *n* (%)	81 (43.5)	28 (30.8)	53 (55.8)	0.001
Coronary heart disease, *n* (%)	24 (12.9)	11 (12.1)	13 (13.7)	0.745
Carotid intima-media thickness (mm)	0.79 ± 0.03	0.79 ± 0.03	0.80 ± 0.02	0.113
Carotid plaque, *n* (%)	98 (52.6)	44 (48.4)	54 (56.8)	0.246
Hypertension, *n* (%)	148 (79.6)	68 (74.7)	80 (84.2)	0.109
Triglyceride (mmol/L)	1.60 ± 1.04	1.58 ± 1.01	1.62 ± 1.08	0.822
Total cholesterol (mmol/L)	3.51 ± 1.47	3.64 ± 1.48	3.39 ± 1.46	0.250
HDL-C (mmol/L)	1.47 ± 0.95	1.54 ± 0.91	1.40 ± 1.00	0.284
LDL-C (mmol/L)	2.59 ± 1.01	2.67 ± 0.94	2.51 ± 1.06	0.268
Non-HDL-C (mmol/L)	2.04 ± 2.07	2.09 ± 2.05	2.00 ± 2.09	0.744
Creatinine (mmol/L)	76.84 ± 31.42	70.82 ± 35.51	82.60 ± 25.82	0.011
Uric acid (mmol/L)	337.20 ± 91.53	324.71 ± 84.90	349.16 ± 96.40	0.068
Fibrinogen (mmol/L)	2.76 ± 0.93	2.55 ± 0.77	2.96 ± 1.03	0.002
Glycated hemoglobin (%)	6.48 ± 1.21	6.30 ± 1.10	6.66 ± 1.28	0.042
Fasting glucose (mmol/L)	6.02 ± 1.90	5.85 ± 1.83	6.18 ± 1.96	0.234
Adiponectin (ug/ml)	2.89 ± 1.23	3.36 ± 1.27	2.43 ± 0.99	<0.001
LDL-C/HDL-C	2.11 ± 1.06	2.06 ± 1.01	2.16 ± 1.11	0.549
TC/HDL-C	3.09 ± 1.64	3.03 ± 1.57	3.15 ± 1.72	0.605
TG/HDL-C	1.42 ± 1.52	1.35 ± 1.35	1.48 ± 1.68	0.553
Non-HDL-C/HDL-C	2.09 ± 1.64	2.03 ± 1.57	2.15 ± 1.72	0.606

Data are presented as mean ± standard deviation or median (interquartile range) and numbers (percentage).
TAT, Total adipose tissue; VAT, Visceral adipose tissue; SAT, Subcutaneous adipose tissue; BMI, Body mass index; NAFLD, Nonalcoholic fatty liver disease; HDL-C, High-density lipoprotein cholesterol; LDL-C, Low-density lipoprotein cholesterol; ICAS, Intracranial atherosclerotic stenosis.

the independent risk factors of intracranial atherosclerosis. The connection between abdominal fat-related measures and adiponectin levels was assessed using the Spearman correlation coefficient. Subjects were placed into three groups with the same sample size based on the tertiles of plasma adiponectin level or VAT/SAT. The prevalence of ICAS was evaluated in each tertile of plasma adiponectin level or VAT/SAT. The efficacy of VAT/SAT and adiponectin to predict cerebral atherosclerosis was assessed using the receiver-operating characteristic (ROC) curve. To distinguish their prediction powers, researchers employed the MedCalc statistical software. The value $p < 0.05$ was regarded as statistically significant, and SPSS v25 was used for statistical analysis (IBM Corporation, New York, United States).

RESULTS

Due to a lack of key clinical data, a history of severe abdominal organ disease or previous abdominal surgery, 40 patients were removed from the data analysis. Finally, 186 patients (59.1% men; mean age: 67.19 ± 8.68 years) were enrolled in the study, including the non-ICAS group ($n = 91$; 48.9%) and the ICAS group ($n = 95$; 51.1%) (**Table 1**). When compared to the non-ICAS group, patients in the ICAS group had a larger VAT/SAT ratio (1.15 ± 0.30 vs. 0.89 ± 0.25, $p < 0.001$), a greater prevalence of NAFLD (37.9% vs. 19.8%, $p = 0.007$), a higher prevalence of diabetes (55.8% vs. 30.8%, $p = 0.001$), higher elevated fibrinogen levels (2.96 ± 1.03 vs. 2.55 ± 0.77, $p = 0.002$), and lower adiponectin levels (2.43 ± 0.99 vs. 3.36 ± 1.27, $p < 0.001$). However, there was no statistical significance in coronary heart disease, carotid intima-media thickness (IMT), carotid plaque, hypertension, triglyceride level, or LDL-C level between the two groups ($p>0.05$ for all). The lipid ratio is considered a good parameter for identifying ICAS (24). Referring to their research, we also included LDL-C/HDL-C, TC/HDL-C, TG/HDL-C, non-HDL-C/HDL-C in the analysis, and there was no statistical difference between the two groups (**Table 1**). Univariate analysis revealed that the ICAS group had a substantially larger abdominal perimeter, VAT area, and VAT/SAT than the non-ICAS group [90.77 ± 10.37 vs. 87.69 ± 10.61, $p = 0.046$; 184.53 ± 57.58 vs. 154.27 ± 52.30, $p < 0.001$; 1.15 ± 0.30 vs. 0.89 ± 0.25, $p < 0.001$] (**Table 1**). In multivariate logistic regression analysis, after controlling for potential confounders, we discovered that the VAT/SAT ratio (OR, 26.08; 95% CI, 5.92–114.83; $p < 0.001$), NAFLD (OR, 2.95; 95% CI, 1.33–6.50; $p = 0.008$), fibrinogen levels (OR, 1.80; 95% CI, 1.12–2.88; $p = 0.014$), diabetes mellitus (OR, 2.51; 95% CI, 1.22–5.18; $p = 0.013$), and comparatively low adiponectin levels (OR, 0.61; 95% CI, 0.44–0.84; $p = 0.002$) were independent predictors of increased ICAS risk (**Table 2**).

We used tertiles to categorize all VAT/SAT ratios and adiponectin levels to further investigate the relationship between ICAS, VAT/SAT, and adiponectin (**Figure 1**). The prevalence of ICAS increased (T1: 27.4%; T2: 50.0%; T3: 75.8%) as VAT/SAT ratio tertile increased ($p < 0.001$). The prevalence of ICAS decreased (T1: 72.6%; T2: 54.8%; T3: 25.8%) as adiponectin tertile increased ($p < 0.001$).

To investigate the relationship between adiponectin and obesity, we performed a Spearman correlation analysis of adiponectin and abdominal fat-related parameters (**Figure 2**; **Table 3**). VAT/SAT ratio ($R = -0.337$, $p < 0.001$) was negatively correlated with adiponectin compared with VAT ($R = -0.239$, $p = 0.001$), abdominal circumference ($R = -0.170$, $p = 0.021$), and BMI ($R = -0.155$, $p = 0.034$).

The ROC curve analysis illustrated the distinctive ability of independent risk factors to predict ICAS (**Figure 3**; **Table 4**). VAT/SAT ratio had sensible accuracy for the prediction of ICAS (AUC: 0.747; $p < 0.001$; sensitivity: 67.4%; specificity: 74.7%). The optimal cut-off value of VAT/SAT ratio was 1.04. The optimal adiponectin cutoff to predict ICAS in this study was 3.03 ug/ml (AUC: 0.716; $p < 0.001$; sensitivity: 75.8%; specificity: 61.5%).

TABLE 2 | Univariate and multivariate analysis of the risk factors for ICAS.

Variables	Univariate		Multivariate	
	OR (95% CI)	*P*	OR (95% CI)	*P*
Male, *n* (%)	2.22 (1.22–4.02)	0.009	–	–
VAT area (cm²)	1.01 (1.00–1.02)	<0.001	–	–
VAT/SAT ratio	37.45 (9.97–140.61)	<0.001	26.08 (5.92–114.83)	<0.001
Abdominal circumference (cm)	1.03 (1.00–1.06)	0.048	–	–
NAFLD, *n* (%)	2.48 (1.28–4.80)	0.007	2.95 (1.33–6.50)	0.008
Diabetes mellitus, *n* (%)	2.84 (1.56–5.18)	0.001	2.51 (1.22–5.18)	0.013
Creatinine (mmol/L)	1.02 (1.00–1.03)	0.016	–	–
Fibrinogen (mmol/L)	1.76 (1.20–2.57)	0.003	1.80 (1.12–2.88)	0.014
Glycated hemoglobin (%)	1.29 (1.00–1.66)	0.046	–	–
Adiponectin (ug/ml)	0.49 (0.37–0.65)	<0.001	0.61 (0.44–0.84)	0.002

P < 0.05 as assessed by the univariate logistic regression, variable was subsequently included in the multivariate analysis.
VAT, Visceral adipose tissue; SAT, Subcutaneous adipose tissue; NAFLD, Nonalcoholic fatty liver disease.

DISCUSSION

In this study, we explored the relationships between abdominal visceral fat content and clinical characteristics in non-ICAS and ICAS patients. We found that male gender, VAT area, VAT/SAT ratio, abdominal circumference, diabetes mellitus, creatinine level, fibrinogen level, glycated hemoglobin level, NAFLD, and adiponectin level were predictors of ICAS. VAT/SAT, NAFLD, diabetes mellitus, fibrinogen level, and lower adiponectin level were found to be independent risk factors for ICAS in a multivariable logistic regression analysis. Obesity is considered a risk factor for atherosclerosis (25). VAT contributed not only to general but also to the advancement of subclinical atherosclerosis, especially in ladies. Both previous research and

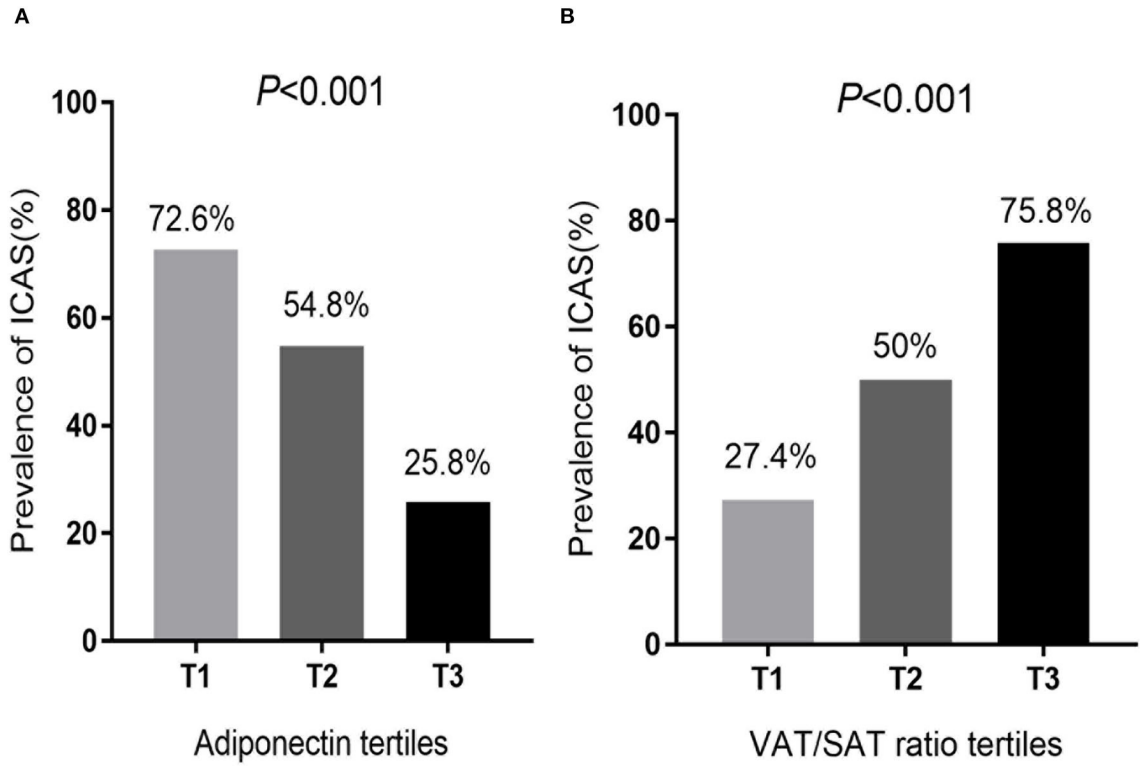

FIGURE 1 | Comparison of **(A)** adiponectin tertiles and **(B)** VAT/SAT ratio tertiles determined according to the prevalence of ICAS. **(A)** Participants were divided into 3 groups, T1: low-adiponectin (0.83–2.09 ug/ml), T2: middle-adiponectin (2.10–3.41 ug/ml), and T3: high-adiponectin (3.42–6.38 ug/ml). **(B)** Participants were divided into 3 groups, T1: low-VAT/SAT (0.30–0.84), T2: middle-VAT/SAT (0.85–1.13), and T3: high-VAT/SAT (1.14–2.06). VAT, Visceral adipose tissue; SAT, Subcutaneous adipose tissue; ICAS, Intracranial atherosclerotic stenosis.

our findings indicate that the particular part of VAT participated in the early advancement of atherosclerosis (26). In a general population sample from Norway, adiposity has consistently been associated with carotid atherosclerotic plaque burden (27). A small number of studies have investigated the association of BMI with ICAS, although they failed to demonstrate a significant association. However, as a measure of adiposity, BMI has limitations. Abdominal circumference is a sign of abdominal obesity, which is more closely related to subclinical atherosclerosis than BMI (28). Abdominal adiposity is associated with insulin resistance and atherosclerosis (29). It is speculated that the increased risk of abdominal obesity may be caused by the accumulation of large amounts of visceral fat tissue. However, abdominal parameters cannot be used to distinguish VAT from SAT, as the former has different biological characteristics and functions (30). Hence, we measured the abdominal fat including TAT, VAT, and SAT using abdominal CT. Previous research has suggested that the absolute value of VAT and SAT, as well as their ratio, may play a significant role in the progression of abdominal atherosclerosis (26). In our study, there was no statistical difference between the two groups in terms of the BMI, TAT area, and SAT.

Notably, VAT area, abdominal circumference, and VAT/SAT ratio are higher in the ICAS group than in the non-ICAS group. After adjusting the traditional cardiovascular risk factors, the VAT/SAT ratio remains an independent predictor. Previous studies have shown that VAT is metabolically active and causes chronic systemic inflammation through the secretion of adipokines, which is an important cause of insulin resistance caused by obesity (31, 32). Several studies have indicated that SAT has a protective effect against insulin sensitivity. When compared to the absolute value of VAT or SAT, the VAT/SAT ratio may be a better predictor of abdominal fat distribution.

Clinical research published over the last few decades has shown higher fibrinogen levels in people with atherosclerotic disease (33). Serum fibrinogen levels over a certain threshold may raise the risk of vascular disease by increasing viscosity, stimulating fibrin formation, or increasing platelet interaction. More inflammatory cytokines are produced as a result of a dysfunctional interaction between fat cells and tissue macrophages, which is linked to obesity (33, 34). Fibrinogen is closely linked with subclinical atherosclerosis in obese individual (35). Increased fibrinogen levels throughout time are closely linked to the occurrence of early carotid lesions, notably plaques. Recent studies have shown that in the Han population, higher fibrinogen levels are also independently related to the risk and severity of coronary atherosclerosis (36). We discovered that a high fibrinogen level was an independent predictor

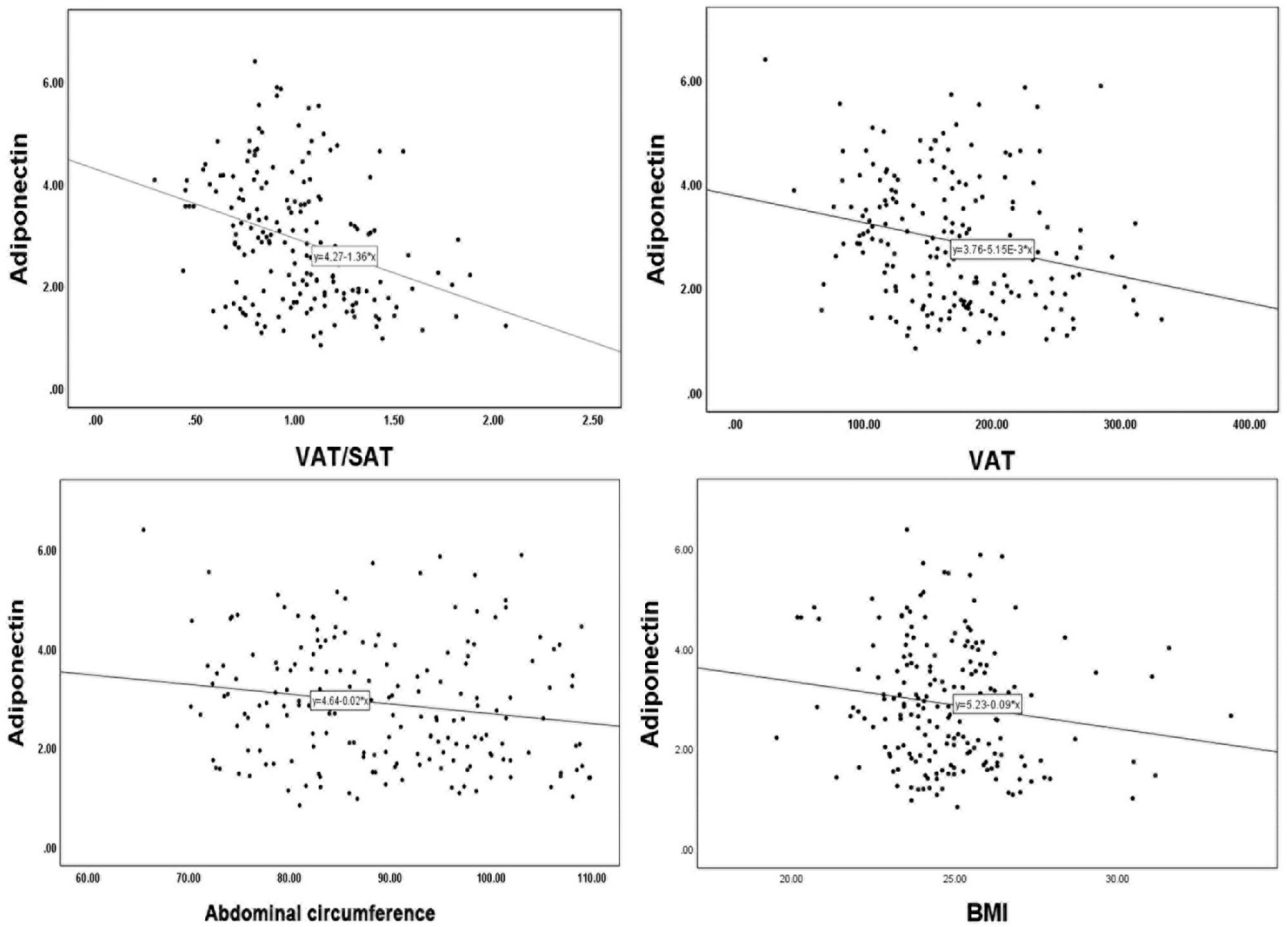

FIGURE 2 | Linear correlation analysis of adiponectin with VAT/SAT, VAT, abdominal circumference, BMI. VAT, visceral adipose tissue; SAT, subcutaneous adipose tissue; BMI, body mass index.

TABLE 3 | Spearman correlation analyses between adiponectin and VAT/SAT, VAT, abdominal circumference, and BMI.

Variables	R	*P* value
VAT/SAT ratio	−0.337	<0.001
VAT	−0.239	0.001
Abdominal circumference	−0.170	0.021
BMI	−0.155	0.034

VAT, Visceral adipose tissue; SAT, Subcutaneous adipose tissue; BMI, Body mass index.

of ICAS in this study. Fibrinogen is a powerful predictor of ischemic stroke, according to some studies, although it does not indicate the type or clinical outcomes of stroke (37). We suggest that high fibrinogen levels may be a predictor of a large atherosclerotic stroke.

Adiponectin is an adipocyte secretory protein whose levels in the blood are reduced in obese and diabetic individuals. It may be beneficial to atherosclerosis, inflammation, insulin resistance pathways, and lipid disorders, making it an appealing biomarker and therapeutic target for cardiometabolic diseases such as coronary heart disease, non–cardiac vascular diseases, MetS, NAFLD, and T2DM (15). Okauchi et al. pointed out that the serum adiponectin concentration is related to BMI, WC, and VAT of middle-aged people (38). The concentration of adiponectin in circulation is negatively correlated with body fat, especially visceral fat (39). In our study, we found that VAT/SAT ratio was more negatively correlated with adiponectin than VAT, BMI, and abdominal circumference (**Figure 2**; **Table 3**). Many studies showed that visceral fat accumulation and decreased plasma adiponectin concentration were associated with insulin sensitivity, insulin resistance, and vascular inflammation (40–42). Patients with large artery atherosclerosis (LAA) strokes reported lower levels of serum adiponectin than those who experienced non-LAA strokes (43). Bang OY et al. found that adiponectin levels were associated with intracranial atherosclerosis. Moreover, adiponectin levels varied by stroke subtype, with the ICAS group having the lowest (44). Their results are similar to our current findings that the lower plasma adiponectin levels were related to the increased

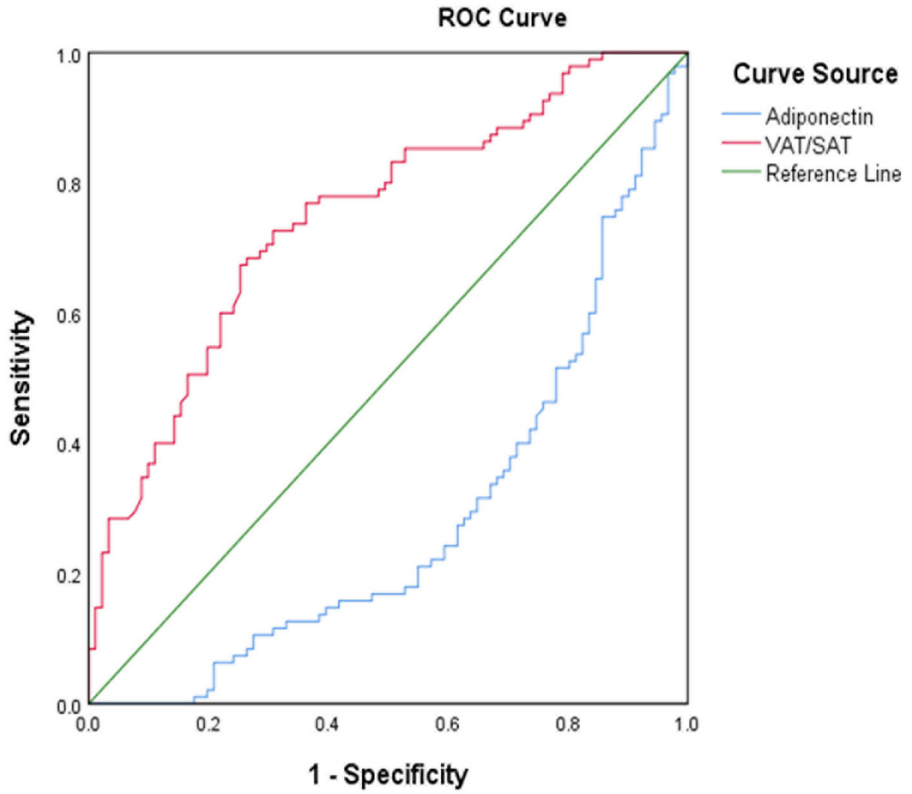

FIGURE 3 | ROC curve for VAT/SAT and adiponectin for distinguish between ICAS and non-ICAS. ROC, receiver operating characteristic curve; VAT, visceral adipose tissue; SAT, subcutaneous adipose tissue; ICAS, intracranial atherosclerotic stenosis.

TABLE 4 | ROC curve for predicting ICAS and cutoff points for maximum sum of sensitivity and specificity.

Variables	ROC (95%CI)	Cutoff point	Sensitivity (%)	Specificity (%)
VAT/SAT	0.75 (0.64–0.79)	1.04	67.4	74.7
Adiponectin	0.72 (0.68–0.82)	3.03	75.8	61.5

VAT, Visceral adipose tissue; SAT, Subcutaneous adipose tissue.

risk of intracranial atherosclerotic stenosis (ICAS). Here, we find that besides adiponectin, the VAT/SAT ratio appears to have a strong predictor for ICAS. Although a majority of clinical studies analyzed and compared total adiponectin levels and found the potential role of adiponectin in cardio-cerebrovascular diseases including cerebral infarction disease, it is also important to further explore the role of each isoform of adiponectin.

Adiponectin as a secreted multimeric protein has three isoforms: low molecular weight (LMW), medium molecular weight (MMW), and high molecular weight (HWM) (45). HMW adiponectin is the most active oligomeric form of adiponectin. There is evidence that circulating levels of total and HWM adiponectin are associated with coronary heart disease, ischemic stroke, and peripheral arterial disease (46). Besides, the research reported a positive association between LMW adiponectin and all-cause mortality in the elderly, which was thought contingent on unbalanced circulating levels of adiponectin isoforms (47). Noriko Tagawa et al. found that decreased total adiponectin, HMW adiponectin, and LMW adiponectin may be associated with atherosclerotic infarction, and that serum LMW adiponectin level was a credible biomarker for cerebrovascular disorders (48).

There are several limitations that need to be emphasized. Firstly, longitudinal observations are required to evaluate the longitudinal effects of visceral fat in the progression of ICAS. Secondly, because of the small sample size, there was no further precise classification of the atherosclerosis stenosis and $\geq$50% was used to determine significant stenosis in this study. Thirdly, previous studies have shown that the apo B/apo A-I ratio is considered to be an excellent surrogate for the prediction of vascular disease risk, such as ICAS (24, 49). Initially we wanted to include this parameter in the study, but for some economic reasons, our center does not routinely screen the two indicators of apo B and apo A-I. Such lipid parameters need to be further explored in a clinical or community study with a larger sample. Finally, the relationship between different isoforms of adiponectin and ICAS has not been studied here partly due to the difficulty in measuring each adiponectin isoform, and we will explore it in the future.

CONCLUSION

In conclusion, the higher VAT/SAT ratio and lower plasma adiponectin levels were closely related to the increased risk of ICAS. The traditional cardiovascular risk factor, diabetes mellitus, is still considered an independent predictor of ICAS. Adiponectin may have a protective effect against atherosclerosis. The VAT/SAT ratio appears to have a strong predictive ability for ICAS.

DATA AVAILABILITY STATEMENT

The raw data supporting the conclusions of this article will be made available by the authors, without undue reservation.

ETHICS STATEMENT

The studies involving human participants were reviewed and approved by Ethics Committee of Shanghai Tenth People's Hospital. The patients/participants provided their written informed consent to participate in this study.

AUTHOR CONTRIBUTIONS

Y-XZ, J-CX, and Q-KB conceived and designed the study. HQ and J-YH collected the clinical data. T-YY performed statistical analyses. F-HW and L-YM analyzed the data and drafted the paper and YT helped. All authors read and approved the final manuscript. All authors contributed to the article and approved the submitted version.

FUNDING

The present study was supported by the Science and Technology Commission of Shanghai Municipality (Grant Number: 20ZR1443500), the Featured Clinical Discipline Project of Shanghai Pudong (PWYst2018-01), Key Discipline Group Construction Project of Shanghai Pudong (PWZxq2017-02), the Clinical Research Project of Shanghai Tenth People's Hospital (YNCR2C030), and Clinical Research Project of Shanghai Municipal Health Commission (201940452).

ACKNOWLEDGMENTS

The authors are grateful to the study participants.

REFERENCES

1. Wong L. Global burden of intracranial atherosclerosis. *Int J Stroke.* (2006) 1:158–9. doi: 10.1111/j.1747-4949.2006.00045.x
2. Gorelick P, Wong K, Bae H, Pandey D. Large artery intracranial occlusive disease: a large worldwide burden but a relatively neglected frontier. *Stroke.* (2008) 39:2396–9. doi: 10.1161/STROKEAHA.107.505776
3. Miao H, Yang Y, Wang H, Huo L, Wang M, Zhou Y, et al. Intensive lipid-lowering therapy ameliorates asymptomatic intracranial atherosclerosis. *Aging Dis.* (2019) 10:258–66. doi: 10.14336/AD.2018.0526
4. Chimowitz M, Lynn M, Howlett-Smith H, Stern B, Hertzberg V, Frankel M, et al. Comparison of warfarin and aspirin for symptomatic intracranial arterial stenosis. *New Eng J Med.* (2005) 352:1305–16. doi: 10.1056/NEJMoa043033
5. Kern R, Steinke W, Daffertshofer M, Prager R, Hennerici M. Stroke recurrences in patients with symptomatic vs asymptomatic middle cerebral artery disease. *Neurology.* (2005) 65:859–64. doi: 10.1212/01.wnl.0000175983.76110.59
6. Ding X, Li C, Yu K, Gao A, Xiao L, Peng F, et al. Different risk factors between intracranial and extracranial atherosclerotic stenosis in Asian population: a systematic review and meta-analysis. *Int J Neurosci.* (2014) 124:834–40. doi: 10.3109/00207454.2013.879580
7. Kim S, Després J, Koh K. Obesity and cardiovascular disease: friend or foe? *Eur Heart J.* (2016) 37:3560–8. doi: 10.1093/eurheartj/ehv509
8. Ma Y, Leng X, Dong Y, Xu W, Cao X, Ji X, et al. Risk factors for intracranial atherosclerosis: a systematic review and meta-analysis. *Atherosclerosis.* (2019) 281:71–7. doi: 10.1016/j.atherosclerosis.2018.12.015
9. Fox C, Massaro J, Hoffmann U, Pou K, Maurovich-Horvat P, Liu C, et al. Abdominal visceral and subcutaneous adipose tissue compartments: association with metabolic risk factors in the framingham heart study. *Circulation.* (2007) 116:39–48. doi: 10.1161/CIRCULATIONAHA.106.675355
10. Bouchi R, Takeuchi T, Akihisa M, Ohara N, Nakano Y, Nishitani R, et al. High visceral fat with low subcutaneous fat accumulation as a determinant of atherosclerosis in patients with type 2 diabetes. *Cardiovasc Diabetol.* (2015) 14:136. doi: 10.1186/s12933-015-0302-4
11. Wong Y, Tse H. Circulating biomarkers for cardiovascular disease risk prediction in patients with cardiovascular disease. *Front Cardiovasc Med.* (2021) 8:713191. doi: 10.3389/fcvm.2021.713191
12. Reiterer M, Rajan M, Gómez-Banoy N, Lau J, Gomez-Escobar L, Ma L, et al. Hyperglycemia in acute COVID-19 is characterized by insulin resistance and adipose tissue infectivity by SARS-CoV-2. *Cell Metab.* (2021) 33:2174–88. doi: 10.1016/j.cmet.2021.10.014
13. Aronne L, Brown W, Isoldi K. Cardiovascular disease in obesity: A review of related risk factors and risk-reduction strategies. *J Clin Lipidol.* (2007) 1:575–82. doi: 10.1016/j.jacl.2007.10.005
14. Wang M, Li Y, Zhang R, Zhang S, Feng H, Kong Z, et al. Adiponectin-transfected endothelial progenitor cells have protective effects after 2-hour middle-cerebral artery occlusion in rats with type 2 diabetes mellitus. *Front Neurol.* (2021) 12:630681. doi: 10.3389/fneur.2021.630681
15. Katsiki N, Mantzoros C, Mikhailidis D. Adiponectin, lipids and atherosclerosis. *Curr Opin Lipidol.* (2017) 28:347–54. doi: 10.1097/MOL.0000000000000431
16. Moradi N, Fouani F, Vatannejad A, Bakhti Arani A, Shahrzad S, Fadaei R. Serum levels of asprosin in patients diagnosed with coronary artery disease (CAD): a case-control study. *Lipids Health Dis.* (2021) 20:88. doi: 10.1186/s12944-021-01514-9
17. Wang Y, Zhao X, Liu L, Soo Y, Pu Y, Pan Y, et al. Prevalence and outcomes of symptomatic intracranial large artery stenoses and occlusions in China: the Chinese intracranial atherosclerosis (CICAS) study. *Stroke.* (2014) 45:663–9. doi: 10.1161/STROKEHA.113.003508
18. Altman DG, Bland JM. Statistics notes: quartiles, quintiles, centiles, and other quantiles. *BMJ.* (1994) 309:996. doi: 10.1136/bmj.309.6960.996
19. Kaess B, Pedley A, Massaro J, Murabito J, Hoffmann U, Fox C. The ratio of visceral to subcutaneous fat, a metric of body fat distribution, is a unique correlate of cardiometabolic risk. *Diabetologia.* (2012) 55:2622–30. doi: 10.1007/s00125-012-2639-5
20. Ho D, Cook N, Britton K, Kim E, Creager M, Ridker P, et al. High-molecular-weight and total adiponectin levels and incident symptomatic peripheral artery disease in women: a prospective investigation. *Circulation.* (2011) 124:2303–11. doi: 10.1161/CIRCULATIONAHA.111.045187
21. Samuels O, Joseph G, Lynn M, Smith H, Chimowitz M, A. standardized method for measuring intracranial arterial stenosis. *AJNR Am J neuroradiol.* (2000) 21:643–6.
22. Gao Y, Wang Y, Lu C, Zeng C, Chang D, Ju S. Correlations between the abdominal fat-related parameters and severity of coronary artery disease

assessed by computed tomography. *Quant Imaging Med Surg.* (2018) 8:579–87. doi: 10.21037/qims.2018.07.06
23. Fox C, Hwang S, Massaro J, Lieb K, Vasan R, O'Donnell C, et al. Relation of subcutaneous and visceral adipose tissue to coronary and abdominal aortic calcium (from the Framingham Heart Study). *Am J Cardiol.* (2009) 104:543–7. doi: 10.1016/j.amjcard.2009.04.019
24. Yang W, Li R, Shen Y, Wang X, Liu Q, Wang H, et al. Importance of lipid ratios for predicting intracranial atherosclerotic stenosis. *Lipids Health Dis.* (2020) 19:160. doi: 10.1186/s12944-020-01336-1
25. Chapman M, Sposito A. Hypertension and dyslipidaemia in obesity and insulin resistance: pathophysiology, impact on atherosclerotic disease and pharmacotherapy. *Pharmacol Ther.* (2008) 117:354–73. doi: 10.1016/j.pharmthera.2007.10.004
26. Gast K, den Heijer M, Smit J, Widya R, Lamb H, de Roos A, et al. Individual contributions of visceral fat and total body fat to subclinical atherosclerosis: the NEO study. *Atherosclerosis.* (2015) 241:547–54. doi: 10.1016/j.atherosclerosis.2015.05.026
27. Imahori Y, Mathiesen E, Leon D, Hopstock L, Hughes A, Johnsen S, et al. The contribution of obesity to carotid atherosclerotic plaque burden in a general population sample in Norway: the Tromsø study. *Atherosclerosis.* (2018) 273:15–20. doi: 10.1016/j.atherosclerosis.2018.04.014
28. Recio-Rodriguez J, Gomez-Marcos M, Patino-Alonso M, Agudo-Conde C, Rodriguez-Sanchez E, Garcia-Ortiz L. Abdominal obesity vs general obesity for identifying arterial stiffness, subclinical atherosclerosis and wave reflection in healthy, diabetics and hypertensive. *BMC Cardiovasc Disord.* (2012) 12:3. doi: 10.1186/1471-2261-12-3
29. Gast K, Smit J, den Heijer M, Middeldorp S, Rippe R, le Cessie S, et al. Abdominal adiposity largely explains associations between insulin resistance, hyperglycemia and subclinical atherosclerosis: the NEO study. *Atherosclerosis.* (2013) 229:423–9. doi: 10.1016/j.atherosclerosis.2013.05.021
30. Després J, Lemieux I. Abdominal obesity and metabolic syndrome. *Nature.* (2006) 444:881–7. doi: 10.1038/nature05488
31. Wensveen F, Jelenčić V, Valentić S, Šestan M, Wensveen T, Theurich S, et al. NK cells link obesity-induced adipose stress to inflammation and insulin resistance. *Nat Immunol.* (2015) 16:376–85. doi: 10.1038/ni.3120
32. Sequeira I, Yip W, Lu L, Jiang Y, Murphy R, Plank L, et al. Visceral adiposity and glucoregulatory peptides are associated with susceptibility to type 2 diabetes: the TOFI_Asia study. *Obesity.* (2020) 28:2368–78. doi: 10.1002/oby.22994
33. Li T, Wang F, Peng R, Pei S, Hou Z, Lu B, et al. Sex-related differences in the association between plasma fibrinogen and non-calcified or mixed coronary atherosclerotic plaques. *Biol Sex Differ.* (2018) 9:51. doi: 10.1186/s13293-018-0210-x
34. Stranahan A. Visceral adiposity, inflammation, and hippocampal function in obesity. *Neuropharmacology.* (2021) 205:108920. doi: 10.1016/j.neuropharm.2021.108920
35. Menti E, Zaffari D, Galarraga T, Lessa J, Pontin B, Pellanda L, et al. Early markers of atherosclerotic disease in individuals with excess weight and dyslipidemia. *Arq Bras Cardiol.* (2016) 106:457–63. doi: 10.5935/abc.20160060
36. Zhang Y, Zhu C, Guo Y, Xu R, Li S, Dong Q, et al. Higher fibrinogen level is independently linked with the presence and severity of new-onset coronary atherosclerosis among Han Chinese population. *PLoS ONE.* (2014) 9:e113460. doi: 10.1371/journal.pone.0113460
37. Peycheva M, Deneva T, Zahariev Z. The role of fibrinogen in acute ischaemic stroke. *Neurol Neurochir Pol.* (2021) 55:74–80. doi: 10.5603/PJNNS.a2020.0094
38. Okauchi Y, Kishida K, Funahashi T, Noguchi M, Ogawa T, Ryo M, et al. Changes in serum adiponectin concentrations correlate with changes in BMI, waist circumference, and estimated visceral fat area in middle-aged general population. *Diabetes Care.* (2009) 32:e122. doi: 10.2337/dc09-1130
39. Maeda N, Funahashi T, Matsuzawa Y, Shimomura I. Adiponectin, a unique adipocyte-derived factor beyond hormones. *Atherosclerosis.* (2020) 292:1–9. doi: 10.1016/j.atherosclerosis.2019.10.021
40. Lee S, Bacha F, Gungor N, Arslanian S. Racial differences in adiponectin in youth: relationship to visceral fat and insulin sensitivity. *Diabetes Care.* (2006) 29:51–6. doi: 10.2337/diacare.29.01.06.dc05-0952
41. Medina-Urrutia A, Posadas-Romero C, Posadas-Sánchez R, Jorge-Galarza E, Villarreal-Molina T, González-Salazar MC, et al. Role of adiponectin and free fatty acids on the association between abdominal visceral fat and insulin resistance. *Cardiovasc Diabetol.* (2015) 14:20. doi: 10.1186/s12933-015-0184-5
42. Hakim O, Bello O, Ladwa M, Shojaee-Moradie F, Jackson N, Peacock J, et al. Adiponectin is associated with insulin sensitivity in white European men but not black African men. *Diabet Med.* (2021) 38:e14571. doi: 10.1111/dme.14571
43. Kim B, Lee S, Ryu W, Kim C, Yoon B. Adipocytokines and ischemic stroke: differential associations between stroke subtypes. *J Neurol Sci.* (2012) 312:117–22. doi: 10.1016/j.jns.2011.08.007
44. Bang O, Saver J, Ovbiagele B, Choi Y, Yoon S, Lee K. Adiponectin levels in patients with intracranial atherosclerosis. *Neurology.* (2007) 68:1931–7. doi: 10.1212/01.wnl.0000263186.20988.9f
45. Wang Y, Lam K, Chan L, Chan K, Lam J, Lam M, et al. Post-translational modifications of the four conserved lysine residues within the collagenous domain of adiponectin are required for the formation of its high molecular weight oligomeric complex. *J Biol Chem.* (2006) 281:16391–400. doi: 10.1074/jbc.M513907200
46. Kizer J, Benkeser D, Arnold A, Djousse L, Zieman S, Mukamal K, et al. Total and high-molecular-weight adiponectin and risk of coronary heart disease and ischemic stroke in older adults. *J Clin Endocrinol Metab.* (2013) 98:255–63. doi: 10.1210/jc.2012-2103
47. Rizza S, Cardellini M, Farcomeni A, Morabito P, Romanello D, Di Cola G, et al. Low molecular weight adiponectin increases the mortality risk in very old patients. *Aging Dis.* (2018) 9:946–51. doi: 10.14336/AD.2017.1117
48. Tagawa N, Fujinami A, Natsume S, Mizuno S, Kato I. Relationship between adiponectin multimer levels and subtypes of cerebral infarction. *PLoS ONE.* (2022) 17:e0262542. doi: 10.1371/journal.pone.0262542
49. Park J, Hong K, Lee E, Lee J, Kim D. High levels of apolipoprotein B/AI ratio are associated with intracranial atherosclerotic stenosis. *Stroke.* (2011) 42:3040–6. doi: 10.1161/STROKEAHA.111.620104

Conflict of Interest: The authors declare that the research was conducted in the absence of any commercial or financial relationships that could be construed as a potential conflict of interest.

Publisher's Note: All claims expressed in this article are solely those of the authors and do not necessarily represent those of their affiliated organizations, or those of the publisher, the editors and the reviewers. Any product that may be evaluated in this article, or claim that may be made by its manufacturer, is not guaranteed or endorsed by the publisher.

Copyright © 2022 Wang, Meng, Yu, Tan, Quan, Hu, Bai, Xie and Zhao. This is an open-access article distributed under the terms of the Creative Commons Attribution License (CC BY). The use, distribution or reproduction in other forums is permitted, provided the original author(s) and the copyright owner(s) are credited and that the original publication in this journal is cited, in accordance with accepted academic practice. No use, distribution or reproduction is permitted which does not comply with these terms.

frontiers | Frontiers in Neurology

ORIGINAL RESEARCH
published: 23 June 2022
doi: 10.3389/fneur.2022.934501

Altered Intrinsic Brain Activity in Patients With Toothache Using the Percent Amplitude of a Fluctuation Method: A Resting-State fMRI Study

Jun Yang[1†], Yi Shao[2†], Yan-Kun Shen[2†], Hong-Shui Zhu[1], Bin Li[3], Qiu-Yue Yu[3], Min Kang[2], San-Hua Xu[2], Ping Ying[2], Qian Ling[2], Jie Zou[2], Hong Wei[2] and Yu-Lin He[3]*

[1] The Affiliated Stomatological Hospital of Nanchang University, The Key Laboratory of Oral Biomedicine, Nanchang, China, [2] Department of Ophthalmology, The First Affiliated Hospital of Nanchang University, Nanchang, China, [3] Department of Radiology, The First Affiliated Hospital of Nanchang University, Nanchang, China

OPEN ACCESS

Edited by:
Yuzhen Xu,
Tongji University, China

Reviewed by:
Xulin Liao,
CUHK Medical Centre, Hong Kong SAR, China
Zhenhao Zhang,
Nanjing Medical University, China

***Correspondence:**
Yu-Lin He
173386424@qq.com

[†]These authors have contributed equally to this work

Specialty section:
This article was submitted to Neurological Biomarkers, a section of the journal Frontiers in Neurology

Received: 02 May 2022
Accepted: 24 May 2022
Published: 23 June 2022

Citation:
Yang J, Shao Y, Shen Y-K, Zhu H-S, Li B, Yu Q-Y, Kang M, Xu S-H, Ying P, Ling Q, Zou J, Wei H and He Y-L (2022) Altered Intrinsic Brain Activity in Patients With Toothache Using the Percent Amplitude of a Fluctuation Method: A Resting-State fMRI Study. Front. Neurol. 13:934501. doi: 10.3389/fneur.2022.934501

Objective: The percent amplitude of fluctuation (PerAF) technique was utilized to evaluate the neural functions of specific cerebrum areas in patients with toothache (TA).

Patients and Methods: An aggregation of 18 patients with TA (eight males and 10 females) were included in the study. We also recruited 18 healthy controls (HCs; eight men and 10 women) aligned for sex and age. Resting functional magnetic resonance imaging (rs-fMRI) scans were obtained. Then, we utilized the PerAF method and a support vector machine (SVM) to analyze the image data and measure neural abnormalities in related cerebrum areas. Receiver operating characteristic (ROC) curve analysis was utilized to appraise the two data sets.

Results: The PerAF signals in the right dorsolateral superior frontal gyrus (RDSFG) and the right posterior central gyrus (RPCG) of TA sufferers were lower than HC signals. These results may reveal neural dysfunctions in relevant cerebrum regions. The AUC values of PerAF in the two areas were 0.979 in the RDSFG and 0.979 in the RPCG. The SVM results suggested that PerAF could be utilized to distinguish the TA group from HCs with a sensitivity of 75.00%, a specificity of 66.67%, and an accuracy of 70.83%.

Conclusion: Patients with TA had marked differences in PerAF values in some regions of the cerebrum. Changes in PerAF values represented distinctions in blood oxygen level dependent semaphore intensity, which reflected the overactivity or inactivation of some cerebrum areas in those suffering from TA. At the same time, we analyzed the PerAF values of TAs with ROC curve, which can be helpful for the diagnosis of TA severity and subsequent treatment. Our results may help to elucidate the pathological mechanism of TA.

Keywords: toothache, percent amplitude of fluctuation, support vector machine, receiver operating characteristic, pathological mechanism

INTRODUCTION

Toothache (TA) is a common oral clinical symptom caused by various stimuli to the tooth itself and its surrounding soft tissues. It can be caused by multiply diseases such as dental caries, pulpitis, periapical periodontitis, gingivitis, periodontitis, and oral ulcers. Due to its innervated nature, pain is the only way the pulp and dentin respond to various external stimuli and the pain manifests as persistent, dull, throbbing, and radiating in a variety of ways (1). Dental pulp is a tissue with high nerve density, it is rich in sensory nerve endings, and it plays a crucial role in regulating odontogenic tooth pain, responses to external stimuli, and detection of potential tooth damage (2). Untreated pain can have physical effects such as dyspnea, ascending heart rate and blood pressure, increased myocardial oxygen demand, increased stress hormones, vomiting, and muscle tension (3). Long-term TA affects the patients' mental state and sleep quality, and even causes the patient to suffer from depression, anxiety, and other psychological conditions, often accompanied by migraines. In addition, it brings a substantial economic burden to society and individuals (4). In general, TA is more common among people of lower socioeconomic status because of their limited access to dental care. In addition, various risk factors, such as education level, smoking, and drinking habits, and race/ethnicity are associated with TA (5). TA can be an early warning mechanism. If the dental disease causing the pain is not treated in time and effectively, it can lead to severe complications, such as infection, that may be life-threatening (6). Despite the rapid progress in treatment methods, such as drugs and surgery, the mechanism of brain structure and function changes in patients with TA remains unclear. In recent years, studies have shown that TA can manifest multiple chronic pains, including paroxysmal throbbing pain in migraines, dull persistent pain in joint dysplasia, or concentrated facial pain. In addition, the degree of TA and the severity of the lesions do not change linearly, and the pain experience is closely related to personal characteristics and psychological factors. (7) Moreover, diagnosis of TA can be complicated. Therefore, exploring brain-related responses to TA has profound theoretical and clinical implications for understanding the cognitive regulation of pain systems.

At present, the use of imaging methods to probe cerebrum area configurations and functions can contribute to exploring the neural mechanisms of TA. Rs-fMRI has been recognized as an appropriate method for assessing TA-related brain damage. Regional homogeneity, low-frequency fluctuation (ALFF) amplitudes, and fractional ALFF (fALFF) amplitudes are three essential rs-fMRI approaches for handling regional cerebrum abnormalities. However, these methods are susceptible to breathing and cardiac noise artifacts and subsequent statistical analysis is complicated due to the arbitrary units of the blood oxygen level dependent (BOLD) signal (8–10). Regional homogeneity (ReHo) is a new method that was developed in recent years. ReHo breakthroughs the theoretical assumption based on linear time invariance and is a new hypothesis for brain fMRI data analysis. However, based on temporal consistency, ReHo cannot be used to analyze the functional state of the cerebrum integrally (11). In recent years, studies have proposed the application of multiple analytical methods for resting-state fMRI, suggesting that many cerebrum areas in patients with TA have abnormalities in intrinsic brain activity. The percent amplitude of fluctuation (PerAF) method can be applied to signal changes in MRI to evaluate the percentage of rs-fMRI (12). PerAF can be used to measure the percentage of BOLD fluctuations and the mean for the whole time series can be calculated. In contrast to ALFF, PerAF is a scale-independent method (13) and is similar to the percent signal change in rs-fMRI. Furthermore, PerAF prevents the confounding variables of voxel-specific fluctuation magnitudes to affect the results (14). Several studies have suggested that PerAF exhibits analogous intra-scanning reliability to ALFF, as it is less affected by BOLD signal intrusion and can be a more reliable indicator (12).

The PerAF has an excellent potential for voxel analysis. However, few investigations have been carried out to probe typical lesions in the cerebrum in patients with TA. Therefore, this study may be very helpful for inchoate studies that can be a basis for diagnosis and prevention of cerebral abnormalities in patients with TA.

METHODS AND SUBJECTS

Subjects

Eighteen patients (eight men, 10 women) with TA were recruited for the study at two hospitals, namely, the Affiliated Stomatological Hospital of Nanchang University and the First Affiliated Hospital of Nanchang University. All subjects conformed to the following criteria: (1) no obvious malformation of the cerebrum on MRI; (2) no history of mental illness; (3) no history of drug or alcohol abuse; and (4) no claustrophobia.

The inclusion standards for the TA group were as follows: (1) pain caused by dental disease or non-dental disease in the pulp and/or periodontal tissue; (2) acute or chronic TA; (3) no other comorbid pain sickness; (4) tolerant of MRI examination; (5) routine MRI T1WI and T2WI sequence examination showing no evident abnormality; and (6) TA with no apparent cause and not attributable to other diseases. The exclusion criteria were as follows: (1) presence of non-dental pain; (2) first-degree relatives with genetic non-dental pain syndromes; (3) suffering from mental disorders; and (4) presence of contraindications for MRI scanning.

This study included 18 healthy controls (HCs; eight men, 10 women) with matched ages and sex. Inclusion criteria for HCs were as follows: (1) no TA symptoms; (2) no parenchymal malformations on MRI; (3) no mental disorder; and (4) feasible MRI examination.

Ethical Approval and Consent to Participate

Based on the Declaration of Helsinki, this research was authorized by the medicinal morality council of Nanchang University's First Affiliated Hospital (Nanchang, China PR). Each participant signed a declaration of informed consent.

MRI Data Acquisition

FMRI Data Parameters

A Trio 3-Tesla MR scanister (Siemens, Munich, Germany) was utilized for MRI scanning. All participants were directed to close their eyes and remain under spontaneous breathing through the scanning. A metamorphic gradient echo sequence was utilized to obtain the data. Then, the desired functional images were received with a 3D metamorphic gradient echo pulse sequence.

FMRI Data Analysis

In this study, we performed an analysis of the aforementioned functional maps. During magnetization equalization, the first 15 time points were abandoned. We utilized Rs-fMRI Advanced Edition (DPARSFA 4.0, http://rfmri.org/DPARSF) software, Rs-fMRI Data Analysis Toolkit (REST, http://www.restfmri.net), and Statistical Parameters Mapping software (SPM8, http://www.fil.ion.ucl.ac.uk/spm) for head motion rectification, dimensional normalization, and slice timing. Then, we applied Digital Imaging Communication system to smooth the data. Subjects were eliminated if they had exorbitant angular movements or a maximal excursion >1.5 mm in the x, y, or z orientation during the fMRI scanning (1). Erroneous variables in the signals from the central white matter region of the brain and the ventricular region of interest (ROI) were dispelled with linear regression. Finally, the functional graphics were normalized utilizing standard echo-plane graphic templates. We creatively utilized the PerAF technique to handle the fMRI datum. The formula for calculating the individual PerAF value is as follows:

$$PerAF = \frac{1}{n}\sum_{i=1}^{n}\left|\frac{x_i - \mu}{\mu}\right| \times 100\% \quad (1)$$

$$\mu = \frac{1}{n}\sum_{i=1}^{n} x_i \quad (2)$$

where x_i portrays the signal intensity at the ith time point, n symbolizes the totality of time points, and μ stands for the average value of the time series.

Support Vector Machine Analysis

We applied the LIBSVM software (http://www.csie.ntu.edu.tw/$\sim$cjlin/libsvm/) to determine whether patients with TA could be differentiated by the increase or decrease in the intensity of PerAF in different brain regions and HCs. SVM was done by "leave one out." At the same time, we validated the SVM results by running the permutation test 10,000 times. Thereby, the global accuracy of each sample could be obtained.

Statistical Analysis

We performed independent-sample *t*-tests with statistical software (SPSS 20.0; SPSS, Chicago, IL, USA) to compare the two groups. Results were statistically significant when $P < 0.05$. Discrepancies in PerAF values between the TA group and HCs were compared with a two-sample *t*-test using the SPM8 toolkit (the statistical threshold was set at $P < 0.05$ for multiple comparisons with a Gaussian random field, and Voxel-level AlphaSim was set at $P < 0.01$ and rectified for cluster sizes >40 voxels).

The PerAF in specific cerebrum areas in the TA group and HCs were analyzed with ROC curve analysis. Pearson's correlation analysis was used to assess the connection between particular cerebrum areas and their clinical manifestations in patients with TA. SVM correlation analysis was performed to obtain and guarantee the global accuracy of each sample.

TABLE 1 | Comparison of baseline data between toothache patients and healthy subjects.

	TA group	HC group	*T*-value	*P*-value
Sex	8/10	8/10	N/A	>0.99
Age	41.18 ± 11.65	40.73 ± 12.48	0.088	0.679
Dominant hand	18 (right hand)	18 (right hand)	N/A	>0.99
Disease duration (years)	2.04 ± 1.08	N/A	N/A	N/A
Visual analog score	6.36 ± 1.49	N/A	N/A	N/A

Two independent t tests were used to compare the baseline data of the two groups ($P < 0.05$ indicates that the difference between the two groups was statistically significant). Data are presented as mean ± standard deviation or n.
TA, toothache; HC, healthy control.

RESULTS

General Situation and Clinical Data Comparisons

There were no noticeable differences in the age and sex distributions between the TA group and the HC group ($P = 0.679$ and $P > 0.99$, respectively). The disease duration of patients with TA was 2.04 ± 1.08 years. More details are summarized in **Table 1**.

PerAF Differences

The PerAF values in the cerebrum areas of the TA group, including the right dorsolateral superior frontal gyrus (RDSFG) and the right posterior central gyrus (RPCG), were decreased to varying degrees (**Figures 1A,B** and **Table 2**). The average ALFF of the two groups is shown in **Figure 1C**. The PerAF values of the two regions in the TA group had no correlation with clinical manifestations ($P > 0.05$).

ROC Curve Analysis

We hypothesized that distinctions in PerAF values could be an underlying helpful diagnostic marker to differentiate the TA group from HCs. ROC curve analysis was utilized to test this hypothesis. Average PerAF values were collected from different regions of the brain and analyzed. The accuracy was deemed low if the area under the curve (AUC) was 0.5–0.7, but high when the AUC was 0.7–0.9. The AUC values of PerAF in the two areas were 0.979 in the RDSFG ($P < 0.0001$; 95% CI: 0.931–1.000) and 0.979 in the RPCG ($P < 0.0001$; 95% CI: 0.931–1.000; **Figure 2**).

SVM Analysis Results

We analyzed PerAF data from the TA group and HCs. The SVM accuracy results suggested that the PerAF data could be utilized to

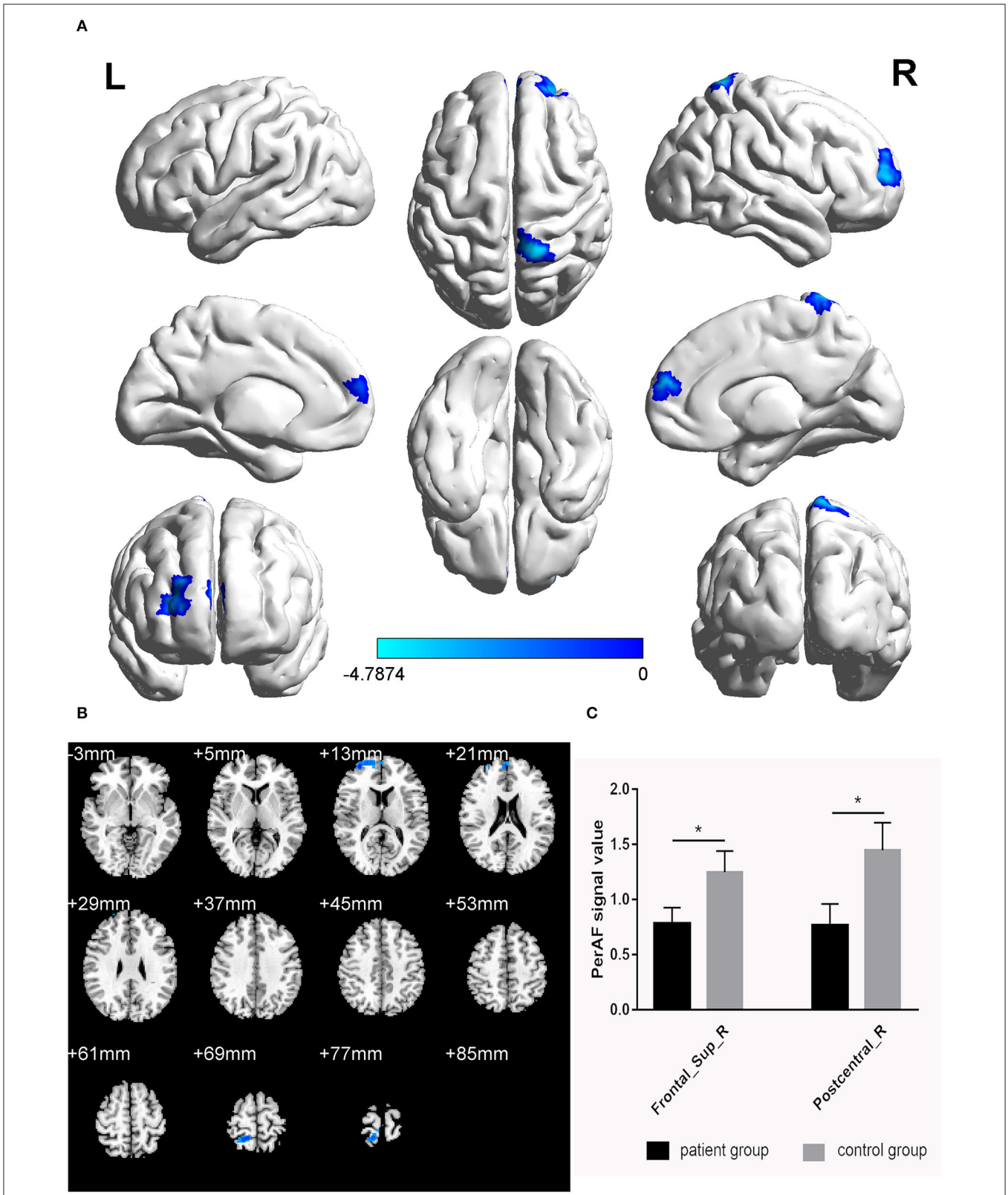

FIGURE 1 | Significant differences in brain activity **(A,B)**. Blue areas indicate lower PerAF values. AlphaSim performed multiple comparisons at cluster sizes >40 voxels and $P < 0.05$, obtained by Gaussian random field theory. **(C)** ALFF mean values between TA group and HC. PerAF, percent amplitude of fluctuation; Frontal_Sup_R, right dorsolateral superior frontal gyrus; Postcentral_R, right posterior central gyrus. *represents significant difference.

distinguish the TA group from HCs with a sensitivity of 75.00%, a specificity of 66.67%, and an accuracy of 70.83% (**Figure 3**). The global accuracy for this combination using the permutation test was 0.6923 ($p < 0.001$), and its ROC curve fitted well (**Figure 4**).

TABLE 2 | Brain regions with significant differences in PerAF between patients and HCs.

Brain areas	MNI coordinates			BA	Number of voxels	*T*-value
	X	Y	Z			
Frontal_Sup_R	33	60	12	4	119	−4.3379
Postcentral_R	15	−48	72	58	82	−4.7874

The statistical threshold was set at P < 0.05 for multiple comparisons with a Gaussian random field, Voxel-level AlphaSim was set at P < 0.01 and rectified for cluster sizes >40 voxels.

PerAF, percent amplitude of fluctuation; HCs', healthy controls; Frontal_Sup_R, right dorsolateral superior frontal gyrus; Postcentral_R, right posterior central gyrus.

DISCUSSION

Since the invention of the electroencephalogram (EEG), humans have begun to explore different neuroimaging tools in a variety of conditions. In recent decades, the characteristics of brain activity in the resting state have become a topic of widespread concern in various medical departments, providing a new perspective for related research on brain functional organization.

Percent amplitude of fluctuation, a new and relatively reliable technique, has been utilized in studies of patients with ophthalmic and neurogenic diseases (**Table 3**). In this investigation, we first utilized the PerAF technique to study neural functions and abnormalities in separate cerebrum areas of patients with TA. The results showed that the signal values of PerAF in the RDSFG and right posterior central gyrus of patients with TA were decreased compared with HCs, and may cause visual impairment (**Figure 5**).

The postcentral gyrus, situated in the lateral parietal lobe of the brain, is known as the primary somatosensory cortex (S1) and acts as a crucial area for touch and nociception (19–21). Pain

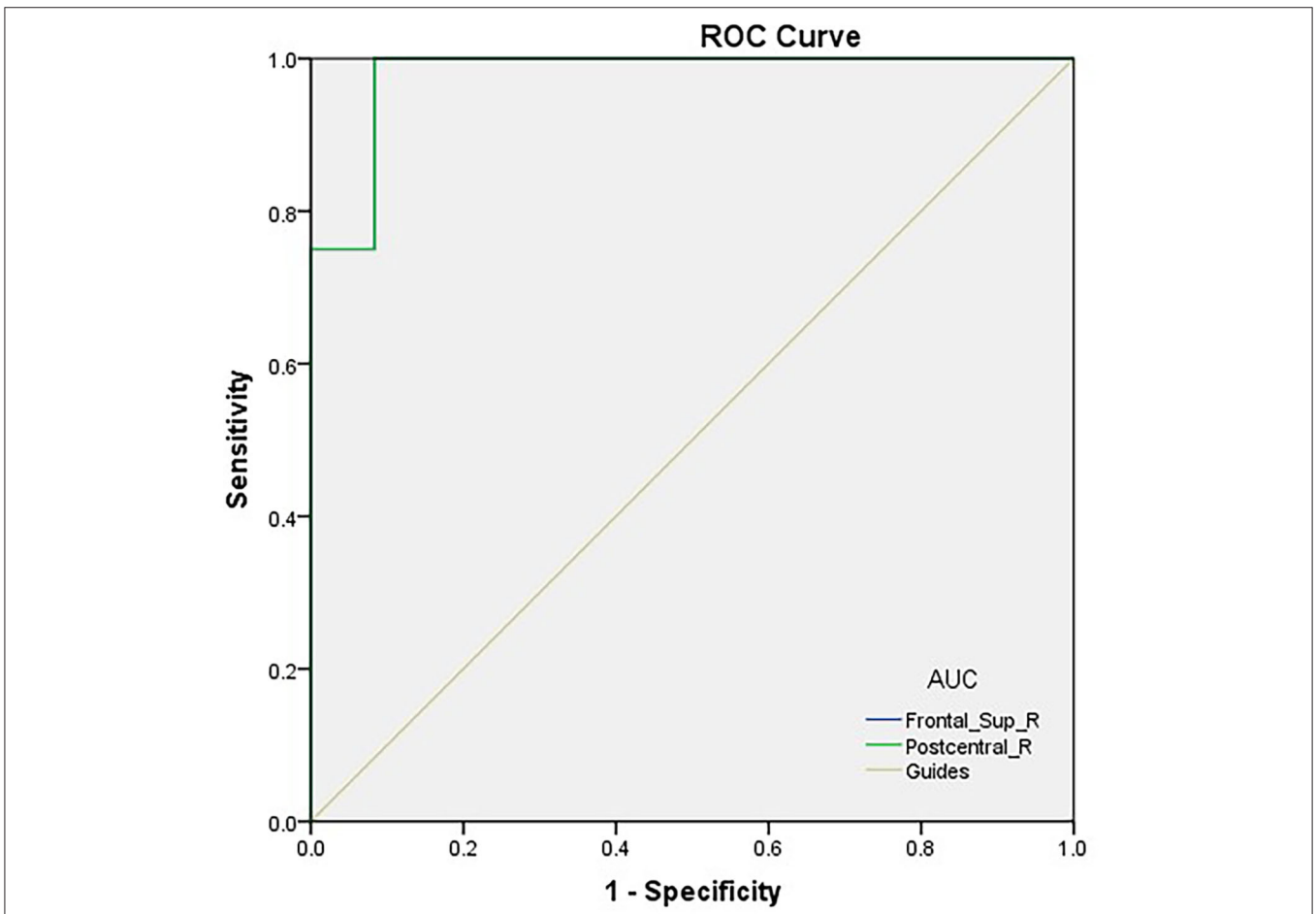

FIGURE 2 | ROC curve analysis of the PerAF values for altered brain regions. ROC curve analysis of the PerAF values for altered brain regions. The area under the ROC curve of the right dorsolateral superior frontal gyrus was 0.979 ($P < 0.0001$; 95% CI: 0.931–1.000); the area under the ROC curve of the right posterior central gyrus was 0.979 ($P < 0.0001$; 95% CI: 0.931–1.000). ROC, receiver operating characteristic; PerAF, percent amplitude of fluctuation; AUC, area under the curve.

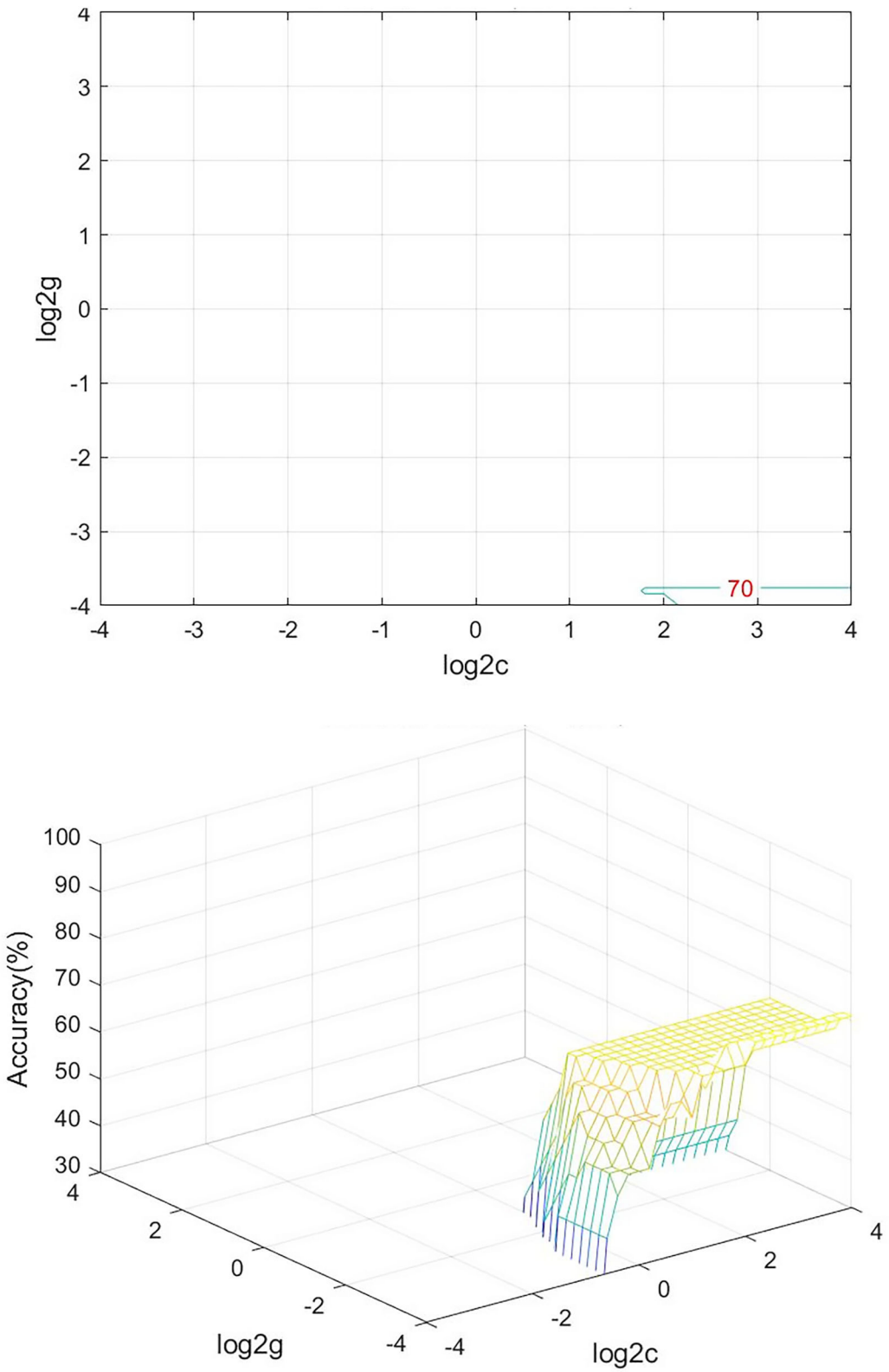

FIGURE 3 | Visualization of SVM results for TA and HC. Left, Visualization of the classification map. Right, 3D view of classification accuracy with best parameters. SVM, support vector machine; TA, toothache; HC, healthy control.

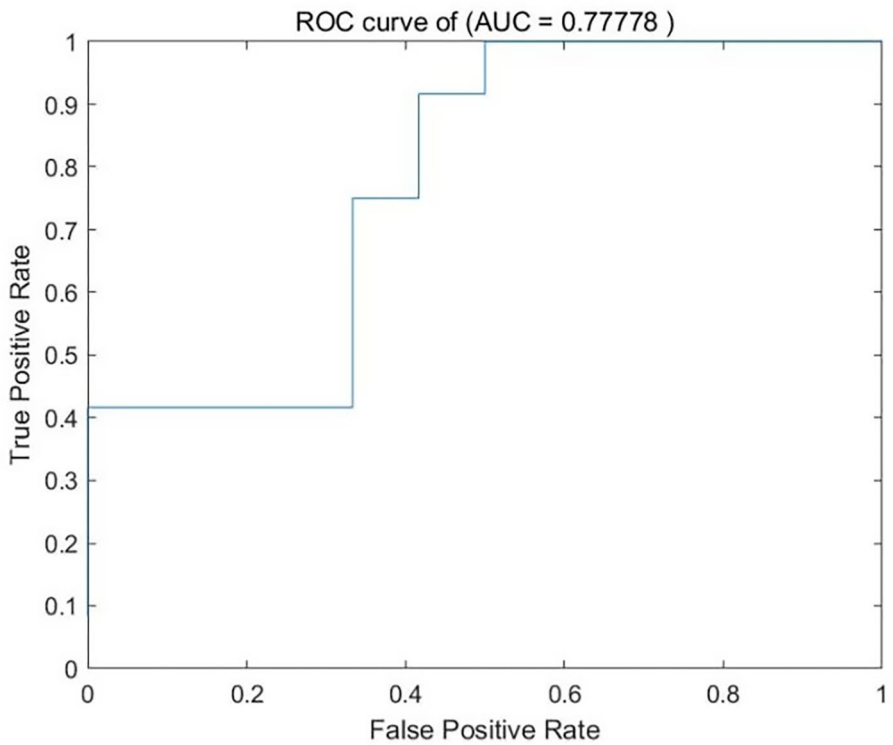

FIGURE 4 | ROC curve of the SVM classifier. SVM, support vector machine; ROC, receiver operating characteristic; AUC, area under the curve.

TABLE 3 | PreAF applied in ophthalmic and neurogenic diseases.

Author	Year	Disease	Brain areas	
			PerAF increased	PerAF decreased
Yang et al. (15)	2021	Retinal detachment	RFG, LITG	— —
Li et al. (16)	2021	Moyamoya disease	LCN	RMSFG,LPG
Yu et al. (17)	2021	Neovascular glaucoma	LITG	RACG, RSOG, LSFG
Yu et al. (18)	2019	Mild cognitive impairment	LP	— —

PerAF, percent amplitude of fluctuation; RFG, right fusiform gyrus; LITG, left inferior temporal gyrus; LCN, left caudate nucleus; RMSFG, right medial superior frontal gyrus; LPG, left precentral gyrus; LITG, left inferior temporal gyrus; RACG, right anterior cingulate and paracingulate gyrus, RSOG, right superior occipital gyrus; LSFG, left superior frontal gyrus; LP, left parahippocampus.

perception is a multi-dimensional experience, including sensory discrimination, emotional motivation, and cognitive evaluation components (22). Downregulation of pain involves cortical and subcortical brain structures, including the dorsolateral prefrontal cortices (DLPFC) and S1. A study of pain induced by thermal stimuli has shown that S1 tissue is typically activated when such incentives are present (23). Previous studies have shown that S1 activity is involved in many pain-related disorders (20, 24, 25). Baciu et al. (24) revealed similar S1 activation in patients with rectal pain, and Binkofski and colleagues (20) described painful esophageal dilation resulting in a marked pattern of brain activation of S1. In another study, somatosensory impairment caused by decreased neural activity in the postcentral gyrus is an early symptom of Parkinson's disease (25).

A previous study has suggested that the DLPFC is often concerned with cognitive and attentive management of algetic stimulus (26). Therefore, a decreased functional correlation between the right S1 and the DLPFC may be associated with altered attentional status to noxious stimuli from T1 to T2. This may explain the simultaneous decline in PerAF values of the RPCG and RDSFG in patients with TA.

Damage to the RPCG results in somatosensory impairment, but experiments have shown that the information processed by the early S1 can distinguish familiar visual objects. This effect was only discovered for familiar objects. This is because correlations from vision to early S1 transmission of content-specific messages about familiar objects only relied on visual facades (27). In another study, when the lesions in the right S1 appeared alone,

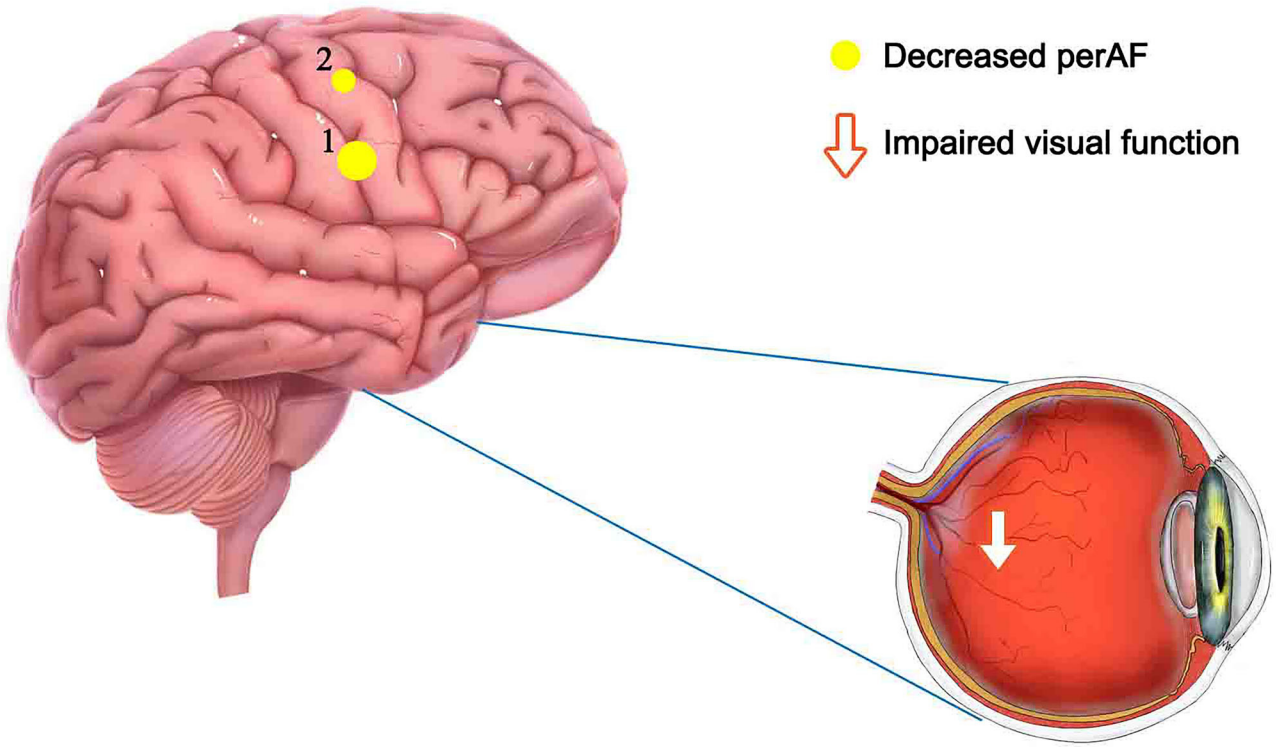

FIGURE 5 | Mean PerAF values for altered brain regions. Compared with HCs, PerAF values in the following regions decreased to varying degrees: 1- right dorsolateral superior frontal gyrus (BA 4, $t = -4.3395$), 2-right posterior central gyrus (BA 58, $t = -4.7844$). PerAF, percent amplitude of fluctuation; HCs, healthy controls; BA, Broadman area.

visual exploration and sensitivity were deviated from the midline and mainly manifested as spatial asymmetry when distinguishing the same target on the retina. This suggested that S1 plays a role in spatial attention allocation, demonstrating a novel role for S1 in visuospatial attention (28). The superior colliculus (SC) is a visual reflex center. The deep layers of SC receive input from S1 (29), and the S1 injury may also cause SC reflex disorders. Therefore, damage to S1 associated with a TA may cause visual impairment.

Specific dystonia is a motion disease that involves abnormal postures of the body. Some regression analysis studies discovered that S1 was markedly connected with variability in fundamental frequency signals related to dystonic symptoms and that somatic assessment portrayed essential distinctions in the right somatosensory cortex (30, 31). Researchers used fMRI data to assess brain activity and physical therapy. The results revealed that the somatosensory representation of S1 was significantly different between dystonic patients and HCs (32). This difference involves the gating system by which the S1 can turn off movement-related sensory input. Such gating systems can filter out redundant inputs, reduce irrelevant information, and play an essential role in organized movement (33, 34). Patients with TA may be at risk of dystonia due to an impaired sensory cortical gating system.

Patients suffering from obsessive-compulsive disorder (OCD) often use repetitive behaviors to relieve anxiety, including touching, counting, and repeated washing. A recent study found an increase in S1 gray matter volume in patients with OCD (35). The manifestations of patients with OCD were similar to sensory-related impulses observed in mental disorders and the impulses were associated with activation of the S1 and insula (36). Motor areas were also regularly connected with heightened sensory impulses and a lack of significant motion, indicating a crucial connection between sensory and action centers in the cerebral cortex that is particularly prominent in disorders such as OCD. Neurologically, schizophrenia severity has been positively correlated with activation in the bilateral somatosensory cortex (postcentral gyrus). Recent findings have shown a connection between somatosensory activation and the severity of OCD, suggesting that the somatosensory areas of OCD patients are functionally and structurally abnormal (37).

In the superior frontal gyrus, researchers observed increased activation associated with various attentional control tasks, including inhibitory control, conflict resolution, and visuospatial interference suppression (38). In addition to interference inhibition, the results of a study suggested that the right DLPFC is involved in adaptive cognitive control, and this brain area participates in cognitive control processing by shielding task-irrelevant interference (39). Corresponding evidence has come from patients with right DLPFC injury who had difficulty developing strategies for coping with interference (40). This

finding suggests that TA-induced impairment of the RDSFG may lead to recurrent inattention and cognitive control impairments that are easily disturbed.

In a study aimed at identifying structural variations in the cerebrum areas of sufferers with vestibular migraines (41), a significant increase in the volume of the superior frontal gyrus was found. Some of these cerebrum areas with increased gray matter volume were involved in evaluating pain and were closely related to emotion and anxiety. In another study, the excitability of the superior frontal gyrus was decreased significantly and was significantly correlated with psychological conditions such as depression (42). Additionally, a decrease in the functional connection of the left medial superior frontal gyrus in patients with an untreated first episode of severe depression was noted in a separate study (43). Further studies described motivational deficits in many psychiatric disorders, including major depressive disorder (MDD). For example, patients with Alzheimer's disease and Parkinson's disease are characterized by cognitive decline associated with the frontal cortico-subcortical network, including the superior frontal gyrus, anterior cingulate gyrus, and ventral striatum (44). More precisely, impaired control of subcortical (inferior) structures (amygdala) by cortical (top) structures, such as the DLPFC and ACC, is considered to be the cause of negative emotions in MDD (45). In one study, researchers captured the role of brain regions that coordinate intra-hemispheric and inter-hemispheric correspondence. The results indicated that the bilateral superior frontal gyrus was related to MDD-related reductions. Damaged functional correlations in this region have been frequently reported in a previous MDD study (46). The results further suggested that the damaged functional connectivity involved the ipsilateral hemisphere and the contralateral hemisphere, so the bilateral superior frontal gyrus is considered a critical functional disconnection node in MDD (47). Therefore, the decreased PerAF value of RDSFG in patients with TA may lead to emotional disturbances, cognitive impairment, and even the onset of MDDs.

People with anxiety disorders exhibit a wide range of symptoms, such as psychological experiences and feelings of excessive worry, as well as nervousness, unmanageable worry, and panic attacks. Anxiety disorders may involve many brain areas (48, 49). In one study, researchers tested the role of the DLPFC in anxiety manifestations with 10 Hz repetitive transcranial magnetic stimulation (rTMS). The findings showed that rTMS in the right DLPFC was associated with increased anxiety, suggesting a mechanical connection between right DLPFC function and anxiety manifestations (50). Another study has also shown that the activity in the DLPFC during threatening situations was negatively correlated with anxiety (51), and activation of the DLPFC reduced anxiety-enhanced startle. These findings suggest that promoting DLPFC activity can reduce anxiety and damage to the DLPFC may lead to symptoms of anxiety in patients.

Dynamic and flexible cognition is one of the fundamental key traits of humans and it manifests as bistable or multi-stable perceptions. Clinically, visual bistable perception disorder is more common. The DLPFC is thought to be involved in such spontaneous perceptual transitions (52, 53). A recent study showed that the DLPFC's causal role in spontaneous perceptual reasoning was behaviorally detectable when tracking brain state dynamics that underpinned this perceptual fluctuation, and its activation enhanced functional integration between frontal and intermediate states (54). Therefore, damage to the GDSFG may cause disturbances of bistable perception, which lead to disturbances in the patient's perception ability.

As mentioned above, OCD is a disabling disorder characterized by recurring persistent urges and repetitive behaviors (35, 55). Evidence from structural neuroimaging studies have highlighted the pivotal character of the DLPFC in the pathology of OCD. Compared with healthy controls, DLPFC volume and thickness were reduced in OCD patients (56). In a resting-state functional connectivity study, DLPFC-related dysconnectivity was recognized in OCD patient ROI-restricted analyses (57). A recent study utilized rs-fMRI to investigate the neural prioritization of the DLPFC in sufferers of OCD. They discovered abnormalities in the DLPFC-right orbitofrontal cortex circuit, DLPFC-inferior temporal gyri circuit, and DLPFC cerebellar circuit, verifying neural circuit abnormalities in an OCD patient alternative model (58). Therefore, DLPFC damage related to TA may cause symptoms of OCD in patients.

We found a close connection between the RDSFG and the RPCG. The decreased association between them may be responsible for the painful sensation of TA. Furthermore, damage to both brain regions may lead to complications, such as OCD and cognitive impairment. These findings have certain implications for the mechanism and neuropathological factors of TA and are helpful for the treatment of subsequent complications of TA. Using the ALFF method to study

TABLE 4 | Brain regions and potential effects.

Brain regions	Experimental results	Brain functions	Expected results
Right dorsolateral superior frontal gyrus	TA<HC	Primary somatosensory, tactile and visual processing	Unbearable pain, early Parkinson's disease, depression, visual impairment
Right posterior central gyrus	TA<HC	Sensory processing, functional connectivity	Pain leads to enlargement of brain area, severe depression and obsessive-compulsive disorder

TA, toothache; HCs, healthy controls.

neural activity of patients with TA (59) showed that the activity of the posterior central gyrus was significantly improved, thus indicating that the PerAF method has a good universality.

CONCLUSION

However, there are some limitations in our study. First, the sample size of this study was small. In order to acquire more representative results, we need to enlarge the sample size in subsequent studies. Second, the inclusion criteria for patients with TA were not strict, and acute and chronic TA were not further distinguished and odontogenic and non-odontogenic pain were not explicitly classified. We discovered that PerAF signal values in the RDSFG and RPCG were markedly lower in patients with TA than in the HCs. These variations may elevate the risk of relevant diseases related to brain dysfunction (**Table 4**). Despite the abovementioned limitations of our study, the potential pathogenesis of TA can still be considered as connected with abnormalities in specific brain areas. It is useful to comprehend pathological mechanisms and relevant diseases of patients with TA. In addition, due to the high sensitivity and specificity of ROC curves and SVM results, alternations in PerAF values in specific cerebrum areas can be utilized as one of the effective indicators to examine pain-related diseases.

DATA AVAILABILITY STATEMENT

The original contributions presented in the study are included in the article/supplementary material, further inquiries can be directed to the corresponding author/s.

ETHICS STATEMENT

The studies involving human participants were reviewed and approved by the Medicinal Morality Council of Nanchang University's First Affiliated Hospital. The patients/participants provided their written informed consent to participate in this study.

AUTHOR CONTRIBUTIONS

All authors listed have made a substantial, direct, and intellectual contribution to the work and approved it for publication.

FUNDING

Key Research Foundation of Jiangxi Province (20203BBG73059, 20181BBG70004, and 20202BBGL73122); Excellent Talents Development Project of Jiangxi Province (20192BCBL23020); Natural Science Foundation of Jiangxi Province (20181BAB205034).

REFERENCES

1. Stormon N, Pradhan A, McAuliffe A, Ford PJ. Does a facilitated pathway improve access to dental services for homeless and disadvantaged adults? *Eval Program Plann.* (2018) 71:46–50. doi: 10.1016/j.evalprogplan.2018.08.002
2. Trowbridge HO. Review of dental pain–histology and physiology. *J Endod.* (1986) 12:445–52. doi: 10.1016/S0099-2399(86)80197-2
3. Lohman D, Schleifer R, Amon JJ. Access to pain treatment as a human right. *BMC Med.* (2010) 20:8. doi: 10.1186/1741-7015-8-8
4. Altan A, Akkoç S, Erdil A, Çolak S, Demir O, Altan H. Effects of pain catastrophizing and anxiety on analgesic use after surgical removal of impacted mandibular third molars. *J Dent Anesth Pain Med.* (2019) 19:379–88. doi: 10.17245/jdapm.2019.19.6.379
5. Ortiz FR, Tomazoni F, Oliveira MD, Piovesan C, Mendes F, Ardenghi TM. Toothache, associated factors, and its impact on oral health-related quality of life (OHRQoL) in preschool children. *Braz Dent J.* (2014) 25:546–53. doi: 10.1590/0103-6440201302439
6. Budenz B, Deters M, Prasa D, Hentschel H. Exposures to dental products, stomatological preparations, and in dental care and toothache reported to the PIC Erfurt (1997 to 2017). *Sci Rep.* (2020) 10:8057. doi: 10.1038/s41598-020-65079-w
7. Wiech K, Ploner M, Tracey I. Neurocognitive aspects of pain perception. *Trends Cogn Sci.* (2008) 12:306–13. doi: 10.1016/j.tics.2008.05.005
8. Smitha KA, Akhil Raja K, Arun KM, et al. Resting state fMRI: a review on methods in resting state connectivity analysis and resting state networks. *Neuroradiol.* (2017) 30:305–17. doi: 10.1177/1971400917697342
9. Dai XJ, Nie X, Liu X, Pei L, Jiang J, Peng DC, et al. Gender differences in regional brain activity in patients with chronic primary insomnia: evidence from a resting -state fMRI study. *J Clin Sleep Med.* (2016) 12:363–74. doi: 10.5664/jcsm.5586
10. Chen LC Li X, Shen L. Self-limited focal epilepsy decreased regional brain activity in sensorimotor areas. *Acta Neurol Scand.* (2021) 143:188–94. doi: 10.1111/ane.13350.Epub2020 13
11. Lin WC, Hsu TW, Chen CL, Lu CH, Chen HL, Cheng YF, et al. Resting state-fMRI with ReHo analysis as a non-invasive modality for the prognosis of cirrhotic patients with overt hepatic encephalopathy. *PLoS ONE.* (2015) 10:e0126834. doi: 10.1371/journal.pone.0126834
12. Zhao N, Yuan LX, Jia XZ, et al. Intra- and inter-scanner reliability of voxel-wise whole-brain analytic metrics for resting state fMRI. *Front Neuroinform.* (2018) 12:54. doi: 10.3389/fninf.2018.00054
13. Li Y, Li M, Feng Y, Ma X, Tan X, Chen Y, et al. Aberrant brain spontaneous activity and synchronization in Type 2 diabetes mellitus subjects without mild cognitive impairment. *Front Neurosci.* (2021) 15:749730. doi: 10.3389/fnins.2021.749730
14. Liu H, Liu J, Liu H, Peng L, Feng Z, Rong P, et al. Pathological between-network positive connectivity in early type 2 diabetes patients without cerebral small vessel diseases. *Front Neurosci.* (2019) 13:731. doi: 10.3389/fnins.2019.00731
15. Yang YC Li QY, Chen MJ, Zhang LJ, Zhang MY, Pan YC, Ge QM, et al. Investigation of changes in retinal detachment-related brain region activities and functions using the percent amplitude of fluctuation method: a resting-state functional magnetic resonance imaging study. *Neuropsychiatr Dis Treat.* (2021) 17:251–60. doi: 10.2147/NDT.S292132
16. Li CQ, Ge QM, Shu HY, Liao XL, Pan YC, Wu JL, et al. Investigation of altered spontaneous brain activities in patients with moyamoya disease using percent amplitude of fluctuation method: a resting-state functional MRI study. *Front Neurol.* (2021) 12:801029. doi: 10.3389/fneur.2021.801029
17. Yu C, Li CQ, Ge QM, Shu HY, Liao XL, Pan YC, et al. Altered resting state functional activity of brain regions in neovascular glaucoma: a resting-state functional magnetic resonance imaging study. *Front Neurosci.* (2021) 15:800466. doi: 10.3389/fnins.2021.800466
18. Yu Y, Li Z, Lin Y, Yu J, Peng G, Zhang K, et al. Depression Affects Intrinsic Brain Activity in Patients With Mild Cognitive Impairment. *Front Neurosci.* (2019) 13:1333. doi: 10.3389/fnins.2019.01333
19. Pihko E, Nangini C, Jousmäki V, Hari R. Observing touch activates human primary somatosensory cortex. *Eur J Neurosci.* (2010) 31:1836–43. doi: 10.1111/j.1460-9568.2010.07192.x

20. Ploner M, Schmitz F, Freund HJ, Schnitzler A. Differential organization of touch and pain in human primary somatosensory cortex. *J Neurophysiol.* (2000) 83:1770–6. doi: 10.1152/jn.2000.83.3.1770
21. Case LK, Laubacher CM, Olausson H, Wang B, Spagnolo PA, Bushnell MC. Encoding of touch intensity but not pleasantness in human primary somatosensory cortex. *J Neurosci.* (2016) 36:5850–60. doi: 10.1523/JNEUROSCI.1130-15.2016
22. Woo CW, Wager TD. What reliability can and cannot tell us about pain report and pain neuroimaging. *Pain.* (2016) 157:511–3. doi: 10.1097/j.pain.0000000000000442
23. Solstrand Dahlberg L, Linnman CN, Lee D, Burstein R, Becerra L, Borsook D. Responsivity of periaqueductal gray connectivity is related to headache frequency in episodic migraine. *Front Neurol.* (2018) 9:61. doi: 10.3389/fneur.2018.00061
24. Binkofski F, Schnitzler A, Enck P, Frieling T, Posse S, Seitz RJ, Freund HJ. Somatic and limbic cortex activation in esophageal distention: a functional magnetic resonance imaging study. *Ann Neurol.* (1998) 5)811–5. doi: 10.1002/ana.410440516
25. Nelson AJ, Hoque T, Gunraj C, Chen R. Altered somatosensory processing in Parkinson's disease and modulation by dopaminergic medications. *Parkinsonism Relat Disord.* (2018) 53:76–81. doi: 10.1016/j.parkreldis.2018.05.002
26. Lorenz J, Minoshima S, Casey KL. Keeping pain out of mind: the role of the dorsolateral prefrontal cortex in pain modulation. *Brain*. (2003) 126(Pt 5):1079–91. doi: 10.1093/brain/awg102
27. Smith FW, Goodale MA. Decoding visual object categories in early somatosensory cortex. *Cereb Cortex.* (2015) 25:1020–31. doi: 10.1093/cercor/bht292
28. Balslev D, Odoj B, Karnath HO. Role of somatosensory cortex in visuospatial attention. *J Neurosci.* (2013) 33:18311–8. doi: 10.1523/JNEUROSCI.1112-13.2013
29. Triplett JW, Phan A, Yamada J, Feldheim DA. Alignment of multimodal sensory input in the superior colliculus through a gradient-matching mechanism. *J Neurosci.* (2012) 32:5264–71. doi: 10.1523/JNEUROSCI.0240-12.2012
30. Konczak J, Abbruzzese G. Focal dystonia in musicians: linking motor symptoms to somatosensory dysfunction. *Front Hum Neurosci.* (2013) 7:297. doi: 10.3389/fnhum.2013.00297
31. Furuya S, Hanakawa T. The curse of motor expertise: Use-dependent focal dystonia as a manifestation of maladaptive changes in body representation. *Neurosci Res.* (2016) 104:112–9. doi: 10.1016/j.neures.2015.12.001
32. Uehara K, Furuya S, Numazawa H, Kita K, Sakamoto T, Hanakawa T. Distinct roles of brain activity and somatotopic representation in pathophysiology of focal dystonia. *Hum Brain Mapp.* (2019) 40:1738–49. doi: 10.1002/hbm.24486
33. Lei Y, Perez MA. Cortical contributions to sensory gating in the ipsilateral somatosensory cortex during voluntary activity. *J Physiol.* (2017) 595:6203–17. doi: 10.1113/JP274504
34. Macerollo A, Brown MJN, Kilner JM, Chen R. Neurophysiological changes measured using somatosensory evoked potentials. *Trends Neurosci.* (2018) 41:294–310. doi: 10.1016/j.tins.2018.02.007
35. Subirà M, Sato JR, Alonso P. do Rosário MC, Segalàs C, Batistuzzo MC, et al. Brain structural correlates of sensory phenomena in patients with obsessive-compulsive disorder. *J Psychiatry Neurosci.* (2015) 40:232–40. doi: 10.1503/jpn.140118
36. Berman BD, Horovitz SG, Morel B, Hallett M. Neural correlates of blink suppression and the buildup of a natural bodily urge. *Neuroimage.* (2012) 59:1441–50. doi: 10.1016/j.neuroimage.2011.08.050
37. Brown C, Shahab R, Collins K, Fleysher L, Goodman WK, Burdick KE, et al. Functional neural mechanisms of sensory phenomena in obsessive-compulsive disorder. *J Psychiatr Res.* (2019) 109:68–75. doi: 10.1016/j.jpsychires.2018.11.018
38. Noonan MP, Crittenden BM, Jensen O, Stokes MG. Selective inhibition of distracting input. *Behav Brain Res.* (2018) 355:36–47. doi: 10.1016/j.bbr.2017.10.010
39. Friehs MA, Klaus J, Singh T, Frings C, Hartwigsen G. Perturbation of the right prefrontal cortex disrupts interference control. *Neuroimage.* (2020) 222:117279. doi: 10.1016/j.neuroimage.2020.117279
40. Cipolotti L, Spanò B, Healy C, Tudor-Sfetea C, Chan E, White M, et al. Inhibition processes are dissociable and lateralized in human prefrontal cortex. *Neuropsychologia*. (2016) 93(Pt A):1–12. doi: 10.1016/j.neuropsychologia.2016.09.018
41. Wang S, Wang H, Zhao D, Liu X. Gray matter changes in patients with vestibular migraine. *Clin Radiol.* (2019) 74:898–e1. doi: 10.1016/S2213-2600(19)30337-6
42. Li Q, Huang X, Ye L, Wei R, Zhang Y, Zhong Y-L, et al. Altered spontaneous brain activity pattern in patients with late monocular blindness in middle-age using amplitude of low frequency fluctuation: a resting-state functional MRI study. *J. Clin Interv Aging.* (2016) 11:1773–80. doi: 10.2147/CIA.S117292
43. Liang Z, Zexuan LI, Xiaowen LU. High efficiency of left superior frontal gyrus and the symptom features of major depressive disorder. *J Cent South Univ*. (2022) 03:15.
44. Nusslock R, Alloy LB. Reward processing and mood-related symptoms: an RDoC and translational neuroscience perspective. *J Affect Disord.* (2017) 216:3–16. doi: 10.1016/j.jad.2017.02.001
45. Robert G, Bannier E, Comte M, Domain L, Corouge I, Dondaine T, et al. Multimodal brain imaging connectivity analyses of emotional and motivational deficits in depression among women. *J Psychiatry Neurosci.* (2021) 46:E303–12. doi: 10.1503/jpn.200074
46. Wang L, Dai Z, Peng H, Tan L, Ding Y, He Z, et al. Overlapping and segregated resting-state functional connectivity in patients with major depressive disorder with and without childhood neglect. *Hum Brain Mapp.* (2014) 35:1154–66. doi: 10.1002/hbm.22241
47. Jiang X, Shen Y, Yao J, Zhang L, Xu L, Feng R, et al. Connectome analysis of functional and structural hemispheric brain networks in major depressive disorder. *Transl Psychiatry*. (2019) 9:136. doi: 10.1038/s41398-019-0467-9
48. American Psychiatric Association. *Diagnostic and Statistical Manual of Mental Disorders: Dsm-5*. Arlington, VA: Amer Psychiatric Pub Incorporated (2013).
49. Grupe DW, Oathes DJ, Nitschke JB. Dissecting the anticipation of aversion reveals dissociable neural networks. *Cereb Cortex.* (2013) 23:1874–83. doi: 10.1093/cercor/bhs175
50. Balderston NL, Liu J, Roberson-Nay R, Ernst M, Grillon C. The relationship between dlPFC activity during unpredictable threat and CO2-induced panic symptoms. *Transl Psychiatry*. (2017) 7:1266. doi: 10.1038/s41398-017-0006-5
51. Balderston NL, Beydler EM, Roberts C, Deng ZD, Radman T, Lago T, et al. Mechanistic link between right prefrontal cortical activity and anxious arousal revealed using transcranial magnetic stimulation in healthy subjects. *Neuropsychopharmacology.* (2020) 45:694–702. doi: 10.1038/s41386-019-0583-5
52. Brascamp J, Sterzer P, Blake R, Knapen T. Multistable perception and the role of the frontoparietal cortex in perceptual inference. *Annu Rev Psychol.* (2018) 69:77–103. doi: 10.1146/annurev-psych-010417-085944
53. Panagiotaropoulos TI, Dwarakanath A, Kapoor V. Prefrontal cortex and consciousness: beware of the signals. *Trends Cogn Sci.* (2020) 24:343–4. doi: 10.1016/j.tics.2020.02.005
54. Watanabe T. Causal roles of prefrontal cortex during spontaneous perceptual switching are determined by brain state dynamics. *Elife.* (2021) 10:e69079. doi: 10.7554/eLife.69079
55. Stein DJ, Costa DLC, Lochner C, Miguel EC, Reddy YCJ, Shavitt RG, et al. Obsessive-compulsive disorder. *Nat Rev Dis Primers.* (2019) 5:52. doi: 10.1038/s41572-019-0102-3
56. Boedhoe PSW, Schmaal L, Abe Y, Alonso P, Ameis SH, Anticevic A, et al. Cortical abnormalities associated with pediatric and adult obsessive-compulsive disorder: findings from the ENIGMA obsessive-compulsive disorder working group. *Am J Psychiatry.* (2018) 175:453–62. doi: 10.1176/appi.ajp.2017.17050485
57. Gürsel DA, Avram M, Sorg C, Brandl F, Koch K. Frontoparietal areas link impairments of large-scale intrinsic brain networks with aberrant fronto-striatal interactions in OCD: a meta-analysis of resting-state functional connectivity. *Neurosci Biobehav Rev.* (2018) 87:151–60. doi: 10.1016/j.neubiorev.2018.01.016
58. Li H, Hu X, Gao Y, Cao L, Zhang L, Bu X, et al. Neural primacy of the dorsolateral prefrontal cortex in patients with obsessive-compulsive disorder. *Neuroimage Clin.* (2020) 28:102432. doi: 10.1016/j.nicl.2020.102432
59. Yang J, Li J, Yu B, Ye QY, Zhu L, Shi PW, et al. Altered intrinsic brain activity in patients with toothaches using the amplitude of low-frequency

fluctuations: a resting -state fMRI study. *Neuropsychiatr Dis Treat*. (2019) 15:283–91. doi: 10.2147/NDT.S189962

Conflict of Interest: The authors declare that the research was conducted in the absence of any commercial or financial relationships that could be construed as a potential conflict of interest.

Publisher's Note: All claims expressed in this article are solely those of the authors and do not necessarily represent those of their affiliated organizations, or those of the publisher, the editors and the reviewers. Any product that may be evaluated in this article, or claim that may be made by its manufacturer, is not guaranteed or endorsed by the publisher.

Copyright © 2022 Yang, Shao, Shen, Zhu, Li, Yu, Kang, Xu, Ying, Ling, Zou, Wei and He. This is an open-access article distributed under the terms of the Creative Commons Attribution License (CC BY). The use, distribution or reproduction in other forums is permitted, provided the original author(s) and the copyright owner(s) are credited and that the original publication in this journal is cited, in accordance with accepted academic practice. No use, distribution or reproduction is permitted which does not comply with these terms.

frontiers | Frontiers in Neurology

REVIEW
published: 23 June 2022
doi: 10.3389/fneur.2022.860144

Application and Research Progress of High Frequency Ultrasound in the Diagnosis of Chronic Inflammatory Neuropathies

Xishun Ma[1], *Lizhen Du*[1], *Wenqing Yuan*[2]* *and Tongliang Han*[1]*

[1] Department of Ultrasound, Qingdao Municipal Hospital, Qingdao, China, [2] Department of Primary Medical Management, Qingdao Municipal Hospital, Qingdao, China

OPEN ACCESS

Edited by:
Yuzhen Xu,
Tongji University, China

Reviewed by:
Huawei Zhang,
Shandong Provincial Hospital, China
Zhibin Wang,
The Affiliated Hospital of Qingdao University, China
Jie Li,
Shandong University, China

***Correspondence:**
Tongliang Han
hantongliang_qd@sina.com
Wenqing Yuan
qdhl720@163.com

Specialty section:
This article was submitted to Neurological Biomarkers, a section of the journal Frontiers in Neurology

Received: 22 January 2022
Accepted: 25 April 2022
Published: 23 June 2022

Citation:
Ma X, Du L, Yuan W and Han T (2022) Application and Research Progress of High Frequency Ultrasound in the Diagnosis of Chronic Inflammatory Neuropathies. Front. Neurol. 13:860144. doi: 10.3389/fneur.2022.860144

In recent years, clinicians have gradually improved their understanding of multiple neuropathy and have done some studies about chronic inflammatory neuropathies, for example, chronic inflammatory demyelinating polyneuropathy, multifocal motor neuropathy, and Lewis-Sumne syndrome. The early diagnosis is very important for the next step treatment and long-term prognosis. At present, the disease mainly depends on clinical and neural electrophysiological examination, but imaging studies are few. In recent years, with the rapid development of high frequency ultrasound, it could clearly show the morphology of the nerve, and it has been an emerging diagnosis tool of polyneuropathies. This article mainly reviews the application and the latest research progress of high frequency ultrasound in these diseases.

Keywords: chronic inflammatory neuropathies, chronic inflammatory demyelinating polyneuropathies, multifocal motor neuropathy (MMN), Lewis-Sumner syndrome, high frequency ultrasound

INTRODUCTION

The diagnosis of chronic inflammatory neuropathies could be challenging (1, 2). The current diagnostic criteria are mainly based on both clinical and electrophysiological parameters. Particularly in chronic inflammatory neuropathies cases with atypical clinical presentation or at early stages of the diseases, the early diagnosis rate is low, and it lacks quantitative criteria for assessing disease activity and treatment response, leading to severely affecting long-term prognostic effects of such diseases. Recent studies have shown that nerve ultrasound has a high sensitivity and acceptable specificity in a cohort of consecutive patients with a clinical suspicion of chronic inflammatory demyelinating polyneuropathy, Lewis-Sumner syndrome, and multifocal motor neuropathy, thereby improving identification of patients who may respond to treatment (3–5). Exploring the imaging characteristics of high-frequency ultrasound could help to establish combined diagnostic criteria for chronic inflammatory neuropathies, improve the accuracy of early diagnosis, and facilitate the follow-up of diseases.

THE ULTRASOUND RESEARCH PROCESS OF CHRONIC INFLAMMATORY NEUROPATHIES

Chronic Inflammatory Demyelinating Polyneuropathy

The Ultrasound Imaging Features of Chronic Inflammatory Demyelinating Polyneuropathy

The chronic inflammatory demyelinating polyneuropathy is an immune-mediated chronic sensorimotor polyneuropathy characterized by proximal limb weakness, weakened tendon reflex, and sensory abnormalities in distal limb, but it also includes rare clinical variants such as simple sensory abnormalities, simple motor abnormalities, and limb asymmetry (6, 7). High-frequency ultrasound can probe the morphological changes in the peripheral nerves to indirectly reflect the neuropathological changes of chronic inflammatory demyelinating polyneuropathy, so it could contribute to diagnosis and treatment (8–10). Several studies confirmed that nerve enlargement occurred in over 90% of patients with chronic inflammatory demyelinating polyneuropathy whether treated or not, but it had a different degree and morphologies. Specific results showed that the cross-sectional area of new chronic inflammatory demyelinating polyneuropathy and long-term-treated chronic inflammatory demyelinating polyneuropathy increased. The ultrasound pattern sum score system: chronic inflammatory demyelinating polyneuropathy scores were higher than new chronic inflammatory demyelinating polyneuropathy. It had also shown that newly developed chronic inflammatory demyelinating polyneuropathy nerve enlargement was mostly localized, however, chronic inflammatory demyelinating polyneuropathy was generalized. The uniformity score results showed that chronic inflammatory demyelinating polyneuropathy had higher points than new chronic inflammatory demyelinating polyneuropathy (11, 12). Nerve enlargement mainly occurred in the upper limb proximal nerve segments and the arm plexus (13, 14), and ultrasound had a high diagnostic rate of evaluation of nerves in these areas (13). In addition to nerve enlargement, there were increased blood flow signals, enhanced echo or disappearance of normal nerve structures (8, 14). Most studies had found a relationship between nerve enlargement and slow motor conduction velocity (9). Padua and colleagues found that nerve enlargement was more pronounced in patients with longer disease duration and that echo at the disappearance of normal nerve tract structure was decreased (14).

In addition, some studies found that chronic inflammatory neuropathies had higher echoes compared to axonal neuropathy in the ulnar nerve of the forearm, the median nerve in the forearm and upper arms, and the arm plexus, which was statistically significant, and it could contribute to the identification of disease. Since most studies are monocentric, further multicentre studies of the ultrasound aspects of chronic inflammatory demyelinating polyneuropathy are required.

Specific cases were shown in **Figures 1**, **2** (15, 16).

Monitoring Disease Treatment Response With HFUS

A scoring tool of standardized method or Ultrasound Pattern Sum Score can better monitor the treatment response, specifically, the changes before and after treatment can be quantified by measuring the cross-sectional area of nerves. Some studies reported that the extent of nerve enlargement attenuated or disappeared after a period of treatment (17). On the other hand, it had been observed that patients with hypoecho nerve enlargement had better treatment effect compared to those with no nerve enlargement or increased echo (13, 14).

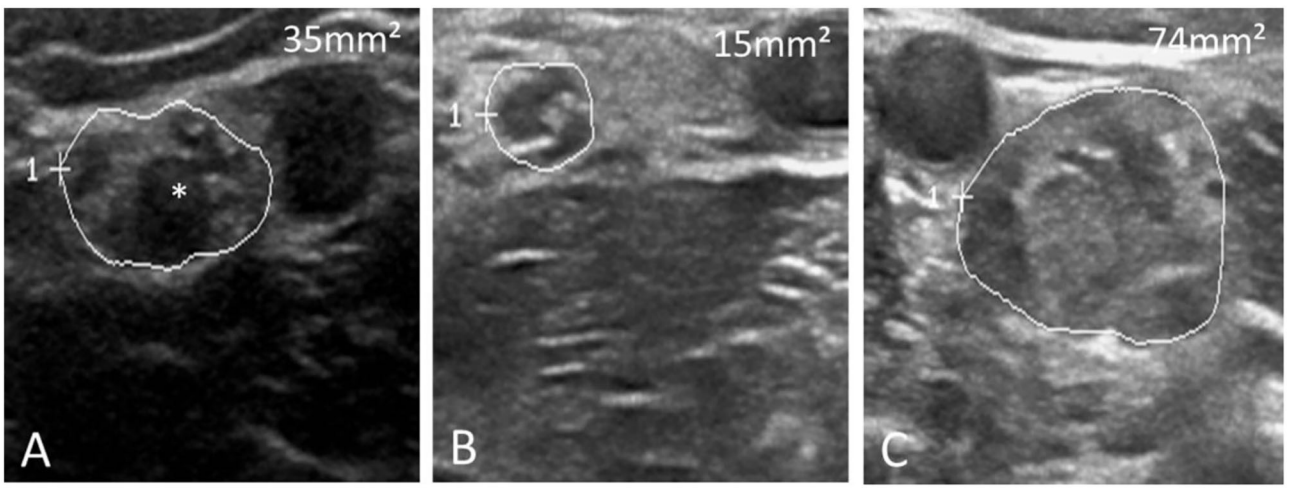

FIGURE 1 | Three distinct ultrasound morphologies in chronic inflammatory demyelinating polyneuropathy. **(A)** Shows an enlarged median nerve (MN, CSA 35 mm^2, normal values 13 mm^2) with reduced echointensity and enlarged fascicles (*), while **(B)** Shows an only slightly enlarged nerve without fascicle enlargement (CSA 15 mm^2). In contrast, in **(C)** the MN is tremendously enlarged (74 mm^2) with otherwise hyperechoic intraneural echo signature. **(A)** Resembles the most common nerve morphology in chronic inflammatory demyelinating polyneuropathy.

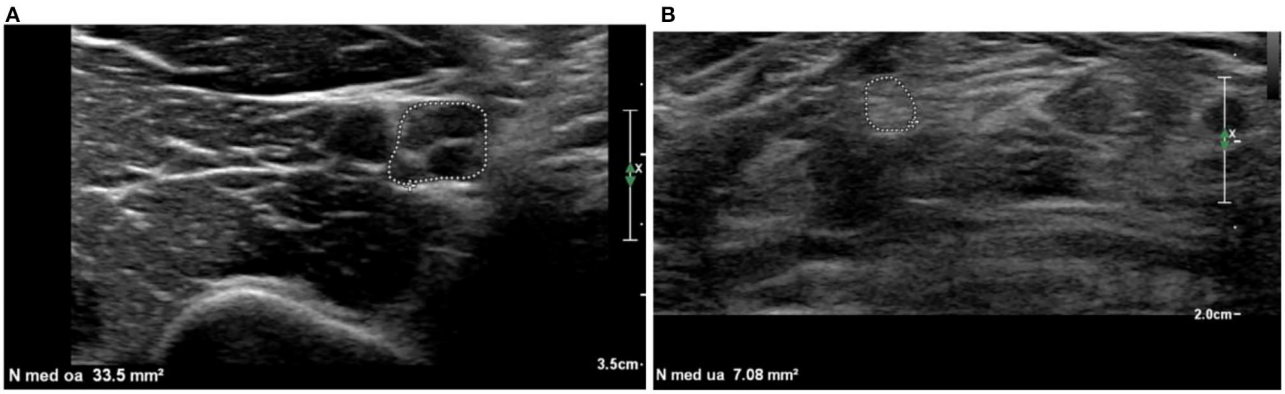

FIGURE 2 | Examples of a hypoechoic **(A)** and hyperechoic **(B)** nerve. **(A)** Median nerve at the upper arm is enlarged (CSA = 33.5 mm^2) and shows enlarged hypoechoic fascicles (fraction of black = 85%). **(B)** Median nerve at the forearm with CSA in normal range, hyperechoic (fraction of black = 9%), fascicles are difficult to distinct. Hyperechoic nerves as in **(B)** can be difficult to distinguish from the surrounding structures. Continuous examination of the whole length of the nerve and identification based on the known anatomical course is necessary to ensure proper identification of the nerve and the nerve outline.

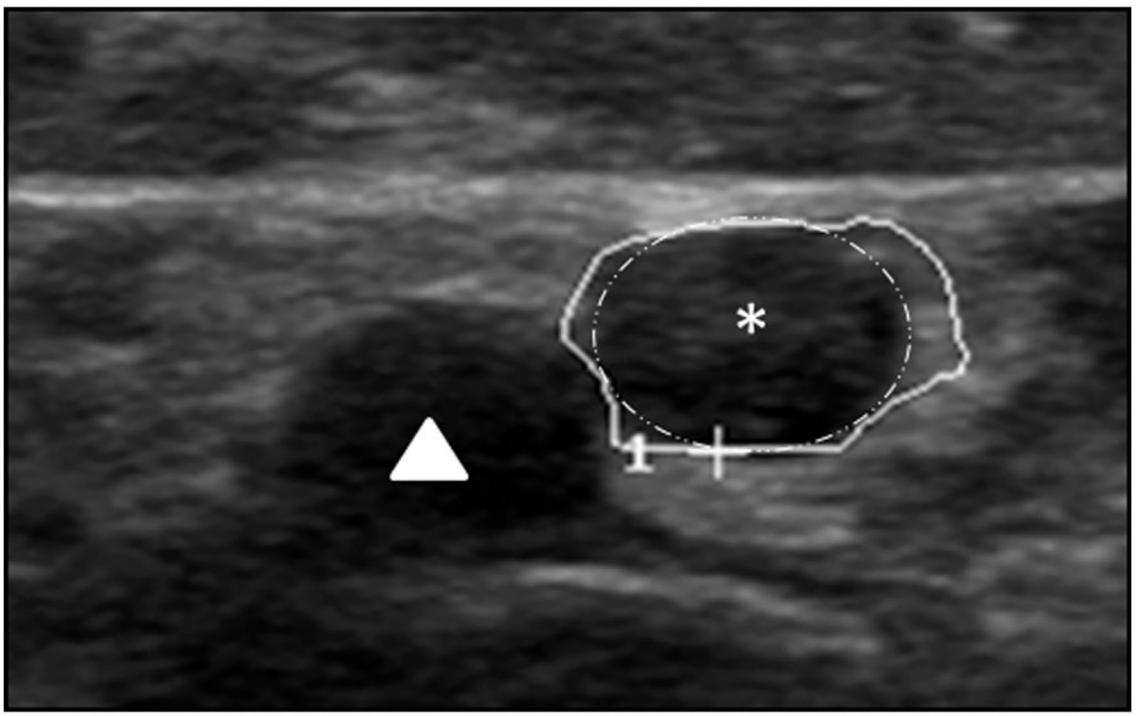

FIGURE 3 | This shows a regionally predominant fascicle enlargement (white surrounding with star) with 9 mm^2 next to normal fascicles in the median nerve (14 mm^2) in a patient with Lewis-Sumner syndrome, accompanied by the brachial artery (triangle). The enlarged fascicle almost covers the whole CSA.

Multifocal Motor Neuropathy

The Ultrasound Imaging Features of Multifocal Motor Neuropathy

Multifocal motor neuropathy is an immune-mediated, simple motor neuropathy characterized by slow disease progression, a typical limb asymmetry muscle weakness that can be accompanied by muscular atrophy (18–21). The characteristic electrophysiological examination criterion for multifocal motor neuropathy is the conduction block at common neurojammed sites (22). Nerve ultrasound imaging features contribute to diagnosis and differential diagnosis of multifocal motor neuropathy.

Nerve enlargement of multifocal motor neuropathy, which often represents mild multifocal and asymmetry compared to chronic inflammatory demyelinating polyneuropathy, was

TABLE 1 | The ultrasonic pattern sum score UPSS.

Measurement	Boundary value in mm^2	Normal <50% >50%	Points
Peripheral nerves			
Median nerve	10.0	<10	0
Upper arm		≥10 ≤ 15	1
		>15	2
Median nerve	11.5	<11.5	0
Elbow		≥11.5 ≤ 17.25	1
		>17.25	2
Median nerve	10.0	<10	0
Forearm		≥10 ≤ 15	1
		>15	2
Ulnar nerve	9.5	<9.5	0
Upper arm		≥9.5 ≤ 14.25	1
		>14.25	2
Ulnar nerve	8.5	<8.5	0
Forearm		≥8.5 ≤ 12.75	1
		>12.75	2
Tibial nerve	29.5	<29.5	0
Popliteal		≥29.5 ≤ 44.25	1
		>44.25	2
Tibial nerve	10.5	<10.5	0
Ankle		≥10.5 ≤ 16.25	1
		>16.25	2
Fibular nerve	11.5	≤11.5	0
Popliteal		≥11.5 ≤ 17.25	1
		>17.25	2
Cervical roots and vagus			
Vagal nerve	3.0	≤3.0	0
Carotid sheath		>3.0	1
C5 longitudinal	2.9 (mm)	≤2.9	0
Transversal process		>2.9	1
C6 longitudinal	3.9 (mm)	≤3.9	0
Transversal process		>3.9	1
Sural nerve			
Sural nerve	3.0	≤3.0	0
Calf		>3.0	1
Ultrasound pattern sum score			

UPS-A. Nerve score: each nerve swelling is assessed with 1 point, each swelling > 50% of the boundary value is assessed with 2 points. UPS-B. Root score: each root swelling or vagal nerve swelling is assessed with 1 point. UPS-C. Sural score: sural nerve swelling is assessed with 1 point. UPSS, ultrasound pattern sum score.

mainly found in the arm plexus and large peripheral nerve in the extremities (23, 24).

The study showed that multifocal nerve enlargement could distinguish multifocal motor neuropathy from healthy control subjects with a sensitivity of 87–100% and a specificity of 94–100% (25–27). The ratio of CSA differences of intra-and internerve and one side and other side [two ultrasound scoring systems (28, 29)] was also increased in multifocal motor neuropathy patients (24, 30). Individual nerve bundles within the nerve may also have varying degrees of enlargement, while adjacent bundles are intact (31). Thus, asymmetric multifocal nerve enlargement may indicate multifocal motor neuropathy, but further studies remain to determine the specificity of this finding, compared to other polynerves, such as asymmetry variants of chronic inflammatory demyelinating polyneuropathy. Some studies showed that the multifocal motor neuropathy group was more pronounced in the median forearm nerve, the ulnar nerve, and the tibia nerve, compared with normal controls. Neuroelectrophysiological examination indicated that it had lower nerve conduction velocity and compound muscle action potential at the upper arm nerve. The multifocal motor neuropathy group had important relationship between CSA of the median nerve in the upper arm and the compound muscle action potential (correlation $r = 0.851$). The multifocal motor neuropathy group had a higher "difference ratio of CSA between one side and the other" in the median, ulnar, and fibula nerve levels, with no significant change in the tibial and brachial plexus levels. Compared with chronic inflammatory demyelinating polyneuropathy, multifocal motor neuropathy patients predominantly showed reduced echo of nerve enlargement areas (31). It rarely found increased echo compared to Lewis-Sumner syndrome and chronic inflammatory demyelinating polyneuropathy, which may contribute to the differential diagnosis of multifocal motor neuropathy and other major motor neuropathies.

Monitoring Disease Treatment Response With HFUS

Recently, it is rarely known about the treatment response and ultrasound application development of multifocal motor neuropathy. A recent study, following up 17 treated multifocal motor neuropathy patients for several months, firstly, demonstrated the degree of nerve enlargement was not proportional to clinical presentation, and secondly, the Ultrasound Pattern Sum Score score demonstrated a significant correlation between changes in motor nerve dysfunction and changes in ultrasound imaging regardless of the disease development (32).

Lewis-Sumner Syndrome

The Ultrasound Imaging Features of Lewis-Sumner Syndrome

Lewis-Sumner syndrome belongs to a variant of chronic inflammatory demyelinating polyneuropathy, an autoimmune disease, mainly showing limb asymmetric sensory, motor peripheral neuropathy. The most commonly involved nerves are the median nerve and the ulnar nerve. The electrophysiological examination has the motor nerve block, and the pathological characteristics are mainly mild demyelinating lesions.

No studies analyzed lewis-sumner syndrome as a single entity, but many studies described its ultrasound performance second only to chronic inflammatory demyelinating polyneuropathy and multifocal motor neuropathy (33). Overall, researchers agreed that most Lewis-Sumner syndrome patients had nerve enlargement. In many cases, neuromorphological changes were similar to chronic inflammatory demyelinating polyneuropathy, with nerve enlargement ranging from mild to widespread.

TABLE 2 | Ultrasound findings in the median nerve at standard sites.

		CSA, wrist		CSA, forearm		CSA, arm		CSA, axilla	
Patient number	**Neuropathy**	**Right**	**Left**	**Right**	**left**	**Right**	**Left**	**Right**	**Left**
1	CIDP	**16**	**12**	**10**	6	**16**	**13**	**16**	**14**
2	CIDP	**15**	**14**	**22**	**21**	**42**	**29**	**32**	**19**
3	MMN	11	**15**	**10**	**17**	**19**	**28**	**23**	**22**
4	MMN	7	8	5	5	5	10	8	8
5	Anti-MAG	9	7	6	**9**	**12**	**13**	15	10
6	Anti-MAG	**13**	10	8	**9**	7	10	8	10

CSA measured in mm^2. Abnormal values shown in bold.

TABLE 3 | Ultrasound findings in the ulnar nerve at standard sites.

		CSA, wrist		CSA, forearm		CSA, elbow		CSA, arm		CSA, axilla	
Patient number	**Neuropathy**	**Right**	**Left**	**Right**	**left**	**Right**	**Left**	**Right**	**Left**	**Right**	**Left**
1	CIDP	6	5	7	7	**16**	**8**	**11**	**12**	**15**	**12**
2	CIDP	**14**	**10**	**18**	**21**	**13**	**17**	**17**	**24**	**21**	**18**
3	MMN	7	4	6	**17**	**14**	**19**	**15**	4	**12**	6
4	MMN	4	6	4	5	**14**	5	**60**	8	6	3
5	Anti-MAG	4	5	6	**9**	**10**	7	**9**	**8**	8	8
6	Anti-MAG	4	4	7	**10**	7	5	7	8	6	9

CSA measured in mm^2. Abnormal values are shown in bold.

However, recent studies showed that Lewis-Sumner syndrome nerve enlargement was mainly regional and limited to a single major nerve tract, rarely affecting asymmetric distributed nerve in the arm and roots (34).

Interestingly, the echo intensity of enlarged nerves usually decreased, but sometimes also increased, with as described by chronic inflammatory demyelinating polyneuropathy, and the cranial nerves were more susceptible in Lewis-Sumner syndrome than in chronic inflammatory demyelinating polyneuropathy, such as vagus enlargement (35, 36). In summary, the Lewis-Sumner syndrome ultrasound morphology behaved similar to an overlapping chronic inflammatory demyelinating polyneuropathy and multifocal motor neuropathy. This may explain the intermediate treatment response and Lewis-Sumner syndrome clinical presentation, sometimes like typical chronic inflammatory demyelinating polyneuropathy, sometimes like multifocal motor neuropathy. However, Lewis-Sumner syndrome generally reflected nerve enlargement of the sensory nerve, which can be distinguished from multifocal motor neuropathy (25).

Specific cases were shown in **Figure 3** (32).

Monitoring Disease Treatment Response With HFUS

With regard to ultrasound changes during treatment, most investigators found recoverance of enlarged nerves in response to treatment (17, 37). It had also been reported that nerve enlargement continued with despite improved clinical symptoms (36). However, prospective studies of disease and ultrasound monitoring remain unknown.

THE CLINICAL ULTRASOUND SCORING SYSTEM

Bochum Scoring

Measuring: the ulnar nerve in the Guyon canal; the ulnar nerve in the upper arm; the radial nerve in the spiral groove; the sural nerve in the calf

Recording: every site scored one point, then added together

Results: identification of chronic inflammatory demyelinating polyneuropathy from multifocal motor neuropathy and Lewis-Sumner syndrome (CSA cutoff value$\geq$ 2). Sensitivity was 80%, and specificity was 87.5% (38).

Ultrasound Pattern Sum Score Scoring

Measuring: median nerve of upper arm, elbow and forearm; ulnar nerve of upper arm and forearm; tibial nerve of popliteal fossa and ankle; peroneal nerve of popliteal fossa; vagus; C5 nerve root; C6 nerve root; sural nerve of calf

Recording:

UPS-A: measuring median nerve, ulnar nerve, tibial nerve, if nerve enlargement <50%, it scored one point. If nerve enlargement >50%, it scored two points.

UPS-B: measuring vagus, C5 and C6 nerve root, every site of nerve enlargement scores one point.

UPS-C: measuring sural nerve, every site of nerve enlargement scores one point.

UPSS: the scores sum of UPS-A, UPS-B and UPS-C

Results: UPSS $\geq$ 10 or UPS-A $\geq$ 7 indicated chronic inflammatory demyelinating polyneuropathy. 3 < UPSS < 10

and UPS-B $\leq$ 1 indicated vascular neuropathy. UPSS $\leq$ 3 indicated axonal neuropathy.

Specific cases were shown **Table 1** (13).

Hhomogeneity Scoring

Measuring: median nerve of forearm, elbow and upper arm; ulnar nerve of forearm and upper arm; tibial nerve of popliteal fossa and ankle

Recording:

0 point: no or regional nerve enlargement; one point:heterogenicity nerve enlargement (enlarged CSA $<$ 50% or $>$ 50%); two points: mild homogeneity nerve enlargement(enlarged CSA $<$ 50%); three points: obvious homogeneity nerve enlargement(enlarged CSA $>$ 50%).

Results: In chronic inflammatory demyelinating polyneuropathy the enlargement was regional, homogeneous, or inhomogeneous with equal contribution. In multifocal motor neuropathy rebional enlargement next to normal segments predominated (25).

Intra-and Internerve CSA Variabiity and Difference Ratio Between One Side and the Other Side

Measuring: any of the two nerves

Recording: Intranerve variability: the ratio of the maximum and the minimum CSA. Internerve variability: the ratio of the maximum and minimum of intranerve variability. The difference ratio between one side and other side: the ratio of maximum and minimum nerve variability.

Results: The ratio of intra-and internerve of multifocal motor neuropathy were higher than chronic inflammatory demyelinating polyneuropathy. Compared with multifocal motor neuropathy, chronic inflammatory demyelinating polyneuropathy had a higher ratio of intra-and internerve, but its ratio of one side and other side were lower.

Specific cases were shown **Tables 2**, **3** (29).

SUMMARY

As clinicians' awareness of chronic inflammatory neuropathy gradually increases, and the continuous development of high-frequency ultrasound, there are increasing studies about the clinical application of nerve ultrasound. The researchers explored the ultrasound characteristics of the disease, and it had a high specificity and sensitivity. The chronic inflammatory neuropathies mainly show nerve enlargement, increased blood flow signals, enhanced echo, or disappearance of normal nerve structures, morever, there are some few differences of them. However, the current study was small-sample studies, there were still limitations, and large-sample multicenter studies are needed in the future. Moreover, researchers should combine with the new ultrasound technology, such as elastography, ultrasound imaging, microvascular imaging, to continue to explore the ultrasound manifestations of such diseases, optimize the neural ultrasound scoring system, quantifying the diagnostic criteria for nerve ultrasound as well as the post-treatment evaluation system to better serve the clinical practice and meet the requirements of precision medicine.

AUTHOR CONTRIBUTIONS

All authors listed have made a substantial, direct, and intellectual contribution to the work and approved it for publication.

FUNDING

This work was supported by grants from Qingdao Medical Research Guidance Plan of 2020 (No. WJZD018).

ACKNOWLEDGMENTS

The authors thank all study participants.

REFERENCES

1. Bunschoten C, Jacobs BC, Van den Bergh PY, Cornblath DR, van Doorn PA. Progress in diagnosis and treatment of chronic inflammatory demyelinating polyradiculoneuropathy. *Lancet Neurol.* (2019) 18:784–94. doi: 10.1016/S1474-4422(19)30144-9
2. Lucke IM, Adrichem ME, Wieske L, van der Kooi AJ, Verhamme C, van Schaik IN, et al. Intravenous immunoglobulins in patients with clinically suspected chronic immune-mediated neuropathy. *J Neurol Sci.* (2019) 397:141–5. doi: 10.1016/j.jns.2018.12.036
3. Herraets IJ, Goedee HS, Telleman JA, van Asseldonk JT, Visser LH, van der Pol WL, et al. High-resolution ultrasound in patients with Wartenberg's migrant sensory neuritis, a case-control study. *Clin Neurophysiol.* (2018) 129:232–7. doi: 10.1016/j.clinph.2017.10.040
4. Telleman JA, Herraets IJ, Goedee HS, Verhamme C, Nikolakopoulos S, van Asseldonk JT, et al. Nerve ultrasound: a reproducible diagnostic tool in peripheral neuropathy. *Neurology.* (2019) 92:443–450. doi: 10.1212/WNL.0000000000006856
5. Herraets IJ, Goedee HS, Telleman JA, van Eijk RP, van Asseldonk JT, Visser LH, et al. Nerve ultrasound improves detection of treatment-responsive chronic inflammatory neuropathies. *Neurology.* (2020) 94:e1470–9. doi: 10.1212/WNL.0000000000008978
6. Joint Task Force of the EPNS. European Federation of Neurological Societies/Peripheral Nerve Society guideline on management of multifocal motor neuropathy. Report of a joint task force of the European Federation of Neurological Societies and the Peripheral Nerve Society—first revision. *J Peripher Nerv Syst.* (2010) 15:295–301. doi: 10.1111/j.1529-8027.2010.00290.x
7. Latov N. Diagnosis and treatment of chronic acquired demyelinating polyneuropathies. *Nat Rev Neurol.* (2014) 10:435–46. doi: 10.1038/nrneurol.2014.117
8. Goedee HS, Brekelmans GJ, Visser LH. Multifocal enlargement and increased vascularization of peripheral nerves detected by sonography in chronic inflammatory demyelinating polyneuropathy: a pilot study. *Clin Neurophysiol.* (2014) 125:154–9. doi: 10.1016/j.clinph.2013.05.025
9. Grimm A, Heiling B, Schumacher U, Witte OW, Axer H. Ultrasound differentiation of axonal and demyelinating neuropathies. *Muscle Nerve.* (2014) 50:976–83. doi: 10.1002/mus.24238
10. Kerasnoudis A, Pitarokoili K, Behrendt V, Gold R, Yoon MS. Nerve ultrasound score in distinguishing chronic from acute inflammatory demyelinating polyneuropathy. *Clin Neurophysiol.* (2014) 125:635–41. doi: 10.1016/j.clinph.2013.08.014

11. Goedee HS, Jongbloed BA, van Asseldonk J-TH, Hendrikse J, Vrancken AFJE, Franssen H, et al. A comparative study of brachial plexus sonography and magnetic resonance imaging in chronic inflammatory demyelinating neuropathy and multifocal motor neuropathy. *Eur J Neurol.* (2017) 24:1307–1313. doi: 10.1111/ene.13380
12. Grimm A, Vittore D, Schubert V, Rasenack M, Décard BF, Heiling B, et al. Ultrasound aspects in therapy-naive chronic inflammatory demyelinating polyneuropathy compared to long-term treated chronic inflammatory demyelinating polyneuropathy. *J Neurol.* (2016) 263:1074–82. doi: 10.1007/s00415-016-8100-9
13. Grimm A, Decard BF, Axer H, Fuhr P. The ultrasound pattern sum score - UPSS. A new method to differentiate acute and subacute neuropathies using ultrasound of the peripheral nerves. *Clin Neurophysiol.* (2015) 126:2216–25. doi: 10.1016/j.clinph.2015.01.011
14. Padua L, Granata G, Sabatelli M, Inghilleri M, Lucchetta M, Luigetti M, et al. Heterogeneity of root and nerve ultrasound pattern in chronic inflammatory demyelinating polyneuropathy patients. *Clin Neurophysiol.* (2014) 125:160–5. doi: 10.1016/j.clinph.2013.07.023
15. Décard BF, Pham M, Grimm A. Ultrasound and MRI of nerves for monitoring disease activity and treatment effects in chronic dysimmune neuropathies - current concepts and future directions. *Clin Neurophysiol.* (2018) 129:155–67. doi: 10.1016/j.clinph.2017.10.028
16. Fisse AL, Pitarokoili K, Motte J, Gamber D, Kerasnoudis A, Gold R, et al. Nerve echogenicity and intranerve CSA variability in high-resolution nerve ultrasound (HRUS) in chronic inflammatory demyelinating polyneuropathy (chronic inflammatory demyelinating polyneuropathy). *J Neurol.* (2019) 266:468–75. doi: 10.1007/s00415-018-9158-3
17. Grimm A, Rasenack M, Athanasopoulou I, Peters N, Fuhr P. Long-term observations in asymmetric immune-mediated neuropathy with vagus hypertrophy using ultrasound of the nerves. *J Neurol Sci.* (2015) 356:205–8. doi: 10.1016/j.jns.2015.06.018
18. Van Asseldonk JT, Franssen H, Van den Berg-Vos RM, Wokke JH, Van den Berg LH. Multifocal motor neuropathy. *Lancet Neurol.* (2005) 4:309–19. doi: 10.1016/S1474-4422(05)70074-0
19. Vlam L, van der Pol WL, Cats EA, Straver DC, Piepers S, Franssen H, et al. Multifocal motor neuropathy: diagnosis, pathogenesis and treatment strategies. *Nat Rev Neurol.* (2012) 8:48–58. doi: 10.1038/nrneurol.2011.175
20. Harschnitz O, Jongbloed BA, Franssen H, Straver DC, van der Pol WL, van den Berg LH. Multifocal motor neuropathy: from immunological cross-talk to conduction block. *J Clin Immunol.* (2014) 34(Suppl. 1):S112–9. doi: 10.1007/s10875-014-0026-3
21. Harschnitz O, van den Berg LH, Johansen LE, Jansen MD, Kling S, Vieira de Sa R, et al. Autoantibody pathogenicity in a multifocal motor neuropathy induced pluripotent stem cell-derived model. *Ann Neurol.* (2016) 80:71–88. doi: 10.1002/ana.24680
22. Ginanneschi F, Filippou G, Giannini F, Carluccio MA, Adinolfi A, Frediani B, et al. Sonographic and electrodiagnostic features of hereditary neuropathy with liability to pressure palsies. *J Peripher Nerv Syst.* (2012) 17:391–8. doi: 10.1111/j.1529-8027.2012.00437.x
23. Zaidman CM, Harms MB, Pestronk A. Ultrasound of inherited vs. acquired demyelinating polyneuropathies. *J Neurol.* (2013) 260:3115–21. doi: 10.1007/s00415-013-7123-8
24. Kerasnoudis A, Pitarokoili K, Behrendt V, Gold R, Yoon MS. Multifocal motor neuropathy: correlation of nerve ultrasound, electrophysiological, and clinical findings. *J Peripher Nerv Syst.* (2014) 19:165–74. doi: 10.1111/jns5.12067
25. Grimm A, Decard BF, Athanasopoulou I, Schweikert K, Sinnreich M, Axer H. Nerve ultrasound for differentiation between amyotrophic lateral sclerosis and multifocal motor neuropathy. *J Neurol.* (2015) 262:870–80. doi: 10.1007/s00415-015-7648-0
26. Loewenbrück KF, Liesenberg J, Dittrich M, Schafer J, Patzner B, Trausch B, et al. Nerve ultrasound in the differentiation of ultifocal motor neuropathy (multifocal motor neuropathy) and amyotrophic lateral sclerosis with predominant lower motor neuron disease (ALS/LMND). *J Neurol.* (2016) 263:35–44. doi: 10.1007/s00415-015-7927-9
27. Nodera H, Izumi Y, Takamatsu N, Kaji R. Cervical root sonography to differentiate multifocal motor neuropathy from ALS. *J Med Invest.* (2016) 63:104–7. doi: 10.2152/jmi.63.104
28. Kerasnoudis A, Pitarokoili K, Behrendt V, Gold R, Yoon MS. Cross sectional area reference values for sonography of peripheral nerves and brachial plexus. *Clin Neurophysiol.* (2013) 124:1881–8. doi: 10.1016/j.clinph.2013.03.007
29. Padua L, Martinoli C, Pazzaglia C, Lucchetta M, Granata G, Erra C, et al. Intra- and internerve cross-sectional area variability: new ultrasound measures. *Muscle Nerve.* (2012) 45:730–3. doi: 10.1002/mus.23252
30. Kerasnoudis A, Klasing A, Behrendt V, Gold R, Yoon MS. Intra- and internerve crosssectional area variability: new ultrasound measures. *Muscle Nerve.* (2013) 47:146–7. doi: 10.1002/mus.23520
31. Rattay T, Winter N, Décard B, Dammeier N, Härtig F, Ceanga M, et al. Nerve ultrasound as follow-up tool in treated multifocal motor neuropathy. *Eur J Neurol.* (2017) 24:1125–1134. doi: 10.1111/ene.13344
32. Gasparotti R, Padua L, Briani C, Lauria G. New technologies for the assessment of neuropathies. *Nat Rev Neurol.* (2017) 13:203–16. doi: 10.1038/nrneurol.2017.31
33. Goedee HS, van der Pol WL, van Asseldonk J-TH, Franssen H, Notermans NC, Vrancken AJFE, et al. Diagnostic value of sonography in treatment-naive chronic inflammatory neuropathies. *Neurology.* (2017) 88:143–51. doi: 10.1212/WNL.0000000000003483
34. Pitarokoili K, Gold R, Yoon M-S. Nerve ultrasound in a case of multifocal motor neuropathy without conduction block. *Muscle Nerve.* (2015) 52:294–9. doi: 10.1002/mus.24583
35. Grimm A, Thomaser A-L, Peters N, Fuhr P. Neurological picture. Vagal hypertrophy in immune-mediated neuropathy visualised with high-resolution ultrasound (HR-US). *J Neurol Neurosurg Psychiatry.* (2015) 86:1277–8. doi: 10.1136/jnnp-2014-308271
36. Scheidl E, Böhm J, Simó M, Rózsa C, Bereznai B, Kovács T, et al. Ultrasonography of MADSAM neuropathy: focal nerve enlargements at sites of existing and resolved conduction blocks. *Neuromuscul Disord.* (2012) 22:627–31. doi: 10.1016/j.nmd.2012.03.005
37. Neubauer C, Gruber H, Bäuerle J, Egger K. Ultrasonography of multifocal acquired demyelinating sensory and motor neuropathy (MADSAM). *Clin Neuroradiol.* (2015) 25:423–5. doi: 10.1007/s00062-014-0364-9
38. Kerasnoudis A, Pitarokoili K, Gold R, Yoon MS. Bochum ultrasound score allows distinction of chronic inflammatory from multifocal acquired demyelinating polyneuropathies. *J Neurol Sci.* (2015) 348:211–5. doi: 10.1016/j.jns.2014.12.010

Conflict of Interest: The authors declare that the research was conducted in the absence of any commercial or financial relationships that could be construed as a potential conflict of interest.

Publisher's Note: All claims expressed in this article are solely those of the authors and do not necessarily represent those of their affiliated organizations, or those of the publisher, the editors and the reviewers. Any product that may be evaluated in this article, or claim that may be made by its manufacturer, is not guaranteed or endorsed by the publisher.

Copyright © 2022 Ma, Du, Yuan and Han. This is an open-access article distributed under the terms of the Creative Commons Attribution License (CC BY). The use, distribution or reproduction in other forums is permitted, provided the original author(s) and the copyright owner(s) are credited and that the original publication in this journal is cited, in accordance with accepted academic practice. No use, distribution or reproduction is permitted which does not comply with these terms.

frontiers | Frontiers in Neurology

ORIGINAL RESEARCH
published: 30 June 2022
doi: 10.3389/fneur.2022.880902

Early Changes in the White Matter Microstructure and Connectome Underlie Cognitive Deficit and Depression Symptoms After Mild Traumatic Brain Injury

Wenjing Huang[1,2,3], *Wanjun Hu*[1,3], *Pengfei Zhang*[1,2,3], *Jun Wang*[1,2,3], *Yanli Jiang*[1,2,3], *Laiyang Ma*[1,2,3], *Yu Zheng*[1,2,3] *and Jing Zhang*[1,3]*

[1] *Department of Magnetic Resonance, Lanzhou University Second Hospital, Lanzhou, China,* [2] *Second Clinical School, Lanzhou University, Lanzhou, China,* [3] *Gansu Province Clinical Research Center for Functional and Molecular Imaging, Lanzhou, China*

OPEN ACCESS

Edited by:
Yuzhen Xu,
Tongji University, China

Reviewed by:
Qian Chen,
Capital Medical University, China
Jian-Jun Yang,
Zhengzhou University, China

***Correspondence:**
Jing Zhang
lztong2001@163.com

Specialty section:
This article was submitted to Neurological Biomarkers, a section of the journal Frontiers in Neurology

Received: *22 February 2022*
Accepted: *01 June 2022*
Published: *30 June 2022*

Citation:
Huang W, Hu W, Zhang P, Wang J, Jiang Y, Ma L, Zheng Y and Zhang J (2022) Early Changes in the White Matter Microstructure and Connectome Underlie Cognitive Deficit and Depression Symptoms After Mild Traumatic Brain Injury. Front. Neurol. 13:880902. doi: 10.3389/fneur.2022.880902

Cognitive and emotional impairments are frequent among patients with mild traumatic brain injury (mTBI) and may reflect alterations in the brain structural properties. The relationship between microstructural changes and cognitive and emotional deficits remains unclear in patients with mTBI at the acute stage. The purpose of this study was to analyze the alterations in white matter microstructure and connectome of patients with mTBI within 7 days after injury and investigate whether they are related to the clinical questionnaires. A total of 79 subjects (42 mTBI and 37 healthy controls) underwent neuropsychological assessment and diffusion-tensor MRI scan. The microstructure and connectome of white matter were characterized by tract-based spatial statistics (TBSSs) and graph theory approaches, respectively. Mini-mental state examination (MMSE) and self-rating depression scale (SDS) were used to evaluate the cognitive function and depressive symptoms of all the subjects. Patients with mTBI revealed early increases of fractional anisotropy in most areas compared with the healthy controls. Graph theory analyses showed that patients with mTBI had increased nodal shortest path length, along with decreased nodal degree centrality and nodal efficiency, mainly located in the bilateral temporal lobe and right middle occipital gyrus. Moreover, lower nodal shortest path length and higher nodal efficiency of the right middle occipital gyrus were associated with higher SDS scores. Significantly, the strength of the rich club connection in the mTBI group decreased and was associated with the MMSE. Our study demonstrated that the neuroanatomical alterations of mTBI in the acute stage might be an initial step of damage leading to cognitive deficits and depression symptoms, and arguably, these occur due to distinct mechanisms.

Keywords: brain injury, DTI, WM microstructure, cognitive deficits, depression symptoms

INTRODUCTION

Mild traumatic brain injury (mTBI), commonly known as concussion, is a significant public health problem. Every year, an estimated 42 million people worldwide suffer from mTBI (1), accounting for approximately 70–90% of all traumatic brain injuries (TBIs). mTBI causes various symptoms, most notably headaches, fatigue, depression, anxiety, and impaired cognitive function, termed as post-concussion syndrome. These symptoms may resolve in most individuals within 3 months post-injury. Nevertheless, mTBI is more likely a progressive injury than a static event (2). Some patients (20–30%) go on to develop persistent physical (headache, dizziness, and fatigue) (3), emotional (irritability, depression, anxiety, and posttraumatic stress) (4), and cognitive deficits (5). Diagnosing and predicting mental and emotional deficits early after an injury is essential to avoid persistent symptoms that may pose a barrier to full recovery.

Diffusion tensor imaging (DTI) and related techniques are sensitive for assessing white matter (WM) microstructure changes after injury, but the results are heterogeneous (6). Changes in WM structural abnormalities have been observed in both animals and humans following brain injury (7, 8). Based on a rodent model of mTBI, it was found that radial diffusivity (RD) and axial diffusivity (AD) decreased one week after injury. Simultaneously, fractional anisotropy (FA) increased and returned to baseline values after 2 weeks (7). In patients with mTBI, DTI found higher FA and lower RD in the corpus callosum when measured 2–20 days after mTBI and higher FA in the genu of the corpus callosum after follow-up (8). Another study showed that patients with persistent post-concussion symptoms had lower FA and higher RD values than patients without symptoms when examined with DTI within 72 h post-injury (9). DTI studies on mTBI have also reported WM structural disruption associated with cognitive and affective impairments after mTBI. For instance, the patient's cognitive information processing speed was associated with FA values recovered in the left anterior limb of the internal capsule (10). Damage to the frontal interhemispheric and thalamic projection tracts can be used to predict processing speed performance in mTBI (11). Damage to the left superior longitudinal fasciculus and right anterior thalamic radiation is closely related to pain emotion regulation (12).

Region-of-interest (ROI)-based research has provided insights into the mechanisms that underlie mTBI-related cognitive and emotional deficits (13, 14). However, the human brain is an integrated network for processing higher-order cognition and emotion. Network theory, especially, the WM structural connectome, provides a way to simplify complex systems into more straightforward representations to investigate brain organization and capture the topological characteristics of the network (15, 16). To date, many studies have used theoretical graph techniques to explore WM structural network alterations in TBI. One study found that patients demonstrated increased shortest path length and decreased the global efficiency of the structural network, which was associated with lower scores on switching tasks (17). Reduced network efficiency is associated with the rupture of long-range WM connections due to axonal injury, which impairs information transfer across distal brain regions (18) and leads to cognitive deficits (19). Although some studies have found TBI-induced structural brain network alterations, others have reported no significant alterations in the global network metrics (20, 21). It is unknown whether patients with mTBI have global and local topologic alterations in the connectome.

In addition, previous studies primarily focused on moderate and severe brain injury or the chronic stages of mTBI (22, 23). Few studies have examined acute brain changes (24). In contrast, acute brain injury is a golden time for mTBI treatment (25). The neuroanatomical abnormalities associated with acute mTBI have not yet been thoroughly investigated. Similarly, the precise position and topological way of WM connectivity are disrupted, and consequently, how much cognitive, and emotional impairments are affected remains unclear. Therefore, this study aimed to assess microstructural changes in the acute phase of mTBI, employ graph theory to explore alterations in the WM connectome, and further explore the potential mechanism of cognitive decline and depressive symptoms at the acute stage of mTBI. We hypothesized that mTBI would change the structural network properties, which might be related to mental/emotional impairments in the acute phase.

MATERIALS AND METHODS

Subjects

In total, forty-eight patients and forty age-, sex-, and education-matched healthy controls (HCs) were recruited from the Lanzhou University Second Hospital. Patients with mTBI were seen at the Department of Emergency and Neurosurgery within 7 days after injury. Most of them were outpatients and emergency patients. The inclusion criteria were as follows: (i) the patient (18–60 years and right-handed) had suffered a brain injury within 7 days; (ii) met at least one of the diagnostic criteria of the American Congress of Rehabilitation Medicine for mTBI (26); (iii) no substantial trauma could be found on brain computed tomography and routine MRI; and (iv) no MRI contraindications. The exclusion criteria were as follows: (i) severe compound injury and multiple injuries; (ii) history of previous TBI or neuropsychological, psychiatric, or neurological disorders; and (iii) history of drug or alcohol abuse. The healthy subjects were carefully screened according to the same exclusion criteria applied to the patient group.

Neuropsychological Assessment

All the subjects underwent the same neuropsychological tests which are commonly affected domains after mTBI. (i) Mini-mental state examination (MMSE) to assess cognitive function. (ii) Self-rating depression scale (SDS) to evaluate adults with depressive symptoms in the last week. (iii) The mTBI group completed the Rivermead post-concussion syndrome questionnaire (RPQ), which provides a symptom questionnaire commonly reported after mTBI to reflect the level of post-concussive symptoms (27).

MRI Data Acquisition

Magnetic resonance imaging data were acquired on a 3T Siemens Verio scanner equipped with an 8-channel phased-array head radiofrequency coil. (i) T2-weighted fluid-attenuated inversion recovery images (FLAIR; TE = 94 ms, TR = 7,000 ms, TI = 2,215.2 ms; FOV: 230 × 230 mm; matrix: 256 × 256; 18 slices) to eliminate cerebral contusion and laceration, subarachnoid hemorrhage, and cerebral softening lesion. (ii) Sagittal three-dimensional T1-weighted images (3D-T1WI) were acquired using turbo spin-echo sequence (TI = 900 ms; flip angle = 12°; FOV: 256 × 256 mm; matrix: 256 × 256; 192 slices). (iii) The diffusion tensor images (DTIs) were acquired using a single-shot echo-planar sequence (TE = 61 ms; TR = 7,100 ms; flip angle = 90°; FOV: 256 × 256 mm; matrix: 128 × 128; 50 slices; 64 diffusion directions, *b* value of 1,000 and 0 s/mm^2).

Tract-Based Spatial Statistics (TBSSs)

The preprocessing and analysis steps based on the TBSS method (28) were performed using the FMRI Software Library (FSL, http://fsl.fmrib.ox.ac.uk/fsl). First, diffusion tensor images were corrected for the eddy current distortions and head motion, and the scalp, skull, and other non-brain tissues were removed from the images. Next, we automatically estimated all the WM tracts using the TBSS method. The FA data of all the subjects were then aligned to the FMRIB Diffusion Toolbox module. A mean FA image was created, and the threshold (0.2) was designed to create a mean FA skeleton. The FA, MD, AD, and RD data aligned for each subject were projected onto this skeleton. The randomization of FSL for nonparametric permutation, 5,000 permutation tests, and threshold-free cluster enhancement and familywise error (FWE) were used for multiple comparisons and corrections. Statistically significant between-group differences were identified using the Johns Hopkins University (JHU) WM tractography atlas.

WM Structural Network Construction and Analyses

The nodes of the brain structural network came from the automated anatomical labeling template, which divides the brain into 90 brain regions (29). MRtrix3's tckgen with constrained spherical deconvolution and anatomically constrained tractography was used for probabilistic tracking of whole-brain WM fibers (step size = 1 mm, angle threshold = 45°, the threshold of FOD = 0.05, 1 million streamlines) (30). The weight of the edges between nodes is defined as the number of streamlines connecting the nodes in the two brain regions. Edges with streamlines <15 were deleted to eliminate potential spurious connections.

Based on MatlabR2013b, GRETNA (http://www.nitrc.org/projects/Gretna/) software was used to generate graph theory metrics (31). Network efficiency was examined at both the global and local levels. For the global network theory analyses, the theoretical network measures calculated were the clustering coefficient (Cp, reflecting the tendency of nodes to cluster together), characteristic path length (Lp, network average of the shortest path lengths), small-worldness (reflecting the ability of integration and segregation in the network), global efficiency (Eg, calculated by taking the mean inverse shortest path length in the network), local efficiency (E_{local}, efficiency of connections between neighbors of a node), and hierarchy (revealing an organizational structure with a high degree of clustering). For the local network theory analyses, the central degree (Dc, the number of edges attached to each node), nodal efficiency (Ne, reflects the efficiency of information dissemination between nodes), and nodal shortest path length (NLp, the size of the shortest path between nodes) were calculated.

A nonparametric one-tailed sign test was used to determine group networks and hub areas. The entire network can be divided into the hub and non-hub nodes. The node of the hub region is higher than the intermediate node with at least one SD, which has the shortest path connection with other nodes and high centrality and efficient information transmission capability (32). Correspondingly, three subnetworks were defined: rich club (connecting hub nodes only), feeder (connecting hub and non-hub nodes), and local connection (connecting non-hub nodes only). The connection strength of each subnetwork (number of streamlines) was calculated for the statistical analyses.

Statistical Analyses

The demographic and neuropsychological data of the mTBI and HC groups were analyzed using SPSS version 22.0, using independent two-sample *t*-tests for continuous variables with a normal distribution (age, MMSE, and SDS) and chi-square tests for sex. Given the non-normal distributions of education years, the Mann–Whitney *U* tests were utilized. Multiple comparisons were corrected using false discovery rate (FDR) correction for local network properties. Nonparametric permutation tests (10,000 times) were used to test for group differences in the three subnetworks of connectivity strength, other network topology metrics, and nodal efficiency with age, sex, and years of education as covariates. Network-based Statistics (NBS) (33) were used to evaluate the abnormalities of anatomical connections in the network between groups. The network connections of each subject were tested using a permutation test (10,000 times) controlled for FWE correction, and the threshold was set to a *p*-value of <0.05. In the mTBI group, clinical assessments were correlated with graph theory outcomes using Spearman's correlation analysis.

RESULTS

Demographic and Clinical Characteristics

In total, six patients and three healthy subjects were excluded due to poor-scan quality from motion artifacts. The final sample consisted of 79 participants, including 42 patients with acute mTBI and 37 HCs (**Table 1**). The two groups did not differ in terms of age, gender, or educational distribution. Patients with mTBI had varying degrees of headaches, fatigue, insomnia, depression, and abnormally increased RPQ scores. Compared with the HCs, patients with mTBI performed worse on the MMSE test ($p < 0.001$) and showed a significantly higher SDS score ($p < 0.001$).

TABLE 1 | Demographic and neuropsychological assessment in patients with mTBI and HCs.

	mTBI ($n = 42$)	HCs ($n = 37$)	p-value
Age, years, mean (SD)[a]	34.17 (11.30)	35.46 (10.72)	0.627
Gender, Male, *n* (%)[b]	23 (54.76)	19 (51.35)	0.762
Education, years, median (IQR)[c]	8 (10)	8 (9.5)	0.660
Injury-to-imaging interval, hours, median (IQR)	72 (78)	–	–
Loss of consciousness (LOC), *n* (%)	15 (35.70)	–	–
Time to resumption of LOC, minutes, median (IQR)[d]	5 (28)	–	–
Posttraumatic amnesia (PTA), *n* (%)	12 (28.60)	–	–
Time to resumption of PTA, hours, median (IQR)[e]	2.25 (3)	–	–
Microbleeds, *n* (%)	14 (33.3)	–	–
Mechanism of injury, *n* (%)			
Vehicle accidents	23 (54.76)	–	–
Violence or assault	10 (23.81)	–	–
Athletic collisions	7 (16.67)	–	–
Others (incidental fall; falling object)	2 (4.76)	–	–
GCS, mean (SD)	14.52 (0.77)	–	–
RPQ, mean (SD)	16.40 (7.86)	–	–
MMSE, mean (SD)[a]	23.98 (6.19)	28.65 (1.95)	<0.001
SDS, mean (SD)[a]	46.67 (11.99)	32.56 (4.75)	<0.001

mTBI, mild traumatic brain injury; HCs, healthy controls; GCS, Glasgow Coma Score; RPQ, Rivermead post-concussion syndromes questionnaire; MMSE, Mini-Mental State Examination; SDS, Self-rating Depression Scale; SD, standard deviation; IQR, interquartile range.

[a] *The independent two-sample t-test was used for the continuous variables.*

[b] *The χ^2 test was used for sex.*

[c] *The Mann–Whitney U test was used for education.*

[d] *$n = 15$.*

[e] *$n = 12$.*

TBSS Results

Voxel-wise analysis using TBSS showed that the mTBI group had a more significant number of clusters with increased FA than the HCs (corrected $p < 0.05$). These clusters belonged to seven tracts of the JHU atlas, including the bilateral inferior frontal-occipital fasciculus, superior longitudinal fasciculus, left uncinate fasciculus, left anterior thalamic radiation, and right inferior longitudinal fasciculus (**Figure 1**). Significantly, different voxels and their corresponding cluster sizes are shown in **Table 2**. The affected tracts were located predominantly in the left uncinate fasciculus and inferior frontal-occipital fasciculus. Voxel-wise analysis showed no significant changes in MD, AD, or RD between the two groups. There was no statistical correlation between FA values and neuropsychological indices in the different areas.

Graph Theory Analyses Results

Small-world organizations of the WM network were detected in both the mTBI and HC groups. An increase in the hierarchy ($p < 0.05$) of patients with acute mTBI was found when compared with the HCs (**Figure 2**). There was no significant difference in the between-group comparison of other global topological properties, including small-worldness, network efficiency, clustering coefficient, and characteristic path length.

More significant results were found in the local networks. Compared with the HCs, the mTBI group showed an increased nodal shortest path length in the bilateral middle temporal gyrus, right insula, right middle occipital gyrus, right putamen, right inferior temporal gyrus, left superior temporal gyrus, left temporal pole of the middle temporal gyrus, and left angular gyrus. Except for the left angular gyrus, nodal efficiency (**Figure 3A**), and nodal degree centrality in the above brain regions were decreased in the mTBI group ($p < 0.05$, FDR). Moreover, Spearman's correlation analysis showed a positive correlation between the total SDS scores and nodal efficiency in the right middle occipital gyrus of patients with acute mTBI ($r = 0.344$, $p = 0.026$) (**Figure 3B**). In addition, a negative correlation between the total SDS scores and the shortest nodal path length in the right middle occipital gyrus of patients was detected ($r = -0.343$, $p = 0.026$) (**Figure 3C**). There was no correlation between local network properties of the right middle occipital gyrus and SDS scores in the healthy controls.

Connected Edge Analyses Results

The distribution of hub nodes in the two groups was similar, including the bilateral precuneus, bilateral middle frontal gyrus, left medial part of the superior frontal gyrus, left dorsolateral part of the superior frontal gyrus, left precentral gyrus, right middle temporal gyrus, and right superior temporal gyrus. Compared with the HC group, the hub of the left calcarine fissure and surrounding cortex was only found in the mTBI group, and there was no hub of the left postcentral gyrus in the mTBI group (**Figure 4A**). Furthermore, the rich club connection strength of the mTBI group was significantly lower ($t = 2.25$, $p = 0.027$),

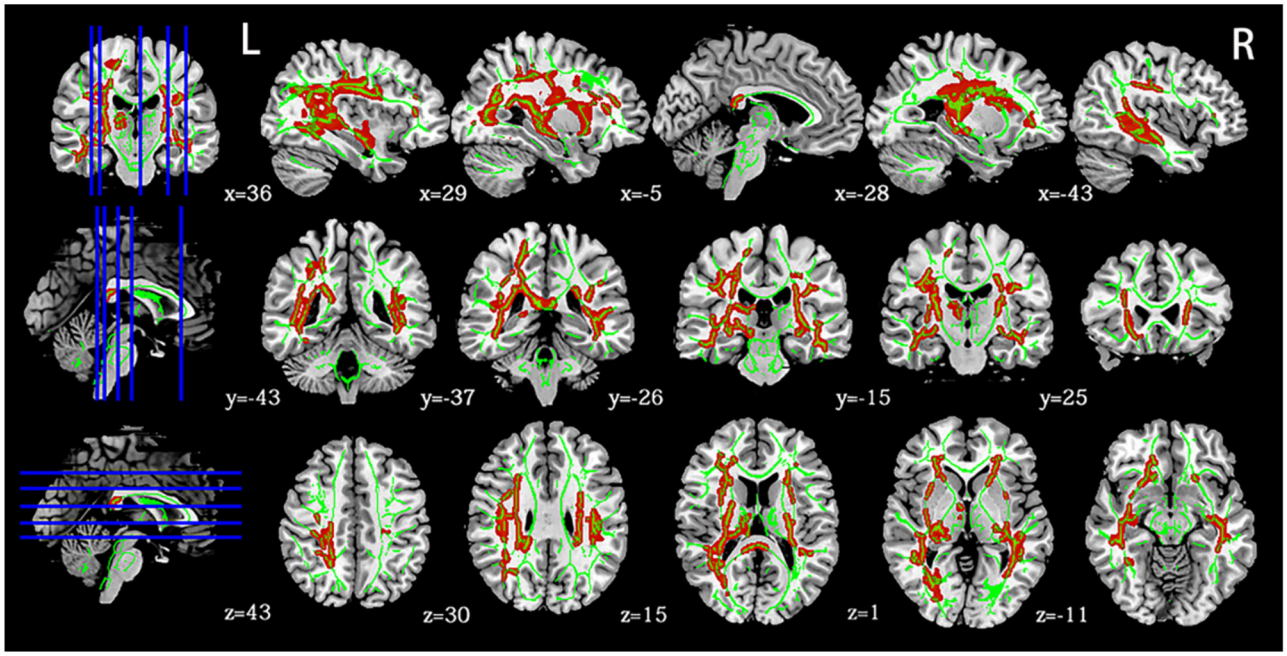

FIGURE 1 | Panel highlights regions with higher FA in mTBI at the acute stage than HCs ($p < 0.05$, FWE). Green indicates a white matter skeleton. Red indicates voxels with higher FA using the "tbss_fill" script. L, left, R, right.

TABLE 2 | The anatomical distribution with increased FA in acute mTBI group.

Cluster	Voxels	min *P*	Anatomical regions
1	10,434	0.014	Uncinate fasciculus, Inferior fronto-occipital fasciculus (left)
2	3,534	0.027	Inferior fronto-occipital fasciculus, Superior longitudinal fasciculus, Uncinate fasciculus (left)
3	538	0.044	Inferior fronto-occipital fasciculus, Anterior thalamic radiation, Uncinate fasciculus (left)
4	34	0.049	Inferior fronto-occipital fasciculus, Superior longitudinal fasciculus, Inferior longitudinal fasciculus (right)

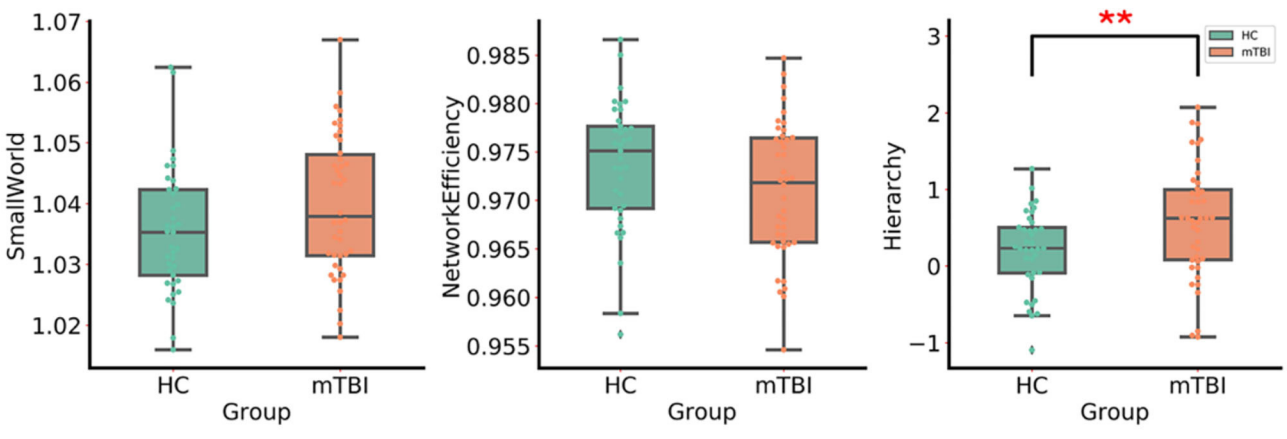

FIGURE 2 | The group differences in the global network metrics of WM structural networks. ** Indicates $p < 0.05$. mTBI, mild traumatic brain injury; HC, healthy control.

while the feeder and local connection strengths did not change (**Figure 4B**). In addition, the rich club connection strength of the mTBI group was positively correlated with the MMSE scores ($r = 0.378$, $p = 0.014$) (**Figure 4C**).

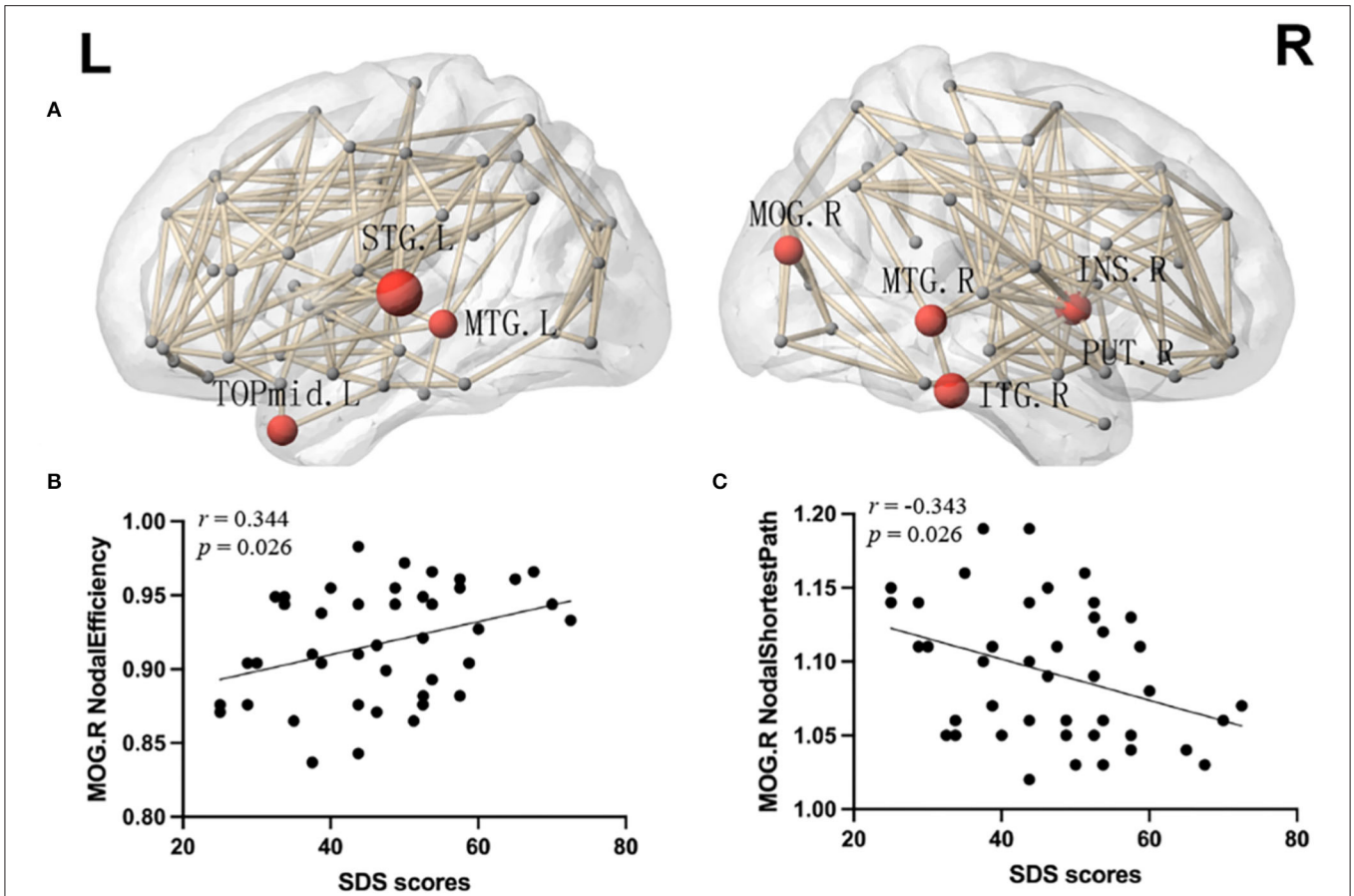

FIGURE 3 | (A) Network hubs were colored in red to indicate significantly lower nodal efficiency and the node sizes indicate the significance ($p < 0.05$, FDR). INS, insular; MOG, middle occipital gyrus; PUT, putamen; STG, superior temporal gyrus; MTG, middle temporal gyrus; TPOmid, temporal pole of middle temporal gyrus; ITG, inferior temporal gyrus; L, left; R, right. **(B)** Correlation analyses between the SDS score and nodal efficiency of the right middle occipital gyrus. **(C)** Correlation analyses between the SDS score and nodal shortest path in the right middle occipital gyrus. SDS, Self-rating Depression Scale.

Analysis of the network-based statistics showed disrupted structural connections in the mTBI group. The disrupted component was mainly distributed in the bilateral inferior temporal gyrus, left parahippocampal gyrus, right caudate nucleus, right thalamus, and right superior occipital gyrus, composed of six nodes and five edges. The thickness of the edges showed significant differences between the groups ($p < 0.05$) (**Figure 5**).

DISCUSSION

In the present study, we investigated the early microstructural changes in WM and topological changes in the brain connectome in patients with mTBI. The results showed that: (i) FA in the mTBI group increased significantly using TBSS compared with the HCs; (ii) graph theory analysis showed less nodal efficiency and increased nodal shortest path length in some areas of mTBI, mainly distributed in the right middle occipital gyrus, which was related to depressive symptoms; and (iii) the rich club connection strength of the patients with mTBI decreased and was positively correlated with the MMSE score.

Using TBSS, we found that the mTBI group in the acute phase showed significantly higher FA than the HC group, suggesting that mTBI may affect the WM integrity. Existing neuroimaging studies have demonstrated acute mTBI with high-anisotropy values (34, 35). The increased FA shortly after injury may be due to secondary injury (ischemia, cerebral hypoxia, and cerebral edema) or compensatory mechanisms (36), which cause cytotoxic swelling. Cytotoxic swelling leads to the excess of sodium ions and intracellular water accumulation. Thus, the cellular swelling narrows the free space between the neighboring axons (37), limiting the uniformity of diffusion and increasing anisotropy. A study showed that FA in patients with mTBI increases even 6 months after injury. These long-term changes may be due to the prolongation of subtle cytotoxic edema, which is more common in the developing brain (38). mTBI can lead to continuous changes in WM tracts. Usually, the WM tracts usually connect or project to the frontal lobe, including the inferior longitudinal fasciculus, inferior frontal-occipital fasciculus, and forceps minor, related to prognosis (8, 34, 39). The high FA values of the inferior frontal-occipital fasciculus and uncinate fasciculus found in the current study are consistent with the results of these

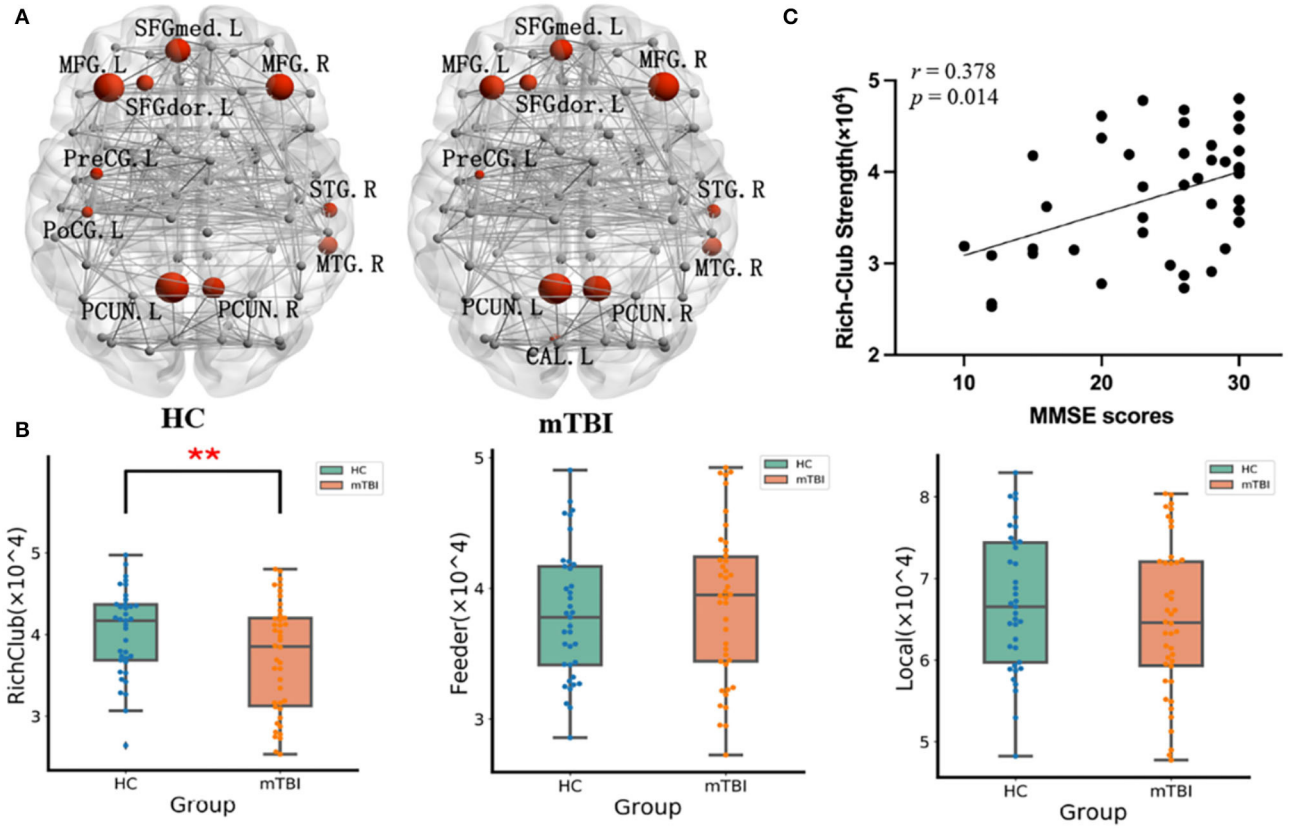

FIGURE 4 | (A) The hubs distribution of the WM networks in the mTBI and HCs group, with hubs colored in red and the hubs sizes indicating the nodal connection strength. PCUN, precuneus; MFG, middle frontal gyrus; SFGmed, medial of superior frontal gyrus; SFGdor, dorsolateral of superior frontal gyrus; PreCG, precentral gyrus; MTG, middle temporal gyrus; STG, superior temporal gyrus; PoCG, postcentral gyrus; CAL, Calcarine fissure and surrounding cortex. **(B)** The mTBI group showed significantly lower strength of the rich-club connection. The feeder and local connections were no significant change compared with HCs. **(C)** Correlation between the MMSE score and rich-club connection strength. ** Indicates $p < 0.05$. mTBI, mild traumatic brain injury; HC, healthy control; MMSE, Mini-Mental State Examination.

previous studies. Interestingly, our study showed that the FA of WM tracts in the left hemisphere is significantly higher than that in the right side, indicating the left hemisphere is more sensitive to concussion, which is consistent with the report of DTI on the left side of football players (39). In the normal population, both DTI and post-mortem studies showed a leftward asymmetry of the WM fiber tracts in the left hemisphere regardless of subject handedness (40, 41), due to more thickly myelinated axons (42). As a result, the leftward lateralization of increased WM structure may be more susceptible to injury from the translational and rotational forces acting in concussions (43), which need further study for clinical application (44).

Global network theory analyses showed that the hierarchical structure of the mTBI group had increased. Hierarchical topology in complex networks reveals an organizational structure in which scale-free properties are combined with a high degree of clustering (45). Hierarchical topology analyses revealed that the patients with mTBI in the acute stage tended to have a more inherent association between connectivity and clustering. Previous theoretical graph theory analysis of children with acute mTBI showed significantly higher small-world properties, clustering coefficients, characteristic path length and modularity, and lower global efficiency (46). Although we found a similar trend of global network properties in the mTBI group, no significant between-group differences were found since mTBI had little effect on adults. Due to the ongoing developmental process, young patients with mTBI may be more vulnerable to brain damage than adults (47).

Compared with the HCs, the mTBI group had reduced nodal degree centrality and nodal efficiency and increased nodal shortest path length, mainly, in the bilateral temporal lobe, right middle occipital gyrus, right insula, and putamen. The changed local network metrics are likely due to disrupted global WM (axonal) integrity, although we did not find regions with changed local network properties corresponding to the regions of increased FA in patients with mTBI. The temporal lobe, located in the middle fossa of the skull, is one of the most vulnerable brain regions to injury due to cerebral trauma (48). Structural changes in the temporal lobe of the GM and WM have consistently been reported (49, 50). Our study results of decreased nodal degree

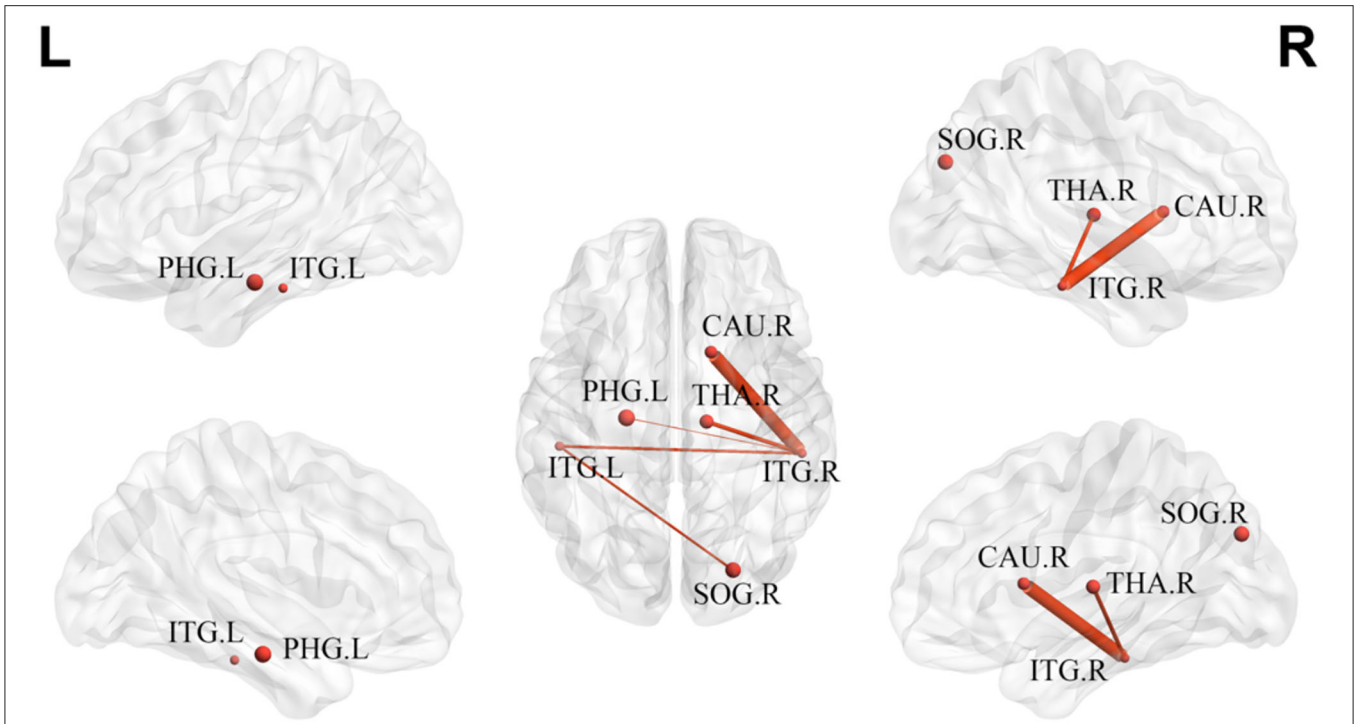

FIGURE 5 | The disrupted component in mTBI group at acute stage. ITG, inferior temporal gyrus; PHG, parahippocampal gyrus; CAU, caudate nucleus; THA, thalamus; SOG, superior occipital gyrus; L, left; R, right.

centrality and nodal efficiency of the structural subnetwork in temporal regions are consistent with a study that found lower eigenvector centrality within the left temporal pole (24). As part of the salience network, the insular cortex has extensive structural connections with the prefrontal, parietal, and central cingulate gyri. It is a critical brain region for integrating processes and controlling cognitive, emotional, and behavioral functions (47). Several studies have reported the insular changes associated with mTBI (51, 52). The occipital lobe contains most of the anatomical areas responsible for visual processing and integration, contributes to communicating visual information and other sensory system information with the cerebral cortex, and plays a role in facial emotion perception (53). We found a correlation between the changed node metrics of the right middle occipital gyrus and the SDS scores in patients with mTBI. Through magnetoencephalography source analysis of untreated patients with depression, one study found that the focal magnetic low-frequency activity in the right occipital lobe was abnormal, and the increased occipital lobe delta dipole density correlated with disease severity (54). The middle occipital gyrus may be involved in the processing of cognitive bias in depression through its connection to the limbic cortex. Changes in the right middle occipital gyrus in acute mTBI may indicate potential structural brain recovery when rapid neurophysiological changes occur.

In this study, both hub and non-hub regions displayed decreased efficiency. Our study found no difference in the distribution of hubs, suggesting that acute mTBI has no significant effect on hub regions, which is consistent with the results of a previous study (46). In addition, our study showed that the strength of the rich club connection in the mTBI group was significantly lower and associated with lower cognitive performance levels. Rich club networks usually consist of highly myelinated FA fiber tracts for effective action potentials and information transmission (55). The high rotational acceleration forces can cause brain damage and changes in fiber bundles, which lead to the deformation of WM fiber bundles widely distributed throughout the brain and increase the maximum principal strains in high-fiber directionality regions compared with regions with lower fiber directionality (56). Rich club constitutes the backbone of a network with highly connected central hubs known to be vulnerable targets susceptible to disturbances in brain trauma and fundamental to high-order cognitive processes (57). One study revealed significantly decreased rich club organization in young patients with chronic TBI, which was related to impaired executive function (58). Our research shows that the subnetworks of rich clubs have changed to more mild damage, which is consistent with the results of other studies (21). As the only sufficiently sensitive subnetwork, the rich club response to mTBI may provide new evidence for the underlying mechanisms of the acute cognitive deficits.

Network-based statistics revealed a disrupted component in the mTBI group, mainly distributed in the bilateral inferior temporal gyrus, left parahippocampal gyrus, right caudate nucleus, right thalamus, and right superior occipital gyrus, including some long- and short-range connections. These results confirmed the overall disruption of structural connectivity in

patients with mTBI, but to a lesser extent. The decline in component connection strength is consistent with our DTI findings that WM abnormalities are widespread in patients with mTBI during the acute phase.

Our study has several limitations. First, the degree of injury was relatively minor (the average Glasgow Coma Score was 14.5) making it difficult to overcome the inter-subject variance. We did not observe significant differences in global network properties in the adult mTBI at the acute stage compared with the HCs, which is similar to a previous study with few positive MRI findings in the mTBI group (59). Second, this study is limited by its cross-sectional design. MRI was performed at a single time point within seven days after the injury. The longitudinal changes in brain structure and the relationship between theoretical graph measures of the structural connectome and improved cognitive/emotional recovery are unclear. Finally, we did not use sufficient standard neuropsychological tests in our current study, which may provide additional factors after being affected by mTBI. This requires a more extensive and detailed description of the neuropsychological changes involved after mTBI and how they map to different injury patterns in the structural connectome. Large-scale longitudinal follow-up studies with complex standard neuropsychological tests will be conducted in the future to identify brain changes in patients with mTBI and precisely predict head trauma outcomes using machine learning methods. Achieving this goal will be the focus of future research.

CONCLUSION

Using TBSS and graph theory analysis, this study found an altered WM structure and disrupted the topological organization of WM networks in mTBI at the acute stage. Re-modularization of the right occipital gyrus associated with mTBI may be linked to depressive symptoms after mTBI. Furthermore, the strength of the rich club connection may provide insight into cognitive decline in acute mTBI.

DATA AVAILABILITY STATEMENT

The raw data supporting the conclusions of this article will be made available by the authors, without undue reservation.

ETHICS STATEMENT

The studies involving human participants were reviewed and approved by Lanzhou University Second Hospital Ethics Committee. The patients/participants provided their written informed consent to participate in this study.

AUTHOR CONTRIBUTIONS

WeH designed and wrote the original draft. WaH and PZ contributed to the data curation and analysis. JW and LM completed the neuropsychological assessment and collected the data. YJ and YZ conceived and revised the manuscript. JZ gave conception and funding acquisition. All authors contributed to the article and approved the submitted version.

FUNDING

This work was supported by the National Natural Science Foundation of China (No. 81960309) and the Science and Technology Project of Gansu Province (No. 21JR7RA403).

REFERENCES

1. Gardner RC, Yaffe K. Epidemiology of mild traumatic brain injury and neurodegenerative disease. *Mol Cell Neurosci.* (2015) 66:75–80. doi: 10.1016/j.mcn.2015.03.001
2. Aiken AH, Gean AD. Imaging of head trauma. *Semin Roentgenol.* (2010) 45:63–79. doi: 10.1053/j.ro.2009.09.007
3. Maleki N, Finkel A, Cai G, Ross A, Moore RD, Feng X, et al. Post-traumatic Headache and Mild Traumatic Brain Injury: Brain Networks and Connectivity. *Curr Pain Headache Rep*. (2021) 25:20. doi: 10.1007/s11916-020-00935-y
4. Delmonico RL, Theodore BR, Sandel ME, Armstrong MA, Camicia M. Prevalence of depression and anxiety disorders following mild traumatic brain injury. *PM&R.* (2021). doi: 10.1002/pmrj.12657
5. Lagarde E, Salmi LR, Holm LW, Contrand B, Masson F, Ribereau-Gayon R, et al. Association of symptoms following mild traumatic brain injury with posttraumatic stress disorder vs. postconcussion syndrome. *JAMA Psychiatry*. (2014) 71:1032–40. doi: 10.1001/jamapsychiatry.2014.666
6. Asken BM, DeKosky ST, Clugston JR, Jaffee MS, Bauer RM. Diffusion tensor imaging (DTI) findings in adult civilian, military, and sport-related mild traumatic brain injury (mTBI): a systematic critical review. *Brain Imaging Behav*. (2018) 12:585–612. doi: 10.1007/s11682-017-9708-9
7. Hoogenboom WS, Rubin TG, Ye K, Cui M-H, Branch KC, Liu J, et al. Diffusion tensor imaging of the evolving response to mild traumatic brain injury in rats. *J Exp Neurosci.* (2019) 13:1179069519858627. doi: 10.1177/1179069519858627
8. Mayer AR, Ling J, Mannell MV, Gasparovic C, Phillips JP, Doezema D, et al. A prospective diffusion tensor imaging study in mild traumatic brain injury. *Neurology*. (2010) 74:643–50. doi: 10.1212/WNL.0b013e3181d0ccdd
9. Stenberg J, Eikenes L, Moen KG, Vik A, Haberg AK, Skandsen T. Acute Diffusion Tensor and Kurtosis Imaging and Outcome following Mild and Traumatic Brain Injury. *J Neurotrauma.* (2021) 38:2560–71. doi: 10.1089/neu.2021.0074
10. Yin B, Li D-D, Huang H, Gu C-H, Bai G-H, Hu L-X, et al. Longitudinal changes in diffusion tensor imaging following mild traumatic brain injury and correlation with outcome. *Front Neural Circ*. (2019) 13. doi: 10.3389/fncir.2019.00028
11. Bai L, Bai G, Wang S, Yang X, Gan S, Jia X, et al. Strategic white matter injury associated with long-term information processing speed deficits in mild traumatic brain injury. *Hum Brain Mapp.* (2020) 41:4431–41. doi: 10.1002/hbm.25135
12. Leung A, Yang E, Lim M, Metzger-Smith V, Theilmann R, Song D, et al. Pain-related white matter tract abnormalities in mild traumatic brain injury patients with persistent headache. *Mol Pain.* (2018) 14:1744806918810297. doi: 10.1177/1744806918810297
13. Chung S, Wang X, Fieremans E, Rath JF, Amorapanth P, Foo FYA, et al. Altered relationship between working memory and brain microstructure after mild traumatic brain injury. *Am J Neuroradiol.* (2019) 40:1438–44. doi: 10.3174/ajnr.A6146
14. van der Horn HJ, Mangina NR, Rakers SE, Kok JG, Timmerman ME, Leemans A, et al. White matter microstructure of the neural emotion regulation

circuitry in mild traumatic brain injury. *Eur J Neurosci.* (2021) 53:3463–75. doi: 10.1111/ejn.15199
15. Chung AW, Schirmer MD, Krishnan ML, Ball G, Aljabar P, Edwards AD, et al. Characterising brain network topologies: A dynamic analysis approach using heat kernels. *Neuroimage.* (2016) 141:490–501. doi: 10.1016/j.neuroimage.2016.07.006
16. Rubinov M, Sporns O. Complex network measures of brain connectivity: Uses and interpretations. *Neuroimage.* (2010) 52:1059–69. doi: 10.1016/j.neuroimage.2009.10.003
17. Caeyenberghs K, Leemans A, Leunissen I, Gooijers J, Michiels K, Sunaert S, et al. Altered structural networks and executive deficits in traumatic brain injury patients. *Brain Struct Funct.* (2014) 219:193–209. doi: 10.1007/s00429-012-0494-2
18. Sharp DJ, Scott G, Leech R. Network dysfunction after traumatic brain injury. *Nat Rev Neurol.* (2014) 10:156–66. doi: 10.1038/nrneurol.2014.15
19. Fagerholm ED, Hellyer PJ, Scott G, Leech R, Sharp DJ. Disconnection of network hubs and cognitive impairment after traumatic brain injury. *Brain.* (2015) 138:1696–709. doi: 10.1093/brain/awv075
20. Kuceyeski AF, Jamison KW, Owen JP, Raj A, Mukherjee P. Longitudinal increases in structural connectome segregation and functional connectome integration are associated with better recovery after mild TBI. *Human Brain Mapp.* (2019) 40:4441–56. doi: 10.1002/hbm.24713
21. Chung AW, Mannix R, Feldman HA, Grant PE, Im K. Longitudinal structural connectomic and rich-club analysis in adolescent mTBI reveals persistent, distributed brain alterations acutely through to one year post-injury. *Sci Rep.* (2019) 9:18833. doi: 10.1038/s41598-019-54950-0
22. Maller JJ, Thomson RHS, Lewis PM, Rose SE, Pannek K, Fitzgerald PB. Traumatic brain injury, major depression, and diffusion tensor imaging: Making connections. *Brain Res Rev.* (2010) 64:213–40. doi: 10.1016/j.brainresrev.2010.04.003
23. Jorge RE, Acion L, White T, Tordesillas-Gutierrez D, Pierson R, Crespo-Facorro B, et al. White Matter Abnormalities in Veterans With Mild Traumatic Brain Injury. *Am J Psychiatry.* (2012) 169:1284–91. doi: 10.1176/appi.ajp.2012.12050600
24. van der Horn HJ, Kok JG, de Koning ME, Scheenen ME, Leemans A, Spikman JM, et al. Altered Wiring of the Human Structural Connectome in Adults with Mild Traumatic Brain Injury. *J Neurotrauma.* (2017) 34:1035–44. doi: 10.1089/neu.2016.4659
25. Jagoda AS, Bazarian JJ, Bruns JJ. Jr., Cantrill SV, Gean AD, Howard PK, et al. Clinical policy: neuroimaging and decisionmaking in adult mild traumatic brain injury in the acute setting. *J Emerg Nurs.* (2009) 35:e5–40. doi: 10.1016/j.jen.2008.12.010
26. Lu L, Wei X, Li M, Li Y, Li W. Emerging MRI and metabolic neuroimaging techniques in mild traumatic brain injury. *Neurol India.* (2014) 62:487–91. doi: 10.4103/0028-3886.144434
27. King NS, Crawford S, Wenden FJ, Moss NEG, Wade DT. The rivermead post concussion symptoms questionnaire—A measure of symptoms commonly experienced after head-injury and its reliability. *J Neurol.* (1995) 242:587–92. doi: 10.1007/BF00868811
28. Smith SM, Jenkinson M, Johansen-Berg H, Rueckert D, Nichols TE, Mackay CE, et al. Tract-based spatial statistics: voxelwise analysis of multi-subject diffusion data. *Neuroimage.* (2006) 31:1487–505. doi: 10.1016/j.neuroimage.2006.02.024
29. Shu N, Wang X, Bi Q, Zhao T, Han Y. Disrupted topologic efficiency of white matter structural connectome in individuals with subjective cognitive decline. *Radiology.* (2018) 286:229–38. doi: 10.1148/radiol.2017162696
30. Smith RE, Tournier JD, Calamante F, Connelly A. Anatomically-constrained tractography: improved diffusion MRI streamlines tractography through effective use of anatomical information. *Neuroimage.* (2012) 62:1924–38. doi: 10.1016/j.neuroimage.2012.06.005
31. Wang J, Wang X, Xia M, Liao X, Evans A, He Y, et al. a graph theoretical network analysis toolbox for imaging connectomics. *Front Hum Neurosci.* (2015) 9:386. doi: 10.3389/fnhum.2015.00386
32. Shu N, Liu Y, Li K, Duan Y, Wang J, Yu C, et al. Diffusion tensor tractography reveals disrupted topological efficiency in white matter structural networks in multiple sclerosis. *Cereb Cortex.* (2011) 21:2565–77. doi: 10.1093/cercor/bhr039
33. Zalesky A, Fornito A, Bullmore ET. Network-based statistic: Identifying differences in brain networks. *Neuroimage.* (2010) 53:1197–207. doi: 10.1016/j.neuroimage.2010.06.041
34. Wilde EA, McCauley SR, Barnes A, Wu TC, Chu Z, Hunter JV, et al. Serial measurement of memory and diffusion tensor imaging changes within the first week following uncomplicated mild traumatic brain injury. *Brain Imaging Behav.* (2012) 6:319–28. doi: 10.1007/s11682-012-9174-3
35. Wang Z, Wu W, Liu Y, Wang T, Chen X, Zhang J, et al. Altered cerebellar white matter integrity in patients with mild traumatic brain injury in the acute stage. *Plos ONE.* (2016) 11:e0151489. doi: 10.1371/journal.pone.0151489
36. Eierud C, Craddock RC, Fletcher S, Aulakh M, King-Casas B, Kuehl D, et al. Neuroimaging after mild traumatic brain injury: review and meta-analysis. *Neuroimage Clin.* (2014) 4:283–94. doi: 10.1016/j.nicl.2013.12.009
37. Alexander AL, Lee JE, Lazar M, Field AS. Diffusion tensor imaging of the brain. *Neurotherapeutics.* (2007) 4:316–29. doi: 10.1016/j.nurt.2007.05.011
38. Wilde EA, McCauley SR, Hunter JV, Bigler ED, Chu Z, Wang ZJ, et al. Diffusion tensor imaging of acute mild traumatic brain injury in adolescents. *Neurology.* (2008) 70:948–55. doi: 10.1212/01.wnl.0000305961.68029.54
39. Veksler R, Vazana U, Serlin Y, Prager O, Ofer J, Shemen N, et al. Slow blood-to-brain transport underlies enduring barrier dysfunction in American football players. *Brain.* (2020) 143:1826–42. doi: 10.1093/brain/awaa140
40. Rademacher J, Bürgel U, Zilles K. Stereotaxic localization, intersubject variability, and interhemispheric differences of the human auditory thalamocortical system. *Neuroimage.* (2002) 17:142–60. doi: 10.1006/nimg.2002.1178
41. Buchel C, Raedler T, Sommer M, Sach M, Weiller C, Koch MA. White matter asymmetry in the human brain: A diffusion tensor MRI study. *Cerebral Cortex.* (2004) 14:945–51. doi: 10.1093/cercor/bhh055
42. Anderson B, Southern BD, Powers RE. Anatomic asymmetries of the posterior superior temporal lobes: a postmortem study. *Neuropsychiatry Neuropsychol Behav Neurol.* (1999) 12:247.
43. Cubon VA, Putukian M, Boyer C, Dettwiler A. A diffusion tensor imaging study on the white matter skeleton in individuals with sports-related concussion. *J Neurotrauma.* (2011) 28:189–201. doi: 10.1089/neu.2010.1430
44. Maruta J, Mallott JM, Sulioti G, Ghajar J, Palacios EM, Mukherjee P. Concussion disrupts normal brain white matter microstructural symmetry. *Front Neurol.* (2020) 11:548220. doi: 10.3389/fneur.2020.548220
45. Ravasz E, Barabasi AL. Hierarchical organization in complex networks. *Phys Rev E.* (2003) 67:026112. doi: 10.1103/PhysRevE.67.026112
46. Yuan W, Wade SL, Babcock L. Structural connectivity abnormality in children with acute mild traumatic brain injury using graph theoretical analysis. *Hum Brain Mapp.* (2015) 36:779–92. doi: 10.1002/hbm.22664
47. Lenroot RK, Giedd JN. Brain development in children and adolescents: Insights from anatomical magnetic resonance imaging. *Neurosci Biobehav Rev.* (2006) 30:718–29. doi: 10.1016/j.neubiorev.2006.06.001
48. Bigler ED. Anterior and middle cranial fossa in traumatic brain injury: relevant neuroanatomy and neuropathology in the study of neuropsychological outcome. *Neuropsychology.* (2007) 21:515–31. doi: 10.1037/0894-4105.21.5.515
49. Holli-Helenius K, Luoto TM, Brander A, Waljas M, Iverson GL, Ohman J. Structural Integrity of Medial Temporal Lobes of Patients with Acute Mild Traumatic Brain Injury. *J Neurotrauma.* (2014) 31:1153–60. doi: 10.1089/neu.2013.2978
50. Govindarajan KA, Narayana PA, Hasan KM, Wilde EA, Levin HS, Hunter JV, et al. Cortical Thickness in Mild Traumatic Brain Injury. *J Neurotrauma.* (2016) 33:1809–17. doi: 10.1089/neu.2015.4253
51. Li F, Lu L, Chen H, Wang P, Zhang H, Chen Y-C, et al. Neuroanatomical and functional alterations of insula in mild traumatic brain injury patients at the acute stage. *Brain Imaging Behav.* (2020) 14:907–16. doi: 10.1007/s11682-019-00053-3
52. Bonnelle V, Ham TE, Leech R, Kinnunen KM, Mehta MA, Greenwood RJ, et al. Salience network integrity predicts default mode network function after traumatic brain injury. Proc Natl Acad Sci U S A. (2012) 109:4690–5. doi: 10.1073/pnas.1113455109
53. Teng C, Zhou J, Ma H, Tan Y, Wu X, Guan C, et al. Abnormal resting state activity of left middle occipital gyrus and its functional connectivity in female patients with major depressive disorder. BMC Psychiatry. (2018) 18:370. doi: 10.1186/s12888-018-1955-9

54. Fernandez A, Rodriguez-Palancas A, Lopez-Ibor M, Zuluaga P, Turrero A, Maestu F, et al. Increased occipital delta dipole density in major depressive disorder determined by magnetoencephalography. *J Psychiatry Neurosci.* (2005) 30:17–23. doi: 10.1111/j.1600-079X.2004.00178.x
55. Collin G, Sporns O, Mandl RCW, van den Heuvel MP. Structural and Functional Aspects Relating to Cost and Benefit of Rich Club Organization in the Human Cerebral Cortex. *Cerebral Cortex.* (2014) 24:2258–67. doi: 10.1093/cercor/bht064
56. Giordano C, Cloots RJH, van Dommelen JAW, Kleiven S. The influence of anisotropy on brain injury prediction. *J Biomech.* (2014) 47:1052–9. doi: 10.1016/j.jbiomech.2013.12.036
57. Dall'Acqua P, Johannes S, Mica L, Simmen H-P, Glaab R, Fandino J, et al. Functional and structural network recovery after mild traumatic brain injury: A 1-year longitudinal study. *Front Human Neurosci.* (2017) 11:280. doi: 10.3389/fnhum.2017.00280
58. Verhelst H, Vander Linden C, De Pauw T, Vingerhoets G, Caeyenberghs K. Impaired rich club and increased local connectivity in children with traumatic brain injury: Local support for the rich? *Hum Brain Mapp.* (2018) 39:2800–11. doi: 10.1002/hbm.24041
59. Bigler ED, Abildskov TJ, Goodrich-Hunsaker NJ, Black G, Christensen ZP, Huff T, et al. Structural Neuroimaging Findings in Mild Traumatic Brain Injury. *Sports Med Arthrosc.* (2016) 24:E42–52. doi: 10.1097/JSA.0000000000000119

Conflict of Interest: The authors declare that the research was conducted in the absence of any commercial or financial relationships that could be construed as a potential conflict of interest.

Publisher's Note: All claims expressed in this article are solely those of the authors and do not necessarily represent those of their affiliated organizations, or those of the publisher, the editors and the reviewers. Any product that may be evaluated in this article, or claim that may be made by its manufacturer, is not guaranteed or endorsed by the publisher.

Copyright © 2022 Huang, Hu, Zhang, Wang, Jiang, Ma, Zheng and Zhang. This is an open-access article distributed under the terms of the Creative Commons Attribution License (CC BY). The use, distribution or reproduction in other forums is permitted, provided the original author(s) and the copyright owner(s) are credited and that the original publication in this journal is cited, in accordance with accepted academic practice. No use, distribution or reproduction is permitted which does not comply with these terms.

frontiers | Frontiers in Neurology

ORIGINAL RESEARCH
published: 07 July 2022
doi: 10.3389/fneur.2022.899470

TGFβ1 as a Predictive Biomarker for Collateral Formation Within Ischemic Moyamoya Disease

Yuanbing Chen[1,2], *Miao Tang*[1,2], *Hui Li*[1,2], *Hongwei Liu*[1,2], *Junyu Wang*[1,2] *and Jun Huang*[1,2]*

[1] *Department of Neurosurgery, Xiangya Hospital, Central South University, Changsha, China,* [2] *National Clinical Research Center for Geriatric Disorders, Xiangya Hospital, Central South University, Changsha, China*

OPEN ACCESS

Edited by:
Wen-Jun Tu,
Chinese Academy of Medical Sciences and Peking Union Medical College, China

Reviewed by:
Rong Wang,
Capital Medical University, China
Marialuisa Zedde,
IRCCS Local Health Authority of Reggio Emilia, Italy
Francesco Acerbi,
IRCCS Carlo Besta Neurological Institute Foundation, Italy

***Correspondence:**
Jun Huang
xyyyhj@csu.edu.cn

Specialty section:
This article was submitted to Neurological Biomarkers, a section of the journal Frontiers in Neurology

Received: *18 March 2022*
Accepted: *25 May 2022*
Published: *07 July 2022*

Citation:
Chen Y, Tang M, Li H, Liu H, Wang J and Huang J (2022) TGFβ1 as a Predictive Biomarker for Collateral Formation Within Ischemic Moyamoya Disease. Front. Neurol. 13:899470. doi: 10.3389/fneur.2022.899470

Objective: Moyamoya disease (MMD) is a unique cerebrovascular occlusive disease characterized by progressive steno-occlusion within the terminal segment of the internal carotid artery. However, good collaterals from an external carotid artery are essential to compensate for the ischemia in moyamoya disease. This study aimed to investigate the transforming growth factor-beta 1 (TGFβ1) in plasma as a potential biomarker for predicting collateral formation in ischemic MMD.

Methods: The transcriptome profile downloaded from Gene Expression Omnibus (GEO) was used to analyze the differential expression of genes between the ischemic MMD and the control groups. We prospectively recruited 23 consecutive patients with ischemic MMD that was diagnosed *via* digital subtraction angiography (DSA). Nine patients with intracranial aneurysms and four healthy people served as controls. The collaterals from the external carotid artery were examined using DSA. We evaluated whether the collateral formation was associated with TGFβ1 in patients with ischemic MMD. Western blot, RT-qPCR, ELISA, and tube formation assay were used to explore the relationship between TGFβ1 and angiogenesis, as well as the potential mechanisms.

Results: The mRNA levels of TGFβ1 were upregulated in the patients with ischemic MMD. The plasma TGFβ1 levels were higher in the patients with ischemic MMD than in the aneurysm and healthy patients ($p < 0.05$). The collateral formation group has higher levels of serum TGFβ1 than the non-collateral formation group ($p < 0.05$). The levels of vascular endothelial growth factor (VEGF) are positively correlated with TGFβ1 levels in the plasma ($R^2 = 0.6115$; $p < 0.0001$). TGFβ1 regulates VEGF expression *via* the activation of the TGFβ pathway within HUVEC cells, as well as TGFβ1 stimulating HUVEC cells to secrete VEGF into the cell culture media. An *in vitro* assay revealed that TGFβ1 promotes angiogenesis within the endothelial cells.

Conclusion: Our findings suggest that TGFβ1 plays a vital role in promoting collateral formation by upregulating VEGF expression in ischemic MMD.

Keywords: moyamoya, TGFβ1, collateral, VEGF, biomarker

INTRODUCTION

Moyamoya disease (MMD) is a rare cerebrovascular occlusive disease characterized by progressive steno-occlusions in the terminal segment of the internal carotid artery (ICA), as well as their proximal branches. Furthermore, the appearance of abnormally dilated compensatory collateral vasculature is revealed upon angiography (1, 2). With the progress of intracranial vascular stenosis, both the intracranial and extracranial vessels are stimulated to develop collateral circulation (3, 4). Those new collaterals are found and considered necessary to maintain perfusion in MMD (5–7). When the collateral circulation is insufficiently compensated, it induces ischemic symptoms (4).

Bypass surgery is recommended as a first-line treatment of MMD, including direct bypass, indirect bypass, and combined strategies (8–10). Moreover, direct bypass surgery can immediately increase blood flow, but indirect bypass requires more time to produce angiogenesis from the muscle and dura (8, 9). Also, there is a lack of effective collateral angiogenesis needed to prevent strokes after indirect bypass surgery immediately (11). Notably, previous research has revealed that transdural collaterals are associated with the capacity to develop collaterals postoperatively (7, 12). Therefore, a comprehensive understanding of the relevant mechanism of preoperative collateral development is expected to guide the establishment of good postoperative collateral. However, the molecular mechanisms regulating angiogenesis in the progression of collateral remain unclear and lack a reliable biomarker to predict the collateral (8, 13–15).

Transforming growth factor-beta 1 (TGFβ1) is secreted as a latent form and functions as a multifunctional polypeptide growth factor acting as a significant modulator of cellular growth and differentiation, also playing a vital role in regulating the expression of potent angiogenic factors (16, 17). There is a high level of TGFβ1 in the serum of patients with MMD that has been shown in previous research (17–19). However, it is only speculated that the expression of TGFβ1 is related to the pathophysiology of moyamoya disease, and the relationship between TGFβ1 and the collateral is still undetermined.

In this research, we sought to explore the genes specifically expressed in the intracranial arteries of MMD and identify the angiogenesis-related genes. In addition, the relationship between TGFβ1 and the collaterals originating from the dura was identified in ischemic MMD. Finally, we investigated the mechanisms of TGFβ1 underlying the regulation and development of collaterals.

MATERIALS AND METHODS

Patients

From September 2019 and November 2021, 23 Asiatic patients diagnosed with ischemic MMD in the department of neurosurgery of Xiangya hospital were recruited for this study. MMD was diagnosed according to the guidelines for diagnosis and treatment of MMD by the Research Committee on Spontaneous Occlusion of the Circle of Willis (20). All patients underwent DSA to evaluate the transdural collaterals from the dura and agreed to have their plasma examined for potential biomarkers that were included in this study. The patients diagnosed with quasi-moyamoya disease (moyamoya syndrome secondary to identified etiologies, including a history of vasculitis, neurofibromatosis, tuberous sclerosis, hypertension, diabetes, and others) were excluded from this study. MMD was categorized into pediatric and adult groups based on age. Nine patients with intracranial aneurysms and four healthy persons were included in the study as controls. Clinical information was collected. The Research Ethics Committee approved this study of the Xiangya hospital. All study participants were given written and informed consent.

Transdural Collaterals

Transdural collaterals are defined as the blood supply to the cerebral cortex from the external cervical artery (ECA). To detect the blood supply from the ECA more accurately, we only selected the middle meningeal artery for evaluation. Transdural collaterals are considered if obvious blood supply from the middle meningeal artery (MMA), according to the DSA (including bilateral ECA injections), is seen (**Figure 1**).

Bioinformatics Analysis

For differentially expressed angiogenesis-related gene screening, the Gene Expression Omnibus (GEO) dataset (GSE157628) was obtained from the GEO database (http://www.ncbi.nlm.nih.gov/geo). The MCA specimen was collected during the STA–MCA anastomosis (21). Data analysis was carried out in the R environment using the limma package. Both upregulated and downregulated differentially expressed genes (DEGs) were used for further study, and statistical significance was set at $p < 0.05$, $|\log2 \text{ fold change}| \geq 2$ in this study. The DEGs were performed for gene ontology (GO) functional enrichment analysis.

ROC Curve Analysis

To evaluate the predictive value of the biomarkers (TGFβ1 and VEGF), the receiver operating characteristic (ROC) curves were conducted to calculate the AUCs. The sensitivity and specificity of the biomarkers' predictability in their capacity to develop transdural collaterals were assessed by calculating the AUC value of the ROC curve using SPSS 21.0 software.

Enzyme-Linked Immunosorbent Assay

Patient plasma was collected before surgery and stored at −80°C. The experimental procedures were carried out according to the manufacturer's instructions for the TGFβ1 (4A Biotech Co, #CHE0029, China) and VEGF (4A Biotech Co, #CHE0043, China) ELISA kit.

Cell Culture

Human umbilical vein endothelial cells (HUVECs) were purchased from the American Type Culture Collection (ATCC). HUVECs were cultured in HUVEC complete medium (CellCook, cat: CM2007, China) supplemented with 10% fetal bovine serum (FBS), 100 U/ml penicillin, and 100 U/ml streptomycin, and maintained at 37°C in a 5% CO_2 atmosphere. HUVECs were collected and seeded at a density of 1×10^6

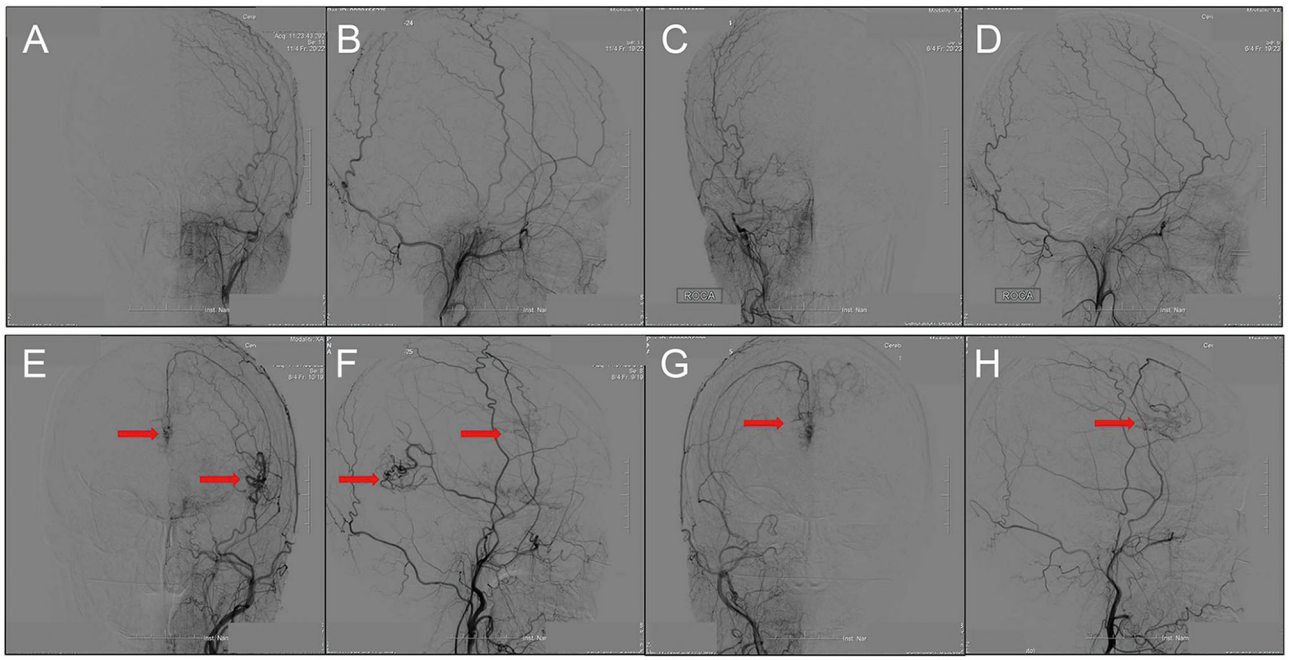

FIGURE 1 | DSA showed the transdural collaterals arising from the middle meningeal artery. **(A–D)**, anteroposterior **(A)** and lateral **(B)** views of left ECA injection, anteroposterior **(C)** and lateral **(D)** views of right ECA injection. There is no MMA supplying blood to the brain cortex through transdural collateral vessels. **(E–H)**, Anteroposterior **(E)** and lateral **(F)** views of left ECA injection, anteroposterior **(G)** and lateral **(H)** views of right ECA injection from the other patient. The MMA provides transdural collateral vessels to the brain cortex (red arrowheads).

cells/well into 6-well-plates. After 4 h, the non-adherent cells were removed and added to the HUVEC complete media (2.5 ml). The TGF-β1 (Cusabio, China) was added to the media with a final concentration of 5 ng/ml. After 24 h, the medium and cells were harvested.

Western Blot

Human umbilical vein endothelial cells were precipitated by centrifugation and lysed in immunoprecipitation (IP) lysis buffer (Containing a protease inhibitor cocktail). A quantity of 40 mg total protein was mixed with 5×loading buffer and heated (100°C for 10 min). The protein lysates were electrophoresed in 10% SDS-PAGE gels and transferred onto polyvinylidene fluoride (PVDF) membranes. The antibody against Smad2 (CST, #5339, 1:1000), p-Smad2 (CST, #18338, 1:1000), Smad3 (Abcam, #ab40854, 1:2000), p-Smad3 (Abcam, #ab52903, 1:2000), VEGF (Abclonal, #A12303, 1:500), and β-actin (Sigma, #A5441, 1:10000) were incubated at 4°C overnight. The membrane was incubated with the corresponding second antibody after washing with TBST at room temperature three times. Antibody signals were detected *via* the ChemiDox XRS+ image-forming system.

RNA Isolation and Quantitative Real-Time PCR

Total RNA was extracted from HUVECs *via* an RNAiso Plus kit (Takara, Japan). The concentrations were measured using a NanoDrop 2000 (Thermo Scientific, USA). gRNA was reverse transcribed into cDNA, according to the manufacturer's protocol using the PrimeScript^{TM}RT reagent Kit with a gDNA Eraser (Takara). The quantitative real-time PCR was conducted using a 7,500 Fast Real-Time PCR System (Applied Biosystems, Life Technologies). The following primers were used: VEGF forward sequence, TTGCCTTGCTGCTCTACCTCCA, and reverse sequence: GATGGCAGTAGCTGCGCTGAT; β-actin forward sequence: CACCATTGGCAATGAGCGGTTC and reverse sequence: AGGTCTTTGCGGATGTCCACGT.

Tube Formation Assay

A total of 100 μL chilled Matrigel was added to a precooled 6-well-plate and solidified at 37°C for 1 h. The HUVEC cells were precipitated by centrifugation and resuspended in HUVEC complete media (1 ml) containing 1% fetal bovine serum. The HUVECs were seeded onto the solidified Matrigel in the 6-well-plates (2×10^4 cells per well). The cells were then supplemented with media from the HUVEC cells treated with TGF-β1 for 24 h or blank and incubated at 37°C in 5% CO_2 for 4 h. A light microscope was used to capture the image of the tube formation using a magnification of ×40. Image J software was used to count the tubes of the branches and loops.

Statistical Analysis

The ROC curve was generated *via* the SPSS 21.0 software. The results are presented as means ± SEM, and statistical analysis was performed between the different groups using Student's *t*-test in GraphPad Prism8.0. The values $p < 0.05$ were considered

A

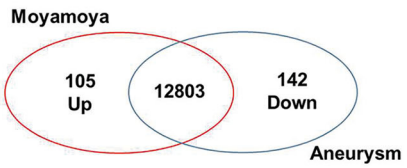

B

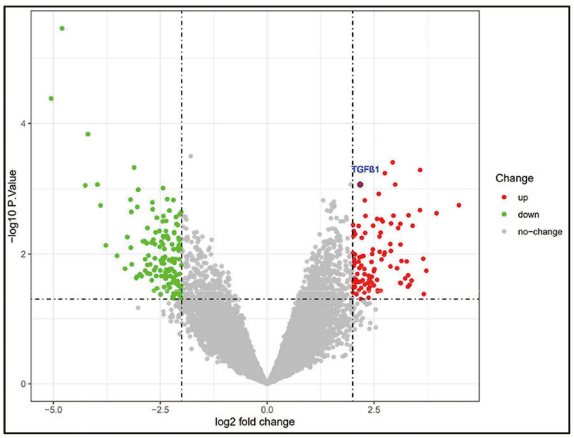

C

PRKCI, MKNK2, REC8, TGFβ1, DWS, LRFN1, STAP1, FOLR2, LGALS9, GPC1, RNF17, WDR70, DDX56, RBP4, GNB5, XCE, TMEM50A, RAB11FIP2, SLC25A3, PRR12, UTRN, CDK5RAP1, KRT6A, MYCNOS, SLC39A6, UGT1A11P, CIAO1, HRH2, SPACA9, ALX3, SEMA6C, UTP18, ANKRD1, COPS3, CNPY3, S100A7, TRBC2, FDXR, PPBP, NPM2, CLUL1, WDR91, FAM20A, HAS3, MT1H, DHRS4-AS1, IL3, IGHD3-10, RIC8B, MARCHF4, CAMK1D, ZZZ3, ARPP19, MKS1, CERS2, ERN1, MIIP, FOXI1, SGCA, ANKLE2, ARHGAP25, CAPN9, B3GNT3, ZNF274, NR0B2, RMC1, CHRNA5, GLYAT, ALB, TM9SF4, SPIB, ABI1, NACAD, ENY2, EP300, NXPE4, UPB1, HGH1, TRBV12-2, TRBV14, DDO, GDF10, IGHV5-10-1, CAPRIN1, ZNF236, MTBP, CLIC3, TRMT6, TACO1, MSI1, SLC6A15, SHFM2, GCA, CFC1, PARP14, STK11, SFN, RXRG, MTERF1, ALOXE3, ZFY, MRC2, CEP162, DNASE2, VPS26C

D

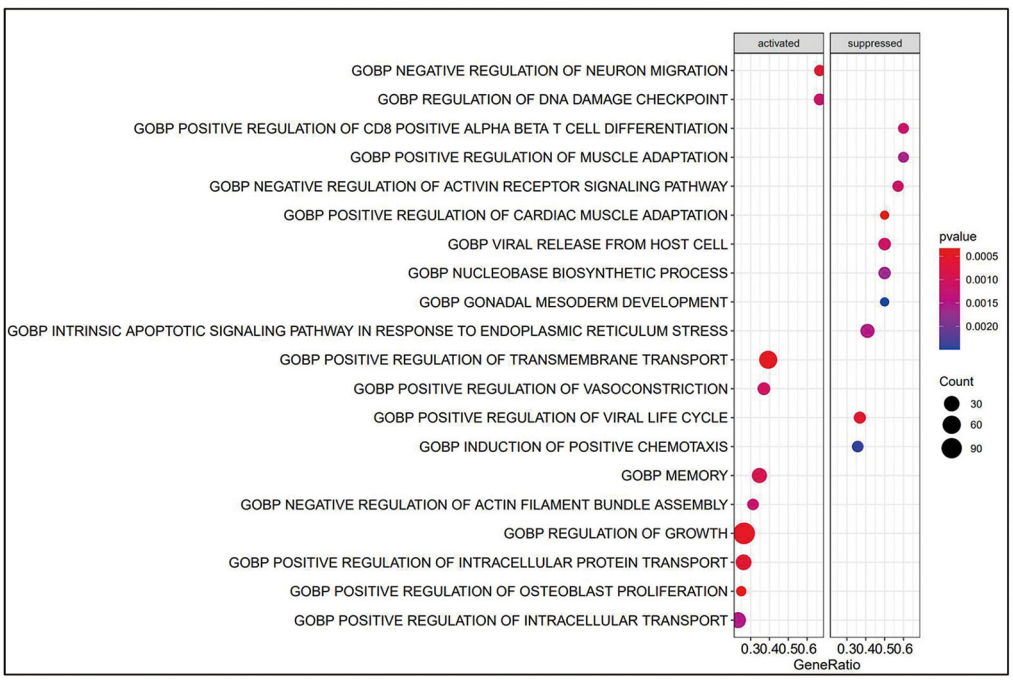

FIGURE 2 | Upregulation of TGFβ1 in the middle cerebral artery(MCA) of MMD. **(A)** Venn diagram showed significantly upregulated genes ($n = 105$) and significantly downregulated genes ($n = 142$). **(B)** Volcano plot to visualize the DEGs in MMD compared to control. The significantly upregulated genes were shown with red dots, and green dots represent significantly downregulated genes. Gray dots represent genes not differentially expressed. **(C)** the upregulated genes were listed. **(D)** GO functional enrichment analysis of sequencing data.

to be significant. $^{*}p < 0.05$, $^{**}p < 0.01$, $^{***}p < 0.001$, and $^{****}p < 0.0001$.

RESULTS

Patient Characteristics

A total of 23 ischemic MMD patients were recruited to the present study, including 9 children (<18 years old) and 14 adults (>18 years old). Among them, 9 patients were women and 14 patients were men. The median age was 29.7 ± 3.6 years and ranged from 7 to 54 years. Transdural collaterals were present in 14 (60.9%) patients. According to the grade of Suzuki, 13 patients in I-III (I, $n = 0$; II, $n = 5$; III, $n = 8$), 10 patients with IV-VI (IV, $n = 6$; V, $n = 4$; VI, $n = 0$); 6 patients presented with transient ischemic attack (TIA) and 17 patients presented with infraction; 13 patients underwent indirect surgery, and 10 patients underwent combined procedures.

Upregulation of TGFβ1 in the Middle Cerebral Artery of MMD

To explore the DEGs in MMD, we analyzed the MCA transcriptomes of patients with MMD compared with those of patients with an aneurysm. We found 105 upregulated and 142 downregulated differentially expressed genes in MMD, which have been visually shown in the volcano plot (**Figures 2A–C**). According to these DEGs, the GO functional enrichment analysis identified several relatively associated terms, including regulation of cell growth, transmembrane transport, and vasoconstriction (**Figure 2D**). There is a distinctive characteristic that the development of abnormal vascular networks and collateral formations of the ECA in moyamoya disease have the ability to promote angiogenesis (3, 22). To further explore the mechanisms of the development of angiogenesis, we identified that the angiogenesis-related genes-TGFβ1 were significantly overexpressed in the MCA of MMD (**Figure 2B**).

TGFβ1 Associated With Transdural Collaterals in Ischemic MMD

The TGFβ1 was observed to be overexpressed in the MCA of MMD, and the TGFβ1 is secreted as a multifunctional polypeptide growth factor in the plasma (16, 17). ELISA was performed to detect the concentration of TGFβ1 in plasma. Compared to patients with aneurysm and healthy controls, the highest levels of TGFβ1 were detected in the MMD group (6,666 ± 1,181 vs. 2,684 ± 399, 2,651 ± 530, $p < 0.05$) (**Figure 3A**). In addition, TGFβ1 was determined at a relatively high level in pediatric groups (9,810 ± 2,260 vs. 4,644 ± 1,025; $p < 0.05$) (**Figure 3B**). Importantly, the concentrations of TGFβ1were significantly increased in the collateral group (8,773 ± 1,708 vs. 3387 ± 460.7; $p < 0.05$) (**Figure 3C**). The ROC curve demonstrated that the levels of TGFβ1 in plasma predicted the formation of transdural collateral with high sensitivity and specificity. The area under the ROC curve was 0.802 (**Figure 3D**). But the level of TGFβ1 without a difference between Suzuki I-III and IV-VI (6,047 ± 1,340 vs. 7,470 ± 2,144; $p = 0.5626$) (**Figure 3E**).

Association Between VEGF and Transdural Collaterals in Ischemic MMD

In previous studies, VEGF, bFGF, and IL8 are included as direct angiogenic growth factors that can stimulate angiogenesis and promote cellular division in endothelial cells, but the TGFβ1 and PDGF belong to the indirect angiogenic growth factors (15). VEGF is reported to be the target gene of TGFβ1 in tumors and inflammation (23–25). Interestingly, the levels of TGFβ1 had a positive correlation with VEGF in the plasma of MMD using multiple linear regression analysis (**Figure 4A**). VEGF was detected at higher concentrations within the pediatric groups and corresponded to the trend seen in TGFβ1 (78.88 ± 14.77 vs. 38.97 ± 5.905; $p < 0.01$) (**Figure 4B**). The levels of VEGF were also significantly upregulated in the collateral group (71.25 ± 10.15 vs. 28.65 ± 5.386; $p < 0.01$) (**Figure 4C**). The concentration of VEGF was used to predict the development of transdural collateral with high sensitivity and specificity which was demonstrated by the curve of ROC, and the area under the ROC curve was 0.897 (**Figure 4D**).

TGFβ1 Upregulated VEGF to Promote the Angiogenesis *via* Activating the TGFβ Signaling Pathway *in vitro*

The expression of VEGF was analyzed further to identify the mechanisms of TGFβ1 regulation on transdural collaterals. The mRNA and protein levels of VEGF were upregulated in HUVEC cells treated with TGFβ1 for 24 h (**Figures 5A,B**). Interestingly, the concentration of VEGF in the cell culture media was significantly higher in cultured HUVEC cells treated with TGFβ1 for 24 h compared to control (**Figure 5C**). Using the tube formation assay, the HUVECs cultured with the media from the HUVEC cells treated with TGF-β1 showed a significantly enhanced ability of angiogenesis (**Figures 5D–F**).

DISCUSSION

This study explored the relationship between the TGFβ1 and transdural collateral. The major findings are as follows: (1) the expression of TGFβ1 was upregulated in patients with MMD; (2) the level of TGFβ1 had a positive correlation with VEGF in plasma, which is related to the transdural collateral in patients with MMD; and (3) TGFβ1 upregulated VEGF to promote angiogenesis through the activation of the TGFβ signaling pathway.

The ischemic events in MMD are attributed to reduced blood flow caused by stenosis arteries (26). The collaterals are important to prevent the occurrence of stroke, reduce the incidence of perioperative complications, and are closely related to clinical outcomes (22, 27). Among collateral circulation, the transdural collaterals play the most important role in the collateral blood supply to the ischemic brain cortex (28). In our study, 60.8% (14/23) of the transdural collaterals were established and supplied blood to the cortex.

In the past few decades, the etiology and pathophysiology of MMD are still unclear (1, 22). It is difficult to extract the samples from the patients with MMD, which restricts the research

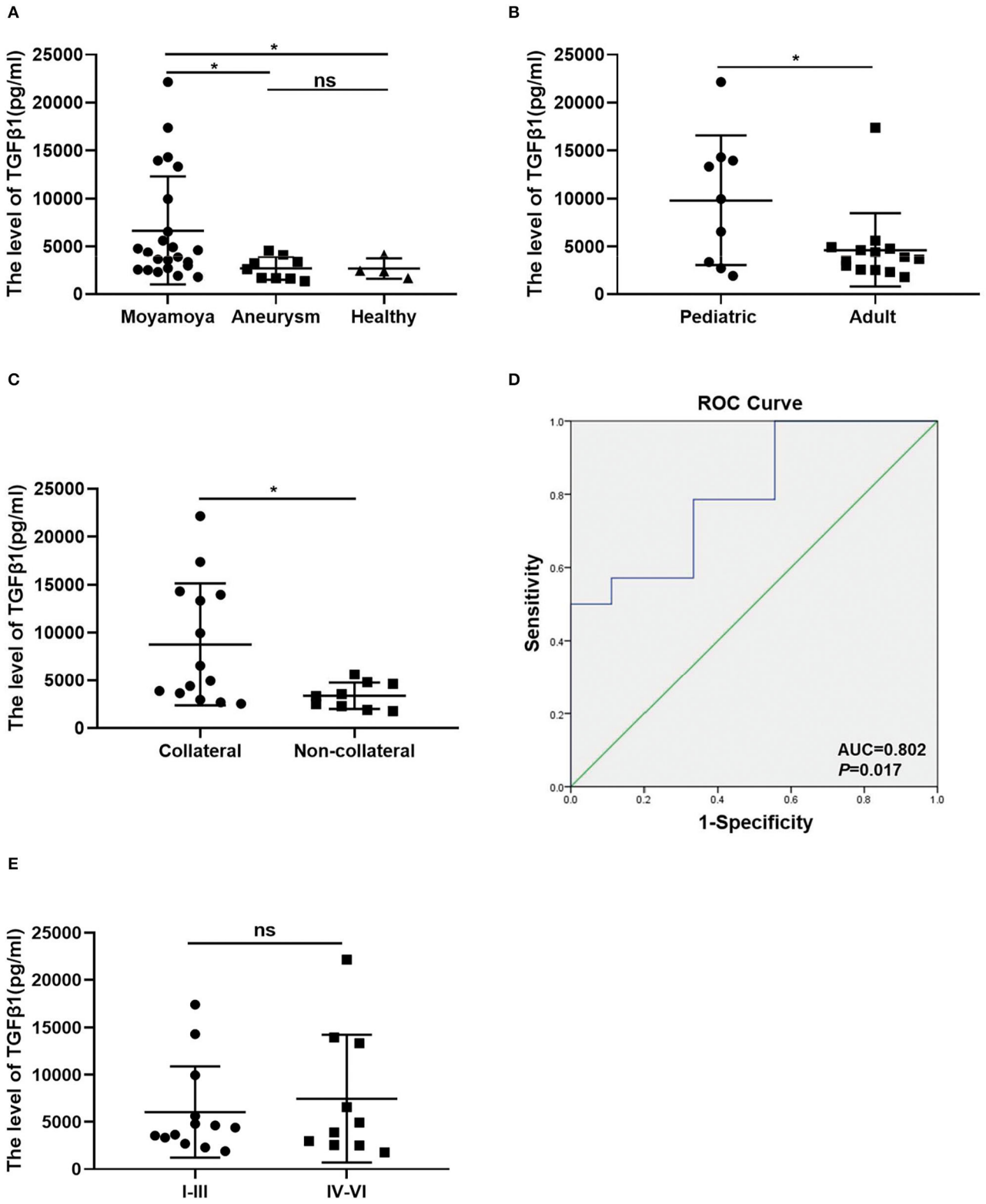

FIGURE 3 | TGFβ1 is associated with transdural collaterals in MMD. **(A)** The levels of TGFβ1 were significantly increased in MMD patients compared to other groups. **(B)** the Expression level of the TGFβ1 in plasma between pediatric group ($n = 9$) and adult group ($n = 14$). **(C)** The different concentration of TGFβ1 between collateral group ($n = 9$) and non-collateral group ($n = 14$). **(D)** The value of the TGFβ1 predicted the collateral formation being analyzed by ROC curves. **(E)** The level of TGFβ1 between Suzuki I-III ($n = 13$) and IV-VI ($n = 10$). ns, non significant ($p > 0.05$), *$p < 0.05$.

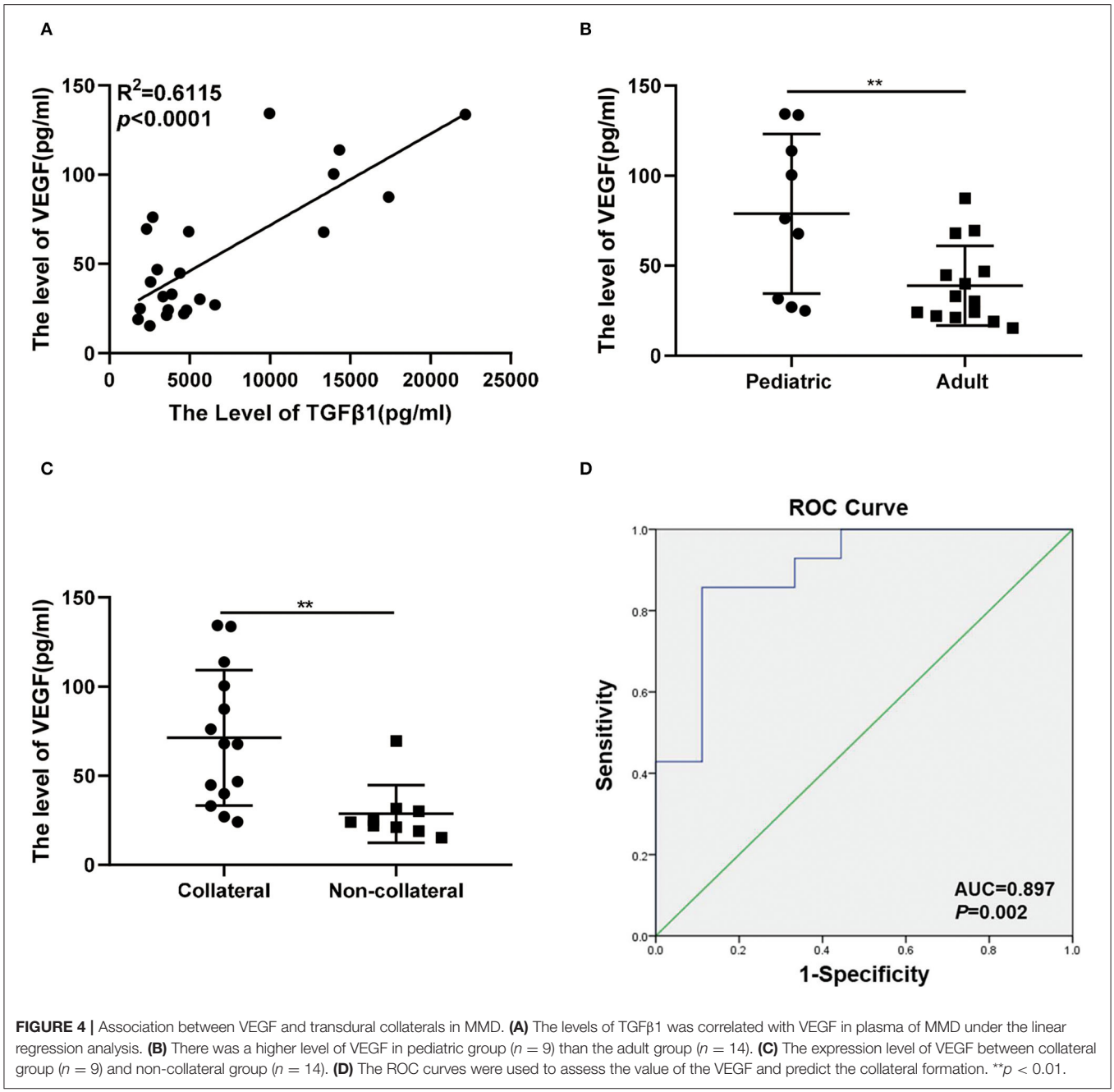

FIGURE 4 | Association between VEGF and transdural collaterals in MMD. **(A)** The levels of TGFβ1 was correlated with VEGF in plasma of MMD under the linear regression analysis. **(B)** There was a higher level of VEGF in pediatric group ($n = 9$) than the adult group ($n = 14$). **(C)** The expression level of VEGF between collateral group ($n = 9$) and non-collateral group ($n = 14$). **(D)** The ROC curves were used to assess the value of the VEGF and predict the collateral formation. $^{**}p < 0.01$.

on the molecular mechanisms of collaterals (21, 29). With the development of technology, facilitating the transcriptome analysis (21), this study revealed that the expression of TGFβ1 was upregulated in MCA, as well as within the plasma extracted from MMD patients. Furthermore, the function of TGFβ1 associated with angiogenesis has been studied (23–25). These changes and functions are consistent with the pathological features of spontaneous transdural collaterals that were shown in patients with MMD (7). Moreover, higher levels of TGFβ1 were observed in MMD accompanied by transdural collaterals. These findings demonstrate that the TGFβ1 may be a unique biomarker for the formation of transdural collaterals.

Vascular endothelial growth factor is one of the direct angiogenic growth factors which can stimulate angiogenesis (15). Our present data revealed that the high concentration of VEGF in the patient's plasma indicates better transdural collaterals. In addition, we observed that the level of TGFβ1 positively correlates with the VEGF pathway in MMD. This result suggests that VEGF levels are also related to transdural collaterals and correlate with the TGFβ1 levels. Interestingly, we found that

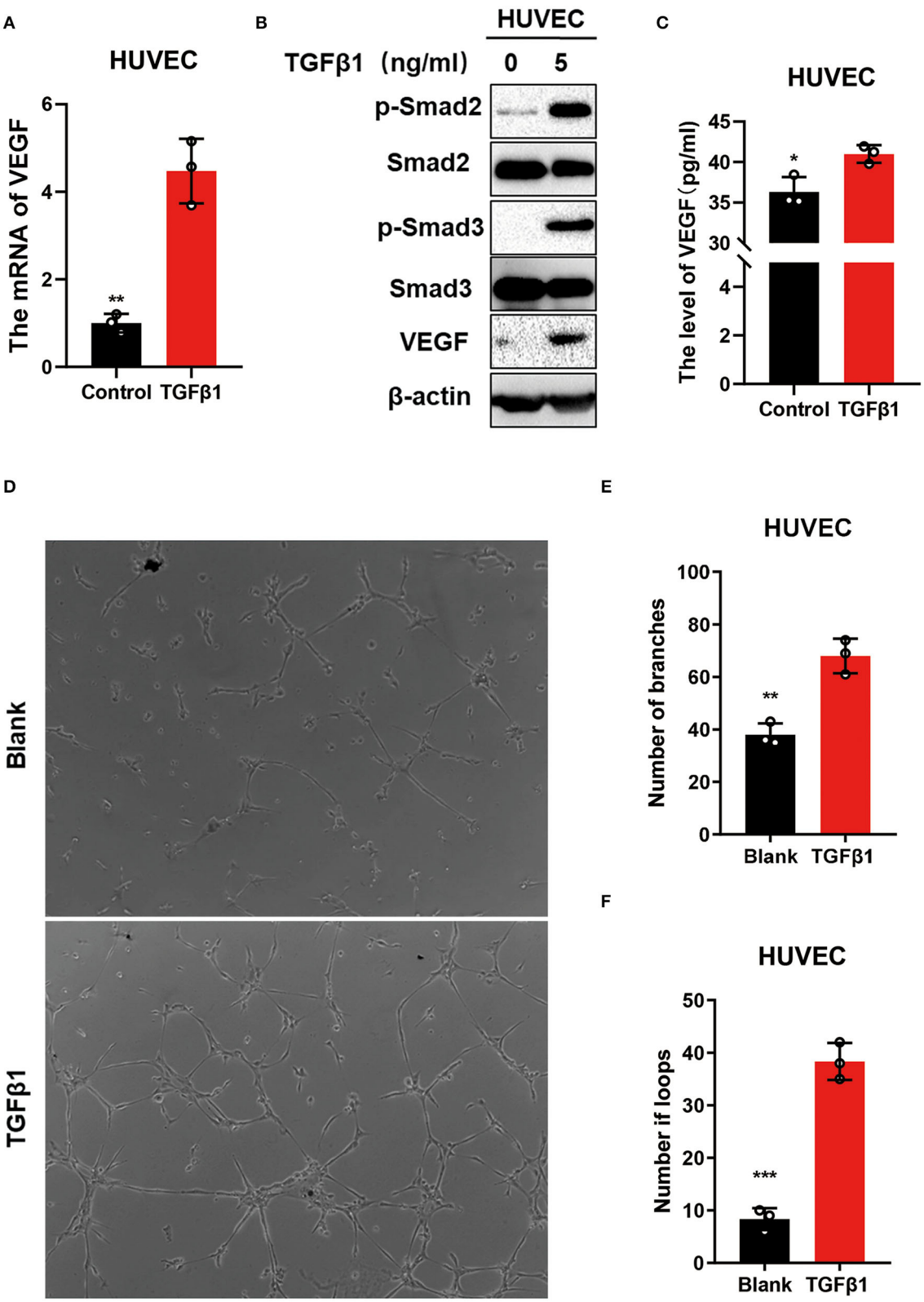

FIGURE 5 | TGFβ1 upregulated VEGF to promote angiogenesis *via* activating the TGFβ signaling pathway *in vitro*. **(A)** The mRNA levels of VEGF in HUVECs after stimulating with TGFβ1(5 ng/ml) for 24 h. **(B)** Western blot was used to detect the molecular of TGFβ pathway. **(C)** ELISA was performed to identify the level of VEGF in medium after the HUVECs were stimulated with TGFβ1(5 ng/ml). **(D–F)** The tube formation assay was conducted to access the ability of angiogenic in which the HUVECs cultured with the medium from the HUVECs treated with TGF-β1. $^{*}p < 0.05$, $^{**}p < 0.01$, $^{***}p < 0.001$.

the TGFβ1 upregulated the protein and mRNA levels of VEGF in HUVEC cells *in vitro*. It was also revealed that TGFβ1 can stimulate the HUVEC cells to secret VEGF into the cell culture media. These results suggest that TGFβ1 promotes the expression of VEGF in HUVEC cells. The function of TGFβ1 and the subsequent regulation of VEGF have been reported in other disease states (30, 31). Furthermore, we conducted a western blot analysis and demonstrated that TGFβ1 promotes the phosphorylation of Smad2 and Smad3, which activate the TGFβ pathway in HUVEC cells. Finally, the TGF-β1 was confirmed to enhance the ability of angiogenesis in HUVEC cells; thus, we concluded that TGF-β1 promotes the formation of transdural collaterals *via* the activation of the TGFβ signaling pathway promoting angiogenesis *in vitro*.

In previous studies, the spontaneous transdural collaterals that appear were considered the brain's ability to promote angiogenesis and served as a radiographic biomarker to predict the collaterals' development after revascularization (7, 8, 12). In this research, we detected that the levels of TGFβ1 were associated with the formation of transdural collaterals, indicating that TGFβ1 may become a vital biomarker in predicting collaterals after revascularization. Furthermore, we found that the relatively high concentrations of TGFβ1 were shown in pediatric patients with MMD. Moreover, an excellent postoperative collateral formation was detected in pediatric patients rather than adult with MMD (32, 33). These findings revealed that high levels of TGFβ1 may promote the formation of the collaterals in pediatric MMD patients and further demonstrates that the levels of TGFβ1 are related to collaterals.

Our study has some limitations. First, we identified the TGFβ1 overexpressed in MCA of MMA through bioinformatics analysis, but it was not verified in blood vessel wall tissue due to the specimen being difficult to obtain. Second, the subjects are patients with ischemic moyamoya disease, and there is a lack of the type of headaches and hemorrhage. In addition, the patients and specimens could be affected *via* selection bias because of the single-center study and the limited sample size. Finally, although we speculate that TGFβ1 may be related to the collaterals after the revascularization, we have not reviewed the follow-up data.

CONCLUSION

The present study showed that TGFβ1 might play an important role in promoting collateral formation by activating the TGFβ pathway and upregulating the VEGF in ischemic MMD, taking into account the function and mechanism of the TGFβ1, which might be an important target for collateral-enhancing and preventing stroke in ischemic MMD.

DATA AVAILABILITY STATEMENT

The original contributions presented in the study are included in the article/**Supplementary Materials**, further inquiries can be directed to the corresponding author.

ETHICS STATEMENT

The Research Ethics Committee approved this study of the Xiangya Hospital. Written informed consent to participate in this study was provided by the participants' legal guardian/next of kin. Written informed consent was obtained from the individual(s), and minor(s)' legal guardian/next of kin, for the publication of any potentially identifiable images or data included in this article.

AUTHOR CONTRIBUTIONS

JH designed the study and wrote the manuscript. YC and JW analyzed the data. MT and HLiu collected clinical data. YC and HLi performed *in vitro* experiments. All authors have contributed to the article and approved the final manuscript.

FUNDING

This work was funded by the National Natural Science Foundation of China [82160554 (JH)] and Natural Science Foundation of Hunan Province [2020JJ8051 (JH)].

ACKNOWLEDGMENTS

The authors thank AiMi Academic Services (www.aimieditor.com) for the English language editing and review services.

SUPPLEMENTARY MATERIAL

The Supplementary Material for this article can be found online at: https://www.frontiersin.org/articles/10.3389/fneur.2022.899470/full#supplementary-material

REFERENCES

1. Scott RM, Smith ER. Moyamoya disease and moyamoya syndrome. *N Engl J Med.* (2009) 360:1226–37. doi: 10.1056/NEJMra0804622
2. Kuroda S, Houkin K. Moyamoya disease: current concepts and future perspectives. *Lancet Neurol.* (2008) 7:1056–66. doi: 10.1016/S1474-4422(08)70240-0
3. Zhao M, Zhang D, Wang S, Zhang Y, Deng X, Zhao J. The collateral circulation in moyamoya disease: a single-center experience in 140 pediatric patients. *Pediatr Neurol.* (2017) 77:78–83. doi: 10.1016/j.pediatrneurol.2017.08.016
4. Liebeskind DS, Cotsonis GA, Saver JL, Lynn MJ, Cloft HJ, Chimowitz MI, et al. Collateral circulation in symptomatic intracranial atherosclerosis. *J Cereb Blood Flow Metab.* (2011) 31:1293–301. doi: 10.1038/jcbfm.2010.224
5. Kluytmans M, van der Grond J, van Everdingen KJ, Klijn CJ, Kappelle LJ, Viergever MA. Cerebral hemodynamics in relation to patterns of collateral flow. *Stroke.* (1999) 30:1432–9. doi: 10.1161/01.STR.30.7.1432
6. Fang H, Song B, Cheng B, Wong KS, Xu YM, Ho SS, et al. Compensatory patterns of collateral flow in stroke patients with unilateral and bilateral carotid stenosis. *BMC Neurol.* (2016) 16:39. doi: 10.1186/s12883-016-0560-0

7. Storey A, Michael Scott R, Robertson R, Smith E. Preoperative transdural collateral vessels in moyamoya as radiographic biomarkers of disease. *J Neurosurg Pediatr.* (2017) 19:289–95. doi: 10.3171/2016.9.PEDS16161
8. Wang G, Wen Y, Chen S, Zhang G, Li M, Zhang S, et al. Use of a panel of four microRNAs in CSF as a predicted biomarker for postoperative neoangiogenesis in moyamoya disease. *CNS Neurosci Ther.* (2021) 27:908–18. doi: 10.1111/cns.13646
9. Deng X, Gao F, Zhang D, Zhang Y, Wang R, Wang S, et al. Direct versus indirect bypasses for adult ischemic-type moyamoya disease: a propensity score-matched analysis. *J Neurosurg.* (2018) 128:1785–91. doi: 10.3171/2017.2.JNS162405
10. Ge P, Zhang Q, Ye X, Liu X, Deng X, Wang J, et al. Postoperative collateral formation after indirect bypass for hemorrhagic moyamoya disease. *BMC Neurol.* (2020) 20:28. doi: 10.1186/s12883-020-1612-z
11. Abe H, Katsuta T, Miki K, Higashi T, Inoue T. Temporary steno-occlusive change in the donor artery during mouth opening (big bite ischemic phenomenon) after superficial temporal artery to middle cerebral artery bypass in adult patients with moyamoya disease and atherosclerosis. *Acta Neurochir Suppl.* (2016) 123:123–8. doi: 10.1007/978-3-319-29887-0_17
12. Bang OY, Fujimura M, Kim SK. The pathophysiology of moyamoya disease: an update. *J Stroke.* (2016) 18:12–20. doi: 10.5853/jos.2015.01760
13. Schoenhagen P, Ziada KM, Kapadia SR, Crowe TD, Nissen SE, Tuzcu EM. Extent and direction of arterial remodeling in stable versus unstable coronary syndromes : an intravascular ultrasound study. *Circulation.* (2000) 101:598–603. doi: 10.1161/01.CIR.101.6.598
14. Chung JW, Kim DH, Oh MJ, Cho YH, Kim EH, Moon GJ, et al. Cav-1 (Caveolin-1) and arterial remodeling in adult moyamoya disease. *Stroke.* (2018) 49:2597–604. doi: 10.1161/STROKEAHA.118.021888
15. Yoshimoto T, Houkin K, Takahashi A, Abe H. Angiogenic factors in moyamoya disease. *Stroke.* (1996) 27:2160–5. doi: 10.1161/01.STR.27.12.2160
16. Lu Q, Sun D, Shivhare SB, Hou H, Bulmer JN, Innes BA, et al. Transforming growth factor (TGF) beta and endometrial vascular maturation. *Front Cell Dev Biol.* (2021) 9:640065. doi: 10.3389/fcell.2021.640065
17. Hojo M, Hoshimaru M, Miyamoto S, Taki W, Nagata I, Asahi M, et al. Role of transforming growth factor-beta1 in the pathogenesis of moyamoya disease. *J Neurosurg.* (1998) 89:623–9. doi: 10.3171/jns.1998.89.4.0623
18. Weng L, Cao X, Han L, Zhao H, Qiu S, Yan Y, et al. Association of increased Treg and Th17 with pathogenesis of moyamoya disease. *Sci Rep.* (2017) 7:3071. doi: 10.1038/s41598-017-03278-8
19. Weinberg DG, Arnaout OM, Rahme RJ, Aoun SG, Batjer HH, Bendok BR. Moyamoya disease: a review of histopathology, biochemistry, and genetics. *Neurosurg Focus.* (2011) 30:E20. doi: 10.3171/2011.3.FOCUS1151
20. Research Committee on the Pathology and Treatment of Spontaneous Occlusion of the Circle of Willis. Guidelines for diagnosis and treatment of moyamoya disease (spontaneous occlusion of the circle of Willis). *Neurol Med Chir.* (2012) 52:245–66. doi: 10.2176/nmc.52.245
21. Kanamori F, Yokoyama K, Ota A, Yoshikawa K, Karnan S, Maruwaka M, et al. Transcriptome-wide analysis of intracranial artery in patients with moyamoya disease showing upregulation of immune response, and downregulation of oxidative phosphorylation and DNA repair. *Neurosurg Focus.* (2021) 51:E3. doi: 10.3171/2021.6.FOCUS20870
22. Liu ZW, Han C, Zhao F, Qiao PG, Wang H, Bao XY, et al. Collateral circulation in moyamoya disease: a new grading system. *Stroke.* (2019) 50:2708–15. doi: 10.1161/STROKEAHA.119.024487
23. Gupta S, Joshi K, Wig JD, Arora SK. Intratumoral FOXP3 expression in infiltrating breast carcinoma: its association with clinicopathologic parameters and angiogenesis. *Acta Oncol.* (2007) 46:792–7. doi: 10.1080/02841860701233443
24. Prete A, Lo AS, Sadow PM, Bhasin SS, Antonello ZA, Vodopivec DM, et al. Pericytes elicit resistance to vemurafenib and sorafenib therapy in thyroid carcinoma via the TSP-1/TGFbeta1 axis. *Clin Cancer Res.* (2018) 24:6078–97. doi: 10.1158/1078-0432.CCR-18-0693
25. Luo H, Zhang Y, Zhang Z, Jin Y. The protection of MSCs from apoptosis in nerve regeneration by TGFbeta1 through reducing inflammation and promoting VEGF-dependent angiogenesis. *Biomaterials.* (2012) 33:4277–87. doi: 10.1016/j.biomaterials.2012.02.042
26. Kim DY, Son JP, Yeon JY, Kim GM, Kim JS, Hong SC, et al. Infarct pattern and collateral status in adult moyamoya disease: a multimodal magnetic resonance imaging study. *Stroke.* (2017) 48:111–6. doi: 10.1161/STROKEAHA.116.014529
27. Fanou EM, Knight J, Aviv RI, Hojjat SP, Symons SP, Zhang L, et al. Effect of collaterals on clinical presentation, baseline imaging, complications, and outcome in acute stroke. *AJNR Am J Neuroradiol.* (2015) 36:2285–91. doi: 10.3174/ajnr.A4453
28. Baltsavias G, Khan N, Valavanis A. The collateral circulation in pediatric moyamoya disease. *Childs Nerv Syst.* (2015) 31:389–98. doi: 10.1007/s00381-014-2582-5
29. Okami N, Aihara Y, Akagawa H, Yamaguchi K, Kawashima A, Yamamoto T, et al. Network-based gene expression analysis of vascular wall of juvenile Moyamoya disease. *Childs Nerv Syst.* (2015) 31:399–404. doi: 10.1007/s00381-014-2605-2
30. Roger I, Milara J, Montero P, Cortijo J. The Role of JAK/STAT molecular pathway in vascular remodeling associated with pulmonary hypertension. *Int J Mol Sci.* (2021) 22:4980. doi: 10.3390/ijms22094980
31. Spittau B, Dokalis N, Prinz M. The role of TGFbeta signaling in microglia maturation and activation. *Trends Immunol.* (2020) 41:836–48. doi: 10.1016/j.it.2020.07.003
32. Ge P, Ye X, Liu X, Deng X, Wang J, Wang R, et al. Angiographic outcomes of direct and combined bypass surgery in moyamoya disease. *Front Neurol.* (2019) 10:1267. doi: 10.3389/fneur.2019.01267
33. Gadgil N, Lam S, Pyarali M, Paldino M, Pan IW, Dauser RC. Indirect revascularization with the dural inversion technique for pediatric moyamoya disease: 20-year experience. *J Neurosurg Pediatr.* (2018) 22:541–9. doi: 10.3171/2018.5.PEDS18163

Conflict of Interest: The authors declare that the research was conducted in the absence of any commercial or financial relationships that could be construed as a potential conflict of interest.

Publisher's Note: All claims expressed in this article are solely those of the authors and do not necessarily represent those of their affiliated organizations, or those of the publisher, the editors and the reviewers. Any product that may be evaluated in this article, or claim that may be made by its manufacturer, is not guaranteed or endorsed by the publisher.

Copyright © 2022 Chen, Tang, Li, Liu, Wang and Huang. This is an open-access article distributed under the terms of the Creative Commons Attribution License (CC BY). The use, distribution or reproduction in other forums is permitted, provided the original author(s) and the copyright owner(s) are credited and that the original publication in this journal is cited, in accordance with accepted academic practice. No use, distribution or reproduction is permitted which does not comply with these terms.

frontiers | Frontiers in Neurology

ORIGINAL RESEARCH
published: 08 July 2022
doi: 10.3389/fneur.2022.938655

Association of Serum Interleukin-8 and Serum Amyloid A With Anxiety Symptoms in Patients With Cerebral Small Vessel Disease

Li-Li Shan[1†], Yi-Lin Wang[2†], Tian-Ci Qiao[1], Yue-Feng Bian[1], Ya-Jing Huo[1], Cen Guo[1], Qian-Yun Liu[1], Zi-Dong Yang[3], Ze-Zhi Li[4], Ming-Yuan Liu[1] and Yan Han[1]**

[1] Department of Neurology, Yueyang Hospital of Integrated Traditional Chinese and Western Medicine, Shanghai University of Traditional Chinese Medicine, Shanghai, China, [2] Georgetown Preparatory School, North Bethesda, MD, United States, [3] Institute of Science and Technology for Brain-Inspired Intelligence, Fudan University, Shanghai, China, [4] Department of Psychiatry, The Affiliated Brain Hospital of Guangzhou Medical University, Guangzhou, China

OPEN ACCESS

Edited by:
Yuzhen Xu,
Tongji University, China

Reviewed by:
Danhong Wu,
Fudan University, China
Xiang Han,
Fudan University, China

***Correspondence:**
Yan Han
hanyan@shutcm.edu.cn
orcid.org/0000-0002-7654-0906
Ming-Yuan Liu
liu.mingyuan@foxmail.com

[†]These authors have contributed equally to this work

Specialty section:
This article was submitted to Neurological Biomarkers, a section of the journal Frontiers in Neurology

Received: 07 May 2022
Accepted: 15 June 2022
Published: 08 July 2022

Citation:
Shan L-L, Wang Y-L, Qiao T-C, Bian Y-F, Huo Y-J, Guo C, Liu Q-Y, Yang Z-D, Li Z-Z, Liu M-Y and Han Y (2022) Association of Serum Interleukin-8 and Serum Amyloid A With Anxiety Symptoms in Patients With Cerebral Small Vessel Disease. Front. Neurol. 13:938655. doi: 10.3389/fneur.2022.938655

Objective: Cerebral small vessel disease (CSVD) is a clinical syndrome caused by pathological changes in small vessels. Anxiety is a common symptom of CSVD. Previous studies have reported the association between inflammatory factors and anxiety in other diseases, but this association in patients with CSVD remains uncovered. Our study aimed to investigate whether serum inflammatory factors correlated with anxiety in patients with CSVD.

Methods: A total of 245 CSVD patients confirmed using brain magnetic resonance imaging (MRI) were recruited from December 2019 to December 2021. Hamilton Anxiety Rating Scale (HAMA) was used to assess the anxiety symptoms of CSVD patients. Patients with HAMA scores $\geq$7 were considered to have anxiety symptoms. The serum levels of interleukin-1β (IL-1β), IL-2R, IL-6, IL-8, IL-10, tumor necrosis factor-α (TNF-α), serum amyloid A (SAA), C-reactive protein (CRP), high-sensitivity C-reactive protein (hs-CRP) and erythrocyte sedimentation rate (ESR) were detected. We compared levels of inflammatory factors between the anxiety and non-anxiety groups. Logistic regression analyses examined the correlation between inflammatory factors and anxiety symptoms. We further performed a gender subgroup analysis to investigate whether this association differed by gender.

Results: In the fully adjusted multivariate logistic regression analysis model, we found that lower levels of IL-8 were linked to a higher risk of anxiety symptoms. Moreover, higher levels of SAA were linked to a lower risk of anxiety symptoms. Our study identified sex-specific effects, and the correlation between IL-8 and anxiety symptoms remained significant among males, while the correlation between SAA and anxiety symptoms remained significant among females.

Conclusions: In this study, we found a suggestive association between IL-8, SAA, and anxiety symptoms in CSVD participants. Furthermore, IL-8 and SAA may have a sex-specific relationship with anxiety symptoms.

Keywords: cerebral small vessel disease, anxiety symptoms, inflammatory factors, SAA, IL-8

INTRODUCTION

Cerebral small vessel disease (CSVD) represents a cluster of disorders in which pathological alterations are found in small arteries, arterioles, venules, and capillaries (1). The alterations of parenchymal visible on brain imaging are considered clinical hallmarks of CSVD (2). CSVD may lead to cognitive decline, dementia, gait impairment, mood disturbance, and stroke through multiple mechanisms (1, 3–5). Importantly, mood disturbances are very commonly identified in patients with CSVD (6–8). There exists evidence that MRI markers of CSVD are consistently associated with a higher incidence of depression (9–11). The vascular depression hypothesis postulates that CSVD leads to mood disorders via damage to brain structures or neural connections involved in mood regulation (9, 12). However, most small vessel disease lesions in CSVD patients are thought to be silent in clinically defined early stages, or clinical symptoms are often highly inconsistent with brain imaging (13). Accordingly, researchers have begun to focus on other predictors relevant to CSVD. Inflammation is attracting more attention as a risk factor and classical pathological feature of CSVD (14, 15).

On the other hand, early studies have suggested that chronic inflammation may potentially trigger mood disorders (16–19). CSVD is often accompanied by anxiety symptoms, and such symptoms might also be correlated with inflammation, as often reported in the healthy population. The relationship between serum inflammatory factor levels and anxiety disorder has been much less studied than its relationship with depression. Recent studies have examined whether low-grade inflammation may be contributing to the connection between anxiety disorders and cardiovascular diseases (CVDs) (20). The mechanism behind the link between inflammation and anxiety may be that inflammatory markers influence metabolic pathways that affect functions of the neurotransmitters, ultimately affecting the neurocircuits that regulate anxiety (21, 22). In the context of anxiety disorders, the most studied inflammatory markers are CRP, interleukin (IL-6), and tumor necrosis factor-**α** (TNF-**α**) (21, 23, 24). However, a prominent role of other inflammation in psychopathology cannot be excluded (25, 26).

To the best of our knowledge, studies on the relationship between inflammatory markers and anxiety symptoms in CSVD patients are sparse, and it is further unknown whether the relationship would differ by gender.

In this study, we hypothesize that inflammatory markers may be one of the possible mechanisms of anxiety symptoms in CSVD patients. We aim to investigate which inflammatory factors or cytokines are the most predictive in explaining anxiety symptoms in CSVD. Further understanding of underlying anxiety mechanisms in CSVD may help identify potential new therapeutic targets.

MATERIALS AND METHODS

Study Design and Participants

The ethics committee of Yueyang Hospital of Integrated Traditional Chinese and Western Medicine, affiliated with the Shanghai University of Traditional Chinese Medicine, approved the study (Approval number: 2020–060). All subjects provided informed written consent. Patients with CSVD diagnosed using brain magnetic resonance imaging (MRI) admitted to the neurology department were sequentially screened from December 2019 to December 2021.

Inclusion criteria: 1. aged between 18 and 80 years, 2. patients with CSVD diagnosed by MRI based on the standards for reporting vascular changes on neuroimaging (STRIVE) (2), including typical radiological findings of lacunes of presumed vascular origin, white matter hyperintensity (WMH), moderate to severe (number of BG-EPVS $>$ 10) basal ganglia enlarged perivascular spaces (BG-EPVS) (27) and cerebral microbleeds (CMB).

Exclusion criteria: 1. presence of speech or hearing impairment, unable to complete the questionnaires due to communication difficulties, 2. presence of severe organ dysfunction (liver and kidney diseases), immune diseases, cancer, acute infections, allergies, 3. presence of severe mental disorders, uncontrolled somatic diseases, 4. presence of contraindications to MRI, 5. presence of hereditary and amyloidosis or WMH caused by other reasons, 6. presence of Parkinson's disease, Alzheimer's disease or any other neurodegenerative disease, 7. presence stenosis of intracranial and extracranial large arteries (stenosis $>$50%), 8. patients treated with antipsychotic drugs within 2 weeks of initial screening.

Inflammatory Markers

Fasting venous blood was collected from each individual in the morning after fasting for 12 h using Vacutainer K2 EDTA Tube (6.0 mL, #367863; Becton Dickinson, Franklin Lakes, NJ, USA) and Vacutainer SST II Tube (5.0 mL, #367955; Becton Dickinson, Plymouth, UK). Serum levels of interleukin-1β (IL-1β), IL-2R, IL-6, IL-8, IL-10, and tumor necrosis factor-α (TNF-α) were detected by using Siemens kits in Immulite 1000 automatic chemiluminescence immunoassay analyzer (Siemens Healthcare Diagnostics GmbH, Berlin, Germany). C-reactive protein (CRP) was measured by scattering immunoturbidimetry using Mindray BC-6800 automated hematology analyzer (Mindray Bio-Medical Electronics Co., Ltd, Shenzhen, China). Serum amyloid A (SAA) was measured by scattering immunoturbidimetry using an Astep Plus protein analyzer (Goldsite Diagnostics Inc., Shenzhen, China). High-sensitivity C-reactive protein (hs-CRP) was detected by immunoturbidimetry using Beckerman AU5841 automatic biochemical analyzer (Beckman Coulter Inc., Brea, CA, USA). Erythrocyte sedimentation rate (ESR) was detected by capillary spectrophotometry using the TEST1 ESR analyzer (Alifax, Padova, Italy). All analyses were performed in the clinical laboratory department, located within the Hospital. The manufacturers provided the kits, and laboratory professionals performed all operations strictly according to the manufacturer's instructions.

Data Collection and Definitions

We evaluated all participants' Hamilton Anxiety Rating Scale (HAMA) scores (28). Demographic characteristics included sex, age, education, marital status (single, married, divorced, widowed, and remarried), living arrangements (living alone or

living with others), and medical history. Since lifestyle was associated with both anxiety and inflammation, we assessed smoking status (never, occasional, current, former), alcohol intake (never, occasional, current, former), salt intake (≥6 g/day), physical activity, and body mass index (BMI, kg/m^2). Patients with HAMA scores≥ 7 were included in the anxiety group and otherwise included in the non-anxiety group.

Statistical Analysis

Continuous variables conforming to normal distribution were presented as mean ± standard deviation (SD), and differences between groups were assessed using an independent *t*-test. Non-normally distributed continuous variables were described with median (quartile), and the Wilcoxon rank-sum test was applied for difference comparison. Frequencies and percentages expressed categorical data, and the Chi-squared test or Fisher's exact test was used for the intergroup comparison. Univariate and multivariate logistic regression analyses examined associations between serum inflammatory factors and anxiety symptoms. We applied restricted cubic spline (RCS) analysis to evaluate further the possible non-linear relationship between the inflammatory markers and anxiety symptoms. Three different models were tested to account for potential confounders: Model 1: unadjusted; Model 2: adjustment for age and sex; Model 3: adjustment for age, sex, passive smoking, and physical activity. In addition, we performed a gender subgroup analysis to examine the above association. Odds ratios (OR) with their 95% confidence interval (CI) were reported. Alpha was set at 0.05. Statistical analyses were performed using SAS 9.4 software (SAS Institute Inc., Cary, NC, USA).

RESULTS

Demographic and Clinical Characteristics of Participants

Two hundred forty-five CSVD patients with an average age of 59 years old were included in this study, and 51% of them were female. The clinical characteristics of CSVD participants with or without anxiety symptoms are presented in **Table 1**. Among CSVD patients, individuals with anxiety symptoms were more physically active ($p = 0.036$), and the proportion of passive smokers was higher ($p = 0.037$) than participants without anxiety symptoms. There were no other statistically significant differences in demographic or clinical characteristics between the anxiety and non-anxiety groups.

Comparison of Inflammatory Markers Levels

The comparison results of the serum inflammatory factors between the two groups are shown in **Table 2**. The serum levels of IL-8 ($p = 0.003$) and SAA ($p = 0.01$) in the anxiety group were significantly lower than those in the non-anxiety group, while other markers of inflammation, including TNF-α, IL-1β, IL-2R, IL-6, IL-10, hs-CRP, CRP, and ESR did not demonstrate significant differences between the two groups.

Association of Inflammatory Markers With Anxiety Symptoms

Restricted cubic spline (RCS) analysis revealed a non-linear relationship between IL-8, SAA, and anxiety symptoms, as shown in **Figure 1**. IL-8 and SAA were grouped in quartiles: first quartile (Q1; IL-8<30 pg/mL), Q2 (30 pg/mL≤ IL-8<58.15 pg/mL), Q3 (58.15 pg/mL≤ IL-8<124 pg/mL) and Q4 (IL-8≥124pg/mL), with the Q4 as the reference group; Q1(SAA <2.5 mg/L), Q2(2.5 mg/L≤SAA< 3.09 mg/L), Q3 (3.09 mg/L≤SAA<8.48 mg/L), Q4(SAA≥8.48 mg/L), with the Q2 as the reference group. Univariate and multivariate logistic regression were used to analyze the association between anxiety symptoms and inflammation markers and to adjust for possible confounding factors in CSVD patients, as shown in **Table 3**.

Model 3 shows the associations after adjustment for age, sex, passive smoking, and physical activity. CSVD patients with lower levels of IL-8 were associated with a higher risk of anxiety symptoms. The odds ratios (OR) in the Q1 and Q2 were 3.32 (95% CI: 1.47–7.53, $p = 0.004$) and 2.28 (95% CI: 1.05–4.91, $p = 0.036$) compared with Q4, respectively. Patients with higher levels of SAA were associated with a lower risk of anxiety symptoms, the OR in Q4 was 0.51 (95%CI: 0.26–0.98, $p = 0.045$) compared with Q2.

Subgroup Analysis in Gender

Significant gender interactions were found between anxiety symptoms and inflammation (29, 30), which led us to perform regression analyses within the subgroups of gender. The results are shown in **Table 4**. CSVD patients with lower IL-8 levels were associated with an increased risk of anxiety in males but not in females, and the adjusted OR with 95%CI were 3.94 (1.22–12.70, $p = 0.022$), 3.93 (1.22–12.62, $p = 0.021$) and 3.32 (1.14-9.61, $p = 0.027$) in Q1, Q2 and Q3 vs. Q4, respectively. Compared with the lower SAA levels in Q2, higher SAA levels in Q4 were associated with a decreased risk of anxiety symptoms in females (OR = 0.33, 95%CI:0.12–0.88, $p < 0.028$) but not males.

DISCUSSION

It was previously shown that inflammation factors might contribute to mood disturbances in cardiovascular disease (CVD) patients (20, 31, 32). Nonetheless, the role of inflammation factors in anxiety symptoms identified in CSVD patients has not been described. Our study indicated that IL-8 or SAA levels in CSVD patients might be negatively correlated with the risk of anxiety symptoms. Furthermore, we found sex differences in the associations between anxiety symptoms and inflammation. However, potential biological mechanisms underlying the relationships between IL-8, SAA, and anxiety symptoms in CSVD patients remain unclear.

Research on serum levels of IL-8 in patients with mood disorders is limited and has yielded different results. Consistent with our findings, previous studies indicated that IL-8 levels were negatively correlated with anxiety symptom severity among suicide attempters displaying anxiety disorders (33–35) or antidepressant drug-naïve patients with major

TABLE 1 | Comparison of demographic information in CSVD patients with and without anxiety symptoms.

Variables	Total ($n = 245$)	Group		$Z/t/\chi^2$	p-Value
		Non-anxiety ($n = 97$)	Anxiety ($n = 148$)		
Female, *n* (%)	126 (51.43)	51 (52.58)	75 (50.68)	0.085	0.771
Age (years), Mean±SD	59.26 ± 11.39	59.68 ± 11.33	58.99 ± 11.47	0.47	0.642
Marital status, *n* (%)				-	0.563
Single	8 (3.27)	3 (3.09)	5 (3.38)		
Married	216 (88.16)	87 (89.69)	129 (87.16)		
Divorced	7 (2.86)	4 (4.12)	3 (2.03)		
Widowed	13 (5.31)	3 (3.09)	10 (6.76)		
Remarried	1 (0.41)	0 (0.00)	1 (0.68)		
Residence, *n* (%)				0.775	0.379
Living alone	16 (6.53)	8 (8.25)	8 (5.41)		
Living with others	229 (93.47)	89 (91.75)	140 (94.59)		
Education level (years), Mean ± SD	11.71 ± 3.70	11.68 ± 3.81	11.74 ± 3.64	−0.12	0.908
BMI, Mean ± SD	24.05 ± 4.24	24.51 ± 4.03	23.76 ± 4.35	1.36	0.175
Smoking, *n* (%)				2.240	0.524
Never	147 (60.00)	60 (61.86)	87 (58.78)		
Occasional	9 (3.67)	2 (2.06)	7 (4.73)		
Current	53 (21.63)	23 (23.71)	30 (20.27)		
Former	36 (14.69)	12 (12.37)	24 (16.22)		
Passive smoking, *n* (%)	49 (20.00)	13 (13.40)	36 (24.32)	4.369	**0.037**
Drinking, *n* (%)				4.480	0.214
Never	113 (46.12)	45 (46.39)	68 (45.95)		
Occasional	78 (31.84)	27 (27.84)	51 (34.46)		
Current	35 (14.29)	19 (19.59)	16 (10.81)		
Former	19 (7.76)	6 (6.19)	13 (8.78)		
Salt intake (≥6 g/day), *n* (%)	52 (21.22)	20 (20.62)	32 (21.62)	0.035	0.851
Physical activity, M (Q_1, Q_3)	15.00 (0.00,20.00)	12.00 (0.00,20.00)	15.00 (0.00,20.00)	−2.095	**0.036**
Cerebrovascular disease, *n* (%)	66 (27.39)	25 (26.04)	41 (28.28)	0.145	0.703
Hypertension, *n* (%)	111 (45.31)	49 (50.52)	62 (41.89)	1.759	0.185
Heart disease, *n* (%)	16 (6.53)	4 (4.12)	12 (8.11)	1.524	0.217
Diabetes, *n* (%)	45 (18.37)	16 (16.49)	29 (19.59)	0.376	0.540
Hyperlipidaemia, *n* (%)	76 (31.40)	24 (24.74)	52 (35.86)	3.336	0.068
Migraine headaches, *n* (%)	64 (26.23)	23 (23.71)	41 (27.89)	0.528	0.468

Statistically significant values are identified in boldface.

depressive disorder (MDD) (36). Under physiologic conditions, inflammatory cytokines play an important role in neuroplasticity and neurogenesis (37). Previous studies have revealed that IL-8 has neuroprotective and neurotrophic properties (38–40), such as IL-8 showed a protective effect on perinatal asphyxia brain injury (41). Mood disturbances in CSVD patients are associated with WMH, lacunar infarcts, and microbleeds (8). Our study indicated that decreased IL-8 levels were associated with an increased risk of anxiety symptoms. Therefore, we considered that IL-8 might play a neuroprotective effect in disrupting brain structures involved in anxiety regulation in CSVD patients.

Additionally, IL-8 can modulate neurotransmitter levels (42) and may be involved in the anxiety-related neuronal circuits, such as attenuating the serotonin and dopamine systems (33, 43). Therefore, we speculate that IL-8 may also involve the biological mechanisms regulating anxiety recovery in CSVD. Indeed, physiologic levels of inflammatory factors are necessary for many neurophysiological processes associated with the protection of mood disturbance (44). When IL-8 levels are too low, the physiological processes of homeostasis may be disrupted.

Accumulating evidence suggests that SAA has proinflammatory properties (45–47). Nevertheless, some of the recent findings on SAA suggested that the primary role of SAA may be associated with homeostasis rather than proinflammatory (48). For example, studies have shown that SAA promotes the resolution of inflammation and tissue repair and regulates the homeostasis of the inflammatory process by inducing M2-like macrophages (49). Furthermore, several studies have found that systemic administration of SAA could not increase the production of proinflammatory cytokines (50, 51). The potential explanations for consideration might be that masses of reports on the proinflammatory effects of SAA were using recombinant human SAA (rhSAA) (45, 52, 53). Nevertheless, natural SAA from serum or plasma lacks most of the proinflammatory activity shown by rhSAA (51, 54, 55).

TABLE 2 | Comparisons of inflammatory markers between the two groups.

Variables	Total (n = 245)	Group		Z/t	p-Value
		Non-anxiety (n = 97)	Anxiety (n = 148)		
TNF-α (pg/ml), M (Q_1, Q_3)	7.35 (5.90,9.10)	7.55 (6.30,9.70)	7.30 (5.85,8.80)	1.272	0.203
CRP (mg/L), M (Q_1, Q_3)	0.88 (0.49,2.21)	0.90 (0.42,2.43)	0.88 (0.53,2.03)	−0.260	0.795
IL-1β (pg/ml), M (Q_1, Q_3)	5.00 (5.00,8.30)	5.00 (5.00,8.65)	5.00 (5.00,8.07)	0.061	0.951
IL-2R (u/ml), M (Q_1, Q_3)	358.00 (283.00,432.00)	371.00 (286.00,425.00)	349.50 (279.00,440.00)	0.115	0.908
IL-6 (pg/ml), M (Q_1, Q_3)	2.56 (2.00,3.59)	2.69 (2.00,4.23)	2.44 (2.00,3.22)	1.829	0.067
IL-8 (pg/ml), M (Q_1, Q_3)	58.15 (30.00,124.00)	84.30 (37.30,155.00)	48.35 (23.50,108.50)	2.922	**0.003**
IL-10 (pg/ml), Mean±SD	5.06 ± 0.57	5.04 ± 0.29	5.08 ± 0.69	−0.64	0.523
SAA (mg/L), M (Q_1, Q_3)	3.09 (2.50,8.48)	5.51 (2.50,8.87)	2.50 (2.50,7.55)	2.583	**0.010**
hs-CRP (mg/L), M (Q_1, Q_3)	0.82 (0.45,1.87)	0.88 (0.43,2.58)	0.78 (0.46,1.47)	0.949	0.343
ESR (mm/h), M (Q_1, Q_3)	11.00 (5.00,18.00)	9.00 (5.00,18.00)	12.50 (5.00,18.00)	−0.500	0.617

TNF-α, tumor necrosis factor α; CRP, C-reactive protein; IL, interleukin; SAA, serum amyloid A; hs-CRP, high-sensitivity C-reactive protein; ESR, erythrocyte sedimentation rate; Statistically significant values are identified in boldface.

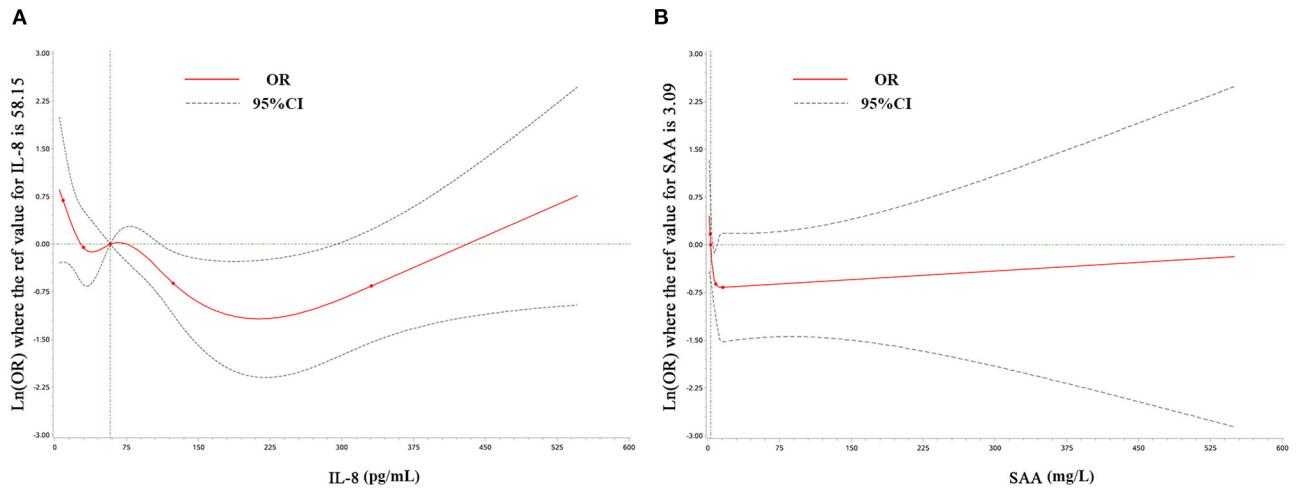

FIGURE 1 | Examination of the relationship between IL-8 **(A)**, SAA **(B)**, and anxiety symptoms by restricted cubic splines analysis. Odds ratios are represented by the solid red line and the 95% confidence interval by the dotted line.

There are few direct clinical studies relating SAA to vascular diseases, and its essential biological role remains poorly understood. The levels of SAA in the blood of healthy individuals are generally below 3 mg/L (56). However, their levels can transiently spike 1000-fold 24 h after the onset of the acute-phase response (57) and then return to a low circulating baseline once the event resolves. The various functions ascribed to SAA are dose-dependent. Their role in inflammation can vary depending on the amount of cytokine expressed and the length of expression or the form of receptor activated by cytokine (55). A stable level of SAA is essential for most biological systems. Small increases in SAA levels may also be associated with the diagnosis or prognosis of a specific disease.

In our study, SAA levels did not show a 1000-fold increase, indicating low levels of peripheral inflammatory activity in the early stage of the CSVD. Compared with the lowest serum SAA levels in Q2 (2.5–3.09 mg/L), the Q4 (≥8.48 mg/L) group was associated with a decreased risk of anxiety symptoms (OR = 0.51, 95%CI: 0.26–0.98, $p = 0.045$), suggesting that significant but smaller increases of SAA levels may protect the patients against the early course of inflammation in CSVD. Additionally, previous studies have found that relatively low concentrations of SAA induce neutrophils to release IL-8 in a dose-dependent manner (46, 58). Thus, it could be hypothesized that IL-8 and SAA may both implicate the underlying pathophysiology of anxiety symptoms in the early stages of CSVD.

There is evidence that inflammatory profiles in mood disorders differ between females and males (30, 59–61). Concerning gender differences, our study found that anxiety symptoms were associated with IL-8 levels (males only) and SAA levels (females only) in CSVD patients. It may be that estradiol increases the secretion of IL-8 in immature dendritic cells, while androgen is generally immunosuppressive (62). Similarly, previous observational studies found higher IL-8 levels associated with decreased depressive symptoms in males (29). In contrast to our findings, Kruse et al. have reported that IL-8

TABLE 3 | Odds ratios (95%CI) of anxiety symptoms associated with IL-8 and SAA.

Variables	Model1		Model2		Model3	
	OR (95%CI)	*p*-Value	OR (95%CI)	*p*-Value	OR (95%CI)	*p*-Value
IL-8						
Q_1 (<30)	3.40 (1.56–7.41)	**0.002**	3.66 (1.65–8.14)	**0.001**	3.32 (1.47–7.53)	**0.004**
Q_2 (30–58.15)	2.15 (1.02–4.49)	**0.043**	2.29 (1.08–4.86)	**0.031**	2.28 (1.05–4.91)	**0.036**
Q_3 (58.15–124)	1.94 (0.93–4.05)	0.078	1.99 (0.95–4.18)	0.069	1.93 (0.90–4.10)	0.089
Q_4 (≥124)	Ref		Ref		Ref	
SAA						
Q_1(<2.5)	–		–		–	
Q_2(2.5–3.09)	Ref		Ref		Ref	
Q_3 (3.09–8.48)	0.64 (0.33–1.23)	0.175	0.63 (0.33–1.23)	0.176	0.62 (0.32–1.22)	0.164
Q_4(≥8.48)	0.46 (0.24–0.88)	**0.020**	0.46 (0.24–0.88)	**0.019**	0.51 (0.26–0.98)	**0.045**

Ref, Reference; Model 1: univariate logistic regression analysis; Model 2, adjusted for age and sex. Model 3, adjusted for age, sex, physical activity, and passive smoking; Statistically significant values are identified in boldface.

TABLE 4 | Odds ratios (95%CI) of anxiety symptoms associated with IL−8 and SAA for gender subgroup analysis.

Variables	Male		Female	
	OR (95%CI)	*p*-Value	OR (95%CI)	*p*-Value
IL−8				
Q_1 (<30)	3.94 (1.22–12.70)	**0.022**	2.53 (0.79–8.13)	0.119
Q_2 (30–58.15)	3.93 (1.22–12.62)	**0.021**	1.32 (0.46–3.81)	0.609
Q_3 (58.15–124)	3.32 (1.14–9.61)	**0.027**	1.12 (0.36–3.47)	0.848
Q_4 (≥124)	Ref		Ref	
SAA				
Q_1(<2.5)	–		–	
Q_2(2.5–3.09)	Ref		Ref	
Q_3 (3.09–8.48)	0.66 (0.23–1.88)	0.441	0.57 (0.23–1.42)	0.228
Q_4(≥8.48)	0.64 (0.25–1.64)	0.351	0.33 (0.12–0.88)	**0.028**

Ref, Reference; Statistically significant values are identified in boldface.

levels are negatively correlated with total HAMD score among females but not males in cross-sectional studies of depressed patients (63). These similar sex-specific effects were also found in electroconvulsive or ketamine therapy studies in depressed patients (64, 65). However, not all studies have been consistent, reflecting the between-study heterogeneity within the diagnostic categories of depression and anxiety or distinct study designs.

CONCLUSION

To sum up, various serum inflammatory factors and mechanisms are in place to maintain homeostasis, but dysregulation of their actions often contributes to diseases, including anxiety symptoms in CSVD patients. The underlying pathophysiology of IL-8 and SAA in CSVD with anxiety symptoms is complex and needs further investigation.

LIMITATIONS

This study is a single-center cross-sectional study based on a relatively small sample. We cannot clarify the causal relationship. A large cohort corroboration is required to explore whether inflammation is a precursor, consequence, or bidirectional relationship in CSVD patients with anxiety symptoms. Additionally, we examined circulating levels of inflammatory factors but did not assess inflammatory factor levels in the cerebrospinal fluid. Further clinical trials are needed to guide the detection of inflammatory factors in CSVD patients with anxiety symptoms.

DATA AVAILABILITY STATEMENT

The raw data supporting the conclusions of this article will be made available by the authors, without undue reservation.

ETHICS STATEMENT

The studies involving human participants were reviewed and approved by Ethics Committee of Yueyang Hospital of Integrated Traditional Chinese and Western Medicine, Shanghai University of Traditional Chinese Medicine (Approval ID: 2020-060). The patients/participants provided their written informed consent to participate in this study.

AUTHOR CONTRIBUTIONS

YH and M-YL designed the study. T-CQ and Y-FB collected data. L-LS and Y-LW analyzed the data and drafted this manuscript. Q-YL, Y-JH, CG, Z-DY, and Z-ZL were involved in the design and revision of the manuscript. All authors contributed to this article and approved the submitted version.

FUNDING

This study was supported, in part, by grants from the National Key Research and Development Program of China (No. 2019YFC1711603), the Major Clinical Study Projects of Shanghai Shenkang Hospital Development Center (No. SHDC2020CR2046B), and Shanghai Science and Technology Development Foundation (No. 19401972802).

REFERENCES

1. Pantoni L. Cerebral small vessel disease: from pathogenesis and clinical characteristics to therapeutic challenges. *Lancet Neurol*. (2010) 9:689–701. doi: 10.1016/S1474-4422(10)70104-6
2. Wardlaw JM, Smith EE, Biessels GJ, Cordonnier C, Fazekas F, Frayne R, et al. Neuroimaging standards for research into small vessel disease and its contribution to ageing and neurodegeneration. *Lancet Neurol*. (2013) 12:822–38. doi: 10.1016/S1474-4422(13)70124-8
3. Pasi M, van Uden IW, Tuladhar AM, de Leeuw FE, Pantoni L. White matter microstructural damage on diffusion tensor imaging in cerebral small vessel disease: clinical consequences. *Stroke*. (2016)47:1679–84. doi: 10.1161/STROKEAHA.115.012065
4. Li Q, Yang Y, Reis C, Tao T, Li W, Li X, et al. Cerebral small vessel disease. *Cell Transplan*. (2018) 27:1711–22. doi: 10.1177/0963689718795148
5. Wardlaw JM, Smith C, Dichgans M. Small vessel disease: mechanisms and clinical implications. *Lancet Neurol*. (2019) 18:684–96. doi: 10.1016/S1474-4422(19)30079-1
6. Castello JP, Pasi M, Kubiszewski P, Abramson JR, Charidimou A, Kourkoulis C, et al. Cerebral small vessel disease and depression among intracerebral hemorrhage survivors. *Stroke*. (2022) 53:523–31. doi: 10.1161/STROKEAHA.121.035488
7. Zhang RT, Yu WK, Wu X, Jiaerken Y, Wang SY, Hong H, et al. Disentangling the pathologies linking white matter hyperintensity and geriatric depressive symptoms in subjects with different degrees of vascular impairment. *J Affective Disord*. (2021) 282:1005–10. doi: 10.1016/j.jad.2020.12.171
8. Direk N, Perez HS, Akoudad S, Verhaaren BF, Niessen WJ, Hofman A, et al. Markers of cerebral small vessel disease and severity of depression in the general population. *Psychiatry Res Neuroimaging*. (2016) 253:1–6. doi: 10.1016/j.pscychresns.2016.05.002
9. van Sloten TT, Sigurdsson S, van Buchem MA, Phillips CL, Jonsson PV, Ding J, et al. Cerebral Small vessel disease and association with higher incidence of depressive symptoms in a general elderly population: the AGES-Reykjavik Study. *Am J Psychiatry*. (2015) 172:570–8. doi: 10.1176/appi.ajp.2014.14050578
10. Fang Y, Qin T, Liu W, Ran L, Yang Y, Huang H, et al. Cerebral small-vessel disease and risk of incidence of depression: a meta-analysis of longitudinal cohort studies. *J Am Heart Assoc*. (2020) 9:e016512. doi: 10.1161/JAHA.120.016512
11. Rensma SP, van Sloten TT, Launer LJ, Stehouwer CDA. Cerebral small vessel disease and risk of incident stroke, dementia and depression, and all-cause mortality: a systematic review and meta-analysis. *Neurosci Biobehav Rev*. (2018) 90:164–73. doi: 10.1016/j.neubiorev.2018.04.003
12. Taylor WD, Aizenstein HJ, Alexopoulos GS. The vascular depression hypothesis: mechanisms linking vascular disease with depression. *Mol Psychiatry*. (2013) 18:963–74. doi: 10.1038/mp.2013.20
13. Clancy U, Gilmartin D, Jochems ACC, Knox L, Doubal FN, Wardlaw JM. Neuropsychiatric symptoms associated with cerebral small vessel disease: a systematic review and meta-analysis. *Lancet Psychiatry*. (2021) 8:225–36. doi: 10.1016/S2215-0366(20)30431-4
14. Low A, Mak E, Rowe JB, Markus HS, O'Brien JT. Inflammation and cerebral small vessel disease: a systematic review. *Ageing Res Rev*. (2019) 53:100916. doi: 10.1016/j.arr.2019.100916
15. Fu Y, Yan YP. Emerging Role of Immunity in Cerebral Small Vessel Disease. *Front Immunol*. (2018) 9:67. doi: 10.3389/fimmu.2018.00067
16. Beurel E, Toups M, Nemeroff CB. The bidirectional relationship of depression and inflammation: double trouble. *Neuron*. (2020) 107:234–56. doi: 10.1016/j.neuron.2020.06.002
17. Miller AH, Raison CL. The role of inflammation in depression: from evolutionary imperative to modern treatment target. *Nat Rev Immunol*. (2016)16:22–34. doi: 10.1038/nri.2015.5
18. Makhija K, Karunakaran S. The role of inflammatory cytokines on the aetiopathogenesis of depression. *Aust N Z J Psychiatry*. (2013) 47:828–39. doi: 10.1177/0004867413488220
19. Łoś K, Waszkiewicz N. Biological markers in anxiety disorders. *J Clin Med*. (2021) 10:008174. doi: 10.3390/jcm10081744
20. Vassou C, Chrysohoou C, Skoumas J, Georgousopoulou EN, Yannakoulia M, Pitsavos C, et al. Irrational beliefs, depression and anxiety, in relation to 10-year cardiovascular disease risk: the ATTICA Epidemiological Study. *Anxiety Stress Coping*. (2022) 7:1–15. doi: 10.1080/10615806.2022.2062331
21. Gaspersz R, Lamers F, Wittenberg G, Beekman ATF, van Hemert AM, Schoevers RA, et al. The role of anxious distress in immune dysregulation in patients with major depressive disorder. *Transl Psychiatry*. (2017) 7:1268. doi: 10.1038/s41398-017-0016-3
22. Capuron L, Miller AH. Immune system to brain signaling: neuropsychopharmacological implications. *Pharmacol Ther*. (2011) 130:226–38. doi: 10.1016/j.pharmthera.2011.01.014
23. Vogelzangs N, Beekman ATF, de Jonge P, Penninx B. Anxiety disorders and inflammation in a large adult cohort. *Transl Psychiatry*. (2013) 3:e249. doi: 10.1038/tp.2013.27
24. Naudé PJW, Roest AM, Stein DJ, de Jonge P, Doornbos B. Anxiety disorders and CRP in a population cohort study with 54,326 participants: The LifeLines study. *World J Biol Psychiatry*. (2018) 19:461–70. doi: 10.1080/15622975.2018.1433325
25. Tang Z, Ye G, Chen X, Pan M, Fu J, Fu T, et al. Peripheral proinflammatory cytokines in Chinese patients with generalised anxiety disorder. *J Affect Disord*. (2018) 225:593–8. doi: 10.1016/j.jad.2017.08.082
26. Hou R, Garner M, Holmes C, Osmond C, Teeling J, Lau L, et al. Peripheral inflammatory cytokines and immune balance in Generalised Anxiety Disorder: Case-controlled study. *Brain Behav Immun*. (2017) 62:212–8. doi: 10.1016/j.bbi.2017.01.021
27. Doubal FN, MacLullich AM, Ferguson KJ, Dennis MS, Wardlaw JM. Enlarged perivascular spaces on MRI are a feature of cerebral small vessel disease. *Stroke*. (2010) 41:450–4. doi: 10.1161/STROKEAHA.109.564914
28. Hamilton M. The assessment of anxiety states by rating. *Br J Med Psychol*. (1959) 32:50–5. doi: 10.1111/j.2044-8341.1959.tb00467.x
29. Moriarity DP, Giollabhui NM, Ellman LM, Klugman J, Coe CL, Abramson LY, et al. inflammatory proteins predict change in depressive symptoms in male and female adolescents. *Clin Psychol Sci*. (2019) 7:754–67. doi: 10.1177/2167702619826586
30. Moieni M, Tan KM, Inagaki TK, Muscatell KA, Dutcher JM, Jevtic I, et al. Sex differences in the relationship between inflammation and reward sensitivity: a randomized controlled trial of endotoxin. *Biol Psychiatry Cogn Neurosci Neuroimaging*. (2019) 4:619–26. doi: 10.1016/j.bpsc.2019.03.010
31. Key KV, Mudd-Martin G, Moser DK, Rayens MK, Morford LA. Inflammatory genotype moderates the association between anxiety and systemic inflammation in adults at risk for cardiovascular disease. *J Cardiovasc Nurs*. (2022) 37:64–72. doi: 10.1097/JCN.0000000000000742
32. Bankier B, Barajas J, Martinez-Rumayor A, Januzzi JL. Association between C-reactive protein and generalized anxiety disorder in stable coronary heart disease patients. *Eur Heart J*. (2008) 29:2212–7. doi: 10.1093/eurheartj/ehn326
33. Janelidze S, Suchankova P, Ekman A, Erhardt S, Sellgren C, Samuelsson M, et al. Low IL-8 is associated with anxiety in suicidal patients: genetic variation and decreased protein levels. *Acta Psychiatr Scand*. (2015) 131:269–78. doi: 10.1111/acps.12339

34. Isung J, Aeinehband S, Mobarrez F, Martensson B, Nordstrom P, Asberg M, et al. Low vascular endothelial growth factor and interleukin-8 in cerebrospinal fluid of suicide attempters. *Transl Psychiatry*. (2012) 2:e196. doi: 10.1038/tp.2012.123
35. Keaton SA, Madaj ZB, Heilman P, Smart L, Grit J, Gibbons R, et al. An inflammatory profile linked to increased suicide risk. *J Affective Disord*. (2019) 247:57–65. doi: 10.1016/j.jad.2018.12.100
36. Zou W, Feng RJ, Yang Y. Changes in the serum levels of inflammatory cytokines in antidepressant drug-naive patients with major depression. *Plos ONE*. (2018)13:197267. doi: 10.1371/journal.pone.0197267
37. Yirmiya R, Goshen I. Immune modulation of learning, memory, neural plasticity and neurogenesis. *Brain Behav Immun*. (2011) 25:181–213. doi: 10.1016/j.bbi.2010.10.015
38. Puma C, Danik M, Quirion R, Ramon F, Williams S. The chemokine interleukin-8 acutely reduces Ca2+ currents in identified cholinergic septal neurons expressing CXCR1 and CXCR2 receptor mRNAs. *J Neurochem*. (2001) 78:960–71. doi: 10.1046/j.1471-4159.2001.00469.x
39. Saas P, Walker PR, Quiquerez AL, Chalmers DE, Arrighi JF, Lienard A, et al. A self-defence mechanism of astrocytes against Fas-mediated death involving interleukin-8 and CXCR2. *Neuroreport*. (2002) 13:1921–4. doi: 10.1097/00001756-200210280-00018
40. Araujo DM, Cotman CW. Trophic effects of interleukin-4,−7 and−8 on hippocampal neuronal cultures: potential involvement of glial-derived factors. *Brain Res*. (1993) 600:49–55. doi: 10.1016/0006-8993(93)90400-H
41. Hussein MH, Daoud GA, Kakita H, Kato S, Goto T, Kamei M, et al. High cerebrospinal fluid antioxidants and interleukin 8 are protective of hypoxic brain damage in newborns. *Free Radical Research*. (2010)44:422–9. doi: 10.3109/10715760903548245
42. Stuart MJ, Singhal G, Baune BT. Systematic review of the neurobiological relevance of chemokines to psychiatric disorders. *Front Cell Neurosci*. (2015) 9:e357. doi: 10.3389/fncel.2015.00357
43. Guyon A, Skrzydelski D, De Giry I, Rovere C, Conductier G, Trocello JM, et al. Long term exposure to the chemokine CCL2 activates the nigrostriatal dopamine system: a novel mechanism for the control of dopamine release. *Neuroscience*. (2009) 162:1072–80. doi: 10.1016/j.neuroscience.2009.05.048
44. Raison CL, Rutherford RE, Woolwine BJ, Shuo C, Schettler P, Drake DF, et al. A randomized controlled trial of the tumor necrosis factor antagonist infliximab for treatment-resistant depression: the role of baseline inflammatory biomarkers. *JAMA Psychiatry*. (2013) 70:31–41. doi: 10.1001/2013.jamapsychiatry.4
45. Furlaneto CJ, Campa A. A novel function of serum amyloid A: a potent stimulus for the release of tumor necrosis factor-alpha, interleukin-1 beta, and interleukin-8 by human blood neutrophil. *Biochem Biophys Res Commun*. (2000) 268:405–8. doi: 10.1006/bbrc.2000.2143
46. He R, Sang HR, Ye RD. Serum amyloid A induces IL-8 secretion through a G protein-coupled receptor, FPRL1/LXA4R. *Blood*. (2003) 101:1572–81. doi: 10.1182/blood-2002-05-1431
47. De Buck M, Gouwy M, Wang JM, Van Snick J, Proost P, Struyf S, et al. The cytokine-serum amyloid A-chemokine network. *Cytokine Growth Factor Rev*. (2016) 30:55–69. doi: 10.1016/j.cytogfr.2015.12.010
48. Ye RD, Sun L. Emerging functions of serum amyloid A in inflammation. *J Leukocyte Biol*. (2015) 98:923–9. doi: 10.1189/jlb.3VMR0315-080R
49. Sun L, Zhou HB, Zhu ZY, Yan Q, Wang LL, Liang Q, et al. *Ex vivo* and *in vitro* effect of serum amyloid A in the induction of macrophage M2 markers and efferocytosis of apoptotic neutrophils. *J Immunol*. (2015) 194:4891–900. doi: 10.4049/jimmunol.1402164
50. Kim M-H, de Beer MC, Wroblewski JM, Webb NR, de Beer FC. SAA does not induce cytokine production in physiological conditions. *Cytokine*. (2013) 61:506–12. doi: 10.1016/j.cyto.2012.10.019
51. Christenson K, Björkman L, Ahlin S, Olsson M, Sjöholm K, Karlsson A, et al. Endogenous acute phase serum amyloid a lacks pro-inflammatory activity, contrasting the two recombinant variants that activate human neutrophils through different receptors. *Front Immunol*. (2013) 4:92. doi: 10.3389/fimmu.2013.00092
52. He RL, Zhou J, Hanson CZ, Chen J, Cheng N, Ye RD. Serum amyloid A induces G-CSF expression and neutrophilia via Toll-like receptor 2. *Blood*. (2009)113:429–37. doi: 10.1182/blood-2008-03-139923
53. Cai H, Song C, Endoh I, Goyette J, Jessup W, Freedman SB, et al. Serum amyloid A induces monocyte tissue factor. *J Immunol*. (2007) 178:1852–60. doi: 10.4049/jimmunol.178.3.1852
54. Björkman L, Raynes JG, Shah C, Karlsson A, Dahlgren C, Bylund J. The proinflammatory activity of recombinant serum amyloid A is not shared by the endogenous protein in the circulation. *Arthritis Rheum*. (2010) 62:1660–5. doi: 10.1002/art.27440
55. De Buck M, Gouwy M, Wang JM, Van Snick J, Opdenakker G, Struyf S, et al. Structure and Expression of Different Serum Amyloid A (SAA) variants and their concentration-dependent functions during host insults. *Curr Med Chem*. (2016) 23:1725–55. doi: 10.2174/0929867323666160418114600
56. Hosman IS, Kos I, Lamot L. Serum amyloid A in inflammatory rheumatic diseases: a compendious review of a renowned biomarker. *Front Immunol*. (2021) 11:631299. doi: 10.3389/fimmu.2020.631299
57. Sack GH. Serum amyloid A - a review. *Mol Med*. (2018) 24:46. doi: 10.1186/s10020-018-0047-0
58. Ribeiro FP, Furlaneto CJ, Hatanaka E, Ribeiro WB, Souza GM, Cassatella MA, et al. mRNA expression and release of interleukin-8 induced by serum amyloid A in neutrophils and monocytes. *Mediators Inflamm*. (2003) 12:173–8. doi: 10.1080/0962935031000134897
59. Labonté B, Engmann O, Purushothaman I, Menard C, Wang JS, Tan CF, et al. Sex-specific transcriptional signatures in human depression. *Nat Med*. (2017) 23:1102–11. doi: 10.1038/nm.4386
60. Rainville JR, Hodes GE. Inflaming sex differences in mood disorders. *Neuropsychopharmacology*. (2019) 44:184–99. doi: 10.1038/s41386-018-0124-7
61. Bangasser DA, Valentino RJ. Sex differences in stress-related psychiatric disorders: Neurobiological perspectives. *Front Neuroendocrinol*. (2014) 35:303–19. doi: 10.1016/j.yfrne.2014.03.008
62. Bengtsson AK, Ryan EJ, Giordano D, Magaletti DM, Clark EA. 17 beta-estradiol (E-2) modulates cytokine and chemokine expression in human monocyte-derived dendritic cells. *Blood*. (2004) 104:1404–10. doi: 10.1182/blood-2003-10-3380
63. Kruse JL, Olmstead R, Hellemann G, Breen EC, Tye SJ, Brooks JO, et al. Interleukin-8 and lower severity of depression in females, but not males, with treatment-resistant depression. *J Psychiatr Res*. (2021) 140:350–6. doi: 10.1016/j.jpsychires.2021.06.009
64. Kruse JL, Olmstead R, Hellemann G, Wade B, Jiang J, Vasavada MM, et al. Inflammation and depression treatment response to electroconvulsive therapy: Sex-specific role of interleukin-8. *Brain Behav Immun*. (2020) 89:59–66. doi: 10.1016/j.bbi.2020.05.069
65. Kruse JL, Vasavada MM, Olmstead R, Hellemann G, Wade B, Breen EC, et al. Depression treatment response to ketamine: sex-specific role of interleukin-8, but not other inflammatory markers. *Transl Psychiatry*. (2021) 11:167. doi: 10.1038/s41398-021-01268-z

Conflict of Interest: The authors declare that the research was conducted in the absence of any commercial or financial relationships that could be construed as a potential conflict of interest.

The reviewer DW declared a shared parent affiliation with the author Z–DY to the handling editor at the time of review.

Publisher's Note: All claims expressed in this article are solely those of the authors and do not necessarily represent those of their affiliated organizations, or those of the publisher, the editors and the reviewers. Any product that may be evaluated in this article, or claim that may be made by its manufacturer, is not guaranteed or endorsed by the publisher.

Copyright © 2022 Shan, Wang, Qiao, Bian, Huo, Guo, Liu, Yang, Li, Liu and Han. This is an open-access article distributed under the terms of the Creative Commons Attribution License (CC BY). The use, distribution or reproduction in other forums is permitted, provided the original author(s) and the copyright owner(s) are credited and that the original publication in this journal is cited, in accordance with accepted academic practice. No use, distribution or reproduction is permitted which does not comply with these terms.

frontiers | Frontiers in Neurology

ORIGINAL RESEARCH
published: 12 July 2022
doi: 10.3389/fneur.2022.905761

Cervical Cancer Imaging Features Associated With *ADRB1* as a Risk Factor for Cerebral Neurovascular Metastases

Xingju Zheng[1†], *Shilin Xu*[2†] *and JiaYing Wu*[3*]

[1] Department of Radiology, Guizhou Provincial People's Hospital, Guiyang, China, [2] Department of Oncology, Xichang People's Hospital, Liangshan High-Tech Tumor Hospital, Xichang, China, [3] Department of Gynaecology and Obstetrics, Zhejiang Xinda Hospital, Huzhou, China

Bioinformatics tools are used to create a clinical prediction model for cervical cancer metastasis and to investigate the neurovascular-related genes that are involved in brain metastasis of cervical cancer. One hundred eighteen patients with cervical cancer were divided into two groups based on the presence or absence of metastases, and the clinical data and imaging findings of the two groups were compared retrospectively. The nomogram-based model was successfully constructed by taking into account four clinical characteristics (age, stage, N, and T) as well as one imaging characteristic (original_glszm_GrayLevelVariance Rad-score). In patients with cervical cancer, headaches and vomiting were more often reported in the brain metastasis group than in the other metastasis groups. According to the TCGA data, mRNA differential gene expression analysis of patients with cervical cancer revealed an increase in the expression of neurovascular-related gene Adrenoceptor Beta 1 (*ADRB1*) in the brain metastasis group. An analysis of the correlation between imaging features and *ADRB1* expression revealed that *ADRB1* expression was significantly higher in the low Rad-score group compared with the high Rad-score group ($P = 0.025$). Therefore, *ADRB1* expression in cervical cancer was correlated with imaging features and was associated as a risk factor for cerebral neurovascular metastases. This study developed a nomogram prediction model for cervical cancer metastasis using age, stage, N, T and original_glszm_GrayLevelVariance. As a risk factor associated with the development of cerebral neurovascular metastases of cervical cancer, *ADRB1* expression was significantly higher in brain metastases from cervical cancer.

Keywords: cervical cancer, brain metastasis, neurovascular, clinical prediction model, radiomics, *ADRB1*, biomarkers

OPEN ACCESS

Edited by:
Yuzhen Xu,
Tongji University, China

Reviewed by:
Jie Yang,
Affiliated Hospital of Shandong University of Traditional Chinese Medicine, China
Su-Ding Fei,
Ningbo College of Health Sciences, China

***Correspondence:**
JiaYing Wu
tinee@21cn.com

[†]*These authors have contributed equally to this work*

Specialty section:
This article was submitted to Neurological Biomarkers, a section of the journal Frontiers in Neurology

Received: *27 March 2022*
Accepted: *20 June 2022*
Published: *12 July 2022*

Citation:
Zheng X, Xu S and Wu J (2022) Cervical Cancer Imaging Features Associated With ADRB1 as a Risk Factor for Cerebral Neurovascular Metastases. Front. Neurol. 13:905761. doi: 10.3389/fneur.2022.905761

INTRODUCTION

The fourth most prevalent cancer among women worldwide is cervical cancer, a common gynecologic malignancy (1). Approximately 570,000 new cases of cervical cancer were reported in 2018, representing 3.15% of all malignant tumor cases. Furthermore, approximately 310,000 cervical cancer-related deaths were reported in 2018, representing 3.26% of all malignant tumor

deaths (1, 2). Cancer metastasis is a major cause of poor prognosis in cervical cancer (3–6). The five-year survival rate for cervical cancer patients with metastasis is only 30–60%, which is significantly lower than that for those without metastasis (7, 8). Cervical cancer metastasis involves complex molecular mechanisms (9). The lack of effective measures to prevent or treat cervical cancer metastasis is attributable to the fact that the mechanism of cervical cancer metastasis remains unclear.

Cervical cancer metastasis occurs mainly via the lymphatic route (10). The most common sites of distant metastases are the lungs, bones, and liver, in order of priority (11). It is rare for cervical cancer to spread to the central nervous system, and very little research has been conducted on this subject (12, 13). When diagnosed with brain metastases, cervical cancer patients typically have a poor prognosis; the median survival period from the time of diagnosis until death is 2–3 months (13). As of now, there is no reliable way to predict early whether cervical cancer will spread to the neurovascular system.

Known as an emerging method of image analysis, radiomics can extract quantitative features from medical images that describe biological information, such as tumor characteristics and heterogeneity, which can serve to guide clinical planning (14). In patients with esophageal cancer, radiomics also proved to be effective for predicting T and N stages as well as lymph node metastasis (15–17). Based on the results of the radiomics study, the model can improve the diagnostic accuracy of differentiating benign and malignant cartilage tumors, as well as benign and low-grade malignant chondrosarcomas (18). An analysis conducted by Zhao et al. of diffusion-weighted images of osteosarcoma was retrospectively screened for four clinical features and eight imaging features, and a combined feature model was constructed for both characteristics, displaying good performance (19). Thus, it is possible to assess a tumor and predict its progression by combining imaging and clinical data. Moreover, imaging analysis is useful in determining the malignant and benign classification and staging of ovarian tumors, monitoring treatment outcomes in patients with metastatic ovarian tumors earlier in the course of treatment, and providing high-precision survival assessment for patients with ovarian tumors (20, 21). Consequently, radiomics is an important tool for predicting tumorigenesis, metastasis, and prognosis.

Radiomics has made significant progress in recent years when it comes to detecting and localizing brain metastases, making a differential diagnosis with other primary brain tumors, and determining the prognosis of the patient. An algorithm based on multi-sequence magnetic resonance imaging (MRI) for example, is capable of automatically detecting and segmenting brain metastases with great precision (22). The best results of glioblastoma multiforme and metastasis differentiation can be obtained by applying an Support Vector Machine (SVM) classifier based on enhanced T1-weighted images (T1W1) radiomics (23). Furthermore, the enhanced T1W1 imaging feature – "zone percentage" is an independent prognostic factor for local tumor control in non-small cell lung cancer brain metastases (24). Researchers from Shen et al. performed a retrospective study using computed tomography (CT) images of patients with bones metastases from lung adenocarcinoma who had genetically confirmed epithelial growth factor receptor (*EGFR*) mutation status. Three features were associated with *EGFR* mutation status (25). Yu et al. demonstrated that high-throughput MRI imaging features extracted from conventional T2 fluid attenuation inversion recovery (T2-FLAIR) images were highly correlated with isocitrate dehydrogenase genotype 1 (*IDH1*) (26). Furthermore, the conventional sequence-based fusion imaging model constructed by Jiang et al. accurately predicted the methylation status of O6-methylguanine-DNA methyltransferase (MGMT) in low-grade gliomas (27). Hence, imaging features have a potential superior predictive efficacy in predicting tumor genotypes (28).

Several studies have reported that neurovascular factors are involved in the development and metastasis of several malignancies (29, 30). The adrenergic receptor gene, a neurovascular-related factor, encodes the adrenergic receptor.

β-adrenergic receptor blockers have the ability to reduce the risk of head and neck cancer, as well as esophageal, gastric, colorectal, and prostate cancer (31, 32). Catecholamines promote ADRB2-dependent pancreatic ductal adenocarcinoma and neurotrophic factor secretion, which is critical to tumor development (33). The induction of angiogenesis by brain endothelial cells was shown to be crucial for the early survival of brain metastatic cells (34). Further, patients with lung cancer with a positive *VEGFC* expression were significantly more likely to develop brain metastases than those with a negative *VEGFC* expression (35). Accordingly, neurovascular-related genes are involved in brain metastasis in cervical cancer, and it may be possible to predict neurovascular-related genes that are associated with brain metastasis by imaging features.

In recent years, bioinformatics has gained significant attention in several fields for its role in exploring disease mechanisms (36–41). The objective of this study was to identify early risk factors and potential targets from an imaging and genomics perspective for patients with brain metastases from cervical cancer in order to improve prognoses. By combining radiomics data and clinical information, a prediction model reflecting the risk of cervical cancer metastasis was constructed in this study that screened neurovascular genes with brain metastases related to cervical cancer.

METHODS

Data Collection

Patients treated at the Guizhou Provincial People's Hospital between January 2010 and January 2021 for CT examinations and a biopsy or surgical pathology that confirmed cervical cancer were included in the study. Inclusion criteria were as follows: I. an accurate pathological diagnosis; II. archived CT examination data; III. comprehensive medical and follow-up records. The following exclusion criteria were applied: I. incomplete clinical information; II. concurrent presence of primary malignant tumors at other sites; III. inadequate image quality. A total of 118

patients with cervical cancer participated in the study. The study was approved by the Ethics Committee of Guizhou Provincial People's Hospital.

Acquisition and Differential Testing of Neurovascular-Related Gene Expression Data

From the TCGA database, clinical information and transcript information were downloaded for two patients with brain metastases and 15 patients with extracerebral metastases from cervical cancer. The RNA transcription data were log-transformed and de-batched. In total, 469 genes related to neural or vascular function were identified through a literature review using PubMed, Web of Science, Google Scholar, and GeneCards databases. These genes regulate the interaction between nerves and blood vessels. The R package "limma" (version 3.50) was used to conduct gene expression analyses of groups with brain metastases and those with extracerebral metastases. Genes with false discovery rate < 0.05 and $|\log2\ \text{FoldChange}| > 1$ were filtered for subsequent analysis.

Image Processing and Radiomics Feature Extraction

GE 16-row spiral CT scanners were used to acquire the imaging data of all patients. All patients were injected with 500 ml of pantethine (Xi'an Hanfeng Pharmaceutical Co., Ltd.), using a 5 mm needle, 30 min before scanning. CT images of patients were read and processed in Digital Imaging and Communications in Medicine (DICOM) format. ITK-SNAP (version 3.8.0; https://www.itksnap.org) was used for image segmentation, whereas the region of interest (ROI) was manually outlined, layer by layer, along the tumor edge. Finally, the segmented images were subjected to radiomics feature extraction using the Pyradiomics (version 3.0.1) package. Spearman's correlation analysis was used to assess the correlation between the radiomics features. For radiomics features with correlation coefficients > 0.85, only one was retained, thus minimizing redundant features.

Logistic Regression Analyses

Clinical and imaging characteristics were subjected to univariate logistics regression analysis, and characteristic variables with $P <$

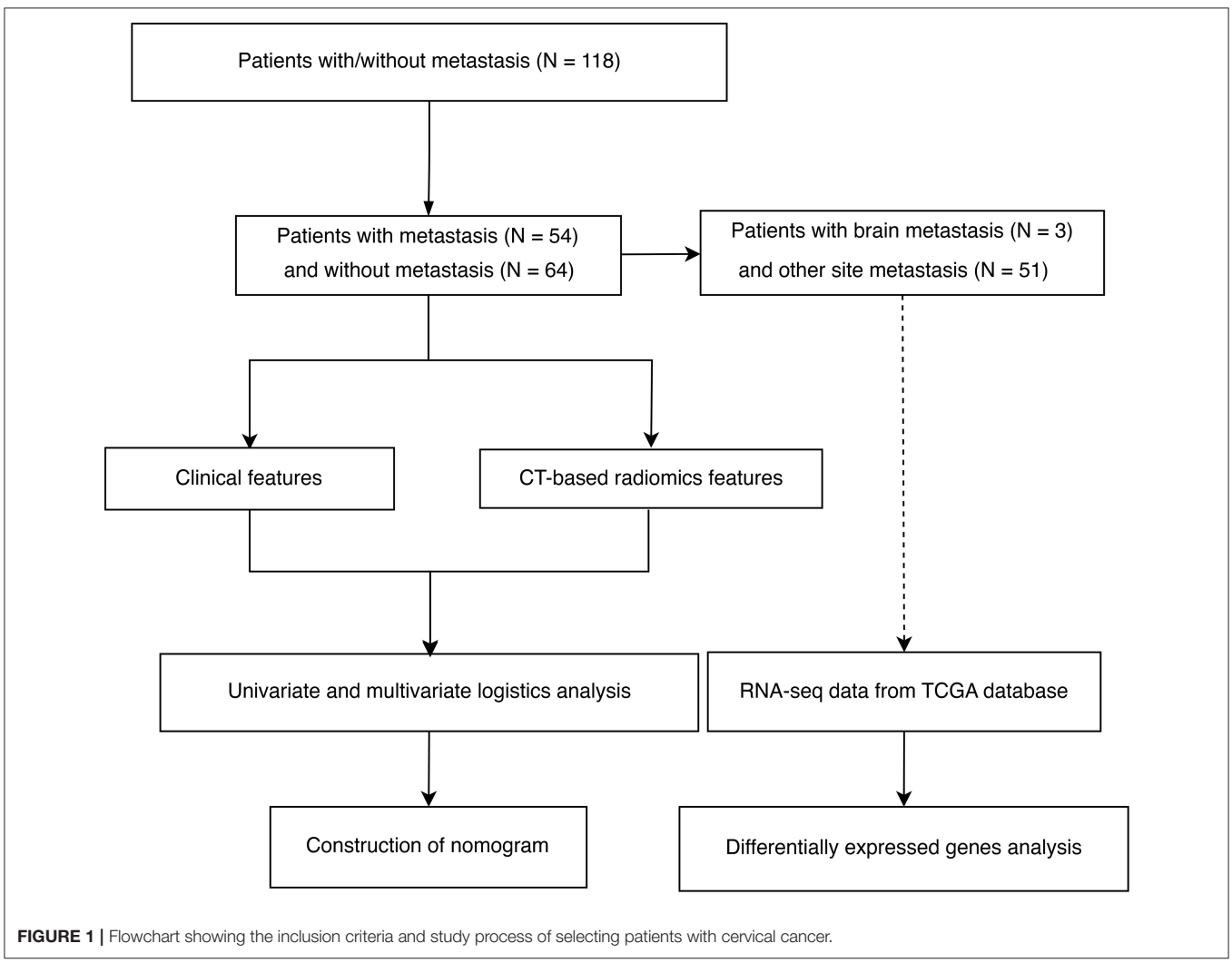

FIGURE 1 | Flowchart showing the inclusion criteria and study process of selecting patients with cervical cancer.

TABLE 1 | Demographic and clinical characteristics of patients with or without metastasis.

Variables	Level	Metastasis		*P*-value
		No (*N* = 64)	Yes (*N* = 54)	
Age [meidan (IQR)]		47.5 (35.75, 53.25)	50 (42.25, 60)	0.022*
Height [meidan (IQR)]		160 (157, 162)	159 (157, 163.5)	0.363
Weight [meidan (IQR)]		66 (56, 73.25)	69 (57.25, 79.75)	0.303
Marital status [N (%)]	Divorced	6 (9.4%)	3 (5.6%)	0.152
	Married	48 (75%)	48 (88.9%)	
	Unmarried	10 (15.6%)	3 (5.6%)	
Stage [N (%)]	I	41 (64.1%)	11 (20.4%)	< 0.001***
	II	17 (26.6%)	15 (27.8%)	
	III	6 (9.4%)	15 (27.8%)	
	IV	0 (0%)	13 (24.1%)	
Histology [N (%)]	Adenosquamous	4 (6.2%)	5 (9.3%)	0.261
	Mucinous Adenocarcinoma	2 (3.1%)	5 (9.3%)	
	Squamous Cell Carcinoma	58 (90.6%)	44 (81.5%)	
Metastasis site [*N* (%)]	Bone	0 (0%)	9 (16.7%)	<0.001***
	Brain	0 (0%)	3 (5.6%)	
	Liver	0 (0%)	8 (14.8%)	
	Lung	0 (0%)	22 (40.7%)	
	No	64 (100%)	0 (0%)	
	Others	0 (0%)	12 (22.2%)	
N [*N* (%)]	N0	46 (71.9%)	9 (16.7%)	<0.001***
	N1	18 (28.1%)	45 (83.3%)	
T [*N* (%)]	T1	37 (57.8%)	11 (20.4%)	<0.001***
	T2	19 (29.7%)	18 (33.3%)	
	T3	7 (10.9%)	11 (20.4%)	
	T4	1 (1.6%)	14 (25.9%)	
Surgery [*N* (%)]	No	28 (43.8%)	42 (77.8%)	<0.001***
	Yes	36 (56.2%)	12 (22.2%)	
Radiation [*N* (%)]	No	23 (35.9%)	7 (13%)	0.008**
	Yes	41 (64.1%)	47 (87%)	

** P <0.05, ** P <0.01, *** P <0.001.*

0.05 were retained. Based on previous studies, we constructed a nomogram prediction model (40, 42–44). The retained imaging and clinical characteristics were included in the multivariate logistics regression analysis together, and characteristics with $P < 0.1$ were retained. The odds ratio (OR) and 95% confidence interval (95% CI) for each variable was determined separately. The receiver operating characteristic curve (ROC) was used to assess the sensitivity and specificity of continuous variables for predicting tumor metastasis.

Nomogram Construction and Clinical Application Validation

A multivariate logistics model was developed using the retained clinical and imaging characteristics. The entire dataset was divided into training and test sets in the ratio of 7:3, and the predictive performance of the model was quantitatively evaluated using the area under the curve (AUC) of the ROC. Decision curve analysis (DCA) calculated the net yield at different threshold probabilities to assess the utility and safety of the clinical prediction model. To facilitate clinical use, "RMS" (version 6.2) was used to visualize this combined multivariate model by constructing a nomogram. Predictors in the nomogram included select clinical and radiomics features. Calibration curves were used to assess the concurrence between predicted probabilities and actual outcomes.

Gene Set Enrichment Analysis

GSEA was performed to identify target neurovascular-related gene pathways using the RNA transcript dataset of patients with cervical cancer from TCGA database (45). The R package cluster profile (version 4.0) was used for GSEA analysis (46). The reference gene set "c2.cp.v7.2.symbols.GMT [Curated]" (MSigDB Collections, https://www.gsea-msigdb.org/gsea/msigdb/) was used for functional pathway annotation. The significant difference was adjusted to $P < 0.05$ as the cut-off criterion.

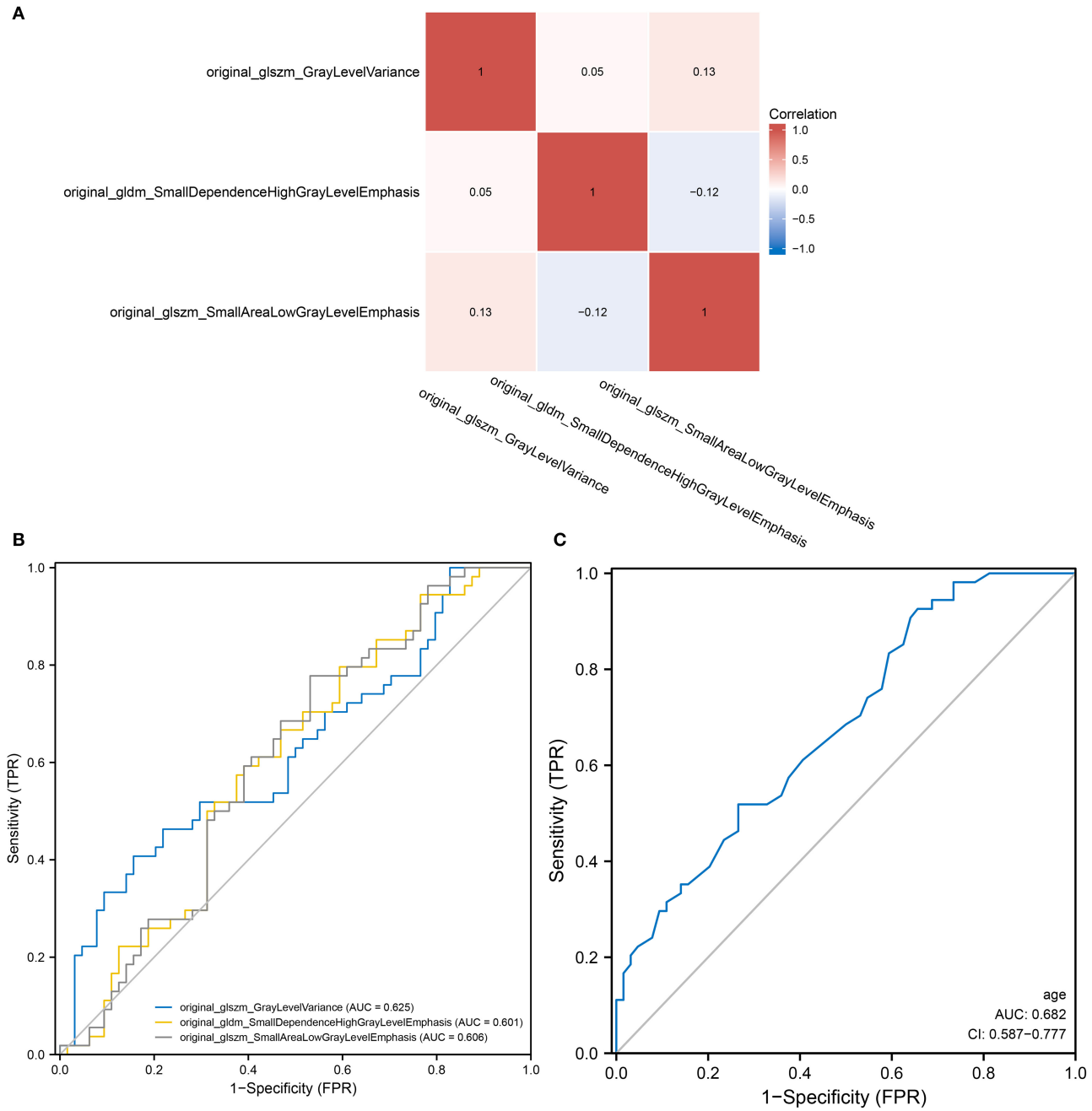

FIGURE 2 | Radiomics and the predictive power of age in predicting tumor metastasis. **(A)** A heat map demonstrating low correlation between the three screened radiomics features; **(B)** A heat map demonstrating low correlation between the three screened radiomics features; **(C)** A ROC curve showing the ability of univariate logistic regression models of age to predict tumor metastasis.

Quantitative Reverse Transcription Polymerase Chain Reaction

Patient tumor tissue samples were analyzed using qRT-PCR to explore the relationship between imaging features and gene expression. TRIzol reagent (Invitrogen) kits were used to extract total RNAs from the samples. According to the manufacturer's instructions, stem-loop antisense primer mix and AMV transcriptase (TaKaRa, China) kits were used to reverse transcribe these total RNAs into cDNAs. Finally, qRT-PCR was performed in the ABI 7500 real-time PCR system (Applied Biosystems, CA, USA) using an SYBR QPCR kit (Toyobo, Osaka, Japan). The primer sequences used are as follows: for *ADRB1*, forward: 5′-TCTACGTGCCCCTGTGCAT-3′ and reverse: 5′-TCGATCTTCTTCACCTGCTTCTG-3′; for

GAPDH, forward: 5′-AAGAAGGTGGTGAAGCAGGC-3′ and reverse: 5′-TCCACCACCCAGTTGCTGTA-3′; for GAPDH, forward: 5′-AAGAAGGTGGTGAAGCAGGC-3′ and reverse: 5′-TCCACCACCCAGTTGCTGTA-3′ (47). *GAPDH* was used as a reference to normalize the same gene expressions between samples. The $2^{-\Delta\Delta Ct}$ method was used to calculate the relative expression of the target gene. Gene expression was further normalized between samples before subsequent analysis.

Statistical Analysis

Demographic variables were divided into categorical and continuous variables, with Pearson's chi-square or Fisher's exact tests being used for categorical variables and Wilcoxon rank sum tests for continuous variables. Statistical analysis was performed using R software (version 4.0.2), and a two-tailed $P < 0.05$ was considered a statistically significant difference.

RESULTS

Demographic Characteristics and Imaging Features of the Patients

The flow chart of patient inclusion and data sources in this study are shown in **Figure 1**. The clinical characteristics and imaging variables of 118 patients with cervical cancer are presented in **Table 1**. Older patients showed a higher incidence of tumor metastasis than younger patients ($p = 0.022$). Additionally, a statistical difference was observed in stage, metastasis, T, N, surgery and radiation between patients with and without metastasis ($P < 0.05$). Patients with metastasis had a higher stage, larger T and N grades and lower surgery and radiation therapy rates than those without metastasis. Analyses of univariate regression and correlation were performed on the features extracted from the enhanced CT images, identifying three most critical variables, namely original_glszm_GrayLevelVariance, original_gldm_SmallDependenceHighGrayLevelEmphasis and original_glszm_SmallAreaLowGrayLevelEmphasis. The correlation heatmap of these three features is shown in **Figure 2A**. Based on the above analysis, we identified the main imaging features of metastases from cervical cancer.

Variable Screening for Univariate and Multivariate Logistic Regression Analysis

Logistic models are commonly used to screen for risk factors for clinical outcomes. The predictors associated with tumor metastasis based on univariate and multivariate logistic regression models are shown in **Table 2**. Based on the filtering conditions of univariate analysis, age, stage, N, T, surgery, radiation, original_glszm_GrayLevelVariance,

TABLE 2 | Univariate and multivariate logistics regression analysis.

Variables	Univariate logistic regression			Multivariate logistic regression		
	OR	95% CI	*P*-value	OR	95% CI	*P*-value
Age*	1.07	1.03, 1.1	<0.001	1.07	1.02, 1.14	0.014
Height*	0.99	0.94, 1.05	0.758	NA	NA	NA
Weight*	1.02	0.99, 1.05	0.325	NA	NA	NA
Marital status (Married)						
Unmarried	0.3	0.06, 1.05	0.081	NA	NA	NA
Divorced	0.5	0.1, 2.01	0.346	NA	NA	NA
Stage (I-II)						
III-IV	10.41	4.07, 30.65	<0.001	6.65	1.67, 32.56	0.011
Histology (adenosquamous)						
Mucinous adenocarcinoma	2	0.26, 19.77	0.518	NA	NA	NA
Squamous cell carcinoma	0.61	0.14, 2.42	0.476	NA	NA	NA
N (N0)						
N1	12.78	5.4, 33.04	<0.001	7.01	1.93, 28.97	0.004
T (T1)						
T2	3.19	1.27, 8.31	0.015	1.91	0.45, 8.16	0.375
T3	6.17	1.92, 21.77	0.003	0.48	0.06, 3.27	0.459
T4	23.55	5.53, 165.7	<0.001	2.11	0.2, 34.99	0.558
Surgery (No)						
Yes	0.22	0.1, 0.49	<0.001	0.13	0.03, 0.43	0.002
Radiation (No)						
Yes	3.77	1.53, 10.33	0.006	1.42	0.33, 6.19	0.634
Original_glszm_GrayLevelVariance*	0.1	0.02, 0.6	0.013	0.08	0, 1.24	0.081
Original_gldm_SmallDependenceHighGrayLevelEmphasis*	0.13	0.02, 0.69	0.022	0.21	0.01, 3.2	0.276
Original_glszm_SmallAreaLowGrayLevelEmphasis*	0.13	0.02, 0.64	0.016	0.25	0.02, 2.31	0.241

**Continuous variable.*

original_gldm_SmallDependenceHighGrayLevelEmphasis and original_glszm_SmallAreaLowGrayLevelEmphasis were able to predict tumor metastasis in patients with cervical cancer ($P < 0.05$). The AUCs for these three radiomics features were 0.625, 0.601, and 0.606 according to the univariate analysis, which means these features can serve as good predictors of cervical cancer (**Figure 2B**). Further multivariate logistic regression analysis showed that age, stage and N were independent predictors of tumor metastasis ($P < 0.05$). According to **Figure 2C**, the AUC on the prediction model constructed based on age was 0.682 (0.587–0.777). Based on predefined filtering conditions, age, stage, N, surgery, and original_glszm_GrayLevelVariance have been incorporated into a multivariate logistic regression model in order to construct a clinical prediction model. In the training, validation, and overall groups, the AUCs of this predictive model were, respectively 0.922, 0.833, and 0.910 (**Figure 3A**). Accordingly, the predictive efficacy and accuracy of the model was enhanced by the inclusion of clinical and imaging factors together. Based on DCA of the training, validation and overall groups shown in **Figure 3B**, the model appears to be user-friendly and has a wide range of clinical applicability. **Figure 3C** depicts the weights assigned to each variable in the model, with the imaging features having the greatest weight (**Table 3**).

Nomogram Construction for Predicting Tumor Metastasis

Based on the regression coefficients of each variable in the constructed multivariate logistic regression model, the nomogram of the clinical prediction model was plotted (**Figure 4A**). The nomogram consists of a series of selected variables and a score corresponding to each featured variable. By calculating the total score of all features in the nomogram, the

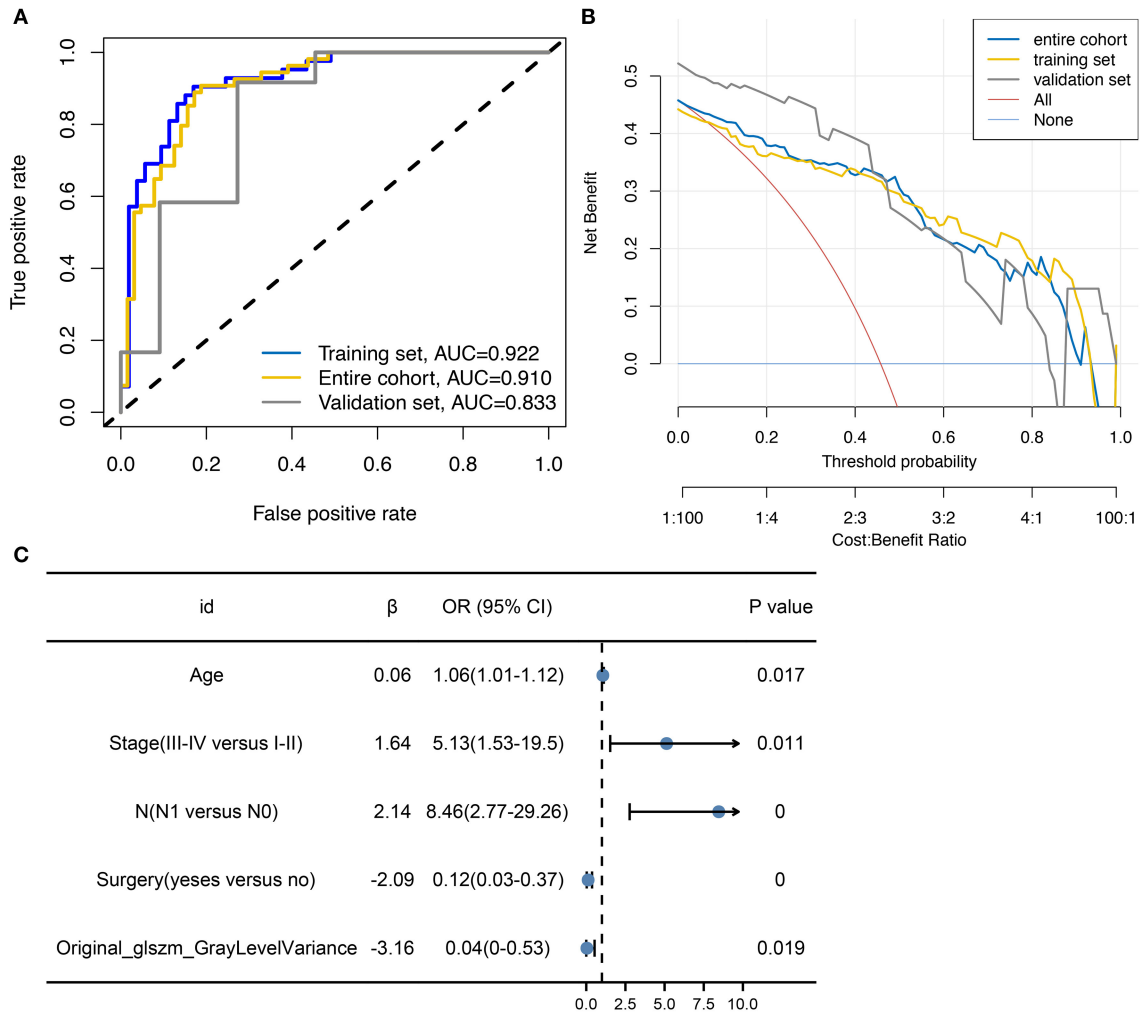

FIGURE 3 | Construction of multifactor models with variable weights. **(A)** ROC curve showing the predictive performance of models based on clinical data and imaging features. **(B)** DCA showing the wide range of clinical utility and safety associated with the built prediction model. **(C)** Forest plot displaying the relative weights and values of the variables included in the model.

likelihood of tumor metastasis can be determined. It is evident in **Figure 4B** that there is a high degree of consistency between the predicted and true values for patients in the multivariate prediction model. Principal component analysis (PCA) reveals that the variables incorporated in the model show significant differences between patients with cervical cancer with and without metastasis (**Figure 4C**). These results suggest that this cervical cancer metastatic prediction model performs well.

TABLE 3 | Prediction factors for nomogram.

Viariable	Prediction model		
	β	OR (95% CI)	*P*-value
(Intercept)	−2.19	0.11 (0.01–1.53)	0.11
Age	0.06	1.06 (1.01–1.12)	0.02
Stage III-IV	1.64	5.13 (1.53–19.50)	0.01
N(N1)	2.14	8.46 (2.77–29.26)	0.00
Surgery (Yes)	−2.09	0.12 (0.03–0.37)	0.00
original_glszm_GrayLevelVariance	−3.16	0.04 (0.00–0.53)	0.02

Comparison of the Brain and Non-brain Metastasis Groups

An examination of clinical differences between patients with brain metastases and those with non-brain metastases was performed to determine the relationship between metastases, neurological and vascular effects. Among the brain metastases group, the incidence of headache and vomiting was 100 and 66.7%, respectively (**Figure 5A**), whereas among the metastases group, the incidence of headache and vomiting was 7.8 and 17.6%, respectively (**Figure 5B**), with a statistically significant difference between the two groups ($p < 0.05$). In addition to

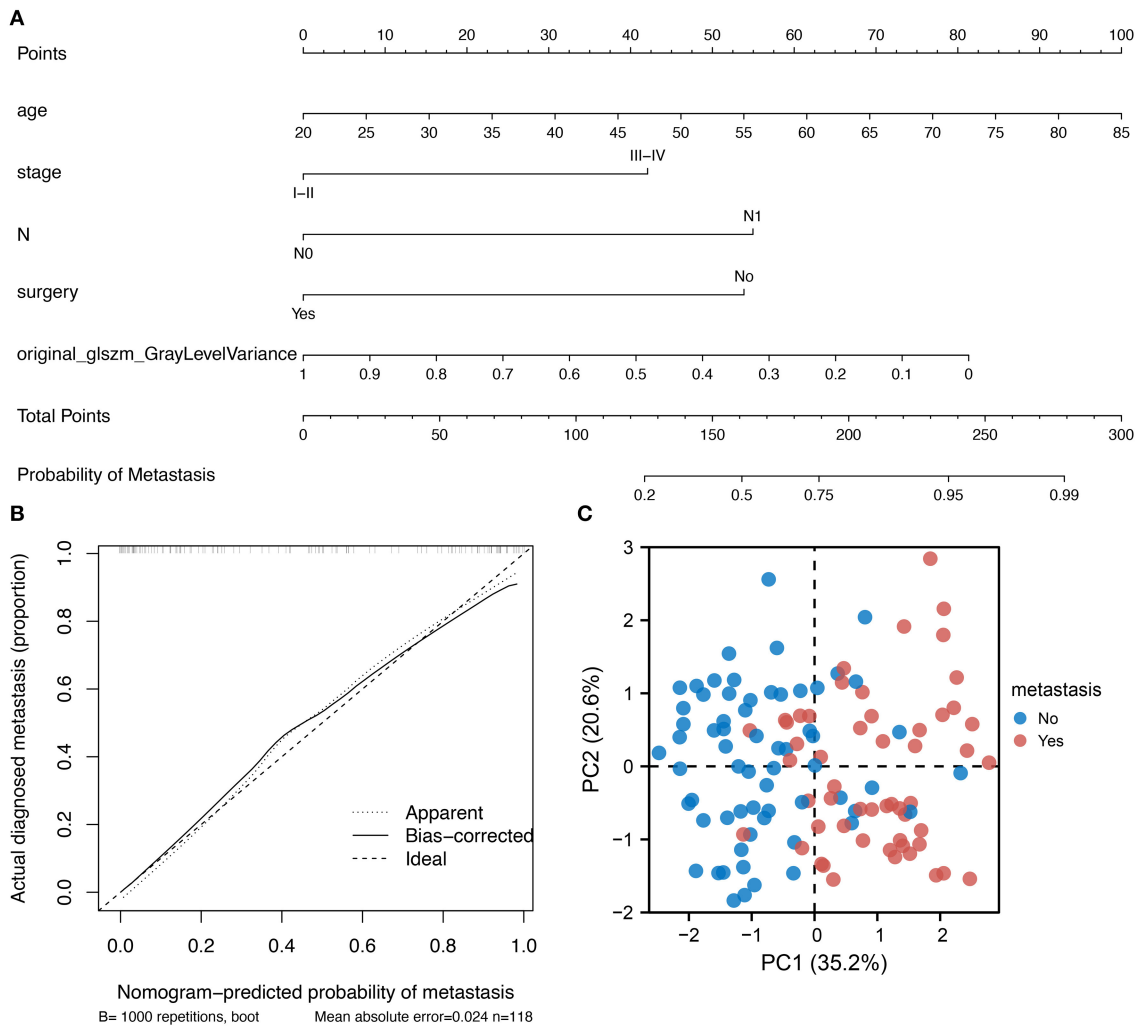

FIGURE 4 | Nomogram development and clinical validation. **(A)** A nomogram was constructed using the multi-factor logistic regression model; **(B)** Calibration plot showing a good fit between the true and predicted values; **(C)** PCA showing the variables incorporated into the model could distinguish between cervical cancer patients with metastasis.

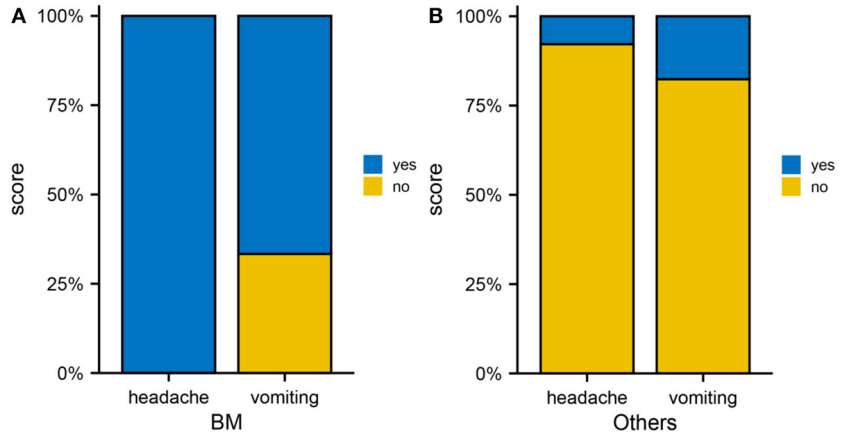

FIGURE 5 | Brain metastases from cervical cancer. **(A)** Occurrence rate of headache as well as vomiting in the brain metastasis group. **(B)** Occurrence rate of headache and vomiting in the non-brain metastasis group.

the increased intracranial pressure due to intracranial occupancy, headache can also be associated with neurological and vascular disorders. Additionally, associated neuropeptide or vasoactive factor release can also result in vomiting in addition to gastrointestinal dysfunction. Consequently, the 469 genes related to neurological and vascular conditions were analyzed.

Variance Analysis in the TCGA Database

RNA transcription data were obtained from the TCGA database for three patients with cervical cancer who had brain metastases and 14 patients with cervical cancer who did not have brain metastases. Differential expression analysis was performed on the 469 genes related to neurological function, which were obtained from the literature review and GeneCards database. Five genes (*CHGB*, *CACNA1B*, *ADRB1*, *PLCG1* and *TSPO*) were found to be statistically significant between the two groups (**Figure 6A**). After ranking the differential genes by significance and investigating the function of each gene, *ADRB1* was identified as a gene that could be involved in nerves and blood vessels. *ADRB1* expression was significantly different in brain metastasis compared to non-brain metastasis groups (**Figure 6B**). In the tumor brain metastasis group, *ADRB1* expression was significantly higher than at other metastasis-site group ($p = 0.003$). In order to further identify the role of *ADRB1* in cervical cancer brain metastasis, the GSEA analysis of RNA transcription data from patients with cervical cancer revealed that the T cell receptor complex pathway was upregulated, while the iron-sulfur cluster assembly pathway was downregulated (**Figure 6C**). This suggests the potential role of *ADRB1* in immune regulation and altered mitochondrial respiratory function in response to hypoxia (48).

Radiomics Features Can Predict *ADRB1* Expression

A correlation analysis was conducted between original_glszm_GrayLevelVariance and *ADRB1* expression in 60 patients to further examine the predictability of the imaging feature in the constructed model. The correlation analysis revealed a negative correlation between the radiomics feature original_glszm_GrayLevelVariance and *ADRB1* expression (**Figure 7A**, Spearman $r = -0.46$, $p < 0.001$). Patients were further divided into high Rad-score and low Rad-score groups according to the value variation of the radiomics feature original_glszm_GrayLevelVariance. The difference in *ADRB1* expression between the high- and low-Rad-score groups is statistically significant (**Figure 7B**). Expression of ADRB1 was higher in the low-Rad-score group than the high-Rad-score group ($p = 0.025$). In light of this, the radiomics feature original_glszm_GrayLevelVariance in the model is likely to be able to predict *ADRB1* expression and, thereby, brain metastasis in cervical cancer. Hence, *ADRB1* expression is associated with radiomics features and is considered a risk factor for cerebral neurovascular metastasis of cervical cancer.

DISCUSSION

The clinical and radiomic features of 118 patients with cervical cancer (with or without tumor metastasis) were retrospectively analyzed. Univariate and multivariate logistic regression analyses screened four clinical features (age, stage, N and T) and one radiomics feature (original_glszm_GrayLevelVariance) associated with cervical cancer metastasis. These features were used to construct clinical prediction models. *ADRB1* was found to be related to radiomic features and was considered as a risk factor associated with the risk of cerebral neurovascular metastasis in cervical cancer.

Radiomics is an emerging field that involves the transformation of various types of images into high-dimensional image feature data, providing a more comprehensive description of tumor tissue heterogeneity (49, 50). In a study, the prediction of cervical cancer metastasis was modeled using multiparametric MRI imaging and seven clinical and pathological characteristics, demonstrating that multisequence MRI features serve as non-invasive biomarkers for the preoperative assessment of cervical

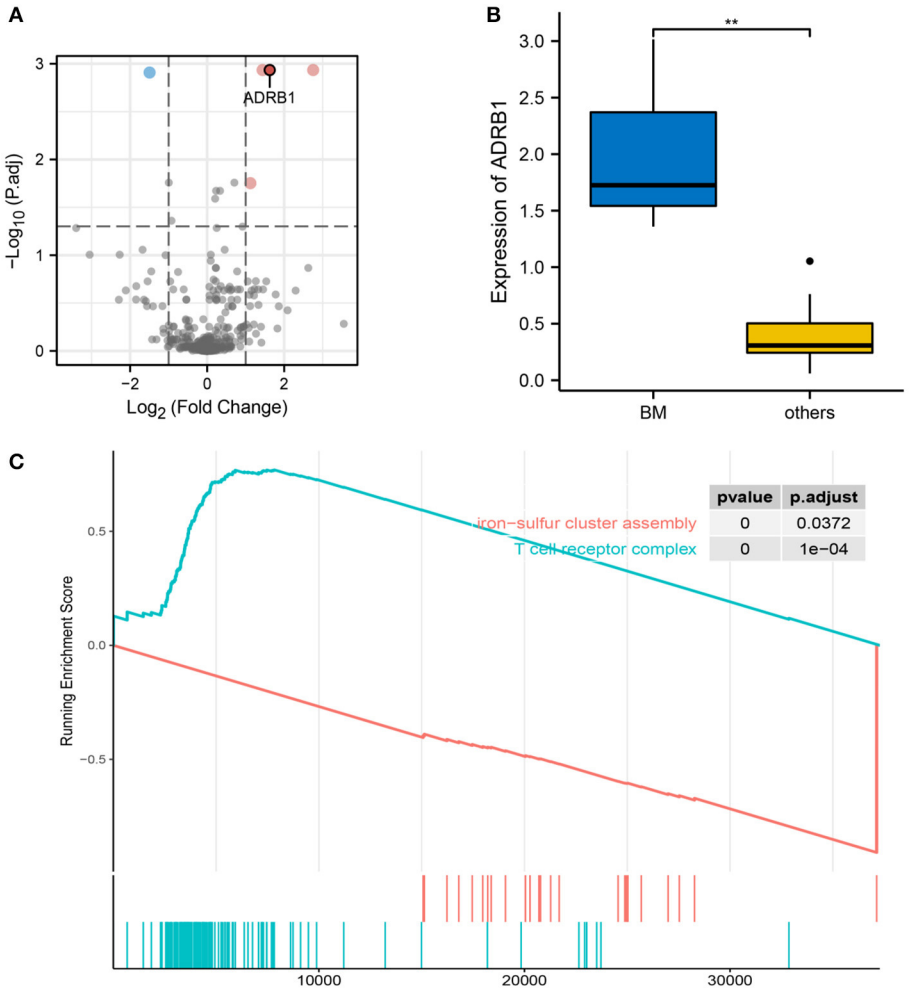

FIGURE 6 | Characteristics of ADRB1. **(A)** Volcano plot showing differentially expressed genes between the brain metastasis and the extracerebral metastasis groups, and *ADRB1* was upregulated in the brain metastasis group. **(B)** Differences in *ADRB1* expression between the brain metastasis and non-brain metastasis groups. **(C)** GSEA showing the upregulation of the T cell receptor complex pathway in the ADRB1-enhanced group and the downregulation of the iron-sulfur cluster assembly pathway.

cancer lymph node status. Furthermore, these characteristics can have an impact on treatment decisions for patients with cervical cancer at an early stage (51). Wu et al. constructed a radiomics model and apparent diffusion coefficients (ADCs) of 189 patients, which was able to predict the development of lymph node metastases in cervical cancer with an AUC of 0.847 (52). Similarly to previous MR-based studies of cervical cancer, this study also observed a better predictability of cervical cancer metastasis using radiomics (53). Based on the original_glszm_GrayLevelVariance feature of enhanced CT images in conjunction with clinical features, the current study developed a clinical prediction model for cervical cancer metastasis. It was demonstrated that the prediction model had good predictive efficacy, a high clinical usefulness and a wide safety range, which successfully differentiated between women with cervical cancer who had metastasized and those who did not. Recent studies have shown that radiomics can be used to investigate the association between histological features and gene mutations by mining high-throughput radiomics features from conventional CT images (54). Similarly, radiomics can also predict genes associated with cervical cancer metastasis.

ADRB1, a β1 adrenergic receptor, is a member of the G protein-coupled receptor family, serving as adrenergic receptors in myocardiocytes (55). The β-adrenergic receptor signaling pathway has also been found to be closely associated with tumor proliferation, apoptosis and microenvironment regulation (56–59). According to previous studies, ADRB family genes play a crucial role in regulating the interaction between the sympathetic drive and the immune system (60). According to previous studies, ADRB family genes play a crucial role in regulating the interaction between the sympathetic drive and

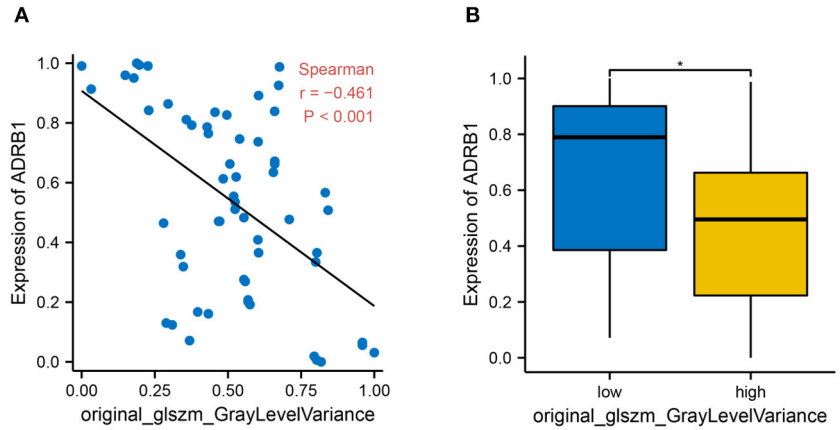

FIGURE 7 | The relationship between histological features and *ADRB1* expression. **(A)** A correlation analysis found a negative relationship between the imaging feature original_glszm_GrayLevelVariance and *ARDB1* expression (Spearman r = −0.46, $P < 0.001$). **(B)** Patients were divided into high Rad-score and low Rad-score groups based on the value of the histological feature original_glszm_GrayLevelVariance; * $p < 0.05$.

the immune system. *ADRB1* is involved in the regulation of tumor development in the lungs, breast and prostate (61–63). Furthermore, *ADRB1* genes may act synergistically with *FOXA1* and *ADRB2* genes to drive tumor formation and development (62). It is also closely associated with metastasis and recurrence of oral squamous cell carcinoma (64). Similarly, this study identified *ADRB1* as a potential oncogene involved in the neurovascular metastasis of cervical cancer. Consistent with previous studies, GSEA revealed that the T cell receptor complex pathway was upregulated, whereas the iron-sulfur cluster assembly pathway was downregulated in the *ADRB1* group, indicating the role of *ADRB1* in immune regulation and altered mitochondrial respiratory function in response to hypoxia. Wang et al. observed that the high expression of *ADRB1* could mediate and maintain a normal immune response by promoting the activity of B cells and dendritic cells (61). Immune infiltration contributes significantly to tumor progression (65). Thus, *ADRB1* serves as an immunomodulator in the process of cerebral neurovascular metastasis in cervical cancer.

Lymph node status in early-stage cervical cancer was found to be associated with the age of the patient (66). Ki et al. report the mean age of diagnosis in patients with cervical cancer metastasis as 55 years (67). Advanced age is a remarkable factor affecting the prognosis of patients with stage IV cervical cancer, with patients ≥70 years of age having the worst prognosis (68). Similar to previous studies, the age of patients with cervical cancer in the non-metastatic group was found to be significantly lower than those with metastasis. Moreover, age turned out to be an independent risk factor for cervical cancer metastasis. Additionally, patients with cervical cancer who had tumor diameters >4 cm were significantly more likely to develop metastasis than those who had tumor diameters <4 cm (69). The incidence of cervical cancer metastasis increases with the progression of the tumor stage (70). Similarly, pelvic lymph node metastasis in patients with cervical cancer could lead to a higher rate of distant metastasis (71).

Neurovascular factors are thought to contribute to headache and vomiting. The incidence of headache and vomiting was higher in patients with cervical cancer in the brain metastasis group when compared to those with other sites of metastasis. Further bioinformatic analysis revealed that the expression of neurovascular-related gene *ADRB1* was elevated in the tumor brain metastasis group. However, the current study has certain limitations: (1) The clinical aspect of this study was retrospective, with possible selection bias and a small sample size. Therefore, further multi-center studies should expand the sample size; (2) The risk factors for brain metastasis in cervical cancer screened in this study were based on bioinformatic analyses, which require further clinical validation; (3) RNA transcription data were downloaded from the TCGA database for two patients with brain metastases and 15 patients with extracerebral metastases from cervical cancer, which may be subject to selection bias due to the limited sample size; (4) Additionally, further experiments to validate the function of *ADRB1* in cervical cancer brain metastasis are required.

CONCLUSION

Based on four clinical features and one radiomic feature, a nomogram-based cervical cancer metastasis prediction model has been developed. A radiomics feature is considered essential for predicting tumor gene expression. *ADRB1* gene expression was significantly higher in cervical cancer brain metastasis than in other metastasis sites. Therefore, features of radiomics that are related to *ADRB1* may be associated with the risk of cerebral neurovascular metastases in cervical cancer.

DATA AVAILABILITY STATEMENT

The datasets presented in this study can be found in online repositories. The names of the repository/repositories

and accession number(s) can be found in the article/supplementary material.

ETHICS STATEMENT

The studies involving human participants were reviewed and approved by Institutional Ethics Review Board of the Guizhou Provincial People' s Hospital. The patients/participants provided their written informed consent to participate in this study.

AUTHOR CONTRIBUTIONS

XZ, SX, and JW reviewed the manuscript, analysis, and analyzed the results. XZ drafted and performed the data curation. All authors read and approved the final manuscript.

ACKNOWLEDGMENTS

The authors wish to thank all the patients and staff who participated in this study. Thanks to Bullet Edits Limited for language editing and proofreading of the manuscript.

REFERENCES

1. Vu M, Yu J, Awolude OA, Chuang L. Cervical cancer worldwide. *Curr Probl Cancer.* (2018) 42:457–65. doi: 10.1016/j.currproblcancer.2018.06.003
2. Arbyn M, Weiderpass E, Bruni L, de Sanjosé S, Saraiya M, Ferlay J, et al. Estimates of incidence and mortality of cervical cancer in 2018: a worldwide analysis. *Lancet Global Health.* (2020) 8:e191–203. doi: 10.1016/S2214-109X(19)30482-6
3. Chen S, Gao C, Wu Y, Huang Z. Identification of Prognostic miRNA signature and lymph node metastasis-related key genes in cervical cancer. *Front Pharmacol.* (2020) 11:544. doi: 10.3389/fphar.2020.00544
4. Zhong Y, Lu Q, Qiu W, Luo Y. LINC00636 promotes lymph node metastasis and cervical cancer through targeting NM23. *Biosci Rep.* (2020) 40:BSR20200367. doi: 10.1042/BSR20200367
5. Gong Y, Wan J-H, Zou W, Lian G-Y, Qin J-L, Wang Q-M. MiR-29a inhibits invasion and metastasis of cervical cancer via modulating methylation of tumor suppressor SOCS1. *Future Oncol.* (2019) 15:1729–44. doi: 10.2217/fon-2018-0497
6. Shi X, Wang J, Dai S, Qin L, Zhou J, Chen Y. Apolipoprotein C1 (APOC1): a novel diagnostic and prognostic biomarker for cervical cancer. *OTT. Volume.* (2020) 13:12881–91. doi: 10.2147/OTT.S280690
7. Wang P, Zhai G, Bai Y. Values of miR-34a and miR-218 expression in the diagnosis of cervical cancer and the prediction of prognosis. *Oncol Lett.* (2018) 15:3580–5. doi: 10.3892/ol.2018.7791
8. Hisamatsu T, Mabuchi S, Yoshino K, Fujita M, Enomoto T, Hamasaki T. Kimura T. Prediction of progression-free survival and response to paclitaxel plus carboplatin in patients with recurrent or advanced cervical cancer. *Int J Gynecol Cancer.* (2012) 22:623–9. doi: 10.1097/IGC.0b013e3182473277
9. Zhou J-Y, Zheng S-R, Liu J, Shi R, Yu H-L, Wei M. MiR-519d facilitates the progression and metastasis of cervical cancer through direct targeting Smad7. *Cancer Cell Int.* (2016) 16:21. doi: 10.1186/s12935-016-0298-1
10. Peng J, Liu X, Li C, Gao M, Wang H. Sema4C modulates the migration of primary tumor-associated lymphatic endothelial cells via an ERK-mediated pathway. *Exp Ther Med.* (2021) 22:1102. doi: 10.3892/etm.2021.10535
11. Qian C, Liu H, Feng Y, Meng S, Wang D, Nie M, et al. Clinical characteristics and risk of second primary lung cancer after cervical cancer: a population-based study. *PLoS ONE.* (2020) 15:e0231807. doi: 10.1371/journal.pone.0231807
12. Piura E, Piura B. Brain metastases from cervical carcinoma: overview of pertinent literature. *Eur J Gynaecol Oncol.* (2012) 33:567–73. doi: 10.5402/2012/581749
13. Cormio G, Pellegrino A, Landoni F, Regallo M, Zanetta G, Colombo A, et al. Brain metastases from cervical carcinoma. *Tumori.* (1996) 82:394–6. doi: 10.1177/030089169608200420
14. Lambin P, Leijenaar RTH, Deist TM, Peerlings J, de Jong EEC, van Timmeren J, et al. Radiomics: the bridge between medical imaging and personalized medicine. *Nat Rev Clin Oncol.* (2017) 14:749–62. doi: 10.1038/nrclinonc.2017.141
15. Liu S, Zheng H, Pan X, Chen L, Shi M, Guan Y, et al. Texture analysis of CT imaging for assessment of esophageal squamous cancer aggressiveness. *J Thorac Dis.* (2017) 9:4724–32. doi: 10.21037/jtd.2017.06.46
16. Shen C, Liu Z, Wang Z, Guo J, Zhang H, Wang Y, et al. Building CT radiomics based nomogram for preoperative esophageal cancer patients lymph node metastasis prediction. *Transl Oncol.* (2018) 11:815–24. doi: 10.1016/j.tranon.2018.04.005
17. Qu J, Shen C, Qin J, Wang Z, Liu Z, Guo J, et al. The MR radiomic signature can predict preoperative lymph node metastasis in patients with esophageal cancer. *Eur Radiol.* (2019) 29:906–14. doi: 10.1007/s00330-018-5583-z
18. Fritz B, Müller DA, Sutter R, Wurnig MC, Wagner MW, Pfirrmann CWA, et al. Magnetic resonance imaging–based grading of cartilaginous bone tumors: added value of quantitative texture analysis. *Invest Radiol.* (2018) 53:663–72. doi: 10.1097/RLI.0000000000000486
19. Zhao S, Su Y, Duan J, Qiu Q, Ge X, Wang A, et al. Radiomics signature extracted from diffusion-weighted magnetic resonance imaging predicts outcomes in osteosarcoma. *J Bone Oncol.* (2019) 19:100263. doi: 10.1016/j.jbo.2019.100263
20. Zhang H, Mao Y, Chen X, Wu G, Liu X, Zhang P, et al. Magnetic resonance imaging radiomics in categorizing ovarian masses and predicting clinical outcome: a preliminary study. *Eur Radiol.* (2019) 29:3358–71. doi: 10.1007/s00330-019-06124-9
21. Kyriazi S, Collins DJ, Messiou C, Pennert K, Davidson RL, Giles SL, et al. Metastatic ovarian and primary peritoneal cancer: assessing chemotherapy response with diffusion-weighted MR imaging—value of histogram analysis of apparent diffusion coefficients. *Radiology.* (2011) 261:182–92. doi: 10.1148/radiol.11110577
22. Grøvik E, Yi D, Iv M, Tong E, Rubin D, Zaharchuk G. Deep learning enables automatic detection and segmentation of brain metastases on multisequence MRI. *J Magn Reson Imaging.* (2020) 51:175–82. doi: 10.1002/jmri.26766
23. Artzi M, Bressler I, Ben Bashat D. Differentiation between glioblastoma, brain metastasis and subtypes using radiomics analysis: radiomics classification of brain tumors. *J Magn Reson Imaging.* (2019) 50:519–28. doi: 10.1002/jmri.26643
24. Huang C-Y, Lee C-C, Yang H-C, Lin C-J, Wu H-M, Chung W-Y, et al. Radiomics as prognostic factor in brain metastases treated with Gamma Knife radiosurgery. *J Neurooncol.* (2020) 146:439–49. doi: 10.1007/s11060-019-03343-4
25. Shen T, Liu L, Li W, Fu P, Xu K, Jiang Y, et al. imaging-based histogram features for prediction of EGFR mutation status of bone metastases in patients with primary lung adenocarcinoma. *Cancer Imaging.* (2019) 19:34. doi: 10.1186/s40644-019-0221-9
26. Yu J, Shi Z, Lian Y, Li Z, Liu T, Gao Y, et al. Noninvasive IDH1 mutation estimation based on a quantitative radiomics approach for grade II glioma. *Eur Radiol.* (2017) 27:3509–22. doi: 10.1007/s00330-016-4653-3
27. Jiang C, Kong Z, Liu S, Feng S, Zhang Y, Zhu R, et al. Fusion radiomics features from conventional MRI predict MGMT promoter methylation status in lower grade gliomas. *Eur J Radiol.* (2019) 121:108714. doi: 10.1016/j.ejrad.2019.108714
28. Aerts HJWL. The potential of radiomic-based phenotyping in precision medicine: a review. *JAMA Oncol.* (2016) 2:1636. doi: 10.1001/jamaoncol.2016.2631
29. Xu K, Wu C, Wang Z, Wang H, Yin F, Li W, et al. Family gene expression as prognostic biomarkers for Alzheimer's disease and primary liver cancer. *Comput Math Methods Med.* (2021) 2021:1–15. doi: 10.1155/2021/3422393

30. Deng C, Guo H, Yan D, Liang T, Ye X, Li Z. Pancancer analysis of neurovascular-related NRP family genes as potential prognostic biomarkers of bladder urothelial carcinoma. *Biomed Res Int.* (2021) 2021:5546612. doi: 10.1155/2021/5546612
31. Chang A, Yeung S, Thakkar A, Huang KM, Liu MM, Kanassatega R-S, et al. Prevention of skin carcinogenesis by the β-blocker carvedilol. *Cancer Prev Res.* (2015) 8:27–36. doi: 10.1158/1940-6207.CAPR-14-0193
32. Chang P-Y, Huang W-Y, Lin C-L, Huang T-C, Wu Y-Y, Chen J-H, et al. Propranolol reduces cancer risk: a population-based cohort study. *Medicine.* (2015) 94:e1097. doi: 10.1097/MD.0000000000001097
33. Renz BW, Takahashi R, Tanaka T, Macchini M, Hayakawa Y, Dantes Z, et al. β2 Adrenergic-neurotrophin feedforward loop promotes pancreatic cancer. *Cancer Cell.* (2018) 33:75–90.e7. doi: 10.1016/j.ccell.2018.10.010
34. Chen G, Liu X, Wang Z, Liu F. Vascular endothelial growth factor C: the predicator of early recurrence in patients with N2 non-small-cell lung cancer. *Eur J Cardiothorac Surg.* (2010) 37:546–51. doi: 10.1016/j.ejcts.2009.08.005
35. Xing F, Liu Y, Sharma S, Wu K, Chan MD, Lo H-W, et al. Activation of the c-Met pathway mobilizes an inflammatory network in the brain microenvironment to promote brain metastasis of breast cancer. *Cancer Res.* (2016) 76:4970–80. doi: 10.1158/0008-5472.CAN-15-3541
36. Martínez-Rodríguez F, Limones-González JE, Mendoza-Almanza B, Esparza-Ibarra EL, Gallegos-Flores PI, Ayala-Luján JL, et al. understanding cervical cancer through proteomics. *Cells.* (2021) 10:1854. doi: 10.3390/cells10081854
37. Sun Y, Sun X, Liu S, Liu L, Chen J. The overlap between regeneration and fibrosis in injured skeletal muscle is regulated by phosphatidylinositol 3-kinase/Akt signaling pathway - a bioinformatic analysis based on lncRNA microarray. *Gene.* (2018) 672:79–87. doi: 10.1016/j.gene.2018.06.001
38. Luo Z, Sun Y, Qi B, Lin J, Chen Y, Xu Y, Chen J. Human bone marrow mesenchymal stem cell-derived extracellular vesicles inhibit shoulder stiffness via let-7a/Tgfbr1 axis. *Bioact Mater.* (2022) 17:344–59. doi: 10.1016/j.bioactmat.2022.01.016
39. Huang J, Liang X, Cai Z, A. Potential ceRNA network for neurological damage in preterm infants. *Biomed Res Int.* (2021) 2021:2628824. doi: 10.1155/2021/2628824
40. Shi Q, Yan X, Wang J, Zhang X. Collagen family genes associated with risk of recurrence after radiation therapy for vestibular schwannoma and pan-cancer analysis. *Dis Markers.* (2021) 2021:1–15. doi: 10.1155/2021/7897994
41. Tang G-Y, Yu P, Zhang C, Deng H-Y, Lu M-X, Le J-H. The neuropeptide-related HERC5/TAC1 interactions may be associated with the dysregulation of lncRNA GAS5 expression in gestational diabetes mellitus exosomes. *Dis Markers.* (2022) 2022:1–12. doi: 10.1155/2022/8075285
42. Balachandran VP, Gonen M, Smith JJ, DeMatteo RP. Nomograms in oncology: more than meets the eye. *Lancet Oncol.* (2015) 16:e173–80. doi: 10.1016/S1470-2045(14)71116-7
43. Ying C, Guo C, Wang Z, Chen Y, Sun J, Qi X, et al. Prediction modeling based on the hospital for special surgery (HSS) knee score for poor postoperative functional prognosis of elderly patients with patellar fractures. *Biomed Res Int.* (2021) 2021:6620504. doi: 10.1155/2021/6620504
44. Sun C, Ma S, Chen Y, Kim NH, Kailas S, Wang Y, et al. Diagnostic value, prognostic value, and immune infiltration of LOX family members in liver cancer: bioinformatic analysis. *Front Oncol.* (2022) 12:843880. doi: 10.3389/fonc.2022.843880
45. Subramanian A, Tamayo P, Mootha VK, Mukherjee S, Ebert BL, Gillette MA, et al. Gene set enrichment analysis: a knowledge-based approach for interpreting genome-wide expression profiles. *Proc Natl Acad Sci USA.* (2005) 102:15545–50. doi: 10.1073/pnas.0506580102
46. Yu G, Wang L-G, Han Y, He Q-Y. clusterProfiler: an R package for comparing biological themes among gene clusters. *OMICS.* (2012) 16:284–7. doi: 10.1089/omi.2011.0118
47. Ranasinghe AM. How does glucose insulin potassium improve hemodynamic performance? evidence for altered expression of beta-adrenoreceptor and calcium handling genes. *Circulation.* (2006) 114(1 Suppl):I239–44. doi: 10.1161/CIRCULATIONAHA.105.000760
48. Chan SY, Zhang Y-Y, Hemann C, Mahoney CE, Zweier JL, Loscalzo J. MicroRNA-210 controls mitochondrial metabolism during hypoxia by repressing the iron-sulfur cluster assembly proteins ISCU1/2. *Cell Metab.* (2009) 10:273–84. doi: 10.1016/j.cmet.2009.08.015
49. Mayerhoefer ME, Materka A, Langs G, Häggström I, Szczypiński P, Gibbs P, et al. Introduction to radiomics. *J Nucl Med.* (2020) 61:488–95. doi: 10.2967/jnumed.118.222893
50. Lee S-H, Park H, Ko ES. Radiomics in breast imaging from techniques to clinical applications: a review. *Korean J Radiol.* (2020) 21:779. doi: 10.3348/kjr.2019.0855
51. Kan Y, Dong D, Zhang Y, Jiang W, Zhao N, Han L, et al. Radiomic signature as a predictive factor for lymph node metastasis in early-stage cervical cancer: radiomic signature of LNM in cervical cancer. *J Magn Reson Imaging.* (2019) 49:304–10. doi: 10.1002/jmri.26209
52. Wu Q, Wang S, Chen X, Wang Y, Dong L, Liu Z, et al. Radiomics analysis of magnetic resonance imaging improves diagnostic performance of lymph node metastasis in patients with cervical cancer. *Radiother Oncol.* (2019) 138:141–8. doi: 10.1016/j.radonc.2019.04.035
53. Li Z, Li H, Wang S, Dong D, Yin F, Chen A, et al. MR-based radiomics nomogram of cervical cancer in prediction of the lymph-vascular space invasion preoperatively: preoperative prediction of LVSI. *J Magn Reson Imaging.* (2019) 49:1420–6. doi: 10.1002/jmri.26531
54. Gillies RJ, Kinahan PE, Hricak H. Radiomics: images are more than pictures, they are data. *Radiology.* (2016) 278:563–77. doi: 10.1148/radiol.2015151169
55. Kelley EF, Snyder EM, Johnson BD. Influence of Beta-1 adrenergic receptor genotype on cardiovascular response to exercise in healthy subjects. *Cardiol Res.* (2018) 9:343–9. doi: 10.14740/cr785
56. Wang F, Liu H, Wang F, Xu R, Wang P, Tang F, et al. Propranolol suppresses the proliferation and induces the apoptosis of liver cancer cells. *Mol Med Rep.* (2018) 17:5213–21. doi: 10.3892/mmr.2018.8476
57. He J-J, Zhang W-H, Liu S-L, Chen Y-F, Liao C-X, Shen Q-Q, et al. Activation of β-adrenergic receptor promotes cellular proliferation in human glioblastoma. *Oncol Lett.* (2017) 14:3846–52. doi: 10.3892/ol.2017.6653
58. Calvani M, Pelon F, Comito G, Taddei ML, Moretti S, Innocenti S, et al. Norepinephrine promotes tumor microenvironment reactivity through β3-adrenoreceptors during melanoma progression. *Oncotarget.* (2015) 6:4615–32. doi: 10.18632/oncotarget.2652
59. Wrobel LJ, Bod L, Lengagne R, Kato M, Prévost-Blondel A, Gal F-AL. Propranolol induces a favourable shift of anti-tumor immunity in a murine spontaneous model of melanoma. *Oncotarget.* (2016) 7:77825–37. doi: 10.18632/oncotarget.12833
60. Ahmari N, Schmidt JT, Krane GA, Malphurs W, Cunningham BE, Owen JL, et al. Loss of bone marrow adrenergic beta 1 and 2 receptors modifies transcriptional networks, reduces circulating inflammatory factors, and regulates blood pressure. *Physiol Genomics.* (2016) 48:526–36. doi: 10.1152/physiolgenomics.00039.2016
61. Wang J, Zhang X, Li J, Ma X, Feng F, Liu L, et al. ADRB1 was identified as a potential biomarker for breast cancer by the co-analysis of tumor mutational burden and immune infiltration. *Aging.* (2021) 13:351–63. doi: 10.18632/aging.104204
62. Lehrer S, Rheinstein PH. The ADRB1 (Adrenoceptor Beta 1) and ADRB2 genes significantly co-express with commonly mutated genes in prostate cancer. *Discov Med.* (2020) 30:163–71.
63. Li C, Chen W, Zhang M, Zhang C, Cao B, Dong B, et al. Modulatory effects of Xihuang Pill on lung cancer treatment by an integrative approach. *Biomed Pharmacother.* (2020) 130:110533. doi: 10.1016/j.biopha.2020.110533
64. Dong H, Liao X-X, Mai H-M, Zhou N, Wang D-Y, Peng J-B, et al. Expression of beta adrenergic receptor in oral squamous cell carcinoma and its significance to the prognosis. *Int J Clin Exp Pathol.* (2017) 10:10431–40.
65. Lois H. New advances in immunotherapy for prostate cancer. *Life Res.* (2019) 2:152. doi: 10.53388/life2019-1025-302
66. Pallavi VR, Devi KU, Mukherjee G, Ramesh C, Bafna UD. Relationship between lymph node metastases and histopathological parameters in carcinoma cervix: a multivariate analysis. *J Obstet Gynaecol.* (2012) 32:78–80. doi: 10.3109/01443615.2011.625455

67. Ki EY, Lee KH, Park JS, Hur SY. A clinicopathological review of pulmonary metastasis from uterine cervical cancer. *Cancer Res Treat.* (2016) 48:266–72. doi: 10.4143/crt.2014.206
68. Zhang J, Qin L, Chen H-M, Hsu H-C, Chuang C-C, Chen D, et al. Overall survival, locoregional recurrence, and distant metastasis of definitive concurrent chemoradiotherapy for cervical squamous cell carcinoma and adenocarcinoma: before and after propensity score matching analysis of a cohort study. *Am J Cancer Res.* (2020) 10:1808–20. doi: 10.2139/ssrn.3582834
69. Blomberg K, Ternestedt B-M, Törnberg S, Tishelman C. How do women who choose not to participate in population-based cervical cancer screening reason about their decision? *Psychooncology.* (2008) 17:561–9. doi: 10.1002/pon.1270
70. Imachi M, Tsukamoto N, Matsuyama T, Nakano H. Pulmonary metastasis from carcinoma of the uterine cervix. *Gynecol Oncol.* (1989) 33:189–92. doi: 10.1016/0090-8258(89)90549-0
71. Shiromizu K, Kasamatsu T, Takahashi M, Kikuchi A, Yoshinari T, Matsuzawa M, et al. Clinicopathological study of postoperative pulmonary metastasis of uterine cervical carcinomas. *J Obstet Gynaecol Res.* (1999) 25:245–9. doi: 10.1111/j.1447-0756.1999.tb01156.x

Conflict of Interest: The authors declare that the research was conducted in the absence of any commercial or financial relationships that could be construed as a potential conflict of interest.

Publisher's Note: All claims expressed in this article are solely those of the authors and do not necessarily represent those of their affiliated organizations, or those of the publisher, the editors and the reviewers. Any product that may be evaluated in this article, or claim that may be made by its manufacturer, is not guaranteed or endorsed by the publisher.

Copyright © 2022 Zheng, Xu and Wu. This is an open-access article distributed under the terms of the Creative Commons Attribution License (CC BY). The use, distribution or reproduction in other forums is permitted, provided the original author(s) and the copyright owner(s) are credited and that the original publication in this journal is cited, in accordance with accepted academic practice. No use, distribution or reproduction is permitted which does not comply with these terms.

frontiers | Frontiers in Neurology

ORIGINAL RESEARCH
published: 13 July 2022
doi: 10.3389/fneur.2022.874158

Detection of Abnormal Spontaneous Brain Activity Patterns in Patients With Orbital Fractures Using Fractional Amplitude of Low Frequency Fluctuation

*Min Kang[1†], YuXuan Gao[2†], LiJuan Zhang[1], RongBin Liang[1], QiuYu Li[1], HuiYe Shu[1], YiCong Pan[1], Ping Ying[1], SanHua Xu[1] and Shao Yi[1]**

[1] Department of Ophthalmology, The First Affiliated Hospital of Nanchang University, Jiangxi Branch of National Clinical Research Center for Ocular Disease, Nanchang, China, [2] Department of Orthopaedics, The Second Affiliated Hospital of Shanxi Medical University, Taiyuan, China

OPEN ACCESS

Edited by:
Yuzhen Xu,
Tongji University, China

Reviewed by:
Yan Zhang,
Jilin University, China
Zhenhao Zhang,
Nanjing Medical University, China

***Correspondence:**
Shao Yi
freebee99@163.com

[†]These authors have contributed equally to this work

Specialty section:
This article was submitted to Neurological Biomarkers, a section of the journal Frontiers in Neurology

Received: 11 February 2022
Accepted: 08 June 2022
Published: 13 July 2022

Citation:
Kang M, Gao Y, Zhang L, Liang R, Li Q, Shu H, Pan Y, Ying P, Xu S and Yi S (2022) Detection of Abnormal Spontaneous Brain Activity Patterns in Patients With Orbital Fractures Using Fractional Amplitude of Low Frequency Fluctuation. Front. Neurol. 13:874158. doi: 10.3389/fneur.2022.874158

Background: To date, no in-depth study has been conducted on the intrinsic pathological relationship between altered brain activity and related behavioral changes in patients with orbital fracture (OF).

Purpose: The present research aimed to explore the potential functional network cerebrum activities in patients with OF using resting state functional magnetic resonance imaging–fractional amplitude of low-frequency fluctuation (rsfMRI-fALFF). This technique can reveal dynamic functional changes in specific cerebrum areas.

Methods: Twenty patients with OF and 20 healthy controls (HCs) were included, closely matched in terms of gender, age, weight, and education level. To record spontaneous cerebral activity changes, the rsfMRI-fALFF tool was applied. Receiver operating characteristic (ROC) curves and Pearson's correlation analysis were used to analyze mean fALFF values in specific cerebrum regions and to explore changes of behavioral changes in patients with OF. The Hospital Depression and Anxiety scale was applied to reveal the relationship between emotional states and fALFF values of the right superior temporal gyrus in patients with OF.

Results: In comparison with HCs, significantly lower fALFF values were detected in the left anterior cingulate gyrus (LACG) and right superior temporal gyrus (RSTG) in patients with OF. ROC curve analysis showed excellent accuracy. The mean fALFF values of the RSTG negatively correlated with the depression score as well as the anxiety score.

Conclusion: The finding of abnormal spontaneous activities in cerebral regions may contribute to more comprehensive understanding of the potential neural network changes in patients with OF. The changes of fALFF value in patients with OF may help to gauge their emotional changes and clinical recovery levels.

Keywords: orbital fractures, fALFF, spontaneous brain activity, resting state, image

INTRODUCTION

The orbital bones are fragile, with no protective surround, making them vulnerable to orbital wall fracture (1), of which trauma is the main cause. Previous research (2) has shown that about half of orbital fractures are isolated and are usually limited to one orbital wall, the orbital floor, and medial wall being the most frequently occurring fracture sites (3). Orbital fractures mostly occur in children and young people, and are more common in males than females (4, 5). Chi et al. reviewed 733 cases of orbital fractures, among which three quarters were male (6). Conservative treatment is often used for small orbital fractures without displacement (7), while, for large displaced fractures, surgical intervention is necessary (8, 9). Orbital fractures may cause exophthalmos (10), enophthalmos (11), diplopia (12), entropion (13), subconjunctival hemorrhage (14), and even blindness (15). Therefore, early monitoring and termination of adverse disease progression in patients with OF are very important. The use of modern imaging technology to study the brain activity of patients with OF may be important as a means by which to improve understanding of the mechanism of potential pathological changes in this condition, and may, therefore, be beneficial to the management of complications. Previous studies have confirmed that the changes of spontaneous brain activity in related brain regions can be used as an indicator of disease progression. Therefore, we tried to explore the value of using modern imaging techniques to explore the value of spontaneous brain activity changes as a marker of disease progression in patients with orbital fractures.

Magnetic resonance imaging (MRI), as a widely used auxiliary imaging technology, was developed in the 1980s and provides us a preliminary understanding of the anatomical structure and operating mechanism of the brain (16, 17). Hemodynamic changes caused by neuronal activity can be qualitatively measured with the help of MRI technology, known as functional magnetic resonance imaging (fMRI). This approach has been used in a variety of studies on the mechanism and effects of spontaneous neuronal activity in the brain, and has been helpful in exploring the pathophysiological changes and pathogenesis of various diseases (18, 19). The fractional amplitude of low frequency fluctuation (fALFF), a resting state fMRI method, has provided an index for the evaluation of spontaneous neural activity, and its accuracy and sensitivity have been widely confirmed (16). To our knowledge, the present experiment was the first attempt to explore the connection between spontaneous brain activity and behavioral performance in patients with OF using the fALFF method as well as to explore the value of fALFF in evaluating the pathological changes and severity of OF.

SUBJECTS AND METHODS

Subjects

In total, 20 patients with OF (12 males, 8 females) and 20 matched healthy controls (HCs) participated in this research. The relevant inclusion criteria were: (1) with optic nerve injury; (2) with diplopia; (3) with orbital collapse; (4) with limited eye movement; (5) with surgical treatment; (6) no other ocular diseases (such as macular degeneration); (7) no brain disease (such as cerebral infarction); (8) no history of mental illness; (9) no organic diseases likely to affect MRI examination.

The 20 HCs (12 males, 8 females) were highly similar to the OF group in sex, age, weight, and education level. Our study met the ethical standards of the Medical Ethics Committee of the First Affiliated Hospital of Nanchang University as well as the principles of the Declaration of Helsinki. After materials, methods, purpose, and underlying risks of this experiment were explained, each participant signed a declaration of informed consents.

MRI Parameters

MRI scanning was conducted using a Trio 3-Tesla MR scanner (Trio; Siemens, Munich, Berlin, Germany) in all the participants. During the MRI scanning, other interference factors were excluded, and the subjects remained awake, breathing normally and with good vital signs. The whole-brainT1-weights were obtained with the application of the spoiled gradient-recalled echo sequence. Relevant corresponding parameter settings of structural images were as follows: echo time = 2.25 ms, repetition time = 1,800 ms, field of view = 250 × 250 mm^2, layer interval = 0.5 mm, flip angle = 90°, matrix = 256 × 256, thickness = 1 mm. Functional images (n = 240) were captured with the following settings: echo time = 30 ms, repetition time = 2,000 ms, field of view = 220 × 220 mm^2, flip angle = 90°, matrix = 64 × 64, thickness = 4 mm.

FMRI Data Processing

All data were pre-filtered using MRIcro (www.MRIcro.com) and then preprocessed the filtered data using SPM8 (https://www.fil.ion.ucl.ac.uk/spm/). In pre-filtering, the first 10 volumes were

TABLE 1 | Basic information of the participants in the study.

Condition	OF	HCs	t	*P*-value
Male/female	12/8	12/8	N/A	>0.99
Age (years)	51.21 ± 11.42	50.96 ± 10.82	0.242	0.871
Weight (kg)	68.32 ± 9.24	69.93 ± 9.54	0.165	0.902
Handedness	20R	20R	N/A	>0.99
Duration of (days)	11.61 ± 4.14	N/A	N/A	N/A
Best-corrected VA-left eye	0.40 ± 0.20	1.05 ± 0.20	−3.763	0.017
Best-corrected VA-right eye	0.45 ± 0.15	1.00 ± 0.15	−3.064	0.011
Latency (ms)-right of the VEP	118.16 ± 8.29	100.98 ± 6.17	3.554	0.017
Amplitudes(uv)-rightof the VEP	6.87 ± 2.42	14.16 ± 1.93	−6.643	0.009
Latency (ms)-left of the VEP	116.12 ± 7.11	101.21 ± 1.32	4.532	0.022
Amplitudes (uv)-left of the VEP	7.42 ± 2.73	16.74 ± 2.52	−5.732	0.012

Compare two groups with independent t-tests ($p < 0.05$). VA, visual acuity; N/A, not applicable; OF, orbital fractures; VEP, visual-evoked potential; HCs, healthy controls.

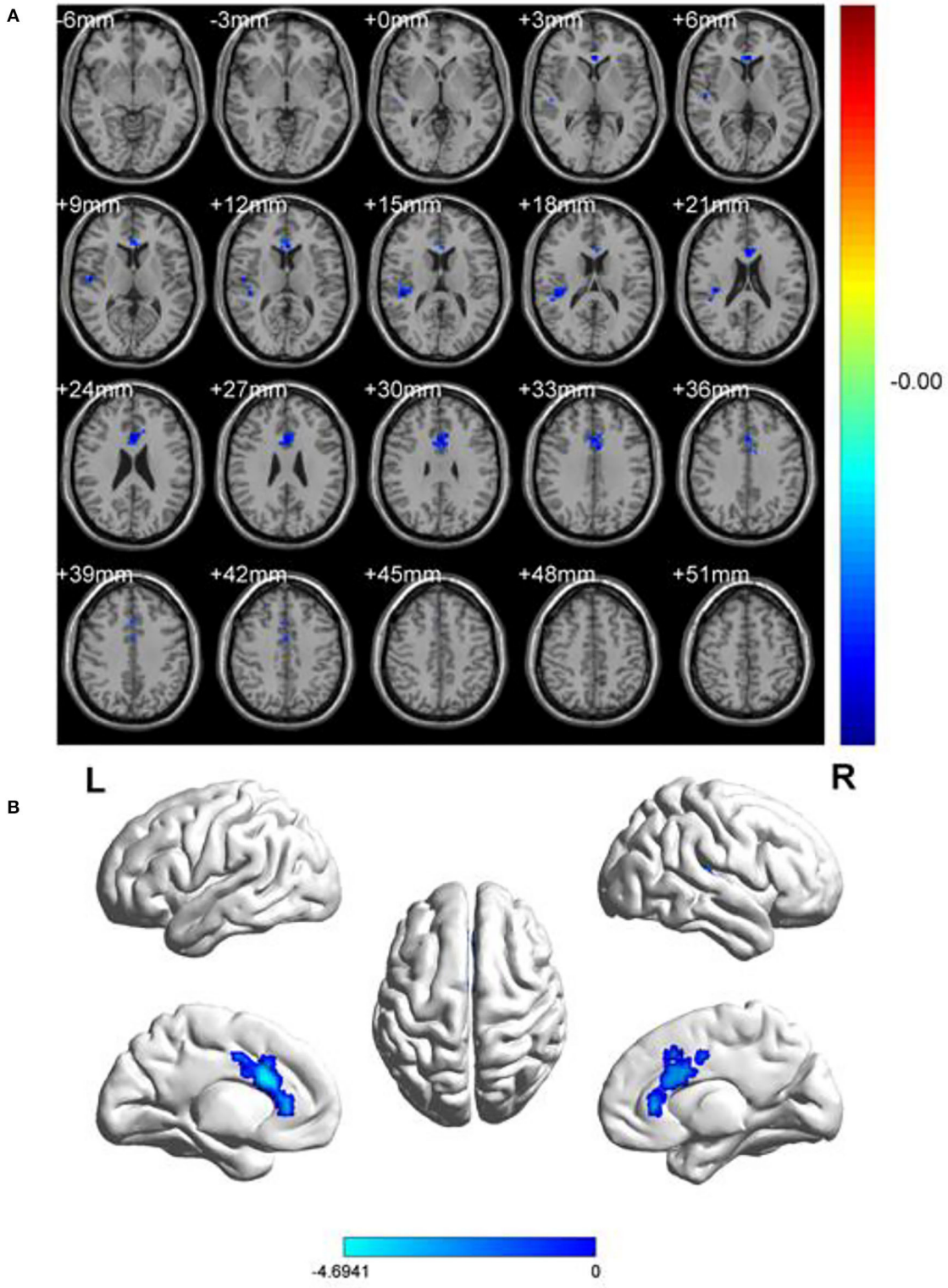

FIGURE 1 | Spontaneous brain activities of and healthy controls. **(A)** Different fALFF areas in patients with OF. **(B)** The blue areas represented lower fALFF values. L, left; R, right.

regarded as invalid data and excluded to ensure steady signals. The volumes were offset by no more than 2 mm in X, Y, or Z directions. On the basis of the standard echo planar imaging template, the images were resampled and normalized (with a standard setting of voxel size 3 × 3 × 3 mm, and were smoothed) to enhance the signal-to-noise ratio. This method has been described in detail previously (20).

FALFF Analysis

To calculate fALFF, a full-width Gaussian kernel (half maximum = 6 × 6 × 6 mm^3) was used to smooth the remaining 230 images. Band-pass (0.01–0.08 Hz) filtering was used to control for movement artifacts and low frequency drift. A fast Fourier transform (FFT) algorithm was used to obtain the signal power spectrum, and fAFLL was calculated as the ratio of the amplitude at each value in the low frequency band (0.01–0.08 Hz) to full-band (0–0.25 Hz) power amplitude.

TABLE 2 | Brain areas with significant differences in fALFF between two groups.

Brain areas	MNI coordinates			BA	Number of voxels	*T* value
	X	Y	Z			
Patient < HC						
Cingulum_Ant_L	0	18	27	31	172	−4.6941
Temporal_Sup_R	45	−30	15	82	82	−4.399

A P-value < 0.05 was significantly different for multiple comparisons using Gaussian random field theory (cluster 0.40 voxels, Alphasim corrected). HC, health control; MNI, Montreal Neurological Institute; BA, Brodmann area; Cingulum_Ant_L, left anterior cingulate gyrus; Temporal_Sup_R, right superior temporal gyrus.

Brain-Behavior Correlation Analysis

To look for any associations between brain activity and behavioral performance, brain regions of interest were determined based on fALFF values, and Pearson's correlation analysis was used to explore the linear relationship between activities in these regions and clinical manifestations.

Statistical Analysis

Using SPSS software version 20.0 (IBM Corp, Armonk, NY, USA), an independent sample *t*-test was conducted on the common clinical variables and demographic data of patients with OF and HCs using a 5% significance level. A two-sample *t*-test was used to compare the functional data. Based on Gaussian random field theory, the statistical threshold of the voxel level in multiple comparisons was set at $p < 0.05$. Gaussian random field theory was used to determine the significance of the functional image at the 5% level with a cluster size > 40 voxels. Using the mean fALFF in various cerebral regions of HCs and patients with OF, the areas under the ROC curves (AUC) were obtained. In addition, Pearson correlation analysis was used to look for associations between the mean fALFF values in multiple cerebrum regions and characteristics of clinical behavior in patients with OF.

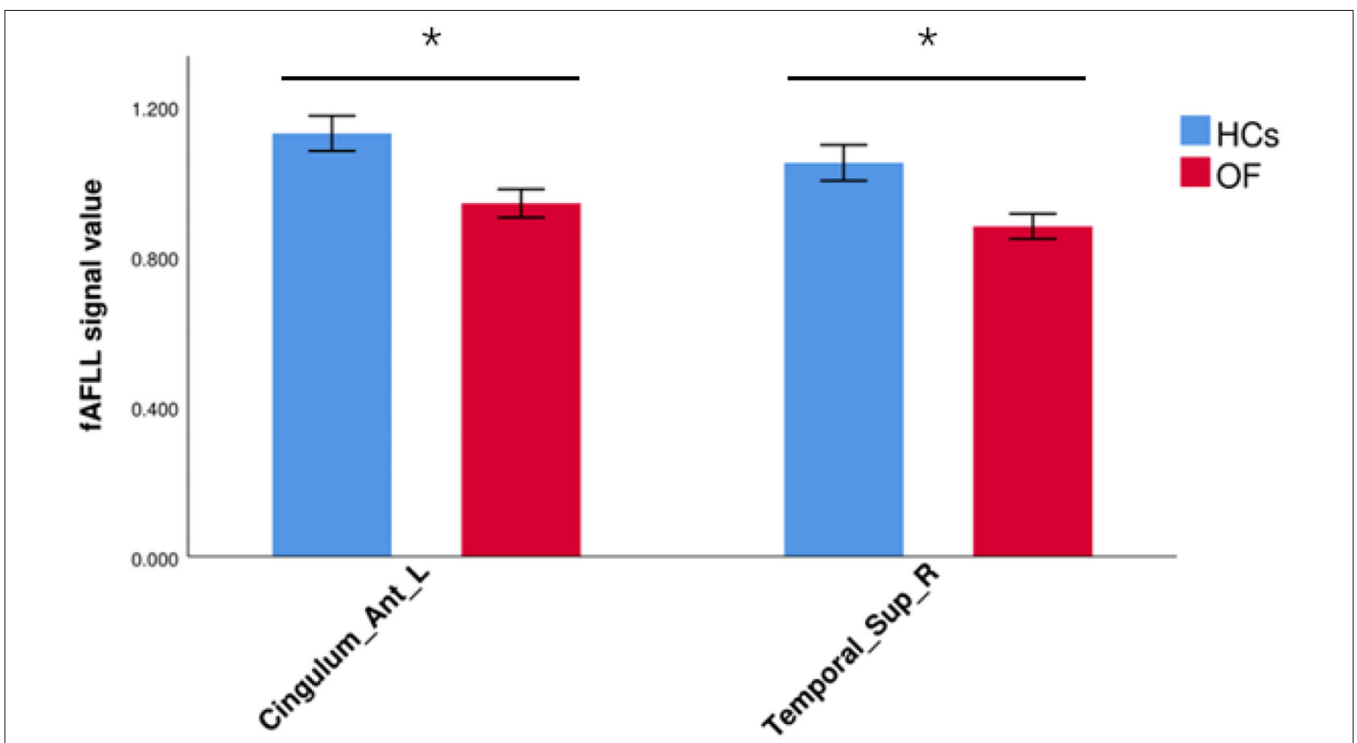

FIGURE 2 | The average fALFF values in OF and HC groups. Cingulum_Ant_L, left anterior cingulate gyrus; Temporal_Sup_R, right superior temporal gyrus; fALFF, fractional amplitude of low-frequency fluctuation; OF, orbital fractures; HC, healthy control. "*" $p < 0.05$.

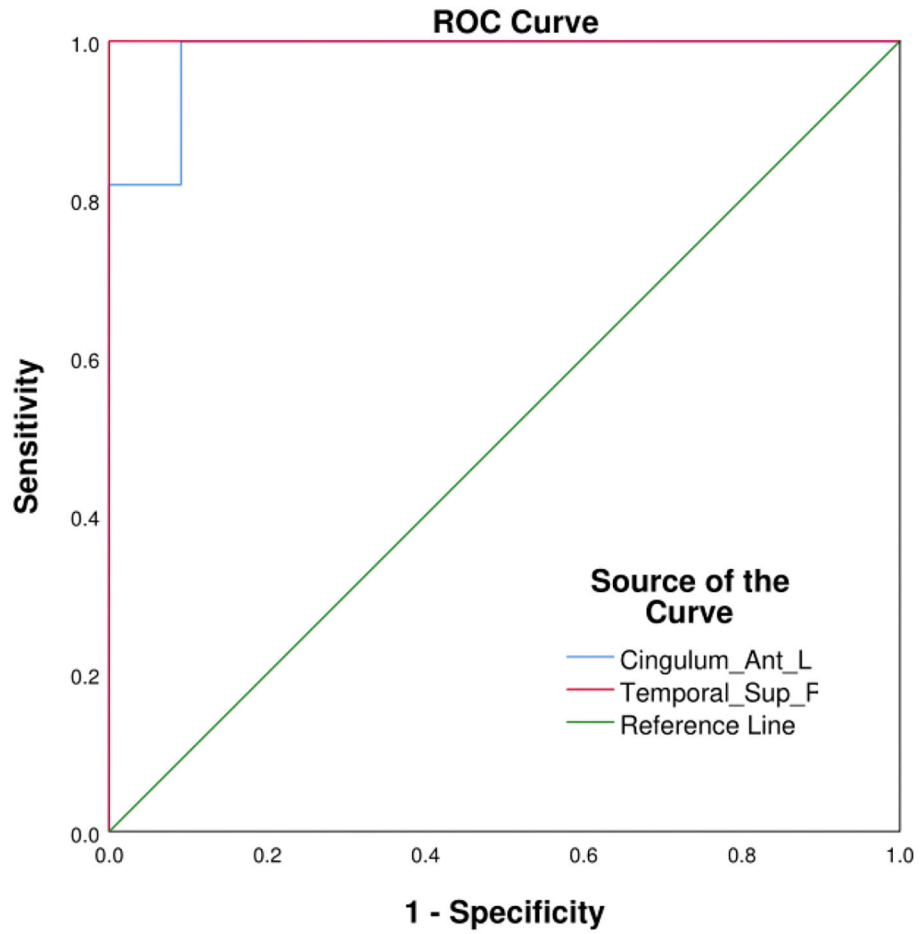

FIGURE 3 | ROC curve analysis of the average fALFF values in different cerebrum areas. AUCs: Cingulum_Ant_L: 0.983, Temporal_Sup_R: 1.000. Cingulum_Ant_L, left anterior cingulate gyrus; Temporal_Sup_R, right superior temporal gyrus; AUC, area under the curve; ROC, receiver operating characteristic.

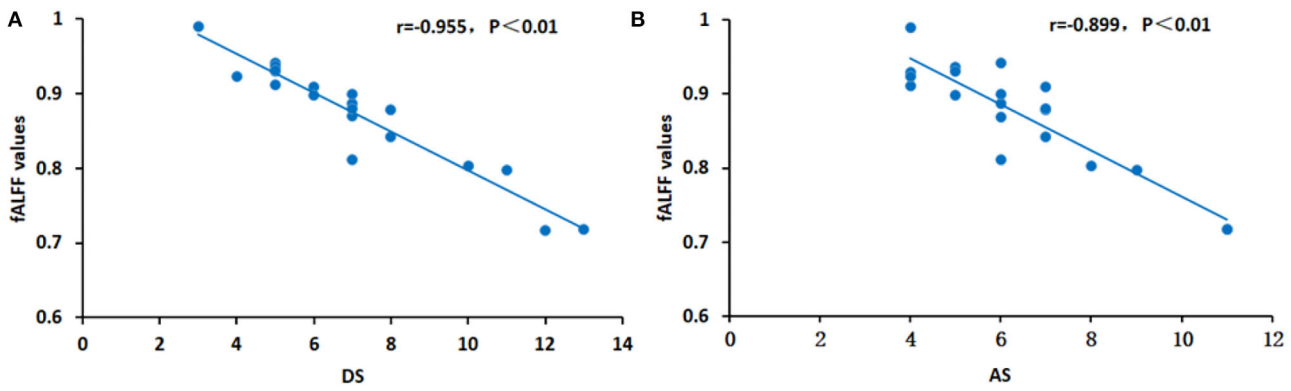

FIGURE 4 | Correlations between the average fALFF values and clinical characteristics in the RSTG. In the RSTG, the DS ($r = -0.955$, $p < 0.01$) **(A)** and AS ($r = -0.899$, $p < 0.01$) **(B)** are both represented by a negative relationship with the fALFF values. fALFF, fractional amplitude of low-frequency fluctuation; DS, depression score; AS, anxiety score; RSTG, right superior temporal gyrus.

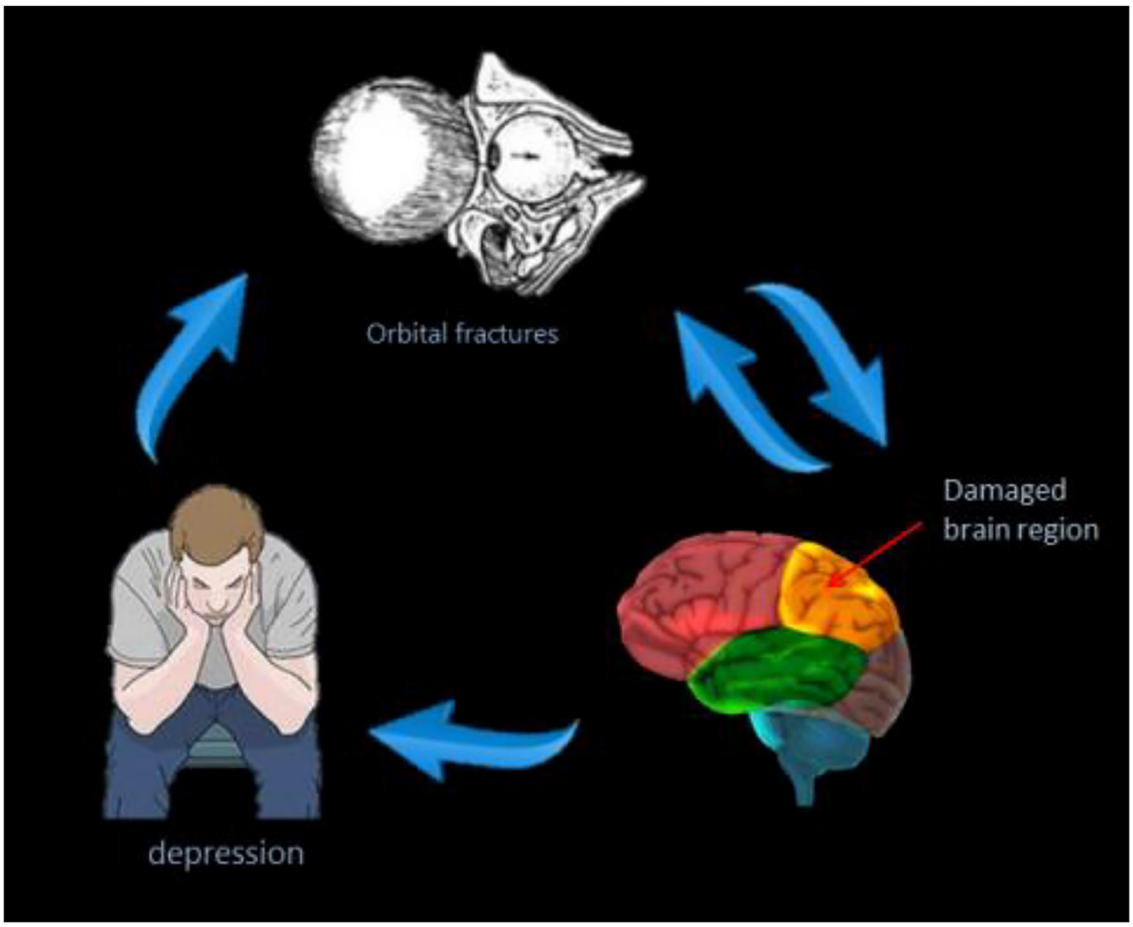

FIGURE 5 | The correlations between average fALFF signal values and clinical manifestation of patients with OF. The patients with OF have lower fALFF values, and they are more likely to develop depressive symptoms. OF, orbital fractures.

RESULTS

Demographics and Visual Measurements

No significant differences were found between groups in terms of gender ($p > 0.99$), weight ($p = 0.902$), or age (OF, 51.21 ± 11.42; HC, 50.96 ± 10.82; $p = 0.871$). However, best corrected monocular visual parameters were significantly different between groups, as follows: visual acuities ($p = 0.017$, left, and 0.011, right eye), visual-evoked potential (VEP) latencies ($p = 0.022$, left, and 0.017, right eye), and amplitudes ($p = 0.012$, left, and 0.009, right eye) (**Table 1**).

Differences in FALFF

In comparison with HCs, the patients with OF showed significant lower fALFF values in the left anterior cingulate gyrus (LACG) and right superior temporal gyrus (RSTG) (**Figure 1**, **Table 2**). The mean fAFLL values are shown in **Figure 2**.

Receiver Operating Characteristic Curves

ROC curves were used to visualize the comparison between average fALFF values of patients with OF and HCs, and the areas under the curves (AUCs) were used as indicators of diagnostic accuracy. Using this approach, AUCs of the LATG and RSTG were found to be 0.983 and 1.000, respectively (**Figure 3**).

Correlation Analysis

In patients with OF, significant correlations were found between fALFF values in the RSTG and depression scores (negative correlation: $r = -0.955$, $p < 0.01$) and anxiety scores (negative correlation: $r = -0.899$, $p < 0.01$) (**Figure 4**).

DISCUSSION

To our knowledge, the ALFF method has not previously been used to study the potential relationship between brain activity changes and clinical manifestations in patients with OF. This study aimed to explore the cerebral neural changes after orbital fracture using the fALFF technique (**Figure 5**). The study found significantly lower fALFF values in the LACG and the RSTG in patients with OF (**Figure 6**). In previous studies, the fALFF method has been applied to a series of ophthalmological diseases, including normal-tension glaucoma (20), monocular blindness (21), retinal vein occlusion (22), diabetic retinopathy,

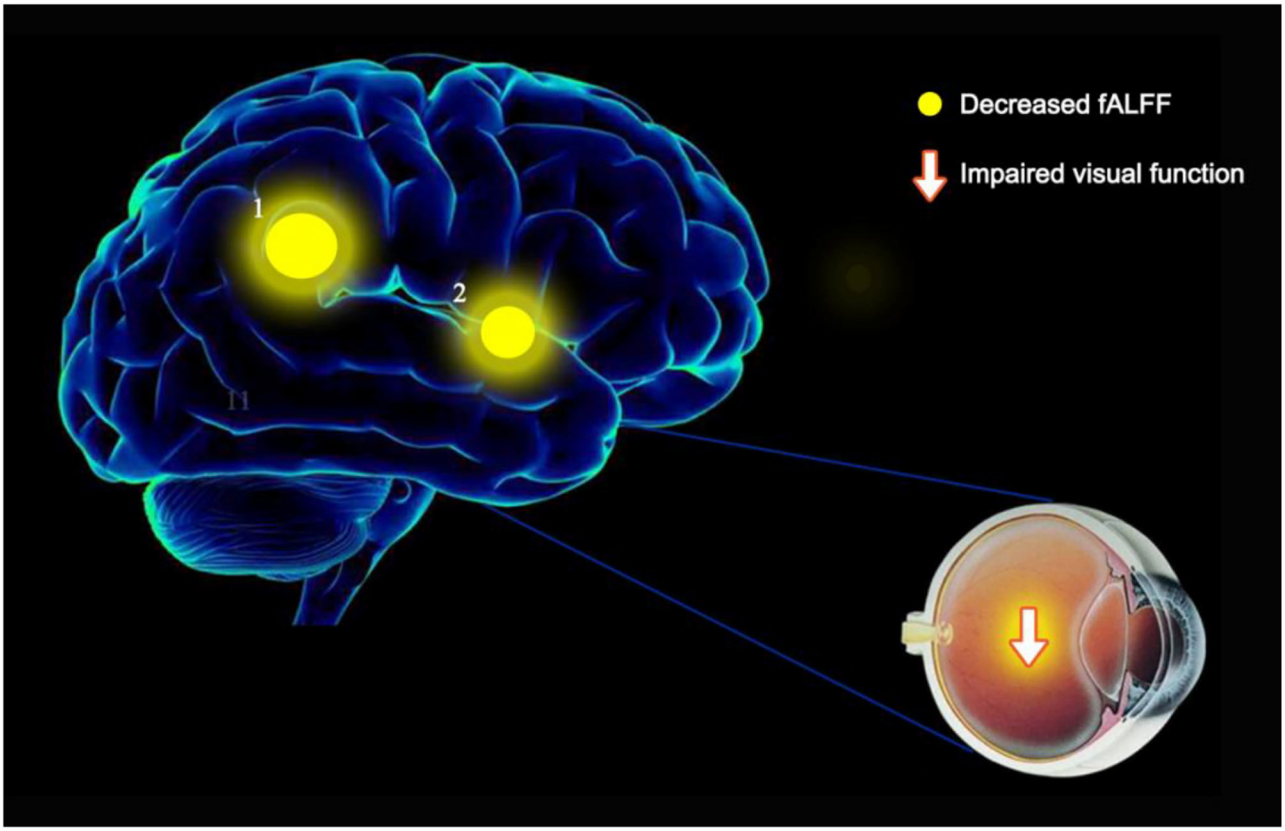

FIGURE 6 | fALFF results of cerebral activity in the OF group. The fALFF values of the cerebral areas in the OF group were in the following: 1- left anterior cingulate gyrus (t = −4.6941), 2 - right superior temporal gyrus (t = −4.399). The intensity, as well as the frequency of brain activity, is reflected by the size of spots.

TABLE 3 | The fALFF method applied in ophthalmological diseases.

Author	Year	Disease	Brain areas	
			Increased fALFF values	Decreased fALFF values
Li et al. (20)	2020	Normal-tension glaucoma	_	RAG, RACL
Fang et al. (21)	2020	Monocular blindness	LP, RPI, LPI	LCA
Tong et al. (22)	2020	Retinal vein occlusion	LC, RC, RB, LI	RC, RT
Wang et al. (23)	2021	Primary angle-closure glaucoma	BSFG	LC, LMTGRMTG, RPG

fALFF, fractional amplitude of low-frequency fluctuation; RAG, right angular gyrus; LP, left precuneus; LMTG, left middle temporal gyrus; LCA, left anterior cingulate; RPI, right inferior parietal lobe; LPI, left inferior parietal lobe; RMTG, right middle temporal gyrus; LC, left cerebellum; RC, right cerebellum; RB, right brainstem; RC, right calcarinesulcus; BSFG, bilateral superior frontal gyrus; LIG, left lingual gyrus; RPG, right precentral gyrus; RT, right thalamus; LI, left insula; RACL, right anterior cuneiform lobe.

and nephropathy (23) (**Table 3**), demonstrating its potential for clinical application.

The anterior cingulate gyrus (ACG) is a functional area associated with many physiological functions, is located in the medial brain and passes longitudinally through the parietal lobe, and its main roles are in memory (24), action – outcome learning (25–27), emotion, and reward-related processing (28). The research of Hornak et al. (29) showed that, in some cases, the ACG plays an important part in voice and facial expression recognition, while Lane et al. (30–32) studied anterior cingulate injury in subjective emotional experience, and found that ventral ACG and Brodmann's area 9 may be activated during mood fluctuations. Based on the functions of the anterior cingulate gyrus, some researchers have explored its diagnostic value in Parkinson's disease (33), depression (34), and acute and chronic pain (35). In addition, a previous study has found that the prefrontal cingulate gyrus can respond to visual stimuli (36). In the present study, given the reduced visual responses in patients with OF, the results may indicate a compensatory mechanism for vision loss in patients with OF.

The superior temporal gyrus (STG) is a functional area of the brain located in the temporal lobe, closely related to emotional

TABLE 4 | Brain areas of altered fALFF values and anticipated results.

Brain regions	Experimental result	Brain function	Anticipated results
Cingulum_Ant_L	OF < HCs	Memory, action–outcome learning, emotion and reward-related processing	Behavioral disorders, memory impairment, depression,
Temporal_Sup_R	OF < HCs	Emotional and speech processing, curative effect index	Mental disorders, speech disorder, reflecting treatment effect

Cingulum_Ant_L, left anterior cingulate gyrus; Temporal_Sup_R, right superior temporal gyrus; OF, orbital fractures; HCs, healthy controls.

and speech processing (37, 38). The STG is a component of the default mode network, which is inhibited during brain activity and excited during rest. Liu et al. (39) used the rsMRI-fALFF method to study the STG in depression. They found that the lower fALFF values of STG correlated greater reductions on the Hamilton rating scale for depression, and inferred that STG neural changes were closely related to the effect of early treatment for depression. In addition, Wang et al. (40) measured functional connectivity density in STG and found that abnormal connectivity is negatively correlated with the treatment effect. In the present experiment, the fALFF value of the right STG in patients with OF was significantly lower than that in healthy controls, and we speculate that this decrease may be a compensatory mechanism for the recovery of brain function in patients with OF. The results suggest that the fALFF value may be used as a reliable index to gauge therapeutic effects of clinical treatment. Moreover, it was discovered that, in the patients with OF, fALFF values in the RSTG were negatively correlated with anxiety and depression scores, which may indicate a self-regulation mechanism in this brain area, with brain function being temporarily inhibited (**Table 4**).

This study has some limitations; one of which is the relatively small sample size, and the other is that the sample source was limited and not completely matched. Third, compared with the simple use of VEP, the use of pattern electro retino grams (PERGs) and pattern visual-evoked potentials (PVEPs) two checks can be more rigorous explanation of the problem. Therefore, future research should use larger and more closely matched samples to further clarify the neural changes in patients with orbital fractures, and to provide a more intuitive clinical efficacy index for treatment. In conclusion, this study has demonstrated that patients with OF have reduced fALFF values in specific cerebrum areas, indicating changes in spontaneous brain activity. Further research on the mechanism underpinning brain activity changes in patients with OF may be helpful to advance understanding of this condition.

DATA AVAILABILITY STATEMENT

The original contributions presented in the study are included in the article/supplementary material, further inquiries can be directed to the corresponding author/s.

ETHICS STATEMENT

The studies involving human participants were reviewed and approved by Ethics Committee of Nanchang University. The patients/participants provided their written informed consent to participate in this study.

AUTHOR CONTRIBUTIONS

YXG, SHX, PY, YCP, HYS, LJZ, RBL, and QYL: Data collation, data analysis, and paper writing and revision. SY: The funding and design of the project and the guidance of the article. All authors contributed to the article and approved the submitted version.

REFERENCES

1. Ramponi DR, Astorino T, Bessetti-Barrett CR. Orbital Floor Fractures. *Adv Emerg Nurs J.* (2017) 39:240–7. doi: 10.1097/TME.0000000000000163
2. Dubois L, Steenen SA, Gooris PJ, Mourits MP, Becking AG. Controversies in orbital reconstruction–I. Defect-driven orbital reconstruction: a systematic review. *Int J Oral Maxillofac Surg.* (2015) 44:308–15. doi: 10.1016/j.ijom.2014.12.002
3. Joseph JM, Glavas IP. Orbital fractures: a review. *Clin Ophthalmol.* (2011) 5:95–100. doi: 10.2147/OPTH.S14972
4. Koenen L, Waseem M. *Orbital Floor Fracture.* StatPearls: StatPearls Internet Treasure Island (FL). (2020).
5. Phan LT, Jordan PW, McCulley TJ. Orbital trapdoor fractures. *Saudi J Ophthalmol.* (2012) 26:277–82. doi: 10.1016/j.sjopt.2012.05.008
6. Cope MR, Moos KF, Speculand B. Does diplopia persist after blow-out fractures of the orbital floor in children? *Br J Oral Maxillofac Surg.* (1999) 37:46–51. doi: 10.1054/bjom.1998.0382
7. Bolling JP, Wesley RE. Conservative treatment of orbital roof blow-in fracture. *Ann Ophthalmol.* (1987) 19:75–6.
8. Sullivan WG. Displaced orbital roof fractures: presentation and treatment. *Plast Reconstr Surg.* (1991) 87:657–61. doi: 10.1097/00006534-199104000-00008
9. Raveh J. Surgical techniques in orbital roof fractures: early treatment and results. *J Craniomaxillofac Surg.* (1995) 23:332–3. doi: 10.1016/S1010-5182(05)80166-0
10. Ha AY, Mangham W, Frommer SA, Choi D, Klinge P, Taylor HO, et al. Interdisciplinary management of minimally displaced orbital roof fractures: delayed pulsatile exophthalmos and orbital encephalocele. *Craniomaxillofac Trauma Reconstr.* (2017) 10:11–5. doi: 10.1055/s-0036-1584395
11. Koryczan P, Zapała J, Gontarz M, Wyszyńska-Pawelec G. Surgical treatment of enophthalmos in children and adolescents with pure orbital blowout fracture. *J Oral Sci.* (2020). doi: 10.2334/josnusd.20-0371
12. Roselló EG, Granado AM, Garcia MA, Martí SJ, Sala GL, Mármol BB, et al. Facial fractures: classification and highlights for a useful report. *Insights Imaging.* (2020) 11:49. doi: 10.1186/s13244-020-00847-w
13. Harish KM, Tulasidas G, Arthanari B, Bhagat JA. Aesthetic outcome of a case of orbital floor fracture treated using a retroseptal transconjunctival approach. *Cureus.* (2019) 11:e4063. doi: 10.7759/cureus.4063

14. Terrill SB, You H, Eiseman H, Rauser ME. Review of ocular injuries in patients with orbital wall fractures: a 5-year retrospective analysis. *Clin Ophthalmol.* (2020) 14:2837–42. doi: 10.2147/OPTH.S274567
15. Scolozzi P. Orbital fractures: enigmatic and insidious entities. *Rev Med Suisse.* (2020) 16:1281–6. doi: 10.53738/REVMED.2020.16.699.1281
16. Shi WQ, Tang LY, Lin Q, Li B, Jiang N, Zhu PW, et al. Altered spontaneous brain activity patterns in diabetic patients with vitreous hemorrhage using amplitude of lowfrequency fluctuation: a restingstate fMRI study. *Mol Med Rep.* (2020) 22:2291–9. doi: 10.3892/mmr.2020.11294
17. Yu YJ, Liang RB, Yang QC, Ge QM Li QY, Li B, et al. Altered spontaneous brain activity patterns in patients after lasik surgery using amplitude of low-frequency fluctuation: a resting-state functional MRI study. *Neuropsychiatr Dis Treat.* (2020) 16:1907–17. doi: 10.2147/NDT.S252850
18. Dai XJ, Liu CL, Zhou RL, Gong HH, Wu B, Gao L, et al. Long-term total sleep deprivation decreases the default spontaneous activity and connectivity pattern in healthy male subjects: a resting-state fMRI study. *Neuropsychiatr Dis Treat.* (2015) 11:761–72. doi: 10.2147/NDT.S78335
19. Bekiesinska-Figatowska M, Helwich E, Rutkowska M, Stankiewicz J, Terczyńska I. Magnetic resonance imaging of neonates in the magnetic resonance compatible incubator. *Arch Med Sci.* (2016) 12:1064–70. doi: 10.5114/aoms.2016.61913
20. Li HL, Chou XM, Liang Y, Pan T, Zhou Q, Pei CG, et al. Use of rsfMRI-fALFF for the detection of changes in brain activity in patients with normal-tension glaucoma. *Acta Radiol.* (2020) 62:414–22. doi: 10.1177/0284185120926901
21. Fang JW Yu YJ, Tang LY, Chen SY, Zhang MY, Sun T, et al. Abnormal fractional amplitude of low-frequency fluctuation changes in patients with monocular blindness: a functional magnetic resonance imaging (MRI) study. *Med Sci Monit.* (2020) 26:e926224. doi: 10.12659/MSM.926224
22. Tong Y, Huang X, Gao Q, Qi CX, Shen Y. Fractional amplitude of low-frequency fluctuations in retinal vein occlusion: a resting-state fMRI study. *Zhonghua Yan Ke Za Zhi.* (2020) 56:266–71. doi: 10.3760/cma.j.cn112142-20200904-00452
23. Tang ZH, Liu TT, Sun XH, Wu LJ, Xiao ZB. Altered spontaneous neuronal activity and functional connectivity pattern in primary angle-closure glaucoma: a resting-state fMRI study. *Neurol Sci.* (2021) 42:243–51. doi: 10.1007/s10072-020-04577-1
24. Rolls ET. The storage and recall of memories in the hippocampo-cortical system. *Cell Tissue Res.* (2018) 373:577–604. doi: 10.1007/s00441-017-2744-3
25. Rushworth MF, Kolling N, Sallet J, Mars RB. Valuation and decision-making in frontal cortex: one or many serial or parallel systems? *Curr Opin Neurobiol.* (2012) 22:946–55. doi: 10.1016/j.conb.2012.04.011
26. Kolling N, Wittmann MK, Behrens TE, Boorman ED, Mars RB, Rushworth MF. Value, search, persistence and model updating in anterior cingulate cortex. *Nat Neurosci.* (2016) 19:1280–5. doi: 10.1038/nn.4382
27. Rolls ET. The orbitofrontal cortex and emotion in health and disease, including depression. *Neuropsychologia.* (2019) 128:14–43. doi: 10.1016/j.neuropsychologia.2017.09.021
28. Rolls ET. The cingulate cortex and limbic systems for emotion, action, and memory. *Brain Struct Funct.* (2019) 224:3001–18. doi: 10.1007/s00429-019-01945-2
29. Hornak J, Bramham J, Rolls ET, Morris RG, O'Doherty J, Bullock PR, et al. Changes in emotion after circumscribed surgical lesions of the orbitofrontal and cingulate cortices. *Brain.* (2003) 126:1691–712. doi: 10.1093/brain/awg168
30. Lane RD, Reiman EM, Ahern GL, Schwartz GE, Davidson RJ. Neuroanatomical correlates of happiness, sadness, and disgust. *Am J Psychiatry.* (1997) 154:926–33. doi: 10.1176/ajp.154.7.926
31. Lane RD, Reiman EM, Bradley MM, Lang PJ, Ahern GL, Davidson RJ, et al. Neuroanatomical correlates of pleasant and unpleasant emotion. *Neuropsychologia.* (1997) 35:1437–44. doi: 10.1016/S0028-3932(97)00070-5
32. Lane RD, Frewen P, Neufeld RW, Densmore M, Stevens T, Lanius R. Neural correlates of levels of emotional awareness. Evidence of an interaction between emotion and attention in the anterior cingulate cortex. *J Cogn Neurosci.* (1998) 10:525–35. doi: 10.1162/089892998562924
33. Vogt BA. Cingulate cortex in Parkinson's disease. *Handb Clin Neurol.* (2019) 166:253–66. doi: 10.1016/B978-0-444-64196-0.00013-3
34. Godlewska BR, Browning M, Norbury R, Igoumenou A, Cowen PJ, Harmer CJ. Predicting treatment response in depression: the role of anterior cingulate cortex. *Int J Neuropsychopharmacol.* (2018) 21:988–96. doi: 10.1093/ijnp/pyy069
35. Bliss TV, Collingridge GL, Kaang BK, Zhuo M. Synaptic plasticity in the anterior cingulate cortex in acute and chronic pain. *Nat Rev Neurosci.* (2016) 17:485–96. doi: 10.1038/nrn.2016.68
36. Sidorov MS, Kim H, Rougie M, Williams B, Siegel JJ, Gavornik JP, et al. Visual sequences drive experience-dependent plasticity in mouse anterior cingulate cortex. *Cell Rep.* (2020) 32:108152. doi: 10.1016/j.celrep.2020.108152
37. Yi HG, Leonard MK, Chang EF. The encoding of speech sounds in the superior temporal gyrus. *Neuron.* (2019) 102:1096–110. doi: 10.1016/j.neuron.2019.04.023
38. Takahashi T, Yücel M, Lorenzetti V, Walterfang M, Kawasaki Y, Whittle S, et al. An MRI study of the superior temporal subregions in patients with current and past major depression. *Prog Neuropsychopharmacol Biol Psychiatry.* (2010) 34:98–103. doi: 10.1016/j.pnpbp.2009.10.005
39. Liu X, Hou ZH, Yin YY, Xie CM, Zhang HS, Zhang HX, et al. Dopamine multilocus genetic profile, spontaneous activity of left superior temporal gyrus, and early therapeutic effect in major depressive disorder. *Front Psychiatry.* (2020) 11:591407. doi: 10.3389/fpsyt.2020.591407
40. Wang J, Wei Q, Yuan XR, Jiang XY, Xu JP, Zhou XQ, et al. Local functional connectivity density is closely associated with the response of electroconvulsive therapy in major depressive disorder. *J Affect Disord.* (2018) 225:658–64. doi: 10.1016/j.jad.2017.09.001

Conflict of Interest: The authors declare that the research was conducted in the absence of any commercial or financial relationships that could be construed as a potential conflict of interest.

Publisher's Note: All claims expressed in this article are solely those of the authors and do not necessarily represent those of their affiliated organizations, or those of the publisher, the editors and the reviewers. Any product that may be evaluated in this article, or claim that may be made by its manufacturer, is not guaranteed or endorsed by the publisher.

Copyright © 2022 Kang, Gao, Zhang, Liang, Li, Shu, Pan, Ying, Xu and Yi. This is an open-access article distributed under the terms of the Creative Commons Attribution License (CC BY). The use, distribution or reproduction in other forums is permitted, provided the original author(s) and the copyright owner(s) are credited and that the original publication in this journal is cited, in accordance with accepted academic practice. No use, distribution or reproduction is permitted which does not comply with these terms.

frontiers | Frontiers in Neurology

ORIGINAL RESEARCH
published: 14 July 2022
doi: 10.3389/fneur.2022.930635

Absence of Susceptibility Vessel Sign in Patients With Malignancy-Related Acute Ischemic Stroke Treated With Mechanical Thrombectomy

Morin Beyeler[1,2†], Nebiyat F. Belachew[3,4†], Moritz Kielkopf[1], Enrique B. Aleman[4], Alejandro Xavier León Betancourt[1], Kotryna Genceviciute[1], Christoph Kurmann[3], Lorenz Grunder[3], Barbara Birner[1], Thomas R. Meinel[1], Adrian Scutelnic[1], Philipp Bücke[1], David J. Seiffge[1], Tomas Dobrocky[3], Eike I. Piechowiak[3], Sara Pilgram-Pastor[3], Heinrich P. Mattle[1], Pasquale Mordasini[3], Marcel Arnold[1], Urs Fischer[1,5], Thomas Pabst[6], Jan Gralla[3], Martin D. Berger[6], Simon Jung[1†] and Johannes Kaesmacher[3*†]*

[1] Department of Neurology, Inselspital, Bern University Hospital, University of Bern, Bern, Switzerland, [2] Graduate School for Health Sciences, University of Bern, Bern, Switzerland, [3] Institute for Diagnostic and Interventional Neuroradiology, Inselspital, Bern University Hospital, University of Bern, Bern, Switzerland, [4] Department of Neuroradiology, Faculty of Medicine, Medical Center – University of Freiburg, University of Freiburg, Freiburg, Germany, [5] Department of Neurology, University Hospital of Basel, University of Basel, Basel, Switzerland, [6] Department of Medical Oncology, Inselspital, Bern University Hospital, University of Bern, Bern, Switzerland

OPEN ACCESS

Edited by:
Wen-Jun Tu,
Chinese Academy of Medical Sciences and Peking Union Medical College, China

Reviewed by:
Yang-Ha Hwang,
Kyungpook National University, South Korea
Neil Haranhalli,
Montefiore Medical Center, United States

***Correspondence:**
Morin Beyeler
morin.beyeler@insel.ch
Johannes Kaesmacher
johannes.kaesmacher@insel.ch

† These authors have contributed equally to this work

Specialty section:
This article was submitted to Neurological Biomarkers, a section of the journal Frontiers in Neurology

Received: 28 April 2022
Accepted: 15 June 2022
Published: 14 July 2022

Citation:
Beyeler M, Belachew NF, Kielkopf M, Aleman EB, León Betancourt AX, Genceviciute K, Kurmann C, Grunder L, Birner B, Meinel TR, Scutelnic A, Bücke P, Seiffge DJ, Dobrocky T, Piechowiak EI, Pilgram-Pastor S, Mattle HP, Mordasini P, Arnold M, Fischer U, Pabst T, Gralla J, Berger MD, Jung S and Kaesmacher J (2022) Absence of Susceptibility Vessel Sign in Patients With Malignancy-Related Acute Ischemic Stroke Treated With Mechanical Thrombectomy. Front. Neurol. 13:930635. doi: 10.3389/fneur.2022.930635

Background and Purpose: Clots rich in platelets and fibrin retrieved from patients with acute ischemic stroke (AIS) have been shown to be independently associated with the absence of the susceptibility vessel sign (SVS) on MRI and active malignancy. This study analyzed the association of SVS and the presence of active malignancy in patients with AIS who underwent mechanical thrombectomy (MT).

Methods: This single-center, retrospective, and cross-sectional study included consecutive patients with AIS with admission MRI treated with MT between January 2010 and December 2018. SVS status was evaluated on susceptibility-weighted imaging. Adjusted odds ratios (aORs) were calculated to determine the association between absent SVS and the presence of active or occult malignancy. The performance of predictive models incorporating and excluding SVS status was compared using areas under the receiver operating characteristics curve (auROC).

Results: Of 577 patients with AIS with assessable SVS status, 40 (6.9%) had a documented active malignancy and 72 (12.5%) showed no SVS. The absence of SVS was associated with active malignancy (aOR 4.85, 95% CI 1.94–12.11) or occult malignancy (aOR 11.42, 95% CI 2.36–55.20). The auROC of predictive models, including demographics and common malignancy biomarkers, was higher but not significant (0.85 vs. 0.81, $p = 0.07$) when SVS status was included.

Conclusion: Absence of SVS on admission MRI of patients with AIS undergoing MT is associated with malignancy, regardless of whether known or occult. Therefore, the SVS might be helpful in detecting paraneoplastic coagulation disorders and occult malignancy in patients with AIS.

Keywords: susceptibility vessel sign, malignancy-related stroke, biomarkers, paraneoplastic coagulation disorders, ischemic stroke, mechanical thrombectomy, thrombus composition/occult malignancy

INTRODUCTION

Patients with malignancy-related strokes are more likely to suffer more severe or fatal or recurrent strokes compared to other patients with stroke (1–3). Identifying patients with malignancy in the acute stroke setting would allow targeted treatment and secondary prevention and might improve outcome (4, 5). Thus, easily accessible biomarkers associated with malignancy are needed. Clots in patients with stroke with active malignancy retrieved *via* mechanical thrombectomy (MT) have been shown to contain more fibrin and platelets than clots from other patients (4, 6). A noninvasive, *in situ* characterization of clots may be achieved through appropriate imaging. Whereas computed tomography (CT) merely provides information on the density of the clot, magnetic resonance imaging (MRI) may allow more sophisticated characterization of their composition. The susceptibility vessel sign (SVS) identified on T2* gradient recalled echo imaging (T2* GRE) and susceptibility-weighted imaging (SWI) in brain MRI may serve this purpose (7, 8). The underlying stroke etiology influences the clot composition and, consequently, the SVS status on cerebral imaging (9). Thrombi from cardioembolic stroke and large artery atherosclerosis stroke (LAA) have a high proportion of erythrocytes in their histopathological composition (10, 11). Interestingly, a study also described a high proportion of platelets in thrombi from patients with LAA (12). Currently, only cardioembolic stroke has been associated with the presence of SVS (13, 14). In opposition, clots due to hypercoagulation states (a.o. disseminated intravascular coagulation by underlying malignancy) tend to be composed of more fibrin and platelet and seem to be more associated with absence of SVS (11, 15). Based on the current data, we hypothesized that the absence of SVS, which may indicate platelet and fibrin-rich thrombi, may also be associated with active malignancy. The aim of this study was to test this hypothesis and analyze models that include the SVS to predict the likelihood of active malignancy in patients with AIS.

METHODS

Study Cohort

This retrospective study evaluated all consecutive patients with stroke treated with MT at our comprehensive stroke center between January 1, 2010, and December 31, 2018. Inclusion criteria were as follows: (1) Ischemic stroke with at least one intracranial symptomatic occlusion on angiography, (2) MRI and SWI performed at admission, (3) SVS status assessable, and (4) MT performed. Patients who received intravenous thrombolytics before blood for laboratory analyses was drawn were excluded from some subanalyses. The local ethics committee approved the study in accordance with Swiss law (reference ID: 2019-00547, Kantonale Ethikkomission Bern). Study approval was restricted to patients treated with MT.

Abbreviations: AIS, acute ischemic stroke; CRP, C-reactive protein; DWI, diffusion-weighted imaging; ESUS, embolic stroke of undetermined source; INR, international normalized ratio; LAA, large artery atherosclerosis stroke; LR, likelihood ratio; MT, mechanical thrombectomy; NPV, negative predictive value; PPV, positive predictive value; SVS, susceptibility vessel sign; SWI, susceptibility-weighted imaging.

Definition of Active Malignancy

Active malignancy was defined according to the Haemostasis and Malignancy Scientific and Standardization Committee of the International Society on Thrombosis and Haemostasis (16, 17). Malignancy diagnosed within 1 year after the index stroke was defined as occult malignancy. However, occult malignancy was also considered active at the time of stroke and thus represented a subset of the active malignancy group (18–20). Patients with focal nonmelanoma skin cancer were excluded due to the nonsystemic nature of the disease and its low risk of metastatic spread (21). Patients receiving secondary prophylactic hormone therapy after breast cancer were considered in complete remission and without active malignancy (22, 23).

Imaging Analysis

Imaging was performed on a 1.5 T or 3 T MR imaging scanner (1.5 T: Magnetom Avanto or Magnetom Aera; 3T: Magnetom Verio; Siemens). Magnetom Avanto 1.5 T SWI and 1.5 T Magnetom Aera SWI were performed with the following parameters: TR, 49 ms; TE, 40 ms; flip angle, 15.0°; section thickness, 1.6, 1.8, or 2.0 mm; and intersection gap, 0 mm. Magnetom Verio 3T SWI was performed with the following parameters: TR, 27 ms; TE, 20 ms; flip angle, 15.0°; section thickness, 2.0 mm; and intersection gap, 0 mm. The detailed method used to determine the presence of SVS in the cohort analyzed in this article was described by N. Belachew et al. in a previous publication (24). To summarize, SVS status was assessed retrospectively by two independent neuroradiologists (N.F.B. and E.B.A.). Both raters were blinded to clinical information and outcome, and were not involved in any patient treatment. Regardless of its diameter, SVS was determined to be present if a distinct signal loss corresponding to an occluded and symptomatic intracranial artery could be identified (**Figures 1A,B**), for which there was no alternative explanation (i.e., neighboring vein, petechial hemorrhage, or microcalcification in the neighboring parenchyma). If no such signal loss could be identified even though a symptomatic vessel occlusion was seen on angiography, SVS was determined to be absent (**Figures 1C,D**). Interrater reliability regarding SVS evaluation for the study cohort analyzed in this article has been assessed and published in a previous study showing very good correlation (Cohen's $\kappa = 0.873$, $p < 0.001$) (24).

Data Collection

Demographics and baseline stroke characteristics were extracted from the local stroke registry. They included gender, age at admission, prestroke independence (defined as a modified Rankin Scale $\leq$ 2), blood pressure at admission, prior anticoagulation/antiplatelet therapy, prior statin therapy, cardiovascular risk factors (such as hypertension, diabetes, hyperlipidemia, smoking), National Institutes of Health Stroke Scale on admission, time between symptom-onset/last-seen-well and admission, intravenous thrombolytics before MT, and site of occlusion. Two neurology fellows (M.B. and M.K.), both blinded

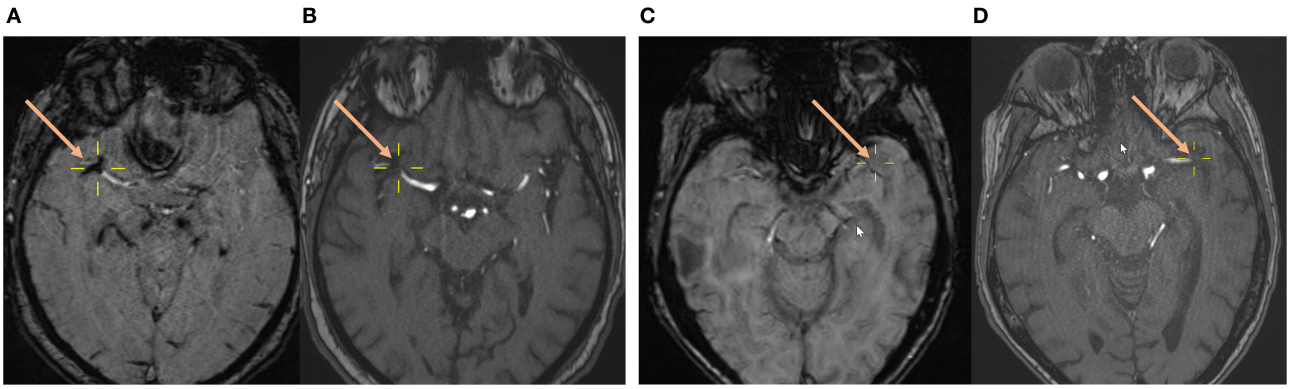

FIGURE 1 | Assessment of the susceptibility vessel sign status on baseline brain MRI. **(A,B)** A 74-year-old male patient with AIS and visible SVS as a circumscribed signal loss on the SWI **(A)** with complete occlusion of the right MCA (M1 segment) on arterial TOF **(B)**. **(C,D)** A 77-year-old female patient with AIS and absent SVS on the SWI **(C)** despite complete occlusion of the left MCA (M1 segment) on arterial TOF **(D)**. *Yellow crosshairs* and *salmon arrows* center, respectively, point to the proximal part of the vessel occlusion on SWI and TOF. AIS, acute ischemic stroke; MCA, middle cerebral artery; SVS, susceptibility vessel sign; SWI, susceptibility-weighted imaging; TOF, time-of-flight angiography.

to the SVS status, retrospectively identified active malignancy (known or occult at the time of stroke) from histological and clinical reports present in the clinical information system. After patients' identification, malignancy localization, histological type, metastatic state, and time metrics related to the malignancy diagnosis and treatment were extracted. The presence of multiterritory infarcts and the assigned stroke etiology at discharge, defined by the Trial of ORG 10172 in Acute Stroke Treatment (TOAST) classification, was also extracted from neuroradiological reports and discharge letters (25). According to the TOAST classification, strokes associated with patent foramen ovale were classified as cardioembolic stroke. A subdivision between intracranial atherosclerosis and artery-to-artery embolism was made for LAA. Embolic stroke of undetermined source (ESUS) was assumed when nonlacunar ischemic stroke occurred in patients in which another underlying stroke etiology in line with the definition of the "NAVIGATE ESUS" trial could not be determined (26). The following laboratory values at admission were extracted from the hospital's clinical information system: D-dimer, fibrinogen, hemoglobin (Hb), C-reactive protein (CRP), leukocytes, thrombocytes, international normalized ratio (INR), thrombin time, and activated partial thromboplastin clotting time.

Statistical Analysis

Baseline characteristics were compared using Fisher's exact test for categorical variables and Mann–Whitney *U*-test for continuous variables. Descriptive statistics were reported as number and percentage for categorical variables, and median and interquartile range (25–75%) for continuous variables. A logistic transformation was applied if the distribution of continuous values was skewed. The association between the SVS status and active malignancy was assessed using simple and multivariable logistic regression models. Results are displayed as odds ratios (ORs) and adjusted odds ratios (aORs). The association of SVS status with occult malignancies was assessed in a sensitivity analysis. All models were adjusted for demographic characteristics (such as gender and age at admission) and malignancy biomarkers known to be associated with malignancy-related stroke such as ESUS, multiterritory infarcts, D-dimer, leukocytes, CRP, INR, and Hb. The predictive value of SVS status was evaluated by assessing sensitivity, specificity, positive predictive value (PPV), negative predictive value (NPV), positive likelihood ratio (LR+), and negative likelihood ratio (LR–). The performance of predictive models, including and excluding SVS status, was assessed by calculating areas under the receiver operating characteristics curve (auROC). The auROCs were cross-validated using bootstrapping, whereas they were compared using the DeLong test. All statistical analyses were performed using the Stata 16 and R software (version 3.6.0, R Core Team). The current STROBE (Strengthening the Reporting of Observational Studies in Epidemiology) checklist for cross-sectional studies was used to report this study.

RESULTS

Study Population

Between January 2010 and December 2018, 1,317 patients with AIS were treated with MT at our stroke center. As already described by Belachew et al. and shown in **Supplementary Figure I** (study flowchart), 577 patients had SWI with assessable SVS status available at admission and met the inclusion criteria (24). Evidence of active malignancy at the time of stroke was found in 40 patients (6.93%), of which a subset of 9 patients (1.56%) had occult malignancy. Active malignancy characteristics are summarized in **Supplementary Figure II**. A total of eight patients (1.39%) were excluded from subgroup analysis of blood markers as they had received intravenous thrombolytics before blood was drawn for further analysis.

Baseline Characteristics

The characteristics of patients with and without active malignancy are summarized in **Supplementary Table I**. SVS was absent in 12.5% of all patients ($n = 72/577$). Of the patients

with active malignancy, SVS was absent in 37.5% ($n = 15/40$), while only 4.3% (57/537, $p < 0.001$) of patients without active malignancy lacked the SVS. Patients with active malignancy were more likely to be functionally dependent before the index stroke, had lower diastolic blood pressure (<90 mmHg), and more often showed anterior and more distal middle cerebral artery occlusions. Intravenous thrombolysis before MT was less often administered to patients with stroke with active malignancy compared to patients without malignancy. ESUS and multiterritory infarcts were more frequent in the group with active malignancy. Active malignancy was associated with elevated D-dimer, low Hb, elevated CRP, elevated leukocytes, and higher INR.

Association of Active Malignancy With Absence of SVS and Other Biomarkers

Simple logistic regression demonstrated absent SVS to be associated with active malignancy, multiterritory infarcts, elevated D-dimer, ESUS, elevated CRP, elevated leukocytes, and low Hb. All simple regression analyses are summarized in **Supplementary Figure III**. Multivariable regression analyses showed significant associations of active malignancy and absent SVS, multiterritory infarcts, elevated D-dimer, elevated leukocytes, and low Hb. Results of multivariable regression analyses, including ORs and 95% confidence intervals, are summarized in **Figure 2**.

Diagnostic Value of SVS Status in Identifying Active Malignancy

Absence of SVS alone predicted active malignancy as follows: sensitivity 20.83%, specificity 95.05%, PPV 37.5%, NPV 89.38%, LR+ 4.21, and LR– 0.83. Predictive models incorporating age at admission, gender, and variables associated with active malignancy in the multivariate logistic regression as well as SVS status were tested. The auROC of the model, including SVS status, was 0.85 (95% CI 0.78–0.92, **Figure 3A**). The internal cross-validation using bootstrapping demonstrated no variation of auROC and 95% CI. If SVS status was excluded, the auROC of the model was 0.81 (95% CI 0.72–0.90, **Figure 3B**) while the internal cross-validation showed an auROC of 0.82 (95% CI 0.68–0.90). The DeLong test did not find a significant difference between the two models ($p = 0.07$).

Subgroup analyses using the same covariates as in the multivariate logistic regression showed that the absence of SVS remained associated with occult malignancy alone (aOR 11.42, 95% CI 2.36–55.20, $p = 0.002$) when patients with active malignancy diagnosed before the stroke were excluded. Absence of SVS predicted occult malignancy as follows: sensitivity 8.06%, specificity 99.17%, PPV 55.50%, NPV 89.38%, LR+ 9.76, and LR– 0.93.

Subgroup Analyses According to the Underlying Stroke Etiology

According to the assigned stroke etiology, the point estimate of the association between absence of SVS and the presence of active malignancy differed slightly (**Supplementary Figure IV**). However, there was no significant heterogeneity of the association between absence of SVS and active malignancy ($p = 0.24$). After excluding patients with LAA ($n = 74$, two without SVS), the aOR for the association decreased from 4.89 (95% CI 1.94–12.11, **Figure 2**) to aOR 3.9 (95% CI 1.42–10.50). Excluding only cases where intracranial stenosis was the stroke etiology ($n = 11$, one without SVS) the aOR decreased to 4.77 (95% CI 1.91–11.89).

DISCUSSION

The main findings of this study are as follows: (1) absence of SVS is associated with both active and occult malignancy in patients with ischemic stroke treated with MT; (2) absence of SVS in admission MRI as imaging biomarker may increase the performance of predictive models for active malignancy in patients with AIS; and (3) the association between the absence of SVS and active malignancy seems not to be influenced by the assigned etiology at discharge. Approximately 8% of patients with acute stroke have a concomitant active malignancy (known or occult) at the time of stroke (4, 27). Identifying the malignancy as the potential cause of the stroke in these patients is essential to guide secondary prevention, which includes therapeutic anticoagulation with low-molecular-weight heparin (4, 5). Strokes with concomitant malignancy are associated with nonspecific biomarkers such as elevated D-dimer, elevated CRP, elevated fibrinogen, elevated lactate dehydrogenase, low Hb, undetermined stroke etiology (especially ESUS), and multiterritorial infarcts in brain imaging (3, 4, 18, 28). These biomarkers may help to detect a malignancy-related coagulation disorder. However, proving the causality between active malignancy and an ischemic stroke event remains difficult. Considering the potential clinical ramifications, the search for further biomarkers that may improve the likelihood of detecting malignancy-related coagulopathy and occult malignancy at the time of stroke is warranted. Finelli et al. were the first to describe multiterritory infarcts seen on diffusion-weighted imaging as an independent imaging biomarker for malignancy-related stroke (29). Guo et al. demonstrated a specificity of 0.65 and a sensitivity of 0.92 for the prediction of occult malignancy in patients with stroke with undetermined stroke etiology if two or more vascular territories are affected (30). The results of our study add to the current evidence regarding the advantage of brain MRI in patients with malignancy-related stroke.

Susceptibility-weighted sequences such as T2* GRE and SWI are central to the MRI-based acute stroke workup (31, 32). SWI sequences provide reliable information on a potential hemorrhagic transformation but may also outline the occluded vessel depending on clot composition (9, 13, 15, 33, 34). Among others, Zhang et al. reported SVS to be present in 90% of cardioembolic strokes ($n = 35/39$), 53.5% of large-artery atherosclerosis strokes ($n = 23/43$), and 75.9% of strokes with undetermined etiology ($n = 22/29$), indicating that SVS status may differ depending on stroke etiology (13, 33, 34). However, a recent meta-analysis confirmed only the association between SVS and cardioembolic stroke (14). Histopathological

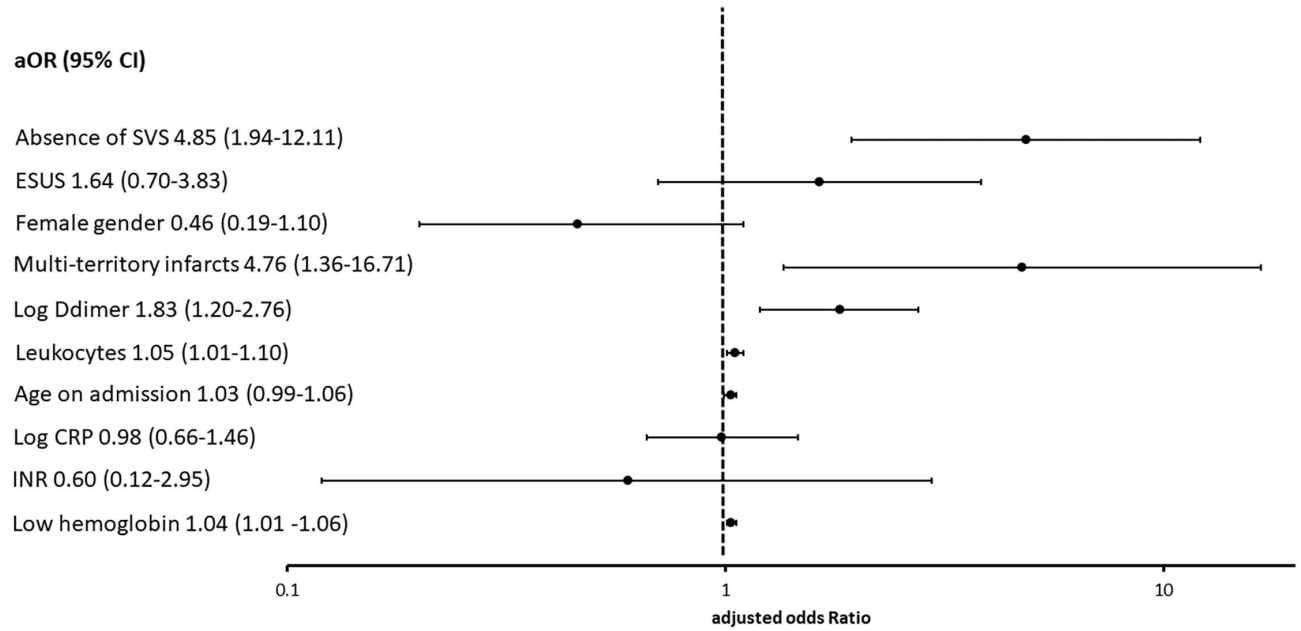

FIGURE 2 | Association between active malignancy, neuroimaging, and blood biomarkers in the multivariable logistic regression. According to the primary goal of this study and previous evidence, adjusted odds ratios (aOR) and their 95% confidence intervals (95% CI) for the association between active malignancy and preselected biomarkers are summarized in this figure. Absence of SVS showed the strongest association with the presence of active malignancy, followed by multiterritory infarcts. CRP, C-reactive protein; ESUS, embolic stroke of undetermined source; INR, international normalized ratio; SVS, susceptibility vessel sign.

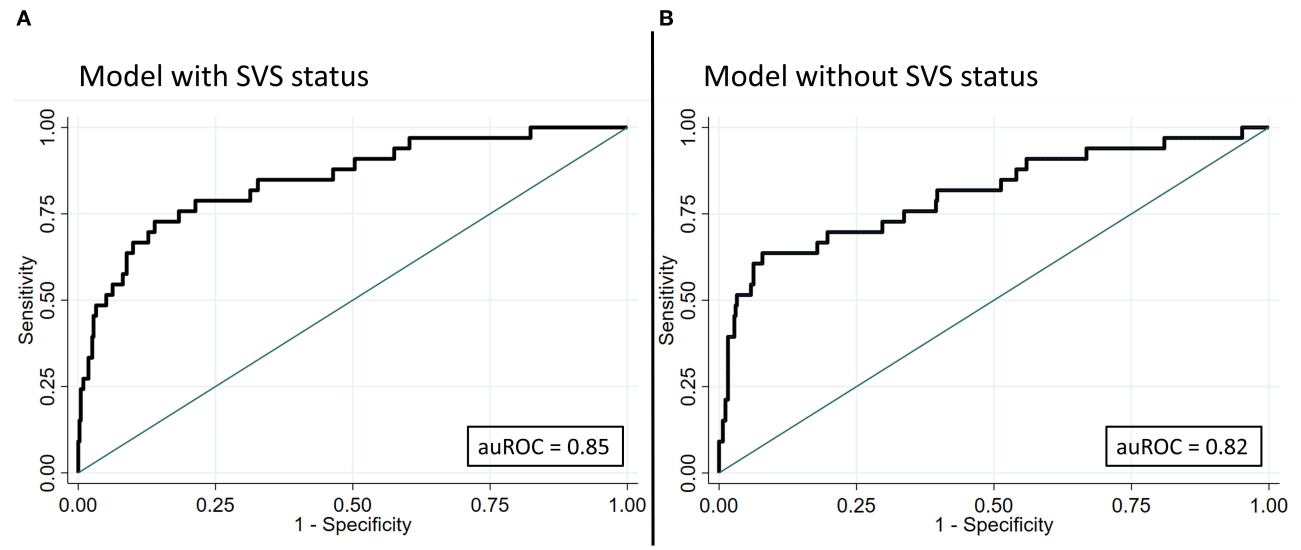

FIGURE 3 | Comparison of predictive models for active malignancy with and without SVS status. The covariables used for the predictive models were age at admission and gender and variables associated with active malignancy in the multivariable logistic regression (ESUS, multiterritory infarcts, D-dimer, Hb, leukocytes). The auROC of the model with SVS status was 0.85 (95% CI 0.78–0.92, **A**). The internal cross-validation demonstrated no variation of the auROC and 95% CI. In the absence of the SVS status, the auROC of the model was 0.81 (95% CI 0.72–0.90, **B**), the internal cross-validation showed an auROC of 0.82 (95% CI 0.68–0.90). The DeLong test did not show a significant difference between the two models ($p = 0.074$). auROC, area under the receiver operating characteristics curve; CRP, C-reactive protein; ESUS, embolic stroke of undetermined source; Hb, hemoglobin; SVS, susceptibility vessel sign.

analyses after MT have shown that thrombi with a cardioembolic genesis predominantly contain erythrocytes (35). Platelet and fibrin-rich thrombi have been shown to be independently associated with malignancy-related stroke, hypercoagulation, and the absence of SVS (4, 6, 11, 15, 36). Our study adds to this knowledge. It demonstrates that absent SVS is associated with active malignancy in AIS treated with MT, irrespective of whether known or unknown at time of stroke. Although the association between the absence of SVS and the presence of malignancy differed slightly by the assigned stroke etiology (**Supplementary Figure IV**), the lack of interaction did not allow any conclusions regarding the role of the assigned etiology on the relation between the absence of SVS and the presence of active malignancy. The exclusion of LAA did not increase the association between the absence of SVS and malignancy in our study population, thus suggesting no association between absent SVS and LAA (13). Predictive models for diagnostic workup are generally developed to help in decision-making for further investigations in complex clinical situations (37, 38). However, this study did not aim to conceptualize a new predictive model for active malignancy but rather to validate the SVS status as an additional biomarker. Although the difference in the auROCs only tended to be greater with SVS included, a more sophisticated SVS evaluation (i.e., quantitative susceptibility mapping) may increase predictive performance (39, 40). As MRI may not always be available or practicable in the acute stroke setting, density, which has also been shown to correlate with erythrocyte content, may be used in patients imaged with CT (33). Furthermore, the macroscopic characteristics of clots retrieved with MT ("white" indicating fibrin-rich thrombi vs. "red-black" indicating erythrocyte-rich thrombi) may provide additional hints about their composition (36, 41). In the same context, Bourcier et al. recently demonstrated an association between "red-black" clots and the presence of SVS, strengthening the evidence that SVS status is a reliable biomarker for their composition (15).

LIMITATIONS

This study has several limitations. First, this was a monocentric and retrospective study, which may limit generalizability of results. Second, in accordance with the terms of the ethical approval, we included only patients who underwent MT. Further studies are needed to confirm our findings in a more general stroke population. Third, although the percentage of malignancies is consistent with studies in the literature, the small number of active or occult malignancies may reduce the statistical power of the results obtained. Additionally, the small number of malignancies precluded accurate subgroups analyses regarding assigned stroke etiology. Because the underlying etiology may influence the thrombus composition, further studies with more patients are needed. Fourth, the high rate of SVS reported in this study may result from a selection bias due to a specific subpopulation of patients with stroke eligible for thrombectomy and the inhomogeneous use of 1.5 and 3 T MRI. Fifth, concomitant microscopic analysis of the retrieved thrombi would have provided a more robust validation of the study hypothesis, assuming that the absence of SVS is a surrogate marker of platelet and fibrin-rich thrombi in case of malignancy-related stroke. Sixth, the comparison of predictive models is limited by the lack of an external validation group and by power considerations comparing auROC of different models according to the number of active malignancies. Finally, levels of lactate dehydrogenase, a well-known marker for the presence of active malignancy, were not available (3).

CONCLUSION

Absent SVS on baseline MRI is associated with active malignancy in patients with AIS undergoing MT, regardless of whether the malignancy is known or unknown at the time of stroke. Using SVS as surrogate marker for clot composition may increase the chances of detecting occult malignancy in patients with AIS, which could be helpful both for the treatment of the malignancy and secondary stroke prevention and thus may lead to better outcomes.

DATA AVAILABILITY STATEMENT

Data are available upon reasonable request, access requests should be directed to the authors.

ETHICS STATEMENT

The studies involving human participants were reviewed and approved by Kantonale Ethikkomission Bern. Written informed consent for participation was not required for this study in accordance with the national legislation and the institutional requirements.

AUTHOR CONTRIBUTIONS

MB contributed to conception and design, data acquisition, analysis and interpretation of data, and writing of the publication. NB contributed to conception and design, data acquisition and writing of the publication. MK and EA contributed to data acquisition and critical revision of the manuscript for important intellectual content. KG and BB contributed to conception and design, and critical revision of the manuscript for important intellectual content. SJ and JK contributed to conception and design, critical revision of the publication for important intellectual content, and supervision. AL, CK, LG, TM, AS, PB, DS, TD, EP, SP-P, HM, PM, MA, UF, TP, JG, and MDB contributed to interpretation of data and critical revision of the manuscript for important intellectual content. All authors contributed to the article and approved the submitted version.

SUPPLEMENTARY MATERIAL

The Supplementary Material and the STROBE checklist for this article can be found online at: https://www.frontiersin.org/articles/10.3389/fneur.2022.930635/full#supplementary-material

REFERENCES

1. Navi B, Sherman C, Genova R, Ryna M, Kelsey L, Lemoss N, et al. Mechanisms of ischemic stroke in patients with cancer : a prospective study. *Ann Neurol.* (2021) 2021:159–69. doi: 10.1002/ana.26129
2. Kneihsl M, Enzinger C, Wünsch G, Khalil M, Culea V, Urbanic-Purkart T, et al. Poor short-term outcome in patients with ischaemic stroke and active cancer. *J Neurol.* (2016) 263:150–6. doi: 10.1007/s00415-015-7954-6
3. Dardiotis E, Aloizou AM, Markoula S, Siokas V, Tsarouhas K, Tzanakakis G, et al. Cancer-associated stroke: pathophysiology, detection and management (Review). *Int J Oncol.* (2019) 54:779–96. doi: 10.3892/ijo.2019.4669
4. Bang OY, Chung JW, Lee MJ, Seo WK, Kim GM, Ahn MJ. Cancer-related stroke: an emerging subtype of ischemic stroke with unique pathomechanisms. *J Stroke.* (2020) 22:1–10. doi: 10.5853/jos.2019.02278
5. Jang H, Lee JJ, Lee MJ, Ryoo S, Yoon CH, Kim G, et al. Comparison of enoxaparin and warfarin for secondary prevention of cancer-associated stroke. *J Oncol.* (2015) 2015:6. doi: 10.1155/2015/502089
6. Fu CH, Chen CH, Lin YH, Lee CW, Tsai L, Tang SC, et al. Fibrin and platelet-rich composition in retrieved thrombi hallmarks stroke with active cancer. *Stroke.* (2020) 51:3723–7. doi: 10.1161/STROKEAHA.120.032069
7. Allibert R, Billon Grand C, Vuillier F, Cattin F, Muzard E, Biondi A, et al. Advantages of susceptibility-weighted magnetic resonance sequences in the visualization of intravascular thrombi in acute ischemic stroke. *Int J Stroke.* (2014) 9:980–4. doi: 10.1111/ijs.12373
8. Cho KH, Kim JS, Kwon SU, Cho AH, Kang DW. Significance of susceptibility vessel sign on T2*-weighted gradient echo imaging for identification of stroke subtypes. *Stroke.* (2005) 36:2379–83. doi: 10.1161/01.STR.0000185932.73486.7a
9. Kang DW, Jeong HG, Kim DY, Yang W, Lee SH. Prediction of stroke subtype and recanalization using susceptibility vessel sign on susceptibility-weighted magnetic resonance imaging. *Stroke.* (2017) 48:1554–9. doi: 10.1161/STROKEAHA.116.016217
10. Niesten JM, Van Der Schaaf IC, Van Dam L, Vink A, Vos JA, Schonewille WJ, et al. Histopathologic composition of cerebral thrombi of acute stroke patients is correlated with stroke subtype and thrombus attenuation. *PLoS ONE.* (2014) 9:12–4. doi: 10.1371/journal.pone.0088882
11. Brinjikji W, Nogueira RG, Kvamme P, Layton KF, Almandoz JE, Hanel R, et al. Association between clot composition and stroke origin in mechanical thrombectomy patients: analysis of the stroke thromboembolism registry of imaging and pathology. *J Neurointerv Surg.* (2021) 13:594–8. doi: 10.1136/neurintsurg-2020-017167
12. Fitzgerald S, Dai D, Wang S, Douglas A, Kadirvel R, Layton K, et al. Platelet-rich emboli in cerebral large vessel occlusion are associated with a large artery atherosclerosis source. *Stroke.* (2019) 50:1907–10. doi: 10.1161/STROKEAHA.118.024543
13. Zhang R, Zhou Y, Liu C, Zhang M, Yan S, Liebeskind D, et al. Overestimation of susceptibility vessel sign: a predictive marker of stroke cause. *Stroke.* (2017) 48:1993–6. doi: 10.1161/STROKEAHA.117.016727
14. Liu M, Li L, Li G. The different clinical value of susceptibility vessel sign in acute ischemic stroke patients under different interventional therapy: a systematic review and meta-analysis. *J Clin Neurosci.* (2019) 62:72–9. doi: 10.1016/j.jocn.2019.01.002
15. Bourcier R, Duchmann Z, Sgreccia A, Desal H, Carità G, Desilles JP, et al. Diagnostic performances of the susceptibility vessel sign on MRI for the prediction of macroscopic thrombi features in acute ischemic stroke. *J Stroke Cerebrovasc Dis.* (2020) 29:105245. doi: 10.1016/j.jstrokecerebrovasdis.2020.105245
16. Frere C, Crichi B, Lejeune M, Spano JP, Janus N. Are patients with active cancer and those with history of cancer carrying the same risks of recurrent VTE and bleeding while on anticoagulants? *Cancers.* (2020) 12:1–9. doi: 10.3390/cancers12040917
17. Khorana AA, Noble S, Lee AYY, Soff G, Meyer G, O'Connell C, et al. Role of direct oral anticoagulants in the treatment of cancer-associated venous thromboembolism: guidance from the SSC of the ISTH. *J Thromb Haemost.* (2018) 16:1891–4. doi: 10.1111/jth.14219
18. Navi BB, Iadecola C. Ischemic stroke in cancer patients: a review of an underappreciated pathology. *Ann Neurol.* (2018) 83:873–83. doi: 10.1002/ana.25227
19. Cocho D, Gendre J, Boltes A, Espinosa J, Ricciardi A, Pons J, et al. Predictors of occult cancer in acute ischemic stroke patients. *J Stroke Cerebrovasc Dis.* (2015) 24:1324–8. doi: 10.1016/j.jstrokecerebrovasdis.2015.02.006
20. Erichsen R, Sværke C, Sørensen HT, Sandler RS, Baron JA. Risk of colorectal cancer in patients with acute myocardial infarction and stroke: a nationwide cohort study. *Cancer Epidemiol Biomarkers Prev.* (2013) 22:1994–9. doi: 10.1158/1055-9965.EPI-13-0444
21. Samarasinghe V, Madan V. Nonmelanoma skin cancer. *J Cutan Aesthet Surg.* (2012) 5:3. doi: 10.4103/0974-2077.94323
22. Burstein HJ, Lacchetti C, Anderson H, Buchholz T, Davidson N, Gelmon K, et al. Adjuvant endocrine therapy for women with hormone receptor–positive breast cancer: ASCO clinical practice guideline focused update. *J Clin Oncol.* (2019) 37:423–38. doi: 10.1200/JCO.18.01160
23. Glassman D, Hignett S, Rehman S, Linforth R, Salhab M. Adjuvant endocrine therapy for hormone-positive breast cancer, focusing on ovarian suppression and extended treatment: an update. *Anticancer Res.* (2017) 37:5329–41. doi: 10.21873/anticanres.11959
24. Belachew NF, Aleman EB, Mordasini P, Aleman E, Meinel T, Hakim A, et al. Susceptibility vessel sign in patients undergoing mechanical thrombectomy for acute ischemic stroke. *AJNR Am J Neuroradiol.* (2021) 42:1949–55. doi: 10.3174/ajnr.A7281
25. Adams HP, Bendixen BH, Kappelle LJ, Biller J, Love B, Gordon D, et al. Classification of subtype of acute ischemic stroke. *Stroke.* (1993) 24:35–41. doi: 10.1161/01.STR.24.1.35
26. Hart RG, Sharma M, Mundl H, Shoamanesh A, Kasner S, Berkowitz S, et al. Rivaroxaban for secondary stroke prevention in patients with embolic strokes of undetermined source: design of the NAVIGATE ESUS randomized trial. *Eur Stroke J.* (2016) 1:146–54. doi: 10.1177/2396987316663049
27. Selvik HA, Thomassen L, Bjerkreim AT, Næss H. Cancer-associated stroke: the bergen NORSTROKE study. *Cerebrovasc Dis Extra.* (2015) 5:107–13. doi: 10.1159/000440730
28. Navi B, Kasner SE, Elkind MSV, Cushman M, Bang OY, Deangelis LM. Cancer and embolic stroke of undetermined source. *Stroke.* (2021) 52:1121–30. doi: 10.1161/STROKEAHA.120.032002
29. Finelli PF, Nouh A. Three-territory DWI acute infarcts: diagnostic value in cancer-Associated hypercoagulation stroke (trousseau syndrome). *Am J Neuroradiol.* (2016) 37:2033–6. doi: 10.3174/ajnr.A4846
30. Guo L, Wang L, Liu W. Ability of the number of territories involved on DWI-MRI to predict occult systemic malignancy in cryptogenic stroke patients. *J Stroke Cerebrovasc Dis.* (2020) 29:104823. doi: 10.1016/j.jstrokecerebrovasdis.2020.104823
31. Hsu CC, Kwan C, Hapugoda S, Craigie M, Watkins T, Haacke E. Susceptibility weighted imaging in acute cerebral ischemia: review of emerging technical concepts and clinical applications. *Neuroradiol J.* (2017) 30:109–19. doi: 10.1177/1971400917690166
32. Naik D, Viswamitra S, Kumar AA, Srinath MG. Susceptibility weighted magnetic resonance imaging of brain: a multifaceted powerful sequence that adds to understanding of acute stroke. (2014) 17:1–4. doi: 10.4103/0972-2327.128555
33. Liebeskind DS, Sanossian N, Yong WH, Starkman S, Tsang M, Moya A, et al. CT and MRI early vessel signs reflect clot composition in acute stroke. *Stroke.* (2011) 42:1237–43. doi: 10.1161/STROKEAHA.110.605576
34. Kim SK, Yoon W, Kim TS, Kim HS, Heo TW, Park MS. Histologic analysis of retrieved clots in acute ischemic stroke: correlation with stroke etiology and gradient-echo MRI. *Am J Neuroradiol.* (2015) 36:1756–62. doi: 10.3174/ajnr.A4402
35. Heo JH, Nam HS, Kim YD, Choi JK, Kim BM, Kim DJ, et al. Pathophysiologic and therapeutic perspectives based on thrombus histology in stroke. *J Stroke.* (2020) 22:64–75. doi: 10.5853/jos.2019.03440
36. Sgreccia A, Duchmann Z, Desilles JP, Lapergue B Labreuche J, Kyheng M, et al. Association between acute ischemic stroke etiology and macroscopic aspect of retrieved clots : is a clot ' s color a warning light for underlying pathologies? *J Neurointerv Surg.* (2019) 11:1197–1200. doi: 10.1136/neurintsurg-2019-014905
37. Vogenberg FR. Predictive and prognostic models: implications for healthcare decision-making in a modern recession. *Am Heal Drug benefits.* (2009) 2:218–22.

38. Shipe ME, Deppen SA, Farjah F, Grogan EL. Developing prediction models for clinical use using logistic regression: an overview. *J Thorac Dis.* (2019) 11 (Suppl. 4):S574–84. doi: 10.21037/jtd.2019.01.25
39. Ruetten PPR, Gillard JH, Graves MJ. Review article: Introduction to quantitative susceptibility mapping and susceptibility weighted imaging. *Br J Radiol.* (2019) 92:1–13. doi: 10.1259/bjr.20181016
40. Chen J, Zhang Z, Nie X, Xu Y, Liu C, Zhao X, et al. Predictive value of thrombus susceptibility for cardioembolic stroke by quantitative susceptibility mapping. *Quant Imaging Med Surg.* (2022) 12:550–7. doi: 10.21037/qims-21-235
41. Kan P, Webb S, Siddiqui AH, Levy EI. First reported use of retrievable stent technology for removal of a large septic embolus in the middle cerebral artery. *World Neurosurg.* (2012) 77:591.e1-e5. doi: 10.1016/j.wneu.2011.05.059

Conflict of Interest: TM reports research support from the Bangerter Rhyner Foundation, Swiss National Foundation, and the Swiss Heart Foundation. HM reports personal consulting fees outside of this study from Servier, Bayer, Medtronic, Stryker and Cerenovus. PM reports receipt of research support from Siemens, Cerenovus, iSchmaview, Medtronic, Stryker, the Swiss Heart Foundation and the Swiss National Foundation, receipt of consultant fees paid to the institution from Medtronic, Cerenovus, Phenox and Microvention during the conduct of the study, unrelated to the submitted work. MA reports personal fees from Bayer, Bristol-Myers Squibb, Medtronic, Amgen, Daiichi Sankyo, Nestlé Health Sciences, Boehringer Ingelheim, and Covidien during the conduct of the study. UF reports grants during the conduct of the study from Medtronic, Stryker, and CSL Behring, unrelated to the submitted work. JK reports grants from the Swiss Academy of Medical Sciences/Bangerter Foundation, Swiss Stroke Society, and Clinical Trials Unit Bern during the conduct of the study. SJ reports grants from the Swiss National Science Foundation and the Swiss Heart Foundation.

The remaining authors declare that the research was conducted in the absence of any commercial or financial relationships that could be construed as a potential conflict of interest.

Publisher's Note: All claims expressed in this article are solely those of the authors and do not necessarily represent those of their affiliated organizations, or those of the publisher, the editors and the reviewers. Any product that may be evaluated in this article, or claim that may be made by its manufacturer, is not guaranteed or endorsed by the publisher.

Copyright © 2022 Beyeler, Belachew, Kielkopf, Aleman, León Betancourt, Genceviciute, Kurmann, Grunder, Birner, Meinel, Scutelnic, Bücke, Seiffge, Dobrocky, Piechowiak, Pilgram-Pastor, Mattle, Mordasini, Arnold, Fischer, Pabst, Gralla, Berger, Jung and Kaesmacher. This is an open-access article distributed under the terms of the Creative Commons Attribution License (CC BY). The use, distribution or reproduction in other forums is permitted, provided the original author(s) and the copyright owner(s) are credited and that the original publication in this journal is cited, in accordance with accepted academic practice. No use, distribution or reproduction is permitted which does not comply with these terms.

frontiers | Frontiers in Neurology

TYPE Original Research
PUBLISHED 28 July 2022
DOI 10.3389/fneur.2022.889213

Check for updates

OPEN ACCESS

EDITED BY
Wen-Jun Tu,
Chinese Academy of Medical Sciences and Peking Union Medical College, China

REVIEWED BY
Anand Singh,
University of Texas MD Anderson Cancer Center, United States
Felix Goehre,
Berufsgenossenschaftliche Kliniken Bergmannstrost Halle, Germany

*CORRESPONDENCE
Elisabeth Bründl
elisabeth.bruendl@ukr.de

SPECIALTY SECTION
This article was submitted to Neurological Biomarkers, a section of the journal Frontiers in Neurology

RECEIVED 03 March 2022
ACCEPTED 05 July 2022
PUBLISHED 28 July 2022

CITATION
Bründl E, Proescholdt M, Störr E-M, Schödel P, Bele S, Zeman F, Hohenberger C, Kieninger M, Schmidt NO and Schebesch K-M (2022) The endogenous neuropeptide calcitonin gene-related peptide after spontaneous subarachnoid hemorrhage–A potential psychoactive prognostic serum biomarker of pain-associated neuropsychological symptoms. *Front. Neurol.* 13:889213. doi: 10.3389/fneur.2022.889213

COPYRIGHT
© 2022 Bründl, Proescholdt, Störr, Schödel, Bele, Zeman, Hohenberger, Kieninger, Schmidt and Schebesch. This is an open-access article distributed under the terms of the Creative Commons Attribution License (CC BY). The use, distribution or reproduction in other forums is permitted, provided the original author(s) and the copyright owner(s) are credited and that the original publication in this journal is cited, in accordance with accepted academic practice. No use, distribution or reproduction is permitted which does not comply with these terms.

The endogenous neuropeptide calcitonin gene-related peptide after spontaneous subarachnoid hemorrhage–A potential psychoactive prognostic serum biomarker of pain-associated neuropsychological symptoms

Elisabeth Bründl[1]*, Martin Proescholdt[1], Eva-Maria Störr[1], Petra Schödel[2], Sylvia Bele[1], Florian Zeman[3], Christoph Hohenberger[1], Martin Kieninger[4], Nils Ole Schmidt[1] and Karl-Michael Schebesch[1]

[1]Department of Neurosurgery, University Medical Center Regensburg, Regensburg, Germany, [2]Section Neurosurgery, Department of Orthopedics, Trauma and Hand Surgery, Medical Center St. Elisabeth, Straubing, Germany, [3]Center for Clinical Studies, University Medical Center Regensburg, Regensburg, Germany, [4]Department of Anesthesiology, University Medical Center Regensburg, Regensburg, Germany

Background: The pronociceptive neuromediator calcitonin gene-related peptide (CGRP) is associated with pain transmission and modulation. After spontaneous subarachnoid hemorrhage (sSAH), the vasodilatory CGRP is excessively released into cerebrospinal fluid (CSF) and serum and modulates psycho-behavioral function. In CSF, the hypersecretion of CGRP subacutely after good-grade sSAH was significantly correlated with an impaired health-related quality of life (hrQoL). Now, we prospectively analyzed the treatment-specific differences in the secretion of endogenous CGRP into serum after good-grade sSAH and its impact on hrQoL.

Methods: Twenty-six consecutive patients (f:m = 13:8; mean age 50.6 years) with good-grade sSAH were enrolled (drop out $n = 5$): $n = 9$ underwent endovascular aneurysm occlusion, $n = 6$ microsurgery, and $n = 6$ patients with perimesencephalic SAH received standardized intensive medical care. Plasma was drawn daily from day 1 to 10, at 3 weeks, and at the 6-month follow-up (FU). CGRP levels were determined with competitive enzyme immunoassay in duplicate serum samples. All patients underwent neuropsychological self-report assessment after the onset of sSAH (t_1: day 11–35) and at the FU (t_2).

Results: During the first 10 days, the mean CGRP levels in serum (0.470 ± 0.10 ng/ml) were significantly lower than the previously analyzed mean CGRP values in CSF (0.662 ± 0.173; $p = 0.0001$). The mean serum CGRP levels within the first 10 days did not differ significantly from the values at 3 weeks ($p = 0.304$). At 6 months, the mean serum CGRP value (0.429 ± 0.121 ng/ml) was

significantly lower compared to 3 weeks ($p = 0.010$) and compared to the first 10 days ($p = 0.026$). Higher mean serum CGRP levels at 3 weeks ($p = 0.001$) and at 6 months ($p = 0.005$) correlated with a significantly poorer performance in the item pain, and, at 3 weeks, with a higher symptom burden regarding somatoform syndrome ($p = 0.001$) at t_2.

Conclusion: Our study reveals the first insight into the serum levels of endogenous CGRP in good-grade sSAH patients with regard to hrQoL. In serum, upregulated CGRP levels at 3 weeks and 6 months seem to be associated with a poorer mid-term hrQoL in terms of pain. In migraineurs, CGRP receptor antagonists have proven clinical efficacy. Our findings corroborate the potential capacity of CGRP in pain processing.

KEYWORDS

biomarker, calcitonin gene-related peptide (CGRP), cognitive impairment, health-related quality of life (hrQoL), neuropeptide, pain, somatoform syndrome, spontaneous subarachnoid hemorrhage

Highlights

- Impairment in health-related quality of life (hrQoL) after treatment of spontaneous subarachnoid hemorrhage (sSAH) is common but underreported.
- Calcitonin gene-related peptide (CGRP), a potent vasoactive and pronociceptive neuromediator, is involved in pain transmission and modulation of psycho-behavioral function.
- This study is the first to correlate endogenous plasma CGRP with mid-term hrQoL outcome in good-grade sSAH.
- During the first 10 days after sSAH, the mean CGRP levels in serum range significantly lower than in CSF and serum CGRP levels decrease significantly over 6 months.
- Upregulated plasma CGRP levels at 3 weeks and 6 months after sSAH seem to be significantly associated with pain and somatoform syndrome.
- As is the case with migraine, after sSAH, upregulated plasma CGRP is suggested to be involved in the pathogenesis of pain and pain processing.

Abbreviations: ANOVA, analysis of variance; aSAH, aneurysmal subarachnoid hemorrhage; AUC, area under the curve; CBF, cerebral blood flow; CGRP, calcitonin gene-related peptide; CSF, cerebrospinal fluid; CT (scan), computed tomography (scan); CV, cerebral vasospasm; DIND, delayed ischemic neurological deficit; DSA, digital subtraction angiography; EIA, enzyme immunoassay; EV, endovascular aneurysm occlusion; EVD, external ventricular drain; FU, 6-month follow-up; GCS, Glasgow Coma Scale; Ghp, general health perceptions; GOS, Glasgow Outcome Scale; h, hour/s; HH, Hunt and Hess; hrQoL, health-related quality of life; ICU, intensive care unit; ISR, ICD-10-Symptom-Rating questionnaire; MCS, mental component summary; Mhi, general mental health; min, minute/s; min-max, minimum – maximum; ml, milliliter; mRS, modified Ranking Scale; MS, microsurgical clipping, microsurgical aneurysm occlusion; ng, nanograms; no., [n], number; NPY, Neuropeptide Y; p, p-value; Pain, bodily pain; PCS, physical component summary; Pfi, physical functioning; pSAH, perimesencephalic subarachnoid hemorrhage; PTSD, posttraumatic stress disorder; Rawhtran, health transition item; Rolem, role limitations because of emotional problems; Rolph, role limitations due to physical health problems; SAH, subarachnoid hemorrhage; SD, standard deviation; SF-36, 36-Item Short Form Health Survey; Social, social functioning; sSAH, spontaneous subarachnoid hemorrhage; TCD, transcranial Doppler ultrasound; (test) t_1, test in the subacute phase after the onset of bleeding (between day 11 to 35 after subarachnoid hemorrhage); (test) t_2, test in the short-term (chronic phase) after treatment at 6-month follow-up; test t_1 - t_2, intergroup development from t_1 to t_2; Vital, vitality; vs., versus; WFNS, World Federation of Neurological Surgeons.

Introduction

Aneurysmal subarachnoid hemorrhage (aSAH) is a serious and highly complex neurovascular insult demanding specialized multidisciplinary therapy concepts during the acute phase, rehabilitation, socio-professional reintegration, and follow-up (FU) care. Over the past few decades, advanced neurovascular treatment strategies, early aneurysm repair, and individualized neuro-intensive care management have not only accounted for declining trends in case-fatality but also for an improvement in functional outcome (1). However, the regained functional independence contrasts with an appallingly low rate of return to work ranging from 70.8% (2) to <50% (3) to merely 3% (4) of the patients surviving spontaneous subarachnoid hemorrhage (sSAH). In up to 50 % of the sSAH patients, the bleeding is accompanied by subtle, yet substantial neuropsychological impairment, fatigue, emotional dysbalance, and somatic problems like bodily pain, which in turn seriously

affect the patients' health-related quality of life (hrQoL) (3, 5). Profound literature on the longitudinal course of sSAH-associated bodily pain, especially headache, and its management is sparse (2). Persistent severe to worst headache, refractory to analgesics (6), is reported by more than 90% of the sSAH patients and represents the second-leading cause for 30-day hospital readmission after sSAH (7). Long-term FU data indicates that–in case of inadequate treatment (6, 8)–sSAH-associated headache may persist for 2–9 years after the hemorrhage (8–10). The pathogenesis of headache after aneurysm rupture is deemed to be multifactorially mediated, but the exact mechanisms remain elusive (11).

In light of the risen clinical awareness of the long-term disabilitiy in cognition and day-to-day functioning, researchers and clinicians strive for the establishment of reliable, clinically relevant biomarkers with a predictive capacity for neurocognitive outcome and hrQoL. Recently, the endogenous 37-amino acid neuropeptide Calcitonin gene-related peptide (CGRP) (12) has gained paramount interest as a potential vasoactive and psychoactive biomarker in cerebrospinal fluid (CSF) and serum after sSAH. CGRP is stored in sensory perivascular nerve fibers which arise from the trigeminal ganglia of Gasseri and acts as a major, highly potent microvascular vasodilator (13). In aSAH, the proven secretion of CGRP into CSF (14, 15) was suggested to be associated with a potential neuroprotective effect by preventing cerebral vasospasm (CV) and cerebral ischemia (15) but with a deleterious effect on the hrQoL in the acute phase (16). Beyond, the neuromodulator CGRP (17) attested a crucial involvement in various neurobehavioral processes (18) like in inflammatory and neuropathic pain (19), and, by unalterable, massive relaxation of cerebral arteries, in migraine (20). In 2018, specifically designed drugs acting antagonistically on CGRP or on the CGRP receptor have ushered in a new era in migraine therapy for acute relief of migraine and effective prevention of migraine attacks (21).

Up to now, no data is yet available on the impact of good-grade sSAH on the intrinsic release of CGRP into serum, on its temporal dynamics, and its pathophysiological interactions with higher integrated behavior. Our study aims to determine whether CGRP could prove to be a useful predictive surrogate parameter in serum for the self-reported hrQoL up to 6 months after sSAH.

Patients and methods

The study protocol, the prospective liquid biobanking, and the clinical database of this prospective single-center investigation were approved by the Local Institutional Ethics Committee (reference number 06-179). The study follows the principles of the Declaration of Helsinki.

Patient population

The cohort has been reported previously (16, 22, 23). A total of 26 consecutive patients, treated for acute non-traumatic, angiographically confirmed aneurysmal or non-aneurysmal perimesencephalic SAH (pSAH) at our University Medical Center between February 2013 and May 2016, fulfilled the beforehand specified eligibility criteria of being native German speakers, aged 18–75 years, who had been admitted to hospital within 48 h of ictus in prognostically favorable, good to moderate neurological condition, defined as a World Federation of Neurological Surgeons (WFNS) score (24) and Hunt and Hess (HH) grading (25) of 1–4, respectively, and an initial Glasgow Coma Scale (GCS) of $\geq$9. Written informed consent was obtained from each individual. In all patients, the diagnosis of sSAH was based on cerebral computed tomography (CT) and a four-vessel digital subtraction angiography (DSA) to visualize the location and morphology of the underlying ruptured aneurysm and to differentiate aneurysmal from perimesencephalic hemorrhages, respectively. Within the first 72 h after the onset of sSAH, all patients received an external ventricular drain (EVD) due to a radiologically confirmed acute occlusive hydrocephalus. Treatment consisted either of endovascular aneurysm occlusion (EV group) or microsurgical clipping (MS group) for aSAH patients, followed by standardized therapy in the intensive care unit (ICU) (pSAH group). Our standardized microsurgical and endovascular procedure protocols (26) and our ICU standard operating protocol (27) have been described elsewhere.

The clinical database comprised all demographic, radiological, and neurological variables, comorbidities, non-/invasive procedures, complications, comprehensive pharmacological screening (at discharge and at the 6-month FU), and outcome grading [Glasgow Outcome Scale (GOS) (28) and modified Ranking Scale (mRS) (29)].

Neuropsychological self-report assessment

Subacutely (between day 11 and 35; t_1) and 6 months (t_2) after the onset of sSAH, all patients completed two well-established generic self-report measures of physical and mental health each: The ICD-10-Symptom-Rating questionnaire (ISR) (30) serves as a score for symptom burden and the German version of the 36-Item Short Form Health Survey (SF-36) (31) represents a performance score.

Laboratory procedures

Within the 10-day period after the onset of sSAH, plasma was drawn directly from the arterial line once daily. At

3 weeks and at the 6 month-FU, blood was collected by venipuncture. Immediately subsequent to sampling, the samples were centrifuged at 1,200 rounds per minute for 10 min, and the supernatants were aliquoted and stored at−80°C until further use. The samples were thawed, aliquoted (1 ml) with columns [STRATA C18-E (55 µm, 70 A) 200 mg/3 ml-columns, Phoenix Pharmaceuticals Inc., Burlingame, USA], purified, evaporated on a vacuum concentrator (Christ RVC 2-25 CD plus; Osterode am Harz, Germany), and dissolved in 250 µl assay-buffer resulting in a fourfold concentration. CGRP levels were measured in duplicate purified serum samples using a competitive enzyme immunoassay (EIA; Phoenix Pharmaceuticals Inc., Burlingame, CA, USA). The cerebral exposure to the endogenously released CGRP into serum over time is expressed as ng/ml.

Statistical analysis

Continuous data and neuropsychological test results are presented as mean ± standard deviation (SD) and range (minimum to maximum) and categorical data as frequency counts.

Neuropsychological assessment: Changes over time within each group were analyzed with a paired *t*-test. Differences between groups at postinterventional assessment were analyzed with an analysis of variance (ANOVA) followed by Fisher's LSD *post-hoc* pairwise comparisons.

Correlation of CGRP with neuropsychological assessment: Regression analyses were conducted for correlations of mean CGRP levels with the hrQoL test scores. Changes over time within each group were analyzed with a paired *t*-test. Intragroup variances (correlations between hrQoL test scores and clinical variables) were analyzed using an analysis of variance (Bartlett's test for equal variances). Statistical analysis was conducted according to Stata procedures (Stata Version 14.2; Stata Corp. College Station, TX, USA).

A $p < 0.05$ was considered statistically significant. A biostatistician was involved in the design and realization of the statistical evaluation.

Results

Demographics and descriptive statistics

A total of $N = 160$ patients with sSAH were treated during the observation period. In accordance with our strict selection criteria, depicted in the Flowchart (Figure 1), five patients were excluded from analysis. Thus, a total of 21 patients (8 men, 13 women) of a mean age of 50.6 years (range 27–72 years) with good-grade sSAH was assigned to statistical evaluation. Four aSAH patients, initially presenting

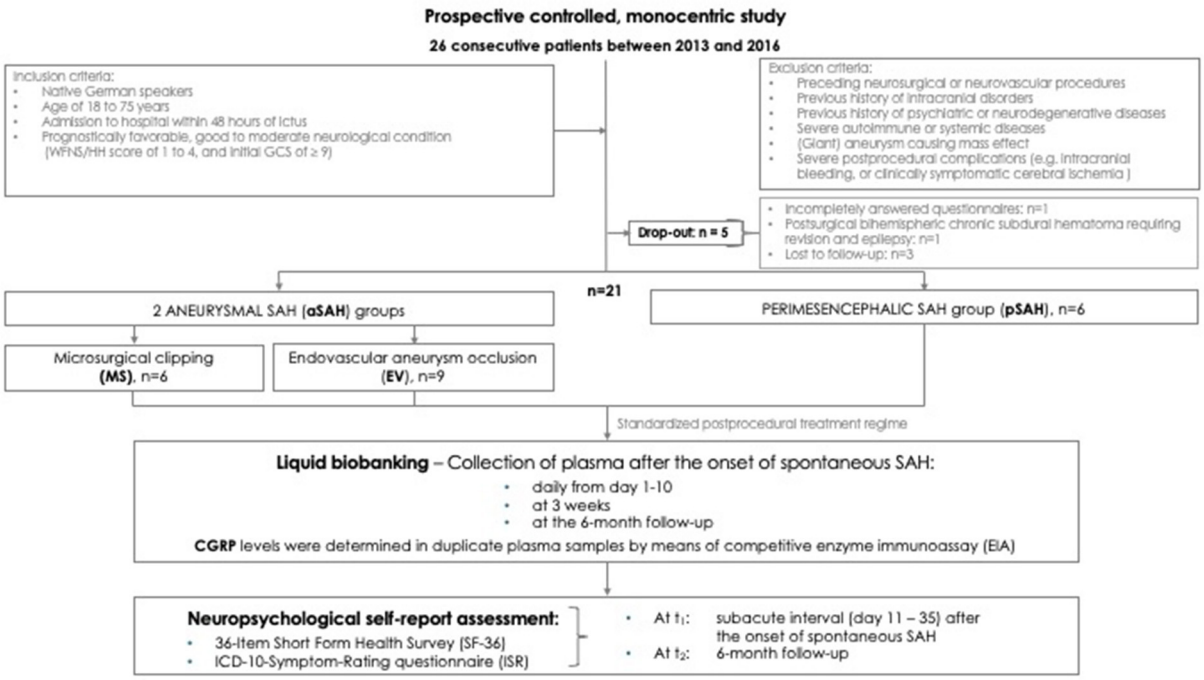

FIGURE 1
Flowchart. Study design and reasons for exclusion of potentially eligible cases.

with HH grade III (14%) or IV (5%), neurologically improved immediately after insertion of an EVD following hospital admission (i.e., HH I or HH II). Thus, the poorer HH score was obviously related to acute occlusive hydrocephalus. With this qualification, we consider the term "good-grade" sSAH patients as appropriate for our cohort. An aneurysmal bleeding source in the anterior ($n = 12$) or posterior circulation was detected in 15 patients (EV $n = 9$: coil $n = 5$, stent-assisted coil $n = 2$; balloon-assisted coil $n = 1$; flow diverter $n = 1$). No patient developed serious procedure-related complications like, for example, periprocedural aneurysm rupture, procedure-related blood transfusion, postprocedural onset of a new neurological deficit, or clinically symptomatic CV-related stroke. Functional outcome was stable or even improved over the 6-month FU. None of these patients required decompressive craniectomy, and, until FU, no late rebleedings or mortalities had occurred. Each individual was able to complete both of our surveys, the ISR and the SF-36, within 10–15 min, and without any signs of (mental or physical) fatigue during the testing, neither at t_1 nor at t_2. Comprehensive information on the baseline data including the aneurysm site, GCS, HH, WFNS and Fisher score, procedure variables, medication, and outcome grading is provided by Table 1.

The presented sSAH cohort exclusively encompassed patients with severe radiological grades of sSAH (Fisher score 3 or 4) and, consecutively, is imbalanced in terms of the overestimation of the true hydrocephalus rate after sSAH. This is all the more remarkable given the inclusion of 6 patients with pSAH. Only four patients, however, required permanent ventriculoperitoneal shunting. Statistical intergroup comparisons yielded no significant differences except for a higher number of middle cerebral artery aneurysms in the MS group ($p = 0.022$), a higher intake of antiplatelets in the EV group ($p = 0.016$) at t_1, an unsurprisingly longer duration of MS vs. EV ($p = 0.004$), and a longer mean time spent on mechanical ventilatory support in the EV group than in the pSAH group (EV vs. pSAH $p = 0.0496$; EV vs. MS $p = 0.864$, MS vs. pSAH $p = 0.065$).

Correlation of neuropsychological performance with CGRP exposure in serum

The self-reported hrQoL perception has been reported previously (22, 23) sum up, our cohort performed significantly worse in several ISR- and SF-36-subscales than the particular population norms, especially at t_1. Within 6 months, sSAH patients had significantly improved with regard to bodily pain (Pain), physical functioning (Pfi), the physical component summary (PCS), depression, anxiety, general health perceptions (Ghp), and social functioning (Social). Poor self-reported neuropsychological performance [physical SF-36 items: Pain, role limitations because of physical health problems (Rolph), Ghp; ISR scores: total, depression, compulsive-obsessive syndrome] in the subacute phase correlated with a worse outcome on the GOS at discharge. And the HH score correlated positively with all psychological SF-36 item scores [vitality (Vital), Social, role limitations because of emotional problems (Rolem), general mental health (Mhi), mental component summary (MCS)] at t_1.

During the first 10 days, the mean CGRP levels in serum (0.470 ± 0.10 ng/ml) were significantly lower than the previously (16) analyzed mean CGRP values in CSF (0.662 ± 0.173; $p = 0.0001$). The mean serum CGRP levels within the first 10 days did not differ significantly from the values at 3 weeks (0.493 ± 0.163 ng/ml; $p = 0.304$). At 6 months, the mean serum CGRP value (0.429 ± 0.121 ng/ml) was significantly lower compared to 3 weeks ($p = 0.010$) and compared to the first 10 days ($p = 0.026$) (cf. Figure 2).

In female patients, CGRP levels at the 6-month FU were significantly higher than in male patients (0.473 ± 0.121 ng/ml vs. 0.358 ± 0.087 ng/ml; $p = 0.016$). Further regression analyses did not reveal any significant correlation between the neuropeptide levels and other patient variables like, for example, the treatment modality.

Higher mean serum CGRP levels at 3 weeks ($p = 0.001$) and at the 6-month FU ($p = 0.005$) correlated with a significantly poorer performance in the SF-36 item pain, and, at 3 weeks, with a higher ISR symptom burden regarding somatoform syndrome ($p = 0.001$) at t_2 (cf. Figure 3). The analysis of cognitive test performances is summarized in Table 2.

Discussion

Our study characterizes the association of elevated serum CGRP on adverse mid-term hrQoL and burdensome pain after sSAH.

Reduced hrQoL after sSAH with a focus on pain processing

Compared to other life-threatening medical events, stroke has been proven to be associated with the strongest reductions in hrQoL and functioning status (32). In stroke patients, the physical hrQoL increased after treatment (except for bodily pain), whereas the psychological quality remained low (33). This equals our results in sSAH which indicate a significant improvement in multiple physical items (Pfi, Pain, Ghp, PCS) within 6 months after sSAH, while most psychological

10.3389/fneur.2022.889213

TABLE 1 Demographic and clinical characteristics of patients.

Patient characteristics	Study population		
	MS	EV	pSAH
Number of patients [*n*]	6	9	6
Male to female ratio	2: 4	3: 6	3: 3
Age [years], mean ± SD	42.0 ± 13.2	50.1 ± 9.3	59.8 ± 7.4
(range)	(27–61)	(30–59)	(53–72)
Calcitonin gene-related peptide in serum			
Level within the first 10 days [ng/ml], mean ± SD	0.535 ± 0.094	0.453 ± 0.135	0.435 ± 0.069
Level at 3 weeks [ng/ml], mean ± SD	0.474 ± 0.134	0.465 ± 0.193	0.554 ± 0.151
Level at 6 months [ng/ml], mean ± SD	0.429 ± 0.111	0.420 ± 0.114	0.442 ± 0.160
Calcitonin gene-related peptide in CSF			
Level within the first 10 days [ng/ml], mean ± SD	0.626 ± 0.155	0.698 ± 0.178	0.645 ± 0.201
Site of aneurysm			
Anterior circulation (ruptured) [n]	8 (6)	7 (6)	1 (0)[a]
Posterior circulation (ruptured) [n]	0 (0)	3 (3)	-
	8	10	1[a]
Side of aneurysm [*n*]			
Left	3	2	1[a]
Right	4	2	–
Side of pterional approach			
Dominant-side	3	–	–
Non-dominant side	3	–	–
Initial neurological status			
GCS [*n*]			
15	1	5	4
14	4	2	1
13	1	0	1
11	0	1	0
9	0	1	0
Hunt and Hess score [*n*]			
0	0	0	0
I	2	5	2
II	2	2	4
III	2	1	0
IV	0	1	0
V	0	0	0
WFNS score [*n*]			
1	1	5	4
2	4	2	2
3	1	0	0
4	0	2	0
5	0	0	0
Fisher score [*n*]			
1	0	0	0
2	0	0	0
3	2	2	2
4	4	7	4

(Continued)

TABLE 1 Continued

Patient characteristics	Study population		
	MS	EV	pSAH
External ventricular drainage			
Implantation after the onset of SAH [d], mean ± SD	0.5 ± 0.6	0.4 ± 0.7	0.5 ± 0.6
(range)	(0–1)	(0–2)	(0–1)
In situ [d], mean ± SD	15.8 ± 4.9	15.1 ± 7.7	12.0 ± 5.0
(range)	(9–23)	(9–30)	(5–18)
Replacement [*n*]	0	2	1
CSF infection [*n*]	1	4	2
Permanent ventriculoperitoneal shunt placement [*n*]	0	2	2
Implantation after the onset of SAH [d], mean ± SD	-	23.5 ± 0.7	29.5 ± 6.4
(range)	-	(23–24)	(25–34)
Vasospasm [*n*]			
DIND	1	1	0
TCD	6	7	3
DSA	0	2	1
Multimodal neuromonitoring	1	1	0
Intraarterial cerebral spasmolysis[a]	0	2	0
Treatment-associated lesions on CT scan [*n*]			
Circumscribed ischemia[b]	2	2	0
Brain edema	3	1	0
Bleeding along the EVD entry route	1	0	1
Hygroma	0	0	1[c]
Medication at discharge / at FU			
Anticonvulsive drugs	1/1	0/1	0/0
Benzodiazepines	0/0	1/0	0/0
Antidepressants	0/0	3/1	1/1
Neuroleptics	0/0	0/0	0/0
Opioid	2/0	1/1	2/0
Nicotine patches	0/1	0/1	0/1
Antihypertensive drugs	4/3	4/6	3/3
Thyroid medication	3/3	2/2	0/0
Antiplatelet agents	0/0	**5***/3	0/0
No medication	0/2	0/1	0/2
Neurological status at discharge / at FU			
GOS [*n*]			
5	4/5	7/7	5/6
4	0/0	1/2	1/0
3	2/1	1/0	0/0
mRS [*n*]			
0	4/2	7/3	4/5
1	0/3	0/3	2/1
2	1/0	1/3	0/0
3	0/1	0/0	0/0
4	1/0	1/0	0 /0
Patients with new neurological deficit [*n*]			
At discharge	0	1	0

(Continued)

TABLE 1 Continued

Patient characteristics	Study population		
	MS	EV	pSAH
At FU	1	3	0
Employment status at FU [*n*]			
Returned to work	1	2	1
Attending vocational integration programs	0	2	0
On sick leave	1	3	0
Unemployed	1	1	0
Unemployed before and after the onset of SAH	0	1	0
Retired at the onset of SAH	0	0	1
No information provided	3	0	4

MS, microsurgical clipping group; EV, endovascular treatment group; pSAH, perimesencephalic subarachnoid hemorrhage group; SD, standard deviation; CSF, cerebrospinal fluid; AUC, area under the curve; ng, nanograms; ml, milliliter; h, hours; GCS, Glasgow Coma Scale; WFNS, World Federation of Neurosurgical Societies; d, days; SAH, subarachnoid hemorrhage; DIND, delayed ischemic neurological deficit; TCD, transcranial Doppler ultrasound; DSA, digital subtraction angiography; [a]Transient placement of transfemoral microcatheters for local intraarterial cerebral spasmolysis (n = 1 continuous nimodipine infusion for 3 and 5 days; n = 1 single shot infusion of milrinone) to reverse severe cerebral vasospasm. [b]Clinically silent ischemia, either in the section of the caudate nucleus after unintended clipping of the recurrent artery of Heubner or diffusely in the periventricular white matter; [c]Conservatively treated bi-hemispheric hygroma due to CSF overdrainage via the EVD; CT scan, computerized axial tomography scan; EVD, external ventricular drainage; FU, 6-month follow-up; GOS, Glasgow Outcome Scale; mRS, modified Rankin Scale. *$p < 0.05$.

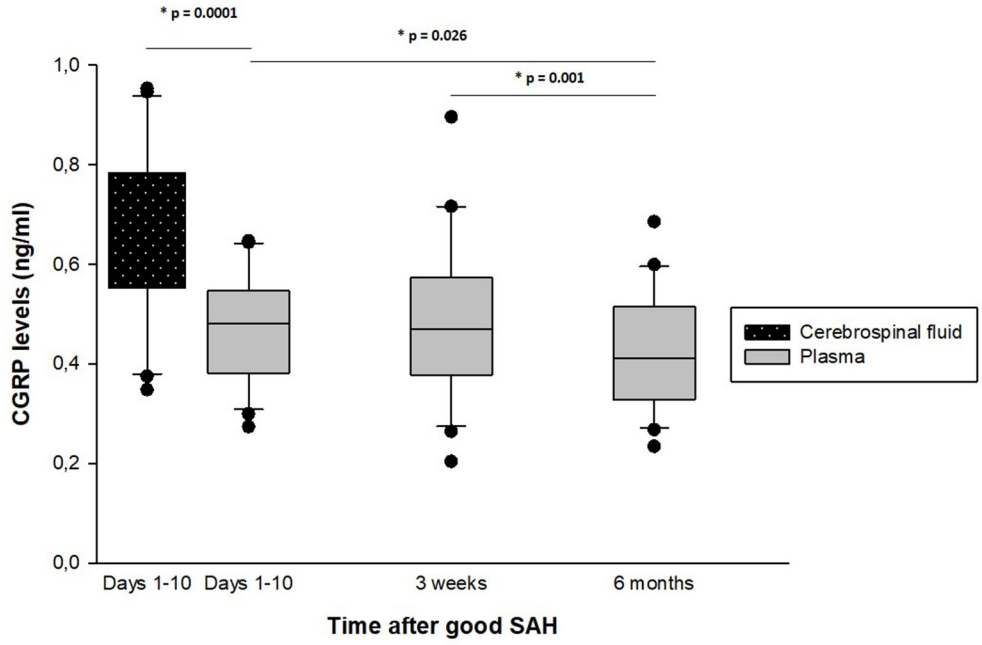

FIGURE 2
Temporal dynamics of CGRP levels in serum and cerebrospinal fluid after good-grade spontaneous subarachnoid hemorrhage. The time interval (1–10 days, 3 weeks, and 6 months) after good-grade spontaneous subarachnoid hemorrhage, plotted vs. the mean endogenous calcitonin gene-related peptide (CGRP) concentrations in serum. During the first 10 days, the mean CGRP levels were significantly lower in serum than in the cerebrospinal fluid (16). At 6 months, the mean serum CGRP value was significantly lower compared to the first 10 days and compared to 3 weeks.

items (Compulsive-obsessive syndrome, somatoform syndrome, nutrition disorder, the ISR supplementary items, the ISR total score, Vital, Rolem, Mhi, and MCS) remained stable.

hrQoL restrictions after sSAH

A considerable proportion of sSAH survivors with "good recovery" experiences impaired hrQoL for several months up to 24.5 years after ictus or even longer (5, 34). In a current

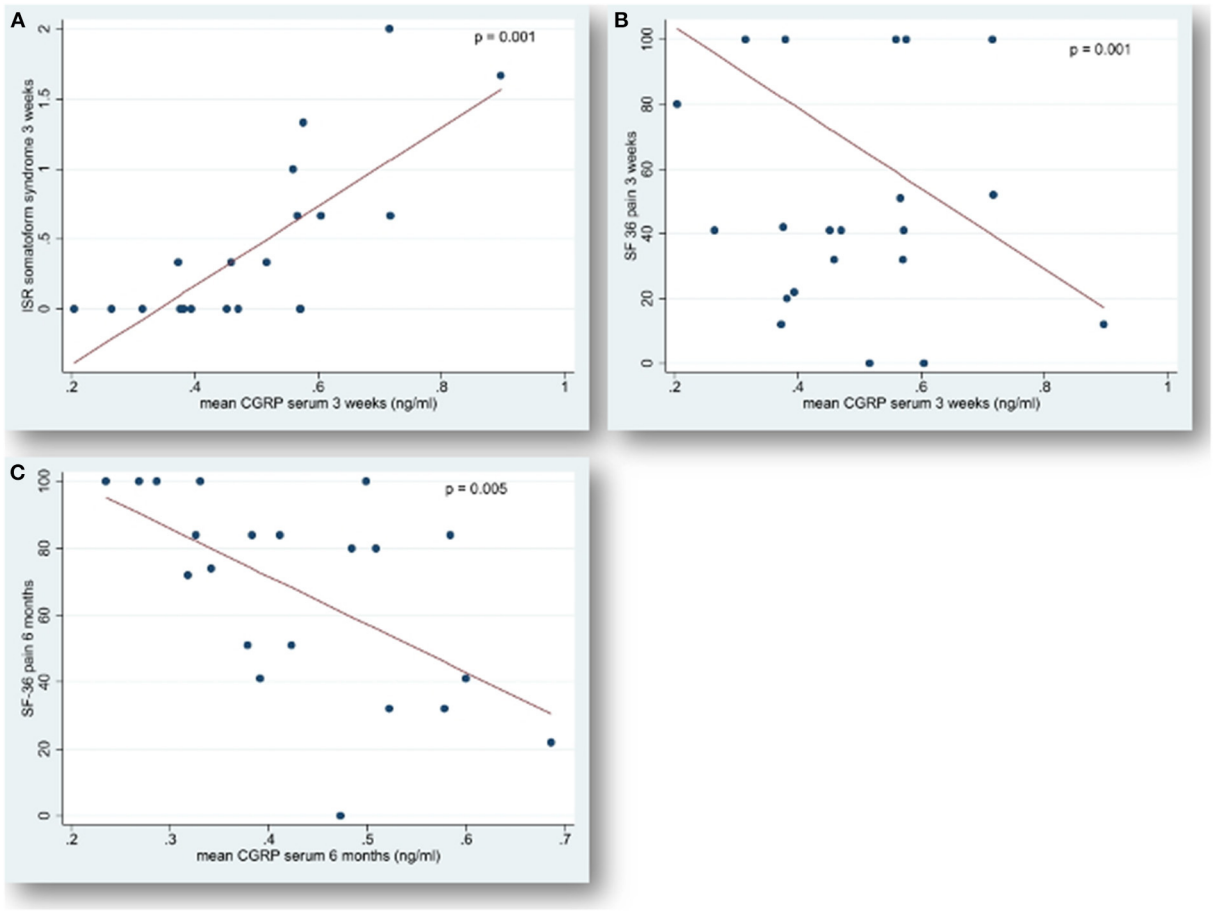

FIGURE 3
Correlation of serum concentrations of CGRP with "somatoform syndrome" and "pain" after spontaneous subarachnoid hemorrhage. Endogenous calcitonin gene-related peptide (CGRP) levels in serum, measured 6 months (t_2) after the onset of spontaneous subarachnoid hemorrhage, plotted versus **(A)** somatoform syndrome 3 weeks after the hemorrhage and versus **(B)** pain 3 weeks and **(C)** pain 6 months after ictus. The ICD-10-Symptom-Rating questionnaire (ISR) (30) with 29 items and 6 syndrome scales aims at comprehensively evaluating the severity of psychological disorders. Each syndrome scale ranges from a minimum of 0 (best performance) to a maximum of 4 points with higher scores indicating a more severe symptom burden. The 36-Item Short Form Health Survey (SF-36) (31) is a 36-item generic general health questionnaire yielding scores on 8 health subscales relating to physical and psychological health. These 8 subscales can be summarized in a corresponding physical component summary and a mental component summary. Each item is scored in the range 0 to 100, and a high score defines a more favorable state of health. Items in the same scale are averaged together to create the 8 scale scores. Each dot represents the mean level of serum CGRP in [ng/ml] for each patient, indicating a significant linear correlation (compare regression line) with higher symptom burden (ISR) and with poorer neurobehavioral performance (SF-36). Statistical significance: $p < 0.05$.

empirical survey (4), one third of the aSAH patients was afflicted with a "post-aSAH syndrome" comprising a self-reported cluster of symptoms like fatigue, cognitive dysfunction (memory, concentration, slowed thought process), emotional problems (anxiety, depression, irritability, and impatience), and somatic problems (headache, sensitivity to sound, and sleep disturbances). The presence of this syndrome–implicating more pain, more pronounced cognitive impairment, and, consecutively, poorer hrQoL–almost invariably kept the patients from returning to work 1 year after the bleeding event (4). This is consistent with our 6-month results (cf. Table 1). Occupational reintegration difficulties and long-term disability after sSAH have a significance extending far beyond socioeconomic terms (8, 34).

Our study emphasizes hrQoL restrictions due to pain conditions. SAH represents a subtype of stroke with a particularly high predisposition to headache in the acute (6) and chronic stage (8, 10). The paucity of analyses available state a higher headache burden in 77% of good-grade SAH patients (35), in 62% of pSAH survivors (10) and 16% of SAH long-term survivors (8) several years after ictus. Most recently, Huckhagel et al. (2) published the first comprehensive data on a significant number of SAH patients with peak rates even reaching up to 40.9% who continued to experience burdensome

TABLE 2 Cognitive performance of the cohort ($n = 21$) in the subacute interval after the onset of spontaneous subarachnoid hemorrhage (t_1) and at 6-month follow-up (t_2).

Neuropsychological assessment	Test scores [mean ± SD]		Difference t_1 vs. t_2 [mean ± SD]	Paired t-Test t_1 vs. t_2 [*p*-value]
	t_1	t_2		
ISR scores				
Depression	1.5 ± 1.2	1.1 ± 0.9	0.4 ± 1.1	**0.046***
Anxiety	1.3 ± 1.1	0.7 ± 0.9	0.7 ± 0.3	**0.019***
Compulsive-obsessive	0.8 ± 1.0	0.8 ± 1.0	0.0 ± 1.4	0.480
Somatoform	0.6 ± 0.7	0.4 ± 0.6	0.1 ± 1.0	0.252
Nutrition disorder	0.6 ± 1.0	0.6 ± 0.7	−0.0 ± 1.2	0.523
Supplementary items	0.7 ± 0.5	0.5 ± 0.6	0.2 ± 0.6	0.064
Total	0.9 ± 0.7	0.7 ± 0.6	0.2 ± 0.8	0.098
SF-36 scores				
Physical items				
Rawhtran	4.5 ± 0.6	2.9 ± 1.4	1.6 ± 1.4	1.000
Pfi	19.5 ± 28.9	72.4 ± 26.3	−52.8 ± 35.5	**0.001***
Rolph	39.3 ± 43.7	47.6 ± 45.3	−8.3 ± 64.4	0.280
Pain	48.5 ± 34.6	67.2 ± 29.9	−18.7 ± 37.9	**0.018***
Ghp	56.3 ± 16.8	74.1 ± 18.2	−17.8 ± 19.0	**0.001***
Psychological items				
Vital	51.0 ± 19.7	51.2 ± 20.3	−0.2 ± 24.4	0.482
Social	66.1 ± 26.0	80.4 ± 25.2	−14.3 ± 28.6	**0.017***
Rolem	61.7 ± 46.2	61.7 ± 45.0	−0.0 ± 58.8	0.500
Mhi	61.1 ± 20.6	68.2 ± 21.7	−7.0 ± 28.6	0.137
PCS	31.0 ± 11.0	46.0 ± 10.0	−13.3 ± 12.7	**0.001***
MCS	49.1 ± 12.5	47.5 ± 10.7	1.4 ± 12.9	0.677

SD, standard deviation; test t_1, test in the subacute phase after the onset of bleeding (between day 11 and 35 after subarachnoid hemorrhage); test t_2, test in the short-term (chronic phase) after treatment at 6-month follow-up; AUC, area under the curve; CGRP, calcitonin gene-related peptide; ISR, ICD-10-Symptom-Rating questionnaire; SF-36, German version of the 36-Item Short Form Health Survey; Rawhtran, health transition item; Pfi, physical functioning; Rolph, role limitations because of physical health problems; Pain, bodily pain; Ghp, general health perceptions; Vital, vitality; Social, social functioning; Rolem, Role limitations because of emotional problems; Mhi, general mental health; PCS, physical component summary; MCS, Mental component summary. ***Statistical significance: $p < 0.05$**.

headaches with a profound negative impact on the hrQoL on average 32.6 months after aSAH. Our study corroborates pain conditions 6 months after ictus. Concordantly, post-stroke headache has been proposed to persist for weeks to months, or even years after the hemorrhage (2, 8, 10). Reduced physical activity not only during the ictal but also during the pain-free interictal phases of migraineurs underlines the intensity-independent disabling effect of headache conditions (36). The SAH headache has been described to be highly refractory and to respond poorly to treatment with standard analgesics (11, 37).

Potential determinants for pain conditions and hrQoL restrictions after sSAH

Potential predictor variables, significantly related to chronic headaches after SAH, were nighttime sleep difficulties with daytime sleepiness (8) and correspondingly, fatigue, an acknowledged risk factor for persistent cephalgia after ischemic stroke (38) and a common feature in systemic autoimmune diseases (39). In our study design, patients with autoimmune or systemic diseases were excluded to minimize confounders. Beyond, comorbidities like depression and mood issues may interfere and exacerbate or perpetuate post-stroke headache (38). Patients with a younger mean age at the onset of SAH and patients with a favorable neurological condition as to the WFNS were more prone to suffer from headache at FU (2). All of our sSAH groups developed a significant deterioration in the health transition item (Rawhtran) implicating recurrent headache. It could be argued that good-grade sSAH patients, being aware of a sudden, life-threatening medical event, might experience a psychological traumatization by the onset of sSAH and the intensive care treatment (40), whereas burdened patients without trauma-related memories or with cognitive deficits are at risk of an

under-reporting of symptoms and minimizing of hrQoL complaints (41).

When previously (23) analyzing our cohort (with similar EV-MS quota) according to the treatment groups, at 6 month-FU, MS patients experienced less Pain ($p = 0.040$) and yielded significantly better Pfi ($p = 0.046$) than the EV group. Interpreting our results with caution due to the small sample size, we argue that headache might be–at least in part–related to the longer persistence of subarachnoid blood in the basal cisterns causing meningeal irritation. MS affords the opportunity to both obliterate the aneurysm and, compared to EV, to reduce the burden of cisternal blood *via* intraoperative irrigation. The majority of authors dismissed the hypothesis of treatment-specific differences (MS vs. EV) in neuropsychological outcome [cf. (23)] and headache (2) after sSAH in most instances.

Pathophysiological considerations

The underlying pathomechanisms contributing to post-sSAH behavioral and cognitive impairment, reduced hrQoL, and associated chronic headache remain to be sufficiently elucidated (1). A diversity of pathophysiological cascades, induced by the hemorrhage and the sharp rise in intracranial pressure itself causing dural stretch as well as the consecutive secondary brain injury, is supposed to be involved (5). Cortical ischemic strokes are more frequently associated with headache than subcortical events (42). Accordingly, it might be argued that SAH affects the subarachnoid space, anatomically a region directly adjacent to the cortex and, thus, sSAH patients tend to be prone to headache. The presence of erythrocytes and blood breakdown products in the subarachnoid space is a potent trigger of meningeal irritation which is further exacerbated by the release of inflammatory cytokines inducing the infiltration of microglia and other immune cells and subsequent pain (11). Beyond, dysfunctions in autoregulatory mechanisms in cerebral perfusion and CV (37), a central sensitization of nociceptive pathways (38), a chronic hyperreactivity of the cerebral vasculature (43), and a stimulation of vascular nerve endings as blood vessels rupture (14, 44) are supposed to aggravate headache.

Pursuing an innovative approach, for the past decade, neuroscientists have increasingly focused on the early identification of valid and easily accessible biomarkers to reliably predict the outcome following sSAH and to design individualized, target-based treatment strategies for improvement of functional outcome and hrQoL (16, 45). Among the molecular genetic, inflammatory, vascular, oxidative stress, and protein biomarkers studied so far, the multifunctional endogenous neuropeptide CGRP appears rather promising (14–16, 44, 46).

Relevance of CGRP in pain processing after sSAH

The trigeminovascular system is involved in the regulation of the cranial vasculature and represents a key element in the transmission of pain (47). Upon activation in primary headaches, in stroke (48), and in SAH (15, 16, 44, 49), the trigeminovascular system, a vasodilator pathway, antidromically releases the peptide neurotransmitter CGRP (13), hereby increasing the cerebral blood flow (CBF) *via* vasodilation (13) and mediating pain by stimulation of the trigeminus nucleus caudalis, respectively (47). The activation of this (putative defense) system is noted clinically as a marked increase in the cranial venous outflow of CGRP during headache attacks or in SAH, where it was elevated in the CSF as well (14). The psychoactive mediator (17) CGRP has been repeatedly attested a crucial involvement in a variety of neurobehavioral and psycho-affective conditions (18), like in depression, anxiety and learning and memory [cf. (16)], as well as in inflammatory and neuropathic pain (19, 50), and, by pronounced arterial cerebral vasodilation, in migraine (20). Congruently, in our series, elevated CGRP levels in serum at 3 weeks and at 6 months significantly correlated with more pain and, at 3 weeks, with a higher symptom burden regarding somatoform syndrome 6 months after sSAH. We qualify the statement with the note that our utilized set of standardized and validated physical and mental health questionnaires refers to bodily pain in general and is therefore incapable to establish a headache-specific diagnosis. However, in the semi-structured interview during FU assessment recurrent headache was a commonly reported symptom in our series. To what extent CGRP is involved in non-headache conditions has not been clarified yet. A recent review article (19) revealed an association between measured CGRP levels and somatic visceral, inflammatory and neuropathic pain. Upregulated CGRP levels were reported in serum, CSF, synovial and tissue biopsies in patients with degenerative disc disease, osteoarthritis, and temporomandibular joint pain. Furthermore, CGRP was elevated in acute pain conditions and pain after exercise. In somatic pain conditions in particular, CGRP levels correlated with pain. This is in concert with our results as to somatoform syndrome after sSAH. Growing evidence indicates that CGRP facilitates nociceptive transmission and contributes to the development and maintenance of a sensitized, hyperresponsive state of the primary and second-order afferent sensory neurons, thus contributing to peripheral and central sensitization. The maintenance of such a sensitized neuronal condition is believed to be a key player underlying migraine pathophysiology (50). In sSAH, the (potentially adverse) effects of CGRP on pain modulation and transmission have not been explored before. Our data conflicts with the substantiated beneficial cerebroprotective role of (endo- and exogenously administered) CGRP in hemodynamics (14, 15, 46).

Upon nerve stimulation, CGRP is released from its storage vesicles in sympathetic perivascular fibers, which form a particularly dense network around the major arteries of the anterior part of the circle of Willis (14), and in free nerve endings in the *dura mater* (51). Pathophysiologically, it is supposed that, at the moment of aneurysm rupture, these CGRP-containing nerve fibers are affected directly or indirectly–by the stimulation of the vessel's wall or surrounding nociceptors or cortical neuronal depolarization secondary to the hemorrhage or by the blood in the subarachnoid space–initiating activity of the trigeminovascular system and inducing an excessive release of CGRP from the perivascular nerve terminals into CSF and serum (14, 15, 44). *Post mortem* analyses after SAH and early observational studies on the cerebral circulation after experimental SAH confirmed a marked decrease in CGRP immunoreactivity in the perivascular nerve fibers, accordingly [cf. (46)]. To date, our study is the first to provide an insight into the temporal dynamic changes of CGRP in serum after good-grade sSAH. Within the first 10 days and 3 weeks after the onset of hemorrhage, CGRP levels did not differ significantly. In contrast, 6 months thereafter, serum CGRP values had significantly declined. Data on the time course of CGRP in the serum is scarce. The most marked suppression of CGRP immunoreactivity in cerebrovascular nerve fibers was documented during the 7th to 14th day after artificial SAH in dogs with a recovery to normal levels by the 42nd day (52). Hypothetically, the CGRP release is followed by an inhibition of the CGRP reuptake at the nerve-ending terminals. CGRP-receptor complexes are formed, and, possibly after a non-competitive saturation of the extra- and intraluminal CGRP receptors, CGRP levels in CSF and serum finally decrease due to the subsequent depletion of the releasing terminal nerve endings. It has further been speculated that different types of stroke like sSAH may alter the synthesis, metabolism, molecule, or receptors of the neurotransmitter CGRP. In the serum of sSAH patients, peak concentrations of CGRP have been measured after rupture of aneuryms of the middle cerebral artery (14, 44) (during days 4–7 after onset of sSAH), in patients with CV-related ischemia (on day 4), and – as to cerebrovascular manipulation–after endoluminal aneurysm treatment *via* coiling (44) (within days 3–5 after sSAH). In our series, the serum CGRP levels did neither differ regarding the anatomical localization of the ruptured aneurysm, nor regarding the treatment-induced mechanical intra- and extraluminal manipulation of the parent vessel in the aneurysm-securing procedure groups and the control group, respectively. Interestingly, in our cohort without gender bias, the female patients expressed significantly higher serum CGRP levels at the 6-month FU than their male counterparts. Although headaches are prevalent in both sexes and in all age groups, women aged 20 up to 50 years are those who have the highest prevalences in Europe (53).

A remarkable and presumably cerebroprotective hypersecretion of CGRP into serum counterbalancing vasoconstriction was previously detected in sSAH patients with vasospasm-related ischemia (44). In our cohort, exclusively comprising good-grade sSAH patients without any CV-related ischemic complications, the excessive release of CGRP into CSF (15, 16) during the first 10 days after ictus contrasts with the significantly lower CGRP levels in serum. This is all the more noteworthy given that even these smaller amounts of CGRP in serum suffice to induce considerable impairment in pain processing and psychosomatic disorders. The sparse neuropeptide findings in serum presumably result from the diluting effect of the nanomolar concentrations of the ventricular CSF CGRP during its absorption into plasma and its clearance over time. On the other hand, our results in a good-grade sSAH collective contradict previous findings in aSAH patients with CV (14, 44), in whom serum CGRP levels have been measured higher than CGRP levels in CSF. To date, it is unclear which source is the best to (non-invasively) access predictive CGRP values, like, recently, in tear fluid (53) of migraine patients.

After three decades of intense research, drugs targeting the trigeminal sensory neuropeptide CGRP or its receptor and, thus, acting on the trigeminal pain system have been specifically designed (21). It is remarkable that, in migraineurs, all CGRP-targeted therapies (CGRP receptor antagonists/gepants and monoclonal antibodies against CGRP or the CGRP receptor) have proven clinical efficacy, whether in preventing attack onset, targeting acute attacks, or reducing attacks in chronic migraine or frequent episodic migraine (21, 54). To date, it is unknown whether CGRP antagonism may provide a beneficial therapeutic approach for the treatment of chronic pain conditions and CV in sSAH as well.

Scrutinizing the frequency and type of self-reported met and unmet needs of SAH survivors 1–2 years and 3–5 years following hemorrhage, headache, fatigue, concentration, memory, and anxiety were the most commonly described, and a large proportion of needs (> 80%) were detected as unmet (55). The pain conditions, real-world deficits, and the neurobehavioral sequelae of an sSAH are not appropriately addressed by current rehabilitation programs, which still mainly focus on physical rehabilitation. Neuroscientists and clinicians should strive for a standardized screening and early identification of patients at-risk and for non-pharmacologic coping strategies that may be effective in pain management and hrQoL improvement to increase patient resiliency (56). Comprehensive rehabilitation programs imply a multidisciplinary approach (57) with physiotherapy, cognitive behavioral therapy, and biofeedback using relaxation techniques in order to reduce pain conditions; in addition, it is recommended to screen for and treat analgesics overuse (38).

In methodological terms, the main strength of our investigation is the prospective, controlled data collection

comprising a throughly selected cohort of a representative neurovascular medium volume center. The study population underwent a meticulous liquid biobanking in combination with a standardized comprehensive hrQoL assessment over a considerable FU period of 6 months. Attributed to the abrupt nature of sSAH, biomarkers are not amenable to baseline data acquisition. Furthermore, the utilized hrQoL questionnaires are not designed to precisely establish pain and headache diagnoses and to specify the psychosomatic symptom burden. A major limitation of our experimental clinical study is the circumscribed sample size demanding a cautious interpretation of our findings. We are aware of the potential bias due to the exclusion of five patients. The results are not applicable for sSAH patients in general since our cohort exclusively encompasses prognostically favorable good-grade individuals with the per-protocol exclusion of non-HC patients.

Conclusion

Our study reveals the first insight into the potential capacity of endogenous CGRP as a predictive psychoactive biomarker in serum after good-grade sSAH. The present data suggests that patients with elevated CGRP levels in serum suffer from sustained pain conditions and psychosomatic symptoms which in turn seriously affect their hrQoL 6 months after sSAH. This investigation serves as a hypotheses-generating clinical-experimental trial. Given that the neurotransmitter CGRP is a certified core element in migraine, nociceptive processing, and in various neurobehavioral disorders, its pathophysiological relevance in post-sSAH pain seems all the more feasible. Considering our interesting results, we advocate and anticipate further basic and clinical research on this issue to characterize the pain syndromes following sSAH and to elucidate the underlying pathopsychological interactions and pathophysiological mechanisms. In the future, the proven efficacy and safety of the CGRP antagonists and antibodies in migraine therapy might pave the way to establish potential, targeted, preventive, and pharmacotherapeutic treatment options for chronic pain conditions.

Data availability statement

The raw data supporting the conclusions of this article will be made available by the authors, without undue reservation.

Ethics statement

The study protocol was approved by the Local Institutional Ethics Committee of the University Medical Center Regensburg (protocol number 06-179). The patients/participants provided their written informed consent to participate in this study. Written informed consent was obtained from the individual(s) for the publication of any potentially identifiable images or data included in this article.

Author contributions

EB, PS, SB, MP, and E-MS: acquisition of data. EB, K-MS, MP, and FZ: analysis, interpretation of data, and statistical analysis. EB: drafting the article. K-MS and EB: study supervision. K-MS: conception and design and approvement of the final version of the manuscript on behalf of all authors. All authors critically revising the article and review of the submitted version of the manuscript.

Conflict of interest

The authors declare that the research was conducted in the absence of any commercial or financial relationships that could be construed as a potential conflict of interest.

Publisher's note

All claims expressed in this article are solely those of the authors and do not necessarily represent those of their affiliated organizations, or those of the publisher, the editors and the reviewers. Any product that may be evaluated in this article, or claim that may be made by its manufacturer, is not guaranteed or endorsed by the publisher.

References

1. La Pira B, Singh TD, Rabinstein AA, Lanzino G. Time trends in outcomes after aneurysmal subarachnoid hemorrhage over the past 30 years. *Mayo Clinic Proceedings*. (2018) 93:1786–93. doi: 10.1016/j.mayocp.2018.06.027

2. Huckhagel T, Klinger R, Schmidt NO, Regelsberger J, Westphal M, Czorlich P. The burden of headache following aneurysmal subarachnoid hemorrhage: a prospective single-center cross-sectional analysis. *Acta Neurochir*. (2020) 162:893–903. doi: 10.1007/s00701-020-04235-7

3. Powell J, Kitchen N, Heslin J, Greenwood R. Psychosocial outcomes at 18 months after good neurological recovery from aneurysmal subarachoid haemorrhage. *J Neurol Neurosurg Psychiatry*. (2004) 75:1119–24. doi: 10.1136/jnnp.2002.000414

4. Haug Nordenmark T, Karic T, Røe C, Sorteberg W, Sorteberg A. The post-Asah syndrome: a self-reported cluster of symptoms in patients with aneurysmal subarachnoid hemorrhage. *J Neurosurg*. (2019) 132:1556–65. doi: 10.3171/2019.1.JNS183168

5. Al-Khindi T, MacDonald RL, Schweizer TA. Cognitive and functional outcome after aneurysmal subarachnoid hemorrhage. *Stroke*. (2010) 41:e519–36. doi: 10.1161/STROKEAHA.110.581975

6. Glisic EK, Gardiner L, Josti L, Dermanelian E, Ridel S, Dziodzio J, et al. Inadequacy of headache management after subarachnoid hemorrhage. *Am J Crit Care*. (2016) 25:136–43. doi: 10.4037/ajcc2016486

7. Singh M, Guth JC, Liotta E, Kosteva AR, Bauer RM, Prabhakaran S, et al. Predictors of 30-day readmission after subarachnoid hemorrhage. *Neurocrit Care*. (2013) 19:306–10. doi: 10.1007/s12028-013-9908-0

8. Ogden JA, Utley T, Mee EW. Neurological and psychosocial outcome 4 to 7 years after subarachnoid hemorrhage. *Neurosurgery*. (1997) 41:25–34. doi: 10.1097/00006123-199707000-00008

9. Greebe P, Rinkel GJE. Life expectancy after perimesencephalic subarachnoid hemorrhage. *Stroke*. (2007) 38:1222–4. doi: 10.1161/01.STR.0000260093.49693.7a

10. Marquardt G, Niebauer T, Schick U, Lorenz R. Long term follow up after perimesencephalic subarachnoid haemorrhage. *J Neurol Neurosurg Psychiatry*. (2000) 127–30. doi: 10.1136/jnnp.69.1.127

11. Rasouli J, Watson C, Yaeger K, Ladner T, Kellner C, Dangayach NS. Pain control after aneurysmal subarachnoid hemorrhage: a contemporary literature review. *J Clin Neurosci*. (2019) 68:9–12. doi: 10.1016/j.jocn.2019.07.057

12. Amara SG, Jonas V, Rosenfeld MG, Ong ES, Evans RM. Alternative Rna processing in calcitonin gene expression generates Mrnas encoding different polypeptide products. *Nature*. (1982) 298:240–4. doi: 10.1038/298240a0

13. McCulloch J, Uddman R, Kingman TA, Edvinsson L. Calcitonin gene-related peptide: functional role in cerebrovascular regulation. *Proc Natl Acad Sci U S A*. (1986) 83:5731–5. doi: 10.1073/pnas.83.15.5731

14. Juul R, Hara H, Gisvold SE, Brubakk AO, Fredriksen TA, Waldemar G, et al. Alterations in perivascular dilatory neuropeptides (Cgrp, Sp, Vip) in the external jugular vein and in the cerebrospinal fluid following subarachnoid haemorrhage in man. *Acta Neurochir*. (1995) 132:32–41. doi: 10.1007/BF01404845

15. Schebesch KM, Herbst A, Bele S, Schödel P, Brawanski A, Stoerr EM, et al. Calcitonin-gene related peptide and cerebral vasospasm. *J Clin Neurosci*. (2013) 20:584–6. doi: 10.1016/j.jocn.2012.07.006

16. Bründl E, Proescholdt M, Störr EM, Schödel P, Bele S, Höhne J, et al. Endogenous calcitonin gene-related peptide in cerebrospinal fluid and early quality of life and mental health after good-grade spontaneous subarachnoid hemorrhage—a feasibility series. *Neurosurg Rev*. (2020) 44:1479–92. doi: 10.1007/s10143-020-01333-z

17. Poyner DR. Calcitonin gene-related peptide: multiple actions, multiple receptors. *Pharmacol Ther*. (1992) 56:23–51. doi: 10.1016/0163-7258(92)90036-Y

18. Van Rossum D, Hanisch UK, Quirion R. Neuroanatomical localization, pharmacological characterization and functions of Cgrp, related peptides and their receptors. *Neurosci Biobehav Rev*. (1997) 21:649–78. doi: 10.1016/S0149-7634(96)00023-1

19. Schou WS, Ashina S, Amin FM, Goadsby PJ, Ashina M. Calcitonin gene-related peptide and pain: a systematic review. *J Headache Pain*. (2017) 18:34. doi: 10.1186/s10194-017-0741-2

20. Charles A, Pozo-Rosich P. Targeting calcitonin gene-related peptide: a new era in migraine therapy. *The Lancet*. (2019) 394:1765–74. doi: 10.1016/S0140-6736(19)32504-8

21. Edvinsson L, Haanes KA, Warfvinge K, Krause DN. Cgrp as the target of new migraine therapies - successful translation from bench to clinic. *Nat Rev Neurol*. (2018) 14:338–50. doi: 10.1038/s41582-018-0003-1

22. Bründl E, Proescholdt M, Schödel P, Bele S, Höhne J, Zeman F, et al. Excessive release of endogenous neuropeptide y into cerebrospinal fluid after treatment of spontaneous subarachnoid haemorrhage and its possible impact on self-reported neuropsychological performance–results of a prospective clinical pilot study on good-G. *Neurol Res*. (2018) 40:1001–13. doi: 10.1080/01616412.2018.1508547

23. Brundl E, Schodel P, Bele S, Proescholdt M, Scheitzach J, Zeman F, et al. Treatment of spontaneous subarachnoid hemorrhage and self-reported neuropsychological performance at 6 months - results of a prospective clinical pilot study on good-grade patients. *Turk Neurosurg*. (2018) 28:369–88. doi: 10.5137/1019-5149.JTN.21825-17.0

24. Teasdale GM, Drake CG, Hunt W, Kassell N, Sano K, Perat B, et al. A universal subarachnoid haemorrhage scale: report of a committee of the world federation of neurosurgical societies. *J Neurol Neurosurg Psychiatry*. (1988) 51:1457. doi: 10.1136/jnnp.51.11.1457

25. Hunt WE, Hess RM. Surgical risk as related to time of intervention in the repair of intracranial aneurysms. *J Neurosurg*. (1968) 28:14–20. doi: 10.3171/jns.1968.28.1.0014

26. Brundl E, Bohm C, Lurding R, Schodel P, Bele S, Hochreiter A, et al. Treatment of unruptured intracranial aneurysms and cognitive performance: preliminary results of a prospective clinical trial. *World Neurosurg*. (2016) 94:145–56. doi: 10.1016/j.wneu.2016.06.112

27. Kagerbauer SM, Kemptner DM, Schepp CP, Bele S, Rothörl RD, Brawanski AT, et al. Elevated premorbid body mass index is not associated with poor neurological outcome in the subacute state after aneurysmal subarachnoid hemorrhage. *Zentralbl Neurochir*. (2010) 71:163–6. doi: 10.1055/s-0030-1249043

28. Jennett B, Bond M. Assessment of outcome after severe brain damage. A practical scale. *The Lancet*. (1975) 1:480–4. doi: 10.1016/S0140-6736(75)92830-5

29. Rankin J. Cerebral vascular accidents in patients over the age of 60: II. Prognosis. *Scott Med J*. (1957) 2:200–15. doi: 10.1177/003693305700200504

30. Tritt K, Von Heymann F, Zacharias I, Loew T, Zaudig M, Söllner W. Development of the "Icd-10-symptom-rating" (Isr) questionnaire. *Z Psychosom Med Psychother*. (2008) 54:409–18. doi: 10.13109/zptm.2008.54.4.409

31. Bullinger M. German translation and psychometric testing of the Sf-36 health survey: preliminary results from the iqola project. *Soc Sci Med*. (1995) 41:1359–66. doi: 10.1016/0277-9536(95)00115-N

32. Bach JP, Riedel O, Pieper L, Klotsche J, Dodel R, Wittchen HU. Health-related quality of life in patients with a history of myocardial infarction and stroke. *Cerebrovasc Dis*. (2010) 31:68–76. doi: 10.1159/000319027

33. Chen Q, Cao C, Gong L, Zhang Y. Health related quality of life in stroke patients and risk factors associated with patients for return to work. *Medicine*. (2019) 98:e15130. doi: 10.1097/MD.0000000000015130

34. Sonesson B, Kronvall E, Säveland H, Brandt L, Nilsson OG. Long-term reintegration and quality of life in patients with subarachnoid hemorrhage and a good neurological outcome: findings after more than 20 years. *J Neurosurg*. (2018) 128:785–92. doi: 10.3171/2016.11.JNS16805

35. Hütter BO, Gilsbach JM, Kreitschmann I. Quality of life and cognitive deficits after subarachnoid haemorrhage. *Br J Neurosurg*. (1995) 9:465–75. doi: 10.1080/02688699550041106

36. Stronks DL, Tulen JHM, Bussmann JBJ, Mulder LJMM, Passchier J. Interictal daily functioning in migraine. *Cephalalgia*. (2004) 24:271–9. doi: 10.1111/j.1468-2982.2004.00661.x

37. Swope R, Glover K, Gokun Y, Fraser JF, Cook AM. Evaluation of headache severity after aneurysmal subarachnoid hemorrhage. *Interdiscip Neurosurg*. (2014) 119–22. doi: 10.1016/j.inat.2014.07.003

38. Lai J, Harrison RA, Plecash A, Field TS. A narrative review of persistent post-stroke headache – a new entry in the international classification of headache disorders, 3rd edition. *Headache*. (2018) 58:1442–53. doi: 10.1111/head.13382

39. Cavestro C, Ferrero M. Migraine in systemic autoimmune diseases. *Endocrin Metab Immune Disord Drug Targets*. (2017) 18:124–34. doi: 10.2174/1871530317666171124124340

40. Hütter BO, Kreitschmann-Andermahr I. Subarachnoid hemorrhage as a psychological trauma: clinical article. *J Neurosurg*. (2014) 120:923–30. doi: 10.3171/2013.11.JNS121552

41. Bryant RA. Posttraumatic stress disorder and mild brain injury: controversies, causes and consequences. *J Clin Exp Neuropsychol*. (2001) 23:718–28. doi: 10.1076/jcen.23.6.718.1024

42. Harriott AM, Karakaya F, Ayata C. Headache after Ischemic stroke: a systematic review and meta-analysis. *Neurology*. (2020) 94:e75–e86. doi: 10.1212/WNL.0000000000008591

43. Muehlschlegel S, Kursun O, Topcuoglu MA, Fok J, Singhal AB. Differentiating reversible cerebral vasoconstriction syndrome with subarachnoid hemorrhage from other causes of subarachnoid hemorrhage. *JAMA Neurol*. (2013) 70:1254–60. doi: 10.1001/jamaneurol.2013.3484

44. Schebesch K-M, Bruendl E, Hochreiter A, Scheitzach J, Bele S, Herbst A, et al. Calcitonin gene-related peptide in serum after spontaneous subarachnoid hemorrhage. *Am J Neurosci*. (2014) 5:10–17. doi: 10.3844/amjnsp.2014.10.17

45. Watson E, Ding D, Khattar NK, Everhart DE, James RF. Neurocognitive outcomes after aneurysmal subarachnoid hemorrhage: identifying inflammatory biomarkers. *J Neurol Sci*. (2018) 394:84–93. doi: 10.1016/j.jns.2018.06.021

46. Kokkoris S, Andrews P, Webb DJ. Role of calcitonin gene-related peptide in cerebral vasospasm, and as a therapeutic approach to subarachnoid hemorrhage. *Front Endocrinol*. (2012) 3:135. doi: 10.3389/fendo.2012.00135

47. Edvinsson L. The trigeminovascular pathway: role of Cgrp and Cgrp receptors in migraine. *Headache*. (2017) 57(Suppl 2):47–55. doi: 10.1111/head.13081

48. Edvinsson L. Aspects on the pathophysiology of migraine and cluster headache. *Pharmacol Toxicol.* (2001) 89:65–73. doi: 10.1111/j.1600-0773.2001.890201.x

49. Juul R, Aakhus S, Björnstad K, Gisvold SE, Brubakk AO, Edvinsson L. Calcitonin gene-related peptide (Human α-Cgrp) counteracts vasoconstriction in human subarachnoid haemorrhage. *Neurosci Lett.* (1994) 170:67–70. doi: 10.1016/0304-3940(94)90240-2

50. Iyengar S, Ossipov MH, Johnson KW. The role of calcitonin gene-related peptide in peripheral and central pain mechanisms including migraine. *Pain.* (2017) 158:543–59. doi: 10.1097/j.pain.0000000000000831

51. Keller JT, Marfurt CF. Peptidergic and serotoninergic innervation of the rat dura mater. *J Comp Neurol.* (1991) 309:515–34. doi: 10.1002/cne.903090408

52. Nozaki K, Kikuchi H, Mizuno N. Changes of calcitonin gene-related peptide-like immunoreactivity in cerebrovascular nerve fibers in the dog after experimentally produced subarachnoid hemorrhage. *Neurosci Lett.* (1989) 102:27–32. doi: 10.1016/0304-3940(89)90302-9

53. Kamm K, Straube A, Ruscheweyh R. Calcitonin gene-related peptide levels in tear fluid are elevated in migraine patients compared to healthy controls. *Cephalalgia.* (2019) 39:1535–1543. doi: 10.1177/0333102419856640

54. Edvinsson L. Calcitonin gene-related peptide (Cgrp) in cerebrovascular disease. *Sci World J.* (2002). doi: 10.1100/tsw.2002.806

55. Dulhanty LH, Hulme S, Vail A, Patel HC, Tyson SF. The self-reported needs of patients following subarachnoid hemorrhage (Sah). *Disabil Rehabil.* (2019) 42:3450–56. doi: 10.1080/09638288.2019.1595748

56. Stonnington CM, Kothari DJ, Davis MC. Understanding and promoting resiliency in patients with chronic headache. *Curr Neurol Neurosci Rep.* (2016) 16:6. doi: 10.1007/s11910-015-0609-2

57. Gaul C, Liesering-Latta E, Schäfer B, Fritsche G, Holle D. Integrated multidisciplinary care of headache disorders: a narrative review. *Cephalalgia.* (2016) 36:1181–91. doi: 10.1177/0333102415617413

frontiers | Frontiers in Neurology

TYPE Original Research
PUBLISHED 01 August 2022
DOI 10.3389/fneur.2022.942023

Check for updates

OPEN ACCESS

EDITED BY
Yuzhen Xu,
Tongji University, China

REVIEWED BY
Jie Tao,
Shanghai General Hospital, China
Wei Gao,
Changxing People's Hospital, China
Jin Huang,
Aviation General Hospital of China Medical University, China

*CORRESPONDENCE
Weidong Wu
wei1318123@163.com

SPECIALTY SECTION
This article was submitted to Neurological Biomarkers, a section of the journal Frontiers in Neurology

RECEIVED 12 May 2022
ACCEPTED 08 July 2022
PUBLISHED 01 August 2022

CITATION
Du Y, Shi H, Yang X and Wu W (2022) Machine learning for infection risk prediction in postoperative patients with non-mechanical ventilation and intravenous neurotargeted drugs. *Front. Neurol.* 13:942023. doi: 10.3389/fneur.2022.942023

COPYRIGHT
© 2022 Du, Shi, Yang and Wu. This is an open-access article distributed under the terms of the Creative Commons Attribution License (CC BY). The use, distribution or reproduction in other forums is permitted, provided the original author(s) and the copyright owner(s) are credited and that the original publication in this journal is cited, in accordance with accepted academic practice. No use, distribution or reproduction is permitted which does not comply with these terms.

Machine learning for infection risk prediction in postoperative patients with non-mechanical ventilation and intravenous neurotargeted drugs

Yi Du, Haipeng Shi, Xiaojing Yang and Weidong Wu*

Department of Intensive Care Medicine, Shanxi Bethune Hospital, Shanxi Academy of Medical Sciences, Taiyuan, China

Drug efficacy can be improved by understanding the effects of anesthesia on the neurovascular system. In this study, we used machine learning algorithms to predict the risk of infection in postoperative intensive care unit (ICU) patients who are on non-mechanical ventilation and are receiving hydromorphone analgesia. In this retrospective study, 130 patients were divided into high and low dose groups of hydromorphone analgesic pump patients admitted after surgery. The white blood cells (WBC) count and incidence rate of infection was significantly higher in the high hydromorphone dosage group compared to the low hydromorphone dosage groups ($p < 0.05$). Furthermore, significant differences in age ($P = 0.006$), body mass index (BMI) ($P = 0.001$), WBC count ($P = 0.019$), C-reactive protein (CRP) ($P = 0.038$), hydromorphone dosage ($P = 0.014$), and biological sex ($P = 0.024$) were seen between the infected and non-infected groups. The infected group also had a longer hospital stay and an extended stay in the intensive care unit compared to the non-infected group. We identified important risk factors for the development of postoperative infections by using machine learning algorithms, including hydromorphone dosage, age, biological sex, BMI, and WBC count. Logistic regression analysis was applied to incorporate these variables to construct infection prediction models and nomograms. The area under curves (AUC) of the model were 0.835, 0.747, and 0.818 in the training group, validation group, and overall pairwise column group, respectively. Therefore, we determined that hydromorphone dosage, age, biological sex, BMI, WBC count, and CRP are significant risk factors in developing postoperative infections.

KEYWORDS

machine learning, post-surgical ICU, neurovascular, anesthesia, infection, hydromorphone

Introduction

Patients in the intensive care unit (ICU) experience varying degrees of pain, delirium, agitation, and arousal. These conditions can lead to prolonged ICU stays and increased morbidity and mortality (1–4). As a result, analgesia and sedation have become part of routine ICU care, leading to the current e-CASH (early comfort using analgesia, minimal sedatives, and maximal humane care) sedation concept (5). The development of clinical drugs used for analgesia and sedation of ICU patients has been increasing in number. Assessing the condition and determining its pharmacology can lead to better analgesia with narcotics (6–9). In the ICU, we are more likely to make better treatment decisions if we understand the different effects of anesthesia on the neurovascular system (10).

Morphine is widely used internationally as a classical neurovascular anesthetic because of its low price and significant effects (11–13). However, repeated administration of morphine can result in serious adverse events (14). Hydromorphone, a new analgesic drug, is a semi-synthetic morphine derivative. The analgesic effect is approximately 8–10 times better than morphine, and it has fast onset of action, fewer side effects, various routes of administration, low risk of hallucination addiction, low risk of gastrointestinal adverse reactions, non-toxic metabolites, and better suitability for patients with decompensated liver and kidney function (13, 15). Hydromorphone has been extensively validated for use in an emergency, day surgery, and perioperative management settings, with significant advantages in reducing respiratory depression and gastrointestinal adverse effects (15–18). However, further studies are needed to assess the effectiveness, safety, and dosage of this medication in the ICU.

In contrast to other analgesics, hydromorphone has been found to reduce the incidence of postoperative pneumonia in patients undergoing thoracic surgery; however, in general, infection remains to be a significant complication of hydromorphone (17, 19, 20). For one, an increased incidence of infective endocarditis has been associated with hydromorphone injection (20). Similarly, intrathecal targeted drug delivery of hydromorphone may lead to device infection (21). These complications may be problematic since inflammation and infection have been shown to reduce the effectiveness of some analgesics (22). Moreover, the postoperative infection has been found to be an important risk factor affecting the survival of patients (23, 24). These suggest that in clinical practice, the risk of infection needs to be predicted.

Machine learning is currently an important means of implementing artificial intelligence technologies, and the application of these algorithms in clinical diagnosis and decision-making has become a research priority in the medical field (25–27). In non-mechanically ventilated ICU, predicting the risk of hydromorphone infection is very challenging and requires an accurate biological classification model utilizing simple and effective decision rules. In relation to this, random forest models and support vector machine models are frequently used in classification tasks to predict treatment effects or complications and to screen for clinically important features related to outcomes (28). Logistic regression analysis is often used to screen for risk factors associated with adverse outcomes, and it can also be utilized in constructing a nomogram that can be easily applied clinically for the accurate detection and treatment of a disease (29, 30). In non-mechanically ventilated ICU patients after surgery, we believe that these machine learning tools can be used to predict the risk of infection with hydromorphone analgesia.

The purpose of this study is to develop a validated tool that can utilize available clinical information to predict the risk of infection in ICU patients receiving post-surgical hydromorphone analgesia. This will ultimately reduce hospital stays, medical costs, and length of hospital stays post-operatively, as well as provide guidance for future studies to improve analgesic outcomes for ICU patients.

Method

Clinical cohort data acquisition

After institutional ethics committee approval, a group of patients admitted to the ICU after surgical procedures and who received analgesic treatment was enrolled in the study. Since this study used a retrospective analysis format, patients' informed consent was waived. The inclusion criteria used were as follows: (1) age between 45 and 90; (2) American Society of Anesthesiologists (ASA) physical score I to II; and (3) cardiac left ventricular ejection fraction greater than 40%. Meanwhile, the exclusion criteria used were as follows: (1) those with significant preoperative heart, liver, or kidney disease; (2) those with neurological or psychiatric diseases; (3) those with lung conditions such as chronic obstructive pulmonary disease or chronic bronchitis; (4) those with allergies to study drugs such as opioid prescriptions; and (5) those with a body mass index of 30 kg/m^2. Overall, a total of 130 patients passed the screening criteria. The general characteristics of these patients, such as biological sex, age, height, weight, BMI, etc., were collected through a clinical history data review. In addition, Acute Physiology and Chronic Health Evaluation (APACHE II) and Sepsis Related Organ Failure Assessment (SOFA) scores were collected in full at the time of patient admission to the ICU.

Hydromorphone dosage calculation

The pumping speed of the micropump was adjusted to achieve satisfactory analgesia. Patients were evaluated for pain

and physiological indicators every 2 h. Patients whose daily hydromorphone dosage exceeded 40 mg/mL were included in the high hydromorphone dosage group, and those who did not exceed 40 mg/mL were included in the low hydromorphone dosage group.

Closing indicators

Physiological and biochemical indices, such as heart rate (HR), mean artery pressure (MAP), respiratory rate (R), C-reactive protein (CRP), white blood cell (WBC) count, platelet (PLT), and Saturation of Pulse Oxygen (SpO2), were recorded completely after 12 h of analgesia, from the moment that the patient was admitted to ICU with self-administered hydromorphone analgesia. In addition, the occurrence of adverse reactions throughout the postoperative treatment period was recorded. In this study, the primary outcome indicator was defined as the occurrence of infection. Postoperative infection was evaluated based on the following indicators: (1) temperature >38 °C; (2) elevated WBC count; (3) positive sputum culture or blood culture showing bacteria; (4) chest X-ray showing abnormal density; and (5) diagnosis of pneumonia, etc. (31).

Machine learning and logistic regression analysis

Firstly, a random forest model was utilized to fit this dataset so as to rank the importance of each clinical feature in terms of the infection outcome (32). Subsequently, in order to screen clinical features related to infection, Support Vector Machine-Recursive Feature Elimination (SVM-RFE) was applied to the general characteristics of patients, secondary indicators for the prediction model of infection important features screening and model construction (33). A support vector machine (SVM) is often used for non-linear classification, and they perform well on small samples. The SVM-RFE technique uses iterative iterations to remove redundant feature variables. Root Mean Squard Error (RMSE) metrics were applied to evaluate the accuracy of the SVM models and to determine the best model variables based on the RMSE minimum. Furthermore, neural networks, a common non-linear algorithmic model in machine learning, were also used to evaluate results as previous researches (34–38).

Univariate and multifactorial logistic regression analyses were also applied to assess the risk ratio of each clinical factor on infection outcome (39). In the first step, we performed univariate logistic regression analysis sequentially and analyzed the characteristics of the patients based upon $P < 0.05$. Those variables that were subjected to multifactor logistic regression analysis were then screened according to $P < 0.2$ to identify the variables obtained from logistic analysis. Based on the odds ratios (ORs) and 95% confidence intervals (95% CIs) for each variable, we calculated how much each characteristic was associated with infection risk. We then applied univariate logistic regression to determine which variables were independent risk factors.

TABLE 1 Comparison of baseline characteristics between the two hydromorphone consumption groups.

Characteristic		Hydromorphone consumption groups		*P*-value
		High ($n = 65$)	Low ($n = 65$)	
Biological sex (%)	Female	20 (30.77)	26 (40.00)	0.271
	Male	45 (69.23)	39 (60.00)	
Age, years		64.23 ± 8.97	61.18 ± 10.14	0.072
Weight, kg		65.98 ± 10.47	65.29 ± 10.96	0.713
Height, cm		170.26 ± 14.51	168.23 ± 13.77	0.415
BMI, kg/m^2		22.74 ± 2.33	23.00 ± 1.98	0.491
Hypertension (%)	No	60 (92.31)	54 (83.08)	0.109
	Yes	5 (7.69)	11 (16.92)	
Diabetes (%)	No	58 (89.23)	51 (78.46)	0.095
	Yes	7 (10.77)	14 (21.54)	
APACHE_II		24.98 ± 5.75	24.09 ± 6.80	0.421
SOFA		4.15 ± 1.03	4.09 ± 1.03	0.734

APACHE II, acute physiology and chronic health evaluation II; BMI, body mass index; SOFA, sepsis related organ failure assessment.

Identification of important characteristics

Intersection analysis was conducted to confirm the shared characteristics between the variables screened using the Support Vector Machine-Recursive Feature Elimination (SVM-RFE) model and those screened using logistic regression analysis (40–45). To determine the amount of information that these shared features can contain about the outcomes, PCA (principle component analysis) is applied to downscale them. In addition, neural network models with multilayer network structures are continuously used in several fields. Furthermore, these shared important features are also passed into the neural network model as input features to measure the classification performance of the variables under the neural network model.

Construction of nomogram model

For the construction of infection prediction models, a multi-factor logistic regression model was used based

TABLE 2 Comparison of clinical outcomes between the two hydromorphone consumption groups.

Characteristic		Hydromorphone consumption groups		*P*
		High ($n = 65$)	Low ($n = 65$)	
HR, min^{-1}		95.77 ± 10.83	98.31 ± 11.38	0.195
MAP, mmHg		76.78 ± 7.47	76.89 ± 6.80	0.932
R, min^{-1}		19.42 ± 3.61	20.52 ± 3.66	0.085
WBC, 10^9/L		12.89 ± 5.11	11.23 ± 3.71	0.036*
PLT, 10^9/L		231.58 ± 62.70	228.45 ± 43.61	0.741
CRP, mg/L		76.32 ± 31.25	74.38 ± 34.21	0.736
SpO_2, %		96.43 ± 1.97	96.37 ± 2.43	0.874
ICU stay, day		2.25 ± 0.71	2.14 ± 0.61	0.354
LOH, day		9.66 ± 1.28	9.26 ± 1.12	0.06
Nausea	No	57 (87.69)	62 (95.38)	0.115
(%)	Yes	8 (12.31)	3 (4.62)	
Infection	No	47 (72.31)	58 (89.23)	0.014*
(%)	Yes	18 (27.69)	7 (10.77)	

CRP, C-reactive protein; HR, heart rate; ICU, intensive care unit; MAP, mean artery pressure; WBC, white blood cell; PLT, platelet; R, respiratory rate; *P < 0.05.

on these important characteristics. By comparing the predicted probability values of the model to the actual results, the calibration curve further evaluates the accuracy of the model. A decision curve analysis (DCA) was used to evaluate the clinical safety of this clinical prediction model by measuring the yield at different prediction probability thresholds (46). The infection prediction model was then plotted using the "rms" package to obtain a clinical visualization tool to facilitate clinical translation.

Statistical analysis

Software R (version 4.0.2) was used for all analyses and graphs. Training and evaluation of the individual prediction models were conducted by dividing the entire dataset into a training and a test set. The receiver operating characteristic curve (ROC) and the area under the curve (AUC) were used to evaluate the predictive performance of the model. PROC was used to plot ROC curves (47). Pearson's chi-square test or Fisher's exact test were used for the difference test analysis on the count data. The measurement data were analyzed using the Wilcoxon rank sum test or unpaired Student's *t*-test. We considered a significance level of p 0.05 to be statistically significant.

TABLE 3 Clinical characteristics between the infected and uninfected groups.

Characteristic		Infection		*P*
		No ($n = 105$)	Yes ($n = 25$)	
Age, years		61.58 ± 9.55	67.44 ± 8.79	0.006**
Weight, kg		66.22 ± 10.32	63.20 ± 12.01	0.205
Height, cm		168.92 ± 13.33	170.60 ± 17.34	0.596
BMI, kg/m^2		23.16 ± 2.14	21.64 ± 1.80	0.001**
APACHE_II		24.34 ± 6.30	25.36 ± 6.32	0.47
SOFA		4.10 ± 1.05	4.20 ± 0.96	0.679
HR, min^{-1}		97.22 ± 11.48	96.28 ± 9.75	0.706
MAP, mmHg		76.75 ± 7.00	77.20 ± 7.74	0.779
R, min^{-1}		19.96 ± 3.69	20.00 ± 3.65	0.963
WBC, 10^9/L		11.61 ± 4.26	13.96 ± 5.18	0.019*
PLT, 10^9/L		232.17 ± 50.04	220.96 ± 67.91	0.351
CRP, mg/L		72.46 ± 30.39	87.52 ± 39.23	0.038*
SpO_2, %		96.40 ± 2.33	96.40 ± 1.61	1
Group (%)	High	47 (44.76)	18 (72.00)	0.014*
	Low	58 (55.24)	7 (28.00)	
Biological sex (%)	Female	42 (40.00)	4 (16.00)	0.024*
	Male	63 (60.00)	21 (84.00)	
Hypertension (%)	No	57 (87.69)	62 (95.38)	0.532
	Yes	8 (12.31)	3 (4.62)	
Diabetes (%)	No	47 (72.31)	58 (89.23)	0.218
	Yes	18 (27.69)	7 (10.77)	

APACHE II, acute physiology and chronic health evaluation II; BMI, body mass index; CRP, C-reactive protein; HR, heart rate; MAP, mean artery pressure; PLT, platelet; SOFA, sepsis related organ failure assessment; *P < 0.05, **P < 0.01.

Results

Comparison of general characteristics and outcomes of patients between the two hydromorphone dosage groups

In the clinical study of 130 patients admitted to the ICU after surgery, 65 patients received an average daily hydromorphone dosage of more than 40 mg/mL and were included in the high hydromorphone dosage group; the remaining 65 patients were included in the low hydromorphone dosage group. An overview of the patients' baseline clinical information is given in Tables 1, 2. Hydromorphone dosage groups did not differ statistically in terms of biological sex, age, weight, height, BMI, hypertension, diabetes, APACHE II, and SOFA scores. However, the high hydromorphone dosage group had a high WBC count ($P = 0.036$) and a high infection risk ($P = 0.014$). This suggests that high hydromorphone dosages may increase the risk of infection.

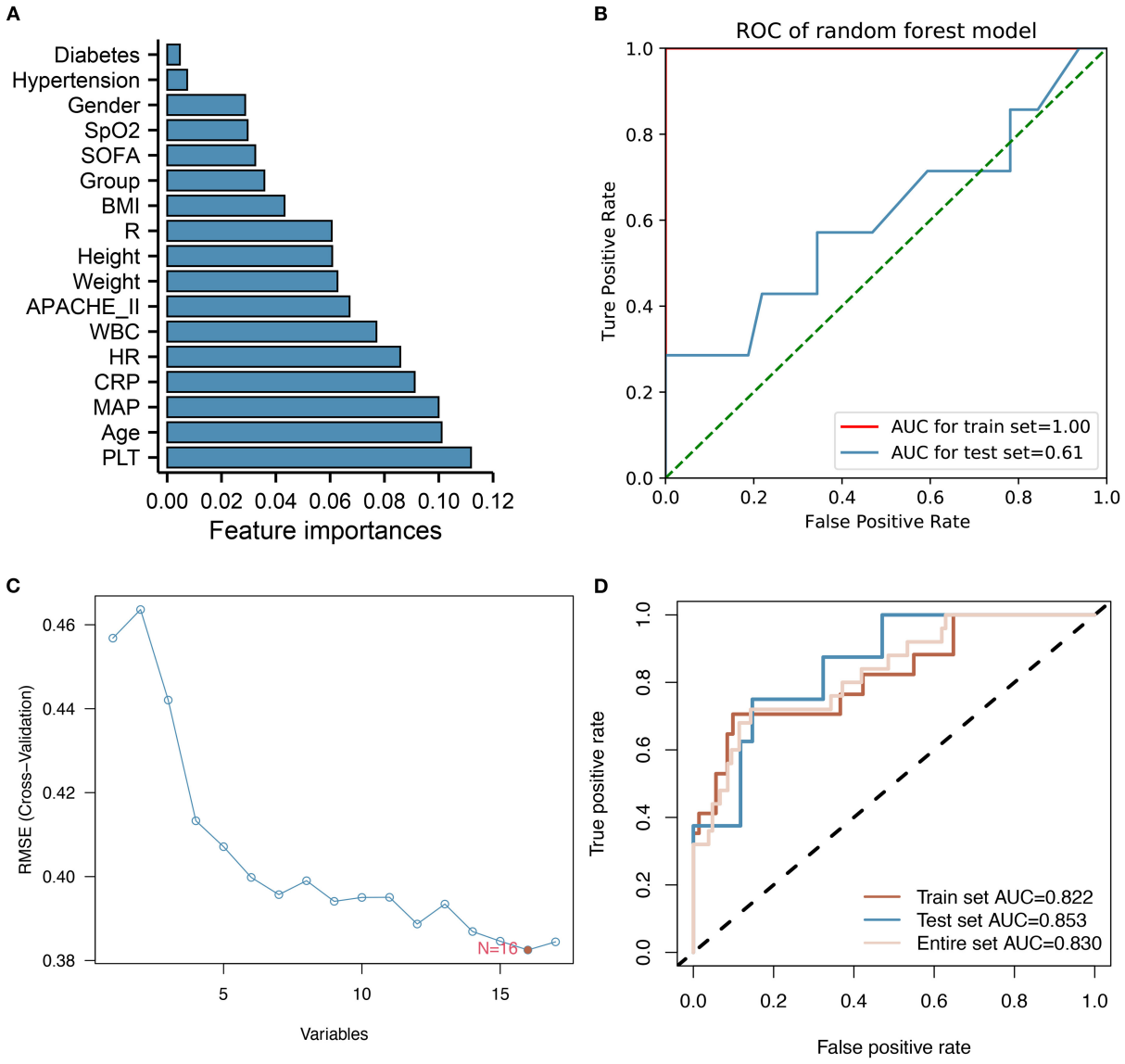

FIGURE 1
Feature ranking and filtering process for Random Forest and SVM-RFE models. **(A)** Bar chart showing a random forest model's importance ranking of each variable. PLT, age, MAP, CRP, and HR are the top five variables identified. **(B)** ROC curves showing the classification ability of the random forest model. **(C)** The feature screening process of SVM-RFE results in the model with the lowest RMSE when 16 variables are selected. **(D)** ROC curves showing training, test, and overall classification performances of the SVM model.

Comparison of characteristics of infected and uninfected groups

Twenty-five patients developed postoperative infections, while the other 105 did not. Table 3 summarizes the clinical characteristics of the infected and uninfected patients. The occurrence of infection was associated with age (P = 0.006), BMI (P = 0.001), WBC count (P = 0.019), CRP (P = 0.038), hydromorphone dosage (P = 0.014), and biological sex (P = 0.024). Infected patients were older, had a lower BMI, higher WBC counts, higher CRP, and used more hydromorphone than non-infected patients. These results suggest that together with hydromorphone use, multiple clinical characteristics can be associated with the occurrence of postoperative infections in surgical patients.

TABLE 4 Univariate and multivariate logistics regression analysis.

Variables	Univariate		Multivariate		
	OR (95% CI)	*P* value	β	OR (95% CI)	*P* value
Group (High vs. Low)	3.17 (1.27–8.76)	0.018*	0.83	2.3 (0.79–7.32)	0.137
Age	1.07 (1.02–1.12)	0.008**	0.06	1.07 (1.01–1.13)	0.02*
Biological sex (Male vs. Female)	3.5 (1.23–12.64)	0.031*	1.1	3.02 (0.9–12.59)	0.094
Weight	0.97 (0.93–1.01)	0.205			
Height	1.01 (0.98–1.04)	0.593			
BMI	0.7 (0.55–0.87)	0.002**	−0.38	0.68 (0.51–0.88)	0.005**
Hypertension (Yes/No)	1.48 (0.38–4.73)	0.534			
Diabetes (Yes/No)	0.39 (0.06–1.49)	0.232			
APACHE_II	1.03 (0.96–1.1)	0.467			
SOFA	1.1 (0.71–1.68)	0.676			
HR	0.99 (0.95–1.03)	0.704			
MAP	1.01 (0.95–1.07)	0.777			
R	1 (0.89–1.13)	0.963			
WBC	1.12 (1.02–1.24)	0.023*	0.14	1.15 (1.02–1.31)	0.031*
PLT	1 (0.99–1)	0.349			
CRP	1.01 (1–1.03)	0.042*	0.01	1.01 (1–1.03)	0.094
SpO2	1 (0.82–1.23)	1			

APACHE II, acute physiology and chronic health evaluation II; BMI, body mass index; CRP, C-reactive protein; HR, heart rate; MAP, mean artery pressure; PLT, platelet; R, respiration; SOFA, sepsis related organ failure assessment; SpO2, Saturation of Pulse Oxygen; WBC, white blood cell; *P < 0.05, **P < 0.01.

Ranking features based on machine learning

Based on a random forest model analysis, PLT, age, MAP, CRP, and HR were the top five clinical features associated with infection (Figure 1A). According to Figure 1B, the ROC curves for training and test sets had AUCs of 1.00 and 0.61, respectively, suggesting that the model was overfitted. After using the SVM-RFE method, we found that the model had the smallest Root Mean Square Error (RMSE) value when 16 variables were included (Figure 1C). AUCs of the SVM model based on these 16 variables were 0.822, 0.853, and 0.830, respectively, for the training, test, and overall datasets (Figure 1D). In the test set, SVM showed better classification ability than random forest model, according to the results of the appeal.

Risk factors associated with infection

Risk factors associated with infection were identified using univariate and multifactorial logistic regression analyses. Univariate logistic regression analysis revealed an association between hydromorphone dosage, group ($P = 0.018$), age ($P = 0.008$), biological sex ($P = 0.031$), BMI ($P = 0.002$), WBC ($P = 0.023$), and CRP ($P = 0.042$). Furthermore, multifactorial logistic regression analysis revealed that age ($P = 0.042$), BMI ($P = 0.005$), and WBC ($P = 0.031$) were independent risk factors for infection (Table 4). Furthermore, a multifactorial logistic regression analysis with $P < 0.2$ as a filter identified Hydromorphone dosage group, age, biological sex, BMI, WBC count, and CRP as clinically important factors that contribute to infection risk.

Variables associated with infection outcome identification

According to the intersection analysis of SVM-RFE and logistic regression analysis, six variables were coinciding with the SVM-RFE and logistic regression analysis, including hydromorphone dosage group, age, biological sex, BMI, WBC count, and CRP (Figure 2A). These six variables have sufficient information to predict infection occurrence according to principal component analysis (PCA) (Figure 2B). According to ROC curve analysis, age (AUC = 0.681), biological sex (AUC = 0.620), BMI (AUC = 0.706), dosage group (AUC = 0.636), WBC count (AUC = 0.626), and CRP (AUC = 0.608) were all predictive of infection (Figures 2C–H). Supplementary figure 1 illustrates

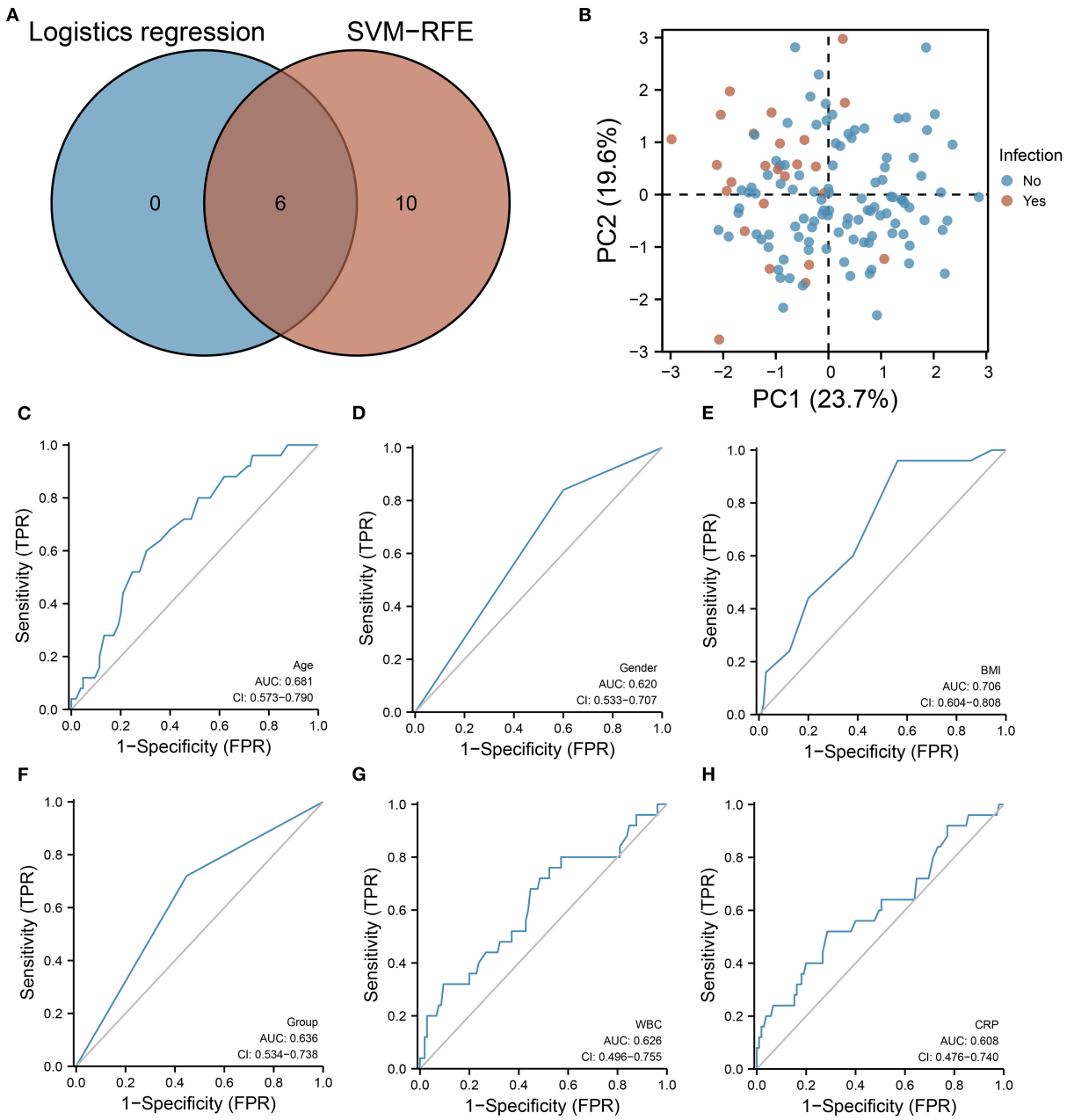

FIGURE 2
SVM-RFE as well as logistic regression models are used for screening important clinical features. **(A)** Venn diagram showing six features associated with infection prediction. **(B)** PCA showing that based on these six characteristics, a better distinction can be made between infected and uninfected patients. **(C–H)** ROC curves showing the predictive performance of **(C)** age, **(D)** biological sex, **(E)** BMI, **(F)** hydromorphone concentration grouping, **(G)** WBC, and **(H)** CRP on infection.

the training process of the neural network model based on these infection-related variables. In both the training and validation sets, the neural network model accurately predicted infection. However, the neural network model only performed 0.539 accurately in the test set. It is possible that this deficiency is due to the small number of patients included in this study.

Construction and evaluation of the nomogram prediction model

Based on the six identified clinical variables, a multifactorial logistic regression algorithm was applied to construct a prediction model to detect the occurrence of infection in relation to the clinical use of hydromorphone. Table 4

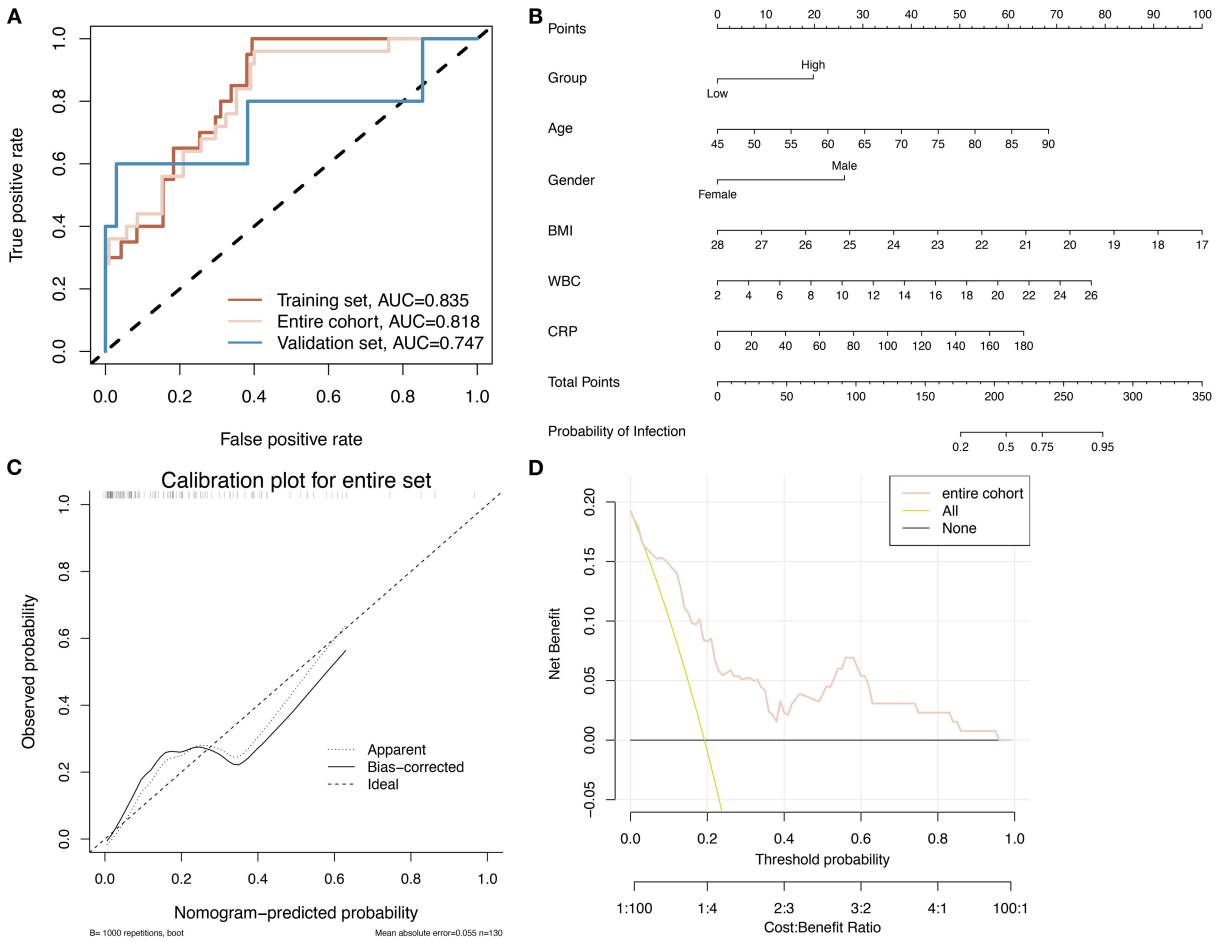

FIGURE 3
A nomogram based on six factors is constructed and its accuracy is assessed. **(A)** The ROC curves for the logistic regression model constructed based on the six identified clinical factors for infection in training, validation, and overall pairwise column sets demonstrate better classification performance in all three datasets. **(B)** The nomogram was constructed using a logistic regression model. **(C)** Calibration plot showing the predicted values of the model are roughly consistent with the true labels, indicating that the model is reasonably accurate. **(D)** Clinical decision curve showing the prediction results in an overall pairwise column.

shows the coefficients of the multifactor logistic regression model based on these six clinical characteristic variables. In the training group, validation group, and overall pairwise column, respectively, the ROC curves showed an AUC of 0.835, 0.818, and 0.747, indicating the model has good predictive ability (Figure 3A). Based on the multifactor logistic regression model, a nomogram was constructed (Figure 3B) to facilitate its clinical application. The correction curves show that the predicted values of the infection prediction model and the true label are in general agreement, further supporting the good predictive power of the model (Figure 3C). Clinical decision curves show that the predictions from the prediction model have clinical value for patients (Figure 3D). Projecting the basic characteristics of the patients and hydromorphone use onto this nomogram allows for the easy calculation of the probability of infection risk, thus guiding hydromorphone use and patient testing in the clinical setting.

In addition, infected patients spent more time in the intensive care unit and hospital overall than their non-infected counterparts (Figure 4). Infections in intensive care units can prolong the stay in the unit, resulting in increased healthcare costs.

Discussion

A machine learning approach was used to predict the risk of infection among non-mechanically ventilated ICU patients receiving hydromorphone analgesia after surgical procedures. According to the study, different factors are associated with the occurrence of postoperative infections in surgical patients

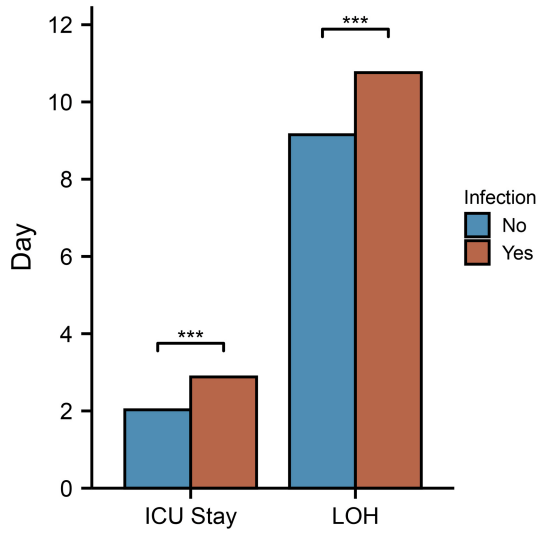

FIGURE 4
Compared between infected and non-infected patients, duration of ICU stay and hospitalization. In the infected group, the hospital stay and ICU stay were longer than in the non-infected group.

based on a cohort study. We identified significant risk factors affecting the development of postoperative infections in patients based on these data, including hydromorphone dosage, age, biological sex, BMI, WBC count, and CRP. Logistic regression was used to construct a predictive model for detecting infection. To assist physicians in assessing the risk of postoperative infections in surgical patients, a nomogram was created based on this model.

In postoperative surgical patients, infections are common adverse effects of opioid analgesics, which can reduce their quality of life, and prolong their length of stay (48–51). A high hydromorphone dosage was associated with a higher incidence of postoperative infections in this study. It has been shown that patients on hydromorphone have less than normal immune system defenses, which may allow bacteria and viruses to infiltrate the body and multiply (20, 52). It has also been shown that hydromorphone, as an opioid analgesic, can cause adverse effects, such as excessive sedation and respiratory depression, pulmonary atelectasis, and infection (53–55). Additionally, hydromorphone promotes bacterial translocation by breaking endothelial tight junctions *via* the Toll-like receptor 2 (20). Opioids increase intestinal bacterial translocation, dysregulated immune responses, and intestinal barrier permeability, thereby increasing the risk of intestinal infections (56). We also found that the WBC count and CRP after 12 h of analgesia were higher in the high hydromorphone dosage group than in the low hydromorphone dosage group. Clinical parameters such as these have been shown to be risk factors for postoperative infection in this study. Infections are more likely to occur in the high hydromorphone dosage group, according to these findings.

Among patients admitted to the ICU after surgery and receiving analgesic treatment, old age was an independent risk factor for infection development. There may be an important correlation between this finding and low immunity in the elderly (57). Similarly, low BMI was identified as an independent risk factor for infection, possibly due to findings that low BMI correlates with worse nutritional status, postoperative recovery, and greater susceptibility to infection (58–60). Furthermore, males had a higher proportion of infections in postoperative ICU admissions than females. Different sex hormones induce different gene expression and immune responses in males and females, which may contribute to different susceptibility to infection (61). Estradiol appears to confer protective immunity, while progesterone and testosterone suppress anti-infection responses (62). Occupational differences and lifestyle differences may also play a role. Therefore, post-analgesic infections should be closely monitored in patients over the age of 65, those with low body mass indexes, and those admitted to the ICU after surgery.

According to our analysis, patients in the infected group spend more time in the ICU and in the hospital, resulting in higher costs and more resource utilization. Infection is a common adverse effect of opioid analgesics in postoperative surgical patients (48, 49). Postoperative infection can negatively impact the patient's prognosis, which negatively impacts their recovery (50, 51). Patients will benefit medically and economically from the early detection and timely treatment of infections after surgery in the ICU.

Despite the higher risk of infection associated with high doses of hydromorphone, postoperative pain control can improve patient recovery. There is evidence that timely and effective relief of postoperative pain enhances recovery, leads to fewer complications, and shortens hospital stays (63). Hydromorphone is commonly used as a bout of pain medication; however, its use also introduces a range of side effects. In order to identify infection-related factors, we used logistic regression to construct infection prediction models and developed an easy-to-use clinical infection prediction nomogram. The tool will help physicians evaluate the risk of infection in surgical patients using hydromorphone for analgesia promptly and may enable early medical intervention, as required by precision medicine. Pain control contributes to the recovery of surgical patients, and timely detection and reduction of analgesic medication use can reduce adverse effects and decrease ICU and hospital stays. A patient-centered big medical data set should be constructed in future studies by collecting all manner of basic patient information, treatment information, and outcomes indicators with the aid of various machine learning predictive models. It is important to design prospective cohort studies to further validate this model, as well as to expand

the study population to include different types of surgical and postoperative infections in order to achieve precision medicine.

Conclusion

This study explores and clarifies hydromorphone's efficacy and safety in the ICU. Hydromorphone dosage, age, biological sex, BMI, WBC count, and CRP have been found to be significant risk factors for developing postoperative infections in non-mechanically ventilated patients in the ICU after surgery. Based on these six clinical variables, infection prediction models have good predictive power and can be used to guide hydromorphone use more safely.

Data availability statement

The original contributions presented in the study are included in the article/Supplementary material, further inquiries can be directed to the corresponding author.

Ethics statement

The studies involving human participants were reviewed and approved by the Ethics Committee of Shanxi Bethune Hospital. The patients/participants provided their written informed consent to participate in this study.

Author contributions

YD and WW: conceptualization and validation. YD: methodology. HS: software. YD and XY: data curation. YD, HS, WW, and XY: writing—original draft preparation. WW: writing—review and editing. All authors contributed to the article and approved the submitted version.

Conflict of interest

The authors declare that the research was conducted in the absence of any commercial or financial relationships that could be construed as a potential conflict of interest.

Publisher's note

All claims expressed in this article are solely those of the authors and do not necessarily represent those of their affiliated organizations, or those of the publisher, the editors and the reviewers. Any product that may be evaluated in this article, or claim that may be made by its manufacturer, is not guaranteed or endorsed by the publisher.

Supplementary material

The Supplementary Material for this article can be found online at: https://www.frontiersin.org/articles/10.3389/fneur.2022.942023/full#supplementary-material

SUPPLEMENTARY FIGURE 1
The training process for the neural network prediction model based on the six identified clinical features. The line graphs illustrate the **(A)** loss of training and validation, and **(B)** changes in AUC values for the prediction models in the training and validation sets during training.

References

1. Skrobik Y, Chanques G. The pain, agitation, and delirium practice guidelines for adult critically ill patients: a post-publication perspective. *Ann Intensive Care.* (2013) 3:9. doi: 10.1186/2110–5820-3–9

2. Wong IMJ, Thangavelautham S, Loh SCH, Ng SY, Murfin B, Shehabi Y. Sedation and delirium in the intensive care unit-a practice-based approach. *Ann Acad Med Singap.* (2020) 49:215–25. doi: 10.47102/annals-acadmed.sg.202013

3. Chanques G, Sebbane M, Barbotte E, Viel E, Eledjam J-J, Jaber S, et al. Prospective study of pain at rest: incidence and characteristics of an unrecognized symptom in surgical and trauma versus medical intensive care unit patients. *Anesthesiology.* (2007) 107:858–60. doi: 10.1097/01.anes.0000287211.98642.51

4. Erstad BL, Puntillo K, Gilbert HC, Grap MJ Li D, Medina J, Mularski RA, et al. Pain management principles in the critically Ill. *Chest.* (2009) 135:1075–86. doi: 10.1378/chest.08–2264

5. Vincent J-L, Shehabi Y, Walsh TS, Pandharipande PP, Ball JA, Spronk P, et al. Comfort and patient-centred care without excessive sedation: the eCASH concept. *Intensive Care Med.* (2016) 42:962–71. doi: 10.1007/s00134–016-4297–4

6. Lee S. Dexmedetomidine: present and future directions. *Korean J Anesthesiol.* (2019) 72:323–30. doi: 10.4097/kja.19259

7. Sahinovic MM, Struys MMRF, Absalom AR. Clinical pharmacokinetics and pharmacodynamics of propofol. *Clin Pharmacokinet.* (2018) 57:1539–58. doi: 10.1007/s40262–018-0672–3

8. Hemmings HC, Riegelhaupt PM, Kelz MB, Solt K, Eckenhoff RG, Orser BA, et al. Towards a comprehensive understanding of anesthetic mechanisms of action: a decade of discovery. *Trends Pharmacol Sci.* (2019) 40:464–81. doi: 10.1016/j.tips.2019.05.001

9. Huang H, Jiang H, Liu J, Chen J, Qiu L, Wang J, et al. Facial nerve monitoring under different levels of neuromuscular blockade with cisatracurium besilate in parotid tumour surgery. *Biomed Res Int.* (2021) 2021:5655061. doi: 10.1155/2021/5655061

10. Masamoto K, Kanno I. Anesthesia and the quantitative evaluation of neurovascular coupling. *J Cereb Blood Flow Metab.* (2012) 32:1233–47. doi: 10.1038/jcbfm.2012.50

11. Richards-Belle A, Canter RR, Power GS, Robinson EJ, Reschreiter H, Wunsch H, et al. National survey and point prevalence study of sedation practice in UK critical care. *Crit Care.* (2016) 20:355. doi: 10.1186/s13054–016-1532-x

12. Borne J, Riascos R, Cuellar H, Vargas D, Rojas R. Neuroimaging in drug and substance abuse part II: opioids and solvents. *Topics Magn Reson Imag.* (2005) 16:239–45. doi: 10.1097/01.rmr.0000192154.34563.6b

13. Solis E, Afzal A, Kiyatkin EA. Opposing mechanisms underlying differential changes in brain oxygen and temperature induced by intravenous morphine. *J Neurophysiol.* (2018) 120:2513–21. doi: 10.1152/jn.00445.2018

14. McDonald DD, Srisopa P. Predictors of serious adverse drug events from opioids: results from the food and drug administration adverse events reporting system. *J Am Assoc Nurse Pract.* (2021) 33:1207–15. doi: 10.1097/JXX.0000000000000545

15. Li Y, Ma J, Lu G, Dou Z, Knaggs R, Xia J, Zhao S, Dong S, Yang L. Hydromorphone for cancer pain. *Cochrane Database Syst Rev.* (2021) 8:CD011108. doi: 10.1002/14651858.CD011108.pub3

16. Nascimento R, Poklis A, Wolf CE. Evaluation of a newly formulated enzyme immunoassay for the detection of hydrocodone and hydromorphone in pain management compliance testing. *J Anal Toxicol.* (2016) 40:583–7. doi: 10.1093/jat/bkw080

17. Yan G, Chen J, Yang G, Duan G, Du Z, Yu Z, et al. Effects of patient-controlled analgesia with hydromorphone or sufentanil on postoperative pulmonary complications in patients undergoing thoracic surgery: a quasi-experimental study. *BMC Anesthesiol.* (2018) 18:192. doi: 10.1186/s12871–018-0657–7

18. Alhabardi S, Almodaimegh H, Alammari M. Pattern of hydromorphone use in King Abdulaziz Medical City-Central Region (KAMC-CR). *Sci Rep.* (2021) 11:8760. doi: 10.1038/s41598–021-88276–7

19. Wasiura J, Segal BH, Mullin KM. Cluster of sphingomonas paucimobilis bacteremias linked to diversion of intravenous hydromorphone. *N Engl J Med.* (2019) 381:584–5. doi: 10.1056/NEJMc1902973

20. Bassareo PP. Hydromorphone and risk of infective endocarditis. *Lancet Infect Dis.* (2020) 20:651–2. doi: 10.1016/S1473–3099(20)30269–3

21. Moman RN, Rogers JM, Pittelkow TP. High cervical intrathecal targeted drug delivery: a case report of refractory oropharyngeal cancer pain. *Case Rep Oncol Med.* (2019) 2019:1–3. doi: 10.1155/2019/2098921

22. Blake KJ, Baral P, Voisin T, Lubkin A, Pinho-Ribeiro FA, Adams KL, et al. Staphylococcus aureus produces pain through pore-forming toxins and neuronal TRPV1 that is silenced by QX-314. *Nat Commun.* (2018) 9:37. doi: 10.1038/s41467–017-0 2448–6

23. Baba Y, Yoshida N, Shigaki H, Iwatsuki M, Miyamoto Y, Sakamoto Y, et al. Prognostic impact of postoperative complications in 502 patients with surgically resected esophageal squamous cell carcinoma: a retrospective single-institution study. *Ann Surg.* (2016) 264:305–11. doi: 10.1097/SLA.0000000000001510

24. Tu R-H, Lin J-X, Li P, Xie J-W, Wang J-B, Lu J, et al. Prognostic significance of postoperative pneumonia after curative resection for patients with gastric cancer. *Cancer Med.* (2017) 6:2757–65. doi: 10.1002/cam4.1163

25. Pattarabanjird T, Cress C, Nguyen A, Taylor A, Bekiranov S, McNamara C, et al. Machine learning model utilizing a novel SNP shows enhanced prediction of coronary artery disease severity. *Genes.* (2020) 11:1446. doi: 10.3390/genes11121446

26. Silcox C, Dentzer S, Bates DW. AI-enabled clinical decision support software: a "trust and value checklist" for clinicians. *NEJM Catalyst.* (2020) 1:CAT.20.0212. doi: 10.1056/CAT.20.0212

27. De Cock M, Dowsley R, Nascimento ACA, Railsback D, Shen J, Todoki A. High performance logistic regression for privacy-preserving genome analysis. *BMC Med Genom.* (2021) 14:23. doi: 10.1186/s12920–020-00869–9

28. Hsieh MH, Hsieh MJ, Chen C-M, Hsieh C-C, Chao C-M, Lai C-C. Comparison of machine learning models for the prediction of mortality of patients with unplanned extubation in intensive care units. *Sci Rep.* (2018) 8:17116. doi: 10.1038/s41598–018-35582–2

29. Huang J, Liu M, He W, Liu F, Cheng J, Wang H. Use of the A2DS2 scale to predict morbidity in stroke-associated pneumonia: a systematic review and meta-analysis. *BMC Neurol.* (2021) 21:33. doi: 10.1186/s12883–021-02060–8

30. Liu H, Yan Y, Chen R, Zhu M, Lin J, He C, et al. Integrated nomogram based on five stage-related genes and TNM stage to predict 1-year recurrence in hepatocellular carcinoma. *Cancer Cell Int.* (2020) 20:140. doi: 10.1186/s12935–020-01216–9

31. Peterson JJ. Postoperative infection. *Radiol Clin North Am.* (2006) 44:439–50. doi: 10.1016/j.rcl.2006.01.007

32. Blanchet L, Vitale R, van Vorstenbosch R, Stavropoulos G, Pender J, Jonkers D, et al. Constructing bi-plots for random forest: tutorial. *Anal Chim Acta.* (2020) 1131:146–55. doi: 10.1016/j.aca.2020.06.043

33. Huang M-L, Hung Y-H, Lee WM Li RK, Jiang B-R. SVM-RFE based feature selection and Taguchi parameters optimization for multiclass SVM classifier. *Sci World J.* (2014) 2014:795624. doi: 10.1155/2014/795624

34. Cao C, Liu F, Tan H, Song D, Shu W, Li W, et al. Deep learning and its applications in biomedicine. *Genom Proteom Bioinform.* (2018) 16:17–32. doi: 10.1016/j.gpb.2017.07.003

35. Feng X, Guan N, Xu E, Miao Y, Li C. Transcription factors leading to high expression of neuropeptide L1CAM in brain metastases from lung adenocarcinoma and clinical prognostic analysis. *Dis Markers.* (2021) 2021:1–15. doi: 10.1155/2021/8585633

36. Chen Y, Sun Y, Luo Z, Lin J, Qi B, Kang X, et al. Potential mechanism underlying exercise upregulated circulating blood exosome miR-215–5p to prevent necroptosis of neuronal cells and a model for early diagnosis of alzheimer's disease. *Front Aging Neurosci.* (2022) 14:860364. doi: 10.3389/fnagi.2022.860364

37. Xuan Z, Ma T, Qin Y, Guo Y. Role of ultrasound imaging in the prediction of TRIM67 in brain metastases from breast cancer. *Front Neurol.* (2022) 13:889106. doi: 10.3389/fneur.2022.889106

38. Hu C, Li Q, Shou J, Zhang F, Li X, Wu M, et al. Constructing a predictive model of depression in chemotherapy patients with non-hodgkin's lymphoma to improve medical staffs' psychiatric care. *Biomed Res Int.* (2021) 2021:9201235. doi: 10.1155/2021/9201235

39. Tripepi G, Jager KJ, Stel VS, Dekker FW, Zoccali C. How to deal with continuous and dichotomic outcomes in epidemiological research: linear and logistic regression analyses. *Nephron Clin Pract.* (2011) 118:c399–c406. doi: 10.1159/000324049

40. Jiang F, Jiang Y, Zhi H, Dong Y, Li H, Ma S, et al. Artificial intelligence in healthcare: past, present and future. *Stroke Vasc Neurol.* (2017) 2:230–43. doi: 10.1136/svn-2017–000101

41. Patel L, Shukla T, Huang X, Ussery DW, Wang S. Machine learning methods in drug discovery. *Molecules.* (2020) 25:5277. doi: 10.3390/molecules25225277

42. Buchlak QD, Esmaili N, Leveque J-C, Farrokhi F, Bennett C, Piccardi M, et al. Machine learning applications to clinical decision support in neurosurgery: an artificial intelligence augmented systematic review. *Neurosurg Rev.* (2020) 43:1235–53. doi: 10.1007/s10143–019-01163–8

43. Liu Z, Li C, A. Predictive model for the risk of cognitive impairment in patients with gallstones. *Biomed Res Int.* (2021) 2021:1–13. doi: 10.1155/2021/3792407

44. Zhang Q, Yang J, Yang C, Yang X, Chen Y. Eucommia ulmoides *Oliver-Tribulus terrestris L.* drug pair regulates ferroptosis by mediating the neurovascular-related ligand-receptor interaction pathway- a potential drug pair for treatment hypertension and prevention ischemic stroke. *Front Neurol.* 13:833922. doi: 10.3389/fneur.2022.833922

45. Kang X-R, Chen B, Chen Y-S, Yi B, Yan X, Jiang C, Wang S, Lu L, Shi R. A prediction modeling based on SNOT-22 score for endoscopic nasal septoplasty: a retrospective study. *PeerJ.* (2020) 8:e9890. doi: 10.7717/peerj.9890

46. Steyerberg EW, Vergouwe Y. Towards better clinical prediction models: seven steps for development and an ABCD for validation. *Eur Heart J.* (2014) 35:1925–31. doi: 10.1093/eurheartj/ehu207

47. Robin X, Turck N, Hainard A, Tiberti N, Lisacek F, Sanchez J-C, et al. pROC: an open-source package for R and S+ to analyze and compare ROC curves. *BMC Bioinform.* (2011) 12:77. doi: 10.1186/1471–2105-12–77

48. Hassan Z, Nisiewicz MJ, Ueland W, Plymale MA, Plymale MC, Davenport DL, et al. Preoperative opioid use and incidence of surgical site infection after repair of ventral and incisional hernias. *Surgery.* (2020) 168:921–5. doi: 10.1016/j.surg.2020.05.048

49. Pirkle S, Reddy S, Bhattacharjee S, Shi LL, Lee MJ. Chronic opioid use is associated with surgical site infection after lumbar fusion. *Spine.* (2020) 45:837–42. doi: 10.1097/BRS.0000000000003405

50. Kato S, Chikuda H, Ohya J, Oichi T, Matsui H, Fushimi K, et al. Risk of infectious complications associated with blood transfusion in elective spinal surgery—a propensity score matched analysis. *Spine J.* (2016) 16:55–60. doi: 10.1016/j.spinee.2015.10.014

51. Tran CW, McGree ME, Weaver AL, Martin JR, Lemens MA, Cliby WA, et al. Surgical site infection after primary surgery for epithelial ovarian cancer: predictors and impact on survival. *Gynecol Oncol.* (2015) 136:278–84. doi: 10.1016/j.ygyno.2014.12.007

52. Khosrow-Khavar F, Kurteva S, Cui Y, Filion KB, Douros A. Opioids and the risk of infection: a critical appraisal of the pharmacologic and clinical evidence. *Expert Opinion Drug Metabolism Toxicol.* (2019) 15:565–75. doi: 10.1080/17425255.2019.1634053

53. Yang Y, Wu J, Li H, Ye S, Xu X, Cheng L, et al. Prospective investigation of intravenous patient-controlled analgesia with hydromorphone or sufentanil:

impact on mood, opioid adverse effects, and recovery. *BMC Anesthesiol.* (2018) 18:37. doi: 10.1186/s12871–018-0500–1

54. Shanthanna H, Paul J, Lovrics P, Vanniyasingam T, Devereaux PJ, Bhandari M, Thabane L. Satisfactory analgesia with minimal emesis in day surgeries: a randomised controlled trial of morphine versus hydromorphone. *Br J Anaesthesia.* (2019) 122:e107–e113. doi: 10.1016/j.bja.2019.03.036

55. Stone AB, Jones MR, Rao N, Urman RD. A dashboard for monitoring opioid-related adverse drug events following surgery using a national administrative database. *Am J Med Qual.* (2019) 34:45–52. doi: 10.1177/1062860618782646

56. Wang F, Roy S. Gut homeostasis, microbial dysbiosis, and opioids. *Toxicol Pathol.* (2017) 45:150–156. doi: 10.1177/0192623316679898

57. Candore G, Caruso C, Jirillo E, Magrone T, Vasto S. Low grade inflammation as a common pathogenetic denominator in age-related diseases: novel drug targets for anti-ageing strategies and successful ageing achievement. *CPD.* (2010) 16:584–596. doi: 10.2174/138161210790883868

58. Cederholm T, Bosaeus I, Barazzoni R, Bauer J, Van Gossum A, Klek S, et al. Diagnostic criteria for malnutrition—an ESPEN consensus Statement. *Clin Nutr.* (2015) 34:335–40. doi: 10.1016/j.clnu.2015.03.001

59. Rajamanickam A, Munisankar S, Dolla CK, Babu S. Diminished systemic and mycobacterial antigen specific anti-microbial peptide responses in low body mass index–latent tuberculosis co-morbidity. *Front Cell Infect Microbiol.* (2020) 10:165. doi: 10.3389/fcimb.2020.00165

60. Chandrasekaran P, Saravanan N, Bethunaickan R, Tripathy S. Malnutrition: modulator of immune responses in tuberculosis. *Front Immunol.* (2017) 8:1316. doi: 10.3389/fimmu.2017.01316

61. McClelland EE, Smith JM. Gender specific differences in the immune response to infection. *Arch Immunol Ther Exp.* (2011) 59:203–13. doi: 10.1007/s00005–011-0124–3

62. Gay L, Melenotte C, Lakbar I, Mezouar S, Devaux C, Raoult D, et al. Sexual dimorphism and gender in infectious diseases. *Front Immunol.* (2021) 12:698121. doi: 10.3389/fimmu.2021.698121

63. Zhu Y, Jing G, Yuan W. Preoperative administration of intramuscular dezocine reduces postoperative pain for laparoscopic cholecystectomy. *J Biomed Res.* (2011) 25:356–61. doi: 10.1016/S1674–8301(11)60047-X

frontiers | Frontiers in Neurology

TYPE Original Research
PUBLISHED 05 August 2022
DOI 10.3389/fneur.2022.937501

Check for updates

OPEN ACCESS

EDITED BY
Wen-Jun Tu,
Chinese Academy of Medical Sciences and Peking Union Medical College, China

REVIEWED BY
Zhenyu Li,
Chongqing University, China
Edith Hofer,
Medical University of Graz, Austria

*CORRESPONDENCE
Li'an Huang
huanglian1306@126.com
Chi Kwan Tsang
tsangch@jnu.edu.cn

SPECIALTY SECTION
This article was submitted to Neurological Biomarkers, a section of the journal Frontiers in Neurology

RECEIVED 06 May 2022
ACCEPTED 11 July 2022
PUBLISHED 05 August 2022

CITATION
Yang Z, Wang G, Luo N, Tsang CK and Huang L (2022) Consensus clustering of gene expression profiles in peripheral blood of acute ischemic stroke patients.
Front. Neurol. 13:937501.
doi: 10.3389/fneur.2022.937501

COPYRIGHT
© 2022 Yang, Wang, Luo, Tsang and Huang. This is an open-access article distributed under the terms of the Creative Commons Attribution License (CC BY). The use, distribution or reproduction in other forums is permitted, provided the original author(s) and the copyright owner(s) are credited and that the original publication in this journal is cited, in accordance with accepted academic practice. No use, distribution or reproduction is permitted which does not comply with these terms.

Consensus clustering of gene expression profiles in peripheral blood of acute ischemic stroke patients

Zhiyong Yang[1,2], Guanghui Wang[1,2], Nan Luo[1,2], Chi Kwan Tsang[1]* and Li'an Huang[1,2]*

[1]Clinical Neuroscience Institute, The First Affiliated Hospital of Jinan University, Guangzhou, China, [2]Department of Neurology, The First Clinical Medical School of Jinan University, Guangzhou, China

Acute ischemic stroke (AIS) is a primary cause of mortality and morbidity worldwide. Currently, no clinically approved immune intervention is available for AIS treatment, partly due to the lack of relevant patient classification based on the peripheral immunity status of patients with AIS. In this study, we adopted the consensus clustering approach to classify patients with AIS into molecular subgroups based on the transcriptomic profiles of peripheral blood, and we identified three distinct AIS molecular subgroups and 8 modules in each subgroup by the weighted gene co-expression network analysis. Remarkably, the pre-ranked gene set enrichment analysis revealed that the co-expression modules with subgroup I-specific signature genes significantly overlapped with the differentially expressed genes in AIS patients with hemorrhagic transformation (HT). With respect to subgroup II, exclusively male patients with decreased proteasome activity were identified. Intriguingly, the majority of subgroup III was composed of female patients who showed a comparatively lower level of AIS-induced immunosuppression (AIIS). In addition, we discovered a non-linear relationship between female age and subgroup-specific gene expression, suggesting a gender- and age-dependent alteration of peripheral immunity. Taken together, our novel AIS classification approach could facilitate immunomodulatory therapies, including the administration of gender-specific therapeutics, and attenuation of the risk of HT and AIIS after ischemic stroke.

KEYWORDS

acute ischemic stroke, molecular subgroups, peripheral immunity, restricted cubic spline functions, immunosuppression, consensus clustering

Introduction

Acute ischemic stroke (AIS) is one of the leading causes of death and disability worldwide, affecting approximately 10 million people each year and resulting in an enormous economic burden for AIS treatment and post-stroke care (1, 2). Recent studies have demonstrated that the immunomodulatory therapy targeting

peripheral immunity is promising for AIS treatment, including attenuation of hemorrhagic transformation (HT) or AIS-induced immunosuppression (AIIS) (3–5). However, there is a complex relationship between peripheral immunity states and stroke pathology. Without careful consideration of AIS patient's peripheral immunity state, broad suppression or modulation of peripheral immunity may impair the normal physiological immune functions, such as the clearance of damaged tissues, subsequent repair responses, or protection against systemic infections, which would result in worsening of stroke prognosis (4, 5). For example, the Enlimomab Acute Stroke Trial, a randomized controlled trial of a murine monoclonal antibody to ICAM-1 for blocking peripheral immunity responses, has shown that the Enlimomab-treated patients exhibited significantly worse outcomes with a higher incidence of fever, infections, and death (6). By far, there are no clinically approved immunotherapeutic drug available (7, 8), partly due to the heterogeneous nature of peripheral immunity states in patients with AIS (9, 10). These results highlight the importance of classification of patients with AIS based on their peripheral immunity states to optimize the efficacy of immunotherapies.

Accumulating evidence has shown that subgrouping patients based on gene expression patterns of peripheral blood plays a key role in patient selection for successful clinical translation of immune interventions in multiple diseases including cancers, systemic lupus erythematous, and sepsis (11–13). In addition, peripheral blood can be conveniently obtained from patients with a quick and easy venous blood collection. As a core component of peripheral immunity, peripheral blood cells such as lymphocytes, monocytes, and granulocytes are intimately involved in many immune responses after AIS (14, 15). Moreover, gene expression profiling of peripheral blood could provide crucial information for the peripheral immunity state after stroke (16, 17). Therefore, we hypothesized that transcriptomic profiling of peripheral blood could be used to establish novel AIS classification for providing important insights into the immune interventions for stroke treatment. In this study, we employed a consensus-clustering approach to classify patients with AIS into major molecular subgroups based on their gene expression profiles in peripheral blood, and we characterized these subgroups by various integrative analyses. To further investigate the role of age and gender in the peripheral immunity states of patients with AIS, we employed a restricted cubic spline analysis to elucidate their relationships with subgroup-specific gene expression. Finally, we evaluated the implication of AIS classification on correlation with hemorrhagic transformation (HT) in patients with AIS, aiming to understand the role of peripheral immunity in HT and to provide new insights into the immune interventions for stroke treatment.

Materials and methods

Data collection

Two datasets (GSE16561 and GSE37587) were extracted from the Gene Expression Omnibus (GEO) by R/Bioconductor package GEOquery, including the gene expression matrix, clinical characteristics, and probe sets. The dataset of samples drawn from non-stroke neurologically healthy participants was used as the control. GSE199435 was extracted from the gene expression dataset of blood samples collected from AIS patients with HT or non-HT ($n = 3$ for each group). The fastq RNA-sequencing data were downloaded from the SRA database (SRP365953). FeatureCounts was used to count the reads mapped to individual genes by processing the sorted bam files with accepted read quality for subsequent analysis.

Removal of batch effect

Since GSE16561 and GSE37587 datasets used the same platform (GPL6883 platform Illumina HumanRef-8 v3.0 expression beadchip), gene expression data were merged for analysis in our study. The expression values merged from both datasets were $\log_2$ transformed, and then ComBat normalization in the SVA package was used to remove batch effects.

Consensus clustering

Consensus clustering was performed by "*ConsensusClusterPlus*" R package as an unsupervised resampling analysis for the detection of high consensus optimal molecular subgroups based on intrinsic molecular characteristics of gene expression features, through robust clustering across multiple runs of a clustering algorithm without external information to mitigate the limitations of individual clustering algorithms by averaging over various clustering methods with random or subjectivity (70). The clustering was performed by a K-means algorithm with the Spearman distance. The maximum cluster number was set to 10. The final cluster number was determined by the consensus matrix and the cluster consensus score (>0.8), as recommended in the literature (70).

Comparing the clinical characteristics of subgroups

The proportion of male patients and different sampling times (within 24 h and 24–48 h after AIS) in the subgroups were compared using the pairwise proportion test. Given that male and female patients may have different patterns of correlation with age, gender-stratified analyses were performed

(18). Pairwise Wilcoxon's rank sum test was used to test whether there was a difference in age among the male and female patients in the subgroups. Since the age of female subjects in subgroups showed no significant difference in Wilcoxon's rank sum test, we used logistic regression models with restricted cubic spline functions to test the potential non-linearity between female age and subgroups as described previously (71).

Identification of subgroup-specific upregulated and downregulated genes

Subgroup-specific upregulated and downregulated genes were identified by comparing the samples in a specified subgroup with samples in the other subgroups using the Wilcoxon rank-sum test (19, 20). To avoid obscuring gene expression features in pathway enrichment analyses and identify the most valuable differentially expressed genes, we used the cutoff criteria defined by Benjamini-Hochberg and adjusted it to $p < 0.05$ and the absolute difference of means > 0.2 (19, 20). Upregulated genes were defined as the subgroup-specific genes with a difference of means > 0.2, while downregulated genes were subgroup-specific genes with a difference of means < -0.2. For any given gene, the difference in mean was calculated by subtracting the mean of expression in the other group from that in the samples of the specified subgroup.

Weighted gene co-expression network analysis

Weighted gene co-expression analysis (WGCNA) was performed under subgroup-specific signatures to identify potential modules with characterized biological functions in each subgroup (21). *FlashClust* function (in "*WGCNA*" package) was used to carry out cluster analysis of samples with appropriate threshold to detect and remove the outliers. The soft thresholding power β-value was screened during module construction by the pick Soft Threshold function in the "*WGCNA*" package. The power of $\beta = 9$ (scale-free $R^2 > 0.8$) was selected as the soft-thresholding parameter. The topological overlap matrix similarity was used to evaluate the distance between each gene pair. Hierarchical clustering analysis with the average and dynamic methods was used to build the cluster tree and classify the genes into modules. After merging the original modules based on their similarity, we finally identified eight modules. In the "*WGCNA*" package, subgroups and gender were converted to numerical values followed by a regression analysis with module eigengene values to visualize the expression tendency of modules. For gender-stratified analysis, Spearman's correlation coefficients and the corresponding *p*-values between age and modules eigengene values were calculated by the "*WGCNA*" package. An alluvial diagram was used to visualize the main distribution and associations between subgroup-specific upregulated and downregulated genes and genes in the eight functional modules using the R software package "*ggalluvial*" and "*ggplot2*."

Pre-ranked gene set enrichment analysis

Gene set enrichment analysis (GSEA) was performed in GSEA Desktop v4.1.0 with GSEAPrerank mode and a false discovery rate (FDR) < 0.05. The gene set databases were generated from the subgroup-specific signature genes. The gene list for each subgroup was ranked by negative $\log_{10}$-transformed adjusted *p*-values for Wilcoxon rank-sum test, which was calculated as each subgroup vs. normal control. We employed a restricted cubic spline analysis to determine the non-linear relationship between co-expression modules and log-transformed age in different gender for pre-ranked GSEA analysis as described (22, 23). To cover the most valuable differentially expressed genes (DEGs) of GSE199435 in the pre-ranked GSEA, we adjusted the cut-off value to $p < 0.05$ and logFC > 0.2 in comparison between AIS patients with HT and patients without HT (non-HT), according to DESeq2. Based on the ranking metric of logFC, the concordance in transcriptional profile between subgroup-specific genes of each WGCNA module and the transcripts was performed by the pre-ranked GSEA (24, 25).

Functional module enrichment analysis

Kyoto Encyclopedia of Genes and Gene Ontology (KEGG) and Reactome pathway enrichment analyses for the subgroup-specific upregulated and downregulated genes were performed for genes in the modules using "*clusterprofiler*" and "*ReactomePA*" R package (26, 27). The pathways with $P < 0.05$ were considered statistically significant for functional modules.

Results

We analyzed a total of 131 peripheral blood samples collected from 107 patients with AIS and 24 healthy individuals from two independent datasets (GSE16561 and GSE37587). We used the ComBat method to process 18,599 genes and eliminated the batch effect by normalization (Figure 1A).

Consensus clustering of AIS cases

Based on the unsupervised consensus clustering method, we classified the 107 patients with AIS into three subgroups

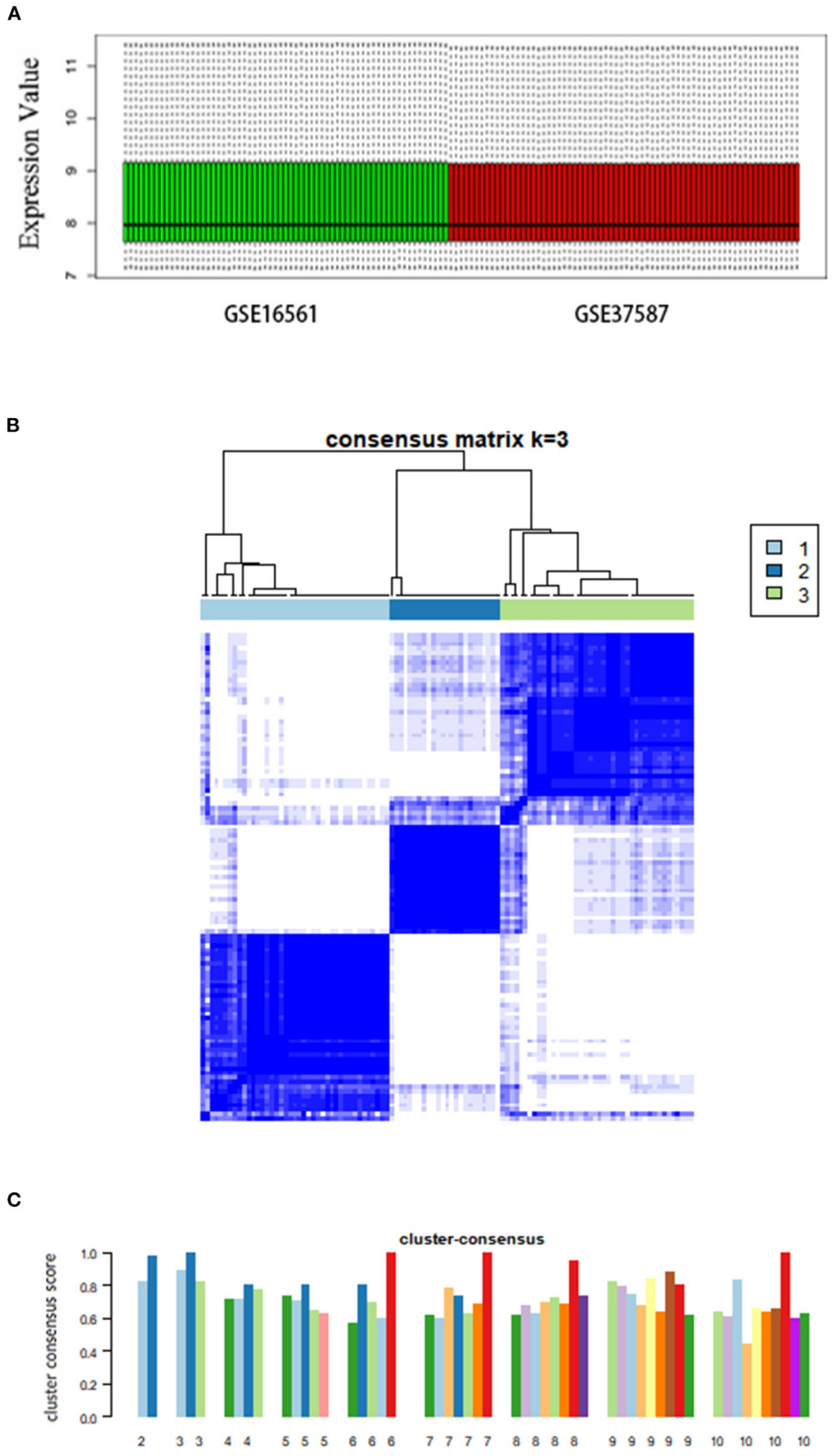

FIGURE 1
Consensus clustering analysis of gene expression profiles of peripheral blood samples in patients with AIS. **(A)** Box plots showing the normalized relative expression (y-axis) of data from genesets GSE16561 and GSE37587. **(B)** The heatmap representing the consensus matrix with a cluster count of 3, which was determined by the minimal consensus scores of >0.8. **(C)** Bar-plots showing the consensus scores (y-axis) and the corresponding numbers of the subgroup. The maximum number of subgroups was set to 10.

based on their gene expression profiles. Subgroups I, II, and III consisted of 41, 24, and 42 patients with AIS, respectively. We showed that the gene expression pattern of each subgroup is highly specific by consensus matrix analysis (Figure 1B). The minimal consensus score analysis for subgrouping indicated that three groups would provide robust classification based on the criteria of cluster count with a consensus score > 0.8 (Figure 1C) (70).

Next, we performed the pair-wise differential expression analysis of each subgroup with the other two subgroups by GSEA. As shown in Figure 2A, we detected 1,372, 1,012, and 712 genes showing subgroup-specific upregulation, as well as 1,363, 609, and 337 genes showing downregulation in subgroups I, II, and III, respectively (Benjamini-Hochberg adjusted $p < 0.05$ and the absolute difference of means > 0.2, Supplementary Figure S1). To investigate the specificity of these differentially expressed genes in each subgroup, we performed a GSEA analysis to compare their gene expression profiles with that of the normal control. The normalized enrichment score revealed that the subgroup-specific genes were also significantly and differentially expressed when compared with the control group (Figures 2A–C, FDR <0.05).

Characterization of subgroups

To characterize the clinical features of the three subgroups, we analyzed the distribution of gender, age, and sampling time after AIS in each subgroup. Intriguingly, the gender distribution among the subgroups was very different. As shown in Figure 3A, the proportion of women in subgroup III was significantly higher than that in subgroup I. Intriguingly, subgroup II consisted of men only (Figure 3A). Therefore, we separated male and female patients for age analysis. We found that the average age of male subjects in subgroup I was significantly younger than subgroups II and III (Figure 3B). In contrast, there was no significant difference between the average age of female subjects in subgroups I and III, as determined by Wilcoxon's rank sum test (Figure 3C). To explore whether there was a non-linear relationship, we performed a logistic regression model analysis with restricted cubic spline (RCS) functions, which revealed a U-shaped relationship between female age and subgroups, without significant linearity ($P_{non-linear} = 0.0223$; Figure 3D). To determine whether the sampling time would affect the pattern of AIS subgrouping, we separated patients into 2 groups (sampling time during 24–48 h and within 24 h), and there was no significant difference among the subgroups in female or male cases (Figures 3E,F).

Next, we conducted pre-ranked GSEA and restricted cubic splines analysis to determine the correlation between age and subgroup-specific gene expression across female and male patients. As shown in Figure 4, the subgroup-specific genes were concentrated in the gene sets with a non-linear correlation with the corresponding age in female patients with AIS (NES $= 1.58$, FDR < 0.001), but not in male patients (NES $= 0.81$, no significant difference). These results demonstrate that gender and age are determining factors for gene expression in the peripheral blood of patients with AIS.

Identification of gene co-expression modules

The weighted gene co-expression network analysis (WGCNA) is a powerful tool to identify modules with a coordinated expression of genes with similar patterns (36). In an attempt to discover unique and specific subgroup signatures, we performed WGCNA of all subgroup-specific genes and control. The specific expression tendency revealed 8 WGCNA modules (Figures 5A,B; Supplementary Table S1). In addition, the cluster analysis by *flashClust* revealed no outlier samples (Supplementary Figure S2A). The power of β was set at 9 to ensure a scale-free network based on the scale-free fit index and the mean connectivity (Supplementary Figure S2B). The topological overlap measure (TOM) for each gene pair was then calculated. Consistently, the hierarchical clustering analysis based on the TOM dissimilarity measure (1-TOM) also revealed eight modules (Supplementary Figure S2C). Then, we used an alluvial diagram to visualize the main distribution and associations between subgroup-specific upregulated and downregulated genes and genes from eight modules (Figure 5C). Based on the main distribution (color bars) and association (lines) of WGCNA modules with the subgroup-specific genes, we identified the upregulated and downregulated associations between WGCNA modules and the corresponding primary subgroups (Table 1). To investigate the relationship between clinical features and gene expression of WGCNA modules, we performed the Pearson correlation analysis, which verified that all modules were correlated with AIS, and this served as the positive control. Importantly, module 6 exhibited the highest degree of negative correlation with AIS (r-value $= -0.35$), while modules 2, 4, 5, and 7 showed comparable levels of positive correlation with AIS with r-values ≥ 0.2 (Figure 5A). With respect to subgroup I, the specific genes from modules 3, 4, 5, and 7 appeared to be independent of gender in patients with AIS (Figure 5A $p > 0.05$ in AIS_Gender_Male column). Notably, we observed a linear relationship between co-expression modules and age in male patients with AIS (except modules 2 and 6) (Figure 6A). In contrast, modules 1 and 8 showed significant linear correlation as shown in the corresponding age bracket in AIS female patients (Figure 6A). Apart from modules 2 and 6, we ascertained the non-linear relationship between most co-expression modules and log-transformed age in female patients with AIS through the incorporation

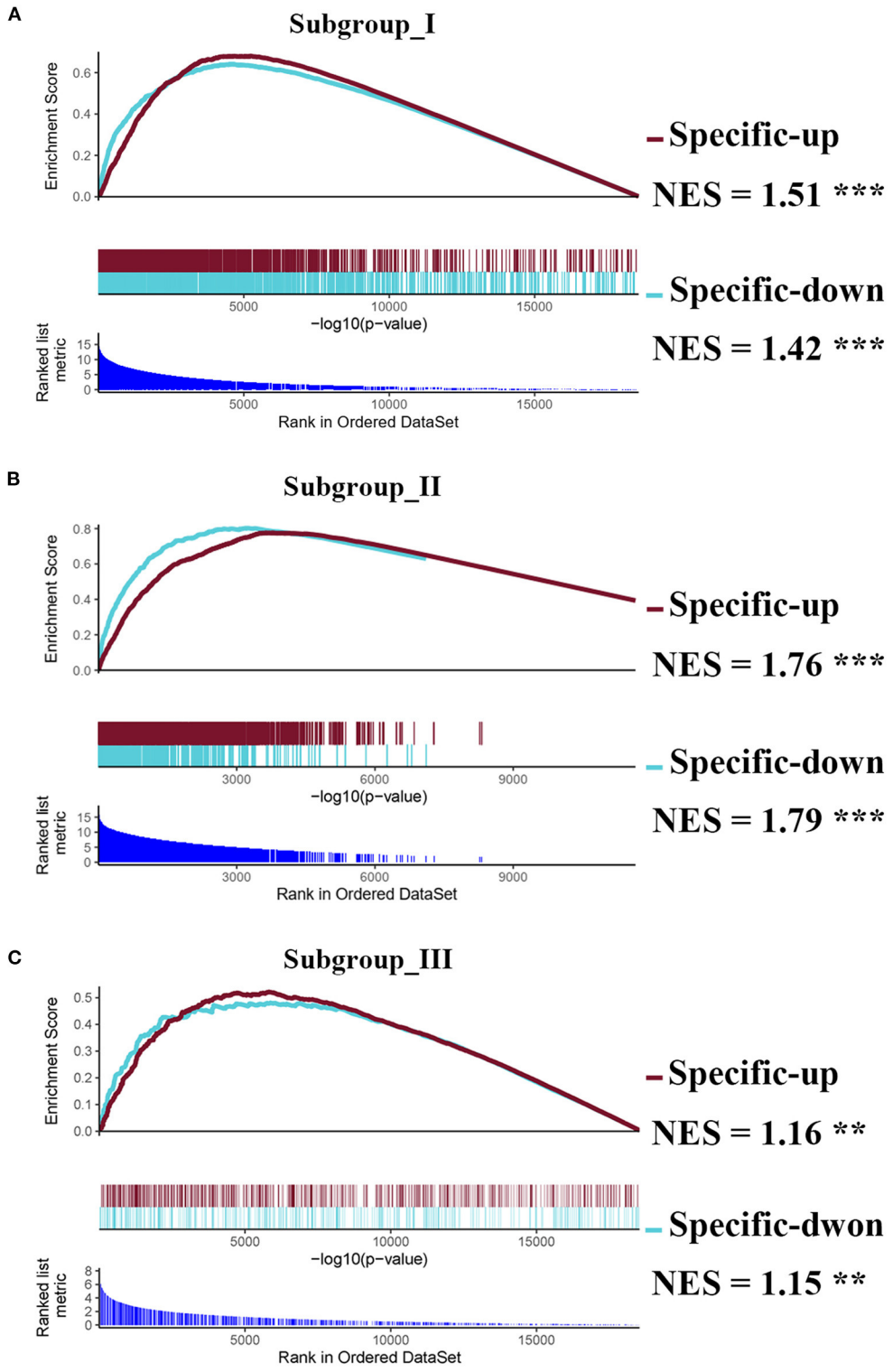

FIGURE 2
Identification of subgroup-specific differentially expressed genes and comparison with control. **(A–C)** GSEA enrichment plots (red lines) showing the subgroup-specific upregulated gene (Specific-up) and subgroup-specific downregulated gene (Specific-down) in subgroup I **(A)**, subgroup II **(B)**, and subgroup III **(C)**. Green lines represent the differentially expressed genes between the corresponding subgroup and the normal controls. NES denotes the normalized enrichment score with FDR (** <0.01, and *** <0.001).

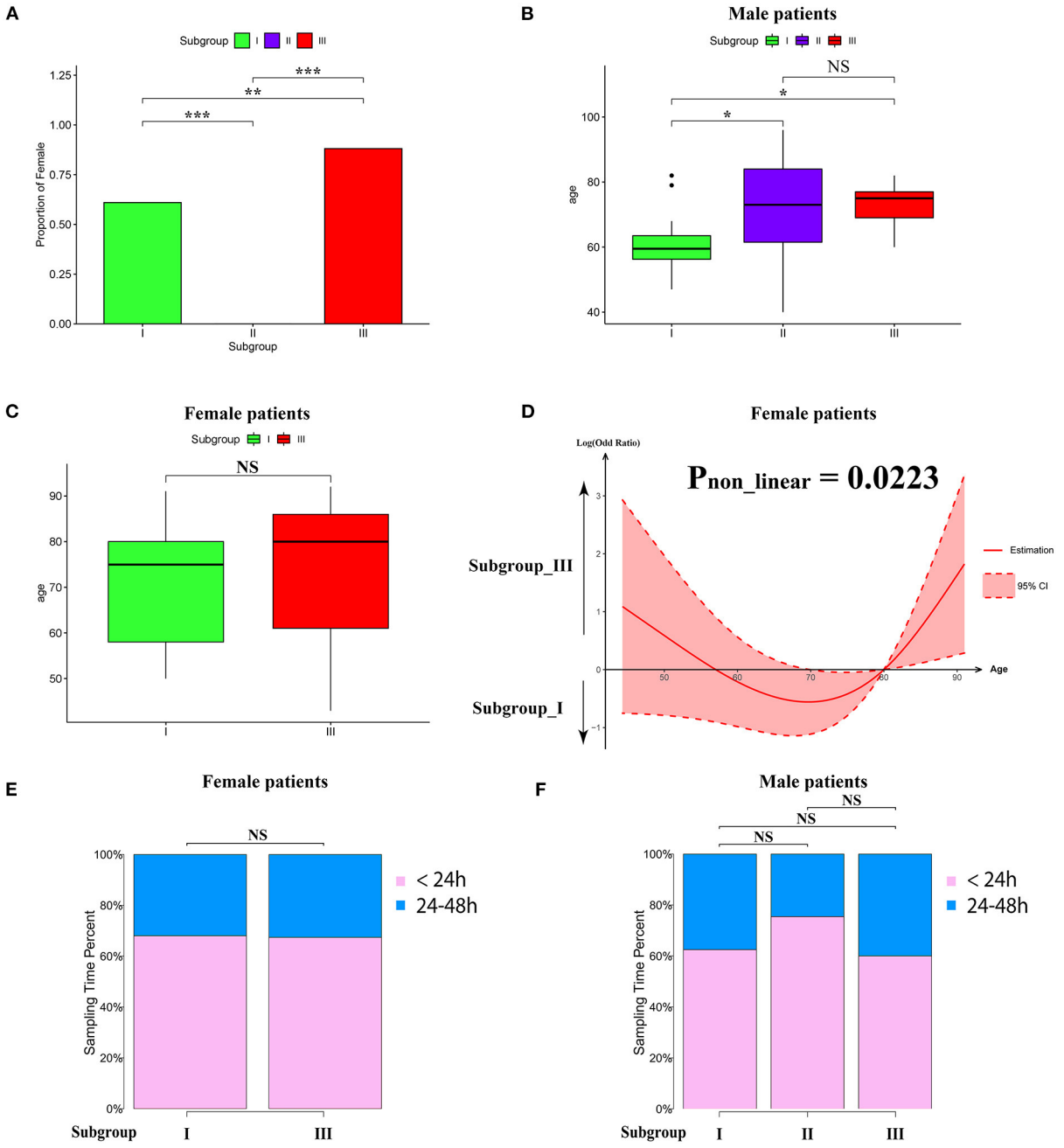

FIGURE 3
Clinical characteristics within subgroups. **(A)** Barplot showing the proportion of male patients in each subgroup. **(B,C)** Barplot showing the age distribution in each subgroup in male **(B)** and female patients **(C)**. Values are means ± SD. NS indicates no significant difference between groups ($p > 0.05$). $^{*}P < 0.05$, $^{**}P < 0.01$, and $^{***}P < 0.001$. **(D)** Non-linear relationship between subgroup and the age of female patients analyzed by restricted cubic spline model. The black line represents the pooled odds ratio (OR), and the red lines indicate a 95% confidence interval (CI). **(E,F)** Box-plots showing the proportion of sampling time (within 24 h and between 24 and 8 h) after AIS in each subgroup of female **(E)** and male **(F)** patients. NS indicates no significant difference between groups ($p > 0.05$).

of the restricted cubic spline analysis with pre-ranked GSEA (Figure 6B). Likewise, the accumulation of gene sets pertaining to a non-linear correlation in the corresponding age in male patients with AIS was not observed except in module 4 (Figure 6C). The linear and non-linear relationships between age and relevant modules in patients with AIS are visualized in the heatmap presentation as shown in Figure 6A. Together with the observation that modules 2 and 6 were primarily

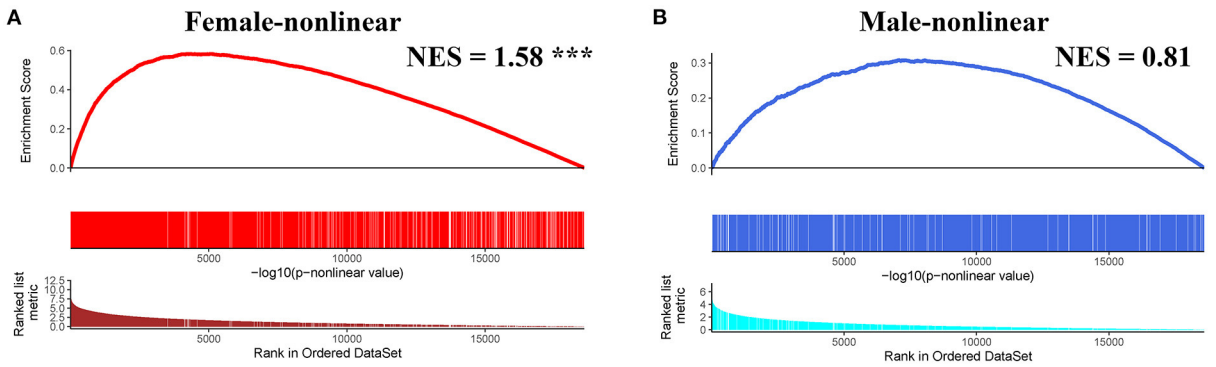

FIGURE 4
GSEA analysis of subgroup-specific differentially expressed genes. **(A)** The enrichment plot illustrates that most subgroup-specific genes had a significantly non-linear relationship with female age. The normalized enrichment score (NES) and FDR (*** <0.001) in the female group. **(B)** The enrichment plot illustrates that most subgroup-specific genes had a significantly non-linear relationship with male age. The normalized enrichment score (NES) is shown without significant difference (FDR > 0.05).

distributed in subgroup III-specific genes (Figure 5C), these results highlight the correlation of gender, rather than age, with gene co-expression in modules.

Functional enrichment analysis of genes in the co-expression modules

KEGG and Reactome pathway analyses were used to identify enriched pathways in the co-expression modules. Interestingly, we found that many of them were related to inflammatory factors, complement synthesis, coagulation factor production, and the expression of C-type lectin receptors (Table 1; Figures 7–10). Notably, modules 4 and 5 primarily constituted of the subgroup I-specific upregulated genes. They were substantially enriched in pathways involved in neutrophil extracellular trap formation, inflammasomes, and metabolism of lipid and lipoprotein (Supplementary Figures S3,S4). With respect to module 4, we found the integration of NLRP3 with the inflammasome pathway (Supplementary Figure S4A). In modules 4 and 5, enriched pathways included platelet activation, thrombus formation, platelet adhesion to exposed collagen, platelet activation, formation of fibrin clot (clotting cascade), and common pathway of fibrin clot formation (Supplementary Figures S3,S4). Analysis of downregulated genes in subgroup I in modules 3, 7, and 8 revealed pathways related to the regulation of the immunocoagulation tangles (Supplementary Figures S3,S4). We also identified the regulation of gene expression by hypoxia-inducible factors in module 8, which suggest improved perfusion and enhanced arterial remodeling in this module (Figures 9, 10B) (28). Additionally, these pathway analyses revealed functions such as nucleotide excision repair, DNA damage bypass, HDR through Homologous Recombination (HRR), and DNA double-strand break repair in tandem with the increased activity of hypoxia-inducible factor and SUMOylation in module 8 (Figure 9), suggesting the anti-hypoxic injury by regulation of gene expression as shown in module 8 (Figures 7–10). Interestingly, module 1 showed the downregulation of genes enriched in proteasome activity in subgroup II (Figure 7, Supplementary Figure S3A). Furthermore, module 6 was related to phosphorylation of CD3 and TCR zeta chains in subgroup III (Figure 9). Genes in this pathway included CD3D, CD3E, CD3F, and CD247 (CD3ζ) which are also the representative markers of T-cells (Figure 10B). We also identified the enhanced normal T-cell function and comparatively lower levels of AIIS in subgroup III (Figure 10) (3). From module 2, specific-downregulated genes in subgroup III encompassed the enrichment of calmodulin-dependent kinase-related genes including CAMK2A and CAMKK2 (29, 30). Consistently, they are known as the fundamental regulators of immune function in conjunction with the enrichment of platelet activation and coagulation-related pathways (Supplementary Figure S4A) (31–33). The identification of these pathways in subgroup III-specific modules 2 and 6 demonstrates the specific peripheral immunological activity in female patients with AIS (Figures 3A, 5C). Another interesting observation was the enrichment of disparate metabolism pathways. For instance, we identified ADH4, DLD, PDK1, ABAT, and SDHD enriched in module 8 that were related to propanoate metabolism, pyruvate metabolism, and tricarboxylic acid (TCA) cycle, whereas ALDOC, PFKI, ALDOA, TKT, RPIA, and FBPI were enriched in the pentose phosphate pathway in modules 1 and 4. These results suggest the diverse regulation of metabolism in periphery immune response in patients with AIS (Supplementary Figures S3,S4). Furthermore, we identified that modules 1 and 6 showed distinct co-expression patterns in relation to oxidative phosphorylation

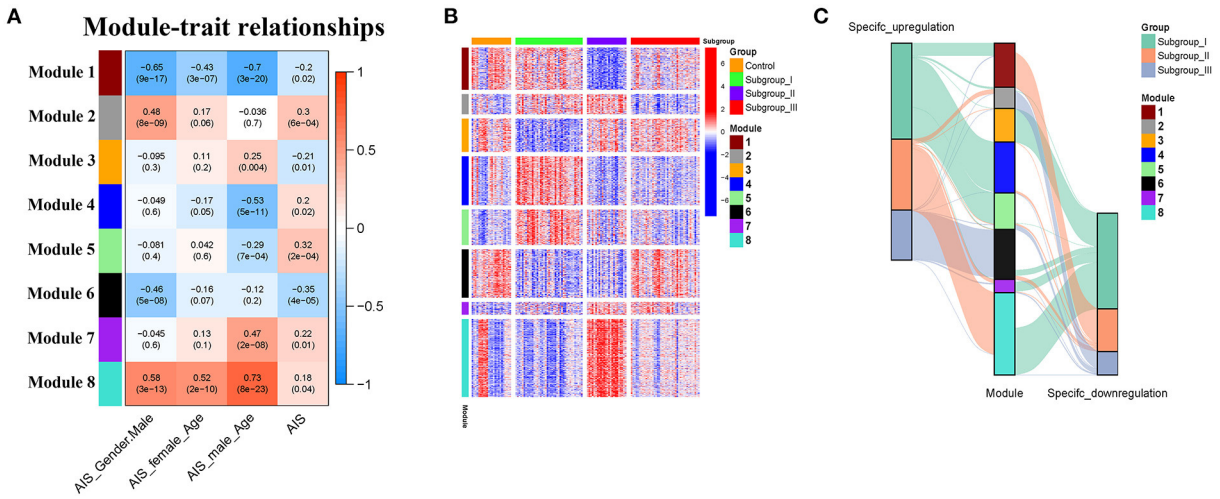

FIGURE 5
Identification and characterization of 8 modules by weighted gene co-expression analysis (WGCNA). **(A)** Module-trait relationship of gender and age in male and female patients. The positive and negative correlation coefficients of WGCNA modules and clinical characteristics are colored from red to blue. Each row corresponds to a module eigengene, each column corresponds to a trait. Each cell depicts the corresponding Pearson correlation r-values and p values in the bracket. **(B)** The scaled expression values of genes in each of the 8 WGCNA modules are displayed in the heatmap. **(C)** Alluvial diagram showing the inherent relationship between modules and subgroups.

TABLE 1 The number of differentially expressed genes by case-control and case-case comparisons and co-expression modules in each subgroup.

Subgroup	Subgroup-control comparison	Subgroup-specific upregulation genes	Subgroup-specific downregulation genes	Modules	
				Up	Down
Subgroup_I	4,092	1,372	1,363	4 and 5	3, 7, and 8
Subgroup_II	2,945	1,012	609	8	1
Subgroup_III	898	712	337	6	2

Supplementary Figure S3B), whereas modules 3 and 6 exhibited different co-expression of genes involved in ribosome biogenesis (Supplementary Figure S3C). Finally, we identified the enrichment pathways involved in protein processing in the endoplasmic reticulum (Figure 7, Supplementary Figure S4B), protein export, and ribosome activity in module 3 (Figures 5C, 7; Table 1; Supplementary Figures S3B,C). These results suggest that the ribosome-related pathways influence protein synthesis and secretion disorders in patients with AIS of subgroup I.

Correlation of transcriptomic pattern in subgroup I with HT

Given that our identified modules in patients with AIS are closely associated with HT, we asked whether our classification could reveal the risk of HT in patients with AIS. To this end, we analyzed an independent dataset (GSE199435) which separated patients with AIS into HT and non-HT groups. We first identified the differentially expressed genes (DEG) in non-HT patients with AIS compared with those of HT. Then, we performed a pre-ranked gene set enrichment analysis to determine the enrichment of HT-related DEG to the co-expression modules with subgroup-specific signature genes. We found that a significant number of genes in modules 4 and 5 in subgroup I-specific upregulated genes were positively enriched in the HT-related upregulated genes (Figure 11A, NES $>$ 1.5, FDR $<$ 0.001). A similar number of genes in modules 3 and 8, mainly from subgroup I that were specific-downregulated genes, was negatively enriched in the HT-related downregulated genes (Figure 11A NES $<$ −1.8, FDR $<$ 0.001). In contrast, a smaller number of genes was observed when analyzing the non-subgroup I modules 1, 2, and 6 (Figure 11A). Therefore, we compared the DEG in modules 3, 4, 5, and 8 with those in HT-specific DEG. As shown in the Venn diagram

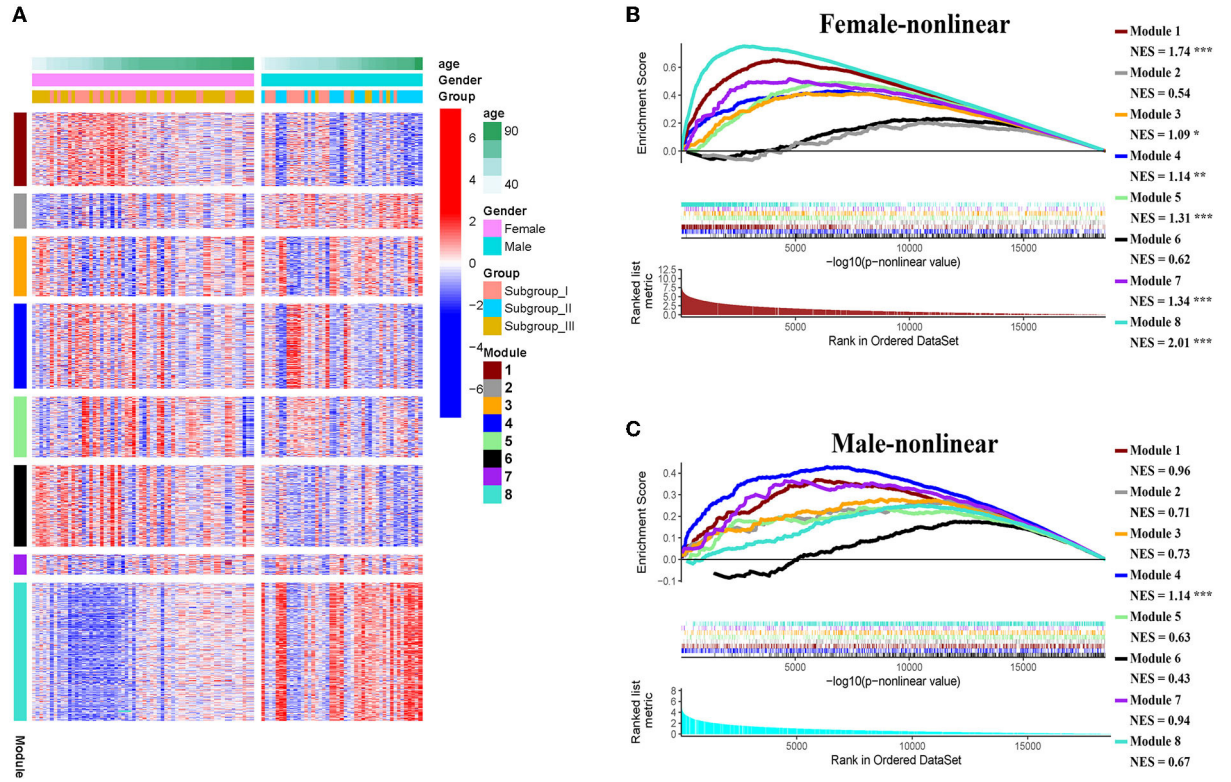

FIGURE 6
(A) Heatmap showing association of gender-specific distribution of age with the expression of subgroup-specific genes in each module. Red and blue indicate upregulation and downregulation, respectively. Samples were ordered by increasing age in each gender. **(B,C)** The enrichment plots of the restricted cubic spline-GSEA showing the significance of the non-linear relationship between all normalized expression of genes in each module and log-transfer age in female patients **(B)** and male patients **(C)**.

in Figure 11B, we identified 267 genes in common (FDR < 0.05). As shown in the heatmap in Figure 11C, their differential expression pattern was highly similar and coordinated in these two sets of genes. Finally, we performed Reactome analysis for the identification of enriched pathways in these 261 genes. Results identified pathways including the activation of matrix metalloproteinases (MMP2 and MMP25), pentose phosphate pathway, DNA double-strand break repair, DNA repair, and translation (Figure 11D, Supplementary Figure S5). Taken together, these results suggest that subgroup I and AIS patients with HT share a similar transcriptional profile.

Discussion

Acute ischemic stroke is a heterogeneous disorder with more than 100 pathologies implicated in its pathogenesis (34, 35). Therefore, it is important to develop various subgroup classification approaches for developing a personalized therapeutic strategy for effective stroke treatment. The advent of the subgroup classification such as the Trial of Org 10172 in Acute Stroke Treatment (TOAST), Causative Classification System (CCS), and Chinese Ischemic Stroke Subclassification (CISS) system during the past decade has facilitated the clinical application of antiplatelet and anticoagulation therapies (36, 37). In addition, the classification of AIS cases improves the clinical feasibility of time-dependent and population-specific revascularization therapies (38, 39). However, current AIS subgroup classification methods, mainly based on clinical evaluation and neuroimaging assessment, fail to address immune interventions that are promising but require personalized medications.

In this study, we developed a novel classification of AIS by consensus clustering of transcriptomic profiles in peripheral blood. Most of the subgroup-specific genes overlap with AIS signature genes as revealed by GSEA (Figure 2) and WGCNA (Figure 5A). These results highlight the importance of subgroup classification for a more precise correlation of peripheral immunity with AIS. Moreover, this study indicates that our subgroup classification is independent of sample collection time for the first 24 h or from 24 to 48 h, making our classification approach more flexible in terms of administration of gender-specific therapeutics for the attenuation of the risk of HT and AIIS, considering that the therapeutic time window of immune

FIGURE 7
Module-based pathway analysis. Visualization of pathways identified by the Kyoto Encyclopedia of Genes and Genomes (KEGG) analysis.

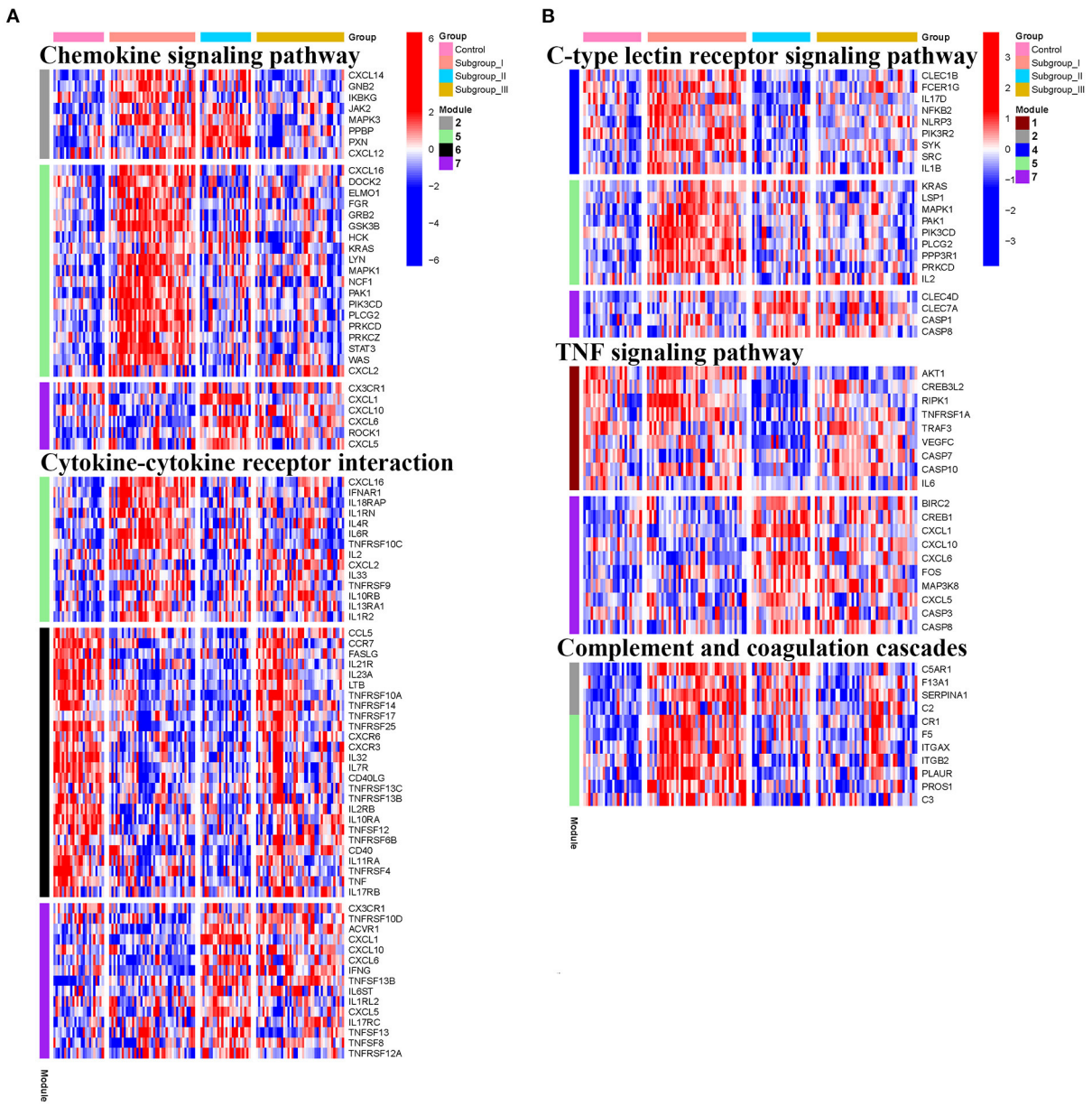

FIGURE 8
Heatmap showing the scaled expression values of genes in representative subgroup-specific KEGG pathways related to inflammation and corresponding signature of each co-expression module among subgroups. **(A)** Chemokine signaling pathway and cytokine-cytokine receptor interation. **(B)** C-type lectin receptor signaling pathway, TNF signaling pathway, and complement and coagulation cascades. Heatmap colors correspond to the level of mRNA expression as indicated in the color rang.

interventions is typically 6–48 h after AIS in clinical studies (40, 41).

Our transcriptome-based classification revealed subgroup-specific functional modules or pathways based on the tendency of co-expression patterns by WGCNA. As an integral component of the peripheral immunity response to AIS, our analysis confirmed that multiple inflammatory factors including chemokines, interleukins, and tumor necrosis factors are secreted from peripheral blood cells to trigger pro- or anti-inflammatory responses as reported previously (31, 42, 43). We also demonstrate that complement synthesis, coagulation factor production, and C-type lectin receptor expression in peripheral blood cells apparently play an instrumental role in peripheral immunity in response to AIS (44–46). Our findings also support the notion that AIS could regulate periphery immune response through the alteration of

FIGURE 9
Module-based pathway analysis. Visualization of pathways identified by the Reactome.

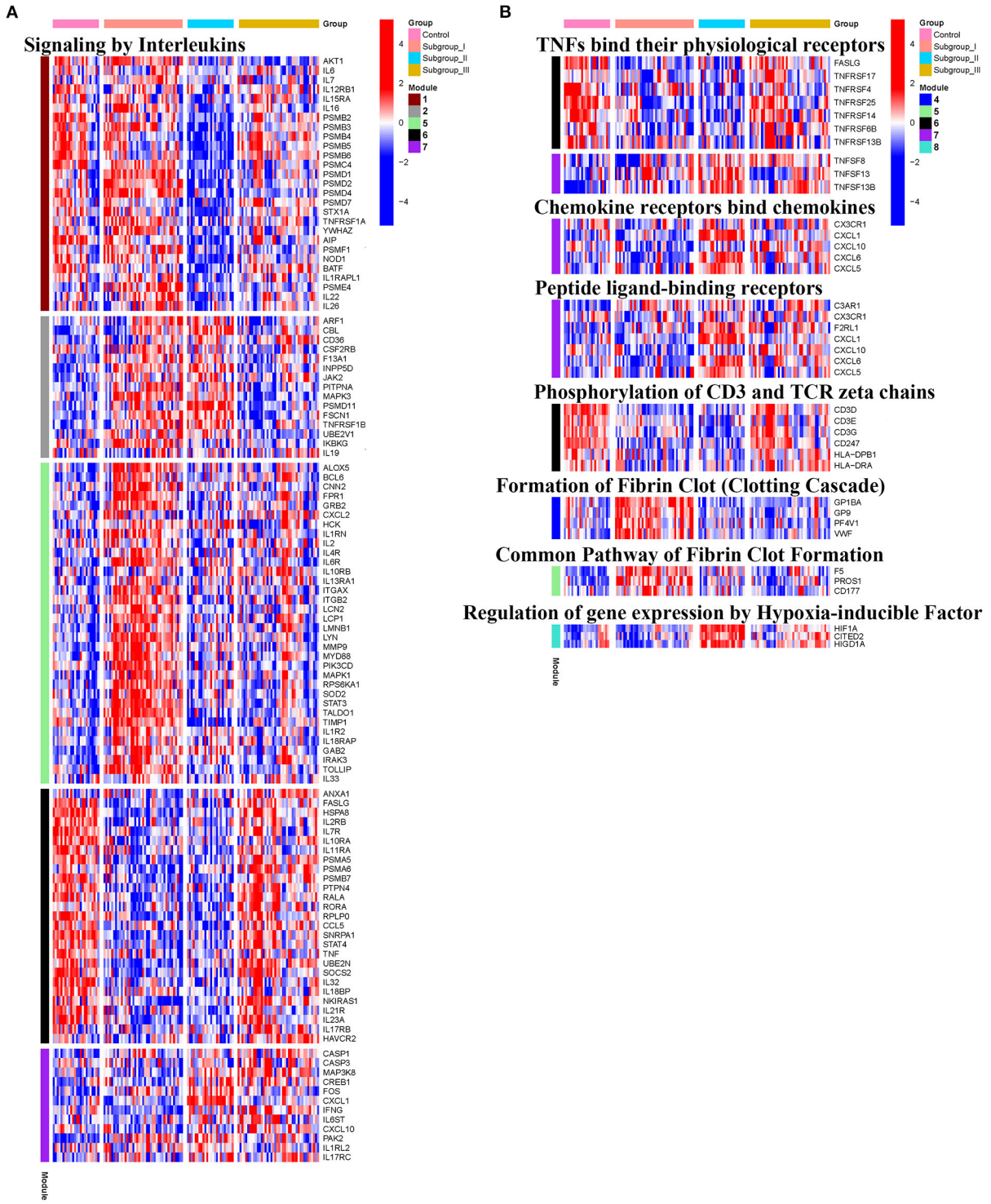

FIGURE 10
Heatmap showing the expression level of genes in representative subgroup-specific Reactome pathways related to inflammation as indicated in Signaling by Interleukins **(A)** and TNFs bind their physiological receptors, Chemokine receptors bind chemokines, Peptide ligand-binding receptors, Phosphorylation of CD3 and TCR zeta chains, Formation of Fibrin Clot Formation, and Relation of gene expression by Hypoxia-inducible Factor **(B)** and corresponding signature of each co-expression module among subgroups, heatmap colors correspond to the level of mRNA expression as indicated in the color rang.

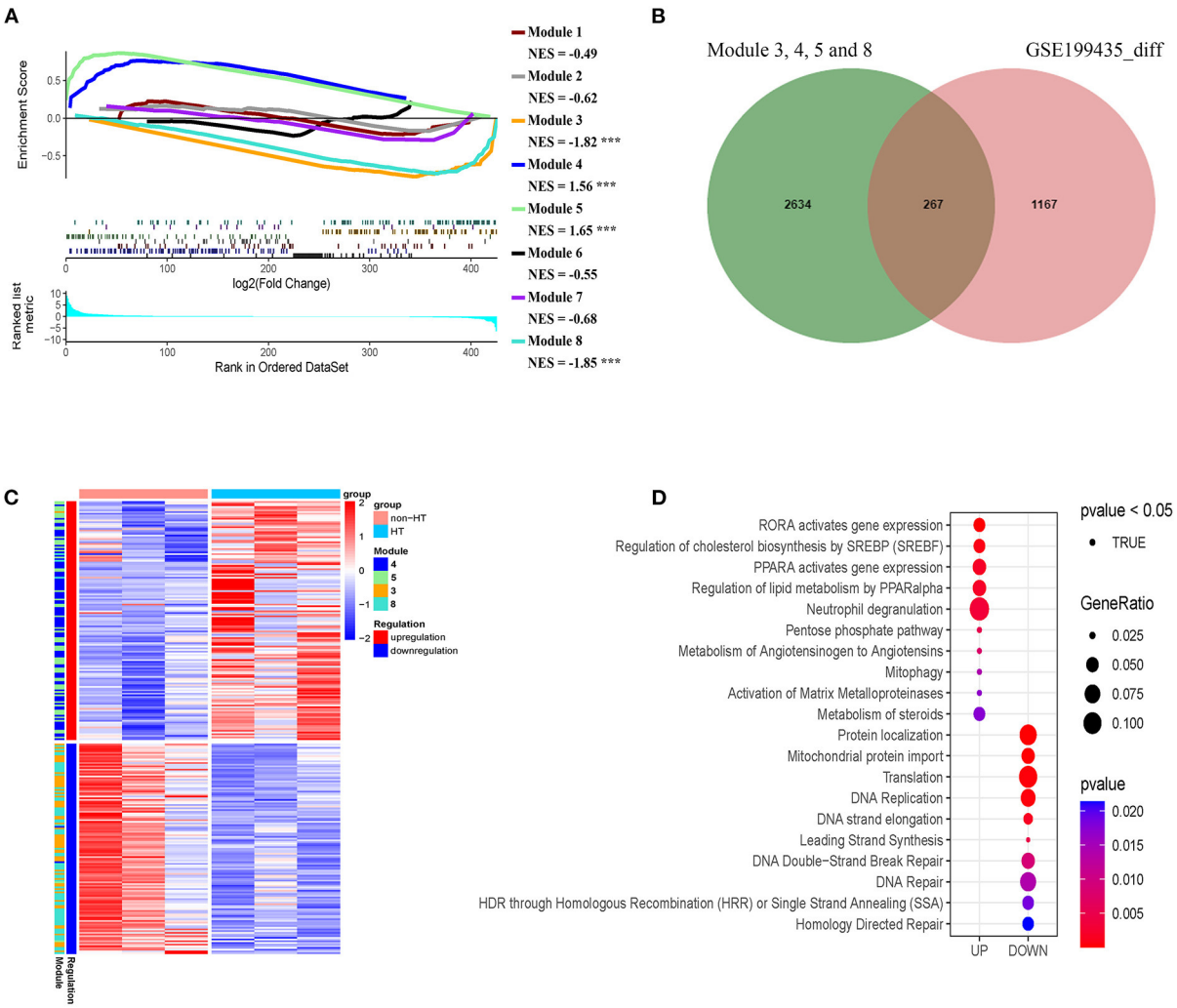

FIGURE 11
Genes in modules in subgroup I overlaps with hemorrhage transformation (HT)-specific differentially expressed genes (DEG). **(A)** Pre-ranked gene set enrichment analysis showing the enrichment of DEG related to HT in the co-expression modules with subgroup I-specific signature genes. **(B)** Venn diagram showing the number of overlapped genes (267) between HT-specific DEG and subgroup I-specific genes. **(C)** Heatmap representing the overlap genes between DEGs related to HT and subgroup I-specific genes. **(D)** Diagram showing pathways identified by Reactome with the negative $\log_{10}$ p-values of the overlapped genes shown in B and C.

immunometabolism, including the tricarboxylic acid (TCA) cycle, the pentose phosphate pathway, propanoate metabolism, oxidative phosphorylation, and pyruvate metabolism (47–49). Our co-expression analysis further suggested a correlation between the immunometabolism and maintenance of DNA stability, consistent with recent studies showing that DNA double-strand break repair, DNA damage bypass, and homologous recombination were allegedly regulated by pyruvate metabolism and TCA cycle (50). In fact, the intricate roles of transcriptional reprogramming and alteration of immunometabolism in peripheral immune cells after AIS remain largely unknown. Our identification of various co-expression patterns within different subgroups could provide a comprehensive insight for future studies on immunotherapy for stroke.

It is worth noting that our pathway analysis in each module reveals the closely intertwined action of peripheral immunity-mediated inflammation, thrombosis-driven friability of cerebral vasculature, and coagulation disequilibrium. In agreement with these findings, recent studies have shown that the ischemic cerebral infarct progression is accompanied by microvascular thrombosis and subsequent HT (51, 52). In fact, these peripheral immunity-mediated inflammatory mechanisms have led to the concept that AIS is a systemic inflammatory and a thrombo-inflammatory disease (31–33). Interestingly, our GSEA analysis demonstrates that the coordinated expression pattern in the

subgroup I-specific DEG is significantly analogous to that in the HT-specific modules (53). We further identified the activation of matrix metalloproteinases (including MMP2 and MMP25) that were enriched in the overlapping genes between these two groups, supporting their possible role in HT as reported previously (54–56). Moreover, we identified the pathways related to ribosome biogenesis and protein translation in both subgroups I and the HT-specific module. Currently, the role of protein translation in HT remains unknown, and obviously future studies will be required to provide the underlying mechanisms. Interestingly, our results suggest a potential mechanism of coagulation by peripheral immunity. We showed that modules 4 and 5, which are mainly from subgroup I specific upregulated genes, are all enriched in a pathway related to neutrophil extracellular trap (NET) formation, which is known to play a key role in hemorrhagic transformation and a thrombus resistant to lytic therapy (57, 58). In addition, our finding is in agreement with previous reports showing that the formation of NET may be induced by IL-1B, CAMP(LL37), and C3 in peripheral blood cells (59–62).

It is not uncommon in clinical settings that AIS induces AIIS, which is characterized by decreased $CD3^{+}$T lymphocyte (3). Our pathway enrichment analysis shows that module 6, which is specifically upregulated in subgroup III (comprised mostly female patients) is plausibly correlated with a lesser degree of AIIS compared to subgroups I and II. Consistently, it has been reported that the female patients showed a reduced level of AIIS compared with male patients, suggesting a gender-specific response in post-AIS peripheral immunity (63–65). In addition, recent studies have shown a diminished level of T cell activity following the release of coagulation factor V(F5), arginase 1 (ARG1), LL33 (CAMP), and IL33 from the periphery immune cells, resulting in peripheral immunosuppression (66–69). We discover the lack of upregulation of ARG1, IL 33, and F5 in subgroup III, which denotes a contrary expression tendency in module 6 (see Supplementary Table S1). In contrast, module 2 consists of calmodulin-dependent kinase-related genes CAMK2A and CAMKK2, which are crucial regulators of peripheral blood cell functions (29, 30). It has been reported that peripheral blood cells are capable of producing complements and factors in coagulation cascades including C2, C5AR1, F13A1 (coagulation factor XIII, A1 Polypeptide), and SERPINA1 (a form of antiplasmin protein) (44). Interestingly, these genes are enriched in module 2 in our study, further supporting a correlation between thromboinflammation and AIIS. Finally, we found that the proteasome activity is decreased specifically in subgroup II. We speculate that peripheral blood cells in this AIS subgroup patients may reduce proteasome activity for alleviating ischemic injury. Since subgroup II is mainly composed of older male patients and subgroup III is mostly of female patients, this gender-dependent characteristic of classification by molecular subgrouping may guide personalized immunotherapeutic treatment for stroke.

Our study has several limitations. Firstly, we only examined 107 AIS cases, and a larger sample size in the future would be necessary to verify the robustness of our classification. Secondly, we could not directly evaluate the prognostic value using this classification method due to the lack of relevant clinical details in the datasets. For example, we were not able to relate the subgroups to clinical information such as comorbidities, demographic characteristics, thrombolysis or types of endovascular treatment, type of hemorrhage transformation (spontaneous HT, thrombolysis-induced HT, etc.), and TOAST classification. Therefore, we could not determine the predictive value of this classification on the prognosis of patients with AIS. Finally, samples were mainly collected from patients in the United States and China. Future prospective validation work is required by using samples collected from other countries.

In conclusion, the peripheral blood transcriptomic profiling for AIS classification reveals distinct and specific expression patterns. Considering the heterogeneity of the peripheral immunity in stroke patients, this molecular classification approach would have a prognostic impact by improving the efficacy of immunotherapies, prediction of the risk of hemorrhagic transformation, and therapeutic time window of immune interventions. Thus, this classification could potentially improve the prognosis of patients with AIS by providing a more informative and personalized medication strategy by the identification of patients with AIS who are vulnerable to stroke-induced immunodeficiency, resistant to gender-specific immunotherapy, and at risk of hemorrhagic transformation and other comorbidities.

Data availability statement

The original contributions presented in the study are included in the article/Supplementary material, further inquiries can be directed to the corresponding authors.

Ethics statement

Ethical review and approval was not required for this study in accordance with the local legislation and institutional requirements. Written informed consent from the patients/participants or patients/participants' legal guardian/next of kin was not required for this study in accordance with the national legislation and the institutional requirements.

Author contributions

ZY: collection and analysis of data, and interpretation of data. ZY and CT: manuscript writing and

revision. GW: project development. NL: technical assistance. CT and LH: direct the overall project. All authors contributed to the article and approved the submitted version.

Funding

This research was funded by grants from the National Nature Science Foundation of China (Grant Number 81971120); the Science and Technology Plan Projects of Guangdong Province (Grant Number 2022A1515012563); the Basic and Applied Basic Research on the Project Jointly Funded by Guangzhou city and Jinan University (Grant Number 202201020062).

Acknowledgments

We owe our gratitude to Mr. Steven Zhou for his technical assistance with the bioinformatics analysis used in this study.

Conflict of interest

The authors declare that the research was conducted in the absence of any commercial or financial relationships that could be construed as a potential conflict of interest.

Publisher's note

All claims expressed in this article are solely those of the authors and do not necessarily represent those of their affiliated organizations, or those of the publisher, the editors and the reviewers. Any product that may be evaluated in this article, or claim that may be made by its manufacturer, is not guaranteed or endorsed by the publisher.

Supplementary material

The Supplementary Material for this article can be found online at: https://www.frontiersin.org/articles/10.3389/fneur.2022.937501/full#supplementary-material

References

1. Benjamin EJ, Blaha MJ, Chiuve SE, Cushman M, Das SR, Deo R, et al. American Heart Association statistics, and s. stroke statistics, heart disease and stroke statistics-2017 update: a report from the American Heart Association. *Circulation*. (2017) 135:e146–603. doi: 10.1161/CIR.0000000000000491

2. GBDS Collaborators. Global, regional, and national burden of stroke, 1990-2016: a systematic analysis for the Global Burden of Disease Study 2016. *Lancet Neurol*. (2019) 18:439–58. doi: 10.1016/S1474-4422(19)30034-1

3. Faura J, Bustamante A, Miro-Mur F, Montaner J. Stroke-induced immunosuppression: implications for the prevention and prediction of post-stroke infections. *J Neuroinflammation*. (2021) 18:127. doi: 10.1186/s12974-021-02177-0

4. Veltkamp R, Gill D. Clinical trials of immunomodulation in ischemic stroke. *Neurotherapeutics*. (2016) 13:791–800. doi: 10.1007/s13311-016-0458-y

5. Smith CJ, Lawrence CB, Rodriguez-Grande B, Kovacs KJ, Pradillo JM, Denes A. The immune system in stroke: clinical challenges and their translation to experimental research. *J Neuroimmune Pharmacol*. (2013) 8:867–87. doi: 10.1007/s11481-013-9469-1

6. Enlimomab acute stroke trial, use of anti-ICAM-1 therapy in ischemic stroke: results of the enlimomab acute stroke trial. *Neurology*. (2001) 57:1428–34. doi: 10.1212/WNL.57.8.1428

7. Lei TY, Ye YZ, Zhu XQ, Smerin D, Gu LJ, Xiong XX, et al. The immune response of T cells and therapeutic targets related to regulating the levels of T helper cells after ischaemic stroke. *J Neuroinflammation*. (2021) 18:25. doi: 10.1186/s12974-020-02057-z

8. Levard D, Buendia I, Lanquetin A, Glavan M, Vivien D, Rubio M. Filling the gaps on stroke research: Focus on inflammation and immunity. *Brain Behav Immun*. (2021) 91:649–67. doi: 10.1016/j.bbi.2020.09.025

9. Pagram H, Bivard A, Lincz LF, Levi C. Immunity and stroke, the hurdles of stroke research translation. *Int J Stroke*. (2017) 12:123–31. doi: 10.1177/1747493016676622

10. Santos Samary C, Pelosi P, Leme Silva P, Rieken Macedo Rocco P. Immunomodulation after ischemic stroke: potential mechanisms and implications for therapy. *Crit Care*. (2016) 20:391. doi: 10.1186/s13054-016-1573-1

11. Agarwal AR, Kadam S, Brahme A, Agrawal M, Apte K, Narke G, et al. Systemic Immuno-metabolic alterations in chronic obstructive pulmonary disease (COPD). *Respir Res*. (2019) 20:171. doi: 10.1186/s12931-019-1139-2

12. Mesko B, Poliska S, Szegedi A, Szekanecz Z, Palatka K, Papp M, et al. Peripheral blood gene expression patterns discriminate among chronic inflammatory diseases and healthy controls and identify novel targets. *BMC Med Genomics*. (2010) 3:15. doi: 10.1186/1755-8794-3-15

13. Krieg C, Nowicka M, Guglietta S, Schindler S, Hartmann FJ, Weber LM, et al. High-dimensional single-cell analysis predicts response to anti-PD-1 immunotherapy. *Nat Med*. (2018) 24:144–53. doi: 10.1038/nm.4466

14. Goossens J, Morrens M, Coppens V. The potential use of peripheral blood mononuclear cells as biomarkers for treatment response and outcome prediction in psychiatry: a systematic review. *Mol Diagn Ther*. (2021) 25:283–99. doi: 10.1007/s40291-021-00516-8

15. Zheng G, Qiu G, Ge M, Meng J, Zhang G, Wang J, et al. miR-10a in peripheral blood mononuclear cells is a biomarker for sepsis and has anti-inflammatory function. *Mediators Inflamm*. (2020) 2020:4370983. doi: 10.1155/2020/4370983

16. Baird AE. Blood genomic profiling: novel diagnostic and therapeutic strategies for stroke? *Biochem Soc Trans*. (2006) 34:1313–7. doi: 10.1042/BST0341313

17. Falcione S, Kamtchum-Tatuene J, Sykes G, Jickling GC. RNA expression studies in stroke: what can they tell us about stroke mechanism? *Curr Opin Neurol*. (2020) 33:24–9. doi: 10.1097/WCO.0000000000000786

18. Liu Q, Liu D, Yan D, Huang W, Ji X, Hui J, et al. Gender-specific association between serum uric acid and incident high intraocular pressure in Chinese population: a cross-sectional study. *Invest Ophthalmol Vis Sci*. (2020) 61:10. doi: 10.1167/iovs.61.11.10

19. Liu S, Lu Y, Geng D. Molecular subgroup classification in alzheimer's disease by transcriptomic profiles. *J Mol Neurosci*. (2022) 72:866–79. doi: 10.1007/s12031-021-01957-w

20. Jiang C, Wang R, Zong B, Wei P, Lu W, Han B, et al. Subgroup identification with gene expression profiles of adipose tissue in patients with coronary artery disease. *Int Heart J*. (2021) 62:1199–206. doi: 10.1536/ihj.21-189

21. Prom-On S, Chanthaphan A, Chan JH, Meechai A. Enhancing biological relevance of a weighted gene co-expression network for functional module identification. *J Bioinform Comput Biol*. (2011) 9:111–29. doi: 10.1142/S0219720011005252

22. Wang Y, Wang Z, Xu J, Li J, Li S, Zhang M, et al. Systematic identification of non-coding pharmacogenomic landscape in cancer. *Nat Commun.* (2018) 9:3192. doi: 10.1038/s41467-018-05495-9

23. Subramanian A, Tamayo P, Mootha VK, Mukherjee S, Ebert BL, Gillette MA, et al. Gene set enrichment analysis: a knowledge-based approach for interpreting genome-wide expression profiles. *Proc Natl Acad Sci U S A.* (2005) 102:15545–50. doi: 10.1073/pnas.0506580102

24. Andersson A, Eden P, Olofsson T, Fioretos T. Gene expression signatures in childhood acute leukemias are largely unique and distinct from those of normal tissues and other malignancies. *BMC Med Genomics.* (2010) 3:6. doi: 10.1186/1755-8794-3-6

25. Verma A, Muthukumar T, Yang H, Lubetzky M, Cassidy MF, Lee JR, et al. Urinary cell transcriptomics and acute rejection in human kidney allografts. *JCI Insight.* (2020) 5:e131552. doi: 10.1172/jci.insight.131552

26. Yu G, He QY. ReactomePA: an R/Bioconductor package for reactome pathway analysis and visualization. *Mol Biosyst.* (2016) 12:477–9. doi: 10.1039/C5MB00663E

27. Yu G, Wang LG, Han Y, He QY. clusterProfiler: an R package for comparing biological themes among gene clusters. *Omics.* (2012) 16:284–7. doi: 10.1089/omi.2011.0118

28. Patel TH, Kimura H, Weiss CR, Semenza GL, Hofmann LV. Constitutively active HIF-1alpha improves perfusion and arterial remodeling in an endovascular model of limb ischemia. *Cardiovasc Res.* (2005) 68:144–54. doi: 10.1016/j.cardiores.2005.05.002

29. Guest CB, Deszo EL, Hartman ME, York JM, Kelley KW, Freund GG. Ca2+/calmodulin-dependent kinase kinase alpha is expressed by monocytic cells and regulates the activation profile. *PLoS ONE.* (2008) 3:e1606. doi: 10.1371/journal.pone.0001606

30. Esteras N, Alquezar C, Bermejo-Pareja F, Bialopiotrowicz E, Wojda U, Martin-Requero A. Downregulation of extracellular signal-regulated kinase 1/2 activity by calmodulin KII modulates p21Cip1 levels and survival of immortalized lymphocytes from Alzheimer's disease patients. *Neurobiol Aging.* (2013) 34:1090–100. doi: 10.1016/j.neurobiolaging.2012.10.014

31. Dziedzic T. Systemic inflammation as a therapeutic target in acute ischemic stroke. *Expert Rev Neurother.* (2015) 15:523–31. doi: 10.1586/14737175.2015.1035712

32. Karim MA, Kartsonaki C, Bennett DA, Millwood IY, Hill MR, Avery D, et al. China Kadoorie Biobank Collaborative, systemic inflammation is associated with incident stroke and heart disease in East Asians. *Sci Rep.* (2020) 10:5605. doi: 10.1038/s41598-020-62391-3

33. Mezger M, Nording H, Sauter R, Graf T, Heim C, von Bubnoff N, et al. Platelets and immune responses during thromboinflammation. *Front Immunol.* (2019) 10:1731. doi: 10.3389/fimmu.2019.01731

34. Liu J, Li M, Liu J. Evaluation of the ESRS and SPI-II scales for short-term prognosis of minor stroke and transient ischemic attack. *Neurol Res.* (2013) 35:568–72. doi: 10.1179/1743132813Y.0000000172

35. Amarenco P, Bogousslavsky J, Caplan LR, Donnan GA, Wolf ME, Hennerici MG. The ASCOD phenotyping of ischemic stroke (Updated ASCO Phenotyping). *Cerebrovascular diseases.* (2013) 36:1–5. doi: 10.1159/000352050

36. Radu RA, Terecoasa EO, Bajenaru OA, Tiu C. Etiologic classification of ischemic stroke: where do we stand? *Clin Neurol Neurosurg.* (2017) 159:93–106. doi: 10.1016/j.clineuro.2017.05.019

37. Chen PH, Gao S, Wang YJ, Xu AD Li YS, Wang D. Classifying ischemic stroke, from TOAST to CISS. *CNS Neurosci Ther.* (2012) 18:452–6. doi: 10.1111/j.1755-5949.2011.00292.x

38. Morotti A, Poli L, Costa P. Acute stroke. *Semin Neurol.* (2019) 39:61–72. doi: 10.1055/s-0038-1676992

39. Herpich F, Rincon F. Management of acute ischemic stroke. *Crit Care Med.* (2020) 48:1654–63. doi: 10.1097/CCM.0000000000004597

40. Grond-Ginsbach C, Hummel M, Wiest T, Horstmann S, Pfleger K, Hergenhahn M, et al. Gene expression in human peripheral blood mononuclear cells upon acute ischemic stroke. *J Neurol.* (2008) 255:723–31. doi: 10.1007/s00415-008-0784-z

41. Sharp FR, Xu H, Lit L, Walker W, Pinter J, Apperson M, et al. Genomic profiles of stroke in blood. *Stroke.* (2007) 38:691–3. doi: 10.1161/01.STR.0000247940.27518.38

42. Lambertsen KL, Biber K, Finsen B. Inflammatory cytokines in experimental and human stroke. *J Cereb Blood Flow Metab.* (2012) 32:1677–98. doi: 10.1038/jcbfm.2012.88

43. Georgakis MK, Gill D, Rannikmae K, Traylor M, Anderson CD, Lee JM, et al. Genetically determined levels of circulating cytokines and risk of stroke. *Circulation.* (2019) 139:256–68. doi: 10.1161/CIRCULATIONAHA.118.035905

44. de Roos B, Duthie SJ, Polley AC, Mulholland F, Bouwman FG, Heim C, et al. Proteomic methodological recommendations for studies involving human plasma, platelets, and peripheral blood mononuclear cells. *J Proteome Res.* (2008) 7:2280–90. doi: 10.1021/pr700714x

45. Galimberti D, Fenoglio C, Ghezzi L, Serpente M, Arcaro M, D'Anca M, et al. Inflammatory expression profile in peripheral blood mononuclear cells from patients with Nasu-Hakola Disease. *Cytokine.* (2019) 116:115–9. doi: 10.1016/j.cyto.2018.12.024

46. Høgåsen AK, Hestdal K, Høgåsen K, Abrahamsen TG. Transforming growth factor beta modulates C3 and factor B biosynthesis and complement receptor 3 expression in cultured human monocytes. *J Leukoc Biol.* (1995) 57:287–96. doi: 10.1002/jlb.57.2.287

47. O'Neill LA, Kishton RJ, Rathmell J, A. guide to immunometabolism for immunologists. *Nat Rev Immunol.* (2016) 16:553–65. doi: 10.1038/nri.2016.70

48. Zhang X, Zink F, Hezel F, Vogt J, Wachter U, Wepler M, et al. Metabolic substrate utilization in stress-induced immune cells. *Intensive Care Med Exp.* (2020) 8:28. doi: 10.1186/s40635-020-00316-0

49. Devanney NA, Stewart AN, Gensel JC. Microglia and macrophage metabolism in CNS injury and disease: the role of immunometabolism in neurodegeneration and neurotrauma. *Exp Neurol.* (2020) 329:113310. doi: 10.1016/j.expneurol.2020.113310

50. Cucchi D, Gibson A, Martin SA. The emerging relationship between metabolism and DNA repair. *Cell Cycle.* (2021) 20:943–59. doi: 10.1080/15384101.2021.1912889

51. Ansari J, Gavins FNE. The impact of thrombo-inflammation on the cerebral microcirculation. *Microcirculation.* (2021) 28:e12689. doi: 10.1111/micc.12689

52. Stoll G, Nieswandt B. Thrombo-inflammation in acute ischaemic stroke - implications for treatment. *Nat Rev Neurol.* (2019) 15:473–81. doi: 10.1038/s41582-019-0221-1

53. Giacomini E, Scotti GM, Vanni VS, Lazarevic D, Makieva S, Privitera L, et al. Global transcriptomic changes occur in uterine fluid-derived extracellular vesicles during the endometrial window for embryo implantation. *Hum Reprod.* (2021) 36:2249–74. doi: 10.1093/humrep/deab123

54. Lyden PD. Hemorrhagic transformation during thrombolytic therapy and reperfusion: effects of age, blood pressure, matrix metalloproteinases. *J Stroke Cerebrovasc Dis.* (2013) 22:532–8. doi: 10.1016/j.jstrokecerebrovasdis.2013.02.001

55. Jickling GC, Liu D, Stamova B, Ander BP, Zhan X, Lu A, et al. Hemorrhagic transformation after ischemic stroke in animals and humans. *J Cereb Blood Flow Metab.* (2014) 34:185–99. doi: 10.1038/jcbfm.2013.203

56. Wang Y, Deng XL, Xiao XH, Yuan BX. A non-steroidal anti-inflammatory agent provides significant protection during focal ischemic stroke with decreased expression of matrix metalloproteinases. *Curr Neurovasc Res.* (2007) 4:176–83. doi: 10.2174/156720207781387187

57. Wang R, Zhu Y, Liu Z, Chang L, Bai X, Kang L, et al. Neutrophil extracellular traps promote tPA-induced brain hemorrhage via cGAS in mice with stroke. *Blood.* (2021) 138:91–103. doi: 10.1182/blood.2020008913

58. Sambola AB, Del Blanco G, Ruiz-Meana M, Francisco J, Barrabes JA, Figueras J, et al. Increased von Willebrand factor, P-selectin and fibrin content in occlusive thrombus resistant to lytic therapy. *Thromb Haemost.* (2016) 115:1129–37. doi: 10.1160/TH15-12-0985

59. Targets in Arterial V. Cancer-associated thrombosis. *Arterioscler Thromb Vasc Biol.* (2019) 39:1724–38. doi: 10.1161/ATVBAHA.119.312463

60. Oikonomopoulou K, Ricklin D, Ward PA, Lambris JD. Interactions between coagulation and complement–their role in inflammation. *Semin Immunopathol.* (2012) 34:151–65. doi: 10.1007/s00281-011-0280-x

61. Mastellos DC, Pires da Silva BGP, Fonseca BAL, Fonseca NP, Auxiliadora-Martins M, Mastaglio S, et al. Complement C3 vs C5 inhibition in severe COVID-19: Early clinical findings reveal differential biological efficacy. *Clin Immunol.* (2020) 220:108598. doi: 10.1016/j.clim.2020.108598

62. Schwabe FV, Happonen L, Ekestubbe S, Neumann A. Host defense peptides LL-37 and lactoferrin trigger ET release from blood-derived circulating monocytes. *Biomedicines.* (2022) 10:469. doi: 10.3390/biomedicines10020469

63. Whisler RL, Chen M, Liu B, Newhouse YG. Age-related impairments in TCR/CD3 activation of ZAP-70 are associated with reduced tyrosine phosphorylations of zeta-chains and p59fyn/p56lck in human T cells. *Mech Ageing Dev.* (1999) 111:49–66. doi: 10.1016/S0047-6374(99)00074-3

64. Yan J, Read SJ, Henderson RD, Hull R, O'Sullivan JD, McCombe PA, et al. Frequency and function of regulatory T cells after ischaemic stroke in humans. *J Neuroimmunol.* (2012) 243:89–94. doi: 10.1016/j.jneuroim.2011.12.019

65. Liesz A, Hu X, Kleinschnitz C, Offner H. Functional role of regulatory lymphocytes in stroke: facts and controversies. *Stroke.* (2015) 46:1422–30. doi: 10.1161/STROKEAHA.114.008608

66. Petrone AB, O'Connell GC, Regier MD, Chantler PD, Simpkins JW, Barr TL. The Role of Arginase 1 in Post-Stroke Immunosuppression and Ischemic Stroke Severity. *Transl Stroke Res.* (2016) 7:103–10. doi: 10.1007/s12975-015-0431-9

67. Zhang SR, Piepke M, Chu HX, Broughton BR, Shim R, Wong CH, et al. IL-33 modulates inflammatory brain injury but exacerbates systemic immunosuppression following ischemic stroke. *JCI Insight.* (2018) 3:e121560. doi: 10.1172/jci.insight.121560

68. Xiao W, Guo S, Chen L, Luo Y. The role of Interleukin-33 in the modulation of splenic T-cell immune responses after experimental ischemic stroke. *J Neuroimmunol.* (2019) 333:576970. doi: 10.1016/j.jneuroim.2019.576970

69. Wang J, Kotagiri P, Lyons PA, Al-Lamki RS, Mescia F, Bergamaschi L, et al. Coagulation factor V is a T-cell inhibitor expressed by leukocytes in COVID-19. *iScience.* (2022) 25:103971. doi: 10.1016/j.isci.2022.103971

70. Seiler M, Huang CC, Szalma S, Bhanot G. ConsensusCluster: a software tool for unsupervised cluster discovery in numerical data. *Omics.* (2010) 14:109–13. doi: 10.1089/omi.2009.0083

71. MacDonald CJ, Madika AL, Gomes R, Severi G, Sibon I, Debette S, et al. Physical activity and stroke among women-a non-linear relationship. *Prev Med.* (2021) 150:106485. doi: 10.1016/j.ypmed.2021.106485

frontiers | Frontiers in Neurology

TYPE Original Research
PUBLISHED 15 September 2022
DOI 10.3389/fneur.2022.875134

Check for updates

OPEN ACCESS

EDITED BY
John Zhang,
Loma Linda University, United States

REVIEWED BY
Danhong Wu,
Fudan University, China
Carlos Garcia Santos-Gallego,
Mount Sinai Hospital, United States

*CORRESPONDENCE
Yuming Xu
xuyuming@zzu.edu.cn
Longde Wang
longed_wang@yeah.net

SPECIALTY SECTION
This article was submitted to Neurological Biomarkers, a section of the journal Frontiers in Neurology

RECEIVED 13 February 2022
ACCEPTED 15 August 2022
PUBLISHED 15 September 2022

CITATION
Wang A, Li Y, Zhou L, Liu K, Li S, Zong C, Song B, Gao Y, Li Y, Tian C, Xing Y, Xu Y and Wang L (2022) Non-HDL-C/HDL-C ratio is associated with carotid plaque stability in general population: A cross-sectional study. *Front. Neurol.* 13:875134. doi: 10.3389/fneur.2022.875134

COPYRIGHT
© 2022 Wang, Li, Zhou, Liu, Li, Zong, Song, Gao, Li, Tian, Xing, Xu and Wang. This is an open-access article distributed under the terms of the Creative Commons Attribution License (CC BY). The use, distribution or reproduction in other forums is permitted, provided the original author(s) and the copyright owner(s) are credited and that the original publication in this journal is cited, in accordance with accepted academic practice. No use, distribution or reproduction is permitted which does not comply with these terms.

Non-HDL-C/HDL-C ratio is associated with carotid plaque stability in general population: A cross-sectional study

Anran Wang[1], Yapeng Li[1], Lue Zhou[1], Kai Liu[1], Shaohua Li[1], Ce Zong[1], Bo Song[1], Yuan Gao[1], Yusheng Li[1], Chuansheng Tian[2], Yurong Xing[3], Yuming Xu[1]* and Longde Wang[1,4]*

[1]Department of Neurology, The First Affiliated Hospital of Zhengzhou University, Zhengzhou, Henan, China, [2]Chinese Preventive Medicine Association, Beijing, China, [3]Physical Examination Center, The First Affiliated Hospital of Zhengzhou University, Zhengzhou, China, [4]The General Office of Stroke Prevention Project Committee, National Health Commission of the People's Republic of China, Beijing, China

Background: Carotid atherosclerosis, especially the rupture of unstable plaques, plays an important role in the development of stroke. A novel lipid ratio, the non-high-density lipoprotein cholesterol (non-HDL-C)/high-density lipoprotein cholesterol (HDL-C) ratio, contains both atherogenic and anti-atherogenic particle information, and has been shown to be associated with carotid atherosclerosis. However, there is no data on evaluating the association between non-HDL-C/HDL-C ratio and carotid plaque stability.

Methods: This study was carried out on 27,436 urban workers aged 20 years or older who participated in a comprehensive health screening between January 2016 and December 2017. Carotid plaque stability was assessed using ultrasonography. Multinomial logistic regression models were used to explore the relationship between the non-HDL-C/HDL-C ratio and carotid plaque stability by odds ratios (*ORs*) and 95% confidence intervals (*CIs*). Subgroup and sensitivity analyses were performed to verify the robustness of the results.

Results: Carotid plaque was detected in 7,161 (26.1%) participants, with stable and unstable plaque accounting for 3,277 (11.9%) and 3,884 (14.2%), respectively. The prevalence of stable carotid plaque substantially increased with increasing non-HDL-C/HDL-C ratio quartile levels (p for trend < 0.001) and with a similar association for unstable carotid plaque (p for trend < 0.001). The mean non-HDL-C/HDL-C ratios (mean $\pm$ *SD*) of non-carotid plaque (2.9 $\pm$ 1.1), stable carotid plaque (3.2 $\pm$ 1.2), and unstable carotid plaque (3.4 $\pm$ 1.4) gradually increased ($p < 0.001$). In multinomial logistic regression, *ORs* (95% *CIs*) for the highest vs. lowest quartile of the non-HDL-C/HDL-C ratio were 1.70 (1.48–1.95) between stable carotid plaques and no carotid plaque, 2.34 (2.06–2.67) between unstable carotid plaques and no carotid plaque, and 1.38 (1.18–1.61) between unstable carotid plaques and stable carotid plaque, after adjusting for common cardiovascular risk factors. The results of subgroup analysis and sensitivity analysis were similar.

Conclusion: Our findings suggested that the non-HDL-C/HDL-C ratio was significantly associated with carotid plaque stability and might be a useful indicator for the early identification of high-risk carotid plaque.

KEYWORDS

lipid ratio, non-HDL-C/HDL-C, carotid plaque, stability, cross-sectional study

Introduction

Stroke is a leading cause of death and disability worldwide (1). Carotid plaque stability plays a fundamental role in the development of ischemic stroke (2, 3). Rupture of unstable carotid plaque can lead to thrombosis, resulting in cerebrovascular occlusion and infarction. Approximately, 18–25% of ischemic stroke thromboembolisms originate from ruptured carotid plaques (4), and carotid plaque is also an important cause of cryptogenic stroke (5). However, carotid ultrasound screening in the general population is not recommended in the current guideline (6). Therefore, early identification of carotid plaque stability could help discover people at high risk of stroke, who might benefit from early pharmacological or surgical intervention.

It is well-known that high-density lipoprotein cholesterol (HDL-C) and non-HDL cholesterol (non-HDL-C) are associated with atherosclerosis (7–9). Non-HDL-C is considered to be a key factor underlying the process contributing to cardiovascular disease and atherosclerosis (10). The National Lipid Association has identified non-HDL-C as a primary therapeutic target (11), HDL-C, which is composed of the smallest and densest lipoprotein particles, inhibits atherosclerosis (12). HDL-C is negatively associated with cardiovascular (CV) events with each 1 mg/dl increase reducing CV events by 2–3% (7, 13, 14), and it exerts cardiovascular protective effects mainly through reverse cholesterol transfer, anti-inflammatory, antioxidant, anti-apoptotic, and vasodilatory effects (14). A novel lipid ratio, the non-HDL-C/HDL-C ratio, contains both atherogenic and anti-atherogenic particles information, and has been shown to be associated with a variety of dyslipidemia-related diseases such as diabetes mellitus (15–17), liver disease (18, 19), metabolic syndrome (20), and previous studies also demonstrated that the non-HDL-C/HDL-C ratio was associated with carotid atherosclerosis (21–23). In addition, the Atherosclerosis Risk in Communities (ARIC) study even found an independent association between non-HDL-C/HDL-C ratio and carotid plaque lipid core (24). The thicker the lipid core, the more likely it is to cause expansion of the necrotic core of the plaque, resulting in plaque rupture (25). Moreover, recently studies showed that the non-HDL-C/HDL-C ratio might be a better predictor of cardiovascular events than traditional lipid indices (26, 27). However, to date, there is no data on evaluating the association between non-HDL-C/HDL-C ratio and carotid plaque stability.

Therefore, we performed this study to clarify whether non-HDL-C/HDL-C ratio is significantly associated with carotid plaque stability.

Methods

Participants

The study population consisted of 28,537 Chinese adults who participated in a health examination in stroke screening sites of the First Affiliated Hospital of Zhengzhou University from January 2016 to December 2017. The exclusion criteria of this study were: subjects with any history of malignancy, infectious diseases, acute inflammation, liver disease, or renal disease. We also excluded subjects with missing data on TC or fasting blood glucose (FBG). After applying our exclusion criteria, a total of 27,436 participants were enrolled in this study.

Data collection

We collected individual sociodemographic information (e.g., sex, age, and education), history of chronic diseases (e.g., diabetes, dyslipidemia, hypertension, coronary heart disease, and stroke), and lifestyle factors (e.g., smoking, drinking, vegetable and fruit consumption, physical activity, etc.) *via* a standard questionnaire by trained interviewers. Definition of history of stroke and coronary artery disease: previously diagnosed by a medical specialist or provided imaging data to support the diagnosis. Smoking, defined as smoking 1 cigarette per day for more than 1 year. Drinking, defined as alcoholic drink of at least $\geq$45 g each time per day during the last year. Vegetable consumption and Fruit consumption were divided into two groups ($\geq$5 days/week and $<$5 days/week) using a standard consumption of 200 g per day. Physical activity, defined as regular exercise for at least 30 min per time in no less than 3 times per week. We measured weight, height, and resting blood pressure such as systolic blood pressure (SBP) and diastolic blood pressure (DBP). Obesity was defined as BMI $\geq$ 28 kg/m^2.

In addition, overnight fasting blood samples were obtained from all subjects. Fasting blood glucose was measured using the

glucose oxidase method. Lipid levels including total cholesterol (TC), triglyceride (TG), HDL-C, and low-density lipoprotein cholesterol (LDL-C) were measured using Olympus Au5400 automated biochemistry analyzer (First Chemical Co, Ltd, Japan). Hypertension was defined as SBP and/or DBP $\geq$ 140/90 mmHg, or the usage of antihypertensive medications. Dyslipidemia was defined as TG $\geq$ 2.26 mmol/L, TC $\geq$ 6.22 mmol/L, HDL-C $<$ 1.04 mmol/L, LDL-C $\geq$ 4.14 mmol/L, self-reported history, or taking lipid-lowering drugs. Diabetes mellitus (DM) was defined as self-reported history, FPG $\geq$ 7.0 mmol/L, or taking antidiabetic agents.

Assessment of carotid plaque stability

Ultrasound technologists evaluated carotid plaques by qualified sonographers using the iU22 (Philips Healthcare), HA500 (Hitachi Healthcare), and DC-8 (Mindray), ultrasound system with 5–10 MHz transmission frequency. Two qualified sonographers measured each participant separately; discrepancies in measurement data were resolved by consensus. We examined plaques of bilateral common carotid artery, internal carotid artery, external carotid artery, and bulb. Carotid plaque was defined as a focal structure encroaching into the arterial lumen by at least 0.5 mm or 50% of the surrounding CIMT value, or CIMT $>$ 1.5 mm (28, 29). Stable carotid plaques had a high level of homogeneous echogenicity and homogeneous texture with a regular smooth morphology. Unstable carotid plaques had an incomplete fibrous cap or ulceration with low level or heterogeneous echogenicity (30).

Statistical analysis

The population was divided into four groups based on the quartiles of the non-HDL-C/HDL-C ratio. Categorical variables were presented as frequency (%), which was compared using chi-square analysis. Continuous variables were described as the median with an interquartile range owing to the skewed distribution, which were compared by variance (ANOVA) or Mann–Whitney *U*-tests for continuous variables.

When participants were divided into 3 groups according to carotid plaque stability (non-carotid plaque, stable carotid plaque, and unstable carotid plaque), multinomial logistic regression models were used to explore the relationship between the non-HDL-C/HDL-C ratio and carotid plaque stability. To adjust for potential confounders, two models were developed: Model 1, adjusted for age, sex, education, smoking status, drinking status, vegetable consumption, fruit consumption, physical activity, BMI $\geq$ 28 kg/m^2 (yes or no), stroke, coronary heart disease, hypertension, antihypertensive agents, diabetes mellitus, antidiabetic agents, lipid-lowering agents; Model 2, further adjusted for TG and FBG. The results were presented as odds ratios (*ORs*) and 95% confidence intervals (*CIs*). To verify the robustness of the relationship between non-HDL-C/HDL-C ratio and carotid plaque stability, analyses were carried out for different subgroups. In view of the effect of lipid-lowering agents on non-HDL-C/HDL-C ratio and carotid plaque stability, sensitivity analysis was performed after excluding people taking lipid-lowering agents.

All analyses above were conducted using R software (version 3.6.3). A two-sided $p < 0.05$ was considered statistically significant.

Results

Baseline characteristics

A total of 27,436 participants were recruited, 12,866 (46.9%) of them were male. The median (IQR) age of overall participants was 48 (41–55) years, and the median non-HDL-C/HDL-C ratio was 2.82 (*IQR*: 2.16–3.60). Compared with participants in the lowest quartile of non-HDL-C/HDL-C ratio, those with higher non-HDL-C/HDL-C ratio were more likely to be older and male; to be smoking, drinking, vegetable, and fruit consumption, active physical activity, obesity; to have a higher prevalence of hypertension, diabetes, and dyslipidemia; to have higher use of antidiabetic, antihypertensive, and lipid-lowering agents use, to have a higher level of SBP, DBP, FBG, TC, TG, LDL-C, and non-HDL level, while more likely to have a lower level of HDL-C. The characteristics of participants according to quartiles of the non-HDL-C/HDL-C ratio are presented in Table 1.

Non-HDL-C/HDL-C ratio and carotid plaque stability

Carotid plaque was detected in 7,161 (26.1%) respondents, with stable and unstable plaque accounting for 3,277 (11.9%) and 3,884 (14.2%), respectively. As non-HDL-C/HDL-C ratio levels increased from the lowest quartile to the highest quartile, the prevalence was increased from 8.2 to 16% for stable carotid plaque (p for trend $<$ 0.001) and from 7.7 to 20.8% for unstable carotid plaque (p for trend $<$ 0.001). The mean non-HDL-C/HDL-C ratios of non-carotid plaque (mean $\pm$ *SD*, 2.9 $\pm$ 1.1), stable carotid plaque (mean $\pm$ *SD*, 3.2 $\pm$ 1.2), and unstable carotid plaque (mean $\pm$ *SD*, 3.4 $\pm$ 1.4) increased gradually and this trend was statistically significant ($p < 0.001$; Figure 1).

In multinomial logistic regression model 1 compared stable carotid plaques with no carotid plaque, the *ORs* (95% *CIs*) for the highest quartile of the non-HDL-C/HDL-C ratios were 1.71 (1.51–1.94). For every 1 unit increase in the non-HDL-C/HDL-C ratio, the prevalence of stable carotid plaque increased by 1.17 times. Compared unstable carotid plaques with no carotid plaque, the *ORs* (95% *CIs*) for the highest quartile of

TABLE 1 Baseline characteristics of the study participants.

Characteristics	Overall	Quartiles of the Non-HDL-C/HDL-C ratio				*P*-value†
		Q1 (<2.16)	Q2 (2.16–2.82)	Q3 (2.82–3.60)	Q4 (>3.60)	
No. of patients	27,436	6,858	6,857	6,863	6,858	
Age, years	48.0 (41.0–55.0)	44.0 (39.0–52.0)	48.0 (41.0–55.0)	49.0 (43.0–56.0)	50.0 (44.0–57.0)	<0.001
Male, sex	12,866 (46.9)	1,812 (26.4)	2,785 (40.6)	3,641 (53.1)	4,628 (67.5)	<0.001
High school or above, *n* (%)	17,032 (62.1)	4,819 (70.3)	4,367(63.7)	4,046 (59.0)	3,800 (55.4)	<0.001
Smoking, *n* (%)	6,548 (23.9)	803 (11.7)	1,335 (19.5)	1,785 (26.0)	2,625 (38.3)	<0.001
Drinking, *n* (%)	5,401 (19.7)	690 (10.1)	1,165 (17.0)	1,547 (22.5)	1,999 (29.1)	<0.001
Vegetable (<5d/w), *n* (%)	12,940 (47.2)	2,692 (43.3)	2,878 (46.3)	2,982 (47.9)	3,060 (49.2)	<0.001
Fruit (<5d/w), *n* (%)	22,734 (82.9)	5,555 (81.0)	5,586 (81.5)	5,747 (83.7)	5,844 (85.2)	<0.001
Active physical activity, n (%)	19,798 (72.2)	4,805 (70.1)	5,046 (73.6)	5,005 (72.9)	4,942 (72.1)	<0.001
BMI ≥ 28 (kg/m^2)	4,595 (16.7)	457 (6.7)	869 (12.7)	1,301 (19.0)	1,968 (28.7)	<0.001
Hypertension, *n* (%)	11,236 (41.0)	1,992 (29.0)	2,510 (36.6)	3,090 (45.0)	3,644 (53.1)	<0.001
Diabetes, *n* (%)	2,914 (10.6)	389 (5.7)	553 (8.1)	746 (10.9)	1,226 (17.9)	<0.001
Dyslipidemia, *n* (%)	10,403 (37.9)	370 (5.4)	1,226 (17.9)	2,997 (43.7)	5,810 (84.7)	<0.001
Antihypertensive agents, *n* (%)	3,580 (13.0)	615 (9.0)	790 (11.5)	973 (14.2)	1,202 (17.5)	<0.001
Antidiabetic agents, *n* (%)	1,305 (4.8)	191 (2.8)	273 (4.0)	348 (5.1)	493 (7.2)	<0.001
Lipid-lowering agents, *n* (%)	731 (2.7)	110 (1.6)	162 (2.4)	165 (2.4)	294 (4.3)	<0.001
Stroke, *n* (%)	487 (1.8)	129 (1.9)	108 (1.6)	123 (1.8)	127 (1.9)	0.520
Coronary heart disease, *n* (%)	617 (2.2)	151 (2.2)	146 (2.1)	144 (2.1)	176 (2.6)	0.224
Carotid plaque						<0.001
No carotid plaque, *n* (%)	20,275 (73.9)	5,768 (84.1)	5,238 (76.4)	4,936 (71.9)	4,333 (63.2)	
Stable carotid plaque, *n* (%)	3,277 (11.9)	564 (8.2)	748 (10.9)	869 (12.7)	1,096 (16.0)	
Unstable carotid plaque, *n* (%)	3,884 (14.2)	526 (7.7)	871 (12.7)	1,058 (15.4)	1,429 (20.8)	
DBP, mm Hg	81.0 (73.0–90.0)	77.0 (70.0–85.0)	80.0 (72.0–89.0)	83.0 (75.0–91.0)	85.0 (77.0–94.0)	<0.001
Fasting blood glucose, mmol/L	5.20 (4.80–5.70)	5.00 (4.70–5.40)	5.10 (4.75–5.60)	5.20 (4.80–5.70)	5.40 (4.90–6.10)	<0.001
Total cholesterol, mmol/L	4.62 (4.07–5.24)	4.06 (3.62–4.52)	4.46 (4.00–4.96)	4.76 (4.29–5.29)	5.27 (4.74–5.88)	<0.001
Triglyceride, mmol/L	1.26 (0.89–1.86)	0.82 (0.66–1.04)	1.10 (0.87–1.43)	1.43 (1.11–1.90)	2.11 (1.58–2.96)	<0.001
HDL cholesterol, mmol/L	1.20 (1.03–1.41)	1.48 (1.31–1.67)	1.28 (1.14–1.43)	1.14 (1.02–1.27)	0.98 (0.88–1.10)	<0.001
LDL cholesterol, mmol/L	2.70 (2.21–3.23)	2.16 (1.84–2.51)	2.66 (2.28–3.03)	2.94 (2.51–3.38)	3.21 (2.66–3.76)	<0.001
Non-HDL cholesterol, (mmol/l)	3.38 (2.82–4.00)	2.57 (2.24–2.91)	3.18 (2.84–3.56)	3.61 (3.25–4.04)	4.28 (3.82–4.80)	<0.001

BMI, body mass index; Continuous variables are expressed as median (interquartile range). Categorical variables are expressed as frequencies (percentage); † *P*-values were derived from Mann–Whitney *U*-tests for continuous variables, and Chi-square tests for categorical variables.

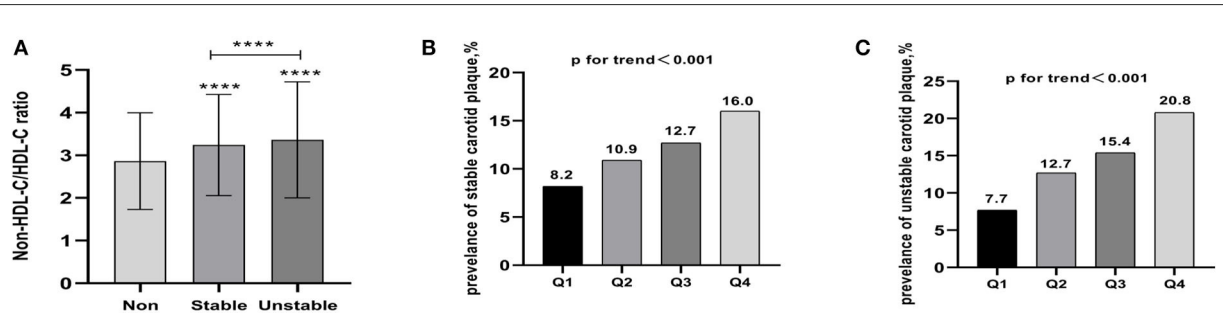

FIGURE 1
(A) The mean non-HDL-C /HDL-C ratios of non-carotid plaque, stable carotid plaque, and unstable carotid plaque (mean ± *SD*) increased gradually and this trend was statistically significant. **(B)** Prevalence of stable carotid plaque stratified by quartile the non-HDL-C/HDL-C ratio. **(C)** Prevalence of unstable carotid plaque stratified by quartile the non-HDL-C/HDL-C ratio. **** $p < 0.001$.

TABLE 2 Multinomial logistic odds ratios (*ORs*) (95% *CI*) of the association of the non-HDL-C/HDL-C ratio with carotid stability.

Outcomes	Quartiles of the Non-HDL-C/HDL-C ratio				*P*-trend	Per 1
	Q1 (<2.16)	Q2 (2.16–2.82)	Q3 (2.82–3.60)	Q4 (>3.60)		unit increase
Stable vs. non-carotid plaque						
Crude model	Reference	1.45 (1.28–1.65)	1.73 (1.52-1.95)	2.37 (2.10-2.67)	<0.001	1.28 (1.24-1.33)
Model 1	Reference	1.24 (1.09–1.42)	1.29 (1.13-1.47)	1.71 (1.51-1.94)	<0.001	1.17 (1.13-1.21)
Model 2	Reference	1.24 (1.09–1.41)	1.29 (1.13-1.47)	1.70 (1.48-1.95)	<0.001	1.21 (1.15-1.27)
Unstable vs. non-carotid plaque						
Crude model	Reference	1.86 (1.64–2.12)	2.32 (2.04–2.63)	3.43 (3.04–3.88)	<0.001	1.36 (1.32–1.41)
Model 1	Reference	1.51 (1.33–1.71)	1.62 (1.44–1.83)	2.21 (1.96–2.49)	<0.001	1.21 (1.18–1.25)
Model 2	Reference	1.52 (1.35–1.73)	1.66 (1.47–1.88)	2.34 (2.06–2.67)	<0.001	1.35 (1.30–1.41)
Unstable vs. stable carotid plaque						
Crude model	Reference	1.29 (1.08–1.53)	1.34 (1.14–1.59)	1.45 (1.24–1.70)	<0.001	1.06 (1.03–1.10)
Model 1	Reference	1.22 (1.04–1.42)	1.26 (1.08–1.46)	1.29 (1.12–1.50)	0.002	1.04 (1.00–1.08)
Model 2	Reference	1.23 (1.05–1.44)	1.29 (1.11–1.51)	1.38(1.18–1.61)	<0.001	1.12 (1.07–1.18)

Model 1: adjusted for age, sex, education, smoking status, drinking status, vegetable consumption, fruit consumption, physical activity, BMI $\geq$ 28 kg/m^2 (yes or no), stroke, coronary heart disease, hypertension, antihypertensive agents, diabetes mellitus, antidiabetic agents, lipid-lowering agents.
Model 2: further adjusted for Triglyceride, Fasting blood glucose.

the non-HDL-C/HDL-C ratios were 2.21 (1.96–2.49). Moreover, for every 1 unit increase in the non-HDL-C/HDL-C ratio, the prevalence of unstable carotid plaque increased by 1.21 times. Compared to unstable carotid plaques with stable carotid plaque, the *ORs* (95% *CIs*) for the highest quartile of the non-HDL-C/HDL-C ratios were 1.29 (1.12–1.50). Moreover, for every 1 unit increase in the non-HDL-C/HDL-C ratio, the prevalence of unstable carotid plaque increased by 1.04 times.

Further adjustment for TG and FBG in model 2 did not change the association between the non-HDL-C/HDL-C ratio and carotid plaque stability. The corresponding *ORs* (95% *CIs*) for the highest vs. lowest quartile of the non-HDL-C/HDL-C ratio were 1.70 (1.48–1.95) between stable carotid plaques and no carotid plaque, 2.34 (2.06–2.67) between unstable carotid plaques and no carotid plaque, and 1.38 (1.18–1.61) between unstable carotid plaques and stable carotid plaque (Table 2).

Subgroup analysis and sensitivity analysis

When the non-HDL-C/HDL-C ratio was considered as a continuous variable, subgroup analysis was conducted by stratification according to sex, age, BMI, hypertension, and diabetes. After the full adjustment variables, the association between non-HDL-C/HDL-C ratio and carotid plaque stability remained significant in gender, age, hypertension, and diabetes subgroups. While in a subgroup analysis of BMI $\geq$ 28 (kg/m^2), there was no statistical significance between unstable carotid plaques and no carotid plaque (*OR* 1.06, 95% *CI* 0.95–1.17; Figure 2).

This sensitivity analysis was performed to assess the relationship between non-HDL-C/HDL-C ratio and carotid plaque stability in the subsample without taking lipid-lowering agents. After multivariable adjustment for the risk factors, sensitivity analyses showed similar results (Table 3).

Discussion

This is the first population-based study to explore the relationship between non-HDL-C/HDL-C ratio and carotid plaque stability. We found that the prevalence of both stable and unstable carotid plaque increased significantly with increasing non-HDL-C/HDL-C ratios, independent of other relevant factors. Meanwhile, the mean non-HDL-C /HDL-C ratio gradually increased for non-carotid plaques, stable carotid plaques, and unstable carotid plaques; and this trend was statistically significant. Our findings, for the first time, demonstrated that non-HDL-C /HDL-C ratio was associated with carotid plaque stability in the general population.

Early atherosclerosis occurs mainly in the peripheral vasculature, such as the femoral and carotid arteries (31). The burden of carotid atherosclerosis has been increasing. A systematic review revealed the global burden of carotid atherosclerotic disease, with 21.1% of people aged 30–79 years suffering from carotid plaque in 2020, equivalent to 815.76 million people (32), and it was known that unstable plaque was an important factor in the development of cardiovascular disease (33). Moreover, many studies had shown that early preventive treatment and risk factor intervention were beneficial (34–36). However, carotid ultrasound screening in the general population is not recommended in the current guideline (6). Therefore,

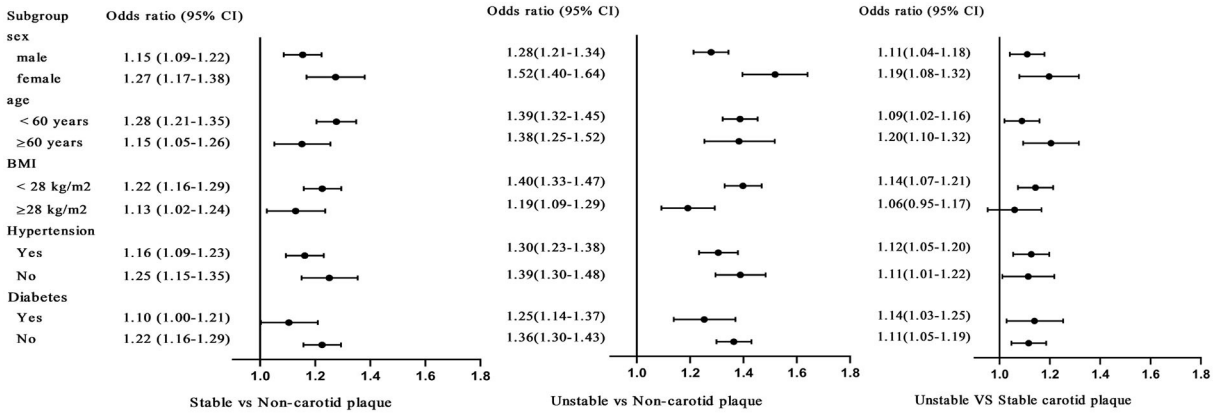

FIGURE 2
Subgroup analysis was conducted by stratification according to sex, age, BMI, hypertension, and diabetes, when the non-HDL-C/HDL-C ratio was considered as a continuous variable. After the fully adjustment, the same variables as Model 3 in Table 2, the odds ratios (*ORs*; 95% *CIs*) of the non-HDL-C/HDL-C ratio and carotid stability.

TABLE 3 Sensitivity analysis[†].

Outcomes	Quartiles of the Non-HDL-C/HDL-C ratio index				*P*-trend	Per 1
	Q1 (<2.16)	Q2 (2.16–2.82)	Q3 (2.82–3.60)	Q4 (>3.60)		Unit increase
Stable vs. no carotid plaque						
Crude model	Reference	1.45 (1.28–1.63)	1.81 (1.61–2.03)	2.64 (2.36–2.96)	<0.001	1.28 (1.24–1.33)
Model 1	Reference	1.23 (1.08–1.41)	1.28 (1.12–1.46)	1.73 (1.52–1.97)	<0.001	1.17 (1.13–1.21)
Model 2	Reference	1.23 (1.07–1.41)	1.27 (1.11–1.45)	1.70 (1.48–1.96)	<0.001	1.21 (1.15–1.27)
Unstable vs. no carotid plaque						
Crude model	Reference	1.82 (1.62–2.04)	2.40 (2.15–2.69)	3.61 (3.24–4.03)	<0.001	1.36 (1.32–1.41)
Model 1	Reference	1.50 (1.32–1.71)	1.64 (1.45–1.86)	2.18 (1.93–2.46)	<0.001	1.21 (1.18–1.25)
Model 2	Reference	1.51 (1.33–1.72)	1.67 (1.48–1.89)	2.28 (2.00–2.60)	<0.001	1.35 (1.30–1.41)
Unstable vs. stable carotid plaque						
Crude model	Reference	1.25 (1.07–1.47)	1.33 (1.14–1.55)	1.37 (1.18–1.58)	<0.001	1.06 (1.03–1.10)
Model 1	Reference	1.22 (1.04–1.43)	1.29 (1.10–1.50)	1.26 (1.08–1.47)	0.002	1.04 (1.00–1.08)
Model 2	Reference	1.23 (1.05–1.45)	1.32 (1.13–1.54)	1.34 (1.14–1.58)	<0.001	1.12 (1.07–1.18)

Multinomial logistic *ORs* (95% *CI*) of the association of the non-HDL-C/HDL-C ratio with carotid plaque and its stability.
Model 1: adjusted for age, sex, education, smoking status, drinking status, vegetable consumption, fruit consumption, physical activity, BMI ≥28 kg/m^2 (yes or no), stroke, coronary heart disease, hypertension, antihypertensive agents, diabetes mellitus, antidiabetic agents, lipid-lowering agents.
Model 2: further adjusted for Triglyceride, Fasting blood glucose.
[†] Sensitivity analysis was performed in participants without taking lipid-lowering agents.

simple and accessible biomarkers for early determination of carotid plaque stability can help improve the understanding of the pathophysiology of cardiovascular disease and identify high-risk patients who may benefit from early intervention.

Our study found a gradual increase in the prevalence of carotid plaque as the non-HDL-C/HDL-C ratio gradually increased. As with our findings, the previous studies had shown that the non-HDL-C/HDL-C ratio was associated with carotid atherosclerosis (21–23). Qin et al. (21) found that carotid intima-media thickness gradually increased in the quartile of non-HDL-CHDL-C ratio in Chinese individuals of metabolic syndrome (p trend < 0.05). A multicenter study (22) found that postmenopausal women with higher non-HDL-C/HDL-C ratios had a greater chance of developing carotid atherosclerotic plaque (*OR*: 1.30, 95% *CI*: 1.07–1.58, $p = 0.009$) when adjusted for other cardiovascular risk factors. Recently, studies found that the non-HDL-C/HDL-C ratio might be a more accurate predictor of cardiovascular disease (26, 27). In addition, an asymptomatic polyvascular abnormalities in Community study (37) found that the odds of unstable carotid plaques at non-HDL-C levels in the middle and highest trilaterals were 1.02 (95% *CI*, 0.84–1.23) and 1.50 (95% *CI*, 1.23–1.82), respectively,

after adjusting for confounders. Moreover, ARIC (24) study even found an independent association between non-HDL-C/HDL-C ratio and carotid plaque lipid core. It is well-known that plaque rich in lipid core is unstable and easy to rupture (25). All the above studies indirectly supported our findings that the non-HDL-C/HDL-C ratio might be associated with carotid plaque stability.

As a clinically easily accessible biomarker, the non-HDL-C/HDL-C ratio collects information on all atherogenic and antiatherogenic lipid particles. Non-high-density lipoprotein cholesterol (non-HDL-C) level is calculated by subtracting high-density lipoprotein cholesterol (HDL-C) from TC. Non-HDL-C consists of LDL-C, very low-density lipoprotein (VLDL-C), intermediate-density lipoprotein (IDL-C), chylomicrons, and their TG-rich lipoprotein remnants, and the protein mainly contains apolipoprotein B, which is a strong indicator of atherogenicity (13, 38). Non-HDL-C is considered to be a key factor underlying the process contributing to most cardiovascular diseases (10). The National Lipid Association has identified non-HDL-C as a primary therapeutic target (11), and the ESC/EAS guidelines for the management of dyslipidemia also recommended the inclusion of non-HDL in the assessment of cardiovascular disease risk (39). HDL-C is composed of the smallest and densest lipoprotein particles and mainly contains apolipoprotein A-I (APOA-I), which inhibits the production and mobilization of inflammatory cells and promotes the reversal of cholesterol transport (RCT) to inhibit atherosclerosis (12). HDL-C is thought to be negatively associated with cardiovascular disease events (7). The non-HDL-C/HDL-C ratio can reflect the balance between atherogenic and anti-atherogenic lipid particles, which may be the underlying mechanism for its relationship with plaque stability.

There are several limitations in our study. First, this is a cross-sectional study and no conclusions can be drawn on the causal relationship between non-HDL-C/HDL-C ratio and carotid plaque stability. Second, carotid plaque stability is assessed using ultrasound, which is not as accurate as MRI or angiography and cannot be verified with pathological specimens. However, we corrected for bias with a two-person blinded assessment. Third, our study did not collect information on HDL functionality, which is a better predictor of CV risk than HDL-C levels (40, 41), and it may be useful for high-risk carotid plaque identification. Finally, we did not collect follow-up information, which limited our ability to prospectively study, the impact of baseline non-HDL-C/HDL-C ratio on the evolution of plaque stability and cardiovascular events. Therefore, future prospective cohort studies are clearly needed.

Conclusions

In conclusion, this study found that the non-HDL-C/HDL-C ratio was associated with carotid plaque stability in the general population. The non-HDL-C/HDL-C ratio was highest in those with unstable carotid plaque, followed by those with stable carotid plaque and lowest in those with no carotid plaque. Our findings suggest that an elevated non-HDL-C/HDL-C ratio is independently associated with carotid plaque and its stability.

Data availability statement

The original contributions presented in the study are included in the article/supplementary material, further inquiries can be directed to the corresponding author/s.

Ethics statement

The studies involving human participants were reviewed and approved by the Ethics Committee of the First Affiliated Hospital of Zhengzhou University. Written informed consent to participate in this study was provided by the patient/participants legal guardian/next of kin.

Author contributions

YMX and LW designed the research. YPL, LZ, YG, KL, SL, CZ, and YRX helped with the acquisition and analysis of the data. AW wrote the article. BS, YG, CT, and YSL contributed to the critical revision of the manuscript. All authors read and approved the final manuscript.

Funding

This work was supported by grant from the Ministry of Science and Technology of the People's Republic of China (2018YFC1311303), the Non-profit Central Research Institute Fund of Chinese Academy of Medical Sciences (2020-PT310-01), the 2021 Youth Talent Promotion Project in Henan Province to KL (Grant No. 2021HYTP054), and 2021 Joint Construction Project of Henan Medical Science and Technology Breakthrough Plan to KL (Grant No. LHGJ20210336).

Acknowledgments

We thank the study participants and the clinical staff for their support and contribution to this study.

Conflict of interest

The authors declare that the research was conducted in the absence of any commercial or financial relationships that could be construed as a potential conflict of interest.

Publisher's note

All claims expressed in this article are solely those of the authors and do not necessarily represent those of their affiliated organizations, or those of the publisher, the editors and the reviewers. Any product that may be evaluated in this article, or claim that may be made by its manufacturer, is not guaranteed or endorsed by the publisher.

References

1. GBD 2019 Stroke Collaborators. Global, regional, and national burden of stroke and its risk factors, 1990-2019: a systematic analysis for the Global Burden of Disease Study 2019. *Lancet Neurol.* (2021) 20:795–820. doi: 10.1016/S1474-4422(21)00252-0

2. Baber U, Mehran R, Sartori S, Schoos MM, Sillesen H, Muntendam P, et al. Prevalence, impact, and predictive value of detecting subclinical coronary and carotid atherosclerosis in asymptomatic adults: the bioimage study. *J Am Coll Cardiol.* (2015) 65:1065–74. doi: 10.1016/j.jacc.2015.01.017

3. Kamtchum-Tatuene J, Noubiap JJ, Wilman AH, Saqqur M, Shuaib A, Jickling GC. Prevalence of high-risk plaques and risk of stroke in patients with asymptomatic carotid stenosis: a meta-analysis. *JAMA Neurol.* (2020) 77:1524–35. doi: 10.1001/jamaneurol.2020.2658

4. Saba L, Saam T, Jäger HR, Yuan C, Hatsukami TS, Saloner D, et al. Imaging biomarkers of vulnerable carotid plaques for stroke risk prediction and their potential clinical implications. *Lancet Neurol.* (2019) 18:559–72. doi: 10.1016/S1474-4422(19)30035-3

5. Kopczak A, Schindler A, Bayer-Karpinska A, Koch ML, Sepp D, Zeller J, et al. Complicated carotid artery plaques as a cause of cryptogenic stroke. *J Am Coll Cardiol.* (2020) 76:2212–22. doi: 10.1016/j.jacc.2020.09.532

6. Krist AH, Davidson KW, Mangione CM, Barry MJ, Cabana M, Caughey AB, et al. Screening for asymptomatic carotid artery stenosis: us preventive services task force recommendation statement. *JAMA.* (2021) 325:476–81. doi: 10.1001/jama.2020.26988

7. Sun L, Clarke R, Bennett D, Guo Y, Walters RG, Hill M, et al. Causal associations of blood lipids with risk of ischemic stroke and intracerebral hemorrhage in chinese adults. *Nat Med.* (2019) 25:569–74. doi: 10.1038/s41591-019-0366-x

8. Holmes MV, Millwood IY, Kartsonaki C, Hill MR, Bennett DA, Boxall R, et al. Lipids, lipoproteins, and metabolites and risk of myocardial infarction and stroke. *J Am Coll Cardiol.* (2018) 71:620–32. doi: 10.1016/j.jacc.2017.12.006

9. Di Angelantonio E, Sarwar N, Perry P, Kaptoge S, Ray KK, Thompson A, et al. Major lipids, apolipoproteins, and risk of vascular disease. *JAMA.* (2009) 302:1993–2000. doi: 10.1001/jama.2009.1619

10. Carr SS, Hooper AJ, Sullivan DR, Burnett JR. Non-HDL-cholesterol and apolipoprotein B compared with LDL-cholesterol in atherosclerotic cardiovascular disease risk assessment. *Pathology.* (2019) 51:148–54. doi: 10.1016/j.pathol.2018.11.006

11. Jacobson TA, Ito MK, Maki KC, Orringer CE, Bays HE, Jones PH, et al. National lipid association recommendations for patient-centered management of dyslipidemia: part 1–full report. *J Clin Lipidol.* (2015) 9:129–69. doi: 10.1016/j.jacl.2015.02.003

12. Di Bartolo BA, Cartland SP, Genner S, Manuneedhi Cholan P, Vellozzi M, Rye KA, et al. HDL improves cholesterol and glucose homeostasis and reduces atherosclerosis in diabetes-associated atherosclerosis. *J Diabetes Res.* (2021) 2021:6668506. doi: 10.1155/2021/6668506

13. Grundy SM, Stone NJ, Bailey AL, Beam C, Birtcher KK, Blumenthal RS, et al. 2018 AHA/ACC/AACVPR/AAPA/ABC/ACPM/ADA/AGS/APHA/ASPC/NLA/PCNA guideline on the management of blood cholesterol: a report of the American College of Cardiology/American Heart Association Task Force on Clinical Practice Guidelines. *Circulation.* (2019) 139:e1082–143. doi: 10.1161/CIR.0000000000000698

14. Badimón JJ, Santos-Gallego CG, Badimón L. [Importance of HDL cholesterol in atherothrombosis: how did we get here? Where are we going?]. *Revista espanola de cardiologia.* (2010) 63(Suppl 2):20–35. doi: 10.1016/S0300-8932(10)70150-0

15. Zhang N, Hu X, Zhang Q, Bai P, Cai M, Zeng TS, et al. Non-high-density lipoprotein cholesterol: high-density lipoprotein cholesterol ratio is an independent risk factor for diabetes mellitus: results from a population-based cohort study. *J Diabetes.* (2018) 10:708–14. doi: 10.1111/1753-0407.12650

16. Lin D, Qi Y, Huang C, Wu M, Wang C, Li F, et al. Associations of lipid parameters with insulin resistance and diabetes: a population-based study. *Clin Nutr.* (2018) 37:1423–9. doi: 10.1016/j.clnu.2017.06.018

17. Du T, Yuan G, Zhang M, Zhou X, Sun X, Yu X. Clinical usefulness of lipid ratios, visceral adiposity indicators, and the triglycerides and glucose index as risk markers of insulin resistance. *Cardiovasc Diabetol.* (2014) 13:146. doi: 10.1186/s12933-014-0146-3

18. Yang S, Zhong J, Ye M, Miao L, Lu G, Xu C, et al. Association between the non-HDL-cholesterol to HDL-cholesterol ratio and non-alcoholic fatty liver disease in chinese children and adolescents: a large single-center cross-sectional study. *Lipids Health Dis.* (2020) 19:242. doi: 10.1186/s12944-020-01421-5

19. Wang K, Shan S, Zheng H, Zhao X, Chen C, Liu C. Non-HDL-cholesterol to HDL-cholesterol ratio is a better predictor of new-onset non-alcoholic fatty liver disease than non-HDL-cholesterol: a cohort study. *Lipids Health Dis.* (2018) 17:196. doi: 10.1186/s12944-018-0848-8

20. Kim SW, Jee JH, Kim HJ, Jin SM, Suh S, Bae JC, et al. Non-HDL-cholesterol/HDL-cholesterol is a better predictor of metabolic syndrome and insulin resistance than apolipoprotein B/apolipoprotein A1. *Int J Cardiol.* (2013) 168:2678–83. doi: 10.1016/j.ijcard.2013.03.027

21. Qin G, Tu J, Zhang C, Tang X, Luo L, Wu J, et al. The value of the apoB/apoA? ratio and the non-HDL-C/HDL-C ratio in predicting carotid atherosclerosis among chinese individuals with metabolic syndrome: a cross-sectional study. *Lipids Health Dis.* (2015) 14:24. doi: 10.1186/s12944-015-0023-4

22. Masson W, Epstein T, Huerín M, Lobo M, Molinero G, Siniawski D. Association between non-HDL-C/HDL-C ratio and carotid atherosclerosis in postmenopausal middle-aged women. *Climacteric.* (2019) 22:518–22. doi: 10.1080/13697137.2019.1631787

23. Liu Y, Zhang Z, Xia B, Wang L, Zhang H, Zhu Y, et al. Relationship between the non-HDLC-to-HDLC ratio and carotid plaques in a high stroke risk population: a cross-sectional study in China. *Lipids Health Dis.* (2020) 19:168. doi: 10.1186/s12944-020-01344-1

24. Virani SS, Catellier DJ, Pompeii LA, Nambi V, Hoogeveen RC, Wasserman BA, et al. Relation of cholesterol and lipoprotein parameters with carotid artery plaque characteristics: the atherosclerosis risk in communities (ARIC) carotid MRI Study. *Atherosclerosis.* (2011) 219:596–602. doi: 10.1016/j.atherosclerosis.2011.08.001

25. Nidorf SM, Fiolet A, Abela GS. Viewing atherosclerosis through a crystal lens: how the evolving structure of cholesterol crystals in atherosclerotic plaque alters its stability. *J Clin Lipidol.* (2020) 14:619–30. doi: 10.1016/j.jacl.2020.07.003

26. Zhu L, Lu Z, Zhu L, Ouyang X, Yang Y, He W, et al. Lipoprotein ratios are better than conventional lipid parameters in predicting coronary heart disease in Chinese Han people. *Kardiologia Polska.* (2015) 73:931–8. doi: 10.5603/KP.a2015.0086

27. Kouvari M, Panagiotakos DB, Chrysohoou C, Georgousopoulou EN, Tousoulis D, Pitsavos AC. Sex-related differences of the effect of lipoproteins and apolipoproteins on 10-year cardiovascular disease risk; insights from the Attica Study (2002-2012). *Molecules.* (2020) 25:1506. doi: 10.3390/molecules25071506

28. Touboul PJ, Hennerici MG, Meairs S, Adams H, Amarenco P, Bornstein N, et al. Mannheim carotid intima-media thickness and plaque consensus (2004-2006-2011). In: *An Update on Behalf of the Advisory Board of the 3rd, 4th and 5th Watching the Risk Symposia, at the 13th, 15th and 20th European Stroke Conferences.* Mannheim; Brussels; Hamburg (2012). p. 290–6. doi: 10.1159/000343145

29. Touboul PJ, Hennerici MG, Meairs S, Adams H, Amarenco P, Desvarieux M, et al. Mannheim intima-media thickness consensus. *Cerebrovasc Dis.* (2004) 18:346–9. doi: 10.1159/000081812

30. Sztajzel R. Ultrasonographic assessment of the morphological characteristics of the carotid plaque. *Swiss Med Weekly.* (2005) 135:635–43.

31. Poredoš P, Cevc M, Blinc A. Characteristics of atherosclerosis in femoropopliteal artery and its clinical relevance. *Atherosclerosis.* (2021) 335:31–40. doi: 10.1016/j.atherosclerosis.2021.09.012

32. Song P, Fang Z, Wang H, Cai Y, Rahimi K, Zhu Y, et al. Global and regional prevalence, burden, and risk factors for carotid atherosclerosis: a systematic review, meta-analysis, and modelling study. *Lancet Global Health.* (2020) 8:e721–9. doi: 10.1016/S2214-109X(20)30117-0

33. Ooi YC, Gonzalez NR. Management of extracranial carotid artery disease. *Cardiol Clin.* (2015) 33:1–35. doi: 10.1016/j.ccl.2014.09.001

34. Naylor AR, Ricco JB, de Borst GJ, Debus S, de Haro J, Halliday A, et al. Editor's choice - management of atherosclerotic carotid and vertebral artery disease: 2017 Clinical Practice Guidelines of the European Society for Vascular Surgery (ESVS). *Eur J Vasc Endovasc Surg.* (2018) 55:3–81. doi: 10.1016/j.ejvs.2017.10.014

35. Saba L, Brinjikji W, Spence JD, Wintermark M, Castillo M, Borst GJD, et al. Roadmap consensus on carotid artery plaque imaging and impact on therapy strategies and guidelines: an international, multispecialty, expert review and position statement. *Am J Neuroradiol.* (2021) 42:1566–75. doi: 10.3174/ajnr.A7223

36. Willeit P, Tschiderer L, Allara E, Reuber K, Seekircher L, Gao L, et al. Carotid intima-media thickness progression as surrogate marker for cardiovascular risk: meta-analysis of 119 clinical trials involving 100 667 patients. *Circulation.* (2020) 142:621–42. doi: 10.1161/CIRCULATIONAHA.120.046361

37. Wu J, Zhang J, Wang A, Chen S, Wu S, Zhao X. Association between non-high-density lipoprotein cholesterol levels and asymptomatic vulnerable carotid atherosclerotic plaques. *Eur J Neurol.* (2019) 26:1433–8. doi: 10.1111/ene.13973

38. Expert Panel on Detection, Evaluation, and Treatment of High Blood Cholesterol in Adults. Executive summary of the third report of the National Cholesterol Education Program (NCEP) expert panel on detection, evaluation, and treatment of high blood cholesterol in adults (adult treatment Panel III). *JAMA.* (2001) 285:2486–97. doi: 10.1001/jama.285.19.2486

39. Mach F, Baigent C, Catapano AL, Koskinas KC, Casula M, Badimon L, et al. 2019 ESC/EAS guidelines for the management of dyslipidaemias: lipid modification to reduce cardiovascular risk. *Atherosclerosis.* (2019) 290:140–205. doi: 10.1093/eurheartj/ehz455

40. Santos-Gallego CG, Rosenson RS. Role of HDL in those with diabetes. *Curr Cardiol Rep.* (2014) 16:512. doi: 10.1007/s11886-014-0512-5

41. Santos-Gallego CG, Giannarelli C, Badimón JJ. Experimental models for the investigation of high-density lipoprotein-mediated cholesterol efflux. *Curr Atheroscler Rep.* (2011) 13:266–76. doi: 10.1007/s11883-011-0177-0

frontiers | Frontiers in Neurology

TYPE Original Research
PUBLISHED 21 September 2022
DOI 10.3389/fneur.2022.944413

Check for updates

OPEN ACCESS

EDITED BY
Yuzhen Xu,
Tongji University, China

REVIEWED BY
Pil-Wook Chung,
Kangbuk Samsung Hospital,
South Korea
Liye Dai,
Beijing Youyi Hospital, China

*CORRESPONDENCE
Qiongqiong Bao
921200479@qq.com

†These authors have contributed equally to this work

SPECIALTY SECTION
This article was submitted to Neurological Biomarkers, a section of the journal Frontiers in Neurology

RECEIVED 15 May 2022
ACCEPTED 06 September 2022
PUBLISHED 21 September 2022

CITATION
He J, Zhu J, Zhang W, Zhan Z, Fu F and Bao Q (2022) Association between serum transthyretin and intracranial atherosclerosis in patients with acute ischemic stroke.
Front. Neurol. 13:944413.
doi: 10.3389/fneur.2022.944413

COPYRIGHT
© 2022 He, Zhu, Zhang, Zhan, Fu and Bao. This is an open-access article distributed under the terms of the Creative Commons Attribution License (CC BY). The use, distribution or reproduction in other forums is permitted, provided the original author(s) and the copyright owner(s) are credited and that the original publication in this journal is cited, in accordance with accepted academic practice. No use, distribution or reproduction is permitted which does not comply with these terms.

Association between serum transthyretin and intracranial atherosclerosis in patients with acute ischemic stroke

Jinfeng He[1†], Jiamin Zhu[2†], Wenyuan Zhang[2,3], Zhenxiang Zhan[2], Fangwang Fu[2] and Qiongqiong Bao[3*]

[1]Department of Neurology, Taizhou Municipal Hospital, Taizhou, China, [2]Department of Neurology, The Second Affiliated Hospital and Yuying Children's Hospital of Wenzhou Medical University, Wenzhou, China, [3]Department of Neurology, Affiliated Yueqing Hospital, Wenzhou Medical University, Yueqing, China

Background: Intracranial atherosclerotic stenosis (ICAS) is a primary cause of ischemic stroke. In addition to dyslipidemia, inflammation has been recognized as a potential pathogenesis of atherosclerosis. It remains unknown whether there is a link between transthyretin and ICAS as an inflammatory index.

Methods: Consecutive patients with acute ischemic stroke admitted to the Second Affiliated Hospital of Wenzhou Medical University between January 2019 and June 2020 were retrospectively analyzed. Blood samples were collected from all patients within 24 h of admission to detect their serum transthyretin levels. ICAS was defined as at least one intracranial artery stenosis on vascular examination with a degree of stenosis ≥50%. Multivariable logistic regression analysis was used to identify independent factors associated with ICAS. Restricted cubic spline models were used to depict patterns in the association between serum transthyretin levels and ICAS.

Results: In total, 637 patients with acute ischemic stroke were included in this study, of whom 267 (41.9%) had ICAS. Compared with the patients without ICAS, serum transthyretin levels in patients with ICAS were significantly lower (226.3 ± 56.5 vs. 251.0 ± 54.9 mg/L; $p < 0.001$). After adjusting for potential confounders, patients in the lowest tertile showed a significant increase in ICAS compared to those in the highest tertile (odds ratio, 1.85; 95% confidence interval, 1.12–3.05; $p = 0.016$). This negative linear association is also observed in the restricted cubic spline model. However, this association may only be observed in men. Age, National Institutes of Health Stroke Scale score, hemoglobin A1c level, and low-density lipoprotein cholesterol level were independently associated with ICAS.

Conclusions: Decreased serum transthyretin levels are associated with a more severe ICAS burden in patients with acute ischemic stroke. Our findings suggest that transthyretin may play a role in the pathogenesis of ICAS and provide insight into the control of inflammation for the treatment of ICAS.

KEYWORDS

transthyretin, intracranial atherosclerosis, acute ischemic stroke, inflammation, biomarker

Introduction

Acute ischemic stroke (AIS) is gradually becoming a major disease threatening the global population's health, particularly in China (1). As the dominant cause of stroke, large artery atherosclerosis is closely related to poor prognoses and high recurrence rates in patients with AIS (2–4). Due to differences in antioxidant content and susceptibility to hemodynamic pressure between the intracranial and extracranial arteries, their responses to different risk factors are inconsistent (5). Compared with Western individuals, intracranial atherosclerotic stenosis (ICAS) affects a larger proportion of Chinese patients than extracranial atherosclerotic stenosis (ECAS) (5). Currently, ICAS is the main cause of the high stroke burden in the Chinese population (6). Recent evidence suggests that inflammation plays a significant role in atherosclerotic disease and is expected to become a therapeutic target (7).

Transthyretin is mainly synthesized in the human liver and plays a role in transporting thyroxine and retinol (8). As a serum protein with a short half-life (approximately 2 days), transthyretin is an ideal index for assessing nutritional status (9). In addition, serum transthyretin concentration decreases in the acute phase of inflammation, malignant tumors, and trauma (8) and is thus a potent inflammatory marker. There is evidence that decreased serum transthyretin levels are associated with poor prognoses in stroke patients, even when stroke severity and vascular risk factors are considered (10–12). In patients with acute coronary syndrome, there is an independent negative relationship between transthyretin levels and coronary stenosis (13).

Consequently, it is speculated that transthyretin is associated with ICAS, although the pathogeneses of ICAS and ECAS are not identical. To our knowledge, no studies have investigated the relationship between transthyretin and ICAS. We aimed to determine whether low serum transthyretin levels are associated with ICAS in patients with AIS.

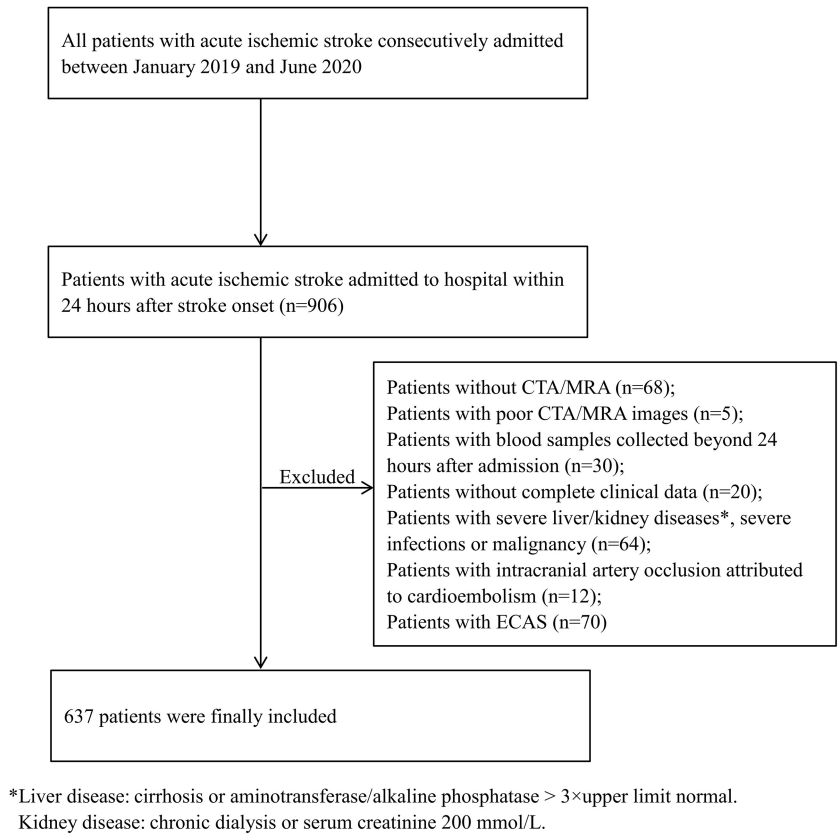

FIGURE 1
Flow chart of patient selection in this study. CTA, computed tomography angiography; ECAS, extracranial atherosclerotic stenosis; MRA, magnetic resonance angiography.

TABLE 1 Clinical characteristics of patients, stratified by the tertiles of transthyretin.

Clinical characteristics	Transthyretin			*P*
	Tertile 1 ($n = 216$)	Tertile 2 ($n = 209$)	Tertile 3 ($n = 212$)	
Transthyretin in mg/L	≤214.0	214.1–265.0	≥265.1	
Age in years, mean ± SD	71.8 ± 11.7	65.6 ± 10.9	59.6 ± 11.6	**<0.001**
Female, *n* (%)	101 (46.8%)	71 (34%)	44 (20.8%)	**<0.001**
Hypertension, *n* (%)	168 (77.8%)	168 (80.4%)	176 (83.0%)	0.39
Diabetes mellitus, *n* (%)	87 (40.3%)	81 (38.8%)	73 (34.4%)	0.44
Hyperlipidemia, *n* (%)	55 (25.5%)	80 (38.3%)	97 (45.8%)	**<0.001**
Atrial fibrillation, *n* (%)	39 (18.1%)	14 (6.7%)	11 (5.2%)	**<0.001**
History of stroke, *n* (%)	47 (21.8%)	29 (13.9%)	30 (14.2%)	**0.046**
Smoking, *n* (%)	59 (27.3%)	69 (33.0%)	75 (35.4%)	0.18
Drinking, *n* (%)	47 (21.8%)	52 (24.9%)	59 (27.8%)	0.29
NIHSS score in point, median (IQR)	4 (2–7)	4 (3–6)	3 (2–5)	**0.003**
NLR, median (IQR)	2.55 (2.02–3.93)	2.35 (1.82–3.28)	2.19 (1.76–2.97)	**<0.001**
Fasting blood glucose in mmol/L, median (IQR)	5.40 (4.57–7.14)	5.18 (4.66–6.67)	5.15 (4.61–6.52)	0.79
HbA1c in %, median (IQR)	6.00 (5.56–7.14)	5.99 (5.50–7.05)	5.90 (5.51–6.88)	0.56
Creatinine in μmol/L, median (IQR)	62.0 (53.8–74.5)	61.1 (54.3–72.2)	69.3 (58.3–81.2)	**<0.001**
Uric acid in μmol/L, median (IQR)	287.5 (240-358)	306 (251–357.5)	354 (293–436.5)	**<0.001**
Homocysteine in μmol/L, median (IQR)	11.3 (8.7–14.7)	10.1 (8.1-13.2)	10.8 (8.8–13.8)	0.08
Total bilirubin in μmol/L, median (IQR)	11.8 (9.2–17.4)	12.7 (8.9-17.6)	12.4 (9.3–16.0)	1.00
Triglyceride in mmol/L, median (IQR)	1.06 (0.80–1.39)	1.47 (1.12-2.01)	1.88 (1.45–2.53)	**<0.001**
Total cholesterol in mmol/L, median (IQR)	4.06 (3.51–4.74)	4.40 (3.87-5.00)	4.55 (3.91–5.19)	**<0.001**
HDL_C in mmol/L, median (IQR)	0.97 (0.82–1.16)	0.97 (0.83-1.14)	0.94 (0.81–1.13)	0.61
LDL_C in mmol/L, median (IQR)	2.60 (2.10–3.15)	2.84 (2.36-3.45)	2.92 (2.15–3.45)	**0.003**
Albumin in g/L, median (IQR)	37.1 (35.3–38.9)	39.2 (37.8-40.8)	40.4 (39.0–42.2)	**<0.001**

HDL_C, high-density lipoprotein cholesterol; IQR, interquartile range; LDL-C, low-density lipoprotein cholesterol; NIHSS, National Institutes of Health Stroke Scale; NLR, neutrophil-to-lymphocyte ratio; SD, standard deviation. Bold values means univariate analysis reached statistical significance ($P < 0.05$).

Methods

Study population

We reviewed the data of consecutive patients with AIS admitted to the Department of Neurology of the Second Affiliated Hospital of Wenzhou Medical University between January 2019 and June 2020. All patients meeting the World Health Organization diagnostic criteria and admitted to the hospital within 24 h of onset were considered in this study (14). Exclusion criteria were as follows: (1) lack of intracranial vascular examination or poor image quality; (2) blood samples collected beyond 24 h after admission; (3) incomplete clinical data; (4) severe liver/kidney disease, infection, or malignancy; (5) intracranial artery occlusion attributed to cardioembolism; and (6) ECAS based on neck vascular ultrasonography.

This study was approved by the Ethics Committee of the Second Affiliated Hospital and Yuying Children's Hospital of the Wenzhou Medical University. The requirement for written informed consent was waived due to the study's retrospective nature.

Data collection

Blood samples were taken from all patients within 24 h after admission, and routine examinations including brain computed tomography (CT)/ magnetic resonance imaging (MRI), intracranial artery CT angiography (CTA)/ MR angiography (MRA), chest CT, 12-lead electrocardiogram (ECG), and B-mode ultrasound (heart, abdomen, and neck vessels) were performed during hospitalization. Hypertension was defined as systolic blood pressure ≥140 mmHg, diastolic blood pressure ≥90 mmHg, or long-term treatment with antihypertensive medication. Diabetes mellitus was defined as fasting blood glucose ≥7.0 mmol/L, blood glucose 2 h after a 75-g glucose load ≥11.1 mmol/L, hemoglobin A1c (HbA1c) ≥6.5%, or long-term treatment with antihyperglycemic medication. Hyperlipidemia was defined as total cholesterol ≥6.2 mmol/L, low-density lipoprotein cholesterol (LDL-C) ≥4.1 mmol/L, or long-term treatment with lipid-lowering medication. Atrial fibrillation was defined as arrhythmia detected on ECG after admission. History of stroke included previous symptomatic ischemic or hemorrhagic stroke. Smoking was defined as

TABLE 2 Clinical characteristics of patients, stratified by the presence of ICAS.

Clinical characteristics	Total ($n = 637$)	Without ICAS ($n = 370$)	With ICAS ($n = 267$)	*P*
Age in years, mean ± SD	65.7 ± 12.4	63.3 ± 12.4	69.1 ± 11.6	**<0.001**
Female, *n* (%)	216 (33.9%)	117 (31.6%)	99 (37.1%)	0.15
Hypertension, *n* (%)	512 (80.4%)	294 (79.5%)	218 (81.6%)	0.49
Diabetes mellitus, *n* (%)	241 (37.8%)	125 (33.8%)	116 (43.4%)	**0.013**
Hyperlipidemia, *n* (%)	232 (36.4%)	130 (35.1%)	102 (38.2%)	0.43
Atrial fibrillation, *n* (%)	64 (10%)	39 (10.5%)	25 (9.4%)	0.63
History of stroke, *n* (%)	106 (16.6%)	55 (14.9%)	51 (19.1%)	0.16
Smoking, *n* (%)	203 (31.9%)	119 (32.2%)	84 (31.5%)	0.85
Drinking, *n* (%)	158 (24.8%)	93 (25.1%)	65 (24.3%)	0.76
NIHSS score in point, median (IQR)	4 (2–5)	3 (2–5)	4 (3–7)	**0.001**
NLR, median (IQR)	2.47 (1.85–3.33)	2.35 (1.81–3.20)	2.49 (1.90–3.50)	0.052
Fasting blood glucose in mmol/L, median (IQR)	5.22(4.61–6.80)	5.09 (4.56–6.39)	5.55 (4.78–7.36)	**0.001**
HbA1c in %, median (IQR)	5.93 (5.53–7.02)	5.82 (5.44–6.79)	6.15 (5.67–7.33)	**<0.001**
Creatinine in μmol/L, median (IQR)	63.9 (55.1–76.1)	66.4 (55.7–77.5)	62.0 (53.9–74.4)	0.069
Uric acid in μmol/L, median (IQR)	312 (260–386)	316.5 (262–393)	304 (252–376)	0.064
Homocysteine in μmol/L, median (IQR)	10.7 (8.6–13.8)	10.7 (8.6–13.6)	10.8 (8.5–14.2)	0.93
Total bilirubin in μmol/L, median (IQR)	12.2 (9.2–17.2)	12.1 (8.8–17.3)	12.2 (9.5–17.1)	0.57
Triglyceride in mmol/L, median (IQR)	1.45 (1.04–2.05)	1.51 (1.05–2.06)	1.34 (1.03–2.00)	0.30
Total cholesterol in mmol/L, median (IQR)	4.33 (3.71–5.00)	4.23 (3.68–4.99)	4.41 (3.82–5.00)	0.16
HDL_C in mmol/L, median (IQR)	0.96 (0.82–1.15)	0.97 (0.82–1.18)	0.96 (0.83–1.11)	0.58
LDL_C in mmol/L, median (IQR)	2.75 (2.21–3.37)	2.70 (2.13–3.28)	2.88 (2.27–3.46)	**0.045**
Albumin in g/L, median (IQR)	39.0 (36.9–40.9)	39.3 (37.4–41.2)	38.7 (36.5–40.2)	**0.001**
Transthyretin in mg/L, mean ± SD	240.6 ± 56.9	251.0 ± 54.9	226.3 ± 56.5	**<0.001**
T1 (≤214.0), *n* (%)	216 (33.9%)	100 (27.0%)	116 (43.4%)	**<0.001**
T2 (214.1–265.0), *n* (%)	209 (32.8%)	121 (32.7%)	88 (33.0%)	
T3 (≥265.1), *n* (%)	212 (33.3%)	149 (40.3%)	63 (23.6%)	

HDL_C, high-density lipoprotein cholesterol; ICAS, intracranial atherosclerotic stenosis; IQR, interquartile range; LDL-C, low-density lipoprotein cholesterol; NIHSS, National Institutes of Health Stroke Scale; NLR, neutrophil-to-lymphocyte ratio; SD, standard deviation. Bold values means univariate analysis reached statistical significance ($P < 0.05$).

smoking at least one cigarette per day for 6 consecutive months. Alcoholism was defined as drinking >14 units of alcohol per week for men or >7 units per week for women. Laboratory findings (including neutrophil-to-lymphocyte ratio [NLR], fasting blood glucose, HbA1c, creatinine, uric acid, homocysteine, total bilirubin, triglycerides, total cholesterol, high-density lipoprotein cholesterol [HDL-C], LDL-C, albumin, and transthyretin levels) were also recorded in detail. Stroke severity was assessed using the National Institutes of Health Stroke Scale (NIHSS) score at admission. Stroke etiology was evaluated according to the Trial of Org10172 in Acute Stroke Treatment (TOAST) classification.

Evaluation of intracranial arteries

The degree of intracranial stenosis was assessed using CTA or MRA according to the WASID method by two independent operators blinded to patient information (15). ICAS was defined as ≥50% stenosis or occlusion of the intracranial artery. Intracranial arteries include the C4-C7 segment of the internal carotid, middle cerebral, anterior cerebral, and posterior cerebral arteries and the V4 segment of the vertebral and basilar arteries. The number of stenotic vessels was recorded and classified as 0, 1, 2, or ≥3. The patients were also divided into three categories according to the site of the stenotic vessels: anterior circulation, posterior circulation, and simultaneous involvement of both the anterior and posterior circulation. ICAS was classified as symptomatic or asymptomatic according to whether the infarction was attributable to ICAS.

Statistical analysis

Normally distributed continuous variables are expressed as mean ± standard deviation, while skewed distributed

continuous variables are expressed as median (interquartile range). Unpaired *t*-tests, Mann-Whitney *U* test, one-way analysis of variance, Kruskal-Wallis test, or LSD-*t*-test were used to compare intergroup differences, as appropriate. Categorical variables are expressed as percentages and were analyzed using Pearson's chi-square test. In addition to the continuous variables, serum transthyretin levels were also divided into tertiles for analysis, and the third tertile was set as the reference group in the logistic regression model. Multivariate logistic regression analysis was used to explore the independent factors related to intracranial atherosclerosis. All variables with $p < 0.1$ in the univariate analysis were entered into the analysis, and the final model was obtained by the backward method. In addition, we used the R package "rms" to construct restricted cubic splines with four knots to understand patterns in the association between serum transthyretin levels and ICAS using the median value of the third tertile of serum transthyretin levels as a reference point (16). All statistical tests were two-tailed, and statistical significance was set at $p < 0.05$. All analyses were performed using SPSS (version 25.0; IBM, Armonk, NY, United States) and R 3.6.3 (R Foundation for Statistical Computing, Vienna, Austria).

Results

Based on the established inclusion and exclusion criteria, 637 patients were included in our study (Figure 1). A total of 556 patients underwent CTA, while 81 underwent MRA to assess their intracranial arteries, and the stenosis rate was similar in both groups (41.2 vs. 46.9%, $p = 0.33$). Among the included patients, 267 (41.9%) presented with ICAS: 111 (17.4%) with one artery involved, 88 (13.8%) with two arteries involved, and 68 (10.7%) with three or more arteries involved.

The average concentration of serum transthyretin across all patients was 240.6 ± 56.9 mg/L. Patients were divided into three groups based on tertiles of serum transthyretin concentration (T1: ≤214.0 mg/L, T2: 214.1–265.0 mg/L, and T3: ≥265.1 mg/L). Patients with lower serum transthyretin levels were older, more likely to be females, and had higher NIHSS scores and NLRs. In contrast, creatinine, uric acid, triglyceride, total cholesterol, LDL-C, and albumin levels were lower. These patients also had larger proportions of atrial fibrillation and a history of stroke, and a smaller proportion of hyperlipidemia (all $p < 0.05$; Table 1). Among the different stroke etiologies, serum transthyretin levels were equivalent between large-artery atherosclerosis and cardioembolism (223.4 ± 56.5 vs. 217.5 ± 64.1 mg/L; $p = 0.50$), and the levels in large-artery atherosclerosis were lower than those in small-vessel occlusion (223.4 ± 56.5 vs. 253.4 ± 52.5 mg/L; $p < 0.001$).

Table 2 shows patients' demographic and clinical data stratified by the presence of ICAS. In patients with ICAS, the serum transthyretin levels decreased significantly (226.3 ± 56.5 vs. 251.0 ± 54.9 mg/L; $p < 0.001$). The greater the burden on intracranial arteries, the greater the decrease in serum transthyretin levels (Figure 2A). Patients with ICAS at any site had decreased serum transthyretin levels, and the average levels were lowest in those with both anterior and posterior circulations (Figure 2B). No difference in serum transthyretin levels was observed between symptomatic and asymptomatic ICAS (223.1 ± 55.9 vs. 237.6 ± 58.2 mg/L; $p = 0.087$). Compared to patients without ICAS, patients with ICAS were older, had higher NIHSS scores, fasting blood glucose, HbA1c, and LDL-C levels, higher

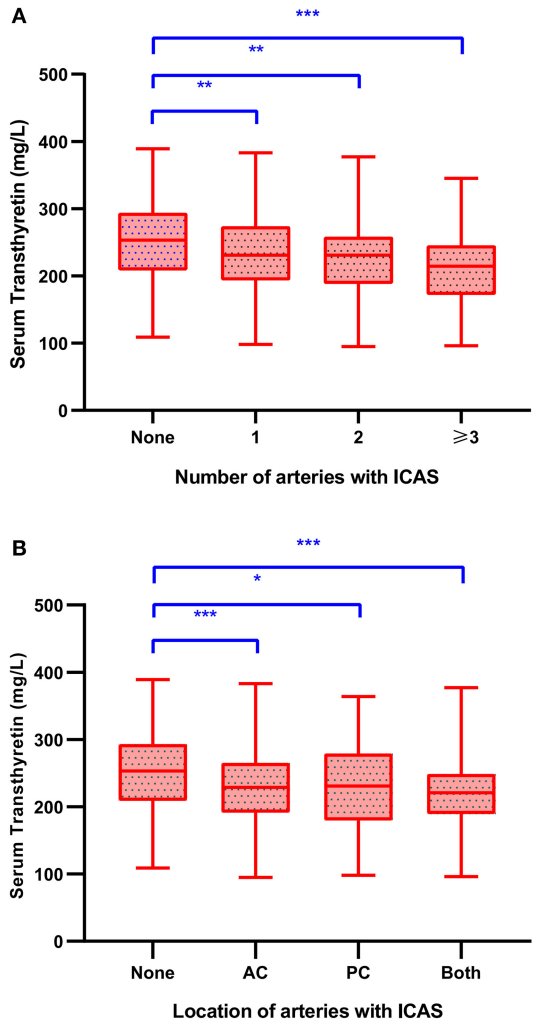

FIGURE 2
Serum transthyretin levels in stroke patients with different number **(A)** and location **(B)** of stenotic intracranial arteries. LSD-*t* test, *$p < 0.05$, **$p < 0.01$, ***$p < 0.001$. AC, anterior circulation; ICAS, intracranial atherosclerotic stenosis; PC, posterior circulation.

TABLE 3 Multiple logistic regression analysis to identify relationships between transthyretin and ICAS.

	Crude OR	*P*	Adjusted OR	*P*
Transthyretin, per SD (56.9 mg/L) increase	0.64 (0.54–0.75)	<0.001	0.74 (0.59–0.93)	0.009
Female	0.66 (0.48–0.91)	0.010	0.70 (0.46–1.08)	0.11
Male	0.63 (0.51–0.77)	<0.001	0.72 (0.55–0.95)	0.019
Transthyretin, tertiles				
T3 (≥265.1 mg/L)	Reference		Reference	
T2 (214.1–265.0 mg/L)	1.72 (1.15–2.57)	0.008	1.37 (0.88–2.15)	0.17
T1 (≤214.0 mg/L)	2.74 (1.84–4.08)	<0.001	1.85 (1.12–3.05)	0.016
P for trend	<0.001		0.016	

Adjusted for age, diabetes mellitus, NIHSS score, NLR, fasting blood glucose, HbA1c, Creatinine, Uric acid, LDL_C, and albumin.
ICAS, intracranial atherosclerotic stenosis; LDL-C, low-density lipoprotein cholesterol; NIHSS, National Institutes of Health Stroke Scale; NLR, neutrophil-to-lymphocyte ratio; OR, Odds ratio; SD, standard deviation.

proportions of diabetes mellitus, and lower albumin levels (all $p < 0.05$).

As shown in Table 3, after adjusting for potential confounders, serum transthyretin was inversely associated with ICAS [odds ratio (OR) per standard deviation (SD) increase, 0.74; 95% confidence interval (CI), 0.59–0.93; $p = 0.009$]. Subgroup analysis showed that this independent association was present in males (OR per SD increase, 0.72; 95% CI, 0.55–0.95; $p = 0.019$) but not in females (OR per SD increase, 0.70; 95% CI, 0.46–1.08; $p = 0.11$). Multivariate analysis suggested that compared with patients in the third transthyretin tertile, those in the first tertile showed a significant increase in ICAS (OR, 1.85; 95% CI, 1.12–3.05; $p = 0.016$), while those in the second tertile showed an insignificant increase (OR, 1.37; 95% CI, 0.88–2.15; $p = 0.17$). As shown in Figure 3, the restricted cubic spline model corroborated the significant negative linear relationship between serum transthyretin level and ICAS. In addition, age, NIHSS score, and HbA1c and LDL-C levels were positively associated with ICAS (Table 4).

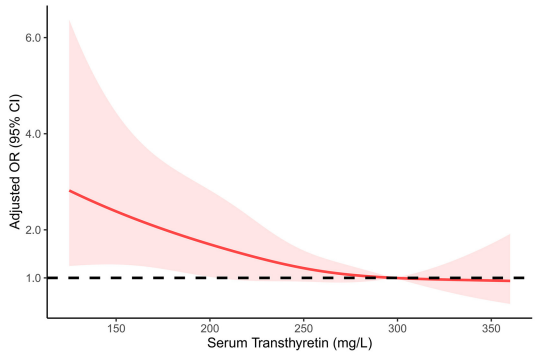

FIGURE 3
Restricted cubic spline regression model of the relationship between serum transthyretin levels and intracranial atherosclerosis.

Discussion

Our study found an inverse association between serum transthyretin levels and ICAS in patients with AIS. The serum transthyretin concentration decreased significantly in patients with a greater burden of ICAS. This is not the first time that serum transthyretin has been associated with atherosclerosis; Zhang et al. (13)found that lower transthyretin levels were associated with severe coronary atherosclerosis in patients with acute coronary syndrome. Similarly, reduced transthyretin levels affect the risk of carotid intima-media thickening in maintenance hemodialysis patients (17). However, previous studies have focused on the extracranial arteries. Because of the differences in pathogenesis between ICAS and ECAS, our results confirmed for the first time that a decrease in serum transthyretin also indicated atherosclerosis in the intracranial artery.

As confirmed by previous studies, increasing age is independently associated with ICAS (18). Patients with lower transthyretin levels were usually older, but the association between transthyretin and ICAS persisted even after adjusting for age in our study. There is no doubt that cholesterol, especially LDL-C, is an important pathogenic factor for atherosclerotic disease (19). Our study also found that LDL-C levels were associated with ICAS. However, patients with decreased serum transthyretin levels tended to have lower cholesterol levels. In summary, other important pathogenic mechanisms link transthyretin to ICAS.

Inflammation is the most promising among these. In addition to dyslipidemia, inflammation has been proven to be important in the pathogenesis of atherosclerosis and is expected to become the next therapeutic target (7). Transthyretin, a negative acute phase protein, decreases due to the inhibition

TABLE 4 Multiple logistic regression analysis to identify independent associated factors with ICAS.

	Crude OR	*P*	Adjusted OR	*P*
Transthyretin, per SD (56.9 mg/L) increase	0.64 (0.54–0.75)	<0.001	0.74 (0.59–0.93)	0.009
Age, per 10-year increase	1.49 (1.30–1.71)	<0.001	1.35 (1.15–1.58)	<0.001
Diabetes mellitus	1.51 (1.09–2.08)	0.013	—	—
NIHSS score, per 1-point increase	1.09 (1.04–1.14)	0.001	1.06 (1.00–1.11)	0.041
NLR, per 1 increase	1.07 (0.97–1.18)	0.17	—	—
Fasting blood glucose, per 1-mmol/L increase	1.11 (1.04–1.18)	0.001	—	—
HbA1c, per 1% increase	1.23 (1.11–1.37)	<0.001	1.30 (1.04–1.62)	0.019
Creatinine, per SD (22.5 μmol/L) increase	0.95 (0.81–1.12)	0.55	—	—
Uric acid, per SD (100 μmol/L) increase	0.87 (0.74–1.02)	0.087	—	—
LDL_C, per 1-mmol/L increase	1.21 (1.01–1.44)	0.035	1.23 (1.02–1.50)	0.035
Albumin, per 1-g/L increase	0.93 (0.88–0.98)	0.005	—	—

ICAS, intracranial atherosclerotic stenosis; LDL-C, low-density lipoprotein cholesterol; NIHSS, National Institutes of Health Stroke Scale; NLR, neutrophil-to-lymphocyte ratio; OR, Odds ratio; SD, standard deviation.

of transthyretin mRNA expression resulting from the increased release of interleukin-6 (IL-6), C-reactive protein (CRP), and other substances in the inflammatory process (8). The NLR is an easily available indicator of the inflammatory response (20), and the inverse association between transthyretin and NLR confirms that decreased transthyretin levels reflect the inflammatory process. Previous studies have reported a significant increase in CRP levels in patients with ICAS (21, 22). A cohort study found that elevated IL-6 levels were closely related to ICAS progression in patients with ischemic stroke (23). These findings support an association between transthyretin and ICAS.

Transthyretin is also a sensitive indicator of nutritional status, as our findings showed that patients with lower serum transthyretin levels had lower albumin levels. Carotid intima-media and plaque thickness are higher in malnourished patients with diabetes (24). Malnutrition is more commonly associated with atherosclerosis in patients with end-stage renal disease, commonly known as malnutrition-inflammation-atherosclerosis syndrome (25). Therefore, malnutrition, inflammation, and atherosclerosis are typically associated with each other. Transthyretin is an indicator of inflammation and nutritional status, which makes it closely related to atherosclerosis.

As a retinol transport protein, a decrease in serum transthyretin concentration is accompanied by a decrease in serum retinol content (26, 27). Retinol has an anti-inflammatory effect and is inversely associated with carotid intima-media thickness (28). A follow-up study of healthy people found that reduced plasma retinol levels were associated with a higher risk of coronary heart disease (29). As anti-inflammatory substance depletion plays an important role in the pathogenesis of ICAS (5), it may also be a potential link between transthyretin and ICAS.

We also found that age, HbA1c, and LDL-C were independently associated with ICAS, in addition to transthyretin. However, age was not a modifiable risk factor. Although univariate analysis suggested that HbA1c level and diabetes mellitus were both risk factors for ICAS, multivariate analysis showed that HbA1c level rather than diabetes mellitus was independently associated with ICAS, which was similar to previous findings (30), implying that it is meaningful to actively control blood glucose levels in patients with diabetes. According to our results, lowering blood lipid levels, especially LDL-C levels, is significant for treating ICAS, and statins have been widely used in treating ICAS (31). Similarly, the association between transthyretin and ICAS suggests that anti-inflammatory and nutritional support may be promising ways to prevent ICAS.

Our study has some limitations. First, this cross-sectional study could not establish a causal relationship between transthyretin and ICAS. Recall bias could not be avoided in the present study. Further cohort studies are needed to explore whether the decrease in serum transthyretin level and its dynamic changes precede stenosis. Second, the mechanism of the relationship between transthyretin and ICAS was deduced based on existing research findings. Indicators such as IL-6 and retinol were not measured in this study. As an alternative, we demonstrated the inflammatory role of transthyretin by evaluating NLRs. Third, the study population included acute stroke patients, and the acute phase response may affect transthyretin levels (10). Although our results considered stroke severity by adjusting for the NIHSS score, the results still need to be validated in the general population. Finally, digital subtraction angiography is the gold standard for judging intracranial artery stenosis; however, our study was based on CTA or MRA findings. However, the latter two inspection

methods have proven to have satisfactory reliability (18). Limited by the fact that high resolution-MRI was not performed, stenosis due to other causes, such as artery dissection and vasculitis, may be overlooked.

In conclusion, lower serum transthyretin levels are associated with more severe ICAS lesions in patients with stroke. These results must be validated in a larger sample and the general population. Our study provides insights into directions for further clinical research exploring whether anti-inflammatory therapy and nutritional supplementation could prevent ICAS.

Data availability statement

The raw data supporting the conclusions of this article will be made available by the authors, without undue reservation.

Ethics statement

The studies involving human participants were reviewed and approved by the Ethics Committee of the Second Affiliated Hospital and Yuying Children's Hospital of the Wenzhou Medical University. The ethics committee waived the requirement of written informed consent for participation.

Author contributions

QB conceived and designed the study. All authors acquired the data, which JH and JZ analyzed. JH, JZ, and WZ assisted in data interpretation and JH wrote the manuscript. All authors participated in revising the article and approved the final version.

Conflict of interest

The authors declare that the research was conducted in the absence of any commercial or financial relationships that could be construed as a potential conflict of interest.

Publisher's note

All claims expressed in this article are solely those of the authors and do not necessarily represent those of their affiliated organizations, or those of the publisher, the editors and the reviewers. Any product that may be evaluated in this article, or claim that may be made by its manufacturer, is not guaranteed or endorsed by the publisher.

References

1. Johnson CO, Nguyen M, Roth GA, Nichols E, Alam T, Abate D, et al. Global, regional, and national burden of stroke, 1990–2016: a systematic analysis for the Global Burden of Disease Study 2016. *Lancet Neurol.* (2019) 18:439–58. doi: 10.1016/S1474–4422(19)30034–1

2. Wang YJ, Zhao XQ, Liu LP, Soo YOY, Pu YH, Pan YS, et al. Prevalence and outcomes of symptomatic intracranial large artery stenoses and occlusions in China the Chinese intracranial atherosclerosis (CICAS) study. *Stroke.* (2014) 45:663–9. doi: 10.1161/STROKEAHA.113.003508

3. Kim B-S, Chung P-W, Park K-Y, Won H-H, Bang OY, Chung C-S, et al. Burden of intracranial atherosclerosis is associated with long-term vascular outcome in patients with ischemic stroke. *Stroke.* (2017) 48:2819–26. doi: 10.1161/STROKEAHA.117.017806

4. Jeng J-S, Hsieh F-I, Yeh H-L, Chen W-H, Chiu H-C, Tang S-C, et al. Impact of MCA stenosis on the early outcome in acute ischemic stroke patients. *Plos One.* (2017) 12. doi: 10.1371/journal.pone.0175434

5. Kim JS, Kim Y-J, Ahn S-H, Kim BJ. Location of cerebral atherosclerosis: why is there a difference between East and West? *Int J Stroke.* (2016) 13:35–46. doi: 10.1177/1747493016647736

6. Li Z, Jiang Y, Li H, Xian Y, Wang Y. China's response to the rising stroke burden. *BMJ.* (2019) 364:l879. doi: 10.1136/bmj.l879

7. Raggi P, Genest J, Giles JT, Rayner KJ, Dwivedi G, Beanlands RS, et al. Role of inflammation in the pathogenesis of atherosclerosis and therapeutic interventions. *Atherosclerosis.* (2018) 276:98–108. doi: 10.1016/j.atherosclerosis.2018.07.014

8. Myron Johnson A, Merlini G, Sheldon J, Ichihara K. Clinical indications for plasma protein assays: transthyretin (prealbumin) in inflammation and malnutrition: international federation of clinical chemistry and laboratory medicine (IFCC): IFCC scientific division committee on plasma proteins (C-PP). *Clin Chem Lab Med.* (2007) 45:419–26. doi: 10.1515/CCLM.2007.051

9. Devoto G, Gallo F, Marchello C, Racchi O, Garbarini R, Bonassi S, et al. Prealbumin serum concentrations as a useful tool in the assessment of malnutrition in hospitalized patients. *Clin Chem.* (2006) 52:2281–5. doi: 10.1373/clinchem.2006.080366

10. Gao C, Zhang B, Zhang W, Pu S, Yin J, Gao Q. Serum prealbumin (transthyretin) predict good outcome in young patients with cerebral infarction. *Clin Exp Med.* (2011) 11:49–54. doi: 10.1007/s10238-010-0103-8

11. Ambrosius W, Michalak S, Kazmierski R, Andrzejewska N, Kozubski W. Predictive value of serum transthyretin for outcome in acute ischemic stroke. *PLoS ONE.* (2017) 12:e0179806. doi: 10.1371/journal.pone.0179806

12. Zhang SQ, Peng B, Stary CM, Jian ZH, Xiong XX, Chen QX. Serum prealbumin as an effective prognostic indicator for determining clinical status and prognosis in patients with hemorrhagic stroke. *Neural Regen Res.* (2017) 12:1097–2. doi: 10.4103/1673-5374.211188

13. Zhang C, Liu P, Xia K, Fang H, Jiang M, Xie Q, et al. Association of serum prealbumin with angiographic severity in patients with acute coronary syndrome. *Med Sci Monitor.* (2017) 23:4041–9. doi: 10.12659/MSM.902348

14. Aho K, Harmsen P, Hatano S, Marquardsen J, Smirnov VE, Strasser T. Cerebrovascular disease in the community: results of a WHO collaborative study. *Bull World Health Organ.* (1980) 58:113–30.

15. Samuels OB, Joseph GJ, Lynn MJ, Smith HA, Chimowitz MZ. A standardized method for measuring intracranial arterial stenosis. *Am J Neuroradiol.* (2000) 21:643–6.

16. Durrleman S, Simon R. Flexible regression models with cubic splines. *Stat Med.* (1989) 8:551–61. doi: 10.1002/sim.4780080504

17. Kuang D, You H, Ding F, Xue J, Chen J, Ronco C, et al. Intima-media thickness of the carotid artery and its correlation factors in maintenance hemodialysis patients: a cross-sectional study. *Blood Purif.* (2009) 28:181–6. doi: 10.1159/000227787

18. Wang Y, Meng R, Liu G, Cao C, Chen F, Jin K, et al. Intracranial atherosclerotic disease. *Neurobiol Dis.* (2019) 124:118–32. doi: 10.1016/j.nbd.2018.11.008

19. Steinberg D. Thematic review series: the pathogenesis of atherosclerosis.An interpretive history of the cholesterol controversy. Part V: the discovery of the statins and the end of the controversy. *J Lipid Res.* (2006) 47:1339–51. doi: 10.1194/jlr.R600009-JLR200

20. Li WX, Hou MM, Ding ZB, Liu XL, Shao Y, Li XY. Prognostic value of neutrophil-to-lymphocyte ratio in stroke: a systematic review and meta-analysis. *Front Neurol.* (2021) 12. doi: 10.3389/fneur.2021.686983

21. Flegar-Meštrić Z, Vrhovski-Hebrang D, Preden-Kereković V, Perkov S, Hebrang A, Grga A, et al. C-reactive protein level in severe stenosis of cerebral arteries. *Cerebrovascul Dis.* (2007) 23:430–4. doi: 10.1159/000101467

22. Su B-J, Dong Y, Tan C-C, Hou X-H, Xu W, Sun F-R, et al. Elevated Hs-CRP levels are associated with higher risk of intracranial arterial stenosis. *Neurotoxicity Res.* (2019) 37:425–32. doi: 10.1007/s12640-019-00108-9

23. Shimizu K, Shimomura K, Tokuyama Y, Sakurai K, Isahaya K, Takaishi S, et al. Association between inflammatory biomarkers and progression of intracranial large artery stenosis after ischemic stroke. *J Stroke Cerebrovascul Dis.* (2013) 22:211–7. doi: 10.1016/j.jstrokecerebrovasdis.2011.07.019

24. Mineoka Y, Ishii M, Hashimoto Y, Nakamura N, Fukui M. Malnutrition assessed by controlling nutritional status is correlated to carotid atherosclerosis in patients with type 2 diabetes. *Endocr J.* (2019) 66:1073–82. doi: 10.1507/endocrj.EJ19-0107

25. Zyga S, Christopoulou G, Malliarou M. Malnutrition-inflammation-atherosclerosis syndrome in patients with end-stage renal disease. *J Ren Care.* (2011) 37:12–5. doi: 10.1111/j.1755-6686.2011.00201.x

26. Smith FR, Goodman DS, Arroyave G, Viteri F. Serum vitamin A, retinol-binding protein, and prealbumin concentrations in protein-calorie malnutrition. II Treatment including supplemental vitamin A. *Am J Clin Nutr.* (1973) 26:982–7. doi: 10.1093/ajcn/26.9.982

27. Forga L, Bolado F, Goni MJ, Tamayo I, Ibanez B, Prieto C. Low serum levels of prealbumin, retinol binding protein, and retinol are frequent in adult type 1 diabetic patients. *J Diabetes Res.* (2016) 2016:2532108. doi: 10.1155/2016/2532108

28. Bobbert T, Raila J, Schwarz F, Mai K, Henze A, Pfeiffer AFH, et al. Relation between retinol, retinol-binding protein 4, transthyretin and carotid intima media thickness. *Atherosclerosis.* (2010) 213:549–51. doi: 10.1016/j.atherosclerosis.2010.07.063

29. Gey KF, Ducimetiere P, Evans A, Amouyel P, Arveiler D, Ferrieres J, et al. Low plasma retinol predicts coronary events in healthy middle-aged men: the PRIME study. *Atherosclerosis.* (2010) 208:270–4. doi: 10.1016/j.atherosclerosis.2009.07.018

30. Choi N, Lee JY, Sunwoo JS, Roh H, Ahn MY, Park ST, et al. Recently uncontrolled glycemia in diabetic patients is associated with the severity of intracranial atherosclerosis. *J Stroke Cerebrovasc Dis.* (2017) 26:2615–21. doi: 10.1016/j.jstrokecerebrovasdis.2017.06.025

31. Chung JW, Cha J, Lee MJ Yu IW, Park MS, Seo WK, et al. Intensive statin treatment in acute ischaemic stroke patients with intracranial atherosclerosis: a high-resolution magnetic resonance imaging study (STAMINA-MRI Study). *J Neurol Neurosurg Psychiatry.* (2020) 91:204–11. doi: 10.1136/jnnp-2019-320893

frontiers | Frontiers in Neurology

TYPE Original Research
PUBLISHED 25 January 2023
DOI 10.3389/fneur.2022.942887

Check for updates

OPEN ACCESS

EDITED BY
Yuzhen Xu,
Tongji University, China

REVIEWED BY
Eugenia Mariela Roldán Olarte,
Universidad Nacional de Tucumán, Argentina
Nikolaos Papagiannakis,
National and Kapodistrian University of Athens, Greece

*CORRESPONDENCE
Xiaoxia Zhao
✉ wsplbb@163.com

SPECIALTY SECTION
This article was submitted to Neurological Biomarkers, a section of the journal Frontiers in Neurology

RECEIVED 13 May 2022
ACCEPTED 23 December 2022
PUBLISHED 25 January 2023

CITATION
Zhao X, Yang S, Lei R, Duan Q, Li J, Meng J and Sun L (2023) Clinical study on the feasibility of new thrombus markers in predicting massive cerebral infarction. *Front. Neurol.* 13:942887. doi: 10.3389/fneur.2022.942887

COPYRIGHT
© 2023 Zhao, Yang, Lei, Duan, Li, Meng and Sun. This is an open-access article distributed under the terms of the Creative Commons Attribution License (CC BY). The use, distribution or reproduction in other forums is permitted, provided the original author(s) and the copyright owner(s) are credited and that the original publication in this journal is cited, in accordance with accepted academic practice. No use, distribution or reproduction is permitted which does not comply with these terms.

Clinical study on the feasibility of new thrombus markers in predicting massive cerebral infarction

Xiaoxia Zhao[1]*, Siyu Yang[2], Ruining Lei[2], Qiaoyan Duan[3], Jundong Li[4], Jiangtao Meng[2] and Lei Sun[5]

[1]Department of Neurology, Shanxi Provincial People's Hospital, Taiyuan, Shanxi, China, [2]Department of Neurology, Fifth Hospital of Shanxi Medical University, Taiyuan, Shanxi, China, [3]Clinical Laboratory, Shanxi Provincial People's Hospital, Taiyuan, Shanxi, China, [4]Medical Imaging Department, Shanxi Provincial People's Hospital, Taiyuan, Shanxi, China, [5]Zhao Furun Famous Doctor Studio in Shanxi Province, Taiyuan, Shanxi, China

Objective: This study investigated the diagnostic performance of the thrombin-antithrombin complex (TAT), plasmin-α2 plasmin inhibitor complex (PIC), tissue plasminogen activator-plasminogen activator inhibitor complex (t-PAIC), and thrombomodulin (TM) in the early identification of massive cerebral infarction.

Method: A total of 423 patients with cerebral infarction confirmed by imaging examination were divided into the massive cerebral infarction (MCI) group and the non-massive cerebral infarction (NMCI) group. TAT, PIC, t-PAIC, and TM were measured immediately after admission. The diagnostic performance was analyzed by the receiver characteristic operating curve (ROC).

Result: The median plasma concentrations of TAT, PIC, and t-PAIC in patients with MCI at early onset were 5.10 ng/ml, 1.11 μg/ml, and 8.80 ng/ml, respectively, which were higher than those in patients with NMCI (2.20 ng/ml, 0.59 μg/ml, and 7.35 ng/ml), and the difference was statistically significant ($P < 0.001$). TAT was shown to be an independent risk factor for the development of massive cerebral infarction by a multivariate logistic regression analysis (OR = 1.138). A ROC curve analysis showed that PIC had the best performance in identifying MCI at an early stage (AUC = 82.8%), with a sensitivity of 80.7% and a specificity of 76.2% when the PIC concentration was ≥0.8 μg/ml; TAT had the highest specificity in identifying MCI, with a specificity of 80.6% when the TAT concentration was ≥3.97 ng/ml.

Conclusion: The detection of PIC, TAT, t-PAIC, and TM is a comprehensive assessment of vascular endothelial damage and activation of the coagulation and fibrinolytic systems and has diagnostic value for early identification of patients with MCI, which, together with its ease of detection, can be used as a plasma marker for early identification of large vessel occlusion.

KEYWORDS

thrombin-antithrombin complex, plasmin-α2 plasmin inhibitor complex, tissue prothrombin activator-prothrombin activator inhibitor complex, thrombomodulin, massive cerebral infarction, diagnosis

1. Introduction

Massive cerebral infarction (MCI) is caused by internal carotid or middle cerebral artery trunk occlusion, with a mortality rate of 53–78% (1). Early diagnosis before admission and transportation to advanced stroke centers for timely thrombolysis or embolectomy treatment is significant to reduce the burden of serious consequences. Although imaging examination is a reliable method to determine vascular occlusion, it is usually not possible to perform it before admission, so it is very critical to find appropriate plasma markers for early identification of massive cerebral infarction.

Ischemic stroke is mostly caused by intravascular thrombosis due to coagulation abnormalities, and the occurrence of ischemic stroke will cause changes in the coagulation and fibrinolytic system; the two interact with each other (2). Previous studies have shown that the plasma concentrations of new thrombus markers are related to the occurrence and development of cardiovascular and cerebrovascular diseases closely. Thrombomodulin (TM) has been confirmed to be involved in the regulation of the body's coagulation and fibrinolytic system (3), and it has been found that the TM content in the plasma is associated with vascular endothelial injurious diseases (4–6). Plasmin-α2 antiplasmin complex (PIC) can reflect the activation of the fibrinolytic system and is more sensitive than D-dimer and fibrinogen degradation products (FDP) (7). Thrombin-antithrombin complex (TAT) is a sensitive marker of thrombin formation and has a certain predictive role in a variety of ischemic diseases (8–10). The high concentration of tissue plasminogen activator-plasminogen activator inhibitor complex (t-PAIC) in the blood indicates damage to the fibrinolytic system and can be used as an independent predictor of cardiovascular mortality (11). These new thrombus markers can be detected by a high-sensitivity chemiluminescence system rapidly and accurately, and the results can be obtained within 17 min (12), offering the possibility of early identification of large vessel occlusions.

To investigate whether the plasma concentrations of novel thrombus markers (TM, PAP, TAT, and t-PAIC) are associated with cerebral infarct size, we measured the plasma concentrations of these thrombus markers in patients with cerebral infarction, assessed their diagnostic performance for massive cerebral infarction for prehospital identification of macrovascular occlusion, and laid the foundation for further exploration of the molecular mechanism of massive cerebral infarction.

2. Materials and methods

2.1. Patients

A total of 423 patients (118 female patients and 305 male patients) with acute ischemic stroke, including 57 patients with massive cerebral infarction, were enrolled in the study from July 2019 to March 2022. The study protocol was reviewed and approved by the Human Ethical Review Committee of Shanxi Provincial People's Hospital. Written informed consent was obtained from the patient or close relatives.

The inclusion criteria were as follows: (1) aged ≥18 years; (2) admitted within 24 h after the onset of acute cerebral infarction; (3) acute cerebral infarction was defined as a rapidly progressive neurological deficit of vascular origin lasting, diagnosed as ischemic stroke by head CT or MRI examination (13); and (4) informed consent.

The exclusion criteria were as follows: (1) traumatic brain injury within the past 1 week; (2) the patient was discharged or transferred due to an unknown prognosis during the observation period (7 days after onset); (3) patients with malignant tumors of any organ or system; (4) patients with severe lung, liver, kidney, blood coagulation system, immune system, and other important organs or systems injury; (5) patients with lower limb thrombosis, pulmonary embolism, and other serious thrombosis diseases affecting coagulation function and injuries using anticoagulant drugs; (6) patients with severe neurological disability (modified Rankin Scale score, mRS ≥2 points) before onset; and (7) patients with cerebral hemorrhage, brainstem infarction, or bilateral cerebral hemispheric infarction.

2.2. Baseline indicator

Patient age, gender, and risk factors for cerebral infarction (hypertension, diabetes, atrial fibrillation, smoking history, and alcohol history) were recorded.

2.3. Imaging examination

After completing magnetic resonance imaging on admission, two senior imaging physicians who ignored the results of plasma tests independently classified the patients into the massive cerebral infarction (MCI) group and the non-massive cerebral infarction (NMCI) group according to the results of the imaging examinations, and in case of disagreement, the decision was made by mutual discussion between the two.

2.4. Blood sampling and assay procedure

Immediately after admission, 2.7 ml of cubital venous blood was collected at one time and injected into BD vacuum blood collection tubes containing 0.3 ml of 0.109 mol/L sodium citrate anticoagulant (9:1 ratio), inverted, and mixed well. After centrifugation at 3,500 r/min for 15 min, platelet-poor plasma was obtained. These plasma samples were all quoted in Eppendorf tubes and then stored at −80°C. The assay was completed within 24 h.

TAT, TM, t-PAIC, and PIC were determined by chemiluminescent enzyme immunoassay (instrument: Sysmex HISCL-5,000 automatic chemiluminescence analyzer and its supporting chemiluminescent enzyme immunoassay reagent). The samples were mixed with reagents for incubation, and then the immune reaction and chemiluminescent enzyme reaction occurred in turn. Using the high specificity of the antigen-antibody reaction and the high sensitivity of luminescence analysis, the content of the analyte in the sample was determined by counting the photons emitted in the enzyme reaction quickly and automatically.

2.5. Criteria for MCI

MCI was defined as the Alberta Stroke Program Early CT Score (ASPECTS) <6 on CT or magnetic resonance diffusion imaging (DWI) images (14), infarct volume ≥70 ml (15), or infarct size ≥2/3 middle cerebral artery territory (16). ASPECTS scoring method: The blood supply area of the middle cerebral artery was divided into 10 regions, i.e., M1–M6, as well as the nucleus accumbens, caudate nucleus, internal capsule, and insula; each region was scored as 1 point, totaling 10 points, and 1 point was subtracted for the presence of 1 EIC region; an ASPECT score of 10 means no early ischemic changes, while a score of 0 indicates the presence of extensive ischemic foci in brain tissue (17).

2.6. Data statistics

Normal distribution continuous variables were expressed as mean ± standard deviation (SD) and compared using the independent sample *t*-test; non normal distribution continuous variables were expressed as median (interquartile range) and compared using the Mann-Whitney U test. Categorical variables were presented as numbers and percentages and compared using the chi-square test. Items with a $P \leq 0.05$ in the univariate analysis were included in the multivariate logistic regression analysis to assess the risk factors for the occurrence of massive cerebral infarction. The receiver operating characteristic curve (ROC) was used to analyze the accuracy of different plasma markers in the diagnosis of MCI, and the Youden index was calculated, where the best cut-off value was obtained when the Youden index was maximum. The area under the ROC curve (AUC) of 70–90% suggested that it was acceptable and had good accuracy. A $p \leq 0.05$ was considered statistically significant. SPSS statistical software, version 25.0 (IBM, Armonk, NY, USA), was used for all statistical analyses.

3. Results

3.1. Baseline data analysis

A total of 423 patients with cerebral infarction were included in the study from July 2019 to March 2022, and 57 patients (13.5%) were diagnosed with massive cerebral infarction by imaging examination.

Differences in gender, age, and risk factors for cerebral infarction such as atrial fibrillation, hypertension, smoking history of diabetes, and drinking history between the MCI group and the NMCI group are not statistically significant (Table 1).

3.2. Plasma concentrations of TM, PIC, TAT, and t-PAIC in different groups

The plasma concentrations of PIC, TAT, and t-PAIC in the MCI group were higher than those in the NMCI group, and the difference between the two groups was statistically significant ($Z = -7.978$, $P < 0.001$; $Z = -6.621$, $P < 0.001$; $Z = -2.709$, $P = 0.007$). There was no significant difference in TM plasma concentrations between the two groups ($Z = -0.119$, $P = 0.905$) (Figure 1).

3.3. Logistic regression analysis of risk factors for massive cerebral infarction

Differences in PIC, TAT, and t-PAIC between the two groups were statistically significant. A multivariable logistic regression analysis showed that the high concentration of TAT plasma was statistically significant and associated with the occurrence of MCI independently (Table 2). When the concentration of plasma TAT in patients with cerebral infarction increased by 1 ng/ml, the probability of MCI increased by 1.138 times (95% CI:1.065, 1.215; $P < 0.001$).

3.4. Diagnostic value of plasma PIC, TAT, and t-PAIC concentrations in massive cerebral infarction

All three novel thrombus markers showed good accuracy (>80%) for the diagnosis of MCI by the Hosmer-Lemeshow goodness-of-fit test analysis (Table 3). By a ROC curve analysis (Figure 2), both PIC and TAT showed good diagnostic performance for MCI (AUC ≥ 70%). PIC showed the best diagnostic performance (AUC = 82.8%) when the plasma concentration of PIC was ≥0.80 μg/ml, the maximum Youden index of 0.569 was obtained, the sensitivity and specificity reached 80.7 and 76.2%, respectively, and the sensitivity was the best among the three markers. The highest specificity of TAT

TABLE 1 Comparison of baseline data between the MCI group and the NMCI group.

Characters		NMCI ($n = 366$)	MCI ($n = 57$)	$\chi 2/Z$	*P*-value
Gender	Male	265 (72.4%)	40 (70.2%)	0.122	0.727
	Female	101 (27.6%)	17 (29.8%)		
Age (years)		64.0 (54.0, 72.0)	64.5 (53.0, 72.5)	−0.098	0.922
Risk factors	Hypertension	240 (65.6%)	37 (64.9%)	0.010	0.922
	Diabetes	118 (32.2%)	18 (31.6%)	0.010	0.921
	Atrial fibrillation	32 (8.7%)	9 (15.8%)	2.798	0.094
	Smoking	225 (61.5%)	32 (56.1%)	0.589	0.443
	Alcohol	155(42.3%)	31 (54.4%)	2.900	0.089

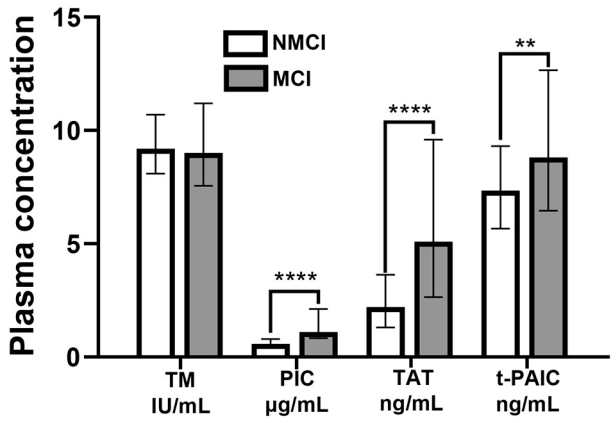

FIGURE 1
Plasma concentrations of TM, PIC, TAT, and t-PAIC in the MCI group and the NMCI group. $^{**}P < 0.01$, $^{****}P < 0.0001$.

TABLE 2 Logistic regression analysis of risk factors for MCI.

Variable	OR (95%CI)	*P*-value
PIC	1.037 (0.986–1.091)	0.162
TAT	1.138 (1.065–1.215)	<0.001
t-PAIC	1.034 (0.969–1.103)	0.307

for the diagnosis of MCI was obtained when the TAT concentration in plasma was ≥3.97 ng/ml, with a maximum Youden index of 0.455, a specificity of up to 80.6%, and a poor sensitivity of 64.9%.

4. Discussion

In this study, we examined the plasma concentrations of novel thrombotic markers in 423 patients with cerebral infarction immediately after admission within 24 h after onset, investigated the correlation between four novel thrombotic markers (TM, PIC, TAT, and t-PAIC) and the occurrence of MCI, and assessed their diagnostic performance for the occurrence of MCI. We found that compared with patients with NMCI, patients with MCI had increased plasma PIC, TAT, and t-PAIC concentrations, which could assist in the identification of MCI in the early stage of cerebral infarction and provide a reference for prehospital identification of macrovascular occlusion.

PIC is the main enzyme that dissolves fibrin *in vivo*, plasmin. In the absence of fibrin, it combines with its representative inhibitor, α2-antiplasmin (α2-PI), 1:1 to form a stable complex (18), which has a half-life of ∼6 h (19) and is easier to measure than plasmin with a half-life of only a few seconds; and its plasma concentration is not affected by antiplatelet and anticoagulant drugs, nor does it affect the production of plasmin, so it can represent the degree of plasmin activation more accurately (20). In this study, we found that the plasma PIC concentration in patients with MCI was higher than that in patients with NMCI ($P < 0.001$), suggesting that the degree of activation of the fibrinolytic system is related to the infarct size, and the fibrinolytic system is more hyperactive in patients with MCI, which is one of the reasons why patients with MCI are more likely to have hemorrhagic transformation. This result is similar to the findings of Sato et al. further confirming that the plasma PIC concentration can reflect the severity of cerebral infarction (21). In addition, a ROC curve analysis revealed that PIC had a high diagnostic value for the occurrence of massive infarction, with an AUC of 82.8% (95% CI: 76.8, 88.9%), and when the plasma concentration of PIC was ≥0.80 μg/ml, the sensitivity and specificity reached 80.7 and 76.2%, respectively. We did not find that high plasma PIC concentration was an independent risk factor for the occurrence of MCI using a multivariable logistic regression analysis, which may be related to the fact that the concentration of PIC in plasma is affected by other cerebrovascular disease risk factors such as atrial fibrillation and atherosclerosis (21, 22).

TAT is produced during the formation of fibrin polymers and is a complex formed by the combination of thrombin and antithrombin in the body. The increase in TAT indicates that thrombin is being generated while antithrombin is continuously consumed. Elevated TAT concentrations have been found in diseases affecting the coagulation system, such as venous thrombosis, malignant tumors, and disseminated intravascular coagulation (DIC), suggesting that the body is in a hypercoagulable state (23–25). Moreover, TAT is upstream of traditional coagulation test items such as D-dimer and FDA and has been confirmed to be more sensitive in reflecting the body's coagulation activation (7). By comparing the plasma TAT concentration between the two groups, we found that the plasma TAT concentration was significantly higher in patients with MCI, and TAT was found to be one of the independent risk factors for the occurrence of massive cerebral infarction by a logistic multivariate regression analysis. Excessive activation of the coagulation system may be one of the mechanisms for the occurrence and development of massive cerebral infarction, or the body may change after the occurrence of massive cerebral infarction. Large-sample prospective studies are needed to explore their causal relationship. The diagnostic performance of TAT for MCI was analyzed by further ROC curve analysis, and it was found that TAT could diagnose the occurrence of MCI and reflect the occurrence of MCI and NMCI accurately, reflecting the possibility of macrovascular occlusion (AUC = 87.0%, 95% CI: 64.9, 80.6%). At the same time, the high concentration of plasma TAT in patients with MCI suggests that the occurrence and development of massive cerebral infarction are accompanied by excessive activation of thrombin, and the increase of TAT suggests the necessity of initiating anticoagulation after the occurrence of MCI. However, patients with MCI are often accompanied by hyperfibrinolysis in the early stages, and the anticoagulation regimen and the time to initiate anticoagulant therapy require further study.

t-PAIC is a complex formed by the combination of tissue-type plasminogen activator (t-PA) and physiological inhibitory factor plasminogen activator inhibitor-1 (PAI-1). t-PA is a key factor in the exogenous activation pathway of the fibrinolytic system *in vivo*, while PAI-1 can specifically bind t-PA to form t-PAIC to interfere with the activation of plasmin. The increased plasma t-PAIC concentration reflects the impairment of the activation pathway in patients (26). In addition, Winter et al. found that damage to endothelial cells also causes increased t-PAIC concentrations in plasma (11). In previous studies, elevated t-PAIC plasma concentrations were observed in patients with both stroke (27) and myocardial infarction (28), and there was a correlation with PAI-1, reflecting impairment of the

TABLE 3 Performance analysis of three markers for diagnosing MCI.

Classifier	Calibration	Discrimination	95% CI	Cut-off value	Sensitivity	Specificity
PIC	86.5%	82.8%	76.8–88.9%	0.80 ng/mL	80.7%	76.2%
TAT	87.0%	77.2%	70.4–84.0%	3.97 ng/ml	64.9%	80.6%
t-PAIC	86.1%	61.1%	52.4–69.9%	9.85 ng/m	43.9%	80.1%

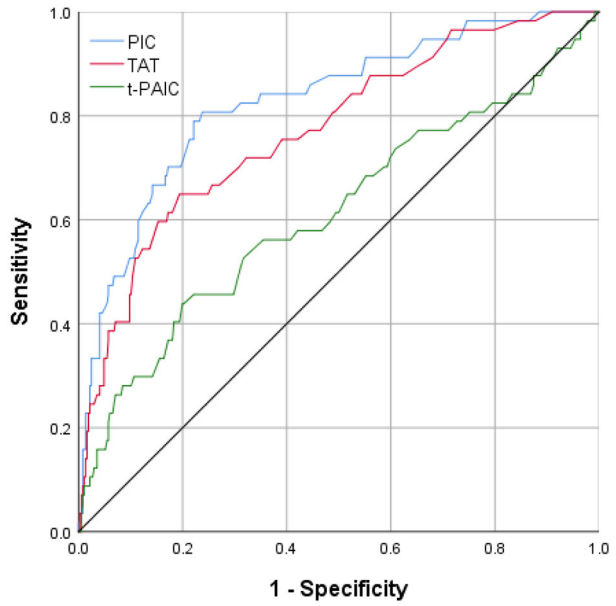

FIGURE 2
The area under ROC curve of the levels of plasma PIC, TAT, and t-PAIC in patients with AIS prediction of MCI.

fibrinolytic activation pathway, which can be used to predict the occurrence of both diseases. However, the relationship between t-PAIC and cerebral infarction size is not clear. In our study, it was found that the plasma t-PAIC concentration in patients with MCI suggested that when MCI occurred in patients, there was not only excessive activation of the coagulation system and increased plasmin production, but also damage to the exogenous activation pathway of the fibrinolytic system, suggesting the necessity of initiating anticoagulant therapy in patients with MCI. In addition, the increase in plasma t-PAIC concentration also reflected that the vascular endothelial cell injury was more severe in patients with MCI, which could cause damage to the integrity of the blood–brain barrier, leading to adverse consequences such as malignant cerebral edema or cerebral hemorrhage.

TM is a transmembrane glycoprotein expressed in vascular endothelial cells and can be released into the blood circulation when the cell membrane is damaged by proteolytic enzymes. Increased concentration of plasma TM has been found to have some correlation with vascular endothelial injury in a variety of diseases with endothelial injury, and increased plasma-free TM is considered to be one of the specific indicators of endothelial cell injury (29). However, there is no consensus in the academic community on the correlation between plasma TM concentration and cerebral infarction, and some studies have shown that plasma TM concentration is increased in stroke patients compared with healthy individuals (30, 31); others have shown that the effect of plasma TM concentration on stroke patients is related to the history of stroke in stroke patients, and for those with a history of stroke, patients with higher plasma TM have a better prognosis after another stroke (32); however, so far there is no literature about the performance of TM in massive cerebral infarction. Through this study, we found that the mean concentration of TM plasma concentration was higher in patients with NMCI and fluctuated more in patients with MCI, but there was no significant statistical difference between the NMCI and MCI groups ($P = 0.905$), which may be affected due to the presence of different stroke subtypes. Cardioembolic stroke patients accounted for a greater proportion of patients with MCI, while patients with NMCI were mostly of the large artery atherosclerotic type. Previous studies have confirmed that plasma TM concentrations were higher in patients with acute stroke accompanied by large artery atherosclerosis (33), while the increase in plasma TM was not significant in patients with cardioembolic stroke (34).

5. Conclusion

The detection of PIC, TAT, t-PAIC, and TM can be used to comprehensively evaluate the vascular endothelial damage and the activation degree of the coagulation and fibrinolysis system. Meanwhile, it is easy to obtain the detection results, so these markers have diagnostic value in identifying patients with MCI and can be used as plasma markers for early detection of macrovascular occlusion. Their wide application will greatly improve the treatment efficiency of patients with macrovascular occlusion. For patients with plasma PIC $\geq$0.80 μg/ml, TAT $\geq$3.97 ng/ml or t-PAIC $\geq$ 9.85 ng/ml, we need to be alert to the possibility of MCI and transport them to advanced stroke centers that can perform thrombolysis or embolectomy as soon as possible, so as to save patients' lives and improve their prognosis.

Data availability statement

The raw data supporting the conclusions of this article will be made available by the authors, without undue reservation.

Ethics statement

The studies involving human participants were reviewed and approved by Human Ethics Review Committee of

Shanxi Provincial People's Hospital. Written informed consent for participation was not required for this study in accordance with the national legislation and the institutional requirements.

Author contributions

XZ: conceptualization, project administration, methodology, and writing–review and editing. SY: investigation, data curation, formal analysis, and writing–original draft. RL: writing–original draft. QD and JL: investigation and supervision. JM: investigation and data curation. LS: investigation. All authors contributed to the article and approved the submitted version.

Conflict of interest

The authors declare that the research was conducted in the absence of any commercial or financial relationships that could be construed as a potential conflict of interest.

Publisher's note

All claims expressed in this article are solely those of the authors and do not necessarily represent those of their affiliated organizations, or those of the publisher, the editors and the reviewers. Any product that may be evaluated in this article, or claim that may be made by its manufacturer, is not guaranteed or endorsed by the publisher.

References

1. Du X, Liu Q, Li Q, Yang Z, Liao J, Gong H, et al. Prognostic value of cerebral infarction coefficient in patients with massive cerebral infarction. *Clin Neurol Neurosurg.* (2020) 196:106009. doi: 10.1016/j.clineuro.2020.106009

2. Yuan Q, Yu L, Wang F. Efficacy of using thromboelastography to detect coagulation function and platelet function in patients with acute cerebral infarction. *Acta Neurol Belg.* (2021) 121:1661–7. doi: 10.1007/s13760-020-01456-6

3. Loghmani H, Conway EM. Exploring traditional and nontraditional roles for thrombomodulin. *Blood.* (2018) 132:148–58. doi: 10.1182/blood-2017-12-768994

4. Khattab AA, Dawood A, Saleh NY. Value of thrombomodulin as a marker for sepsis in critically ill children. *Indian J Pediatr.* (2021) 88:864–71. doi: 10.1007/s12098-020-03564-w

5. Pletsch-Borba L, Watzinger C, Turzanski Fortner R, Katzke V, Schwingshackl L, Sowah SA, et al. Biomarkers of vascular injury and type 2 diabetes: a prospective study, systematic review and meta-analysis. *J Clin Med.* (2019) 8:2075. doi: 10.3390/jcm8122075

6. Tao J, Guo X, Li D, Li Y. Increased level of thrombomodulin is associated with endothelial injury in patients with sepsis-induced disseminated intravascular coagulation. *Clin Lab.* (2021) 67. doi: 10.7754/Clin.Lab.2020.201204

7. Liu Y, Ma J, Shi Q, Xin S, Yu H, Liu Z, et al. Quantitatively monitoring acute ischemic stroke patients post recombinant tissue plasminogen activator treatment. *Health Sci Rep.* (2021) 4:e218. doi: 10.1002/hsr2.218

8. Piazza O, Scarpati G, Cotena S, Lonardo M, Tufano R. Thrombin antithrombin complex and IL-18 serum levels in stroke patients. *Neurol Int.* (2010) 2:1–6. doi: 10.4081/ni.2010.e1

9. Gulba DC, Barthels M, Reil GH, Lichtlen PR. Thrombin/antithrombin-III complex level as early predictor of reocclusion after successful thrombolysis. *Lancet.* (1988) 2:97. doi: 10.1016/S0140-6736(88)90021-9

10. Marcucci R, Gori AM, Giannotti F, Baldi M, Verdiani V, Del Pace S, et al. Markers of hypercoagulability and inflammation predict mortality in patients with heart failure. *J Thromb Haemost.* (2006) 4:1017–22. doi: 10.1111/j.1538-7836.2006.01916.x

11. Winter MP, Kleber ME, Koller L, Sulzgruber P, Scharnagl H, Delgado G, et al. Prognostic significance of Tpa/Pai-1 complex in patients with heart failure and preserved ejection fraction. *Thromb Haemost.* (2017) 117:471–8. doi: 10.1160/TH16-08-0600

12. Mei H, Jiang Y, Luo L, Huang R, Su L, Hou M, et al. Evaluation the combined diagnostic value of tat, pic, tpaic, and stm in disseminated intravascular coagulation: a multi-center prospective observational study. *Thromb Res.* (2019) 173:20–6. doi: 10.1016/j.thromres.2018.11.010

13. Mendelson SJ, Prabhakaran S. Diagnosis and management of transient ischemic attack and acute ischemic stroke: a review. *JAMA.* (2021) 325:1088–98. doi: 10.1001/jama.2020.26867

14. Jovin TG, Chamorro A, Cobo E, de Miquel MA, Molina CA, Rovira A, et al. Thrombectomy within 8 hours after symptom onset in ischemic stroke. *N Engl J Med.* (2015) 372:2296–306. doi: 10.1056/NEJMoa1503780

15. Campbell BC, Mitchell PJ, Kleinig TJ, Dewey HM, Churilov L, Yassi N, et al. Endovascular therapy for ischemic stroke with perfusion-imaging selection. *N Engl J Med.* (2015) 372:1009–18. doi: 10.1056/NEJMoa1414792

16. Torbey MT, Bösel J, Rhoney DH, Rincon F, Staykov D, Amar AP, et al. Evidence-based guidelines for the management of large hemispheric infarction: a statement for health care professionals from the neurocritical care society and the German society for neuro-intensive care and emergency medicine. *Neurocrit Care.* (2015) 22:146–64. doi: 10.1007/s12028-014-0085-6

17. Barber PA, Demchuk AM, Zhang J, Buchan AM. Validity and reliability of a quantitative computed tomography score in predicting outcome of hyperacute stroke before thrombolytic therapy. ASPECTS study group alberta stroke programme early CT score. *Lancet.* (2000) 355:1670–4. doi: 10.1016/S0140-6736(00)02237-6

18. Guo X, Tao H, Li D, Li Y. The A2-plasmin inhibitor-plasmin complex is a potential biomarker of venous thromboembolism in orthopedic trauma patients. *Clin Lab.* (2021). doi: 10.7754/Clin.Lab.2020.200856

19. Nielsen VG, Matika RW, Ley ML, Waer AL, Gharagozloo F, Kim S, et al. Tissue-type plasminogen activator-induced fibrinolysis is enhanced in patients with breast, lung, pancreas and colon cancer. *Blood Coagul Fibrinolysis.* (2014) 25:248–53. doi: 10.1097/MBC.0000000000000040

20. Yagi K, Tao Y, Hara K, Kanda E, Hirai S, Takai H, et al. Increased plasma plasmin-alpha2-plasmin inhibitor complex levels correlate with postoperative rebleeding after endoscopic surgery for spontaneous intracerebral hemorrhage. *Acta Neurochir.* (2020) 162:3129–36. doi: 10.1007/s00701-019-04154-2

21. Sato M, Suzuki A, Nagata K, Uchiyama S. Increased von willebrand factor in acute stroke patients with atrial fibrillation. *J Stroke Cerebrovasc Dis.* (2006) 15:1–7. doi: 10.1016/j.jstrokecerebrovasdis.2005.09.005

22. Côté R, Wolfson C, Solymoss S, Mackey A, Leclerc JR, Simard D, et al. Hemostatic markers in patients at risk of cerebral ischemia. *Stroke.* (2000) 31:1856–62. doi: 10.1161/01.STR.31.8.1856

23. Pottier P, Fouassier M, Hardouin JB, Volteau C, Planchon B. D-dimers, thrombin-antithrombin complexes, and risk factors for thromboembolism in hospitalized patient. *Clin Appl Thromb Hemost.* (2009) 15:666–75. doi: 10.1177/1076029608321436

24. Lundbech M, Krag AE, Christensen TD, Hvas AM. Thrombin generation, thrombin-antithrombin complex, and prothrombin fragment F1+2 as biomarkers for hypercoagulability in cancer patients. *Thromb Res.* (2020) 186:80–5. doi: 10.1016/j.thromres.2019.12.018

25. Koyama K, Madoiwa S, Nunomiya S, Koinuma T, Wada M, Sakata A, et al. Combination of thrombin-antithrombin complex, plasminogen activator inhibitor-1, and protein C activity for early identification of severe coagulopathy in initial phase of sepsis: a prospective observational study. *Crit Care.* (2014) 18:R13. doi: 10.1186/cc13190

26. Zunker P, Schick A, Padro T, Kienast J, Phillips A, Ringelstein EB. Tissue plasminogen activator and plasminogen activator inhibitor in patients with acute ischemic stroke: relation to stroke etiology. *Neurol Res.* (1999) 21:727–32. doi: 10.1080/01616412.1999.11741005

27. Johansson L, Jansson JH, Boman K, Nilsson TK, Stegmayr B, Hallmans G. Tissue plasminogen activator, plasminogen activator inhibitor-1, and tissue plasminogen activator/plasminogen activator inhibitor-1 complex as risk factors for the development of a first stroke. *Stroke.* (2000) 31:26–32. doi: 10.1161/01.STR.31.1.26

28. Nordenhem A, Leander K, Hallqvist J, de Faire U, Sten-Linder M, Wiman B. The complex between Tpa and Pai-1: risk factor for myocardial infarction as studied in the sheep project. *Thromb Res.* (2005) 116:223–32. doi: 10.1016/j.thromres.2004.12.007

29. Maruyama I, Bell CE, Majerus PW. Thrombomodulin is found on endothelium of arteries, veins, capillaries, and lymphatics, and on syncytiotrophoblast of human placenta. *J Cell Biol.* (1985) 101:363–71. doi: 10.1083/jcb.101.2.363

30. Zhang X, Hu Y, Hong M, Guo T, Wei W, Song S. Plasma thrombomodulin, fibrinogen, and activity of tissue factor as risk factors for acute cerebral infarction. *Am J Clin Pathol.* (2007) 128:287–92. doi: 10.1309/HB6AB1YR4DQUT5AU

31. Pletsch-Borba L, Grafetstatter M, Husing A, Johnson T, Gonzalez Maldonado S, Gross ML, et al. Vascular injury biomarkers and stroke risk: a population-based study. *Neurology.* (2020) 94:e2337–e45. doi: 10.1212/WNL.0000000000009391

32. Olivot JM, Labreuche J, Aiach M, Amarenco P, Investigators G. Soluble thrombomodulin and brain infarction: case-control and prospective study. *Stroke.* (2004) 35:1946–51. doi: 10.1161/01.STR.0000133340.37712.9b

33. Kamtchum-Tatuene J, Mwangalika Kachingwe G, Mwandumba HC, Solomon T, Benjamin LA. Endothelial dysfunction and carotid atherosclerosis in Malawian adults: a cross-sectional study. *eNeurologicalSci.* (2020) 20:100252. doi: 10.1016/j.ensci.2020.100252

34. Nomura E, Kohriyama T, Kozuka K, Kajikawa H, Nakamura S, Matsumoto M. Significance of serum soluble thrombomodulin level in acute cerebral infarction. *Eur J Neurol.* (2004) 11:329–34. doi: 10.1111/j.1468-1331.2004.00776.x

Frontiers in Neurology

Explores neurological illness to improve patient care

The third most-cited clinical neurology journal explores the diagnosis, causes, treatment, and public health aspects of neurological illnesses. Its ultimate aim is to inform improvements in patient care.

Discover the latest Research Topics

See more →

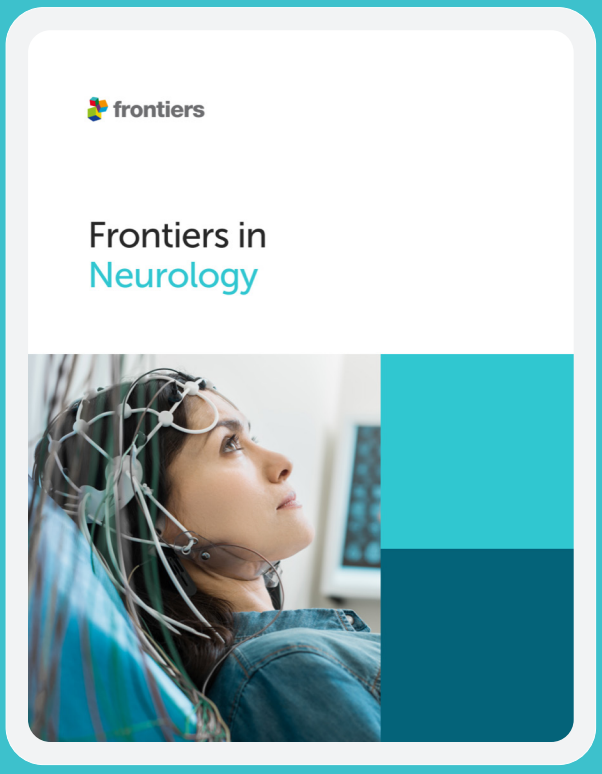

Frontiers

Avenue du Tribunal-Fédéral 34
1005 Lausanne, Switzerland
frontiersin.org

Contact us

+41 (0)21 510 17 00
frontiersin.org/about/contact